



## UNIVERSITY OF CALCUTTA

### Notification No. CSR/ 68 /18

It is notified for information of all concerned that the Syndicate in its meeting held on 13.07.2018 (vide Item No.11) approved the Syllabus of Two-Year (Four-Semester) M.Sc. Course of Study in Chemistry under CBCS in the Post-Graduate Departments of the University and in the affiliated Colleges offering Post-Graduate Courses under this University, as laid down in the accompanying pamphlet.

The above shall be effective from the academic session 2018-2019.

SENATE HOUSE  
KOLKATA-700073  
The 17<sup>th</sup> August, 2018

  
(Debabrata Manna)

Deputy Registrar (Acting)

# **SYLLABUS**

FOR

TWO-YEAR FOUR-SEMESTER COURSE IN

## **CHEMISTRY**

2018

# **UNIVERSITY OF CALCUTTA**

# DEPARTMENT OF CHEMISTRY

## UNIVERSITY OF CALCUTTA

### TWO YEAR FOUR-SEMESTER M.Sc. COURSE IN CHEMISTRY

#### COURSE STRUCTURE

DURATION	SEMESTER				TOTAL MARKS
	I JULY-DEC	II JAN-JULY	III JULY-DEC	IV JAN-JUNE	
MARKS	250	250	250	250	1000
COURSE TYPE	THEO PRACT	THEO PRACT	THEO PRACT	THEO PRACT	
GENERAL (G)	150 100	150 100	50		650
CREDIT POINTS	(12) (8)	(12) (8)	(4)		(52)
CBCS			100		
CREDIT POINTS			(8)		

<b>SPECIAL (S)</b>			<b>100</b>	<b>150 100</b>	<b>350</b>
<b>CREDIT POINTS</b>			<b>(8)</b>	<b>(12) (8)</b>	<b>(28)</b>
<b>Total Marks</b>	<b>150 100</b>	<b>150 100</b>	<b>150 100</b>	<b>150 100</b>	<b>1000 (80)</b>

Total credit points: **80**

Special Courses (S) in Four Branches of Chemistry are

- (i) Analytical Special (SA)
- (ii) Inorganic Special (SI)
- (iii) Organic Special (SO)
- (iv) Physical Special (SP)

**SEMESTER – I (Marks – 250)**

Course ID	Marks/Credit			
	Theo	Credit	Pract	Credit
<b>CHEM – G11</b>	50	4	-	-
<b>CHEM – G12</b>	50	4	-	-
<b>CHEM – G13</b>	50	4	-	-
<b>CHEM – G14</b>	-	-	100	8
<b>Total</b>	150	12	100	8

**SEMESTER –II (Marks – 250)**

Course ID	Marks/Credit			
	Theo	Credit	Practical	Credit
<b>CHEM – G21</b>	50	4	-	-
<b>CHEM – G22</b>	50	4	-	-
<b>CHEM – G23</b>	50	4	-	-
<b>CHEM – G24</b>	-	-	100	8
<b>Total</b>	150	12	100	8

**SEMESTER –III (Marks – 250)**

Course ID	Marks/Credit			
	Theo	Credit	Practical	Credit
<b>CHEM – G31</b>	50	4	-	-
<b>CBCC-A</b>	50	4	-	-

CBCC-B	50	4	-	-
CHEM–SA31/SI31/SO31/SP31	-	-	100	8
<b>Total</b>	150	12	100	8

#### SEMESTER –IV (Marks – 250)

Course ID	Marks/Credit			
	Theo	Credit	Practical	Credit
**CHEM – SA41/SI41/SO41/SP41	50	4	-	-
**CHEM – SA42/SI42/SO42/SP42	50	4	-	-
**CHEM – SA43/SI43/SO43/SP43	50	4	-	-
*CHEM – SA44/SI44/SO44/SP44	-	-	100	8
<b>Total</b>	150	12	100	8

\* Review and project work

\*\* One special course to be opted and continued systematically

## Course Structure and marks distribution

### 1. Theoretical papers

Full marks: 50, each paper

Each unit 10 marks, two questions per unit to be set and any one to be answered

### 2. Practical Papers

Full Marks: 100, each paper

Course ID	Experiment	General Laboratory performance	*Seminar
CHEM-G14	45	45	10
CHEM-G24	45	45	10
CHEM – SA31/SI31/SO31/SP31	50	50	-

- Topic should be outside the UG curriculum of CU; use of overhead/LCD projector is mandatory ; time 10m, followed by discussion

Course ID	*Continuous assessment	Review	Project	Grand Viva
CHEM – SA44/SI44/SO441/SP44	10	25	40	25

\*Continuous assessment to be assessed by the guide

Review (maximum 3000 words excluding references and figures) and Project to be assessed by External Expert

Grand Viva to be taken by Sectional Faculty members and assessed by them

## SYLLABUS



**INDUSTRIAL DELIGNIFICATION PROCESS AND**  
**ROLE OF SUPPORTED POLYOXOMETALATES**  
**IN THE PROCESS**

SCOTTISH CHURCH COLLEGE  
UNIVERSITY OF CALCUTTA

C.U Roll No.: 223/CEM/191020

C.U REGISTRATION No.: 014-1221-0403-16

SPECIAL PAPER: SI 44

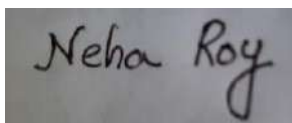
NAME OF CANDIDATE

NAME OF SUPERVISOR/EXAMINER

**NEHA ROY**

SIGNATURE OF CANDIDATE

SGNATURE OF SUPERVISOR/EXAMINER



.....

.....

## **Self Declaration**

This is to certify that, I, Neha Roy, Roll No. 223/CEM/191020, Registration No. 014-1221-0403-16, a student of MSc. in the department of Chemistry, Scottish Church College, (2019-2021) has worked on the project titled “ **INDUSTRIAL DELIGNIFICATION METHODS AND ROLE OF POLYOXOMETALATES IN THE DELIGNIFICATION PROCESS**” for the partial fulfilment of requirements of matter of science in Chemistry under the University Of Calcutta , Scottish Church College, under my supervision .To the best of my knowledge, this work has not been submitted to any other university for the award of any other degree.

## Table of Contents-

1. Introduction
2. Importance of delignification in the Industry
3. Different Methods of Delignification
  - Kraft Method
  - Oxygen Delignification
4. Merits and demerits of the methods
  - Merits and Demerits of the Kraft method
  - Merits and Demerits of the Oxygen delignification method
5. Alternative methods to counter the demerits
6. Polyoxometalates in bleaching
  - Polyoxometalate bleaching in anaerobic condition
  - Polyoxometalate bleaching in aerobic condition
7. Conclusion
8. References

## **1.Introduction**

Lignin is an integral cell wall constituent in cell vascular plants. Lignin provides rigidity, water impermeability and resistance against microbial attack. Lignin is an aromatic polymer consisting of guaiacyl (G), syringyl- (S) ,and p- hydroxyphenyl –(H) Phenyl propanoid units, whose proportion differ with botanical origin of the lignin.

The phenylpropanoid units are attached to each other by a series of C-O-C and C-C bonds such as beta-O-4 , beta-5 , alpha-O-4, beta-beta and 5-5. The polymer is branched and cross linking occurs.

The lignin in the cell wall is intimately mixed with the polysaccharides, and there are indications of the occurrence of linkages between lignin and carbohydrates. Among the proposed chemical linkages, the benzyl ether and ester types, whose formation is associated with quinone methide re aromatization reactions during lignin bio synthesis, have been considered the most probable.

## **2.Importance of delignification in the industry-**

Delignification causes disruption of lignin structure, resulting in biomass swelling, increase in internal surface area, and accessibility of enzymes to cellulose fibres.

Lignocellulosic biomass utilization as a source of clean energy and chemicals has attracted attention in recent years in the context of the fossil fuel energy drive. Lignocellulosic biomass consists of cellulose, hemi cellulose and lignin fractions, which quantitatively and qualitatively vary according to the plant material. Unlike cellulose and hemi cellulose, lignin is a cross linked hydrophobic polymerization is insoluble in most solvents and fairly resistant to anaerobic degradation. Hence, a pretreatment of Lignocellulosic materials to dissolve the lignin structure (delignification) and cleave the chains seems to be necessary before enzymatic and chemical thermal process to avail important chemicals from biomass. Delignification of the lignocellulosic biomass has been investigated in many studies, recently in the production of kraft pulps , lactic acid, bio ethanol. Recently molecular oxygen delignification in alkaline media had been widely reported as a potential technique for lignin degradation.

## **3. Different methods of delignification**

There are several delignification process and oxygen delignification in general use, with the kraft process and oxygen delignification being the most common.

The kraft process is a high temperature and pressure digestion system that breaks down the lignin in wood pulp chemically.

Oxygen based lignin removal process utilize oxygen activation to remove the lignin and are often used as supplementary steps at the brown stock washing stage of the kraft process.

### **Kraft Process –**

The Kraft process has been the most common form of chemical pulping throughout the years. It involves the digestion of wood chips at elevated temperature (423-453K) and pressure in white liquor. The white liquor is a water solution of sodium hydroxide with sulfides.

This process is done for nearly 2 hours to separate the lignin from cellulose under high pH condition. The higher pH leads to ionization of the phenolic hydroxide groups of the lignin, which in result solubilizes the lignin content of lignocellulosic biomass. After separation of

cellulose from lignocellulosic biomass, lignin is recovered from the final combined liquid, which is referred to as black liquor. Thus a concentrated and lignin rich solid is obtained although the lignin obtained from this process emits poisonous gas.

The lignin can also be recovered from the black liquor by lowering the pH of the solution with carbon di oxide. In this process the lignin is precipitated on the surface. The precipitated lignin can be recovered by simple filtration and washing. Although, the lignin obtained in process is free from Sulphur and sugar, this hypothesis is under examination for use.

### **Oxygen delignification-**

Oxygen delignification is nowadays one the most used process in pulp industry for ECF (Elemental Chlorine Free) and TCF (Total Chlorine Free) bleached pulp production.

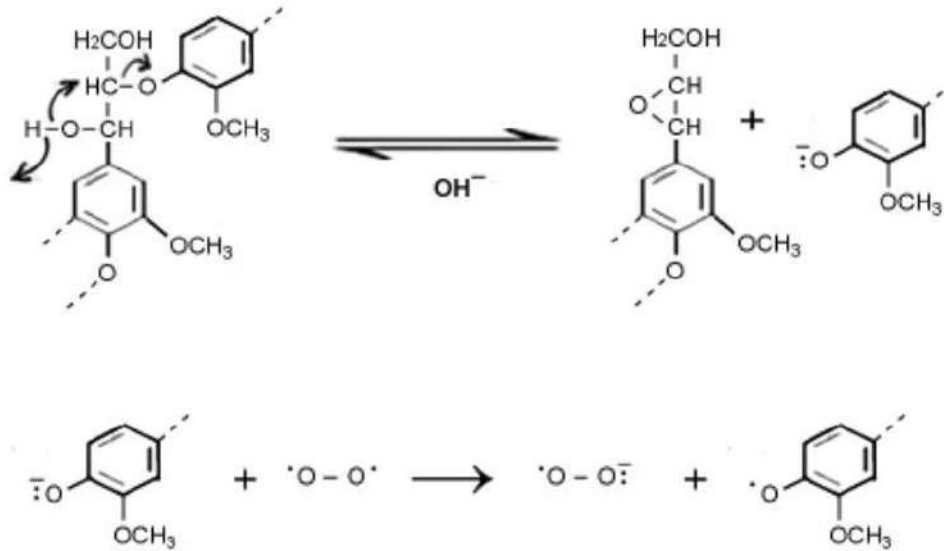
This process is done in elevated temperature, in the range of 80° – 120° and in pressure from 6- 8 bars to increase the rate. But above 120° a degradation of polysaccharides can occur. Amount of NaOH and pH is very significant in oxygen delignification. The pH value should be higher than 10 and better effectiveness it should be 12.

At lowest energy state Oxygen molecule contains two unpaired electrons has an affinity to opposite spin of other electrons. Therefore it can act as Free radical. At higher temperature and strong alkaline condition it can act with organic compounds.

At initiated state the phenolic group of lignin reacts with the alkali and forms a phenolate ion. The phenolate ion then reacts with oxygen, forming a resonance stabilized phenoxy radical and a superoxide anion.

The phenoxy radical undergo reaction with themselves or with oxygen species radical, such as hydroxyl (HO•), hydroperoxy (HOO•) and superoxide (O<sup>2•-</sup>) and produce different organic acids, carbon di oxide, and other lower mass organic compounds through side chain elimination, ring opening and de methoxylation reactions.

The reaction can is shown as below-



#### 4. Merits and demerits of the methods

##### Merits of Kraft methods-

The Kraft process is the most popular method for producing wood pulp in the US due to advantages over soda and sulfite pulping, any wood species can be used. Additionally cooking times are reduced and waste recovery is more efficient. Kraft process tends to be stronger than other types of pulps, but actual strength varies by species. When stained with Graff "C" stain, Kraft pulp can appear in a range of colors on the wood type and the amount of bleaching. Unbleached Kraft pulps will appear Yellow or blue/Grey. With increased bleaching, pulps will appear lighter and tend more towards red when treated with stain. The stained color of kraft pulp tends to be darker than sulfite pulp.

##### Demerits of Kraft method-

One of the major disadvantages of Kraft process is that the Kraft lignin is highly contaminated with carbohydrates coming from hemicellulose as well as some fatty acids. Also, substantial amount of Sulphur is usually covalently bound to Kraft lignin in the form of thiols.

##### Merits of Oxygen delignification-

a. Environment friendly, which helps to reduce the uses of chlorinated chemicals in next steps. The other environmental benefits are lower BOD, COD and fewer colours in effluent, as the effluent from the Oxygen bleaching is recycled back to the recovery boiler.

b. The process is cost effective, as it significantly reduce the consumption of bleaching chemicals, such as Chlorine gas, Chlorine di oxide, Ozone, Hydrogen peroxide in the next stages. Overall Oxygen production is minimal.

All the effluent containing spent chemicals and reaction products is recycled back in this process. Without this, all the effluent would go to waste water treatment plant due to presence of corrosive chlorinated compounds. So it reduces the chemical consumption cost.

### Demerits of Oxygen delignification-

Oxygen bleaching process is less selective compared to other bleaching agents, as the process undergoes with the free radical reaction system. This can lead to significant degradation of polysaccharides .

Another disadvantage is that it is weak reactive oxidant. So, it required alkaline conditions, high temperature and pressure to obtain a reasonable reaction state. Raising the alkali charge also creates negative effect. Moreover, primary high installation cost of Oxygen delignification is another drawback.

### 5. Alternative methods to counter the de merits

In counter to the demerits mentioned above, alternative methods can be used. Currently, delignification supported by polyoxometalates is catching the attention in the industry. Polyoxometalates , also called as POMs, favorably embraced the advantages of both chemical (active at elevated temperature) and biological (highly selective) lignin oxidizing agents. Also, these reagents are chlorine free and can be used under conditions wherein they oxidize lignin and chromophores in wood pulp fibres while leaving the cellulose undamaged. They can be reactivated with oxygen under conditions that result in oxidation of the organic by products of the delignification process. Thus, they can be recycled in a closed system, that promises to provide the basis for a new class of closed milled technologies in which, the consumable oxidant is oxygen and primary by products are Carbon di Oxide and water.

The POMs used as delignification agents are transition metal substituted cluster ions similar in structure to many mineral ores. They are entirely chlorine free and can be used under conditions that make them very selective in their action on pulp fibre constituents. When used in active states, they can oxidize lignin and related chromophores while leaving the polysaccharides undamaged.

### *6. Polyoxometalates in bleaching*

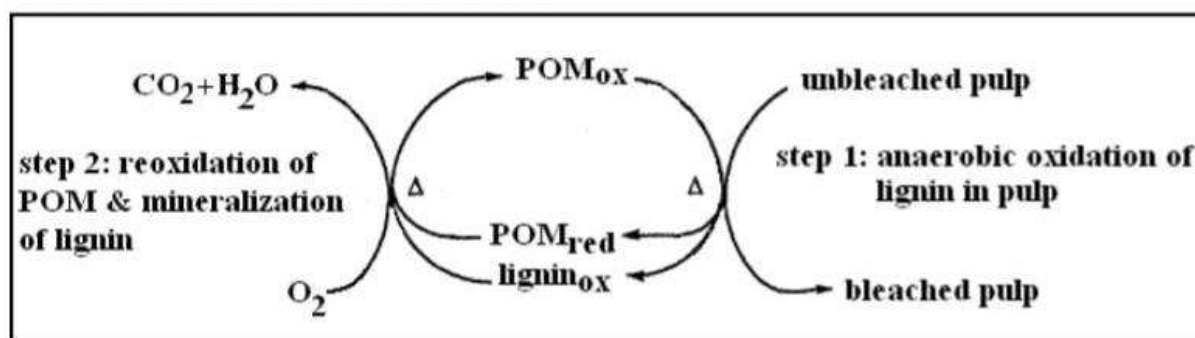
Among a large no. Of variation, the keggin type Polyoxometalates have been recognized as the most suitable POMs for use in oxidative delignification. The advantages of keggin type Polyoxometalates include a range of redox potentials, solubility and molecular charges which can be adjusted during synthesis and relatively easy regeneration by Oxygen, Hydrogen peroxide or Ozone.

Keggin type hetero poly oxy anions are described by the general formula  $X M'_a M''_{12-a} O_b^{m-}$  where  $X^{n+}$  is a d or p-block hetero atom ( $Al^{3+}$ ,  $Si^{4+}$ ,  $P^{5+}$ ) and  $M'$  and  $M''$  are  $d^n$  and  $d^0$  metal centers respectively.

The concept of delignification with POMs as robust inorganic systems which provide controlled environments with transition metal ions, has been developed to mimic the action of fragile lignin peroxidases containing iron proto porphyrin IX, in selective oxidation of lignin. POMs are reduced while lignin is oxidized. POMs may be re oxidized by Oxygen, Hydrogen peroxide or Ozone.

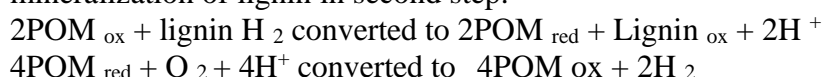
POMs with the redox potential in the range of +0.7 to +0.8 V vs NHE have been used for delignification. Delignification by POMs can be carried out in anaerobic condition and in aerobic condition.

### *Delignification by PMOs in Anaerobic condition-*



This is 2 step process. In the first step, performed under anaerobic conditions at elevated temperature (100-140°C), lignin is oxidized and dissolved in an aqueous solution of POMs, which are simultaneously reduced. After being treated with POMs, the pulp is separated from the spent POM liquor and washed. Polyoxometalates are readily washed from the pulp with high efficiency of 99.9%. The reduced POMs are regenerated, using oxygen, for the next bleaching process. Under the aggressive conditions of this step, POMs initiate and catalyse the wet air oxidation of dissolved lignin degradation compounds and other potentially present organic compounds, which are converted to  $CO_2$  and  $H_2O$ . During the development of POM bleaching technique, a number of anions have been used,  $[PV_2MO_{10}O_{40}]^{5-}$ . Further progress has been made by using  $[SiVW_{11}O_{40}]$  which is stable at neutral pH levels.

An important aspect of this POM delignification is that the protons released during lignin oxidation in the first step are consumed by Oxygen during the re oxidation of POMs and mineralization of lignin in second step.



The 2 step delignification process have a lot of advantages. These include an acceptable selectivity of POM delignification performed in a radical free condition which can be improved by conducting the process in less acidic conditions and an effective regeneration of POMs, which provides the basis of an effluent free technology.



But also, to apply the two step POM based delignification on a commercial scale, an improvement of the process related to the efficiency of lignin oxidation with POMs is required.

POMs such as  $[\text{PMo}_{10}\text{V}_2\text{O}_{40}]^{5-}$  ( $\text{PMo}_{10}\text{V}_2$ ),  $[\text{PW}_{11}\text{VO}_{40}]^{4-}$  ( $\text{PW}_{11}\text{V}$ ),  $[\text{SiW}_{11}\text{VO}_{40}]^{5-}$ ,  $[\text{BW}_{11}\text{VO}_{40}]^{6-}$  and  $[\text{SiW}_{11}\text{Mn}(\text{H}_2\text{O})\text{O}_{39}]^{5-}$  ( $\text{SiW}_{11}\text{Mn}$ ) (all a isomers) have been used for delignification processes of pine kraft pulp under anaerobic conditions. All studied POMs were able to delignify the pulp the best results being obtained with  $\text{SiW}_{11}\text{V}$  and  $\text{SiW}_{11}\text{Mn}$ . Considerable cellulose degradation occurred with  $[\text{PW}_{11}\text{VO}_{40}]^{4-}$ , due to the lower pH used (on account of the stability of this POM at pH , 2) which promoted cellulose acid hydrolysis. The delignification effectiveness of different POMs is related to their redox potentials. POMs with lower redox potentials ( $\text{PMo}_{10}\text{V}_2$  and  $\text{BW}_{11}\text{V}$ ) presented a lower degree of delignification whereas those of  $\text{SiW}_{11}\text{V}$  and  $\text{SiW}_{11}\text{Mn}$ , with a higher redox potential, were the most effective for the delignification of pulps. Polyoxometalate re-oxidation was demonstrated for  $\text{PMo}_{10}\text{V}_2$  at  $150^\circ\text{C}$ , since its reduced form was rapidly re-oxidised by oxygen, despite its low effectiveness for anaerobic delignification.

In contrast, for the  $\text{SiW}_{11}\text{V}$  and  $\text{SiW}_{11}\text{Mn}$  anions the re-oxidation of the reduced anions by oxygen was slow, even at conditions of elevated temperature and oxygen pressure, limiting the useful application of this system.

A second generation of POMs emerged as suitable for both delignification and wet oxidation, which are also stable above pH 7 so that hydrolysis of the cellulose can be significantly reduced. These include  $[\text{SiW}_{10}\text{V}_2\text{O}_{40}]^{6-}$  ( $\text{SiW}_{10}\text{V}_2$ ),  $[\text{AlW}_{11}\text{VO}_{40}]^{6-}$  ( $\text{AlW}_{11}\text{V}$ ), and ‘ $\text{SiW}_{10.1}\text{Mo}_{1.0}\text{V}_{0.9}\text{O}_{40}$ ’.

Another important advance associated with this new generation of POMs was the development of a new synthetic procedure (using hydrothermal methods) that results in an equilibrium composition which is inherently stable and, therefore, can be recycled repeatedly in a closed system.

The reactivity of phenolic and non-phenolic lignin structural units has been studied using monomeric and dimeric lignin model compounds (LMCs). A possible reaction pathway for a cleavage of the phenolic lignin model compounds has been proposed; this pathway would include two one-electron oxidation steps producing cyclohexadienyl cations from the initially formed phenoxy radicals.

In contrast to phenolic LMCs, the etherified LMCs follow a different mechanism and the

experiments on non-phenolic lignin subunits have revealed that the reaction may proceed via

successive oxidation of the benzylic carbon atom. Model studies, however, do not reflect all the reactions that lignin might undergo as a macromolecule in the pulp

matrix. Oxidation of pine milled wood lignin (MWL) with POMs has also been explored.

The MWL was insoluble under the conditions studied, and oxidative reactions were found to be taking place primarily at the surface of the suspended lignin macromolecules, providing incomplete information on the lignin reactivity. To understand the changes which lignin undergoes

during POM treatment of softwood and hardwood pulps, residual lignin has been isolated from pulps at different levels of POM delignification and analysed. In addition, the nature of lignin degradation compounds dissolved during POM delignification has been explored to help elucidate lignin cleavage reactions. Whereas the efforts to isolate higher-molecular weight lignin have been unsuccessful, low-molecular weight aromatic compounds have been identified in the POM spent liquor. This may be an indicator of the lignin reactions occurring on its surface; or, on the other hand, it could indicate the continuation of the degradation of higher-molecular weight lignin after dissolution, if the reactions took place in the bulk of the lignin. Among the lignin degradation products of POM treatment of different kraft pulps were acetosyringone and acetovanillone, as the products of the C<sub>β</sub>-C<sub>γ</sub> bond cleavage; vanillin, vanillic acid, and syringaldehyde, which are the products of the C<sub>α</sub>-C<sub>β</sub> bond cleavage; and 2,6-dimethoxy benzoquinone, which confirms the C<sub>1</sub>-C<sub>α</sub> bond cleavage in lignin. The presence of 3,4-dimethoxy carbonyl and carboxyl aromatic compounds, veratraldehyde, and veratric acid, respectively, reveals a potential methylation reaction taking place with methanol released during the lignin demethylation reaction in POM treatment of kraft pulps, since these structures are not naturally present in lignin.

The results obtained using the different lignin-related substrates revealed that phenol oxidation reactions are the most significant reactions occurring during lignin oxidation with POMs. LMCs with free phenolic hydroxyl groups (PhOH) reacted both faster and at lower temperature (room temperature) than the etherified forms, which reacted only at temperatures  $\geq 120$  °C. Fast oxidation of phenolic units was confirmed in POM oxidation of kraft pulps when the content of PhOH groups rapidly decreased in the corresponding residual lignin with the progress of POM delignification.

Since POM oxidation of phenols yields quinones, it is expected that the quinone content in pulps will increase with the progress of POM delignification. For example, *ortho*- and *para*-quinone structures resulted from POM treatment of different lignin model compounds *para*quinone was detected in the solution of unbleached birch kraft pulp treated with POMs a reddish orange hue of the pulps, which is commonly noticed after treatment with POMs, was

also attributed to the formation of quinones. In addition, *ortho*-quinone formation in lignin is consistent with a loss of methoxyl groups. Lignin demethylation has been observed in the POM treatment of pine MWL [28] and in the residual lignin of hardwood kraft pulps

with the progress of POM delignification. Conversely, *para*-quinone products give evidence for the occurrence of the C<sub>1</sub>-C<sub>α</sub> cleavage reactions.

An abundance of quinone structures in residual lignin after POM treatment of pulp may be an important reason for a successful brightening of POM treated pulps with sodium hydroxide and hydrogen peroxide, as they are efficient quinone-removing agents.

In addition to quinone formation confirmed in different model studies and studies on MWL and kraft pulps, an increase in other carbonyl groups, such as -C<sub>α</sub>HO and -C<sub>α</sub> = O, has been observed in the remaining POM-treated MWL and residual lignin of kraft pulps [28,34]. This result corroborates a reaction mechanism based on the successive oxidations of the benzylic carbon atoms, as proposed in the studies on etherified LMCs.

Even though in kraft pulping lignin is primarily degraded through the cleavage of its most abundant β-O-4 structure, some β-O-4 bonds are still present in residual lignin of kraft pulps. Because the bleaching result depends considerably on the agent's ability to cleave this structure, the POM treatment of β-O-4 dimers was performed, whereby the researchers observed cleavage of the C<sub>1</sub>-C<sub>α</sub> bond in phenolic guaiacyl- and syringyl- glycerol β-aryl ethers. This finding is consistent with the observed reduction in the content of the β-O-4 bonds resulting from the POM treatment of pine MWL. The 2D NMR HSQC analysis of residual lignin isolated from kraft pulps also indicated a weakening of the correlations assigned to this lignin bond.

Moreover, the products of the β-O-4 bond cleavage, identified in the LMC studies, were also identified in the POM spent liquor of the treatment of kraft pulps. This finding corroborates the delignification mechanism, which includes C<sub>1</sub>-C<sub>α</sub> bond cleavage. The lignin model studies, however, did not support the claim that the delignification mechanism includes C<sub>α</sub>-C<sub>β</sub> bond cleavage (C<sub>α</sub>-aldehyde and C<sub>α</sub>-carboxyl acid aromatic structures). Nevertheless, the cleavage of the β-O-4 bonds, the most abundant bonds in native lignin, and important bonds in residual lignin, which was revealed in the POM experiments on LMCs, MWL and kraft pulps, would contribute positively to the total delignification result in the POM treatment of kraft pulps.

*Delignification by PMOs in Aerobic condition-*

POMs have been studied as catalysts in oxygen delignification of unbleached pulps in aqueous or organic solvent- water media to increase the selectivity of delignification. For this purpose, the hetero poly anions HAA-n of the general formula  $[P Mo_{12-n} V_n O_{40}]^{(3+n)-}$  (n= 1-6) have been used. The most important properties of the HPA-n series of polyoxometalates are their re oxidation with oxygen, a property, which enables the two reactions to occur in the same step and their stability at pH 2.5-5 , a property which requires

acidic process conditions. The redox potential of the HPA-n series of POMs decreases with increasing n and catalytic action in oxidative delignification is performed with HPA-5 in particular  $[P Mo_7 V_5 O_{40}]$ . Vanadium is responsible for the oxidation- reduction path of the

HPA-n polyoxometalates; while oxidizing lignin, HPA-5 is reduced in the reaction  $V^{5+}$  to  $V^{4+}$ , reduced HPA-5 is re oxidized with oxygen in the reaction  $V^{4+}$  to  $V^{5+}$ . The  $VO_2^+$  formed via dissociation of HPA-n is characterized by higher redox potential than the parent HPA-n.

HPA-n converted to  $HPA-(n-1) + VO_2^+$

Due to higher redox potential,  $VO_2^+$  ions are less selective oxidizing agents leading to the oxidative degradation of polysaccharides. Moreover, the free  $VO_2^+$  ions are not oxidized by

$O_2$  in acidic solution which means that they cannot be recycled. Therefore it is desirable to suppress HPA-5 dissociation, which can be done by pH control by addition of polar organic solvents (ethanol) or by increasing the ionic strength of solution. Adding ethanol into the system in the amount of up to 40-50 % improves delignification selectivity due to partial reduction of the concentration of  $VO_2^+$  in the solution. The pH of the system also strongly influences the delignification and while degradation of polysaccharides increases with decreasing pH, the delignification efficiency decreases at pH higher than 2.

Studies of the effect of HPA-5/ $O_2$  and HPA-5-MnII/ $O_2$  on lignin have been performed using hardwood (eucalyptus) and softwood (spruce) species, monomeric and dimeric lignin model compounds, and dioxane lignin adsorbed on pulp. The results of these studies indicated that the conversion of phenolic lignin units occurs 5–6 times faster than that of non-phenolic lignin units and that the syringyl units are more readily oxidized than the guaiacyl analogues. A simplified reaction scheme has been suggested by Evtuguin and Pascoal Neto. They suggested that similarly to the mechanism of POM delignification in the anaerobic system, the reaction starts with one-electron oxidation of lignin phenolic units resulting in phenoxy radicals, which lose one more electron and form cyclohexadienyl cations. In contrast to anaerobic POM treatment delignification, participation of oxygen is suggested in lignin autooxidation during aerobic delignification catalysed by POMs/HPA-5. The role of the  $VO_2^+$  released from the HPA-5 is demonstrated in the suppression of these lignin autooxidation

reactions, and even more in the oxidation of non-phenolic structures for which the  $\text{VO}_2^+$  ions were suggested to be the active catalysts. The rate-determining step of the oxidative delignification of both phenolic and non-phenolic lignin units is the first one-electron oxidation step. Similar to the studies of anaerobic POM delignification, the studies of aerobic POM delignification indicated that the delignification includes cleavages of the  $\text{C}_\alpha\text{-C}_\beta$  and  $\text{C}_1\text{-C}_\alpha$  bonds, demethylation, and formation of quinone structures. The comparative analysis of lignin before and after HPA-5/ $\text{O}_2$  treatment of dioxane lignin adsorbed on pulp showed that the content of the  $\beta\text{-O-4}$ ,  $\beta\text{-}\beta$ , and  $\beta\text{-5}$  bonds was reduced, which is the same result observed in the POM anaerobic delignification of MWL and kraft pulps.

### HPA-5/ $\text{O}_2$ system

The hetero polyanion  $[\text{PMo}_7\text{V}_5\text{O}_{40}]^{8-}$  in solution (HPA-5 for short) has shown catalytic activity under  $\text{O}_2$  for the delignification of eucalyptus sawdust and for the delignification of kraft pulp, in water or ethanol–water medium under appropriate conditions. Delignification of kraft pulp at temperatures of  $90^\circ\text{C}$  and at an optimized pH of 1.8–2.0 and

an oxygen pressure of 0.6 MPa originated pulps with significantly lower kappa numbers than those of the experiments performed with no POM after 2 h of reaction. However, owing to the low pH used, polysaccharide destruction also occurred. This was assumed to be mainly related to the hydrolysis reactions by acid catalysis, as similar intrinsic viscosities were obtained for the experiment carried out with no POM. Notwithstanding, the delignification process catalysed by the HPA-5/ $\text{O}_2$  system was more selective than the conventional oxygen delignification in alkaline medium, when the oxidative degradation was carried out to a kappa number of around 6–7. It was demonstrated that the HPA-5/ $\text{O}_2$  system could be used in multiple delignification cycles without losing its activity for the

delignification of the pulp. These results showed that no catalyst deactivation occurred. The chemical oxygen demand index, after the second cycle, indicated that the oxidised organic materials accumulation and their dissolution in the multiple delignification liquors was roughly the same. This fact indicates that the HPA-5/ $\text{O}_2$  system yields the total oxidation of lignin to carbon dioxide and water. These results are extremely important for a possible application of HPA-5 as a catalyst for an oxygen delignification stage in a totally effluent-free (TEF) bleaching plant. Since the delignification liquor may be continuously re-used it could be carried out in a closed system. In this way, POM delignification opens new perspectives for the implementation of the closed-mill concept and for the reduction of the environmental impact of the bleached kraft pulp mill.

### HPA-5- $\text{Mn}^{\text{II}}$ / $\text{O}_2$ system

$\text{Mn}^{\text{II}}$ -assisted HPA-5 as a catalyst. In spite of the good delignification extent obtained during oxygen delignification catalysed by HPA-5, the selectivity of residual lignin oxidation was restricted by two main factors: a. the low pH of the best delignification medium (ca. pH 2), which promotes acid catalysed hydrolysis of polysaccharides; and b. the undesirable and not easily controllable degradation of polysaccharides with  $\text{VO}_2^+$  ions dissociated from parent structure of HPA-5. To overcome these drawbacks, new development was carried out

on the preparation and structure of the catalyst. Manganese (II) ions in the form of manganese diacetate were added in the last stage of the synthesis of HPA-5 under acidic conditions with the purpose of preparing Mn-substituted HPA-5 structures (HPA-5-MnII for short) as suggested by electrochemical experiments. This experiment accounted for the partial dissociation of HPA-5 at pH 3, leading to the formation of the so-called lacunary derivatives of the parent Keggin polyoxoanions. Moreover, the synthesis of POMs, based on the reactions of lacunary Keggin structures and transition metal ions is well documented. Regarding the catalytic features of Mn-substituted polyoxometalates in oxygen delignification, the use of a lacunary structure of HPA-5 acting as a multidentate ligand to the manganese ions (HPA-5- Mn II) on the oxygen delignification catalysis was investigated. The delignification degree achieved with HPA-5/O<sub>2</sub> or HPA- 5-MnII/O<sub>2</sub> systems was considerably higher than that obtained by oxygen without a catalyst. Comparing the two reaction systems HPA-5/O<sub>2</sub> and HPA-5-MnII/O<sub>2</sub>, the latter showed a slightly lower delignification efficiency but a remarkably improved selectivity, proving a positive influence of the presence of manganese in the substituted HPA-5. The VO<sub>2</sub><sup>+</sup> ions present in the acidic HPA-5 solution play a key role in the oxidative delignification because they were considered as the main active species in the catalytic oxidation of lignin.

At the same time, however, VO<sub>2</sub><sup>+</sup> ions oxidise the polysaccharides, thus decreasing the selectivity of the delignification.

The introduction of Mn in the synthesis of HPA-5- Mn II could control, to some extent, the VO<sub>2</sub><sup>+</sup> ions released.

The lower concentrations of VO<sub>2</sub><sup>+</sup> in the HPA-5-MnII solution could explain the slightly lower delignification efficiency but better selectivity. The molar ratio between HPA-5 and Mn<sup>2+</sup> ions used in the synthesis of HPA-5-MnII also influenced the delignification results. The selectivity of the lignin oxidation was fairly constant when the ratio [HPA-5]/[Mn<sup>2+</sup>] was higher than 1.5. The catalyst HPA-5-1.5MnII ([HPA-5]/[Mn<sup>2+</sup>] = 1.5) was suggested as being the best for the catalytic needs.<sup>54</sup> About 15–20% higher viscosity of the delignified

pulp was achieved with HPA-5-1.5MnII when compared with HPA-5 catalysis at the same degree of delignification. Delignification parameters in the system HPA-5-1.5MnII/O<sub>2</sub> were also optimized. The best delignification selectivity with HPA-5-1.5MnII was observed at a pH between 3 and 4. The temperature of 100<sup>o</sup>C seemed to be a good compromise for selective delignification. After 4 h of reaction at 100<sup>o</sup>C, it was possible to reach up to 70% of residual lignin removal with a viscosity drop of only 26%.

### Oxygen delignification with polyoxometalates and Laccase

As laccase may be an efficient catalyst of re-oxidation of different kinds of POMs, biocatalytic reoxidation of reduced POMs with laccase has been proposed as a method that will enhance re-oxidation efficiency in aerobic delignification. In a first approach, POMs were used as inorganic mediators to laccase-catalysed delignification of pulp at temperatures typically around 45–60<sup>o</sup>C. This followed observation that some of the

POMs that were hardly re-oxidised by oxygen, such as  $\text{SiW}_{11}\text{Mn}^{\text{II}}$  and  $\text{SiW}_{11}\text{V}^{\text{IV}}$ , could be re-oxidised by the enzyme even at room temperature ( $T \approx 25\text{ }^{\circ}\text{C}$ ) and atmospheric pressure (ca. 0.02 MPa). When using POMs as inorganic mediators for pulp delignification (laccase-mediator system – LMS), the POM oxidises the residual lignin in the pulp and the reduced POM is re-oxidised by laccase at the same stage. Finally, the cycle is completed by re-oxidation of the copper centres of the prosthetic group of laccase in the presence of oxygen. The application of the LMS to the delignification of kraft pulps has not produced high delignification. No more than 35% delignification was achieved, even after 48 h of reaction. The low delignification rate was suggested to be due to the scarce reactivity of the POM with the substrate under the applied conditions. In fact, the optimal conditions required for kraft pulp delignification with the POM are typically around 90–110  $^{\circ}\text{C}$ , in contrast to the applied temperatures lower than 60  $^{\circ}\text{C}$ .

In a second approach, an alternative multi-stage process was developed in which the pulp is treated with a POM at high temperature (100–110  $^{\circ}\text{C}$ ) in a first stage, followed by the POM re-oxidation with laccase at moderate temperatures (30–60  $^{\circ}\text{C}$ ) in a separate stage. The application of this multi-stage process brought delignification around 50% when applied to  $\text{SiW}_{11}\text{Mn}^{\text{III}}$  and  $\text{SiW}_{11}\text{V}^{\text{V}}$ .  $\text{SiW}_{11}\text{Mn}^{\text{III}}$  was found to be more selective, while  $\text{SiW}_{11}\text{V}^{\text{V}}$

was more effective in the oxidative delignification. After the laccase stage (POM-L) the complete re-oxidation of polyoxometalates  $\text{SiW}_{11}\text{V}$  (and  $\text{SiW}_{11}\text{Mn}$ , respectively) was verified. Furthermore, no indications of degradation of the Keggin structure were found under the experimental conditions used.

## 7. Conclusion-

As a promising alternative to chlorine based bleaching, oxidative delignification with POMs has been suggested. Both of the approaches, one based on the anaerobic process in which POMs are used as oxidative delignification agents and second based on aerobic process in which POMs are used as catalysts, have their advantages and disadvantages. The most effective and selective polyoxometalates found for the delignification process were  $\text{SiW}_{11}\text{V}^{\text{V}}$ ,  $\text{SiW}_{11}\text{Mn}^{\text{III}}$ ,  $\text{AlW}_{11}\text{V}^{\text{V}}$ ,  $\text{SiW}_{10}\text{V}_2$ , ' $\text{SiW}_{10.1}\text{Mo}_{1.0}\text{V}_{0.9}\text{O}_{40}$ ' and the above-mentioned HPA-5- $\text{Mn}^{\text{II}}$ .

Work on both of the process is going on currently in the industry. A very satisfying result of up to 70% of delignification can be achieved and a saving of 56% of chlorine oxide has also been achieved. In the future it is expected that, new direction of application of other POMs can be achieved, and more selectivity can also be achieved. Alternatively, the development/optimization of new/known processes incorporating delignification and re-oxidation of the POM in different stages should be considered. In the future, these processes

should be optimized and costs evaluated and compared with those of industrial processes in order to evaluate the possibility of incorporating new POM-based delignification processes into industrial applications.

## 8. References

1. Antonio Pineda<sup>1</sup> · Adam F.Lee<sup>1</sup>. Heterogenously catalysed lignin depolymerization. 2016
2. Mark Gale, Charles Cai, Kandis Leslie Abdul Aziz. Heterogenous Catalyst Design Principles for the conversion of Lignin into High Value Commodity Fuels and Chemicals.
3. Javier Fernandez- Rodriguez, Jalel Labidi, in separation of Functional Molecules in Food by Membrane Technology. Lignin Separation and Fractionation by Ultrafiltration. 2019
4. Eja Ahmad, Kamal K. Pant, in West Biorefinery. Lignin Conversion: A Key to the Concept of Lignocellulosic Biomass – Based Integrated Biorefinery. 2018
5. Armindo R.Gaspar, Jose A. F. Gamelas, Dmitry V.Evtuguin and Carlos Pascol Neto. Green Chemistry. Alternative for lignocellulosic pulp delignification using polyoxometalates and oxygen: a review. 2007
6. Pratima Bajpai , in Biermann's Handbook of Pulp and Paper (Third Edition), 2018
7. R.H.Atalla, I.A.Weinstock, R.S.Reiner, C.J.Houtman, S.Reichel, and C.G.Hill . USDA Forest Service, Forest Products Laboratory. Department of Chemical Engineering University of Wisconsin-Madison, USA. C.L.Hill , M.Wemple, J.Cowan, E.M.G.Barbuzzi. Emory University, Department of Chemistry Altana, Georgia, USA. RECENT ADVANCES IN POLYOXOMETALATE BASED DELIGNIFICATION.
8. Armindo R. Gaspar,<sup>a</sup> Jose´ A. F. Gamelas,<sup>\*b</sup> Dmitry V. Evtuguin<sup>b</sup> and Carlos Pascoal Neto<sup>b</sup>. Alternative for lignocellulosic pulp delignification using polyoxometalates and oxygen: a review . 2007
9. Biljana Bujanovic , Sally Ralph 2, Richard Reiner, Kolby Hirth and Rajai Atalla. Polyoxometalates in Oxidative Delignification of Chemical Pulps: Effect on Lignin. 2010.
10. Oxygen Delignification: Pulp and Paper Processes: PRAXAIR'S OXIGEN DELIGNIFICATION AND EXTRACTIVE OXIDATION.



**METAL ORGANIC FRAMEWORK WITH POTENTIAL  
APPLICATION OF TOXIC GASES SEPARATION.**

**SCOTTISH CHURCH COLLEGE**  
**UNIVERSITY OF CALCUTTA**

**C.U. ROLL NO : 223/CEM/191019**

**C.U. REGISTRATION NO : 223-1211-0012-19**

**SPECIAL PAPER : SI/44**

**NAME OF CANDIDATE**

**Bipasha Banerjee**

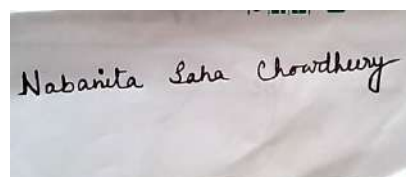
**NAME OF THE SUPERVISER**

**Nabanita Saha Chowdhury**

**SIGNATURE OF CANDIDATE**

A rectangular box containing a handwritten signature in black ink on a light background. The signature reads "Bipasha Banerjee".

**SIGNATURE OF SUPERVISER**

A rectangular box containing a handwritten signature in black ink on a light background. The signature reads "Nabanita Saha Chowdhury".

## **DECLARATION**

This review work accomplished by the undersigned under supervision of **Dr. Nabanita Saha Chowdhury**. Assistant professor of Scottish Church College, during 4<sup>th</sup> and final semester(April-August,2021)in partial fulfilment of M.Sc.(Chemistry) degree of Scottish Church College under Calcutta University.

I hereby declare that the work is done by me and it is fundamental and not submitted anywhere before for the publication or any other purpose.



-----  
(Signature of the student )

**Name: Bipasha Banerjee.**

**University Roll No : 223/CEM/191019**

**Registration No : 223-1211-0012-19**

**College Roll No : 19PG-C-28**

**Date : 19/07/2021**

**Place : Scottish Church College , Kolkata**

## **CONTENTS**

## **PAGE**

<b>1. Abstract</b>	<b>5</b>
<b>2. Introduction</b>	<b>6-7</b>
<b>3. What's MOF?</b>	<b>7-8</b>
<b>3.1 Structural Feathure</b>	<b>8-10</b>
<b>3.2 MOF Synthesis</b>	<b>11-12</b>
<b>4. Applications of MOFs</b>	<b>13</b>
<b>5. Applications of MOFs in     toxic gases separation</b>	<b>14-28</b>
<b>6. Future scope</b>	<b>28</b>
<b>7. Conclusion</b>	<b>29</b>
<b>8. Acknowledgement</b>	<b>29</b>
<b>9. References</b>	<b>30-36</b>

## **PREFACE**

It is both privileged and a formidable challenge for me to write a review on the subject of **“Metal organic frame work with potential applications for toxic gases separation.”**

In writing this review different journal published in different scientific magazine has been followed. The emphasis is given on synthetic reaction on **“Metal organic frame work with potential applications for toxic gases separation.”**

The review has been thoroughly revised and updated where required with major changes by **Dr. Nabanita Saha Chowdhury**, the assistant professor of Scottish Church College.

I also like to give thank **Dr. Nabanita Saha Chowdhury**, the assistant professor of Scottiosh Church College, who distinguished services has helped me a lot in writing this review.

**Bipasha Banerjee**

**Date : 19/7/2021**

**Kolkata**

## **1.ABSTRACT**

The release of phylogenic toxic impurity into the atmosphere is a world wide threat of growing concern. The toxic gases ( $\text{NH}_3$ ,  $\text{NO}$ ,  $\text{CO}_2$ ,  $\text{CO}$ ,  $\text{SO}_2$ ,  $\text{H}_2\text{S}$  etc.) are impure the air, that causes serious environmental problems and pose substantial health hazard.<sup>1</sup> How to increase safety with regard to personal protection in the event of toxic gas exposure is a critical question for an ever-growing population spending most of their lifetime indoors, but in order to protect future generations of employes from potential hazards it is also crucial for the chemical industry. "In this review, we highlight the state-of-the-art examples in which metal organic frame works (MOFs), an emerging class of porous sorbents, have been applied to the desorptive removal of toxic gases." MOFs can also simultaneously shows better adsorption capacities and exponential selectivities for toxic  $\text{SO}_2$ ,  $\text{NO}_2$  and other flue and exhaust gases while maintaining their structural integrity.<sup>2</sup> The highly crystalline nature and rich chemical functionality of MOFs have assisted the elucidation of host-guest inactions at a molecular level to afford insights and new knowledge that will inspire and inform the design of new generations of adsorbents.<sup>1,2</sup>

## 2.INTRODUCTION

The liberation of anthropogenic toxic pollutants in the environment/atmosphere, which include products of combustion or chemical reactions, leaks of harmful industrial gases and vapours as well as the deliberate emission of chemical warfare agents, is a world wide risk of growing concern. For environment air pollution, common hazardous compounds such as NO, SO<sub>2</sub>, CO<sub>2</sub>, H<sub>2</sub>S, CO, NH<sub>3</sub> other nitrogen (e.g. hydrogen cyanide) or sulphur –containing compounds (e.g, organo thiols), hydrocarbons, volatile organic compounds (benzene, toluene, methanol, etc.) are major concern. The main sources of these gases are anthropogenic. SO<sub>x</sub> and NO<sub>x</sub> are taken part into the formation of acid rain and the photo chemical smog. Emissions of SO<sub>2</sub>, NO<sub>2</sub> and CO are mainly due to the burning of fossil fuels that cover the current high energy demand. The another poisonous, corrosive and odorous gas is H<sub>2</sub>S. The purification of these gases prior to their use implies the recovery of this acid contaminant.<sup>2</sup>

In review of all the above, “the effective sensing, capture and eventually the degradation of these harmful chemicals is of the great importance both for the protection of the environment and for health issues.” Notably, porous materials are at the front line of minimizing the efficiency of industrial and regeneration processes. With respect to, a new class of crystalline nano-porous materials known as metal-organic frameworks (MOFs) has emerged, as an alternative to zeolites, as a consequence of their enchanting potential applications in adsorption, sensing and catalyst.<sup>2,5</sup>

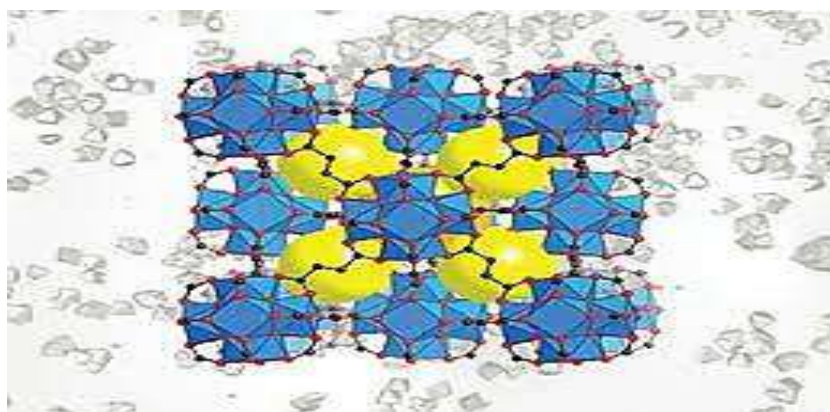
Accordingly, one of the main scientific

challenges to be achieved in the field of MOF research should be to maximize the performance of these solids towards the sensing capture and degradation of harmful gases and vapours by means of a rational control of size and reactivity of the pore walls that are directly accessible by guest molecules.<sup>3</sup>

In this review, “the features of classical MOFs as well as hybrid materials based on MOFs suitable for the selective, sensing, capture, and catalytic degradation of toxic gases and vapours.”<sup>3,4,5</sup>

### 3. What is MOFs?<sup>7</sup>

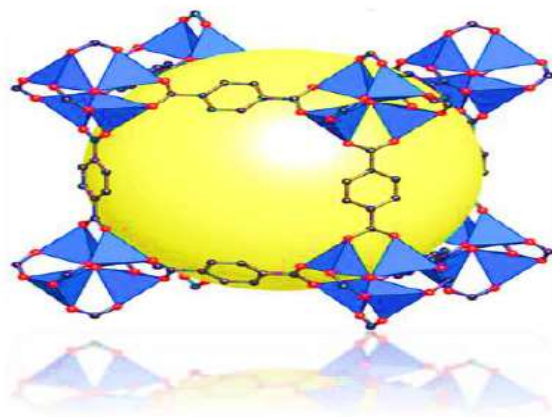
Metal–organic frameworks (MOFs) are a class of compounds comprising of metal ions or clusters coordinated to organic ligands to form two-, or three-dimensional structures.<sup>7</sup>



- MOFs are self-combined metal clusters with organic framework, are well known for their structure, permanent porosity, and have shown various prospect for various applications.<sup>7</sup>
- Metal–organic framework is a coordination network with organic ligands containing potential voids.

### 3.1. Structural Feature<sup>4,8,9,10</sup>

MOFs are structures made up of inorganic nodes, which can either ions or clusters of ions, and organic linkers.

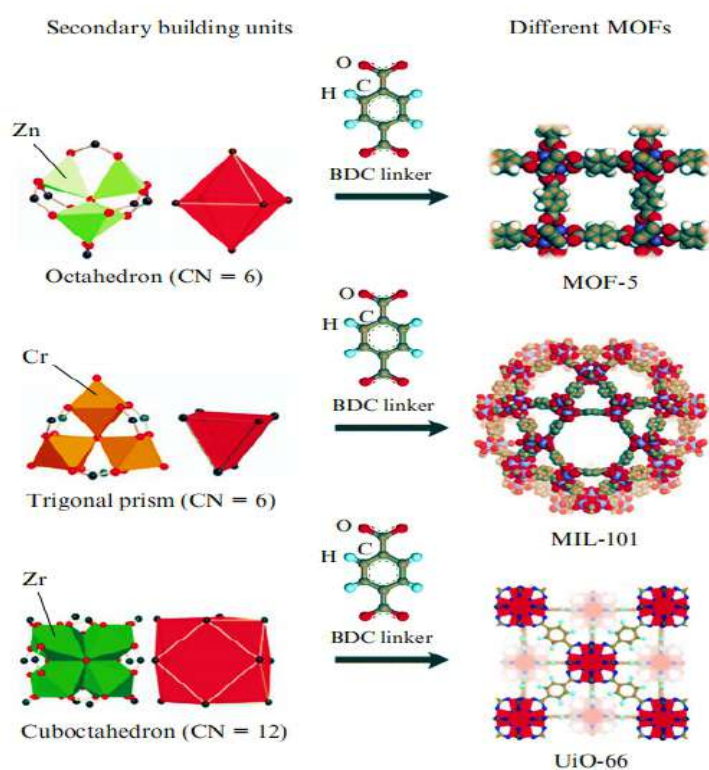


MOFs can be obtained using rigid molecular building blocks under reaction conditions that maintain their structural integrity throughout the synthesis regime. In this context, reticular synthesis can be described as the process of assembling judicious primary building blocks to form to SBUs (Secondary building units) which predetermine ordered structures held together by strong co-ordination bonds. In a nutshell



with this strategy it is possible to control the overall co-ordination number of the inorganic and organic building units, and it then becomes important to identify the networks that can be expected result from a topological point of view.<sup>8,10</sup>

Typically MOFs are built from two types of primary building units or points extension. “One type is basically organic ligands, which could be multitopic in nature. Another type is a metal atom or finite polyatomic cluster, which have two or more metal atoms of same (homometallic, e.g.  $Zn_4O, Zr_6O_4$ ) or different type (heterometallic, e.g. poly-oxometallates).” The two types of building reveal characteristics roles in the formation of secondary building units (SBUs). To construct the MOF architecture these SBUs finally self-gathered in higher dimensions. According to the classification co-ordination number of

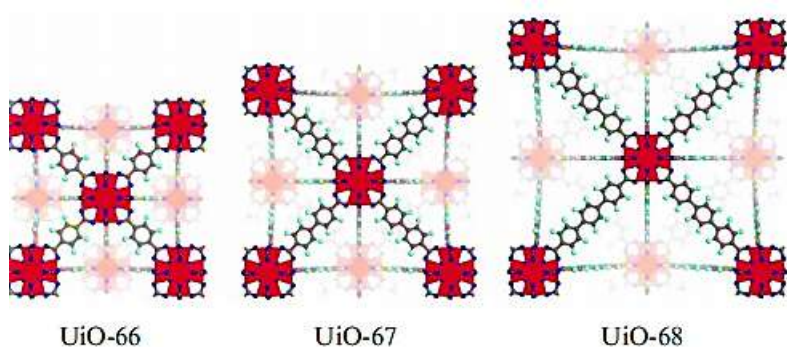


Structures of different MOFs Terephthalate(BDC) dianion as a linker.

secondary building units can vary from 3 to 66.<sup>4</sup>

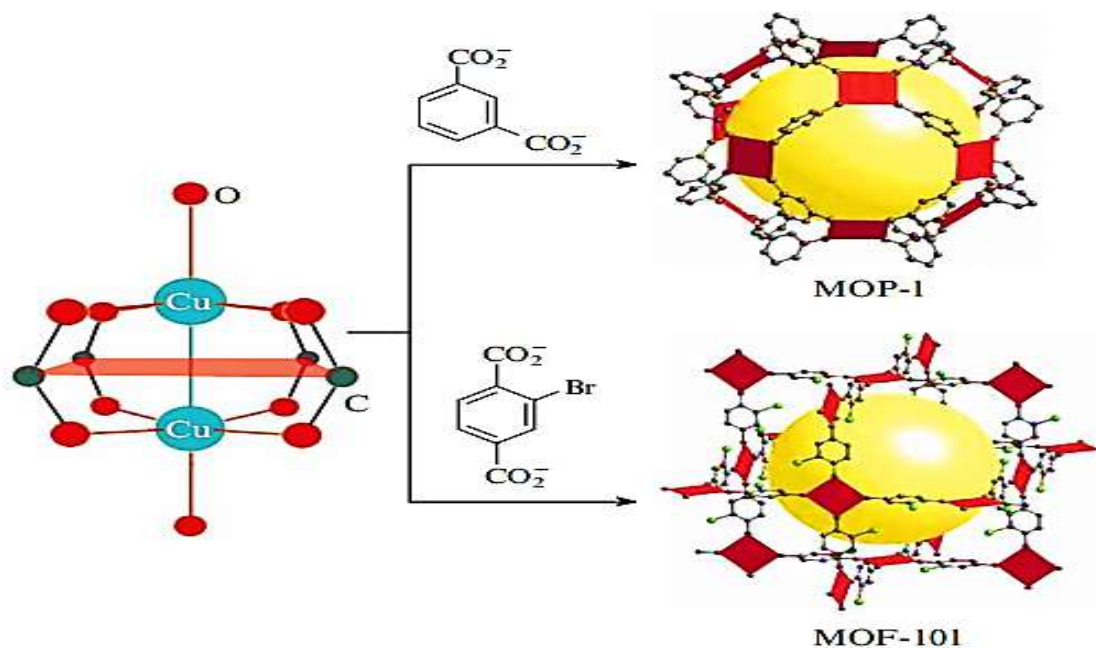
Through the different linkers SBUs can be combined into a framework structure. Two situations can be arrived by the leading of the selection and substitution of a linker: either the symmetry of the structure is maintained when another linker is used and

because of the elongation of carbon chain only the unit cell parameters change



“(for example, when going from UiO-66 to UiO-68)”<sup>11,12,13</sup> or the change in the mutual arrangement of functionalities, change the symmetry.

As already mentioned, MOFs are distinguished by the diversity of their structure, different symmetry and pore sizes and, hence, by their characteristics. The pore size is determined by the carbon chain length of the number of benzene rings in it, whereas the introduction of different substituents and functional groups into the linker is responsible for the additional selectivity and unique chemical properties of the pore.<sup>4,9</sup>



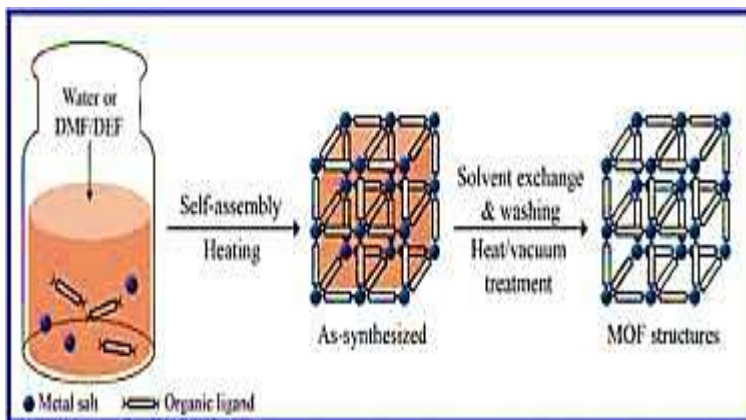
Depending upon the mutual arrangement of substituents in the linker molecule, example of the change in geometry of MOFs.

## 3.2. MOFs SYNTHESIS<sup>3,4,10,14,53</sup>

MOFs can be synthesized in **5 ways**.

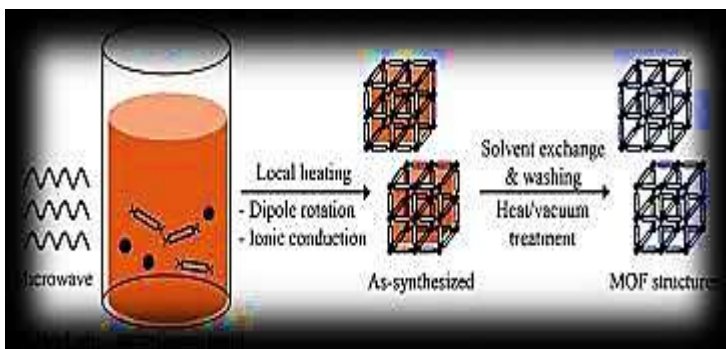
- a) **Hydro thermal/ Solvothermal Synthesis.**
- b) **Microwave assisted synthesis.**
- c) **Ultrasonic synthesis.**
- d) **Electrochemical synthesis.**
- e) **oCentrifugal synthesis.**

### a) Hydrothermal / Solvothermal Synthesis:



Solvothermal synthesis is carried out at the boiling temperature of the solvent or above this boiling point in special closed chemical reactors at elevated pressure caused by solvent vapour or produced by a pump.<sup>10,53</sup>

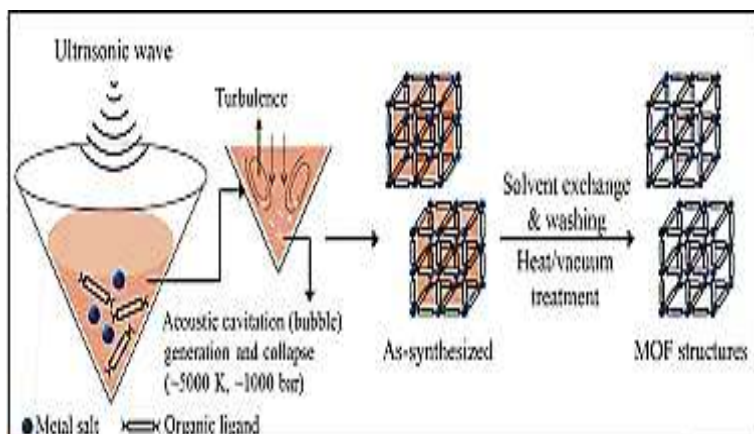
### b) Microwave assisted synthesis:



MW impact on a substance that leads to heating: the action on polar molecules and on free ions. In both cases, polar molecules and ions try to align with the alternating field. In an electrolyte solution, electric current is generated and, hence, heating occurs due to

resistance.<sup>4,10,14,53</sup>

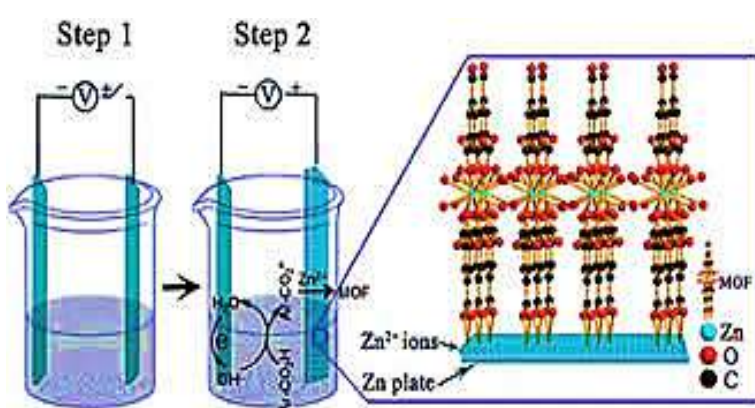
### c) Ultrasonic irradiation synthesis:



Ultrasound is known to synthesize MOFs rapidly under mild process conditions, such as solvent-free, at room temperature and under ambient pressure. Studies have shown that MOFs can be produced cost-effectively at high

yield via sonochemical route. Finally, the sonochemical synthesis of MOFs is a green, environmentally friendly method.<sup>10,53</sup>

### d) Electrochemical synthesis:



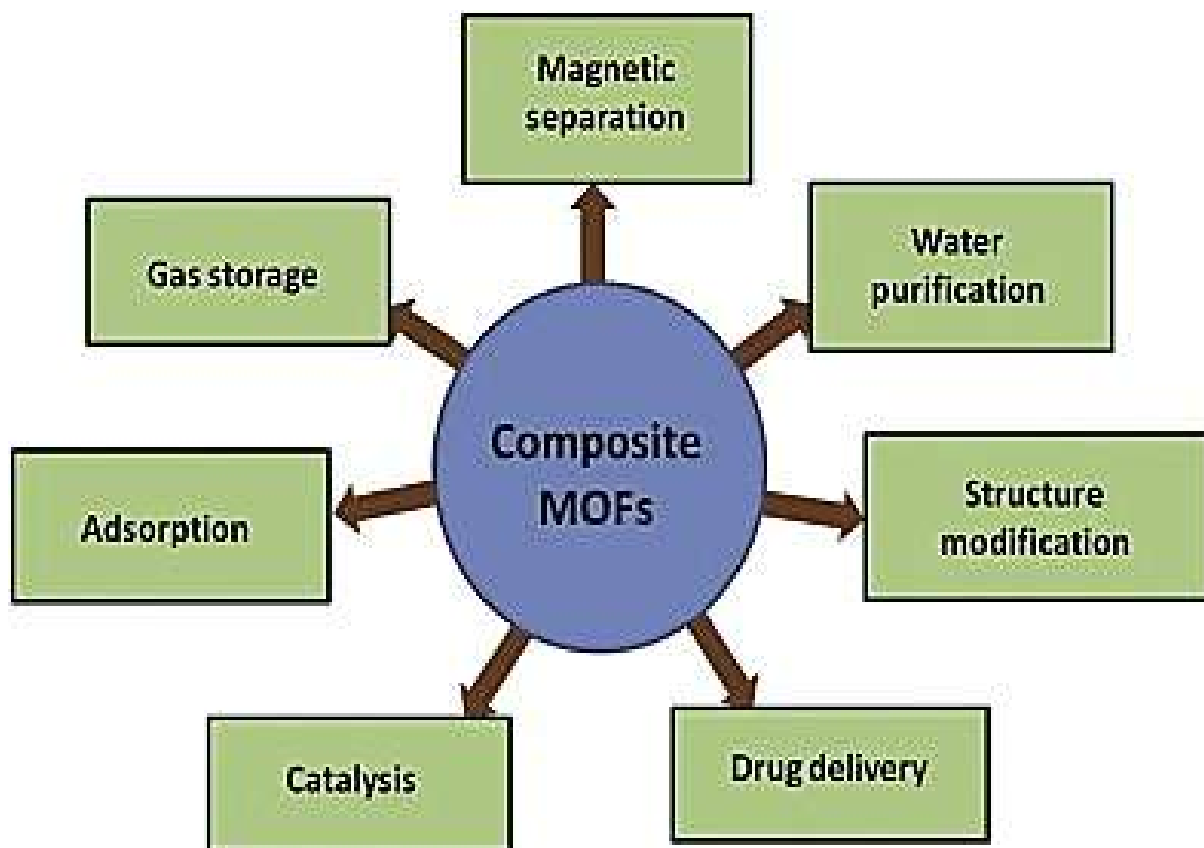
Electrochemical synthesis of MOFs is that metal ions are introduced not from a solution of the corresponding salt or through the formation of these ions during the reaction of a metal with an acid, but as a result of

electrochemical process.<sup>3,53</sup>

## 4. APPLICATIONS OF MOFs:

Numerous applications of MOFs in many fields are being developed that exploit MOFs' cage-like structure, such as:

- Gas storage and separation,
- Liquid separation and purification,
- Electro chemical energy storage,
- Catalysis and sensing,
- Drug delivery,
- Structure modification, etc.



## **5. APPLICATION OF MOFs IN TOXIC GASES**

### **SEPARATION:**

#### **(COMMON TRACE AND TOXIC GASES:<sup>15-20</sup>**

Maximum values for a large number of toxic industrial chemicals (TICs) are given by the “Air Quality Guidelines for Europe published by the World Health Organization (WHO).”<sup>15,16</sup>

For noncarcinogenic substances, stress thresholds are given, below which a significant risk for people’s health is not expected. From known lowest observed adverse effect levels and/or no observed adverse effect level, divided by a protection factor, these values are calculated. In some cases, where unpleasant smells caused because of the concentration below any health-adverse limit, odor limits are described. For the same pollutant varying values are listed, depending on variable exposure times typical for different exposure situations. Carcinogenic substances can cause cancer regardless of the concentration. In this case, “life time risks” are given instead of thresholds. The statistical probability of developing cancer caused by long-term exposition to a well-defined concentration of the substance during lifetime is the “life time risk.” These guidelines are included into national laws, standards, and guidelines, in the US<sup>17</sup> (e.g., the publication “Building Air Quality—a guide for Building Owners and Facility Managers”<sup>18</sup> of the “National Institute for Occupational Safety and Health, NIOSH”). An air conditioner filter for buildings or cars should be capable of reducing the concentrations of toxic components at least below the given limits. Organic compounds with measurable vapor pressures are referred to as VOCs.

It is very common to judge the indoor VOC concentration as “total volatile organic compounds, TVOC” with respect to the technical feasibility of measurements in parts per million (ppm) range.<sup>18,19</sup> Neither health nor general well-being are assumed to be affected by a TVOC average concentration below  $0.2 \text{ mg m}^{-3}$  and provides a challenging target for filter materials.<sup>19</sup> Another field of filter application is “CBRN filtration for extreme situations”, like industrial accidents or terrorist attacks. The CBRN filtration has been an exclusive domain of the military. However, the increasing outbreak and ever present threat of “chemical warfare agent (CWA)” use, as well as the more easily available TICs, has expanded the interest in such filters.<sup>20</sup> Many commercially available filters for use against toxic gases are certified against the NIOSH standards. As an example, “the NIOSH Standard for CBRN full facepiece air purifying respirators (APR) specifies performance levels against ten representative chemicals”.

In the same way, the equivalent European Standard (DIN EN 14387, DIN = Deutsches Institut für Normierung, [German Institute for Standardization]; EN = European Standard) specifies performance levels against ammonia, cyclohexane, chlorine, hydrogen sulfide, hydrogen cyanide, and sulfur dioxide. With the exception of chlorine, which is not explicitly covered in the NIOSH standard. However, the specification of concentrations and protection times is handled differently in each standard. Beyond the detection and separation of CWAs or VOCs, the detection of explosives is also a challenging task. Critical properties of explosives are pressure sensitivity, impact sensitivity or spontaneous combustion.<sup>15</sup> The class of explosive agents is highly diversified, and most explosives are based on

nitrocompounds. Because of their organic backbone they can be divided in different groups -

i) aromatic structure such as 2,4,6-trinitrotoluene (TNT), picric acid (2,4,6-trinitrophenol, TNP) or *N*-methyl-*N*-2,4,6-tetranitroanilin (tetryl); (ii) aliphatic backbones such as nitroglycerin, pentaerythritol tetranitrate (PETN) or (iii) cyclic backbones like hexahydro-1,3,5-trinitro-1,3,5-triazin (hexogen, RDX), and cyclotetramethylene tetranitramine (octogen, HMX). Also explosive agents with a large percentage of inorganic components such as gunpowder or ammonium nitrate fuel oils (ANFO) are known. ANFOs are a physical mixture of ammonium nitrate and mineral oil or diesel and hence are very cheap. There are also explosives without nitro groups such as triacetone triperoxide (APEX, TATP), which is often used by terrorists because of a cheap and easy synthesis route. Maximum allowable concentrations of explosives are given by different institutions, like NIOSH or the Occupational Safety and Health Administration (OSHA).<sup>15</sup> )

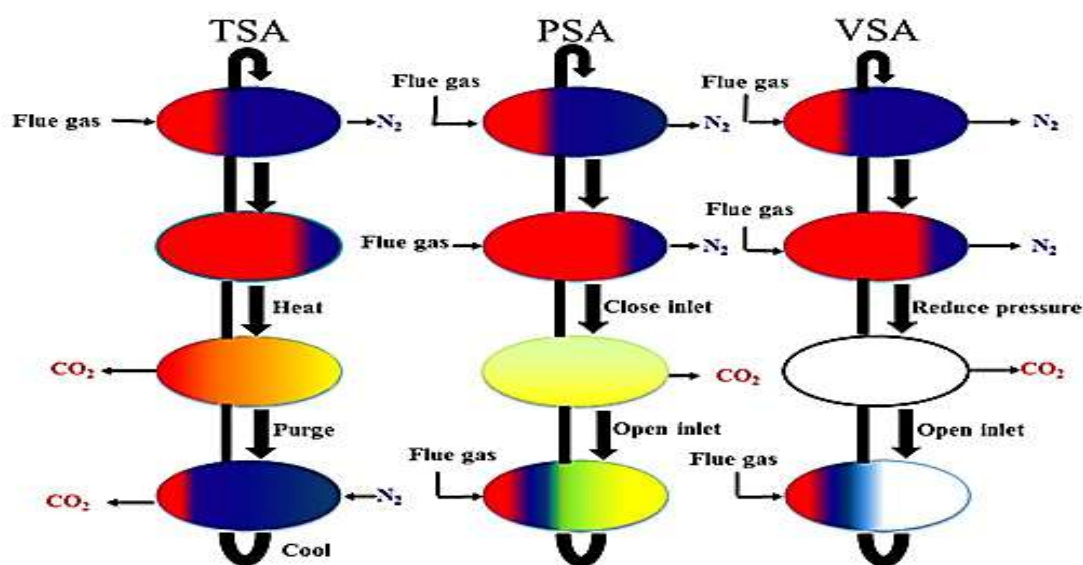
## **5.1.Principles and methods of adsorptive gas separation:<sup>21-25</sup>**

Separation is a method to detach the components of a mixture, whose procedure often requires large amounts of energy for dividing the substances of a mixture.<sup>21,22</sup> Furthermore, separation can be attained via selective adsorption and this takes place when the components on the surface of the adsorbent have different affinities to adsorb the diffused guest molecule. Gas



separation methods comprise membrane-based, cryogenic distillation, absorption and adsorption based technologies.<sup>23</sup> Among these methods, adsorptive separation has a greater attraction due to potentially lower energy consumption, easier maintenance, flexibility in the design for different applications, a simple operation and the environment-friendly characteristic of this method.<sup>24</sup> Generally, in the process of adsorptive gas separation, two main steps are involved; adsorption and desorption processes. In the adsorption stage, a mixture of the gases is passed through a fixed-bed adsorber or a column packed with the adsorbents. Then this process is ensued by the desorption step to remove the component attached on the surface of the adsorbent for reuse. Therefore, the gas adsorption process is dependent on the desorption methods used for regeneration of the adsorbent. Several cyclic adsorption processes are used in the gas separation technology including the inert purge cycles, the displacement cycles, the temperature swing adsorption the pressure swing adsorption (PSA), the vacuum swing adsorption (VSA) and the electrical swing adsorption (ESA). Although all these methods are expedient for gas separation and purification, the TSA and PSA are more commonly used in CO<sub>2</sub> segregation. The TSA desorption occurs by heating the adsorbent, has albeit its long cycle time due to the heating/cooling stage that requires a few hours up to over a day. On the other hand, the PSA is the process whereby regeneration is achieved by lowering the pressure of the adsorbent. This cycle has some advantages over the TSA such as a higher throughput of the cycle (the process usually occur in seconds or minutes) and a temperature-independent process. The PSA is predominantly used for bulk separation.

Another more recent method is the VSA that is of a greater interest for the researchers because it operates at near ambient pressure and most flue gas streams pressures are approximately atmospheric. As opposed to the other methods, the PSA and VSA have typically more desirability thanks to fewer energy requirements of these cycles.<sup>25</sup>



Schematic representation of TSA, PSA and VSA cyclic processes for regeneration of MOFs in the fixed-bed column.

It should be noted that adsorptive gas separation is attained when different components of the adsorbent have different abilities to adsorb. Also, a promising adsorbent should contain acceptable mechanical properties such as high selectivity, capacity, regenerability as well as promising adsorption kinetics.<sup>21</sup>

## 5.2 Selection of adsorbent and its criteria:<sup>21,26,27</sup>

Adsorbent selection is one of the important parts of adsorptive separation. Generally, the best adsorbent is the one that has both high selectivity and

capacity of adsorbing the targeted molecules. Hence, for choosing the adsorbent, the followings are to be considered: the nature of the adsorbent (also nature of its pores) and the adsorption process. For instance, in the bulk gas separation process, the adsorbent must be selected based on the ease of desorption. If the separation process is not considered, the nature of the adsorbent is the key criterion for choosing the adsorbent including the size and the shape of the adsorbate molecule, the dipole moment, the quadrupole moment, and the polarizability.<sup>21</sup>

For example, the adsorbents with high polarized surfaces are ideal if, the targeted molecule has a high dipole moment. “For the targeted molecule with a high quadrupole moment (like CO<sub>2</sub> molecules), the desirable adsorbent should contain a surface with high electric field gradients whereas for the adsorption of a non-polar molecule with high polarizability, an adsorbent with a high surface area could be appropriate.”<sup>26</sup> Moreover, due to the formation of complexation bonds and H-bonds (weak chemical bonding)  $\pi$  bond between the adsorbates molecules and the adsorbent numerous important separations and purifications are accomplished. Finally, the most important and basic point of selecting the adsorbent is “the equilibrium isotherm, followed by diffusivity.”<sup>27</sup>

### **5.a. Removal of Ammonia(NH<sub>3</sub>) gas by using**

#### **MOFs: 15,28,29,30,31,32**

The use of MOFs to remove ammonia has been extensively reviewed elsewhere. Ammonia is toxic and is a severe irritant to the eyes and respiratory system;

therefore, effective methods of capturing ammonia are needed to protect industrial and emergency workers who may be at risk of exposure in the event of an accidental spill. The most common porous material used for this application is activated carbon, but activated carbon is better fitted to capturing organic molecules than highly polar gases, like ammonia, and its ammonia capacity is fairly low (1.8 mg NH<sub>3</sub> per g carbon from humid air at 40°C).<sup>28</sup>

The adsorption capacity and selectivity of MOFs for NH<sub>3</sub>, improved through the judicious addition of functional groups to the framework. Groups that form strong hydrogen bonds with ammonia have been experimentally shown to greatly increase ammonia uptake.<sup>29</sup> “For example, in IRMOF-3, which is an amino functionalized analogue of IRMOF-1 (MOF-5), ammonia capacity is nearly 18 times greater than in IRMOF-1.” Additionally, functionalizing MOF-205 with –OH groups results in substantial enhancement in ammonia uptake at low pressure compared to the parent MOF-205.<sup>30</sup> A hierarchical modeling approach was used to predict NH<sub>3</sub> uptake capacity in four MOFs (MIL-47, IRMOF-1, IRMOF-10, and IRMOF-16) functionalized with –OH, –C=O, –Cl, and –COOH groups.<sup>31</sup> They used single-point energies computed at the MP2 level of theory to fit force fields to use in grand canonical Monte Carlo (GCMC) calculations because conventional force fields like UFF(Universal Force Field) and DREIDING are not adequate to capture the strong interactions between polar adsorbates and polar functional groups. They found that functionalized MOFs have higher NH<sub>3</sub> uptake at low pressure, but at high pressure the overall capacity may be lower due to the decrease in pore volume from large functional groups. Among these latter studies is the work of “Kim et al., who modeled a wide range of metal catecholates, which could potentially be incorporated as linkers within MOFs.” Out of the various

functionalities considered, R-COOCu groups were calculated to have the highest binding energy with ammonia. In response to this, it is recently reported that the synthesis of a series of functionalized UiO-66 MOFs containing copper carboxylate groups.<sup>32</sup> The materials showed high ammonia removal capacities under both dry and humid conditions and retained the framework structure. The highest ammonia breakthrough capacities are obtained for UiO-66-(COOCu)<sub>2</sub> with 6.38 mmol g<sup>-1</sup> under dry conditions and in the presence of humidity 6.84 mmol g<sup>-1</sup>. This work provides an excellent example of the interaction between the modeling and experimental communities, leading to materials with enhanced performance over those tested previously. The limits of ammonia removal by MOFs continue to be extended. The ammonia uptakes of these materials are among the highest reported to date (>12 mmol g<sup>-1</sup>) and they also appear to be stable toward repeated adsorption / desorption cycling of ammonia.<sup>15</sup>

### **5.b. Removal of Hydrogen Sulphid(H<sub>2</sub>S) gas by using MOFs:<sup>33-39</sup>**

H<sub>2</sub>S is a toxic compound used as a reagent in a number of industrial processes.<sup>33</sup> It is also a significant component of natural gas, biogas, and flue gas, and commonly found in ground water sources used for human consumption. There is a significant body of research on removing H<sub>2</sub>S from these sources.<sup>34,35</sup> Here, we focus on desulfurization in the context of removing toxic compounds from

the atmosphere. Hamon et al. Demonstrated how MOFs like, (MIL 47(V), MIL-53(Al,Cr,Fe), MIL-100 and MIL-101) are used for H<sub>2</sub>S capture at 303 K (up to 20 bar).<sup>36</sup> They showed that H<sub>2</sub>S adsorption isotherms in MOFs with microporous structures (MIL-53(Al,Cr) and MIL-47(V)) are fully reversible, with steps at low pressure and loadings reaching as high as 13 mmol g<sup>-1</sup> for MIL-53(Cr) at 16 bar. A structural change in MIL-53(Cr) upon H<sub>2</sub>S adsorption was observed, while MIL-47(V) stayed rigid. H<sub>2</sub>S adsorption in MOFs with mesoporous structures (MIL-100 and MIL-101) was measured to be partially irreversible. This behavior can be attributed to partial framework collapse caused by strong interactions between the framework and H<sub>2</sub>S molecules. Due to the large pore volume in MIL 101, a significant amount of H<sub>2</sub>S adsorption (-38 mmol g<sup>-1</sup> at 20 bar) was recorded. Additionally, Hamon et al. showed that MIL-53(Fe) decomposes to form black powder (iron sulfur) upon H<sub>2</sub>S exposure.<sup>37</sup> Typically, H<sub>2</sub>S will bind to open metal sites, such as those in the extensively reported HKUST-1, resulting (in that case) in breakdown of the MOF structure and the formation of copper sulfide. Interestingly, several composites of this MOF have shown apparently synergistic effects, including the graphite oxide/MOF composites reported by Bandosz and co-workers<sup>38</sup> and also the MOF/activated carbon composites reported by Shi *et al*<sup>39</sup>. In the latter study incorporation of less than 2% of activated carbon into the composites resulted in a 51% increase in H<sub>2</sub>S uptake; this was attributed to increased microporosity and availability of copper sites for reaction.

### **5.c. Removal of Carbon dioxide(CO<sub>2</sub>) gas by using MOFs:<sup>8,40,41,42</sup>**

The rising level of CO<sub>2</sub> in atmosphere is one of the hottest topics worldwide and its consequence is considered to provided major threat towards living beings.<sup>8,40,41</sup> The emission from coal,oil and natural gas due to rapid industrial development is mostly responsible for the rising CO<sub>2</sub> level in the atmosphere. Zeolites and activated porous carbons were explored for CO<sub>2</sub> adsorption, and other classes of porous materials, like MOFs, have now picked up attention as potential adsorbents. Very high internal surface area with polar functional groups decorating the pores provides opportunities for high CO<sub>2</sub> uptake capacity in MOFs.<sup>8</sup> CO<sub>2</sub> capture trials were performed *via* TGA. A small amount of sample (~10–35 mg) was placed in a platinum sample pan. At 25°C under a pure nitrogen flow, the system was equilibrated, after which the sample was heated to 100°C at a rate of 5°C min<sup>-1</sup>. This temperature was held for 180 mins to desorb species adsorbed from air without damaging the impregnated amines. The system was then cooled back to 25 °C and held under nitrogen flow at this temperature for 60 min. Then, the gas was switched to a pure CO<sub>2</sub> stream to perform CO<sub>2</sub> capture at 25 °C for 600 min. The weight gain during the adsorption step was then analyzed to determine the CO<sub>2</sub> adsorption capacity values (pseudo-equilibrium capacity). “The amine efficiency (moles of CO<sub>2</sub> captured per moles of N present on the amine) was achieved on NEU-2 PEI(x%wt).” The weight percent of the amine-containing molecules was converted into the molar content of nitrogen groups and compared to the capacity of carbon dioxide captured. All amine groups present on the impregnated PEI were assumed to be equally capable of capturing CO<sub>2</sub>.<sup>42</sup>

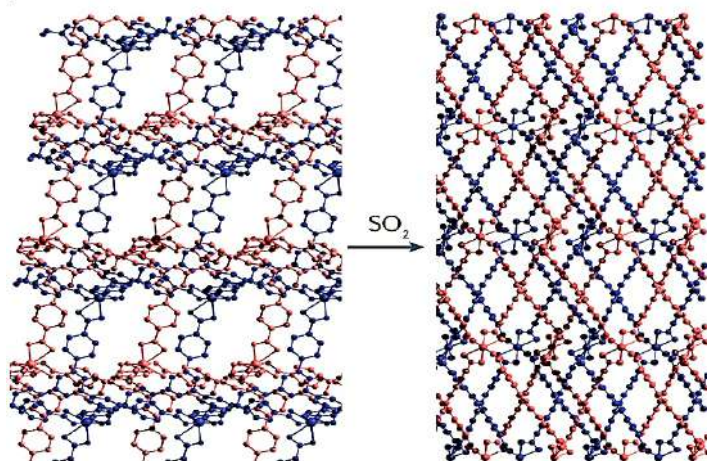
## **5.d. Removal of Sulphur dioxide(SO<sub>2</sub>) gas by using MOFs:<sup>43-48</sup>**

Several MOFs (MOF-5, IRMOF-3, MOF-74, MOF-177, MOF-199 and IRMOF-62) were examined for adsorptive removal of SO<sub>2</sub>.<sup>43,44</sup> These materials feature a wide range of BET surface areas (632–3,875 m<sup>2</sup> g<sup>-1</sup>) and have pores with a large variety of functionalities (for example, amines, aromatics, alkynes, coordinatively unsaturated metal sites and framework catenation) and sizes. MOF-74(Zn) composed of [Zn<sub>2</sub>O<sub>2</sub>(CO<sub>2</sub>)<sub>2</sub>]<sub>∞</sub> chains bridged by benzene-2,5-dihydroxy-1,4-dicarboxylate linkers, exhibits a significant increase in the dynamic adsorption capacity for SO<sub>2</sub>. HKUST-1 is a MOF that features Cu(II) ions bridged by benzene-1,3,5-tricarboxylate linkers to give [Cu<sub>2</sub>(O<sub>2</sub>CR)<sub>4</sub>] paddlewheel fragments. This MOF exhibits comparable SO<sub>2</sub> sorption capacity to that of granular activated- carbon (Calgon Carbon BPL carbon), whereas the other MOFs tested in this study showed negligible retention of SO<sub>2</sub>. An irreversible colour change was observed for MOF-74(Zn) upon adsorption of SO<sub>2</sub>, which was assigned to the interaction of SO<sub>2</sub> with the five-coordinate Zn(II) centre species and/or with the potentially reactive hydroxy groups. Motivated by the previous work, the complexes MOF-74(M) (M = Co, Mg, Ni or Zn) were screened for their capacity to remove trace SO<sub>2</sub> from air using fixed-bed breakthrough experiments under both dry and humid conditions. Under dry conditions, MOF74(Mg) shows higher SO<sub>2</sub> adsorption than MOF-74(Co), MOF-74(Zn) or MOF74(Ni), but the presence of water was found to have a detrimental effect on both framework stability and SO<sub>2</sub> adsorption for all MOF-74 series.<sup>45</sup> The organic linker can also influence the SO<sub>2</sub> adsorption capacity of MOFs. For example, micro-breakthrough measurements have been



performed to test the sorptive properties of UiO-66-ox, a UiO-66 analogue featuring free carboxylic acid groups, when exposed to a gas stream containing SO<sub>2</sub>.<sup>46</sup> Interestingly, UiO-66-ox shows an eightfold enhancement of the adsorption capacity of SO<sub>2</sub> in comparison with UiO-66, and this was attributed to chemisorption of SO<sub>2</sub> to the free carboxylic acid groups in UiO-66-ox.

The stability of MOFs upon adsorption of SO<sub>2</sub> is crucial for reversible gas uptake. However, porous MOFs can show structural flexibility, as they may convert reversibly between a narrow-pore phase and a large-pore phase under external stimuli (for example, temperature, pressure, guest inclusion and light). Thus, structural transitions of MOFs upon adsorption of SO<sub>2</sub> can lead to increased observed gas uptakes. In situ PXRD investigation revealed that MFM-202a undergoes an irreversible phase change to MFM-202b upon adsorption of SO<sub>2</sub>. The phase change leads to an increase in pore volume owing to the formation of triple  $\pi$ - $\pi$  interactions between the phenyl rings on the backbone of MFM-202b,



Example of MOF Applicable for SO<sub>2</sub> removal. (MFM-202a and MFM-202b before and after SO<sub>2</sub> adsorption)

which lead to an increase in the stability, SO<sub>2</sub> uptake and selectivity of the overall framework. Thus, the SO<sub>2</sub>-induced framework transition from MFM-202a to MFM-202b leads to both additional uptake and high SO<sub>2</sub> selectivity of 132 at 273K and 84.5 at 293K.<sup>47</sup> The dense packing of SO<sub>2</sub> clusters was reported for SIFSIX materials, which are copper coordination networks constructed by inorganic hexafluorosilicate anions, SiF<sub>6</sub><sup>2-</sup>, and heterocyclic organic linkers. SIFSIX-1-Cu (1 = 4,4'-bipyridine) shows an ultrahigh SO<sub>2</sub> adsorption capacity of 11.0 mmol g<sup>-1</sup> at 298K and 1 bar owing to its unique pore chemistry, which enables the absorption of four SO<sub>2</sub> molecules per unit cell owing to S<sup>δ+</sup>⋯F<sup>δ-</sup> and O<sup>δ-</sup>⋯H<sup>δ+</sup> interactions. SIFSIX-2-Cu-i exhibits high SO<sub>2</sub> capacity at low pressures and SO<sub>2</sub> selectivities of 86–89, confirming its potential in removing trace SO<sub>2</sub> from gas mixtures.<sup>48</sup> Very recently, the zirconium-based MFM-601 was reported to show the highest SO<sub>2</sub> uptake capacity.

### **5.e. Removal of carbon monoxide(CO) gas by using MOFs:<sup>28,49,50</sup>**

MOFs have also been considered for removal of CO via adsorption. The performance of the M-MOF-74 (a.k.a. M-CPO-27; M = Ni<sup>2+</sup>, Co<sup>2+</sup>, Fe<sup>2+</sup>, Mg<sup>2+</sup>, Mn<sup>2+</sup>, Zn<sup>2+</sup>) series has been extensively studied, and the Ni, Co, and Fe analogues have been shown to take up nearly one CO molecule per open metal site.<sup>28</sup> CO uptake capacities are reported to be high as 6 mmol g<sup>-1</sup> in the case of Fe-MOF-74. Also binding energies more than 50 kJ mol<sup>-1</sup> are reported for Ni-

MOF-74. Recently, Long *et al.* reported on an Fe-triazolate based MOF where high-spin  $\text{Fe}^{2+}$  centers are converted to low spin  $\text{Fe}^{2+}$  centers upon CO exposure.<sup>49</sup> Due to the high affinity of the framework towards CO gas, significant CO uptake is possible at very low pressures. Due the  $\pi$ -acidity of CO, very high selectivities for CO over other gases such as  $\text{CO}_2$ ,  $\text{O}_2$ ,  $\text{N}_2$  and  $\text{C}_2\text{H}_4$  can be achieved. A  $\text{Cu}^{2+}$  based MOF (PCP-2) that undergoes a structural change when the CO partial pressure is above 0.05 bar at 120 K and shows a steep uptake in the CO isotherm.<sup>50</sup> Analyses revealed that CO binding facilitates further accommodation of CO molecules in a self-accelerating sorption manner and therefore results in very high selectivity of CO over  $\text{N}_2$ . PCP-2 (Purkinje cell protein-2) can take up 2.1 CO molecules per  $\text{Cu}^{2+}$  site at 0.8 bar and 120 K. Importantly, PCP-2 can be recovered in its original form upon CO removal.

### **5.f. Removal of Nitric oxide(NO) gas by using MOFs:**<sup>8,51,52</sup>

Separation of hazardous gas, NO from gas mixtures is very important, and MOFs with pores compatible with the kinetic diameter of these gas could be useful for this purpose. "MOFs have been used for ultrahigh selectivity of NO gas over other gases, for example Cu-SIP-3 and  $\text{Zn}(\text{TCNQ-TCNQ})(\text{bipy})$ ."<sup>8,51</sup> Usually these two MOFs do not absorb gases like Ar,  $\text{N}_2$ ,  $\text{CO}_2$  etc, are nonporous in nature. But above gate-opening pressure they take up NO gas. On reduction of the pressure, the desorption path is not like adsorption, due to strong coordination to coordinatively unsaturated metal sites (CUMs) in the case of Cu-SIP-3, while for  $[\text{Zn}(\text{TCNQ-TCNQ})(\text{bipy})]$ , charge transfer plays a crucial role for high NO capture. Ni- and Co-MOF-74 also show very high NO uptake ( 7.0 mmol NO per g of activated material) at room temperature.<sup>52</sup>

## **6.FUTURE SCOPE**

The knowledge about metal organic frameworks is growing rapidly during recent few years but there are still significant gaps in the completeness of our understanding of their structure, stability and properties. Detailed investigations on factors responsible for destruction of crystal structure of certain MOFs with time stability and decomposition mechanism have still not been carried out systematically. There are some reports on application of MOFs in toxic gases separation from environment. MOFs can be explored for such application . Detailed toxicological investigation should be carried out commercialization of such products.

## **7.Conclusion**

In this review article, we have discussed various synthetic methods of MOFs along with their applications. Different methods lead to the MOFs having different properties. MOFs introduced a huge number of applications including gas storage and separation. The use of MOFs with adequate pore size/shape is not enough for an efficient capture of hazardous gases/vapors and other more specific interactions between the harmful adsorbates and the host are desirable. MOF's exceptional design flexibility and structural diversity and the already vast database of MOFs provide an excellent platform to drive future studies in the search of efficient capture systems that afford high capacity, selectivity, stability and reversibility in operation. MOFs with open metal sites could enhance H<sub>2</sub> and CO<sub>2</sub> uptake to reach the DOE targets for the benefit of mankind. Thus, the opportunity to utilize MOF

architectures is limited only by imagination and our ability to prepare and characterize adequately well designed structures.

## **8.ACKNOWLEDGEMENT:**

I would like to thank **Dr. Nabanita Saha Chowdhury** for her valuable support and suggestions which have helped me immensely to complete this review work.

I would also like to thank my friends for helping me with this work.

I would also like to thank SCOTTISH CHURCH COLLEGE DEPARTMENT OF CHEMISTRY for providing me an opportunity to work in this review.

## **9.REFERENCES:**

1. Han. X., Yang. S., Schroder. M. Porous metal–organic frameworks as emerging sorbents for clean air. *Review. 2019. Volume 3.*
2. Barea. E., Montoro. C., Navarro. J. A. R., Toxic gas removal-metal–organic frameworks for the capture and degradation of toxic gases and vapours. *Chem. Soc. Rev., 2014, 43, 5419.*

3. Stock. N., Biswas. S., Synthesis of Metal-Organic Frameworks (MOFs): Routes to Various MOF Topologies, Morphologies, and Composites. |*Chem. Rev.* 2012, 112, 933–969.
4. Butova. V. V., Soldatov. M. A., Guda. A. A., Lomachenko. K. A., Lamberti. C., Metal-organic frameworks: structure, properties, methods of synthesis and characterization. *Russ. Chem. Rev.* 85 (3) 280-307 (2016).
5. Kokotailo. G. T., Lawton. S. L., Olson. D. H., Meier. W. M., Structure of synthetic Zeolite ZSM-5. *Nature (London)* 272 437 (1978).
6. Davis. M. E., Lobo. R. F., Zeolite and molecular sieve synthesis. *Chem. Mater.* 4 756 (1992).
7. Li. S., Huo. F., Metal-Organic Framework Composites: From Fundamentals to Applications. *J. Name.*, 2013, 00, 1-3.
8. Dey. C., Kundu. T., Biswas. B. P., Mallick. A., Banerjee. R., Crystalline metal-organic frameworks (MOFs): synthesis, structure and function. *Acta Cryst.* (2014). B70, 3–10.
9. Jiao. L., Seow. J. R. Y., Skinner. W. S., Wang. Z. U., Jiang. H-L., Metal-organic frameworks: Structure and functional applications. *Materials Today. Volume xxx.* 2018.
10. Yan. B., Yan. C., Dahl. D., SYNTHESSES, STRUCTURES, AND PROPERTIES OF METAL-ORGANIC FRAMEWORKS. *TopSCHOLAR.* 5-2015.
11. Chavan. S., Vitillo. J. G., Gianolio. D., Zavorotynska. O., Civalleri. B., Jakobsen. S., Nilsen. M. H., Valenzano. L., Lamberti. C., Lillerud. K. P.,

Bordiga. S., H<sub>2</sub>storage in isostructural UiO-67 and UiO-66 MOFs. *Phys. Chem. Chem. Phys.* . 14 1614 (2012).

12. Cavka. J. H., Jakobsen. S., Olsbye. U., Guillou. N., Lamberti. C., Bordiga. S., Lillerud. K. P., A new zirconium inorganic building brick forming metal organic frameworks with exceptional stability. *J. Am. Chem. Soc.* . 130 13850 (2008).

13. Valenzano. L., Civalleri. B., Chavan. S., Bordiga. S., Nilsen. M. H., Jakobsen. S., Lillerud. K. P., Lamberti. C., Disclosing the Complex Structure of UiO-66 Metal Organic Framework: A Synergic Combination of Experiment and Theory. *Chem. Mater.* . 23 1700 (2011).

14. Hessel, V.; Löwe, H., Microchemical Engineering: Components, Plant Concepts User Acceptance – Part I. *Chemical Engineering & Technology.* 2003, 26 (1), 13-24.

15. Woellner. M., Housdrof. S., Klein. N., Mueeler. P., Smith. M. W., Kaskel. S., Adsorption and Detection of Hazardous Trace Gases by Metal–Organic Frameworks. *Adv. Mater.* 2018, 1704679.

16. World Health Organization, *Air Quality Guidelines for Europe*, WHO Regional Office for Europe, Copenhagen 2000.

17. Fromme. H., Debiak. M., Sagunski. H., Röhl. C., M. Craft., Gehring. M. K., The German approach to regulate indoor air Contaminants. *International Journal of Hygiene and Environmental Health.* 222 (2019) 347-354.

- 18.** U.S. Environmental Protection Agency/National Institute for Occupational Safety and Health, *Building Air Quality: A Guide for Building Owners and Facility Managers*, U.S. Government Printing Office, Washington, DC 1991.
- 19.** Hincal. F., Erkekoglu. P., Toxic Industrial Chemicals (TICs) – Chemical Warfare Without Chemical Weapons. *FABAD J. Pharm. Sci.* 2006, 31, 220.
- 20.** NIOSH, *Approved Respiratory Standards: Statement of Standard for Chemical, Biological, Radiological, and Nuclear (CBRN) Full Facepiece. Air Purifying Respirator (APR) 2014.*
- 21.** Ghanbari. T., Abnisa. F., Daud. W. M. A. W., A Review on Production of Metal Organic Frameworks (MOF) for CO<sub>2</sub> Adsorption. *Journal Pre-proofs.* 2019.
- 22.** Yang, R. T. (2003). *Adsorbents: fundamentals and applications*: John Wiley & Sons.
- 23.** King, C. J. (2013). *Separation processes*: Courier Corporation.
- 24.** Rouquerol, J., Rouquerol, F., Llewellyn, P., Maurin, G., & Sing, K. S. (2013). *Adsorption by powders and porous solids: principles, methodology and applications*: Academic press.
- 25.** Yang, R., Gas Separation by Adsorption Progress. In: Butterworth, Boston.1987.
- 26.** Yang, R. T. *Adsorbents: fundamentals and applications*: John Wiley & Sons. (2003).
- 27.** Li, J.-R., Kuppler, R. J., & Zhou, H.-C. (2009). Selective gas adsorption and separation in metal– organic frameworks. *Chem Soc Rev*, 38(5), 1477-1504.



- 28.** Bobbitt. N. S., Mendonca. M. L., Howarth. A. J., Islamoglu. T., Hupp. J. T., Farha. O. K., Snurr. R. Q., Metal–organic frameworks for the removal of toxic industrial chemicals and chemical warfare agents. *Chem. Soc. Rev.* 2017.
- 29.** G. W. Peterson, J. B. DeCoste, F. Fatollahi-Fard and D. K. Britt, Engineering UiO-66-NH<sub>2</sub> for toxic gas removal, *Ind. Eng. Chem. Res.*, 2014, 53(2), 701–707.
- 30.** I. Spanopoulos, P. Xydias, C. D. Malliakas and P. N. Trikalitis, A Straight Forward Route for the Development of Metal–Organic Frameworks Functionalized with Aromatic–OH Groups: Synthesis, Characterization, and Gas (N<sub>2</sub>, Ar, H<sub>2</sub>, CO<sub>2</sub>, CH<sub>4</sub>, NH<sub>3</sub>) Sorption Properties, *Inorg. Chem.*, 2013, 52(2), 855–862.
- 31.** D. Yu, P. Ghosh and R. Q. Snurr, Hierarchical modeling of ammonia adsorption in functionalized metal–organic frameworks, *Dalton Trans.*, 2012, 41(14), 3962.
- 32.** J. N. Joshi, E. Y. Garcia-Gutierrez, C. M. Moran, J. I. Deneff, K. S. Walton, *J. Phys. Chem. C* 2017, 121, 3310.
- 33.** N. S. Bobbitt, M. L. Mendonca, A. J. Howarth, T. Islamoglu, J. T. Hupp, O. K. Farha, R. Q. Snurr, *Chem. Soc. Rev.* 2017, 46, 3357.
- 34.** I. Ahmed and S. H. Jung, Adsorptive desulfurization and denitrogenation using metal–organic frameworks, *J. Hazard. Mater.*, 2016, 301, 259–276.

- 35.** X. Peng and D. Cao, Computational screening of porous carbons, zeolites, and metal organic frameworks for desulfurization and decarburization of biogas, natural gas, and flue gas, *AIChE J.*, 2013, 59(8), 2928–2942.
- 36.** L. Hamon, C. Serre, T. Devic, T. Loiseau, F. Millange, G. Férey and G. D. Weireld, Comparative study of hydrogen sulfide adsorption in the MIL-53(Al,Cr,Fe), MIL-47(V), MIL-100(Cr), and MIL-101(Cr) metal–organic frameworks at room temperature, *J. Am. Chem. Soc.*, 2009, 131(25), 8775–8777.
- 37.** C. Petit, B. Mendoza and T. J. Bandoz, Hydrogen sulfide adsorption on MOFs and MOF/graphite oxide composites, *ChemPhysChem*, 2010, 11(17), 3678–3684.
- 38.** C. Petit, B. Mendoza, T. J. Bandoz, *ChemPhysChem* 2010, 11, 3678.
- 39.** R.-H. Shi, Z.-R. Zhang, H.-L. Fan, T. Zhen, J. Shanguan, J. Mi, *Appl. Surf. Sci.* 2017, 394, 394.
- 40.** Sumida, K., Rogow, D. L., Mason, J. A., McDonald, T. M., Bloch, E. D., Herm, Z. R., Bae, T.-H. & Long, J. R. (2012). *Chem. Rev.* 112, 724–781.
- 41.** Sakakura, T., Choi, J.-C. & Yasuda, H. (2007). *Chem. Rev.* 107, 2365– 2387.
- 42.** Fonseca. J., Choi. Sunho., Synthesis of a novel amorphous metal organic framework with hierarchical porosity for adsorptive gas separation. *Microporous and Mesoporous Materials* 310 (2021) 110600 .

43. Han, X., Yang, S., Schroder, M. Porous metal–organic frameworks as emerging sorbents for clean air. *Review*. 2019. Volume 3.
44. Britt, D., Tranchemontagne, D. & Yaghi, O. M. Metal-organic frameworks with high capacity and selectivity for harmful gases. *PNAS* **105**, 11623–11627 (2008).
45. Glover, T. G., Peterson, G. W., Schindler, B. J., Britt, D. & Yaghi, O. M. MOF-74 building unit has a direct impact on toxic gas adsorption. *Chem. Eng. Sci.* **66**, 163–170 (2011).
46. DeCoste, J. B., Demasky, T. J., Katz, M. J., Farha, O. K. & Hupp, J. T. A. UiO-66 analogue with uncoordinated carboxylic acids for the broad-spectrum removal of toxic chemicals. *New J. Chem.* **39**, 2396–2399 (2015).
47. Yang, S. et al. Irreversible network transformation in a dynamic porous host catalyzed by sulfur dioxide. *J. Am. Chem. Soc.* **135**, 4954–4957 (2013).
48. Cui, X. et al. Ultrahigh and selective SO<sub>2</sub> uptake in inorganic anion-pillared hybrid porous materials. *Adv. Mater.* **29**, 1606929 (2017).
49. D. A. Reed, D. J. Xiao, M. I. Gonzalez, L. E. Darago, Z. R. Herm, F. Grandjean and J. R. Long, Reversible CO Scavenging via Adsorbate-Dependent Spin State Transitions in an Iron(II)–Triazolate Metal–Organic Framework, *J. Am. Chem. Soc.*, 2016, 138(17), 5594–5602.
50. H. Sato, W. Kosaka, R. Matsuda, A. Hori, Y. Hijikata, R. V. Belosludov, S. Sakaki, M. Takata and S. Kitagawa, Self-Accelerating CO Sorption in a Soft Nanoporous Crystal, *Science*, 2014, 343(6167), 167–170.

- 51.** Shimomura, S., Higuchi, M., Matsuda, R., Yoneda, K., Hijikata, Y., Kubota, Y., Mita, Y., Kim, J., Takata, M. & Kitagawa, S. (2010). *Nat. Chem.* 2, 633–637.
- 52.** McKinlay, A. C., Xiao, B., Wragg, D. S., Wheatley, P. S., Megson, I. L. & Morris, R. E. (2008). *J. Am. Chem. Soc.* 130, 10440–10444.
- 53.** Lee, Y. R., Kim, J., Ahn, W. A., Synthesis of metal-organic frameworks: A mini review. *Korean J. Chem. Eng.*, 30(9), 1667-1680 (2013).

**CATALYTIC APPLICATION OF IRON –N**  
**HETEROCYCLIC CARBENE COMPLEXES.**

**Scottish Church College, Kolkata, 2021.**

**ROLL NO: 223/CEM/191016.**

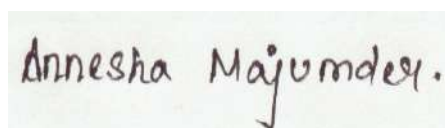
**REGISTRATION NO: 613-1221-1465-15.**

**Special Paper:SI44.**

**NAME OF CANDIDATE**

**Annesha Majumder**

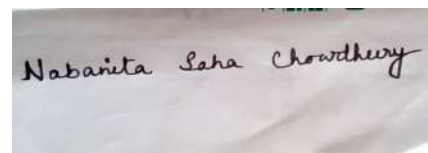
**Signature of Candidate**



**NAME OF THE SUPERVISOR**

**Nabanita Saha Chowdhury**

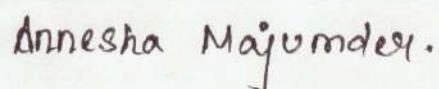
**Signature of Supervisor**



**Project work accomplished in partial fulfilment of M.Sc.  
(Chemistry). Degree of the University under Calcutta  
Scottish Church College Kolkata, 2021.**

## **DECLARATION**

This review work accomplished by the undersigned under supervision of **Dr. Nabanita Saha Chowdhury**. Assistant Professor of Scottish Church College, during 4th and final Semester (April – July 2021 in partial fulfilment of M.Sc CHEMISTRY degree of Scottish Church College under Calcutta University.



Annesha Majumder.

**(Signature of the student)**

**Name: Annesha Majumder.**

**University Roll No: 223/CEM/191016.**

**Registration No: 613-1221-1465-15.**

**College Roll No: 19 PG- C- 26.**

**Date:**

**Place: Scottish Church College, Kolkata .**

<b><u>Contents</u></b>	<b><u>page</u></b>
1. Abstract.	5
2. Introduction.	5
3. Catalysis.	5-6
3.1 C-C Bond Formation.	6
3.1.1 Coupling Reaction.	6-13
3.1.2 Allylic Alkylation.	13-15
3.2 C-X Bond Formation.	15
3.2.1 C-B Bond Formation.	15
3.2.2 C-S Bond Formation.	16
3.3 Reduction.	17
3.3.1 Hydrosilylation Reaction.	17-21
3.3.2 Hydrogenation Reaction.	21-22
3.4 Cyclisation Reaction.	22-23
3.5 Polymerisation Reaction.	23-24
3.6 Dehydration Reaction.	24-25
4. Conclusion.	25
5. Acknowledgement.	26
6. References.	26-32

## **PREFACE**

It is both privileged and a formidable challenge for me to write a review on the subject of **“Catalytic Application Of Iron-N Heterocyclic Carbene Complexes.”**

In writing this review different journal published in different scientific magazine has been followed. The emphasis is given on **“Catalytic Application Of Iron-N Heterocyclic Carbene Complexes.”**The review has been thoroughly revised and updated where required with major changes by **Dr. Nabanita Saha Chowdhury**.

I also like to give thank **Dr. Nabanita Saha Chowdhury**, the assistant professor of Scottish Church College, who’s distinguished services has helped me a lot in writing this review.



## **1. Abstract.**

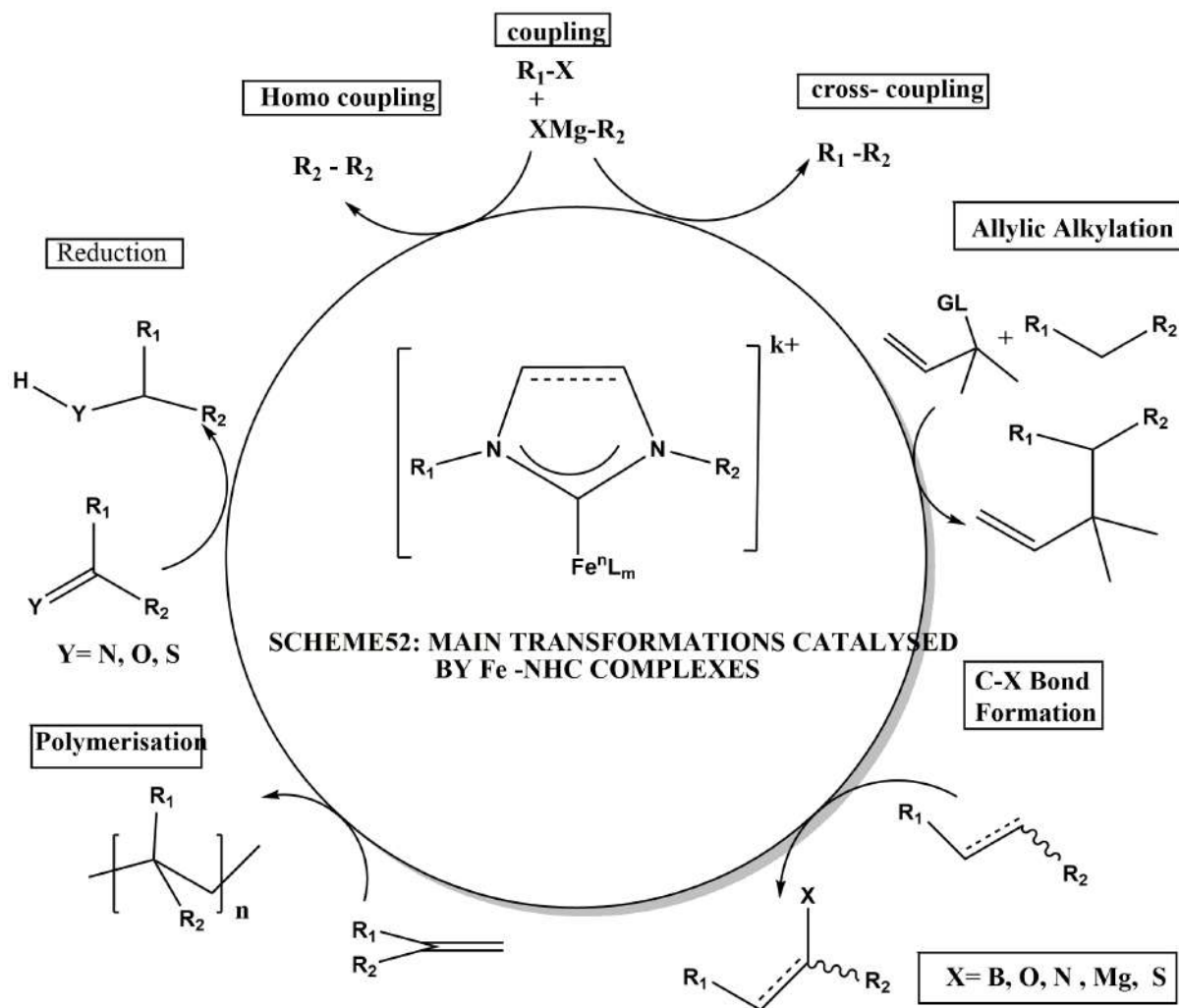
First iron containing NHC complex was synthesised in 1969. First catalytic application of Fe-NHC complexes was reported in early 2000. Since then the catalytic application of these complexes are still not much explored. In this review we will mainly discuss about the different catalytic applications of Fe-NHC complexes. E.g C-C bond formation C-B bond formation , reduction reactions, cyclisation reactions, polymerisation reaction and etc. we will discuss about the various publications on the catalysis of Fe-NHC compounds till date. We will see the use of structurally well defined Fe-NHC complexes and also non coordinated NHC along with Fe precursor i.e in situ generation of Fe-NHC catalyst in various examples.

## **2. Introduction.**

Iron is the most abundant 3d block transition metal in earth crust<sup>1</sup>. Nowadays different catalyst systems are based on rare/heavy transition metals such as : Ru, Rh, Pd, Pt, Ir, Au etc<sup>5</sup>. These are not only expensive but also very toxic as they interact with enzymes, nucleic acid and other biological entities<sup>6</sup>. But on the other hand Fe based catalysts are cheap ,non toxic and environment friendly. Iron is considered as a good candidate for catalysis as it has numerous examples in the field of biology<sup>2</sup>. NHC carbenes are very popular and well known ligands and has wide application in the field of organometallic catalysis. NHC s are neutral sigma donor (2 e) ligands but has no pi acid character. NHC complexes have some advantages, 1. Being a good sigma donor it forms strong bond with metal centres and hence M-NHC complexes are resistant towards decomposition .2. NHC 's are easily accessible and they can be tuned both sterically and electronically very easily. 3. NHC ligands being good sigma donors can stabilise high valent Fe intermediates by increasing the electron density of Fe thus improving its catalytic efficiency.

## **3. Catalysis.**

The first well defined Fe-NHC catalyst for atom transfer radical polymerisation was introduced by the research group of Grubb in the year 2000. Transformations catalysed by Fe-NHC complexes are shown in the **scheme -52**.



## 3.1 C-C Bond Formation :

### 3.1.1 Coupling reactions

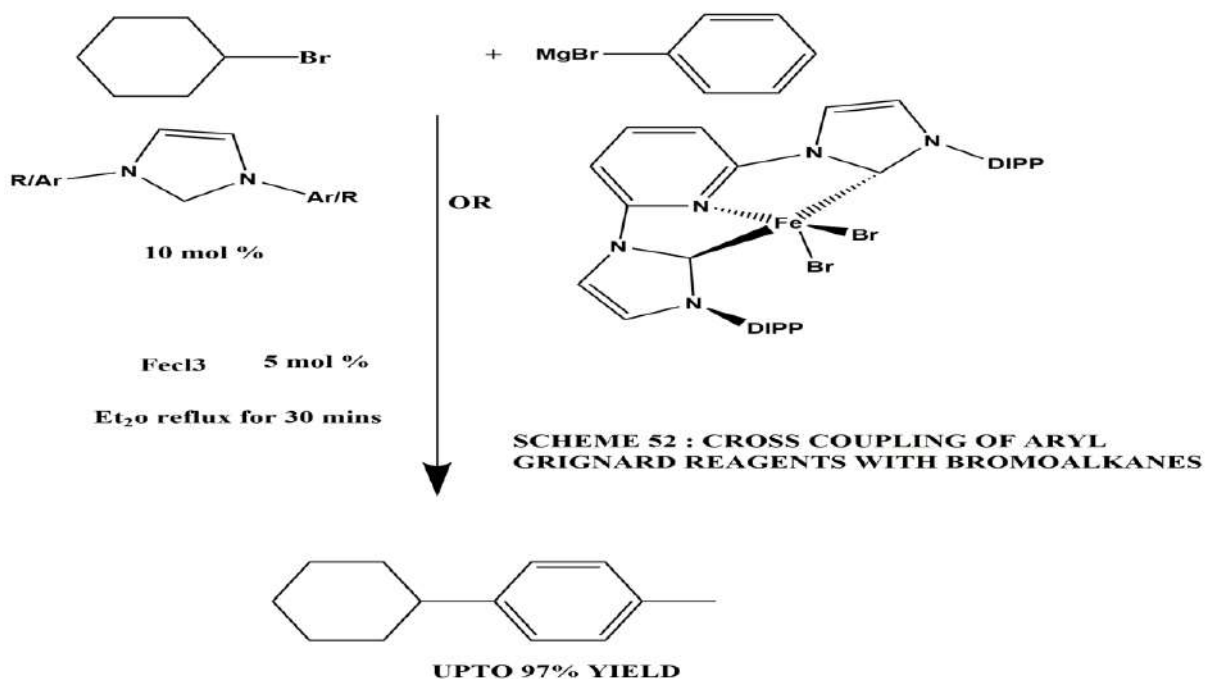
One of the most important type of reactions are cross coupling reactions. Noble prize in Chemistry for 2010 was awarded to Negishi, Suzuki and Heck for their incredible work in the field<sup>121</sup>.

#### Scheme -53 kumada type cross coupling:

##### C(Sp<sup>3</sup>-Sp<sup>2</sup>) bond formation

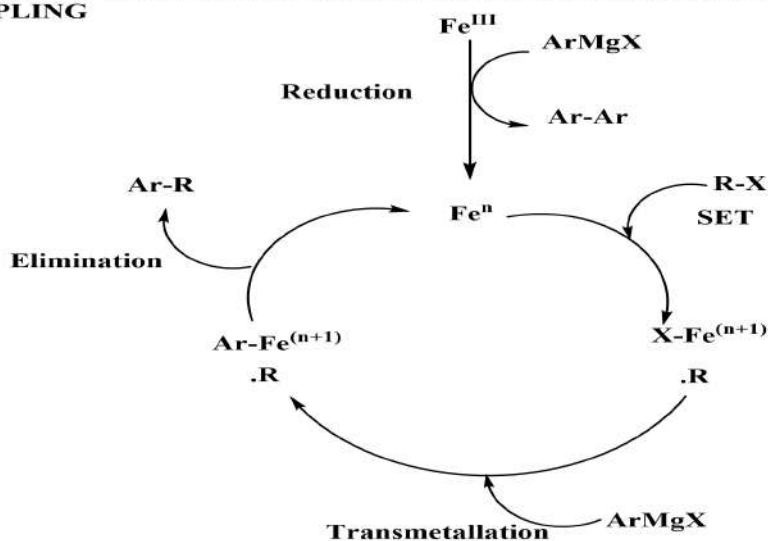
In 2006 Bedford and co-workers first introduced NHC's to the field of Fe catalysed kumada type cross coupling. They performed a reaction between bromocyclohexane and p-tolylmagnesium bromide catalysed by 100a and other NHC Fe catalyst.<sup>62</sup> The NHC's were either generated via in situ deprotonation

or thermal decomposition. For 100a a isolated yield of **94%** was obtained which was quite impressive.

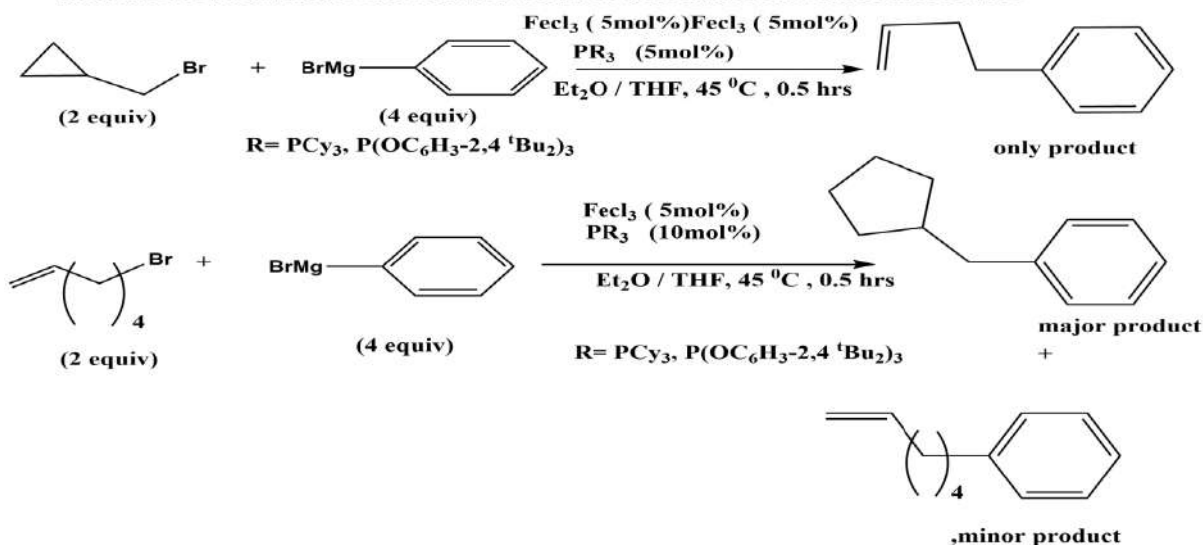


Instead of the **oxidative addition** the authors put forward a mechanism involving radical intermediates based on the previous research works of Kochi, Funstrer and Nakamura.<sup>62</sup>

**SCHEME 54 : SIMPLIFIED REACTION MECHANISM FOR KUMADA TYPE CROSS COUPLING**



**SCHEME 55: CONTROL EXPERIMENTS SUPPORTING A RADICAL PATHWAY**

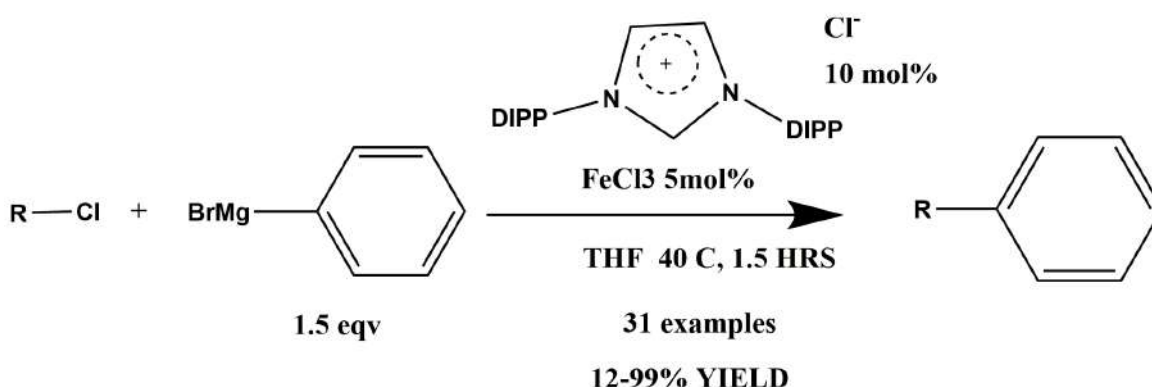


**Scheme 56,57 Cross Coupling Reaction of chloroalkanes**

**With BrMgPh**

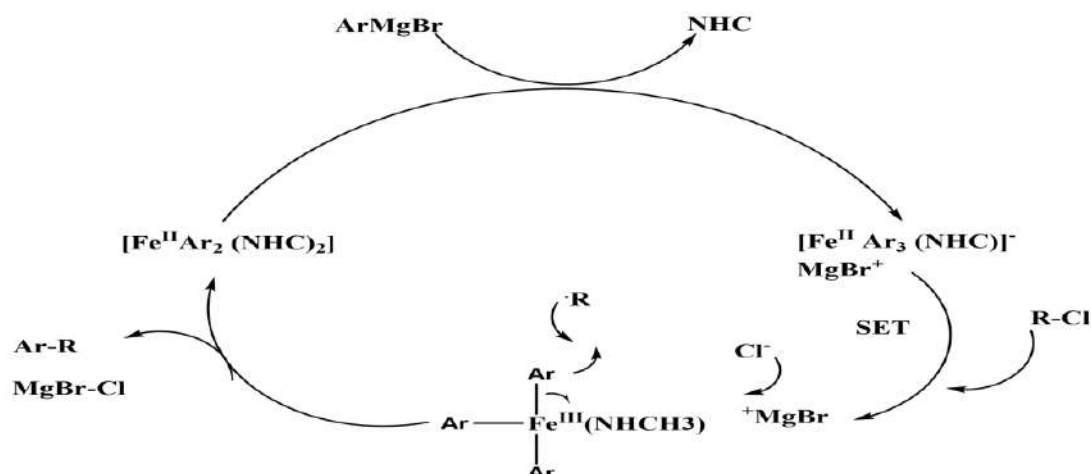
Chloroalkanes are much more difficult substrate to deal with than bromoalkanes as they are selective and result in lower yields. Nakamura and co-workers successfully resulted the cross coupling reactions of not only monochlorinated substrates but also di and tri chlorinated substrates as well.

**SCHEME 56: CROSS COUPLING OF CHLOROALKANES WITH PHENYLMAGNESIUM BROMIDE**



5 eqv of grignard reagent is required for the above scheme . 2 eqv is used for the deprotonation of the ligand precursor and the rest 3 eqv is used for the formation of a Fe (+2) biaryl compound i.e [ Fe Ar<sub>2</sub> (NHC)<sub>2</sub>].

**SCHEME 57: PROSTULATED REACTION MECHANISM FOR KUMADA TYPE CROSS COUPLING WITH SINGLE ELECTRON TRANSFER**

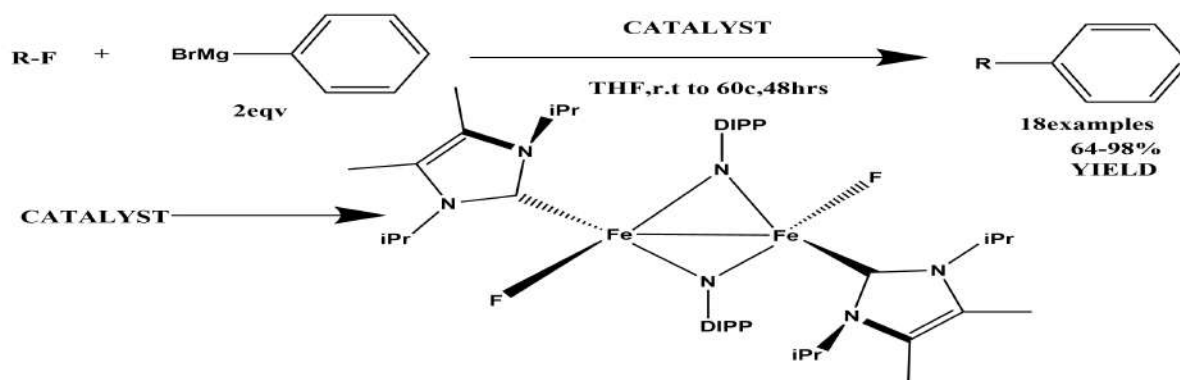


Scientist Meyer and others used biscarbene chelated Fe complexes **64c**, **65b-d**, **66 a-b** to the above transformations, but the yields were comparatively lower. So an idea was developed that biscarbene chelating ligands may not give effective catalysis i.e. higher yields compared to their mono-carbene analogues.<sup>39a, 127</sup>

**Scheme 58, 59 Kumada type coupling of primary alkyl fluorides<sup>41</sup> :**

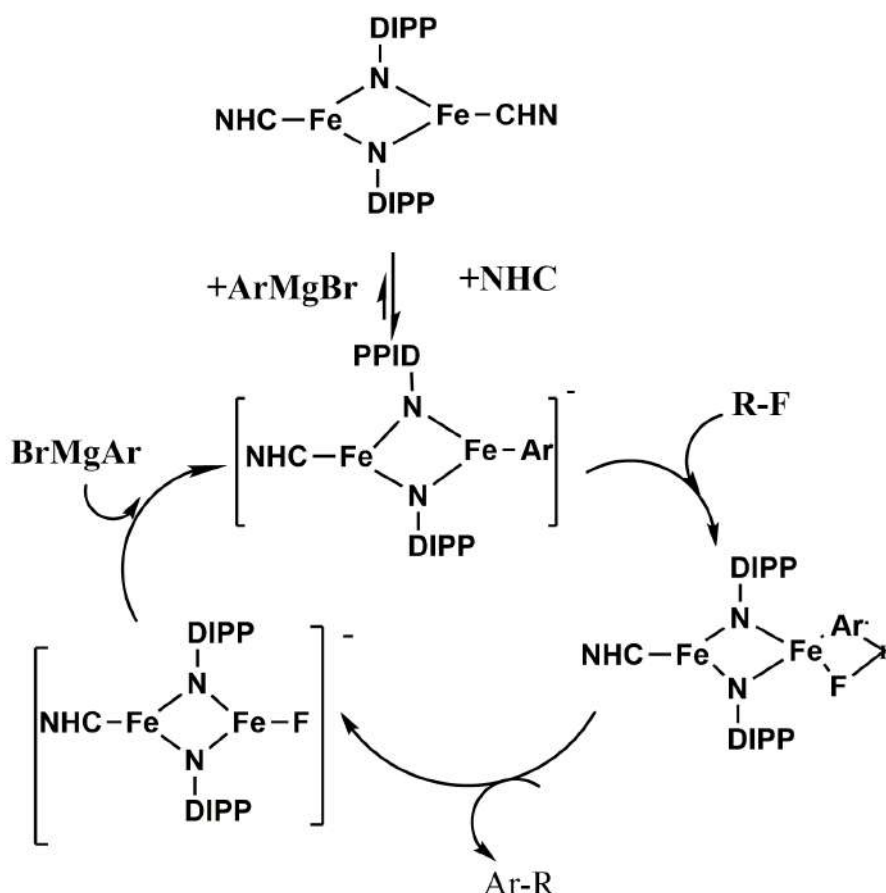
For coupling reactions one of the most challenging substrates are alkyl fluorides. In the year 2012 Scientist Deng and coworkers introduced a Fe–NHC catalyst **48a** which not only gave good yields but also good selectivity. The unique structure of the catalyst i.e. two Fe centres bridged with two imido ligands was the key to the success of the reactions. In spite of this much appreciated result the catalyst system was only applicable to primary alkyl fluorides.<sup>41</sup>

**SCHEME 58: KUMADA TYPE COUPLING OF PRIMARY ALKYL FLUORIDES WITH ARYL GRIGNARD REAGENTS**



Further mechanistic study revealed a **radical mediated pathway**.<sup>41</sup>

**SCHEME 59 : PROPOSED MECHANISM FOR KUMADA TYPE COUPLING OF ALKYL FLUORIDES**



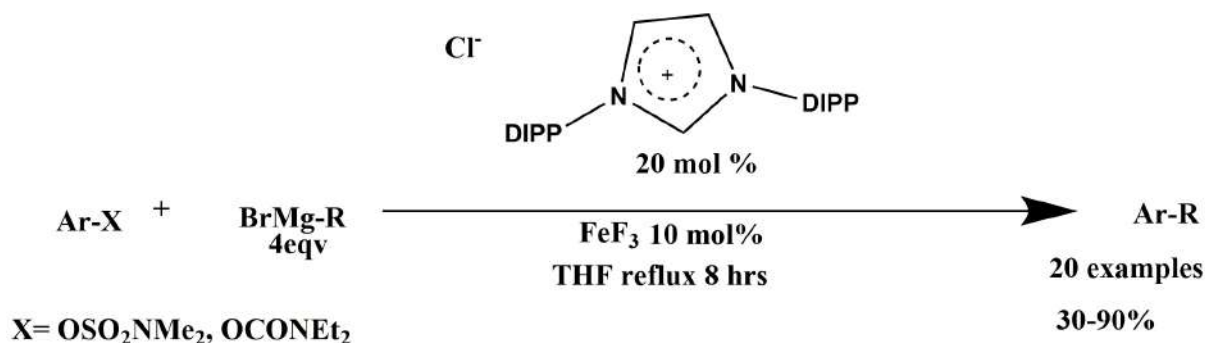
**Scheme 61, Alkyl Grignard coupling with  $\text{FeF}_3$  /NHC as the catalyst system<sup>129</sup>** : Researchers Cook and Agarwal used  $\text{FeF}_3$  in combination with an NHC precursor as the catalyst system in the coupling reaction of primary and secondary alkyl grignard reagent with aryl sulfamates and tosylates. With the help of this catalyst they achieved higher yields , greater functional group tolerance and high selectivity than previous catalyst systems. The only drawback of this catalyst system is steric factor as with ortho substituted aryl compounds give low yield in the coupling reactions. Isomerisation of secondary grignard reagent is a common

problem in alkyl cross coupling reactions. Depending on the Fe source **branched: linear** product ratio was obtained. 129

<b>Iron Source</b>	<b>Branched :linear</b>
<i>FeCl<sub>3</sub>, Fe(acac)<sub>3</sub>, Fe(otf)<sub>3</sub>, Fe(BF<sub>4</sub>)<sub>2</sub></i>	<i>0.2:1 to 0.9:1</i>
<i>FeF<sub>3</sub></i>	<i>6.5:1</i>

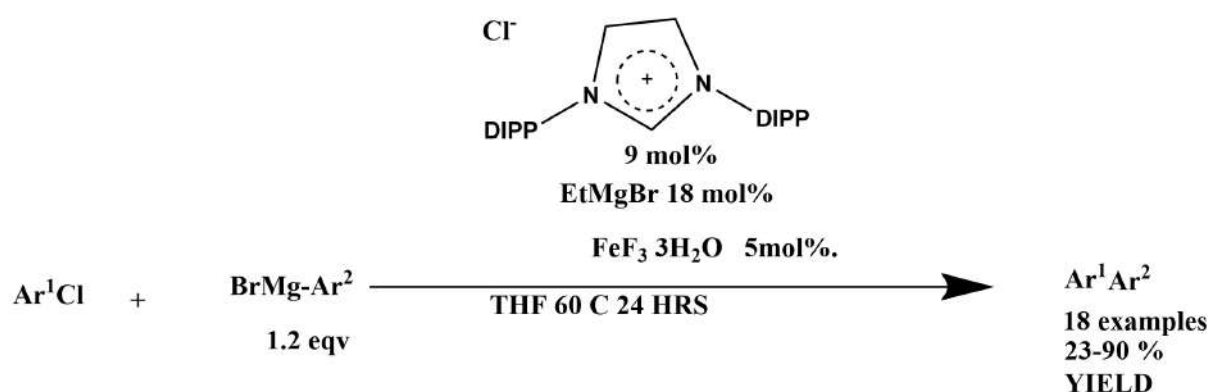
The higher ratio of branched product to linear product was due to very strong coordination of the fluoride, which prevents open coordination sites for  $\beta$  agostic interactions and hence slows the isomerisation of the Grignard reagent.

**SCHEME 61: ALKYL GRIGNARD COUPLING WITH FeF<sub>3</sub>/ NHC AS THE CATALYST SYSTEM**



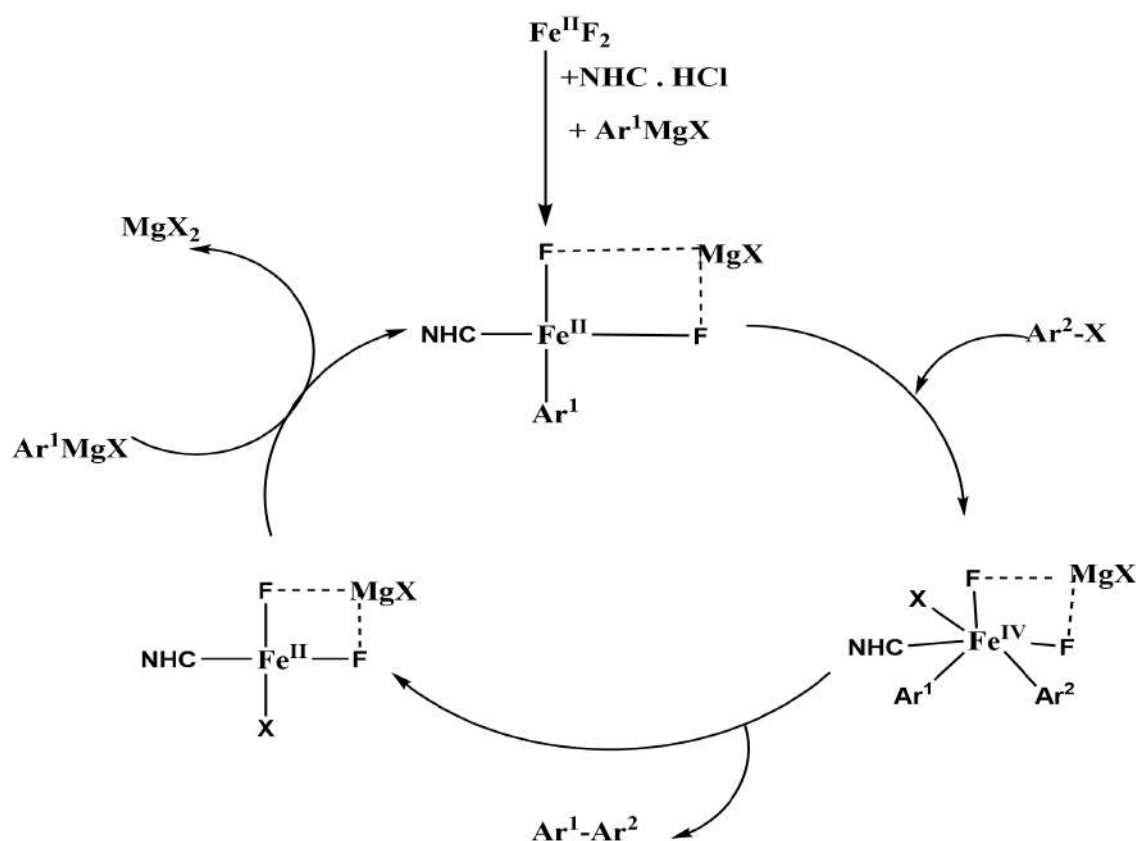
**Scheme 62,63 Aryl-Aryl coupling C(Sp<sup>2</sup>)- C(Sp<sup>2</sup>) bond formation<sup>130</sup>** : scientist Nakamura and coworkers first established Aryl-Aryl coupling i.e C(Sp<sup>2</sup>)-C(Sp<sup>2</sup>) catalysed by Fe NHC complexes. Previously the main problem scientists faced while dealing with aryl-aryl coupling was the formation of homocoupling products. They overcame this problem by using the iron fluoride salts or addition of KF+ FeCl<sub>3</sub>. EtMgBr was used to deprotonate the ligand precursor i.e a saturated DIPP substituted imidazolium chloride.<sup>130</sup>

**SCHEME 62: ARYL-ARYL COUPLING**



Later different metal fluoride catalysts were established<sup>131</sup>. Iron fluoride catalyst systems showed much promise in coupling of aryl chlorides, Cobalt for hetero aromatic coupling, Nickel for aryl bromides and sterically hindered substrates.<sup>131</sup>

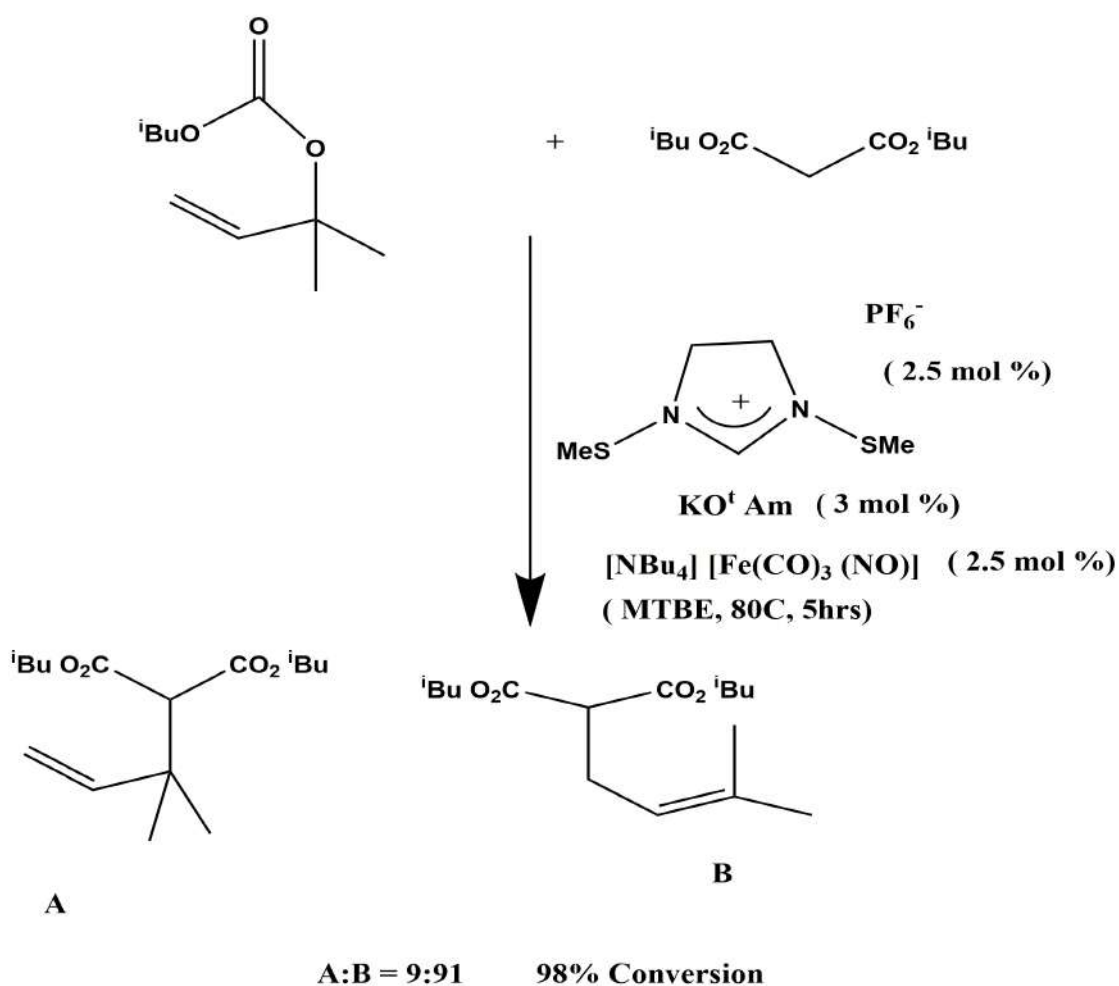
**SCHEME 63: PROPOSED METALATE MECHANISM IN ARYL ARYL COUPLING**





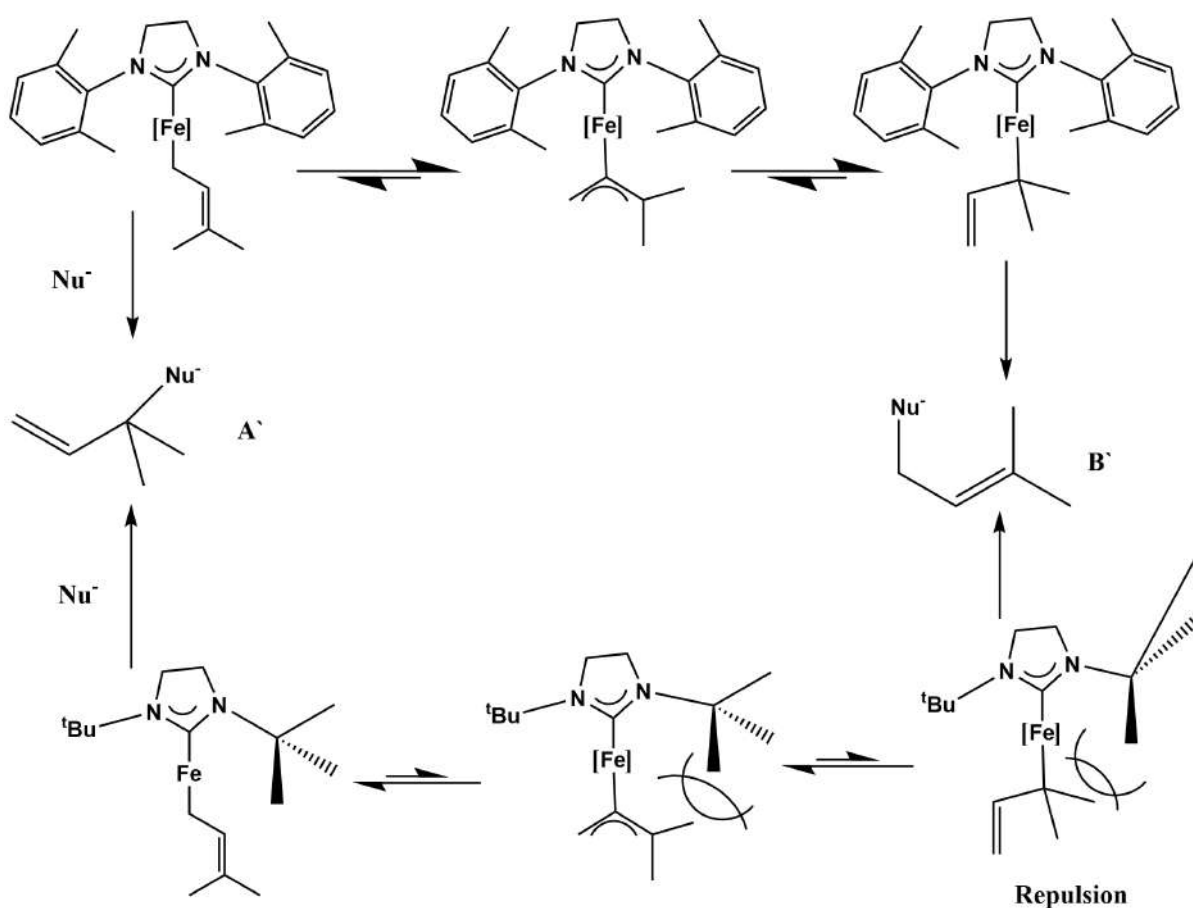
**3.1.2 Allylic Alkylation<sup>133,135,136,138</sup>** : Transition metals like Mo, W, Pd, Pt, Ru, Ir, Fe can facilitate this type of catalysis. Initial trials for allylic alkylation with these transition metal catalysts resulted in low selectivity, and high catalyst loading. Scientist Plietker and other's addressed this issue of regioselectivity by using  $[\text{NBu}_4][\text{Fe}(\text{CO})_3(\text{NO})][(\text{TBA})\text{Fe}]$  along with other ligands which resulted in higher yields. A significantly improved synthetic method was obtained by the use of NHC ligands in the later parts of 2000. In the scheme 67 an allyl carbonate was reacted with a Michael donor which gave two products A and B.<sup>136</sup>

**SCHEME 67 : ALLYLIC ALKYLATION CATALYSED BY (TBA)Fe/ NHC**



Product A was formed due to ipso substitution and B is regioisomer. B was formed via a  $\sigma$ - $\pi$ - $\sigma$  isomerisation mechanism which is a rare case in the field of iron catalysed allylic alkylation reaction. Various parameters like reaction condition, solvent, stoichiometry, which may influence the product formation was investigated and were optimized. It was seen that with increasing steric demand of NHC substituents the isomerisation was inhibited, which in turn increase the non isomeric ipso substituted product A. It was also observed that if we increase the reactivity of the nucleophile (Michael donor) formation of the ipso substituted product was high as isomerisation is a comparatively slow process. It was also observed that the  $\sigma$ -allyliron species can react via two different routes **Scheme-68**

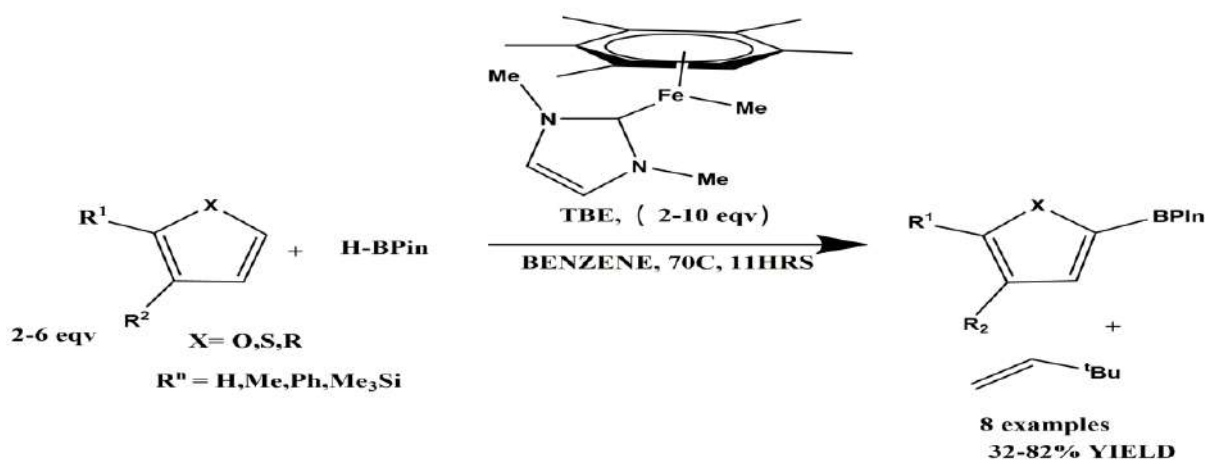
**SCHEME 68: MECHANISTIC PROPOSAL FOR ALLYLIC ALKYLATION**



A' was formed by a direct substitution reaction. If the steric demand of the coordinated ligands allows isomerisation to a  $\pi$  allyl complex the formation of the regiomer  $\sigma$  allyl complex yields B'. When we use a planar aryl substituent on the NHC ligand B is facilitated. But if the substituent is a tert butyl group then the formation of A was favoured due to steric demand. Based on this results Plietker and coworkers used various  $\pi$  allyliron complexes which improved catalytic activity and the product formation was controlled by a  $\pi$  allyl mechanism. After many trials with different catalytic system the catalyst load can be reduced to as low as 1 mol %. Several allyl carbonates were substituted with impressive yields with various nucleophiles. This same group later in 2012 achieved a regioselective allylic alkoxylation. Best results were obtained with (TBA) Fe as the catalyst precursor along with diphenyl benzimidazolium salt.<sup>136,138</sup>

**3.2.1 C-B Bond Formation<sup>88,140</sup>:** Scientist's Tatsumi, Ohki and Hantaka in the year 2010 reported selective Fe-NHC catalysed borylation of furans and thiophenes. Methylated piano stool complex **190** was used in a reaction between the employed heterocycle and pinacol borane giving moderate to high yields (**Scheme-73**).

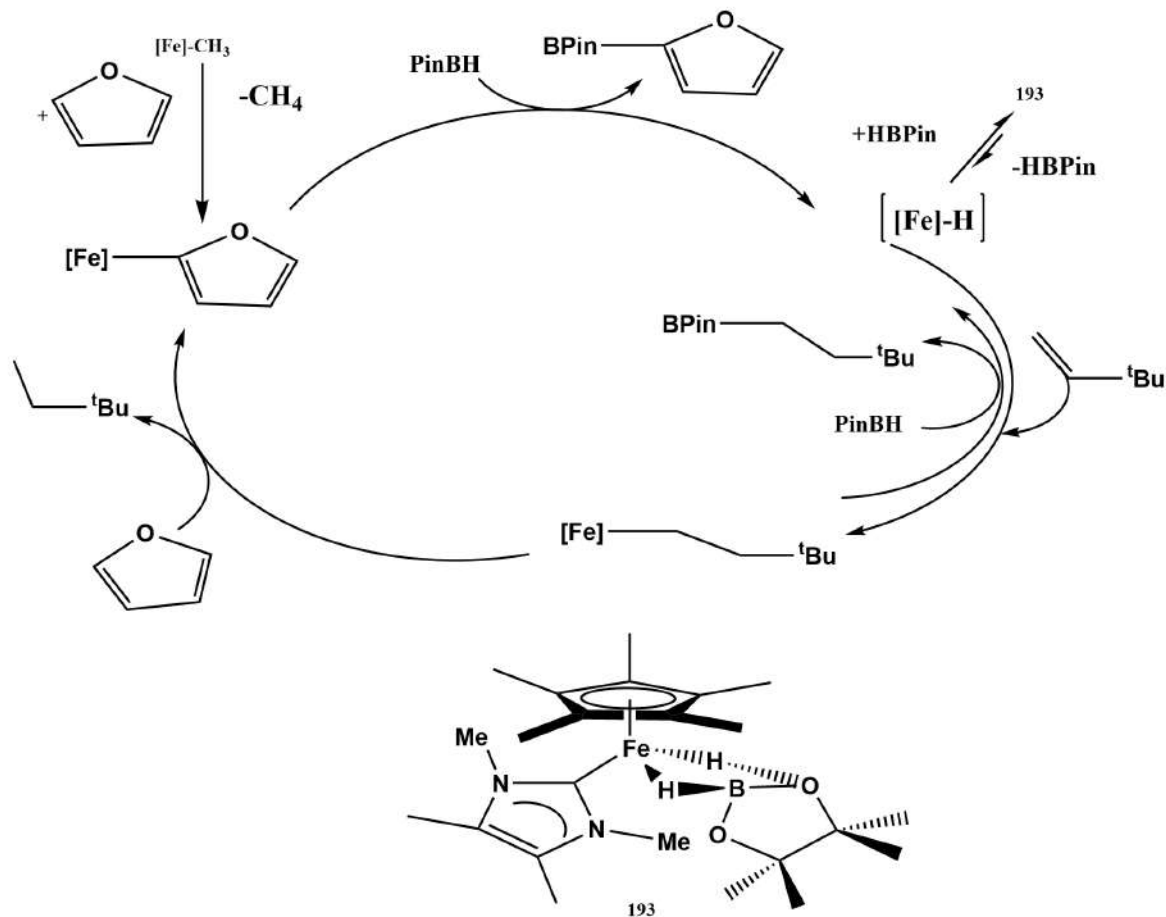
**SCHEME 73: Fe-NHC CATALYSED BORYLATIONS OF FURANS AND THIOPHENES**



The mechanism for this reaction is depicted in the **scheme 74** below. At first the [Fe]-CH<sub>3</sub> (methylated iron complex) activates the 2 position of the heterocycle and CH<sub>4</sub> was released. This resulted in the furanyl group coordinating to the Fe center and sequential borylation was followed. The borane stabilizes the Fe-hydrido complex which is formed as an intermediate. The borohydrido complex can also be isolated and characterized. The TBE (tert butyl ethylene) then breaks into the Fe-H bond to form a iron-alkyl intermediate which activates the next heterocycle. The borohydride complex cannot activate the heterocycle as it

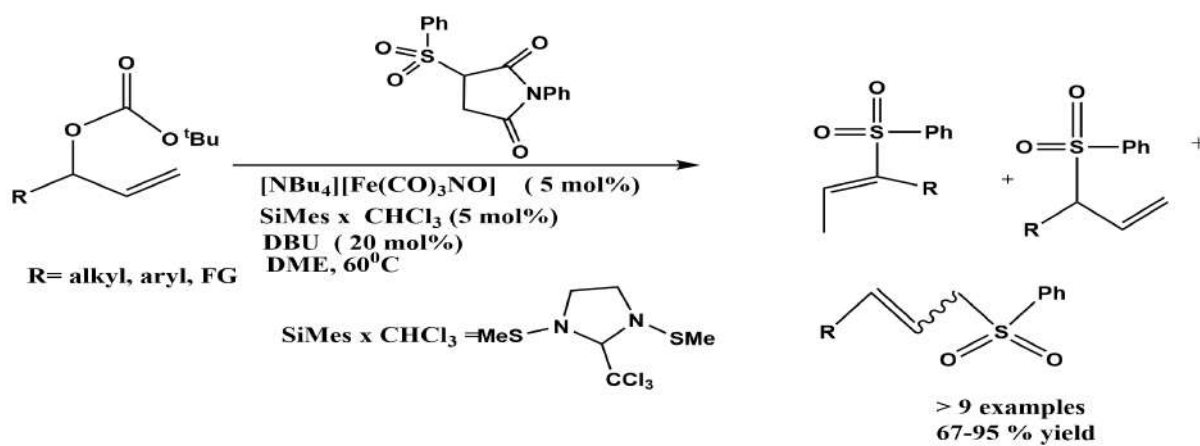
decomposes on heating with an excess of the heterocycle.

**SCHEME 74 : PROSTULATED MECHANISM FOR THE BORYLATION OF FURANS**



**3.2.2 C-S Bond Formation 145**

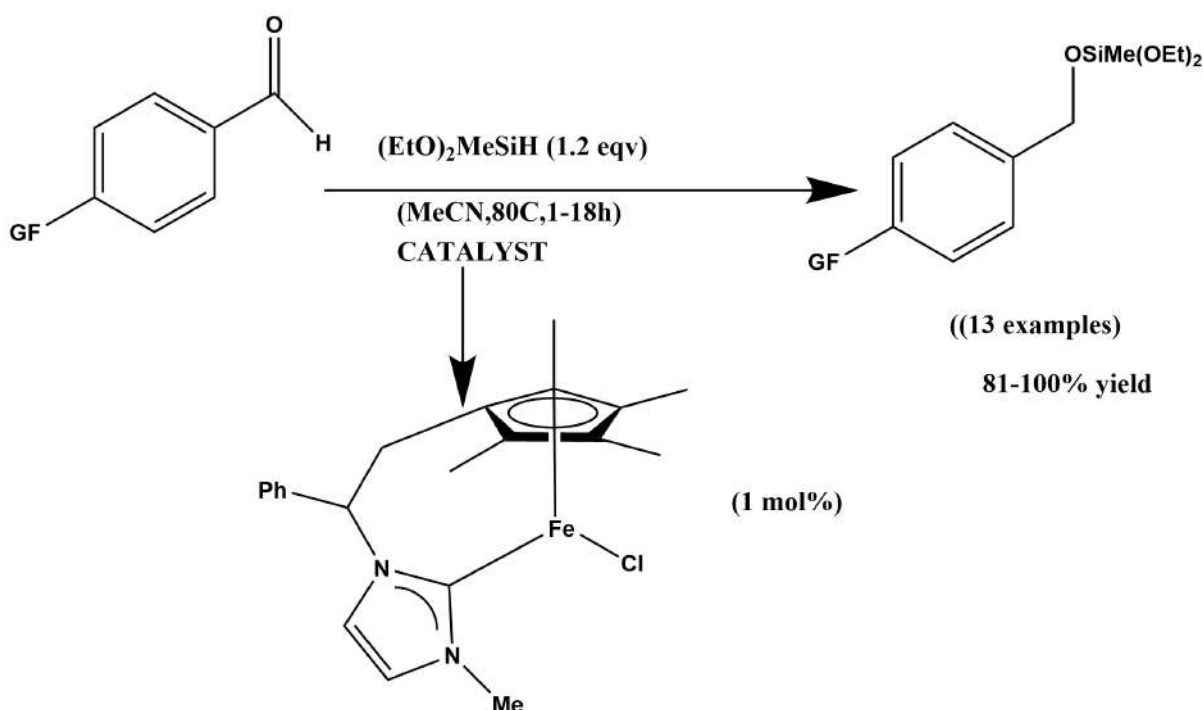
**SCHEME 83: ONE POT SULFONYLATION FOLLOWED BY ISOMERISATION**



**3.3 Reduction 4e, 5a-e, 146 :** selective / specific reduction of double bond bonds is a key step to achieve a synthetic strategy. Rh, Ru, Pd, Pt, Ir, metal based hydrogenation and hydrosilylation is now much in practice instead of inorganic hydridic agents. The first Fe based active catalyst was prepared by the group of Marko ( $[\text{FeH}(\text{Co})_3]$ ) in the year 1980. It was prepared from  $\text{Fe}(\text{Co})_5$  with  $\text{NEt}_3$  as a solvent and base along with hydrogen pressure. Later Chirik and coworkers synthesized Fe NNN pincer compounds which showed greater catalytic efficiency i.e TOF than Wilkinson catalyst. ( $\text{Rh}(\text{PPh}_3)_3$ ).

**3.3.1 Hydrosilylation Reaction Of C=O Bonds (Scheme 84)<sup>92</sup> :** The first example in this field was shown using a Fe NHC piano tool complex (215) by Royo and coworkers. They exemplified the hydrosilylation of several activated Benzaldehydes. It was observed that Para-aryl substituted aldehydes were much successful as substrates as they give higher yields but unfortunately alkyl substituted aldehydes or ketones were not converted.<sup>92</sup>

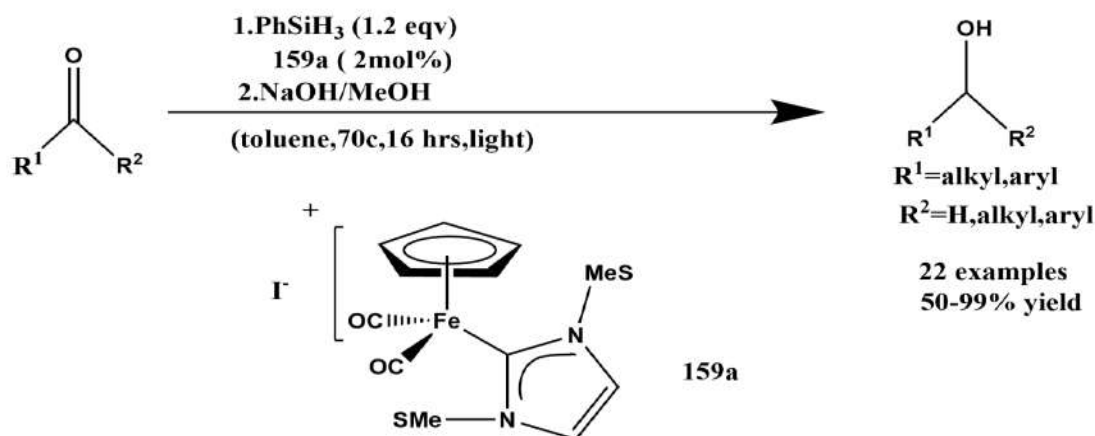
**SCHEME 84: HYDROSILYLATION OF BENZALDEHYDE DERIVATIVES**



**First Fe-NHC catalysed reduction of ketones and aldehydes via hydrosilylation (Scheme 85)<sup>82c</sup>:**

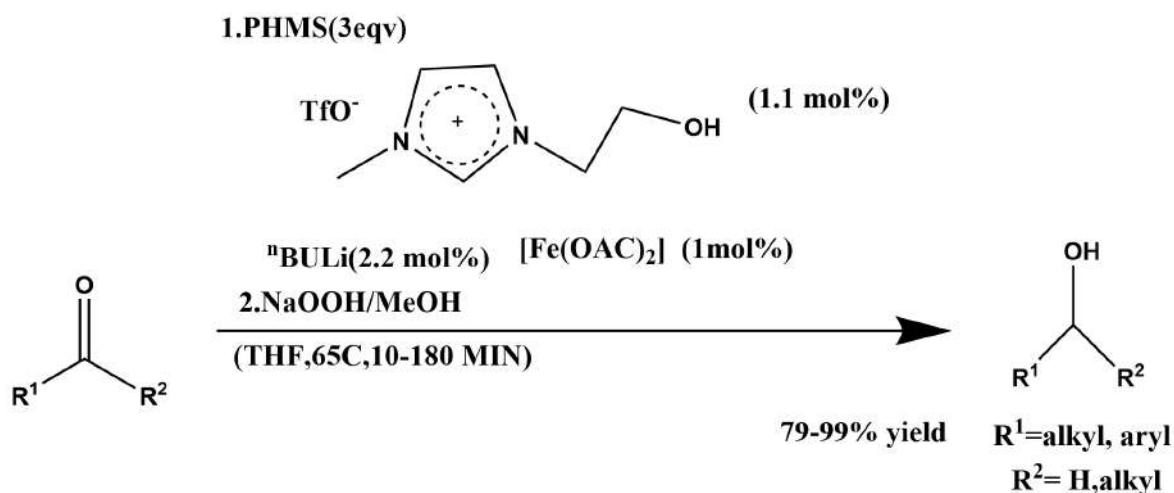
Darcel and coworkers used Fe-NHC piano stool complexes 159a and 165a for the reduction of aldehydes and ketones. They published a paper in 2011.

**SCHEME 85: FIRST Fe-NHC CATALYSED REDUCTION OF KETONES AND ALDEHYDES VIA HYDROSILYLATION**



**Reduction Of Ketones via hydrosilylation with an O-functionalised ligand system ( scheme 89)<sup>151</sup>:**

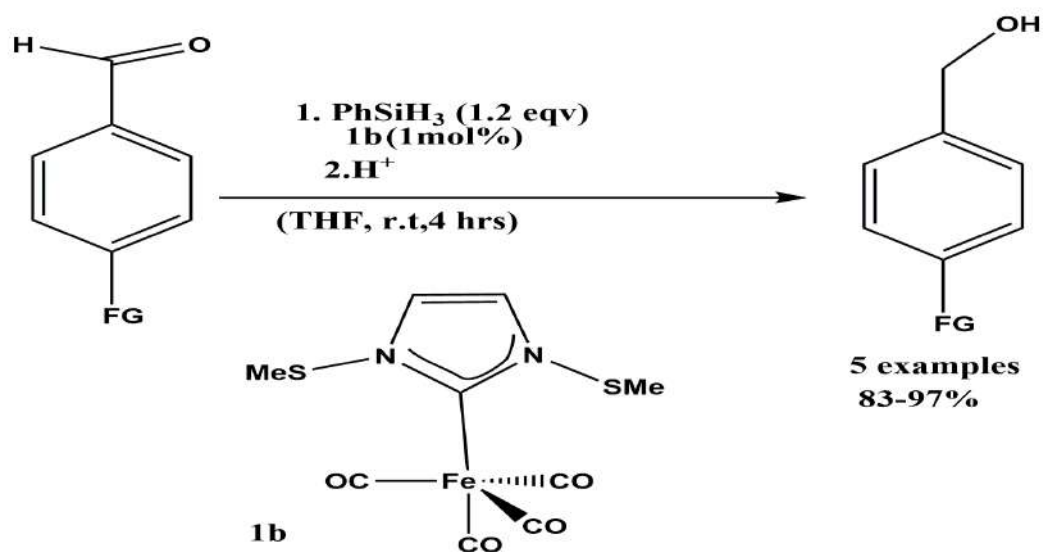
**SCHEME 89: REDUCTION OF KETONES VIA HYDROSILYLATION WITH AN ORTHO FUNCTIONALISED LIGAND SYSTEM**



## Reduction Of Benzaldehyde Derrivatives Via Hydrosilylation

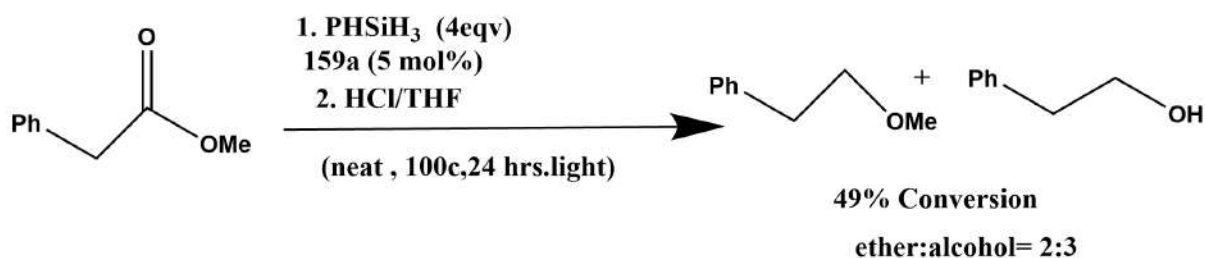
**(scheme 92)<sup>26a</sup>:** Royo and co-workers employed zero valent [ Fe(CO)<sub>4</sub> NHC] complexes **1a to 1d** for the hydrosilylation of the benzaldehyde derivatives. Benzaldehydes containg different functional groups including reducible ones were also converted succesfully by this method.

### SCHEME 92: REDUCTION OF BENZALDEHYDE DERRIVATIVES VIA HYDROSILYLATION



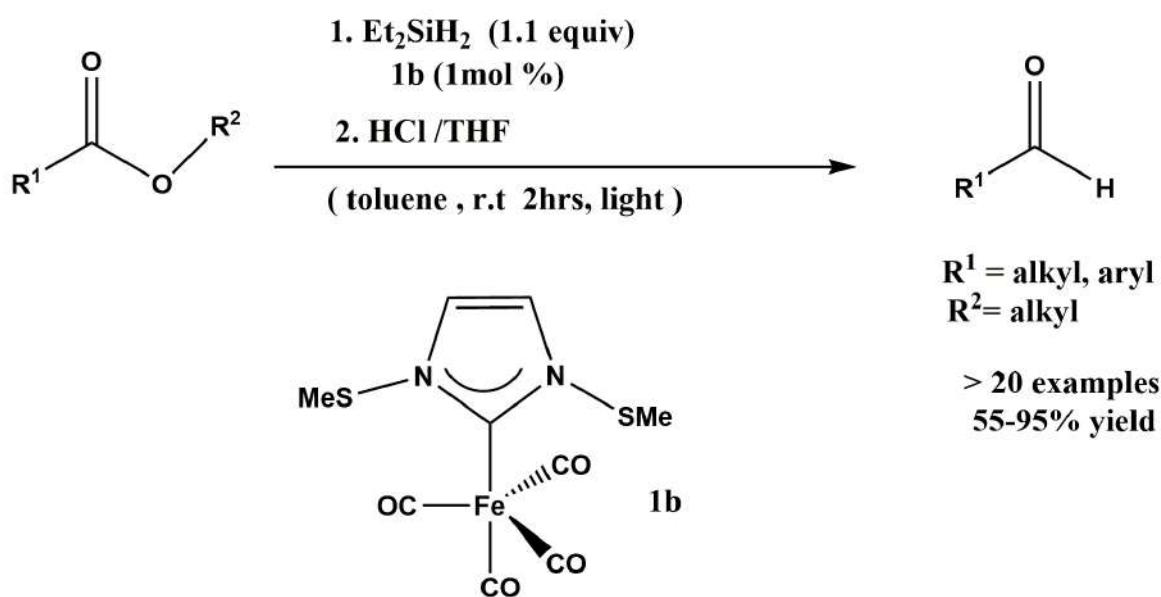
**Reduction Of Esters Via Hydrosylliation (scheme 94)<sup>152</sup>:** Scientists Darcel and coworkers applied a series of piano stool complexes of the type [ Fe (cp) (CO)<sub>2</sub> L] for the hydrosilylation of ester compounds. However they found out later that two products were formed in this reaction alcohol and ether. It was also observed that by varying the ligand system product ratio can also be varied. The **159a** Fe –NHC complex showed far less conversion rate ( 49%) than its tricyclohexyl phosphine analogue (97%). The Fe-NHC complex showed a higher selectivity towards ether whereas, the phosphine analogue preferentially yilded the alcohol as a major product. This method lacked selectivity of products.

**SCHEME 94: REDUCTION OF ESTERS VIA HYDROSILYLATION**



Selective Reduction Of Esters To Aldehydes Via Hydrosilylation  
(scheme 95)<sup>26e</sup>:

**SCHEME 95: SELECTIVE REDUCTION OF ESTERS TO ALDEHYDES VIA HYDROSILYLATION**

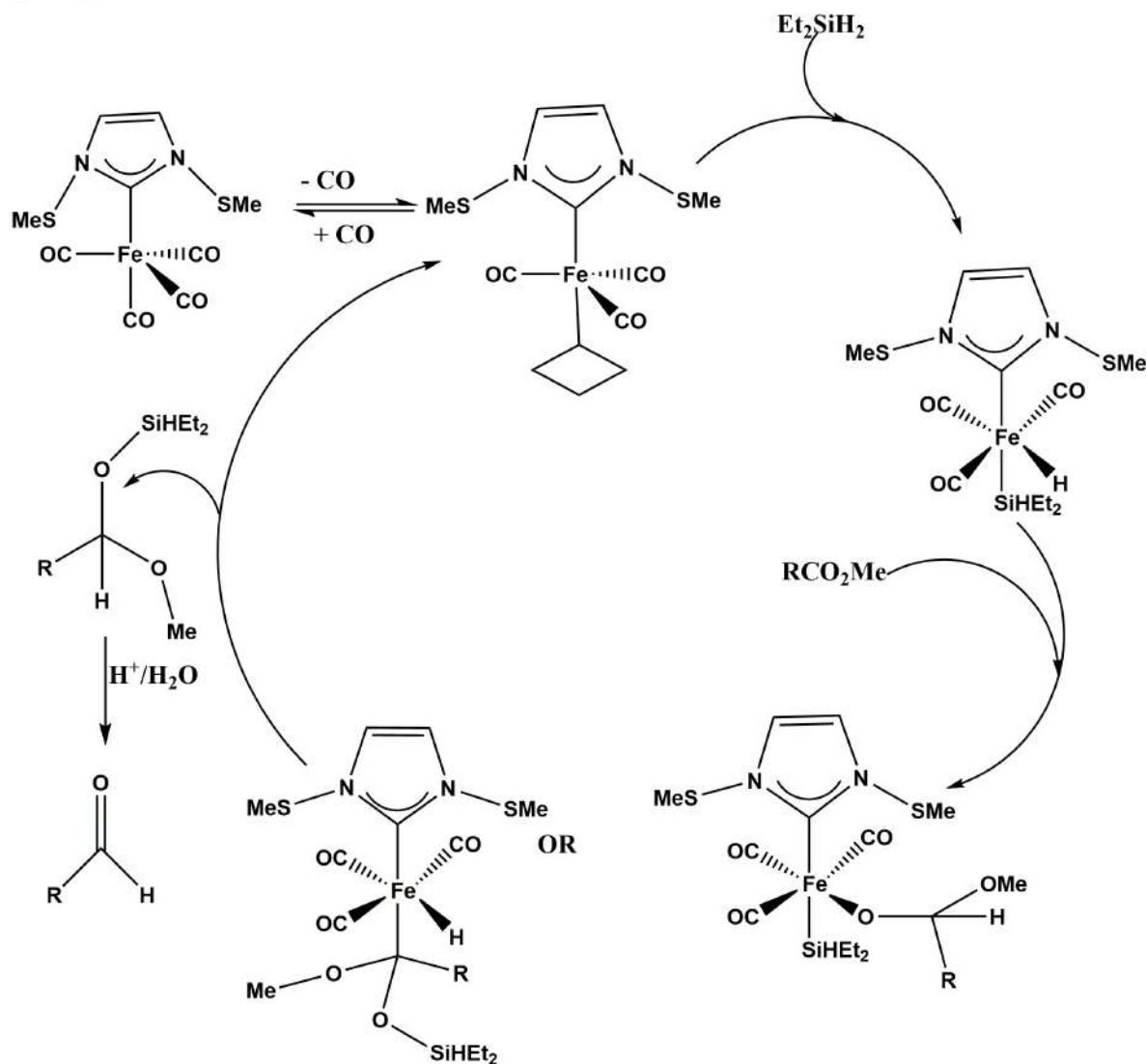


The same group of scientists as stated above achieved selective reduction of esters to aldehydes via hydrosilylation with the use of Fe(0) carbonyl NHC complexes (1a, 1c, 2d). High product selectivities were only observed when secondary silanes were used, but either no reduction or selective reduction to alcohol instead of aldehyde were observed when primary or tertiary silanes were used. (Irradiation of 350nm is also crucial for this method). Alkyl, benzyl, phenyl substituted esters were successfully reduced with a yield of 65-95%. Only in case of electron deficient aromatic esters this method was not so



successful. Several lactones converted to lactols or ring opened aldehydes depending on the ring size. A possible mechanism is depicted for this method in the **scheme 96**.

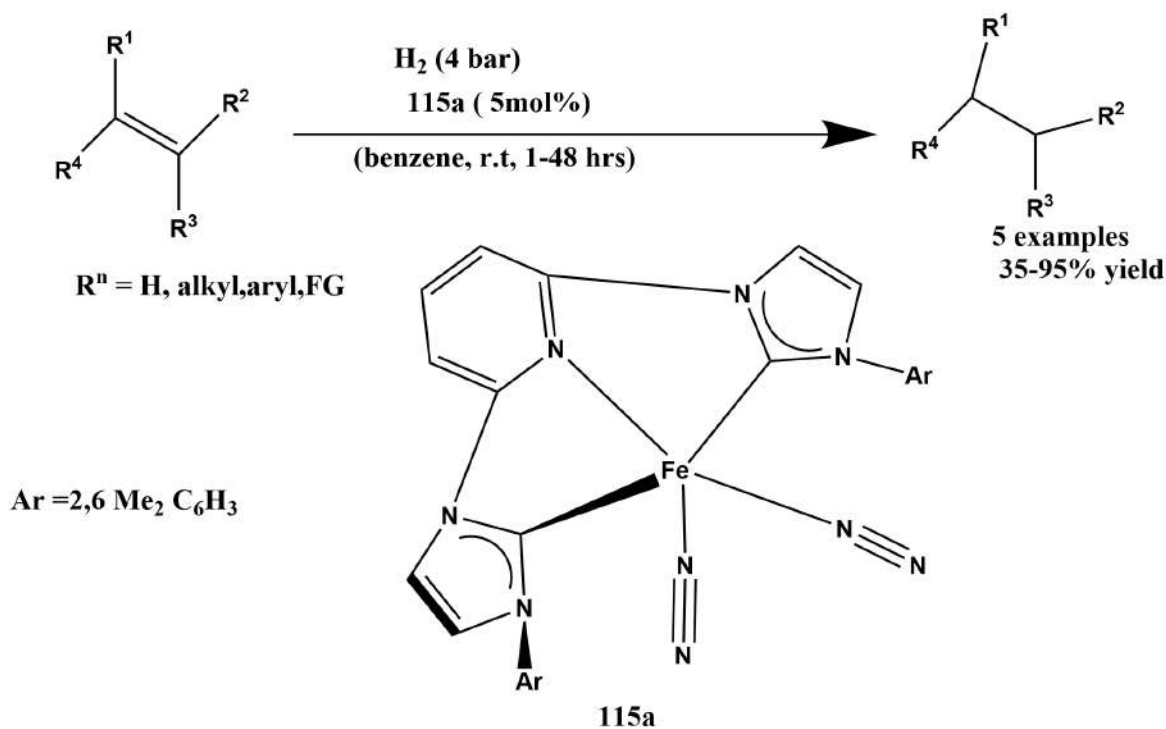
**SCHEME 96 PROPOSED MECHANISM FOR THE Fe-NHC CATALYSED REDUCTION OF ESTERS**



### 3.3.2 Hydrogenation61a :

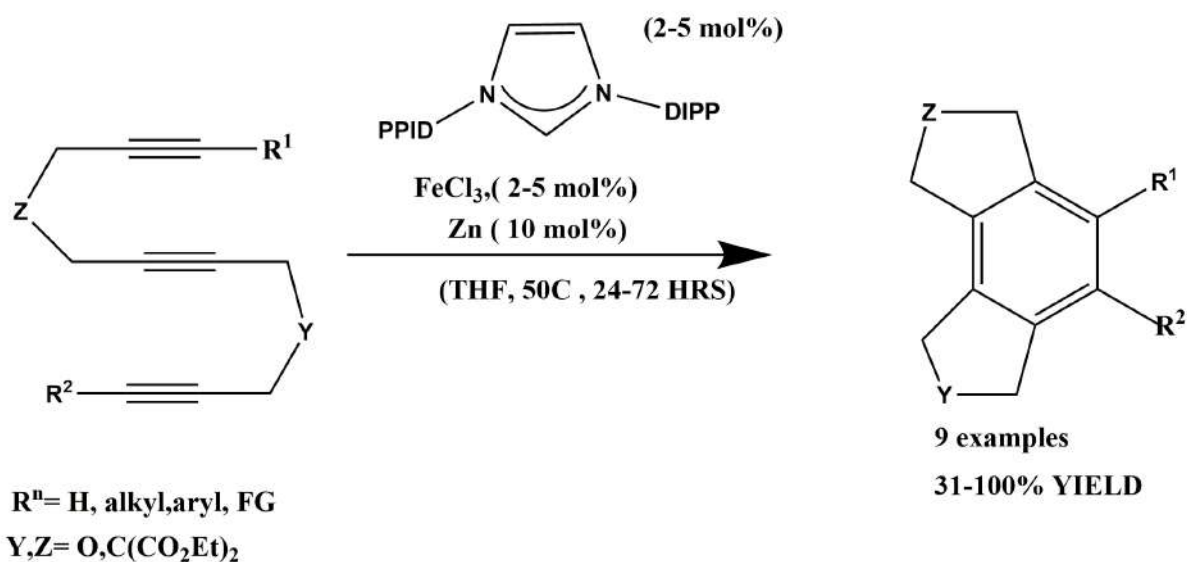
**Hydrogenation of olefins( scheme 104) :** Low valent electron rich Fe(0) NHC complexes 105 and 115a were used to hydrogenate unfunctionalised alkenes producing moderate to excellent yields. This discipline was established by Chirik and coworkers in the year 2012.**3.4**

**SCHEME 104 : HYDROGENATION OF OLEFINS**



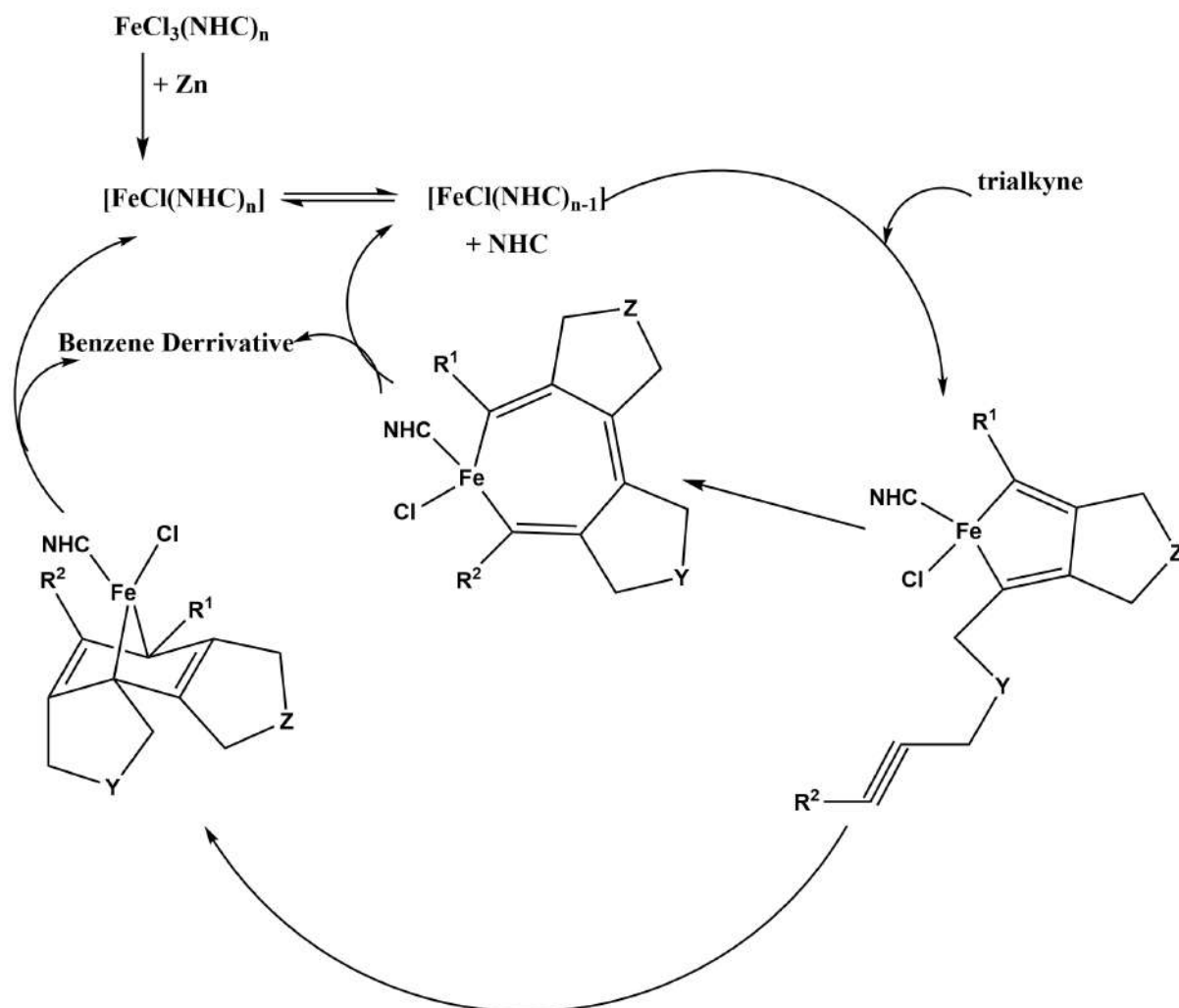
**2012.3.4 Cyclisation reaction ( scheme 105 and 106)<sup>156</sup> :**

**CATALYTIC [ 2+2+2] CYCLOADDITION**



Maintainence and formation of ring structures of organic molecules are very important and has a wide application in pharmaceutical , chemical, cosmetic and agricultural industry.

**SCHEME 106: PROPOSED MECHANISM FOR CATALYTIC [2+2+2] CYCLOADDITION**

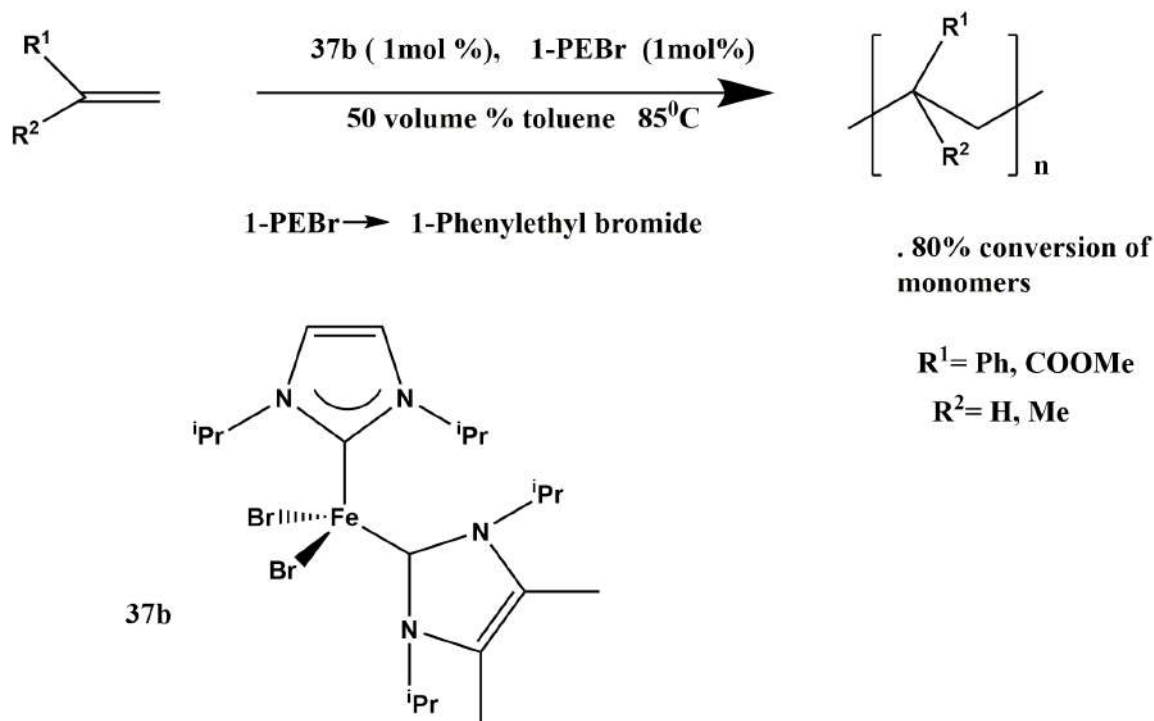


### 3.5 Polymerisation Reaction<sup>159,11a</sup> :

**Atom Transfer Radical Polymerisation (scheme 109):** Atom Transfer Radical Polymerisation has become an important method of polymerization since its inception in 1995. Tolerance of various functional groups and low concentration of radicals are the salient features of ATRP. First Fe-NHC catalysed ATRP was reported by Grubbs and coworkers in the year 2000. The reaction ( scheme 109) follows a pseudo first order kinetics which establishes the fact that the radical concentration remains constant throughout the reaction. Among the catalyst 37a and 37b the bromo complex 37b was more active than the chloro complex 37a and could be employed with a very low catalyst load

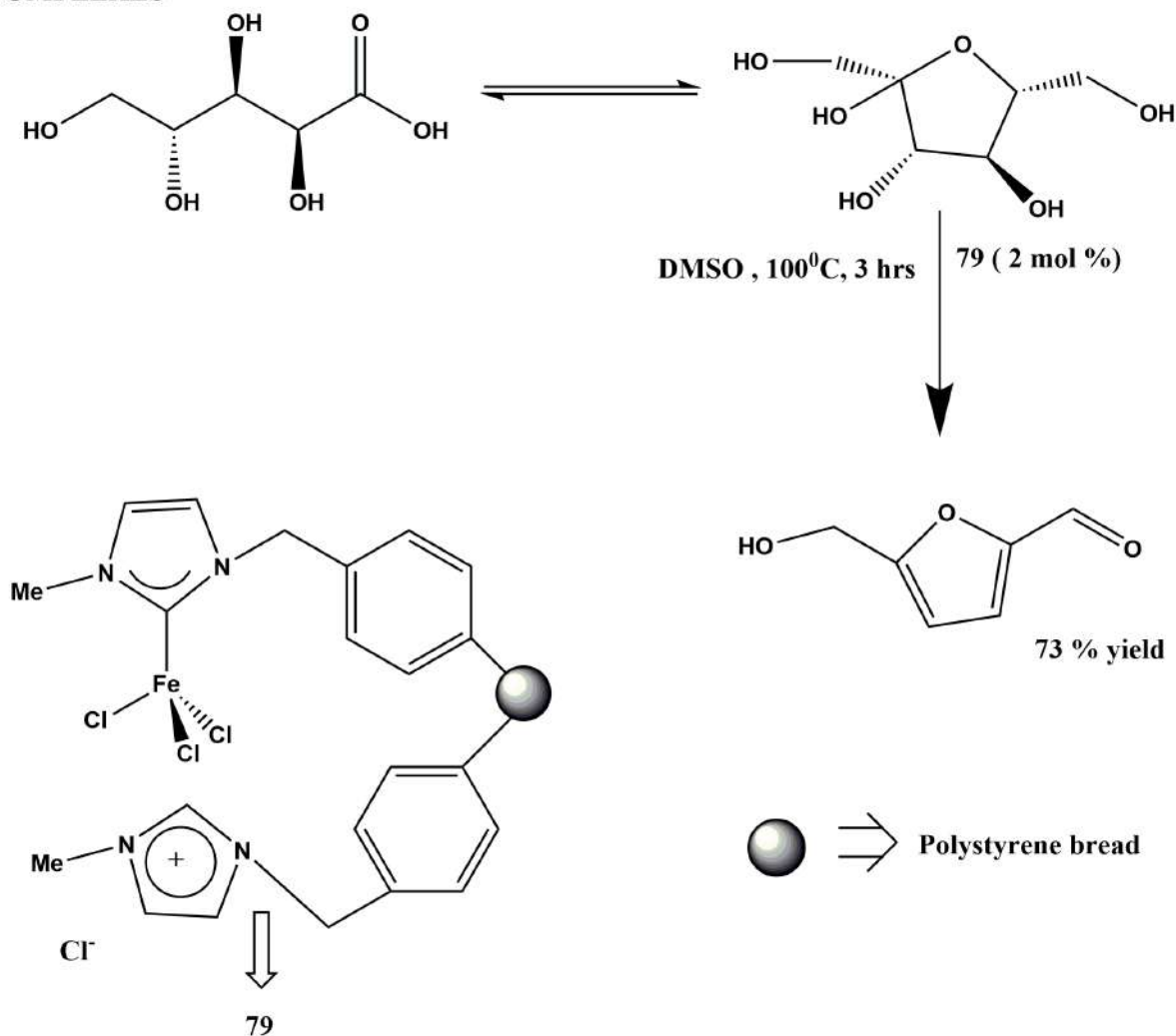
as low as 1%. Polydispersity of the reaction (MW/MN) was found to be 1:1. At that time this rate of polymerization was highest for ATRP'S in organic solvents.

**SCHEME 109: ATOM TRANSFER RADICAL POLYMERISATIONS OF OLEFINS**



**3.6 Dehydration Reaction (scheme 113)<sup>50</sup>:** Cho , Lee and coworkers used Fe –NHC complex 79 as a catalyst for the dehydration of fructose to 5-(hydroxymethyl)-2 furfural (HMF) . They obtained an isolated yield of 73%. The catalyst can be recycled 10 times without any or little loss of activity.

**SCHEME 113: DEHYDRATION OF FRUCTOSE CATALYSED BY IMMOBILISED Fe- NHC COMPLEXES**



**4. Conclusion:** The field of Fe-NHC catalysis has evolved to be quite a promising research area in the past few decades. A various Fe-NHC complexes with different oxidation states, geometries and substitution patterns have been synthesized in recent times. The application of these various complexes has also been successfully demonstrated in many of the above examples. These Fe-NHC complexes may also have major role in industrial and pharmaceutical applications as they are cheap and non toxic. Though at present Fe-NHC catalysis is facing a lot of challenges , efforts must be made to understand mechanistically on a molecular level which may in future lead to significant breakthroughs in this field not only to replace classical rare/heavy metal based catalysis but also to expand new horizons in this field.

**5. Acknowledgement:** I would like to thank Dr. Nabanita Saha Chowdhury for her valuable support and suggestions which have helped me immensely to complete this review work.

I would also like to thank all the teachers and my friends for helping me with this work.

I would also like to thank SCHOTTISH CHURCH DEPARTMENT OF CHEMISTRY for providing me an opportunity to work in this review project.

**6. Reference:** (1) Huheey, J. E.; Keiter, E. A.; Keiter, R. L.; Medhi, O. K. *Inorganic Chemistry: Principles of Structure and Reactivity*; Pearson Education: Upper Saddle River, NJ, 2006. (2) (a) Lippard, S. J.; Berg, J. M. *Principles of Bioinorganic Chemistry*; University Science Books: Mill Valley, CA, 1994. (b) Kraatz, H. B.; Metzler-Nolte, N. *Concepts and Models in Bioinorganic Chemistry*; Wiley-VCH: Weinheim, Germany, 2006. (c) Metzler-Nolte, N.; Schatzschneider, U. *Bioinorganic Chemistry: A Practical Course*; de Gruyter: Berlin, Germany, 2009. (d) Ochiai, E. I. *Bioinorganic Chemistry: A Survey*; Academic Press: Waltham, MA, 2010. (3) (a) Bolm, C.; Legros, J.; Le Paih, J.; Zani, L. *Chem. Rev.* 2004, 104, 6217. (b) Sherry, B. D.; Fürstner, A. *Acc. Chem. Res.* 2008, 41, 1500.

(c) Correa, A.; Garcia Mancheño, O.; Bolm, C. *Chem. Soc. Rev.* 2008, 37, 1108. (d) Gaillard, S.; Renaud, J.-L. *ChemSusChem* 2008, 1, 505. (e) Enthaler, S.; Junge, K.; Beller, M. *Angew. Chem., Int. Ed.* 2008, 47, 3317. (f) Sarhan, A. A. O.; Bolm, C. *Chem. Soc. Rev.* 2009, 38, 2730. (g) Kleimark, J.; Hedström, A.; Larsson, P.-F.; Johansson, C.; Norrby, P.-O. *ChemCatChem* 2009, 1, 152. (h) Czaplik, W. M.; Mayer, M.; Cvengroš, J.; von Wangelin, A. J. *ChemSusChem* 2009, 2, 396. (i) Morris, R. H. *Chem. Soc. Rev.* 2009, 38, 2282. (j) Fürstner, A. *Angew. Chem., Int. Ed.* 2009, 48, 1364. (k) Sun, C.-L.; Li, B.-J.; Shi, Z.-J. *Chem. Rev.* 2011, 111, 1293. (l) Zhang, M.; Zhang, A. *Appl. Organomet. Chem.* 2010, 24, 751. (m) Nakamura, E.; Yoshikai, N. *J. Org. Chem.* 2010, 75, 6061. (n) Jana, R.; Pathak, T. P.; Sigman, M. S. *Chem. Rev.* 2011, 111, 1417. (o) Le Bailly, B. A. F.; Thomas, S. P. *RSC Adv.* 2011, 1, 1435. (p) Junge, K.; Schröder, K.; Beller, M. *Chem. Commun.* 2011, 47, 4849. (q) García Mancheño, O. *Angew. Chem., Int. Ed.* 2011, 50, 2216. (r) Blanchard, S.; Derat, E.; Desage-El Murr, M.; Fensterbank, L.; Malacria, M.; Mouriès-Mansuy, V. *Eur. J. Inorg. Chem.* 2012, 2012, 376. (s) Darwish, M.; Wills, M. *Catal. Sci. Technol.* 2012, 2, 243. (t) Mousseau, J. J.; Charette, A. B. *Acc. Chem. Res.* 2012, 46, 412. (u) Gopalaiah, K. *Chem. Rev.* 2013, 113, 3248. (v) Plietker, B. *Iron Catalysis in Organic Chemistry: Reactions and Applications*; Wiley-VCH: Weinheim,

Germany, 2008. (w) Plietker, B.; Beller, M. *Iron Catalysis: Fundamentals and Applications*; Springer: Berlin, Germany, 2011. (x) Knölker, H.-J. *Organoirron Chemistry. Organometallics in Synthesis*; Wiley: Hoboken, NJ, 2013. (4) (a) Van Santen, R. A.; van Leeuwen, P. W. N. M.; Moulijn, J. A.; Averill, B. A. *Catalysis: An Integrated Approach*; Elsevier: Amsterdam, The Netherlands, 2000. (b) Hagen, J. *Industrial Catalysis: A Practical Approach*; Wiley-VCH: Weinheim, Germany, 2006. (c) Lloyd, L. *Handbook of Industrial Catalysts*; Springer: Berlin, Germany, 2011. (d) Bartholomew, C. H.; Farrauto, R. J. *Fundamentals of Industrial Catalytic*

*Processes*; Wiley: Hoboken, NJ, 2011. (e) Beller, M.; Renken, A.; van Santen, R. A. *Catalysis*; Wiley-VCH: Weinheim, Germany, 2012. (5) (a) Beller, M.; Bolm, C. *Transition Metals for Organic Synthesis: Building Blocks and Fine Chemicals*; Wiley-VCH: Weinheim, Germany, 1998. (b) Cornils, B.; Herrmann, W. A. *Applied Homogeneous Catalysis with Organometallic Compounds*; Wiley-VCH: Weinheim, Germany, 2002. (c) Hartwig, J. F. *Organotransition Metal Chemistry: From Bonding to Catalysis*; University Science Books: Mill Valley, CA, 2010. (d) Crabtree, R. H. *The Organometallic Chemistry of the Transition Metals*; Wiley: Hoboken, NJ, 2011. (e) Bates, R. *Organic Synthesis Using Transition Metals*; Wiley: Hoboken, NJ, 2012. (f) Behr, A.; Neubert, P. *Applied Homogeneous Catalysis*; Wiley-VCH: Weinheim, Germany, 2012. (6) Wasi, S.; Tabrez, S.; Ahmad, M. *Environ. Monit. Assess.* 2013, 185, 2585. (7) (a) Lappert, M. F. *J. Organomet. Chem.* 1988, 358, 185. (b) Herrmann, W. A.; Köcher, C. *Angew. Chem., Int. Ed. Engl.* 1997, 36, 2162. (c) Herrmann, W. A. *Angew. Chem., Int. Ed.* 2002, 41, 1290. (d) Cavallo, L.; Correa, A.; Costabile, C.; Jacobsen, H. J. *Organomet. Chem.* 2005, 690, 5407. (e) Crabtree, R. H. *J. Organomet. Chem.* 2005, 690, 5451. (f) Hahn, F. E. *Angew. Chem., Int. Ed.* 2006, 45, 1348. (g) Díez-González, S.; Nolan, S. P. *Coord. Chem. Rev.* 2007, 251, 874. (h) Köhl, O. *Chem. Soc. Rev.* 2007, 36, 592. (i) Liddle, S. T.; Edworthy, I. S.; Arnold, P. L. *Chem. Soc. Rev.* 2007, 36, 1732. (j) Mata, J. A.;

*Chemical Reviews Review*

[dx.doi.org/10.1021/cr4006439](https://doi.org/10.1021/cr4006439) | *Chem. Rev.* 2014, 114, 5215–52725268

Poyatos, M.; Peris, E. *Coord. Chem. Rev.* 2007, 251, 841. (k) Pugh, D.; Danopoulos, A. A. *Coord. Chem. Rev.* 2007, 251, 610. (l) Hahn, F. E.; Jahnke, M. C. *Angew. Chem., Int. Ed.* 2008, 47, 3122. (m) Díez-González, S.; Marion, N.;

Nolan, S. P. *Chem. Rev.* 2009, 109, 3612. (n) Jacobsen, H.; Correa, A.; Poater, A.; Costabile, C.; Cavallo, L. *Coord. Chem. Rev.* 2009, 253, 687. (o) Köhl, O. *Coord. Chem. Rev.* 2009, 253, 2481. (p) Poyatos, M.; Mata, J. A.; Peris, E. *Chem. Rev.* 2009, 109, 3677. (q) Dröge, T.; Glorius, F. *Angew. Chem., Int. Ed.* 2010, 49, 6940. (r) Schuster, O.; Mercks, L.; Albrecht, M. *Chimia* 2010, 64, 184. (s) Edwards, P. G.; Hahn, F. E. *Dalton Trans.* 2011, 40, 10278. (t) Benhamou, L.; Chardon, E.; Lavigne, G.; Bellemin-Laponnaz, S.; César, V. *Chem. Rev.* 2011, 111, 2705. (u) Ingleson, M. J.; Layfield, R. A. *Chem. Commun.* 2012, 48, 3579. (v) Bézier, D.; Sortais, J.-B.; Darcel, C. *Adv. Synth. Catal.* 2013, 355, 19. (w) Schaper, L.-A.; Hock, S. J.; Herrmann, W. A.; Kühn, F. E. *Angew. Chem., Int. Ed.* 2013, 52, 270. (x) Hock, S. J.; Schaper, L.-A.; Herrmann, W. A.; Kuhn, F. E. *Chem. Soc. Rev.* 2013, 42, 5073. (y) Nelson, D. J.; Nolan, S. P. *Chem. Soc. Rev.* 2013, 42, 6723. (z) Petz, W. *Iron-Carbene Complexes*; Springer: Berlin, Germany, 1993. (aa) Glorius, F.; Bellemin-Laponnaz, S. *N-Heterocyclic Carbenes in Transition Metal Catalysis*; Springer: Berlin, Germany, 2007. (bb) Nolan, S. P. *N-Heterocyclic Carbenes in Synthesis*; Wiley-VCH: Weinheim, Germany, 2006. (cc) Köhl, O. *Functionalised N-Heterocyclic Carbene Complexes*; Wiley: Chichester, U.K., 2010. (dd) Cazin, C. S. J. *Heterocyclic Carbenes in Transition Metal Catalysis and Organocatalysis*; Springer: Berlin, Germany, 2011. (ee) Díez-González, S. *N-Heterocyclic Carbenes: From Laboratory Curiosities to Efficient Synthetic Tools*; Royal Society of Chemistry: Cambridge, U.K., 2011. (8) (a) Öfele, K. J. *Organomet. Chem.* 1968, 12, P42. (b) Wanzlick, H. W.; Schönherr, H. J. *Angew. Chem., Int. Ed. Engl.* 1968, 7, 141. (9) Öfele, K. *Angew. Chem., Int. Ed. Engl.* 1969, 8, 916. (10) Herrmann, W. A.; Elison, M.; Fischer, J.; Köcher, C.; Artus, G. R. J. *Angew. Chem., Int. Ed. Engl.* 1995, 34, 2371. (11) Louie, J.; Grubbs, R. H. *Chem. Commun.* 2000, 1479. (12) (a) Igau, A.; Grutzmacher, H.; Baceiredo, A.; Bertrand, G. J. *Am. Chem. Soc.* 1988, 110, 6463. (b) Melaimi, M.; Soleilhavoup, M.; Bertrand, G. *Angew. Chem., Int. Ed.* 2010, 49, 8810. (c) Martin, D.; Melaimi, M.; Soleilhavoup, M.; Bertrand, G. *Organometallics* 2011, 30, 5304. (d) Martin, C. D.; Soleilhavoup, M.; Bertrand, G. *Chem. Sci.* 2013, 4, 3020. (13) (a) Crossland, J. L.; Tyler, D. R. *Coord. Chem. Rev.* 2010, 254, 1883. (b) Smith, J. M.; Subedi, D. *Dalton Trans.* 2012, 41, 1423. (14) Öfele, K.; Kreiter, C. G. *Chem. Ber.* 1972, 105, 529. (15) Cetinkaya, B.; Dixneuf, P.; Lappert, M. F. J. *Chem. Soc., Chem. Commun.* 1973, 206. (16) Lappert, M. F.; Pye, P. L. J. *Chem. Soc., Dalton Trans.* 1977, 2172. (17) Quick, M. H.; J. Angelici, R. J. *Organomet. Chem.* 1978, 160, 231.



(18) Albano, V. G.; Bordoni, S.; Braga, D.; Busetto, L.; Palazzi, A.; Zanotti, V. *Angew. Chem., Int. Ed. Engl.* 1991, 30, 847. (19) Kernbach, U.; Ramm, M.; Luger, P.; Fehlhammer, W. P. *Angew. Chem., Int. Ed. Engl.* 1996, 35, 310. (20) Nieto, I.; Cervantes-Lee, F.; Smith, J. M. *Chem. Commun.* 2005, 3811. (21) Liu, B.; Zhang, Y.; Xu, D.; Chen, W. *Chem. Commun.* 2011, 47, 2883. (22) Danopoulos, A. A.; Monakhov, K. Y.; Braunstein, P. *Chem. Eur. J.* 2013, 19, 450. (23) Wacker, A.; Yan, C. G.; Kaltenpoth, G.; Ginsberg, A.; Arif, A. M.; Ernst, R. D.; Pritzkow, H.; Siebert, W. J. *Organomet. Chem.* 2002, 641, 195. (24) Danopoulos, A. A.; Tsoureas, N.; Wright, J. A.; Light, M. E. *Organometallics* 2004, 23, 166. (25) Huttner, G.; Gartzke, W. *Chem. Ber.* 1972, 105, 2714. (26) (a) Warratz, S.; Postigo, L.; Royo, B. *Organometallics* 2013, 32, 893. (b) Cardin, D. J.; Cetinkaya, B.; Cetinkaya, E.; Lappert, M. F.; Randall, E. W.; Rosenberg, E. J. *Chem. Soc., Dalton Trans.* 1973, 1982. (c) Cetinkaya, B.; Dixneuf, P.; Lappert, M. F. *J. Chem. Soc., Dalton Trans.* 1974, 1827. (d) Lappert, M. F.; MacQuitty, J. J.; Pye, P. L. J.

*Chem. Soc., Dalton Trans.* 1981, 1583. (e) Li, H.; Misal Castro, L. C.; Zheng, J.; Roisnel, T.; Dorcet, V.; Sortais, J.-B.; Darcel, C. *Angew. Chem., Int. Ed.* 2013, 52, 8045. (27) (a) Müller, J.; Öfele, K.; Krebs, G. J. *Organomet. Chem.* 1974, 82, 383. (b) Böhm, M. C.; Daub, J.; Gleiter, R.; Hofmann, P.; Lappert, M. F.; Öfele, K.

*Chem. Ber.* 1980, 113, 3629. (c) Öfele, K.; Herrmann, W. A.; Mihalios, D.; Elison, M.; Herdtweck, E.; Scherer, W.; Mink, J. J. *Organomet. Chem.* 1993, 459, 177. (d) Jacobsen, H.; Correa, A.; Costabile, C.; Cavallo, L. J. *Organomet. Chem.* 2006, 691, 4350. (28) (a) Lappert, M. F.; MacQuitty, J. J.; Pye, P. L. J. *Chem. Soc., Chem. Commun.* 1977, 411. (b) Hitchcock, P. B.; Lappert, M. F.; Thomas, S. A.; Thorne, A. J.; Carty, A. J.; Taylor, N. J. J. *Organomet. Chem.* 1986, 315, 27. (29) Carty, A. J.; Taylor, N. J.; Smith, W. F.; Lappert, M. F.; Pye, P. L. J. *Chem. Soc., Chem. Commun.* 1978, 1017. (30) Li, B.; Liu, T.; Popescu, C. V.; Bilko, A.; Darensbourg, M. Y. *Inorg. Chem.* 2009, 48, 11283. (31) Hsieh, C.-H.; Darensbourg, M. Y. *J. Am. Chem. Soc.* 2010, 132, 14118. (32) Vanin, A. F. *Nitric Oxide* 2009, 21, 1. (33) Hsieh, C.-H.; Pulukkody, R.; Darensbourg, M. Y. *Chem. Commun.* 2013, 49, 9326. (34) Hsieh, C.-H.; Chupik, R. B.; Pinder, T. A.; Darensbourg, M. Y. *Polyhedron* 2013, 58, 151. (35) Brothers, S. M.; Darensbourg, M. Y.; Hall, M. B. *Inorg. Chem.* 2011, 50, 8532. (36) Hess, J. L.; Hsieh, C.-H.; Reibenspies, J. H.; Darensbourg, M. Y. *Inorg. Chem.* 2011, 50, 8541. (37) Pulukkody, R.; Kyran, S. J.; Bethel, R. D.; Hsieh, C.-H.; Hall, M. B.;

Darensbourg, D. J.; Darensbourg, M. Y. *J. Am. Chem. Soc.* 2013, 135, 8423. (38) Holzwarth, M. S.; Frey, W.; Plietker, B. *Chem. Commun.* 2011, 47, 11113. (39) (a) Xiang, L.; Xiao, J.; Deng, L. *Organometallics* 2011, 30, 2018. (b) Danopoulos, A. A.; Braunstein, P.; Stylianides, N.; Wesolek, M. *Organometallics* 2011, 30, 6514. (c) Hashimoto, T.; Urban, S.; Hoshino, R.; Ohki, Y.; Tatsumi, K.; Glorius, F. *Organometallics* 2012, 31, 4474. (d) Przyojski, J. A.; Arman, H. D.; Tonzetich, Z. J. *Organometallics* 2012, 31, 3264. (40) Zhang, Q.; Xiang, L.; Deng, L. *Organometallics* 2012, 31, 4537. (41) Mo, Z.; Zhang, Q.; Deng, L. *Organometallics* 2012, 31, 6518. (42) Gao, H.-h.; Yan, C.-h.; Tao, X.-P.; Xia, Y.; Sun, H.-M.; Shen, Q.; Zhang, Y. *Organometallics* 2010, 29, 4189. (43) (a) Layfield, R. A.; McDouall, J. J. W.; Scheer, M.; Schwarzmaier, C.; Tuna, F. *Chem.*

*Commun.* 2011, 47, 10623. (b) Day, B. M.; Pugh, T.; Hendriks, D.; Guerra, C. F.; Evans, D. J.; Bickelhaupt, F. M.; Layfield, R. A. *J. Am. Chem. Soc.* 2013, 135, 13338. (44) Danopoulos, A. A.; Braunstein, P.; Wesolek, M.; Monakhov, K. Y.; Rabu, P.; Robert, V. *Organometallics* 2012, 31, 4102. (45) Wang, X.; Mo, Z.; Xiao, J.; Deng, L. *Inorg. Chem.* 2013, 52, 59. (46) (a) Meyer, S.; Orben, C. M.; Demeshko, S.; Dechert, S.; Meyer, F. *Organometallics* 2011, 30, 6692. (b) Zlatogorsky, S.; Muryn, C. A.; Tuna, F.; Evans, D. J.; Ingleson, M. J. *Organometallics* 2011, 30, 4974. (c) Zlatogorsky, S.; Ingleson, M. J. *Dalton Trans.* 2012, 41, 2685. (47) Wu, J.; Dai, W.; Farnaby, J. H.; Hazari, N.; Le Roy, J. J.; Mereacre, V.; Murugesu, M.; Powell, A. K.; Takase, M. K. *Dalton Trans.* 2013, 42, 7404. (48) Grohmann, C.; Hashimoto, T.; Fröhlich, R.; Ohki, Y.; Tatsumi, K.; Glorius, F. *Organometallics* 2012, 31, 8047. (49) (a) Lavallo, V.; Grubbs, R. H. *Science* 2009, 326, 559. (b) Lavallo, V.; El-Batta, A.; Bertrand, G.; Grubbs, R. H. *Angew. Chem., Int. Ed.* 2011, 50, 268. (50) Kim, Y.-H.; Shin, S.; Yoon, H.-J.; Kim, J. W.; Cho, J. K.; Lee, Y.S. *Catal. Commun.* 2013, 40, 18. (51) Nehete, U. N.; Anantharaman, G.; Chandrasekhar, V.; Murugavel, R.; Walawalkar, M. G.; Roesky, H. W.; Vidovic, D.; Magull, J.; Samwer, K.; Sass, B. *Angew. Chem., Int. Ed.* 2004, 43, 3832. (52) Chen, M.-Z.; Sun, H.-M.; Li, W.-F.; Wang, Z.-G.; Shen, Q.; Zhang, Y. *J. Organomet. Chem.* 2006, 691, 2489. *Chemical Reviews Review*

[dx.doi.org/10.1021/cr4006439](https://doi.org/10.1021/cr4006439) | *Chem. Rev.* 2014, 114, 5215–52725269

(53) Wang, Y.; Sun, H.; Tao, X.; Shen, Q.; Zhang, Y. *Chin. Sci. Bull.* 2007, 52, 3193. (54) (a) Al Thagfi, J.; Lavoie, G. G. *Organometallics* 2012, 31, 2463. (b) Thagfi, J. A.; Lavoie, G. G. *Organometallics* 2012, 31, 7351. (55) Kaplan, H. Z.; Li, B.; Byers, J. A. *Organometallics* 2012, 31, 7343. (56) Kaufhold, O.; Hahn, F. E.; Pape, T.; Hepp, A. J. *Organomet. Chem.* 2008, 693, 3435. (57) Zhang, Y.; Liu, B.; Wu, H.; Chen, W. *Chin. Sci. Bull.* 2012, 57, 2368. (58) Liu, B.; Xia, Q.;

Chen, W. *Angew. Chem., Int. Ed.* 2009, 48, 5513. (59) Raba, A.; Cokoja, M.; Ewald, S.; Riener, K.; Herdtweck, E.; Pöthig, A.; Herrmann, W. A.; Kühn, F. E. *Organometallics* 2012, 31, 2793. (60) Smith, J. M.; Long, J. R. *Inorg. Chem.* 2010, 49, 11223. (61) (a) Yu, R. P.; Darmon, J. M.; Hoyt, J. M.; Margulieux, G. W.; Turner, Z. R.; Chirik, P. J. *ACS Catal.* 2012, 2, 1760. (b) Danopoulos, A. A.; Pugh, D.; Smith, H.; Sassmannshausen, J. *Chem. Eur. J.* 2009, 15, 5491. (c) Mc Guinness, D. S.; Gibson, V. C.; Steed, J. W. *Organometallics* 2004, 23, 6288. (62) Bedford, R. B.; Betham, M.; Bruce, D. W.; Danopoulos, A. A.; Frost, R. M.; Hird, M. J. *Org. Chem.* 2006, 71, 1104. (63) Danopoulos, A. A.; Wright, J. A.; Motherwell, W. B. *Chem. Commun.* 2005, 784. (64) Zhang, X. *Int. J. Quantum Chem.* 2010, 110, 1880. (65) Obligacion, J. V.; Chirik, P. J. *Org. Lett.* 2013, 15, 2680. (66) Pugh, D.; Wells, N. J.; Evans, D. J.; Danopoulos, A. A. *Dalton Trans.* 2009, 7189. (67) Fränkel, R.; Kernbach, U.; Bakola-Christianopoulou, M.; Plaia, U.; Suter, M.; Ponikwar, W.; Nöth, H.; Moinet, C.; Fehlhammer, W. P. J. *Organomet. Chem.* 2001, 617–618, 530. (68) (a) Nieto, I.; Ding, F.; Bontchev, R. P.; Wang, H.; Smith, J. M. *J. Am. Chem. Soc.* 2008, 130, 2716. (b) Scepaniak, J. J.; Fulton, M. D.; Bontchev, R. P.; Duesler, E. N.; Kirk, M. L.; Smith, J. M. *J. Am. Chem. Soc.* 2008, 130, 10515. (69) (a) Scepaniak, J. J.; Young, J. A.; Bontchev, R. P.; Smith, J. M. *Angew. Chem., Int. Ed.* 2009, 48, 3158. (b) Scepaniak, J. J.; Vogel, C. S.; Khusniyarov, M. M.; Heinemann, F. W.; Meyer, K.; Smith, J. M. *Science* 2011, 331, 1049. (c) Scepaniak, J. J.; Bontchev, R. P.; Johnson, D. L.; Smith, J. M. *Angew. Chem., Int. Ed.* 2011, 50, 6630. (70) (a) Scepaniak, J. J.; Margarit, C. G.; Harvey, J. N.; Smith, J. M. *Inorg. Chem.* 2011, 50, 9508. (b) Scepaniak, J. J.; Harris, T. D.; Vogel, C. S.; Sutter, J.; Meyer, K.; Smith, J. M. *J. Am. Chem. Soc.* 2011, 133, 3824. (71) Vogel, C.; Heinemann, F. W.; Sutter, J.;

Anthon, C.; Meyer, K. *Angew. Chem., Int. Ed.* 2008, 47, 2681. (72) Vogel, C. S.; Heinemann, F. W.; Khusniyarov, M. M.; Meyer, K. *Inorg. Chim. Acta* 2010, 364, 226. (73) (a) Cramer, S. A.; Jenkins, D. M. *J. Am. Chem. Soc.* 2011, 133, 19342. (b) Lu, Z.; Cramer, S. A.; Jenkins, D. M. *Chem. Sci.* 2012, 3, 3081. (74) (a) Rohde, J.-U.; In, J.-H.; Lim, M. H.; Brennessel, W. W.; Bukowski, M. R.; Stubna, A.; Münck, E.; Nam, W.; Que, L. *Science* 2003, 299, 1037. (b) Nam, W. *Acc. Chem. Res.* 2007, 40, 522. (75) Meyer, S.; Klawitter, I.; Demeshko, S.; Bill, E.; Meyer, F. *Angew. Chem., Int. Ed.* 2013, 52, 901. (76) Zanotti, V.; Bordoni, S.; Busetto, L.; Carlucci, L.; Palazzi, A.; Serra, R.; Albano, V. G.; Monari, M.; Prestopino, F. *Organometallics* 1995, 14, 5232. (77) (a) McCormick, F. B.; J. Angelici, R. *Inorg. Chem.* 1979, 18, 1231. (b) Fehlhammer, W. P.; Bar, E.; Boyadjiev, B. Z. *Naturforsch., B: Chem. Sci.* 1986,

41, 1023. (78) Rieger, D.; Lotz, S. D.; Kernbach, U.; André, C.; Bertran-Nadal, J.; Fehlhammer, W. P. J. *Organomet. Chem.* 1995, 491, 135. (79) Buchgraber, P.; Toupet, L.; Guerchais, V. *Organometallics* 2003, 22, 5144. (80) (a) Merces, L.; Labat, G.; Neels, A.; Ehlers, A.; Albrecht, M. *Organometallics* 2006, 25, 5648. (b) Bézier, D.; Jiang, F.; Roisnel, T.; Sortais, J.-B.; Darcel, C. *Eur. J. Inorg. Chem.* 2012, 2012, 1333. (81) Merces, L.; Neels, A.; Stoeckli-Evans, H.; Albrecht, M. *Dalton Trans.* 2009, 7168. (82) (a) Bézier, D.; Venkanna, G. T.; Sortais, J.-B.; Darcel, C. *ChemCatChem* 2011, 3, 1747. (b) Misal Castro, L. C.; Sortais, J.-B.; Darcel, C. *Chem. Commun.* 2012, 48, 151. (c) Jiang, F.; Bézier, D.; Sortais, J.-B.; Darcel, C. *Adv. Synth. Catal.* 2011, 353, 239. (83) Merces, L.; Neels, A.; Albrecht, M. *Dalton Trans.* 2008, 5570. (84) Kumar, M.; DePasquale, J.; Zeller, M.; Papish, E. T. *Inorg. Chem. Commun.* 2013, 32, 55. (85) Llewellyn, S. A.; Green, M. L. H.; Green, J. C.; Cowley, A. R. *Dalton Trans.* 2006, 2535. (86) Ohki, Y.; Hatanaka, T.; Tatsumi, K. *J. Am. Chem. Soc.* 2008, 130, 17174. (87) Hatanaka, T.; Ohki, Y.; Tatsumi, K.

**INDUSTRIAL DELIGNIFICATION PROCESS AND**  
**ROLE OF SUPPORTED POLYOXOMETALATES**  
**IN THE PROCESS**

SCOTTISH CHURCH COLLEGE  
UNIVERSITY OF CALCUTTA

C.U Roll No.: 223/CEM/191020

C.U REGISTRATION No.: 014-1221-0403-16

SPECIAL PAPER: SI 44

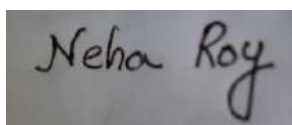
NAME OF CANDIDATE

**NEHA ROY**

NAME OF SUPERVISOR/EXAMINER

**Dr. Chandan Kumar Pal**

SIGNATURE OF CANDIDATE

A rectangular box containing the handwritten signature "Neha Roy" in black ink on a light grey background.

SGNATURE OF SUPERVISOR/EXAMINER

*Chandan kumar Pal*

## **Self Declaration**

This is to certify that, I, Neha Roy, Roll No. 223/CEM/191020, Registration No. 014-1221-0403-16, a student of MSc. in the department of Chemistry, Scottish Church College, (2019-2021) has worked on the project titled “ **INDUSTRIAL DELIGNIFICATION METHODS AND ROLE OF POLYOXOMETALATES IN THE DELIGNIFICATION PROCESS**” for the partial fulfilment of requirements of matter of science in Chemistry under the University Of Calcutta , Scottish Church College, under my supervision .To the best of my knowledge, this work has not been submitted to any other university for the award of any other degree.

## Table of Contents-

1. Introduction
2. Importance of delignification in the Industry
3. Different Methods of Delignification
  - Kraft Method
  - Oxygen Delignification
4. Merits and demerits of the methods
  - Merits and Demerits of the Kraft method
  - Merits and Demerits of the Oxygen delignification method
5. Alternative methods to counter the demerits
6. Polyoxometalates in bleaching
  - Polyoxometalate bleaching in anaerobic condition
  - Polyoxometalate bleaching in aerobic condition
7. Conclusion
8. References

## **1.Introduction**

Lignin is an integral cell wall constituent in cell vascular plants. Lignin provides rigidity, water impermeability and resistance against microbial attack. Lignin is an aromatic polymer consisting of guaiacyl (G), syringyl- (S) ,and p- hydroxyphenyl –(H) Phenyl propanoid units, whose proportion differ with botanical origin of the lignin.

The phenylpropanoid units are attached to each other by a series of C-O-C and C-C bonds such as beta-O-4 , beta-5 , alpha-O-4, beta-beta and 5-5. The polymer is branched and cross linking occurs.

The lignin in the cell wall is intimately mixed with the polysaccharides, and there are indications of the occurrence of linkages between lignin and carbohydrates. Among the proposed chemical linkages, the benzyl ether and ester types, whose formation is associated with quinone methide re aromatization reactions during lignin bio synthesis, have been considered the most probable.

## **2.Importance of delignification in the industry-**

Delignification causes disruption of lignin structure, resulting in biomass swelling, increase in internal surface area, and accessibility of enzymes to cellulose fibres.

Lignocellulosic biomass utilization as a source of clean energy and chemicals has attracted attention in recent years in the context of the fossil fuel energy drive. Lignocellulosic biomass consists of cellulose, hemicellulose and lignin fractions, which quantitatively and qualitatively vary according to the plant material. Unlike cellulose and hemicellulose, lignin is a cross linked hydrophobic polymerization is insoluble in most solvents and fairly resistant to anaerobic degradation. Hence, a pretreatment of Lignocellulosic materials to dissolve the lignin structure (delignification) and cleave the chains seems to be necessary before enzymatic and chemical thermal process to avail important chemicals from biomass. Delignification of the lignocellulosic biomass has been investigated in many studies, recently in the production of kraft pulps , lactic acid, bio ethanol. Recently molecular oxygen delignification in alkaline media had been widely reported as a potential technique for lignin degradation.

## **3. Different methods of delignification**

There are several delignification process and oxygen delignification in general use, with the kraft process and oxygen delignification being the most common.

The kraft process is a high temperature and pressure digestion system that breaks down the lignin in wood pulp chemically.

Oxygen based lignin removal process utilize oxygen activation to remove the lignin and are often used as supplementary steps at the brown stock washing stage of the kraft process.



## **Kraft Process –**

The Kraft process has been the most common form of chemical pulping throughout the years. It involves the digestion of wood chips at elevated temperature (423-453K) and pressure in white liquor. The white liquor is a water solution of sodium hydroxide with sulfides.

This process is done for nearly 2 hours to separate the lignin from cellulose under high pH condition. The higher pH leads to ionization of the phenolic hydroxide groups of the lignin, which in result solubilizes the lignin content of lignocellulosic biomass. After separation of

cellulose from lignocellulosic biomass, lignin is recovered from the final combined liquid, which is referred to as black liquor. Thus a concentrated and lignin rich solid is obtained although the lignin obtained from this process emits poisonous gas.

The lignin can also be recovered from the black liquor by lowering the pH of the solution with carbon di oxide. In this process the lignin is precipitated on the surface. The precipitated lignin can be recovered by simple filtration and washing. Although, the lignin obtained in process is free from Sulphur and sugar, this hypothesis is under examination for use.

## **Oxygen delignification-**

Oxygen delignification is nowadays one the most used process in pulp industry for ECF (Elemental Chlorine Free) and TCF (Total Chlorine Free) bleached pulp production.

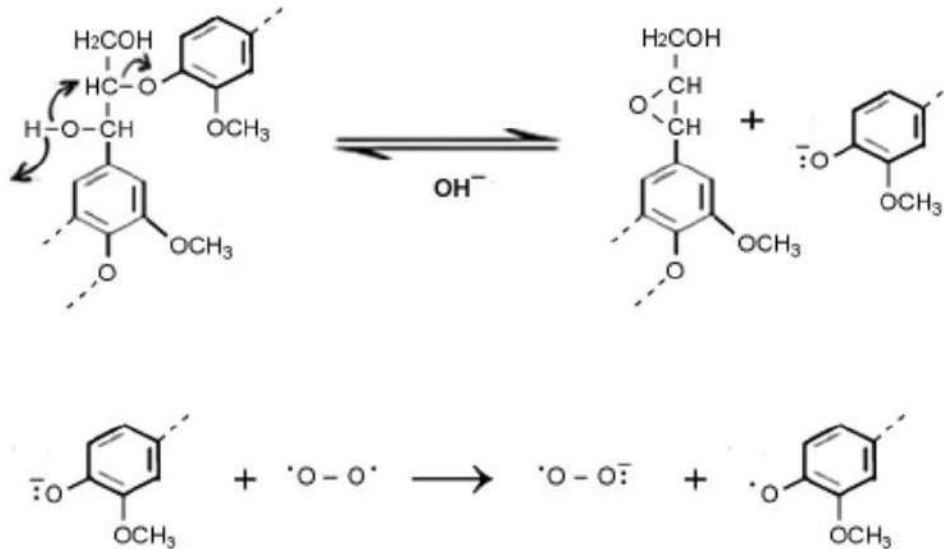
This process is done in elevated temperature, in the range of 80° – 120° and in pressure from 6- 8 bars to increase the rate. But above 120° a degradation of polysaccharides can occur. Amount of NaOH and pH is very significant in oxygen delignification. The pH value should be higher than 10 and better effectiveness it should be 12.

At lowest energy state Oxygen molecule contains two unpaired electrons has an affinity to opposite spin of other electrons. Therefore it can act as Free radical. At higher temperature and strong alkaline condition it can act with organic compounds.

At initiated state the phenolic group of lignin reacts with the alkali and forms a phenolate ion. The phenolate ion then reacts with oxygen, forming a resonance stabilized phenoxy radical and a superoxide anion.

The phenoxy radical undergo reaction with themselves or with oxygen species radical, such as hydroxyl (HO•), hydroperoxy (HOO•) and superoxide (O<sup>2•-</sup>) and produce different organic acids, carbon di oxide, and other lower mass organic compounds through side chain elimination, ring opening and de methoxylation reactions.

The reaction can is shown as below-



#### 4. Merits and demerits of the methods

##### Merits of Kraft methods-

The Kraft process is the most popular method for producing wood pulp in the US due to advantages over soda and sulfite pulping, any wood species can be used. Additionally cooking times are reduced and waste recovery is more efficient. Kraft process tends to be stronger than other types of pulps, but actual strength varies by species. When stained with Graff "C" stain, Kraft pulp can appear in a range of colors on the wood type and the amount of bleaching. Unbleached Kraft pulps will appear Yellow or blue/Grey. With increased bleaching, pulps will appear lighter and tend more towards red when treated with stain. The stained color of kraft pulp tends to be darker than sulfite pulp.

##### Demerits of Kraft method-

One of the major disadvantages of Kraft process is that the Kraft lignin is highly contaminated with carbohydrates coming from hemicellulose as well as some fatty acids. Also, substantial amount of Sulphur is usually covalently bound to Kraft lignin in the form of thiols.

##### Merits of Oxygen delignification-

a. Environment friendly, which helps to reduce the uses of chlorinated chemicals in next steps. The other environmental benefits are lower BOD, COD and fewer colours in effluent, as the effluent from the Oxygen bleaching is recycled back to the recovery boiler.

b. The process is cost effective, as it significantly reduce the consumption of bleaching chemicals, such as Chlorine gas, Chlorine di oxide, Ozone, Hydrogen peroxide in the next stages. Overall Oxygen production is minimal.

All the effluent containing spent chemicals and reaction products is recycled back in this process. Without this, all the effluent would go to waste water treatment plant due to presence of corrosive chlorinated compounds. So it reduces the chemical consumption cost.

### Demerits of Oxygen delignification-

Oxygen bleaching process is less selective compared to other bleaching agents, as the process undergoes with the free radical reaction system. This can lead to significant degradation of polysaccharides .

Another disadvantage is that it is weak reactive oxidant. So, it required alkaline conditions, high temperature and pressure to obtain a reasonable reaction state. Raising the alkali charge also creates negative effect. Moreover, primary high installation cost of Oxygen delignification is another drawback.

### 5. Alternative methods to counter the de merits

In counter to the demerits mentioned above, alternative methods can be used. Currently, delignification supported by polyoxometalates is catching the attention in the industry. Polyoxometalates , also called as POMs, favorably embraced the advantages of both chemical (active at elevated temperature) and biological (highly selective) lignin oxidizing agents. Also, these reagents are chlorine free and can be used under conditions wherein they oxidize lignin and chromophores in wood pulp fibres while leaving the cellulose undamaged. They can be reactivated with oxygen under conditions that result in oxidation of the organic by products of the delignification process. Thus, they can be recycled in a closed system, that promises to provide the basis for a new class of closed milled technologies in which, the consumable oxidant is oxygen and primary by products are Carbon di Oxide and water.

The POMs used as delignification agents are transition metal substituted cluster ions similar in structure to many mineral ores. They are entirely chlorine free and can be used under conditions that make them very selective in their action on pulp fibre constituents. When used in active states, they can oxidize lignin and related chromophores while leaving the polysaccharides undamaged.

### *6. Polyoxometalates in bleaching*

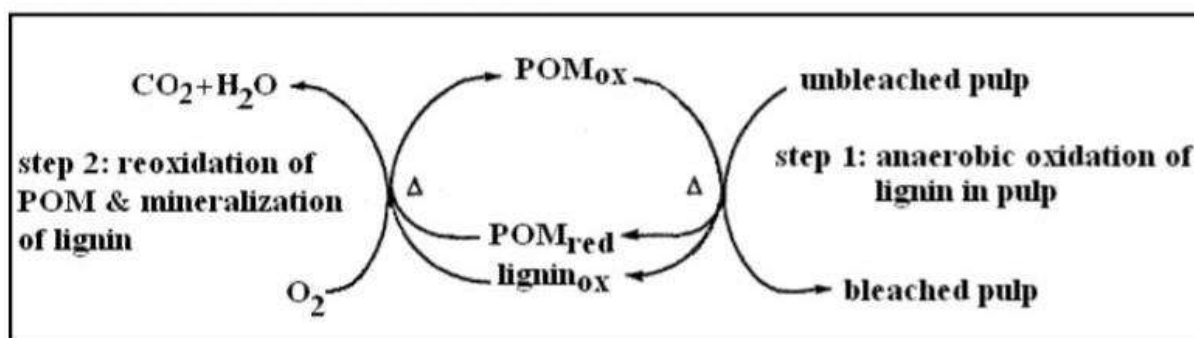
Among a large no. Of variation, the keggin type Polyoxometalates have been recognized as the most suitable POMs for use in oxidative delignification. The advantages of keggin type Polyoxometalates include a range of redox potentials, solubility and molecular charges which can be adjusted during synthesis and relatively easy regeneration by Oxygen, Hydrogen peroxide or Ozone.

Keggin type hetero poly oxy anions are described by the general formula  $X M'_a M''_{12-a} O_b^{m-}$  where  $X^{n+}$  is a d or p-block hetero atom ( $Al^{3+}$ ,  $Si^{4+}$ ,  $P^{5+}$ ) and  $M'$  and  $M''$  are  $d^n$  and  $d^0$  metal centers respectively.

The concept of delignification with POMs as robust inorganic systems which provide controlled environments with transition metal ions, has been developed to mimic the action of fragile lignin peroxidases containing iron proto porphyrin IX, in selective oxidation of lignin. POMs are reduced while lignin is oxidized. POMs may be re oxidized by Oxygen, Hydrogen peroxide or Ozone.

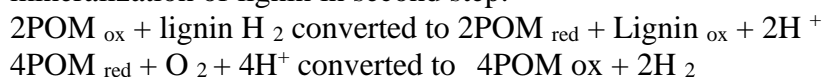
POMs with the redox potential in the range of +0.7 to +0.8 V vs NHE have been used for delignification. Delignification by POMs can be carried out in anaerobic condition and in aerobic condition.

### *Delignification by PMOs in Anaerobic condition-*



This is 2 step process. In the first step, performed under anaerobic conditions at elevated temperature (100-140°C), lignin is oxidized and dissolved in an aqueous solution of POMs, which are simultaneously reduced. After being treated with POMs, the pulp is separated from the spent POM liquor and washed. Polyoxometalates are readily washed from the pulp with high efficiency of 99.9%. The reduced POMs are regenerated, using oxygen, for the next bleaching process. Under the aggressive conditions of this step, POMs initiate and catalyse the wet air oxidation of dissolved lignin degradation compounds and other potentially present organic compounds, which are converted to  $CO_2$  and  $H_2O$ . During the development of POM bleaching technique, a number of anions have been used,  $[PV_2MO_{10}O_{40}]^{5-}$ . Further progress has been made by using  $[SiVW_{11}O_{40}]$  which is stable at neutral pH levels.

An important aspect of this POM delignification is that the protons released during lignin oxidation in the first step are consumed by Oxygen during the re oxidation of POMs and mineralization of lignin in second step.



The 2 step delignification process have a lot of advantages. These include an acceptable selectivity of POM delignification performed in a radical free condition which can be improved by conducting the process in less acidic conditions and an effective regeneration of POMs, which provides the basis of an effluent free technology.

But also, to apply the two step POM based delignification on a commercial scale, an improvement of the process related to the efficiency of lignin oxidation with POMs is required.

POMs such as  $[\text{PMo}_{10}\text{V}_2\text{O}_{40}]^{5-}$  ( $\text{PMo}_{10}\text{V}_2$ ),  $[\text{PW}_{11}\text{VO}_{40}]^{4-}$  ( $\text{PW}_{11}\text{V}$ ),  $[\text{SiW}_{11}\text{VO}_{40}]^{5-}$ ,  $[\text{BW}_{11}\text{VO}_{40}]^{6-}$  and  $[\text{SiW}_{11}\text{Mn}(\text{H}_2\text{O})\text{O}_{39}]^{5-}$  ( $\text{SiW}_{11}\text{Mn}$ ) (all isomers) have been used for delignification processes of pine kraft pulp under anaerobic conditions. All studied POMs were able to delignify the pulp the best results being obtained with  $\text{SiW}_{11}\text{V}$  and  $\text{SiW}_{11}\text{Mn}$ . Considerable cellulose degradation occurred with  $[\text{PW}_{11}\text{VO}_{40}]^{4-}$ , due to the lower pH used (on account of the stability of this POM at pH 2) which promoted cellulose acid hydrolysis. The delignification effectiveness of different POMs is related to their redox potentials. POMs with lower redox potentials ( $\text{PMo}_{10}\text{V}_2$  and  $\text{BW}_{11}\text{V}$ ) presented a lower degree of delignification whereas those of  $\text{SiW}_{11}\text{V}$  and  $\text{SiW}_{11}\text{Mn}$ , with a higher redox potential, were the most effective for the delignification of pulps. Polyoxometalate re-oxidation was demonstrated for  $\text{PMo}_{10}\text{V}_2$  at  $150^\circ\text{C}$ , since its reduced form was rapidly re-oxidised by oxygen, despite its low effectiveness for anaerobic delignification.

In contrast, for the  $\text{SiW}_{11}\text{V}$  and  $\text{SiW}_{11}\text{Mn}$  anions the re-oxidation of the reduced anions by oxygen was slow, even at conditions of elevated temperature and oxygen pressure, limiting the useful application of this system.

A second generation of POMs emerged as suitable for both delignification and wet oxidation, which are also stable above pH 7 so that hydrolysis of the cellulose can be significantly reduced. These include  $[\text{SiW}_{10}\text{V}_2\text{O}_{40}]^{6-}$  ( $\text{SiW}_{10}\text{V}_2$ ),  $[\text{AlW}_{11}\text{VO}_{40}]^{6-}$  ( $\text{AlW}_{11}\text{V}$ ), and ‘ $\text{SiW}_{10.1}\text{Mo}_{1.0}\text{V}_{0.9}\text{O}_{40}$ ’.

Another important advance associated with this new generation of POMs was the development of a new synthetic procedure (using hydrothermal methods) that results in an equilibrium composition which is inherently stable and, therefore, can be recycled repeatedly in a closed system.

The reactivity of phenolic and non-phenolic lignin structural units has been studied using monomeric and dimeric lignin model compounds (LMCs). A possible reaction pathway for a cleavage of the phenolic lignin model compounds has been proposed; this pathway would include two one-electron oxidation steps producing cyclohexadienyl cations from the initially formed phenoxy radicals.

In contrast to phenolic LMCs, the etherified LMCs follow a different mechanism and the

experiments on non-phenolic lignin subunits have revealed that the reaction may proceed via

successive oxidation of the benzylic carbon atom. Model studies, however, do not reflect all the reactions that lignin might undergo as a macromolecule in the pulp

matrix. Oxidation of pine milled wood lignin (MWL) with POMs has also been explored.

The MWL was insoluble under the conditions studied, and oxidative reactions were found to be taking place primarily at the surface of the suspended lignin macromolecules, providing incomplete information on the lignin reactivity. To understand the changes which lignin undergoes

during POM treatment of softwood and hardwood pulps, residual lignin has been isolated from pulps at different levels of POM delignification and analysed. In addition, the nature of lignin degradation compounds dissolved during POM delignification has been explored to help elucidate lignin cleavage reactions. Whereas the efforts to isolate higher-molecular weight lignin have been unsuccessful, low-molecular weight aromatic compounds have been identified in the POM spent liquor. This may be an indicator of the lignin reactions occurring on its surface; or, on the other hand, it could indicate the continuation of the degradation of higher-molecular weight lignin after dissolution, if the reactions took place in the bulk of the lignin. Among the lignin degradation products of POM treatment of different kraft pulps were acetosyringone and acetovanillone, as the products of the C<sub>β</sub>-C<sub>γ</sub> bond cleavage; vanillin, vanillic acid, and syringaldehyde, which are the products of the C<sub>α</sub>-C<sub>β</sub> bond cleavage; and 2,6-dimethoxy benzoquinone, which confirms the C<sub>1</sub>-C<sub>α</sub> bond cleavage in lignin. The presence of 3,4-dimethoxy carbonyl and carboxyl aromatic compounds, veratraldehyde, and veratric acid, respectively, reveals a potential methylation reaction taking place with methanol released during the lignin demethylation reaction in POM treatment of kraft pulps, since these structures are not naturally present in lignin.

The results obtained using the different lignin-related substrates revealed that phenol oxidation reactions are the most significant reactions occurring during lignin oxidation with POMs. LMCs with free phenolic hydroxyl groups (PhOH) reacted both faster and at lower temperature (room temperature) than the etherified forms, which reacted only at temperatures  $\geq 120$  °C. Fast oxidation of phenolic units was confirmed in POM oxidation of kraft pulps when the content of PhOH groups rapidly decreased in the corresponding residual lignin with the progress of POM delignification.

Since POM oxidation of phenols yields quinones, it is expected that the quinone content in pulps will increase with the progress of POM delignification. For example, *ortho*- and *para*-quinone structures resulted from POM treatment of different lignin model compounds *para*quinone was detected in the solution of unbleached birch kraft pulp treated with POMs a reddish orange hue of the pulps, which is commonly noticed after treatment with POMs, was

also attributed to the formation of quinones. In addition, *ortho*-quinone formation in lignin is consistent with a loss of methoxyl groups. Lignin demethylation has been observed in the POM treatment of pine MWL [28] and in the residual lignin of hardwood kraft pulps

with the progress of POM delignification. Conversely, *para*-quinone products give evidence for the occurrence of the C<sub>1</sub>-C<sub>α</sub> cleavage reactions.

An abundance of quinone structures in residual lignin after POM treatment of pulp may be an important reason for a successful brightening of POM treated pulps with sodium hydroxide and hydrogen peroxide, as they are efficient quinone-removing agents.

In addition to quinone formation confirmed in different model studies and studies on MWL and kraft pulps, an increase in other carbonyl groups, such as -C<sub>α</sub>HO and -C<sub>α</sub> = O, has been observed in the remaining POM-treated MWL and residual lignin of kraft pulps [28,34]. This result corroborates a reaction mechanism based on the successive oxidations of the benzylic carbon atoms, as proposed in the studies on etherified LMCs.

Even though in kraft pulping lignin is primarily degraded through the cleavage of its most abundant β-O-4 structure, some β-O-4 bonds are still present in residual lignin of kraft pulps. Because the bleaching result depends considerably on the agent's ability to cleave this structure, the POM treatment of β-O-4 dimers was performed, whereby the researchers observed cleavage of the C<sub>1</sub>-C<sub>α</sub> bond in phenolic guaiacyl- and syringyl- glycerol β-aryl ethers. This finding is consistent with the observed reduction in the content of the β-O-4 bonds resulting from the POM treatment of pine MWL. The 2D NMR HSQC analysis of residual lignin isolated from kraft pulps also indicated a weakening of the correlations assigned to this lignin bond.

Moreover, the products of the β-O-4 bond cleavage, identified in the LMC studies, were also identified in the POM spent liquor of the treatment of kraft pulps. This finding corroborates the delignification mechanism, which includes C<sub>1</sub>-C<sub>α</sub> bond cleavage. The lignin model studies, however, did not support the claim that the delignification mechanism includes C<sub>α</sub>-C<sub>β</sub> bond cleavage (C<sub>α</sub>-aldehyde and C<sub>α</sub>-carboxyl acid aromatic structures). Nevertheless, the cleavage of the β-O-4 bonds, the most abundant bonds in native lignin, and important bonds in residual lignin, which was revealed in the POM experiments on LMCs, MWL and kraft pulps, would contribute positively to the total delignification result in the POM treatment of kraft pulps.

*Delignification by PMOs in Aerobic condition-*

POMs have been studied as catalysts in oxygen delignification of unbleached pulps in aqueous or organic solvent- water media to increase the selectivity of delignification. For this purpose, the hetero poly anions HAA-n of the general formula  $[P Mo_{12-n} V_n O_{40}]^{(3+n)-}$  (n= 1-6) have been used. The most important properties of the HPA-n series of polyoxometalates are their re oxidation with oxygen, a property, which enables the two reactions to occur in the same step and their stability at pH 2.5-5 , a property which requires

acidic process conditions. The redox potential of the HPA-n series of POMs decreases with increasing n and catalytic action in oxidative delignification is performed with HPA-5 in particular  $[P Mo_7 V_5 O_{40}]$ . Vanadium is responsible for the oxidation- reduction path of the

HPA-n polyoxometalates; while oxidizing lignin, HPA-5 is reduced in the reaction  $V^{5+}$  to  $V^{4+}$ , reduced HPA-5 is re oxidized with oxygen in the reaction  $V^{4+}$  to  $V^{5+}$ . The  $VO_2^+$  formed via dissociation of HPA-n is characterized by higher redox potential than the parent HPA-n.

HPA-n converted to  $HPA-(n-1) + VO_2^+$

Due to higher redox potential,  $VO_2^+$  ions are less selective oxidizing agents leading to the oxidative degradation of polysaccharides. Moreover, the free  $VO_2^+$  ions are not oxidized by

$O_2$  in acidic solution which means that they cannot be recycled. Therefore it is desirable to suppress HPA-5 dissociation, which can be done by pH control by addition of polar organic solvents (ethanol) or by increasing the ionic strength of solution. Adding ethanol into the system in the amount of up to 40-50 % improves delignification selectivity due to partial reduction of the concentration of  $VO_2^+$  in the solution. The pH of the system also strongly influences the delignification and while degradation of polysaccharides increases with decreasing pH, the delignification efficiency decreases at pH higher than 2.

Studies of the effect of HPA-5/ $O_2$  and HPA-5-MnII/ $O_2$  on lignin have been performed using hardwood (eucalyptus) and softwood (spruce) species, monomeric and dimeric lignin model compounds, and dioxane lignin adsorbed on pulp. The results of these studies indicated that the conversion of phenolic lignin units occurs 5–6 times faster than that of non-phenolic lignin units and that the syringyl units are more readily oxidized than the guaiacyl analogues. A simplified reaction scheme has been suggested by Evtuguin and Pascoal Neto. They suggested that similarly to the mechanism of POM delignification in the anaerobic system, the reaction starts with one-electron oxidation of lignin phenolic units resulting in phenoxy radicals, which lose one more electron and form cyclohexadienyl cations. In contrast to anaerobic POM treatment delignification, participation of oxygen is suggested in lignin autooxidation during aerobic delignification catalysed by POMs/HPA-5. The role of the  $VO_2^+$  released from the HPA-5 is demonstrated in the suppression of these lignin autooxidation



reactions, and even more in the oxidation of non-phenolic structures for which the  $\text{VO}_2^+$  ions were suggested to be the active catalysts. The rate-determining step of the oxidative delignification of both phenolic and non-phenolic lignin units is the first one-electron oxidation step. Similar to the studies of anaerobic POM delignification, the studies of aerobic POM delignification indicated that the delignification includes cleavages of the  $\text{C}_\alpha\text{-C}_\beta$  and  $\text{C}_1\text{-C}_\alpha$  bonds, demethylation, and formation of quinone structures. The comparative analysis of lignin before and after HPA-5/ $\text{O}_2$  treatment of dioxane lignin adsorbed on pulp showed that the content of the  $\beta\text{-O-4}$ ,  $\beta\text{-}\beta$ , and  $\beta\text{-5}$  bonds was reduced, which is the same result observed in the POM anaerobic delignification of MWL and kraft pulps.

### HPA-5/ $\text{O}_2$ system

The hetero polyanion  $[\text{PMo}_7\text{V}_5\text{O}_{40}]^{8-}$  in solution (HPA-5 for short) has shown catalytic activity under  $\text{O}_2$  for the delignification of eucalyptus sawdust and for the delignification of kraft pulp, in water or ethanol–water medium under appropriate conditions. Delignification of kraft pulp at temperatures of  $90^\circ\text{C}$  and at an optimized pH of 1.8–2.0 and

an oxygen pressure of 0.6 MPa originated pulps with significantly lower kappa numbers than those of the experiments performed with no POM after 2 h of reaction. However, owing to the low pH used, polysaccharide destruction also occurred. This was assumed to be mainly related to the hydrolysis reactions by acid catalysis, as similar intrinsic viscosities were obtained for the experiment carried out with no POM. Notwithstanding, the delignification process catalysed by the HPA-5/ $\text{O}_2$  system was more selective than the conventional oxygen delignification in alkaline medium, when the oxidative degradation was carried out to a kappa number of around 6–7. It was demonstrated that the HPA-5/ $\text{O}_2$  system could be used in multiple delignification cycles without losing its activity for the

delignification of the pulp. These results showed that no catalyst deactivation occurred. The chemical oxygen demand index, after the second cycle, indicated that the oxidised organic materials accumulation and their dissolution in the multiple delignification liquors was roughly the same. This fact indicates that the HPA-5/ $\text{O}_2$  system yields the total oxidation of lignin to carbon dioxide and water. These results are extremely important for a possible application of HPA-5 as a catalyst for an oxygen delignification stage in a totally effluent-free (TEF) bleaching plant. Since the delignification liquor may be continuously re-used it could be carried out in a closed system. In this way, POM delignification opens new perspectives for the implementation of the closed-mill concept and for the reduction of the environmental impact of the bleached kraft pulp mill.

### HPA-5- $\text{Mn}^{\text{II}}$ / $\text{O}_2$ system

$\text{Mn}^{\text{II}}$ -assisted HPA-5 as a catalyst. In spite of the good delignification extent obtained during oxygen delignification catalysed by HPA-5, the selectivity of residual lignin oxidation was restricted by two main factors: a. the low pH of the best delignification medium (ca. pH 2), which promotes acid catalysed hydrolysis of polysaccharides; and b. the undesirable and not easily controllable degradation of polysaccharides with  $\text{VO}_2^+$  ions dissociated from parent structure of HPA-5. To overcome these drawbacks, new development was carried out

on the preparation and structure of the catalyst. Manganese (II) ions in the form of manganese diacetate were added in the last stage of the synthesis of HPA-5 under acidic conditions with the purpose of preparing Mn-substituted HPA-5 structures (HPA-5-MnII for short) as suggested by electrochemical experiments. This experiment accounted for the partial dissociation of HPA-5 at pH 3, leading to the formation of the so-called lacunary derivatives of the parent Keggin polyoxoanions. Moreover, the synthesis of POMs, based on the reactions of lacunary Keggin structures and transition metal ions is well documented. Regarding the catalytic features of Mn-substituted polyoxometalates in oxygen delignification, the use of a lacunary structure of HPA-5 acting as a multidentate ligand to the manganese ions (HPA-5- Mn II) on the oxygen delignification catalysis was investigated. The delignification degree achieved with HPA-5/O<sub>2</sub> or HPA- 5-MnII/O<sub>2</sub> systems was considerably higher than that obtained by oxygen without a catalyst. Comparing the two reaction systems HPA-5/O<sub>2</sub> and HPA-5-MnII/O<sub>2</sub>, the latter showed a slightly lower delignification efficiency but a remarkably improved selectivity, proving a positive influence of the presence of manganese in the substituted HPA-5. The VO<sub>2</sub><sup>+</sup> ions present in the acidic HPA-5 solution play a key role in the oxidative delignification because they were considered as the main active species in the catalytic oxidation of lignin.

At the same time, however, VO<sub>2</sub><sup>+</sup> ions oxidise the polysaccharides, thus decreasing the selectivity of the delignification.

The introduction of Mn in the synthesis of HPA-5- Mn II could control, to some extent, the VO<sub>2</sub><sup>+</sup> ions released.

The lower concentrations of VO<sub>2</sub><sup>+</sup> in the HPA-5-MnII solution could explain the slightly lower delignification efficiency but better selectivity. The molar ratio between HPA-5 and Mn<sup>2+</sup> ions used in the synthesis of HPA-5-MnII also influenced the delignification results. The selectivity of the lignin oxidation was fairly constant when the ratio [HPA-5]/[Mn<sup>2+</sup>] was higher than 1.5. The catalyst HPA-5-1.5MnII ([HPA-5]/[Mn<sup>2+</sup>] = 1.5) was suggested as being the best for the catalytic needs.<sup>54</sup> About 15–20% higher viscosity of the delignified

pulp was achieved with HPA-5-1.5MnII when compared with HPA-5 catalysis at the same degree of delignification. Delignification parameters in the system HPA-5-1.5MnII/O<sub>2</sub> were also optimized. The best delignification selectivity with HPA-5-1.5MnII was observed at a pH between 3 and 4. The temperature of 100<sup>o</sup>C seemed to be a good compromise for selective delignification. After 4 h of reaction at 100<sup>o</sup>C, it was possible to reach up to 70% of residual lignin removal with a viscosity drop of only 26%.

### Oxygen delignification with polyoxometalates and Laccase

As laccase may be an efficient catalyst of re-oxidation of different kinds of POMs, biocatalytic reoxidation of reduced POMs with laccase has been proposed as a method that will enhance re-oxidation efficiency in aerobic delignification. In a first approach, POMs were used as inorganic mediators to laccase-catalysed delignification of pulp at temperatures typically around 45–60<sup>o</sup>C. This followed observation that some of the

POMs that were hardly re-oxidised by oxygen, such as  $\text{SiW}_{11}\text{Mn}^{\text{II}}$  and  $\text{SiW}_{11}\text{V}^{\text{IV}}$ , could be re-oxidised by the enzyme even at room temperature ( $T \approx 25\text{ }^{\circ}\text{C}$ ) and atmospheric pressure (ca. 0.02 MPa). When using POMs as inorganic mediators for pulp delignification (laccase-mediator system – LMS), the POM oxidises the residual lignin in the pulp and the reduced POM is re-oxidised by laccase at the same stage. Finally, the cycle is completed by re-oxidation of the copper centres of the prosthetic group of laccase in the presence of oxygen. The application of the LMS to the delignification of kraft pulps has not produced high delignification. No more than 35% delignification was achieved, even after 48 h of reaction. The low delignification rate was suggested to be due to the scarce reactivity of the POM with the substrate under the applied conditions. In fact, the optimal conditions required for kraft pulp delignification with the POM are typically around 90–110  $^{\circ}\text{C}$ , in contrast to the applied temperatures lower than 60  $^{\circ}\text{C}$ .

In a second approach, an alternative multi-stage process was developed in which the pulp is treated with a POM at high temperature (100–110  $^{\circ}\text{C}$ ) in a first stage, followed by the POM re-oxidation with laccase at moderate temperatures (30–60  $^{\circ}\text{C}$ ) in a separate stage. The application of this multi-stage process brought delignification around 50% when applied to  $\text{SiW}_{11}\text{Mn}^{\text{III}}$  and  $\text{SiW}_{11}\text{V}^{\text{V}}$ .  $\text{SiW}_{11}\text{Mn}^{\text{III}}$  was found to be more selective, while  $\text{SiW}_{11}\text{V}^{\text{V}}$

was more effective in the oxidative delignification. After the laccase stage (POM-L) the complete re-oxidation of polyoxometalates  $\text{SiW}_{11}\text{V}$  (and  $\text{SiW}_{11}\text{Mn}$ , respectively) was verified. Furthermore, no indications of degradation of the Keggin structure were found under the experimental conditions used.

## 7. Conclusion-

As a promising alternative to chlorine based bleaching, oxidative delignification with POMs has been suggested. Both of the approaches, one based on the anaerobic process in which POMs are used as oxidative delignification agents and second based on aerobic process in which POMs are used as catalysts, have their advantages and disadvantages. The most effective and selective polyoxometalates found for the delignification process were  $\text{SiW}_{11}\text{V}^{\text{V}}$ ,  $\text{SiW}_{11}\text{Mn}^{\text{III}}$ ,  $\text{AlW}_{11}\text{V}^{\text{V}}$ ,  $\text{SiW}_{10}\text{V}_2$ , ' $\text{SiW}_{10.1}\text{Mo}_{1.0}\text{V}_{0.9}\text{O}_{40}$ ' and the above-mentioned HPA-5- $\text{Mn}^{\text{II}}$ .

Work on both of the process is going on currently in the industry. A very satisfying result of up to 70% of delignification can be achieved and a saving of 56% of chlorine oxide has also been achieved. In the future it is expected that, new direction of application of other POMs can be achieved, and more selectivity can also be achieved. Alternatively, the development/optimization of new/known processes incorporating delignification and re-oxidation of the POM in different stages should be considered. In the future, these processes

should be optimized and costs evaluated and compared with those of industrial processes in order to evaluate the possibility of incorporating new POM-based delignification processes into industrial applications.

## 8. References

1. Antonio Pineda<sup>1</sup> · Adam F.Lee<sup>1</sup>. Heterogenously catalysed lignin depolymerization. 2016
2. Mark Gale, Charles Cai, Kandis Leslie Abdul Aziz. Heterogenous Catalyst Design Principles for the conversion of Lignin into High Value Commodity Fuels and Chemicals.
3. Javier Fernandez- Rodriguez, Jalel Labidi, in separation of Functional Molecules in Food by Membrane Technology. Lignin Separation and Fractionation by Ultrafiltration. 2019
4. Eja Ahmad, Kamal K. Pant, in West Biorefinery. Lignin Conversion: A Key to the Concept of Lignocellulosic Biomass – Based Integrated Biorefinery. 2018
5. Armindo R.Gaspar, Jose A. F. Gamelas, Dmitry V.Evtuguin and Carlos Pascol Neto. Green Chemistry. Alternative for lignocellulosic pulp delignification using polyoxometalates and oxygen: a review. 2007
6. Pratima Bajpai , in Biermann's Handbook of Pulp and Paper (Third Edition), 2018
7. R.H.Atalla, I.A.Weinstock, R.S.Reiner, C.J.Houtman, S.Reichel, and C.G.Hill . USDA Forest Service, Forest Products Laboratory. Department of Chemical Engineering University of Wisconsin-Madison, USA. C.L.Hill , M.Wemple, J.Cowan, E.M.G.Barbuzzi. Emory University, Department of Chemistry Altana, Georgia, USA. RECENT ADVANCES IN POLYOXOMETALATE BASED DELIGNIFICATION.
8. Armindo R. Gaspar,<sup>a</sup> Jose´ A. F. Gamelas,<sup>\*b</sup> Dmitry V. Evtuguin<sup>b</sup> and Carlos Pascoal Neto<sup>b</sup>. Alternative for lignocellulosic pulp delignification using polyoxometalates and oxygen: a review . 2007
9. Biljana Bujanovic , Sally Ralph 2, Richard Reiner, Kolby Hirth and Rajai Atalla. Polyoxometalates in Oxidative Delignification of Chemical Pulps: Effect on Lignin. 2010.
10. Oxygen Delignification: Pulp and Paper Processes: PRAXAIR'S OXIGEN DELIGNIFICATION AND EXTRACTIVE OXIDATION.

**Immunomodulatory Properties**  
**and**  
**Anticancer activities of  $\beta$ -glucan**

**Review work submitted in partial fulfilment of requirement for  
M.Sc(Chemistry) degree**

**From**

**SCOTTISH CHURCH COLLEGE  
UNIVERSITY OF CALCUTTA**

**SULAGNA PAUL**

**(M.Sc, 4<sup>th</sup> Semester)**

**University Registration No: 211-1221-0869-14**

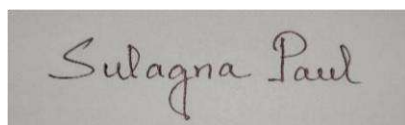
**University Roll No: 223/CEM/191033**

**Special paper : CHEM-SO44**

**Name of Candidate**

**Sulagna Paul**

**(M.Sc, 4<sup>th</sup> Semester)**

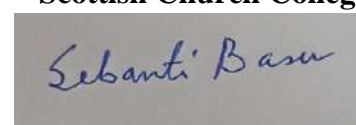


.....  
**Signature of candidate**

**Name of Examiner**

**Dr. Sebanti Basu**

**Associate Professor  
Scottish Church College**



.....  
**Signature of Examiner**

## **ACKNOWLEDGEMENT**

I gratefully thank Dr. Asish Kumar Sen, Ex. Chief Scientist and Emeritus Scientist-CSIR; Associate professor, Indian Institute of Chemical Biology, under his supervision and unending support this review work was accomplished during my 4<sup>th</sup> and final semester in partial fulfilment of M.Sc (chemistry) degree in the University of Calcutta under Scottish Church College, Kolkata. Also I would like to thank the University of Calcutta and my respected college professors for giving me the opportunity to write this review paper.

## **Content**

**Page No.**

1. Introduction .....	4
2. Sources of $\beta$ -glucan .....	4
3. Structure variation and types of $\beta$ -glucan .....	5
➤ Backbone .....	5
➤ Side chain .....	5
➤ Types of $\beta$ -glucan .....	6
➤ Conformations .....	6
4. Immunomodulation: an introduction .....	7
5. Pharmacodynamics and pharmacokinetics of $\beta$ -glucan .....	9
➤ Animal studies .....	9
➤ Human studies .....	10
➤ $\beta$ -Glucan as immunomodulating agent .....	11
6. Tumour and cancer : an introduction .....	13
7. Anticancer activity .....	14
8. Anticancer activity of $\beta$ -glucan .....	14
➤ Clinical trials on anticancer effects of natural products with $\beta$ -glucan .....	14
➤ Medicinal mushroom with $\beta$ -glucans as active components .....	15
9. Conclusion .....	16
10. References .....	17

## **1. Introduction:**

Cereal and fungal products[1-5] have been used for centuries for medicinal and cosmetic purposes; however, the particular role of  $\beta$ -glucan was not traversed until the 20<sup>th</sup> century.  $\beta$ -Glucan, a polysaccharide in the form of dietary fibre was first discovered in lichens (comprise a fungus living in a symbiotic relationship with an algae or cyanobacterium) [6] and shortly thereafter in barley. Dietary fiber has been extensively studied [7] in last few decades for their physiological health benefits. We get dietary fiber from the plant-based foods we eat. Fiber supports good health by helping human body reduce cholesterol and control blood sugar levels. Depending on its solubility dietary fibres are classified in two groups- soluble and insoluble dietary fiber.  $\beta$ -glucans are one form of water-soluble dietary fibre and also regarded as bioactive functional food ingredient due to its various health benefits like improving cholesterol levels, weight reduction, immune modulator and anti-carcinogenic effects. They comprise a group of  $\beta$ -D-glucose polysaccharides naturally occurring in the cell walls of cereals, bacteria, fungi, mushrooms ( $\beta$ -glucans are principally obtained in fruit body of various type of mushrooms) with significantly differing physicochemical properties depending on source[8].

Typically,  $\beta$ -glucans (other than cellulose) form a linear backbone with 1–3  $\beta$ -glycosidic bonds but vary with respect to molecular mass, solubility, branching structure, viscosity hence causing diverse physiological effects in animals, bacteria, yeast, algae and mushrooms. The evaluation of mushroom derivatives and their medical properties are important part of these studies. For dietary intake levels of at least 3 g per day, oat fiber  $\beta$ -glucan decreases blood levels of LDL cholesterol and reduce the risk of cardiovascular diseases (CVD).  $\beta$ -glucans are used as modifying and texturing substrate in various bioceutical and cosmetic products, and as soluble fiber supplements.

## **2. Sources of $\beta$ -glucan[10-15]:**

$\beta$ -Glucan is not naturally found in human body. It is acquired through dietary supplements. There are a number of foods high in  $\beta$ -glucan including :

- Cereals - barley fiber, millets, oats and whole grains.
- Microorganisms – yeast (Cell wall of the baker's yeast that is *Saccharomyces cerevisiae*), fungi, bacteria.
- Reishi, maitake, and shiitake mushrooms.
- Lichens (*Cetraria islandica*).



- Seaweeds/algae [ *Laminariasp.* (brown algae) , *Phytophthorasp.*]

A lesser amount of  $\beta$ -glucan is found in wheat, rye and sorghum. Among these sources, barley typically has the highest  $\beta$ -glucan content and oats the second highest.

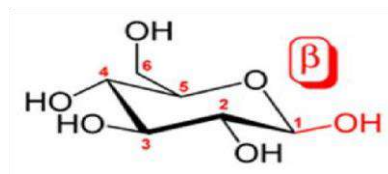


Various sources of  $\beta$ -Glucan

### **3. Structure variation and types of $\beta$ -glucan:**

- **Backbone :**

$\beta$ -Glucans (excluding cellulose) are polymers of D-glucose having linear  $\beta$ -(1 $\rightarrow$ 3) linkage backbone. The most common  $\beta$ -glucans from various sources include a linear  $\beta$ -(1 $\rightarrow$ 3) glycosidic bond (a glycosidic bond is a type of covalent bond that joins a carbohydrate molecule to another molecule) to form polymer. Some  $\beta$ -glucans, isolated from certain sources, can be branched having  $\beta$ -(1 $\rightarrow$ 3) linkage as backbone and  $\beta$ -(1 $\rightarrow$ 6) as branching linkage.



Glucose molecule with carbon numbering notation and  $\beta$  orientation

- **Side-chain :**

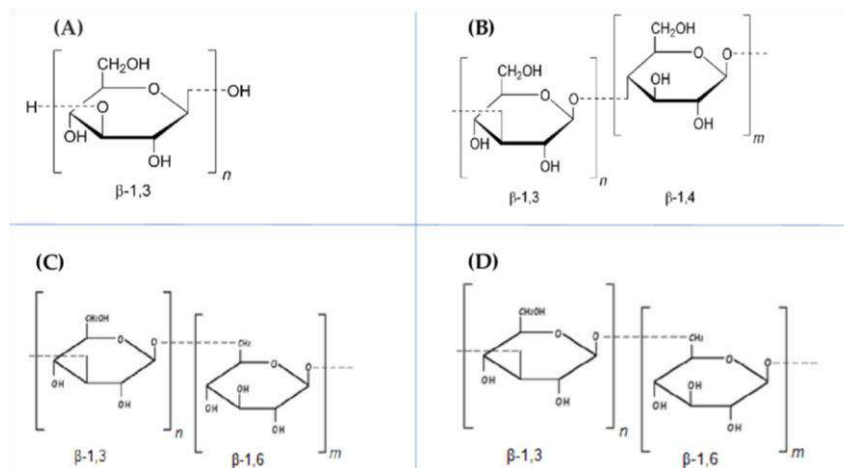
Some  $\beta$ -glucan molecules have branched glucose side-chains attached to their positions on the main D-glucose chain, which branch off the  $\beta$ -glucan backbone. Additionally, these side-chains can be attached to other types of molecules, like proteins as in Polysaccharide-K.

Polysaccharide-K or PSK is protein bound polysaccharide consists of a  $\beta$ -glucan-(1 $\rightarrow$ 4) main chain with  $\beta$ -(1 $\rightarrow$ 3) and  $\beta$ -(1 $\rightarrow$ 6) side-chains.

- **Types :**

Each type of  $\beta$ -glucan comprises a different molecular backbone, degree of branching and molecular weight and solubility. Cereal-derived  $\beta$ -glucans are predominantly mixtures of  $\beta$ (1 $\rightarrow$ 3) and  $\beta$ -(1 $\rightarrow$ 4) glycosidic linkages without any  $\beta$ -(1 $\rightarrow$ 6) bonds. Beta-glucans from yeasts (e.g., *Saccharomyces cerevisiae*) are mixtures of linear  $\beta$ -(1 $\rightarrow$ 3) backbones containing 30-residue straight chains. They are connected to these are long branches attached via  $\beta$ -(1 $\rightarrow$ 6) linkages. Yeast  $\beta$ -glucans contains backbone containing  $\beta$ -(1 $\rightarrow$ 3) glycosidic linkage with elongated  $\beta$ -(1 $\rightarrow$ 6) branches.

Bacterial  $\beta$ -glucans (e.g., *Agrobacterium imbiobaris*) have main and unbranched  $\beta$ (1 $\rightarrow$ 3) D-glucan backbones, while seaweed  $\beta$ -glucans (such as those found in brown kelp, *Laminaria*) are species-dependent. They may contain straight chain of  $\beta$ -(1 $\rightarrow$ 3) linkages or the straight chain backbone together with high levels of  $\beta$ -(1 $\rightarrow$ 6) glycosidic linkages.



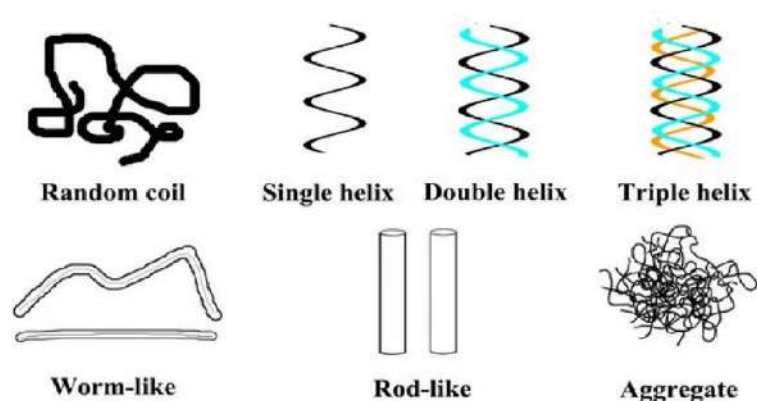
Types of  $\beta$ -Glucan

- **Conformations :**

The branching alignment follow a particular ratio and branches can arise from branches (secondary branches). In aqueous solution, based on origin and processing method used in their extraction and

modification,  $\beta$ -glucans can exist in a range of conformations. The most widely observed conformations are random coils, helices (single, double, or triple), worm-like shapes, rod-like shapes, or aggregates. The molecular weight (MW) of  $\beta$ -glucan ranges from 102 to 106

Da, depending on the source. For example, soluble  $\beta$ -glucans from two edible mushroom varieties *maitake* and *shiitake* were estimated to have MW of about 400 kDa. Cereal  $\beta$ -glucans are also soluble and may reach MW of between 1.1 and 1.6 MDa (for oats) and around 49 MDa for barley. The immune functions of  $\beta$ -glucans are apparently dependent on their conformational complexity. It has been suggested that higher degree of structural complexity is associated with more potent immunomodulatory and anti-cancer effects.[15-20]



Various conformations of  $\beta$ -glucan

#### 4. Immunomodulation:

The immune system is a complex network of cells and proteins that defends the body against infections. The immune system attacks germs and keeps a record of every microbe (germ) it has ever defeated in types of white blood cells (B and T-lymphocytes). They are known as memory cells, so it can quickly recognise and destroy the microbe before it starts multiplication after entering the body again. Immunomodulation is the modification of the immune system. It has natural as well as human-induced forms. Improvement of the immune response is desirable to prevent various infection in e of immunodeficiency.[21]

- T lymphocyte :T lymphocyte or T cell, a type of white blood cell(Leukocyte) is an essential part of the immune system. In mammals, T cells originate in the bone marrow(at the core of the bones) and mature in the thymus (pyramid-shaped lymphoid organ). In the thymus, T cells multiply and transform into :

# regulatory - This T cells act to control immune reactions, hence their name

# helper - This T cells play a role in normal immune responses

# cytotoxic T cells - This T cells recognize antigens on the surface of a cell infected with a virus, allowing the T cells to bind to and kill the infected cell

# memory T cell – This T cells are antigen specific T cells that remain long term after an infection has been eliminated. These cells have a memory for the antigen survive for a long time, respond quickly following a second exposure to the same antigen.

These T cells are then sent to peripheral tissues or circulate in the blood or lymphatic system.

- B Lymphocyte : B-Lymphocytes also known as B cells are a type of white blood cell of the lymphocyte subtype. They function in the antibody-mediated immunity component of the adaptive immune system. B cells produce antibody molecules (these are not secreted) which when inserted into the plasma membrane serve as a part of B cell receptors. In mammals, B cells mature in the bone marrow. B cells bind to an antigen, receive help from a cognate helper T cell, and differentiate into a plasma cell that secretes large amount of antibodies. Different types of Lymphocyte are:

# Plasmablast–A short-lived antibody secreting cell arising from B cell differentiation. They are generated early in an infection having antibodies with very weak affinity towards antigen.

# Plasma cell – A long-lived antibody secreting cell arising from B cell differentiation. They are generated later in an infection having antibodies with higher affinity towards target antigen.

# Memory B cell – Their function is to circulate through the body and generate a stronger, more rapid antibody response if they detect the antigen.

# Regulatory B cell – These B cell type stops the expansion of pathogenic, pro-inflammatory lymphocytes through the secretion of various antibodies.

- Acquired Immunity : Acquired immunity is immunity which is developed over lifetime. It can come from of:

# a vaccine

# exposure to an infection or disease

When pathogens are introduced into a person's body from a vaccine or a disease, this type of immunity develops. The two types of acquired immunity are adaptive and passive. Adaptive

immunity occurs in response to being infected with or vaccinated against a microorganism. Passive immunity occurs when a person receives antibodies to a disease or toxin.

- **Innate Immunity:** Innate immunity is also known as natural immunity because it is present at birth and does not have to be learned through exposure to an foreign element. It provides an immediate response to the foreign elements. The innate immunity system includes:

# Physical Barriers such as skin, the gastrointestinal tract, the respiratory tract, the nasopharynx, cilia, eyelashes and other body hair.

# Defence Mechanism such as secretions, mucous, bile, gastric acid, saliva, tears and sweat. #

General Immune Responses

## **5. Pharmacodynamics & Pharmacokinetics of $\beta$ -glucan:**

Most  $\beta$ -glucans are considered as non-digestible carbohydrates and are fermented to various degrees by the intestinal microbial flora [22–24]. Therefore, it has been speculated that their immunomodulatory properties may be partly attributed to a microbial dependent effect. However,  $\beta$ -glucans in fact can directly bind to specific receptors of immune cells, suggesting a microbial independent immunomodulatory effect [25]. The pharmacodynamics and pharmacokinetics of  $\beta$ -glucans have been studied in animal and human models.

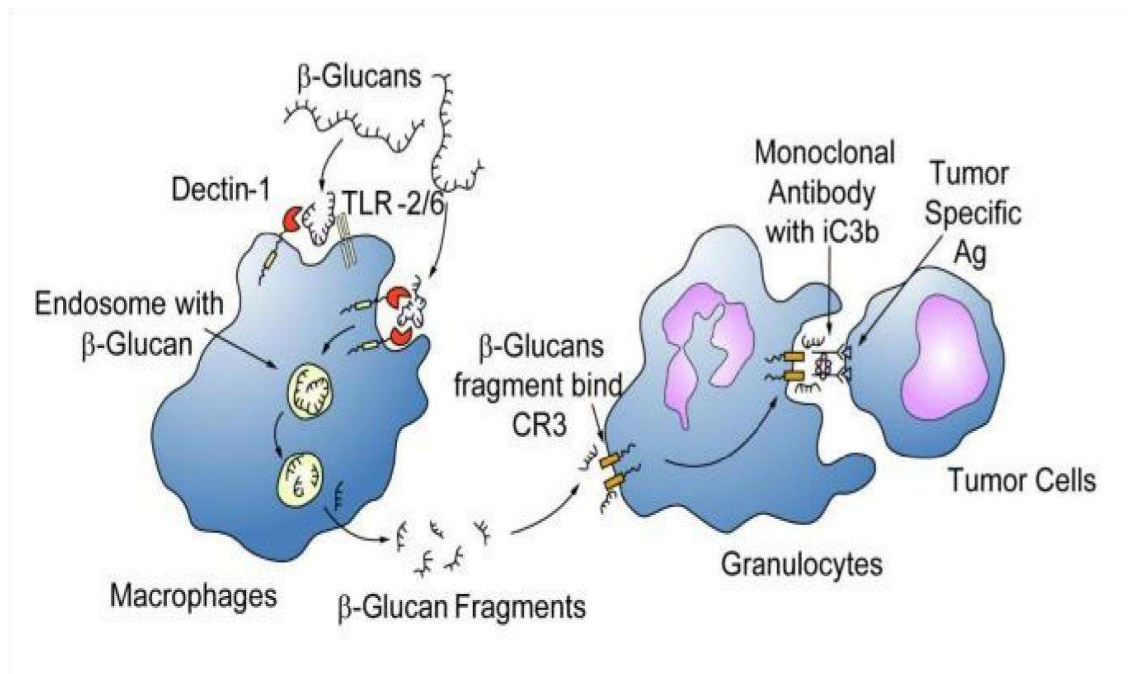
- **Animal Studies**

Study using a suckling rat model (rodent, easily available and managed in the laboratory) for evaluation of the absorption and tissues distribution of internally administered radioactive labelled  $\beta$ -glucan, it was found that the majority of  $\beta$ -glucan was detected in the stomach and duodenum 5 minutes after the administration [26]. This amount rapidly decreased during first 30 minutes. A significant amount of  $\beta$ -glucan entered the proximal intestine (the first and middle part of the colon) shortly after ingestion. Its transit through the proximal intestine decreased with time with a simultaneous increase in the ileum. Despite low systemic blood levels (less than 0.5%), significant systemic immunomodulating effects in terms of humoral and cellular immune responses were demonstrated.

The pharmacokinetics following intravenous administration of 3 different highly purified and previously characterized  $\beta$ -glucans were studied using carbohydrates covalently labelled with a fluorophore on the reducing terminus. The variations in molecular size, branching frequency and

solution conformation were shown to have an impact on the elimination half-life, volume of distribution and clearance [27].

After ingestion the low systemic blood level of  $\beta$ -glucans does not reflect the pharmacodynamics of  $\beta$ -glucans and does not exclude its *in vivo* effects. Cheung-VKN *et al.* labeled  $\beta$ -glucans with fluorescein to track their oral uptake and processing *in vivo*. The orally administered  $\beta$ -glucans were taken up by macrophages (specialised cells involved in the detection and destruction of bacteria) via the Dectin-1 (a type II transmembrane protein which binds  $\beta$ -1,3 and  $\beta$ -1,6 glucans) receptor and was subsequently transported to the spleen, lymph nodes, and bone marrow. Within the bone marrow, the macrophages degraded the large  $\beta$ -1,3-glucans into smaller soluble  $\beta$ -1,3glucan fragments. These fragments were subsequently taken up via the complement receptor 3 (CR3) (a human cell surface receptor found on B and T lymphocytes, neutrophils and macrophages) of margined granulocytes. These granulocytes with CR3-bound  $\beta$ -glucanfluorescein were shown to kill inactivated complement 3b (iC3b)-opsonised tumour cells after they were recruited to a site of complement activation such as tumour cells coated with monoclonal antibody [28]. It was also shown that intravenous administered soluble  $\beta$ -glucans can be delivered directly to the CR3 on circulating granulocytes.



The uptake and subsequent actions of beta-glucan on immune cells

$\beta$ -glucans are captured by the macrophages via the Dectin-1 receptor with or without TLR-2/6. The large  $\beta$ -glucan molecules are then internalized and fragmented into smaller sized  $\beta$ -glucan fragments within the macrophages. They are carried to the marrow and endothelial reticular system and subsequently released. These small  $\beta$ -glucan fragments are eventually taken up by the circulating granulocytes, monocytes or macrophages via the complement receptor (CR)-3. The immune response will then be turned on, one of the actions is the phagocytosis of the monoclonal antibody tagged tumour cells.

Furthermore, Rice PJ et al. showed that soluble  $\beta$ -glucans such as laminarin and scleroglucan can be directly bound and internalized by intestinal epithelial cells and gut associated lymphoid tissue (GALT) cells [28]. Unlike macrophage, the internalization of soluble  $\beta$ -glucan by intestinal epithelial cells is not Dectin-1 dependent. However, the Dectin-1 and TLR-2 are accountable for uptake of soluble  $\beta$ -glucan by GALT cells. Another significant finding of this study is that the absorbed  $\beta$ glucans can increase the resistance of mice to bacterial infection challenge.

- **Human Studies**

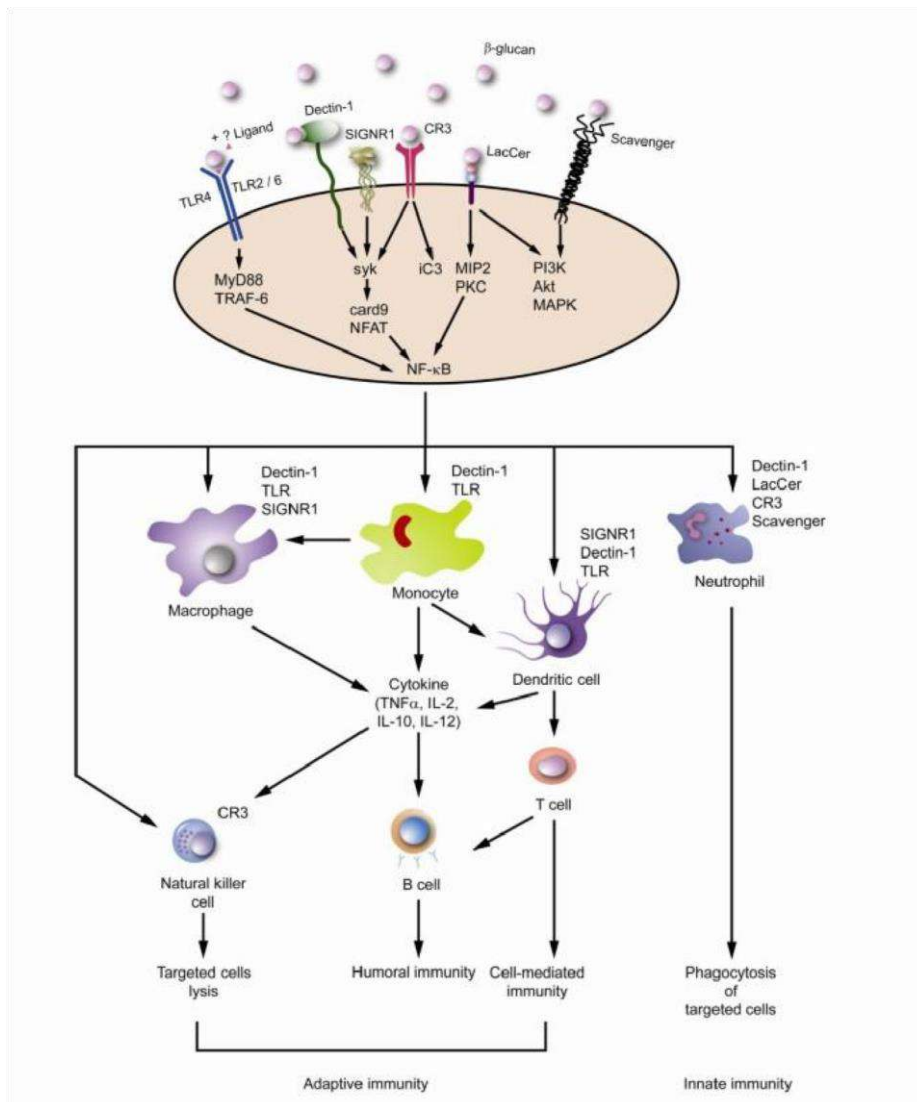
After ingestion how  $\beta$ -glucans mediate their effects in human remained to be defined. In a phase I study the assessment of safety and tolerability of a soluble form oral  $\beta$ -glucans is done [29]. B Glucans of different doses (100 mg/day, 200 mg/day or 400 mg/day) were given respectively for 4 consecutive days. No drug-related adverse events were observed. Repeated measurements of  $\beta$ glucans in serum, however, revealed no systemic absorption of the agent following the oral administration. In spite of that, the immunoglobulin A concentration in saliva increased significantly for the 400 mg/day arm, suggesting a systemic immune effect has been elicited. One limitation of this study is the low sensitivity of serum  $\beta$ -glucans determination.

In summary, based on mostly animal data,  $\beta$ -glucans enter the proximal small intestine rapidly and are captured by the macrophages after oral administration. The  $\beta$ -glucans are then internalized and fragmented into smaller sized  $\beta$ -glucans and are carried to the marrow and endothelial reticular system. The small  $\beta$ -glucans fragments are then released by the macrophages and taken up by the circulating granulocytes, monocytes and dendritic cells. The immune response will then be elicited. However, we should interpret this information with caution as most of the proposed mechanisms are based on *in vitro* and *in vivo* animal studies. Indeed, there is little to no evidence for these hypothesized mechanisms of action and pharmacokinetics occurred in human subjects at the moment.

- **$\beta$ -glucans as immunomodulating agent**

Current data suggests that  $\beta$ -glucans are potent immunomodulators with effects on both innate and adaptive immunity. The ability of the innate immune system to quickly recognize and respond to an invading pathogen is essential for controlling infection. Dectin-1, which is a type II transmembrane protein receptor that binds  $\beta$ -1,3 and  $\beta$ -1,6 glucans, can initiate and regulate the innate immune response [31–33]. It recognizes  $\beta$ -glucans found in the bacterial or fungal cell wall with the advantage that  $\beta$ -glucans are absent in human cells. It then triggers effective immune responses including phagytosis and pro-inflammatory factors production, leading to the elimination of infectious agents. Dectin-1 is expressed on cells responsible for innate immune response and has been found in macrophages, neutrophils, and dendritic cells. The Dectin-1 cytoplasmic tail contains an immunoreceptor tyrosine based activation motif (ITAM) that signals through the tyrosine kinase in collaboration with Toll-like receptors 2 and 6 (TLR-2/6) [34, 37, 38]. The entire signalling pathway downstream to dectin-1 activation has not yet been fully mapped out but several signalling molecules have been reported to be involved. They are NF- $\kappa$ B (through Syk-mediate pathway), signalling adaptor protein CARD9 and nuclear factor of activated T cells (NFAT). This will eventually lead to the release of cytokines including interleukin (IL)-12, IL-6, tumour necrosis factor (TNF)- $\alpha$ , and IL10. Some of these cytokines may play important role in the cancer therapy. On the other hand, the dendritic cell-specific ICAM-3-grabbing non-integrin homolog, SIGN-related 1 (SIGNR1) is another major mannose receptor on macrophages that cooperates with the Dectin-1 in non-opsonic recognition of  $\beta$ -glucans for phagocytosis [30]. Furthermore, it was found that blocking of TLR-4 can inhibit the production of IL-12 p40 and IL-10 induced by purified Ganoderma glucans (PS-G), suggesting a vital role of TLR-4 signalling in glucan induced dendritic cells maturation. Such effect is also operated via the augmentation of the I $\kappa$ B kinase, NF- $\kappa$ B activity and MAPK phosphorylation [31]. One additional point to note is that those studies implied the interaction between  $\beta$ -glucans and TLR all used nonpurified  $\beta$ -glucans, therefore the actual involvement of pure  $\beta$ -glucans and TLR remains to be proven.





### Immune activation induced by $\beta$ -glucans.

$\beta$ -glucans can act on a variety of membrane receptors found on the immune cells. It may act singly or in combine with other ligands. Various signalling pathway are activated and their respective simplified downstream signalling molecules are shown. The reactors cells include monocytes, macrophages, dendritic cells, natural killer cells and neutrophils. Their corresponding surface receptors are listed. The immunomodulatory functions induced by  $\beta$ -glucans involve both innate and adaptive immune response.  $\beta$ -glucans also enhance opsonic and non-opsonic phagocytosis and trigger a cade of cytokines release, such as tumour necrosis factor(TNF)- $\alpha$  and various types of interleukins (ILs).

In summary,  $\beta$ -glucans act on a diversity of immune related receptors in particularly Dectin-1 and CR3, and can trigger a wide spectrum of immune responses. The targeted immune cells of  $\beta$ -glucans include macrophages, neutrophils, monocytes, NK cells and dendritic cells. The immunomodulatory functions induced by  $\beta$ -glucans involve both innate and adaptive immune response.  $\beta$ -glucans also

enhance opsonic and non-opsonic phagocytosis. Whether  $\beta$ -glucans polarize the T cells subset towards a particular direction remains to be explored.

## **6. Tumour and cancer: an introduction:**

In a healthy body, cells grow, divide and replace each other in the body. As new cells form, the older ones die. Tumours develop when cells reproduce very quickly.

A tumour is a mass or lump of tissue that may resemble swelling. The National Cancer Institute define a tumour as ‘an abnormal mass of tissue that results when cells divide more than they should or do not die when they should’.

Tumours can vary in size from a tiny nodule to a large mass, they can appear almost anywhere on the body. There are three types of tumour [37]-

# Benign – They are not cancerous. They either cannot spread or grow, or they do so very slowly and after removal they do not generally return.

# Premalignant – This tumour cells are not cancerous but they have the potential to become malignant or cancerous.

# Malignant – Malignant tumours are cancerous. The cells can grow and spread to other parts of the body.

Cancer cells are formed when normal cells lose the normal regulatory mechanisms that control growth and multiplication. They become ‘rogue cells’ and often lose the specialized characteristics that distinguish one type of cell from another (for example a liver cell from a blood cell). This is called a loss of differentiation. Malignant tumour cells grow uncontrollably and due to the heavy growth and spreading of these cells the disease can become life threatening. Malignant tumours can grow quickly and spread over new areas of the body often by way of the lymph system or bloodstream in a process called metastasis. A major problem in treating cancer is the fact that it is not a single disease. There are more than 200 different cancers resulting from different cellular defects, and so a treatment that is effective in controlling one type of cancer may be ineffective on another.

Different types of malignant tumour originate in different type of cell [36] such as Carcinoma, Sarcoma, Germ cell tumour, Blastoma.

## **7. Anticancer activity [38]:**

Anticancer drug, also called antineoplastic drug, any drug that is effective in the treatment of malignant or cancerous disease. There are several major classes of anticancer drugs; these include alkylating agents, antimetabolites, natural products and hormones. The term chemotherapy frequently is equated with the use of anticancer drugs, though it refers more accurately to the use of chemical compounds to treat disease generally. From recent studies it has been proved that natural products may exert significant cytotoxic and immunomodulatory effects. Plant derived chemotherapeutic agents such as taxol, etoposide or vincristine, currently used in cancer therapy are prominent examples in this e. However, there is a need for new and natural anticancer compounds with low or without toxicity to normal cells. One of the active compounds responsible for the immune effects is beta-glucan derived from cereals, fungi, seaweeds, yeasts and bacteria.

## **8. Anticancer activity of $\beta$ -glucan[39]:**

In the literature, there are no clinical trials that directly assessed the anti-cancer effects of purified  $\beta$ -glucans in cancer patients. Most studies were assessing the toxicity profile or underlying immune changes of the cancer patients without addressing on the change of cancer status. In addition, most of the related studies used either crude herbal extracts or a fraction of the extracts instead of purified  $\beta$ -glucans. Therefore, it is difficult to identify whether the actual effects were related to  $\beta$ -glucans or other confounding chemicals found in the mixture.

In a prospective clinical trial of short term immune effects of oral  $\beta$ -glucan in patients with advanced breast cancer, 23 female patients with advanced breast cancer were compared with 16 healthy females control. Oral  $\beta$ -1,3;1,6-glucan was taken daily. Blood samples were recollected on the day 0 and 15. It was found that despite a relatively low initial white cell count, oral  $\beta$ -glucan can stimulate proliferation and activation of peripheral blood monocytes in patients with advanced breast cancer.

Whether that can be translated into clinical benefit remains unanswered.

- **Clinical trials on anti-cancer effects of natural products with  $\beta$ -glucan:**

Many edible fungi particularly in the mushroom species yield immunogenic substances with potential anticancer activity [40].  $\beta$ -glucans are one of the common active components . In limited clinical trials on human cancers, most were well tolerated. Among them, lentinan derived from *Lentinusedodes* is a form of  $\beta$ -glucans [41]. Since it has poor enteric absorption, intrapleural, intra-peritoneal [42] or intravenous routes had been adopted in clinical trials which showed some clinical benefit when used as

an adjuvant to chemotherapy [43]. Schizophyllan (SPG) or sizofiran is another  $\beta$ -glucan derived from *Schizophyllum commune*. Its triple helical complex  $\beta$ -glucans structure prevents it from adequate oral absorption so an intratumoral route or injection to regional lymph nodes had been adopted [44]. In a randomized trial, SPG combined with conventional chemotherapy improved the long term survival rate of patients with ovarian cancer [45]. But whether the prolonged survival can subsequently led to a better cure rate remain unanswered.

- **Medicinal mushroom with  $\beta$ -glucans as active components**

*Maitake* D-Fraction extracted from *Grifolafrondosa* (*Maitake* mushroom) was found to decrease the size of the lung, liver and breast tumours in >60% of patients when it was combined with chemotherapy in a 2 arms control study comparing with chemotherapy alone [46]. The effects were less obvious with leukemia, stomach and brain cancer patients [47]. But the validity of the clinical study was subsequently questioned by another independent observer [48]. Two proteoglycans from *Coriolusversicolor* (Yun Zhi) – PSK (Polysaccharide-K) and PSP (Polysaccharopeptide) – are among the most extensively studied  $\beta$ -glucan containing herbs with clinical trials information. However, both PSK and PSP are protein-bound polysaccharides, so their actions are not necessary directly equivalent to pure  $\beta$ -glucans [49]. In a series of trials from Japan and China, PSK and PSP were well tolerated without significant side effects [50,51-53]. They also prolonged the survival of some patients with carcinoma and non-lymphoid leukemia.

*Ganoderma* polysaccharides are  $\beta$ -glucans derived from *Ganodermalucidum* (Lingzhi, Reishi). While  $\beta$ -glucan is the major component of the *Ganoderma* mycelium, it is only a minor component in the *Ganoderma* spore [54]. The main active ingredient in the *Ganoderma* spore extract is triterpenoid which is cytotoxic in nature. In an open-label study on patients with advanced lung cancer, thirty-six patients were treated with 5.4 g/day *Ganoderma* polysaccharides for 12 weeks with inconclusive variable and results on the cytokines profiles [55]. Another study on 47 patients with advanced colorectal cancer using the same dosage and period again demonstrated similar variable immune response patterns [56]. These results highlight the inconsistency of clinical outcomes in using immune enhancing herbal extracts clinically, which may partly be due to the impurity of the products used.

## **9. Conclusion:**

$\beta$ -Glucans have been investigated for their ability to protect against infection and cancer and more recently for their therapeutic potential when combined with cancer therapy.  $\beta$ -Glucans are natural polysaccharides present in fungi, algae, bacteria, and plants, which differ in structure, size, branching frequency, and conformation. These polysaccharides (excluding cellulose) commonly consist of a main

chain of  $\beta$ -(1,3) and/or  $\beta$ -(1,6)-glucopyranosyl units in non-repeating non-random order, with side chains of varying lengths. The intrinsic differences of the  $\beta$ -glucans derived from different sources will elicit variable immunomodulatory and anti-cancer responses. In this review we have summarized the immunomodulatory and anti-cancer effect of  $\beta$ -glucans as well as the current limitations of  $\beta$ -glucan research.

$\beta$ -Glucans have a potent immunomodulating activity; their action is mediated through receptors present on immune cells. Their immune modulating effects are attributed to the ability to bind to pattern recognition receptors.

So far, there are very few clinical trial data on using purified  $\beta$ -glucans for cancer patients. Most of the available evidence comes from preclinical data and human studies are just now beginning to appear in the literature, therefore firm conclusions on its clinical importance cannot yet be made. Perhaps the most promising evidence to date in human trials has come from recent studies on a benefit of  $\beta$ -glucan on quality of life and survival when given in combination with cancer treatment.

Studies on  $\beta$ -glucan are complicated by the fact that many studies on  $\beta$ -glucan related herbs often used crude extracts rather than purified compounds, therefore, the confounding effects of other chemicals cannot be totally ruled out. Careful selection of appropriate  $\beta$ -glucan products with good pre-test quality control is essential if we want to understand and compare the results on how  $\beta$ -glucans act on our immune system and exerting anti-cancer effects. A possibly well-defined  $\beta$ -glucan standard is urgently needed in this field for controlled experiments.

There is urgent need for future studies that compare purified forms of  $\beta$ -glucans from different sources to further the understanding of the mechanisms of action and aid in the development of clinical studies for its anti-cancer and immunomodulatory effects.

## **10. Reference:**

1. Henrion, M.; Francey, C.; Lê, K.-A.; Lamothe, L. Cereal  $\beta$ -Glucans: The Impact of Processing and How It Affects Physiological Responses. *Nutrients* 2019, 11, 1729.
2. Lamothe, L.M.; Lê, K.-A.; Samra, R.A.; Roger, O.; Green, H.; Macé, K. The scientific basis for healthful carbohydrate profile. *Crit. Rev. Food Sci. Nutr.* 2019, 59, 1058–1070. doi:10.1080/10408398.2017.1392287.
3. Ferretti, F.; Mariani, M. Simple vs. Complex Carbohydrate Dietary Patterns and the Global Overweight and Obesity Pandemic. *Int. J. Environ. Res. Public Health* 2017, 14, 1174. doi:10.3390/ijerph14101174.

4. Qiao, F.; Liu, Y.K.; Sun, Y.H.; Wang, X.D.; Chen, K.; Li, T.Y.; Li, E.C.; Zhang, M.L. Influence of different dietary carbohydrate sources on the growth and intestinal microbiota of *Litopenaeus vannamei* at low salinity. *Aquac. Nutr.* 2017, 23, 444–452. doi:10.1111/anu.12412.
5. Ahmad, A.; Kaleem, M.  $\beta$ -Glucan as a Food Ingredient. In *Biopolymers for Food Design*; Elsevier: Amsterdam, Netherlands, 2018; pp. 351–381. doi:10.1016/b978-0-12-811449-0.00011-6.
6. de Souza Bonfim-Mendonça, P.; Capoci, I.R.G.; Tobaldini-Valerio, F.K.; Negri, M.; Svidzinski, T.I.E. Overview of  $\beta$  Glucans from *Laminaria* spp.: Immunomodulation Properties and Applications on Biologic Models. *Int. J. Mol. Sci.* 2017, 18, 1629. doi:10.3390/ijms18091629.
7. Chen, J. Editorial (Hot Topic: Recent Advance in the Studies of  $\beta$ -glucans for Cancer Therapy). *AntiCancer Agents Med. Chem.* 2013, 13, 679–680. doi:10.2174/1871520611313050001.
8. Ina, K.; Kataoka, T.; Ando, T. The use of lentinan for treating gastric cancer. *Anti-Cancer Agents Med. Chem.* 2013, 13, 681–688. doi:10.2174/1871520611313050002.
9. Jayachandran, M.; Chen, J.; Chung, S.S.M.; Xu, B. A critical review on the impacts of  $\beta$ -glucans on gut microbiota and human health. *J. Nutr. Biochem.* 2018, 61, 11–110.
10. Lazaridou, A.; Biliaderis, C.G.; Izydorczyk, M.S. Cereal  $\beta$ -glucans: Structures, physical properties, and physiological functions. In *Functional Food Carbohydrates*; CRC Press: Boca Raton, FL, USA, 2006; pp. 15–86.
11. H. V.; Sievenpiper, J. L.; Zurbau, A.; Blanco Mejia, S.; Jovanovski, E.; Au-Yeung, F.; Jenkins, A. L.; Vuksan, V (2016). "The effect of oat  $\beta$ -glucan on LDL-cholesterol, non-HDL-cholesterol and apoB for CVD risk reduction: A systematic review and meta-analysis of randomised-controlled trials". *British Journal of Nutrition.* 116 (8): 1369–1382. doi:10.1017/S000711451600341X.
12. Kirby RW, Anderson JW, Sieling B, Rees ED, Chen WJ, Miller RE, Kay RM (1981). "Oat-bran intake selectively lowers serum low-density lipoprotein cholesterol concentrations of hypercholesterolemic men". *Am. J. Clin. Nutr.* 34 (5): 824–9. doi:10.1093/ajcn/34.5.824. PMID 6263072.
13. 21 CFR 101.81 Health Claims: Soluble fiber from certain foods and risk of coronary heart disease (CHD)
14. Zeković, Djordje B. (10 October 2008). "Natural and Modified (1→3)- $\beta$ -D-Glucans in Health Promotion and Disease Alleviation". *Critical Reviews in Biotechnology.* 25 (4): 205–230. doi:10.1080/07388550500376166. PMID 16419618. S2CID 86109922
15. Sikora, Per (14 June 2012). "Identification of high  $\beta$ -glucan oat lines and localization and chemical characterization of their seed kernel  $\beta$ -glucans". *Food Chemistry.* 137 (1–4): 83–91. doi:10.1016/j.foodchem.2012.10.007. PMID 23199994
16. Chu, YiFang (2014). *Oats Nutrition and Technology*. Barrington, Illinois: Wiley Blackwell. ISBN 978-1-118-35411-7.

17. Volman, Julia J (20 November 2007). "Dietary modulation of immune function by  $\beta$ glucans". *Physiology & Behavior*. 94 (2): 276–284. doi:10.1016/j.physbeh.2007.11.045. PMID 18222501. S2CID 24758421
18. Ruiz-Herrera J, Ortiz-tellanos L (May 2010). "Analysis of the phylogenetic relationships and evolution of the cell walls from yeasts and fungi". *FEMS Yeast Research*. 10 (3): 225–43. doi:10.1111/j.1567-1364.2009.00589.x. PMID 19891730.
19. McIntosh, M (19 October 2004). "Curdlan and other bacterial (1→3)- $\beta$ -D-glucans". *Applied Microbiology and Biotechnology*. 68 (2): 163–173. doi:10.1007/s00253-005-1959-5. PMID 15818477. S2CID 13123359.
20. Han, Man Deuk (March 2008). "Solubilization of water-insoluble  $\beta$ -glucan isolated from *Ganoderma lucidum*". *Journal of Environmental Biology*.
21. Manners, David J. (2 February 1973). "The Structure of a  $\beta$ -(1→3)-D-Glucan from Yeast Cell Walls". *Biochemical Journal*. 135 (1): 19–30. doi:10.1042/bj1350019. PMC 1165784. PMID 4359920.
22. Teas, J (1983). "The dietary intake of Laminarin, a brown seaweed, and breast cancer prevention". *Nutrition and Cancer*. 4 (3): 217–222. doi:10.1080/01635588209513760. ISSN 01635581. PMID 6302638.
23. Vannucci, L; Krizan, J; Sima, P; Stakheev, D; Caja, F; Rajsiglova, L; Horak, V; Saieh, M (2013). "Immunostimulatory properties and antitumour activities of glucans (Review)". *International Journal of Oncology*. 43 (2): 357–64. doi:10.3892/ijo.2013.1974. PMC 3775562. PMID 23739801.
24. Jump up to:<sup>a b</sup> McRorie Jr, J. W; McKeown, N. M (2017). "Understanding the Physics of Functional Fibers in the Gastrointestinal Tract: An Evidence-Based Approach to Resolving Enduring Misconceptions about Insoluble and Soluble Fiber". *Journal of the Academy of Nutrition and Dietetics*. 117 (2): 251–264. doi:10.1016/j.jand.2016.09.021. PMID 27863994.
25. Keenan, M. J.; Martin, R. J.; Raggio, A. M.; McCutcheon, K. L.; Brown, I. L.; Birkett, A.; Newman, S. S.; Skaf, J.; Hegsted, M.; Tulley, R. T.; Blair, E.; Zhou, J. (2012). "High-Amylose Resistant Starch Increases Hormones and Improves Structure and Function of the Gastrointestinal Tract: A Microarray Study". *Journal of Nutrigenetics and Nutrigenomics*. 5(1): 26–44. doi:10.1159/000335319. PMC 4030412. PMID 22516953.
26. Simpson, H. L.; Campbell, B. J. (2015). "Review : dietary fibre–microbiota interactions". *Alimentary Pharmacology & Therapeutics*. 42 (2): 158–79. doi:10.1111/apt.13248. PMC 4949558. PMID 26011307.
27. Othman, R. A; Moghadasian, M. H; Jones, P. J (2011). "Cholesterol-lowering effects of oat  $\beta$ glucan". *Nutrition Reviews*. 69 (6): 299–309. doi:10.1111/j.1753-4887.2011.00401.x. PMID 21631511.

28. Frey A, Giannasca KT, Weltzin R, Giannasca PJ, Reggio H, Lencer WI, Neutra MR (1 September 1996). "Role of the glycocalyx in regulating access of microbes to apical plasma membranes of intestinal epithelial cells: implications for microbial attachment and oral vaccine targeting". *The Journal of Experimental Medicine*. 184 (3): 1045–1059. doi:10.1084/jem.184.3.1045. PMC 2192803. PMID 9064322.
29. Tsukagoshi S, Hashimoto Y, Fujii G, Kobayashi H, Nomoto K, Orita K (June 1984). "Krestin (PSK)". *Cancer Treatment Reviews*. 11 (2): 131–155. doi:10.1016/0305-7372(84)90005-7. PMID 6238674.
30. Hong, F; Yan J; Baran JT; Allendorf DJ; Hansen RD; Ostroff GR; Xing PX; Cheung NK; Ross GD (15 July 2004). "Mechanism by which orally administered  $\beta$ -1,3-glucans enhance the tumoricidal activity of antitumour monoclonal antibodies in murine tumour models". *Journal of Immunology*. 173 (2): 797–806. doi:10.4049/jimmunol.173.2.797. ISSN 0022-1767. PMID 15240666.
31. Obayashi T, Yoshida M, Mori T, et al. (1995). "Plasma (13)- $\beta$ -D-glucan measurement in diagnosis of invasive deep mycosis and fungal febrile episodes". *Lancet*. 345 (8941): 17–20. doi:10.1016/S0140-6736(95)91152-9. PMID 7799700. S2CID 27299444.
32. Ostrosky-Zeichner L, Alexander BD, Kett DH, et al. (2005). "Multicenter clinical evaluation of the (1 $\rightarrow$ 3) $\beta$ -D-glucan assay as an aid to diagnosis of fungal infections in humans". *Clin Infect Dis*. 41 (5): 654–659. doi:10.1086/432470. PMID 16080087.
33. Odabasi Z, Mattiuzzi G, Estey E, et al. (2004). " $\beta$ -D-glucan as a diagnostic adjunct for invasive fungal infections: validation, cutoff development, and performance in patients with acute myelogenous leukemia and myelodysplastic syndrome". *Clin Infect Dis*. 39 (2): 199–205. doi:10.1086/421944. PMID 15307029.
34. Mennink-Kersten MA, Warris A, Verweij PE (2006). "1,3- $\beta$ -D-Glucan in patients receiving intravenous amoxicillin–clavulanic acid". *NEJM*. 354 (26): 2834–2835. doi:10.1056/NEJMc053340. PMID 16807428.
35. Mennink-Kersten MA, Ruegebrink D, Verweij PE (2008). "Pseudomonas aeruginosa as a cause of 1,3- $\beta$ -D-glucan assay reactivity". *Clin Infect Dis*. 46 (12): 1930–1931. doi:10.1086/588563. PMID 18540808.
36. Lahmer, Tobias; da Costa, Clarissa Prazeres; Held, Jürgen; Rasch, Sebastian; Ehmer, Ursula; Schmid, Roland M.; Huber, Wolfgang (4 April 2017). "Usefulness of 1,3  $\beta$ -D-Glucan Detection in non-HIV Immunocompromised Mechanical Ventilated Critically Ill Patients with ARDS and Suspected Pneumocystis jirovecii Pneumonia". *Mycopathologia*. 182 (7–8): 701–708. doi:10.1007/s11046-017-0132-x. ISSN 1573-0832. PMID 28378239. S2CID 3870306.
37. He, Song; Hang, Ju-Ping; Zhang, Ling; Wang, Fang; Zhang, De-Chun; Gong, Fang-Hong (August 2015). "A systematic review and meta-analysis of diagnostic accuracy of serum 1,3- $\beta$ -D-glucan for invasive fungal infection: Focus on cutoff levels". *Journal of Microbiology, Immunology, and*



- Infection = Wei Mian Yu Gan Ran Za Zhi. 48 (4): 351–361. doi:[10.1016/j.jmii.2014.06.009](https://doi.org/10.1016/j.jmii.2014.06.009). ISSN 1995-9133. PMID [25081986](https://pubmed.ncbi.nlm.nih.gov/25081986/).
38. Kullberg, Bart Jan; Arendrup, Maiken C. (8 October 2015). "Invasive Candidiasis". *The New England Journal of Medicine*. 373 (15): 1445–1456. doi:[10.1056/NEJMra1315399](https://doi.org/10.1056/NEJMra1315399). hdl:[2066/152392](https://hdl.handle.net/2066/152392). ISSN 1533-4406. PMID [26444731](https://pubmed.ncbi.nlm.nih.gov/26444731/).
  39. Ostrosky-Zeichner, Luis; Alexander, Barbara D.; Kett, Daniel H.; Vazquez, Jose; Pappas, Peter G.; Saeki, Fumihiko; Ketchum, Paul A.; Wingard, John; Schiff, Robert (1 September 2005). "[Multicenter clinical evaluation of the \(1→3\)- \$\beta\$ -D-glucan assay as an aid to diagnosis of fungal infections in humans](#)". *Clinical Infectious Diseases*. 41 (5): 654–659. doi:[10.1086/432470](https://doi.org/10.1086/432470). ISSN 1537-6591. PMID [16080087](https://pubmed.ncbi.nlm.nih.gov/16080087/).
  40. Karumuthil-Melethil S, Perez N, Li R, Vasu C: Induction of innate immune response through TLR2 and dectin 1 prevents type 1 diabetes. *J Immunol*. 2008, 181 (12): 8323-8334.
  41. Klein E, Di Renzo L, Yefenof E: Contribution of CR3, CD11b/CD18 to cytolysis by human NK cells. *Molecular immunology*. 1990, 27 (12): 1343-1347. 10.1016/0161-5890(90)90041-W.
  42. Di Renzo L, Yefenof E, Klein E: The function of human NK cells is enhanced by  $\beta$ -glucan, a ligand of CR3 (CD11b/CD18). *European journal of immunology*. 1991, 21 (7): 1755-1758. 10.1002/eji.1830210726.
  43. Cheung NK, Modak S, Vickers A, Knuckles B: Orally administered  $\beta$ -glucans enhance antitumour effects of monoclonal antibodies. *Cancer Immunol Immunother*. 2002, 51 (10): 557-564.
- 
44. Modak S, Koehne G, Vickers A, O'Reilly RJ, Cheung NK: Rituximab therapy of lymphoma is enhanced by orally administered (1→3),(1→4)- $\beta$ -D-glucan. *Leuk Res*. 2005, 29 (6): 679-683. 10.1016/j.leukres.2004.10.008.
  45. Dushkin MI, Safina AF, Vereschagin EI, Schwartz Y: Carboxymethylated  $\beta$ -1,3-glucan inhibits the binding and degradation of acetylated low density lipoproteins in macrophages in vitro and modulates their plasma clearance in vivo. *Cell Biochem Funct*. 1996, 14 (3): 209-217.
  46. Zimmerman JW, Lindermuth J, Fish PA, Palace GP, Stevenson TT, DeMong DE: A novel carbohydrate-glycosphingolipid interaction between a  $\beta$ -(1–3)-glucan immunomodulator, PGGglucan, and lactosylceramide of human leukocytes. *The Journal of biological chemistry*. 1998, 273 (34): 22014-22020. 10.1074/jbc.273.34.22014.
  47. Iwabuchi K, Nagaoka I: Lactosylceramide-enriched glycosphingolipid signalling domain mediates superoxide generation from human neutrophils. *Blood*. 2002, 100 (4): 1454-1464.

48. Vereschagin EI, van Lambalgen AA, Dushkin MI, Schwartz YS, Polyakov L, Heemskerk A, Huisman E, Thijs LG, van den Bos GC: Soluble glucan protects against endotoxin shock in the rat: the role of the scavenger receptor. *Shock* (Augusta, Ga). 1998, 9 (3): 193-198.
49. Wakshull E, Brunke-Reese D, Lindermuth J, Fisette L, Nathans RS, Crowley JJ, Tufts JC, Zimmerman J, Mackin W, Adams DS: PGG-glucan, a soluble  $\beta$ -(1,3)-glucan, enhances the oxidative burst response, microbicidal activity, and activates an NF-kappa B-like factor in human PMN: evidence for a glycosphingolipid  $\beta$ -(1,3)-glucan receptor. *Immunopharmacology*. 1999, 41 (2): 89-107. 10.1016/S0162-3109(98)00059-9.
50. Tang W, Liu JW, Zhao WM, Wei DZ, Zhong JJ: Ganoderic acid T from *Ganoderma lucidum* mycelia induces mitochondria mediated apoptosis in lung cancer cells. *Life Sci*. 2006, 80 (3): 205-211. 10.1016/j.006.09.001.
51. Lin SB, Li CH, Lee SS, Kan LS: Triterpene-enriched extracts from *Ganoderma lucidum* inhibit growth of hepatoma cells via suppressing protein kinase C, activating mitogen-activated protein kinases and G2-phase cell cycle arrest. *Life Sci*. 2003, 72 (21): 2381-2390. 10.1016/S00243205(03)00124-3.
52. Min BS, Gao JJ, Nakamura N, Hattori M: Triterpenes from the spores of *Ganoderma lucidum* and their cytotoxicity against meth-A and LLC tumour cells. *Chem Pharm Bull (Tokyo)*. 2000, 48 (7): 1026-1033.

---

53. Muller CI, Kumagai T, O'Kelly J, Seeram NP, Heber D, Koeffler HP: *Ganoderma lucidum* causes apoptosis in leukemia, lymphoma and multiple myeloma cells. *Leukemia research*. 2006, 30 (7): 841-848. 10.1016/j.leukres.2005.12.004.
54. Chan WKD, Cheung CC, Law HKD, Lau YLD, Chan GCD: *Ganoderma lucidum* polysaccharides can induce human monocytic leukemia cells into dendritic cells with immuno-stimulatory function. *J Hematol Oncol*. 2008, 1 (1): 9-10.1186/1756-8722-1-9.
55. Demir G, Klein HO, Mandel-Molinas N, Tuzuner N:  $\beta$ -Glucan induces proliferation and activation of monocytes in peripheral blood of patients with advanced breast cancer. *Int Immunopharmacol*. 2007, 7 (1): 113-116. 10.1016/j.intimp.2006.08.011.
56. Kidd PM: The use of mushroom glucans and proteoglycans in cancer treatment. *Altern Med Rev*. 2000, 5 (1): 4-27.
57. Miyakoshi H, Aoki T, Mizukoshi M: Acting mechanisms of Lentinan in human – II. Enhancement of non-specific cell-mediated cytotoxicity as an interferon inducer. *International journal of immunopharmacology*. 1984, 6 (4): 373-379. 10.1016/0192-0561(84)90057-2

**NITRIC OXIDE: A CHEMICAL ENTITY OF  
BIOLOGICAL INTEREST**

**Scottish Church College**

**UNIVERSITY OF CALCUTTA**

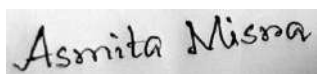
**UNIVERSITY ROLL NO. 223/CEM/191017**

**REGISTRATION NO. 223-1211-0007-19**

**SPECIAL PAPER: SI 44**

**NAME OF CANDIDATE**

ASMITA MISRA



**SIGNATURE OF CANDIDATE**

**NAME OF SUPERVISOR/EXAMINER**

Dr. CHANDAN KUMAR PAL



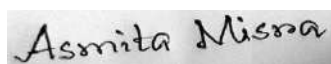
**SIGNATURE OF SUPERVISOR/EXAMINER**

No. \_\_\_\_\_

Date: \_\_\_\_\_

## **SELF DECLARATION**

This is to certify that I am ASMITA MISRA (Roll No. **19PG-C10**), Reg. No. **223-1211-0007-19** of (2019-2021), a student of MSc. in the Department of Chemistry as worked on the project entitled “**NITRIC OXIDE: A CHEMICAL ENTITY OF BIOLOGICAL INTEREST**” for the partial fulfilment of requirements of matter of science in CHEMISTRY under the **UNIVERSITY OF CALCUTTA, SCOTTISH CHURCH COLLEGE**, under my supervision. To the best of my knowledge this work has not been submitted to any other universities for the award of any other degree.



**Signature of Student**

**University Roll NO. 223/CEM/191017**

**Registration No. 223-1211-0007-19**

**Date: 19.07.2021**

**Place- SCOTTISH CHURCH COLLEGE, KOLKATA**

## Content

## Page No.

• ACKNOWLEDGEMENT.....	4
• INTRODUCTION.....	5-7
• DISCUSSION.....	8-12
• BIO RELEVANCE OF NO.....	12
• NITRITE AS A STORAGE FORM OF NO.....	13-14
• NO-NO <sub>2</sub> SYSTEM IN CARDIOVASCULAR HOMEOSTASIS...	14
• NITRIC OXIDE AND GENE THERAPY.....	14-15
• HEME ANALOGUES AND RELATED MACROCYCLIC COMPLEX...	15-16
• NON-HEME MODEL COMPLEXES.....	17
• OTHER IRON COMPLEXES.....	17-18
• COMPLEXES OF OTHER METALS.....	18-19
• CONCLUSION.....	20-21
• REFERENCE.....	22-25

# **ACKNOWLEDGEMENT**

I am very much grateful to the former and present Head of the Department of Chemistry, Scottish Church College for permitting me to carry out project work.

I wish to express my heartiest sense of gratitude to Dr. SUDIPTA CHATTERJEE, Department of Chemistry, SERAMPORE COLLEGE, for introducing me to field of '**Nitric Oxide: A chemical entity of biological interest**' and supervision, advice, helpful discussion, constant encouragement and insightful guidance from the very early stage of project work.

I convey my warmest thanks to my parents, and all of my friends.

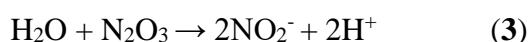
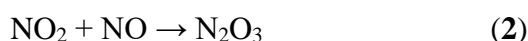
## ❖ Introduction:

Nitric oxide is among the simplest of molecules and for many years its structure and reaction chemistry have been the subject of study by chemists. The recent two decades have revealed a new and unexpected role for NO as a key physiological regulator despite the apparent wealth of knowledge. This new type of role for NO has reinvigorated research in the fundamental chemistry of this simple molecule and led many researchers to revisit the characteristic chemistry of metal-NO compounds to decipher the biological role of NO.

Because of remarkable flexibility of NO the interaction between metal centers and nitric oxide (nitrogen monoxide) has long been of interest to chemists as either a net electron donor or electron acceptor in metal-NO binding interactions.<sup>1</sup> Early concerns with the biology of NO was largely focused on the known toxicities of NO and other reactive nitrogen oxide species as constituents of air pollution including cigarette smoke.<sup>2</sup> However, this topic's appeal expanded significantly upon the discoveries in the late 1980's that endogenously formed NO play a key role in mammalian biology and this activity could be attributed to the formation of nitrosyl complexes of metallo-proteins. These roles include functions in vascular regulation, neurotransmission, and immuno-cytotoxicity.<sup>3,4</sup> Furthermore, numerous disease have been shown to be characterized by the over- or underproduction of nitric oxide.<sup>5</sup> This type of observations have stimulated extensively research activity in the chemistry, biology, and pharmacology of NO. In the solution-phase reaction of NO, "this has led to new interest in this type"; it may provide new insights regarding the physiological roles of this "simple" molecule to understand the fundamental chemistry.

Nitric oxide ( $\cdot\text{NO}$ ); was discovered by the British chemist **Joseph Priestley** contemporaneous with his discovery of oxygen in 1776. It was long thought of as a poisonous, pungent-smelling gas: also an unpleasant and dangerous product of the oxidation of ammonia and of incomplete combustion of gasoline in motor vehicle exhausts, this simple molecule is now treated as generally injurious to health.<sup>6</sup> It is a colourless gas with solubility in water 2-3 mM. With various atoms and radicals it may proceed many chemical reactions; it reacts readily with  $\text{O}_2$  to form nitrogen dioxide ( $\text{NO}_2$ ). The reaction of NO with superoxide anion ( $\text{O}_2^{\cdot-}$ ) generates peroxynitrite ( $\text{ONOO}^-$ ). It is an oxidative species which is responsible for certain types of NO-

mediated toxicity *in vivo*. To form methaemoglobin and nitrate it can react with oxyhemoglobin. In contrast, the reaction of NO with O<sub>2</sub> (autoxidation) formed N<sub>2</sub>O<sub>3</sub>, as well as the NO/O<sub>2</sub><sup>-</sup> which is a mild oxidant and prefers to nitrosate nucleophiles such as amines and thiols<sup>7-9</sup> In the case of the autoxidation in hydrophobic environments, NO<sub>2</sub> is first generated but as NO levels increase there is rapid formation of N<sub>2</sub>O<sub>3</sub> [Eqs. (1) and (2)], ultimately forming nitrite in water [Eqs. (3)]



Between NO and NO<sub>2</sub> an equilibrium is formed and the proportion of oxidation *vs.* nitrosation is determined by the amount of substrate present.

Conventional understanding of Nitric Oxide (NO); its signalling properties is biology that it simply diffuses random manner from its site of production by NO synthases to its site of action or inactivation. However, on biological systems the discovery of mammalian ·NO production and its protean effects profoundly changed this view. The enormous importance of this shift in view is reflected by the award of the Nobel Prize in Physiology or Medicine in 1998 to Furchgott, Ignarro, and Murad, which is shared for their seminal roles in the discovery “Concerning NO as a signaling molecule in the cardiovascular system.” After the discovery they were endogenously produced it, and its role in pathophysiology was re-evaluated. We now know that these “toxic” species not only are endogenously generated but are an essential part of the immune response and many physiological signal transduction pathways.<sup>10-13</sup> Toxicity is lead by their chemical activity, this same reactive species, whose biological properties can be very much beneficial and it also explain their apparently dichotomous actions.

From its electronic structure, it is shown that, nitric oxide is in a free radical form but also it works as a powerful oxidising and reducing agent. In drinking water as a final oxidation product nitrate is present, is also a known risk especially to the health of the foetus and the very young. The unpaired electron makes NO highly reactive and displays an ultra-short half-life (less than 1 second).<sup>14</sup>

As a simple diatomic free radical, NO is generally considered to represent the biologically important form of the endothelium-derived relaxing factor (EDRF).<sup>15</sup> Cellular NO is almost exclusively generated via five-electron oxidation of L-arginine, which is catalyzed by nitric



oxide synthases (NOS). NO directly activates soluble guanylate cyclase (sGC) to transform guanosine triphosphate (GTP) into cyclic guanosine monophosphate (cGMP) and it fully followed by kinase-mediated signal transduction in physiological condition.

From the chemical biology of nitric oxide, it gives us a framework to understand how this simple diatomic molecule could have a lot of biological properties, which is simply based on its concentration in terms of chemical toxicology. In vascular and stromal cells i.e., from endothelial (eNOS) and neuronal (nNOS) NO synthase regulate normal physiological processes are mainly occurred in low concentration of NO and the high levels such as those expected in activated macrophages (via inducible, iNOS) are thought to serve a cytotoxic/cytostatic function.<sup>16-18</sup> However at these higher concentrations cell death is not always happened.

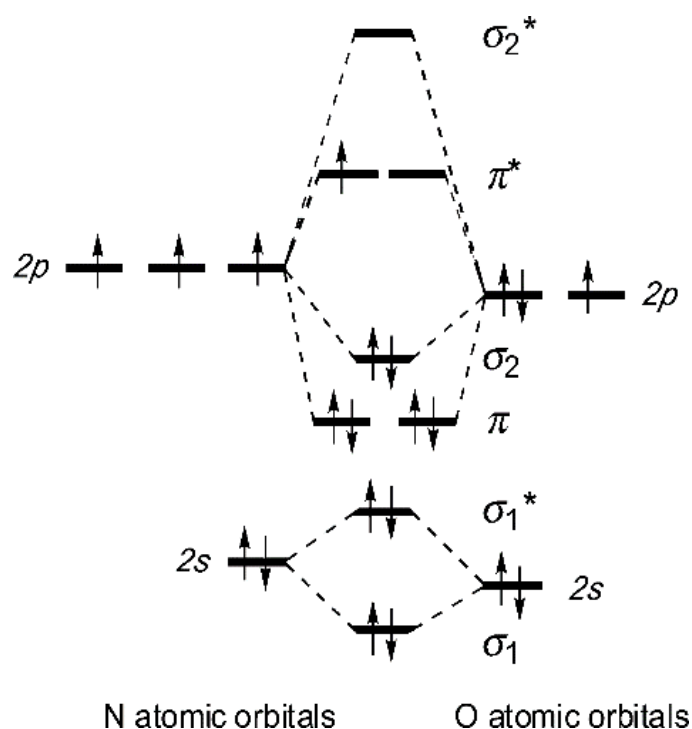
In recent years to elucidate the fundamental coordination chemistry of the metal ions and their interactions with NO<sub>x</sub> species many bioinorganic researchers, including biophysicists, biochemists, and synthetic inorganic chemists, have joined. This information adds insight into aspects of the active site structure or reaction mechanism for each of these metalloenzymes. By virtue of these discoveries, it seems to us that interest in NO, is not going to abate any time soon. Thus the purpose of this review is to highlight recent studies relating nitric oxide production in vivo in health and disease related to clinical nutrition and metabolism and insight in the mechanisms that regulate NO production under many conditions and the potential options for nutrition-based therapy through the study of the biomimicking nitric oxide complexes of different metal ions.

### ❖ Discussion:

It was a sensation that NO, which is a simple, common air pollutant, it formed when nitrogen burns, for instance in automobile exhaust fumes, could exert important functions in the organism. It is so surprising that NO is totally different from any other known signal molecule and also very much unstable that within 10 seconds it is easily converted to nitrate and nitrite. NO was discovered to be one of the most important physiological regulators, playing a key role in signalling and cytotoxicity, possibly now a days one of the biggest surprises in biological chemistry and obviously one of the most significant in co-ordination chemistry in the decade.

#### • Nitric Oxide: The molecule

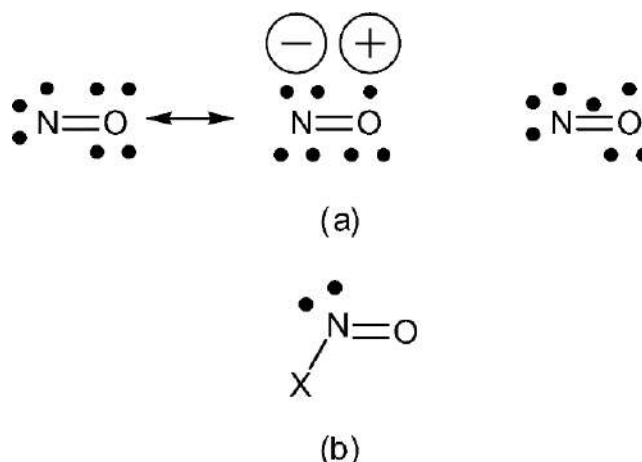
Nitric oxide is a stable free radical. From the molecular orbital diagram of NO (**Figure 1**) it is clear that an unpaired electron in this molecule resides in a  $\pi^*$  molecular orbital. The singly electron occupied the  $\pi^*$  orbital, but polarized toward nitrogen in a manner opposing the polarization of the lower energy  $\pi_b$  orbitals. The result is that it is a relatively nonpolar diatomic molecule.



**Figure 1:** Molecular Orbital Energy Level Diagram of NO.

This electronic configuration explains the high reactivity of the NO molecule, in particular the ease of oxidation to the nitrosonium ion ( $\text{NO}^+$ ), the probability of reduction to the

nitroxide ion ( $\text{NO}^-$ ), the facile attack by oxygen leading to the formation of  $\text{NO}_2$ , and reaction with halogens ( $\text{X}_2$ ) affording  $\text{XNO}$  (**Figure 2**).

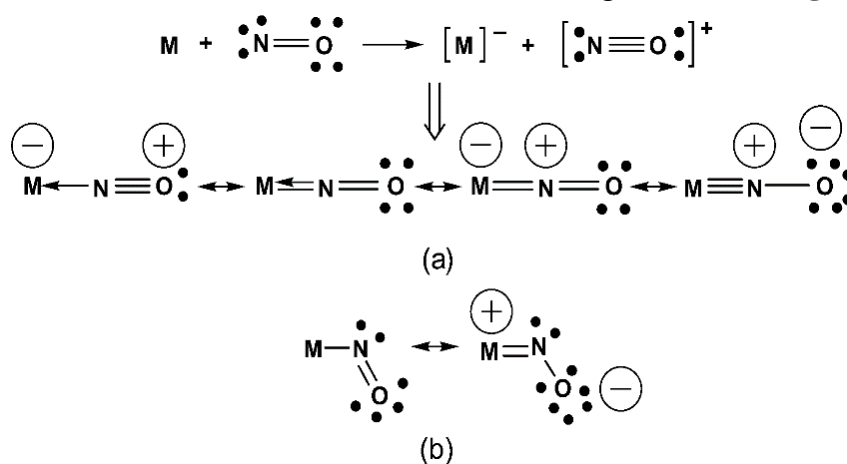


**Figure 2:** (a) Valence bond and other representations of NO  
(b) Structure of nitrosyl halide and related species having a “bent” X-N-O bond.

NO is isoelectronic with  $\text{O}_2^+$  and  $\text{NO}^+$  is isoelectronic with CO and  $\text{CN}^-$ , while  $\text{NO}^-$  is isoelectronic with  $\text{O}_2$ . Thus, a formal analogy is often drawn between the linear bonding modes of these ligands.

$\text{NO}^+$  is isoelectronic with CO; therefore, in its bonding to metals, linear NO is considered as  $\text{NO}^+$ , a 2-electron donor where N and O are  $sp$  hybridized.

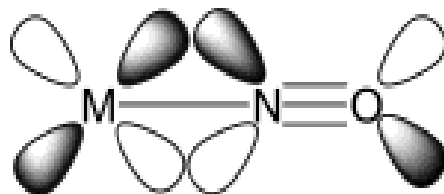
It is considered that  $\text{NO}^-$  is the best co-ordination mode of NO, and also it has bent geometry, suggesting  $sp^2$  hybridization at the nitrogen. Therefore, it is considered that bent NO is 2-electron donor  $\text{NO}^-$ . Resonance forms of  $\text{M}-\text{N}-\text{O}$  binding is shown in **Figure 3**.



**Figure 3.** Valence bond representation of metal-nitrosyl bonding (a) involving  $\text{NO}^+$  and (b) involving  $\text{NO}^-$

Although linear coordination usually gives rise to N – O stretching vibrations at higher energy than the bent mode, there is enough overlap in the ranges of these bands so distinguish between them IR spectra alone may not be sufficient.

From the molecular orbital approach, the bonding of NO to metal is thought of as having two components. The first one is a donation of electron density from NO to the metal, involving a  $\sigma$  orbital on the N atom ( $\sigma_2$  in MO scheme, **Figure 1**) and the second one is back donation from metal  $d\pi$  orbitals to the  $\pi^*$  orbitals of NO. The  $d\pi$ - $\pi^*$  interaction is shown in **Figure 4**.



**Figure 4.** Molecular orbitals involved in  $d\pi$ - $\pi^*$  bonding between metal and NO

This type of bonding description is very similar to that between CO and metal, however as NO is more electronegative than CO, so it is a better electron acceptor than CO. From the valance bond picture (**Figure 3**) it is clear that within the M—N—O group, the metal-nitrogen bond is usually strong, whereas the N—O bond is relatively weak.

The ionization potential of NO is 9.26 eV and the electron affinity is 0.024 eV.<sup>19</sup> Nitrosonium ion ( $\text{NO}^+$ ) is isolated as a series of stable salts and is a useful synthetic and oxidizing agent. In biological media  $\text{NO}^+$  has an extremely short independent life, so metal-complexes may function as a transport agent. Later it is reported that, the independent chemistry of reduced nitric oxide ( $\text{NO}^-$ ) is currently minimal, although in binding with transition metals the anion formally plays a significant role. In a solution nitric oxide is redox active, this is a most important property which has a major influence on the chemistry of its transition metal complexes. The reversible process for  $\text{NO} \rightleftharpoons \text{NO}^+ + e^-$ ; the value of redox potential is strongly solvent dependent and in water it is also pH dependent.<sup>20, 21</sup> In strongly basic conditions, NO is reducing, i.e.  $\text{NO}_2^- + \text{H}_2\text{O} + e^- \rightarrow \text{NO} + 2\text{OH}^-$ ,  $E^\circ = -0.46 \text{ V vs. NHE}$ . For reduction of  $\text{NO}^+$  to NO; the standard potential value has been estimated to be *ca.* +1.2V vs. NHE. The reduction of NO to triplet and singlet  $\text{NO}^-$  has been estimated as lying between +0.39 and -0.35 V vs. NHE.

The bond length of free NO is lying between that of a double and a triple bond (**Table 1**). Convention regarding this bond length is equivalent to a bond order of 2.5, consistent with the MO diagram shown in **Figure 1**. Oxidation of NO to  $\text{NO}^+$  causes contraction of bond length

and bond order is equivalent to 3; again reduction of NO to NO<sup>-</sup> causes an increase in bond length because of the further population of the  $\pi^*$  orbital.<sup>22,23</sup>

Component	Bond Length (Å)	Stretching Frequency (cm <sup>-1</sup> )	Bond Order
NO <sup>+</sup>	1.06	2377	3
NO	1.154	1875	2.5
NO <sup>-</sup>	1.26	1470	2

**Table 1:** Comparison of different parameters of NO, NO<sup>+</sup> and NO<sup>-</sup>.

The change in the bond length for this simple diatomic molecule is also reflected in the IR stretching frequency value.  $\bar{\nu}_{NO}$  decreasing with increasing charge.<sup>24</sup> The nitrosyl halides, alkanes, and arenes are “bent” molecules, the N = O distance varying from 1.13 to 1.22 Å, and the X—N = O bond angle falling in the range from 101° to 134°, both are dependent on the substituent.<sup>25</sup> These bond lengths are strongly dependent on the electronegativity of the substituents and these substituent effects also influence  $\bar{\nu}_{NO}$ , which occurs between 1621 and 1363 cm<sup>-1</sup>, broadly equivalent to bond order 2, as shown in **Figure 2(b)**.

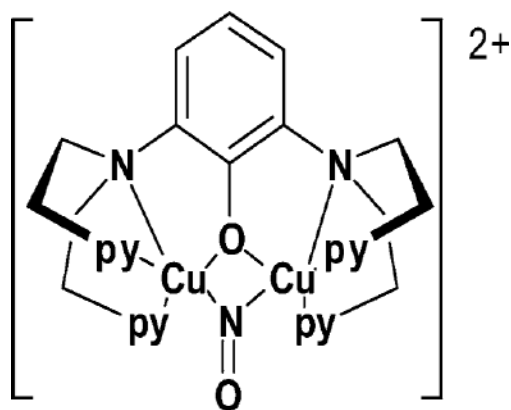
### ❖ Bonding of NO to Transition metals:

#### (a) Terminal metal nitrosyl complexes:

In normal conditions, the bonding of NO with transition metals is M—N—O i.e. attachment of the N atom to the metal. Many other types of bonding are there in different conditions. In biomimetic systems, generally metals can bind one or two NO groups, and the M—N—O bond angles may be actually linear or bent. NO also bridged two or three metal centers, although this is not so encountered in the biomimetic systems.

#### (b) Bridging Nitrosyl complexes:

Like CO, NO also can bridge two, three, or even four metal atoms, but the dinuclear arrangement M—N(O)—M which is most likely to be encountered in systems of relevance to biology, although it is currently rare. The only structurally characterized biomimetic example is the di-copper complex is [2,6-bis{bis(2-pyridylethyl)aminomethyl}phenolate]<sup>26</sup> (**Figure 5**)



**Figure 5:** Biomimetic example of dicopper complex of the type  $M-N(O)-M$ .

(c) *Isonitrosyl and Other Types of Metal-NO Bonding* :

Here two metastable states are formed corresponding to an isonitrosyl,  $M-O-N$  and a  $\kappa^2$ - $M(NO)$  species respectively and it is studied carefully in low temperature X-ray crystallographic method.<sup>27</sup> Among the complexes clearly exhibiting this behaviour are  $[Fe(NO)CN)_5]^{2-}$  and  $[Ru(NO)(NH_3)_5]^{2+}$ , both of which are known to act as “NO donors” under physiological conditions and has been used as a vasodilator in the treatment of high blood pressure. Surely, indications of unconventional NO bonding in porphyrin complexes have been observed. DFT calculations of model species  $[M(NO)(porph)]$  {porph = porphyrinate(2-)} containing  $\{M(NO)\}^n$ , here  $n = 6-8$  and  $M = Fe, Ru, Co, Mn, Rh$ , indicated that both isonitrosyl and sideways bound  $M(NO)$  systems could exist.

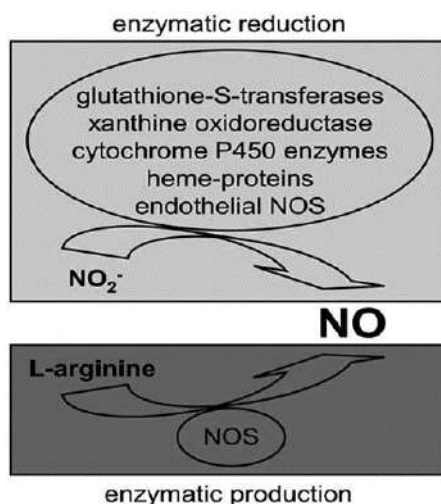
❖ **Bio Relevance of NO:**

The principal targets for NO under bioregulatory conditions are metal centres, primarily iron proteins.<sup>28</sup> The best characterized example is the Ferro-heme enzyme soluble guanylyl cyclase (sGC).<sup>29</sup> In the protein backbone formation of a nitrosyl complex with Fe(II) leads to labialization of a trans axial (proximal) histidine ligand, and as a result change in the protein conformation which is believed to activate the enzyme for the catalytic formation of the secondary messenger cyclic-guanylyl monophosphate (cGMP) from guanylyl triphosphate (GTP). The reason for lowering the blood pressure is enzymatic formation of cGMP leads to relaxation of smooth muscle tissue of blood vessels. Other reports describe the roles of NO as an inhibitor for metalloenzymes such as cytochrome P450,<sup>30a</sup> cytochrome oxidase,<sup>30b</sup> nitrile hydratase,<sup>31</sup> and catalase,<sup>32</sup> as a substrate for mammalian peroxidases,<sup>33</sup> and as a contributor to the vasodilator properties of a salivary Fe-heme protein of blood-sucking insects.<sup>34</sup> Heme centres are also involved in the in vivo generation of NO by oxidation of arginine catalyzed by

nitric oxide synthase (NOS) enzymes.<sup>35</sup> For bioregulatory purposes, NO concentrations generated are low, and [NO] values less than 1  $\mu\text{M}$  has been reported to be generated in endothelium cells for blood pressure control.<sup>36</sup> Thus, reactions with targets such as sGC must be very fast to compete effectively with other physical and chemical processes that deplete free NO. However, the NO concentrations produced during the immune response to pathogen invasion are much higher, and under these conditions, reactive nitrogen species such as peroxynitrite anion ( $\text{OONO}^-$ ) and  $\text{N}_2\text{O}_3$  may have physiological importance.

### ❖ Nitrite as a storage form of NO:

NO is produced not only through a classical NOS dependent pathway but also through the alternative NOS-independent nitrite reduction (**Figure 6**).



**Fig 6:** NOS-dependent and NOS-independent pathways of NO production.

In concentrations of about 150-1000nM in the plasma, it represents the largest vascular storage pool of NO; here nitrite anion is present. A high concentration of nitrite was used in the treatment of cyanide poisoning in order to oxidize hemoglobin to methemoglobin, which will bind cyanide. But Gladwin and colleagues denied this belief, since they discovered that nitrite is reduced to NO *in vivo* and causes a reduction of blood pressure and an increase in blood flow, at doses (as low as 0.9 $\mu\text{M}$ ) that do not produce clinically significant methemoglobinemia. Nitrite enters the red blood cells and reacts with deoxy-Hb to form NO and methemoglobin. Nitrite is converted to NO to an extent that depends on the degree of deoxygenation, NO escapes from the red blood cells producing vasodilation, and blood flow increases to an extent that matches oxygen requirements.

The reduction of  $\text{NO}_2^-$  to NO represents an important step in cytoprotection and appears to involve mitochondrial respiration and functional resilience to I/R (**ischemia-reperfusion**). Several experimental evidences demonstrated that nitrite-dependent cytoprotection involves the reduction of nitrite to  $\text{NO}^{37}$  and the formation of NO-modified proteins.<sup>38</sup>

Impressively, now it is accepted that the nitrite reduction to NO enhances under hypoxic conditions but occurs also under normoxia. Then it is valued that nitrite mediated NO formation through different methods i.e. electron paramagnetic resonance and chemiluminescence, and from this it is tested that nitrite-dependent NO generation is involved in both physiological and pathological responses.<sup>39</sup>

### ❖ NO- $\text{NO}_2^-$ System in Cardiovascular Homeostasis:

The generation of up to 70% of plasma nitrite originates from NOS-derived NO, mainly in the endothelium by endothelial NOS. In fact, nitrite has been reported as an index of NOS activity. These enzymes synthesize NO from the amino acid L-arginine and molecular oxygen to accomplish vasodilation, blood pressure regulation and platelet aggregation inhibition.<sup>40</sup>

NO itself represents a significant molecule within the cardio-vascular system, preventing various types of cardiovascular disease such as hypertension, atherosclerosis and stroke. Moreover, it also acts as a messenger molecule in the local control of vascular homeostasis regulating vessel tone and inhibiting smooth muscle cell proliferation and blood cell adhesion.<sup>41</sup>

NO regulates blood perfusion by inducing vessel dilation and by enhancing the formation of collateral vessels. For this reason, it is considered that NO has been a candidate for the revascularization and protection of ischemic tissues. However, despite its beneficial actions, at high concentrations NO could have many toxic effects. In contrast, under ischemic conditions nitrite is reduced to NO, while in well-oxygenated tissues it is oxidized to evidently harmless nitrate.

### ❖ Nitric oxide and gene therapy:

Given the importance of NO in cellular signalling, and in particular its effects on the cardiovascular system, increasing NO production was deemed an important area for drug development. In the promotion of NO production, gene therapy is an alternative to traditional medication. A reduction in intimal hyperplasia (IH) in rodent models of vascular injury was achieved by delivering NO to the injury site including supplementing dietary L-arginine and using NO donor compounds. Furthermore, several groups using either liposomal or adenoviral



gene delivery methods have successfully transferred eNOS into sites of vascular injury resulting in a reduction in intima-media ratio shown in (Table 2).<sup>42</sup>

NOS isoform	Vector	Animal model
eNOS (bovine)	Fusigenic liposomes (HVJ <sup>§</sup> )	Rat and rabbit carotid artery
	Adenovirus	
eNOS (human)	Adenovirus	Pig and rat carotid artery
	Adenovirus (SMC <sup>#</sup> )	
iNOS (human)	Adenovirus	Pig coronary artery
	Cationic liposome	Rat aorta allograft model, porcine femoral artery stent model

<sup>§</sup>HVJ: haemagglutinating virus Japan,

<sup>#</sup>SMC: smooth muscle cell.

**Table 2:** NOS gene transfer: vectors and models

iNOS gene transfer in various models of vascular injury in rats and pigs abolished myointimal thickening, inhibition of IH, and protection against graft IH by 37% and this has been shown by many groups. For the prevention of IH, these studies also suggest the great potential utility of NOS gene therapy. Thus, in view of the non-viral character of this gene therapy method, the results of this study may be a very important outcome for the transition of NOS-based gene therapy to clinical practice.

### ❖ Biomimetic Complex:

In metal nitrosyl chemistry, the role of biochemistry; is to throw light on molecular and/or electronic structural issues, and to make it easier for understanding of the reactivity of the coordinated NO group. For categorizing the complexes it is appropriate to do by generic types: heme analogues and related macrocyclic species, non-heme iron complexes, other iron complexes, and complexes of other metals.<sup>43</sup>

#### (a) Heme Analogues and Related Macrocyclic Complexes:

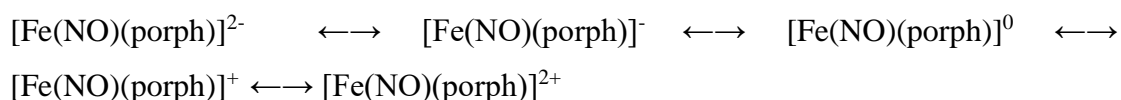
For NO synthases an enzyme produces NO in the body and a soluble guanylyl cyclase. For NO enzymatic receptor is present, they both contain heme, here iron nitrosyl porphyrinato

complexes have received substantial attention. The iron heme nitrosyl containing  $\{\text{Fe}(\text{NO})\}^7$  appears, to be more prevalent than their oxidized  $\{\text{Fe}(\text{NO})\}^6$  counterparts.

- **Iron complexes:**

In a biological system NO has numerous possible targets; it reacts with many transition metals, i.e. molecules containing Fe-heme moiety. Fe-nitrosyl porphyrins may be five or six-coordinate and here the sixth ligand is the well-characterized examples of the latter being either a N-heterocycle, water, alkyl/aryl, or  $\text{NO}_2^-$ . In the diamagnetic  $\{\text{Fe}(\text{NO})\}^6$  group of complexes here metal-NO bond angles lie between  $169^\circ$  and  $180^\circ$ , it is actually linear, and the bond distance of Fe-N(O) are in the range between 1.63-1.67 Å, which is in general independent of co-ordination number.<sup>44</sup> The nature of the trans axial ligand in the six co-ordinate species has relatively little effect on the Fe-N(O) bond length. From the electronic structure of this group of complexes, it is shown that be they are five- or six-coordinate, the nature of the ligand which is trans to NO are very much sensitive, on the Fe-N-O bond angle the distorted porphyrinato ligand do not seem to have a significant effect.<sup>45</sup>

Compared with other small, diatomic molecules (e.g.,  $\text{O}_2$ , CO) the co-ordination chemistry of NO is unique in nature, in that case it can react with both ferric  $\text{Fe}^{\text{III}}$  and ferrous  $\text{Fe}^{\text{II}}$  heme proteins (that contain an open coordination site). Sometimes reaction with  $\text{Fe}^{\text{III}}$ -hemes, results in a reduction form of  $\text{Fe}^{\text{II}}$ -hemes, with the sequential generation of nitrite. The relatively stable  $\text{Fe}^{\text{II}}$ -NO complex is formed, and these formed by coordination of NO with  $\text{Fe}^{\text{II}}$ -heme. In  $\{\text{Fe}(\text{NO})\}^7$  group, here the Fe-N-O bond angles are  $140^\circ$ - $150^\circ$  and the Fe-N(O) bond distances lie between 1.72-1.74 Å, hence the NO stretching frequencies range from 1625 to  $1690\text{ cm}^{-1}$ , it is dependent on the coordination number and nature of the trans axial ligand in the six-coordinated species. These species are paramagnetic ( $S=1/2$ ) in nature, and the Mössbauer spectral isomer shifts vary from 0.22 to 0.35 mm/s.<sup>46</sup> The five-coordinate Fe complexes are electrochemically active, these exist mainly within a five-membered electron-transfer chain:



The anionic species formally contains both  $\{\text{Fe}(\text{NO})\}^8$  and  $\{\text{Fe}(\text{NO})\}^9$ ; although there is a possibility that the porphyrin ring may be reduced rather than the metal nitrosyl core. Particularly in the presence of alternative donor ligands, some of these anionic species are

unstable and readily dissociating NO. Nevertheless, the chemically generated  $[\text{Fe}(\text{NO})(\text{porph})]^-$  may be reoxidized to its neutral precursor form. The monocations presumably contain  $\{\text{Fe}(\text{NO})\}^6$  which are stable, although the porphyrin rings in these and related dications could be oxidized rather than the metal.<sup>47</sup>

**(b) Non-Heme Model Complexes:**

The mononuclear high-spin  $\text{Fe}^{\text{II}}$  state of nonheme iron proteins; is not generally spectroscopically accessible. However, most effectively NO can be used as a probe of such  $\text{Fe}^{\text{II}}$  centers, and it can usually convert the EPR-silent  $S=2$  state into an EPR-active  $S=3/2$  state. In bio-catalysis for serve as an enzyme-NO adduct, unstable  $\text{O}_2$  intermediate is used, thereby it makes easier the identification of exogenous ligands such as substrate and solvent molecules in the metal coordination environment.

Various physical methods have been used *i.e.* single-crystal X-ray crystallography, magnetic susceptibility measurements, IR, resonance Raman, EPR, Mossbauer, X-ray absorption spectroscopy, and magnetic circular dichroism and other calculations to probe the molecular and electronic complexities of the enzymatic species and appropriate model complexes. Mainly model complexes are contained five- and six-coordinate  $\{\text{Fe}(\text{NO})\}^7$  core and these are stabilized by a range of donor atoms incorporated in multidentate or macrocyclic ligands. While  $\{\text{Fe}(\text{NO})\}^6$  species are not common among presently characterized enzyme -NO adducts, they are occasionally prepared by oxidation of  $\{\text{Fe}(\text{NO})\}^7$  species.

**(c) Other iron complexes:**

The few species containing  $\{\text{Fe}(\text{NO})\}^6$  are diamagnetic, with  $\nu_{\text{NO}} > 1850 \text{ cm}^{-1}$ , it is known from various studies of heme and related complexes. The NO stretching frequencies in the  $\{\text{Fe}(\text{NO})\}^7$  species are partly a function of donor atom set and also of charge, falling in the range  $1620\text{-}1810 \text{ cm}^{-1}$ .

It is suggested that, oxidation of  $\{\text{Fe}(\text{NO})\}^7$  to  $\{\text{Fe}(\text{NO})\}^6$ , results in a major reduction in population of the NO  $\pi^*$  orbitals. The Fe-N(O) bond distance in most  $\{\text{Fe}(\text{NO})\}^7$  complexes in this group are in the range  $1.68\text{-}1.76 \text{ \AA}$ . The specific coordination number of the species was not established, but the dimensions are consistent with a  $\{\text{Fe}(\text{NO})\}^7$  configuration, the EPR spectrum indicating that  $S=3/2$  is a ground state. Both  $\{\text{Fe}(\text{NO})\}^7$  and  $\{\text{Fe}(\text{NO})\}^6$  are six coordinated complex.

Tetragonal pyramidal five coordinated  $\{\text{Fe}(\text{NO})\}^7$  complexes, towards the NO group the Fe atoms are displaced from the basal donor atom planes. The Fe-N(O) bond lengths are similar to those of their six-coordinate analogues, averaging 1.72 Å. The Fe-N-O bond angle is always significantly bent (122-150°), with one exception,  $[\text{Fe}(\text{NO})(\text{tmc})]^{2+}$  [ tmc= tetramethylcyclam] (178°), which has a distorted geometry; midway between tetragonal pyramidal and trigonal bipyramidal. There are very few examples of  $\{\text{Fe}(\text{NO})\}^7$  complexes which have trigonal-bipyramidal coordination and an S=3/2 ground state, and this geometry has not yet been identified in non-heme iron proteins. The anionic species  $[\text{Fe}(\text{NO})(\text{R}_3\text{-tcbma})]^-$ ; [ R= <sup>i</sup>pr, cyclopentyl (cyp), 3,5-dimethylphenyl (dmp)], were designed to have this structure and a quartet ground state, but the Fe-N-O bond angles vary according to the substituent, R, viz., 178° (R= <sup>i</sup>pr), 173° (R=cyp), and 160° (R=dmp), respectively. These are all trigonal bipyramidal non-heme protein.

**(d) Example of Metal-nitrosyl Complexes of other metals:**

- **Ruthenium-nitrosyl complexes:**

Like the Fe atom analogue, a number of ruthenium complexes, have the ability to scavenge and release NO, being therefore of considerable interest in environmental remediation and in biomedical applications. Between ruthenium complexes and Fe analogue; ruthenium complexes are more kinetically stable, and the relevant oxidation states are Ru<sup>II</sup> and Ru<sup>III</sup>, are low spin, in contrast to the variable spin behaviour of Fe<sup>II</sup> and Fe<sup>III</sup>.

**Table 3:** Ruthenium nitrosyl complexes and their stretching frequencies. <sup>48</sup>

Compound	Reduction form of compound	Stretching frequency of compound (cm <sup>-1</sup> )
$[\text{Ru}(\text{NO})(\text{hedta})]$	$\{\text{Ru}(\text{NO})\}^6$	1846
$[\text{Ru}(\text{NO})(\text{hedta})]^-$	$\{\text{Ru}(\text{NO})\}^7$	1858
$[\text{Ru}(\text{NO})(\text{hedta})]^{2-}$	$\{\text{Ru}(\text{NO})\}^8$	1383

From extensive electrochemical and <sup>15</sup>N NMR spectral examination, it has been concluded that the monoanion is best described as Ru<sup>II</sup> (S=0) coupled to NO (S=1/2) and the dianion also as Ru<sup>II</sup> (S=0) but coupled to singlet NO<sup>-</sup> (S=0). In  $[\text{Ru}(\text{NO})(\text{hedta})]^{2-}$  complex are consistent a bent Ru-N-O bond and it is obtained from <sup>15</sup>N NMR spectral data. This complex is very rare

in coordination complexes of  $\sigma$ -bonding ligands but has been identified in complexes containing  $\pi$ -acceptor ligands.

However,  $\text{Ru}^{\text{II}}$  is a strong  $\pi$  donor, and  $d\pi-\pi^*(\text{NO})$  back-donation will be more efficient in the neutral species than in the monoanion, which contains an unpaired electron in the  $\pi^*(\text{NO})$  orbital.

- **Cobalt-nitrosyl complexes:**

Schiff base neutral Co-nitrosyl complexes expected to contain bent Co-N-O bonds; have the configuration  $\{\text{Co}(\text{NO})\}_8$ . This has been confirmed by several crystallographic studies, and by judicious use of  $^{14/15}\text{N}$  NMR spectroscopy in solution and in the solid state.<sup>49</sup> These diamagnetic complexes, like their porphyrinato analogues, it has also very much interest because of the relative ease with which the Co-NO bond may be photolyzed. The electronic description cannot be effectively probed of these complexes, but the alternatives are  $\text{Co}^{\text{III}}$  ( $S=0$ ) bonded to  $\text{NO}^-$  ( $S=0$ ) or  $\text{Co}^{\text{II}}$  ( $S=1/2$ ) antiferromagnetically coupled with  $\text{NO}\cdot$  ( $S=1/2$ ). The former is preferred since  $^{59}\text{Co}$  NMR chemical shifts of the nitrosyls are quite similar to those of  $\text{Co}^{\text{III}}$  complexed; by “innocent”  $\sigma$ -bonding ligands.

- **Copper-nitrosyl complexes:**

In denitrification copper enzyme plays a vital role, but as a terminal electron acceptors uses  $\text{NO}_3^-$  and  $\text{NO}_2^-$ , ultimately producing  $\text{NO}$ ,  $\text{N}_2\text{O}$ , and/or  $\text{N}_2$ . In biological nitrogen oxide reduction proposed a Cu-NO species as a key intermediate, and NO adducts of other copper proteins have been proposed. A single copper nitrosyl species in nitrite reductase obtained from *Achromo-bacter cycloclastes* has been proposed as an intermediate involved in conversion of  $\text{NO}_2^-$  to  $\text{NO}$  or, in some instances, to  $\text{N}_2\text{O}$ . The site binding  $\text{NO}_2^-$  or  $\text{NO}$  is believed to be pseudo-tetrahedral, and the nitrosyl adduct, which has the configuration  $\{\text{Cu}(\text{NO})\}^{10}$ , is described as  $\text{Cu}^{\text{I}}$  bound by  $\text{NO}^+$ .<sup>50</sup>

### ❖ Conclusion:

Nitric oxide is a common free radical produced in living cells through the enzymatic degradation of L-arginine. It displays a number of regulatory functions: it is involved in the processes of neural conduction, regulation of cardiac function and immune defence, it triggers the pathways leading to the controlled cell death – apoptosis. One of the most important and earliest discovered functions of NO was to stimulate vasodilation. At the same time, being a free radical, NO is deleterious to the components of living cells.

NO in the unbound form has a very short lifetime in the cell but can be stabilized by the formation of complexes, i.e. metal–porphyrin nitrosyl, dinitrosyl–iron complexes and S-nitrosothiols, which are considered to be its biological transporters. Nitric oxide has a very high affinity for iron contained in the active sites of proteins

The various possibilities of biological responses to NO make it a fascinating molecule for study. A complex relationship is present between the fundamental chemistry of NO and the influences of the cellular microenvironment. Due to the extraordinary significance of nitric oxide in biological systems as a signalling molecule, immune defence (antimicrobial) agent and metabolite/intermediate in the global nitrogen cycle, the coordination chemistry of hemes with NO and its derivatives remains a primary research target. Much progress has been made in the understanding of the geometric and electronic structures of ferrous and ferric heme–nitrosyls as a function of the properties of the heme, the trans ligand to NO, and the environment of the heme in a protein active site. Thus it can be expected that key breakthroughs in the mechanistic understanding of NO and (multielectron) nitrite reductase, NO–nitrite interconversions in mammals, and of multielectron oxidases that involve ammonia and hydroxylamine will be achieved in the coming years.

There is also considerable biological interest in NO reactions with ligands coordinated to a redox-active metal. For example, the facile second-order trapping of NO by Mb(O<sub>2</sub>) or Hb(O<sub>2</sub>) is very fast and is mechanistically very distinct from the third order autoxidation of NO. The result is the oxidation of Fe(II) to Fe(III) concomitant with NO oxidation to NO<sub>3</sub><sup>-</sup>. In contrast, the facile reaction of M<sup>IV</sup>=O species (M = Fe or Cr) with NO to give M<sup>III</sup> – (ONO) leads to reduction of the metal along with oxidation of NO. The reaction with Hb(O<sub>2</sub>) is an important sink for NO in the cardiovascular system, while trapping of ferryl intermediates (or other strong oxidants) by NO may play a role in reducing oxidative stress. Oxidative stress may also be reduced by NO coordination with metal centres catalytic for Fenton chemistry (the generation of strongly oxidizing intermediates from H<sub>2</sub>O<sub>2</sub>). On the other hand, the ambiguous nature of

possible NO function in oxidative stress is illustrated by its inhibition of catalase; therefore, the protective function of this enzyme in removing endogenous  $H_2O_2$ . Once formed, the nitrosyl complex can serve to activate the coordinated NO toward either nucleophilic or electrophilic attack depending on the nature of the metal and its oxidation state and the ligand field.

Key biological roles not only involve the formation and decay of nitrosyl complexes but also how NO coordination affects the reactivities of the metal and other ligands and how the metal mediates the chemistry of the coordinated NO. Understanding the dynamics, thermodynamics, and mechanisms of the relevant fundamental processes provides insight into how the chemical biology of NO and other relevant nitrogen oxides function.

Obviously, understanding bacterial denitrification is relevant to the complex role of NO in human health. It can also be so in the design of iron and copper coordination complex-based systems with the ability to limit or reduce  $NO_x$  emission in the environment. Hence, the careful design and synthesis of  $NO_x$  selective iron or copper complexes might be extremely useful in the production of pollution-reducing components that might be employed at the source of  $NO_x$  emissions (e.g., in an automobile muffler).

**References:**

1. (a) Mingos, D. M. P.; Sherman, D. J. *Adv. Inorg. Chem.* **1989**, *34*, 293. (b) Richter-Addo, G. B.; Legzdins, P. *Metal Nitrosyls*; Oxford University Press: New York, **1992**.
2. Schwartz, S. E.; White, W. H. *Trace Atmospheric Constituents. Properties, Transformation and Fates*; J. Wiley & Sons: New York, **1983**.
3. (a) Moncada, S.; Palmer, R. M. J.; Higgs, E. A. *Pharmacol. Rev.* **1991**, *43*, 109. (b) Feldman, P. L.; Griffith, O. W.; Stuehr, D. J. *Chem. Eng. News* **1993**, *71*, 10, 26. (c) Butler, A. R.; Williams, D. L. *Chem. Soc. Rev.* **1993**, 233. (d) *Methods in Nitric Oxide Research*; Feelisch, M., Stamler, J. S., Eds.; John Wiley and Sons: Chichester, England, 1996 and references therein. (e) Wink, D. A.; Hanbauer, I.; Grisham, M. B.; Laval, F.; Nims, R. W.; Laval, J.; Cook, J.; Pacelli, R.; Liebmann, J.; Krishna, M.; Ford, P. C.; Mitchell, J. B. *Curr. Top. Cell. Regul.* **1996**, *34*, 159.
4. *Nitric Oxide: Biology and Pathobiology*; Ignarro, L. J., Ed.; Academic Press: San Diego, CA, **2000**.
5. *Nitric Oxide and Infection*; Fang, F. C., Ed.; Kluwer Academic/ Plenum Publishers: New York, **1999**.
6. Koshland, D. E. *Science* **1992**, *258*, 1861.
7. Wink, D. A.; Darbyshire, J. F.; Nims, R. W.; Saveedra, J. E.; Ford, P. C. *Reactions of the bio regulatory agent nitric oxide in oxygenated aqueous media: determination of the kinetics for oxidation and nitrosination by intermediates generated in the NO/O<sub>2</sub> reaction*. *Chem. Res. Toxicol.* *6*:23-27; **1993**.
8. Wink, D. A.; Nims, R. W.; Darbyshire, J. F.; Christodoulou, D.; Hanbauer, I.; Cox, G. W.; Laval, F.; Laval, J.; Cook, J. A.; Krishna, M. C.; DeGraff, W.; Mitchell, J. B. *Reaction kinetics for nitrosation of cysteine and glutathione in aerobic nitric oxide solutions at neutral pH: insights into the fate and physiological effect of intermediates generated in the NO/O<sub>2</sub> reaction*. *Chem. Res. Toxicol.* *7*:519-525; **1994**.
9. Wink, D. A.; Cook, J. A.; Kim, S.; Vodovotz, Y.; Pacelli, R.; Krishna, M. C.; Russo, A.; Mitchell, J. B.; Jourdeuil, D.; Miles, A. M.; Grisham, M. B. *Superoxide modulates the oxidation and nitrosation of thiols by nitric oxide derived reactive intermediates*. *J. Biol. Chem.* *272*:11147-11151; **1997**.
10. Ignarro, L. J. *Biosynthesis and metabolism of endothelium-derived nitric oxide*. *Annu. Rev. Pharmacol. Toxicol.* *30*:535-560; **1990**.
11. *Free Radicals in Biology and Medicine* (Life Chemistry Reports Series). Clarendon Press, Oxford Press, New York, NY USA; **1985**.
12. *Signal Transduction by Reactive Oxygen and Nitrogen Species: Pathways and Chemical Principles*. Lavoisier; **2003**.



13. Wink, D. A.; Feelisch, M.; Fukuto, J.; Chistodoulou, D.; Jour'd'heil, D.; Grisham, M. B.; Vodovotz, Y.; Cook, J.A.; Krishna, M.; DeGraff, W. G.; Kim, S.; Gamson, J.; Mitchell, J.B. *The cytotoxicity of nitroxyl: possible implications for the pathophysiological role of NO*. Arch. Biochem. Biophys. 351:66-74; **1998**.
14. Kelm, M. *Nitric oxide metabolism and breakdown*. Biochem. Biophys. Acta, **1999**, 1411(2-3), 273-289.
15. Ignarro, L.J. *Endothelium-derived nitric oxide: actions and properties*. FASEB J., **1989**, 3, 31-36.
16. Stuehr, D. J.; Santolini, J.; Wang, Z. Q.; Wei, C. C.; Adak, S. *Update on mechanism and catalytic regulation in the NO synthases*. J. Biol. Chem. 279: 36167-360; **2004**.
17. Knowles, R. G.; Moncada, S. *Nitric oxide synthases in mammals*. Biochem. J. 298: 249-258; **1994**.
18. Ignarro, L. J. *Physiology and pathophysiology of nitric oxide*. Kidney Int. Suppl. 55: S2-S5; **1996**.
19. Natalis, P.; Collin, J. E.; Delwiche, J.; Caprace, G.; Hubin, M. J. J. *Electron Spectrosc. Relat. Phenom.* **1979**, 17, 421.
20. Lee, K. Y.; Kuchnya, D. L.; Kochi, J. K. Inorg. Chem. **1990**, 29, 4196. Kim, E.; Kochi, J. K. J. Am. Chem. Soc. **1991**, 113, 4962.
21. Stanbury, D. M. Adv. Inorg. Chem. **1989**, 33, 69.
22. Teillet-Billy, D.; Fiquet-Fayard, F. J. Phys. Chem. **1990**, 94, 3450
23. Siegel, M. W.; Celotta, R. J.; Hall, J. L.; Levine, J.; Bennett, R.A. Phys. Rev. A **1972**, 6, 607.
24. Teillet-Billy, D.; Fiquet-Fayard, F. J. Phys. **1977**, 10B, L111.
25. Lee, J.; Chen, L, West, A. H.; Richter-Addo, G. B. Chem. Rev. **2002**, 102, 1019 and references therein.
26. Paul, P. P.; Tyeklar, Z.; Farooq, A.; Karline, K. D.; Liu S.; Zubieta, J. J. Am. Chem. Soc. **1990**, 112, 2430.
27. Coppens, P.; Novozhilova, I.; Kovalevsky, A. Chem. Rev. **2002**, 102, 861 and references therein.
28. (a) Traylor, T. G.; Sharma, V. S. *Biochemistry* **1992**, 31, 2847. (b) Radi, R. Chem. Res. Toxicol. **1996**, 9, 828.
29. (a) Kim, S.; Deinum, G.; Gardner, M. T.; Marletta, M. A.; Babcock, G. T. J. Am. Chem. Soc. **1996**, 118, 8769 and references therein. (b) Burstyn, J. N.; Yu, A. E.; Dierks, E. A.; Hawkins, B. K.; Dawson, J. H. *Biochemistry* **1995**, 34, 5896.
30. (a) Minamiyama, Y.; Takemura, S.; Imaoka, S.; Funae, Y.; Tanimoto, Y.; Inoue, M. J. Pharmacol. Exp. Ther. **1997**, 283, 1479. (b) Cleeter, M. W. J.; Cooper, J. M.; Darley-Usmar, V. M.; Moncada, S.; Scapira, A. H. V. FEBS Lett. **1994**, 345, 50.
31. (a) Noguchi, T.; Hoshino, M.; Tsujimura, M.; Odaka, M.; Inoue, Y.; Endo, I. *Biochemistry* **1996**, 35, 16777. (b) Odaka, M.; Fujii, K.; Hoshino, M.; Noguchi, T.; Tsujimura, M.; Nagashima, S.; Yohda, M.; Nagamune, T.; Inoue, Y.; Endo, I. J. Am.

- Chem. Soc. **1997**, *119*, 3785. (c) Tsujimura, M.; Dohmae, N.; Odaka, M.; Chijimatsu, M.; Takio, K.; Yohda, M.; Hoshino, M.; Nagashima, S.; Endo, I. *J. Biol. Chem.* **1997**, *272*, 29454.
32. Brown, G. C. *Eur. J. Biochem.* **1995**, *232*, 188.
  33. Abu-Soud, H. M.; Khassawneh, M. Y.; Sohn, J.-T.; Murray, P.; Haxhiu, M. A.; Hazen, S. L. *Biochemistry* **2001**, *40*, 11866.
  34. (a) Ribiero, J. M. C.; Hazzard, J. M. H.; Nussenzveig, R. H.; Champagne, D. E.; Walker, F. A. *Science* **1993**, *260*, 539. (b) Walker, F. A.; Ribiero, J. M. C.; Monfort, W. R. *Metal Ions in the Biological System*; Sigel, H., Sigel, A., Eds.; M. Dekker: New York, **1998**; Vol. 36, p 621.
  35. (a) Tayeh, M. A.; Marletta, M. A. *J. Biol. Chem.* **1989**, *264*, 19654. (b) Abu-Soud, H. M.; Ichimori, K.; Nakazawa, H.; Stuehr, D. J. *Biochemistry* **2001**, *40*, 6876. (c) Stuehr, D.; Pou, S.; Rosen, G. M. *J. Biol. Chem.* **2001**, *276*, 14533 and references therein.
  36. Malinski, T.; Czuchajowski, C. *Methods in Nitric Oxide Research*; Feelisch M., Stamler, J. S., Eds.; John Wiley and Sons: Chichester, England, **1996**; Chapter 22.
  37. Webb A, Bond R, McLean P, Uppal R, Benjamin N, Ahluwalia A. *Reduction nitrite to nitric oxide during ischemia protects against myocardial ischemia-reperfusion damage.* *Proc Natl Acad Sci USA* **2004**; *101*: 13683-8
  38. Duranski MR, Greer JJ, Dejam A, Jaganmohan S, Hogg N, Langston W, *et Cytoprotective effects of nitrite during in vivo ischemia-reperfusion of the heart and liver.* *J Clin Invest* **2005**; *115*:1232-40.
  39. Zweier JL, Lia H, Samouilova A, Liua X. *Mechanisms of nitrite reduction to nitric oxide the heart and vessel wall.* *Nitric Oxide*, **2010**; *22*: 83-90
  40. Lundberg JO, Weitzberg E, Gladwin MT. *The nitrate-nitrite-nitric oxide pathway in physiology and therapeutics.* *Nat Rev Drug Discov* **2008**; *7*: 156-67.
  41. Moncada S, Higgs A. *The L-arginine-nitric oxide pathway.* *N Engl J Med* **1993** 2002-42.
  42. Von der Leyen et al., **1995**; Kullo et al., **1997**; Varenne et al., **1998**.
  43. Lee, J.; Chen, L, West, A. H.; Richter-Addo, G. B. *Chem. Rev.* **2002**, *102*, 1019 and references therein Coppens, P.; Novozhilova, I.; Kovalevsky, A. *Chem. Rev.* **2002**, *102*, 861 and references therein.
  44. McCleverty, J. A. *Chem. Rev.* **1979**, *7*, 53. Wolak, M.; van Eldik, R. *Chem. Rev.* **2002**, *102*, 263. Ford, P. C.; Lorkovic, I. M. *Chem. Rev.* **2002**, *102*, 993.
  45. Wyllie, R. A.; Scheidt, W. R. *Chem. Rev.* **2002**, *102*, 1067.
  46. Ellison, M. K.; Schulz, C. E.; Scheidt, W. R. *J. Am. Chem. Soc.* **2002**, *124*, 13833.
  47. Nasri, H.; Ellison, M. K.; Chen, S.; Huynh, B. H.; Scheidt, W. R. *J. Am. Chem. Soc.* **1997**, *119*, 6274'
  48. Chen, Y.; Lin, F.-T.; Shepherd, R. E. *Inorg. Chem.* **1999**, *38*, 973

49. Groombridge, C. J.; Larkworthy, L. F.; Marecaux, A.; Povey, D. C.; Smith, G. W.; Mason, J. J. *Chem. Soc., Dalton Trans.* **1992**
50. Ruggiero, C. E.; Carrier, S. M.; Antholine, W. E.; Whittaker, J. W.; Cramer, C. J.; Tolman, W. B. *J. Am. Chem. Soc.* **1993**, *115*, 11285

**SYNTHESIS OF ZEOLITE 13X, FOR THE**  
**USE IN OXYGEN CONCENTRATOR -A**  
**REVIEW**

**SCOTTISH CHURCH COLLEGE, UNIVERSITY OF  
CALCUTTA**



University Registration no. = **223-1221-0167-16**

University Roll no. = **223/CEM /191022**

SPECIAL PAPER = **CHEM -S044**

NAME OF CANDIDATE: **PAPRI MITRA**

NAME OF EXAMINER: **Dr. SEBANTI BASU**

*Papri Mitra*

Signature of the Candidate

Signature of the Examiner

## **ACKNOWLEDGEMENT**

I gratefully thank Dr. Rama Ranjan Bhattacharjee, Associate Professor, Amity University, under his supervision and unending support this review work was accomplished during my 4<sup>th</sup> and final semester (Jan-July 2021) in partial fulfillment of M.Sc (Chemistry) degree in the University of Calcutta under Scottish Church College, Kolkata. And also I would like to thank the University of Calcutta and my college professors for giving me the opportunity to write this review paper.

# **CONTENT**

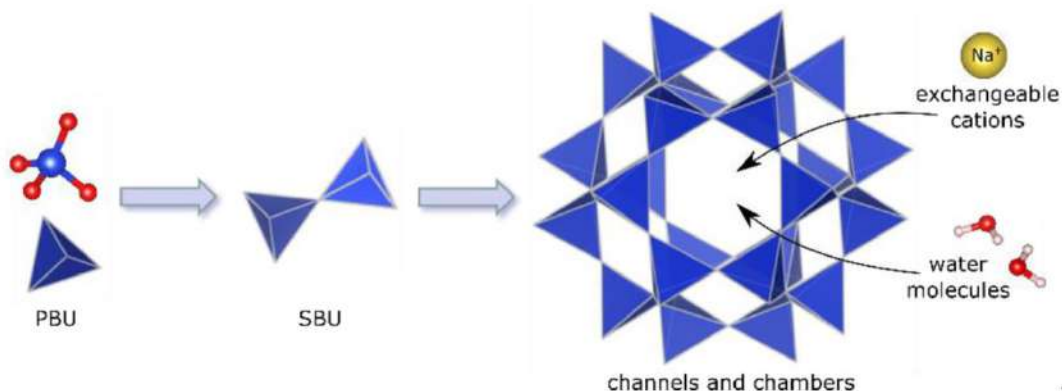
1. INTRODUCTION.
2. EXPERIMENTAL.
  - 2.1 Synthesis from coal fly ash (CFA).
    - 2.1.1 Materials
    - 2.1.2 Processes
  - 2.2 Synthesis from natural halloysite.
    - 2.2.1 Materials
    - 2.2.2 Processes
  - 2.3 Synthesis from natural kaolin.
    - 2.3.1 Materials
    - 2.3.2 Processes
3. RESULT AND DISCUSSION
  - 3.1 Characterization of Zeolite 13X
    - 3.1.1 X-Ray Diffraction Analysis
    - 3.1.2 FT-IR Analysis
    - 3.1.3 Scanning Electron Microscope Analysis
    - 3.1.4 Thermal Analysis
    - 3.1.5 Adsorption Properties
  - 3.2 Effects of Parameters on Zeolite 13X Synthesis
    - 3.2.1 Crystallization temperature
    - 3.2.2 Alkalinity
    - 3.2.3  $\text{SiO}_2/\text{Al}_2\text{O}_3$  Molar Ratio
    - 3.2.4 Synthesis time
4. CONCLUSION
5. REFERENCE

## 1. INTRODUCTION

The second wave of COVID-19 saw a huge shortage of medical oxygen in different parts of India. While meeting the current demand, manufacturing medical oxygen also became important to ensure the country has adequate in the future. Apart from medical use, it is also used by various chemical industries for various processes such as: refiner industries, steel construction, paper industries, wastewater treatment and glass production and other industrial operations. The high rise in oxygen demand made industrial consumption of oxygen practically zero as the entire capacity has been converted for medical usage. Still there is a huge shortage of oxygen with the rise of COVID cases daily.

Thus there is a growing need to address the health and quality of life through a light-weight and portable oxygen concentrator with a medical grade oxygen supply ( $O_2$  concentration: ~88–92 vol %). Now this problem can be solved by using air as the source and separating oxygen from it in the pure form. Generally, the common adsorption process of air separation consists of procedures which make use of zeolites as nitrogen adsorbent under the equilibrium conditions and oxygen is a process product.

Zeolites (from the Greek “zein” and “lithos”, meaning “stones that boil”) are microporous aluminosilicate materials of alkali or earth alkaline elements with crystalline frameworks structure of three-dimensional tetrahedral units of  $SiO_4$  and  $AlO_4$  which are connected by their common oxygen atoms, generating a network of pores and cavities having molecular dimensions with uniform pore sizes ranging from 0.3–1.0 nm, which are occupied by water and cations. [1,2]. The uniqueness of zeolites originate from the fact that their surfaces are formed with negatively charged oxides and also the presence of isolated cations above their surface structure.



Zeolites are obtained from nature and can also be prepared synthetically. The formation of natural zeolites occurs when the volcanic rocks and the ash layers react with alkaline groundwater. Generally synthesized zeolites have some advantages over their natural counterparts i.e., [3, 4]

- The synthetic zeolites can be designed to have structures that do not occur in nature, structures that optimize their intended purpose.
- They can be produced in a phase-pure, uniform state without the presence of impurities.
- In synthetic zeolite the content of aluminium and silicone can be adjusted.
- Synthetic zeolites have better ion exchange capabilities than the natural zeolites.

Zeolites as molecular sieves are used in various air separation processes such as cryogenic technique, membrane separation and pressure swing adsorption (PSA) that can effectively produce enriched oxygen using ambient air as the source. PSA technique has an advantage over others because of its lower consumption of energy. This technique can absorb nitrogen from air and output an enriched oxygen stream under high-pressure conditions [42]. The most commonly used zeolite for the air separation for oxygen production is Zeolite 13X adsorbent as it has an outstanding nitrogen to oxygen adsorption selectivity. The selectivity for zeolite to adsorb nitrogen compared to oxygen is due to the interaction between electrostatic field of the cationic zeolite and the quadrupole moment of the nitrogen and oxygen. The quadrupole moment of nitrogen is three times higher than that of oxygen, which leads to a selective adsorption onto the zeolite surface [6].

Zeolite 13X (Molecular formula =  $\text{Na}_{86}[(\text{AlO}_2)_{86} (\text{SiO}_2)_{106}] \cdot \text{H}_2\text{O}$ ) is a Faujasite-type zeolite having three dimensional pore structures linked by circular 12-ring apertures, which leads to a larger cavity diameter of 12 Å, restricted by 10 sodalite cages in a hexagonal structure. The effective pore diameter in this type of zeolite is relatively large at 7.4 Å [7]. Sodium cations in zeolite 13X balances the negative charge of the zeolite framework and also creates an electrostatic field in the zeolite structural environment. Some of the relevant properties of 13X are listed in Table 1 [8-11].



Chemical Formula	$\text{Na}_{36}[(\text{AlO}_2)_{86}(\text{SiO}_2)_{106}]\cdot\text{H}_2\text{O}$
Pore Diameter	$\sim 8 \text{ \AA}$
Mesopore Volume	$0.165 \text{ cm}^3/\text{g}$
Micropore Volume	$0.17 \text{ cm}^3/\text{g}$
Langmuir Surface Area	$571 \text{ m}^2/\text{g}$
Mass of Pellet Sample	2.37 g
Mass of Crushed sample	2.49 g

**Table 1: Properties of zeolite 13X**

The growing need for oxygen economy invokes much interest in molecular sieves and its cost effective synthesis. Usually, synthesis of zeolites takes place from freshly prepared sodium aluminosilicate gel, obtained from various silica and alumina sources by hydrothermal treatment. However, it is very expensive to prepare synthetic zeolites from chemical sources of silica and alumina. Therefore, in order to obtain low-cost and effective synthetic zeolite, many researchers have studied the synthesis of zeolite from kaolinite [12], waste porcelain [13], illite [14], bentonite [15] and montmorillonite [16], coal fly ash [17], kaolinite [18], oil shale ash [19], bagasse fly ash [20], paper sludge [21], high silicon fly ash [22], waste sandstone cake [23,24], halloysite [25] and lithium slag [26].

In this paper we will study the synthesis of zeolite 13X from (i) coal fly ash (ii) natural halloysite and (iii) natural kaolin with alkali fusion followed by hydrothermal treatment. And to confirm the successful zeolite production we compare the properties, and characterized utilizing various techniques, such as X-ray diffraction (XRD), the Brunauer–Emmett–Teller (BET) method, scanning electron microscopy (SEM), X-ray fluorescence (XRF), thermo gravimetric analysis (TGA), differential thermal analysis (DTA), X-ray diffraction (XRD), and differential thermal gravimetry (DTG).

### **COAL FLY ASH**

Coal fly ash (CFA) is a solid waste product obtained from the combustion of pulverized coal in electric power generating plants. Large number of thermal power plants generates huge quantities of fly ash causing serious environmental problem mainly due to its structure and toxic elements. There are many processes to recycle and reuse the CFA to reduce the environmental pollution and one of it is synthesis of zeolites from it. The major component of CFA is silicone dioxide

(SiO<sub>2</sub>), Aluminium oxide (Al<sub>2</sub>O<sub>3</sub>) and calcium oxide (CaO). Thus the synthesis of aluminosilicates porous material from CFA is possible. And is done by alkali fusion followed by hydrothermal synthesis.[27]

### **NATURAL HALLOYSITE**

Halloysite having empirical formula - Al<sub>2</sub>Si<sub>2</sub>O<sub>5</sub> (OH)<sub>4</sub>, is a double-layered aluminosilicate clay mineral, consisting of one alumina octahedron sheet and one silica tetrahedron sheet in a 1:1 stoichiometric ratio. It has a high specific surface area and hollow structure, and also from its composition it acts as a promising material with high reactivity to synthesize zeolite of high purity. Synthetic zeolite products produced from halloysite are generally found to be non-toxic, odorless, environment-friendly, acid and alkali resistant, thermally stable and do not generate secondary pollution.[25]

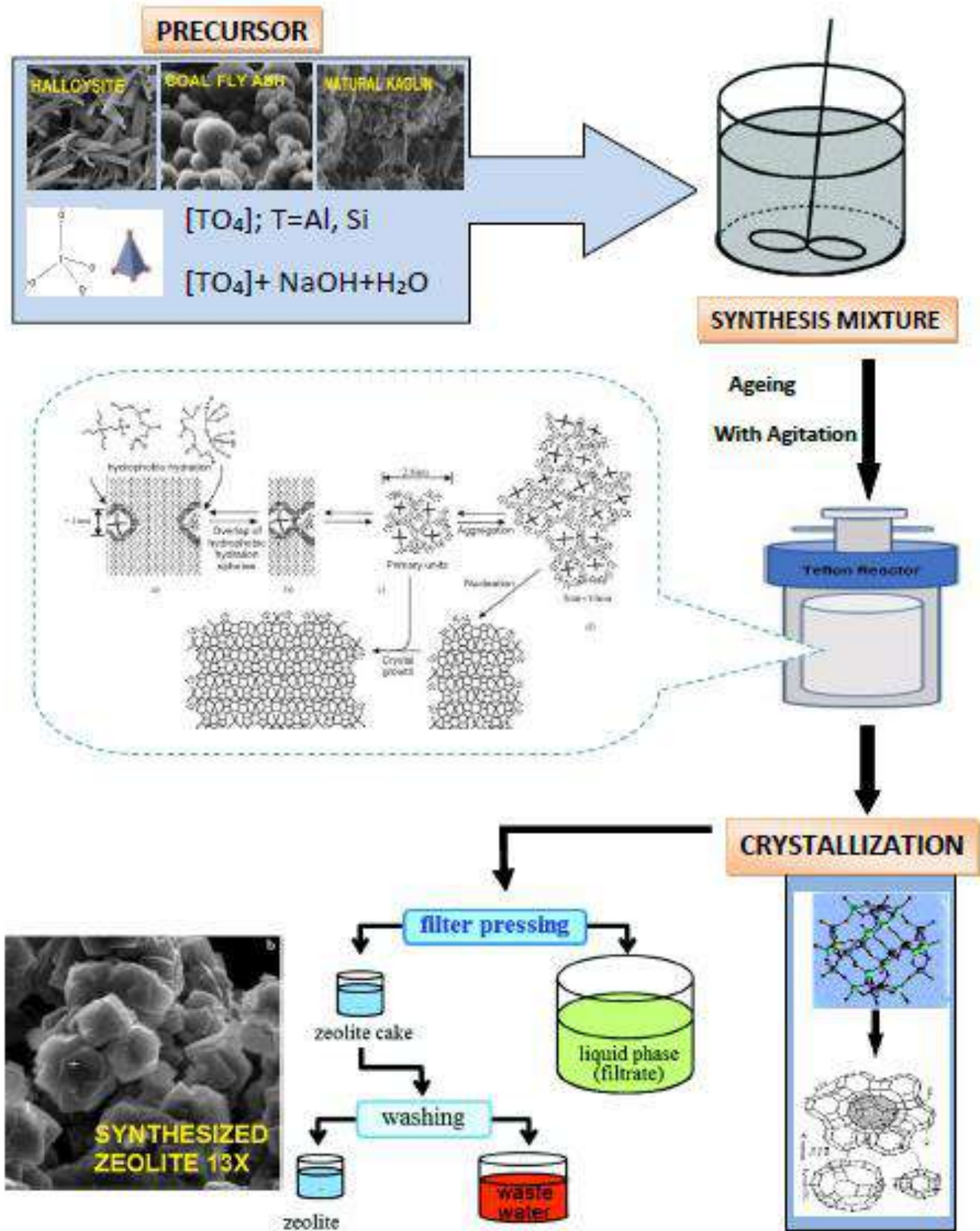
### **NATURAL KAOLIN**

Natural kaolin is a clay material mainly consists of kaolinite, illite and trace of quartz. Kaolinite is a clay mineral, with the chemical composition [Al<sub>2</sub>Si<sub>2</sub>O<sub>5</sub> (OH)<sub>4</sub>]. It is a two-layered aluminosilicate clay mineral, consisting of one alumina octahedron sheet and one silica tetrahedron sheet in a 1:1 stoichiometric ratio. And Illite (K<sub>1-2</sub> Al [Si<sub>7-6.5</sub>Al<sub>1-1.5</sub>O<sub>20</sub>](OH)<sub>4</sub>) is a phyllosilicate or layered aluminosilicate with high Si content. Expanding from these empirical findings, it can be further deduced that it will be possible to directly synthesize zeolite X from natural kaolin via alkali fusion followed by hydrothermal treatment.[28]

## **1. EXPERIMENTAL**

The zeolite synthesis process is done using alkali fusion followed by hydrothermal process shown in scheme 1. The hydrothermal processes have some advantages which includes, high reactivity of reactants, low energy consumption, low air pollution, easy to control the solution, formational of metastable phases, and unique condensed phase.

## Scheme 1



## 2.1 SYNTHESIS FROM COAL FLY ASH (CFA).

### 2.1.1 Materials

The CFA is collected at the top of burners using cyclones, electric precipitators or mechanic filters. X- ray diffraction analysis shows that it is mainly composed of amorphous  $\text{SiO}_2$  and  $\text{Al}_2\text{O}_3$  with some crystals such as quartz(  $\text{SiO}_2$ ), mullite ( $2\text{SiO}_2.3\text{Al}_2\text{O}_3$ ), hematite ( $\text{Fe}_2\text{O}_3$ ) and magnetite( $\text{Fe}_3\text{O}_4$ ). The chemical composition of coal fly ash is shown in table 2;

composition	Wt%
$\text{SiO}_2$	71.0
$\text{Al}_2\text{O}_3$	8.3
$\text{CaO}$	0.8
$\text{K}_2\text{O}$	0.7
$\text{Na}_2\text{O}$	0.3
$\text{Fe}_2\text{O}_3$	3.6
C	1.0

**Table 2:** Chemical Composition CFA



### 2.1.2 Synthesis process

The CFA was pre-treated by magnetic separation using a high intensity magnetic separator which results in the reduction of about 65% of iron components and increases of nearly 34% and 3.5% silicone and aluminium compounds respectively.[34] The total amount of  $\text{SiO}_2$  and  $\text{Al}_2\text{O}_3$  can be reach to approximately 89.96%. In the experiment the fly ash was mixed and grounded with sodium hydroxide (NaOH) to obtain a homogeneous mixture. Then the mixture was heated with a weight ratio of 1 : 1 ( CFA, NaOH ) at  $850^\circ\text{C}$  for 2hours in a muffle furnace. The obtained mixture was treated with deionized water by magnetic stirring. Then it was followed by an ageing process with vigorous agitation for 12 hours at room temperature in the Teflon reactor with proper sealing. At last, the mixture was crystallized at static condition at  $100^\circ\text{C}$  for 14 hours. At end of the process solid products were filtered-off, and the solid phase was washed thoroughly using deionized water for several times until the drained water's pH reached below 10.5. after that it was dried at  $100^\circ\text{C}$  for 12 hours and saved in dry container.[27]



## 2.2 SYNTHESIS FROM NATURAL HALLOYSITE

### 2.2.1 Materials.

The natural halloysite mineral was used as the source of silicon–aluminum. Sodium hydroxide (NaOH) was used as the alkali source and sodium silicate (Na-SiO<sub>3</sub>·9H<sub>2</sub>O) as the sodium and silicone source. The X-ray diffraction (XRD) pattern and the chemical analysis showed that the main constituents of the raw material were silica (45.04 %) and alumina (38.31 %), whereas the loss of ignition (LOI) is 17.94 %. The chemical composition of halloysite determined by chemical analysis is given in Table 3;

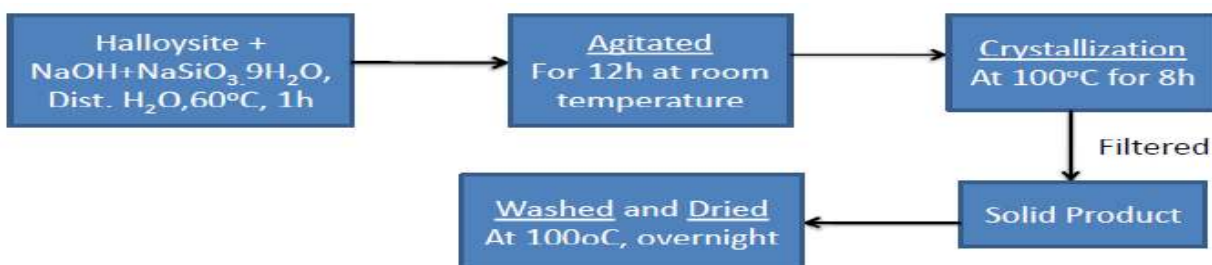


Component	Content (%)	Component	Content (%)
SiO <sub>2</sub>	45.04	K <sub>2</sub> O	0.03
Al <sub>2</sub> O <sub>3</sub>	38.31	TiO <sub>2</sub>	0.04
TFe <sub>2</sub> O <sub>3</sub>	0.16	P <sub>2</sub> O <sub>5</sub>	0.02
MgO	0.05	MnO	0.002
CaO	0.05	H <sub>2</sub> O	2.27
Na <sub>2</sub> O	0.05	LOI	17.94

Table3: Chemical compositions of the raw material (wt%)

### 2.2.2 Synthesis process

The process was done using 3 g of halloysite which was calcined at 500°C for 2 h, and was mixed with 5.7 g NaOH and 8.2 g NaSiO<sub>3</sub>·9H<sub>2</sub>O, the mixture were dispersed in 67 mL distilled water with constant stirring for 1 hours at 60°C in a water bath. Then the slurry was aged for 12 hours at room temperature in the sealed Teflon reactor to rearrange the reactant for the formation of nuclei. After this the mixture was crystallized at 100 °C for 8 hours under static conditions. At last, the solid was separated by filtration and washed thoroughly several times with deionized water until the filtrate pH was reduced to less than 10. The precipitated solid was dried at 100°C overnight and finely crushed.[25]



## 2.3 SYNTHESIS FROM NATURAL KAOLIN

### 2.3.1. Materials

The kaolin was taken as the starting material for the experiment as silica–alumina source after was it was crushed and air-dried. NaOH was taken as the alkali source for the alkali fusion followed by hydrothermal treatment.[30] The main constituents of the low grade natural kaolin can be seen in table 4;



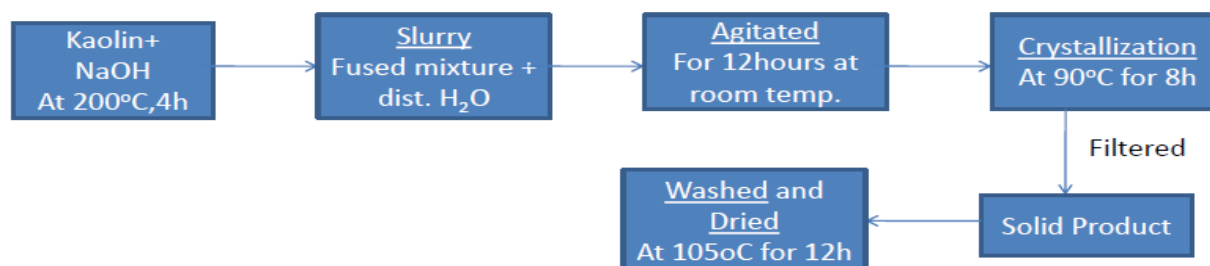
**Natural Kaolin**

Component	Content (%)
SiO <sub>2</sub>	56.30
Al <sub>2</sub> O <sub>3</sub>	29.52
TFe <sub>2</sub> O <sub>3</sub>	1.32
MgO	0.35
CaO	0.056
Na <sub>2</sub> O	0.056
K <sub>2</sub> O	2.99
TiO <sub>2</sub>	0.28
P <sub>2</sub> O <sub>5</sub>	0.32
MnO	0.012
H <sub>2</sub> O	0.28
LOI	9.18

Table 4: Chemical Characterization of natural kaolin (wt%)

### 2.3.2 Synthesis Process

Low grade natural kaolin was mixed with sodium hydroxide (NaOH) powder with the weight ratio of 2:1 and fused in an MgO ceramic crucible at 200 °C for 4 hours. The fused mixture was cooled at room temperature and grounded and then was added to distilled water. The slurry obtained was vigorously agitated for 12 hours at room temperature for homogenization with constant stirring at 800 r/min. Then the homogenized material was crystallized at 90 °C for 8 hours. Finally, the solid was separated by filtration and washed thoroughly several times with deionized water until the pH was reached around 8, then was dried at 105°C and crushed.[30,31]



## 3.RESULT AND DISCUSSION

### 3.1 Characterization of zeolite 13X

#### 3.1.1 XRD Analysis

The synthesized zeolite product from coal fly ash was analyzed using X-Ray Diffraction (XRD) method for the identification of crystalline material and its structure. The XRD pattern of the synthesized product is shown in Fig 2; From the figure we can see that the XRD pattern indicates the presence of X-type zeolite with the largest peak at  $2\theta = 6.16^\circ$ , which is in a good agreement with the standard JCPDS Card (PDF 38-0237).

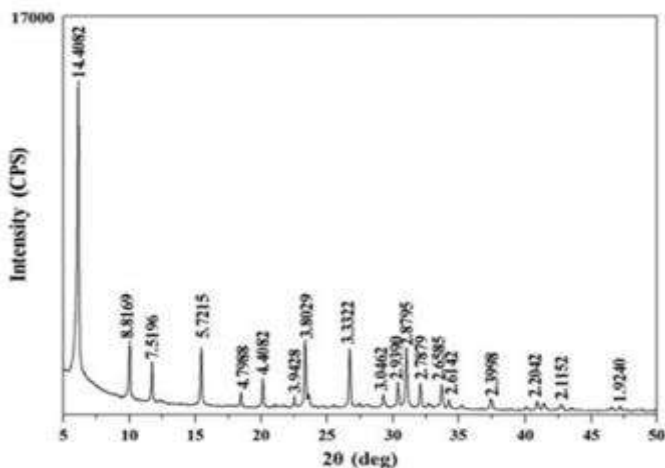


Fig.3. XRD pattern of synthesized zeolite 13X from halloysite

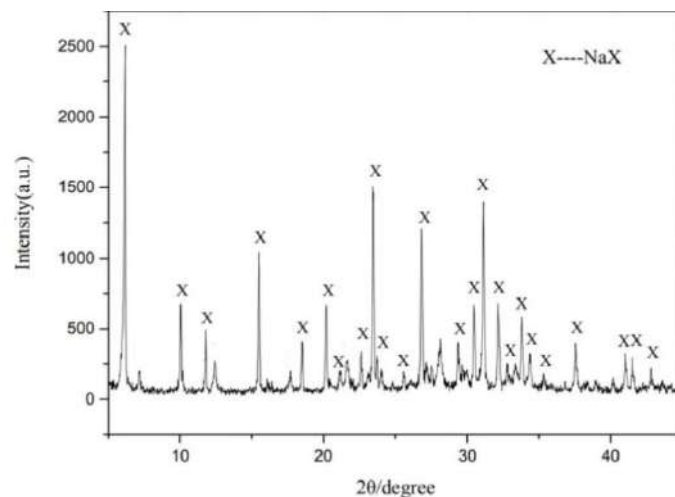


Fig.2. XRD pattern of zeolite 13X produced from coal fly ash

The synthesized product from natural halloysite was also analyzed using XRD to corroborate the structure of the newly formed zeolite 13X. The XRD pattern of the zeolite is given in Fig. 3, which also matches with the standard JCPDS Card (PDF 38-0237).[25] The XRD pattern obtained from the synthesized zeolite from natural kaolin is shown in figure.4, which also matches with that of standard JCPDS Card (PDF 38-0237).[31]

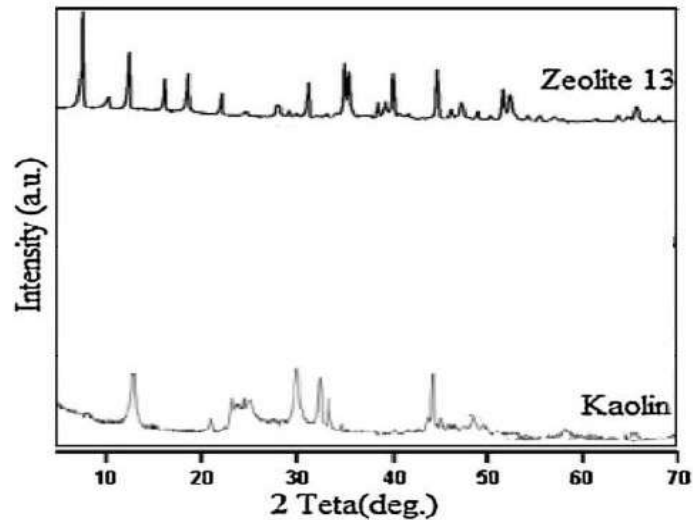


Fig.4. XRD pattern of natural kaolin and zeolite 13X

From the three figures (fig.2,3,4) we can see that there was no other diffraction peaks which indicated that only one pure phase of 13X zeolite was synthesized. Also the observed diffraction peaks were sharp and intense confirming a high degree of crystallinity of the synthesized 13X zeolite.

### 3.1.2 FT-IR analysis

Apart from FT-IR analysis, it is well known that spectroscopic method provide useful information about the structure of zeolites and about other functional groups which may be present during the synthesis and post treatment. The IR spectra of the synthesized zeolite 13X obtained from the halloysite, CFA and kaolin are shown in fig. 5,6 and 7 respectively.

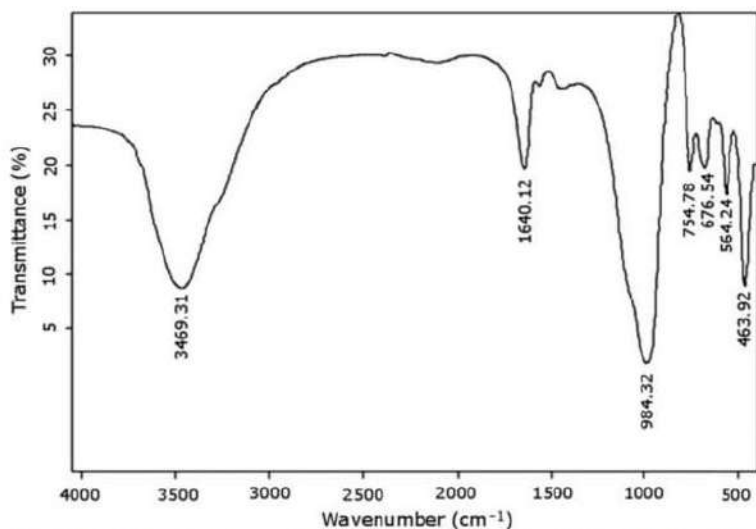


Fig.5. FT-IR spectrum of zeolite 13X synthesized from halloysite

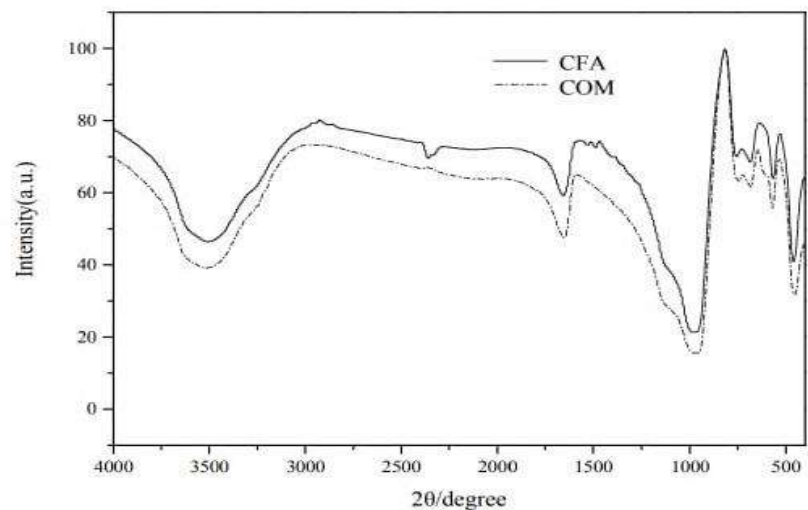
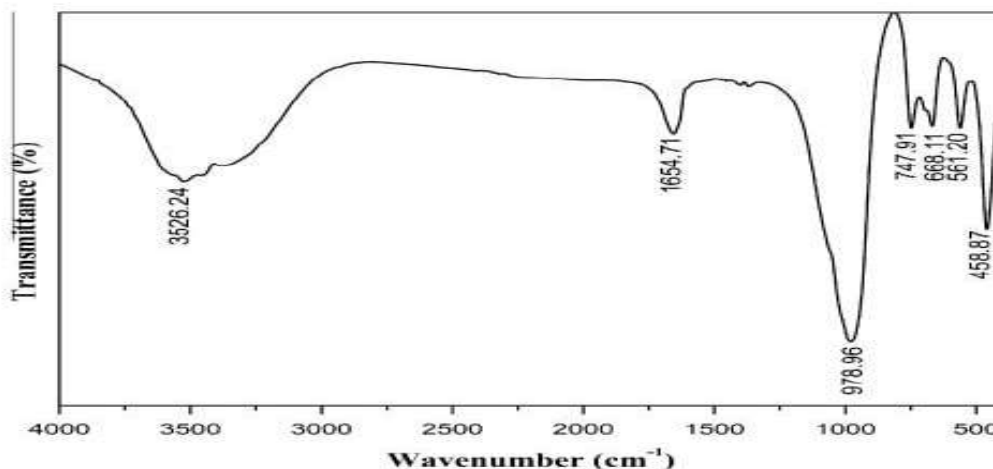


Fig.6. IR spectra of the synthesized zeolite from CFA and commercial zeolite(COM)





**Fig. 7.** FT-IR spectrum of 13X zeolite obtained at the optimum synthesis conditions from low-grade natural kaolin.

From the IR spectra of the synthesized zeolite we get the band at about 420-500 $\text{cm}^{-1}$  due to the T-O bending vibration of the zeolite interior and for the double-six member ring bond vibration zone there is a band at about 561  $\text{cm}^{-1}$ . The peaks centered at around 978- 984 and 676-678  $\text{cm}^{-1}$  corresponded to the TO4 [19] (T = Si or Al) asymmetric and symmetric stretching vibration respectively. The appearance of band at 1640  $\text{cm}^{-1}$  could be assigned to the  $\text{H}_2\text{O}$  having (H-O-H-) vibration band and the observed broad adsorption band at 3464  $\text{cm}^{-1}$  was ascribed to OH-stretching of water molecules that are present in the cavities and channels in the zeolite due its incomplete dehydration. All these data comes in good agreement with reported values of commercial 13X zeolite [26].

### **3.1.3. Scanning Electron Microscope Analysis**

The morphology of the zeolite product matches with that of 13X zeolite having an octahedral shape which is confirmed by scanning electron microscope (SEM) analysis, and present of no other structures suggests that the obtained 13X zeolite product is in phase pure state. The images obtained from SEM is shown in fig. 8,9,10 [27,25,28] for the synthesized zeolite 13X from CFA, halloysite and kaolin

respectively.

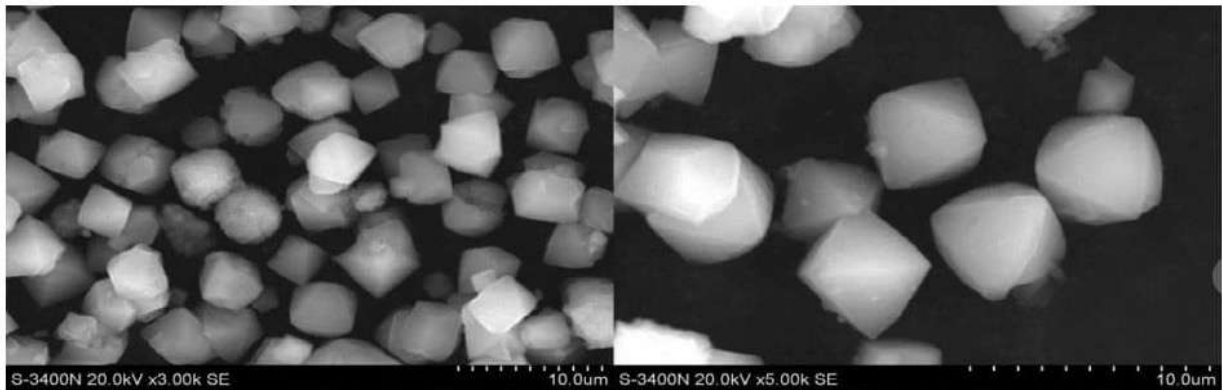


Fig. 8 SEM photographs of zeolite 13X produced from fly ash

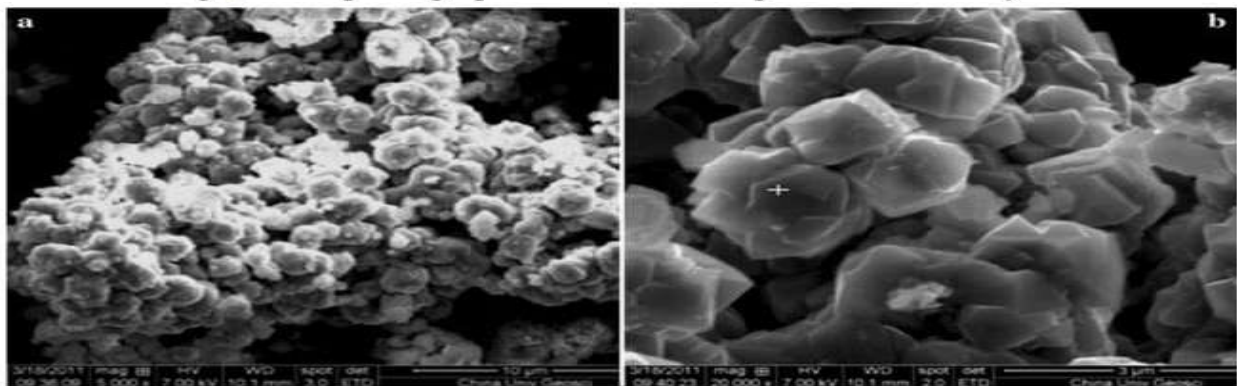


fig.9. FE-SEM images of 13X zeolite synthesized from halloysite

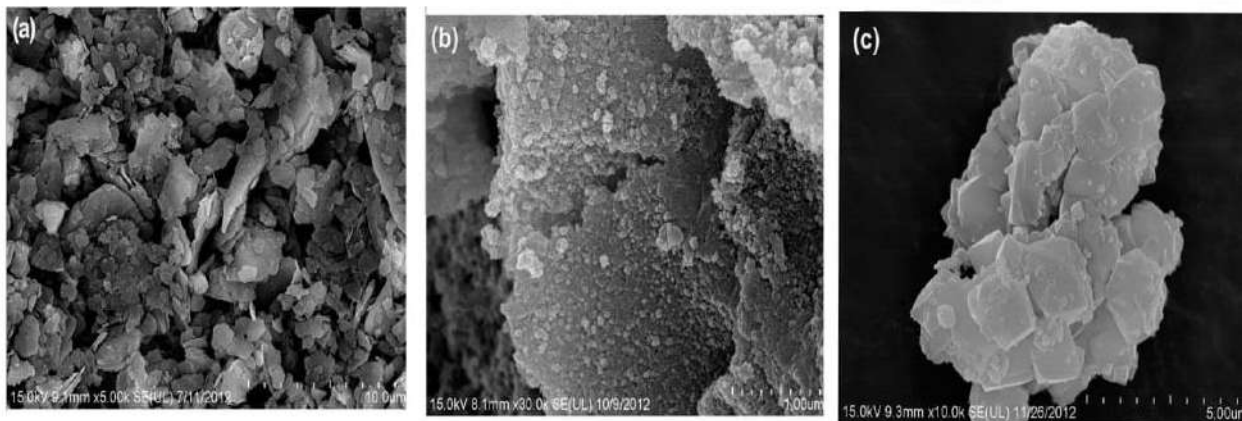
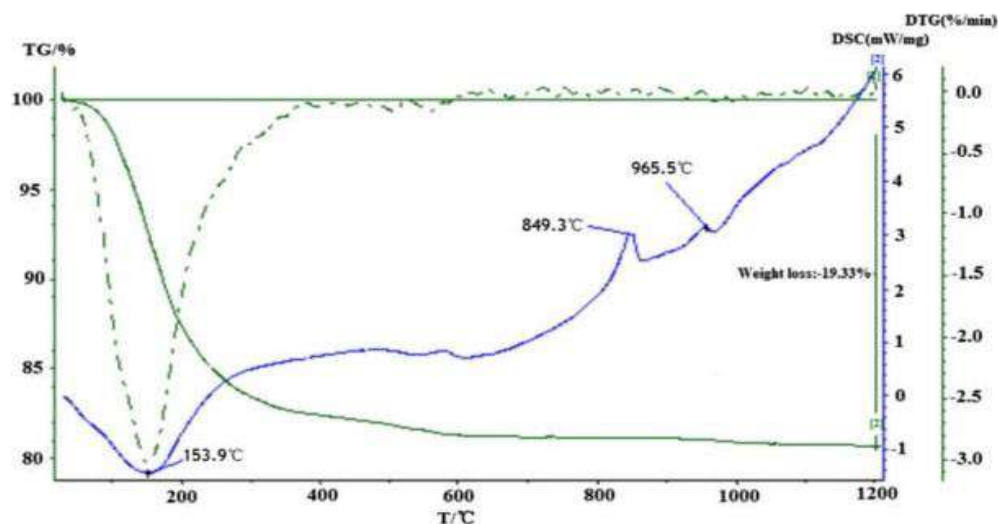


fig.10.SEM images of (a)kaolin, (b)fused material, and (c) synthesized zeolite obtained from natural kaolin

### 3.1.4. Thermal Analysis

The thermal stability of the synthesized zeolite was characterized using thermogravimetry (TG) and differential scanning calorimetry (DSC) in the presence of nitrogen flow. The TG analysis showed a weight loss at temperature below 600°C due to the loss of adsorbed water molecules in the surface and

cavities of the synthesized 13X zeolite. This comes in good agreement with the endothermic peak at 153.9°C in DSC analysis. In the DSC curve [fig.11][25] it was observed that there are two endothermic peaks- one at 849.3 °C, where the zeolite framework collapsed and one at 965.5 °C where it is attributed to crystal transformation. This concludes that the synthesized zeolite 13X has a heat resistance at 849.3 °C. [28,32].



**Fig. 11 TG/DSC data of synthesized 13X zeolite obtained by halloysite**

### **3.1.5. Adsorption Property.**

The surface area and the micropore volume of the synthesized zeolite was measured by Langmuir method, t-plot method and BET method and shown in table 5, 6, and 7[25,27, 31]. The specific surface area of the zeolite obtained from kaolin, CFA and halloysite are  $591\text{m}^2\text{g}^{-1}$ ,  $607.95\text{m}^2\text{g}^{-1}$  and  $725.80\text{m}^2\text{g}^{-1}$  respectively[27,25,31]. There is a large mass transfer zone (MTZ) for zeolite 13X and so the adsorption rate of zeolite 13X is comparatively high. The nitrogen adsorption on the adsorbent site of 13X is stronger compared to oxygen making zeolite 13X a better option for oxygen concentrator[41].

**Table 5:** Comparison of zeolite properties from CFA and commercial zeolite 13X

<b>Parameter</b>	<b>S(m<sup>2</sup>/g)</b>	<b>V(ml/g)</b>	<b>D(nm)</b>	<b>A(mg/L)</b>
COM	469.67	0.2023	2.53	130.11
CFA	607.95	0.2818	2.72	182.20

S= Surface area, V= pore volume, D= pore diameter, A= adsorption volume

**Table 6:** Volume and surface area of synthesized zeolite 13X from halloysite

Volume		Surface area		
V total	V t-plot	S Langmuir	S t-plot	S BET
0.27 cm <sup>3</sup> /g	0.24 cm <sup>3</sup> /g	725.80 cm <sup>3</sup> /g	513.19 cm <sup>3</sup> /g	55.16 cm <sup>3</sup> /g

*V total*= total pore volume, *V t-plot*= t-plot micropore volume, *S Langmuir*= Langmuir surface area, *S t-plot*= t-plot micropore area, *S BET*= BET surface area

**Table 7:** Properties of synthesized zeolite 13X from natural kaolin and commercial zeolite 13x.

	BET Surface Area (m <sup>2</sup> /g)	Micropore Surface Area (m <sup>2</sup> /g)	Micropore Volume (cm <sup>3</sup> /g)	External Surface
13X-COM	588	566	0.240	33
13X-Kaolin	591	576	0.250	34

## **3.2 EFFECTS OF PARAMETERS ON 13X ZEOLITE PREPARATION**

Synthesizing zeolites is very complex because it is affected by a number of parameters as a slight change may result in formation of different types of zeolite and may create a barrier in producing pure state zeolite. According to Plackett—Burman and the Taguchi methods- the synthesis gel SiO<sub>2</sub>/Al<sub>2</sub>O<sub>3</sub> molar ratio, alkalinity (H<sub>2</sub>O/Na<sub>2</sub>O) and water content (H<sub>2</sub>O/SiO<sub>2</sub>) and the zeolite synthesis temperature were found as the most affective parameters on the synthesized zeolites' crystallinities and growth.

### **3.2.1 Crystallization Temperature**

The crystallization temperature greatly influences the nucleation and growth mechanism in zeolite formation. When the experiments is conducted at a temperature range of 90°C -100°C, pure form of zeolites 13X were formed which was further verified by XRD pattern[ [fig.12,16](#)]. Around this temperature range zeolite 13X showed a high cation exchange capacity. Below 60°C there is the formation of zeolite type A [29] and at a temperature more than 100°C hydroxysodalite zeolites are formed [33]. This phenomenon occurs because of different rates of dissolution of aluminium and silicone. The aluminium dissolution rate tends to be faster than that of silicone at lower temperature ranges, and with increase in temperature the dissolution of silicone increases and thus favors' in the formation pure of zeolite 13X.

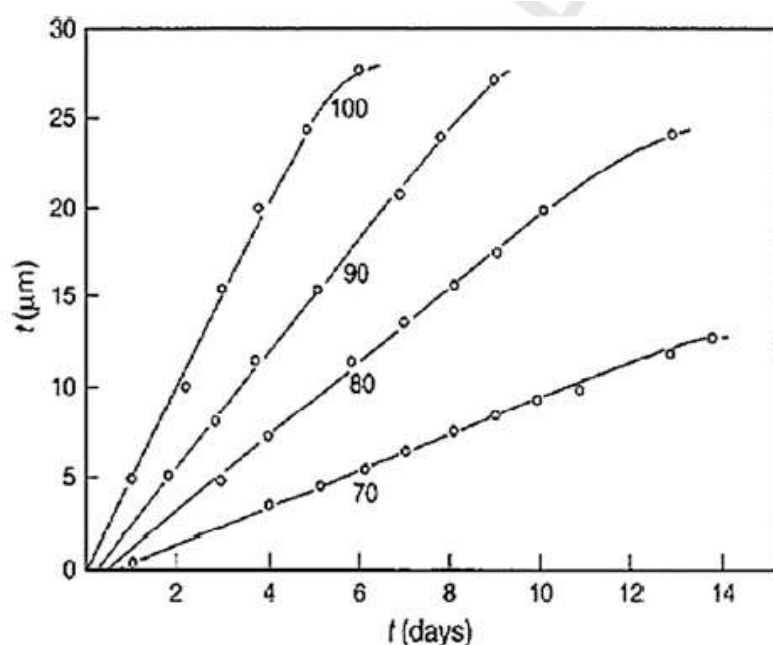


Fig.12 Influence of temperature on the growth rates of zeolite NaX (FAU)

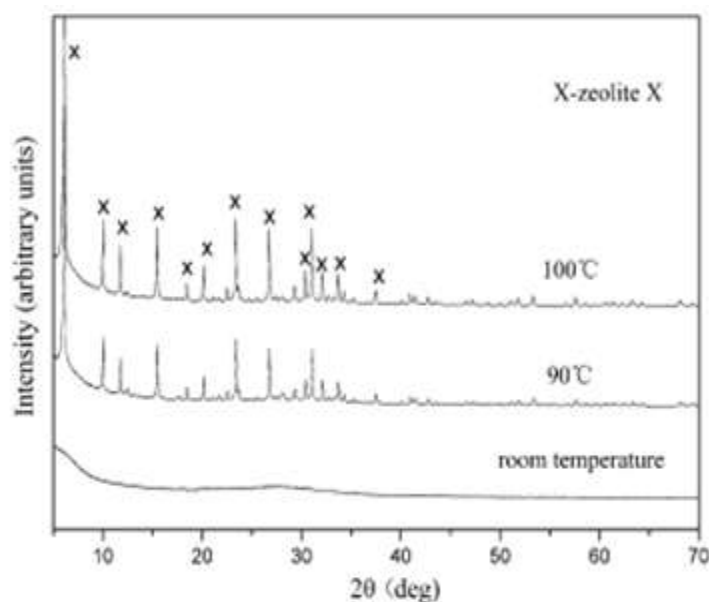


Fig.16 XRD patterns of the synthesized products obtained at room temperature, 90–100 °C

### 3.2.2 The Alkalinity

The second most important factor is the alkalinity of the synthesis solution, where the resultant zeolite crystallinity increases as this factor increases[34-36]. NaOH not only affects the degree of zeolitisation but also the type of zeolite obtained as a product. The zeolite 13X is highly favored when the NaOH concentration is in the range of 1M to 4M[31] and this further proved by the given figure 14 . At low NaOH concentration ranges the cations cannot enter the lattice and thus new structure could not be formed because of the lack of crystallization. Also, the alkalinity should not cross the optimum value as silicate anions polymerization degree decreases while polysilicate and aluminate anions polymerization accelerates and also results in the lower supersaturation of the gel[37]. At high NaOH value, the zeolite 13X is converted to P-type zeolite.

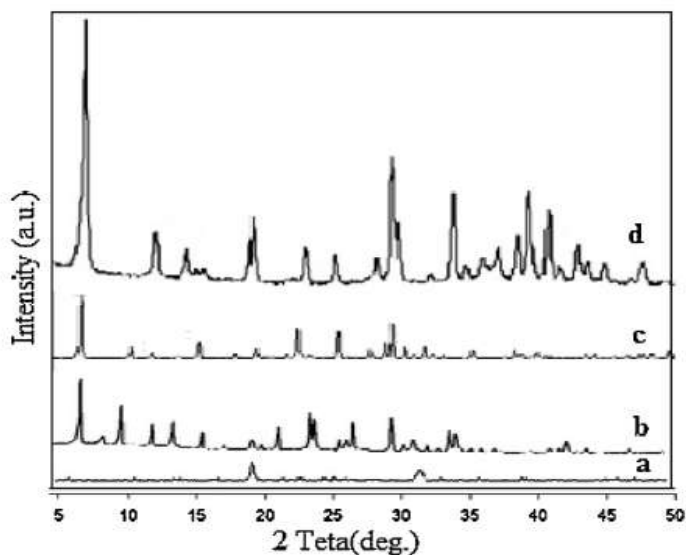


Fig.14 XRD pattern of zeolite 13X and associated phases obtained by hydrothermal synthesis: (a) 1.0M NaOH, (b) 2.0 M NaOH, (c) 3.0M NaOH, (d) 4.0M NaOH.

### 3.2.3. Effect of $\text{SiO}_2/\text{Al}_2\text{O}_3$ Molar Ratio

The  $\text{SiO}_2/\text{Al}_2\text{O}_3$  ratio plays an important role in the hydrothermal synthesis of zeolite[38]. All zeolites have distinct framework structures established by adjoining oxide tetrahedral to form the Framework. Thus different types of zeolites are formed at different  $\text{SiO}_2/\text{Al}_2\text{O}_3$  molar ratios. In the synthesis, at a molar ratio of 2.0, it is found that both zeolite A and X type is present, when the molar ratio of  $\text{SiO}_2/\text{Al}_2\text{O}_3$  was changed to 4.3 pure X type zeolite was formed[28] which was further confirmed by the XRD pattern shown in figure 15 [25]. Further increasing at a ratio of 5.0 hydroxysodalite and zeolite beta are formed. Comparing the silicate and alluminate content from the tables 2,3,4,; sodium silicate was added to the synthesis mixture from halloysite as formation of zeolite 13X requires high silica content.

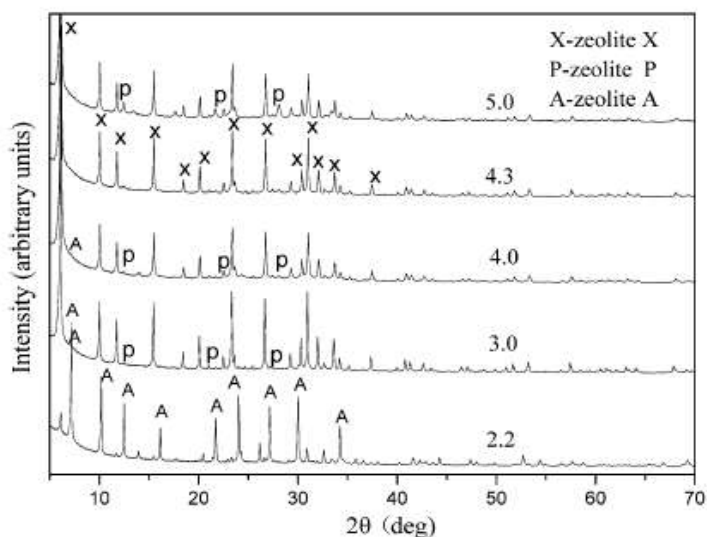


Fig.15 XRD data of different molar ratios of  $\text{SiO}_2/\text{Al}_2\text{O}_3$

### 3.2.4 Synthesis Time.

The zeolite crystallinity is observed to increase with time. Zeolite 13X requires a relatively longer crystallization time and increasing the temperature from 5 hours to 16 hours improved its crystallinity. This is observed because the framework is formed by connection of sodalite cages through double 6 member rings (D6R) and sparser structure [39]. At a synthesis temperature higher than 12 hours porosity of the formed zeolite layers increases as a result the permeability of the gaseous penetration increases[40]. Fig. 13, 17[25] shows the sequence of transformation of the zeolites with the synthesis time. At lower time period type A zeolite is formed which on further increase in time changes to zeolite type X and at time greater hydroxysodalite and P type is formed.[29] Thus the synthesis time suitable for zeolite 13X is found between the time ranges of 8 hours to 14 hours.

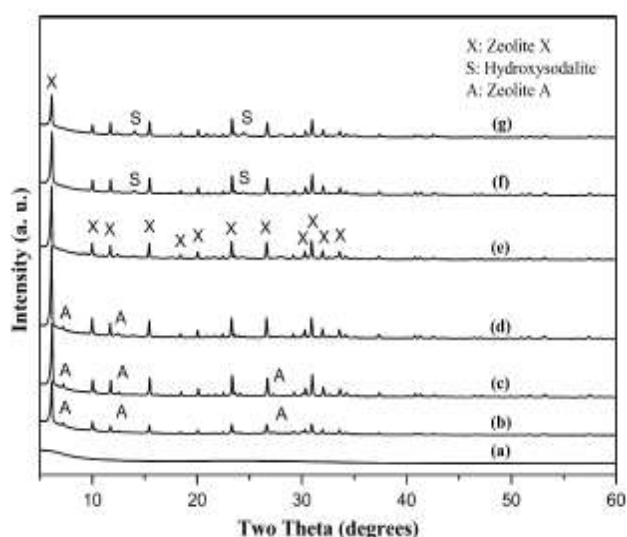


Fig. 13 XRD patterns of the reaction as-synthesized products obtained at different crystallization times (a) 0 h, (b) 1 h, (c) 4 h, (d) 6 h, (e) 8 h, (f) 12 h, and (g) 24 h.

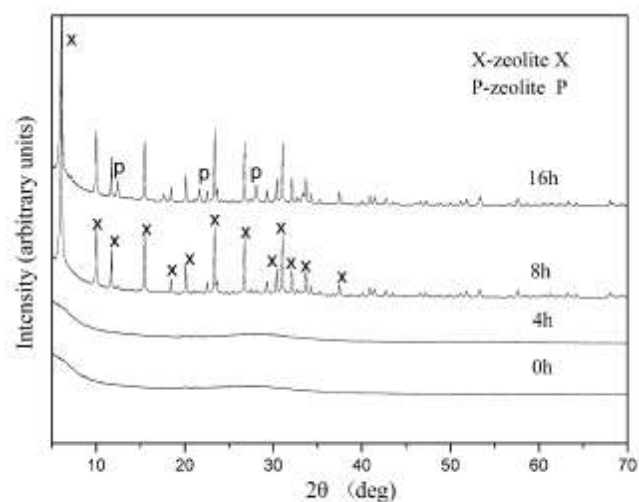


Fig.17 XRD patterns of the reaction as-synthesized products obtained at 100 °C for 0, 4, 8 and 16 h crystallization time

## **4.CONCLUSION**

The lab-scale formation of zeolite 13X from low grade natural kaolin, natural halloysite and coal fly ash was successful and was confirmed by the XRD, FT-IR and SEM analysis. The analysis of the morphology and structural properties are in good agreement with reported standard properties of the 13X zeolite. The surface area and micropore volume of the synthesized zeolite obtained was much higher than that of the commercial zeolite and hence showed excellent adsorption property. Also, the effects of different parameters showed that a slight change of values may lead to the production of different types of zeolites such as P type, A-type, hydroxysodalite, etc. So the synthesis temperature, time, amount of aluminosilicate, amount of sodium hydroxide should be in proper ranges for the formation of pure zeolite 13X type. Since a natural source that is halloysite and kaolin was used it ensured cost effective and environmental friendly synthesis and had no toxic effect or threats to individuals using them. The use of CFA ensured its proper recycling and reduction in pollution as the most part of it is dumped in ash fields causing hazardous problems. The main idea for this topic was to produce cost effective zeolite 13X which can be used by portable oxygen concentrator and give one pure form oxygen taking air as a source.



## 5. REFERENCES

1. D.W. Breck. Zeolite Molecular Sieves: Structure, Chemistry and Use. *Analytica Chimica Acta* 1975, 75 (2), 493.
2. Cundy, C.; Cox, P. The Hydrothermal Synthesis of Zeolites: History And Development From The Earliest Days To The Present Time. *ChemInform* 2003, 34 (19).
3. Zeolite - Wikipedia. <http://en.wikipedia.org/wiki/Zeolite>.
4. Król, M. Natural Vs. Synthetic Zeolites. *Crystals* 2020, 10 (7), 622.
5. Shokroo, E.; Kakavandi, I.; Baghbani, M.; Farniaei, M. Dynamic Modeling Of Nitrogen Adsorption On Zeolite 13X Bed. *Fluid Mechanics Research International Journal* 2017, 1 (1).
6. Drain, L. Permanent Electric Quadrupole Moments Of Molecules And Heats Of Adsorption. *Transactions of the Faraday Society* 1953, 49, 650-654.
7. Xu, R.; Pang, W.; Yu, J.; Huo, Q.; Chen, J. Chemistry Of Zeolites And Related Porous Materials: Synthesis And Structure; John Wiley & Sons, 2009. *John Wiley & Sons* 2009.
8. Material Safety Data Sheet. [http://www.ecompressedaircom/pdf/13x\\_msd](http://www.ecompressedaircom/pdf/13x_msd)
9. LBC Zeolite Molecular Sieves Characteristics. [http://www.sinolbc.com/Professional\\_View.asp:Professional\\_Id=11](http://www.sinolbc.com/Professional_View.asp:Professional_Id=11)
10. CO2 emission and its mitigation by adsorption on zeolites and activated carbon, <http://www.ias.as.in/currsci/mar252007/724.pdf>
11. How Does the Size of a Nitrogen Molecule Compare to That of Oxygen?, [http://wiki.answers.com/q/How\\_does\\_the\\_size\\_of\\_a\\_nitrogne\\_molecule\\_compare\\_to\\_that\\_of\\_oxygen](http://wiki.answers.com/q/How_does_the_size_of_a_nitrogne_molecule_compare_to_that_of_oxygen)
12. Chandrasekhar, S.; Pramada, P. *Journal of Porous Materials* 1999, 6 (4), 283-297
13. Wajima, T.; Ikegami, Y. Synthesis Of Crystalline Zeolite-13X From Waste Porcelain Using Alkali Fusion. *Ceramics International* 2009, 35 (7), 2983-2986.
14. Mezni, M.; Hamzaoui, A.; Hamdi, N.; Srasra, E. Synthesis Of Zeolites From The Low-Grade Tunisian Natural Illite By Two Different Methods. *Applied Clay Science* 2011, 52 (3), 209-218.

15. Ruiz, R.; Blanco, C.; Pesquera, C.; González, F.; Benito, I.; López, J. Zeolitization Of A Bentonite And Its Application To The Removal Of Ammonium Ion From Waste Water. *Applied Clay Science* 1997, 12 (1-2), 73-83.
16. Lee, S.; Han, Y.; Choy, J. 2D→3D Transformation Of Layered Aluminosilicate Upon Base Treatment. *Solid State Ionics* 2002, 151 (1-4), 343-346
17. Tanaka, H.; Fujii, A. Effect Of Stirring On The Dissolution Of Coal Fly Ash And Synthesis Of Pure-Form Na-A And -X Zeolites By Two-Step Process. *Advanced Powder Technology* 2009, 20 (5), 473-479.
18. Colina, F.; Llorens, J. Study Of The Dissolution Of Dealuminated Kaolin In Sodium–Potassium Hydroxide During The Gel Formation Step In Zeolite X Synthesis. *Microporous and Mesoporous Materials* 2007, 100 (1-3), 302-311.
19. Fernandes Machado, N.; Malachini Miotto, D. Synthesis Of Na–A And –X Zeolites From Oil Shale Ash. *Fuel* 2005, 84 (18), 2289-2294.
20. Purnomo, C.; Salim, C.; Hinode, H. Synthesis Of Pure Na–X And Na–A Zeolite From Bagasse Fly Ash. *Microporous and Mesoporous Materials* 2012, 162, 6-13.
21. WAJIMA, T.; HAGA, M.; KUZAWA, K.; ISHIMOTO, H.; TAMADA, O.; ITO, K.; NISHIYAMA, T.; DOWNS, R.; RAKOVAN, J. Zeolite Synthesis From Paper Sludge Ash At Low Temperature (90°C) With Addition Of Diatomite. *Journal of Hazardous Materials* 2006, 132 (2-3), 244-252.
22. Kazemian, H.; Naghdali, Z.; Ghaffari Kashani, T.; Farhadi, F. Conversion Of High Silicon Fly Ash To Na-P1 Zeolite: Alkaline Fusion Followed By Hydrothermal Crystallization. *Advanced Powder Technology* 2010, 21 (3), 279-283.
23. Wajima, T.; Munakata, K. Material Conversion From Waste Sandstone Cake Into Cation Exchanger Using Alkali Fusion. *Ceramics International* 2012, 38 (2), 1741-1744.
24. Wajima, T.; Munakata, K.; Ikegami, Y. Conversion Of Waste Sandstone Cake Into Crystalline Zeolite X Using Alkali Fusion. *MATERIALS TRANSACTIONS* 2010, 51 (5), 849-854.
25. Zhou, C.; Alshameri, A.; Yan, C.; Qiu, X.; Wang, H.; Ma, Y. Characteristics And Evaluation Of Synthetic 13X Zeolite From Yunnan'S Natural Halloysite. *Journal of Porous Materials* 2012, 20 (4), 587-594.
26. Chen, D.; Hu, X.; Shi, L.; Cui, Q.; Wang, H.; Yao, H. Synthesis And Characterization Of Zeolite X From Lithium Slag. *Applied Clay Science* 2012, 59-60, 148-151.
27. Tu, W.; Zhang, Y.; Bai, J.; Liu, W. Synthesis Of Zeolite 13X From Coal Fly Ashes And Properties Of The Zeolite Products. *Applied Mechanics and Materials* 2014, 675-677, 724-727.

28. Ma, Y.; Yan, C.; Alshameri, A.; Qiu, X.; Zhou, C.; Li, D. Synthesis And Characterization Of 13X Zeolite From Low-Grade Natural Kaolin. *Advanced Powder Technology* 2014, 25 (2), 495-499.
29. Molina, A.; Poole, C. A Comparative Study Using Two Methods To Produce Zeolites From Fly Ash. *Minerals Engineering* 2004, 17 (2), 167-173.
30. Ma, Y.; Yan, C.; Alshameri, A.; Qiu, X.; Zhou, C.; Li, D. Synthesis And Characterization Of 13X Zeolite From Low-Grade Natural Kaolin. *Advanced Powder Technology* 2014, 25 (2), 495-499.
31. Garshasbi, V.; Jahangiri, M.; Anbia, M. Equilibrium CO<sub>2</sub> Adsorption On Zeolite 13X Prepared From Natural Clays. *Applied Surface Science* 2017, 393, 225-233.
32. Fischer, F.; Lutz, W.; Buhl, J.; Laevemann, E. Insights Into The Hydrothermal Stability Of Zeolite 13X. *Microporous and Mesoporous Materials* 2018, 262, 258-268.
33. Pourazar, M.; Mohammadi, T.; Jafari Nasr, M.; Javanbakht, M.; Bakhtiari, O. Preparation Of 13X Zeolite Powder And Membrane: Investigation Of Synthesis Parameters Impacts Using Experimental Design. *Materials Research Express* 2020, 7 (3), 035004.
34. Plant, D.; Maurin, G.; Deroche, I.; Llewellyn, P. Investigation Of CO<sub>2</sub> Adsorption In Faujasite Systems: Grand Canonical Monte Carlo And Molecular Dynamics Simulations Based On A New Derived Na<sup>+</sup>-CO<sub>2</sub> Force Field. *Microporous and Mesoporous Materials* 2007, 99 (1-2), 70-78.
35. Bkour, Q.; Faqir, N.; Shawabkeh, R.; Ul-Hamid, A.; Bart, H. Synthesis Of A Ca/Na-Aluminosilicate From Kaolin And Limestone And Its Use For Adsorption Of CO<sub>2</sub>. *Journal of Environmental Chemical Engineering* 2016, 4 (1), 973-983.
36. Ayele, L.; Pérez-Pariente, J.; Chebude, Y.; Díaz, I. Synthesis Of Zeolite A From Ethiopian Kaolin. *Microporous and Mesoporous Materials* 2015, 215, 29-36.
37. Subhapriya, S.; Gomathipriya, P. Synthesis And Characterization Of Zeolite X From Coal Fly Ash: A Study On Anticancer Activity. *Materials Research Express* 2018, 5 (8), 085401.
38. Ojha, K.; Pradhan, N.; Samanta, A. Zeolite From Fly Ash: Synthesis And Characterization. *Bulletin of Materials Science* 2004, 27 (6), 555-564.
39. Zhang, X.; Tang, D.; Zhao, J.; Li, X.; Yang, R. Hydrothermal Synthesis Of Nanocrystalline Na<sub>x</sub> Zeolite At Room Temperature. *Journal of Nanoscience and Nanotechnology* 2014, 14 (7), 5552-5560.

- 
40. Mohammadi, T.; Maghsoodloorad, H. Synthesis And Characterization Of Ceramic Membranes (W-Type Zeolite Membranes). *International Journal of Applied Ceramic Technology* 2012, 10 (2), 365-375.
  41. Shokroo, E.; Kakavandi, I.; Baghbani, M.; Farniaei, M. Dynamic Modeling Of Nitrogen Adsorption On Zeolite 13X Bed. *Fluid Mechanics Research International Journal* 2017, 1 (1), 20-24.
  42. Thomas, W.; Crittenden, B. *Adsorption technology and design*; Butterworth-Heinemann: Oxford, 1998.

**SYNTHESIS OF ZEOLITE 13X, FOR THE**  
**USE IN OXYGEN CONCENTRATOR -A**  
**REVIEW**

**SCOTTISH CHURCH COLLEGE, UNIVERSITY OF  
CALCUTTA**



University Registration no. = **223-1221-0167-16**

University Roll no. = **223/CEM /191022**

SPECIAL PAPER = **CHEM -S044**

NAME OF CANDIDATE: **PAPRI MITRA**

NAME OF EXAMINER: **Dr. SEBANTI BASU**

*Papri Mitra*

*Sebanti Basu*

Signature of the Candidate

Signature of the Examiner

## **ACKNOWLEDGEMENT**

I gratefully thank Dr. Rama Ranjan Bhattacharjee, Associate Professor, Amity University, under his supervision and unending support this review work was accomplished during my 4<sup>th</sup> and final semester (Jan-July 2021) in partial fulfillment of M.Sc (Chemistry) degree in the University of Calcutta under Scottish Church College, Kolkata. And also I would like to thank the University of Calcutta and my college professors for giving me the opportunity to write this review paper.

# **CONTENT**

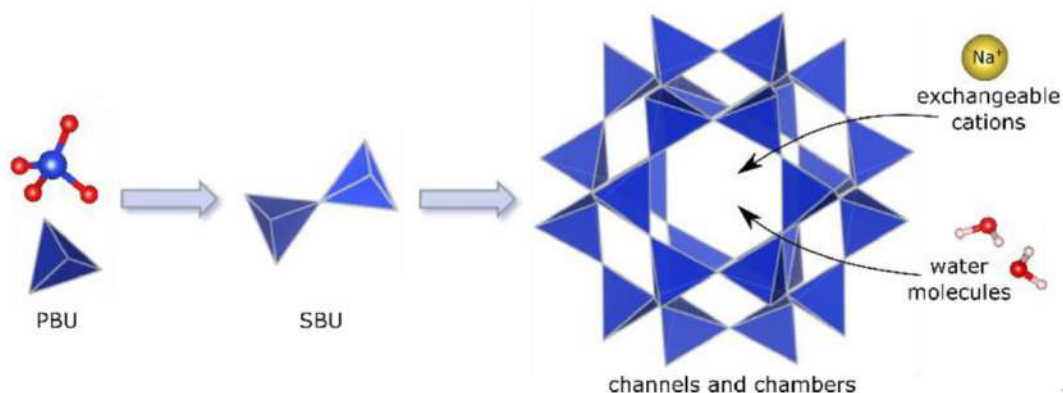
1. INTRODUCTION.
2. EXPERIMENTAL.
  - 2.1 Synthesis from coal fly ash (CFA).
    - 2.1.1 Materials
    - 2.1.2 Processes
  - 2.2 Synthesis from natural halloysite.
    - 2.2.1 Materials
    - 2.2.2 Processes
  - 2.3 Synthesis from natural kaolin.
    - 2.3.1 Materials
    - 2.3.2 Processes
3. RESULT AND DISCUSSION
  - 3.1 Characterization of Zeolite 13X
    - 3.1.1 X-Ray Diffraction Analysis
    - 3.1.2 FT-IR Analysis
    - 3.1.3 Scanning Electron Microscope Analysis
    - 3.1.4 Thermal Analysis
    - 3.1.5 Adsorption Properties
  - 3.2 Effects of Parameters on Zeolite 13X Synthesis
    - 3.2.1 Crystallization temperature
    - 3.2.2 Alkalinity
    - 3.2.3  $\text{SiO}_2/\text{Al}_2\text{O}_3$  Molar Ratio
    - 3.2.4 Synthesis time
4. CONCLUSION
5. REFERENCE

## 1. INTRODUCTION

The second wave of COVID-19 saw a huge shortage of medical oxygen in different parts of India. While meeting the current demand, manufacturing medical oxygen also became important to ensure the country has adequate in the future. Apart from medical use, it is also used by various chemical industries for various processes such as: refiner industries, steel construction, paper industries, wastewater treatment and glass production and other industrial operations. The high rise in oxygen demand made industrial consumption of oxygen practically zero as the entire capacity has been converted for medical usage. Still there is a huge shortage of oxygen with the rise of COVID cases daily.

Thus there is a growing need to address the health and quality of life through a light-weight and portable oxygen concentrator with a medical grade oxygen supply ( $O_2$  concentration: ~88–92 vol %). Now this problem can be solved by using air as the source and separating oxygen from it in the pure form. Generally, the common adsorption process of air separation consists of procedures which make use of zeolites as nitrogen adsorbent under the equilibrium conditions and oxygen is a process product.

Zeolites (from the Greek “zein” and “lithos”, meaning “stones that boil”) are microporous aluminosilicate materials of alkali or earth alkaline elements with crystalline frameworks structure of three-dimensional tetrahedral units of  $SiO_4$  and  $AlO_4$  which are connected by their common oxygen atoms, generating a network of pores and cavities having molecular dimensions with uniform pore sizes ranging from 0.3–1.0 nm, which are occupied by water and cations. [1,2]. The uniqueness of zeolites originate from the fact that their surfaces are formed with negatively charged oxides and also the presence of isolated cations above their surface structure.





Zeolites are obtained from nature and can also be prepared synthetically. The formation of natural zeolites occurs when the volcanic rocks and the ash layers react with alkaline groundwater. Generally synthesized zeolites have some advantages over their natural counterparts i.e., [3, 4]

- The synthetic zeolites can be designed to have structures that do not occur in nature, structures that optimize their intended purpose.
- They can be produced in a phase-pure, uniform state without the presence of impurities.
- In synthetic zeolite the content of aluminium and silicone can be adjusted.
- Synthetic zeolites have better ion exchange capabilities than the natural zeolites.

Zeolites as molecular sieves are used in various air separation processes such as cryogenic technique, membrane separation and pressure swing adsorption (PSA) that can effectively produce enriched oxygen using ambient air as the source. PSA technique has an advantage over others because of its lower consumption of energy. This technique can absorb nitrogen from air and output an enriched oxygen stream under high-pressure conditions [42]. The most commonly used zeolite for the air separation for oxygen production is Zeolite 13X adsorbent as it has an outstanding nitrogen to oxygen adsorption selectivity. The selectivity for zeolite to adsorb nitrogen compared to oxygen is due to the interaction between electrostatic field of the cationic zeolite and the quadrupole moment of the nitrogen and oxygen. The quadrupole moment of nitrogen is three times higher than that of oxygen, which leads to a selective adsorption onto the zeolite surface [6].

Zeolite 13X (Molecular formula =  $\text{Na}_{86}[(\text{AlO}_2)_{86}(\text{SiO}_2)_{106}] \cdot \text{H}_2\text{O}$ ) is a Faujasite-type zeolite having three dimensional pore structures linked by circular 12-ring apertures, which leads to a larger cavity diameter of 12 Å, restricted by 10 sodalite cages in a hexagonal structure. The effective pore diameter in this type of zeolite is relatively large at 7.4 Å [7]. Sodium cations in zeolite 13X balances the negative charge of the zeolite framework and also creates an electrostatic field in the zeolite structural environment. Some of the relevant properties of 13X are listed in Table 1 [8-11].

Chemical Formula	$\text{Na}_{36}[(\text{AlO}_2)_{86}(\text{SiO}_2)_{106}]\cdot\text{H}_2\text{O}$
Pore Diameter	$\sim 8 \text{ \AA}$
Mesopore Volume	$0.165 \text{ cm}^3/\text{g}$
Micropore Volume	$0.17 \text{ cm}^3/\text{g}$
Langmuir Surface Area	$571 \text{ m}^2/\text{g}$
Mass of Pellet Sample	2.37 g
Mass of Crushed sample	2.49 g

**Table 1: Properties of zeolite 13X**

The growing need for oxygen economy invokes much interest in molecular sieves and its cost effective synthesis. Usually, synthesis of zeolites takes place from freshly prepared sodium aluminosilicate gel, obtained from various silica and alumina sources by hydrothermal treatment. However, it is very expensive to prepare synthetic zeolites from chemical sources of silica and alumina. Therefore, in order to obtain low-cost and effective synthetic zeolite, many researchers have studied the synthesis of zeolite from kaolinite [12], waste porcelain [13], illite [14], bentonite [15] and montmorillonite [16], coal fly ash [17], kaolinite [18], oil shale ash [19], bagasse fly ash [20], paper sludge [21], high silicon fly ash [22], waste sandstone cake [23,24], halloysite [25] and lithium slag [26].

In this paper we will study the synthesis of zeolite 13X from (i) coal fly ash (ii) natural halloysite and (iii) natural kaolin with alkali fusion followed by hydrothermal treatment. And to confirm the successful zeolite production we compare the properties, and characterized utilizing various techniques, such as X-ray diffraction (XRD), the Brunauer–Emmett–Teller (BET) method, scanning electron microscopy (SEM), X-ray fluorescence (XRF), thermo gravimetric analysis (TGA), differential thermal analysis (DTA), X-ray diffraction (XRD), and differential thermal gravimetry (DTG).

### **COAL FLY ASH**

Coal fly ash (CFA) is a solid waste product obtained from the combustion of pulverized coal in electric power generating plants. Large number of thermal power plants generates huge quantities of fly ash causing serious environmental problem mainly due to its structure and toxic elements. There are many processes to recycle and reuse the CFA to reduce the environmental pollution and one of it is synthesis of zeolites from it. The major component of CFA is silicon dioxide

(SiO<sub>2</sub>), Aluminium oxide (Al<sub>2</sub>O<sub>3</sub>) and calcium oxide (CaO). Thus the synthesis of aluminosilicates porous material from CFA is possible. And is done by alkali fusion followed by hydrothermal synthesis.[27]

### **NATURAL HALLOYSITE**

Halloysite having empirical formula - Al<sub>2</sub>Si<sub>2</sub>O<sub>5</sub> (OH)<sub>4</sub>, is a double-layered aluminosilicate clay mineral, consisting of one alumina octahedron sheet and one silica tetrahedron sheet in a 1:1 stoichiometric ratio. It has a high specific surface area and hollow structure, and also from its composition it acts as a promising material with high reactivity to synthesize zeolite of high purity. Synthetic zeolite products produced from halloysite are generally found to be non-toxic, odorless, environment-friendly, acid and alkali resistant, thermally stable and do not generate secondary pollution.[25]

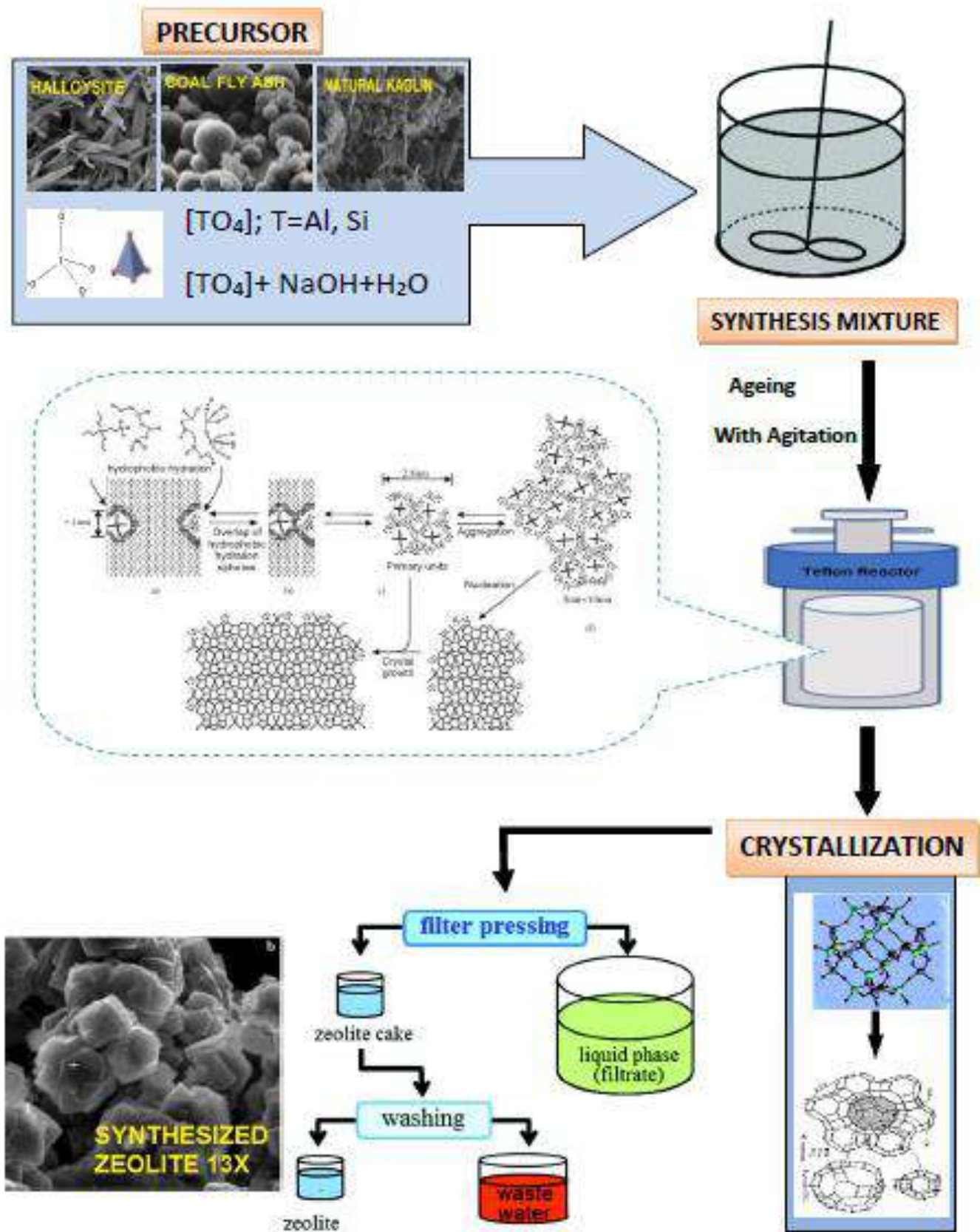
### **NATURAL KAOLIN**

Natural kaolin is a clay material mainly consists of kaolinite, illite and trace of quartz. Kaolinite is a clay mineral, with the chemical composition [Al<sub>2</sub>Si<sub>2</sub>O<sub>5</sub> (OH)<sub>4</sub>]. It is a two-layered aluminosilicate clay mineral, consisting of one alumina octahedron sheet and one silica tetrahedron sheet in a 1:1 stoichiometric ratio. And Illite (K<sub>1-2</sub> Al [Si<sub>7-6.5</sub>Al<sub>1-1.5</sub>O<sub>20</sub>](OH)<sub>4</sub>) is a phyllosilicate or layered aluminosilicate with high Si content. Expanding from these empirical findings, it can be further deduced that it will be possible to directly synthesize zeolite X from natural kaolin via alkali fusion followed by hydrothermal treatment.[28]

## **1. EXPERIMENTAL**

The zeolite synthesis process is done using alkali fusion followed by hydrothermal process shown in scheme 1. The hydrothermal processes have some advantages which includes, high reactivity of reactants, low energy consumption, low air pollution, easy to control the solution, formational of metastable phases, and unique condensed phase.

## Scheme 1



## 2.1 SYNTHESIS FROM COAL FLY ASH (CFA).

### 2.1.1 Materials

The CFA is collected at the top of burners using cyclones, electric precipitators or mechanic filters. X- ray diffraction analysis shows that it is mainly composed of amorphous  $\text{SiO}_2$  and  $\text{Al}_2\text{O}_3$  with some crystals such as quartz(  $\text{SiO}_2$ ), mullite ( $2\text{SiO}_2.3\text{Al}_2\text{O}_3$ ), hematite ( $\text{Fe}_2\text{O}_3$ ) and magnetite( $\text{Fe}_3\text{O}_4$ ). The chemical composition of coal fly ash is shown in table 2;

composition	Wt%
$\text{SiO}_2$	71.0
$\text{Al}_2\text{O}_3$	8.3
CaO	0.8
$\text{K}_2\text{O}$	0.7
$\text{Na}_2\text{O}$	0.3
$\text{Fe}_2\text{O}_3$	3.6
C	1.0

**Table 2:** Chemical Composition CFA



### 2.1.2 Synthesis process

The CFA was pre-treated by magnetic separation using a high intensity magnetic separator which results in the reduction of about 65% of iron components and increases of nearly 34% and 3.5% silicone and aluminium compounds respectively.[34] The total amount of  $\text{SiO}_2$  and  $\text{Al}_2\text{O}_3$  can be reach to approximately 89.96%. In the experiment the fly ash was mixed and grounded with sodium hydroxide (NaOH) to obtain a homogeneous mixture. Then the mixture was heated with a weight ratio of 1 : 1 ( CFA, NaOH ) at  $850^\circ\text{C}$  for 2hours in a muffle furnace. The obtained mixture was treated with deionized water by magnetic stirring. Then it was followed by an ageing process with vigorous agitation for 12 hours at room temperature in the Teflon reactor with proper sealing. At last, the mixture was crystallized at static condition at  $100^\circ\text{C}$  for 14 hours. At end of the process solid products were filtered-off, and the solid phase was washed thoroughly using deionized water for several times until the drained water's pH reached below 10.5. after that it was dried at  $100^\circ\text{C}$  for 12 hours and saved in dry container.[27]



## 2.2 SYNTHESIS FROM NATURAL HALLOYSITE

### 2.2.1 Materials.

The natural halloysite mineral was used as the source of silicon–aluminum. Sodium hydroxide (NaOH) was used as the alkali source and sodium silicate (Na-SiO<sub>3</sub>·9H<sub>2</sub>O) as the sodium and silicone source. The X-ray diffraction (XRD) pattern and the chemical analysis showed that the main constituents of the raw material were silica (45.04 %) and alumina (38.31 %), whereas the loss of ignition (LOI) is 17.94 %. The chemical composition of halloysite determined by chemical analysis is given in Table 3;

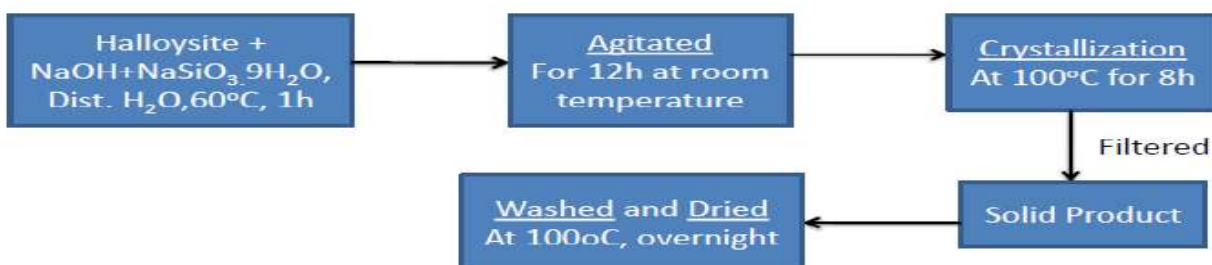


Component	Content (%)	Component	Content (%)
SiO <sub>2</sub>	45.04	K <sub>2</sub> O	0.03
Al <sub>2</sub> O <sub>3</sub>	38.31	TiO <sub>2</sub>	0.04
TFe <sub>2</sub> O <sub>3</sub>	0.16	P <sub>2</sub> O <sub>5</sub>	0.02
MgO	0.05	MnO	0.002
CaO	0.05	H <sub>2</sub> O	2.27
Na <sub>2</sub> O	0.05	LOI	17.94

Table3: Chemical compositions of the raw material (wt%)

### 2.2.2 Synthesis process

The process was done using 3 g of halloysite which was calcined at 500°C for 2 h, and was mixed with 5.7 g NaOH and 8.2 g NaSiO<sub>3</sub>·9H<sub>2</sub>O, the mixture were dispersed in 67 mL distilled water with constant stirring for 1 hours at 60°C in a water bath. Then the slurry was aged for 12 hours at room temperature in the sealed Teflon reactor to rearrange the reactant for the formation of nuclei. After this the mixture was crystallized at 100 °C for 8 hours under static conditions. At last, the solid was separated by filtration and washed thoroughly several times with deionized water until the filtrate pH was reduced to less than 10. The precipitated solid was dried at 100°C overnight and finely crushed.[25]



## 2.3 SYNTHESIS FROM NATURAL KAOLIN

### 2.3.1. Materials

The kaolin was taken as the starting material for the experiment as silica–alumina source after was it was crushed and air-dried. NaOH was taken as the alkali source for the alkali fusion followed by hydrothermal treatment.[30] The main constituents of the low grade natural kaolin can be seen in table 4;



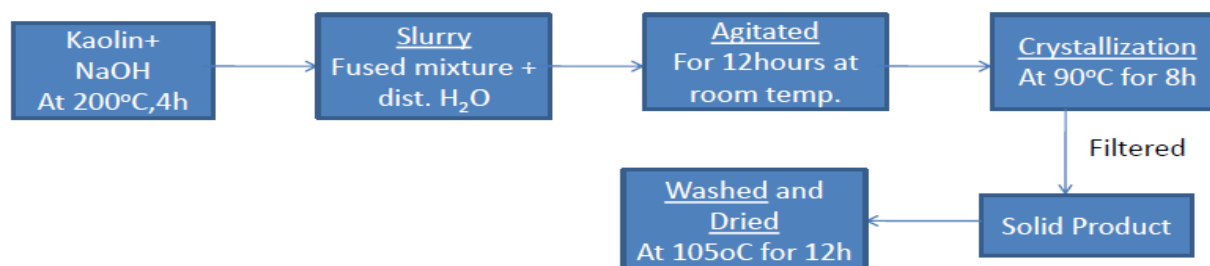
**Natural Kaolin**

Component	Content (%)
SiO <sub>2</sub>	56.30
Al <sub>2</sub> O <sub>3</sub>	29.52
TFe <sub>2</sub> O <sub>3</sub>	1.32
MgO	0.35
CaO	0.056
Na <sub>2</sub> O	0.056
K <sub>2</sub> O	2.99
TiO <sub>2</sub>	0.28
P <sub>2</sub> O <sub>5</sub>	0.32
MnO	0.012
H <sub>2</sub> O	0.28
LOI	9.18

Table 4: Chemical Characterization of natural kaolin (wt%)

### 2.3.2 Synthesis Process

Low grade natural kaolin was mixed with sodium hydroxide (NaOH) powder with the weight ratio of 2:1 and fused in an MgO ceramic crucible at 200 °C for 4 hours. The fused mixture was cooled at room temperature and grounded and then was added to distilled water. The slurry obtained was vigorously agitated for 12 hours at room temperature for homogenization with constant stirring at 800 r/min. Then the homogenized material was crystallized at 90 °C for 8 hours. Finally, the solid was separated by filtration and washed thoroughly several times with deionized water until the pH was reached around 8, then was dried at 105°C and crushed.[30,31]



## 3.RESULT AND DISCUSSION

### 3.1 Characterization of zeolite 13X

#### 3.1.1 XRD Analysis

The synthesized zeolite product from coal fly ash was analyzed using X-Ray Diffraction (XRD) method for the identification of crystalline material and its structure. The XRD pattern of the synthesized product is shown in Fig 2; From the figure we can see that the XRD pattern indicates the presence of X-type zeolite with the largest peak at  $2\theta = 6.16^\circ$ , which is in a good agreement with the standard JCPDS Card (PDF 38-0237).

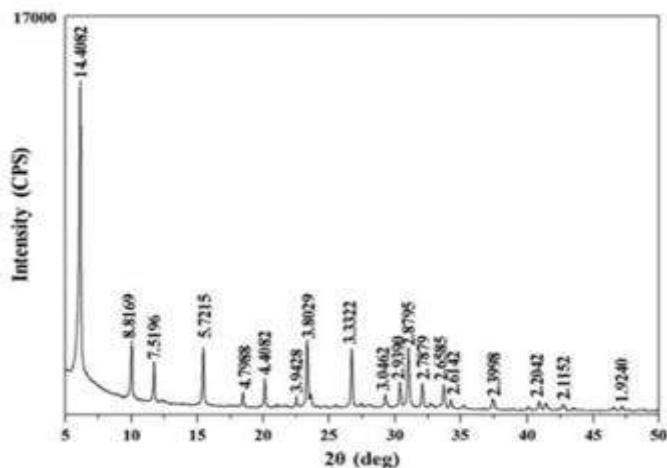


Fig.3. XRD pattern of synthesized zeolite 13X from halloysite

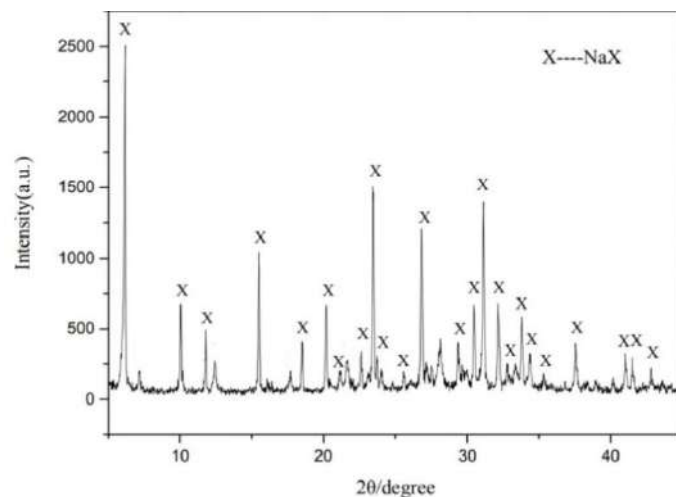


Fig.2. XRD pattern of zeolite 13X produced from coal fly ash

The synthesized product from natural halloysite was also analyzed using XRD to corroborate the structure of the newly formed zeolite 13X. The XRD pattern of the zeolite is given in Fig. 3, which also matches with the standard JCPDS Card (PDF 38-0237).[25] The XRD pattern obtained from the synthesized zeolite from natural kaolin is shown in figure.4, which also matches with that of standard JCPDS Card (PDF 38-0237).[31]



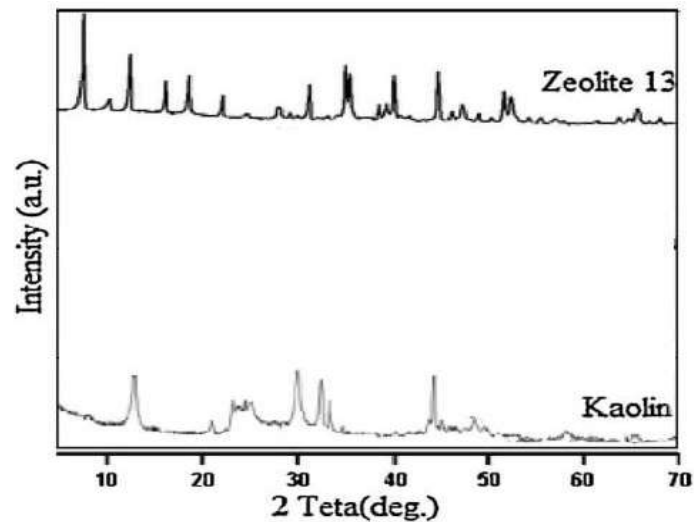


Fig.4. XRD pattern of natural kaolin and zeolite 13X

From the three figures (fig.2,3,4) we can see that there was no other diffraction peaks which indicated that only one pure phase of 13X zeolite was synthesized. Also the observed diffraction peaks were sharp and intense confirming a high degree of crystallinity of the synthesized 13X zeolite.

### 3.1.2 FT-IR analysis

Apart from FT-IR analysis, it is well known that spectroscopic method provide useful information about the structure of zeolites and about other functional groups which may be present during the synthesis and post treatment. The IR spectra of the synthesized zeolite 13X obtained from the halloysite, CFA and kaolin are shown in fig. 5,6 and 7 respectively.

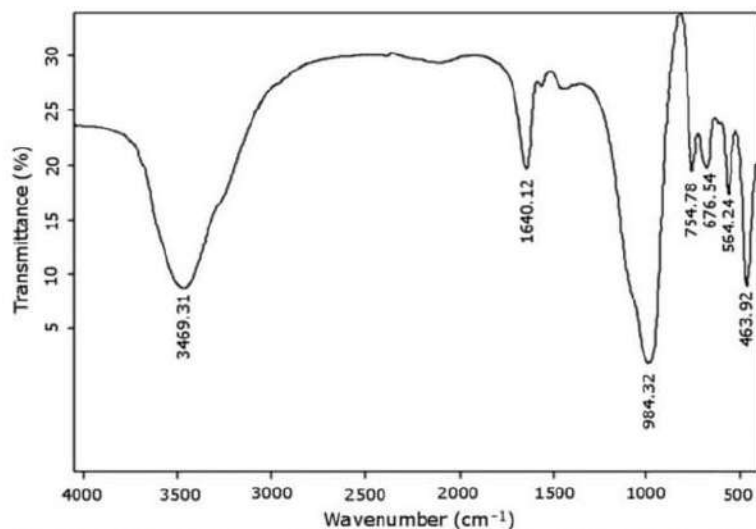


Fig.5. FT-IR spectrum of zeolite 13X synthesized from halloysite

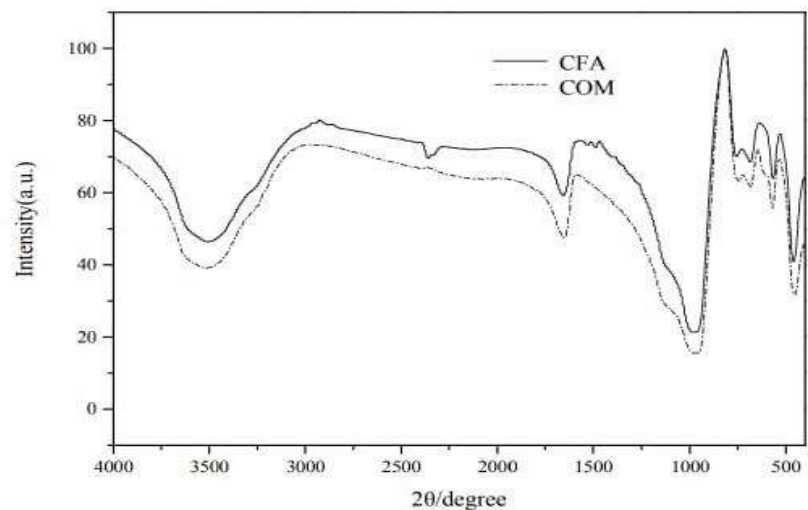
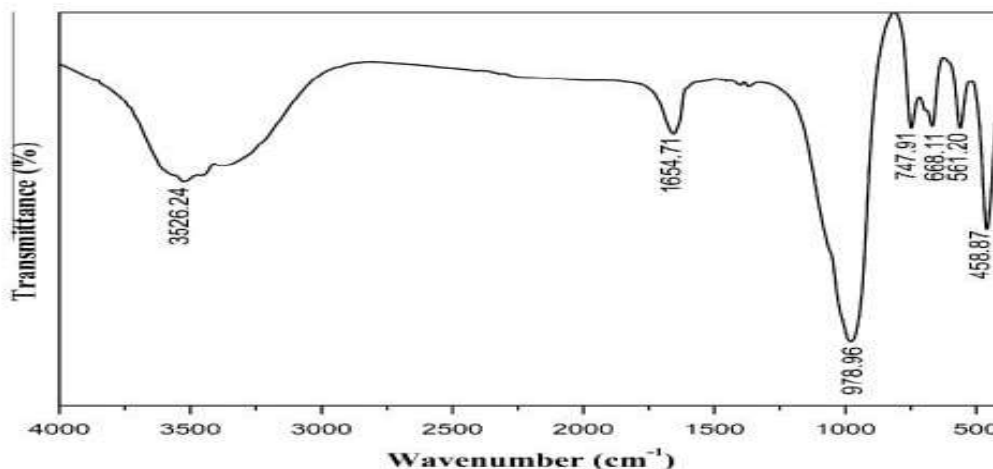


Fig.6. IR spectra of the synthesized zeolite from CFA and commercial zeolite (COM)



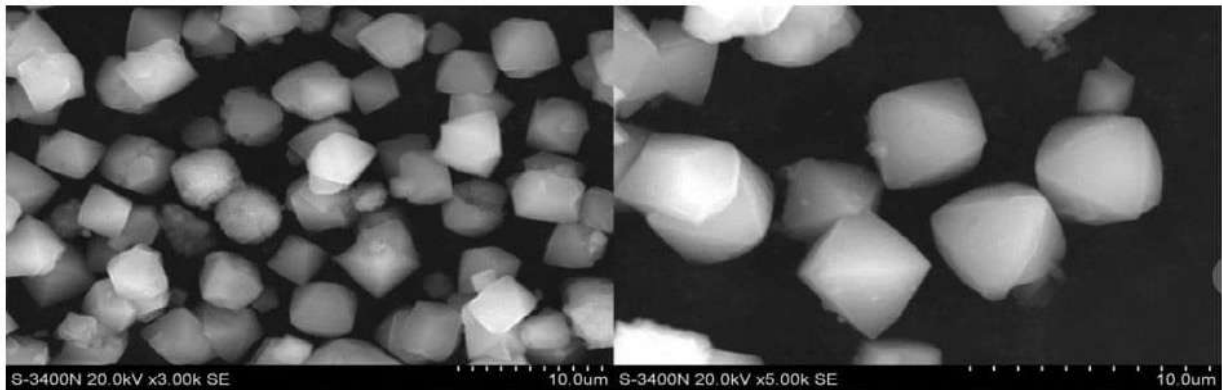
**Fig. 7.** FT-IR spectrum of 13X zeolite obtained at the optimum synthesis conditions from low-grade natural kaolin.

From the IR spectra of the synthesized zeolite we get the band at about 420-500 $\text{cm}^{-1}$  due to the T-O bending vibration of the zeolite interior and for the double-six member ring bond vibration zone there is a band at about 561  $\text{cm}^{-1}$ . The peaks centered at around 978- 984 and 676-678  $\text{cm}^{-1}$  corresponded to the TO4 [19] (T = Si or Al) asymmetric and symmetric stretching vibration respectively. The appearance of band at 1640  $\text{cm}^{-1}$  could be assigned to the  $\text{H}_2\text{O}$  having (H-O-H-) vibration band and the observed broad adsorption band at 3464  $\text{cm}^{-1}$  was ascribed to OH-stretching of water molecules that are present in the cavities and channels in the zeolite due its incomplete dehydration. All these data comes in good agreement with reported values of commercial 13X zeolite [26].

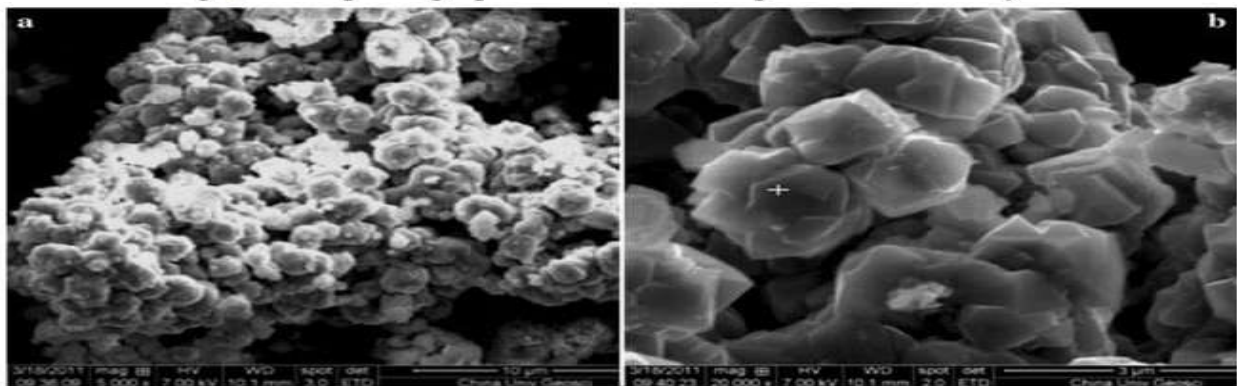
### **3.1.3. Scanning Electron Microscope Analysis**

The morphology of the zeolite product matches with that of 13X zeolite having an octahedral shape which is confirmed by scanning electron microscope (SEM) analysis, and present of no other structures suggests that the obtained 13X zeolite product is in phase pure state. The images obtained from SEM is shown in fig. 8,9,10 [27,25,28] for the synthesized zeolite 13X from CFA, halloysite and kaolin

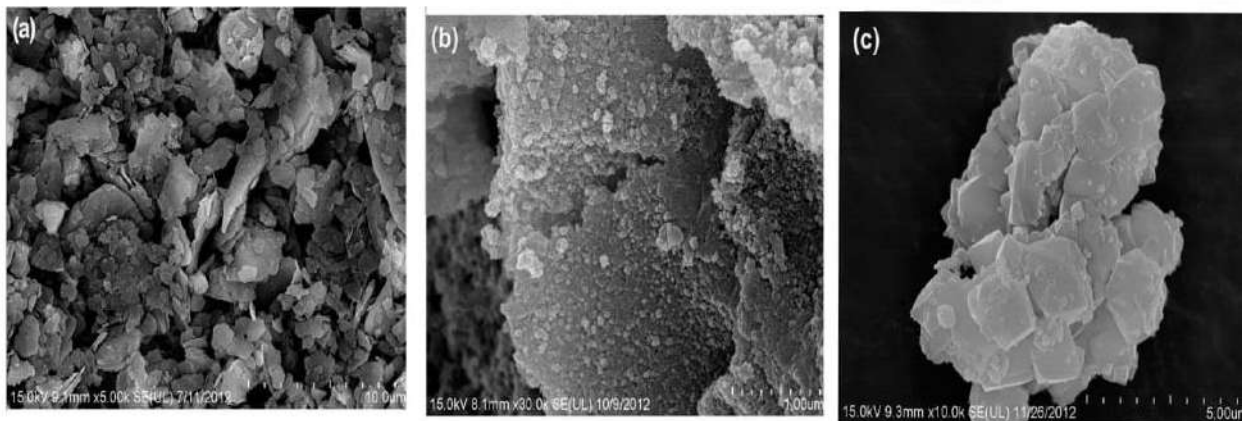
respectively.



**Fig. 8** SEM photographs of zeolite 13X produced from fly ash



**fig.9.** FE-SEM images of 13X zeolite synthesized from halloysite

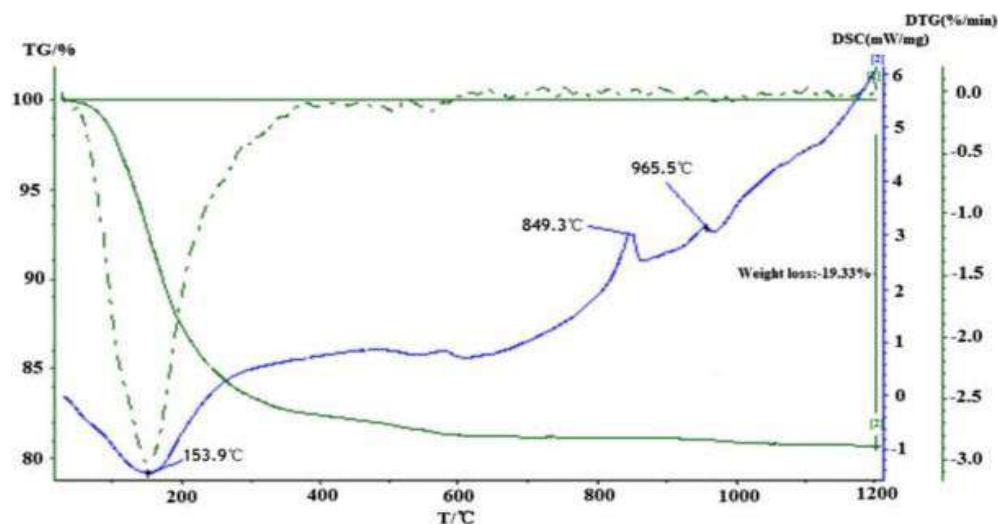


**fig.10.** SEM images of (a)kaolin, (b)fused material, and (c) synthesized zeolite obtained from natural kaolin

### **3.1.4. Thermal Analysis**

The thermal stability of the synthesized zeolite was characterized using thermogravimetry (TG) and differential scanning calorimetry (DSC) in the presence of nitrogen flow. The TG analysis showed a weight loss at temperature below 600°C due to the loss of adsorbed water molecules in the surface and

cavities of the synthesized 13X zeolite. This comes in good agreement with the endothermic peak at 153.9°C in DSC analysis. In the DSC curve [fig.11][25] it was observed that there are two endothermic peaks- one at 849.3 °C, where the zeolite framework collapsed and one at 965.5 °C where it is attributed to crystal transformation. This concludes that the synthesized zeolite 13X has a heat resistance at 849.3 °C. [28,32].



**Fig. 11 TG/DSC data of synthesized 13X zeolite obtained by halloysite**

### **3.1.5. Adsorption Property.**

The surface area and the micropore volume of the synthesized zeolite was measured by Langmuir method, t-plot method and BET method and shown in table 5, 6, and 7[25,27, 31]. The specific surface area of the zeolite obtained from kaolin, CFA and halloysite are  $591\text{m}^2\text{g}^{-1}$ ,  $607.95\text{m}^2\text{g}^{-1}$  and  $725.80\text{m}^2\text{g}^{-1}$  respectively[27,25,31]. There is a large mass transfer zone (MTZ) for zeolite 13X and so the adsorption rate of zeolite 13X is comparatively high. The nitrogen adsorption on the adsorbent site of 13X is stronger compared to oxygen making zeolite 13X a better option for oxygen concentrator[41].

**Table 5:** Comparison of zeolite properties from CFA and commercial zeolite 13X

Parameter	S( $\text{m}^2/\text{g}$ )	V( $\text{ml}/\text{g}$ )	D(nm)	A( $\text{mg}/\text{L}$ )
COM	469.67	0.2023	2.53	130.11
CFA	607.95	0.2818	2.72	182.20

S= Surface area, V= pore volume, D= pore diameter, A= adsorption volume

**Table 6:** Volume and surface area of synthesized zeolite 13X from halloysite

Volume		Surface area		
V total	V t-plot	S Langmuir	S t-plot	S BET
0.27 cm <sup>3</sup> /g	0.24 cm <sup>3</sup> /g	725.80 cm <sup>3</sup> /g	513.19 cm <sup>3</sup> /g	55.16 cm <sup>3</sup> /g

*V total*= total pore volume, *V t-plot*= t-plot micropore volume, *S Langmuir*= Langmuir surface area, *S t-plot*= t-plot micropore area, *S BET*= BET surface area

**Table 7:** Properties of synthesized zeolite 13X from natural kaolin and commercial zeolite 13x.

	BET Surface Area (m <sup>2</sup> /g)	Micropore Surface Area (m <sup>2</sup> /g)	Micropore Volume (cm <sup>3</sup> /g)	External Surface
13X-COM	588	566	0.240	33
13X-Kaolin	591	576	0.250	34

## **3.2 EFFECTS OF PARAMETERS ON 13X ZEOLITE PREPARATION**

Synthesizing zeolites is very complex because it is affected by a number of parameters as a slight change may result in formation of different types of zeolite and may create a barrier in producing pure state zeolite. According to Plackett—Burman and the Taguchi methods- the synthesis gel SiO<sub>2</sub>/Al<sub>2</sub>O<sub>3</sub> molar ratio, alkalinity (H<sub>2</sub>O/Na<sub>2</sub>O) and water content (H<sub>2</sub>O/SiO<sub>2</sub>) and the zeolite synthesis temperature were found as the most affective parameters on the synthesized zeolites' crystallinities and growth.

### **3.2.1 Crystallization Temperature**

The crystallization temperature greatly influences the nucleation and growth mechanism in zeolite formation. When the experiments is conducted at a temperature range of 90°C -100°C, pure form of zeolites 13X were formed which was further verified by XRD pattern[ [fig.12,16](#)]. Around this temperature range zeolite 13X showed a high cation exchange capacity. Below 60°C there is the formation of zeolite type A [29] and at a temperature more than 100°C hydroxysodalite zeolites are formed [33]. This phenomenon occurs because of different rates of dissolution of aluminium and silicone. The aluminium dissolution rate tends to be faster than that of silicone at lower temperature ranges, and with increase in temperature the dissolution of silicone increases and thus favors' in the formation pure of zeolite 13X.

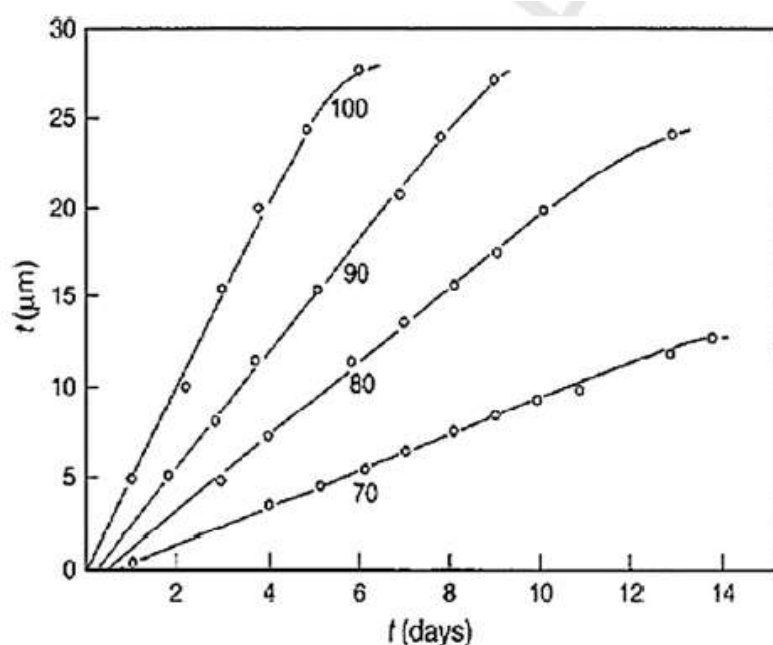


Fig.12 Influence of temperature on the growth rates of zeolite NaX (FAU)

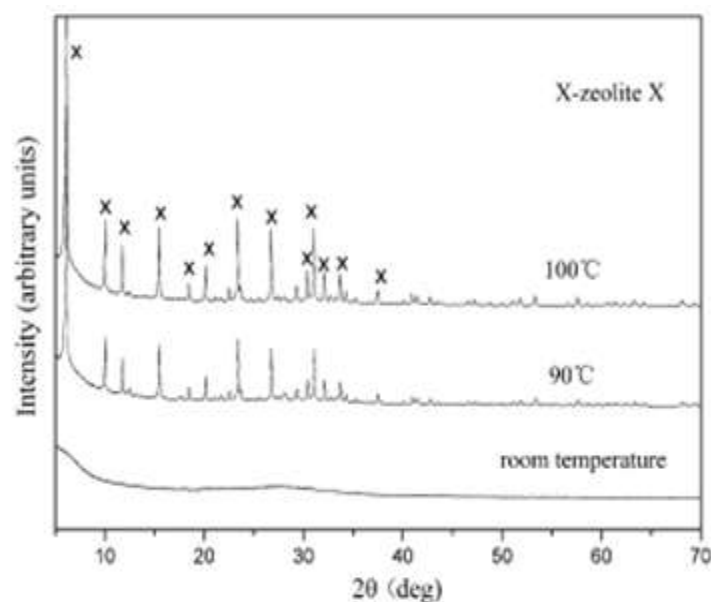


Fig.16 XRD patterns of the synthesized products obtained at room temperature, 90–100 °C

### 3.2.2 The Alkalinity

The second most important factor is the alkalinity of the synthesis solution, where the resultant zeolite crystallinity increases as this factor increases[34-36]. NaOH not only affects the degree of zeolitisation but also the type of zeolite obtained as a product. The zeolite 13X is highly favored when the NaOH concentration is in the range of 1M to 4M[31] and this further proved by the given figure 14 . At low NaOH concentration ranges the cations cannot enter the lattice and thus new structure could not be formed because of the lack of crystallization. Also, the alkalinity should not cross the optimum value as silicate anions polymerization degree decreases while polysilicate and aluminate anions polymerization accelerates and also results in the lower supersaturation of the gel[37]. At high NaOH value, the zeolite 13X is converted to P-type zeolite.

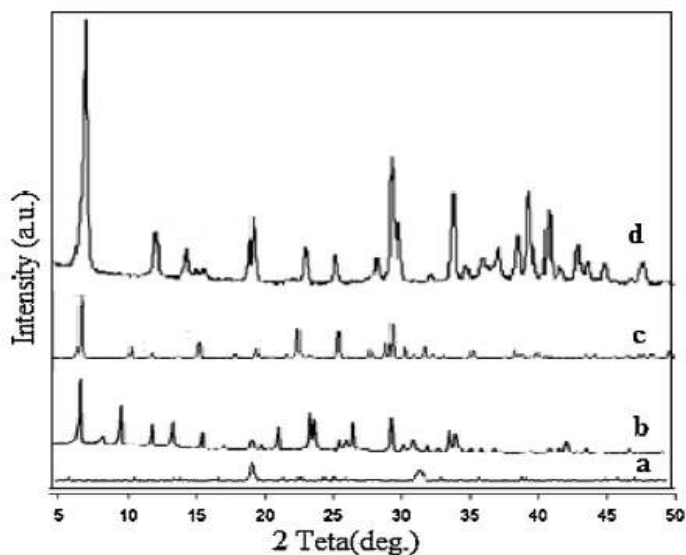


Fig.14 XRD pattern of zeolite 13X and associated phases obtained by hydrothermal synthesis: (a) 1.0M NaOH, (b) 2.0 M NaOH, (c) 3.0 M NaOH, (d) 4.0 M NaOH.

### 3.2.3. Effect of $\text{SiO}_2/\text{Al}_2\text{O}_3$ Molar Ratio

The  $\text{SiO}_2/\text{Al}_2\text{O}_3$  ratio plays an important role in the hydrothermal synthesis of zeolite[38]. All zeolites have distinct framework structures established by adjoining oxide tetrahedral to form the Framework. Thus different types of zeolites are formed at different  $\text{SiO}_2/\text{Al}_2\text{O}_3$  molar ratios. In the synthesis, at a molar ratio of 2.0, it is found that both zeolite A and X type is present, when the molar ratio of  $\text{SiO}_2/\text{Al}_2\text{O}_3$  was changed to 4.3 pure X type zeolite was formed[28] which was further confirmed by the XRD pattern shown in figure 15 [25]. Further increasing at a ratio of 5.0 hydroxysodalite and zeolite beta are formed. Comparing the silicate and alluminate content from the tables 2,3,4,; sodium silicate was added to the synthesis mixture from halloysite as formation of zeolite 13X requires high silica content.

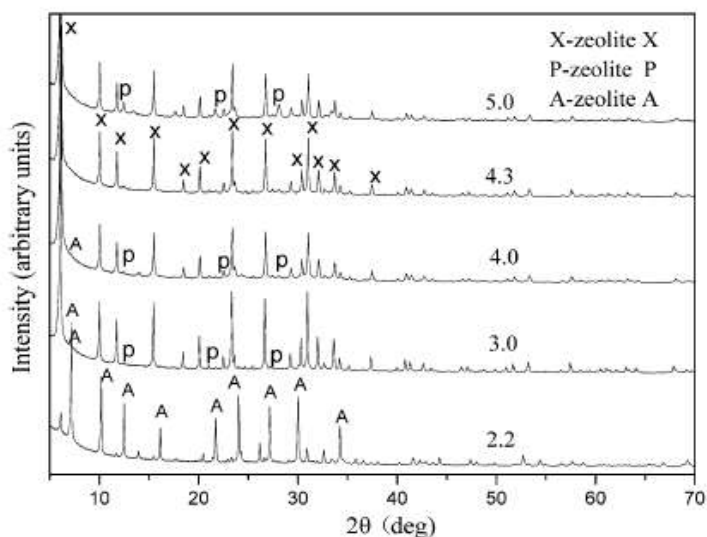


Fig.15 XRD data of different molar ratios of  $\text{SiO}_2/\text{Al}_2\text{O}_3$

### 3.2.4 Synthesis Time.

The zeolite crystallinity is observed to increase with time. Zeolite 13X requires a relatively longer crystallization time and increasing the temperature from 5 hours to 16 hours improved its crystallinity. This is observed because the framework is formed by connection of sodalite cages through double 6 member rings (D6R) and sparser structure [39]. At a synthesis temperature higher than 12 hours porosity of the formed zeolite layers increases as a result the permeability of the gaseous penetration increases[40]. Fig. 13, 17[25] shows the sequence of transformation of the zeolites with the synthesis time. At lower time period type A zeolite is formed which on further increase in time changes to zeolite type X and at time greater hydroxysodalite and P type is formed.[29] Thus the synthesis time suitable for zeolite 13X is found between the time ranges of 8 hours to 14 hours.

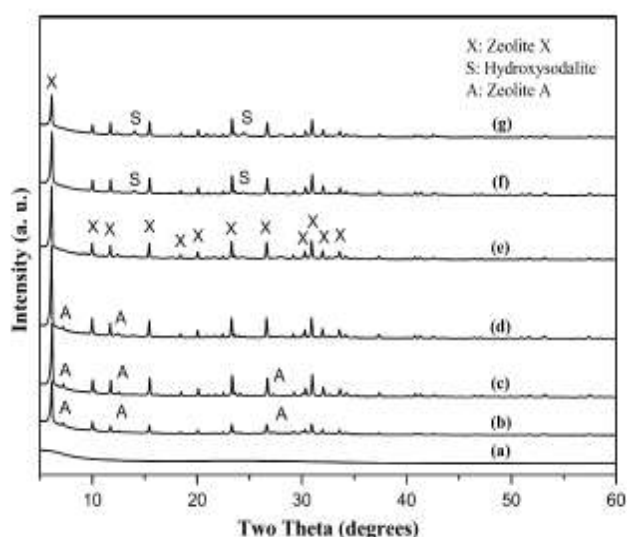


Fig. 13 XRD patterns of the reaction as-synthesized products obtained at different crystallization times (a) 0 h, (b) 1 h, (c) 4 h, (d) 6 h, (e) 8 h, (f) 12 h, and (g) 24 h.

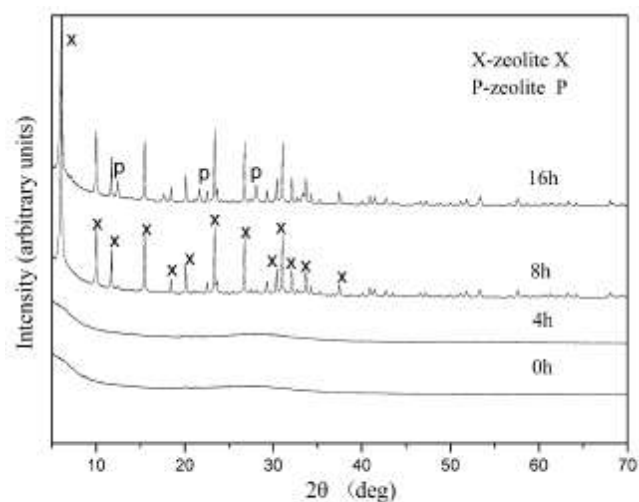


Fig.17 XRD patterns of the reaction as-synthesized products obtained at 100 °C for 0, 4, 8 and 16 h crystallization time



## **4.CONCLUSION**

The lab-scale formation of zeolite 13X from low grade natural kaolin, natural halloysite and coal fly ash was successful and was confirmed by the XRD, FT-IR and SEM analysis. The analysis of the morphology and structural properties are in good agreement with reported standard properties of the 13X zeolite. The surface area and micropore volume of the synthesized zeolite obtained was much higher than that of the commercial zeolite and hence showed excellent adsorption property. Also, the effects of different parameters showed that a slight change of values may lead to the production of different types of zeolites such as P type, A-type, hydroxysodalite, etc. So the synthesis temperature, time, amount of aluminosilicate, amount of sodium hydroxide should be in proper ranges for the formation of pure zeolite 13X type. Since a natural source that is halloysite and kaolin was used it ensured cost effective and environmental friendly synthesis and had no toxic effect or threats to individuals using them. The use of CFA ensured its proper recycling and reduction in pollution as the most part of it is dumped in ash fields causing hazardous problems. The main idea for this topic was to produce cost effective zeolite 13X which can be used by portable oxygen concentrator and give one pure form oxygen taking air as a source.

## 5. REFERENCES

1. D.W. Breck. Zeolite Molecular Sieves: Structure, Chemistry and Use. *Analytica Chimica Acta* 1975, 75 (2), 493.
2. Cundy, C.; Cox, P. The Hydrothermal Synthesis of Zeolites: History And Development From The Earliest Days To The Present Time. *ChemInform* 2003, 34 (19).
3. Zeolite - Wikipedia. <http://en.wikipedia.org/wiki/Zeolite>.
4. Król, M. Natural Vs. Synthetic Zeolites. *Crystals* 2020, 10 (7), 622.
5. Shokroo, E.; Kakavandi, I.; Baghbani, M.; Farniaei, M. Dynamic Modeling Of Nitrogen Adsorption On Zeolite 13X Bed. *Fluid Mechanics Research International Journal* 2017, 1 (1).
6. Drain, L. Permanent Electric Quadrupole Moments Of Molecules And Heats Of Adsorption. *Transactions of the Faraday Society* 1953, 49, 650-654.
7. Xu, R.; Pang, W.; Yu, J.; Huo, Q.; Chen, J. Chemistry Of Zeolites And Related Porous Materials: Synthesis And Structure; John Wiley & Sons, 2009. *John Wiley & Sons* 2009.
8. Material Safety Data Sheet. [http://www.ecompressedaircom/pdf/13x\\_msd](http://www.ecompressedaircom/pdf/13x_msd)
9. LBC Zeolite Molecular Sieves Characteristics. [http://www.sinolbc.com/Professional\\_View.asp:Professional\\_Id=11](http://www.sinolbc.com/Professional_View.asp:Professional_Id=11)
10. CO2 emission and its mitigation by adsorption on zeolites and activated carbon, <http://www.ias.as.in/currsci/mar252007/724.pdf>
11. How Does the Size of a Nitrogen Molecule Compare to That of Oxygen?, [http://wiki.answers.com/q/How\\_does\\_the\\_size\\_of\\_a\\_nitrogne\\_molecule\\_compare\\_to\\_that\\_of\\_oxygen](http://wiki.answers.com/q/How_does_the_size_of_a_nitrogne_molecule_compare_to_that_of_oxygen)
12. Chandrasekhar, S.; Pramada, P. *Journal of Porous Materials* 1999, 6 (4), 283-297
13. Wajima, T.; Ikegami, Y. Synthesis Of Crystalline Zeolite-13X From Waste Porcelain Using Alkali Fusion. *Ceramics International* 2009, 35 (7), 2983-2986.
14. Mezni, M.; Hamzaoui, A.; Hamdi, N.; Srasra, E. Synthesis Of Zeolites From The Low-Grade Tunisian Natural Illite By Two Different Methods. *Applied Clay Science* 2011, 52 (3), 209-218.

15. Ruiz, R.; Blanco, C.; Pesquera, C.; González, F.; Benito, I.; López, J. Zeolitization Of A Bentonite And Its Application To The Removal Of Ammonium Ion From Waste Water. *Applied Clay Science* 1997, 12 (1-2), 73-83.
16. Lee, S.; Han, Y.; Choy, J. 2D→3D Transformation Of Layered Aluminosilicate Upon Base Treatment. *Solid State Ionics* 2002, 151 (1-4), 343-346
17. Tanaka, H.; Fujii, A. Effect Of Stirring On The Dissolution Of Coal Fly Ash And Synthesis Of Pure-Form Na-A And -X Zeolites By Two-Step Process. *Advanced Powder Technology* 2009, 20 (5), 473-479.
18. Colina, F.; Llorens, J. Study Of The Dissolution Of Dealuminated Kaolin In Sodium–Potassium Hydroxide During The Gel Formation Step In Zeolite X Synthesis. *Microporous and Mesoporous Materials* 2007, 100 (1-3), 302-311.
19. Fernandes Machado, N.; Malachini Miotto, D. Synthesis Of Na–A And –X Zeolites From Oil Shale Ash. *Fuel* 2005, 84 (18), 2289-2294.
20. Purnomo, C.; Salim, C.; Hinode, H. Synthesis Of Pure Na–X And Na–A Zeolite From Bagasse Fly Ash. *Microporous and Mesoporous Materials* 2012, 162, 6-13.
21. WAJIMA, T.; HAGA, M.; KUZAWA, K.; ISHIMOTO, H.; TAMADA, O.; ITO, K.; NISHIYAMA, T.; DOWNS, R.; RAKOVAN, J. Zeolite Synthesis From Paper Sludge Ash At Low Temperature (90°C) With Addition Of Diatomite. *Journal of Hazardous Materials* 2006, 132 (2-3), 244-252.
22. Kazemian, H.; Naghdali, Z.; Ghaffari Kashani, T.; Farhadi, F. Conversion Of High Silicon Fly Ash To Na-P1 Zeolite: Alkaline Fusion Followed By Hydrothermal Crystallization. *Advanced Powder Technology* 2010, 21 (3), 279-283.
23. Wajima, T.; Munakata, K. Material Conversion From Waste Sandstone Cake Into Cation Exchanger Using Alkali Fusion. *Ceramics International* 2012, 38 (2), 1741-1744.
24. Wajima, T.; Munakata, K.; Ikegami, Y. Conversion Of Waste Sandstone Cake Into Crystalline Zeolite X Using Alkali Fusion. *MATERIALS TRANSACTIONS* 2010, 51 (5), 849-854.
25. Zhou, C.; Alshameri, A.; Yan, C.; Qiu, X.; Wang, H.; Ma, Y. Characteristics And Evaluation Of Synthetic 13X Zeolite From Yunnan'S Natural Halloysite. *Journal of Porous Materials* 2012, 20 (4), 587-594.
26. Chen, D.; Hu, X.; Shi, L.; Cui, Q.; Wang, H.; Yao, H. Synthesis And Characterization Of Zeolite X From Lithium Slag. *Applied Clay Science* 2012, 59-60, 148-151.
27. Tu, W.; Zhang, Y.; Bai, J.; Liu, W. Synthesis Of Zeolite 13X From Coal Fly Ashes And Properties Of The Zeolite Products. *Applied Mechanics and Materials* 2014, 675-677, 724-727.

28. Ma, Y.; Yan, C.; Alshameri, A.; Qiu, X.; Zhou, C.; li, D. Synthesis And Characterization Of 13X Zeolite From Low-Grade Natural Kaolin. *Advanced Powder Technology* 2014, 25 (2), 495-499.
29. Molina, A.; Poole, C. A Comparative Study Using Two Methods To Produce Zeolites From Fly Ash. *Minerals Engineering* 2004, 17 (2), 167-173.
30. Ma, Y.; Yan, C.; Alshameri, A.; Qiu, X.; Zhou, C.; li, D. Synthesis And Characterization Of 13X Zeolite From Low-Grade Natural Kaolin. *Advanced Powder Technology* 2014, 25 (2), 495-499.
31. Garshasbi, V.; Jahangiri, M.; Anbia, M. Equilibrium CO<sub>2</sub> Adsorption On Zeolite 13X Prepared From Natural Clays. *Applied Surface Science* 2017, 393, 225-233.
32. Fischer, F.; Lutz, W.; Buhl, J.; Laevemann, E. Insights Into The Hydrothermal Stability Of Zeolite 13X. *Microporous and Mesoporous Materials* 2018, 262, 258-268.
33. Pourazar, M.; Mohammadi, T.; Jafari Nasr, M.; Javanbakht, M.; Bakhtiari, O. Preparation Of 13X Zeolite Powder And Membrane: Investigation Of Synthesis Parameters Impacts Using Experimental Design. *Materials Research Express* 2020, 7 (3), 035004.
34. Plant, D.; Maurin, G.; Deroche, I.; Llewellyn, P. Investigation Of CO<sub>2</sub> Adsorption In Faujasite Systems: Grand Canonical Monte Carlo And Molecular Dynamics Simulations Based On A New Derived Na<sup>+</sup>-CO<sub>2</sub> Force Field. *Microporous and Mesoporous Materials* 2007, 99 (1-2), 70-78.
35. Bkour, Q.; Faqir, N.; Shawabkeh, R.; Ul-Hamid, A.; Bart, H. Synthesis Of A Ca/Na-Aluminosilicate From Kaolin And Limestone And Its Use For Adsorption Of CO<sub>2</sub>. *Journal of Environmental Chemical Engineering* 2016, 4 (1), 973-983.
36. Ayele, L.; Pérez-Pariente, J.; Chebude, Y.; Díaz, I. Synthesis Of Zeolite A From Ethiopian Kaolin. *Microporous and Mesoporous Materials* 2015, 215, 29-36.
37. Subhapriya, S.; Gomathipriya, P. Synthesis And Characterization Of Zeolite X From Coal Fly Ash: A Study On Anticancer Activity. *Materials Research Express* 2018, 5 (8), 085401.
38. Ojha, K.; Pradhan, N.; Samanta, A. Zeolite From Fly Ash: Synthesis And Characterization. *Bulletin of Materials Science* 2004, 27 (6), 555-564.
39. Zhang, X.; Tang, D.; Zhao, J.; Li, X.; Yang, R. Hydrothermal Synthesis Of Nanocrystalline Na<sub>x</sub> Zeolite At Room Temperature. *Journal of Nanoscience and Nanotechnology* 2014, 14 (7), 5552-5560.

- 
40. Mohammadi, T.; Maghsoodloorad, H. Synthesis And Characterization Of Ceramic Membranes (W-Type Zeolite Membranes). *International Journal of Applied Ceramic Technology* 2012, 10 (2), 365-375.
  41. Shokroo, E.; Kakavandi, I.; Baghbani, M.; Farniaei, M. Dynamic Modeling Of Nitrogen Adsorption On Zeolite 13X Bed. *Fluid Mechanics Research International Journal* 2017, 1 (1), 20-24.
  42. Thomas, W.; Crittenden, B. *Adsorption technology and design*; Butterworth-Heinemann: Oxford, 1998.

# QUANTUM-DOT LASERS: AN OVERVIEW

## LITERATURE REVIEW (SEMESTER-4) -2021



**SCOTTISH CHURCH COLLEGE  
(UNIVERSITY OF CALCUTTA)**

**C.U. ROLL NO: 223/CEM/191023  
C.U. REGISTRATION NO: 223-1211-0014-19  
SPECIAL PAPER: SP 44**

**NAME OF THE CANDIDATE:**

**PRIYANKA CHATTERJEE**

**SUPERVISED BY:**

**DR. ANIRUDDHA GANGULY**

*Priyanka Chatterjee*

SIGNATURE OF CANDIDATE

*Aniruddha Ganguly*

SIGNATURE OF SUPERVISOR

## Table of Contents

<b>Sl. No</b>	<b>Content</b>	<b>Page No.</b>
1	<b>Abstract</b>	3
2	<b>Introduction</b> a) Quantum-Dot b) Concept of Quantum Confinement c) Fabrication of Quantum-Dots d) development of Quantum Dot LASER	3-5
3	<b>Why we would choose Quantum dots in laser</b> ➤ Size Factor and tunability of QDs ➤ Gain in Quantum-Dot LASERS: ➤ Temperature dependence of threshold energy ➤ Self-organized growth of quantum dots ➤ Electronic spectrum	5-8
4	<b>Construction Of laser</b> ➤ Instrumentation ➤ Kinetic Equation ➤ Optical quality change in output light	8-13
5	<b>Experiment</b>	13-16
6	<ul style="list-style-type: none"><li>• <b>Practical Uses of Quantum-Dot lasers</b></li><li>• <b>Future fabrication of Quantum Dot lasers</b></li></ul>	16
7	<b>Conclusion</b>	17
8	<b>Reference</b>	17

# 1. Abstract:

In this literature survey, I shall discuss the applications of Quantum -Dot lasers in the recent era of technology. Limitless opportunities are provided to create new technologies by these types of nanostructures. To understand the applications of Quantum-Dots, I have discussed about the basic characteristics of quantum dots and the Confinement effect in the Introduction part. Then, I have discussed the construction of Quantum-Dot laser with the corresponding instrumentations. Finally, I have made a scholarly search on the practical usage of Quantum-Dot lasers and tried to predict the future of this technology.

# 2. Introduction:

## a) Quantum-Dot:

Quantum dots are the semiconductor nano structures with vast application across many industries. In such systems, motion of the electron is confined in three spatial directions and they cannot move freely to any spatial direction. Unique tunability is obtained by their small size (~2-10 nanometres or ~10-50 atoms in diameter). Like that of traditional semiconductors, the importance of QDs is originated from the fact that their electrical conductivity can be altered by an external stimulus such as voltage or photon flux. One of the main differences between quantum dots and traditional semiconductors is that the peak emission frequencies of quantum dots are very sensitive to both the dot's size and composition. [Ref: 1, 2]

## b) Concept of Quantum Confinement [Ref: 2]

According to Heisenberg Uncertainty Principle, if a moving quantum particle with non-relativistic mass  $m$  is confined to a region, say a length of  $\Delta x$  along  $x$  axis, then the uncertainty in its momentum ( $\Delta p_x$ ) is given by,

$$\Delta p_x \approx h/2\pi\Delta x \dots\dots\dots (1)$$

$\Delta p_x$  may be considered as the measure of momentum of the particle along the  $x$  direction. This confinement along the  $x$  axis, gives the particle an additional amount of kinetic energy given by:

$$E_{\text{confinement}} = \frac{(\Delta p_x)^2}{2m} = h^2/8m\pi^2\Delta x^2 \dots\dots\dots(2)$$

This confinement energy is meaningful, if it is comparable to the kinetic energy  $E_{x(T)}$  of the particle due to its thermal motion along the  $x$  direction. Thus the condition is:

$$\frac{1}{2}k_B T = h^2/8m\pi^2\Delta x^2$$

$$\text{or, } \Delta x \approx \sqrt{\frac{h^2}{4m\pi^2 k_B T}} \dots\dots\dots(3)$$

The **de Broglie wavelength**,  $\lambda$  (dB) of the particle for its thermal motion along  $x$  axis is given by:

$$\lambda \text{ (dB)} = \frac{h}{p_x(T)} = \frac{h}{\sqrt{2mE_x(T)}} = \sqrt{\frac{h^2}{mk_B T}} \approx \Delta x$$

Thus the condition of quantum confinement of a particle along a particular dimension is:  
The dimension of confinement must be of the order the de Broglie wavelength for the thermal motion of the particle in the direction. The above condition tells us how small the dimension must be if we want to observe the size dependent quantum confinement. In general it can be stated that a nan omaterial is in the state of quantum confinement when its size is in the order of de Broglie wavelength of the charge carrier (i.e. electron or hole).  
Quantum confinement occurs when one or more of the dimensions of a nano crystal approach the **Exciton Bohr radius**. The concepts of energy levels, band gap, conduction band and valence band still apply. However, the electron energy levels can no longer be treated as continuous - they must be treated as discrete.



[QDs utilize the motion of conduction band electrons, valence band holes or excitons. Excitons are pairs of conduction band electrons and valence band holes.]

Quantum well, or quantum wire confinements provide the electron at least one degree of freedom. Although this kind of confinement leads to quantization of the electron spectrum which changes the density of states, and results in one or two-dimensional energy sub bands, it still gives the electron at least one direction to propagate. On the other hand, today's technology allows us to create QD structures, in which all existing degrees of freedom of electron propagation are quantized. We can think this confinement as a box of volume  $d_1d_2d_3$ . The energy is therefore quantized to:

$$E = E_{q_1} + E_{q_2} + E_{q_3} \quad \text{where,} \quad E_{q_n} = \frac{h^2}{2m} \left( \frac{q_n}{d_n} \right)^2 \quad \dots\dots\dots (5)$$

$q_1$ ,  $q_2$  and  $q_3$  are the quantum numbers associated with an energy sub band. Since the allowed energy levels are discrete and separated, we can represent the density of states as delta functions. The energy levels of a QD can be adjusted with proper designs according to the needs of the application. For instance, the addition or subtraction of just a few atoms to the QD has the effect of altering the boundaries of the band gap. Changing the geometry of the surface of the QD also changes the band gap energy, owing again to the small size of the dot, and the effects of quantum confinement. [Ref: 1, 2]

- **Electronic Density of States:** [Ref: 3]

Semiconductor quantum dots can be thought of qualitatively as the textbook case of a **particle-in-a-box**. The three dimensional quantum confinement provided by band offsets between the narrow gap dot material and surrounding matrix was initially predicted to lead to full discretization of the energy levels into delta-function-like states possessing atom-like degeneracy, in contrast to the step-function-like QW density of states (DOS),  $\rho(E)$  see Fig. 1.. Analogous to the particle-in-a-box, the energy levels of a QD are determined by the size of the dot and height of the potential barrier. **In real semiconductor systems the idea of the particle-in-a-box picture begins to disappear.** The random, self-assembled process of QD formation in crystal growth leads to no uniformity in the size distribution, strain profile, and compositional fluctuations if non-binary alloys are used for the dots or surrounding matrix. These fluctuations lead to *inhomogeneous broadening*,  $\Delta E_{inh}$ , of the optical properties of a dot ensemble. The broadening effectively leads to the formation of a quasi-band of states representing the weighed superposition of the discrete states of individual dots, as illustrated in Fig. 1(a). Fortunately, the energy level spacing between principal quantum states can be a few times larger than the inhomogeneous broadening such that the quantized separation can be maintained. An important result of this statistical broadening is that it yields a highly symmetric, Gaussian gain spectrum for the QD states. The extent of inhomogeneous broadening is dependent on crystal growth conditions and provides additional tunability to the gain spectrum in QD devices, which can be advantageous for broad bandwidth applications such as for optical amplifiers, tuneable lasers, and mode-locked lasers. For single mode lasing with low threshold and high efficiency, a smaller inhomogeneous broadening is desirable, since off-resonance dots will still capture charge carriers and result in unclamped spontaneous emission. In state-of-the-art QD material, inhomogeneous broadenings, as measured from the photoluminescence spectrum, as low as 24 meV have been realized at room temperature. In further departure from the depiction of Fig.1(b), the well-developed QD material systems form via the **Stranski-Krastanov** growth mode which yields a thin wetting layer of dot material that acts as a QW connecting all the dots in a layer. A more realistic representation of the DOS of QD material is shown in Fig. 1(b).

Fig.2 shows variation of density of states With Energy in case of 3D,2D,1D and 0D nano structures.

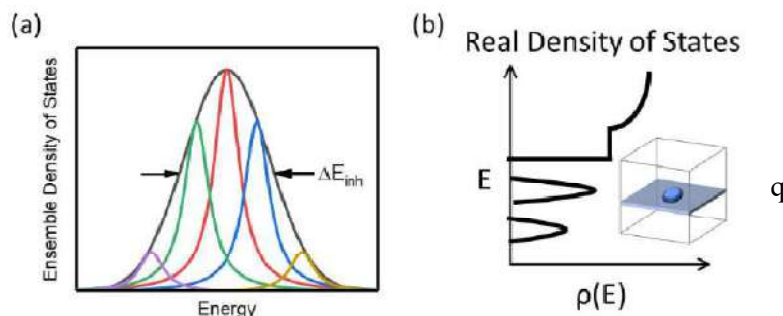
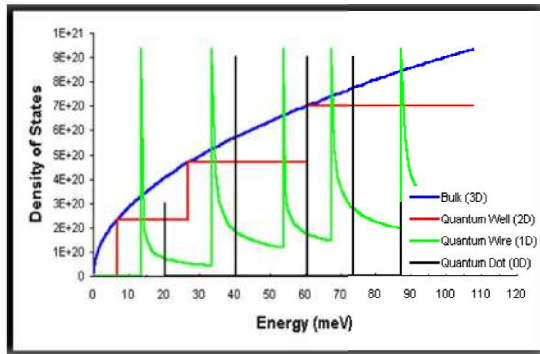


Fig. 1. (a) Schematic illustration of inhomogeneous broadening for a quantum dot state. (b) A realistic schematic of the density of states,  $\rho(E)$ , of a quantum dot structure including inhomogeneous broadening and the wetting layer



**Fig:2.** Variation of density of states With Energy in case of 3D,2D,1D and 0D nano structures.

### The confinement of the motion of holes and electrons can be created by:

- electrostatic potentials
  - e.g. doping, strain, impurities, external electrodes
- the presence of an interface between different semiconductor materials
  - e.g. in the case of self-assembled QDs
- the presence of the semiconductor surface
  - e.g. in the case of a semiconductor nanocrystal
- or by a combination of these.[ref: 1]

### c) Fabrication of Quantum-Dots in QD lasers:

- **Core-Shell Quantum Structures:** QDs are small regions of one material buried in another with a larger band gap.[Ref:4]
- **Self-Assembled QDs:** self-assembled quantum dots are semiconductor heterostructures that confine charge carriers in three directions. A quantum well, which confines carriers in only one direction, is the most straightforward confinement structure to produce. This structure is produced by growing epitaxial layers of at least two different materials, and sandwiching a lower band gap layer between regions of higher band gap. Quantum dots and quantum wires cannot be produced by such a layer wise approach. Micro fabrication techniques involving lithography and etching can be used here. [Ref: 4]

Self-assembled QDs nucleate spontaneously under certain conditions during **molecular beam epitaxy (MBE)** and **metalorganics vapor phase epitaxy (MOVPE)**

- **MOVPE:** is a chemical vapor deposition method of epitaxial growth of materials, especially compound semiconductors from the surface reaction of organic compounds or metalorganics and metal hydrides containing the required chemical elements. In contrast to molecular beam epitaxy (MBE) the growth of crystals is by chemical reaction and not physical deposition. This takes place not in a vacuum, but from the gas phase at moderate pressures (2 to 100 kPa).[Ref: 4]
- **MBE:** A technique that grows atomic-sized layers on a chip rather than creating layers by diffusion.[Ref: 5]
- **Monolayer fluctuations:** QDs can occur spontaneously in QW structures due to monolayer fluctuations in the Quantum well's thickness.[Ref: 6]
- **Individual QDs:** Individual QDs can be created from two-dimensional electron or hole gases present in remotely doped quantum wells or semiconductor hetero-structures. The sample surface is coated with a thin layer of resist. A lateral pattern is then defined in the resist by electron beam lithography. This pattern can then be transferred to the electron or hole gas by etching, or by depositing metal electrodes (lift-off process) that allow the application of external voltages between the electron gas and the electrodes. Such QDs are mainly of interest for experiments and applications involving electron or hole transport, i.e., an electrical current.

#### d) Development of QD LASER:

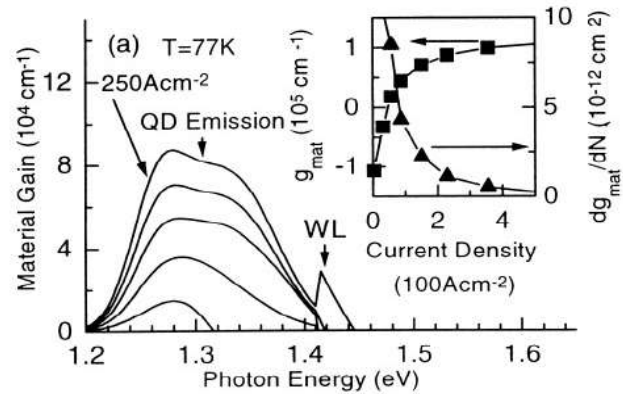
- The advantages of quantum well lasers on traditional lasers first predicted in 1970s (*Dingle and Henry 1976*), and first quantum well lasers which were very inefficient were demonstrated at those dates (*van der Ziel et al. 1975*). The advantages recognized were:
  - The confinement and nature of the electronic density of states result in more efficient devices operating at lower threshold currents than lasers with bulk active layers. The laser threshold current density can be reduced by decreasing the thickness of the active layer. Discrete energy levels provide a means of "**tuning**" the resulting wavelength of the material. Since the thickness of the quantum well depends on the desired spacing between energy levels, tuning can be done by changing the quantum well dimensions or thickness. For energy levels of greater than a few tens of meV's, the critical dimension is approximately a few hundred angstroms. [Ref:7]
- The inefficiency of quantum well lasers were eliminated in 1980s by the use of new materials growth capabilities (molecular beam epitaxy), and optimization of the hetero structure laser design.
- The concept of semiconductor QDs was proposed for semiconductor laser applications by Arakawa and Sakaki in 1982, predicting suppression of temperature dependence of the threshold current. Henceforth, reduction in threshold current density, reduction in total threshold current, enhanced differential gain and high spectral purity/no-chirping were theoretically discussed in 1980's.
- QD lasers acquired more importance after significant progress in nanostructure growth in the 1990's such as the self-assembling growth technique for InAs QDs. The first demonstration of a quantum dot laser with high threshold density was reported by Ledentsov and colleagues in 1994.
- Bimberg (1996) achieved improved operation by increasing the density of the QD structures, stacking successive, strain-aligned rows of QDs and therefore achieving vertical as well as lateral coupling of the QDs. In addition to utilizing their quantum size effects in edge emitting lasers, self-assembled QDs have also been incorporated within vertical cavity surface emitting lasers. [Ref:8]

### 3. Why we would choose Quantum dots in laser

- **Size Factor and tunability of QDs:** As the quantum confinement in a QD is in all three dimensions, tunability of a quantum dot laser (QDL) is higher than a quantum well laser (QWL). To be useful for devices, a QD should satisfy several important requirements. A lower limit of the QD size is defined by the condition that at least one electron level in a quantum dot is available. This critical size ( $D_{min}$ ) is strongly related to the conduction band offset ( $D_{Ec}$ ) in the material system used. Assuming a conduction band offset of, 0.3 eV for, e.g. direct band gap GaAs - Al<sub>0.4</sub>Ga<sub>0.6</sub>As QWs, this would mean that the diameter of the QD should not be smaller than 40 Å. This is an absolute lower limit of the QD size, since for QDs of this or even slightly larger size the separation between the electron level and the barrier continuum energy is very small and at finite temperatures evaporation of carriers from QDs will result in their depletion. For the InAs - AlGaAs system the conduction band offset is larger, while the electron effective mass is smaller, and the critical size is similar. If the separation between energy levels becomes comparable to the thermal energy (KT), population of higher-lying energy levels cannot be neglected. This equation establishes an upper limit for GaAs-AlGaAs QDs of, 120 Å, and of 200 Å for InAs-GaAs QDs, due to the much lower electron effective mass in the latter case. Efficient hole confinement requires even smaller sizes. However, if the optical transition matrix element between a ground state electron and a hole excited state is small, population of excited hole sublevels will not result in significant broadening of the gain spectra. In the last decade two principally different approaches have been explored to fabricate quantum dots. One way to fabricate QDs, by selective etching, or intermixing of quantum well structures, suffered either from insufficient resolution, or from defects introduced upon patterning and etching, from or both. For laser applications this way was originally followed. Using patterning techniques InGaAs/InGaAsP QD lasers were successfully realized, but they still showed a very high threshold current density of 7.6 kA/cm<sup>2</sup> at 77 K. The real breakthrough in QD lasers is related to self-organized growth at crystal surfaces. [Ref: 3,8]

- **Gain in Quantum-Dot LASERS:** Gain characteristics of QD lasers based on self-organized quantum dots (QD) were studied for two systems: InGaAs QDs in AlGaAs matrix on GaAs substrate and InAs QDs in an InGaAs matrix on an InP substrate. A ground to excited state transition was observed with increasing threshold gain. The current density of the model gain was calculated for the QD-on-GaAs and the QD-on-InP injection lasers. Two characteristic regions are observed in the dependences of the gain and the lasing wavelength on current density in both systems of QDs. These regions are attributed to the ground and excited state lasing in a QD array, respectively. Raising the current leads first to saturation of the QD ground state gain and then to a transition to lasing via excited states of QDs. The latter is characterized by three times higher gain saturation level. The higher the QD density, the higher will be both the transparency current -density and also the gain saturation level. (Fig: 3a) [Ref: 8,9,10]

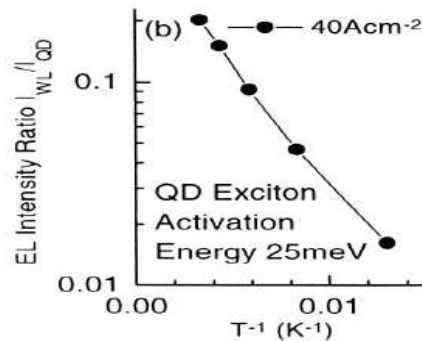
**Fig: 3a:** Calculated material gain spectra as a function of excitation for an ensemble of InAs dots having a base length of 7 nm and a size distribution of 13%. The WL is assumed to be a ,0.5 nm thick, single quantum well. The inset shows the peak material gain ( $g_{mat}$ ) at ,1.28 eV and the differential material gain ( $dg_{mat}/dN$ ) as a function of current density.



Since the total number of dots in the recombination volume of a typical ridge-waveguide laser exceeds a value of,  $10^6$ , the very narrow gain spectrum of a single dot transition (demonstrated by Grundmann) transforms to a broad gain spectrum. Based on the structural parameters of the laser and the transition energies of ground and excited states one can calculate the material gain. Since the Bloch matrix element and the overlap integral are not exactly known in the case of a QD laser, one has to calibrate the gain spectra to absolute values by using the well known equilibrium value of the absorption coefficient from bulk GaAs.[Ref:8]

Due to the lateral separation of the dots, carriers in different dots are thermally coupled only via the wetting layer (WL) and GaAs barrier states [Ref: 8]. this fact is directly proved by the intensity ratio of QD and WL electroluminescence (EL) at different temperatures and at constant injection level, which follows an Arrhenius dependence (see Fig. 6b). The intensity ratio fits to activation energy for the QD exciton to the WL of 25 meV. It was suggested,[Ref.10]

**Fig: 3.b)** Arrhenius plot of threshold current density of WL and QD electro luminescence (EL), proving thermal equilibrium of carriers between QD and WL states.



- **Self-organized growth of quantum dots :** A solution to the problem of reliable quantum dot fabrication is based on an effect, previously considered an undesirable by crystal growers. A layer of a material having a lattice constant different from that of the substrate, after some critical thickness is deposited can spontaneously transform to an array of three-dimensional islands. More recently, it was shown that there can exist a range of deposition parameters, where the islands are small (10 nm), have a similar size and shape, and form dense arrays. Theoretical considerations show that due to the strain-induced renormalization of the surface energy of the facets, an array of equalized and equishaped 3D islands can represent a stable state of the system. This is directly confirmed for the most extensively studied MBE grown InAs-GaAs material system by the reversibility of the islanding surface planarization process. The reversible transition occurs when the surface stoichiometry is changed from As-rich (islanding) to In rich

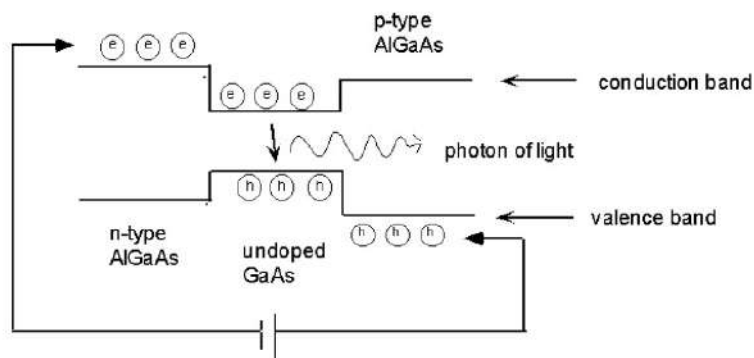
(planarization), and vice versa. High arsenic pressure results in a reduction of the characteristic QD size and in formation of high concentrations of dislocated InAs clusters. Thus, a stable array of 3D InAs islands on a GaAs (100) substrate exists only in some part of the 'arsenic overpressure ± substrate temperature' phase diagram as is demonstrated also for MOCVD growth. When the surface density of the QDs is high, interaction of the islands via the substrate makes also their lateral ordering favourable. If strained InAs islands are covered with a thin GaAs layer, the islands in the second sheet are formed on top of the dots in the first sheet, resulting in a three-dimensional ordered array of QDs being either isolated or strongly vertically coupled as resolved by transmission electron microscopy and X-ray diffraction. The size and the shape of InAs islands can be changed by changing the deposition mode. Bright luminescence (300 K) from InGaAlAs QDs in (Al,Ga)As matrices can be tuned in the range 0.7-1.39 micro meter. Modification of the QDPL energy is also possible via post-growth annealing. Self-organization effects are also observed in the growth of  $\text{In}_x\text{Ga}_{1-2x}\text{As}$ , GaSb or InSb on (100). Growth GaAs shows the formation of large islands with a disk like shape, with a diameter too large to show clear QD effects. Since the first presentation of a photo pumped lasing in self-organized QDs obtained using molecular beam epitaxy (MBE) and, soon after, an injection laser, efforts were undertaken to decrease the threshold current density to its ultimate limit determined by the transparency condition for the dot states. For this purpose one has to increase the internal efficiency of irradiative recombination and the carrier capture rate into the dots. This was considered to be the most serious limitation for QD lasers. However, soon after the first realization of lasers based on self-organized QDs in 1994, the threshold density was dramatically decreased and currently no fundamental obstacle for using QDs for lasers can be foreseen. [Ref: 11,12]

➤ **Temperature dependence of threshold energy:**

[QD lasers are not as temperature dependent as traditional semiconductor lasers. This theory was utilized by applications and in 2004; temperature-independent QD lasers were invented in Fujitsu Laboratories.](#)

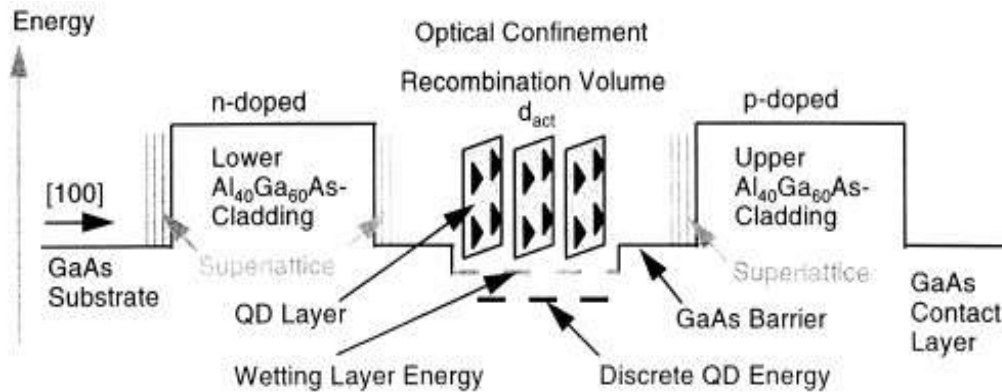
A non-equilibrium distribution of carriers between all dots in a dot-ensemble should prohibit thermal broadening of the gain spectrum. If this condition is strictly fulfilled, the peak gain should remain constant as a function of temperature (T) at constant injection level. An enhancement of T due to carrier confinement was reported for bulk lasers (As mentioned in development of QD laser at point no:2.d) placed in a magnetic field. Then a dramatic increase of T for a true single layer QD laser up to 425 K was reported in the latter structure, however, the breakdown of the non-equilibrium carrier distribution and the temperature dependent current leakage reduces the value of T at temperatures above 100 K. The carriers in the dots are thermally coupled to the WL (wetting layer) and the GaAs barrier, one can expect two loss mechanisms. First of all, with increasing temperature, the injected carriers start to populate the barrier states due to thermal coupling, thus increasing the injection current to maintain the threshold gain of the QD laser. Secondly, non-radiative recombination in the barrier might increase current leakage. This leakage current is related to the quality of the epitaxial barrier layer (in particular the low temperature GaAs) and does not present a principal limitation of the threshold current the differential internal efficiency of a single layer QD laser was originally about 40%. This value was improved to 50% by introducing multi layer QD structures. For a  $\text{In}_{0.5}\text{Ga}_{0.5}\text{As}/\text{GaAs}$  and  $\text{In}_{0.3}\text{Ga}_{0.7}\text{As}/\text{GaAs}$  QD laser the value is almost 70% and 81% respectively. [Ref: 8]

**Figure 4:** stimulated recombination of electron-hole pairs takes place in the GaAs quantum well region, where the confinement of carriers and the confinement of the optical mode enhance the interaction between carriers and radiation.[1]



➤ **Electronic spectrum:**

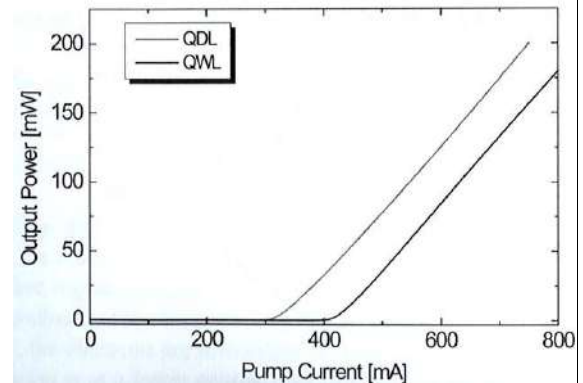
Experimentally observed energy levels for electrons and holes agree with theoretical calculations based solely on the QD geometry derived by HRTEM images. Remarkable property of a QD is a narrow (FWHM, 0.1 meV) atomic like luminescence line, which does not show broadening with temperature, directly manifesting formation of an electronic QD. The transparency condition in a QD with a two-fold degenerate electron and whole ground state is reached when it captures one exciton. Then, the probability to emit or to absorb light is equal. This statement is correct if the separation between exciton and biexciton energy levels is smaller than the inhomogeneous broadening. If this separation is larger, a QD occupied by an exciton cannot absorb a second photon having the exciton-energy but will show stimulated emission. Thus, in this case, which is, e.g. realized in II-VI materials, finite gain appears also for single excitons. Increase in the excitation density results in saturation of QD excitonic gain followed by its decrease, due to the larger fraction of QDs filled with biexcitons. On the other hand, biexciton absorption first increases and then drops to zero and converts to gain, when most of the QDs become populated with two electron-hole pairs. Charged excitons and biexcitons provide finite gain since ground state absorption is no longer possible. If there is no transport between QDs (particularly at low temperatures) the population of QDs with electrons, holes and excitons is defined by the capture and recombination probabilities and is not a function of temperature. The gain-current relation depends on the capture mechanism, whether electrons and holes are captured in a correlated or uncorrelated manner. We note that there combination current is not simply given by the product of electron and hole density. At high temperatures, thermal evaporation of carriers from dots may result in the predominant population of deeper QDs and in a negative  $T_0$  value. The gain behaviour is different in these cases: the gain maximum keeps its maximum energy with excitation density in the first case while it shifts to higher photon energies in the second. [Ref: 8]



**Fig: 5** Schematic band structure of a quantum dot laser with self-organized dots under forward bias. A 3D array of dots vertically aligned along the growth direction, which is formed during the growth, of multiple QD layers is illustrated schematically. Typically the dot area density in the (100) plane is  $4 \times 10^{10} \text{ cm}^{-2}$  and the dot size distribution is around 10%. The distance between the dot layers is 5 nm and the real dot density in the recombination volume with a thickness of 200 nm is  $6 \times 10^{15} \text{ cm}^{-3}$  for three QD layers.

In order for QD lasers compete with QW lasers, two major issues have to be addressed:

- A large array of QDs has to be used because their active volume is very small. An array of QDs with a narrow size distribution has to be produced to reduce inhomogeneous broadening. Furthermore, that array has to be without defects that degrade the optical emission by providing alternate nonradiative defect channels.
- The phonon bottleneck created by confinement limits the number of states that are efficiently coupled by phonons due to energy conservation. Therefore, it also limits the relaxation of excited carriers into lasing states. This bottleneck causes degradation of stimulated emission (Benisty et al., 1991). However, other mechanisms can be used to suppress that bottleneck effect. (e.g. Auger interactions) [Ref: 3, 11, 13]



**Figure: 6 – comparison of efficiency between a QWL and a QDL**

## 4. Construction Of laser

### 4.1 Optical cavity [Ref: 9,14]

Lasing action is similar to LED emission, but there are some additional device structures that need to be incorporated. The main requirement for an LED is that one side of the device should have transparent conductors and the other side should be reflecting so that the light can be extracted from one side. In lasers, the intensity of the emitted radiation should be high. To build up intensity, optical cavities are used where light is bounced back and forth to develop the high intensity. A schematic of an optical cavity is shown in **figure 8**. An optical cavity or optical resonator has two reflecting mirrors. One of the mirrors is made totally reflecting, while the other side is partially reflective, so that radiation is emitted from the other side. Typical resonators are called Fabry-Perot resonators **fig: 7**, which consist of smooth parallel walls perpendicular to the junction. The optical resonators are so placed that the distance between them (L) is related to the wavelength of the emitted laser( $\lambda$ ), given by

$$L = m \frac{\lambda}{\eta} \dots\dots\dots (6)$$

m is an integer and  $\eta$  is the refractive index of the lasing medium. Typically, L is much larger than  $\lambda$ . The Fabry Perot cavity laser device arrangement is shown in figure 11. [Ref: 9, 14]

R1 and R2 are the reflectivity of the two mirrors. Lasing occurs when the gain due to emission (g) is greater than the loss due to absorption ( $\alpha$ ). The net gain for this system, as a function of distance within the cavity, is written as

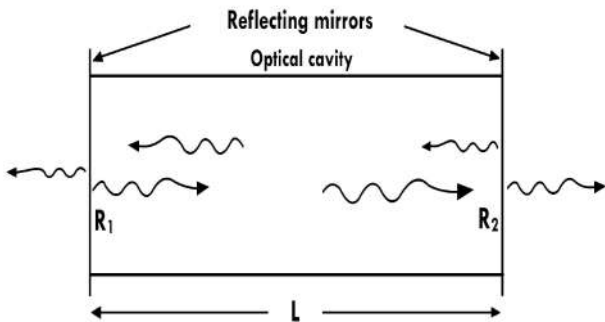
$$\phi(z) = R_1 R_2 \exp [(g - \alpha) z] \dots\dots\dots (7)$$

For the arrangement shown in figure 5 the total path length is 2L. So then net gain occurs when

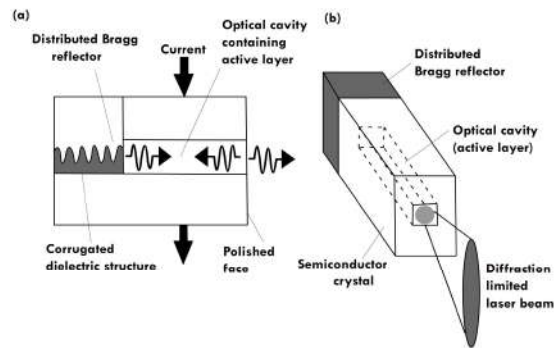
$$\phi(z) = R_1 R_2 \exp [(g - \alpha) z] > 1 \dots\dots\dots (8)$$

It is possible to define an threshold gain for lasing as

$$g_{th} = \alpha + \frac{1}{2L} \ln \left( \frac{1}{R_1 R_2} \right) \dots\dots\dots (9)$$



**Fig: 7** Fabry-Perot cavity for lasing action. The two surfaces have reflectivity R1 and R2, with transmission coefficient equal to 1- R. If R1 > R2, then light will be emitted from the second surface and vice versa. Adapted from Physics of semiconductor devices - S.M. size.



**Figure 8:** Schematic of the laser optical cavity (a) Side view (b) Front view.

The optical cavity is located at the centre of the device. Carriers are injected into the centre to create population inversion and stimulated emission. The laser light generated is built up in this layer, before it is finally emitted.

Higher the values of reflectivity smaller are the threshold gain required for lasing action. Similarly, lower the losses due to absorption, smaller is the threshold gain for lasing.

**4.2 Wave guiding [Ref:9]**

The optical cavity helps in building up the laser intensity but it also important to confine the beam within the lasing medium i.e. the beam must be confined in the direction parallel to the light propagation. This is done by wave guiding and it makes use of the concept of total internal reflection. The wave guiding arrangement for a double hetero junction based laser is shown in **figure 9**. The active region is the GaAs region which is confined between two AlGaAs regions. The higher band gap AlGaAs regions serve to confine the charge carriers within the GaAs region and increase recombination efficiency. This is similar to the band structure in a double hetero-junction LED. Also, the refractive indices of the materials are such that the AlGaAs regions also confine the emitted radiation within the active region. Let  $n_{r1}$ ,  $n_{r2}$ , and  $n_{r3}$  be the refractive indices of the AlGaAs, GaAs, and AlGaAs layer respectively, from **figure 10**. The the condition for total internal reflection in the active region is that

$$n_{r2} > n_{r1} \ \& \ n_{r3}$$

The band gap ( $E_g$ ) and refractive index ( $n_r$ ) of AlGaAs (formula  $Al_xGa_{1-x}As$ ) depends on the value of  $x$  and is given by

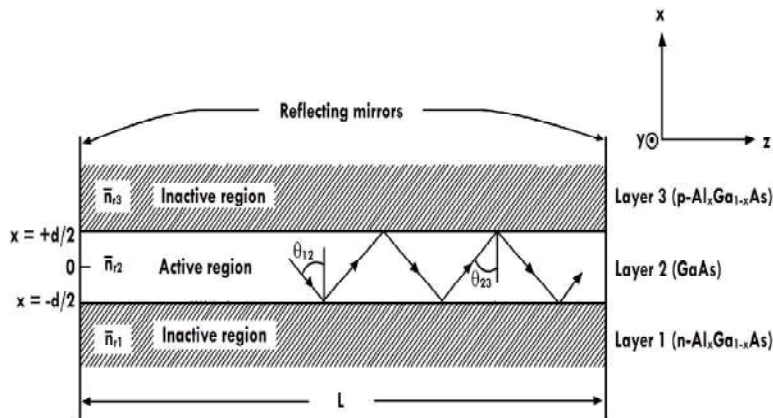
$$E_g = 1.42 + 1.247X \dots\dots\dots (10)$$

$$n_r = 3.590 - 0.710X - 0.091X^2 \dots\dots\dots (11)$$

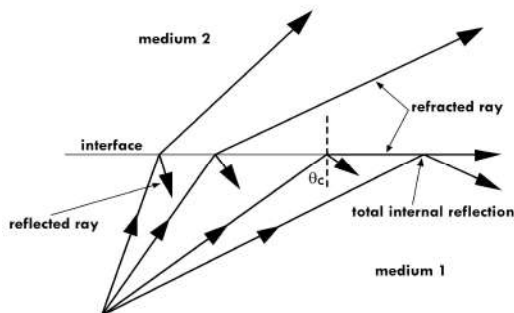
The AlGaAs performs the dual role of band gap engineering (as in LEDs) and also optical engineering. For a value of  $x = 0.3$ ,  $E_g$  is 1.8 eV and  $n_r$  is 3.38. This is lower than the refractive index of GaAs, which is 3.59. It is possible to calculate a critical angle for total internal reflection ( $\theta_c$ ), with respect to the normal to the interface, as shown in figure 7. This is given by

$$\theta_c = \sin^{-1} \left( \frac{n_2}{n_1} \right) \dots\dots\dots (12)$$

Below  $\theta_c$ , only partial reflection occurs, while above  $\theta_c$  there is total internal reflection. For  $x = 0.3$ , this critical angle is  $70.3^\circ$  with increasing  $x$ ,  $n_2$  reduces even further and the value of  $\theta_c$  reduces. Also, increasing  $x$  increases band gap and carrier confinement. Hence, these two effects go together in improving lasing efficiency.



**Figure 9 :**Wave guiding in a hetero-junction laser. The beam is confined to the active GaAs region by total internal reflection at the GaAs-AlGaAs layer. This is because the refractive index of the GaAs is higher than AlGaAs.



**Figure 10:** Critical angle for total internal reflection when light passes from a medium with higher refractive index to one with a lower refractive index. At angles above the critical angle, total internal reflection occurs, while refraction occurs for lower angles.



### 4.3 Quantum Dot Gain Simulator:

Gain is very important information when working with lasers. And it is the light produced by stimulated emission and we need energy source to sustain the gain. Moreover gain happens inside the laser cavity [9]. Quantum-dot (QD) lasers that exhibit broad gain bandwidths and ultrafast carrier dynamics represent compact sources for the generation of ultra short pulses. A model of the gain and threshold current density of a semiconductor quantum dot (QD) laser has been developed. Optimization of the structure has been carried out, aimed at minimizing the threshold current density. Expression for the gain is as follows:

$$g = g^{stat} [1 - \exp \{-\frac{\gamma(j-j_0)}{j_0}\}] \dots \dots \dots (13)$$

Where,  $j_0, \gamma$  factor and  $g^{stat}$  are, respectively, the transparency current density, an additional gain parameter that must be of the order unity in a real QD array and the saturation gain level.

#### o Kinetic Equations:

- **Multimode rate equations:** In the multimode formulation, the rate equations model a laser with multiple optical modes. This formulation requires one equation for the carrier density, and one equation for the photon density in each of the optical cavity modes: [Ref: 1]

$$\begin{aligned} \frac{dN}{dt} &= \frac{I}{eV} - \frac{N}{\tau_n} - \sum_{\mu=1}^{\mu=M} \Gamma_{\mu} G_{\mu} P_{\mu} \\ \frac{dP_{\mu}}{dt} &= (\Gamma_{\mu} G_{\mu} - \frac{1}{\tau_p}) P_{\mu} + \beta_{\mu} \frac{N}{\tau_r} \end{aligned} \quad (14)$$

- o where: N is the carrier density, P is the photon density, I is the applied current, e is the elementary charge, V is the volume of the active region,  $\tau_n$  is the carrier lifetime, G is the gain coefficient ( $s^{-1}$ ),  $\Gamma$  is the confinement factor,  $\tau_p$  is the photon lifetime,  $\beta$  is the spontaneous emission factor,  $\tau_r$  is the radiative recombination time constant, M is the number of modes modelled,  $\mu$  is the mode number, and subscript  $\mu$  has been added to G,  $\Gamma$ , and  $\beta$  to indicate these properties may vary for the different modes.
- o The first term on the right side of the carrier rate equation is the injected electrons rate ( $I/eV$ ), the second term is the carrier depletion rate due to all recombination processes (described by the decay time  $\tau_n$ ) and the third term is the carrier depletion due to stimulated recombination, which is proportional to the photon density and medium gain. In the photon density rate equation, the first term  $\Gamma GP$  is the rate at which photon density increases due to stimulated emission (the same term in carrier rate equation, with positive sign and multiplied for the confinement factor  $\Gamma$ ), the second term is the rate at which photons leave the cavity, for internal absorption or exiting the mirrors, expressed via the decay time constant  $\tau_n$  and the third term is the contribution of spontaneous emission from the carrier radiative recombination into the laser mode. [Ref:14]

**The Modal Gain:**  $G_{\mu}$ , the gain of the  $\mu^{th}$  mode, can be modelled by a parabolic dependence of gain on wavelength as follows:

$$G_{\mu} = \frac{\alpha N [1 - (2 \frac{\lambda(t) - \lambda_{\mu}}{\delta \lambda_g})^2] - \alpha N_0}{1 + \epsilon \sum_{\mu=1}^{\mu=M} P_{\mu}} \quad (15)$$

Where:  $\alpha$  is the gain coefficient and  $\epsilon$  is the gain compression factor (see below).  $\lambda_{\mu}$  is the wavelength of the  $\mu^{\text{th}}$  mode,  $\delta\lambda_g$  is the full width at half maximum (FWHM) of the gain curve, the centre of which is given by:

$$\lambda(t) = \lambda_0 + \frac{k(N_{th} - N(t))}{N_{th}} \quad (16)$$

Where  $\lambda_0$  is the centre wavelength for  $N = N_{th}$  and  $k$  is the spectral shift constant (see below).  $N_{th}$  is the carrier density at threshold and is given by:

$$N_{th} = N_{tr} + \frac{1}{\alpha\tau_p\Gamma} \quad (17)$$

Where  $\beta_0$  is the spontaneous emission factor,  $\lambda_s$  is the centre wavelength for spontaneous emission and  $\delta\lambda_s$  is the spontaneous emission FWHM. Finally,  $\lambda_{\mu}$  is the wavelength of the  $\mu^{\text{th}}$  mode and is given by:

$$\lambda_{\mu} = \lambda_0 - \mu\delta\lambda + \frac{(n-1)\delta\lambda}{2} \quad (18)$$

Where  $\delta\lambda$  is the mode of spacing.

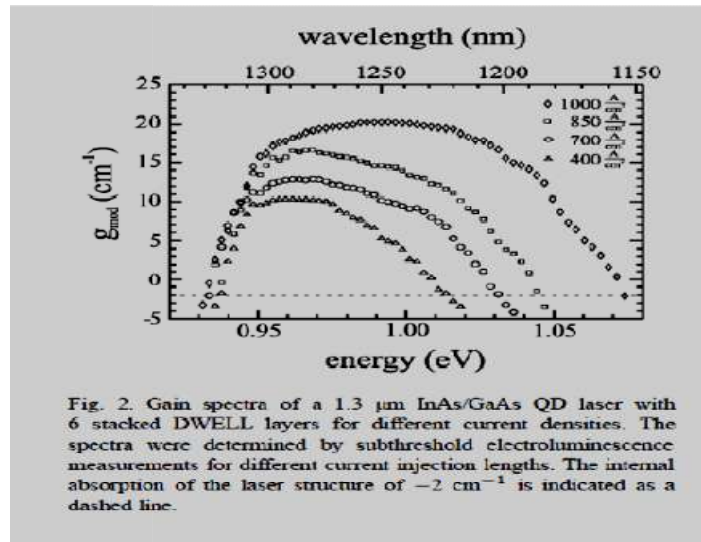


Fig:11, Ref: Recent advances in semiconductor quantum-dot lasers  
Johann Peter Reithmaier , Alfred Forchel

The gain term,  $G$ , cannot be independent of the high power densities found in semiconductor laser diodes. There are several phenomena which cause the gain to 'compress' which are dependent upon optical power. The two main phenomena are [spatial hole burning](#) and [spectral hole burning](#). To account for gain compression due to the high power densities in semiconductor lasers, the gain equation is modified such that it becomes related to the inverse of the optical power. Hence, the following term in the denominator of the following gain equation:

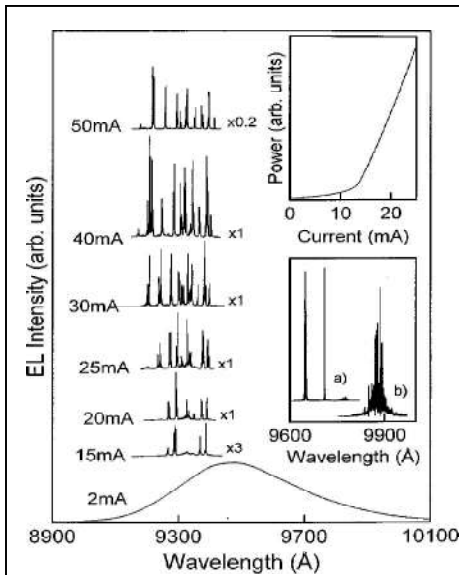
$$1 + \epsilon \sum_{\mu=1}^{\mu=M} P_{\mu} \quad (19)$$

- **Spectral Shift:** A complete analysis of spectral shift during direct modulation found that the refractive index of the active region varies proportionally to carrier density and hence the wavelength varies proportionally to injected current.

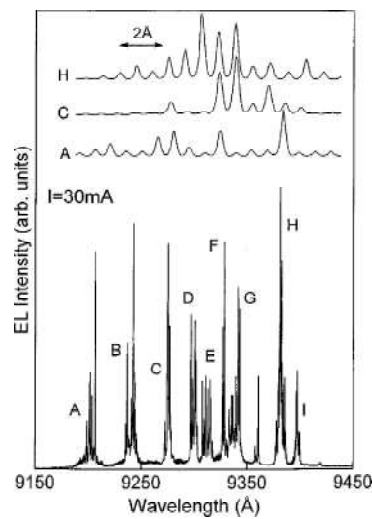
$$\delta\lambda = k \left( \sqrt{\frac{I_0}{I_{th}}} - 1 \right) \quad (20)$$

### ➤ Optical Quality Change in Output light: InAs/GaAs self-organized quantum dot lasers

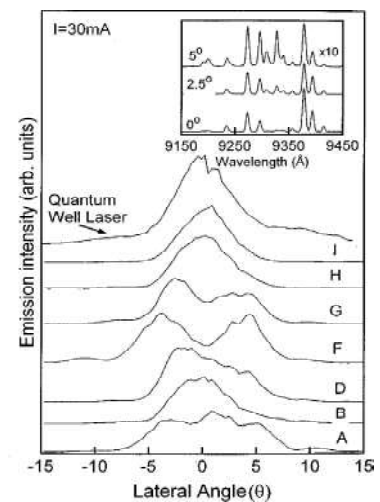
- In contrast to conventional bulk or quantum well lasers, physical processes in QD lasers are expected to be considerably modified. Carriers localized in different dots may be unable to interact directly, resulting in a system without a global Fermi function and exhibiting a non-homogeneously broadened gain spectrum.
- A QD laser may therefore behave as a collection of quasi-independent lasers with important consequences for device characteristics, including the form of the lasing spectra; the subject of this letter.
- The laser device consists of ten layers of InAs self-organized QDs grown in a GaAs matrix.<sup>4</sup> The dot layers are separated by 250 Å of GaAs, resulting in electronically uncoupled dots<sup>5</sup> and hence a true zero-dimensional system. The ten dot layers are confined by 1000 Å of GaAs followed by *n*- and *p*-type doped Al<sub>0.6</sub>Ga<sub>0.4</sub>As cladding layers of which the initial 1000 Å is undoped. SiN coated ridge devices of width 5–25 mm were fabricated using standard techniques.
- High resolution optical spectra at 77 K were recorded using a double grating 0.85 m spectrometer and a liquid nitrogen cooled Ge-*p-i-n* photodiode.[10]



12. a



12. b



12. c

- **Fig 12.a)** Emission spectra recorded as a function of current for a 2 mm 315mm cavity QD laser device. The upper inset shows the  $L$  vs  $I$  characteristic of the device. The lower inset compares lasing spectra of a QD ( $J52.2JTH$ ) and a QW, both with a 0.5 mm 320 mm cavity ~the QD spectrum has been shifted by 1600 Å for ease of display.
- **Fig. 12.b).** High resolution emission spectrum of the QD laser for 1530 mA. The upper three traces are expanded spectra of mode groups  $A$ ,  $C$ , and  $H$ .
- **Fig. 12.c).** Far-field lateral mode patterns obtained by scanning the tip of an optical fibre in the junction plane. Each pattern corresponds to analysis of the emitted light at the centre wavelength ~bandwidth 4.5 Å! of a given mode group as indicated in Fig.12.b. The uppermost curve is for the QW laser. The inset shows QD laser emission spectra recorded for different angular positions of the optical fibre.
- The far-field patterns demonstrate that the spectrally separated groups of longitudinal modes correspond to different lateral intensity profiles although, in general, more than one group of modes exhibits the same far-field pattern. The angular width of the single peak patterns (e.g., the QW laser, QD profiles  $I$  and  $H$ ) is consistent with a value obtained from the Fourier transform of the fundamental lateral mode, indicating that the far-field patterns correspond to true lateral modes of the cavity. The inset to Fig. 15.c shows emission spectra recorded as a function of angle in the junction plane. Although the low spectral resolution does not allow the observation of individual longitudinal modes, the spectra clearly show the different angular dependencies of the various groups of modes.
- Higher order lateral modes are observed at high injection currents in conventional lasers where inhibited carrier diffusion, due to the stimulated emission reduction of the carrier lifetime, results in spatial hole burning. The energy extraction efficiency of the fundamental mode is reduced and lasing occurs via higher order modes which have a different spatial profile. In a QD laser in-plane carrier diffusion will be severely inhibited for all currents by the rapid dot carrier capture which occurs on a time scale of 30 ps. The observed modal behaviour of the QD laser can be explained assuming a dot carrier capture rate which decreases as the dot carrier population increases. Lasing dots, which will on average have a lower population than non lasing dots, will act as a local trap for injected carriers resulting in an effective depletion of carriers following the profile of the corresponding lateral mode. Because of this spatial depletion, additional groups of dots which subsequently reach threshold lase via different lateral modes.

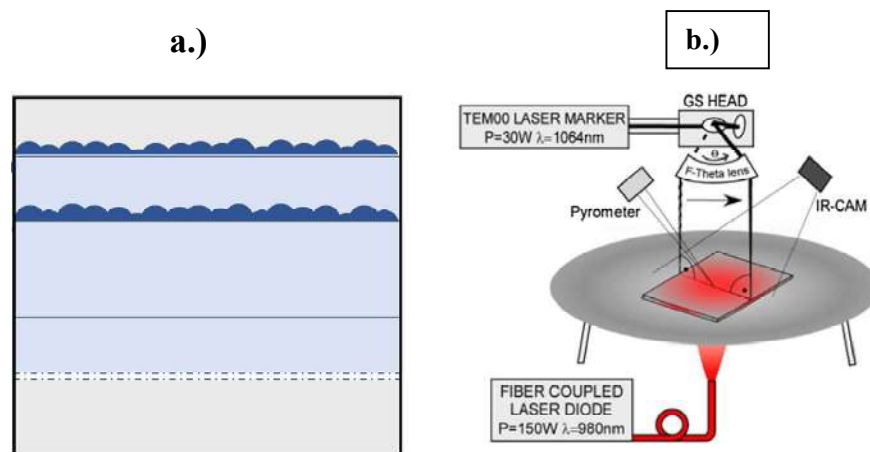
## 5. Experiment

- **Precision tuning of InAs quantum dot emission wavelength by iterative laser annealing:**

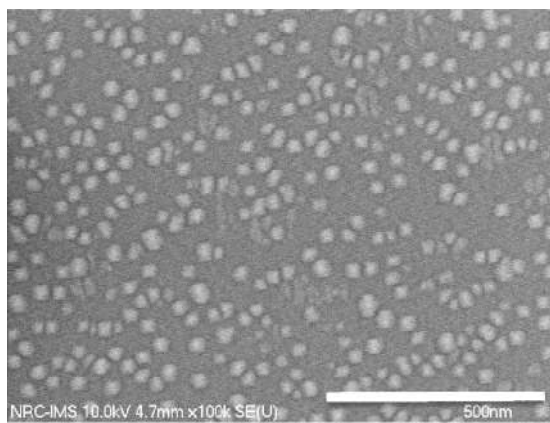
- **[Ref: 15]**

- The QD microstructure (sample 02-161A) used in this study was grown on an S-doped ( $1 \times 10^{-18} \text{ cm}^{-3}$ ) InP (0 0 1) wafer using chemical beam epitaxy A 3.3 monolayer (ML) thick InAs was grown on a 230 nm thick InP buffer to form the QDs. This was capped with a 150 nm InP layer and a further 3.3 ML of InAs to form QDs on the surface of the wafer. The surface dots were examined using scanning electron microscopy to provide an indication of buried dot density. All growth was performed at a temperature of 510°C .
- A 20mm× 10 mm sample was cleaved from the 2-inch diameter wafer and its back and front surfaces were coated, respectively, with 500 and 50 nm thick SiO<sub>2</sub> films to prevent material decomposition during high-temperature annealing. A cross-section view of the investigated QD microstructure is shown in **Fig 13.a)** before annealing, the sample was cleaned sequentially with Opticlear, acetone, and isopropyl alcohol and rinsed with deionised water.
- The laser annealing setup is shown schematically in **Fig.13.)b**. It includes a 150W 980 nm fibre-coupled laser diode (LD) designed for irradiation of the backside of the sample. The irradiation increases the temperature of a 10 mm diameter spot to a maximum of 500°C, which is below the threshold for intermixing of the investigated microstructure.
- Note that direct heating of a semiconductor wafer with LD, as opposed to using a conventional hot plate, allows rapid cooling of the wafer between processing steps. This is advantageous for rapid employment of photoluminescence (PL) diagnostics and, although not applied in the current experiment, it would also allow processing without the need of relocating the wafer between the laser and diagnostics stations.

- A closed loop system consisting of an IR camera coupled with the LD power supply was employed to provide a stable background temperature. The sample background temperature was monitored with a custom IR camera capable of collecting temperature maps at 10 Hz. By irradiating the front surface of the sample with a focused beam of a CW 1064 nm Nd:YAG laser operating in a TM00 mode, a series of high-temperature spots were created, one after another.
- The temperature of each spot was set at 700°C and measured with a Micron M680 infrared (IR) pyrometer collecting data from a 400 mm diameter area. The use of two laser sources allowed to avoid excessive heating of the sample with just the Nd:YAG laser and thus reduced the potential for damage of the sample surface.
- Room temperature PL measurements were carried out with a commercial mapper (Philips, PLM-150) at a step resolution of 10 mm. The emission from as-grown samples was observed in the range of 1495–1500 nm. With a 0.5 mm diameter Nd:YAG laser spot, the average diameter of the intermixing inducing spots was approximately 100 μm, which covered approximately 107 QDs.
- A visible range camera operating at 15 Hz recorded images of the sample, which allowed relocation to its original position each time it was removed for collecting PL measurements. An image recognition procedure was employed to identify the position of individual spots. The computer-based procedure employed a Lab-VIEW interface, which allowed the precision of spatial and rotational positioning of samples to within ±5 mm and 0.05 deg, respectively



**Fig. 13:** Cross-section view of the QD microstructure (a) investigated with the ILA technique that makes use of a laser diode (980 nm) and a CW Nd:YAG laser (1064 nm) for selective area annealing of a sample installed on a graphite plate (b).



**Fig. 14.** Scanning electron micrograph of the InAs/InP QD sample surface before any processing

## Results and discussion

Fig. 13 shows a scanning electron microscope image of the surface of the sample before any processing was performed. A surfacedensity of 320/mm<sup>2</sup> InAs dots was measured, typical for self assembled dot structure on InP. To investigate the effect of selective-area QD intermixing, we first fabricated two series of 3 spots annealed either for 30 or 15 sec. This produced spots emitting at 1483 nm (A1), 1478 nm (A2) and 1482 nm (A3) in the first series, and at 1485 nm (B1), 1492 nm (B2) and 1494 nm (B3) in the second series. The PL wavelength maps of a sample processed under these conditions are shown in Fig. 15a and c. At this point, the goal was to demonstrate the fabrication of spots emitting at 1475 nm in the first series, and at 1485 nm in the second series. This was achieved with 3 separate follow up steps, where individual spots were processed for empirically determined annealing times. For instance, a 3 nm blue shift of A1 from the initial 1483 nm was obtained following a 5s anneal

**Table 1**

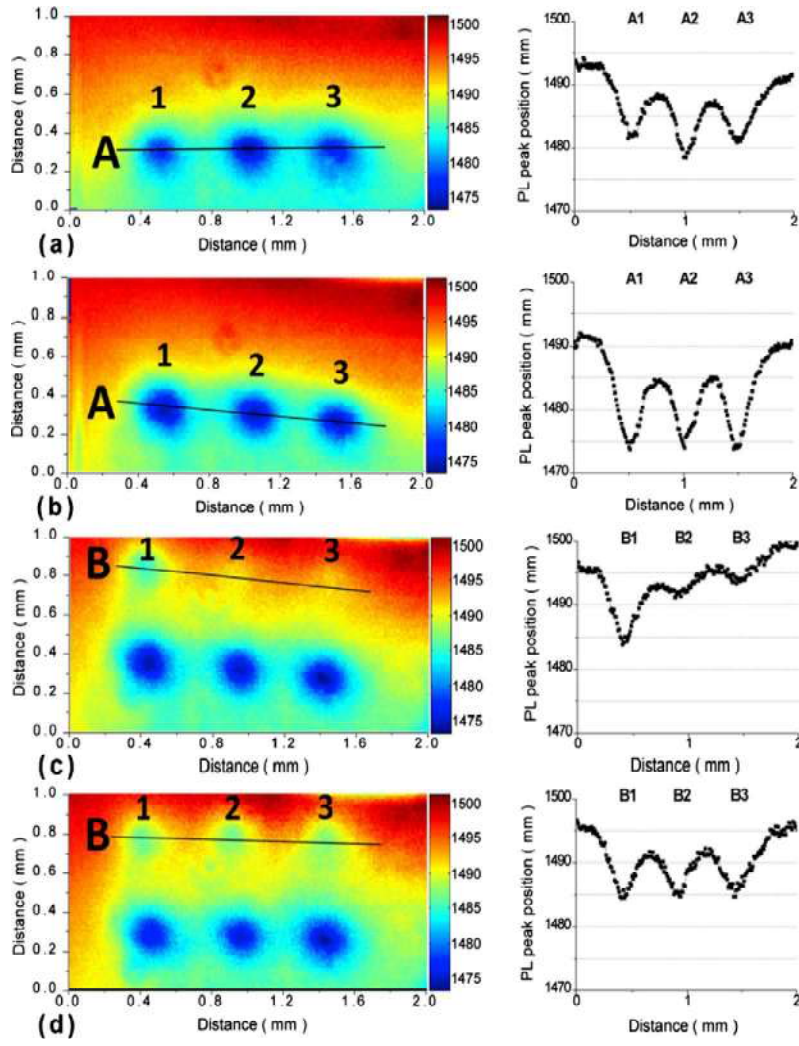
Details of the 4-step annealing procedure of two series of InAs QD sites carried out with the iterative laser annealing technique.

Site	Step 1 Time [s]	PL peak $\lambda$ [nm]	Step 2 Time [s]	PL peak $\lambda$ [nm]	Step 3 Time [s]	PL peak $\lambda$ [nm]	Step 4 Time [s]	PL peak $\lambda$ [nm]	Time Total [s]
A1	30	1483	5	1480	3	1477	2	1475	40.0
A2	30	1478	3	1477	2	1476	0.5	1475	35.5
A3	30	1482	7	1479	7	1475	0	1475	44.0
B1	15	1485	0	1485	0	1485	0	1485	15.0
B2	15	1492	16	1489	2	1488	2.5	1485	35.5
B3	15	1494	16	1491	2	1489	3.8	1485	36.8

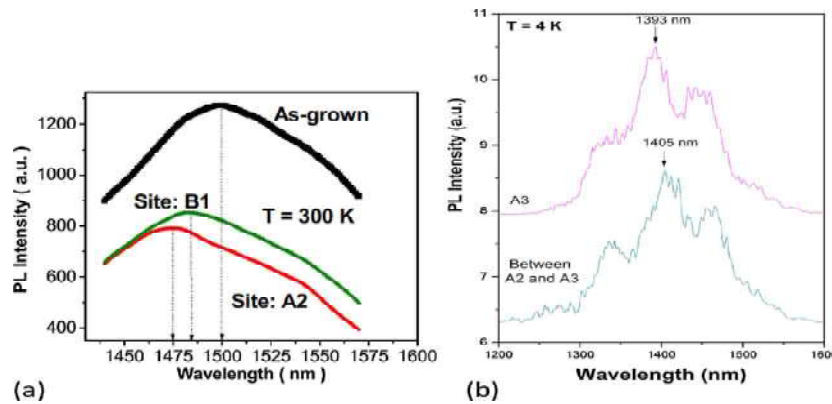
(Always at 700 °C), and additional 3 and 2 s anneals blue shifted the emission of that spot by a further 3 and 2 nm, respectively. This procedure allowed us to tune all the spots in this series to emit at 1475 nm, as illustrated in Fig. 15b. By applying a similar procedure, we fabricated a series of spots emitting at 1485 nm, as illustrated in Fig. 15d. Details of the annealing conditions and values of the most blue shifted wavelengths for processed spots are presented in Table 1. Note that a meaningful annealing at 0.5 s is feasible with this technique thanks to the simultaneous application of the LD and Nd:YAG laser for heating of the wafer.

Being able to carry out selective-area annealing is of practical importance for the development of a method capable of wafer level tuning of the QD emission. With the Nd:YAG laser delivering a 0.5 mm diameter spot, and driven by the requirement of interference-free annealing conditions, we have carried out processing of sites separated by 0.6 mm. The associated cross-section PL scans in Fig. 15 illustrate wavelength profiles of the QD intermixed material. It is noticeable that the processing of spots A1-A3 had relatively weak to negligible influence on the results of processing B1-B3. We estimate that with a Nd:YAG laser delivering a 20 mm diameter spot, this approach should allow the fabrication of at least 4000 individual regions per mm<sup>2</sup> emitting nominally at the same wavelength. Using selective-area growth techniques, each of these regions could be made to contain just a single QD, allowing our ILA technique to fabricate arrays of single QDs all emitting at nominally the same wavelength. Due to the large ratio of the QD diameter to its thickness, the main effect of the observed intermixing (band gap shifting) is due to diffusion in the growth direction. Previously, we discussed the amplitude of the ground state blue shifting as a function of the thickness of InAs QDs grown on GaAs, and we demonstrated that the intermixing leads to narrowing of the spectral emission from the intermixed material. The contour of PL scans characterizing each spot is determined by the profile of a laser-induced temperature, the number of different thickness QDs annealed within a spot and, ultimately, narrowing of the spectral emission of the intermixed material. For instance, a 3.8 times narrower emission from the ground state ( $E_1 = 1078$  nm) of InAs QDs on GaAs (001) blue shifted by 251 meV was observed by us previously. A similar effect, however, would be more difficult to observe in the current experiment due to the relatively small blue shift amplitudes. As illustrated by room-temperature PL spectra shown in Fig. 15a, following the 4-step ILA procedure, blue shift amplitudes of 14 and 8.3 meV have been induced between the as-grown material ( $k = 1500$  nm) and that fabricated in the centre of sites A2 ( $k_{\text{blue}} = 1475$  nm) and B1 ( $k_{\text{blue}} = 1485$  nm). The relatively large width of these spectra is the result of a dense population of self assembled QDs and a scatter in their height of the order of three monolayers. It can also be seen that PL intensity of the intermixed QDs is slightly reduced in comparison to that of the as-grown material. The source of this degradation is most likely related to the laser-induced modification of the structural and optical properties of the SiO<sub>2</sub> film employed for protecting the surface of annealed QDs. In addition to the increased surface roughness, densification of a laser annealed dielectric film is another parameter that could influence the PL signal. The effect of the PL intensity degradation after laser annealing requires detailed studies that

exceed the scope of this publication. **Fig. 15b** shows 4 K PL spectra of the InAs QD microstructures probed at site A3, and between sites A2 and A3 fabricated by the ILA technique. The three maxima observed in these plots indicate the presence of three families of InAs/InP islands where each family has a thickness strongly peaked around an integer number of monolayers. An approximate blue shift of 12 nm ( $\sim 7.5$  meV) has been observed in this case although this amplitude is more resolvable for the centre and low-energy maxima. A reduced intensity of the high-energy feature at  $k \sim 1330$  nm, following the annealing step, seems to be related to a reduced number of the family of thinner QDs contributing to the observed PL spectrum. It is worth mentioning that these observations are consistent with the results of intermixing InAs/InP QDs induced with conventional annealing techniques where the relatively small wavelength shifts, as observed here, correspond to small changes in dot morphology.



**Fig:15** Photoluminescence wavelength maps of a laser annealed QD sample at selective sites for 30 s (a) and 15 s (c), and following a series of ILA steps designed to fabricate QDs emitting at 1475 nm (b) and 1485 nm (d). Cross-section PL scans along the indicated black lines illustrate wavelength profiles of the QD intermixed material.



**Fig: 16** Room-temperature photoluminescence of as-grown InAs QDs and 15 nm (B1) and 25 nm (A2) blue shifted material (a), and low-temperature photoluminescence of InAs QD microstructures probed at site A3, and between sites A2 and A3 (b).

## 6. Practical Application of QD lasers: [Ref:16]

- **Large market anticipated for direct retinal imaging laser eyewearolution:**

A visible semiconductor laser module is installed in a pair of spectacles and is used to directly project images on to the retina of the wearer. Clinical trials are currently being conducted for this eye wear which will be used in the medical treatment for the vast number of low vision patients around the world. By using this laser eye wear those with poor eyesight will experience improvement in visibility in their everyday life. The global market for this laser eye wear is anticipated to reach about 150 billion yen by 2020.

- **World's longest single photon source quantum cryptography communication:**

A breakthrough achievement has been made in the development of quantum-key distribution through the telecommunication wave length band using a single photon source based on quantum dots. The world's longest Quantum key distribution – distance of 120 km has been reached, which will enable secure intercity communication. Laser beams are strongly attenuated to a pseudo single photon limit. However, when QDs are used ,high purity single photons can be generated .such single photon source quantum cryptography holds a key advantage in practical application and also the system operation and management.

- **Cancer cell treatment: Laser ablation process for Hyperthermia:**

Ball shaped nano shells or QDs with a non conducting core like silica coated with silver and gold nano materials are when injected into cancer affected area of the body. When it is concentrated with the cancer cells, a laser beam (NIR, i.e. Near Infrared Radiation) is illuminated to produce heat and destroy the heat sensitive cancer cells. It is called photo-thermal effect.

➤ **Future fabrication of Quantum Dot lasers:** The advantages of quantum dot based lasers compared to other conventional technologies have been realized for several years. Especially the free geometric parameters of quantum dot layers give probabilities to tailor the spectral gain profile applied to different types of QD lasers applications. Nevertheless, due to the intrinsic limitation of technologies, to realize quantum dot lasers with predicted properties met several difficulties. The requirement of further widening the parameters range in order to reducing the inhomogeneous line width broadening (we need homogeneous line width) is one of the aspects of developing quantum dot lasers. Using surface preparation technologies, lots of groups are working on the issue of further controlling the position and dot size for the self-organized technology. Once the developed methods can be implemented in the high density systems, the new technology will become the breakthrough in the history of quantum dot lasers development. Since the speed of carrier capture extremely increase the transport time and affects the modulation bandwidth, it is required to decouple the carrier capture from the escape procedure. Employing tunnel injections to quantum dots is a choice. Allowing the injection of cooled carriers, this method is able to achieve good performance without losing the extra carriers which often happens before due to the thermal relaxation. With the experiment done by comparing the QW lasers and QD lasers in term of raised gain at the fundamental transition energy with the constant broad band characteristics of quantum dot lasers, it is concluded the combination use of quantum dot and quantum well would tailor the material properties in a much wider range than using quantum dots or quantum wells alone. With the employment of further control of parameters and better



coupling technology and the breakthroughs which are already done, realizing quantum dot lasers as well as other quantum dot optoelectronic devices in commercial market is not so far away. [17]

## **7. Conclusion:**

In summary, quantum dot lasers enable substantial performance improvements over quantum well devices due to their unique atom-like energy level structure properties that can be finely tuned by changing growth conditions. Their discrete density of states and in homogeneously broadened gain lead to lasers with low threshold, high continuous wave operating temperature, ultrahigh stability against optical feedback, and ultrafast gain recovery. Each of these concepts has been experimentally demonstrated, and due to the reduced sensitivity of quantum dots to crystalline defects, their advantageous properties are also starting to be shown for epitaxially integrated lasers on silicon, enabling significant improvements in manufacturing scalability.

## **8. References:**

1. Evident Technologies, “*How Quantum Dots Work*”.
2. An introduction to nano materials and nano science. (Ashim K. Das & Mahua Das.)
3. A Review of High-Performance Quantum Dot Lasers on Silicon (IEEE JOURNAL OF QUANTUM ELECTRONICS, VOL. 55, NO. 2, APRIL 2019)
4. An introduction to self-assembled quantum dots.
5. Molecularbeam epitaxy growth of quantum dots from strained coherent uniform islands of InGaAs on GaAs D. Leonard, M. Krishnamurthy, S. Fafard, J. L. Merz, and P. M. Petroff
6. Effect of Monolayer Thickness Fluctuations on Coherent Exciton Coupling in Single Quantum Wells
7. Quantum Dot Lasers: Lecture in Modern Optics by Björn Agnarsson
8. Quantum dot lasers: breakthrough in optoelectronics  
D. Bimberg, M. Grundmanna, F. Heinrichsdorffa, N.N. Ledentsov, c, V.M. Ustinov, A.E. Zhukov, A.R. Kovsh, M.V. Maximov, Y.M. Shernyakov, B.V. Volovik, A.F. Tsatsul'nikov, P.S. Kop'ev, Zh.I. Alferov
9. Solid state semiconductor LASERS
10. Emission spectra and mode structure of InAs/GaAs self-organized quantum dot lasers  
L. Harris, D. J. Mowbray, M. S. Skolnick, M. Hopkinson, and G. Hill,
11. Quantum-Dot Lasers: Physics and Applications  
P. M. Snowton (School of Physics and Astronomy, Cardiff University, Queens Buildings, The Parade, Cardiff, CF24 3AA U.K. )
12. Quantum dot optoelectronic devices: lasers, photo detectors and solar cells
13. Directly Modulated Single-Mode Tunable Quantum Dot Lasers at 1.3  $\mu\text{m}$   
Yating Wan, Sen Zhang, Justin C. Norman, MJ Kennedy, William He, Yeyu Tong, Chen Shang, Jian-Jun He, Hon Ki Tsang, Arthur C. Gossard, and John E. Bowers.(2015)
14. Dynamics of quantum dot lasers subject to optical feedback and external optical injection  
(vorgelegt von, Diplom-Physiker, Christian Otto aus Wuppertal)
15. Precision tuning of InAs quantum dot emission wavelength by iterative laser annealing  
Jan J. Dubowski , Radoslaw Stanowski , Dan Dalacu , Philip J. Poole
16. Pipelining innovation developed around quantum dots: putting Quantum dot lasers to practical use by Yasuhiko Arakawa.
17. Perspective: The future of quantum dot photonic integrated circuits  
(Cite as: APL Photonics 3, 030901 (2018);

**18. Theoretical Characteristics of Quantum Dot Laser through Modelling (M. B. El\_Mashade Engineering Dept., NRC, AL Azhar University Cairo, )**

**ACKNOWLEDGEMENT**

I take this opportunity to express my sincere gratitude to the entire Physical Chemistry faculty of Scottish Church College, Kolkata.

Special thanks to my mentor Prof. Rana Sen, Our beloved teacher Dr. Susmita Kar, and Dr. Aniruddha Ganguly, respected Prof. Dulal Chandra Mukherjee, Prof. Priyatosh Dutta, who helped me in my every footstep of this journey.

I also want to recall the names of Dr. Soma Gorai, Dr. Surajit Jana and Dr. Tapan kumar Si (of Kazi Najrul University) who encouraged me every time. How I can forget my dearest friends, Sumanna, Rohini, Susmita, Shramana and Sayan. Without their support, I won't be able to do this work perfectly.

**DIOXYGEN ACTIVATION BY**  
**NONHEME IRON ENZYMES AND MODELS**

**SCOTTISH CHURCH COLLEGE**

**UNIVERSITY OF CALCUTTA**

UNIVERSITY ROLL NO: 223/CEM/191021

REGISTRATION NO: 012-1124-2090-16

SPECIAL PAPER: SI 44

NAME OF THE CANDIDATE

NILAY PUSTI

NAME OF THE SUPERVISOR

Dr. PARTHA HALDER

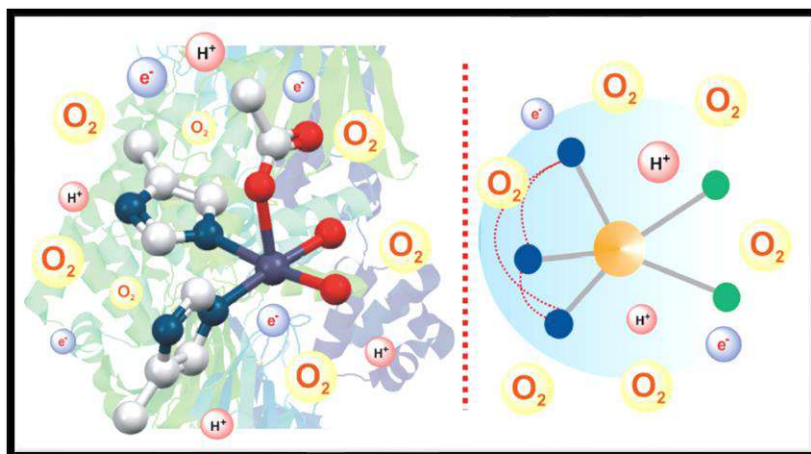


SIGNATURE OF THE CANDIDATE



SIGNATURE OF THE SUPERVISOR

# DIOXYGEN ACTIVATION BY NONHEME IRON ENZYMES AND MODELS



**NILAY PUSTI**

UNIVERSITY ROLL NO: 223/CEM/191021

REGISTRATION NO: 012-1124-2090-16

PROJECT WORK ACCOMPLISHED IN PARTIAL  
FULFILMENT OF M.Sc. (CHEMISTRY) DEGREE OF  
THE UNIVERSITY OF CALCUTTA UNDER SCOTTISH  
CHURCH COLLEGE, KOLKATA, 2021.

## SELF DECLARATION

This review work has accomplished by the undersigned under supervision of Dr. Partha Halder, Assistant Professor of Scottish Church College, Kolkata during 4<sup>th</sup> and final semester (Apr-July 2021) in partial fulfillment of M.Sc. (Chemistry) degree of the University of Calcutta under Scottish Church College, Kolkata.

I hereby declare that the work is done by me and it is fundamental and not submitted anywhere before for publication or any other purpose.



-----  
Signature of the Student

University Roll No: 223/CEM/191021

University Registration No: 012-1124-2090-16

College Roll No: 19PG-C-25

Scottish Church College, Kolkata

July, 2021



Counter Signature of Guide

## Table of Contents

---

---

Preface -----	04
Acknowledgment-----	05
Abstract-----	06
Introduction-----	06
Function of Dioxygen-----	07
Why Dioxygen needs to be activated-----	07
Nature's strategy for Dioxygen activation-----	08
Specific selectivity of Iron-----	08
Category of Iron Enzymes-----	09
Heme Oxygenase-----	09
Non heme Oxygenase-----	10
2-His-1- carboxylate: General aspects-----	11
Enzyme Group-----	12
Versatile oxidation reaction by nonheme oxygenease-----	12
Reactive Intermediates-----	13-14
Rieske Dioxygenase-----	15-17
Biomimetic Approach-----	18-19
Nucleophilic Iron Oxidant-----	20-22
Results and Discussion-----	22
Dioxygen Reactivity-----	22-24
Interception of the Active Oxidant with Thioanisole-----	25-27
Interception of the Active Oxidant with Alkanes-----	28-29
Proposed Mechanism-----	30
Experimental Section-----	31
Iron-oxygen Intermediate in model Complex-----	32-34
Role of Lewis acidic metal ion-----	35
Conclusion-----	36
References-----	36

## PREFACE

---

I am very happy to get this wonderful opportunity to do the review article on the topic “Dioxygen activation by Nonheme Iron enzymes and models”. It is a new kind of job I have done for first time. I have gained different experiences in this review work; I would cover fundamental aspects like Function of Dioxygen, why Dioxygen needs to be activated, the strategy of nature’s Dioxygen activation for serving the purpose and very interestingly how nonheme oxygenases enzymes activates Dioxygen and incorporated Dioxygen in various catalytic reaction.

Also I have somewhat understood how chemists are trying to mimic nature’s strategy. In the biomimetic approach for the reductive activation of  $O_2$ , and many modeling studies for developing variety of iron-oxygen oxidants from  $O_2$  in presence of sacrificial reductants.

And I have found different reaction intermediates where high oxidation states of Iron center is shown and well described by many experimental results.

Finally I have gone through many research papers on the topic so I studied new things which enriched my knowledge.

## Acknowledgement

---

I would like to express my gratitude to **Dr. Partha Halder** for providing his valuable time and inputs without which the completion of this project would not have been possible. I am extremely thankful to him not only for his valuable assistance but also for his moral support which motivated me every time to complete this project.

I would like to thank my friends and classmates for their help and support during the making of this project in the stipulated time frame.

I would like to thank my parents for giving me encourage and providing me all sufficient resources which were needed for the successful completion of this project.

Lastly, I would like to thank Chemistry Department of Scottish Church College as well as other teachers for giving us a positive support always to successfully carry out the steps required for moving forward.

Finally, I bow down to the **Supremacy** with all my sincere gratitude to thank Him for everything.



## **Abstract:**

---

Nature always prefers iron containing metalloenzymes for biological transformation. Recent days nonheme iron enzymes are received more attention for recent availability of different crystal structure of different enzymes, so 2-Histidine-1-Carboxylate facial triad motif a new structural motif for activation of dioxygen.

Iron-Oxygen Oxidant catalyses various types of reaction most common oxyfunctionalization of hydrocarbons, cis-dihydroxylation. So active site non heme iron enzymes studied here, trapping the intermediates finding the mechanisms and biomimetic approach done to make bioinspired iron oxidants, thus with the help of synthetic ligand small models are done and mimicking nature's strategy towards oxygen activation.

Synthesis of The ternary iron(II)-benzilate complex [(TpPh<sub>2</sub>)FeII(benzilate)] shown here, and detailed study of high valent Iron intermediates done with spectroscopic evidences.

## **Introduction:**

---

Most organic substances are diamagnetic and oxygen is in triplet ground state, so reaction between them is spin forbidden process, thus dioxygen needs to be activated.

Nature has well defined strategy to overcome the kinetic barrier through some metalloenzymes, nature has chosen the enzymes for their unique active site structure and hydrolytic and redox behavior.

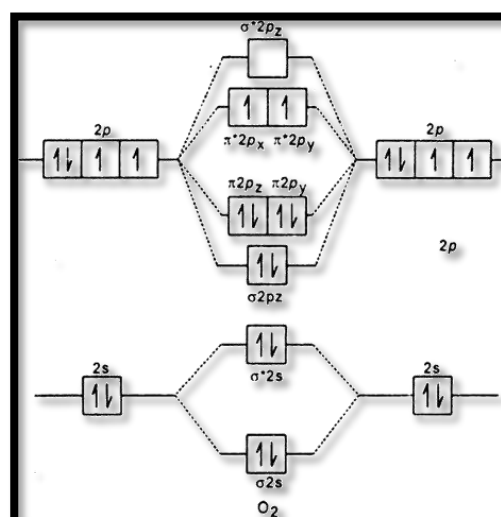
But recently nonheme iron enzymes are mainly focused for activation of dioxygen and then performing many catalytic reactions, in this review the activation strategy and catalytic reactions are explained; also small models studies are performed for generate bioinspired iron oxidants.

## 1. Biological Functions of Dioxygen:

Aerobic organisms depend on dioxygen ( $O_2$ ) for the life processes. The major pathway of dioxygen use in aerobic organisms is the four-electron reduction to give two molecules of water per dioxygen molecule. This reaction, coupled with the oxidation of electron-rich organic foodstuffs such as glucose, is the major source of energy in aerobic organisms. However, this apparent simple biological oxidation reaction involves a series of complicated enzyme-catalyzed reactions to synthesize one of the most important biomolecule ATP, the 'energy currency' for the organism. Another use of dioxygen in aerobic organisms is to function as the source of oxygen atoms in the biosynthesis of various molecules in metabolic pathways or in the process of biodegradation of toxic compounds. Dioxygen converts lipid-soluble molecules to water-soluble forms for purposes of excretion. These reactions are also enzyme-catalyzed, and the enzymes involved are either monooxygenase or dioxygenase enzymes depending on whether one or both of the oxygen atoms from dioxygen are incorporated into the final oxidized organic product.

## 2. Why Dioxygen needs to be activated?

The reaction of dioxygen with majority of organic substrates is exothermic and thermodynamically favorable. However, molecular oxygen is relatively inert toward organic substrates at ambient temperature due to its triplet ground state ( $3O_2$ ). The sluggishness of Dioxygen reactions with the biological substrates having singlet ground state ( $1S$ ) is due to the kinetic barrier of these reactions. Hence dioxygen needs to be 'activated' for aerobic life processes. The obvious question that arises at this point is how dioxygen gets activated to carry out the oxygen-dependent metabolic processes in the biological systems and how nature manages the processes with such efficiency.



### **3. Nature's strategy for Dioxygen activation:**

---

Nature has a well define strategy for dioxygen activation involving many metalloenzymes that carry out various biologically relevant oxidation reactions with high selectivity under ambient conditions. Metalloenzymes act as mediators between dioxygen and organic molecules to overcome the kinetic barrier. The metal centre in the active site of a metalloenzyme is often referred to as the 'heart' of the metalloenzyme and is coordinated by different amino acid residues from the protein backbone. This constitutes the primary coordination sphere of a metalloenzyme. Apart from the primary coordination sphere, the catalytic activity and selectivity of an enzymatic reaction is controlled by the adjacent non coordinating amino acid side chains and various non-covalent interactions. Metalloenzymes carry out a myriad of biological functions such as oxygen transport/storage, electron transport, metal transport, hydrolysis and many others. Transition metals in appropriate oxidation states react directly with triplet O<sub>2</sub> to form Dioxygen adducts that can participate in reaction pathways leading either to the incorporation of oxygen atoms into organic molecules or to the oxidation of organic substrates Thus, in general, Nature's strategy of dioxygen activation involves either transition metal ion (generally iron, copper, manganese, cobalt) or organic/inorganic cofactor (flavin, pterin) or both.

### **4. Why Nature's evolutionary selection of iron in various metalloproteins:**

---

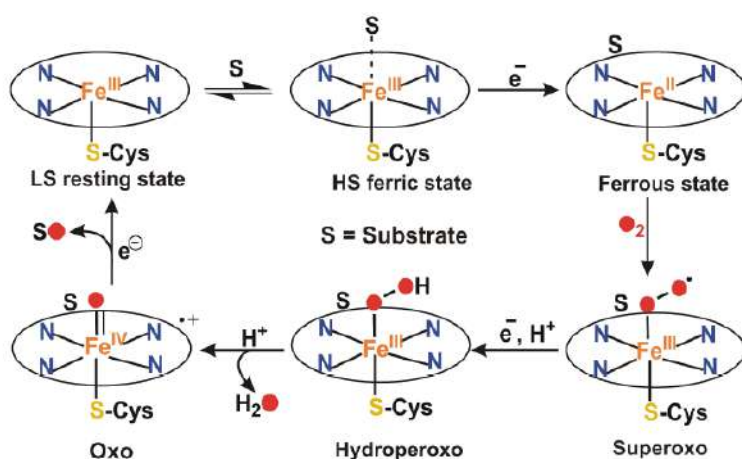
Nature's selection of a particular metal ion as the cofactor for a particular enzymatic reaction, excluding the others, owes its origin in the unique coordination chemistry of the metal ion, together with its hydrolytic and redox properties. Nature choose Iron in various metalloproteins due to its natural abundance (4th most abundant element on earth) and variable oxidation states. The bioinorganic chemistry of iron is rich and diverse. Iron containing enzymes catalyze a wide range of reactions such as oxygen transport/storage, electron transfer, oxidation and oxygenation. Thus, there exists an ancient and intimate relationship between iron and dioxygen.

## 5. Category of Iron Enzymes: Heme and Non heme

Depending upon the diverse structure of the active site, iron containing metalloenzymes that activate dioxygen are classified into two main categories: heme and nonheme. In spite of the diversity in the active sites of these iron containing enzymes, a common mechanistic hypothesis for dioxygen activation, has been put forward, in which dioxygen first binds to the reduced iron centre. Depending upon the substrate/cofactor, different iron-oxygen oxidants are formed that carry out various biologically relevant oxidative transformation reactions.

### 5.1 Heme Containing Oxygenases:

Hemes are chemical groups that consist of a porphyrin ligand backbone, where the four equatorial nitrogen atoms of the porphyrin ring are coordinated to the iron centre. The iron centre may also have one or two axial ligands, typically histidine and/or cysteine. They are found in the active sites of many proteins involved in the metabolic oxidation reactions and in the transportation of oxygen gas. Oxygen binds to the iron centre and the reduced iron acts as a source or sink of electrons for redox reactions. In some enzymes, the porphyrin ring also acts as an electron source.



**Scheme 1:** Proposed mechanism of Dioxygen activation at the iron center by heme Cytochrome P-450

The Cytochrome P-450 is an important family of heme enzymes, which activate dioxygen and incorporate one of the oxygen atoms into a variety of biologically important substrates with concomitant two-electron reduction of the other oxygen atom to water. These groups of enzymes are known to catalyze hydroxylation, epoxidation, *N*-, *S*-, *O*-dealkylation, *N*-oxidation, sulfoxidation, and dehalogenation. These oxidative transformations have significant role in carcinogen activation, drug, xenobiotic detoxification, and for the metabolism of steroid and prostaglandin.

In the resting state, the enzyme has a low-spin ferric center (Scheme1), which is converted to a high-spin ferric center upon binding of substrate. Reduction of the ferric cytochrome P-450 by one electron forms the ferrous cytochrome P-450. Dioxygen then binds to the iron (II) center to form an O<sub>2</sub>-adduct. Transfer of a second electron to the iron (II)-O<sub>2</sub> adduct forms a peroxyiron (III) complex. Heterolytic O-O bond cleavage of the resulting peroxy complex in the presence of proton forms the reactive iron-oxo intermediate, often referred to as the  $\pi$ -cation radical oxoferryl state, with concurrent production of water this iron-oxo intermediate oxidizes various substrates and release of product regenerates the resting site of the enzyme for further catalytic cycles. NADPH acts as the source of electrons and protons in the catalytic cycle.

## 5.2 Nonheme Oxygenases:

---

Nonheme enzymes are a group of iron containing metalloenzymes which have received most attention recently due to the explosion in the number of crystal structures available for different enzymes. In fact, this emerging class of enzymes now rivals the heme enzymes in terms of diversity of the versatile Oxidation reactions they catalyze. However, unlike heme enzymes, mononuclear nonheme iron enzymes employ a variety of sacrificial reductants (organic/inorganic cofactors, often bonded to the active metal site of the enzyme) ligands to the metal center imparts these groups of enzymes to adopt a more flexible metal-coordination environment. Nonheme enzymes either have monoiron or diiron center for catalytic reactivity. Dinuclear for the reductive activation of dioxygen. Such mechanistic scenario of binding a number of exogenous enzymes have two iron centers that are bridged by carboxylate or

oxo/hydroxo, and are coordinated by imidazole, carboxylate and sometimes by phenolate group of amino acid residues or by labile solvent molecules. These proteins are involved in oxygen binding (hemerythrin) and activation (methane monooxygenase, ribonucleotide reductase,  $\Delta 9$  desaturase), and hydrolysis reactions (purple acid phosphatase).

## 6. '2-His-1-Carboxylate Facial Triad' Motif: General Aspect

---

Accumulations of crystallographic data of a superfamily of mononuclear nonheme enzymes have unfolded a common structural motif at the active site. This structural motif consists of a mononuclear iron(II) center coordinated facially by two nitrogen atoms from histidine residues and one carboxylate oxygen from either a glutamate or aspartate residue (Fig 1.). The remaining three vacant sites are coordinated by labile water molecules in the resting state of the enzymes. This structural motif has been coined as the '2-His-1-carboxylate facial triad' and serves as a versatile platform for dioxygen activation. In the presence of suitable cofactors/exogenous ligand and dioxygen, the labile water/solvent molecules are replaced to generate the substrate bound form of the active enzyme, which efficiently participates in the dioxygen activation pathway. This flexibility in the metal coordination chemistry is perhaps the reason for which this superfamily of enzymes catalyze an array of diverse oxidative transformations, many of which are of medical, pharmaceutical and environmental significance.

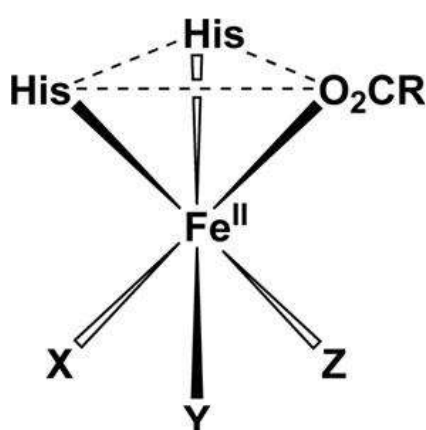


Fig 1: Schematic representation of the 2-His-1-carboxylate facial triad (X, Y and Z denote weakly bound solvent molecules or vacant sites).

## 7. The 2-His-1-carboxylate facial triad: enzyme groups

The enzymes featuring the 2-His-1-carboxylate facial triad can be classified into five different groups based on their structural characteristics, reactivity, and specific requirements for catalysis. These groups are the (1) extradiol cleaving catechol dioxygenases, (2) Rieske oxygenases, (3)  $\alpha$ -ketoglutarate dependent enzymes, (4) pterin-dependent hydroxylases, and finally (5) a miscellaneous, catch-all category. The basic characteristics, recent developments, and illustrative examples of each group will be discussed. (Fig 2)

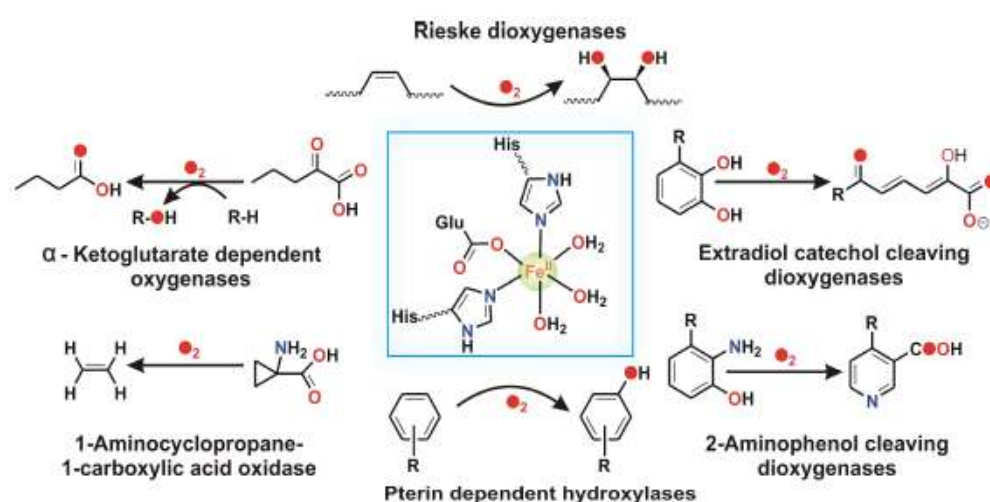
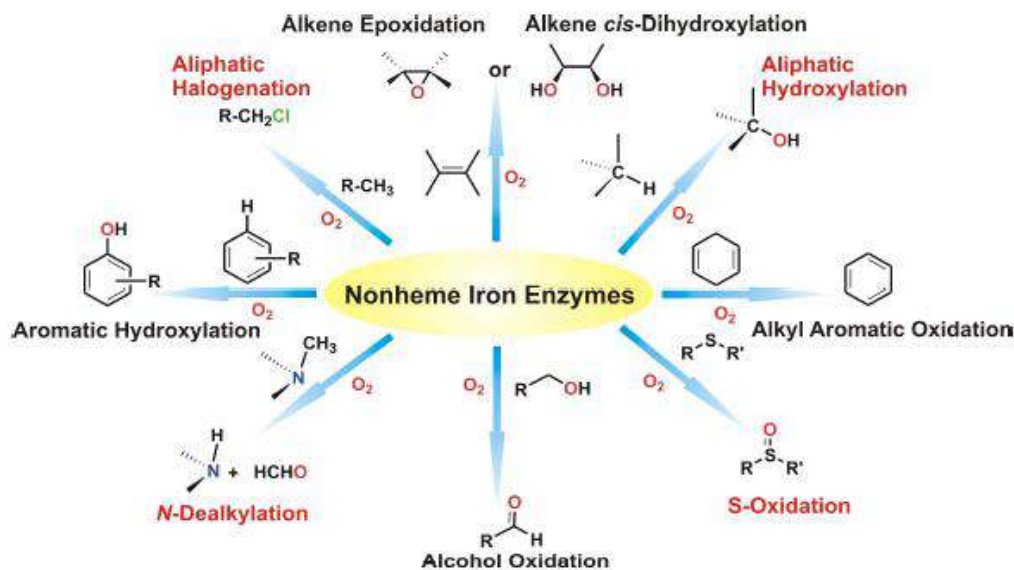


Fig 2: Reactions catalyzed by nonheme iron enzymes with the '2-His-1-carboxylate facial triad' motif.

## 8. Versatile Oxidation Reactions Catalyzed by Nonheme Oxygenases

Nonheme iron oxygenases catalyze a diverse array of challenging metabolic transformations which are fundamentally important to life. Selective oxidation of alkenes and alkanes by molecular oxygen is the strategy for synthesis of key metabolic components in biology.



Scheme 2: Versatile oxidation reactions catalyzed by nonheme enzymes.

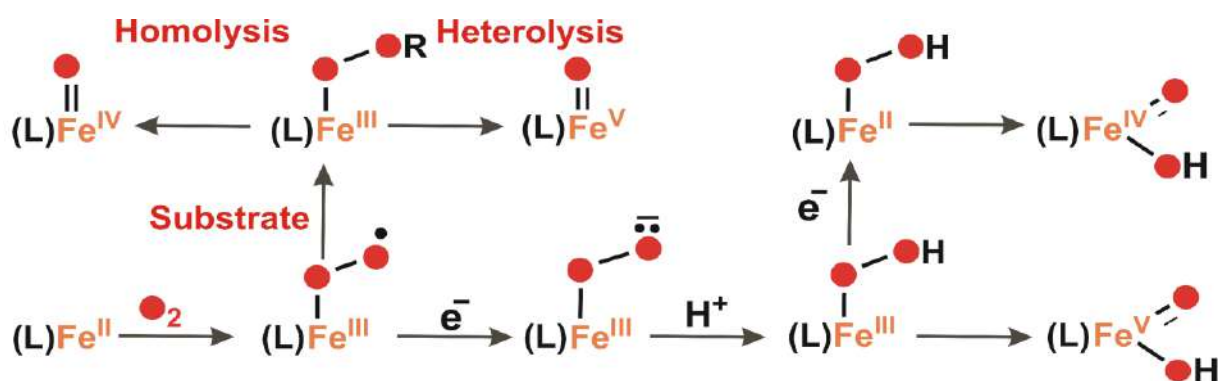
The most important reactions catalyzed by the nonheme enzymes are the insertion of oxygen into unactivated C-H bonds (hydroxylation) of alkanes and *cis*-dihydroxylation of olefins. Other reactivities shown by nonheme enzymes include halogenation, desaturation, cyclization, ring expansion, epoxidation, aromatic hydroxylation, alkyl aromatic oxidation, alcohol oxidation, oxo transfer to sulfides, *P*-oxidation, *N*-dealkylation and decarboxylation (Scheme 2). Selective C-C bond cleavage reactions performed by nonheme oxygenases are an efficient approach adopted by Nature for the degradation of aromatic molecules to aliphatic products, which is an important step in the biodegradation of aromatics in the soil and groundwater.

## 9. Reactive intermediates Nonheme Enzymes:

To activate Dioxygen and to overcome the low one electron redox potential of dioxygen, additional reducing equivalents (sacrificial reductants) are necessary in the enzymatic cycle. Thus reductive activation of dioxygen leads to formation of different Iron-oxygen oxidants, which are oxidizing agents in enzymatic reactions. It is important to understand the reaction intermediates for the clear concept about the reaction, and also the role of co-factors in the dioxygen activation.



In the nonheme superfamily, the six-coordinate resting state of an enzyme is unreactive towards dioxygen. The binding of a substrate or co factor results in the formation of a coordinatively unsaturated five-coordinate species, which triggers the attack of dioxygen. After dioxygen binds to the iron(II)center, different iron-oxygen intermediates are generated depending upon the cofactors (Scheme 3). In the first step of the reaction with dioxygen, an iron(III)-superoxo species is formed. The fate of the iron(III)-superoxo species varies depending upon the subtle role played by the cofactor. The iron(III)-superoxo species may undergo one-electron reduction by receiving electron from the co-reductant to form an iron(III)-peroxo species. The iron(III)-peroxo on protonation forms an iron(III)-(hydro)peroxo intermediate. The iron(III)-(hydro)peroxo species itself, or after reduction to an iron(II)-hydroperoxo species may undergo heterolytic O-O bond cleavage leading to the generation of high-valent iron-oxo-oxidants (Scheme 3). Alternatively, the iron(III)-superoxo species can abstract hydrogen from substrate to generate an iron(III)-hydroperoxo species. The mode of O-O bond cleavage of the resulting iron(III)-hydroperoxo species determines whether an iron(IV)-oxo or iron(V)-oxo species would form in the catalytic cycle (Scheme 3). In addition to high-valent iron-oxo oxidants, metal-superoxo, peroxo and hydroperoxo are key intermediates involved in the oxidation by nonheme oxygenases.



Scheme 3: Possible iron-oxygen intermediates formed in the reductive activation of dioxygen at mononuclear iron center.

## 10. Rieske Dioxygenases:

Aromatic compounds are common contaminants in the soil and groundwater. The nonheme iron enzymes, Rieske dioxygenases, catalyze the *cis*-dihydroxylation of arenes in the first step of the bioremediation of aromatic pollutants. Apart from *cis*-dihydroxylation of arenes, Rieske dioxygenases efficiently catalyze the hydroxylation, oxo atom transfer to sulfides, *O*- and *N* dealkylation, and desaturation reactions. Over the last decades, Crystallographic data of several Rieske dioxygenases dioxygenase, have been reported. Among others, the well studied enzyme in this family is naphthalene dioxygenase. Rieske dioxygenases contain the '2 His-1-carboxylate facial triad' motif at the mononuclear active site. Additionally, there is an adjacent reductase component, called the reduced Rieske centre (Fe<sub>2</sub>S<sub>2</sub>cluster) for providing electrons between the NADPH and the oxygenase site of the enzyme (Figure 3). Thus the enzymes consume equivalent amounts of dioxygen and substrate, and two equivalents of external electrons from the reductase unit. In a single subunit of each Rieske dioxygenase, the Rieske cluster and the mononuclear nonheme iron center are too far (~ 45 Å) apart for electron transport. However, the quaternary structure allows the electron transfer from a Rieske cluster to the mononuclear iron center from another subunit situated at a distance of 12 Å.

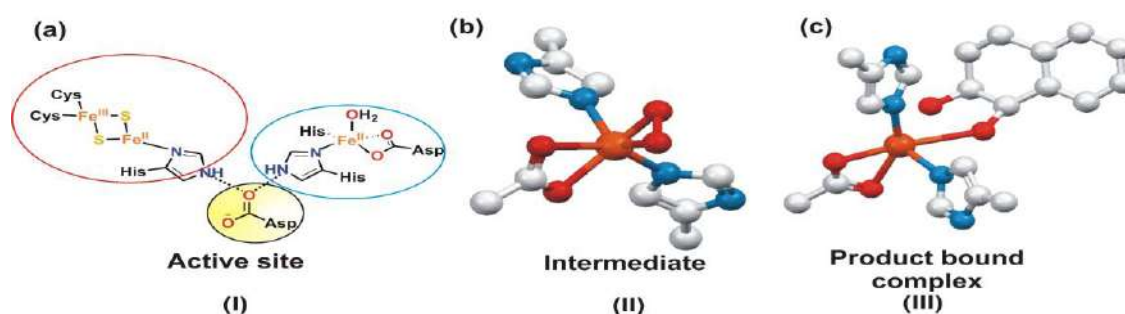


Fig 3:

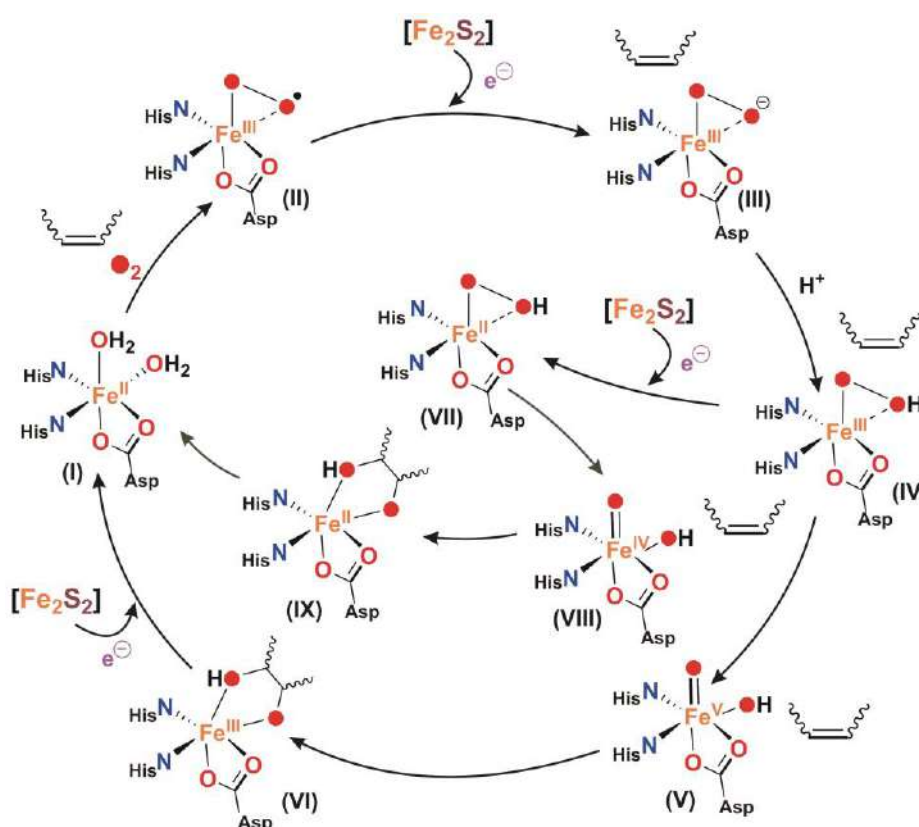
(a) Active site of the nonheme iron center and the reductase unit of naphthalene-1,2-dioxygenase (NDO) within  $\alpha$ -subunits of the enzyme. A conserved aspartate acts as a bridge between the two  $\alpha$ -subunits. Crystal structures of (b) the iron-oxygen intermediate and (c) the product bound iron center.

In the electron transfer process, a fully conserved aspartate residue acts as a bridge between the oxygenase and reductant component of the Rieske enzymes (Figure 3). Mutation studies have revealed the loss of catalytic reactivity upon substitution of the aspartate residue by

other amino acids. Thus, for the four-electron reductive activation of dioxygen concomitant with the *cis*-dihydroxylation of alkenes, two electrons are provided by the substrate(alkene) itself and the other two electrons are supplied by NADPH via the Rieske cluster to the nonheme iron active site .Crystal structures of naphthalene-1,2-dioxygenase (NDO), isolated from *Pseudomonas putida*, as adduct an oxygen as well as in the product bound form provide useful insights into the nature of active intermediate responsible for *cis-dihydroxylation* reaction of alkenes (Figure 3b and Figure 3c). The oxidized substrate bound structure of NDO reveals an FeIII centre coordinated by a bidentate naphthalene *cis*-1,2-dihydrodiol. Crystal structure of the oxidized form of NDO, under controlled oxygen environment and in the absence of substrate, reveals a side-on bound iron-oxygen adduct with asymmetric Fe-O bond distances of 2.24 and 2.32 Å (Figure 3b). The O-O bond distance of 1.46 Å is similar to that of reported synthetic iron(III)-peroxo intermediates. The intermediate was thus suggested to be a side-on bound iron(III)-hydroperoxide. The structure clearly indicates that the formation of an iron(III)-superoxide intermediate initiates the reaction with dioxygen to form the corresponding peroxide/hydroperoxide species.

Findings from enzymatic studies have revealed a general mechanism involved in the catalytic cycle of Rieske dioxygenases (Scheme 4). The substrate binds to the active site only when the Rieske cluster is reduced by receiving one electron from the redox partner (NADPH). This causes several conformational changes in the protein backbone creating space for dioxygen binding. Dioxygen bonded to the iron center undergoes reductive activation to form a side-on bound iron(III)-peroxide and subsequently a hydroperoxo intermediate upon protonation. This hydroperoxo moiety may react directly, or may undergo heterolytic O-O bond cleavage for generation of highvalent iron-oxo oxidants to carry out *cis*-dihydroxylation of alkenes. Heterolytic O-O cleavage of iron(III)-hydroperoxide would form an iron(V)-oxo-hydroxo intermediate. The final iron(III)-diol complex, undergoes one-electron reduction at the nonheme iron center to form ferrous(FeII) state at the active site. The resulting iron(II) complex releases the *cis* dihydroxylated product and regenerates the enzyme to its resting state for further catalytic cycles (Scheme 4). However, there is a debate as to whether the iron(III)-(hydro)peroxo species itself performs the *cis*-dihydroxylation or the OO bond is cleaved to form a high-valent iron(V)-oxo-hydroxo oxidant prior to *cis*-dihydroxylation. Different mechanisms for the actual oxygen insertion step have been proposed. Theoretical calculations

suggest a concerted pathway where the O-O bond is cleaved concomitantly with the formation of an epoxide which then subsequently form an arene cation, and finally to the *cis* diol. A high activation barrier is found for the mechanism involving O-O bond cleavage prior to attack of the substrate. On the other hand, O-O cleavage prior to substrate oxidation would give rise to an Fe(V)-(oxo)(hydroxo) intermediate. Isotope labelling experiments with H<sub>2</sub><sup>18</sup>O in the dihydroxylation reaction by H<sub>2</sub>O<sub>2</sub> in enzymatic studies support the O-O bond cleavage prior to *cis*-dihydroxylation.



Scheme 4: Proposed mechanism for the *cis*-dihydroxylation reaction catalyzed by Rieske dioxygenases.

Interestingly, while studying the mechanism of benzoate dioxygenase, Ballou *et al.* have proposed that the iron(III)-hydroperoxide species may undergo one electron reduction to an iron(II)-hydroperoxide (Scheme 4), which decays to an iron(IV)-oxo-hydroxo intermediate upon heterolytic O-O bond cleavage. From the above mechanistic considerations, it is evident that Rieske dioxygenases employ an ordered mechanism in which dioxygen binds to the

active site only after the substrate (alkene) is bound and the Rieske Fe<sub>2</sub>S<sub>2</sub> cluster is reduced. This ordered dioxygen activation mechanism is a clever strategy adopted by nature that prevents the oxidative inactivation of the enzyme in its resting state.

Note: Other reactions catalyzed by nonheme iron enzymes with 2-His-1-Carboxylate facial triad motif, are not explained here.

## **11. Biomimetic Approach:**

---

Biomimetic approach towards oxygen activation is a way to unfold the mystery of Nature's dioxygen activation strategy. Metalloenzyme catalyzed oxidations often exhibit exquisite substrate specificity as well as regioselectivity and/or stereo selectivity, and operate under mild conditions. Understanding the structure-function relationship of O<sub>2</sub>-activating metalloenzyme is important to find out mechanism of an enzymatic reaction. The bioinspired approach aims at reproducing specific structural features of the active site of the natural enzymes into the synthetic system. With these features incorporated, the synthetic systems are expected to perform the same catalytic transformation as the natural enzyme. Trapping of intermediates and probing the mechanism of enzymatic reaction would be much easier with small molecule model complexes. Furthermore, mechanistic studies of biomimetic catalysts would provide important insights into biological reaction pathways, thus completing a feedback loop relating studies of metalloenzymes to their synthetic models.

However, development of efficient synthetic models is truly challenging. Ligand design, to replicate the primary coordination sphere around the active site of enzyme. Moreover, assistance from outer sphere residues similar to the enzymatic system in small molecule models is a challenge for the bioinorganic researchers. A thorough characterization of reactive intermediates by various spectroscopic tools as well as detailed mechanistic investigations are equally important to elucidate the nature of the reactive oxidant and are important steps in the design of bioinspired oxidation catalysts. In nonheme chemistry, several bioinspired models of different oxygenases have been developed.

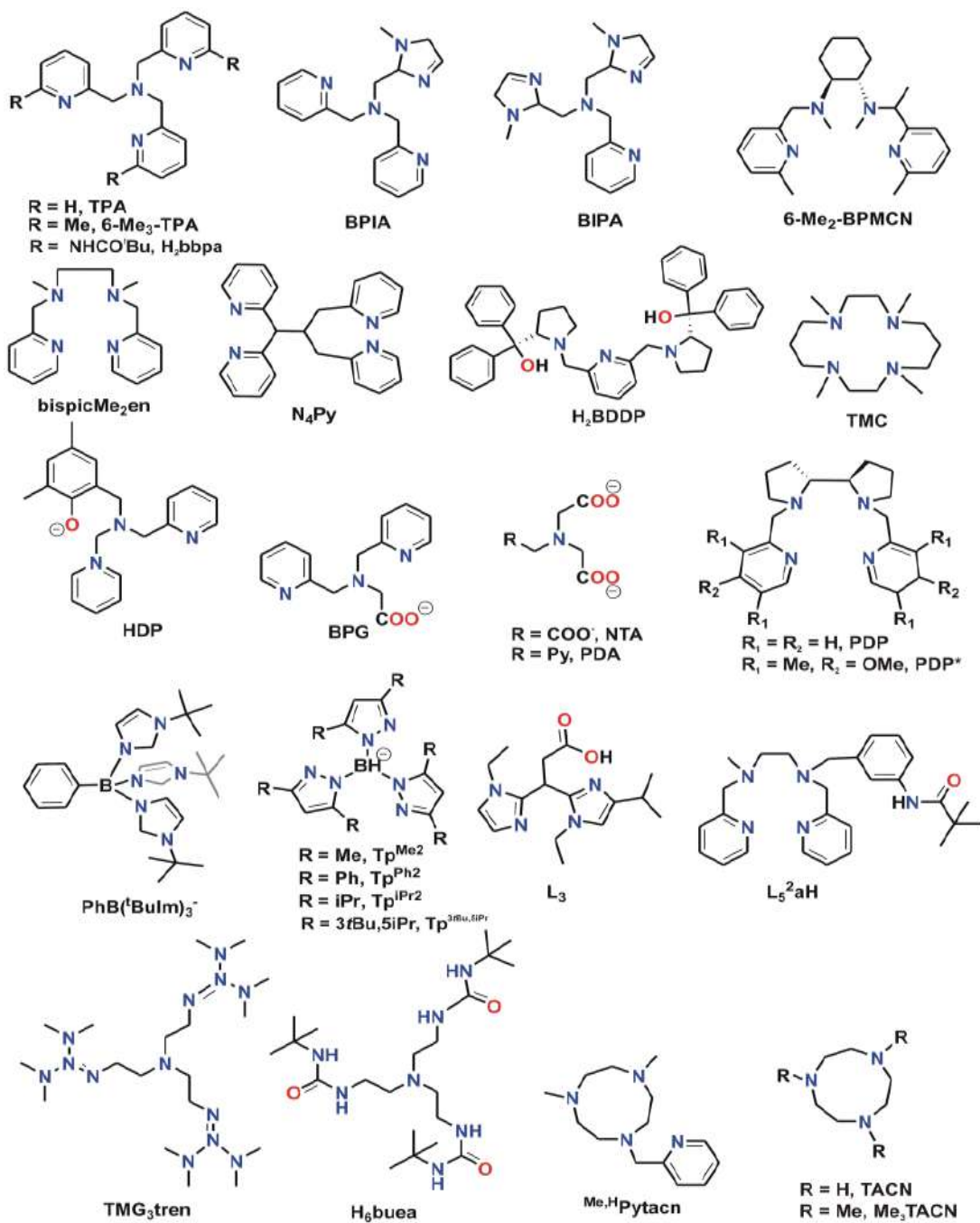
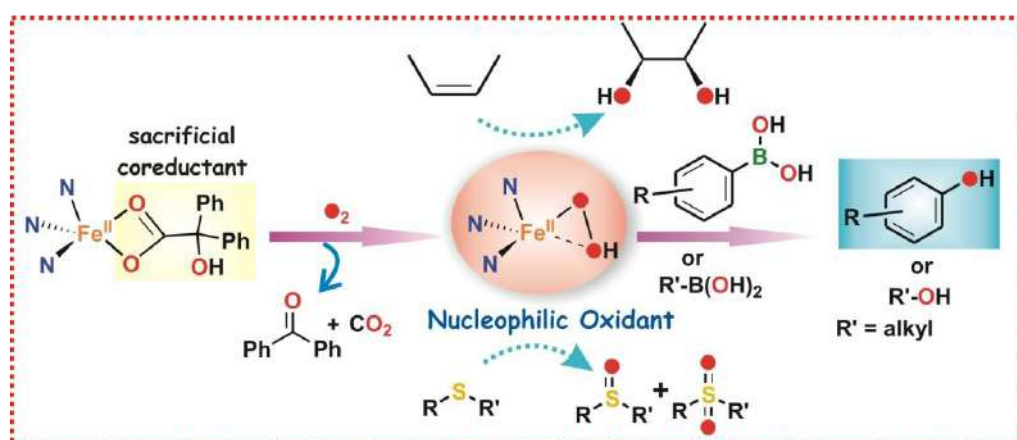


Fig 4: There are many others ligands used in biomimetic studies, these are not shown here.

## 12. Nucleophilic Iron-Oxygen Oxidant Derived from a Biomimetic Iron (II)- $\alpha$ -Hydroxy Acid Complex



The nonheme iron enzymes Rieske dioxygenases catalyze the cis-dihydroxylation of arenes in the biodegradation of aromatic compounds. It is postulated that an iron(V)-oxo-hydroxo oxidant is responsible for the dihydroxylation reaction. An iron(IV)-oxo-hydroxo species has also been proposed as the active oxidant in benzoate dioxygenase. However, there is no direct experimental evidence for such oxidant in the catalytic cycle of Rieske dioxygenases. Inspired by the novel reactions catalyzed by Rieske dioxygenases, a number of nonheme iron complexes have been reported for bioinspired oxidation catalysis. The reported complexes have been shown to dihydroxylate or epoxidize olefins with excess hydrogen peroxide. The presence of 'ready oxidant'  $H_2O_2$  and alkene together allowed the complexes to exhibit catalytic reactivity through putative high-valent iron-oxo oxidant. An iron(V)-oxo-hydroxo oxidant has been implicated to carry out the cis-dihydroxylation of aromatic rings in the reaction by a nonheme iron catalyst. Costas *et al.* have shown the existence of an iron(V)-oxo-hydroxo species by variable-temperature mass spectrometry. Que *et al.* have proposed an iron(IV)-dihydroxy intermediate responsible for olefin *cis*-dihydroxylation.

Studies on enzymatic and model systems have unfolded the necessity of sacrificial coreductants to generate useful metal-oxo oxidants. Taking lessons from nature, we have selected a series of  $\alpha$ -hydroxy acids which serve as bioinspired sacrificial reductants to provide electrons and proton for the reductive activation of dioxygen. Of various  $\alpha$ -hydroxy

acids that act as two electron reductants, they have selected benzoic acid as the sacrificial reductant

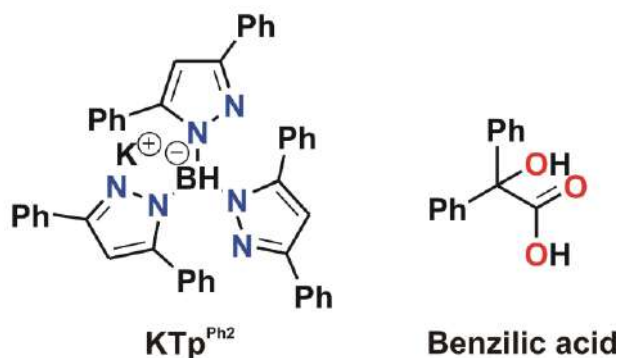


Fig 5: Ligands used.

Paria *et al.* have shown that benzoic acid underwent decarboxylation to form benzophenone in the reaction of an iron(II)-benzoate complex  $[(\text{TpPh}_2)\text{FeII}(\text{benzoate})]$  (**1**) of a facial  $\text{N}_3$  ligand, hydrotris(3,5-diphenylpyrazol-1-yl)borate ( $\text{TpPh}_2$  in Figure 5) with dioxygen. The iron(II)-benzoate complex was capable of doing *cis*-dihydroxylation of cyclohexene with the incorporation of both the oxygen atoms of molecular oxygen into the diol product. In the oxidative transformation, an iron(IV)-oxo-hydroxo oxidant was proposed as the active oxidant. To get deeper insight into the role of  $\alpha$ -hydroxy acid as the sacrificial reductant and also to elucidate the nature of the active oxidant, we have explored the reactivity of the iron(II)-benzoate complex  $[(\text{TpPh}_2)\text{FeII}(\text{benzoate})]$  (**1**) toward external substrates. In this chapter, we have tried to establish the nature of the oxidant derived from the iron(II) benzoate complex and have demonstrated a protocol for harnessing the oxidizing capability of molecular oxygen in presence of electron and proton source to carry out various important oxidative transformation reactions.



## 12.1 Results and Discussion

---

### . Synthesis and Characterization

The ternary iron(II)-benzilate complex [(TpPh<sub>2</sub>)FeII(benzilate)] (**1**) was synthesized by mixing the ligand KTpPh<sub>2</sub>, iron(II) perchlorate with a basic solution of benzoic acid in methanol. The <sup>1</sup>H NMR spectrum of complex **1** in benzene-*d*<sub>6</sub> displays paramagnetically shifted proton resonances supporting the high-spin state of iron(II) center in complex **1**. Complex **1** crystallizes in a triclinic system with *P1* space group. The X-ray crystal structure of **1** shows a distorted square-pyramidal iron(II) center ( $\tau = 0.46$ ) coordinated by the facial tridentate TpPh<sub>2</sub> ligand and a monoanionic benzilate. The carboxylate group of benzilate coordinates to the iron center in a bidentate mode. The average Fe–N bond length of 2.092 Å is comparable to that of other reported FeII(TpPh<sub>2</sub>) complexes, while the iron–O(carboxylate) distances indicate an unsymmetric bidentate binding mode ( $r(\text{Fe1-O1}), 2.346(3)$  and  $r(\text{Fe1-O2}), 2.008(3)$  Å). The hydroxyl group of the benzilate does not coordinate to the iron center possibly due to the steric crowding from the phenyl rings on the TpPh<sub>2</sub> ligand. The five-coordinate iron(II)-benzilate complex (**1**) has a vacant coordination site for binding of dioxygen.

### 12.2 Dioxygen Reactivity of Complex 1

The reaction of iron(II)-benzilate complex (**1**) with dioxygen was carried out in benzene. When exposed to dioxygen, the colorless solution of **1** forms a green solution over a period of 20 min. The oxidized solution shows a characteristic charge-transfer band at 600 nm in the UV-Vis spectrum (Figure 5). The green species corresponds to an iron(III)-phenolate species of TpPh<sub>2</sub>\* ligand in which the *ortho* carbon of one of the 3-phenyl rings on the ligand gets hydroxylated. This is also evident from the ESI-mass spectrum of the final oxidized solution, which exhibits ion peak at  $m/z = 740.2$  attributable to [(TpPh<sub>2</sub>\*)Fe]<sup>+</sup> (Figure 6a). Moreover, the X-band EPR spectrum at 77 K shows a rhombic signal at  $g = 4.3$ , (Figure 5) typical of a high-spin iron(III) complex. <sup>1</sup>H NMR and GC-MS analyses of organic products obtained from the oxidized solution clearly establish the quantitative decarboxylation of benzilate to benzophenone.

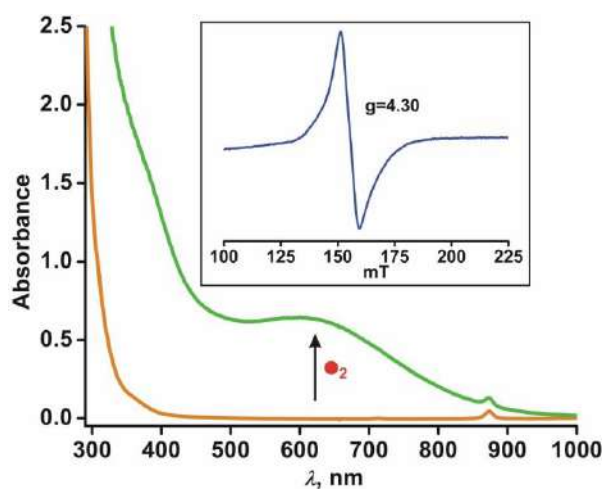


Fig 5:  
Optical spectra of **1** under nitrogen (orange line) and of **1** after reaction with dioxygen (green line) in benzene (0.5 mM) at 298 K. Inset: EPR spectrum of the oxidized solution of **1** at 77 K.

To understand the source of the atomic constituents of dioxygen, labeling experiments were performed. The ESI-MS of the oxidized solution of **1** after the reaction with  $^{18}\text{O}_2$  in benzene displays an ion peak at  $m/z = 742.2$  with the expected isotope distribution pattern attributable to  $[(\text{TpPh}_2^*)\text{Fe}]^+$  (Figure 6b). This indicates that one oxygen atom from  $^{18}\text{O}_2$  is incorporated into the ligand backbone. However the ketonic product benzophenone derived from **1** does not contain any labeled oxygen, as confirmed by GC-MS analysis. A mixed labeling experiment with  $^{16}\text{O}_2$  and  $\text{H}_2^{18}\text{O}$  reveals no incorporation of labeled oxygen into the hydroxylated ligand backbone. It is clear from the dioxygen reactivity of **1** that the  $\alpha$ -hydroxy acid (benzilate) coordinated to the iron(II) centre undergoes oxidative decarboxylation to form the corresponding carbonyl compound (benzophenone). The importance of -OH group of  $\alpha$ -hydroxy acid in the oxidative decarboxylation mechanism has already been reported, where it has been shown that 2-methoxy-2-phenylacetate (which lacks a -OH group) or 2-methoxy-2-methylpropanoate (MMP) (which has neither an  $\alpha$ -C-H bond nor an O-H bond) did not undergo oxidative decarboxylation;  $\alpha$ -methoxy acids were isolated quantitatively. These results unambiguously established the involvement of O-H group to initiate the decarboxylation reaction.

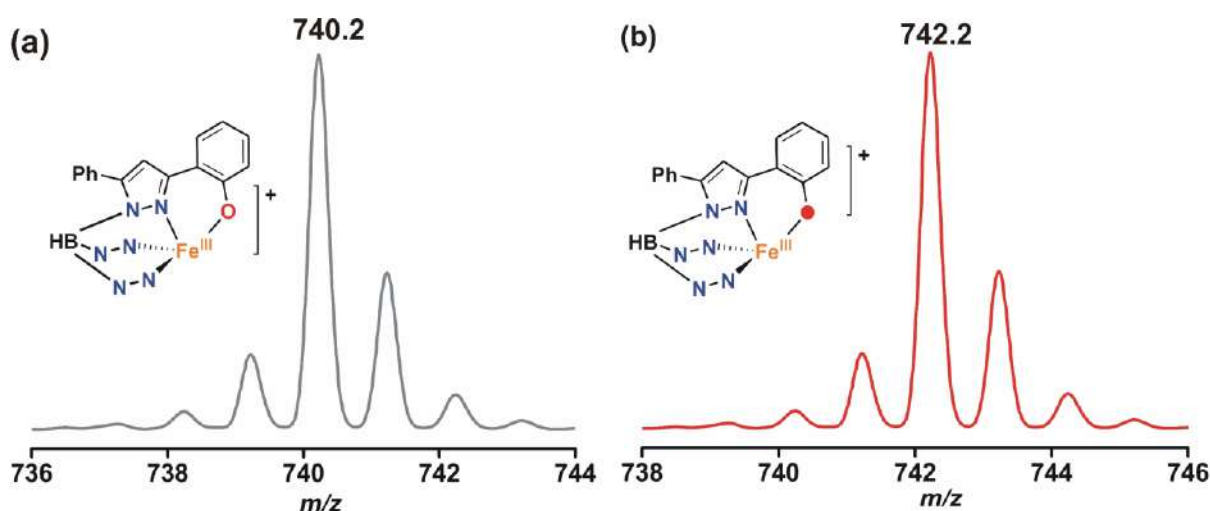
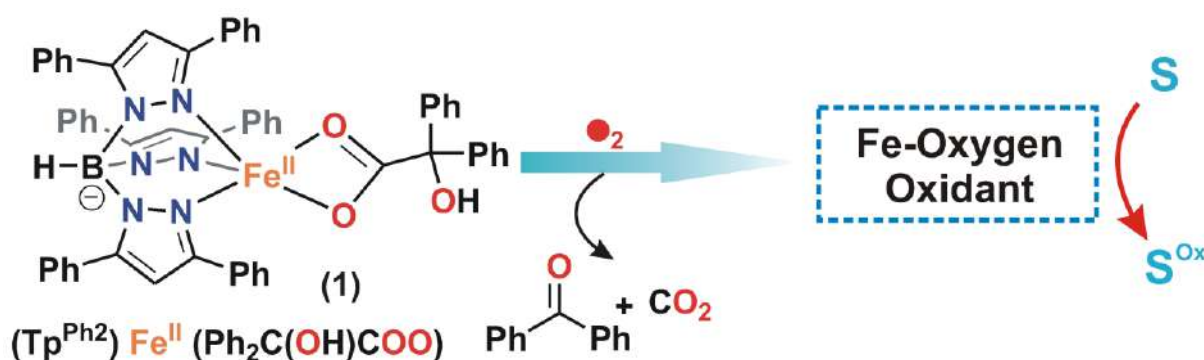


Fig 6: Comparison of ESI-mass spectra of the oxidized solution after the reaction of **1** with (a)  $^{16}\text{O}_2$  and (b)  $^{18}\text{O}_2$ .

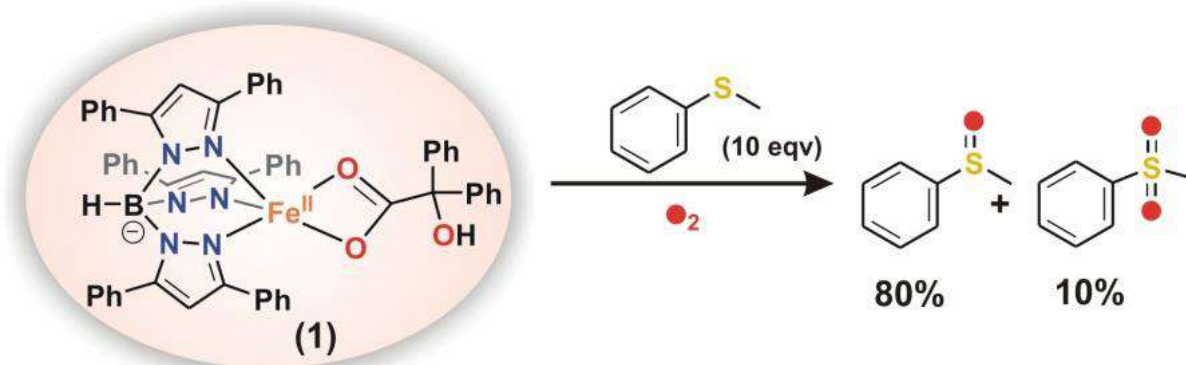
Based on the absorption spectrum of the final oxidized solution of **1** (Figure 5), around 90% intra-ligand hydroxylation was estimated. The formation of benzoic acid and concomitant ring hydroxylation of TpPh<sub>2</sub> ligand has been reported for iron(II)-benzoylformate. A high-spin Fe(IV)=O intermediate was implicated in the hydroxylation of phenyl ring during the oxidative decarboxylation of iron(II)-benzoylformate complex. Although no iron-oxygen oxidant could be detected for spectroscopic characterization from **1**, the oxidant generated in oxidative decarboxylation of  $\alpha$ -hydroxy acid was intercepted by indirect probes (Scheme 5). In the presence of excess external intercepting agents, the intra-ligand hydroxylation could be inhibited almost completely.



Scheme 5: Iron-oxygen oxidant generated in the reaction of an iron(II)-benzilate complex of a monoanionic facial N<sub>3</sub> ligand with O<sub>2</sub>.

### 12.3 Interception of the Active Oxidant with Thioanisole:

Reaction of **1** with sulfide affords a mixture of sulfoxide and sulfone. Using 10 equiv of thioanisole, around 80% thioanisole oxide and 10% methylphenyl sulfone is formed with almost no intra-ligand hydroxylation (Scheme 6.). However, with decreasing amount of sulfide, the amount of sulfone formation increases and the yield of sulfoxide decreases. With 1 equiv thioanisole, 34% sulfone is formed as the only product without any sulfoxide. Thus the distribution of thioanisole-derived products strongly depends on the concentration of thioanisole added in the reaction.



Scheme 6: Thioanisole derived oxidized products in the reaction of **1** with dioxygen in benzene in the presence of 10 equiv thioanisole

To assess the source of oxygen atoms in thioanisole-derived products, labeling experiments were carried out with complex **1** and <sup>18</sup>O<sub>2</sub> in the presence of thioanisole (10 equiv). The GC-mass spectra of the organic products display ion peaks at *m/z* 140 and 156 corresponding to [C<sub>6</sub>H<sub>5</sub>S<sup>16</sup>OCH<sub>3</sub>]<sup>+</sup> (Figure 7a) and [C<sub>6</sub>H<sub>5</sub>S<sup>16</sup>O<sub>2</sub>CH<sub>3</sub>]<sup>+</sup> (Figure 7b) that shift to *m/z* 142 (Figure 7c) and *m/z* 160 (Figure 7d), respectively, in the presence of <sup>18</sup>O<sub>2</sub>. Therefore, the oxygen atoms in thioanisole-derived products originate from molecular oxygen.

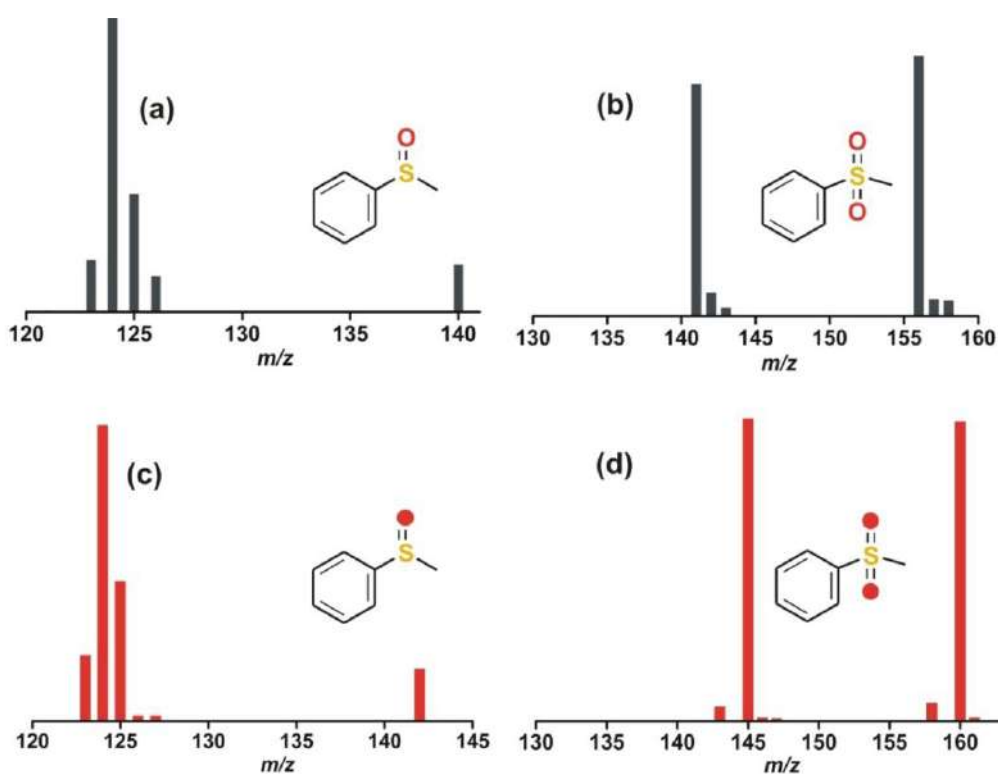


Fig 7: Thioanisole derived products after reaction of complex **1** with  $^{16}\text{O}_2$ , (a and b) and with  $^{18}\text{O}_2$  (c and d).

The oxidation of sulfide to sulfoxide is a well-known reaction that takes place in the presence of a high-valent iron-oxo intermediate. A variety of synthetic iron(IV) oxo complexes have been shown to oxidize thioanisole to thioanisole oxide. A high-spin iron(III)-hydroperoxo intermediate has also been proposed to oxidize sulfide to sulfoxide. The two-electron oxidative decarboxylation of  $\alpha$ -hydroxy acid in **1** rules out the involvement of an iron(III)-hydroperoxo or superoxo species.

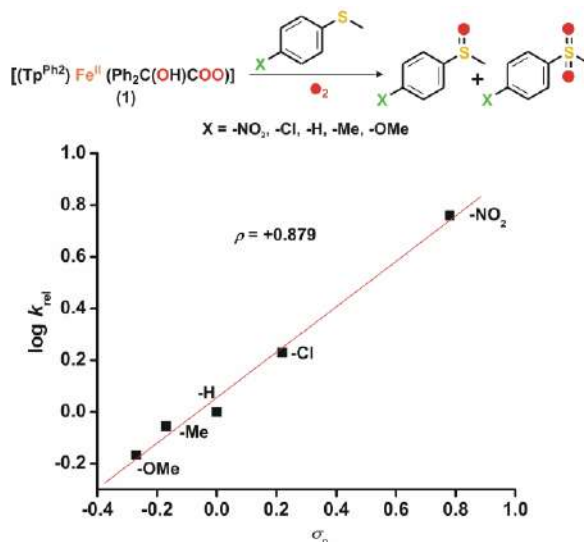


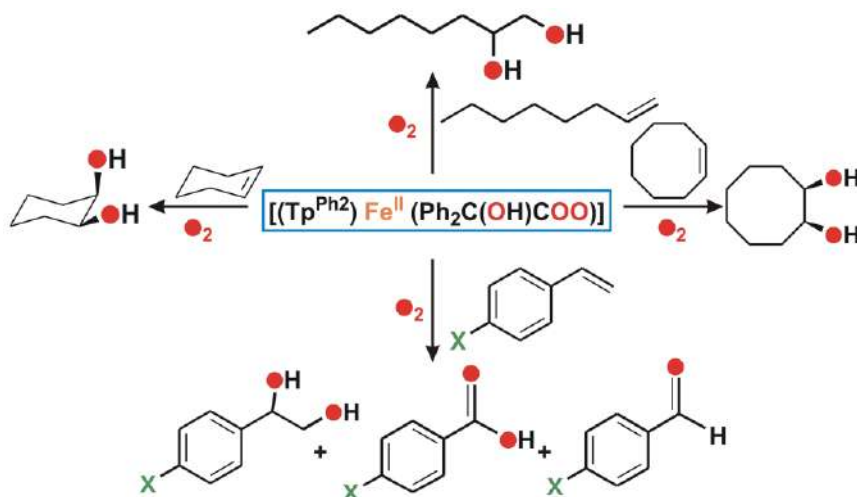
Fig 8: Hammett plot of  $\log k_{\text{rel}}$  versus  $\sigma_p$  for  $p\text{-XC}_6\text{H}_4\text{SCH}_3$ . The  $k_{\text{rel}}$  value was calculated by dividing the concentration of the product from  $p\text{-XC}_6\text{H}_4\text{SCH}_3$  by the concentration of the product from  $\text{C}_6\text{H}_5\text{SCH}_3$ . (Scheme above: Products obtained from  $p\text{-XC}_6\text{H}_4\text{SCH}_3$  in the reaction with **1** and oxygen.)

The observed oxidation of thioanisole to a mixture of thioanisole oxide and methyl phenyl sulfone suggests that the nature of the iron–oxygen species from **1** must be different from those reported. A Hammett analysis would provide useful information regarding the nature of the active oxidant. Since the intermediate is not observed, no absolute reaction rate can be obtained. However, relative rates can be obtained from product analysis of the competition oxidation of pairs of sulfides. For Hammett analysis with complex **1**, competitive reactions were carried out with 1:1 mixtures of thioanisole and different *para*-substituted thioanisoles ( $p\text{-XC}_6\text{H}_4\text{SCH}_3$  where  $\text{X} = \text{NO}_2, \text{Cl}, \text{H}, \text{Me}, \text{OMe}$ ). A  $\rho$  value of +0.88 was obtained from the Hammett plot of the relative rates ( $k_{\text{rel}}$ ) versus  $\sigma_p$  (Figure 8). The data clearly indicate that the oxidant responsible for oxygen-atom transfer to thioanisole has nucleophilic character.

#### **12.4 Interception of the Oxidant with Alkenes:**

The active oxidant, generated in the oxidative decarboxylation of **1**, oxidizes alkenes to the corresponding *cis*-diols (Scheme 7). Cyclohexene forms *cis*-cyclohexane-1,2-diol to an extent of 60%. When 1-octene is used as a substrate, the formation of octane-1,2-diol is observed in

85% yield (Figure 9a). Cyclooctane affords 80% *cis*-cyclooctane-1,2-diol Unlike other alkenes, styrene forms 1-phenylethane-1,2-diol(20%), benzaldehyde (50%), and benzoic acid (30%) in the reaction with **1** and dioxygen



Scheme 7: Oxidation products of different alkenes in the reaction with **1** and dioxygen in benzene

The use of molecular oxygen in generating an oxidant capable of performing *cis*-dihydroxylation of olefin is quite intriguing. The oxidation of alkene to *cis*-diol takes place only in the presence of an oxidant with two oxygen atoms disposed in a *cis* position as in osmium tetroxide, potassium permanganate, etc. To explore the nature of the oxidant, Hammett analysis was performed by product analysis of the competition oxidation of pairs of styrenes (Figure 9). For Hammett analysis, competitive reactions were carried out with 1:1 mixtures of styrene and different *para*-substituted styrenes ( $p\text{-XC}_6\text{H}_4\text{CH}=\text{CH}_2$ , where X = CN, Cl, H, Me, OMe). A  $\rho$  value of +0.95 was obtained from the Hammett plot of the relative rates ( $k_{\text{rel}}$ ) versus  $\sigma_p$  for  $p\text{-XC}_6\text{H}_4\text{CH}=\text{CH}_2$ . The result strongly indicates that the intermediate responsible for *cis*-dihydroxylation of styrene has nucleophilic character.

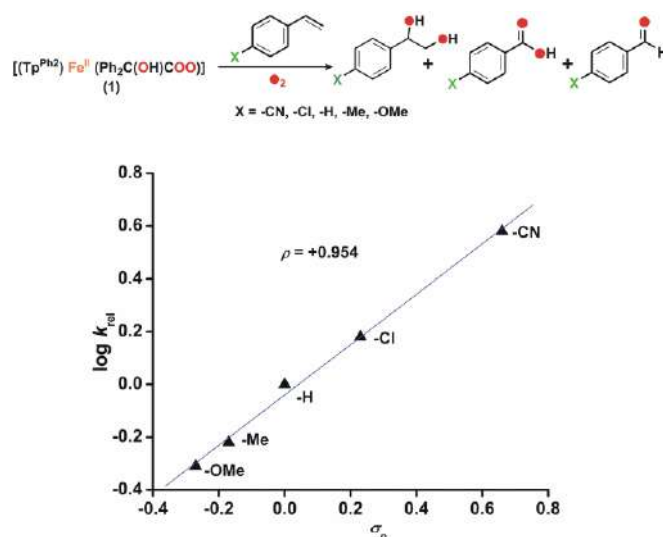


Fig9: Hammett plot of  $\log k_{rel}$  versus  $\sigma_p$  for  $p\text{-XC}_6\text{H}_4\text{CH=CH}_2$ . The  $k_{rel}$  value was calculated by dividing the concentration of the product from  $p\text{-XC}_6\text{H}_4\text{CH=CH}_2$  by the concentration of the product from  $C_6H_5CH=CH_2$ . (Scheme above: Products obtained from  $p\text{-XC}_6\text{H}_4\text{CH=CH}_2$  in the reaction with **1** and dioxygen.)

Labeling experiments using  $^{18}O_2$  in the presence of alkenes strongly support the incorporation of both atoms of molecular oxygen into the *cis*-diol product (Figure 10). High-valent iron-oxo intermediates have been reported to show electrophilic character and can exchange their oxygen atoms with water. On the contrary, the *cis*-diol products obtained in the reactions of alkenes derive both oxygen atoms from molecular oxygen, and the oxidant does not exchange its oxygen atoms with water. An iron(IV)-oxo-hydroxo oxidant is likely to exchange its oxygen atoms with water. The active oxidant was thus proposed to be a nucleophilic side-on bound iron(II)-hydroperoxo species (Scheme 8).

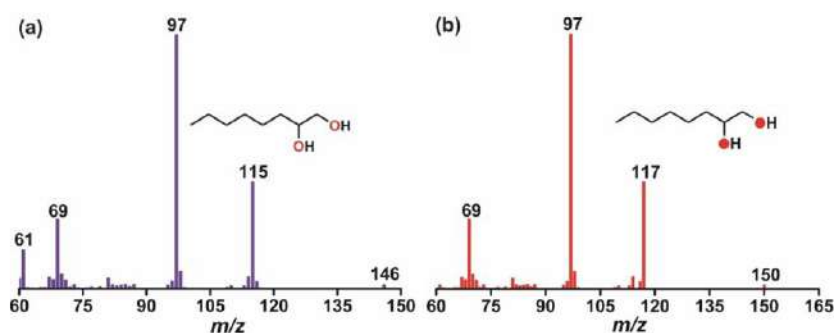
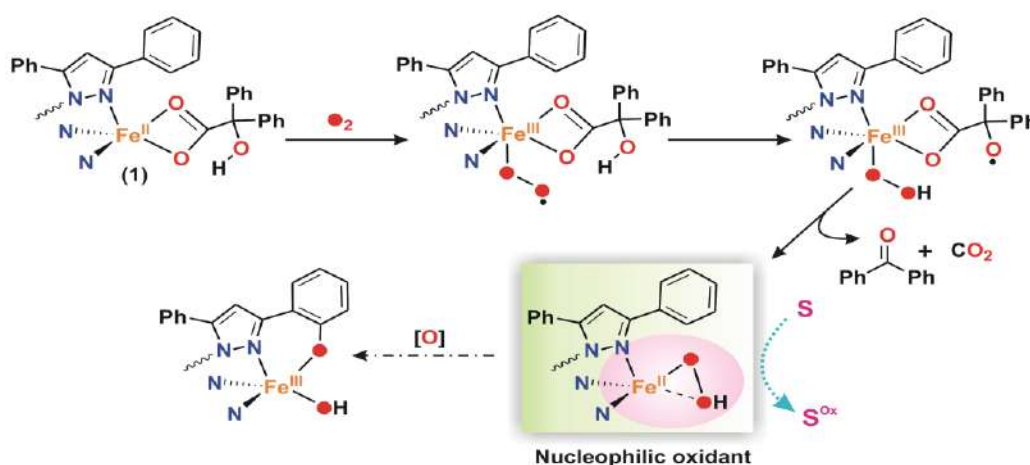


Fig 10: GC-mass spectra of octane-1,2-diol formed in the reaction of **1** with (a)  $^{16}O_2$  (b)  $^{18}O_2$  in the presence of 100 equiv of 1-octene.



## 12.5 Proposed Mechanism

Based on the reactivity studies described above, it is proposed that an iron(III) superoxide species, formed initially upon activation of O<sub>2</sub> at the iron(II) center, abstracts the hydrogen atom from the O-H group of  $\alpha$ -hydroxy acid (scheme 8). The iron(III) hydroperoxo species with a coordinated radical then rearranges to an iron(II) hydroperoxo via decarboxylation of the  $\alpha$ -hydroxy acid to the corresponding carbonyl compound. The iron(II)-hydroperoxo intermediate oxidizes sulfide to a mixture of sulfoxide and sulfone and *cis*-dihydroxylates alkenes. In the absence of any external substrate, the oxidant species hydroxylates one of the 3-phenyl rings of the TpPh<sub>2</sub> ligand. The resulting iron(II)phenolate complex readily reacts with the residual O<sub>2</sub> and gets oxidized to an iron(III) phenolate species exhibiting a broad CT band at 600 nm for **1**.



Scheme 8: Proposed pathway for the formation of a nucleophilic iron oxygenoxidant upon oxidative decarboxylation of the iron(II)-benzilate complex.

## 12.6 Experimental Section

The ligand KTpPh<sub>2</sub> was prepared according to a procedure reported in the literature.

### [Fe(II)(TpPh<sub>2</sub>)(benzilate)] (**1**)

To a suspension of KTpPh<sub>2</sub> (0.35 g, 0.5 mmol) and Fe(ClO<sub>4</sub>)<sub>2</sub>·6H<sub>2</sub>O (0.18g, 0.5 mmol) in methanol (5 mL) was added a methanolic solution (5 mL) of benzilic acid (0.114 g, 0.5 mmol) and triethylamine (70  $\mu$ L). The resulting white Yield: 0.41 g (86%). Elemental analysis calcd

(%) for  $C_{59}H_{46}BFeN_6O_3$  (953.69 g mol<sup>-1</sup>): C 74.30, H 4.86, N 8.81; found: C 73.9, H 4.75, N 8.59. IR (KBr): 3466(br), 2924(vs), 2856(s), 1741(m), 1639(br), 1553(m), 1468(m), 1354(m), 1169(s), 1068(s), 764(vs), 694(vs), 403(vs) cm<sup>-1</sup>.

### Reaction of 1 with Dioxygen.

The iron(II)-benzilate complex (0.020 mmol) was dissolved in 10 mL of a dioxygen-saturated organic solvent. The solution was allowed to stir at room temperature. After the reaction, the solution was removed under a vacuum and the residue was treated with 10 mL of a 3 M hydrochloric acid (HCl) solution. The organic products were extracted with diethyl ether (3 × 15 mL), and the organic layer was dried over anhydrous sodium sulfate. After removal of the solvent, the colorless residue was analyzed by GC-MS and <sup>1</sup>H NMR spectroscopy.

### Reactions of 1 with O<sub>2</sub> in the Presence of External Substrates.

The iron(II) benzilate complex (0.02 mmol) was dissolved in 10 mL of benzene under a nitrogen atmosphere. Dioxygen was purged through the solution for 2 min, and then an external reagent was added and the reaction solution was allowed to stir at room temperature for 20-25 min. After oxidation, the solvent was removed under reduced pressure and the iron complex was decomposed by addition of 10 mL of 3 M HCl solution. Organic products were extracted by either diethyl ether or chloroform (3 × 15 mL), and the organic layer was dried over anhydrous sodium sulfate. After removal of the solvent, organic products were analyzed by GC-MS and <sup>1</sup>H NMR spectroscopy. Quantification of the oxidized organic products by NMR was done by comparing the peak area of four aromatic *ortho* protons (d 7.81 ppm) of benzophenone. For GC analyses, naphthalene was used as an internal standard and the products were identified by comparison of their GC retention times and GC-MS with those of authentic compounds. <sup>1</sup>H NMR (500 MHz, CDCl<sub>3</sub>) data of the oxidized products are provided below.

<sup>1</sup>H NMR data were compared with the literature values.

Benzophenone:  $\delta = 7.80$  (d, 4H), 7.59 (t, 2H), 7.50 (t, 4H) ppm. Thioanisole

oxide:  $\delta = 7.66$  (m, 2H), 7.52 (m, 3H), 2.73 (s, 3H) ppm. Methyl phenyl

sulfone:  $\delta = 7.96$  (d, 2H), 7.60 (m, 3H), 3.06 (s, 3H) ppm. cis-Cyclohexane-1,2-

diol:  $\delta = 3.77-3.82$  (m, 2H) 3.58 (br s, 2H), 1.73-1.82 (m, 2H), 1.51-1.64 (m,

4H), 1.27-1.35 ppm (m, 2H) ppm. 1-Phenylethane-1,2-diol:  $\delta = 7.37$  ppm (m, 4H), 7.30 (m, 1H), 4.85 (m, 1H), 3.80 (m, 1H), 3.70 (m, 1H) ppm. Octane-1,2-diol:  $\delta = 3.80-3.63$  (m, 2H), 3.49 (m, 1H), 1.44-1.40 (m, 2H), 1.30-1.24 (m, 6H), 0.92-0.86 (m, 3H) ppm. cis-Cyclooctane-1,2-diol:  $\delta = 3.94$  (d, 2H), 1.93-1.86 (m, 2H), 1.70-1.63 (m, 4H), 1.55-1.49 (m, 6H) ppm.

## 13. Iron-Oxygen Intermediates in Model Complexes

---

### **13.1 Iron(III)-Superoxide (Fig 10)**

An iron(III)-superoxo species, the key intermediate in the dioxygenactivation pathway of nonheme iron enzymes, has been recently crystallized and characterized by Nam and coworkers. The intermediate was isolated at  $-20^\circ$  by the reaction of iron(III) complex supported by a tetraamido macrocyclic ligand (TAML) and potassium superoxide. The intermediate shows an electronic absorption band at  $\lambda_{\text{max}} = 490$  nm ( $\epsilon = 2,600$  M<sup>-1</sup> cm<sup>-1</sup>). Labeling experiments with K<sub>18</sub>O<sub>2</sub> confirm the incorporation of superoxide moiety from potassium superoxide into the iron complex. Resonance Raman and Mössbauer data establish the intermediate to be a mononuclear iron(III)-superoxide species. Finally, the X-ray crystal structure of the intermediate unambiguously established a mononuclear side-on 1:1 iron complex of O<sub>2</sub> with the triangular Fe-O<sub>2</sub> moiety in a pseudo square pyramidal geometry. The O-O bond length of 1.323 Å is shorter than the iron(III)-peroxo intermediate of nonheme naphthalene dioxygenase (1.45 Å), but is comparable to the Fe(II)-superoxo species of homoprotocatechuate dioxygenase. The iron(III)-superoxo species undergoes both electrophilic and nucleophilic oxidation reactions. Another iron(III)-superoxo complex [(BDDP)Fe<sup>III</sup>(O<sub>2</sub>)] [where H<sub>2</sub>BDDP = 2,6-bis(((S)-2-(diphenylhydroxymethyl)-1-pyrrolidinyl)methyl)pyridine] has been spectroscopically characterized at low temperature. Resonance Raman, Mössbauer and EPR spectroscopic studies support the binding of superoxo ligand to the iron(III)-center.

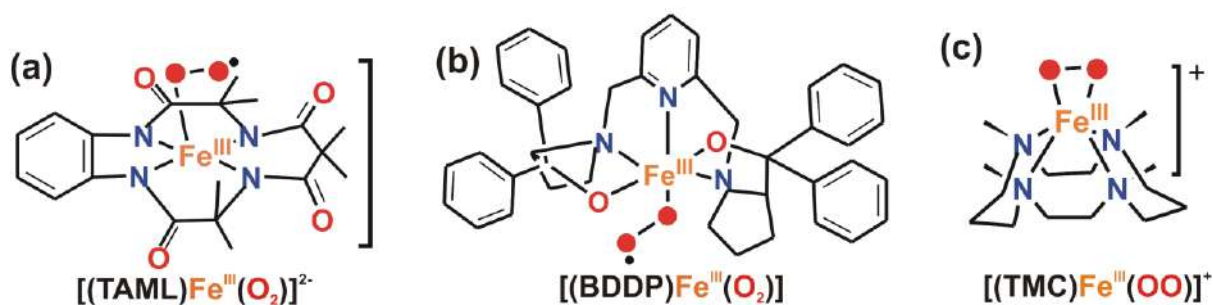


Fig 10: Biomimetic iron(III)-superoxo and peroxo complexes.

### 13.2 Iron(III)-Peroxides and Hydroperoxides

Iron(III)-hydroperoxo or peroxo species is the one-electron reduced form of superoxo species and holds a key position among the intermediates involved in the dioxygen reaction pathway of nonheme metalloenzymes. A number of mononuclear iron(III)-hydroperoxide complexes have been reported, supported by different polydentate ligands such as  $\text{N}_4\text{PyTPAH}_2\text{bbpaRtpen}$  and bispidine-derived ligands which were generated from the corresponding iron(II) complexes in the presence of  $\text{H}_2\text{O}_2$  at low temperature and characterized by different spectroscopic techniques. The first example of iron(III) hydroperoxide complex was evident from the reaction of a diferric complex  $[\text{Fe}_2(\text{quin})(\text{OH})_2]$  (qn= quinaldinate) in the presence of  $\text{H}_2\text{O}_2$  and base. The study also provided the first evidence of reversible O-O bond cleavage of the peroxo group via the formation of  $\text{Fe}^{\text{IV}}\text{O}$  or  $\text{Fe}^{\text{V}}\text{O}$  species, which was confirmed by the Resonance Raman and ESI-TOF/MS measurements. Banseet *al.* have reported the formation of a low-spin iron(III)-hydroperoxide  $[(\text{L}_5\ 2\text{aH})\text{Fe}^{\text{III}}(\text{OOH})]_2^{2+}$  intermediate upon addition of  $\text{H}_2\text{O}_2$  into a methanolic solution of  $[(\text{L}_5\ 2\text{aH})\text{Fe}^{\text{II}}]^+$  at  $-80^\circ\text{C}$ . The intermediate exhibits the absorbance maxima at 515 nm in the UV-vis spectrum and features of low-spin iron(III) species in the EPR spectrum. High-spin  $[\text{Fe}^{\text{III}}(\eta^1\text{-OOH})(\text{L})]_{\text{n}+}$  complexes have also been obtained with sterically hindered  $\text{H}_2\text{bbpa}$  ligand and anionic quin Ligand The iron(III)-(hydro)peroxide complexes of  $\text{N}_4\text{Py}$  ligand show reversible acid-base chemistry. The only crystallographically characterized mononuclear nonheme iron(III)-peroxo complex  $[(\text{TMC})\text{Fe}^{\text{III}}(\text{OO})]^+$  was reported by Nam, Solomon and Valentine The complex exhibits absorption band at 526 nm in the UV-vis spectrum, and was also characterized by Resonance Raman, IR, EPR and EXAFS studies. X-ray crystallographic studies reveal the peroxo coordinated iron(III) complex with the Fe-O bond distances of  $1.906(4)\text{\AA}$  and  $1.904(4)\text{\AA}$  and the O-O bond length of  $1.463\text{\AA}$ . The

conversion of iron(III)-peroxo species to an iron(III)-hydroperoxo via protonation and then its final conversion to an iron(IV)-oxo species via homolytic O-O bond cleavage by chemical means have also been documented. The reactivity of all these oxidants have been explored in various oxidation reactions. Que and coworkers have isolated the same high-spin Fe<sup>III</sup>-OOH complex via protonation of its conjugate base. This Fe<sup>III</sup>-OOH species can be converted quantitatively to an Fe<sup>IV</sup>=O complex via heterolytic O-O bond cleavage. The conversion is promoted by two factors: the strong Fe<sup>III</sup>-OOH bond, which inhibits Fe-O bond lysis, and the addition of protons, which facilitates O-O bond cleavage. In a subsequent study, using the same TMC ligand, Nam group have explored the one electron reduction of iron(III)-hydro/alkyl peroxo complexes by ferrocene derivatives to generate the corresponding iron(IV)-oxo complexes, via rapid heterolytic O-O bond cleavage of a transient iron(II)-hydro/alkylperoxo species. Nam and co-workers have explored the reactivity of a high-spin iodosylarene intermediate [(13-TMC)Fe<sup>III</sup>-(O-IAr)]<sup>3+</sup> bearing an N-methylated cyclam ligand which has been proposed to be more reactive than the corresponding iron(IV)-oxo complex. Recent research by the same group have revealed that the iron(III)-iodosylarene intermediates epoxidize olefins, with high stereospecificity and enantioselectivity. displays absorbance maxima at 400 (9800), 825 (260), 866 (250) nm, whereas complex [(H<sub>3</sub>buea)Fe<sup>IV</sup>O]<sub>2</sub><sup>2+</sup> shows absorbance maxima at 350 (4200), 440 (3100), 550 (1900), 808 (280) nm. (Fig 11)

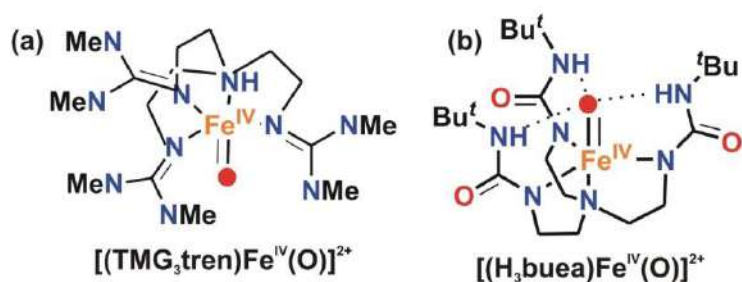


Fig 11: High-spin ( $S = 2$ ) iron(IV)-oxo complexes supported by (a)TMG<sub>3</sub>tren ligand and (b) H<sub>3</sub>buea<sub>3</sub>- ligand.

### 13.4 Iron(V)-Oxo Oxidants

An iron(III)-hydroperoxide intermediate may convert to an iron(V)-oxo species by heterolytic O-O bond cleavage. Such iron(V) oxo species has been implicated as the key

oxidant in several nonheme enzymes such as Rieske dioxygenases, methane monooxygenases etc. Indirect evidence for such an oxidant has been obtained in biomimetic oxidations by [(TPA)Fe<sup>II</sup>]<sub>2</sub><sup>+</sup> and related catalysts using H<sub>2</sub>O<sub>2</sub> as oxidant. The spectroscopically characterized iron(V)-oxo intermediate [(TAML)Fe<sup>V</sup>=O]<sup>-</sup> species reported by Collins *et al.* supported by a tetradentate ligand TAML exhibits an S = ½ spin state, exhibiting EPR signals at g = 1.99, 1.97, 1.74. Costas *et al.* have characterized an iron(V)-oxo-hydroxo intermediate namely [(Me<sub>6</sub>HPytacn)Fe<sup>V</sup>(O)(OH)]<sup>+</sup> by cryospray ESI-mass spectroscopy. Collins *et al.* and subsequently Sengupta and coworkers have reported the reactivity of a synthetic iron(V)-oxo intermediate appended by modified TAML ligands toward different organic substrates.

#### 14. Role of Lewis Acidic Metal Ions in the Stabilization and Reactivity of Iron-Oxo Oxidants

Lewis acidic metal ions or protons have invoked interesting chemistry in the area of nonheme iron-oxygen intermediates. Extensive studies by Nam, Que, Fukuzumi, Ray and many others have led to the isolation of metal peroxo and high-valent metal-oxo species bonded by redox-inactive metal ions, which results in remarkable change in their chemical properties. In high-valent metal oxo complexes, binding of metal ions or protons resulted in positive shifts in the one-electron reduction potentials. Nam and coworkers have reported that such positive shift in the one-electron redox potential of metal-oxo oxidants change the mechanism of oxygen atom transfer (OAT) and of hydrogen atom transfer (HAT) to metal coupled electron transfer (MCET) and proton coupled electron transfer (PCET) in the presence of metal ions or protons, respectively. In a subsequent work, Nam *et al.* have proposed the reduction of iron(III)-peroxo complexes with coordinated redox inactive metal ions facilitates the cleavage of O-O bond to form the corresponding iron(IV)-oxo intermediate. (Scheme 9)



Scheme 9: Lewis acid promoted conversion of iron(III)-peroxide to high valent iron-oxo oxidants.

## Conclusion:

---

So, in this review we can understand various catalytic reaction performed by nonheme oxygenase with 2-His-1-carboxylate facial triad motif. And from biomimetic approach we can find how synthetic ligands are used to generate iron oxygen oxidant and mimic nature's activity, also we can understand about the reaction intermediates, and their importance for knowing the actual mechanism.

## References:

---

1. Solomon, E. I., Goudarzi, S., & Sutherlin, K. D. O<sub>2</sub> Activation by Non-Heme Iron Enzymes. *J. Am. Chem. Soc.*, **2016**, 55(46), 6363–6374.
2. Kal, S., & Que, L, Dioxygen activation by nonheme iron enzymes with the 2-His-1-carboxylate facial triad that generate high-valent oxoiron oxidants. *J. Biol. Inorg. Chem.*, **2017**, 22, 339–365.
3. Koehntop, K. D., Emerson, J. P., & Que, L The 2-His-1-carboxylate facial triad: a versatile platform for dioxygen activation by mononuclear non-heme iron(II) enzymes.). *J. Biol. Inorg. Chem.* (**2005**), 10(2), 87–93.
4. Kovaleva, E. G., & Lipscomb, J. D. Versatility of biological non-heme Fe(II) centers in oxygen activation reactions. *Nature Chemical Biology*, **2008**, 4(3), 186–193.
5. Costas, M., Mehn, M. P., Jensen, M. P., & Que, L. Dioxygen Activation at Mononuclear Nonheme Iron Active Sites: Enzymes, Models, and Intermediates. *Chem. Rev.*, **2008**, 104(2), 939–986.
6. S. Paria, P. Halder, T. K. Paine, “A functional model of extradiol-cleaving catechol dioxygenases: mimicking the 2-his-1-carboxylate facial triad” *Inorg. Chem.* **2010**, 49, 4518.
7. (a) S. Paria, S. Chatterjee, and T. K. Paine, “Reactivity of an Iron-Oxygen Oxidant Generated upon Oxidative Decarboxylation of Biomimetic Iron(II)- $\alpha$ -Hydroxy Acid Complexes” *Inorg. Chem.* **2014**, 53, 2810-2821

8. P. C. A. Bruijninx, G. van Koten, R. J. M. Klein Gebbink, “Mononuclear non-heme iron enzymes with the 2-His-1-carboxylate facial triad: recent developments in enzymology and modeling studies” *Chem. Soc. Rev.* **2008**, 37, 2716
9. O. Hayashi, *Molecular Mechanisms of Oxygen Activation*, Academic Press, New York and London, **1974**.
10. Sayanti Chatterjee, thesis entitled *Dioxygen Activation by Functional Models of Nonheme Iron Enzymes: Mechanistic Studies and Catalytic Applications*, Thesis, **2015**, 35-82.



**POROUS CARBON AND ITS APPLICATION AS  
HYDROGEN STORAGE MATERIALS.**

**SCOTTISH CHURCH COLLEGE  
UNIVERSITY OF CALCUTTA**

**C.U. ROLL NO. 223/CEM/191029**

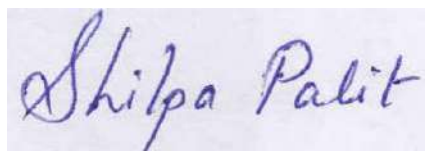
**C.U. REGISTRATION NO. 223-1211-0008-19**

**SPECIAL PAPER: SI 44**

NAME OF CANDIDATE

**SHILPA PALIT**

SIGNATURE OF CANDIDATE



-----

NAME OF SUPERVISOR/EXAMINER

**DR. CHANDAN KUMAR PAL**

SIGNATURE OF SUPERVISER/EXAMINER



-----

**REVIEW ON-‘Porous Carbon and Its Application as H-storage material’**

**PROJECT WORK SUBMITTED FOR THE PARTIAL FULFILMENT OF  
MASTERS DEGREE OF MASTER OF SCIENCE IN CHEMISTRY OF  
THE UNIVERSITY OF CALCUTTA UNDER SCOTTISH CHURCH  
COLLEGE, 2021**

**BY - SHILPA PALIT**

REGISTRATION NO: 233-1211-0008-19 OF 2019-2021

CU ROLL: 223/CEM/191029

**UNDER SUPERVISION OF  
DR. CHANDAN KUMAR PAL**



**SCOTTISH CHURCH COLLEGE  
UNIVERSITY OF CALCUTTA  
DEPARTMENT OF CHEMISTRY**

**DEDICATED WITH OUTMOST  
RESPECT  
TO  
MY PARENTS**



Dr. CHANDAN KUMAR PAL

Associate Professor

*ckpchem@scottishchurch.ac.in*

DEPARTMENT-CHEMISTRY

Ph. 033 2350 3862

email: *scottish.cal@gmail.com*

13 July 2021

## **TO WHOM IT MAY CONCERN**

This is to certify that SHILPA PALIT ( Roll-19PG-C-07 ), Reg.No.-223-1211-0008-19 (of 2019-2021), a student of MSC in the academic year session 2019-2021 has worked on the project entitled '**Porous Carbon and Its Application as H-storage material.**' for the partial fulfillment of requirement of Master of Science in CHEMISTRY under the University of CALCUTTA, SCOTTISH CHURCH COLLEGE, under my supervision. To the best of my knowledge this work has not been submitted to any other universities for the award of any other degree.

Dr. CHANDAN KUMAR PAL

Associate Professor

Department of ChemistryS

Scottish Church College, Kolkata

**University of Calcutta**  
**Scottish Church College**  
**Faculty of science**  
**Department of chemistry**



**DECLARATION**

I, Shilpa Palit hereby declare that the dissertation entitled '**Porous Carbon and Its Application as H-storage material**' submitted to the Chemistry Department of the SCOTTISH CHURCH COLLEGE, University of Calcutta, for the degree of Master of Science in Chemistry is my original work and the dissertation has not been submitted for the award of any degree, a diploma, to any other University or Institution.

Date: ...13/07/2021.....

Place: ...KOLKATA...

-----  
Full Signature student

# ACKNOWLEDGEMENT

This study was carried out at Department of chemistry, Faculty of Science, SCOTTISH CHURCH COLLEGE, University of Calcutta, West Bengal, India.

I am grateful to the former and present Head of the Department of Chemistry, Scottish Church College for permitting me to carry out project work.

I wish to express my heartiest sense of gratitude to prof. CHANDAN KUMAR PAL, Department of CHEMISTRY, SCOTTISH CHURCH COLLEGE, for introducing me to field of **‘Porous Carbon and Its Application as H-storage material’** and his supervision, advice, helpful discussion, constant encouragement and insightful guidance from the very early stage of project work.

I convey my warmest thanks to my parents, and all my friends.

# INDEX

## CHAPTERS

- + TO WHOM IT MAY CONCERN
- + DECLARATION
- + ACKNOWLEDGEMENT
- + INTRODUCTION
- + SYNTHESIS OF ACTIVATED CARBON
- + PYROLYSIS ACTIVATION
- + HYDROGEN STORAGE IN CARBON MATERIAL
- + MECHANISM OF HYDROGEN STORAGE
- + COMPARISON OF H<sub>2</sub> STORAGE CAPACITY OF DIFFERENT  
CARBON MATERIALS
- + CONCLUSION
- + REFERENCE

## **INTRODUCTION**

The 3<sup>rd</sup> and 5<sup>th</sup> most abundant element of the universe and in human body respectively is carbon, a vital constituent of the universe and all organisms. In recent decades, a great deal of attention have been attracted by porous carbon on chemistry, physical, material science etc. Carbon materials are identified with their excellent properties like high chemical stability, good electrical conductivity and low cost. However, the rich pore structure differentiated porous carbon from traditional carbon materials in the field of large specific surface area, pore volume, size and adjustable channels. Thus, these carbons can be used for adsorption of wide distribution of molecules from gas to liquid.

A high performance porous carbon HPC (Hierarchical Porous Carbon), defined as carbon materials containing interconnected pores of any two or all three types, exhibits many applications like energy storage, catalysis and adsorption. The International Union of Pure and Applied Chemistry classified pore sizes as micropores, having pore sizes <2nm, mesopores, 2-50nm, and lastly macropores, >50nm. They work differently. Micropores are distinguished in providing large surface area; mesopores enhance mass transfer because of their mass-transfer resistance and ultimately macropores, acting as reactant reservoirs and shorten mass-transfer pathways.

Porous carbons are categorized into two namely, (i) Carbon foam with desired porous architecture used for thermal and structural applications and (ii) Activated carbons having porous carbon with added surface activating chemical groups [1]. These carbons have been in use for thousands of years and are regarded as one of the most important types of industrial carbons. These materials, having highly developed internal surface area and porosity, has vivid applications (mainly as versatile absorbents) of industrial significance.

Some highlighted and advanced applications of porous carbons and HPCs are mainly as super capacitors, capacitive deionization, Li-S battery, CO<sub>2</sub> capture, catalysis, hydrogen storage materials etc.



Hydrogen can be considered as the cleanest fuel, due to depletion of petroleum resources and problems related to fossil fuels. Hydrogen has high calorific value, 3 times as high as petroleum. Its energy is denser with respect to fossil fuels i.e. have high gravimetric energy density. So, if hydrogen energy can be produced cheaply, then common energy system can be changed from fossil fuel based to hydrogen fuel based. Thus, storage of hydrogen is becoming an important research interest day by day. Carbon materials, especially activated carbons can be served as well known precursors in the H storage due to its great adsorption properties. This review paper mainly focuses on activated porous carbon and their vivid applications as hydrogen storage materials.

## **SYNTHESIS OF ACTIVATED CARBONS**

Activated carbons are mainly prepared by the process of pyrolysis of carbonaceous materials, biomass and waste. Biological organisms have their hierarchical structures, which are naturally organized, from chemical substances to organelles, then to cells, tissues and ultimately an entire organism. The processing of activated carbons mainly involves raw material selection, then carbonization and lastly activation.

### ➤ **RAW MATERIALS OR PRECURSORS-**

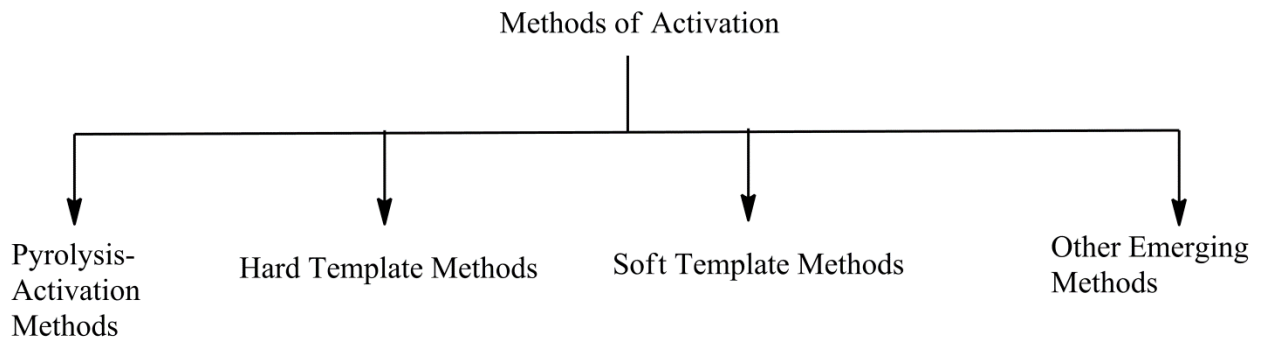
Appropriate raw material selection is an important factor. They should be of low cost with high carbon content and low inorganic content. Wood, coal, peat, fruit stones, coffee beans, cornstalks, shells, etc. can be used as precursors for pyrolysis [2]. Mainly cellulose, lignin and hemicelluloses are the organic components of biomass. During pyrolysis they are converted into volatile substances and residual biochar which is essential for making activated carbons. Amongst woods, one of the precursors for largest production of activated carbon is from pine, forming 50% of precursor. Moreover, the precursor must have high density, to enhance structural strength of carbon.

### ➤ **CARBONISATION AND PYROLYSIS**

Carbonisation involves steps like thermal decomposition of raw materials, non- carbon species elimination, thus giving a fixed carbon mass and rudimentary pore structure. Non-carbon materials i.e. oxygen and hydrogen are to be needed to removed by pyrolysis of the starting materials, carried out usually at a temperature below 800 degree C, in inert atmosphere. At a temperature of about 500 degree Celsius, the basic structures of micropores of biochar with microporosity are formed. Further heat treatment of about 800 °C is given to remove the tarry products evolved during pyrolysis, that block the pores, thus making the pores available. Generally, further increase in pyrolysis temperature to about 1000 °C, heating rate and residence time would decrease the yield of biochar as more volatile substance would release. Though, this produces pores in biochar but too much release of volatile substances could lead to the collapse of pores. Detailed mechanism and kinetics of pyrolysis of biomass can be found in review by Liu et al [3].

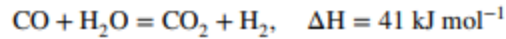
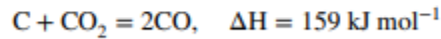
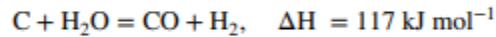
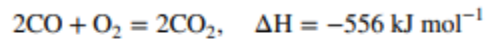
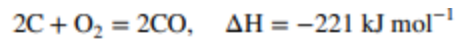
### ➤ ACTIVATION

The process of activation is mainly carried out to enlarge the diameter of pores that are created during carbonization process and to create some new porosity, resulting in the formation of readily accessible and well developed pore structure, with very large internal surface area.



### **PYROLYSIS ACTIVATION:**

**i) Physical Activation:** In the presence of suitable oxidizing agent like air, CO<sub>2</sub> and steam, gasification of carbon materials by physical activation can be done, mostly at a temperature of about 800-1000 °C. Some of the endothermic reaction taking place by the process is:

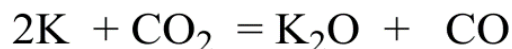
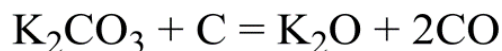
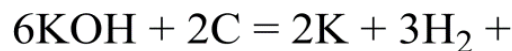


Reaction with steam is faster than that with CO<sub>2</sub> because H<sub>2</sub>O being smaller than CO<sub>2</sub> molecule which diffuses faster in pores of carbon. But at the same time, external oxidation is promoted by activation of CO<sub>2</sub> and large pores development as compared to steam activation.

Due to some exothermic reactions, excessive burning takes place and the reaction becomes difficult to control. As a result, weight loss of the carbon material takes place in physical activation.

ii) **CHEMICAL ACTIVATION:** This process is mainly carried with biomass (like wood) as starting material. Chemical activating agents are impregnated in the precursor materials, then at temperature between 400 °C and 600 °C, pyrolysis is carried out in inert atmosphere. Some of the surface active agents H<sub>3</sub>PO<sub>4</sub>, ZnCl<sub>2</sub>, H<sub>2</sub>SO<sub>4</sub>, K<sub>2</sub>S, KSNS, KOH, chlorides and carbonates of Fe<sup>2+</sup>, Mg<sup>2+</sup>, etc. All of them mostly are dehydrating agents causing inhibition of tar formation. KOH acts as the most widely and efficiently used activating agent.

The equations for KOH activation mechanism are illustrated [4] below



From

equation (1) and (3), the production

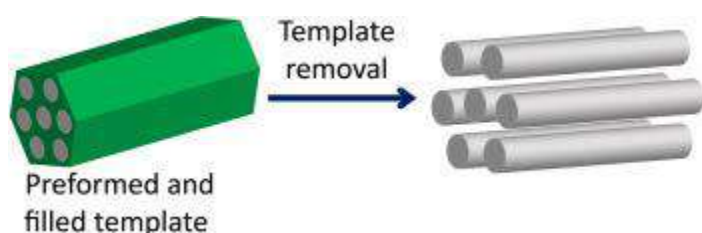
of carbon dioxide by decomposition of  $K_2CO_3$ , above  $700\text{ }^\circ\text{C}$  contributes to further developments of pores by carbon gasification [5].

Moreover, for the instances,  $K_2CrO_4$  (potassium oxalate) can also be used as activating agent, especially in synthesis of hierarchical porous carbon for high capacitance and energy density from cornstalk [6], along with calcium carbonate,  $CaCO_3$ , as hard template.

Chemical activation has several advantages over physical, including shorter reaction time, high microporosity and lower processing temperature.

## ii) **HARD TEMPLATE METHOD:**

The hard-templating synthetic route, also known as “nanocasting,” is another straightforward technique to obtain mesoporous structures [7]. This technique is based on the use of preformed templates made from aggregates of nanoparticles, carbon or mesoporous silica. The use of a hard template overcomes the need to control hydrolysis and condensation of guest species and their interactions with surfactants. The hard template method ensures that the meso-channels are completely filled. Therefore, hard templating can prepare a wide range of materials, in particular highly crystalline and even single-crystal materials due to the resistance of the rigid template to high temperatures. Nonetheless, this method presents its disadvantages, for example there are far fewer hard templates rather than soft templates available for use, hence the procedure is more elaborate and time consuming.



Commonly covalent compounds, usually rigid and solid materials are referred as hard templates. For synthesizing HPC, having well controlled porosity, templates methods can be used. Silica is considered as the most popular hard template. But use of silica can be somewhat expensive. A much cheaper and environment friendly material that can work as template is ice. Here, aqueous

solution of carbon source is frozen and it forms internal ice crystals, thus acting as template. Some more hard templates are fish scale, yeast cell, wood, cotton fabrics etc.

iii) **SOFT TEMPLATE METHODS:** The soft-templating approach aims for the co-assembly of surfactant molecules and guest species into an ordered mesoporous structure, which is obtained after the removal of the template. This method has become a general synthetic pathway for ordered mesoporous materials. Organic molecules or block copolymers are generally used as soft templates. These organic molecules spontaneously form ordered micelles and evaporates during carbonization. Thus, soft template methods are more convenient as compared to hard template methods.

Surfactants like SDS etc have bipolar structure and micelle forming ability, thus can be used as soft templates as they create mesopores and macropores. But, most biomass and waste are insoluble in surfactants and cannot form stable colloids.

#### IV) **OTHER EMERGING METHODS:**

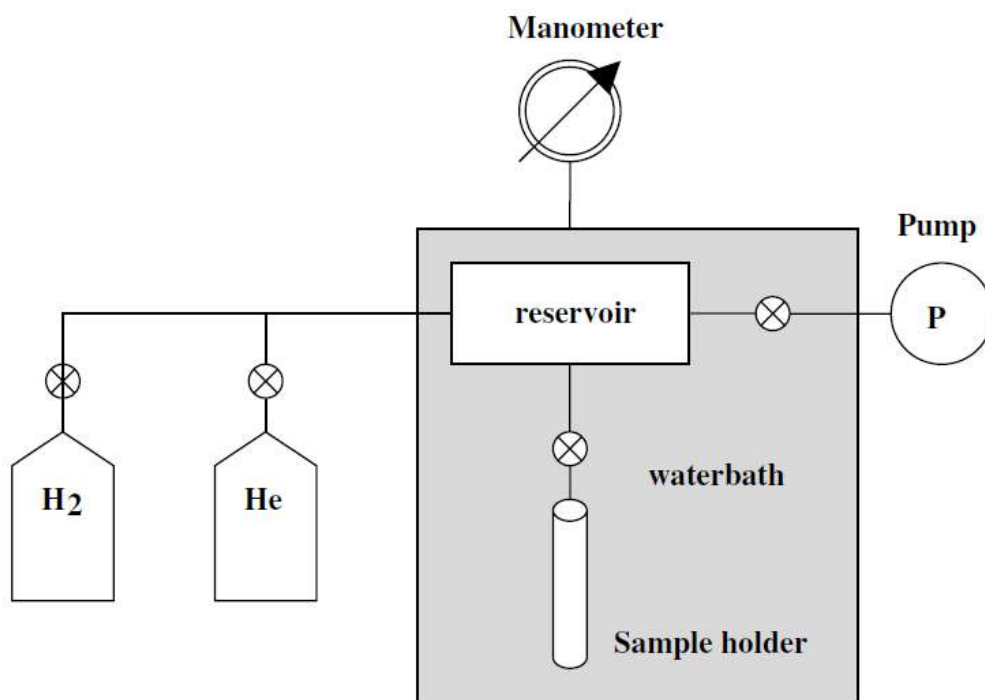
Besides template methods, other methods also have been investigated for preparing HPC from non-structured materials. These techniques include hydrothermal carbonization, spray pyrolysis, [8], chemical vapor deposition (CVD) and autogenic pressure carbonization.

## HYDROGEN STORAGE IN CARBON MATERIALS

Hydrogen, an efficient alternative fuel, can be utilized widely in different sectors. However, the production of hydrogen is not conveniently obtainable; also, for its storage and transportation, the hydrogen technology suffers many major challenges [10].

The hydrogen adsorption has been measured by a manually controlled Sieverts' apparatus, consisting of two volumes connected through a valve, i.e., sample holder and gas inlet chamber of constant volume. Owing to the design with small volumes, the apparatus is used to investigate

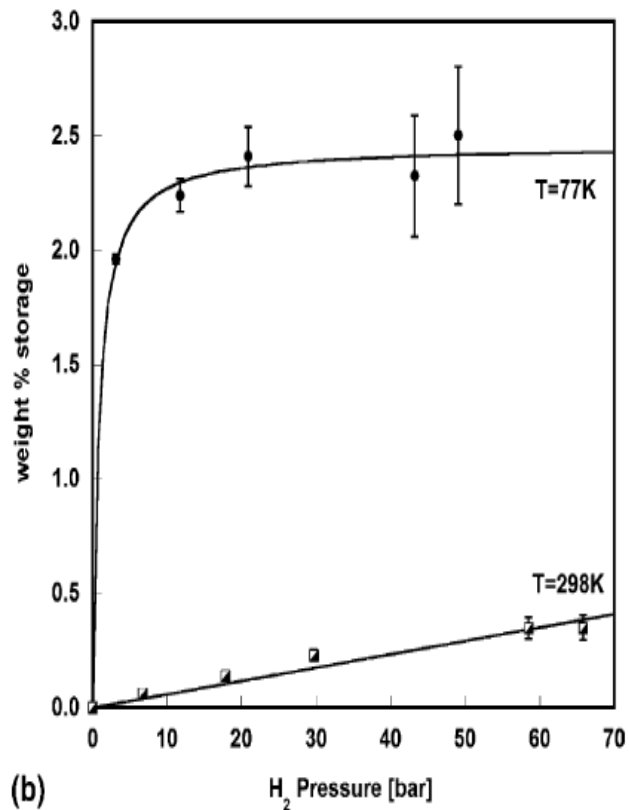
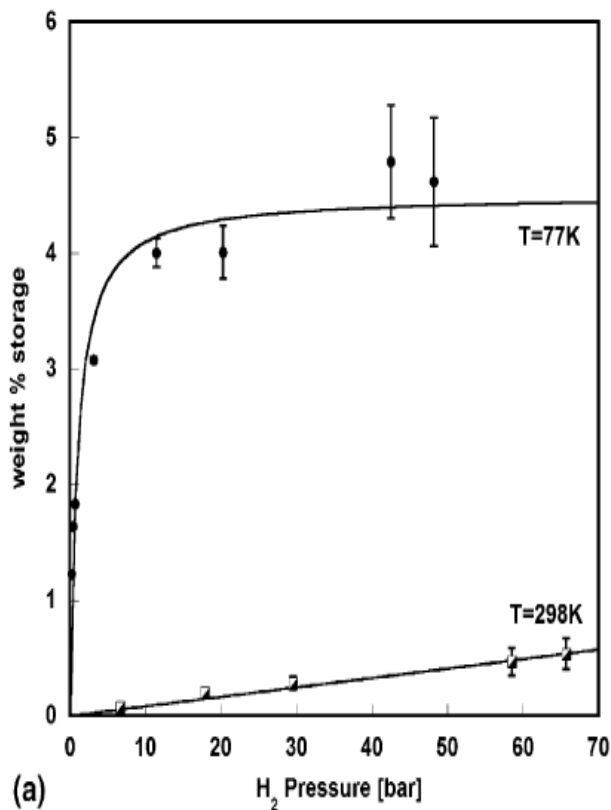
even very small quantities of materials of carbon. A schematic diagram of the apparatus is shown in figure.



**For measurements at room temperature, reservoir and sample holder are immersed in the water bath. For measurements at 77 K, the sample holder is immersed in liquid nitrogen.**

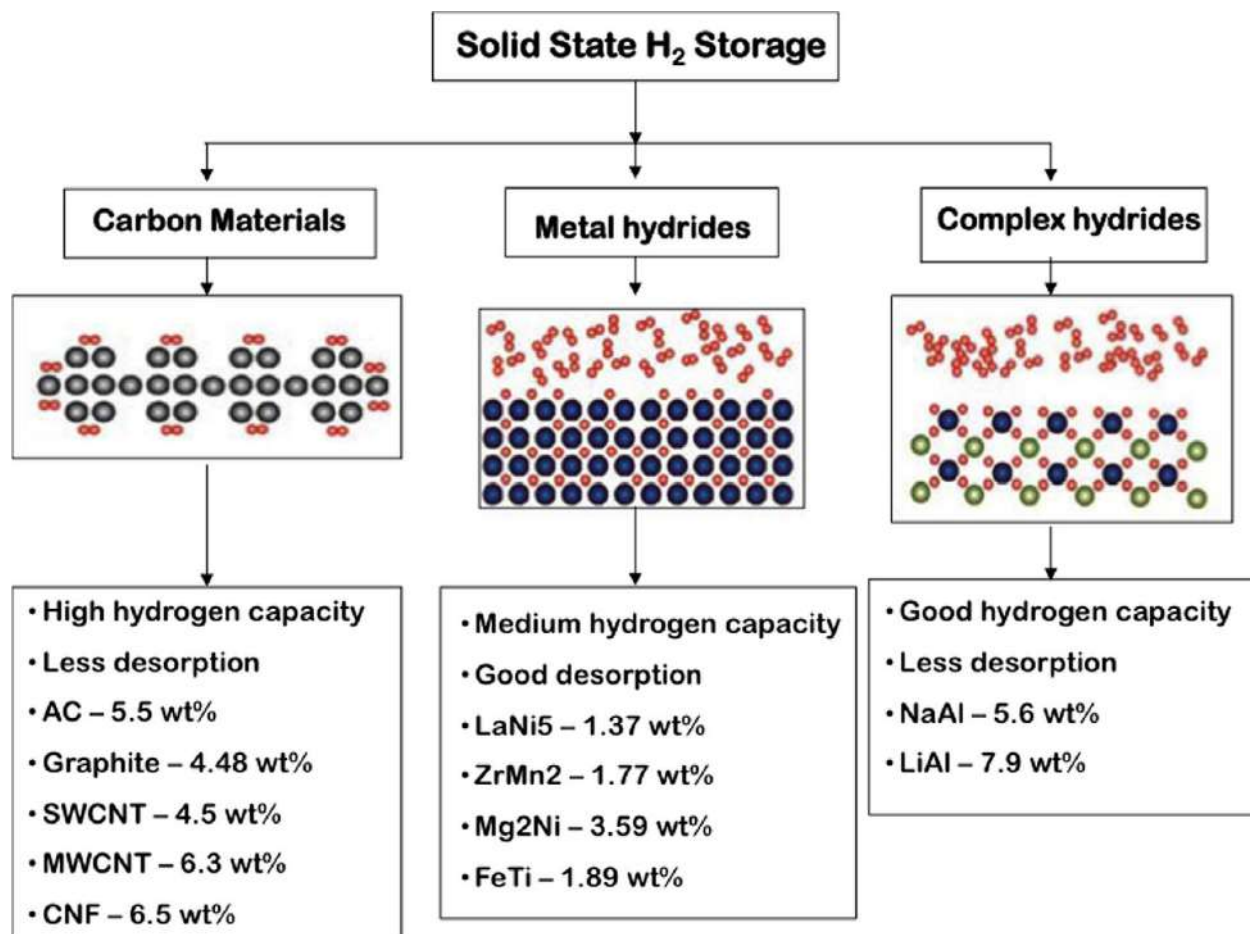
Hydrogen is stored reversibly in these carbon materials which are proved by the fact that the hydrogen storage capacity is totally independent of the number of adsorption cycles.

The hydrogen adsorption isotherms of activated carbon and of purified SWCNTs at 77 K and at room temperature are given below. Even though, both the materials possess a completely different nanostructure, the shape of the isotherms is however very similar. This shape is characteristic for all investigated carbon materials. At 298 K, the hydrogen uptake is a linear function of pressure, which is explained with Henry's law. At room temperature, no saturation occurs in the investigated pressure range and as a result, the adsorbed hydrogen layer on the carbon surface is found to be much diluted. At low temperature, the isotherms are similar with Langmuir type equation (type I isotherm), which indicates that saturation takes place with a hydrogen monolayer formation, which is as usual for microporous surfaces. [11], [12]. In fact, the hydrogen adsorption mainly gets limited to one molecular layer in microporous structures by its pore dimensions.



**Hydrogen adsorption isotherms at room temperature and at 77 K fitted with a Henry type and a Langmuir type equation, respectively (a) for activated carbon, (b) for purified SWCNTs.**

Hydrogen can be stored in three ways: compressed gas, cryogenic liquid and as solid-state storage. Storage of hydrogen in solid form is considered as safest mode in which hydrogen combines with materials through physisorption or chemisorption.



The hydrogen storage options are given in the above three in solid state. Among these three, carbon materials are considered to be the most efficient because of high capacity of hydrogen, less desorption, larger surface area and low cost.

A range of carbon nanostructures like that of activated carbon (AC), carbon nanotubes (CNTs), activated carbon fibers, carbon nanofibers (CNFs), and carbon nanohorns are examined in literature in order to identify their capacity of hydrogen storage. Hydrogen adsorption occurs in micropores where the density of unadsorbed gaseous phase is lower than that of hydrogen adsorbed phase at above the critical point.

For any carbon material, the bond between hydrogen to material is not so strong, and low adsorption energy ruled out the possibility of the hydrogen adsorbed in the narrow interstitial



channels between the nanotubes. This means that with higher available surface area, higher will be the storage capacity similar to that in case of ACs. [13].

Materials such as CNTs, ACs, zeolites, graphene, and metal organic frameworks, by physical and chemical treatments, can be optimized for higher storage capacities of hydrogen.

## **MECHANISM OF HYDROGEN STORAGE:**

### **PHYSISORPTION:**

The phenomenon of physisorption is mainly based on van der Waals force of interaction between hydrogen molecules and materials of carbon. The interaction energy between solid material and hydrogen molecules can be estimated by:

$$E = \alpha H_2 \text{ substrate} / R^6$$

Where,  $\alpha$  = the polarizability and  $R$  = the interaction distance.

Here, hydrogen has fixed polarizability; therefore, the only way to increase the interaction energy is by selecting materials of high polarizability. Average interaction energy mainly ranges from 4 to 5 kJ mol which shows a weak interaction between the hydrogen molecules and the carbon materials. As a result, increase in temperature can desorb hydrogen and consequently, at high temperature low storage capacity can be observed.

### **CHEMISORPTION:**

Each and every carbon atom can be utilized as site of interaction for chemisorption, if the covalent chemical bonding between carbon atoms is effectively used. It is reported that on CNTs, a dissociative chemisorptions of hydrogen is mostly feasible on carbon materials. At high pressure, the hydrogen molecules gets broken into atoms, thus facilitating the formation of two C-H bonds and resulting in shortening of distance between two adjacent tubes thus leading to dissociative hydrogen adsorption. Here, also, at higher temperatures desorption takes place and is not very useful for practical storage of hydrogen.

Moreover, it has also been suggested, [15], that two different mechanisms are mainly responsible for adsorption of hydrogen on materials of carbon. In first mechanism, hydrogen molecules are adsorbed on the surface of carbon materials. In the second mechanism, hydrogen molecules penetrate in between the interlayer space. This showed that the higher hydrogen adsorption occurs by first mechanism where the specific surface area plays a very important role, which concludes that high hydrogen storage capacity could be achieved by high specific surface area.

## **COMPARISION OF HYDROGEN STORAGE CAPACITY OF DIFFERENT CARBON MATERIALS.**

### **I) FOR ACTIVATED CARBONS:**

Activated carbon is cheap and has good availability for industrial purpose; for this reason, it receives high interest for hydrogen storage application. The potential for storage in this form of carbon is determined by the microstructure of the carbon material.

Activated carbon is a form of processed carbon that comprises graphite crystallites and amorphous carbon, and normally have pore diameter of <1 nm. The experimentally measured hydrogen storage capacity depends also on the material employed (doping, etc), that ranges between 0.5 and 5 wt%. ACs possesses low mass density and a high specific surface area. Weak van der Waal's forces enhance the physisorption of hydrogen molecules as they get adsorbed and diffuse into the pores of the ACs. [16].

A mathematical model has been developed by to calculate the net hydrogen storage capacity by carbon materials over a wide temperature and pressure range. It has been shown that hydrogen adsorption in AC is more efficient than compressed gas at cryogenic temperature.[17]

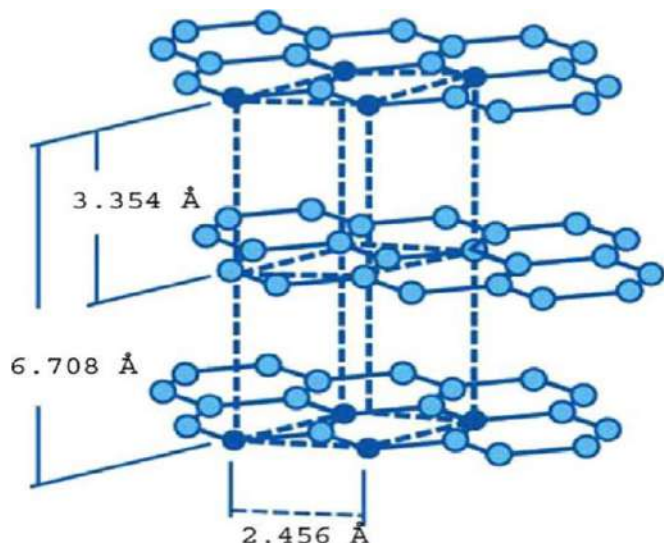
**Hydrogen storage capacity of AC:** The ability of hydrogen adsorption on activated carbon was first investigated in early 1980s at low temperatures. A table has been shown, having different hydrogen storage capacities that are reported in similar operating conditions. [18], [19], [20], [21].

Adsorbent	Hydrogen storage (wt%)	Conditions-temp, pressure
AC	0.67	303 K, 10 MPa
AC	1.4	77 K, 0.1 MPa
AC	1.6	296 K, 13 MPa
AC	4.5	77.4 K
AC	5.7	77 K, 3 MPa
AC (KOH-treated)	6.6	77 K, 4 MPa
AC (Ni-doped)	1.8	77 K, 0.1 MPa
AC (Pt-doped)	2.3	298 K, 10 MPa
AC (Pd-doped)	5.5	298 K, 8 MPa

Abbreviation: AC, activated carbon.

## II] **GRAPHITE:-**

Graphite is  $sp^2$  hybridized, with a sheet like structure where all atoms are weakly bonded and exist in a plane, is held together by van der Waal's forces of attraction to the sheets above and below.



Graphite structure

## **HYDROGEN STORAGE CAPACITY OF GRAPHITE:**

Since, adsorption of gas mainly occurs in volume of micropores, the SSA of carbon materials is of great concern. Hence, storage capacity of hydrogen decreased with Pt decoration as a result of the decrease in SSA and micropore volume. It was observed that the hydrogen storage capacity increased with Pt content up to certain level and then decreased. These results concluded that the hydrogen storage capacity of graphite depends on their metal content and also on dispersion rate. Also, the total amount of hydrogen adsorption may decrease, if the hydrogen storage capacity is a function mainly of SSA and micropore volume.

Summary of hydrogen storage capacities of various graphite samples is presented in Table below. [22]

Adsorbent	Hydrogen storage (wt%)	Conditions temp, pressure
G (Ni-doped)	0.92 (experimental)	-
G (Cu-doped)	0.97 (experimental)	-
G (Co-doped)	1.8 (experimental)	-
G (Fe-doped)	3.9 (experimental)	-
G (Al-doped)	3.48 (Theoretical)	300 K, 100 MPa
G (Li-doped)	6.5 (Theoretical)	298 K, 2 MPa
Ni/porous graphite	4.48 (experimental)	298 K, 10 MPa

### III) SPHERICAL FULLERENE:

Popular and well-known fullerene include  $C_{70}$ ,  $C_{76}$ ,  $C_{84}$ ,  $C_{240}$ , and  $C_{540}$ , but however, the most common is  $C_{60}$  constituting of 60 carbon atoms bounded in an almost spherical condition.

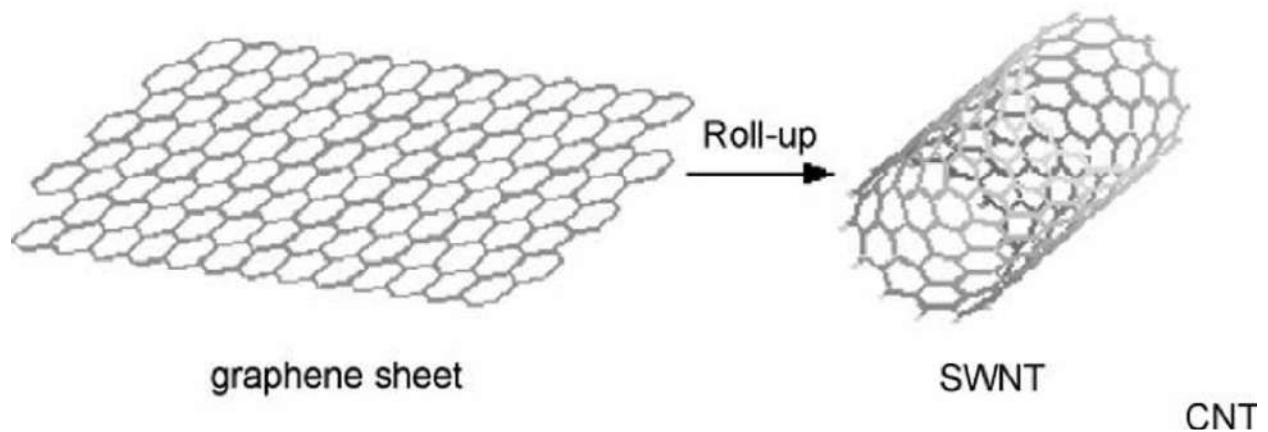
#### **HYDROGEN STORAGE CAPACITY:**

Theoretical hydrogen storage capacity of approximately 8 wt% with titanium and scandium with 0.3 to 0.5 eV binding energy is observed. It was further noted that bonding of heavy metals such as cobalt, manganese, and iron is at all not possible with  $C_{60}$ .

The “molecular surgical method,” have helped to develop buckyballs in which, every ball is perforated with a sulfur atom in its rim. The buckyball can be closed by series of chemical reactions once after the hydrogen molecules entered that hole and then, all the gaps can be filled by heating it up to 340°C for 2 hours.

#### IV) **CARBON NANOTUBES:**

Carbon nanotubes can be considered as a single rolled graphene layer with an inner diameter starting from 0.7 nm up to several nanometers and a length of 10 to 100  $\mu\text{m}$ . Three different kinds of CNTs exist, they are, “armchair,” “zigzag,” and “chiral” subjected to the way in which the graphene sheet are folded into a tube. The rolling up of multiple graphene sheets ultimately results in the formation of multiwalled nanotubes (MWNTs) and that of single graphene sheet results in single walled nanotubes (SWNTs). The diameter of SWNTs varies from 0.671 to 3nm, whereas MWNTs show typical diameters of 30 to 50nm.



#### **HYDROGEN STORAGE CAPACITY:**

Experimentally measured hydrogen storage capacities of carbon nanotubes are given in the table below. [22], [23].

Adsorbent	Hydrogen storage (wt%)	Conditions-temp (K)/ pressure (Mpa)
SWNT (low purity)	5–10	406/0.04
SWNT (high purity)	3.5-4.5	298/0.04
SWNT (high purity)	8.25	80/7
SWNT (50% purity)	4.2	300/10.1
SWNT (80%-90%)	7	273/0.04
Aligned SWNT (Purified)	4	298/11
SWNT (Monte Carlo Simulation)	11.2	77/10
Li-doped MWNT	20	200-400/0.1
K-doped MWNT	14	300/0.1
K-doped MWNT	1.8	<313/0.1
Well-aligned MWNT	3	290/10

Abbreviations: MWNT, multiwalled nanotube; SWNT, single-walled nanotube.

## v) **CARBON NANOFIBRES:**

Carbon nanofibers consist of platelets of graphite, which are fixed in several alignments to the fiber axis. This can be produced through decomposition of ethylene, hydrogen, and carbon monoxide mixture on catalyst with three distinct structures namely, tubular (90°), platelet (~0°), and herringbone (45°), where the angle indicates the direction of the fiber axis which is relative to the vector normal to the graphene sheets.

### **HYDROGEN STORAGE CAPACITY:**

The most astonishing hydrogen storage capacity at 278 K and 12 MPa is 67 weight fraction of hydrogen in graphite nanofibers with herringbone structured and 54 weight fraction with platelet structures. On the other hand, some scientists have experimentally measured and reported the hydrogen storage capacity of 10 wt% at 27°C and 120 atm pressure.

Different hydrogen storage capacity of CNF reported by different researchers is given in the table below. [24], [25].

<b>Adsorbent</b>	<b>Hydrogen storage (wt%)</b>	<b>Conditions-temp (K)/pressure (MPa)</b>
GNF	0.08	77-300/0.8-1.8
GNF	0.7	300/10.5
CNF	1	293/10
CNF	1.6	300/12.5
CNF	1.4	298/12
CNF	6.5	300/12
GNF	10	300/12
CNF	12.38	77/12
Ball-milled CNF	0.5	Ambient/0.9

Hydrogen penetrates into the nanopores which are formed by the layers of CNF and the interior of CNT forming an intercalated layer of hydrogen. In addition to this, the nanopores could undergo expansion so that they accommodate hydrogen in a multilayer configuration. The edge sites that are exposed in the graphene sheets act as catalytic site for the dissociation of hydrogen followed by intercalation of the graphene layers. The presence of functional groups has also been helped in the enhancement of hydrogen storage capacities by facilitating stronger bonding.



# **COMPARISON OF HYDROGEN STORAGE CAPACITY OF DIFFERENT CARBON MATERIAL:**

Material	Adsorption capacity	Adsorption temp./ pressure	Desorption capacity	Desorption temp/pressure
AC (Pt-doped)	2.3	298 K, 10 MPa	2.3	298 K, 10 MPa
AC (Ni-B-doped)	1.8	77 K, 0.1 MPa	1.8	Small hysteresis 77 K, 0.1 MPa
AC (derived from tamarind seeds and KOH-treated)	4.73	303 K, 4 MPa	4.73	303 K, 4 MPa
Nitrogen containing activated carbons	2.94	77 K, 1 bar	2.94	77 K, 1 bar
Ni-ACF/CNF	0.75	298 K, Up to 50 bar	0.75	298 K, Up to 50 bar
Carbon hollow nanobubbles on porous CNF	7.4	598 K	5.9	Heated up to 523 K, 200 min
Heat-treated MWCNT/SnO <sub>2</sub>	2.62	673 K	2.13	493-783 K
Nitrogen-doped carbon nanotubes	2.0	298 K, 10 MPa	2.0	1173 K

Abbreviations: AC, activated carbon; CNF, carbon nanofiber; MWCNT, multi walled carbon nanotubes.

# ***CONCLUSION***

Hydrogen can provide energy for use in diverse applications, including distributed or combined-heat-and-power; backup power; systems for storing and enabling renewable energy; portable power; auxiliary power for trucks, aircraft, rail.etc

Due to their high efficiency and zero-or near zero-emissions operation, hydrogen a have the potential to reduce greenhouse gas emission in many applications.

There are many ways to produce hydrogen using sunlight, including photo biological, photoelectrochemical, photovoltaic-driven electrolysis, and solar thermochemical processes. Thus storage and study to increase its efficiency is a important task to achieve.

Hydrogen is a never ending source of energy. As long as water will be available on earth, sources of hydrogen will also be available. It is a green source of energy and recyclable and a future fuel of low cost.

The disadvantage of Hydrogen used as a fuel is its storage, its highly flammable nature, transportation and cost effectiveness.

Despite all the pros and cons we have tried to use as much low cost material like porous carbon materials for storage of hydrogen, which is easily accessible, have better resistance to temperature and environmental conditions, have better storage capabilities and wide range of varieties.

.

## **REFERENCES**

[1]. Porous carbons. Article *in* Sadhana · February 2003

DOI: <https://doi.org/10.1007/BF02717142>

[2]. Nature's hierarchical material. Peter Fratzl \*, Richard Weinkamer Max-Planck-Institute of Colloids and Interfaces, Department of Biomaterials, 14424 Potsdam, Germany

[3]. Development of Biochar-Based Functional Materials: Toward a Sustainable Platform Carbon Material. Wu-Jun Liu, Hong Jiang, \* and Han-Qing Yu\* CAS Key Laboratory of Urban Pollutant Conversion, Department of Chemistry, University of Science & Technology of China, Hefei 230026, China.

[4]. Preparation and Application of Hierarchical Porous Carbon Materials from Waste and Biomass: A Review Xiao-Li Zhou<sup>1</sup> · Hua Zhang<sup>1</sup> · Li-Ming Shao<sup>2, 3</sup> · Fan Lü<sup>1, 3</sup> · Pin-Jing He<sup>2, 3</sup>

Received: 1 February 2020 / Accepted: 25 May 2020 © Springer Nature B.V. 2020.

<https://doi.org/10.1007/s12649-020-01109-y>

[5]. High Hydrogen Storage Capacity of Porous Carbons Prepared by Using Activated Carbon

Huanlei Wang, Qiuming Gao,\* and Juan Hu State Key Laboratory of High Performance Ceramics and Superfine Microstructures, Graduate School, Shanghai Institute of Ceramics, Chinese Academy of Sciences, 1295 Dingxi Road, Shanghai 200050, People's Republic of China.

[6]. Simple and scalable synthesis of hierarchical porous carbon derived from cornstalk without pith for high capacitance and energy density†. Jiaming Li, ‡ Qimeng Jiang, ‡

Lansheng Wei, Linxin Zhong \* and Xiaoying Wang \* DOI:

10.1039/c9ta07864a

[7]. Mesoporous Composite Nanomaterials for Dye Removal and Other Applications Mariana Marcos-HernándezDino Villagrán, in Composite Nanoadsorbents

[8]. Guo, M., Guo, J., Tong, F., Jia, D., Jia, W., Wu, J., Wang, L., Sun, Z.: Hierarchical porous carbon spheres constructed from coal as electrode materials for high performance supercapacitors. RSC Adv. 7(72), 45363–45368 (2017). <https://doi.org/10.1039/C7RA08026C>

[9]. Progress on Synthesis and Applications of Porous Carbon Materials Bowen Li, He Xiong, Yang Xiao\*,

Doi: 10.20964/2020.02.04 [10] Hydrogen adsorption in different carbon nanostructures. Barbara Panella a,\*, Michael Hirscher a, Siegmund Roth b a Max-Planck-Institut für Metallforschung, Heisenbergstr. 3, D-70569 Stuttgart, Germany b Max-Planck-Institut für Festkörperforschung, Heisenbergstr. 1, D-70569 Stuttgart, Germany.

[11]. Lowell S, Shields Powder JE. Surface area and porosity. 3<sup>rd</sup> edition. Chapman & Hall; 1991; 14.

[12]. Kadono K, Kajijura H, Shiraishi M. Dense hydrogen adsorption in carbon subnanopores at 77 K. Appl Phys Lett 2003;83:3392–4.

[13]. Schimmel HG, Kearley GJ, Nijkamp MG, Visser CT, De Jong KP, Mulder FM. Hydrogen adsorption in carbon nanostructures: comparison of nanotubes, fibers, and coals. *Chemistry*. 2003;9:4764-4770

[14]. Hydrogen storage ability of porous carbon material fabricated from coffee bean wastes

Hiroki Akasaka a,\* , Tomokazu Takahata a, Ikumi Toda a, Hiroki Ono a, Shigeo Ohshio a,  
Syuji Himeno b, Toshinori Kokubu c, Hidetoshi Saitoh

[15]. Li Y, Zhao D, Wang Y, Xue R, Shen Z, Li X. The mechanism of hydrogen storage in carbon materials. *Int J Hydrogen Energy*. 2006; 32:2513-2517

[16]. High Hydrogen Storage Capacity of Porous Carbons Prepared by Using Activated Carbon Huanlei Wang, Qiuming Gao,\* and Juan Hu *State Key Laboratory of High Performance Ceramics and Superfine Microstructures, Graduate School, Shanghai Institute of Ceramics, Chinese Academy of Sciences, 1295 Dingxi Road, Shanghai 200050, People's Republic of China*

[17] Benard P, Chahine R. Modelling of adsorption storage of hydrogen on activated carbons. *Int J Hydrogen Energy*. 2001;26: 849-855.

[18] Lee SY, Park SJ. Effect of platinum doping of activated carbon on hydrogen storage behaviors of metal-organic frameworks-5. *Int J Hydrogen Energy*. 2011; 36:8381-8387.

[19] Hirscher M, Panella B. Nanostructures with high surface area for hydrogen storage. *J Alloys Compd*. 2005;404-406:399-401.

[20] Zhao A, Fierro V, Zlotea C, et al. Activated carbons doped with Pd nanoparticles for hydrogen storage. *Int J Hydrogen Energy*. 2012;37:5072-5080.

[21] Xu WC, Takahashi K, Matsuo Y, et al. Investigation of hydrogen storage capacity of various carbon materials. *Int J Hydrogen Energy*. 2007;32:2504-2512

[22] Broom DP, Webb CJ, Hurst KE, Parilla PA, Gennett T, Brown CM. Outlook and challenges for hydrogen storage in nanoporous materials. *Appl Phys A*. 2016; 122:151.

[23] Liu C, Chen Y, Wu CZ, Xu ST, Cheng HM. Hydrogen storage in carbon nanotubes revisited. *Carbon*. 2010;48:452-455.

[24] Guo T, Nikolaev P, Thess A, Colbert DT, Smalley RE. Catalytic growth of single-walled nanotubes by laser vaporization. *Chem Phys Lett*. 1995;243:49-54.

**[25]** Ariharan A, Viswanathan B, Nandhakumar V. Nitrogenincorporated carbon nanotube derived from polystyrene and polypyrrole as hydrogen storage material. *Int J Hydrogen Energy*. 2018;43:5077-5088.

**PARAMAGNETIC METAL-METAL BONDED  
HETEROBIMETALLIC COMPLEXES**

**SCOTTISH CHURCH COLLEGE**

**UNIVERSITY OF CALCUTTA**

**UNIVERSITY ROLL No.: 223/CEM/191018**

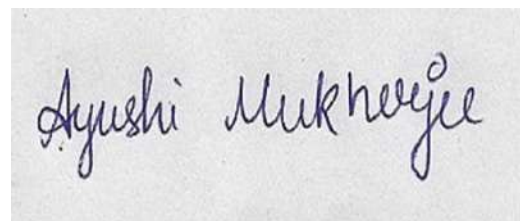
**REGISTRATION NO.: 544-1221-1159-16**

**SPECIAL PAPER: SI 44**

NAME OF CANDIDATE

**AYUSHI MUKHERJEE**

SIGNATURE OF CANDIDATE



NAME OF SUPERVISER EXAMINER

**Dr. PARTHA HALDER**

SIGNATURE OF SUPERVISER EXAMINER



# **PARAMAGNETIC METAL-METAL BONDED HETEROBIMETALLIC COMPLEXES**

**AYUSHI MUKHERJEE**

UNIVERSITY ROLL No.: 223/CEM/191018

REGISTRATION No.: 544-1221-1159-16

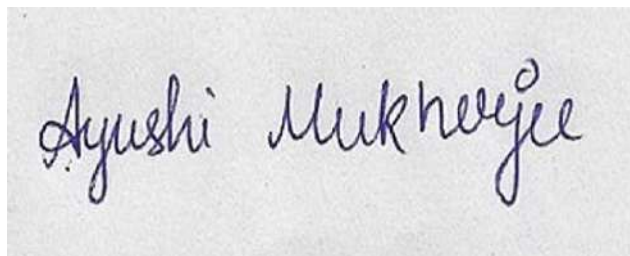
PROJECT WORK ACCOMPLISHED IN PARTIAL FULFILMENT OF MASTER DEGREE (M.Sc in CHEMISTRY) OF THE UNIVERSITY OF CALCUTTA UNDER SCOTTISH CHURCH, KOLKATA, 2021.



## **SELF-DECLARATION**

This review work was accomplished by the undersigned under supervision of Dr. Partha Halder, Associate Professor of Scottish Church College, Calcutta University during 4<sup>th</sup> and final semester (Mar- Jul 2021) in partial fulfilment of M.Sc. (Chemistry) degree of the University of Calcutta under Scottish Church College, Kolkata.

I hereby declare that the work is done by me and it is fundamental and not submitted anywhere before for publication or any other purpose.



Signature of the Student

University Roll No.:223/CEM/191018

Registration No.:544-1221-1159-16

College Roll No.: 19PG-C-24

Date: 19/7/2021

Place: SCOTTISH CHURCH COLLEGE, KOLKATA



Counter signature of Guide

## CONTENTS:

Preface-----	6
Abstract -----	7
1. Introduction and Overview -----	8
2. Development of metal-metal bonding:	
From homometallic to heterometallic -----	8
3. Guiding principles in controlling spin states -----	10
3.1. Localized versus Delocalized unpaired electrons -----	10
3.2. Direct Exchange -----	10
3.3. Superexchange -----	10
3.4. Double Exchange -----	11
4. Early examples of Paramagnetic Heterometallic metal-metal bonded compounds -----	12
5. Paramagnetic Heterobimetallic complexes -----	13
6. Synthetic methods used to form heterobimetallic compounds and their structural characterization -----	13
6.1.1. Synthesis of $\text{PtNi}(\text{tba})_4\text{OH}_2$ (1)-----	14
6.1.2. Structure of $\text{PtNi}(\text{tba})_4\text{OH}_2$ (1)-----	14
6.2.1. Synthesis of $[\text{PtCr}(\text{tba})_4(\text{NCS})_2]$ (2)-----	14
6.2.2. Structure of $[\text{PtCr}(\text{tba})_4(\text{NCS})_2]$ (2)-----	15
6.3.1. Synthesis of $\text{K}(\text{crypt-222})[\text{CrFeL}_1]$ (3) -----	15
6.3.2. Structure of $\text{K}(\text{crypt-222})[\text{CrFeL}_1]$ (3) -----	16

6.4.1. Synthesis of $\text{CoCr}(\text{N}(\text{o}-(\text{NCH}_2\text{P}^i\text{Pr}_2)\text{C}_6\text{H}_4)_3)(4)$ -----	16
6.4.2. Structure of $\text{CoCr}(\text{N}(\text{o}-(\text{NCH}_2\text{P}^i\text{Pr}_2)\text{C}_6\text{H}_4)_3)(4)$ -----	16
6.5.1. Synthesis of $\text{NiV}(\text{N}(\text{o}-(\text{NCH}_2\text{P}^i\text{Pr}_2)\text{C}_6\text{H}_4)_3)$ (5) -----	17
6.5.2. Structure of $\text{NiV}(\text{N}(\text{o}-(\text{NCH}_2\text{P}^i\text{Pr}_2)\text{C}_6\text{H}_4)_3)$ (5) -----	17
6.6.1. Synthesis of $[\text{Cr}(^i\text{PrNPPH}_2)_3\text{Fe-I}]$ (6) -----	17
6.6.2. Structure of $[\text{Cr}(^i\text{PrNPPH}_2)_3\text{Fe-I}]$ (6) -----	18
6.7.1. Synthesis of $\text{V}(\text{XylNP}^i\text{Pr}_2)_3\text{FeI}$ (7) -----	18
6.7.2. Structure of $\text{V}(\text{XylNP}^i\text{Pr}_2)_3\text{FeI}$ (7) -----	18
6.8.1. Synthesis of $[\text{ClCr}(\mu\text{-}^i\text{PrNP}^i\text{Pr}_2)_2\text{Rh}(\eta^2\text{-}^i\text{PrNP}^i\text{Pr}_2)]$ (8) -----	19
6.8.2. Structure of $[\text{ClCr}(\mu\text{-}^i\text{PrNP}^i\text{Pr}_2)_2\text{Rh}(\eta^2\text{-}^i\text{PrNP}^i\text{Pr}_2)]$ (8) -----	19
6.9.1. Synthesis of $[\text{ClCr}(\mu\text{-}^i\text{PrNP}^i\text{Pr}_2)_2\text{Ir}(\eta^2\text{-}^i\text{PrNP}^i\text{Pr}_2)]$ (9) -----	19
6.9.2. Structure of $[\text{ClCr}(\mu\text{-}^i\text{PrNP}^i\text{Pr}_2)_2\text{Ir}(\eta^2\text{-}^i\text{PrNP}^i\text{Pr}_2)]$ (9) -----	20
7. Electronic Spectra of the Heterobimetallic complexes -----	20
7.1. Spectra of $\text{PtNi}(\text{tba})_4\text{OH}_2$ (1) -----	20
7.2. Spectra of $[\text{PtCr}(\text{tba})_4(\text{NCS})_2]$ (2) -----	20
7.3. Spectra of $\text{K}(\text{crypt-222})[\text{CrFeL}_1]$ (3) -----	20
7.4. Spectra of $\text{CoCr}[\text{N}(\text{o}-(\text{NCH}_2\text{P}^i\text{Pr}_2)\text{C}_6\text{H}_4)_3]$ (4) -----	20
7.5. Spectra of $\text{NiV}(\text{N}(\text{o}-(\text{NCH}_2\text{P}^i\text{Pr}_2)\text{C}_6\text{H}_4)_3)$ (5) -----	21
7.6. Spectra of $[\text{Cr}(^i\text{PrNPPH}_2)_3\text{Fe-I}]$ (6) -----	21
7.7. Spectra of $\text{V}(\text{XylNP}^i\text{Pr}_2)_3\text{FeI}$ (7) -----	21
7.8. Spectra of $[\text{ClCr}(\mu\text{-}^i\text{PrNP}^i\text{Pr}_2)_2\text{Rh}(\eta^2\text{-}^i\text{PrNP}^i\text{Pr}_2)]$ (8) -----	21
7.9. Spectra of $[\text{ClCr}(\mu\text{-}^i\text{PrNP}^i\text{Pr}_2)_2\text{Ir}(\eta^2\text{-}^i\text{PrNP}^i\text{Pr}_2)]$ (9) -----	21
8. Electronic Structure of Heterobimetallic Compounds -----	21

8.1. Electronic Structure of $C_4$ Symmetric Heterobimetallics -----	22
8.2. Electronic Structure of $C_3$ Symmetric Heterobimetallics -----	23
9. Magnetic Properties of Heterobimetallic Compounds -----	26
9.1. Isolated Magnetic Ions -----	26
9.2. Spin-coupled magnetic centers -----	28
10. Conclusion -----	28
11. Acknowledgements -----	29
12. References -----	29

## PREFACE

I have brought very different experiences in this review work and I would cover the fundamental aspects like synthesis, structural characterization, spectroscopic data, electronic structure and magnetic properties of different paramagnetic metal-metal bonded heterobimetallic complexes. The paramagnetic heterobimetallic complexes are very interesting and are a new area of research with a variety of metal-metal bonds, different types of magnetic coupling, and spin exchanges.

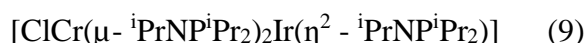
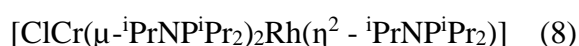
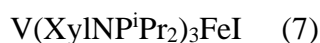
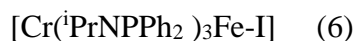
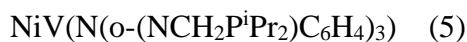
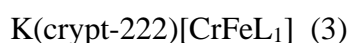
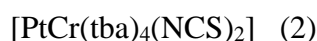
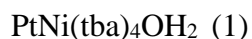
Development of heterobimetallic complexes which are paramagnetic from homometallic complexes are described in this review. The review also contains guiding principles which controls the different spin states in various complexes. Paramagnetic heterobimetallic complex is a vast and recent topic. Researchers are introducing various synthetic strategies as synthesizing heterometallic complexes are very challenging.

I would like to sincerely thank Dr. Partha Halder, Associate Professor of Scottish Church College, Calcutta University, for writing of this review, which has benefitted from his valuable guidance and helpful advice for successful completion. I am also Grateful to Dr. Chandan Kumar Pal, Associate Professor of Scottish Church College, Calcutta University for further help and support. As well as, thanks to my Chemistry Department for making possible completion of this review.

## ABSTRACT:

Noteworthy advancement has been made in the formerly 10–15 years on the sketch, synthesis, and magnetic and spectroscopic patrimony of multimetallic coordination complexes with paramagnetic heterometallic metal–metal bonds. Various imprecise classes have been surveyed like the different types of structures (linear, quasi 1D chain like structure, triangular geometry, square planar, octahedral, etc.) and polymeric design with a heterometallic metal–metal bonded backbone. In this article, our kingpin is on the synthetic scheme implemented to access these compounds, their structural attributes, magnetic characteriation, spectroscopic data and electronic structure. The magnetic properties of these compounds hang on the location of the unpaired electrons and the energies of the d orbitals they indwell in; unpaired electrons may be localized to one metal center or be delocalized over both centers and coupling can be ferro- or antiferromagnetic.

This review contains characterization of 9 different heterobimetallic compounds:



## 1. INTRODUCTION AND OVERVIEW

Metal–metal bonded coordination compounds represent an important extension of Werner’s classical coordination theory. The first molecular heterometallic metal–metal bond compound was reported by Wilkinson and co-workers in the year 1960. The diamagnetic complex was a symmetric dimer,  $\text{Cp}(\text{CO})_3\text{Mo}-\text{WCp}(\text{CO})_3$ .

It was around 1969–1970 when it was recognized that metal–metal bonded complexes could also be paramagnetic. There were comparatively few paramagnetic complexes with heterometallic metal–metal bonds reported before  $\sim 2007$ . Around early 2007, a combined effort began to prepare new examples of paramagnetic heterometallic metal–metal bonded complexes, and the outcome of these studies will be the major topic of discussion in this Review.

## 2. DEVELOPMENT OF METAL-METAL BONDING: FROM HOMOMETALLIC TO HETEROMETALLIC

One of the utmost important questions is how homometallic meta-metal bonds differ from heterometallic metal-metal bonds. To explore this question from a theoretical standpoint, at first homometallic metal–metal multiple bonds need to be described; the  $\text{Re}\equiv\text{Re}$  quadruple bond in the  $[\text{Re}_2\text{Cl}_8]^{2-}$  ion, shown in Figure 1A below.

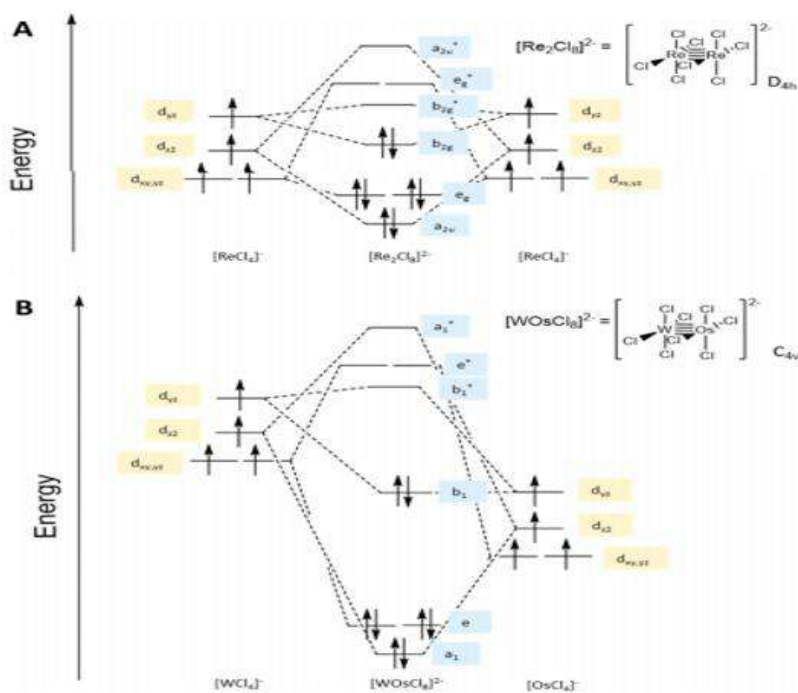


Figure 1: Qualitative molecular orbital (MO) diagram for (A)  $[\text{Re}_2\text{Cl}_8]^{2-}$  and (B)  $[\text{WOsCl}_8]^{2-}$

Ligand field analysis indicates the availability of  $dz^2$ ,  $dxy$ ,  $dxz$ , and  $d_{yz}$  Re valence orbitals to engage in metal–metal bonds of  $\sigma$ ,  $2 \times \pi$ , and  $\delta$  symmetry, respectively. In the  $D_{4h}$  symmetry of the  $[\text{Re}_2\text{Cl}_8]^{2-}$  ion, the two Re  $dz^2$  orbitals shows the strongest overlap to yield  $\sigma$  type bonding ( $a_{2u}$ ) and antibonding ( $a_{2u}^*$ ) combinations. The overlap of  $\pi$ -symmetry orbitals is less intense than the  $\sigma$ , and  $\delta$  bonds being the weakest of all. Nevertheless, the  $\sigma^2 \pi^4 \delta^2$  quadruple bond is the most effective and appropriate description of the ground state configuration of the  $[\text{Re}_2\text{Cl}_8]^{2-}$  ion<sup>1</sup> as shown in figure 1A.

For the study of heterometallic complex, a hypothetical heterometallic complex was chosen which isoelectronic with  $[\text{Re}_2\text{Cl}_8]^{2-}$  ion is:  $[\text{WOsCl}_8]^{2-}$ . The polarity of the heterometallic bond lowers the molecular symmetry to  $C_{4v}$ . As it is isoelectronic, the four valence orbitals that were available in the  $\text{Re}_2$  system were similarly still available for the WOs compound:  $dz^2$ ,  $dxy$ ,  $dxz$ , and  $d_{yz}$ . However, as mentioned in the Figure 1B, there is a difference in effective nuclear charge between W and Os budding from the difference in their columns in the periodic table ( $\Delta N$ ). With  $\Delta N = 2$ , the W 5d orbitals lie uniformly higher in energy than the Os 5d orbitals. Overlapping of the W and Os  $dz^2$  orbitals will result in a  $\sigma$  bonding ( $a_1$ ) and antibonding ( $a_1^*$ ) combination, but the interaction is not as strongly covalent as in the case of  $\text{Re}_2$ . The  $a_1$  orbital will be polarized toward Os while,  $a_1^*$  polarized toward W (as Os is energetically lower than W). Similar effects will happen in the  $\pi$  and  $\delta$  symmetry orbitals, and these orbitals already have weaker overlap than the  $\sigma$  orbitals. Thus, the result is that the  $b_1^*$  orbitals may have close to 100% W character and in that limit would be considered nonbonding (refer to Figure 1B).

An issue that arises in Figure 1 is about the oxidation state of the ions. For the  $[\text{Re}_2\text{Cl}_8]^{2-}$  ion, most chemists (although not all) are comfortable assigning an uniform oxidation states between the two Re ions,  $\text{Re}^{3+}$  oxidation state. This is mentioned in the left and the right sides of the MO where  $[\text{Re}_2\text{Cl}_8]^{2-}$  was split hypothetically in  $[\text{ReCl}_4]^-$  fragments each with a  $d^4$  valence electronic configuration. A similar deconstruction of the  $[\text{WOsCl}_8]^{2-}$  ion yields  $d^3$   $[\text{WCl}_4]^-$  and  $d^5$   $[\text{OsCl}_4]^-$  fragments (both having a similar distribution of charge). But it can also be written as  $d^4$   $[\text{WCl}_4]^{2-}$  and  $d^4$   $\text{OsCl}_4$  fragments with an uneven distribution of charge. Moreover, the facts that all of the valence electrons in the  $[\text{WOsCl}_8]^{2-}$  ion is concentrated to the bonding orbitals that are polarized toward Os suggest electron transfer significantly from  $\text{W} \rightarrow \text{Os}$  toward a limit of  $\text{W}^{6+}/\text{Os}^0$  (i.e.,  $d^0/d^8$ ). Thus, there lies confusion in stating the specific oxidation states to these metal atoms in these heterometallic complexes. Hence, the  $[\text{WOsCl}_8]^{2-}$  compound was described as having a  $\{\text{WOs}\}^8$  configuration: eight electrons occupying the valence orbitals.

While dealing with the metal-metal bond distances it was noticed that the Re–Re distance in the  $[\text{Re}_2\text{Cl}_8]^{2-}$  ion is not directly comparable to the W–Os distance in  $[\text{WOsCl}_8]^{2-}$  because the atoms involved here have slight difference in sizes. A normalization procedure for the metal–metal bond distances was required; the earliest, simplest, and still most widely used normalization procedure is Cotton’s formal shortness ratio (FSR), defined as  $FSR = \frac{d}{R_{1,A} + R_{1,B}}$ ; where,  $d$  is the observed metal–metal distance, and the  $R_1$  values are



metallic radii given by Pauling<sup>2</sup>. In essence, the FSR describes how much longer (or shorter) a distance is than that of a neutral metallic sample of the elements involved in the complex.

### **3. GUIDING PRINCIPLES IN CONTROLLING SPIN STATES**

#### **3.1. Localized versus Delocalized Unpaired Electrons -**

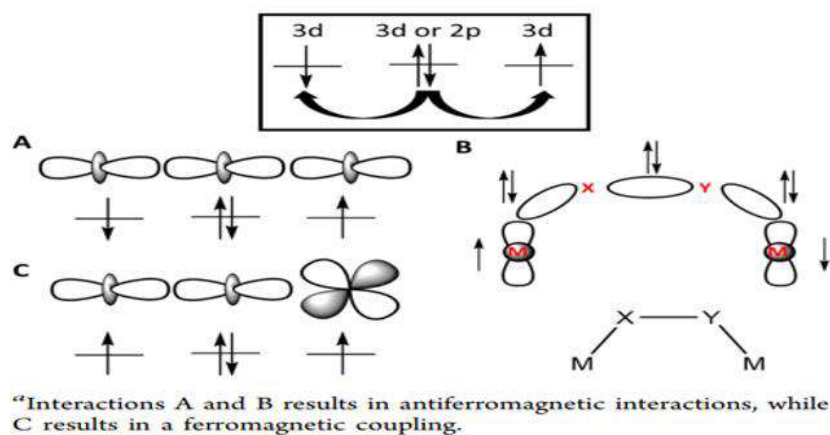
Ability to control spin at the single electron level is one of the greatest challenges and goal in molecular magnetism. It is important to determine whether the unpaired electron resides in the localised or the delocalised orbital in a heterometallic complexes. Localized orbitals tend to be of either  $\pi$  or  $\delta$  symmetry with respect to the metal–metal bond whereas delocalized orbitals tend to be of  $\sigma$  symmetry. Double exchange mechanism significantly illustrates the electron delocalisation in molecular magnetism (that is deals with the electrons residing in  $\sigma$  symmetric orbitals). Whereas in localised orbital (i.e., electrons residing in  $\pi$  or  $\delta$  orbitals) either the direct or the superexchange mechanism and antiferromagnetic coupling occurs if the orbital overlaps or ferromagnetic coupling takes place if the orbitals are orthogonal.

#### **3.2. Direct Exchange –**

As mentioned above direct exchange mechanism is for electrons present in localised orbitals. It happens when 2 paramagnetic ions are close enough in space to allow overlap of their magnetic orbitals. For better understanding of direct exchange mechanism, it can be envisioned that two ions each having an unpaired electron such that there exist two probability of spin states;  $S=0$  &  $S=1$ . To satisfy the Pauli Exclusion Principle, the electrons must be of opposite spins, leading to an antiferromagnetic interaction with an  $S = 0$  ground state. Though the direct exchange mechanism is strong, it is only applicable within minuscule range as the coupling strength,  $J$ , which is the difference in energy between  $S=0$  and 1 state, rapidly lessens in magnitude when the distance between the two centre enlarges.

#### **3.3. Superexchange –**

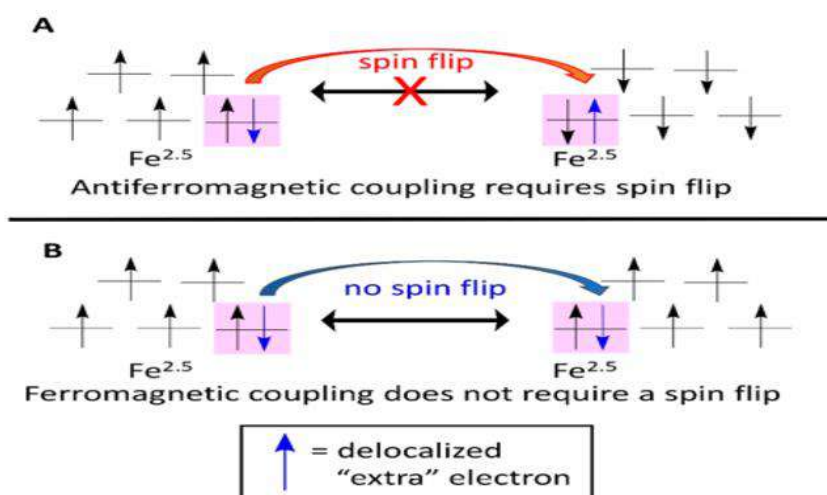
The superexchange mechanism is described as the interactivity of spins confined on two paramagnetic ions via a bridging diamagnetic ion. The main scheme behind superexchange is that unpaired electrons confined on two metal centres may interact with filled orbitals either from bridging ligands or from a third central atom (here, a metal atom). As emphasized in Scheme 1A and 1B (below), these situations both tend to be antiferromagnetic interactions. Ferromagnetic interactions may result from the example situation in Scheme 1C in which the magnetic orbitals are rigorously orthogonal.



Scheme 1: General Mechanism for Superexchange (Top) and Orbital Interactions that give rise to Different Magnetic Coupling (Bottom)

### 3.4. Double Exchange –

The double exchange mechanism occurs frequently in systems containing two magnetic centers that contain a different number of valence electrons from one another. The magnetic centers themselves may differ from one another. The key trait is the presence of one or more “extra” electrons that are delocalized between two metal atoms. If the other spins on the two magnetic centers all assemble in a parallel (i.e., ferromagnetic) arrangement, an “extra” electron does not need to roll over spins as it resonates between the two metal centers. An antiferromagnetic state requires the “extra” electron to undergo a spin flip to form a Pauli-allowed state, which is not commending. This effect is exemplified in  $[\text{Fe}_2(\mu\text{OH})_3(\text{tmtacn})_2]^{2+}$  (tmtacn = 1,4,7-trimethyl-1,4,7-triazacyclononane), where a mixed valent  $\text{Fe}^{(\text{II/III})}$  system presents an overall  $S = 9/2$  ground state as a result of the double exchange mechanism (Scheme 2).



Ferromagnetic alignment is energetically favorable.

Scheme 2: Mechanism by which Double Exchange occurs using a Bimetallic Mixed Valent  $\text{Fe}^{(\text{II/III})}$  System

#### 4. Early Examples of Paramagnetic Heterometallic Metal–Metal Bonded Compounds

Before 2007, few examples of paramagnetic heterometallic metal–metal bonded compounds were reported. Lippert and co-workers introduced paramagnetic heterometallic metal–metal bonded chains in 1981. Their synthetic strategy was to use Pt(II)–nucleobase complexes as metalloligands, producing an extensive diversity of Pt–M–Pt heterotrimetallic compounds having paramagnetic central M atoms. For example, the methylthymine complex with a central Pd(III) ion. Analysis of the electronic transitions and EPR spectra of these compounds led to the conclusion that the filled Pt  $d_{z^2}$  orbitals act as ligands to the central metal atom.

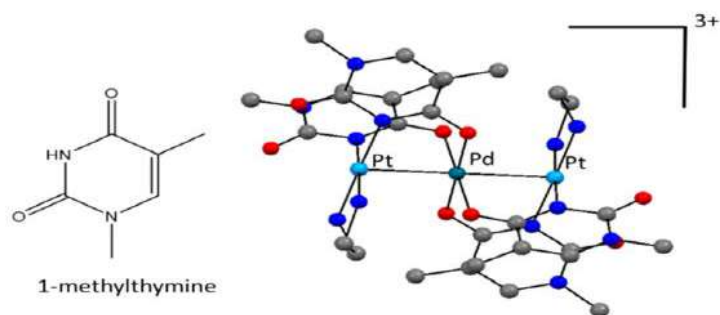


Figure 2: Paramagnetic heterotrimetallic Pt(II)-Pd(III)-Pt(II) complex supported by N-methylthymine ligands.

In 2005, Matsumoto, Uemura, and co-workers reported a quasi-1D system of paramagnetic Pt–Rh octomers bridged by Cl ions. Each chain contains a  $[-\text{Pt}-\text{Rh}-\text{Pt}-\text{Pt}-\text{Pt}-\text{Pt}-\text{Rh}-\text{Pt}-]$  metal core with one unpaired electron per octomer unit. In this case, the unpaired electron does not occupy the  $d_{z^2}$  orbitals of Pt; rather it occupies the  $d_{xy}$  orbital of Rh and “hops” from one Rh to another.

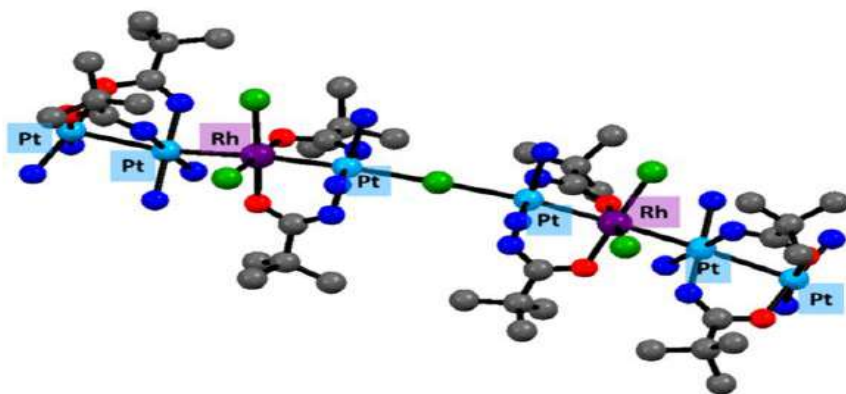


Figure 3: Repeating unit of a quasi-1D chain complex containing Pt and Rh synthesized by Matsumoto, Uemura, and co-workers.

## **5. PARAMAGNETIC HETEROBIMETALLIC COMPLEXES**

Heterobimetallics represent the unadorned way to perceive the impact of two different metals on one another. To support the two metals, research groups have focused on providing either a 3-fold symmetric or a 4-fold symmetric coordination environment. The heterobimetallic compounds nurtured in this section all contain a M–M bond and either three or four equatorial bridging ligands that pier the M–M bonded unit.

In this review the discussion would be about various types of paramagnetic heterobimetallic complexes, their synthesis, spectroscopic data, magnetism and electronic structure.

The compounds discussed in this review are:

- (1) PtNi(tba)<sub>4</sub>OH<sub>2</sub>
- (2) [PtCr(tba)<sub>4</sub>(NCS)<sub>2</sub>]
- (3) K(crypt-222)[CrFeL<sub>1</sub>]
- (4) CoCr(N(o-(NCH<sub>2</sub>P<sup>i</sup>Pr<sub>2</sub>)C<sub>6</sub>H<sub>4</sub>)<sub>3</sub>)
- (5) NiV(N(o-(NCH<sub>2</sub>P<sup>i</sup>Pr<sub>2</sub>)C<sub>6</sub>H<sub>4</sub>)<sub>3</sub>)
- (6) [Cr(<sup>i</sup>PrNPPh<sub>2</sub>)<sub>3</sub>Fe-I]
- (7) V(XylNP<sup>i</sup>Pr<sub>2</sub>)<sub>3</sub>FeI
- (8) [ClCr(μ-<sup>i</sup>PrNP<sup>i</sup>Pr<sub>2</sub>)<sub>2</sub>Rh(η<sup>2</sup>-<sup>i</sup>PrNP<sup>i</sup>Pr<sub>2</sub>)]
- (9) [ClCr(μ-<sup>i</sup>PrNP<sup>i</sup>Pr<sub>2</sub>)<sub>2</sub>Ir(η<sup>2</sup>-<sup>i</sup>PrNP<sup>i</sup>Pr<sub>2</sub>)]

## **6. Synthetic Methods Used to Form Heterobimetallic Compounds and Their Structural Characterization**

In comparison to homometallic metal–metal bonded heterobimetallic compounds, heterometallic analogs are much rarer. Synthesis of any heterobimetallic complex, metal–metal bonded or not, involves inherent provocations, the most prominent of which is how to avoid formation of the homometallic species. The synthetic procedures outlined below are those that have led to successes in forming the paramagnetic heterobimetallic complexes addressed in this review.

### 6.1.1. Synthesis of $\text{PtNi}(\text{tba})_4\text{OH}_2$ (1)<sup>3</sup>

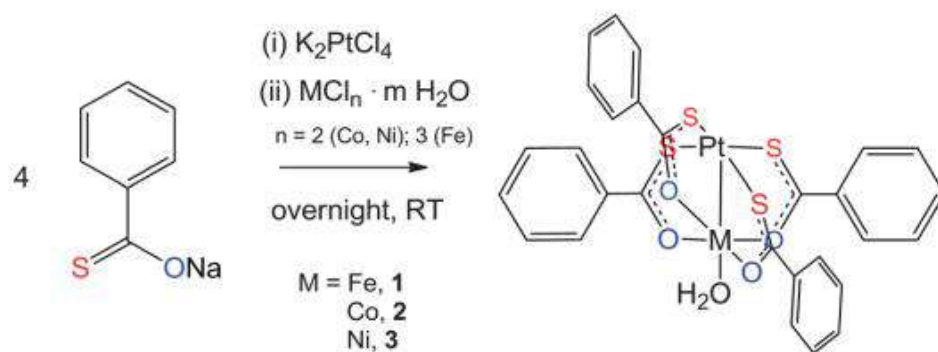


Figure 4: Synthesis of  $[\text{PtNi}(\text{tba})_4(\text{OH}_2)]$  compound

As shown in Figure 4, a sodium thiobenzoate solution was prepared in situ to which was added first  $\text{K}_2\text{PtCl}_4$  and then nickel chloride hydrate in rapid succession. The solution was stirred overnight and the resulting precipitate isolated by filtration and recrystallized from organic solvents.

### 6.1.2. Structure of $\text{PtNi}(\text{tba})_4\text{OH}_2$ (1)<sup>3</sup>

Lantern structures with two different donor atoms, hard O and soft S, were chosen in order to selectively bind Pt and Ni at separate sites, while minimizing ligand exchange. The structure of (1) is a dimer of lanterns with a Pt–Ni distance of 2.570 Å and a Pt····Pt distance of 3.0823 Å. The two  $[\text{PtNi}(\text{tba})_4(\text{OH}_2)]$  units are again unbridged and in a staggered configuration such that the sulfur atoms are not closer than 3.56 Å. One  $\text{H}_2\text{O}$  molecule is bound to each Ni atom. The Ni derivatives exhibit dimeric structures in the solid state via Pt/Pt metallophilic interactions that result in magnetic coupling across the  $\{\text{MPtPtM}\}$  unit between the two 3d metal ions.

### 6.2.1. Synthesis of $[\text{PtCr}(\text{tba})_4(\text{NCS})_2]$ (2)<sup>4</sup>

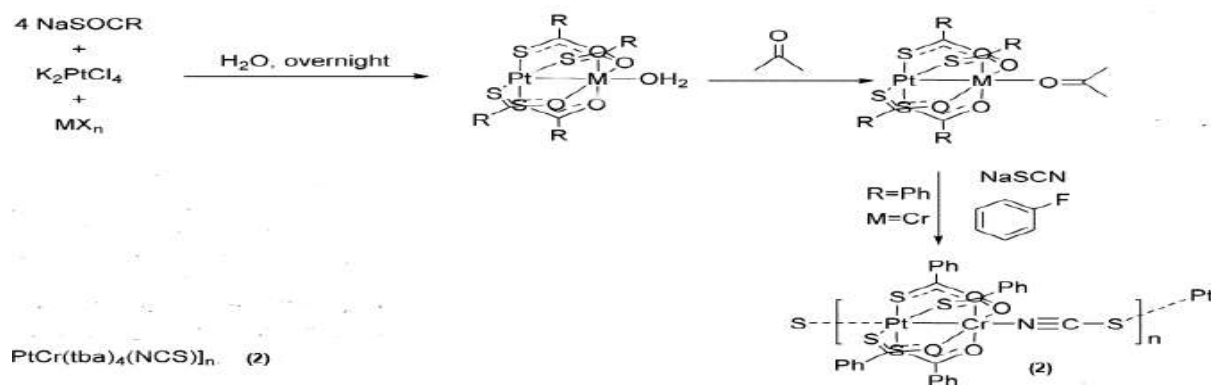


Figure 5: Synthesis of  $[\text{PtCr}(\text{tba})_4(\text{NCS})_2]$  compound

A portion of potassium thiobenzoate was dissolved in minimal H<sub>2</sub>O, yielding a yellow solution. Separately, a sample of K<sub>2</sub>PtCl<sub>4</sub> was dissolved in H<sub>2</sub>O and added, and the two were allowed to mix for 15 min. A solution of CrCl<sub>3</sub>·6H<sub>2</sub>O in H<sub>2</sub>O was added, yielding a green precipitate. The precipitate was recovered by vacuum filtration and dissolved in acetone, yielding an olive green solution. This solution was layered on top of a solution of NaSCN in cold acetone and fluorobenzene. Insoluble green crystals suitable for X-ray analysis grew within 48 h. (Fig 5)

### 6.2.2. Structure of [PtCr(tba)<sub>4</sub>(NCS)<sub>2</sub>] (2)<sup>4</sup>

Compound (2) displays a quasi-1D infinite chain linked in a zig zag pattern with the isothiocyanate N-bound to Cr and S-bound to the Pt on an adjacent lantern. The Pt–Cr distance is 2.5252 Å. The SNCS–Pt bond distance of 2.702 Å is longer than the Cr–NNCS distance of 2.00 Å.

### 6.3.1. Synthesis of K(crypt-222)[CrFeL<sub>1</sub>] (3)<sup>5</sup>

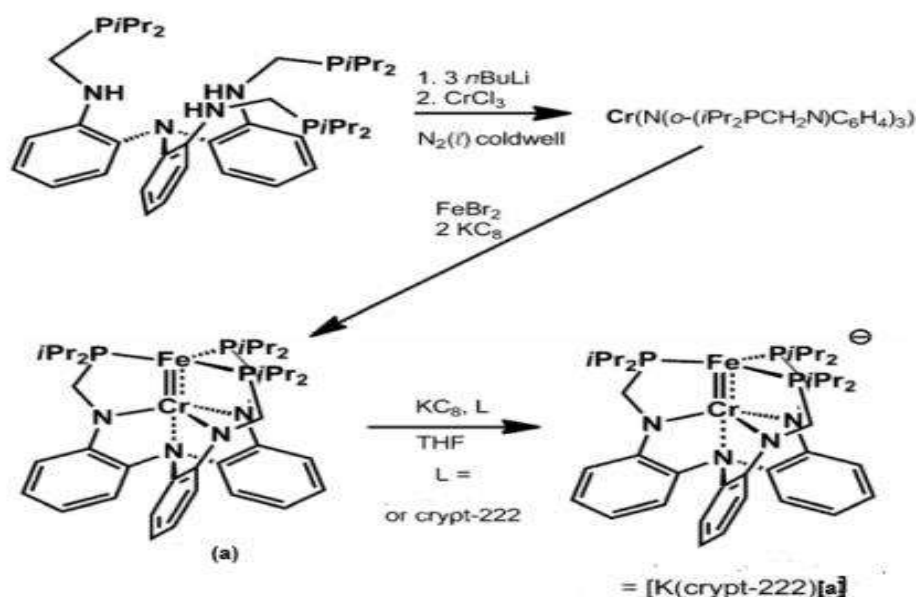


Figure 6: Synthesis of K(crypt-222)[CrFeL<sub>1</sub>]

To prepare the iron–chromium complexes herein, the ligand was first deprotonated and metalated with CrCl<sub>3</sub>. The resulting monometallic species, [Cr(N(o-(*i*Pr<sub>2</sub>PCH<sub>2</sub>N)C<sub>6</sub>H<sub>4</sub>)<sub>3</sub>)], which was confirmed by combustion analysis, acts as a metalloligand in a subsequent metalation (Figure 6). For example, reaction of [Cr(N(o-(*i*Pr<sub>2</sub>PCH<sub>2</sub>N)C<sub>6</sub>H<sub>4</sub>)<sub>3</sub>)] with FeBr<sub>2</sub> and two equiv KC<sub>8</sub> resulted in a color change from dark brown to green brown within minutes. The product, (a) is reduced with 1 equiv KC<sub>8</sub> generating a red-brown solution of paramagnetic [K(solv)<sub>n</sub>][a]. Encapsulation of the potassium ion with crypt-222 enabled the isolation of crystalline [K(crypt-222)][a] (3).

### 6.3.2. Structure of $\text{K}(\text{crypt-222})[\text{CrFeL}_1]$ (3)<sup>5</sup>

The solid-state structures revealed Fe-Cr bond lengths of 1.97 Å of (3). It is  $C_3$  symmetric. The average Fe-P bond lengths in (3) are between those reported for this  $\text{Fe}^{\text{I}}$  (2.29 Å) and  $\text{Fe}^0$  (2.20 Å) pair. Based on these values, the Fe oxidation states in (3) would be consistent with  $\text{Fe}^0$ , but also  $\text{Fe}^{\text{I}}$ . The formal oxidation states is  $\text{Fe}^0/\text{Cr}^{\text{II}}$  for (3).

### 6.4.1. Synthesis of $\text{CoCr}[\text{N}(\text{o}-(\text{NCH}_2\text{P}^i\text{Pr}_2)\text{C}_6\text{H}_4)_3]$ (4)<sup>6</sup>

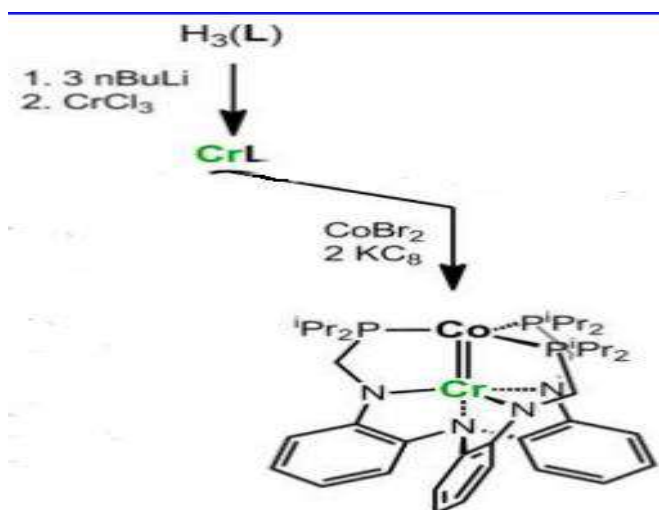


Figure 7: Synthesis of  $\text{CoCr}[\text{N}(\text{o}-(\text{NCH}_2\text{P}^i\text{Pr}_2)\text{C}_6\text{H}_4)_3]$

A solution of  $\text{Cr}[\text{N}(\text{o}-(\text{NCH}_2\text{P}^i\text{Pr}_2)\text{C}_6\text{H}_4)_3]$  was dissolved in THF and added to a slurry of  $\text{CoBr}_2$  in THF. After stirring the dark green brown solution for 1 h, slurry of  $\text{KC}_8$  in THF was added. After stirring for an additional hour, the solution was then filtered through a Celite pad, which was washed with THF until the washings were clear. The solution was dried in vacuo to give a brown powder (Figure 7).

### 6.4.2. Structure of $\text{CoCr}[\text{N}(\text{o}-(\text{NCH}_2\text{P}^i\text{Pr}_2)\text{C}_6\text{H}_4)_3]$ (4)<sup>6</sup>

The complex is essentially three-fold symmetric. The solid-state structure of (4) reveals short Co-Cr bond distances of 2.14 Å. The complementary nature of the bonds along the three-fold axis suggests that the position of the chromium atom is sufficiently flexible to accommodate a full range of Co-Cr interactions.

### 6.5.1. Synthesis of $\text{NiV}[\text{N}(\text{o}-(\text{NCH}_2\text{P}^i\text{Pr}_2)\text{C}_6\text{H}_4)_3]$ (5)<sup>7</sup>

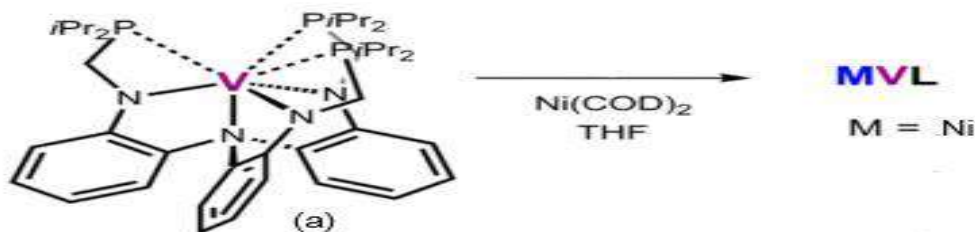


Figure 8: Synthesis of  $\text{NiV}(\text{N}(\text{o}-(\text{NCH}_2\text{P}^i\text{Pr}_2)\text{C}_6\text{H}_4)_3)$

The monovanadium(III) compound,  $\text{V}(\text{N}(\text{o}-(\text{NCH}_2\text{P}^i\text{Pr}_2)\text{C}_6\text{H}_4)_3)$  (a, abbreviated as VL), was obtained in good yield from the reaction of  $\text{VCl}_3(\text{THF})_3$  (THF = tetrahydrofuran) and the triply deprotonated ligand  $[\text{N}(\text{o}-(\text{NCH}_2\text{P}^i\text{Pr}_2)\text{C}_6\text{H}_4)_3]^{3-}$ . Brown (a) was used as a metalloligand in a subsequent metalation to install zero valent nickel (Figure 8). Complex NiVL (5) was produced from (a) and  $\text{Ni}(\text{COD})_2$ , where COD = 1,5-cyclooctadiene.

### 6.5.2. Structure of $\text{NiV}(\text{N}(\text{o}-(\text{NCH}_2\text{P}^i\text{Pr}_2)\text{C}_6\text{H}_4)_3)$ (5) <sup>7</sup>

The average  $\text{V}-\text{N}_{\text{amide}}$  bond length is 1.93 Å. There V has a +3 oxidation state. The apical  $\text{V}-\text{N}_{\text{amine}}$  bond length is 2.30 Å. Of note, the  $\text{V}-\text{N}_{\text{amine}}$  and  $\text{Ni}-\text{V}$  bond lengths are inversely related in that the former contracts when  $\text{Ni}-\text{V}$  interactions are absent or weak, and it elongates with increasing  $\text{Ni}-\text{V}$  multiple bonding.

### 6.6.1. Synthesis of $[\text{Cr}(\text{}^i\text{PrNPPH}_2)_3\text{Fe-I}]$ (6) <sup>8</sup>

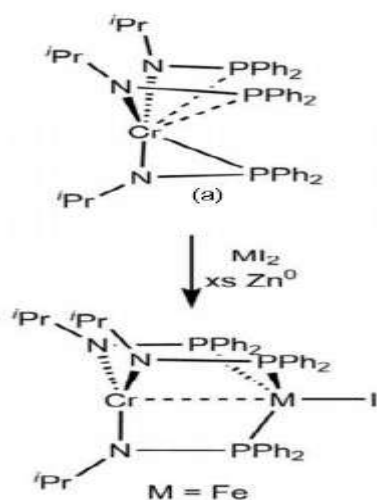


Figure 9: Synthesis of  $[\text{Cr}(\text{}^i\text{PrNPPH}_2)_3\text{Fe-I}]$

Treatment of  $\text{CrCl}_3(\text{THF})_3$  with three equivalents of  $\text{Li}[\text{}^i\text{PrNPPH}_2]$  (generated in situ) in diethyl ether afforded the green chromium tris(phosphinoamide),  $[\text{Cr}(\text{}^i\text{PrNPPH}_2)_3]$  (a). Complex  $[\text{Cr}(\text{}^i\text{PrNPPH}_2)_3\text{Fe-I}]$  (6)



can be synthesized upon treatment of an equimolar ratio of (a) and  $MI_2$  ( $M = Fe$ ) in the presence of excess Zn powder under ambient conditions (Figure 9).

### 6.6.2. Structure of $[Cr(iPrNPPh_2)_3Fe-I]$ (6)<sup>8</sup>

The compound is isomorphous and crystallizes in the cubic space group with an ideal  $C_3$ -symmetric geometry in the solid state. In the trigonal lantern geometries of (6) Cr adopts a trigonal monopyramidal geometry. The Fe center in 6 has a distorted trigonal bipyramidal geometry with Fe 0.80 Å above the plane of the three phosphorus atoms.

### 6.7.1. Synthesis of $V(XylNP^iPr_2)_3FeI$ (7)<sup>9</sup>

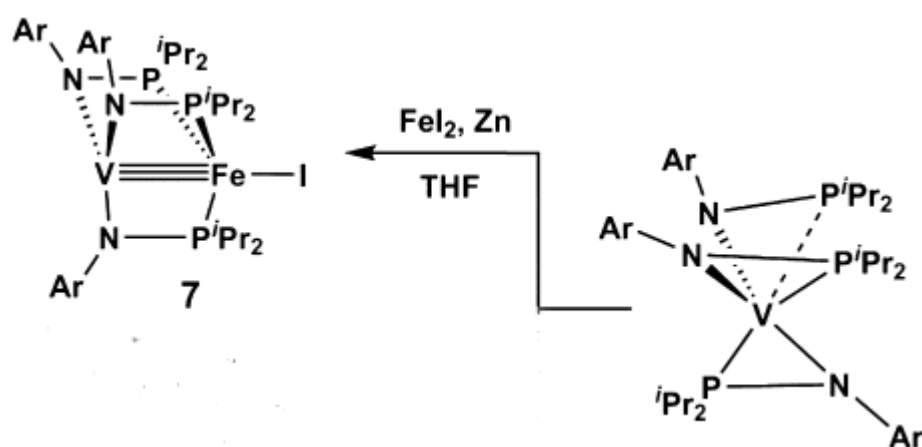


Figure10: Synthesis of  $V(XylNP^iPr_2)_3FeI$

A solution of  $V(XylNP^iPr_2)_3$  in THF was chilled to  $-35$  °C, and then this solution was added to solid  $FeI_2$  and Zn powder over a period of 5 min (Figure 10). The reaction mixture was stirred at room temperature for 12h to ensure completion of the reaction. The excess Zn powder and other insoluble residues were removed by filtration.

### 6.7.2. Structure of $V(XylNP^iPr_2)_3FeI$ (7)<sup>9</sup>

The V/Fe complex 7 is  $C_3$ -symmetric in the solid state with a trigonal planar geometry at the V center and a distorted tetrahedral geometry at Fe if the metal–metal bond is not taken into consideration. The V–Fe bond lengths in the two molecules of complex 7 in the asymmetric unit are 2.0186 Å and 2.0195 Å. The stronger interaction between V and Fe in complex 7 is the result of the more electron donating phosphine substituents, which render the iron center more electron profuse.

### 6.8.1. Synthesis of $[ClCr(\mu-iPrNP^iPr_2)_2Rh(\eta^2-iPrNP^iPr_2)]$ (8)<sup>10</sup>

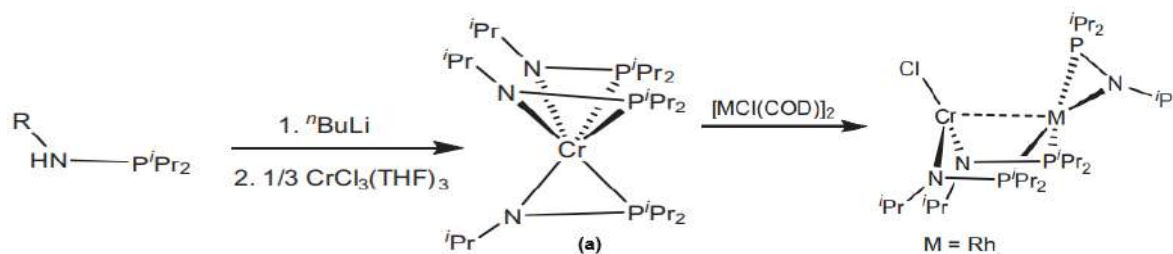


Figure11: Synthesis of  $[\text{ClCr}(\mu\text{-}^i\text{PrNP}^i\text{Pr}_2)_2\text{Rh}(\eta^2\text{-}^i\text{PrNP}^i\text{Pr}_2)]$

Using a salt metathesis route, complex (a) was synthesized by treating  $\text{CrCl}_3(\text{THF})_3$  with three equivalents of  $[\text{}^i\text{PrNP}^i\text{Pr}_2]\text{Li}$  in diethyl ether at room temperature. A solution of (a) in  $\text{Et}_2\text{O}$  was chilled to  $-32^\circ\text{C}$  and then added to solid  $[\text{RhCl}(\text{COD})]_2$  over 5 min. The reaction mixture was stirred at room temperature for 12 h to ensure completion of reaction. Insoluble by-products were removed via filtration through Celite and the volatiles were removed from the filtrate in vacuo.

### 6.8.2. Structure of $[\text{ClCr}(\mu\text{-}^i\text{PrNP}^i\text{Pr}_2)_2\text{Rh}(\eta^2\text{-}^i\text{PrNP}^i\text{Pr}_2)]$ (8)<sup>10</sup>

The Cr–N–P–Rh–P–N six-membered ring adopts a boat configuration, thus permitting orbital overlap between the two metals. If the metal–metal interaction is ignored, the geometry about Cr in (8) is trigonal pyramidal whereas the Rh centers adopt a distorted square planar geometry. The average Cr–N distances of 8 is significantly short (1.875 Å) which is because of the interactions between the amides and the more coordinatively unsaturated Cr center in 8.

### 6.9.1. Synthesis of $[\text{ClCr}(\mu\text{-}^i\text{PrNP}^i\text{Pr}_2)_2\text{Ir}(\eta^2\text{-}^i\text{PrNP}^i\text{Pr}_2)]$ (9)<sup>10</sup>

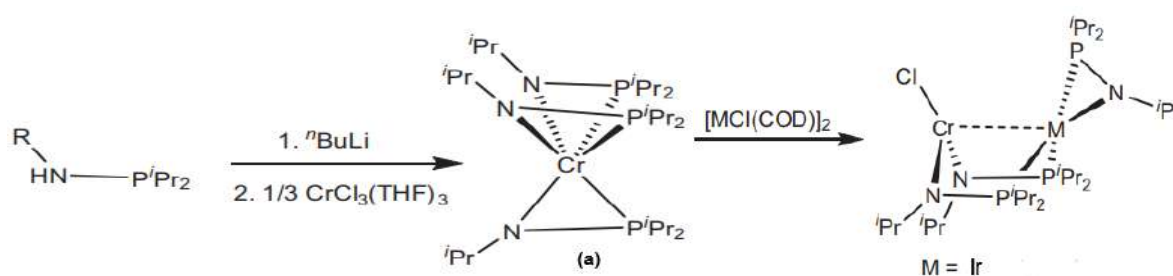


Figure12: Synthesis of  $[\text{ClCr}(\mu\text{-}^i\text{PrNP}^i\text{Pr}_2)_2\text{Ir}(\eta^2\text{-}^i\text{PrNP}^i\text{Pr}_2)]$

Using a salt metathesis route, complex (a) was synthesized by treating  $\text{CrCl}_3(\text{THF})_3$  with three equivalents of  $[\text{}^i\text{PrNP}^i\text{Pr}_2]\text{Li}$  in diethyl ether at room temperature. A solution of (a) in  $\text{Et}_2\text{O}$  was chilled to  $-32^\circ\text{C}$  and then added to solid  $[\text{IrCl}(\text{COD})]_2$  over 5 min. The reaction mixture was stirred at room temperature for 12 h to ensure completion of reaction. Insoluble by-products were removed via filtration through Celite and the volatiles were removed from the filtrate in vacuo.

### 6.9.2. Structure of $[\text{ClCr}(\mu\text{-}^i\text{PrNP}^i\text{Pr}_2)_2\text{Ir}(\eta^2\text{-}^i\text{PrNP}^i\text{Pr}_2)]$ (9)<sup>10</sup>

The Cr–N–P–Ir–P–N six-membered ring adopts a boat configuration in both cases, thus permitting orbital overlap between the two metals. If the metal–metal interaction is ignored, the geometry about Cr in (8) is trigonal pyramidal whereas the Ir centers adopt a distorted square planar geometry. The average Cr–N distances of 8 is significantly short (1.883 Å) which is because of the interactions between the amides and the more coordinatively unsaturated Cr center in 8.

## 7. Electronic Spectra of the Heterobimetallic Compounds

### 7.1. Spectra of PtNi(tba)<sub>4</sub>OH<sub>2</sub> (1) <sup>3</sup>

A series of UV-Vis spectra for 1 in THF in the concentration range 0.5–10 mM showed no changes attributable to monomer–dimer equilibrium. It exhibit weak absorbances in solution in the NIR at 1337 nm ( $\epsilon = 10 \text{ M}^{-1} \text{ cm}^{-1}$ ), consistent with intermetallic d–d charge transfer.

### 7.2. Spectra of [PtCr(tba)<sub>4</sub>(NCS)<sub>2</sub>] (2) <sup>4</sup>

UV–vis–NIR (diffuse reflectance) ( $\lambda_{\text{max}}$ ): 257, 660, 1672.

IR ( $\text{cm}^{-1}$ ): 2100 s, 1594 w, 1505 s, 1487 w, 1461 m, 1435 m, 1310 w, 1219 s, 1173 m, 1000 w, 963 s, 770 w, 723 m, 680 m, 645 m, 586 m.

### 7.3. Spectra of K(crypt-222)[CrFeL<sub>1</sub>] (3) <sup>5</sup>

The complex has been investigated by Mössbauer spectroscopy. The isomer shift value is 0.29 mm s<sup>-1</sup>. This proves that Fe has a 0 oxidation state.

### 7.4. Spectra of CoCr[N(o-(NCH<sub>2</sub>P<sup>i</sup>Pr<sub>2</sub>)C<sub>6</sub>H<sub>4</sub>)<sub>3</sub>] (4) <sup>6</sup>

<sup>1</sup>H NMR (ppm, THF-d<sub>8</sub>, 500 MHz): 10.5, 6.1, 2.4, 0.7, –1.0, –4.8.

UV–vis–NIR (THF)  $\lambda_{\text{max}}$ , nm ( $\epsilon$ , M<sup>-1</sup> cm<sup>-1</sup>): 325 sh (24 000), 440 sh (4400), 520 sh (2600), 840 sh (650), 1420 (950).

### 7.5. Spectra of NiV(N(o-(NCH<sub>2</sub>P<sup>i</sup>Pr<sub>2</sub>)C<sub>6</sub>H<sub>4</sub>)<sub>3</sub>) (5) <sup>7</sup>

<sup>1</sup>H NMR (ppm, C<sub>6</sub>D<sub>6</sub>, 400 MHz): 13.9, 6.9, 2.6, 1.2, 0.9, 0.5 (brsh).

UV–vis–NIR [THF;  $\lambda_{\text{max}}$ , nm ( $\epsilon$ , M<sup>-1</sup> cm<sup>-1</sup>): 410 (5200), 905 (500).

## 7.6. Spectra of $[\text{Cr}(\text{iPrNPPh}_2)_3\text{Fe-I}]$ (6)<sup>8</sup>

<sup>1</sup>H NMR (400 MHz, C<sub>6</sub>D<sub>6</sub>, ppm): δ 18.6, -2.0, -11.6.

UV-vis-NIR (C<sub>6</sub>H<sub>6</sub>) λ<sub>max</sub>, nm (ε, L mol<sup>-1</sup> cm<sup>-1</sup>): 340 (5900), 490 (900), 670 (600), 760 (400), 980 (310), 1170 (450).

## 7.7. Spectra of $\text{V}(\text{XylNP}^{\text{iPr}}\text{Pr}_2)_3\text{FeI}$ (7)<sup>9</sup>

<sup>1</sup>H NMR (400 MHz, C<sub>6</sub>D<sub>6</sub>): δ 30.2 (401), 5.3 (19), 4.8 (48), 1.6 (18), -0.4 (116), -1.6 (148).

UV-vis-NIR (C<sub>6</sub>H<sub>6</sub>) λ<sub>max</sub>, nm (ε, L mol<sup>-1</sup> cm<sup>-1</sup>): 490 (940), 610 (520), 880 (340).

## 7.8. Spectra of $[\text{ClCr}(\mu\text{-iPrNP}^{\text{iPr}}\text{Pr}_2)_2\text{Rh}(\eta^2\text{-iPrNP}^{\text{iPr}}\text{Pr}_2)]$ (8)<sup>10</sup>

The <sup>1</sup>H NMR spectra of 8 show nine paramagnetically broadened resonances, suggesting asymmetric structures with the three phosphinoamide ligands in at least two different environments. <sup>1</sup>H NMR (400 MHz, C<sub>6</sub>D<sub>6</sub>): δ 22.3, 12.5, 11.0, 10.4, 8.7, 4.9, 0.7, 0.3, -0.6.

## 7.9. Spectra of $[\text{ClCr}(\mu\text{-iPrNP}^{\text{iPr}}\text{Pr}_2)_2\text{Ir}(\eta^2\text{-iPrNP}^{\text{iPr}}\text{Pr}_2)]$ (9)<sup>10</sup>

The <sup>1</sup>H NMR spectra of 8 show nine paramagnetically broadened resonances, suggesting asymmetric structures with the three phosphinoamide ligands in at least two different environments. <sup>1</sup>H NMR (400 MHz, C<sub>6</sub>D<sub>6</sub>): δ 16.4, 11.9, 10.7 (2 signals overlapping), 9.0, 6.0, 4.8, 0.05, -2.2.

# 8. Electronic Structure of Heterobimetallic Compounds

The electronic structure of each complex featured in this section can be derived from either an idealized C<sub>3</sub>-symmetric or C<sub>4</sub>-symmetric structure. Those derived from the idealized C<sub>3</sub>-symmetry structure can be further classified into one of two generalized structures depending on the π donor ability of the equatorial ligand set.

## 8.1. Electronic Structure of C<sub>4</sub> Symmetric Heterobimetallics.

In a  $C_4$  symmetric structure, the five metal d orbitals transform into 1  $\sigma$ , 2  $\pi$ , and 2  $\delta$  symmetry orbitals representing the  $d_{z^2}$ ,  $dxz$ ,  $dyz$ ,  $d_{xy}$ , and  $dx^2 - y^2$  orbitals, respectively. The  $\delta$  symmetry  $dx^2 - y^2$  orbital is predominantly involved in metal–ligand bonding and hence is typically vacant unless the metal ions are high-spin.

Among the following compounds mentioned in the review  $\{PtNi\}^{16}$  (where 16 is the total number of d electrons) complex (1) has a  $C_4$  symmetry. Only four d-orbitals were included for each metal center, excluding the  $dx^2 - y^2$  orbital on the basis that it is involved predominantly in metal–ligand bonding.

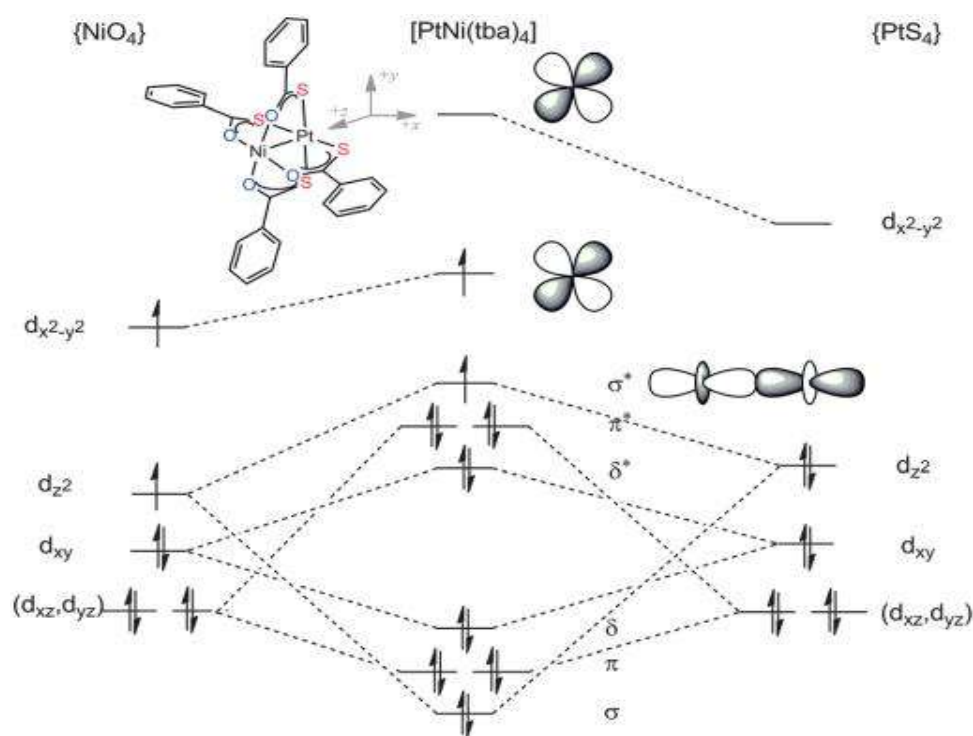


Figure 13: MO Diagram for Pt–Ni interaction in  $[PtNi(tba)_4(OH_2)]$ .<sup>3</sup>

The sides of Figure 13 show the qualitative ligand-field splitting and high-spin engagement is expected for a  $\{NiO_4\}$  environment and the low-spin environment for  $\{PtS_4\}$ . The midsection of Figure 13 shows how these two square planar centers overlap to form a new high spin system. Here, the 16 electrons fill up to the  $\sigma^*$  and Ni  $dx^2 - y^2$  levels, resulting in an  $S = 1$  ground state configuration. In this case, the small difference in effective nuclear charge of the metal atoms ( $\Delta N = 0$ ) gives rise to delocalized  $\sigma$ ,  $\pi$ , and  $\delta$  orbitals. Increasing  $\Delta N$  is expected to lead to localization of the  $\pi$  and  $\delta$  orbitals, and polarization of the  $\sigma$  orbitals. Therefore (1) is best reported as containing a two-center/three-electron  $\sigma$  bond between the metal atoms.

## 8.2. Electronic Structure of $C_3$ Symmetric Heterobimetallics

The trigonal ligand field found within  $C_3$ -symmetric structures allows all five metal d orbitals to engage in metal–metal bonding. In a  $C_3$  structure, the  $d_{xy}$  and  $d_{x^2-y^2}$  orbitals become degenerate orbitals of  $\delta$  symmetry.

Here, a comparative study has been made between complexes (3), (4) and (5). All these three compounds are having a  $\{MM'\}^{12}$  electron count (where 12 is the number of d electrons present in the complex). At first glance, the orbital diagrams and electron configurations appear to be identical. But on inspecting the metal–metal distance range from 1.97 Å for (3) to 2.49 Å for (5), a major distinction in the electronic structure that affect metal–metal bonding was observed.<sup>1</sup>

In complex (3), the d-orbital manifold is comprised of delocalized  $\sigma/\sigma^*$  and  $\pi/\pi^*$  MOs as well as localized  $d_{x^2-y^2}/d_{xy}$  orbitals. No  $\delta$ -bonding is evident.

In complex (4), the weak ligand field of trigonal coordination geometries, all five d-orbitals can potentially participate in metal–metal bonding. Hence, the d-orbitals can combine to form one  $\sigma$  ( $dz^2$ ), two  $\pi$  ( $dxz$ ,  $dyz$ ), and two  $\delta$  ( $d_{xy}$ ,  $d_{x^2-y^2}$ ) bonds. Here, the  $\delta$ -symmetric d-orbitals are localized.

In complex (5), the  $\sigma$ - and  $\pi$ -symmetric MOs become increasingly localized and, hence, nonbonding. In (5), the unpaired spin is predicted to be centered at V. For the NiV species, only nonbonding, localized MOs are present, and hence the formal bond order is 0. But experimental values suggest some bonding interaction in 5. A natural bond orbital (NBO) analysis reveals this interaction to be dative,  $Ni \rightarrow V$ . The interaction of lone pair of electrons in the Ni  $dz^2$  orbital and an empty V  $dz^2$  orbital provides an estimated electronic stabilization of  $\sim 20$  kcal/mol.<sup>7</sup>

All three compounds have an  $S = 1$  ground spin state with the two unpaired electrons in  $\delta$ -symmetry orbitals localized on the more electropositive metal atom. The major difference in going from (3) to (4) to (5) is a change in  $\Delta N$  from 2 to 3 to 5 ( $\Delta N$  = the difference in the d- electrons of the 2 participating metal ions). This change affects the polarization of the orbitals according to their symmetry. Compounds (3) and (4) are alike in that they have delocalization in both the  $\sigma$  and  $\pi$  symmetry orbitals. The composition of the  $\sigma$  bonding orbitals is  $\sim 33:66$  polarized toward the more electronegative metal in both cases.<sup>1</sup> The  $\pi$  bonding orbitals, however, are more responsive to the change in  $\Delta N$ , changing from a 27:73 Cr:Fe split in (3) to 16:84 Cr:Co in (4). This weakening of the metal–metal  $\pi$  bonding is manifested in a 0.17 Å elongation of the metal–metal distance from (3) to (4)<sup>1</sup>. With (5), the  $\Delta N$  value is 5. In this case, all of the orbitals localize to one metal center or the other. Only the  $\sigma$  bonding orbitals shows slight delocalization with a 10:90 V:Ni polarization.<sup>1</sup> This trend is due to the energy mismatch of the participating orbitals budding from differences in the effective nuclear charge. Large differences in energy prevent delocalized bonds from forming as in the case of (5) described as having only a dative interaction. A notable feature of this data set is that it shows clearly that the symmetry of the d orbitals strongly affects the degree of energy mismatch. Thus,  $\delta$ -symmetry orbitals, which have relatively poor overlap to begin with, are the first orbitals to “localize” when  $\Delta N$

increases. Thus, (3) can be described as having only a  $\sigma^2 \pi^4$  configuration contributing to its metal–metal bonding despite being a  $\{MM'\}^{12}$  complex. (Refer Figure 14).

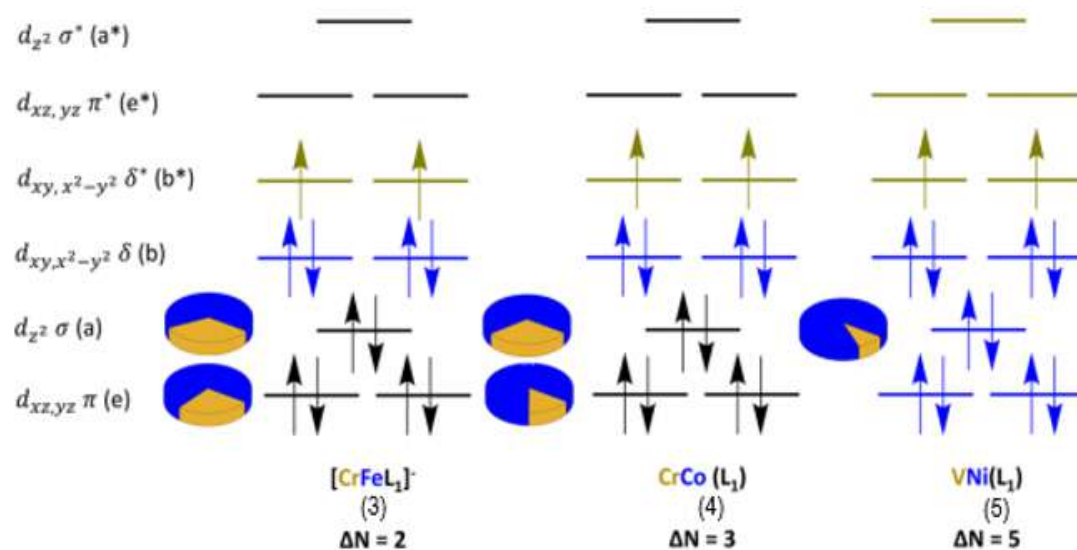


Figure 14: Qualitative MO Diagram for (3), (4) and (5). These compounds range from having a triple bond (left) to a dative interaction (right). Orbitals depicted in black represent highly delocalised orbitals across the chain. As the difference in group number  $\Delta N$  increases, the orbitals become localised onto one metal center. These localised orbitals are denoted in either blue or gold and correlate to the metal of that colour<sup>11</sup>.

In complex (7), due to the large differences in atomic orbital energies between the two different metals involved, there is no significant  $\delta$ -bonding overlap in V/Fe heterobimetallic complexes, and the existing  $\pi$  interactions are highly polarized. For the  $C_3$ -symmetric V/Fe complex 7, the calculated MO diagrams predict both  $\sigma$  and  $\pi$  overlap. From EPR spectroscopy it is observed that the SOMO of 7 is predicted to be a Fe-localized orbital that is nonbonding with respect to V. (Figure 15)

In complex (6), the differing atomic orbital energies of the two transition metals involved prevent orbital overlap of  $\delta$  symmetry. While each of the complexes has the symmetry to form both  $\sigma$  and  $\pi$  metal-metal bonds, this does not occur in all cases and the overlap that does occur is relatively weak. The  $\{CrFe\}^{10}$  complex 6 (where the  $\{M_1M_2\}^n$  notation is meant to represent the number of total d electrons “n” in the d-orbital manifold) adopts a  $(\sigma)^2 (\pi)^4 (\pi^*)^2 (Fe_{nb})^2$  configuration with the intermediate spin  $S = 2$  state allowing the  $\sigma^*$  and  $Cr_{nb}$  orbitals to remain unpopulated. From this configuration, the formal Cr-Fe bond order is 2. The metal-metal  $\pi$  bonding orbitals of 6 show substantial  $\pi$ -anti-bonding character with respect to the I-terminal ligand, which likely weakens the metal-metal  $\pi$  bonding in 6. The  $\pi^*$  orbitals of the complex 6 is invariably lower in energy than the localized Fe non-bonding orbitals ( $dx^2-dy^2$ ,  $dxy$ ). As a consequence, electrons populate both the M non-bonding orbitals and the metal-metal  $\pi^*$  orbitals in (6), leading to lower bond orders and higher spin state configurations. The weaker  $\pi$  overlap (and weaker metal-metal bonding in general) between Fe and Cr may be the result of a number of different factors stemming from the inherent geometric differences between this complex. (Figure 15)

Generally, as  $\Delta N$  increases the overlap between the orbitals of the two transition metals decreases hence increasing the metal-metal bond length. But the  $(\sigma)^2 (\pi)^4 (\text{Fe}_{\text{nb}})^3$  configuration for complex 7 gives rise to a V–Fe triple bond order (a  $\sigma$  bond and two  $\pi$  bonds), resulting in extremely short bonds. Turning to complex 6, in contrast to the VFe species and despite the more favourable  $\Delta N = 2$ , the Cr and Fe complex contain longer metal–metal distances because of lowering of the  $\pi^*$  orbital energy of (6) below the localized  $\delta$ -symmetry nonbonding Fe d orbitals (as mentioned above).

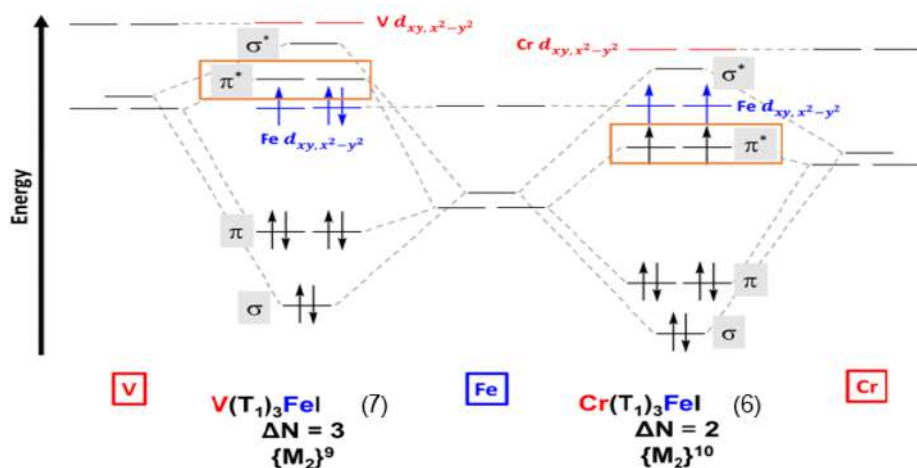


Figure 15: Qualitative MO diagrams for the bonding manifolds for (6) and (7) that give rise to multiple bonds or dative interactions, respectively. Orbitals that are in red or blue are localized to the corresponding colour metal. The  $\pi^*$  orbitals have been emphasized with a box<sup>1</sup>.

In complex (9) and (10), both the complexes show quite similar MOs. Since the inherent electronegativities of  $Cr^{III}$  and  $Rh^I$  or  $Ir^I$  should differ substantially, it is expected that the interaction between the two metals in complexes 9 and 10 is polar and perhaps better represented as a donor–acceptor interaction.

In 9, there is actually substantial orbital overlap between the two metals, with many of the frontier molecular orbitals containing significant contributions from both Cr and Rh. Most notably, a relatively covalent doubly-occupied Cr–Rh bonding orbital is found, along with a singly-occupied molecular orbital corresponding to a Rh–Cr antibonding orbital. Thus, if these two orbital interactions are considered, the Cr–Rh bond order is predicted to be  $\sim 0.5$ . The relative covalency of the metal–metal bond is somewhat unexpected given the vastly different electronic nature of Cr and Rh. However, if one considers that the increased electronegativity of Rh lowers the energy of its frontier MOs, the well-matched energy of the overlapping Cr 3d orbitals and Rh 4d orbitals in 9 can be justified.



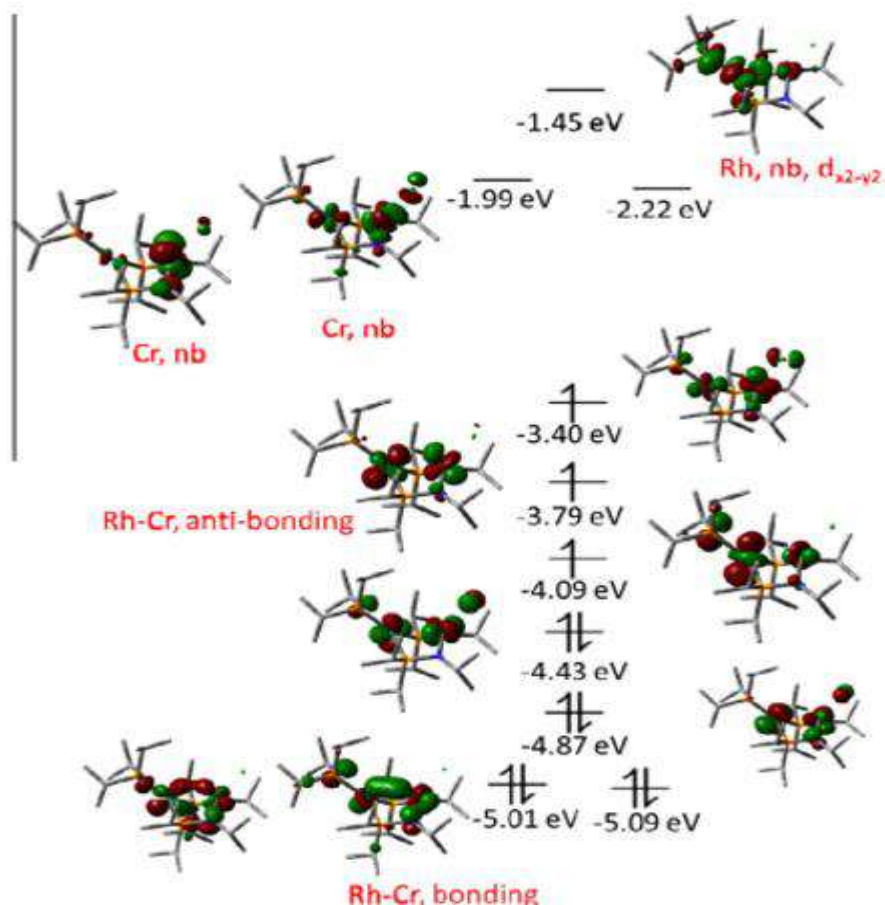


Figure 16: Pictorial representation of the frontier molecular orbitals of complex (9) derived from DFT calculations.

## 9. Magnetic Properties of Heterobimetallic Compounds

Despite containing only two metals, the diversity of magnetic interactions presented by the heterobimetallic compounds discussed here is wide-ranging. Depending on the position of the unpaired electrons and the energies of the d orbitals they reside in, unpaired electrons may be confined to one metal center or be delocalized over both centers and coupling can be ferro- or antiferromagnetic.

### 9.1. Isolated Magnetic Ions

Compounds containing isolated magnetic ions are those in which the spins are concentrated to a single metal atom.

The Evans method susceptibility values of  $3.11 \mu_B$  is consistent with high spin first-row transition metal centers as expected from the oxygen carboxylate donors and pseudo-octahedral coordination geometry. Variable-temperature solid-state susceptibility measurements revealed much more interesting behaviour in complex 1, however, the data for 1 show antiferromagnetic coupling, this time of two  $S = 1$  ions to give a singlet ground state. At 295 K, the  $\chi_M T$  product for crystalline 1 is  $1.81 \text{ emu K mol}^{-1}$  ( $\mu_{\text{eff}} = 3.80 \mu_B$ ). This

value is only slightly lower than expected for two magnetically isolated Ni (II) ions with  $g = 2$  (2.00 emu K mol<sup>-1</sup> expected). The susceptibility decreases monotonically upon cooling, reaching 0.02 emu K mol<sup>-1</sup> at 25 K and 0.01 emu K mol<sup>-1</sup> at 5 K. The main pathway for antiferromagnetic exchange is through the Ni dz<sup>2</sup>-Pt dz<sup>2</sup>-Pt dz<sup>2</sup>-Ni dz<sup>2</sup> alignment.<sup>3</sup>

The complex (3) is paramagnetic. The magnetic moment of (3) is 2.69  $\mu_B$  and is temperature-independent from 20 to 290 K. Thus, complex (3) has an  $S = 1$  ground state that is energetically well-isolated.<sup>5</sup>

Evans' method (C<sub>6</sub>D<sub>6</sub>):  $\mu_{\text{eff}} = 2.76 \mu_B$  for complex (4). The magnetic susceptibility plots of (4) are essentially temperature independent from 40 to 300 K, with value of 3.22  $\mu_B$ . This value is most consistent with  $S = 1$  (spin-only magnetic moment,  $\mu_{\text{SO}} = 2.83 \mu_B$ ) for cobalt-chromium (4).<sup>6</sup>

Complex (5) is paramagnetic and shows 6 proton resonances that are significantly broadened. It owes its paramagnetic nature due to  $S=1$  V<sup>III</sup> center. The effective magnetic moment of NiVL (5) was determined by Evan's NMR solution method at room temperature (rt) to be 2.39  $\mu_B$ , which is significantly below the spin-only moment for  $S = 1$  (2.83  $\mu_B$ ), suggesting that the  $g$  value associated with the V(III) d<sup>2</sup> spin is significantly less than 2. Specifically, the susceptibility of 5 would be consistent with a low  $g$  value of 1.7. Of relevance, low  $g$  values of 1.7 have been corroborated by high field EPR and/or variable-temperature magnetic susceptibility measurements for octahedral V<sup>III</sup> species.<sup>7</sup>

Solution magnetic moments measurements of 6 suggest  $S = 2$  ( $\mu_{\text{eff}} = 4.83 \mu_B$ ) ground states<sup>8</sup> because it has 4 unpaired electrons in the ground state (as mentioned above, in complex 6 the  $\pi^*$  orbital is located below the Fe<sub>nb</sub> orbital; hence it has 4 unpaired electrons).

The <sup>1</sup>H NMR spectrum of (7) displays 6 well-defined paramagnetically shifted resonances, consistent with a 3-fold symmetric complex, and the solution magnetic moment of 7 ( $\mu_{\text{eff}} = 1.82 \mu_B$ ) indicates a  $S=1/2$  ground state which is centred in the Fe<sub>nb</sub> orbital.

The magnetic moment of 8 ( $\mu_{\text{eff}} = 3.83 \mu_B$ ) indicates that this contain Cr<sup>III</sup> and possess an overall  $S = \frac{3}{2}$  ground state.<sup>10</sup>

Therefore, in complex 9 and 10 containing interactions between Cr<sup>III</sup> and either Rh<sup>I</sup> or Ir<sup>I</sup> species, both compounds have spin states of  $S = \frac{3}{2}$ . This is attributable to a diamagnetic Rh or Ir species and Cr(III) ion housing the localized d- electrons.

## 9.2. Spin-coupled magnetic centers:

In the case where both metal atoms in a heterobimetallic complex are high spin and paramagnetic, the magnetic properties can be difficult to rationalize.

Perhaps the most surprising compound in this class is complex (2) which behaves as a one-dimensional infinite chain linked in a zigzag pattern through thiocyanate ligands. The bridging isothiocyanate ligand can only transmit spin density via orbitals with  $\pi$  symmetry. These orbitals are orthogonal to the Pt-based  $dz^2$  ( $\sigma^*$ ) orbital on an adjacent {PtCr} unit. In turn, this orthogonality results in intrachain ferromagnetic interactions between the Cr(III) centers via Hund's rule ( $J = +1.18 \text{ cm}^{-1}$ ). At  $\pm 5 \text{ T}$ , the magnetization values approach saturation near  $3 \mu_B$ , consistent with an  $S = 3/2$  ground state spin for each Cr(III) ion. At  $4 \text{ K}$ , the smooth and monotonic increase in magnetization with increasing field ( $0$  to  $5 \text{ T}$ ) is consistent with paramagnetic behaviour. At fields lower than  $4000 \text{ Oe}$  and  $T < 4 \text{ K}$ , the magnetization trace shows some discontinuities, suggesting possible rearrangements of chain magnetic moments. Indeed, the hysteresis field sweep collected at  $1.8 \text{ K}$  exhibits butterfly-like hysteresis loops observed between  $0$  to  $1 \text{ T}$  and  $0$  to  $-1 \text{ T}$ . Given the zigzag nature of the {Pt-Cr-NCS} chains, it is reasonable to attribute the discontinuities to rearrangement of the net ferromagnetic chain moments as the external field is changed due to canting of the Cr(III) magnetic axes.<sup>4</sup> (Figure 17)

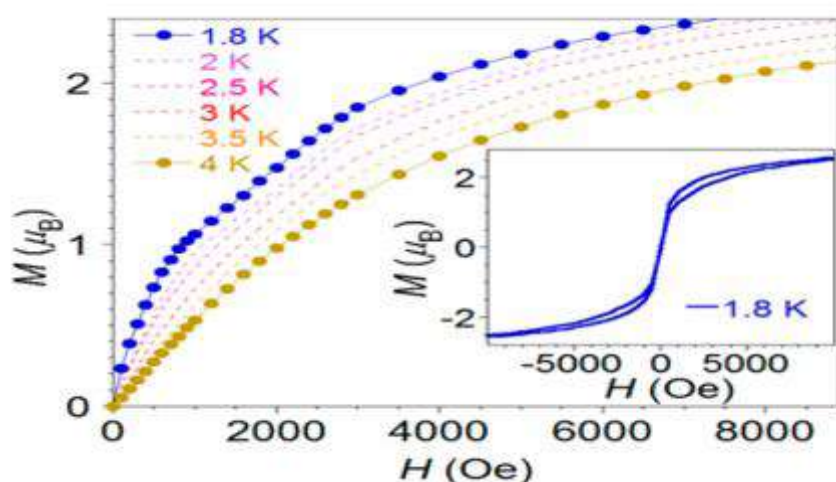


Figure 17: Field dependence of magnetization for (2) acquired at selected temperatures between  $1.8 \text{ K}$  to  $4 \text{ K}$ ; lines are guides to the eye. (inset) Expansion of  $M$  Vs  $H$  plot obtained at  $1.8 \text{ K}$  to show butterfly-like hysteresis.

## 10. Conclusion

In the dawn of 2007, the sphere of paramagnetic metal–metal bonded compounds has experienced a resurrection. This resurrection has incorporated the debut of various new types of bonds, inclusive of multiple bonds, heterobimetallic compounds evincing unusually large ferromagnetic coupling, new electron transfer properties, that crystallize into tetramers with long-range coupling, and heterometallic 1D zigzag

chain compounds. The relevant choice of ligand for axial position and metal–metal pairing allows for long-range polymeric interactions. Continued evolution of other diamagnetic or new paramagnetic mediators between magnetic centers may be a way to endow heterobimetallic complexes with further engrossing magnetic properties.

## 11. Acknowledgements

I thank my professor Dr. Partha Halder for numerous insightful conversations, formatting advice and for providing his valuable time and suggestions without which the completion of this project wouldn't have been possible.

I would like to thank my parents for encouraging and providing me all sort of moral support which motivated me every time to complete this review.

I am also grateful to the Chemistry Department of Scottish Church College for support of this work.

## 12. References:

1. Chipman, J.A; Berry, J.F; “Paramagnetic Metal-Metal Bonded Heterometallic Complexes.” *Chem. Rev.* **2020**, 120, 5, 2409-2447
2. Pauling, L. “Atomic Radii and Interatomic Distances in Metals.” *J. Am. Chem. Soc.* **1947**, 69, 542-553
3. Dahl, E. W.; Baddour, F. G.; Fiedler, S. R.; Hoffert, W. A.; Shores, M. P.; Yee, G. T.; Djukic, J.-P.; Bacon, J. W.; Rheingold, A. L.; Doerrer, L. H. Antiferromagnetic Coupling Across a Tetrametallic Unit Through Noncovalent Interactions. *Chem. Sci.* **2012**, 3, 602–609.
4. Guillet, J. L.; Bhowmick, I.; Shores, M. P.; Daley, C. J. A.; Gembicky, M.; Golen, J. A.; Rheingold, A. L.; Doerrer, L. H. Thiocyanate-Ligated Heterobimetallic {PtM} Lantern Complexes Including a Ferromagnetically Coupled 1D Coordination Polymer. *Inorg. Chem.* **2016**, 55, 8099–8109.
5. Rudd, P. A.; Liu, S.; Planas, N.; Bill, E.; Gagliardi, L.; Lu, C. C. Multiple Metal–Metal Bonds in Iron–Chromium Complexes. *Angew. Chem., Int. Ed.* **2013**, 52, 4449–4452.
6. Clouston, L. J.; Siedschlag, R. B.; Rudd, P. A.; Planas, N.; Hu, S.; Miller, A. D.; Gagliardi, L.; Lu, C. C. Systematic Variation of Metal–Metal Bond Order in Metal–Chromium Complexes. *J. Am. Chem. Soc.* **2013**, 135, 13142–13148.
7. Clouston, L. J.; Bernales, V.; Cammarota, R. C.; Carlson, R. K.; Bill, E.; Gagliardi, L.; Lu, C. C. Heterobimetallic Complexes That Bond Vanadium to Iron, Cobalt, and Nickel. *Inorg. Chem.* **2015**, 54, 11669–11679.
8. Kuppaswamy, S.; Bezpalko, M. W.; Powers, T. M.; Wilding, M. J. T.; Brozek, C. K.; Foxman, B. M.; Thomas, C. M. A Series of C<sub>3</sub>-Symmetric Heterobimetallic Cr–M (M = Fe, Co and Cu) Complexes. *Chem. Sci.* **2014**, 5, 1617–1626.

9. Wu, B.; Wilding, M. J. T.; Kuppaswamy, S.; Bezpalko, M. W.; Foxman, B. M.; Thomas, C. M. Exploring Trends in Metal–Metal Bonding, Spectroscopic Properties, and Conformational Flexibility in a Series of Heterobimetallic Ti/M and V/M Complexes (M = Fe, Co, Ni, and Cu). *Inorg. Chem.* **2016**, *55*, 12137–12148.
10. Kuppaswamy, S.; Cass, T. R.; Bezpalko, M. W.; Foxman, B. M.; Thomas, C. M. Synthesis and Investigation of the Metal–Metal Interactions in Heterobimetallic Cr/Rh and Cr/Ir Complexes. *Inorg. Chim. Acta* **2015**, *424*, 167–172.
11. Eisenhart, R. J.; Clouston, L. J.; Lu, C. C. Configuring Bonds between First-Row Transition Metals. *Acc. Chem. Res.* **2015**, *48*, 2885– 2894.

***A LITERATURE REVIEW ON***  
**POLYMERIC MICELLES AS DRUG DELIVERY AGENTS**

**SCOTTISH CHURCH COLLEGE**

**(UNIVERSITY OF CALCUTTA)**

**ROLL NO.- 223/CEM/191035**

**REGISTRATION NO.- 136-1221-0629-15**

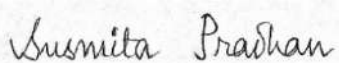
**SPECIAL PAPER: SP44**

**NAME OF THE CANDIDATE**

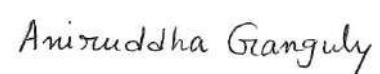
SUSMITA PRADHAN

**NAME OF SUPERVISOR**

Dr. ANIRUDDHA GANGULY



**SIGNATURE OF CANDIDATE**



**SIGNATURE OF SUPERVISOR**

# **POLYMERIC MICELLES AS DRUG DELIVERY AGENTS**

**Susmita Pradhan**

*Department of Chemistry, Scottish Church College, Kolkata, India*

---

## **Abstract**

Polymeric micelles that are formed by self-assembled amphiphilic block copolymers may serve as nanoscopic, long-circulating carriers of hydrophobic drugs. Among the different polymer-based drugs, these micelles generally display smaller size, easier preparation, sterilization processes and good solubilization properties (in order to improve bioavailability of the poorly soluble drugs). These properties of the polymeric micelles make them very stable in vivo and can accumulate in tumoral tissues. This article puts special emphasis on the use of polymeric micelles as pharmaceutical carriers, drug loading procedures and potential medical applications in treatment of human diseases.

**Keywords:** Polymeric micelles; amphiphilic block copolymer; drug loading.

## **1. Introduction**

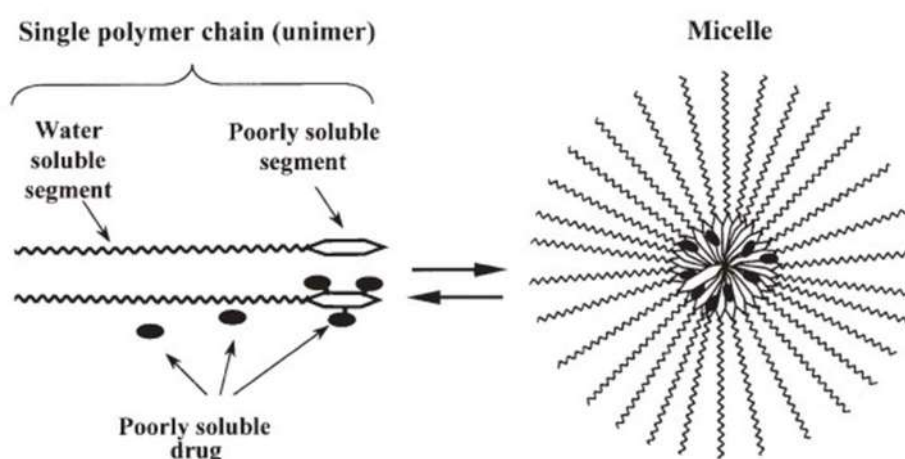
It has been long recognized that improving one or more of the intrinsic adsorption, distribution, metabolism and excretion (ADME) properties of a drug is a critical step in developing more effective drug therapies [1]. Oral administration is the most convenient route for drug delivery because of its simplicity convenience and patient acceptance specially in the case of repeated dosing for chronic therapy [2]. To minimize drug degradation and loss upon administration, prevent harmful or undesirable side-effects and increase drug bioavailability and fraction of the drug accumulated in the pathological zone, various drug delivery and drug targeting systems are currently being developed or under development. Among drug carriers one can find soluble polymers, microparticles made of natural and synthetic polymers, microcapsules, cells, cell ghosts, lipoproteins, liposomes and micelles. Each of those carrier types offers its own advantages and all those carriers can be made slowly degradable, stimuli reactive (for example, pH or temperature sensitive) and even targeted (for example, by conjugating them with specific antibodies against certain characteristic components of the area of interest) [3-6]. Fast clearance of the drug carrier is prevented since the glomerular filtration in the kidney has a molecular weight cut-off of approximately 50,000 g/mol [7]. The clearance of the drug was also found to be considerably lowered for particles less than 200 nm, which was assigned to a higher surface curvature [8]. Nanotechnology brings some advantages to the drug delivery, particular for oral drug. One approach to enhance the absorption efficiency and bioavailability of highly lipophilic drugs consists in using a particulate delivery system soluble or dispersible in an aqueous environment. This strategy is based on the following premises: particulate systems (a) provide the drug with some level of protection against degradation within the gastrointestinal tract (GI) tract; (b) prolong the drug transit time and facilitate translocation of the drug across epithelial barriers, thus improving drug absorption; and (c) may be targeted to specific sites and carry functionalities that assist specific absorption pathways [9].

In this review, after a short description of micelles characteristics, different aspects will be addressed, from the micelles basic characteristics (CMC, size, surface charge, solubilization, drug loading, drug release rate) to applications of polymeric micelles in drug delivery.

## 2. Micelles and micellization: relevance to drug delivery

### 2.1 Micelle and its solubilization

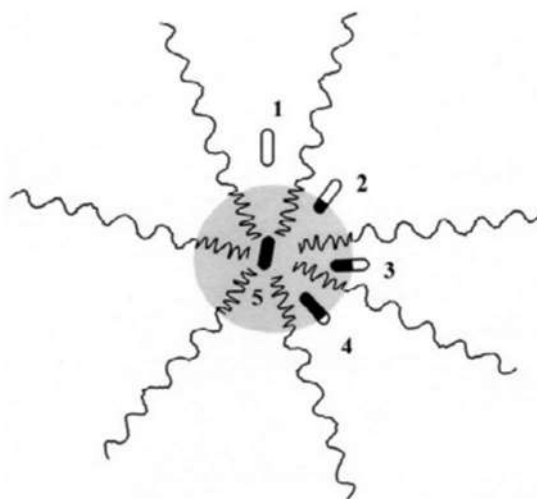
A micelle or micella is an aggregate of surfactant molecules dispersed in a liquid, forming a colloidal suspension. The particle size of the micelle is normally within the 5-100nm range [10]. Micelles consist of an inner core of an assembled hydrophobic segments capable of solubilizing lipophilic substances and an outer hydrophilic corona serving as a stabilizing interface between the hydrophobic core and the external aqueous environment, i.e., they belong to amphiphilic colloids [11]. The concentration of a monomeric amphiphile at which micelle appear is known as critical micelle concentration (CMC), while the temperature below which the amphiphilic molecules exists as unimers and above which it aggregates is called the critical micellization temperature (CMT). The CMC and CMT determine the threshold of the micelle formation [12,13]. Figure 1 shows the scheme of micelle formation from an amphiphilic molecule and its loading with a poorly soluble drug.



**Fig 1.** Micelle formation from amphiphilic unimers and drug incorporation into the micelle core by both covalent attachment to the hydrophobic fragment of the unimer and by non-covalent incorporation into the hydrophobic core micelle.

Generally, the CMC of a block copolymer decrease with the increase of block length of the core forming hydrophobic block and thus increasing the whole molecular weight. The important property of micelles as drug carriers is that they entrap sparingly soluble drugs and deliver them to the active site at concentrations that exceed their solubility and thus improve their bioavailability, reduce their toxicity and enhanced permeability across the physiological barriers [14,15]. Micelles made of non-ionic surfactants are most frequently used as adjuvants and drug carriers in pharmaceuticals [16-18]. They have an anisotropic water distribution where concentration of water decreases from the surface towards the core of the micelle. Due to this, micelles show a polarity gradient from the highly hydrated surface to the hydrophobic core. As a result, the position of the drug within a micelle will depend on its polarity. The non-polar molecules are solubilized in aqueous solution within the micelle core whereas the polar molecules are adsorbed on the surface of the micelle. In the meantime, the substances having the intermediate polarity are distributed along the surfactant molecules in a certain intermediate position.





**Fig. 2** Possible patterns of drug association with a micelle depending on the drug hydrophobicity (black color on a 'drug molecule' shows the hydrophobic area; white, the hydrophilic area). Completely water-soluble hydrophilic drug can only be adsorbed within the micelle corona compartment (case 1); while completely insoluble hydrophobic molecule can only be incorporated in the micelle core compartment (case 5). Drug molecules with intermediate hydrophobic/hydrophilic ratio will have intermediate positions within the micelle particle (cases 2 to 4).

Surfactant micelles which are formed above CMC rapidly break apart on dilution, thus result in primitive leakage of drug and its precipitation in situ. These limitations as drug carriers instigate the high stability and the solubility of micelles [19].

## 2.2 Biological significance of micellization

Micellization of biologically-active substances is a phenomenon where it is believed that the increase in the bioavailability of a lipophilic drug upon oral administration is caused by drug solubilization in the gut by naturally occurring fatty acid-containing mixed micelles (biliary lipid) produced by the organism as a result of the digestion of dietary fat [20]. The micellar form of the drug is transferred across the intestinal mucosal membrane into the enterocyte where it enters the lipoprotein biosynthetic pathway and eventually is released into the intestinal lymphatics being incorporated into chylomicron particles [21]. Here, mixed micelles play a key role in the transport of drug across the mucosal membrane. Amid other micelle-forming amphiphilic substances, low-molecular-weight oligoethylene glycol-based surfactants are especially widely used in pharmaceutical technology as solubilizers for poorly water-soluble or water-insoluble drugs for parenteral and oral routes of drug delivery like, for example, Polysorbate 80 [22-24]. The main advantage of this surfactants for pharmacological applications is their reported low toxicity [25]. The mechanism of the bioavailability enhancement is apparently close to the one for the biliary lipids: direct disturbance of the absorbing membrane. The structure of micelles makes them suitable carriers for poorly water-soluble drugs that account for approximately 25% of conventional, commercially available therapeutics and nearly 50% of them identified through screening techniques. The definite drawback is that mixed micelles composed of low molecular weight surfactants are thermodynamically not stable in aqueous media and are subject to dissociation upon dilution. Hence, in terms of drug delivery carrier development, there is a need to find a delivery carrier development, new class of surfactant molecules able to form more stable micelles with lower CMC values. Hence, a class of amphiphilic polymers known to form polymeric micelles in aqueous solutions, has been proposed as a drug carrier [26].

### 3. Polymeric Micelles

#### General Features

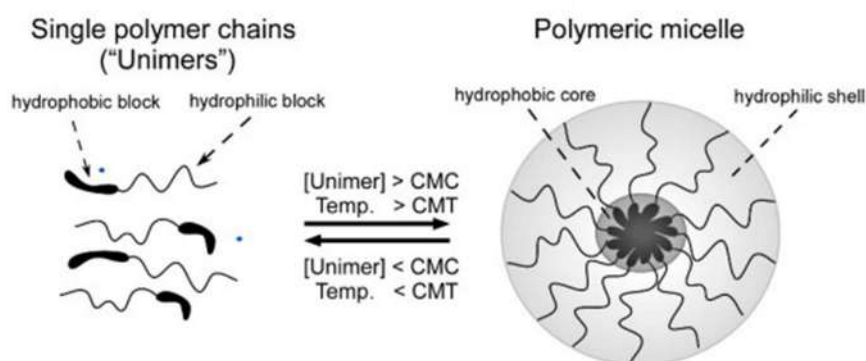
Polymeric micelles are self-assembled core-shell structures originated from amphiphilic block copolymers (ABCs) in an aqueous solution. The size of the polymeric micelle ranges from ~10 to ~100 nm and usually this size distribution is narrow. Hydrophobic segments of amphiphilic di- or tri-block copolymers self-assembled spontaneously into a supramolecular core above CMC. The hydrophobic core acts as a reservoir for solubilization of poorly water-soluble drugs whereas a hydrophilic shell interfaces the aqueous milieu. The major driving force behind self-assembly of amphiphilic polymers is the decrease of free energy of the system due to removal of hydrophobic fragments from aqueous environment with the formation of a micelle core and reestablishment of hydrogen bond network in water [27,28].

The CMC value is the most important parameter that defines micelles' thermodynamic stability [29]. The relative thermodynamic stability of polymer micelles primarily depends on the length of the hydrophobic block. An increase in the length of the hydrophobic block significantly decreases the CMC of the unimer construct, i.e., increases the thermodynamic stability of the micelle, whereas an increase in hydrophilic block alone slightly increases the CMC, i.e., decreases the thermodynamic stability of the polymeric micelle. Another fundamental parameter is kinetic energy which is an index of the micelle, tendency to disassembly over time when the system is diluted below the CMC. Due to the higher kinetic stability and lower toxicity, polymeric micelles are preferred to low molecular weight (MW) surfactants-composed micelles as drug delivery systems [30-32].

#### 3.1 Polymer micelle structures

##### 3.1.1 Self-Assembled Micelles

Self-assembled micelles are created from amphiphilic polymers that spontaneously form nano-sized aggregates when the unimers (individual polymer chains) are directly dissolved in aqueous solution by dissolution method above CMC and CMT. The process of self-assembly is driven by a gain in entropy of the solvent molecules since the hydrophobic polymer segments aggregate and withdraw from aqueous solution [33,34].

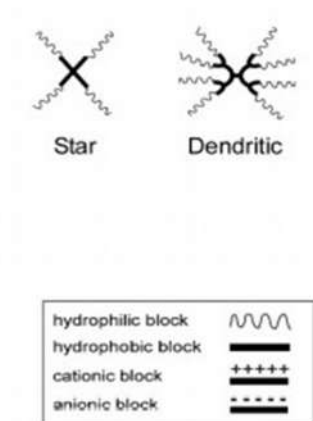


**Fig. 3** Self-assembly of block copolymer micelles

If the mass of the hydrophilic block is too great, the copolymers exist as unimers in aqueous medium, whereas if the mass of the hydrophobic block is too great, unimer aggregates with non-micellar morphology are formed. Otherwise, if the mass of the hydrophilic block is similar or slightly greater than the hydrophobic block then micelle core will be formed [35].

### 3.1.2 Unimolecular Micelles (Covalently Assembled Micelles)

These are topologically similar to the self-assembled micelles but consist of single polymer molecules with covalently linked amphiphilic chains. For example, copolymers with star-like or dendritic structure can either aggregate into multimolecular micelles or exist as unimolecular micelles [36]. Star-like micelles have a corona significantly bigger than the core, while the dendritic aggregates are dominated by a substantially bigger core.



**Fig. 4** Star-like & Dendritic micelle

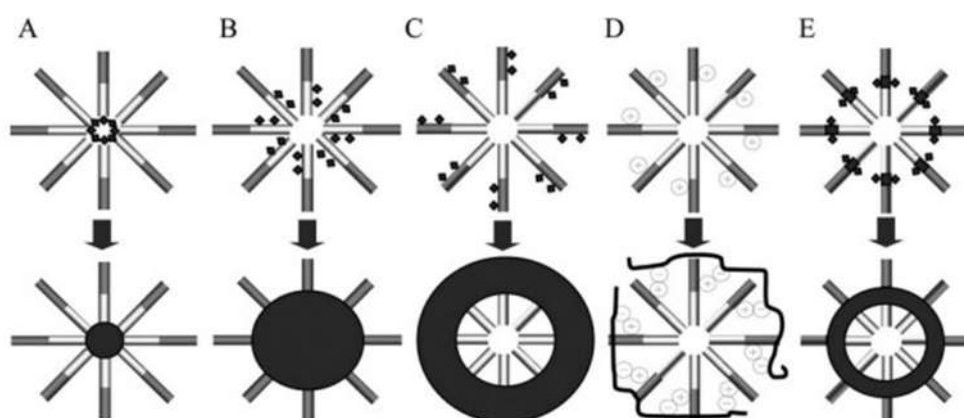
Multi-arm star-like block copolymers are synthesized by either the arm-first or core-first methods. In this method, monofunctional living linear macromolecules are prepared and then either cross-linked through propagation using a bio-functional comonomer or by adding a multifunctional terminating agent to connect to precise number of arms to the centre. These polymers are directly soluble in water and formed unimolecular micelles. In addition, star-copolymers with polyelectrolyte arms can be synthesized to develop pH-sensitive unimolecular micelles as drug carriers [9].

Dendrimers are widely used as building blocks to prepare unimolecular micelles because they are highly-branched, have distinct globular shape and controlled surface functionality. The dendritic cores can entrap various drug molecules. These unimolecular micelles encapsulate a hydrophobic drug, etoposide with high drug loading capacity [37].

Multi-arm star-like block copolymers are synthesized by either the arm-first or core-first methods. In this method, monofunctional living linear macromolecules are prepared and then either cross-linked through propagation using a bio-functional comonomer or by adding a multifunctional terminating agent to connect to precise number of arms to the centre. These polymers are

### 3.1.3 Cross-linked Micelles

Cross-linking of the micellar shell is a very promising approach to improve the stability of micelles without affecting the loading capacity in the core (C) [44,45]. It leads to a nano-sized structure (around 20-200 nm) that are stable upon dilution and shear forces with an immobile but permeable cross-linked peripheral layer and a mobile non-cross-linked core region and environmental variation (e.g. changes in pH values, ionic strength, solvents etc.) [38,39].



**Fig. 5** Crosslinking of micelles via functional groups at the end of hydrophobic chain (inner-core crosslinked, A), functional groups along hydrophobic chain (core crosslinked, B), functional groups along hydrophilic chain (shell crosslinked, C), polyelectrolyte complex formation (D), functional group along middle block of triblock (interface crosslinking, E).

There are range of pathways to achieve stabilization of self-aggregation of the cross-linked micelle. The introduction of reactive or polymerizable end groups to the hydrophobic block of an amphiphilic block copolymer enables the fixation of the micelle within the micelle core (A) [40,41]. The random distribution of the functional groups along with hydrophobic block promotes the stabilization of structure (B) [42]. This approach, however, limits the loading capacity and effects the release of the drug. The formation of a triblock copolymer with subsequent crosslinking of the middle block copolymer results interface cross-linking between hydrophobic and hydrophilic blocks (E) [43]. For charged block copolymers a different approach has been employed. The negative or positive charges distributed along either block can form strong complexes with polyelectrolytes of the opposite charge. These micellar-complex can either be very stable or the cross-linking can be reversed depending on the ionic strength (D) [46].

## **4. Polymeric Micelles for drug delivery**

Polymeric micelles have been widely studied as delivery medium for poorly water-soluble drugs, such as paclitaxel, indomethacin, amphotericin B, Adriamycin and dihydrotestosterone. The key physicochemical considerations of polymeric micelles for drug delivery include nanoscopic dimensions, drug loading capacity, release kinetics and physical stability against drug precipitation. The advantage of polymer particles as drug carriers in contrast to oral administration lies in the increased circulation time in the body. Poly(ethylene) glycol (PEG), the most widely used hydrophilic block, is well-known to enhance the circulation time substantially in order for the particles to remain undetected [47]. Polymer encapsulated drugs becomes superior for the treatment of solid tumours. The so-called enhanced permeability and retention (EPR) effect leads to preferred accumulation of polymers in the tumour while the ineffective lymph drainage of tumours hampers the clearance of drug carrier [48].

### **4.1 Block copolymers for polymeric micelles**

Di-block copolymers can be obtained using a range of techniques, such as free radical polymerization, anionic polymerization, cationic polymerization, living/controlled radical polymerization (such as atom transfer radical polymerization (ATRP), nitroxide mediated polymerization (NMP) and reversible addition fragmentation chain transfer (RAFT)), polycondensation, ring-opening polymerization and further novel techniques are all mentioned as successful pathways to block copolymers.

### **4.2 Proteins or Peptides**

Proteins or peptides may have many therapeutic uses but here the main focus is on the protein/peptides building blocks in amphiphilic block copolymers. Proteins/peptides can be treated as a water-soluble block with potentially high biocompatibility. Several proteins or peptides are known to allow the targeted delivery of drugs such as transferrin. These receptors are abundant to different cancer cell lines. Thus, transferrin bound to amphiphilic block copolymers can be a promising pathway in targeting specifically tumour cells [49]. Another drug carrier Liposomes which are extensively studied and the most widely used, have suitable characteristics for protein or peptide encapsulation. These vesicles are formed by concentric spherical phospholipid bilayers encapsulating an aqueous milieu. Liposomes are completely biocompatible, biologically inert and cause little toxic or antigenic reactions. Many techniques for liposome preparation require only manipulations that are compatible with peptide and protein integrity [50]. Furthermore, new approaches to intracellular drug delivery including the use of transduction proteins and peptides are also being developed.

### 4.3 Drug loading

Polymeric micelles are generally investigated to encapsulate hydrophobic drugs to increase their solubility in an aqueous milieu. The delivery of hydrophilic drugs increases the circulation time on the surface of the system. In order to achieve high loading, the hydrophilic molecules need to conjugate chemically with the unimers or via electrostatic interactions by using polyion complex micelles. The amount of loading strictly depends on the hydrophobic interactions occurring between the drug and the micellar core. This compatibility is based on drug characteristics such as polarity, hydrophobicity and charge. To assess compatibility between the polymer and solubilized drug, the Flory–Huggins interaction parameter may be used. The parameter,  $\chi_{sp}$  is defined as,

$$\chi_{sp} = (\delta_s - \delta_p)^2 V_s / RT$$

where is  $\chi_{sp}$  the interaction parameter between solubilized drug (s) and core-forming polymer block (p),  $\delta$  is the Scatchard–Hildebrand solubility parameter of the core-forming polymer block and  $V_s$  is the molar volume of the solubilized drug. The lower is the parameter  $\chi_{sp}$ , the greater the compatibility between the drug and the micelle core [51].

The definition of the loading capacity, also called drug loading (DL), and the entrapment efficiency (EE) should be carried out to evaluate the suitability of the excipients as well as to select the preparation method ensuring an efficient encapsulation of the selected drug. DL and EE can be calculated as:

$$\%DL = \frac{\text{amount of drug in the micelles}}{\text{total micelles weight (drug + polymer)}} \times 100$$

$$\%EE = \frac{\text{amount of drug in the micelles}}{\text{total amount of drug initially added}} \times 100$$

where the amount of drug in the micelles, in case of lipophilic compounds, can be quantified spectrophotometrically or via HPLC analysis after separation of the undissolved drug [52].

### 4.4 Drug release studies

Drugs must be released slowly from polymeric micelles for drug targeting. This process is called depot effect. Fast release of drugs from polymeric micelles which is also known as dose dumping, potentially causes precipitation of hydrophobic drug in the vascular system.

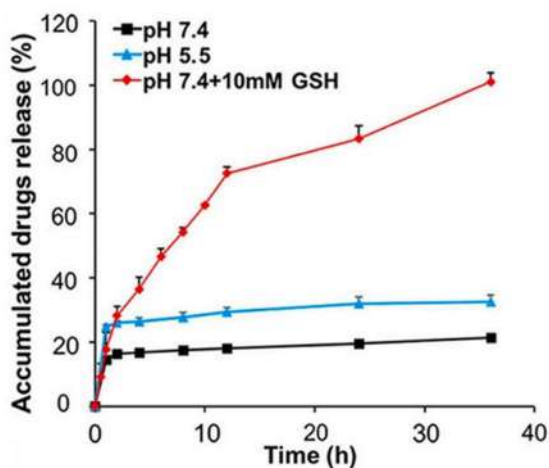
The most common method used for describing drug release from micelles is the dialysis process. In this method, the micellar formulation is introduced into a dialysis bag which is immersed in a recipient filled with the release medium maintained at constant temperature and stirring speed. While the released drug can diffuse from inside the bag to the outer medium, the micelle is prevented to cross the membrane due to its size. Thus, by analysing samples withdrawn from the external medium at different time points, the release profile can be built [53,55]. Moreover, an adequate cut-off must be chosen to ensure the complete release of a drug. The small molecules easily diffuse across dialysis membranes while the large cut-off values are necessary in the case of proteins and antibodies. To ensure accuracy of the results, the volume and the composition of the acceptor medium should be selected in such a way that guaranteed the sink conditions; most of the times the formulation volume inside the membrane is in the range 1-10 ml, while the outer volume is between the range 40 and 90 ml [54]. So, it should be considered that the amount of drug found in the receptor is the result of two processes – (1) the effective release of the drug from the micelle and (2) the permeation of drug across the dialysis membrane.

In some special cases, the drug release studies are carried out without dialysis membrane, for example, polarity-sensitive fluorescent probes and FRET (Foerster Resonance Energy Transfer).

#### 4.5 Drug release studies in biorelevant conditions

A drug release study is mostly performed to have knowledge about micelles behaviour in common buffers such as PBS (Phosphate Buffered Saline buffer) and HEPES (4-(2-hydroxyethyl)-1-piperazineethanesulfonic acid buffer) to select the most appropriate polymers for development of micelles or to investigate the mechanisms of drug release.

Drug release studies can also be used as a proof-of-concept of stimuli-responsiveness of the micellar systems. Stimuli like pH (typically lower in endosomes or lysosomes, in tumour cells and in inflamed tissues), presence of reducing agents (such as glutathione), specific enzymes (for instance matrix metalloproteinases over-expressed at tumour sites or matrix metalloproteinases-13 over-expressed in osteoarthritis) show changes in structure of micelles and trigger drug release [56]. External stimuli including UV-radiation or ultrasound treatment also results in triggered drug release. Zhu *et al.* measured the release profile of doxorubicin-loaded polymeric micelles. The Fig. 6 (below) shows at pH 7.4 less than 25% of doxorubicin was released, whereas at pH 5.5, an improved release was observed reproducing the endosomal and lysosomal conditions. At the end, in presence of 10mM glutathione (GSH), more than 70% and more 90% of the drug was released respectively reproducing tumour cells environment after 12h and 36h of incubation.



**Fig. 6** Release profile of drug doxorubicin from micelles in PBS at different pH (7.4 and 5.5) and in PBS (pH 7.4) added with 10 mM glutathione, working as reducing agent (Adapted from American Chemical Society).

Again, controlled release of metoprolol, a  $\beta$ 1-selective adrenergic blocking agent, in the form of its succinate or tartrate salt in the gastrointestinal tract (duodenum or stomach). Since the half-life of the bare drug is  $\sim$ 3 to 4 h, multiple doses are needed to maintain a constant plasma concentration for improved patient compliance. To counter this problem, usually, a double layer coating is used to prepare the oral dose. The outer layer is mixture of a swelling controlling agent such as magnesium alumina metasilicate (MAS) and a buoyancy agent such as sodium alginate (SA) and a disintegrant such as Na-carboxymethylcellulose (NaCMC). After oral administration, MAS produces swelling of the tablet via adsorption of water while SBC, in the presence of HCl, generates  $\text{CO}_2$  which gets entrapped in the pores of MAS. This leads to reduction in the density of the tablet, thereby producing floating. NaCMC then facilitates the breakup of the tablet, the rate of which is controlled by SA. Thus, we have a controlled release of the drug a constant plasma concentration can be maintained[71].

Other drug release studies like the release of anti-cancer drug chlorambucil from micelle composed of 2-(N,N-dimethyl amino) ethyl methacrylate (PDMAEMA) (Sam Miguel *et al.*) and release of doxorubicin from PEG-b-PEYM (poly(ethylene glycol)-block-polymethacrylate) micelles due to presence of acid-labile ortho ester side-chains in the polymer (Gao *et al.*) are also the relevant ones [57-60].

## 5. Applications of Drug Delivery

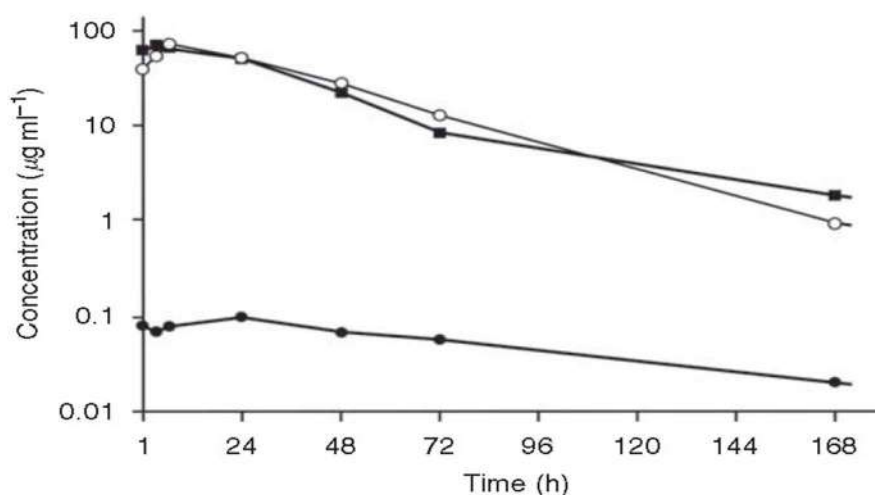
The studies on application of polymer micelles in drug delivery have mostly focused of the following areas: 1) delivery of anticancer agents to treat tumours; 2) drug delivery to the brain to treat neurodegenerative diseases; 3) delivery of antifungal agents; 4) delivery of imaging agents for diagnostic applications; and 5) delivery of polynucleotide therapeutics. Here two applications - Chemotherapy of cancer and drug delivery to the brain are discussed below.

### 5.1 Chemotherapy of cancer

Chemotherapy is an essential component in the multidisciplinary management of most cancers. Drugs directed at killing or controlling cancerous cells also tend to be toxic to normal cells. The reliance on toxic actives or their adjuvants calls for improvements in dosage forms, one of the main challenges in chemotherapy. In that regard, polymer nanoparticles or self-assembled aggregates (micelles and liposomes) that are capable of encapsulating drugs and escaping from the macrophage uptake and yet are small enough to allow intra- or transcapillary passage are gaining prominence as a means to address this issue.

Four major approaches were employed to enhance chemotherapy of tumours using polymer micelles : 1) passive targeting of polymer micelles to tumours due to EPR effect; 2) targeting of polymer micelles to specific antigens overexpressed at the surface of tumour cells; 3) enhanced drug release at the tumours sites having low pH; and 4) sensitization of drug resistant tumours by block copolymers.

A series of pioneering studies by Kataoka's group used polymer micelles for passive targeting of various anticancer agents and chemotherapy of tumours. Injectable formulations based on copolymers of PEG and poly (aspartic acid) have advanced into Phase I clinical trials. In this phase I clinical trial polymer micelles of PEO-b-poly (L-aspartic acid) incorporates CDDP (cis-dichlorodiaminoplatinum (II)) or cis-platin (Fig. 7) [61,63].



**Fig. 7** A Phase I clinical study of cisplatin-incorporated polymeric micelles (NC-6004) in patients with solid tumours: Plasma Pt concentration–time curve from a patient treated at  $90 \text{ mgm}^{-2}$  of NC-6004. ■ - total Pt, ○ - gel-filterable Pt, ● - ultra filterable Pt.

Evaluation of anticancer activity using murine colon adenocarcinoma C26 as an in vivo tumour model demonstrated that CDDP in polymer micelles had significantly higher activity than the free CDDP,

resulting in complete eradication of the tumour. A phase II clinical trial on Genexol-PM, a Cremophor EL-free PEG-b-PLA polymeric micelle for PTX (paclitaxel), showed favourable efficacy in patients with metastatic breast cancer MCF7 (45.3–72.3% response rate) and human ovarian carcinoma OVCAR-3, compared with the conventional Cremophor EL-based PTX. Micelles based on PEG-poly (aspartic acid) typically possess a core-shell structure with water-soluble PEG in the outer shell and a sufficiently hydrophobic complex formed between the poly (aspartic acid) and doxorubicin conjugate in the core [62]. This approach can result in high selectivity of binding, internalization, and effective retention of the micelles in the tumour cells. Micelles of PEO- b-poly( $\epsilon$ -caprolactone) loaded with doxorubicin (DOX) were covalently bound with cRGD. As a result of such modification the uptake of doxorubicin-containing micelles in in vitro human endothelial cell from Kaposi's sarcoma was profoundly increased.

A pH-sensitive system that has been advanced for oral administration of hydrophobic and other drugs for chemotherapy is based on a family of graft-comb poly(ethylene oxide)-block-poly(propylene oxide)-block-poly(ethylene oxide)-graft-poly(acrylic acid) copolymers (PEO-PPO-PEO-PAA, or Pluronic-PAA). The Pluronic-PAA copolymers, typically of high ( $>10^5$  Da) molecular weight, possess many physical and pharmacological features that make dosage forms based on such polymers and chemotherapeutic agents well adapted for treatment of cancers involving oral administration. Studies by Alakhov et al. demonstrated that Pluronic block copolymers can sensitize MDR (multidrug resistant) cells resulting in increased cytotoxic activity of DOX and PTX. Pluronic can enhance drug effects in MDR cells through multiple effects including 1) inhibiting drug efflux transporters, such as Pgp (P-glycoprotein), 2) abolishing drug sequestration within cytoplasmic vesicles; 3) inhibiting the glutathione/glutathione S-transferase detoxification system; and 4) enhancing proapoptotic signalling in MDR cells [64-66].

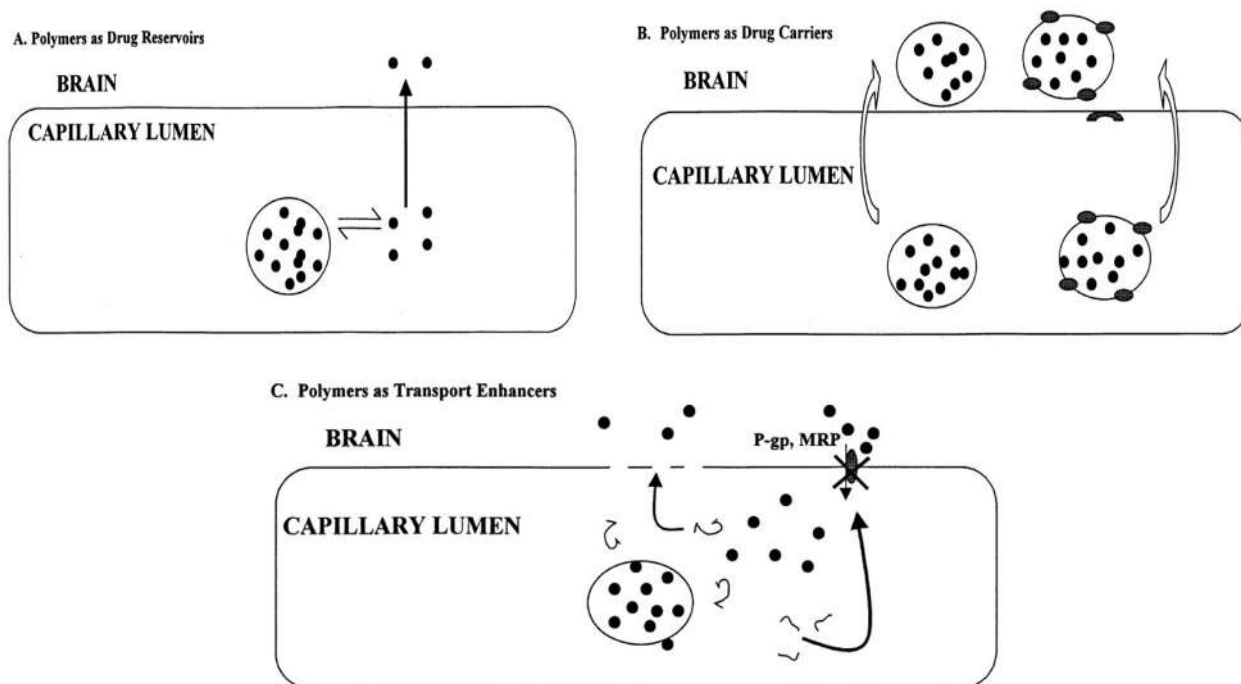
The detailed clinical studies of these reinforce that block copolymers comprising the micelles can serve as biological response modifying agents that can have beneficial effects in chemotherapy of tumours.

## 5.2 Drug Delivery to the Brain

By restricting drug transport to the brain, the blood brain barrier (BBB) represents a formidable impediment for treatment of brain tumours and neurodegenerative diseases, such as HIV-associated dementia, stroke, Parkinson's and Alzheimer's diseases. Two strategies using polymer micelles have been evaluated to enhance delivery of biologically active agents to the brain. The first strategy is based on modification of polymer micelles with antibodies or ligand molecules capable of transcytosis across brain micro-vessel endothelial cells comprising the BBB. The second strategy uses Pluronic block copolymers to inhibit drug efflux systems, particularly Pgp, and selectively increase the permeability of BBB to Pgp substrates [68].

An early study used micelles of Pluronic block copolymers for delivery of the CNS drugs to the brain [67]. These micelles were surface-modified by attaching to the free PEO ends either polyclonal antibodies against brain-specific antigen,  $\alpha$ 2-glycoprotein, or insulin to target the receptor at the luminal side of BBB.





**Fig. 8** Potential strategies for enhancing the delivery of drugs to the brain using polymer-based formulations. The closed circles represent drug, grey ellipses represent proteins, and the various short lines represent individual polymer strands.

Subsequent studies using in vitro BBB models demonstrated that the micelles vectorized by insulin undergo receptor-mediated transport across brain micro-vessel endothelial cells [68]. Based on these observations one should expect development of novel polymer micelles that target specific receptors at the surface of the BBB to enhance transport of the incorporated drugs to the brain.

The studies by our group have also demonstrated that selected Pluronic block copolymers, such as Pluronic P85 are potent inhibitors of Pgp and increase entry of the Pgp-substrates to the brain across BBB. Pluronic did not induce toxic effect in BBB as revealed by lack of alteration in paracellular permeability of the barrier and in histological studies using specific markers for brain endothelial cells. Overall, this strategy has a potential in developing novel modalities for delivery of various drug to the brain, including selected anti-cancer agents to treat metastatic brain tumours as well as HIV protease inhibitors to eradicate HIV virus in the brain [68,69].

## 6. Conclusions

Drug delivery using polymeric micelles grew out of its infant state with some block copolymers being currently tested in clinical trials. About two decades novel biocompatible and/or biodegradable block copolymer chemistries have been researched, the block ionomer complexes capable of incorporating DNA and other charged molecules have been discovered, the pH and other chemical signal sensitive micelles have been developed. Many drug combinations have been very successful in the treatment of cancer, and they continue to be widely researched in preclinical and clinical studies with expanding focus on targeting aberrant signalling pathways in solid tumours [70]. Notable achievements also include the studies demonstrating the possibilities for overcoming multidrug resistance in cancer and enhance drug delivery to the brain using block copolymer micelles systems. Sequential drug delivery of polymeric micelles may be used for “tumour priming” to enhance tumour penetration and uptake of anticancer agents beyond the scope of the EPR effect. Polymeric micelles are uniquely suited for multi-drug delivery in the search for synergistic, selective, and safe anticancer drug combinations.

## Acknowledgement

I'm grateful to Dr. Aniruddha Ganguly (Scottish Church College, Kolkata) for his support and guidance in my work.

## References

- [1] Ehrlich P (1956), *The relationship existing between chemical constitution, distribution, and pharmacological action*. In Himmelweite F, Marquardt M and Dale H (eds.), *The Collected Papers of Paul Ehrlich*. Pergamon, Elmsford, New York, Vol. 1, pp. 596-618.
- [2] E. C. Lavelle, S. Sharif, N. W. Thomas, J. Holland, S. S. Davis., *Adv. Drug Delivery Rev.* 18, 5–22 (1995).
- [3] R.H. Muller, *Colloidal Carriers for Controlled Drug Delivery and Targeting*, Wissenschaftliche Verlagsgesellschaft, Stuttgart, Germany, and CRC Press, Boca Raton, FL, 1991.
- [4] D.D. Lasic, F. Martin (Eds.), *Stealth Liposomes*, CRC Press, Boca Raton, FL, 1995.
- [5] S. Cohen, H. Bernstein (Eds.), *Microparticulate Systems for the Delivery of Proteins and Vaccines*, Marcel Dekker, Inc New York, 1996.
- [6] V.P. Torchilin, V.S. Trubetskoy, *Which polymers can make nanoparticulate drug carriers long circulating? nanoparticulate drug carriers long-circulating?* *Adv. Drug Deliv. Rev.* 16 (1995) 141–155.
- [7] L. W. Seymour, R. Duncan, J. Strohmalm and J. Kopecek, *J. Biomed. Mater. Res.*, 1987, 21, 1341.
- [8] L. Hongbo, S. Farrell and K. Uhrich, *J. Controlled Release*, 2000, 68, 167.
- [9] Mira F. Francis, Mariana Cristea, and Françoise M. Winnik, *Polymeric micelles for oral drug delivery: Why and how*, *Pure Appl. Chem.*, Vol. 76, No. 7–8, pp. 1321–1335, 2004.
- [10] Mittal K. L. and Lindman B. (eds) (1991), *Surfactants in Solution*, vols 1–3, Plenum Press, New York.
- [11] K. Kataoka, G. S. Kwon, M. Yokoyama, T. Okano, Y. Sakurai., *J. Controlled Release* 24, 119–132 (1993).
- [12] J.-F. Gohy, *Adv. Polym. Sci.*, 2005, 190, 65
- [13] G. S. Kwon, M. Naito, M. Yokoyama, Y. Sakurai and K. Kataoka, *Langmuir*, 1993, 9, 945.
- [14] K. Kataoka. *J. Macromol. Sci., Pure Appl. Chem.* A31, 1759–1769 (1994).
- [15] M. Yokoyama (Ed.), *Novel Passive Targetable Drug Delivery with Polymeric Micelles*, pp. 193–229, Academic Press, San Diego (1998).
- [16] S. N. Malik, D. H. Canaham, M. W. Gouda., *J. Pharm. Sci.* 64, 987–990 (1975).
- [17] K. Takada, H. Yoshimura, N. Shibata, Y. Masuda, H. Yoshikawa, S. Muranishi, T. Yasumura, T. Oka., *J. Pharmacobio-Dyn.* 9, 156–160 (1986).
- [18] H. A. Bardelmeijer, M. Ouweland, M. M. Malingre, J. H. Schellens, J. H. Beijnen, O. van Tellingen. *Cancer Chemother. Pharmacol.* 49, 119–125 (2002).
- [19] A. K. Andrianov and L. G. Payne., *Adv. Drug Delivery Rev.* 34, 155–170 (1998)

- [20] G.S. Kwon, K. Kataoka, *Block copolymer micelles as long circulating drug vehicles*, *Adv. Drug Deliv. Rev.* 16 (1995), 295–309.
- [21] W.N. Charman, *Lipid vehicle and formulation effects on intestinal lymphatic drug transport*, in: W.N. Charman, V.J. Stella (Eds.), *Lymphatic Transport of Drugs*, CRC Press, Boca Raton, FL, 1992, pp. 113–179.
- [22] A. Martinez-Coscolla, E. Miralles-Loyola, T.M. Garrigues, M.D. Sirvent, E. Salinas, V.G. Casabo, *Studies on the reliability of novel absorption–lipophilicity approach to interpret the effects of the synthetic surfactants on drug and xenobiotics absorption*, *Drug. Res.* 43 (1993) 699–705.
- [23] Y. Masuda, H. Yoshikawa, K. Takada, S. Muranishi, *The mode of enhanced enteral absorption of macromolecules by lipid-surfactant mixed micelles*, *J. Pharmacobio. - Dyn.* 9 (1986).
- [24] D.D. Lasic, *Mixed micelles in drug delivery*, *Nature* 355 (1992) 279–280.
- [25] G. Magnusson, T. Olsson, J.-A. Nyberg, *Toxicity of Pluronic F-68*, *Toxicol. Lett.* 30 (1986) 203–207.
- [26] M. Yokoyama, *Block copolymers as drug carriers*, *CRC Crit. Rev. Ther. Drug Carrier Syst.* 9 (1992) 213–248.
- [27] M.-C. Jones, J.-C. Leroux, *Polymeric micelles — a new generation of colloidal drug carriers*, *Eur. J. Pharm. Biopharm.* 48 (1999) 101–111.
- [28] A. Martin, in: *Physical Pharmacy*, 4th Edition, Williams and Wilkins, Baltimore, MD, 1993, pp. 396–398.
- [29] *Stability Issues of Polymeric Micelles*, *J. Control. Release* 131 (2008) 2–4.
- [30] R. Trivedi, U.B. Kompella, *Nanomicellar formulations for sustained drug delivery: strategies and underlying principles*, *Nanomedicine* 5 (2010) 485–505.
- [31] R. Wakaskar, *Polymeric micelles and their properties*, *J. Nanomed. Nanotechnol.* 08 (2017).
- [32] *Application of solid phase peptide synthesis to engineering PEO–peptide block copolymers for drug delivery*, *Colloids Surf. B: Biointerfaces* 30 (2003) 323–334.
- [33] Kabanov AV, Nazarova IR, Astafieva IV, Batrakova EV, Alakhov VY, Yaroslavov AA and Kabanov VA (1995), *Micelle formation and solubilization of fluorescent probes in poly (oxyethylene-b-oxypropylene-b oxyethylene) solutions*. *Macromolecules.* 28: 2303-2314.
- [34] Allen C, Maysinger D and Eisenberg A (1999), *Nano-engineering block copolymer aggregates for drug delivery*. *Coll. Surfaces, B: Biointerfaces.* 16: 3-27.
- [35] Zhang L, Yu K and Eisenberg A (1996), *Ion-Induced morphological changes in "crew-cut" aggregates of amphiphilic block copolymers*. *Science.* 272: 1777-9.
- [36] Hawker CJ, Wooley KL and Frechet JMJ (1993), *Unimolecular micelles and globular amphiphiles: dendritic macromolecules as novel recyclable solubilization agents*. *Journal of the Chemical Society, Perkin Transactions 1: Organic and Bio-Organic Chemistry (1972-1999):* 1287-97.
- [37] Antoun S, Gohy JF and Jerome R (2001), *Micellization of quaternized poly(2-(dimethylamino)ethyl methacrylate)-block-poly (methyl methacrylate) copolymers in water*. *Polymer.* 42: 3641-3648.

- [38] K.B. Thurmond, T. Kowalewski, K.L. Wooley, *Water-soluble knedel-like structures: the preparation of shell-cross-linked small particles*, *J. Am. Chem. Soc.* 118 (30) (1996) 7239–7240.
- [39] K.B. Thurmond II, H. Huang, C.G. Clark Jr., T. Kowalewski, K.L. Wooley, *Shell cross-linked polymer micelles: stabilized assemblies with great versatility and potential*, *Colloids Surf. B* 16 (1999) 45–54.
- [40] M. Iijima, Y. Nagasaki, T. Okada, M. Kato and K. Kataoka, *Macromolecules*, 1999, 32, 1140–1146.
- [41] K. Emoto, Y. Nagasaki and K. Kataoka, *Langmuir*, 1999, 15, 5212
- [42] Y. Y. Won, H. T. Davis and F. S. Bates, *Science*, 1999, 283, 960.
- [43] Y. Li, B. S. Lockitz, S. P. Armes and C. L. McCormick, *Macromolecules*, 2006, 39, 2726.
- [44] R. K. O'Reilly, C. L. Hawker and K. L. Wooley, *Chem. Soc. Rev.*, 2006, 35, 1068.
- [45] R. K. O'Reilly, M. J. Joralemon, C. J. Hawker and K. L. Wooley, *J Polym Sci. Part A: Polym. Chem.*, 2006, 44, 5203.
- [46] E. S. Read and S. P. Armes, *Chem. Commun.*, 2007, 3021.
- [47] S. Stolnik, L. Illum and S. S. Davis, *Adv. Drug Delivery Rev.*, 1995, 16, 195.
- [48] Y. Matsumura and H. Maeda, *Cancer Res.*, 1986, 46, 6387.
- [49] E. Ryschich, G. Huszty, H. Knaebel, M. Hartel, M. Buchler and J. Schmidt, *Eur. J. Cancer*, 2004, 40, 1418; T. Szekeres, J. Sedlak and L. Novotny, *Curr. Med. Chem.*, 2002, 9, 759.
- [50] Lasic, D.D. and Papahadjopoulos, D., eds (1998) *Medical Applications of Liposomes*, Elsevier.
- [51] Martina Heide Stenzel, *RAFT polymerization: an avenue to functional polymeric micelles for drug delivery*, The Royal Society of Chemistry, 2008, DOI: 10.1039/b805464a
- [52] Y. Shi, H. Zhu, Y. Ren, K. Li, B. Tian, J. Han, D. Feng, *Preparation of protein-loaded PEG-PLA micelles and the effects of ultrasonication on particle size*, *Colloid Polym. Sci.* 295 (2017) 259–266.
- [53] M. Imran, M.R. Shah, Shafiullah, *Chapter 10 - Amphiphilic block copolymers-based micelles for drug delivery*, in: A.M. Grumezescu (Ed.), *Design and Development of New Nanocarriers*, William Andrew Publishing, 2018, pp. 365–400.
- [54] S. D'Souza, *A review of in vitro drug release test methods for nano-sized dosage forms*, *Adv. Pharm.* 2014.
- [55] V. Gupta, P. Trivedi, *Chapter 15 - In vitro and in vivo characterization of pharmaceutical topical nanocarriers containing anticancer drugs for skin cancer treatment*, in: A.M. Grumezescu (Ed.), *Lipid Nanocarriers for Drug Targeting*, William Andrew Publishing, 2018, pp. 563–627.
- [56] Y. Dai, X. Chen, X. Zhang, *Recent advances in stimuli-responsive polymeric micelles via click chemistry*, *Polym. Chem.* 10 (2019) 34–44.
- [57] V. San Miguel, A.J. Limer, D.M. Haddleton, F. Catalina, C. Peinado, *Biodegradable and thermo-responsive micelles of triblock copolymers based on 2- (N, N- dimethylamino) ethyl methacrylate and  $\epsilon$ -caprolactone for controlled drug delivery*, *Eur. Polym. J.* 44 (2008) 3853–3863.

- [58] R. Tang, W. Ji, D. Panus, R.N. Palumbo, C. Wang, *Block copolymer micelles with acid-labile ortho ester side-chains: synthesis, characterization, and enhanced drug delivery to human glioma cells*, J. Control. Release 151 (2011) 18–27.
- [59] Y. Zhu, T. Meng, Y. Tan, X. Yang, Y. Liu, X. Liu, F. Yu, L. Wen, S. Dai, H. Yuan, F. Hu, *Negative Surface Shielded Polymeric Micelles with Colloidal Stability for Intracellular Endosomal/Lysosomal Escape*, Mol. Pharm. 15 (2018) 5374–5386.
- [60] X. Gao, Z. Yu, B. Liu, J. Yang, X. Yang, Y. Yu, *A smart drug delivery system responsive to pH/enzyme stimuli based on hydrophobic modified sodium alginate*, Eur. Polym. J. 133 (2020) 109779.
- [61] Matsumura Y, Kataoka K. Preclinical and clinical studies of anti-cancer agent-incorporating polymer micelles. Cancer Sci. 2009; 100:572–9.
- [62] Lee KS, Chung HC, Im SA, Park YH, Kim CS, Kim SB, et al., *Multi-centre phase II trial of Genexol-PM, a Cremophor-free, polymeric micelle formulation of paclitaxel, in patients with metastatic breast cancer*. Breast Cancer Res Treat. 2008;108.
- [63] R Plummer, RH Wilson, H Calvert, AV Boddy, M Griffin, J Sludden, MJ Tilby, M Eatock, DG Pearson, CJ Ottley, Y Matsumura, K Kataoka and T Nishiya, *A Phase I clinical study of cisplatin-incorporated polymeric micelles (NC-6004) in patients with solid tumours*, British Journal of Cancer (2011), 104, 593– 598.
- [64] Kabanov AV, Batrakova EV and Alakhov VY (2002), *Pluronic block copolymers for overcoming drug resistance in cancer*. Adv. Drug Deliv. Rev. 54: 759-779.
- [65] Alakhov VY, Moskaleva EY, Batrakova EV and Kabanov AV (1996), *Hypersensitization of multidrug resistant human ovarian carcinoma cells by pluronic P85 block copolymer*. Bioconjug. Chem. 7: 209-216.
- [66] Lee ES, Shin HJ, Na K and Bae YH (2003), *Poly(L-histidine)- PEG block copolymer micelles and pH induced destabilization*. J Control Release. 90: 363-74.
- [67] Miller DW, Batrakova EV, Waltner TO, Alakhov V and Kabanov AV (1997), *Interactions of pluronic block copolymers with brain micro-vessel endothelial cells: evidence of two potential pathways for drug absorption*. Bioconjug. Chem. 8: 649-657.
- [68] Donald W. Miller, Alexander V. Kabanov (1999), *Potential applications of polymers in the delivery of drugs to the central nervous system*, Elsevier, Colloids and Surfaces B: Biointerfaces 16 (1999), 321-330.
- [69] Kabanov AV and Batrakova EV (2004), *New technologies for drug delivery across the blood brain barrier*. Curr Pharm Des. 10: 1355-1363.
- [70] Hyunah Cho, Tsz Chung Lai, Keishiro Tomoda and Glen S. Kwon, *Polymeric Micelles for Multi-Drug Delivery in Cancer*, AAPS Pharm SciTech, Vol. 16, No. 1, 2015.
- [71] Boldhane SP, Kuchekar BS, *Development and optimization of metoprolol succinate gastroretentive drug delivery system*, Acta Pharm. 60 (2010) 415-425.

NON-INNOCENT LIGANDS AND THEIR EFFECT ON  
COORDINATION CHEMISTRY

**SCOTTISH CHURCH COLLEGE**

**UNIVERSITY OF CALCUTTA**

Roll No.: 223/CEM/191024

Registration No.: 223-1211-0007-19

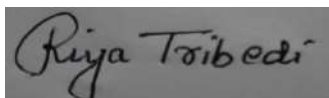
Special Paper SI 44

NAME OF THE CANDIDATE

*RIYA TRIBEDI*

NAME OF SUPERVISOR/ EXAMINER

*Dr. CHANDAN KUMAR PAL*



SIGNATURE OF CANDIDATE



SIGNATURE OF SUPERVISOR/EXAMINER

No. \_\_\_\_\_

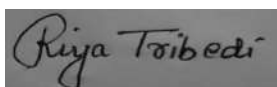
DATE: 19/07/2021

## **SELF DECLARATION**

I Riya Tribedi declare that the project report “ **NON- INNOCENT LIGAND AND EFFECT ON COORDINATION CHEMISTRY** ” is based on my own work carried out during the course of our study under the supervision of **Dr. Kausikisankar Paramanik** .

I assert the statement made and conclusion drawn are an outcome of my research work.

To the best of my knowledge this work has not been submitted to any other universities for the award of any other degree .



**Signature of Student**

**University Roll NO. 223/CEM/191024**

**Registration No. 223-1211-0007-19**

**Date: 19/07/2021**

**Place- SCOTTISH CHURCH COLLEGE, KOLKATA**

## Abstract.

An aspect of metal complexes with the so-called non-innocent ligands in the realm of redox chemistry is an active and intriguing area of current research due to their facile electron transfer ability at low to moderate potentials (approx.  $\pm 1$  V vs Ag/AgCl). Like metal centres, they can actively participate in redox reactions to augment the overall transportations of electrons. Accordingly, they either act as electron-sink or electron-reservoir depending on their structural and compositional characteristics, which are very crucial in various biochemical and catalytic processes. It is worth noting that the oxidation state of the central metal atom as well as the electronic structure of these compounds are very difficult to determine a priori and such unambiguous conclusion make them more challenging to the chemists. Nonetheless, a number of experimental studies (spectroscopic, electrochemical, structural) are indispensable to elucidate for appropriate assignment electronic structure of ligand, metal and their composites.

## Introduction

The existence of complexes of that display non-innocence has been of interest in the field of coordination chemistry. The term “innocent” and “non-innocent” was first coined in chemistry by a Danish scientist Christian Klixbüll Jørgensen in 1966.<sup>1</sup> According to him, a ligand is termed innocent if its oxidation state (OS) can be determined with certainty while an unambiguous determination of the OS of the ligands results non-innocent nature of the ligands, which eventually impede the rigorous assignment of OS of the metal centre. Transition metal complexes with the so-called non-innocent ligands have been known in coordination chemistry since the 1960s, when square planar dithiolene compounds of Ni(II) were synthesized.[Ref]<sup>2</sup>

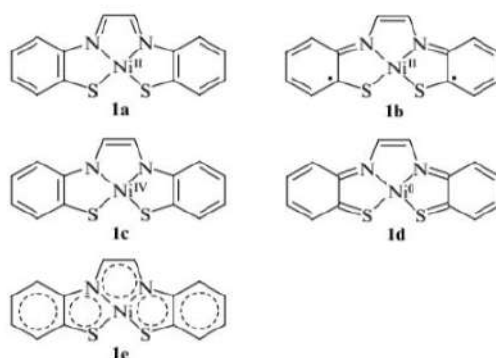
A redox-active ligand (L) is an organic molecule that can act effortlessly transfer electron(s) in fluid solution and thereby behave as an electron acceptor ( $L^{\bullet-}$ ), electron donor ( $L^{\bullet+}$ ) or even neutral (L) molecule upon coordination to a metal centre. Because of their flexibility to adopt a number of OS by virtue of their inherent electron-transfer behaviour, redox-active ligands often exhibit non-innocent behaviour in the course of metal-ligand bond formation. The situation would be even more intricated regarding



the rigorous assignment of OS for both metal and ligand especially when the coordinated metal also partakes in the redox reactions. Accordingly, one can expect a rich chemistry from such class i.e., they are expected to exhibit a wide variety of physico-chemical properties e.g., conductivity, magnetism, dielectric and optical properties in the condensed phase. The electron transfer between a redox-active ligand and metal centre induces various intriguing dynamic phenomena, such as valence tautomerism, and other electron-transfer-induced magnetic and dielectric transitions. Moreover, the recent development of electrically conducting metal–organic frameworks (MOF) opens the possibility of using redox-active ligand complexes for novel practical applications (such as sensory materials). As such, redox-active ligand chemistry has attracted significant attention not only within coordination chemistry research but also in materials science.

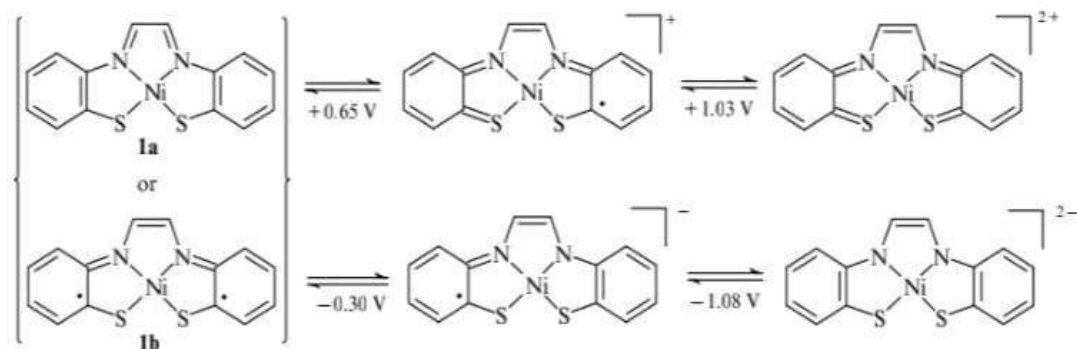
## Discussion

Example A- An example of complexes with a non-innocent ligand is the neutral nickel complex with glyoxalbis(2-mercaptoanil) **Ni(gma)<sub>2</sub>** (**1**) characterised by the presence of an extensive of  $\pi$ -conjugated system.[Ref]3. This complex can be considered as a 16-electron Ni<sup>II</sup> complex with diiminodithiolate (**1a**) or di(iminothiosemiquinonate) (**1b**), as a 14-electron Ni<sup>IV</sup> complex (**1c**) or, alternatively, as an 18-electron Ni<sup>0</sup> complex (**1d**).<sup>3</sup>



**Figure 1 . Nickel complex with glyoxa bis (2-mercaptoanil)**

Consequently, neither the OS of the central metal atom nor the ligand can be precisely defined unless electrochemical, theoretical and a number of spectroscopic, and studies have been performed.



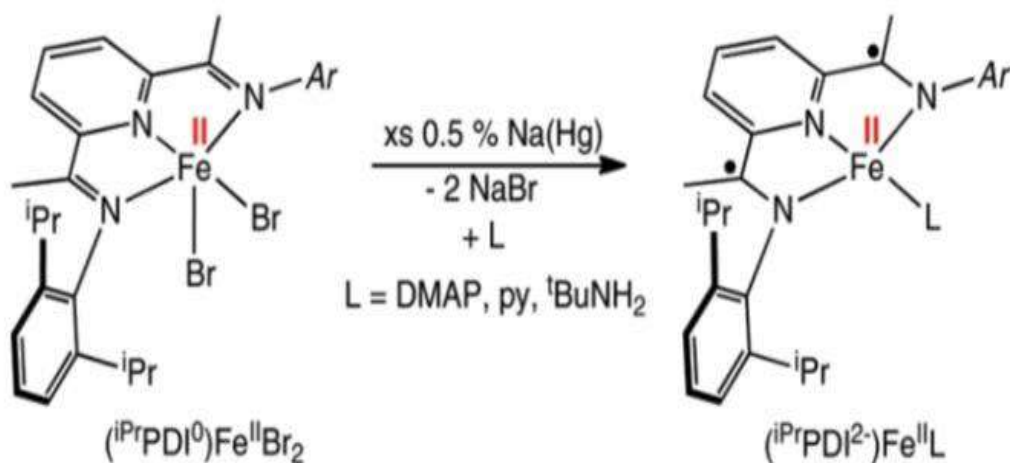
**Figure 2 .**

Here in this example of Ni – diiminodithiolate , two one electron oxidation process and two one electron reduction process in diiminodithiolate complexes whereas metal remains unchanged .

In dithiolene complexes the oxidation state of the metal and ligand also could not be unambiguously determined , which result in confusion in the interpretation of electrochemical data (whether the metal or ligand take place in oxidation and reduction and UV – Visible spectroscopic data .

**Example B -** Bis (imino) pyridine an important class of redox active ligand , developed in 1960s. This ligand gets interest because of their success in olefin polymerization catalysis . Bis ( imino) pyridine ligands, 2,6-(R<sup>1</sup>N=CR<sup>2</sup>)<sub>2</sub>C<sub>5</sub>H<sub>3</sub>N (R= ALKYL,ARYL, AMINO,;R<sup>2</sup> =H, Me).<sup>4</sup>

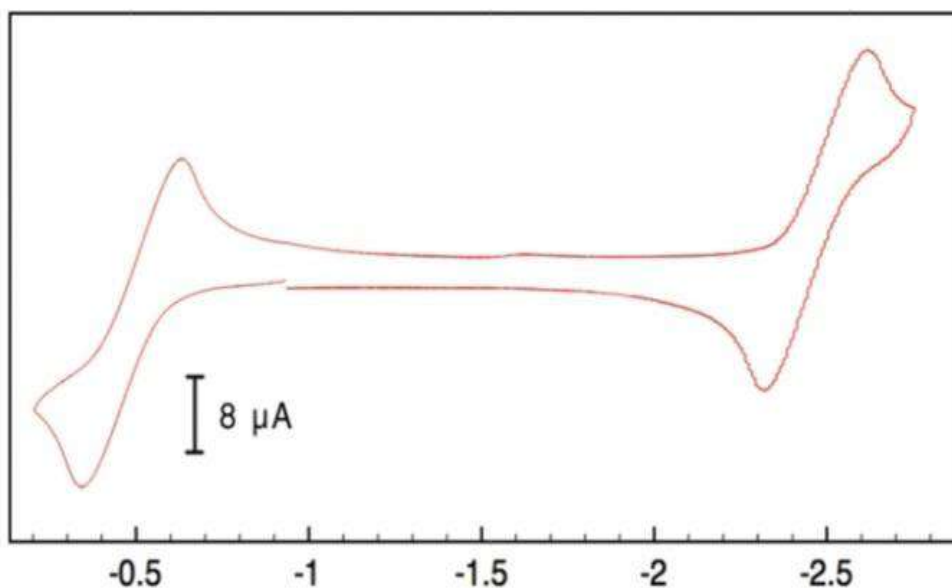
Spectroscopic and computational studies on compound with principally  $\sigma$  ligands such as N,N dimethylamino) pyridine established that the formal Fe<sup>0</sup> oxidation states are deceiving and that these molecules are best described as intermediate spin ferrous compound ( $S_{Fe} = 1$ ) antiferromagnetically coupled to a triplet ( $S_{pd} = 1$ ) bis(imino) pyridine diradical in figure shown3.



**Figure 3** . Electronic structures of two electron reduced bis (imino ) pyridine iron compounds bearing  $\sigma$  donating ligand .

The discovery that two electron reduction in bis(imino) pyridine based the fundamental question of “how many electrons are required to reduced the iron?”

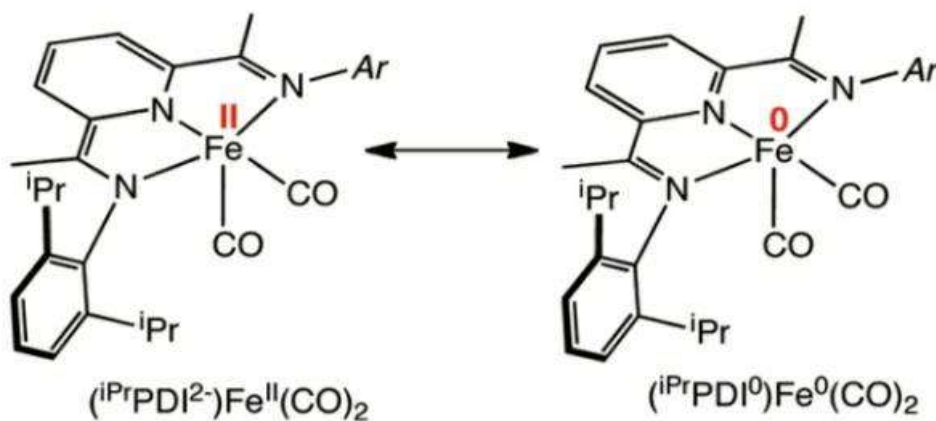
RESULT and DISCUSSION;- Oxidation and reduction of the bis(imino) pyridine Iron Dicarbonyl compound [(iPrPDI<sub>2</sub>)Fe(CO)<sub>2</sub>] . The redox chemistry of bis(imino)pyridine is initially explored electrochemically to determine the chemical accessibility of the oxidized reduced compounds. Cyclic voltammogram (CV) shows an +oxidation wave at -0.49V and reduction at -2.46V , indicating that both oxidised and reduced bis (imino) pyridine iron carbonyl compound should be occurred in figure4 .



Potential (V) v/s Fc/Fc +

**Figure 4** . CV of [(iPrPDI2)Fe(CO)2] ( glassy carbon working electrode , 0.1 M [nBu4N] [PF6] , scan rate 100 m V/s in THF at 295 K versus ferrocene<sup>0/+</sup>).

Before the chemical oxidation and reduction chemistry is presented it is useful to review the electronic structure of the neutral derivative compound [(iPrPDI2)Fe(CO)2]. Spectroscopic and computational studies that the establishment of the ground state for this molecule can be described either as a low spin iron(II) complex with a singlet triplet ( $S_{pd} = 0$ ) dianionic chelate or as a traditional  $Fe^0 d^8$  complex with neutral bis(imino)pyridine ligand in figure.



**Figure 5** .Electronic structure of [(iPrPDI)Fe(CO)<sub>2</sub>] highlighting the hybrid between the of [(iPrPDI<sup>2-</sup>)Fe<sup>II</sup>(CO)<sub>2</sub>] and [(iPrPDI<sup>0</sup>)Fe<sup>0</sup>(CO)<sub>2</sub>] resonance forms.

**Example C:- Study of Bis – azoaromatic – Centered diradical complexes of Rh(III)<sup>5</sup>**



**Figure 6** . bis- azoaromatic-Centred diradical [(L·)M(L·)] complexes of Rh(III).

Ligand centered radical are of current interest due to the capacity of gain and release electron during catalytic transformation in chemical reaction . Two ligand  $\pi$  – orbital connected by a diamagnetic metal center leads to us singlet diradical owing to an antiparallel spin exchange interaction . The electron transfer process occurs exclusively within the princer type NNN ligand backbone . The orthogonal of two ligand  $\pi$  orbital linked via closed shell metal center (  $t_{2g}^6$ ) take part significant coupling between the radical . By the DFT theory shows weak antiferromagnetic intramolecular spin – spin interaction between two ligand  $\pi$  array [ (  $1^-$ )Rh<sup>III</sup>( $1^-$ )].

Redox,EPR, and Magnetic Properties;- Electron-transfer properties of the free ligand and their complexes was studied by cyclic voltammetry in acetonitrile solution by using a platinum working electrode.The redox potentials are referenced to the ferrocenium/ ferrocene couple (Fc<sup>+</sup>/Fc).The value of of the Fc<sup>+</sup>/Fc couple under similar experimental condition is found to be 0.462 V vs Ag/AgCl. The observed

magnetic moment  $[(1^{\bullet})\text{Rh}^{111}(1^{\bullet})] + ([2])^+$  lies nearly  $\sim 2.3\mu$  over the temperature range 50-300k.

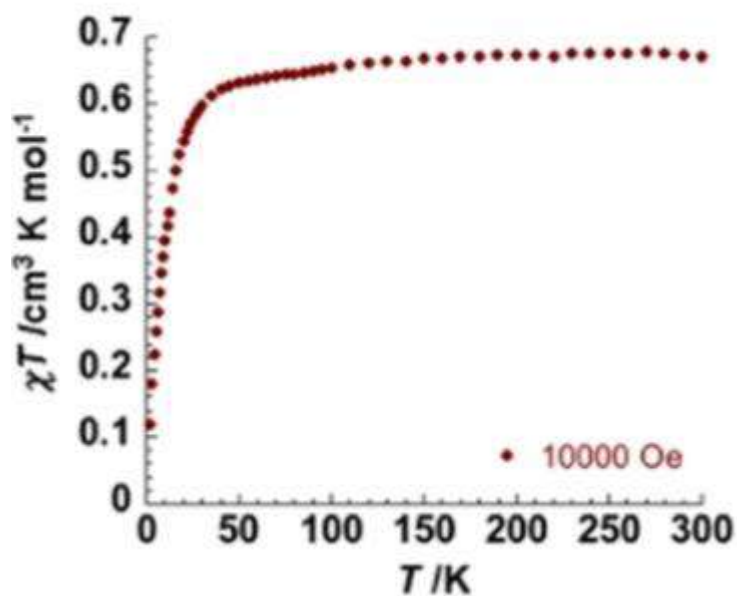


Figure 7 . Plot of  $\chi T$  vs  $T$

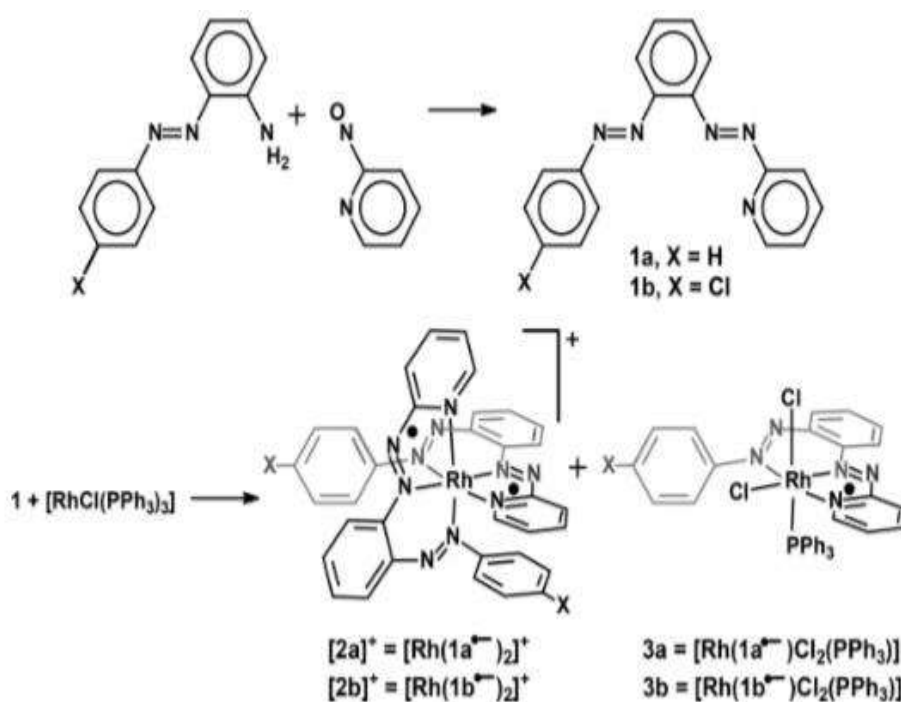
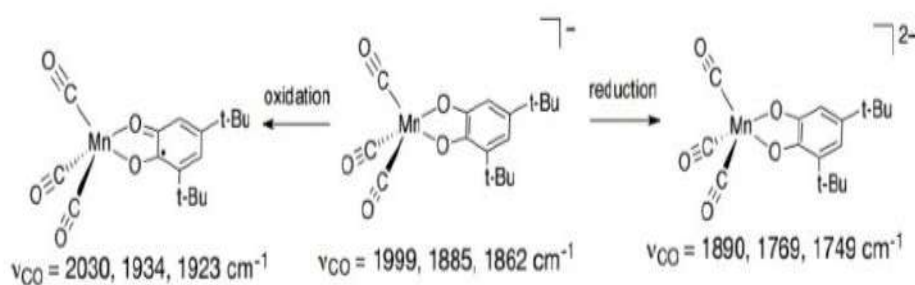


Figure 8 . Synthesis of ligand and their radical anion complexes;

Bis-azoaromatic electron traps viz 2-(2-pyridylazo)azoarene(1) have been synthesized by electron deficient pyridine and azoarene moieties and they act as opposite radical formation of stable open shell diradical complexes  $[(1^\bullet)\text{Rh}^{111}(1^\bullet)]^+$ . In this work we have performed to get a pair of ambient stable diradical  $[(1^\bullet)\text{Rh}^{111}(1^\bullet)]^+$ . Along with monoradical  $[\text{Rh}(1^\bullet)\text{Cl}_2(\text{PPh}_3)]$  (3) via simultaneous metal oxidation and ligand reduction reaction.

**Example D:- Oxidation and Reduction of manganese catecholate and the resulting change in  $\nu_{\text{CO}}$ .**<sup>6</sup>

The complex  $[(t\text{-Bu cat})\text{Mn}(\text{CO})_3]$ , ( $t\text{-Bu cat}$  is 3, 5 – di- tert – butyl catecholate) is capable of ligand and metal reactivity. The highest occupied molecular orbital (HOMO) in  $[(t\text{-Bu cat})\text{Mn}(\text{CO})_3]$  is on the catecholate ligand while the lowest unoccupied molecular orbital (LUMO) is on the metal.



**Figure 9 . Oxidation and Reduction of  $[\text{Mn}(\text{CO})_3(t\text{-Bu cat})]$  and the resulting change in  $\nu_{\text{CO}}$**

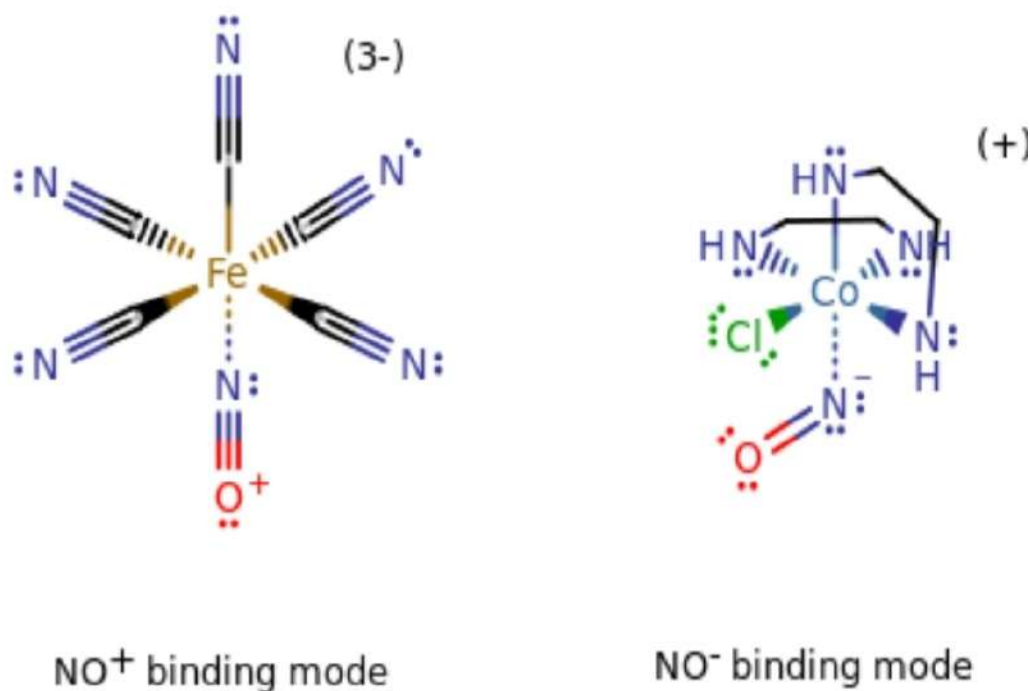
Reduction of  $[(t\text{-Bu cat})\text{Mn}(\text{CO})_3]$  to form of  $[(t\text{-Bu cat})\text{Mn}(\text{CO})_3]^{\bullet-}$  decreases the  $\nu_{\text{CO}}$ , with the average change  $\Delta\nu_{\text{CO}} = 160 \text{ cm}^{-1}$ . Oxidation of  $[(t\text{-Bu cat})\text{Mn}(\text{CO})_3]$  occurs on the ligand; the one electron oxidation increases the  $\nu_{\text{CO}}$  with the average shift  $\Delta\nu_{\text{CO}} = 47 \text{ cm}^{-1}$ .

Observations from EPR, UV, Vis, Raman, and DFT calculations show the location of the radical. Reduction results in the radical to be predominantly metal in character, while oxidation is ligand in character. Metal redox causes large changes in  $\nu_{\text{CO}}$  and ligand redox causes small changes in  $\nu_{\text{CO}}$ .

**Example E:- The nitrosyl ligand is noninnocent <sup>7</sup>**

(a)  $[\text{Co}(\text{en})_2(\text{NO})\text{Cl}]^{+}$  (with a bent nitrosyl )

(b)  $[\text{Fe}(\text{CN})_5(\text{NO})]^{3-}$  ( with linear nitrosyl)



**Figure 10 .**

In the iron compound we have five  $\text{CN}^-$  and one  $\text{NO}^+$  each contributing to the overall charge =  $+1 -5 +1 = -3$  charge , we know that iron is  $+1$  charge . In this case  $\text{NO}^+$  is linear bonding mode . Iron in this case is a  $d^7$  metal . For this compound we have 6  $\pi$ -compatible electrons on the iron compound favors a linear  $\text{NO}^+$ .

**WHY THE DIFFERENCE IN BONDING MODE FAVORABILITY?** If you're curious, the difference in the bonding modes can be explained by the extent of  $\pi$  **back-bonding** from the metal to the ligand.

This is a *stabilizing* interaction between the compatible metal d orbitals and  $\pi^*$  ligand LUMOs because the former is *lower* in energy and the latter is *higher* in energy (**the orbitals lower in energy become stabilized**).

**LINEAR NITROSYL**



Basically,  $\text{NO}^+$  has a  $\pi^*$  orbital aligned with a metal  $t_{2g}$  orbital (such as  $3d_{xz}$ ), so it can **accept electron density** from a *compatible* d bonding MO from the metal to *stabilize* this **linear** bonding configuration.

If we take the plane of the screen to be the  $xz$  plane, then we have this metal-to-ligand  $\pi^*$  acceptance:



**Figure 11.** Bonding Configuration

A similar  $\pi$  acceptance can work with the  $3d_{yz}$  orbital and the  $\pi^*_y$  MO.

### **BENT NITROSYL**

On the other hand,  $\text{NO}^-$  is bent away from the vertical axis, so the orbitals that contain the lone pairs of electrons are **not compatible** with the  $3d_{xy}$ ,  $3d_{xz}$ , or  $3d_{yz}$  orbitals of the metal.

They are compatible with only the  $d_{z^2}$  and  $d_{x^2-y^2}$  orbitals via  **$\sigma$  donation**, rather than  $\pi$  acceptance.

So, we have the issue that the nitrogen contributes no  $\pi$ -compatible orbitals required to accept electrons; they're aligned for  $\sigma$  donation instead, which conflicts with the "desire" of the metal to  $\pi$ -donate:

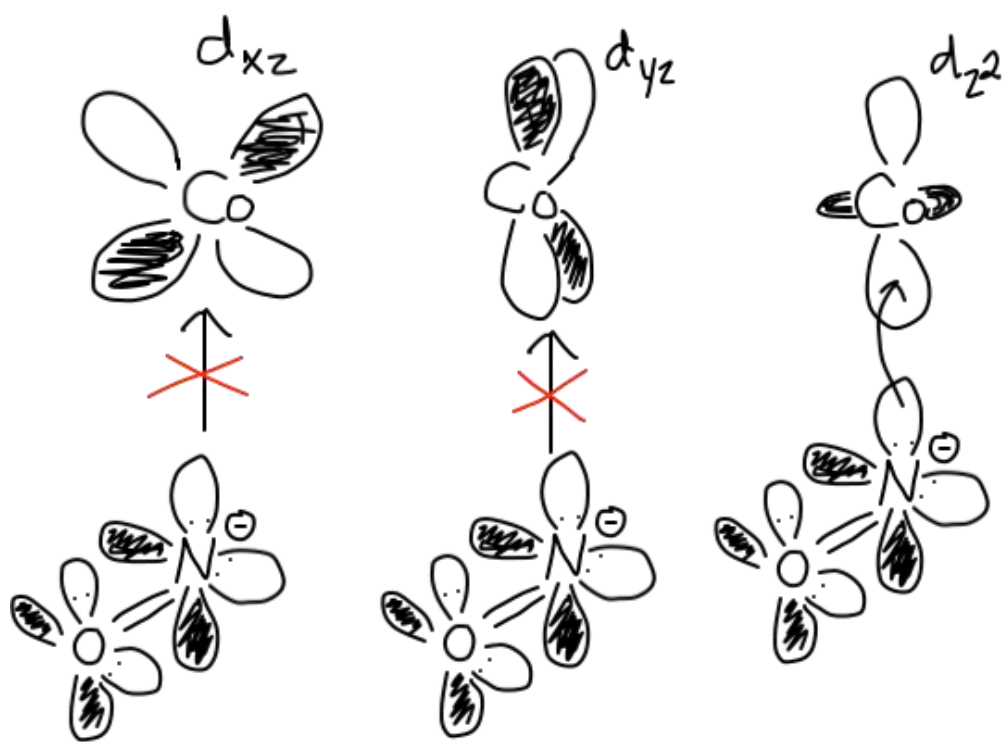


Figure 12. (a) ,(b), (c)

As a result, electron density **cannot** be donated into the  $\pi^*$  MOs of  $\text{NO}^-$  in a  $\pi$  fashion, and a linear configuration is *not* stabilized enough. Thus, its bonding mode stays **bent**. Usually textbooks will specify which bonding mode they want to use for a given non-innocent ligand; mine specifies  $\text{NO}^+$  but doesn't use  $\text{NO}^-$ , because it is nice to analog  $\text{NO}^+$  with  $\text{CO}$ , as they are isoelectronic.

- **Manifestation of non-innocent ligand behaviour:-**

The potential of redox active ligand to behave non-innocently in transition metal coordination compound is reflected with respect to various aspects and situation. These include the question of establishing correct oxidation states, the identification and characterization of differently charged radical ligand, the listing of structural and other consequences of ligand redox reaction, and the distinction between barrierless delocalized resonance cases  $\text{M}^n/\text{L}^{\cdot} \leftrightarrow \text{M}^{n+1}/\text{L}^{\ominus}$  versus separated valence tautomer equilibrium situation  $\text{M}^n/\text{L}^{\cdot} \leftrightarrow \text{M}^{n+1}/\text{L}^{\ominus}$ . Further ambivalence arises for dinuclear system with radical bridge  $\text{M}^n(\mu\text{-L}^{\cdot})\text{M}^n$  versus mixed-valent alternatives  $\text{M}^{n+1}(\mu\text{-L}^{\ominus})\text{M}^n$ , for non-innocent ligand bridged coordination compounds of higher nuclearity such as  $(\mu_3\text{-L})\text{M}_3$ ,  $(\mu_4\text{-L})\text{M}_4$ ,  $(\mu\text{-L})_4\text{M}_4$  or coordination polymers. Conversely, the presence of more than one noninnocently behaving ligand at a single transition metal site in situation such as  $\text{L}^{\cdot} - \text{M} - \text{L}^{\ominus}$  or  $\text{L}^{\cdot} - \text{M} - \text{L}^{\cdot}$  may give rise to corresponding

ligand to ligand interaction phenomenon(charge transfer,electron hopping and spin spin coupling) and to redox –induced electron transfer with counterintuitive oxidation-state changes.The relationship of non innocent ligand behaviour with excited state descriptions and perspectives regarding material properties and single-electron or multielectron reactivity.<sup>1</sup>

- **Reaction at coordinated ligand :-**

The type of reaction in coordination chemistry are substitution , addition , ligand re-arrangement , metal redox and reaction at coordinated ligand . While the first four cases constitute majority of coordination chemistry over the past 100 years , the last case stands out against the more classic reaction in that reactivity at the metal is not the central focus . Changing a ligand from donor to an acceptor by reaction at the ligand changes the reactivity at the metal . A large enough change in ligand porality can affect oxidation state at the metal , similar to the concept of umpolung inorganic chemistry . The changes in ligand oxidation state and polarity and the affect on reactivity at metal have not been widely explored in catalysis . Remote activation of a metal center through reaction at coordinated ligand is exploring .<sup>6</sup>

- **CONCLUSION**

The aim of the present review is to attract attention to the result of investigation on the nature of bonding between metal and ligand in noninnocent metal complexes . There is a great diversity of structural type of noninnocent ligand, from small molecules (NO) to macrocycles . In most cases , these ligand contains conjugated  $\pi$  system capable of either accepting or donating electrons . In many cases ligand rather than the central metal atom are redox active . As mentioned above noninnocent ligand is a property not only of ligand but of complexes as whole , because of the central metal atom can have strong effect on the electronic structure of the ligand , if there is a strong mixing of the ligand and metal orbitals . Due to the charge transfer between the metal and the ligand valence of the metal in the complex can vary even with changes in temperature of the sample . Electrochemical and spectrochemical method , X- ray diffraction analysis , low temperature ESR and UV – Vis and near – IR spectroscopy are most informative and are most widely used to study the nature of bonding in noninnocent complexes

## REFERENCE

1. C. K. Jorgensen, *Coord. Chem. Rev.*, **1966**, 1, 1164
2. (a) L. A. Berben, Bas de Bruin and A. F. Heyduk, *Chem. Commun.*, **2015**, 51, 1553; (b) A. Davinson, N. Edelstein, R. H. Holm, A. H. Maki, *J. Am. Chem. Soc.*, **1963**, 85, 2029; (c) A. Davinson, N. Edelstein, R. H. Holm, A. H. Maki, *Inorg. Chem.*, **1963**, 2, 1227.
3. K. P. Butin, E. Beloglazkina, N. V. Zyk, *Russian Chemical Reviews.*, **2007**, 74, 531.
4. A. M. Tondreau, C. Nilsman, E. Lobkovsky and P. J. Chirik, *Inorg. Chem.*, **2011**, 50, 9895; (b) P. J. Chirik, *Inorg. Chem.*, **2011**, 9740; (c) R. Raucoules, Theodorus de Bruin, P. Raybaud, and C. Adamo, *Organometallic.*, **2008**, 27, 3377.
5. S. Roy, S. Pramanik, S. C. Patra, B. Adhikari, A. Mondal, S. Ganguly and K. Pramanik, *Inorg. Chem.*, **2017**, 56, 12774.
6. M. R. Ringenberg, *J. Am. Chem. Soc.*, **2011**, 1, 240; (b) N. Leconte, J. Moutet, k. Herasymchuk, M.R. Clarke, C. Philouze, D. Luneau, T. Storr, F. Thomas, *Chem. Commun.*, **2017**, 53, 2767.
7. N.S Truong, *Inorg. Chem.*, **2016**, 58, 223.

**Immunomodulatory Properties**  
**and**  
**Anticancer activities of  $\beta$ -glucan**

**Review work submitted in partial fulfilment of requirement for  
M.Sc(Chemistry) degree**

**From**

**SCOTTISH CHURCH COLLEGE**

**UNIVERSITY OF CALCUTTA**

**SULAGNA PAUL**

**(M.Sc, 4<sup>th</sup> Semester)**

**University Registration No: 211-1221-0869-14**

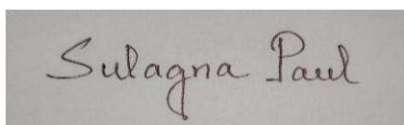
**University Roll No: 223/CEM/191033**

**Special paper : CHEM-SO44**

**Name of Candidate**

**Sulagna Paul**

**(M.Sc, 4<sup>th</sup> Semester)**



.....  
**Signature of candidate**

**Name of Examiner**

**Dr. Sebanti Basu**

**Associate Professor  
Scottish Church College**

.....  
**Signature of Examiner**

## **ACKNOWLEDGEMENT**

I gratefully thank Dr. Asish Kumar Sen, Ex. Chief Scientist and Emeritus Scientist-CSIR; Associate professor, Indian Institute of Chemical Biology, under his supervision and unending support this review work was accomplished during my 4<sup>th</sup> and final semester in partial fulfilment of M.Sc (chemistry) degree in the University of Calcutta under Scottish Church College, Kolkata. Also I would like to thank the University of Calcutta and my college professors for giving me the opportunity to write this review paper.

## **Content**

**Page No.**

1. Introduction .....	4
2. Sources of $\beta$ -glucan .....	4
3. Structure variation and types of $\beta$ -glucan .....	5
➤ Backbone .....	5
➤ Side chain .....	5
➤ Types of $\beta$ -glucan .....	6
➤ Conformations .....	6
4. Immunomodulation: an introduction .....	7
5. Pharmacodynamics and pharmacokinetics of $\beta$ -glucan .....	9
➤ Animal studies .....	9
➤ Human studies .....	10
➤ $\beta$ -Glucan as immunomodulating agent .....	11
6. Tumour and cancer : an introduction .....	13
7. Anticancer activity .....	14
8. Anticancer activity of $\beta$ -glucan .....	14
➤ Clinical trials on anticancer effects of natural products with $\beta$ -glucan .....	14
➤ Medicinal mushroom with $\beta$ -glucans as active components .....	15
9. Conclusion .....	16
10. References .....	17

## **1. Introduction:**

Cereal and fungal products[1-5] have been used for centuries for medicinal and cosmetic purposes; however, the particular role of  $\beta$ -glucan was not traversed until the 20<sup>th</sup> century.  $\beta$ -Glucan, a polysaccharide in the form of dietary fibre was first discovered in lichens (comprise a fungus living in a symbiotic relationship with an algae or cyanobacterium) [6] and shortly thereafter in barley. Dietary fiber has been extensively studied [7] in last few decades for their physiological health benefits. We get dietary fiber from the plant-based foods we eat. Fiber supports good health by helping human body reduce cholesterol and control blood sugar levels. Depending on its solubility dietary fibres are classified in two groups- soluble and insoluble dietary fiber.  $\beta$ -glucans are one form of water-soluble dietary fibre and also regarded as bioactive functional food ingredient due to its various health benefits like improving cholesterol levels, weight reduction, immune modulator and anti-carcinogenic effects. They comprise a group of  $\beta$ -D-glucose polysaccharides naturally occurring in the cell walls of cereals, bacteria, fungi, mushrooms ( $\beta$ -glucans are principally obtained in fruit body of various type of mushrooms) with significantly differing physicochemical properties depending on source[8].

Typically,  $\beta$ -glucans (other than cellulose) form a linear backbone with 1–3  $\beta$ -glycosidic bonds but vary with respect to molecular mass, solubility, branching structure, viscosity hence causing diverse physiological effects in animals, bacteria, yeast, algae and mushrooms. The evaluation of mushroom derivatives and their medical properties are important part of these studies. For dietary intake levels of at least 3 g per day, oat fiber  $\beta$ -glucan decreases blood levels of LDL cholesterol and reduce the risk of cardiovascular diseases (CVD).  $\beta$ -glucans are used as modifying and texturing substrate in various bioceutical and cosmetic products, and as soluble fiber supplements.

## **2. Sources of $\beta$ -glucan[10-15]:**

$\beta$ -Glucan is not naturally found in human body. It is acquired through dietary supplements. There are a number of foods high in  $\beta$ -glucan including :

- Cereals - barley fiber, millets, oats and whole grains.
- Microorganisms – yeast (Cell wall of the baker's yeast that is *Saccharomyces cerevisiae*), fungi, bacteria.
- Reishi, maitake, and shiitake mushrooms.
- Lichens (*Cetraria islandica*).



- Seaweeds/algae [ *Laminariasp.* (brown algae) , *Phytophthorasp.*]

A lesser amount of  $\beta$ -glucan is found in wheat, rye and sorghum. Among these sources, barley typically has the highest  $\beta$ -glucan content and oats the second highest.

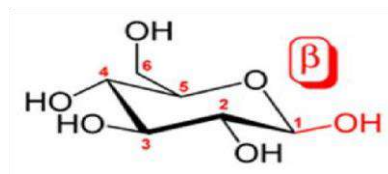


Various sources of  $\beta$ -Glucan

### **3. Structure variation and types of $\beta$ -glucan:**

- **Backbone :**

$\beta$ -Glucans (excluding cellulose) are polymers of D-glucose having linear  $\beta$ -(1 $\rightarrow$ 3) linkage backbone. The most common  $\beta$ -glucans from various sources include a linear  $\beta$ -(1 $\rightarrow$ 3) glycosidic bond (a glycosidic bond is a type of covalent bond that joins a carbohydrate molecule to another molecule) to form polymer. Some  $\beta$ -glucans, isolated from certain sources, can be branched having  $\beta$ -(1 $\rightarrow$ 3) linkage as backbone and  $\beta$ -(1 $\rightarrow$ 6) as branching linkage.



Glucose molecule with carbon numbering notation and  $\beta$  orientation

- **Side-chain :**

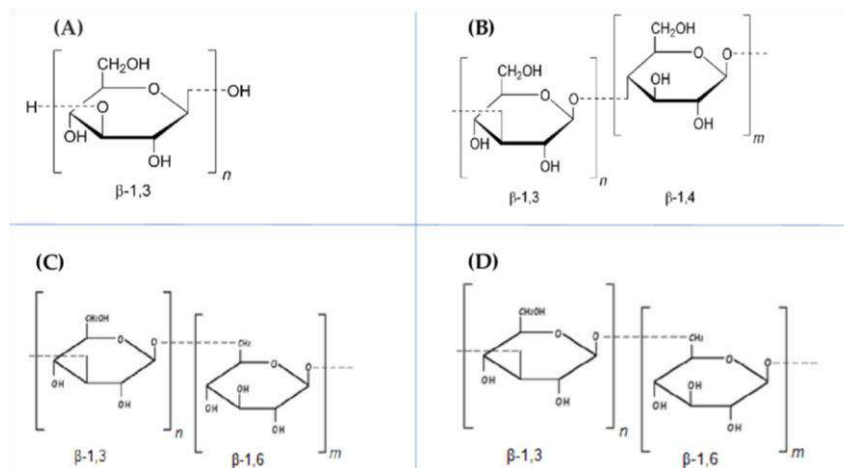
Some  $\beta$ -glucan molecules have branched glucose side-chains attached to their positions on the main D-glucose chain, which branch off the  $\beta$ -glucan backbone. Additionally, these side-chains can be attached to other types of molecules, like proteins as in Polysaccharide-K.

Polysaccharide-K or PSK is protein bound polysaccharide consists of a  $\beta$ -glucan-(1 $\rightarrow$ 4) main chain with  $\beta$ -(1 $\rightarrow$ 3) and  $\beta$ -(1 $\rightarrow$ 6) side-chains.

- **Types :**

Each type of  $\beta$ -glucan comprises a different molecular backbone, degree of branching and molecular weight and solubility. Cereal-derived  $\beta$ -glucans are predominantly mixtures of  $\beta$ (1 $\rightarrow$ 3) and  $\beta$ -(1 $\rightarrow$ 4) glycosidic linkages without any  $\beta$ -(1 $\rightarrow$ 6) bonds. Beta-glucans from yeasts (e.g., *Saccharomyces cerevisiae*) are mixtures of linear  $\beta$ -(1 $\rightarrow$ 3) backbones containing 30-residue straight chains. They are connected to these are long branches attached via  $\beta$ -(1 $\rightarrow$ 6) linkages. Yeast  $\beta$ -glucans contains backbone containing  $\beta$ -(1 $\rightarrow$ 3) glycosidic linkage with elongated  $\beta$ -(1 $\rightarrow$ 6) branches.

Bacterial  $\beta$ -glucans (e.g., *Agrobacterium imbiobaris*) have main and unbranched  $\beta$ (1 $\rightarrow$ 3) D-glucan backbones, while seaweed  $\beta$ -glucans (such as those found in brown kelp, *Laminaria*) are species-dependent. They may contain straight chain of  $\beta$ -(1 $\rightarrow$ 3) linkages or the straight chain backbone together with high levels of  $\beta$ -(1 $\rightarrow$ 6) glycosidic linkages.



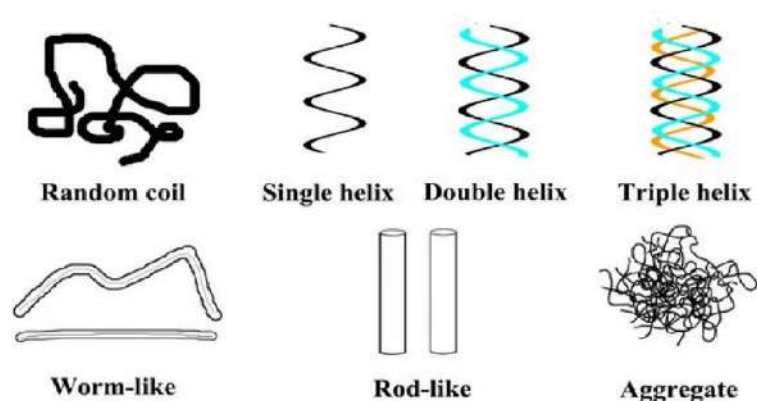
Types of  $\beta$ -Glucan

- **Conformations :**

The branching alignment follow a particular ratio and branches can arise from branches (secondary branches). In aqueous solution, based on origin and processing method used in their extraction and

modification,  $\beta$ -glucans can exist in a range of conformations. The most widely observed conformations are random coils, helices (single, double, or triple), worm-like shapes, rod-like shapes, or aggregates. The molecular weight (MW) of  $\beta$ -glucan ranges from 102 to 106

Da, depending on the source. For example, soluble  $\beta$ -glucans from two edible mushroom varieties *maitake* and *shiitake* were estimated to have MW of about 400 kDa. Cereal  $\beta$ -glucans are also soluble and may reach MW of between 1.1 and 1.6 MDa (for oats) and around 49 MDa for barley. The immune functions of  $\beta$ -glucans are apparently dependent on their conformational complexity. It has been suggested that higher degree of structural complexity is associated with more potent immunomodulatory and anti-cancer effects.[15-20]



Various conformations of  $\beta$ -glucan

#### 4. Immunomodulation:

The immune system is a complex network of cells and proteins that defends the body against infections. The immune system attacks germs and keeps a record of every microbe (germ) it has ever defeated in types of white blood cells (B and T-lymphocytes). They are known as memory cells, so it can quickly recognise and destroy the microbe before it starts multiplication after entering the body again. Immunomodulation is the modification of the immune system. It has natural as well as human-induced forms. Improvement of the immune response is desirable to prevent various infection in e of immunodeficiency.[21]

- T lymphocyte :T lymphocyte or T cell, a type of white blood cell(Leukocyte) is an essential part of the immune system. In mammals, T cells originate in the bone marrow(at the core of the bones) and mature in the thymus (pyramid-shaped lymphoid organ). In the thymus, T cells multiply and transform into :

# regulatory - This T cells act to control immune reactions, hence their name

# helper - This T cells play a role in normal immune responses

# cytotoxic T cells - This T cells recognize antigens on the surface of a cell infected with a virus, allowing the T cells to bind to and kill the infected cell

# memory T cell – This T cells are antigen specific T cells that remain long term after an infection has been eliminated. These cells have a memory for the antigen survive for a long time, respond quickly following a second exposure to the same antigen.

These T cells are then sent to peripheral tissues or circulate in the blood or lymphatic system.

- B Lymphocyte : B-Lymphocytes also known as B cells are a type of white blood cell of the lymphocyte subtype. They function in the antibody-mediated immunity component of the adaptive immune system. B cells produce antibody molecules (these are not secreted) which when inserted into the plasma membrane serve as a part of B cell receptors. In mammals, B cells mature in the bone marrow. B cells bind to an antigen, receive help from a cognate helper T cell, and differentiate into a plasma cell that secretes large amount of antibodies. Different types of Lymphocyte are:

# Plasmablast–A short-lived antibody secreting cell arising from B cell differentiation. They are generated early in an infection having antibodies with very weak affinity towards antigen.

# Plasma cell – A long-lived antibody secreting cell arising from B cell differentiation. They are generated later in an infection having antibodies with higher affinity towards target antigen.

# Memory B cell – Their function is to circulate through the body and generate a stronger, more rapid antibody response if they detect the antigen.

# Regulatory B cell – These B cell type stops the expansion of pathogenic, pro-inflammatory lymphocytes through the secretion of various antibodies.

- Acquired Immunity : Acquired immunity is immunity which is developed over lifetime. It can come from of:

# a vaccine

# exposure to an infection or disease

When pathogens are introduced into a person's body from a vaccine or a disease, this type of immunity develops. The two types of acquired immunity are adaptive and passive. Adaptive

immunity occurs in response to being infected with or vaccinated against a microorganism. Passive immunity occurs when a person receives antibodies to a disease or toxin.

- **Innate Immunity:** Innate immunity is also known as natural immunity because it is present at birth and does not have to be learned through exposure to an foreign element. It provides an immediate response to the foreign elements. The innate immunity system includes:

# Physical Barriers such as skin, the gastrointestinal tract, the respiratory tract, the nasopharynx, cilia, eyelashes and other body hair.

# Defence Mechanism such as secretions, mucous, bile, gastric acid, saliva, tears and sweat. #

General Immune Responses

## **5. Pharmacodynamics & Pharmacokinetics of $\beta$ -glucan:**

Most  $\beta$ -glucans are considered as non-digestible carbohydrates and are fermented to various degrees by the intestinal microbial flora [22–24]. Therefore, it has been speculated that their immunomodulatory properties may be partly attributed to a microbial dependent effect. However,  $\beta$ -glucans in fact can directly bind to specific receptors of immune cells, suggesting a microbial independent immunomodulatory effect [25]. The pharmacodynamics and pharmacokinetics of  $\beta$ -glucans have been studied in animal and human models.

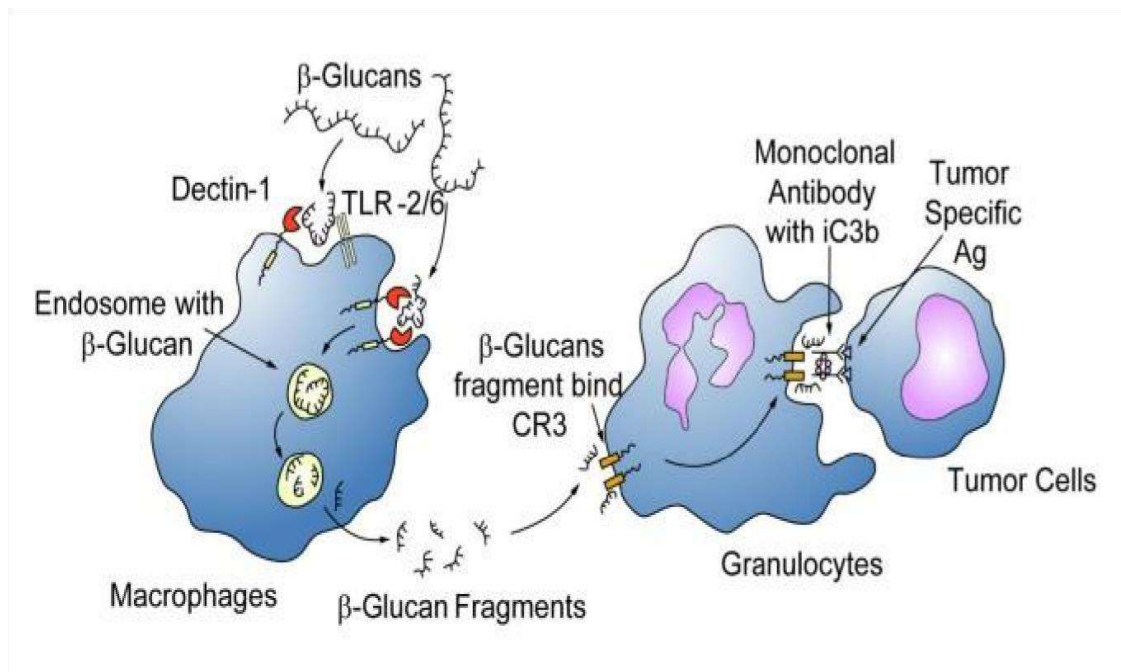
- **Animal Studies**

Study using a suckling rat model (rodent, easily available and managed in the laboratory) for evaluation of the absorption and tissues distribution of internally administered radioactive labelled  $\beta$ -glucan, it was found that the majority of  $\beta$ -glucan was detected in the stomach and duodenum 5 minutes after the administration [26]. This amount rapidly decreased during first 30 minutes. A significant amount of  $\beta$ -glucan entered the proximal intestine (the first and middle part of the colon) shortly after ingestion. Its transit through the proximal intestine decreased with time with a simultaneous increase in the ileum. Despite low systemic blood levels (less than 0.5%), significant systemic immunomodulating effects in terms of humoral and cellular immune responses were demonstrated.

The pharmacokinetics following intravenous administration of 3 different highly purified and previously characterized  $\beta$ -glucans were studied using carbohydrates covalently labelled with a fluorophore on the reducing terminus. The variations in molecular size, branching frequency and

solution conformation were shown to have an impact on the elimination half-life, volume of distribution and clearance [27].

After ingestion the low systemic blood level of  $\beta$ -glucans does not reflect the pharmacodynamics of  $\beta$ -glucans and does not exclude its *in vivo* effects. Cheung-VKN *et al.* labeled  $\beta$ -glucans with fluorescein to track their oral uptake and processing *in vivo*. The orally administered  $\beta$ -glucans were taken up by macrophages (specialised cells involved in the detection and destruction of bacteria) via the Dectin-1 (a type II transmembrane protein which binds  $\beta$ -1,3 and  $\beta$ -1,6 glucans) receptor and was subsequently transported to the spleen, lymph nodes, and bone marrow. Within the bone marrow, the macrophages degraded the large  $\beta$ -1,3-glucans into smaller soluble  $\beta$ -1,3glucan fragments. These fragments were subsequently taken up via the complement receptor 3 (CR3) (a human cell surface receptor found on B and T lymphocytes, neutrophils and macrophages) of margined granulocytes. These granulocytes with CR3-bound  $\beta$ -glucanfluorescein were shown to kill inactivated complement 3b (iC3b)-opsonised tumour cells after they were recruited to a site of complement activation such as tumour cells coated with monoclonal antibody [28]. It was also shown that intravenous administered soluble  $\beta$ -glucans can be delivered directly to the CR3 on circulating granulocytes.



The uptake and subsequent actions of beta-glucan on immune cells

$\beta$ -glucans are captured by the macrophages via the Dectin-1 receptor with or without TLR-2/6. The large  $\beta$ -glucan molecules are then internalized and fragmented into smaller sized  $\beta$ -glucan fragments within the macrophages. They are carried to the marrow and endothelial reticular system and subsequently released. These small  $\beta$ -glucan fragments are eventually taken up by the circulating granulocytes, monocytes or macrophages via the complement receptor (CR)-3. The immune response will then be turned on, one of the actions is the phagocytosis of the monoclonal antibody tagged tumour cells.

Furthermore, Rice PJ et al. showed that soluble  $\beta$ -glucans such as laminarin and scleroglucan can be directly bound and internalized by intestinal epithelial cells and gut associated lymphoid tissue (GALT) cells [28]. Unlike macrophage, the internalization of soluble  $\beta$ -glucan by intestinal epithelial cells is not Dectin-1 dependent. However, the Dectin-1 and TLR-2 are accountable for uptake of soluble  $\beta$ -glucan by GALT cells. Another significant finding of this study is that the absorbed  $\beta$ glucans can increase the resistance of mice to bacterial infection challenge.

- **Human Studies**

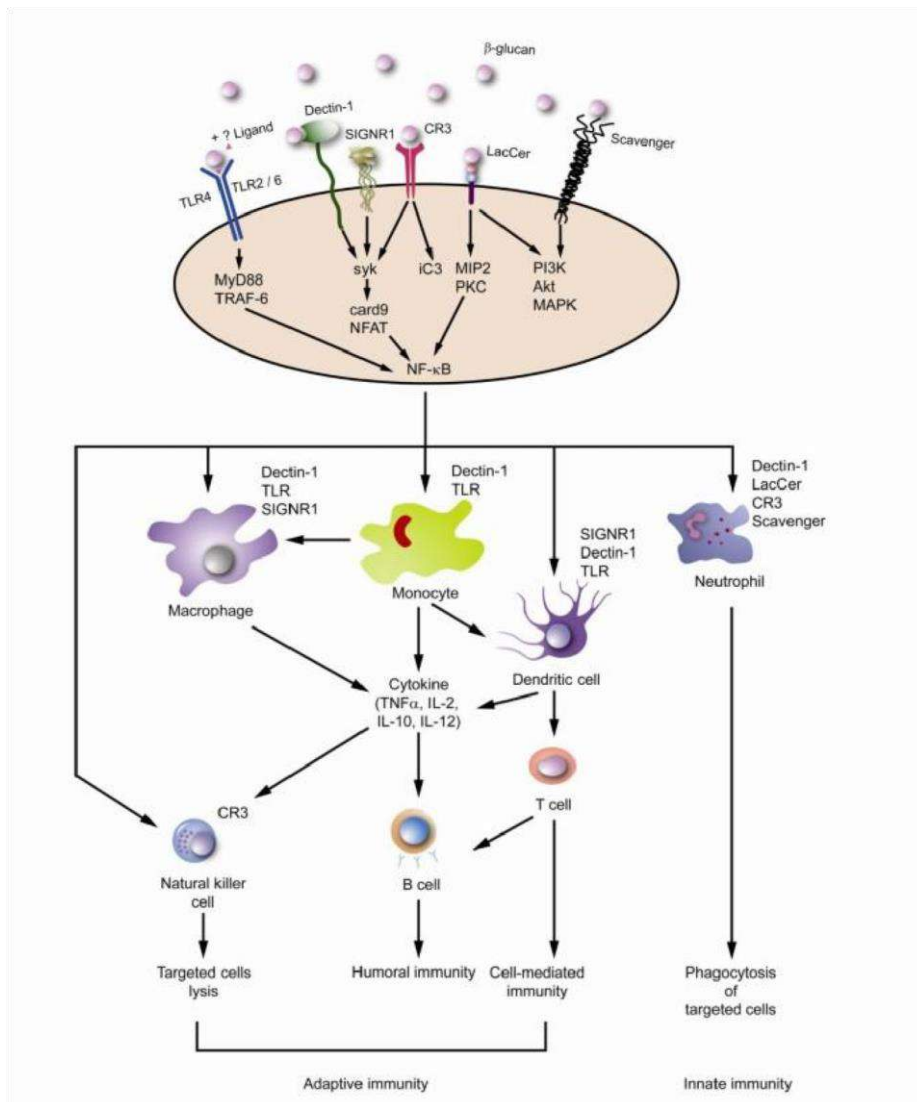
After ingestion how  $\beta$ -glucans mediate their effects in human remained to be defined. In a phase I study the assessment of safety and tolerability of a soluble form oral  $\beta$ -glucans is done [29]. B Glucans of different doses (100 mg/day, 200 mg/day or 400 mg/day) were given respectively for 4 consecutive days. No drug-related adverse events were observed. Repeated measurements of  $\beta$ glucans in serum, however, revealed no systemic absorption of the agent following the oral administration. In spite of that, the immunoglobulin A concentration in saliva increased significantly for the 400 mg/day arm, suggesting a systemic immune effect has been elicited. One limitation of this study is the low sensitivity of serum  $\beta$ -glucans determination.

In summary, based on mostly animal data,  $\beta$ -glucans enter the proximal small intestine rapidly and are captured by the macrophages after oral administration. The  $\beta$ -glucans are then internalized and fragmented into smaller sized  $\beta$ -glucans and are carried to the marrow and endothelial reticular system. The small  $\beta$ -glucans fragments are then released by the macrophages and taken up by the circulating granulocytes, monocytes and dendritic cells. The immune response will then be elicited. However, we should interpret this information with caution as most of the proposed mechanisms are based on *in vitro* and *in vivo* animal studies. Indeed, there is little to no evidence for these hypothesized mechanisms of action and pharmacokinetics occurred in human subjects at the moment.

- **$\beta$ -glucans as immunomodulating agent**

Current data suggests that  $\beta$ -glucans are potent immunomodulators with effects on both innate and adaptive immunity. The ability of the innate immune system to quickly recognize and respond to an invading pathogen is essential for controlling infection. Dectin-1, which is a type II transmembrane protein receptor that binds  $\beta$ -1,3 and  $\beta$ -1,6 glucans, can initiate and regulate the innate immune response [31–33]. It recognizes  $\beta$ -glucans found in the bacterial or fungal cell wall with the advantage that  $\beta$ -glucans are absent in human cells. It then triggers effective immune responses including phagytosis and pro-inflammatory factors production, leading to the elimination of infectious agents. Dectin-1 is expressed on cells responsible for innate immune response and has been found in macrophages, neutrophils, and dendritic cells. The Dectin-1 cytoplasmic tail contains an immunoreceptor tyrosine based activation motif (ITAM) that signals through the tyrosine kinase in collaboration with Toll-like receptors 2 and 6 (TLR-2/6) [34, 37, 38]. The entire signalling pathway downstream to dectin-1 activation has not yet been fully mapped out but several signalling molecules have been reported to be involved. They are NF- $\kappa$ B (through Syk-mediate pathway), signalling adaptor protein CARD9 and nuclear factor of activated T cells (NFAT). This will eventually lead to the release of cytokines including interleukin (IL)-12, IL-6, tumour necrosis factor (TNF)- $\alpha$ , and IL10. Some of these cytokines may play important role in the cancer therapy. On the other hand, the dendritic cell-specific ICAM-3-grabbing non-integrin homolog, SIGN-related 1 (SIGNR1) is another major mannose receptor on macrophages that cooperates with the Dectin-1 in non-opsonic recognition of  $\beta$ -glucans for phagocytosis [30]. Furthermore, it was found that blocking of TLR-4 can inhibit the production of IL-12 p40 and IL-10 induced by purified Ganoderma glucans (PS-G), suggesting a vital role of TLR-4 signalling in glucan induced dendritic cells maturation. Such effect is also operated via the augmentation of the I $\kappa$ B kinase, NF- $\kappa$ B activity and MAPK phosphorylation [31]. One additional point to note is that those studies implied the interaction between  $\beta$ -glucans and TLR all used nonpurified  $\beta$ -glucans, therefore the actual involvement of pure  $\beta$ -glucans and TLR remains to be proven.





### Immune activation induced by $\beta$ -glucans.

$\beta$ -glucans can act on a variety of membrane receptors found on the immune cells. It may act singly or in combine with other ligands. Various signalling pathway are activated and their respective simplified downstream signalling molecules are shown. The reactors cells include monocytes, macrophages, dendritic cells, natural killer cells and neutrophils. Their corresponding surface receptors are listed. The immunomodulatory functions induced by  $\beta$ -glucans involve both innate and adaptive immune response.  $\beta$ -glucans also enhance opsonic and non-opsonic phagocytosis and trigger a cade of cytokines release, such as tumour necrosis factor(TNF)- $\alpha$  and various types of interleukins (ILs).

In summary,  $\beta$ -glucans act on a diversity of immune related receptors in particularly Dectin-1 and CR3, and can trigger a wide spectrum of immune responses. The targeted immune cells of  $\beta$ -glucans include macrophages, neutrophils, monocytes, NK cells and dendritic cells. The immunomodulatory functions induced by  $\beta$ -glucans involve both innate and adaptive immune response.  $\beta$ -glucans also

enhance opsonic and non-opsonic phagocytosis. Whether  $\beta$ -glucans polarize the T cells subset towards a particular direction remains to be explored.

## **6. Tumour and cancer: an introduction:**

In a healthy body, cells grow, divide and replace each other in the body. As new cells form, the older ones die. Tumours develop when cells reproduce very quickly.

A tumour is a mass or lump of tissue that may resemble swelling. The National Cancer Institute define a tumour as ‘an abnormal mass of tissue that results when cells divide more than they should or do not die when they should’.

Tumours can vary in size from a tiny nodule to a large mass, they can appear almost anywhere on the body. There are three types of tumour [37]-

# Benign – They are not cancerous. They either cannot spread or grow, or they do so very slowly and after removal they do not generally return.

# Premalignant – This tumour cells are not cancerous but they have the potential to become malignant or cancerous.

# Malignant – Malignant tumours are cancerous. The cells can grow and spread to other parts of the body.

Cancer cells are formed when normal cells lose the normal regulatory mechanisms that control growth and multiplication. They become ‘rogue cells’ and often lose the specialized characteristics that distinguish one type of cell from another (for example a liver cell from a blood cell). This is called a loss of differentiation. Malignant tumour cells grow uncontrollably and due to the heavy growth and spreading of these cells the disease can become life threatening. Malignant tumours can grow quickly and spread over new areas of the body often by way of the lymph system or bloodstream in a process called metastasis. A major problem in treating cancer is the fact that it is not a single disease. There are more than 200 different cancers resulting from different cellular defects, and so a treatment that is effective in controlling one type of cancer may be ineffective on another.

Different types of malignant tumour originate in different type of cell [36] such as Carcinoma, Sarcoma, Germ cell tumour, Blastoma.

## **7. Anticancer activity [38]:**

Anticancer drug, also called antineoplastic drug, any drug that is effective in the treatment of malignant or cancerous disease. There are several major classes of anticancer drugs; these include alkylating agents, antimetabolites, natural products and hormones. The term chemotherapy frequently is equated with the use of anticancer drugs, though it refers more accurately to the use of chemical compounds to treat disease generally. From recent studies it has been proved that natural products may exert significant cytotoxic and immunomodulatory effects. Plant derived chemotherapeutic agents such as taxol, etoposide or vincristine, currently used in cancer therapy are prominent examples in this e. However, there is a need for new and natural anticancer compounds with low or without toxicity to normal cells. One of the active compounds responsible for the immune effects is  $\beta$ -glucan derived from cereals, fungi, seaweeds, yeasts and bacteria.

## **8. Anticancer activity of $\beta$ -glucan[39]:**

In the literature, there are no clinical trials that directly assessed the anti-cancer effects of purified  $\beta$ glucans in cancer patients. Most studies were assessing the toxicity profile or underlying immune changes of the cancer patients without addressing on the change of cancer status. In addition, most of the related studies used either crude herbal extracts or a fraction of the extracts instead of purified  $\beta$ glucans. Therefore, it is difficult to identify whether the actual effects were related to  $\beta$ -glucans or other confounding chemicals found in the mixture.

In a prospective clinical trial of short term immune effects of oral  $\beta$ -glucan in patients with advanced breast cancer, 23 female patients with advanced breast cancer were compared with 16 healthy females control. Oral  $\beta$ -1,3;1,6-glucan was taken daily. Blood samples were recollected on the day 0 and 15. It was found that despite a relatively low initial white cell count, oral  $\beta$ -glucan can stimulate proliferation and activation of peripheral blood monocytes in patients with advanced breast cancer.

Whether that can be translated into clinical benefit remains unanswered.

- **Clinical trials on anti-cancer effects of natural products with  $\beta$ -glucan:**

Many edible fungi particularly in the mushroom species yield immunogenic substances with potential anticancer activity [40].  $\beta$ -glucans are one of the common active components . In limited clinical trials on human cancers, most were well tolerated. Among them, lentinan derived from *Lentinusedodes* is a form of  $\beta$ -glucans [41]. Since it has poor enteric absorption, intrapleural, intra-peritoneal [42] or intravenous routes had been adopted in clinical trials which showed some clinical benefit when used as

an adjuvant to chemotherapy [43]. Schizophyllan (SPG) or sizofiran is another  $\beta$ -glucan derived from *Schizophyllum commune*. Its triple helical complex  $\beta$ -glucans structure prevents it from adequate oral absorption so an intratumoral route or injection to regional lymph nodes had been adopted [44]. In a randomized trial, SPG combined with conventional chemotherapy improved the long term survival rate of patients with ovarian cancer [45]. But whether the prolonged survival can subsequently led to a better cure rate remain unanswered.

- **Medicinal mushroom with  $\beta$ -glucans as active components**

*Maitake* D-Fraction extracted from *Grifolafrondosa* (*Maitake* mushroom) was found to decrease the size of the lung, liver and breast tumours in >60% of patients when it was combined with chemotherapy in a 2 arms control study comparing with chemotherapy alone [46]. The effects were less obvious with leukemia, stomach and brain cancer patients [47]. But the validity of the clinical study was subsequently questioned by another independent observer [48]. Two proteoglycans from *Coriolusversicolor* (Yun Zhi) – PSK (Polysaccharide-K) and PSP (Polysaccharopeptide) – are among the most extensively studied  $\beta$ -glucan containing herbs with clinical trials information. However, both PSK and PSP are protein-bound polysaccharides, so their actions are not necessary directly equivalent to pure  $\beta$ -glucans [49]. In a series of trials from Japan and China, PSK and PSP were well tolerated without significant side effects [50,51-53]. They also prolonged the survival of some patients with carcinoma and non-lymphoid leukemia.

*Ganoderma* polysaccharides are  $\beta$ -glucans derived from *Ganodermalucidum* (Lingzhi, Reishi). While  $\beta$ -glucan is the major component of the *Ganoderma* mycelium, it is only a minor component in the *Ganoderma* spore [54]. The main active ingredient in the *Ganoderma* spore extract is triterpenoid which is cytotoxic in nature. In an open-label study on patients with advanced lung cancer, thirty-six patients were treated with 5.4 g/day *Ganoderma* polysaccharides for 12 weeks with inconclusive variable and results on the cytokines profiles [55]. Another study on 47 patients with advanced colorectal cancer using the same dosage and period again demonstrated similar variable immune response patterns [56]. These results highlight the inconsistency of clinical outcomes in using immune enhancing herbal extracts clinically, which may partly be due to the impurity of the products used.

## **9. Conclusion:**

$\beta$ -Glucans have been investigated for their ability to protect against infection and cancer and more recently for their therapeutic potential when combined with cancer therapy.  $\beta$ -Glucans are natural polysaccharides present in fungi, algae, bacteria, and plants, which differ in structure, size, branching frequency, and conformation. These polysaccharides (excluding cellulose) commonly consist of a main

chain of  $\beta$ -(1,3) and/or  $\beta$ -(1,6)-glucopyranosyl units in non-repeating non-random order, with side chains of varying lengths. The intrinsic differences of the  $\beta$ -glucans derived from different sources will elicit variable immunomodulatory and anti-cancer responses. In this review we have summarized the immunomodulatory and anti-cancer effect of  $\beta$ -glucans as well as the current limitations of  $\beta$ -glucan research.

$\beta$ -Glucans have a potent immunomodulating activity; their action is mediated through receptors present on immune cells. Their immune modulating effects are attributed to the ability to bind to pattern recognition receptors.

So far, there are very few clinical trial data on using purified  $\beta$ -glucans for cancer patients. Most of the available evidence comes from preclinical data and human studies are just now beginning to appear in the literature, therefore firm conclusions on its clinical importance cannot yet be made. Perhaps the most promising evidence to date in human trials has come from recent studies on a benefit of  $\beta$ -glucan on quality of life and survival when given in combination with cancer treatment.

Studies on  $\beta$ -glucan are complicated by the fact that many studies on  $\beta$ -glucan related herbs often used crude extracts rather than purified compounds, therefore, the confounding effects of other chemicals cannot be totally ruled out. Careful selection of appropriate  $\beta$ -glucan products with good pre-test quality control is essential if we want to understand and compare the results on how  $\beta$ -glucans act on our immune system and exerting anti-cancer effects. A possibly well-defined  $\beta$ -glucan standard is urgently needed in this field for controlled experiments.

There is urgent need for future studies that compare purified forms of  $\beta$ -glucans from different sources to further the understanding of the mechanisms of action and aid in the development of clinical studies for its anti-cancer and immunomodulatory effects.

## **10. Reference:**

1. Henrion, M.; Francey, C.; L  , K.-A.; Lamothe, L. Cereal  $\beta$ -Glucans: The Impact of Processing and How It Affects Physiological Responses. *Nutrients* 2019, 11, 1729.
2. Lamothe, L.M.; L  , K.-A.; Samra, R.A.; Roger, O.; Green, H.; Mac  , K. The scientific basis for healthful carbohydrate profile. *Crit. Rev. Food Sci. Nutr.* 2019, 59, 1058–1070. doi:10.1080/10408398.2017.1392287.
3. Ferretti, F.; Mariani, M. Simple vs. Complex Carbohydrate Dietary Patterns and the Global Overweight and Obesity Pandemic. *Int. J. Environ. Res. Public Health* 2017, 14, 1174. doi:10.3390/ijerph14101174.

4. Qiao, F.; Liu, Y.K.; Sun, Y.H.; Wang, X.D.; Chen, K.; Li, T.Y.; Li, E.C.; Zhang, M.L. Influence of different dietary carbohydrate sources on the growth and intestinal microbiota of *Litopenaeus vannamei* at low salinity. *Aquac. Nutr.* 2017, 23, 444–452. doi:10.1111/anu.12412.
5. Ahmad, A.; Kaleem, M.  $\beta$ -Glucan as a Food Ingredient. In *Biopolymers for Food Design*; Elsevier: Amsterdam, Netherlands, 2018; pp. 351–381. doi:10.1016/b978-0-12-811449-0.00011-6.
6. de Souza Bonfim-Mendonça, P.; Capoci, I.R.G.; Tobaldini-Valerio, F.K.; Negri, M.; Svidzinski, T.I.E. Overview of  $\beta$  Glucans from *Laminaria* spp.: Immunomodulation Properties and Applications on Biologic Models. *Int. J. Mol. Sci.* 2017, 18, 1629. doi:10.3390/ijms18091629.
7. Chen, J. Editorial (Hot Topic: Recent Advance in the Studies of  $\beta$ -glucans for Cancer Therapy). *AntiCancer Agents Med. Chem.* 2013, 13, 679–680. doi:10.2174/1871520611313050001.
8. Ina, K.; Kataoka, T.; Ando, T. The use of lentinan for treating gastric cancer. *Anti-Cancer Agents Med. Chem.* 2013, 13, 681–688. doi:10.2174/1871520611313050002.
9. Jayachandran, M.; Chen, J.; Chung, S.S.M.; Xu, B. A critical review on the impacts of  $\beta$ -glucans on gut microbiota and human health. *J. Nutr. Biochem.* 2018, 61, 11–110.
10. Lazaridou, A.; Biliaderis, C.G.; Izydorczyk, M.S. Cereal  $\beta$ -glucans: Structures, physical properties, and physiological functions. In *Functional Food Carbohydrates*; CRC Press: Boca Raton, FL, USA, 2006; pp. 15–86.
11. H. V.; Sievenpiper, J. L.; Zurbau, A.; Blanco Mejia, S.; Jovanovski, E.; Au-Yeung, F.; Jenkins, A. L.; Vuksan, V (2016). "The effect of oat  $\beta$ -glucan on LDL-cholesterol, non-HDL-cholesterol and apoB for CVD risk reduction: A systematic review and meta-analysis of randomised-controlled trials". *British Journal of Nutrition.* 116 (8): 1369–1382. doi:10.1017/S000711451600341X.
12. Kirby RW, Anderson JW, Sieling B, Rees ED, Chen WJ, Miller RE, Kay RM (1981). "Oat-bran intake selectively lowers serum low-density lipoprotein cholesterol concentrations of hypercholesterolemic men". *Am. J. Clin. Nutr.* 34 (5): 824–9. doi:10.1093/ajcn/34.5.824. PMID 6263072.
13. 21 CFR 101.81 Health Claims: Soluble fiber from certain foods and risk of coronary heart disease (CHD)
14. Zeković, Djordje B. (10 October 2008). "Natural and Modified (1→3)- $\beta$ -D-Glucans in Health Promotion and Disease Alleviation". *Critical Reviews in Biotechnology.* 25 (4): 205–230. doi:10.1080/07388550500376166. PMID 16419618. S2CID 86109922
15. Sikora, Per (14 June 2012). "Identification of high  $\beta$ -glucan oat lines and localization and chemical characterization of their seed kernel  $\beta$ -glucans". *Food Chemistry.* 137 (1–4): 83–91. doi:10.1016/j.foodchem.2012.10.007. PMID 23199994
16. Chu, YiFang (2014). *Oats Nutrition and Technology*. Barrington, Illinois: Wiley Blackwell. ISBN 978-1-118-35411-7.

17. Volman, Julia J (20 November 2007). "Dietary modulation of immune function by  $\beta$ glucans". *Physiology & Behavior*. 94 (2): 276–284. doi:10.1016/j.physbeh.2007.11.045. PMID 18222501. S2CID 24758421
18. Ruiz-Herrera J, Ortiz-tellanos L (May 2010). "Analysis of the phylogenetic relationships and evolution of the cell walls from yeasts and fungi". *FEMS Yeast Research*. 10 (3): 225–43. doi:10.1111/j.1567-1364.2009.00589.x. PMID 19891730.
19. McIntosh, M (19 October 2004). "Curdlan and other bacterial (1→3)- $\beta$ -D-glucans". *Applied Microbiology and Biotechnology*. 68 (2): 163–173. doi:10.1007/s00253-005-1959-5. PMID 15818477. S2CID 13123359.
20. Han, Man Deuk (March 2008). "Solubilization of water-insoluble  $\beta$ -glucan isolated from *Ganoderma lucidum*". *Journal of Environmental Biology*.
21. Manners, David J. (2 February 1973). "The Structure of a  $\beta$ -(1→3)-D-Glucan from Yeast Cell Walls". *Biochemical Journal*. 135 (1): 19–30. doi:10.1042/bj1350019. PMC 1165784. PMID 4359920.
22. Teas, J (1983). "The dietary intake of Laminarin, a brown seaweed, and breast cancer prevention". *Nutrition and Cancer*. 4 (3): 217–222. doi:10.1080/01635588209513760. ISSN 01635581. PMID 6302638.
23. Vannucci, L; Krizan, J; Sima, P; Stakheev, D; Caja, F; Rajsiglova, L; Horak, V; Saieh, M (2013). "Immunostimulatory properties and antitumour activities of glucans (Review)". *International Journal of Oncology*. 43 (2): 357–64. doi:10.3892/ijo.2013.1974. PMC 3775562. PMID 23739801.
24. Jump up to:<sup>a b</sup> McRorie Jr, J. W; McKeown, N. M (2017). "Understanding the Physics of Functional Fibers in the Gastrointestinal Tract: An Evidence-Based Approach to Resolving Enduring Misconceptions about Insoluble and Soluble Fiber". *Journal of the Academy of Nutrition and Dietetics*. 117 (2): 251–264. doi:10.1016/j.jand.2016.09.021. PMID 27863994.
25. Keenan, M. J.; Martin, R. J.; Raggio, A. M.; McCutcheon, K. L.; Brown, I. L.; Birkett, A.; Newman, S. S.; Skaf, J.; Hegsted, M.; Tulley, R. T.; Blair, E.; Zhou, J. (2012). "High-Amylose Resistant Starch Increases Hormones and Improves Structure and Function of the Gastrointestinal Tract: A Microarray Study". *Journal of Nutrigenetics and Nutrigenomics*. 5(1): 26–44. doi:10.1159/000335319. PMC 4030412. PMID 22516953.
26. Simpson, H. L.; Campbell, B. J. (2015). "Review : dietary fibre–microbiota interactions". *Alimentary Pharmacology & Therapeutics*. 42 (2): 158–79. doi:10.1111/apt.13248. PMC 4949558. PMID 26011307.
27. Othman, R. A; Moghadasian, M. H; Jones, P. J (2011). "Cholesterol-lowering effects of oat  $\beta$ glucan". *Nutrition Reviews*. 69 (6): 299–309. doi:10.1111/j.1753-4887.2011.00401.x. PMID 21631511.

28. Frey A, Giannasca KT, Weltzin R, Giannasca PJ, Reggio H, Lencer WI, Neutra MR (1 September 1996). "Role of the glycocalyx in regulating access of microbes to apical plasma membranes of intestinal epithelial cells: implications for microbial attachment and oral vaccine targeting". *The Journal of Experimental Medicine*. 184 (3): 1045–1059. doi:10.1084/jem.184.3.1045. PMC 2192803. PMID 9064322.
29. Tsukagoshi S, Hashimoto Y, Fujii G, Kobayashi H, Nomoto K, Orita K (June 1984). "Krestin (PSK)". *Cancer Treatment Reviews*. 11 (2): 131–155. doi:10.1016/0305-7372(84)90005-7. PMID 6238674.
30. Hong, F; Yan J; Baran JT; Allendorf DJ; Hansen RD; Ostroff GR; Xing PX; Cheung NK; Ross GD (15 July 2004). "Mechanism by which orally administered  $\beta$ -1,3-glucans enhance the tumoricidal activity of antitumour monoclonal antibodies in murine tumour models". *Journal of Immunology*. 173 (2): 797–806. doi:10.4049/jimmunol.173.2.797. ISSN 0022-1767. PMID 15240666.
31. Obayashi T, Yoshida M, Mori T, et al. (1995). "Plasma (13)- $\beta$ -D-glucan measurement in diagnosis of invasive deep mycosis and fungal febrile episodes". *Lancet*. 345 (8941): 17–20. doi:10.1016/S0140-6736(95)91152-9. PMID 7799700. S2CID 27299444.
32. Ostrosky-Zeichner L, Alexander BD, Kett DH, et al. (2005). "Multicenter clinical evaluation of the (1 $\rightarrow$ 3) $\beta$ -D-glucan assay as an aid to diagnosis of fungal infections in humans". *Clin Infect Dis*. 41 (5): 654–659. doi:10.1086/432470. PMID 16080087.
33. Odabasi Z, Mattiuzzi G, Estey E, et al. (2004). " $\beta$ -D-glucan as a diagnostic adjunct for invasive fungal infections: validation, cutoff development, and performance in patients with acute myelogenous leukemia and myelodysplastic syndrome". *Clin Infect Dis*. 39 (2): 199–205. doi:10.1086/421944. PMID 15307029.
34. Mennink-Kersten MA, Warris A, Verweij PE (2006). "1,3- $\beta$ -D-Glucan in patients receiving intravenous amoxicillin–clavulanic acid". *NEJM*. 354 (26): 2834–2835. doi:10.1056/NEJMc053340. PMID 16807428.
35. Mennink-Kersten MA, Ruegebrink D, Verweij PE (2008). "Pseudomonas aeruginosa as a cause of 1,3- $\beta$ -D-glucan assay reactivity". *Clin Infect Dis*. 46 (12): 1930–1931. doi:10.1086/588563. PMID 18540808.
36. Lahmer, Tobias; da Costa, Clarissa Prazeres; Held, Jürgen; Rasch, Sebastian; Ehmer, Ursula; Schmid, Roland M.; Huber, Wolfgang (4 April 2017). "Usefulness of 1,3  $\beta$ -D-Glucan Detection in non-HIV Immunocompromised Mechanical Ventilated Critically Ill Patients with ARDS and Suspected Pneumocystis jirovecii Pneumonia". *Mycopathologia*. 182 (7–8): 701–708. doi:10.1007/s11046-017-0132-x. ISSN 1573-0832. PMID 28378239. S2CID 3870306.
37. He, Song; Hang, Ju-Ping; Zhang, Ling; Wang, Fang; Zhang, De-Chun; Gong, Fang-Hong (August 2015). "A systematic review and meta-analysis of diagnostic accuracy of serum 1,3- $\beta$ -D-glucan for invasive fungal infection: Focus on cutoff levels". *Journal of Microbiology, Immunology, and*



- Infection = Wei Mian Yu Gan Ran Za Zhi. 48 (4): 351–361. doi:[10.1016/j.jmii.2014.06.009](https://doi.org/10.1016/j.jmii.2014.06.009). ISSN 1995-9133. PMID [25081986](https://pubmed.ncbi.nlm.nih.gov/25081986/).
38. Kullberg, Bart Jan; Arendrup, Maiken C. (8 October 2015). "Invasive Candidiasis". *The New England Journal of Medicine*. 373 (15): 1445–1456. doi:[10.1056/NEJMra1315399](https://doi.org/10.1056/NEJMra1315399). hdl:[2066/152392](https://hdl.handle.net/2066/152392). ISSN 1533-4406. PMID [26444731](https://pubmed.ncbi.nlm.nih.gov/26444731/).
  39. Ostrosky-Zeichner, Luis; Alexander, Barbara D.; Kett, Daniel H.; Vazquez, Jose; Pappas, Peter G.; Saeki, Fumihiko; Ketchum, Paul A.; Wingard, John; Schiff, Robert (1 September 2005). "[Multicenter clinical evaluation of the \(1→3\)-β-D-glucan assay as an aid to diagnosis of fungal infections in humans](#)". *Clinical Infectious Diseases*. 41 (5): 654–659. doi:[10.1086/432470](https://doi.org/10.1086/432470). ISSN 1537-6591. PMID [16080087](https://pubmed.ncbi.nlm.nih.gov/16080087/).
  40. Karumuthil-Melethil S, Perez N, Li R, Vasu C: Induction of innate immune response through TLR2 and dectin 1 prevents type 1 diabetes. *J Immunol*. 2008, 181 (12): 8323-8334.
  41. Klein E, Di Renzo L, Yefenof E: Contribution of CR3, CD11b/CD18 to cytolysis by human NK cells. *Molecular immunology*. 1990, 27 (12): 1343-1347. 10.1016/0161-5890(90)90041-W.
  42. Di Renzo L, Yefenof E, Klein E: The function of human NK cells is enhanced by β-glucan, a ligand of CR3 (CD11b/CD18). *European journal of immunology*. 1991, 21 (7): 1755-1758. 10.1002/eji.1830210726.
  43. Cheung NK, Modak S, Vickers A, Knuckles B: Orally administered β-glucans enhance antitumour effects of monoclonal antibodies. *Cancer Immunol Immunother*. 2002, 51 (10): 557-564.
- 
44. Modak S, Koehne G, Vickers A, O'Reilly RJ, Cheung NK: Rituximab therapy of lymphoma is enhanced by orally administered (1→3),(1→4)-β-D-glucan. *Leuk Res*. 2005, 29 (6): 679-683. 10.1016/j.leukres.2004.10.008.
  45. Dushkin MI, Safina AF, Vereschagin EI, Schwartz Y: Carboxymethylated β-1,3-glucan inhibits the binding and degradation of acetylated low density lipoproteins in macrophages in vitro and modulates their plasma clearance in vivo. *Cell Biochem Funct*. 1996, 14 (3): 209-217.
  46. Zimmerman JW, Lindermuth J, Fish PA, Palace GP, Stevenson TT, DeMong DE: A novel carbohydrate-glycosphingolipid interaction between a β-(1–3)-glucan immunomodulator, PGGglucan, and lactosylceramide of human leukocytes. *The Journal of biological chemistry*. 1998, 273 (34): 22014-22020. 10.1074/jbc.273.34.22014.
  47. Iwabuchi K, Nagaoka I: Lactosylceramide-enriched glycosphingolipid signalling domain mediates superoxide generation from human neutrophils. *Blood*. 2002, 100 (4): 1454-1464.

48. Vereschagin EI, van Lambalgen AA, Dushkin MI, Schwartz YS, Polyakov L, Heemskerk A, Huisman E, Thijs LG, van den Bos GC: Soluble glucan protects against endotoxin shock in the rat: the role of the scavenger receptor. *Shock* (Augusta, Ga). 1998, 9 (3): 193-198.
  49. Wakshull E, Brunke-Reese D, Lindermuth J, Fisette L, Nathans RS, Crowley JJ, Tufts JC, Zimmerman J, Mackin W, Adams DS: PGG-glucan, a soluble  $\beta$ -(1,3)-glucan, enhances the oxidative burst response, microbicidal activity, and activates an NF-kappa B-like factor in human PMN: evidence for a glycosphingolipid  $\beta$ -(1,3)-glucan receptor. *Immunopharmacology*. 1999, 41 (2): 89-107. 10.1016/S0162-3109(98)00059-9.
  50. Tang W, Liu JW, Zhao WM, Wei DZ, Zhong JJ: Ganoderic acid T from *Ganoderma lucidum* mycelia induces mitochondria mediated apoptosis in lung cancer cells. *Life Sci*. 2006, 80 (3): 205-211. 10.1016/j.006.09.001.
  51. Lin SB, Li CH, Lee SS, Kan LS: Triterpene-enriched extracts from *Ganoderma lucidum* inhibit growth of hepatoma cells via suppressing protein kinase C, activating mitogen-activated protein kinases and G2-phase cell cycle arrest. *Life Sci*. 2003, 72 (21): 2381-2390. 10.1016/S00243205(03)00124-3.
  52. Min BS, Gao JJ, Nakamura N, Hattori M: Triterpenes from the spores of *Ganoderma lucidum* and their cytotoxicity against meth-A and LLC tumour cells. *Chem Pharm Bull (Tokyo)*. 2000, 48 (7): 1026-1033.

---

  53. Muller CI, Kumagai T, O'Kelly J, Seeram NP, Heber D, Koeffler HP: *Ganoderma lucidum* causes apoptosis in leukemia, lymphoma and multiple myeloma cells. *Leukemia research*. 2006, 30 (7): 841-848. 10.1016/j.leukres.2005.12.004.
  54. Chan WKD, Cheung CC, Law HKD, Lau YLD, Chan GCD: *Ganoderma lucidum* polysaccharides can induce human monocytic leukemia cells into dendritic cells with immuno-stimulatory function. *J Hematol Oncol*. 2008, 1 (1): 9-10.1186/1756-8722-1-9.
  55. Demir G, Klein HO, Mandel-Molinas N, Tuzuner N:  $\beta$ -Glucan induces proliferation and activation of monocytes in peripheral blood of patients with advanced breast cancer. *Int Immunopharmacol*. 2007, 7 (1): 113-116. 10.1016/j.intimp.2006.08.011.
  56. Kidd PM: The use of mushroom glucans and proteoglycans in cancer treatment. *Altern Med Rev*. 2000, 5 (1): 4-27.
  57. Miyakoshi H, Aoki T, Mizukoshi M: Acting mechanisms of Lentinan in human – II. Enhancement of non-specific cell-mediated cytotoxicity as an interferon inducer. *International journal of immunopharmacology*. 1984, 6 (4): 373-379. 10.1016/0192-0561(84)90057-2
-

A LITERATURE SURVEY ON:

**APPLICATION OF FLUORESCENCE**  
**SPECTROSCOPY IN DETECTION OF CANCER**

SCOTTISH CHURCH COLLEGE

(UNIVERSITY OF CALCUTTA)

ROLL NUMBER: 223/CEM/191030

REGISTRATION NUMBER: 223-1221-0192-16

P.G. SEMESTER IV

PHYSICAL CHEMISTRY SPECIAL PAPER: SP 44

*Shramana Palit*

---

SHRAMANA PALIT

*Aniruddha Ganguly*

---

DR. ANIRUDDHA GANGULY  
(SUPERVISOR)

# **APPLICATION OF FLUORESCENCE SPECTROSCOPY IN DETECTION OF CANCER IN BIOLOGICAL MEDIUM**

## **ABSTRACT**

Diagnostic techniques based on optical spectroscopy have the potential to link biochemical and morphological properties of tissues to individual patient care. In particular, these techniques are fast, non-invasive, and quantitative. Furthermore, they can be used to elucidate key tissue features, such as cellular metabolic rate, vascularity, intravascular oxygenation, and alterations in tissue morphology. Here we will focus on fluorescence spectroscopy whose applications are being widely explored in the detection of endoscopically visible neoplastic growth.

If fluorescence spectroscopy can be applied as a diagnostic technique in this clinical context, it may increase potential for curative treatment, and thus reduce complications and health care costs. Steady state, fluorescence measurements from small tissue regions as well as relatively large tissue fields have been performed. To a much lesser extent, time resolved fluorescence spectroscopy measurements have also been used for tissue characterization.

Fluorescence spectroscopy has been the most widely explored mainly because fluorescence is highly sensitive to the biochemical makeup of tissues. It has been shown that tumours were easily detected on account of altered fluorescence properties with respect to fluorescence of ordinary tissue

The goal of this article is to review development and applications of fluorescence spectroscopy as a diagnostic tool in clinical applications. Emphasis has been placed on detection of cancer and pre-cancer in biological medium. We will also look into the applications of fluorescence spectroscopy in the diagnosis of particularly breast cancer and skin cancer.

# INTRODUCTION

## SPECTROSCOPY

Spectroscopy is the study of the interaction of electromagnetic radiation with matter. There are three aspects to a spectroscopic measurement: irradiation of a sample with electromagnetic radiation; measurement of the absorption, spontaneous emission (fluorescence, phosphorescence), and/or scattering (Rayleigh, Raman inelastic scattering) from the sample; and analysis and interpretation of these measurements.

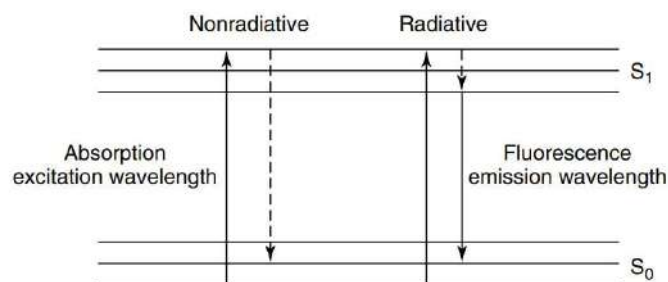
## ENERGY LEVELS PROBING

Energy level of a molecule is defined as its characteristic state, which is related to the molecular structure of the molecule and to energetics and dynamics of any chemical processes that the molecule may undergo. The ground state of a molecule is defined as the state of lowest energy. States of higher energy are called excited states. A molecule possesses several distinct reservoirs of energy levels, including electronic, vibrational, rotational, translational, and those associated with nuclear and electron spin. At any finite temperature, molecules will be distributed among energy levels available to them because of thermal agitation. The exact distribution will depend on the temperature ( $T$ ) and on the separation between energy levels in the energy ladder. At a given temperature, the number of molecules in an upper level ( $n_{\text{upper}}$ ) relative to that in a lower level ( $n_{\text{lower}}$ ) is given by the Boltzmann distribution, as shown in Equation (1):

$$n(\text{upper})/n(\text{lower}) = \exp^{(-\Delta E/ kT)} \quad (1),$$

where  $k$  is the Boltzmann constant ( $1.38 \times 10^{-23} \text{ J K}^{-1}$ ). When electromagnetic radiation is applied to a molecule, it is just as likely to cause transitions from a higher to a lower energy level as it is to cause transitions from a lower to a higher energy level. Consequently, net absorption or transition to a higher energy level can occur only if the difference between populations of the energy levels concerned is significant, with the lower one being significantly higher.

## FLUORESCENCE SPECTROSCOPY

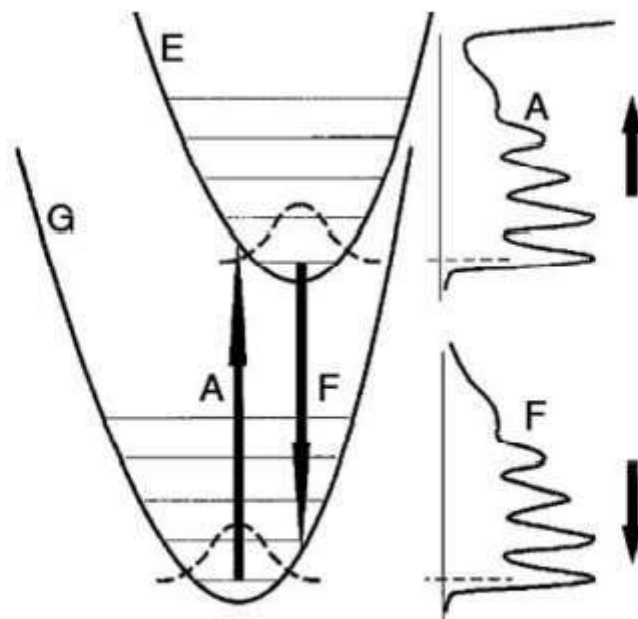


**Figure 1** Energy level diagram illustrating the phenomena of absorption and fluorescence of a molecule.

The above figure displays an energy level diagram with ground electronic state ( $S_0$ ) and lowest excited one ( $S_1$ ), as well as vibrational energy levels within each electronic state of a molecule. When a molecule is excited at a wavelength that lies within absorption spectrum of that molecule, it will absorb the energy and be activated from its ground state ( $S_0$ ) to the excited singlet state ( $S_1$ ), with the electron in the same spin as its ground state. The molecule can then relax back from the excited state to the ground state by generating energy either non-radiatively or radiatively, depending on

the local environment. In a nonradiative transition, relaxation occurs by thermal generation. In a radiative transition, relaxation occurs via fluorescence at specific emission wavelengths. Fluorescence generation occurs in three steps: thermal equilibrium is achieved rapidly as the electron makes a nonradiative transition to the lowest vibrational level of the first excited state; the electron then makes a radiative transition to a vibrational level of the ground state; and finally the electron makes a nonradiative transition to the lowest vibrational level of the ground state. When there is intersystem crossing, in which the spin of the electron is flipped in the excited state, the time for radiative transition from the excited state to ground state is longer because the transition must occur with a spin change. This excited state is termed the triplet state. Radiative transition from the excited triplet state is termed phosphorescence. Tissue absorption, fluorescence, and phosphorescence monitor changes in electronic energy levels, to provide biochemical information from biological molecules.

A scheme in the Figure shows a simple state diagram of an aromatic molecule and the basic molecular processes leading to absorption and fluorescence emission. The ground (G) and excited state (E) energy surfaces are shown as parabolas; i.e., a harmonic potential along a basic vibrational coordinate. The allowed vibrational states are shown as equidistant lines.



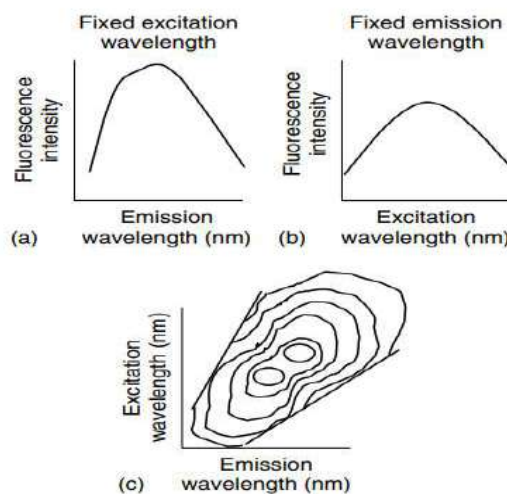
**Figure 1.** Basic principles of absorption (A) and fluorescence (F) spectroscopy. (G denotes the electronic ground state and E the lowest electronic excited state of the molecule.)

In thermal equilibrium only the lowest vibrational state of the molecule is populated and the probability for the position of the nuclei in that level is shown by the dashed line. Absorption of a photon is observed when its energy fits exactly to the energy distance between the lowest vibrational level of the ground state and one vibrational level of the excited state. An electronic transition is generally a vertical transition; i.e., that the absorption of the photon is much faster (ca. 0.1 fs) in comparison to the movement of the nuclei (ca. 0.1 ps for one period of vibration). Under that condition, neither the position nor the velocity of the nuclei, nearly resting in the ground state, should change—this is the well-known Franck-Condon principle, which states that whenever a higher vibrational level is occupied by the electronic transition this should occur at the turning point of the motion. It gives rise to an absorption spectrum similar to that plotted to the right of the state

diagram. A typical example similar to that plotted is the absorption spectrum of anthracene in a hydrocarbon solvent. In many cases, however, vibronic features are washed out by overlapping transition, coupling of different vibrations, influence of solvent, etc. After excitation, additional nuclear energy due to motion of the nuclei is quickly dissipated to the solvent in a liquid medium and thermal equilibrium is established in the excited state. Because the lifetime of the excited states before returning to the ground state is generally some few nanoseconds, all further processes, as, for example, fluorescence or intersystem-crossing to triplet states, originate from the lowest vibronic level of the excited state. This is shown in the scheme for fluorescence F and all principles discussed first for absorption apply in a similar manner for fluorescence. This gives rise to an emission spectrum, which should show nearly a mirror image about the energy difference between the two lowest vibrational levels. Therefore, the shift of fluorescence versus absorption to lower energies should generally be small. In cases where this is not observed an additional process is indicated, occurring in the excited state.

## METHODOLOGY AND PRINCIPLES

The fluorescence of a biological molecule is characterized by its quantum yield and lifetime. (1) The quantum yield is simply the ratio of the no. of photons emitted to the no. absorbed. The lifetime is defined as the average time the biological molecule spends in the excited state before returning to the ground state. Fluorescence quantum yield and lifetime are modified by a no. of factors that can increase or decrease the energy losses. For example, a molecule may be non-fluorescent as a result of large of non-radiative decay (thermal generation) or a slow rate of radiative decay (fluorescence). Fluorescence spectroscopy is the measurement and analysis of various features related to fluorescence quantum yield or lifetime of a biological molecule. The fluorescent intensity of a biological molecule is a function of its concentration, its extinction coefficient (absorbing power) at its excitation wavelength, and its quantum yield at its emission wavelength. (2) Fluorescence emission spectrum represents the fluorescence intensity measured over a range of emission wavelengths at a fixed excitation wavelength. On the other hand, a fluorescence excitation spectrum is a plot of fluorescence intensity at a particular emission wavelength for a range of excitation wavelengths.



A fluorescence excitation–emission matrix (EEM) is a two-dimensional contour plot that displays the fluorescence intensities as a function of a range of excitation and emission wavelengths. Each contour represents points of equal fluorescence intensity.

Fluorescence spectroscopy of turbid media such as tissue depends on one or more of the following:

- specifically, it depends on the concentration and distribution of fluorophore(s) present in the tissue as well as the biochemical/biophysical environment, which may alter the quantum yield and lifetime of the fluorophore(s).
- Fluorescence spectroscopy of turbid media such as tissue also depends on absorption and scattering that result from the concentration and distribution of nonfluorescent absorbers and scatterers, respectively, within the different sublayers of the tissue.

The effect of aforementioned variables on fluorescence spectroscopy of tissue is wavelength dependent. First, endogenous fluorophores having absorption bands that lie in the same wavelength range as the excitation light will be excited and hence will emit fluorescence. Absorption and scattering properties of the tissue will affect light at both the excitation and emission wavelengths. Therefore, only those fluorophores contained in the tissue layers to which excitation light penetrates and from which emitted light can escape the tissue surface will produce measurable fluorescence. Elastic scattering events in tissue are caused by random spatial variations in the density, refractive index, and dielectric constants of extracellular, cellular, and subcellular components. Tissue scattering generally decreases monotonically with increasing wavelength over the UV, VIS, and NIR spectral regions. (3,5)



## FACTORS AFFECTING THE FLUORESCENCE OF TISSUES

Haemoglobin, which is contained in red blood cells, serves as oxygen carrier in blood and also plays a vital role in the transport of carbon dioxide and hydrogen ions. (6) Capacity of haemoglobin to bind oxygen depends on the presence of a non-polypeptide unit, namely, a heme group. The heme consists of an organic part, a protoporphyrin ring, and an iron atom. The absorption spectra are characterized by the decreasing absorption of deoxygenated haemoglobin and the increasing absorption of oxygenated haemoglobin as a function of increasing wavelength.

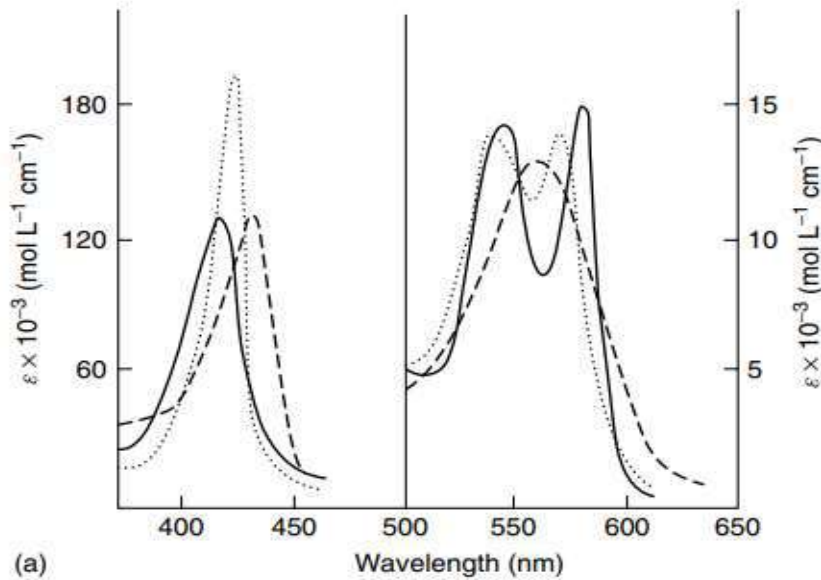


Figure of absorption spectra of oxygenated and deoxygenated haemoglobin in the UV/VIS region

Illumination and collection geometry of excitation and emitted light, respectively, can also affect fluorescence measurements from tissue with respect to both intensity and line shape. (7,8) This may be attributed to the fact that, although fluorescence is generated iso-tropically from the fluorophores within the biological medium, fluorescence emitted from the surface of the medium may range from isotropic to anisotropic, depending on whether the medium is highly absorbing, dilute, or turbid.

For a turbid medium such as tissue that contains  $k$  fluorophores, the fluorescence intensity can be rewritten to include a transfer function (TF) which describes attenuation of excited and emitted light due to the absorption and scattering properties of the tissue at these wavelengths. This is defined in Equation

$$F(\lambda x, \lambda m) = P_0(\lambda x) \int_0^\infty dz \sum_{k=1}^N \mu_a k$$

where  $z$  refers to the depth within the medium. Here, the transfer function for a particular depth can be determined from the absorption coefficient, scattering coefficient, and anisotropy factor of the tissue. The wavelength-dependent absorption coefficient  $\mu_a$  denotes the probability of photon absorption per unit path length, whereas the scattering coefficient  $\mu_s$  denotes the probability of photon scattering per unit path length. The anisotropy factor ( $g$ ) denotes the cosine of the average scattering angle. The reduced or isotropic scattering coefficient  $\mu_s$  is the product of the scattering coefficient  $\mu_s$  and one minus the anisotropy parameter ( $1 - g$ ). (3) Models of light transport can be used to deduce the absorption and scattering coefficients and the anisotropy parameter needed to compute the transfer function in the equation. (9)

## TYPES OF FLUOROPHORES

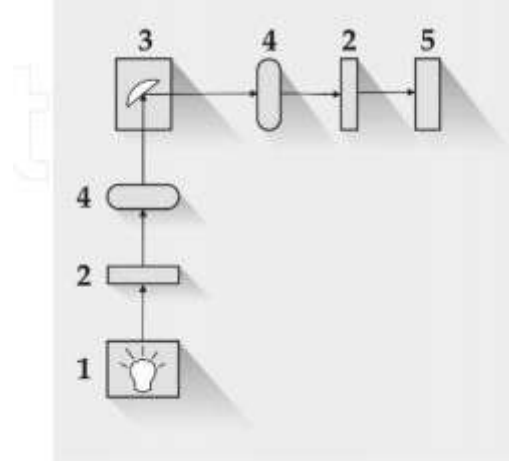
**Endogenous fluorophore-** fluorophores present natively inside the cell (4,5)

**Table 1** Excitation and emission maxima of biological molecules that exhibit endogenous fluorescence

Endogenous fluorophores	Excitation maxima (nm)	Emission maxima (nm)
<b>Amino acids</b>		
Tryptophan	280	350
Tyrosine	275	300
Phenylalanine	260	280
<b>Structural proteins</b>		
Collagen	325	400, 405
Elastin	290, 325	340, 400
<b>Enzymes and coenzymes</b>		
FAD, flavins	450	535
NADH	290, 351	440, 460
NADPH	336	464
<b>Vitamins</b>		
Vitamin A	327	510
Vitamin K	335	480
Vitamin D	390	480
<b>Vitamin B<sub>6</sub> compounds</b>		
Pyridoxine	332, 340	400
Pyridoxamine	335	400
Pyridoxal	330	385
Pyridoxic acid	315	425
Pyridoxal 5'-phosphate	330	400
Vitamin B <sub>12</sub>	275	305
<b>Lipids</b>		
Phospholipids	436	540, 560
Lipofuscin	340–395	540, 430–460
Ceroid	340–395	430–460, 540
Porphyrins	400–450	630, 690

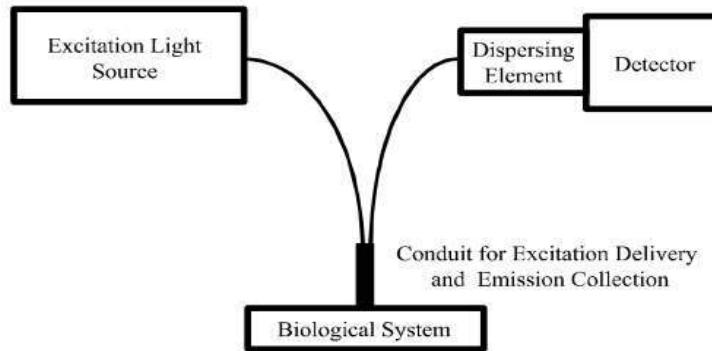
## INSTRUMENTATION

To stimulate and measure fluorescence from a sample, one needs to use instrument with five basic components: (1) light source, (2) wavelength selector elements on the excitation and emission paths to/from sample, (3) sample holder/positioner, (4) polarizers, and (5) detector



A schematic of the basic components of an instrument used for fluorescence and/or reflectance spectroscopy of tissues is shown in the figure below. It consists of a light source, a flexible conduit that contains optical fibres for illumination and collection of light, a dispersing element that separates emitted light into its respective wavelengths, and a detector that measures the intensity at these wavelength(s). In this scenario, fluorescence emission and reflectance are measured in a re-emission geometry in which illumination and collection are performed on the same surface of the tissue.

Polychromatic light from light source is dispersed on a dispersing element from which light beam of selected wavelength is directed on a sample to excite fluorescence. Most frequently, Xe arc lamps are used. These days, deuterium, tungsten, or halogen lamps are rarely utilized for excitation, since they are relatively weak sources for fluorescence. Lasers, laser diodes, and light-emitting diodes (LEDs) are also frequently used. They produce intense monochromatic light, so there is no need for the wavelength-selecting element on the excitation path. The drawback is that excitation spectra cannot be measured with these light sources. Tuneable and supercontinuum lasers are an exception, which can produce emissions over the given spectral interval, but these are rather expensive devices. Light dispersion can be accomplished with prisms and diffraction gratings; the latter is dominantly used in the modern spectrofluorometers. The detector can be either single-channelled or multi-channelled. The single-channelled detector, usually photomultiplier tube (PMT) or semiconductor, detects the intensity of one wavelength at a time. Multi-channelled detectors, such as charge-coupled device cameras (CCDs), record the intensity of emission over the range of wavelengths simultaneously. In addition, modern instruments include some other important components, such as polarizers, filters, and optical fibre connectors. Laboratory spectrometers are complex and robust devices capable of versatile and sensitive measurements. However, for many applications, and for the convenience and mobility of measurements fluorimeters can be designed as miniaturized devices. These devices are particularly suitable for clinical investigations of tissue fluorescence.



**Figure 3.** Schematic of the basic components of an instrument employed for fluorescence spectroscopy of biological media.

## What are the advantages of using fluorescence spectroscopy in cancer detection?

Cancer is one of the major killer diseases throughout the world. According to statistics of the American Cancer Society, cancer accounts for nearly one quarter of deaths in the United States. In the United States, lung cancer is the most common fatal cancer in men (30%), followed by prostate cancer (9%) and colon and rectal cancers (9%). In women, the most common fatal cancers are lung (26%), breast (15%), and colon and rectal (9%) cancers. It is expected that about 1.5 million new cases of cancer will be diagnosed in the United States in 2009. The United States has an estimated population of around 300 million and the world has an estimated population of around 6 billion. Therefore, by extrapolation, cancer is fatal to millions of people throughout the world on a yearly basis. Almost all cancers from all anatomical sites face some kind of diagnostic problems. There are many reasons for this; many cancers have vague symptoms and signs, and some are difficult to visualize due to deeper anatomical sites inside the body. As a result, many cancers are diagnosed at a late stage and treatment at these stages usually fails to cure the cancer, resulting in high mortality rate by different types of cancers throughout the world. Therefore, there is great need for technology that can diagnose or assist current investigation tools to diagnose premalignant or malignant lesions at an early stage.

Fluorescence spectroscopy is a well-known and promising non-invasive optical diagnostic technique that aims to characterize biological tissue on the basis of its emission spectra. Over the past few decades, it has emerged as a powerful biomedical diagnostic tool because of its sensitivity to probe the biochemical changes, which occur inside the body during disease progression. These biochemical changes lead to changes in the endogenous fluorophores concentrations, quantum efficiencies, and the local environment. Consequently, the contrast in the fluorescence spectra obtained from normal and diseased tissue sites has been reported to be useful for cancer diagnostics.

# USING FLUORESCENCE SPECTROSCOPY TO DETECT CANCER

There are three main types of fluorophores used for cancer diagnostic studies: exogenous fluorophores, endogenous fluorophores, and fluorophores synthesized in the tissue from a precursor molecule that is given externally. Endogenous fluorophores give rise to autofluorescence phenomenon. Examples of endogenous fluorophores include collagen, elastin, nicotinamide adenine dinucleotide (NADH), tryptophan, porphyrins, and flavin adenine dinucleotide (FAD). Collagen and elastin are mainly responsible for spectral changes associated with structural changes within the tissues and cells. Other fluorophores like FAD, NADH, tryptophan, and porphyrins are mainly responsible for spectral changes associated with changes in cellular metabolism and functional processes. (10,11,12,13)

Cancer tissues have an increased rate of metabolism, which gives rise to alternation in endogenous fluorophores, giving rise to spectral characteristics different from normal tissue. Many groups have performed studies to explore various endogenous fluorophores. They all observed a marked decrease in the fluorescence intensity in case of premalignant and malignant tissues. (14,15)

In 1965, Lycette and Leslie (16) suggested that fluorescence spectroscopy could be used to discriminate between normal tissues and malignant tumours. Fluorescence emission spectra were recorded from excised normal tissue and malignant tumours of the oesophagus, stomach, breast, and thyroid at 330-nm excitation. All tissues fluoresced in the range 360–600 nm. It was found that the fluorescence intensities of malignant tumours were less than that of normal tissue from the same patient. Subsequently, the groups of Profio, Alfano, Lohmann, and Yang (17,18,19) carried out pioneering studies on in vitro and in vivo fluorescence spectroscopy of neoplastic and nonneoplastic animal and human tissues. (Neoplastic-tumour growths either malignant or benign). Fluorescence spectroscopy has been used to evaluate neoplastic and nonneoplastic tissues in vitro and in vivo. Generally, the results of in vitro studies have been used to guide the design of experimental parameters for in vivo studies.

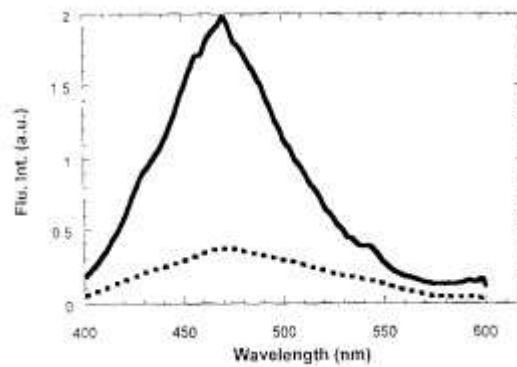
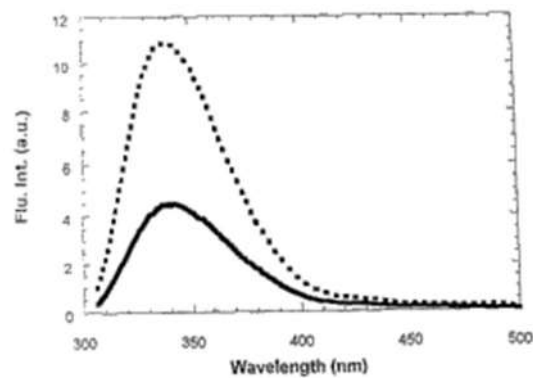
Autofluorescence phenomenon has been used for diagnosis of premalignant or malignant lesions in various organs of the body including the oral cavity, cervix, skin, lungs, breast, oesophagus, head and neck, and colon. These studies proposed promising results for using fluorescence spectroscopy as a possible diagnostic tool for early-stage cancers. But, there are some undesirable features associated with autofluorescence; for example, there might be some broad structureless emissions caused by some nonspecific fluorophores. We will briefly discuss fluorescence spectroscopy's application in three types of cancers; that is, oral cavity, breast, and skin cancers.

## Oral cavity cancers

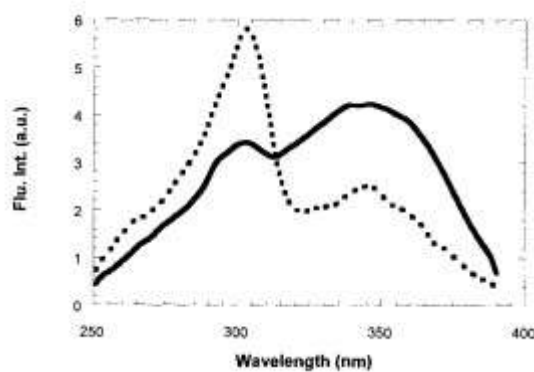
Fluorescence spectroscopy has been proved by many groups to be highly valuable for early detection of oral cavity cancers with high sensitivity and specificity. Gillenwater et al. used fluorescence spectroscopy for non-invasive diagnosis of oral neoplasia with sensitivity of 88% and specificity of 100%. They applied a fluorescence spectroscopy system to record emission spectra at 337,365 and 410 nm excitation wavelengths. They did a comparison of fluorescence peak intensities and spectral shapes from normal and abnormal oral sites. They found that fluorescence intensity of normal oral mucosa was higher compared to abnormal areas. Also, they observed that the ratio of red region to blue region intensities was higher in abnormal areas. (20)

## SKIN CANCER

Fluorescence spectroscopy has also proved beneficial for early diagnosis of skin premalignant and malignant lesions. Bracheleon et al. collected 33 samples of freshly frozen tissues sections of tumours. Results showed that upon excitation at 295nm the lesions showed higher fluorescence than the normal surrounding skin (emission spectra). Upon excitation at 350nm the fluorescence intensity was lower than surrounding normal skin. The trend was reversed in case of excitation spectra.

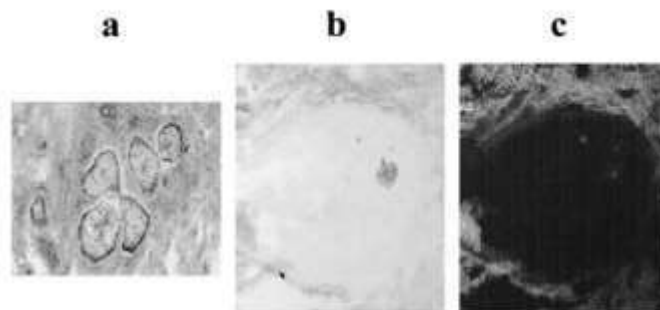


The above figure represents emission spectra for excitation at 295nm and 350nm respectively. The dotted line is for the tumour and the solid line is for normal skin.



The above figure represents the excitation spectra for tumour and normal skin.

Autofluorescence image of the frozen tissue sections shows a dark area with a marked loss of collagen autofluorescence of the tumour loci and surrounding dermal tissue. The areas characterized by the loss of autofluorescence were two- to three-fold larger than the actual tumour size estimated from the H&E images. In a limited number of cases the autofluorescence pattern showed sharply demarcated “dark” areas amidst brightly fluorescent dermal collagen fibrils.



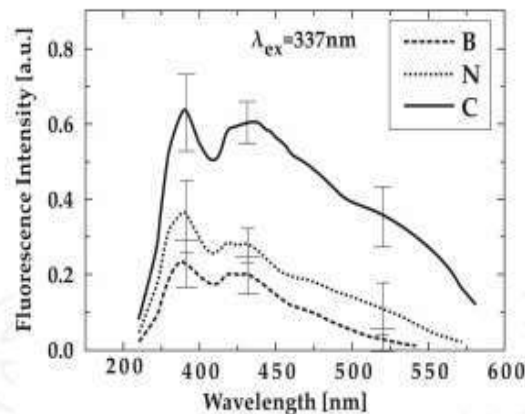
**Figure 4.** Fluorescence microscopy image: (a) white light H&E stained image of a NMSC section. The tumor nests can be distinguished by the lighter appearance delimited by a dark purple rim; (b) white light image of the same area in a section adjacent to the one in (a); and (c) fluorescent image of (b). Excitation at  $360 \pm 5$  nm; emission at  $428 \pm 5$  nm. The area where the tumor nests are located result in a dark, nonfluorescent region surrounded by a brighter area where fibrous structures (from collagen fibrils) can be observed. The nonfluorescent area is larger than the area occupied by the tumor nests in (a).

The most striking observation among those reported was the increase of fluorescence in the tumour with respect to normal skin. This is probably due to hyperactivity or hyperproliferation. Upon excitation at 350nm the in vivo fluorescence spectra normal skin and tumour, the fluorescence of collagen crosslinks in tumours decreases drastically in comparison to surrounding skin due to tumour induced changes in connective tissue. (21,22)

## BREAST CANCER

Breast tissue optical characters show glandular, adipose and fibrous tissues. The autofluorescence of these tissues comes from the structural and compositional differences in the concentration of fluorophores and their distribution. The first report on the characterization of human breast tissues by fluorescence emission spectroscopy has been published by Alfano et al. (23). They have obtained normal and cancerous breast tissues from two different individuals and have measured emission spectra (460–700 nm) after excitation with an argon ion laser (at 488 and 457.9 nm). However, the assessment of method's capability for diagnosis has been impossible because of small number of investigated samples.

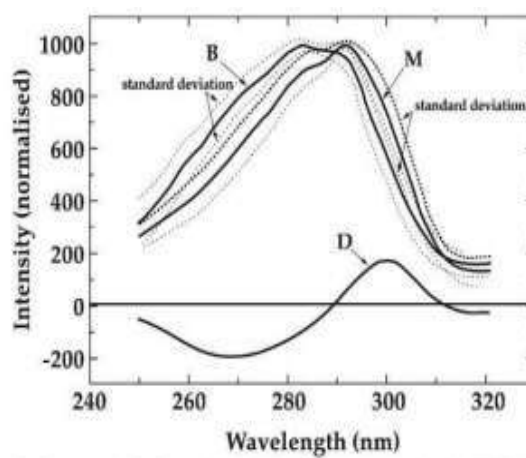
Gupta et al. (24) have measured N<sub>2</sub> laser-excited (337 nm) emission spectra (360–560 nm) from different sites on benign (fibroadenomas, 35 patients), cancerous (ductal carcinomas, 28 patients), and normal specimens (the uninvolved areas of the resected cancerous specimens). Intensities of emission were much higher from cancerous sites compared to those of benign tumour and normal breast tissue sites. In this ex vivo study, cancer tissues have been discriminated from benign and normal ones with a sensitivity and specificity of up to 99.6% using absolute intensity of emission (with aid of stepwise multivariate linear regression statistical method).



**Figure 4.** Mean emission spectra from 245 cancerous (C), 230 normal (N), and 436 benign (B) breast tissue sites. (Adapted from Gupta et al. [16] with permission of John Wiley and Sons.)



Yang et al. (25) have reported the use of excitation spectra for breast cancer detection. They have measured excitation spectra in the 250–320-nm spectral region recording emission at 340 nm from 103 malignant and 63 benign breast tissues. The averaged spectra and their difference distinct spectral features can be clearly evidenced. Authors have estimated above 90% sensitivity and specificity of cancer diagnosis for this method.



**Figure 5.** Averaged excitation spectra for emission at 340 nm from 103 malignant and 63 breast tissues. D is the difference spectrum ( $M - B$ ). B is benign; M is malignant. (Adapted from Yang et al. [17] with permission of John Wiley and Sons.)

## CONCLUSION

Fluorescence spectroscopy has potential for use as a routine diagnostic tool for premalignant and malignant lesions but needs more research studies and clinical trials. There are many aspects that should be discussed in future research. To differentiate between inflammatory and cancerous lesions is a major challenge. Some fluorophores produce broad and overlapping absorption and emission spectra, which makes quantitative measurements very difficult. Also, absorption and scattering phenomena may interfere with the acquired signals from superficial tissue layers.

Improvement in instrumentation and single analysis algorithms will help to increase the sensitivity and efficiency of fluorescence spectroscopy-based diagnostic techniques for cancer diagnostics. Also, there is great need to develop new highly selective fluorophores along with higher emission bands. Skin photosensitization is another challenge that should be overcome with modern research. Time gating of a charge-coupled device camera's intensifier may be helpful to improve the signal-to-noise ratio in fluorescence imaging of cancerous lesions. Combining fluorescence spectroscopy with endoscopy will greatly facilitate the early diagnosis of cancers anatomically deeper inside the human body. Flexible fibres and body core should be designed to meet the demands of a daily medical care practice. Active collaboration between medical scientists, physicians, surgeons, biochemists, and biophysicists is necessary for accommodating fluorescence spectroscopy in daily medical practice in the near future. With advancement in technology and overcoming of limitations, we expect that fluorescence spectroscopy will be a routine diagnostic technique for cancers. Cancer diagnosis at early stages by means of fluorescence spectroscopy will result in early treatment and survival rate will increase greatly.

## REFERENCES

1. J.R. Lakowicz, *Principles of Fluorescence Spectroscopy*, Plenum Press, New York, 1983
2. I.D. Campbell, R.A. Dwek, *Biological Spectroscopy*, Benjamin/Cummings Publishing Co., Menlo Park, CA, 1984. Richards-Kortum, E. Sevick-Muraca, 'Quantitative Optical Spectroscopy for Tissue Diagnosis', *Annu. Rev. Phys. Chem.*, 47, 555–606 (1996).
3. R. Richards-Kortum, 'Fluorescence Spectroscopy of Turbid Media', in *Optical–Thermal Response of Laser Irradiated Tissue*, eds. A.J. Welch, M.J.C. van Gemert, Plenum Press, New York, 667–706, 1995.
4. M.B. Silberberg, H.E. Savage, G.C. Tang, P.G. Sacks, R.R. Alfano, S.P. Schantz, 'Detection of Retinoic Acid Induced Biochemical Alterations in Squamous Cell Carcinoma Using Intrinsic Fluorescence Spectroscopy', *Laryngoscopy*, 104(3), 278–282 (1994)
5. R. Richards-Kortum, E. Sevick-Muraca, 'Quantitative Optical Spectroscopy for Tissue Diagnosis', *Annu. Rev. Phys. Chem.*, 47, 555–606 (1996).
6. L. Stryer, *Biochemistry*, WH Freeman and Company, New York, 1988
7. R. Richards-Kortum, A. Mehta, G. Hayes, R. Cothren, T. Kolubayev, C. Kitrell, N.B. Ratliff, J.R. Kramer, M.S. Feld, 'Spectral Diagnosis of Atherosclerosis Using an Optical Fiber Laser Catheter', *Am. Heart J.*, 118(2), 381 (1989).
8. M. Keijzer, R. Richards-Kortum, S.L. Jacques, M.S. Feld, 'Fluorescence Spectroscopy of Turbid Media: Autofluorescence of the Human Aorta', *Appl. Opt.*, 28, 4286–4292 (1989)
9. S. Prahl, M.J.C. van Gemert, A.J. Welch, 'Determining the Optical Properties of Turbid Media by Using the Adding–Doubling Method', *Appl. Opt.*, 32, 559–568 (1993)
10. Papazoglou, T.G. (1995) Malignancies and atherosclerotic plaque diagnosis—Is laser induced fluorescence spectroscopy the ultimate solution? *J. Photochem. Photobiol.*, 28: 3–11.
11. Vengadesan, N., Aruna, P., and Ganesan, S. (1998) Characterization of native fluorescence from DMBA-treated hamster cheek pouch buccal mucosa for measuring tissue transformation. *Br. J. Canc.*, 77: 391–395.
12. Parmeswaran, D., Ganesan, S., Nalini, R., Aruna, P., Veeraganesh, V., and Alfano, R.R. (1997) Native fluorescence characteristics of normal and malignant epithelial cells of human larynx. *Proc. SPIE*, 2979: 759–764.
13. Alfano, R.R., Tata, D.B., Cordero, J., Tomashefsky, P., Longo, F.W., and Alfano, M.A. (1984) Laser induced fluorescence spectroscopy from native cancerous and normal tissues. *IEEE J. Quant. Electron.*, 20: 1507–1510.
14. Kennedy, J.C. and Pottier, R.H. (1992) Endogenous protoporphyrin IX, a clinically useful photosensitizer for photodynamic therapy. *J. Photochem. Photobiol.*, 14: 275–292.
15. Schomacker, K.T., Frisoli, J.K., Compton, C.C., Flotte, T.J., Richter, J.M., Nishioka, S., and Deutsch, T.F. (1992) UV laser induced fluorescence of colonic tissue. *Laser. Surg. Med.*, 12: 63–78
16. R.M. Lycette, R.B. Leslie, 'Fluorescence of malignant tissue', *Lancet*, 2, 436 (1965)
17. A.E. Profio Profio, D.R. Doiron, E.G. King, 'Laser Fluorescence Bronchoscope for Localization of Occult Lung Tumors', *Med. Phys.*, 6(6), 523–525 (1979).
18. R.R. Alfano, D.B. Tata, J. Cordero, P. Tomashefsky, F.W. Longo, M.A. Alfano, 'Laser Induced Fluorescence Spectroscopy from Native Cancerous and Normal Tissue', *IEEE J. Quantum Electron.*, 20, 1507–1511 (1984).
19. W. Lohmann, 'In Situ Detection of Melanomas by Fluorescence Measurements', *Maturwissenschaften*, 75, 201–202 (1988).
20. Gillenwater, A., Jacob, R., Ganeshappa, R., Kemp, B., El-Naggar, A.K., Palmer, J.L., Clayman, G., Mitchell, M.F., and Richards-Kortum, R. (1998) Noninvasive diagnosis of oral neoplasia based

on fluorescence spectroscopy and native tissue autofluorescence. *Arch. Otolaryngol. Head Neck Surg.*, 124: 1251–1258

21. . Zeng, H., C. MacAulay, D. McLean and B. Palcic (1995) Spectroscopic and microscopic characteristics of human skin autofluorescence emission. *Photochem. Photobiol.* 61, 639–645.
22. Kollias, N., R. Gillies, M. Moran, I. E. Kochevar and R. R. Anderson (1998) Endogenous skin fluorescence includes bands that may serve as quantitative markers of aging and photoaging. *J. Investig. Dermatol.* 111, 776–780
23. Alfano RR, Tang GC, Pradhan A, Lam W, Choy DSJ, Orpher E. Fluorescence spectra from cancerous and normal human breast and lung tissues. *IEEE Journal of Quantum Electronics.* 1987;23:1806–1811. DOI: 10.1109/JQE.1987.1073234
24. Gupta PK, Majumder SK, Uppal A. Breast cancer diagnosis using nitrogen laser excited autofluorescence spectroscopy. *Lasers in Surgery and Medicine.* 1997;21:417–422. DOI: 10.1002/(SICI)1096-9101(1997)21:53.0.CO;2-T
25. Yang Y, Katz A, Celmer EJ, Zurawska-Szezepaniak M, Alfano RR. Fundamental differences of excitation spectrum between malignant and benign breast tissues. *Photochemistry and Photobiology.* 1997;66:518–522. DOI: 10.1111/j. 1751-1097.1997.tb03183.

TITLE OF REVIEW - Producing Oxygen using 13X zeolite by PSA method.

NAME OF THE INSTITUTION - Scottish Church College

C.U. ROLL NO - 223/CEM/191026

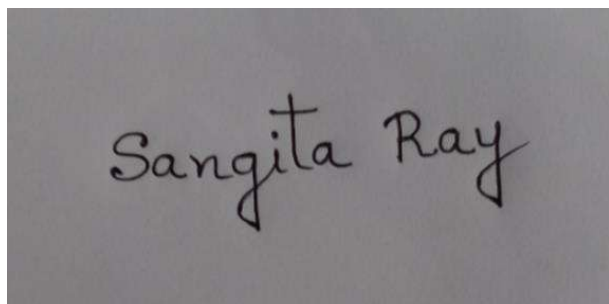
C.U. REGISTRATION NO - 613-1221-0683-16

SPECIAL PAPER : CHEM- SO 44

NAME OF CANDIDATE

Sangita Ray

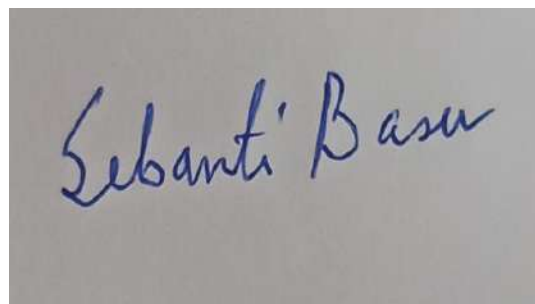
SIGNATURE OF CANDIDATE

A photograph of a handwritten signature in black ink on a light-colored background. The signature reads "Sangita Ray" in a cursive script.

NAME OF EXAMINER

Dr. Sebanti Basu

SIGNATURE OF EXAMINER

A photograph of a handwritten signature in blue ink on a light-colored background. The signature reads "Sebanti Basu" in a cursive script.

## ACKNOWLEDGEMENT:

The review 'Producing Oxygen using 13X zeolite by PSA method' has provided me with an ample scope of learning through collaborative activities. I consider myself fortunate enough to work under Dr. Rama Ranjan Bhattacharjee whose guidance made my review work learning quite joyful. He has given important suggestions for the improvement of the review work. I am grateful to him.

I am also very thankful to Dr. Sebanti Basu, Associate professor, Scottish Church College for her continuous support.

I would like also to thank Dr. Sourav Chakrabarty, Assistant Professor, Scottish Church College for his precise suggestions which were very helpful to the accomplishment of the review work.

And I am also grateful to my parents and my friends who have helped me to carry out the review.

## CONTENT:

Introduction	1
Reason behind choosing zeolite	1
Why 13X zeolite	2
Table – 1 (Properties of zeolite)	3
Adsorption phenomena	4
A short view of PSA process	4-7
Methods of pressure swing adsorption	7-9
Table – 2 (Details of PSA Columns and Adsorbent)	9
Discussion of experimental work (two columns 4 step and 6 step)	9-15
Animation picture of PSA method	16
Consideration for Mathematical Model	17
Result and discussion (for Dynamic modeling of N <sub>2</sub> adsorption on 13X bed)	17-21
Conclusion	21
Future Scope	21
References	22-24

## Introduction:-

One of the most important clinical gas used in health care center is oxygen. There are no modern hospitals and nursing home which can manage without oxygen. Pure oxygen is too much essential for the respiration of the patients during anesthesia and in the intensive care or neonatal units<sup>[1]</sup>. Now in this covid pandemic situation oxygen is really too much necessary for survival of covid +ve patients. The challenge is appeared by increasing supply of medicinal oxygen with reducing cost<sup>[2]</sup>. In 1907, Linde built a first cryogenic distillation bed for air separation and this time oxygen was first produced<sup>[3]</sup>. Besides this in chemical industries oxygen is too much necessary for various processes like refinery industries, manufacturing metal etc. The most commonly adsorbent used in air separation for producing oxygen is zeolite 13X<sup>[4]</sup>. Here desorption and adsorption process mainly occurs. There are many process exists for separation of air to produce purified oxygen. Among them pressure swing adsorption (PSA) is very popular in the market because it is a safe process with reasonable energy and area requirements<sup>[1]</sup>. At first Skarstrom in 1958 proposed the simplest PSA process. Till now there are many process arises using different types of adsorbent for this purposes to purify oxygen. Farooq et al,(1989) used zeolite-5A for producing oxygen using PSA method by performing Sakrstrom cycle. In 1990 Keny and Liow used 5A zeolite for air separation<sup>[5]</sup>. But zeolite 13X is used in a wide range because it has outstanding nitrogen to oxygen adsorption selectivity. In recent time 13X zeolite is modified with Li<sup>+</sup> exchange method which shows a higher nitrogen adsorption capacity at the active cation sites of the zeolite framework<sup>[6]</sup>. Besides this zeolite 13X has large mass transfer zone, so the adsorption rate is high. Nitrogen concentrations mainly drop in the outlet of the zeolite 13X at the time of about 125 seconds and the concentrations reaches zero after about 180 seconds<sup>[3]</sup>.

## Reason behind choosing zeolite as a molecular sieve :

Porous materials are those materials which contain void space. There are many types of porous materials such as rocks and soil, zeolites, biological tissues and artificial materials such as cements and ceramics etc. The characteristics of a porous material vary depending on the size, arrangement and shape of the pores, as well as the porosity and composition of the material itself (porous materials latest research). According to the IUPAC, pores are classified into three categories, these are micropore – (pore sizes less than 2nm), mesopore (between 2 and 50 nm) and macropore ( with pore size larger than 50 nm)<sup>[8]</sup>. For PSA method zeolite is chosen as adsorbent. Zeolite has microporous crystalline structures. Zeolite framework is an assemblage of SiO<sub>4</sub> and AlO<sub>4</sub> tetrahedral joined together by sharing oxygen atoms<sup>[9]</sup>. This type of microporous solid such as zeolite (aluminosilicate member) is known as molecular sieves. Zeolite molecular sieve contains very small pores of uniform size<sup>[10]</sup>. Zeolite adsorbent has the selectivity to adsorb



nitrogen compared to oxygen because of the interaction between electrostatic field of the cationic zeolite and the quadrupole moment of the nitrogen and oxygen. The quadrupole of oxygen is three times lesser than that of nitrogen. And this fact leads to a selective adsorption on to the zeolite surface<sup>[6]</sup>.

## Why 13X zeolite:

So zeolite adsorbs nitrogen like it sponge adsorbs water . Converting medical air to medical oxygen using 13X zeolite is very practical. However LiX material is a good adsorbent for adsorption of nitrogen at ambient pressure and releases under vacuum. The operations are simpler and the system built will be simple and accomplished. But Lithium X can not be easily sourced in India. So the technology has to be based on more readily available 13X molecular sieve zeolite. Substitution of LiX by 13X change the operation from vacuum based to a pressure based (VPSA to PSA)<sup>[11]</sup>. There are three types of zeolite structure become dominant such as A,X and Y<sup>[1]</sup>. 13X zeolite is the sodium form of the type X crystal. It has pore diameter of 1nm . So it will adsorb molecules of A crystalline form that is 3 Angstrom,4 Angstrom and 5 Angstrom<sup>[7]</sup>. Zeolite 13X has the chemical formula  $\text{Na}_{86}[(\text{AlO}_2)_{86}(\text{SiO}_2)_{106}] \cdot \text{H}_2\text{O}$  having pore diameter less than 10 Angstrom( 1nm). X crystalline foam has a larger pore size than other types .

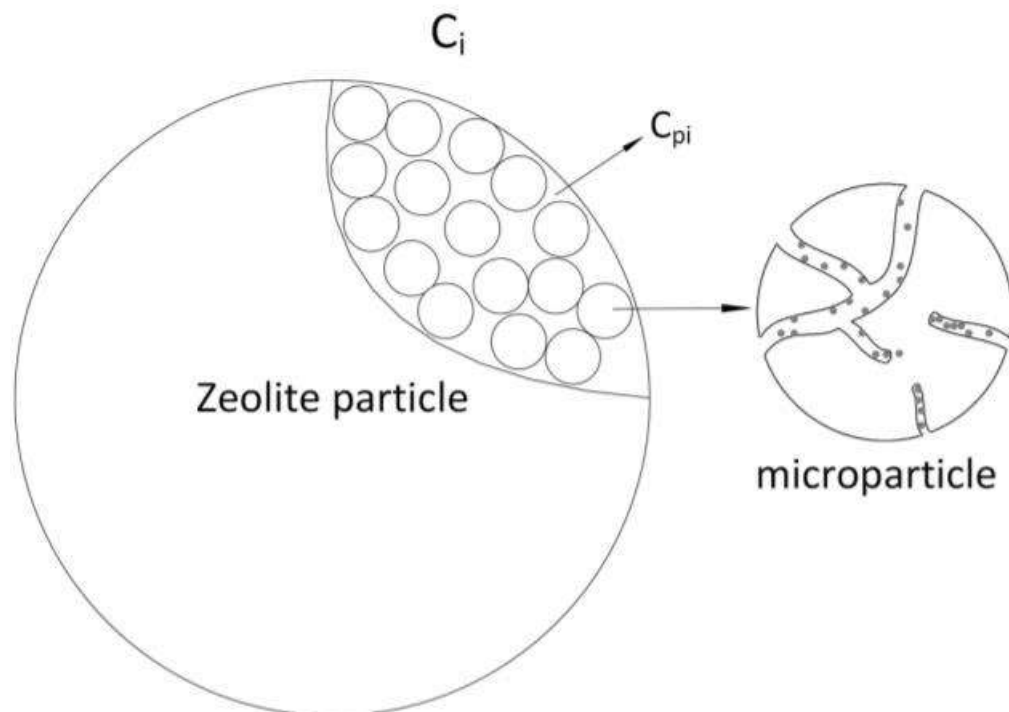
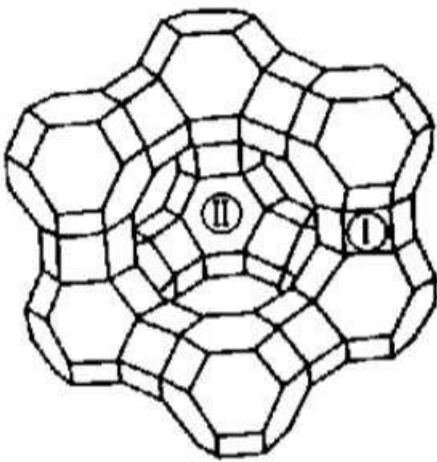


Figure-1 Schematics of zeolite particle structure<sup>[6]</sup>.

Table – 1 (Properties of zeolite)<sup>[19]</sup>

Chemical name	Na <sub>86</sub> [(AlO <sub>2</sub> ) <sub>86</sub> (SiO <sub>2</sub> ) <sub>106</sub> ]•H <sub>2</sub> O
Pore Diameter	~8Å
Mesopore volume	0.165 cm <sup>3</sup> /g
Micropore volume	0.17 cm <sup>3</sup> /g
Langmuir surface area	571 m <sup>2</sup> /g
Mass of pellet sample	2.37 g
Mass of crushed sample	2.49 g



Zeolite 13X molecular structure

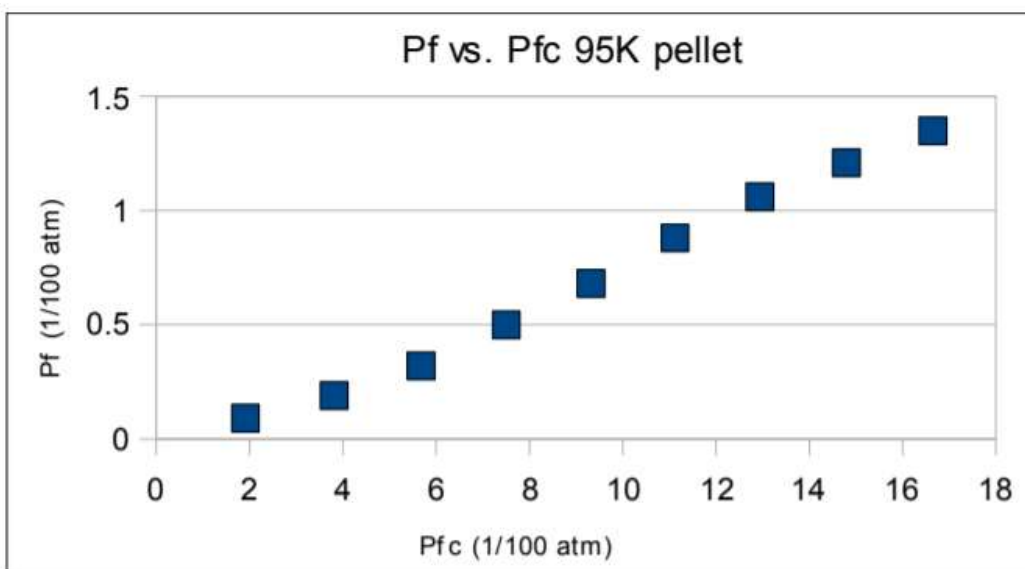
Figure-2<sup>[19]</sup>

Figure-3

Adsorption of nitrogen in zeolite 13X pellet at 95K<sup>[19]</sup>.

## Adsorption phenomena in PSA method:

Adsorption is the phenomenon where molecules of one phase remain preferentially concentrated at the surface of another phase<sup>[22]</sup>. Generally, gas adsorption in zeolite are of two types named physisorption and chemisorption. But physisorption is more preferable method for gas separation and purification because of the fact that the adsorbent can be regenerated by heating or flushed to remove the adsorbed gas molecules attaching to the solid. This make the process more economical and profitable<sup>[9]</sup>.

## A short view of PSA process:

Pressure swing adsorption is an industrial process which is generally used for the bulk separation of gas mixtures. It is a cyclic operation<sup>[12]</sup>. In 1960, Skarstrom patented the first PSA unit which was composed of two beds and using a zeolite<sup>[13]</sup>.

Stage 1- Compressed air is passed into the first bed. Nitrogen molecules are trapped and oxygen molecules is allowed to flow through.

Stage -2- At the time of saturation of the adsorbent in the first bed with nitrogen, the air flow feed is directed towards the second bed.

Stage -3- Nitrogen was adsorbed by the adsorbent (13X zeolite) in the second bed. The first bed is depressurized allowing nitrogen to be loosen out of the system and released to the atmosphere.

Stage- 4- The process starts over. Again compressed air is fed into the first bed. The second bed is relaxed by releasing nitrogen and oxygen to the atmosphere. The process is repeated continuously producing a constant flow of purify oxygen<sup>[14]</sup>.

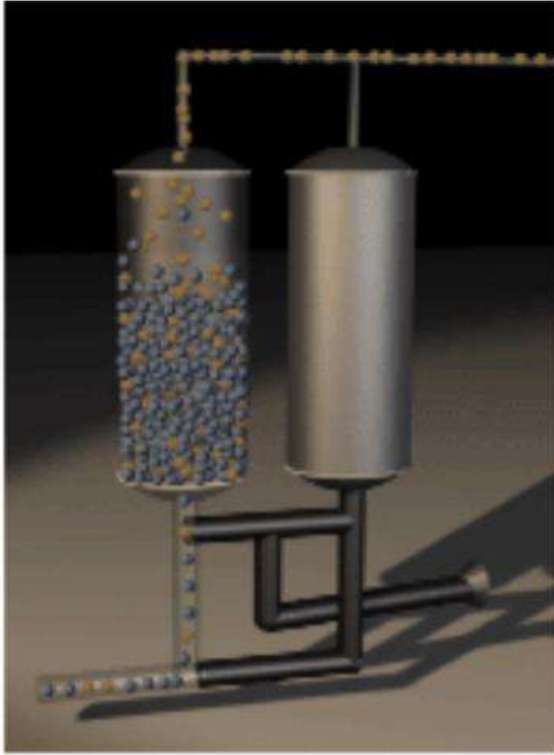


Figure-4<sup>[14]</sup> Stage – 1

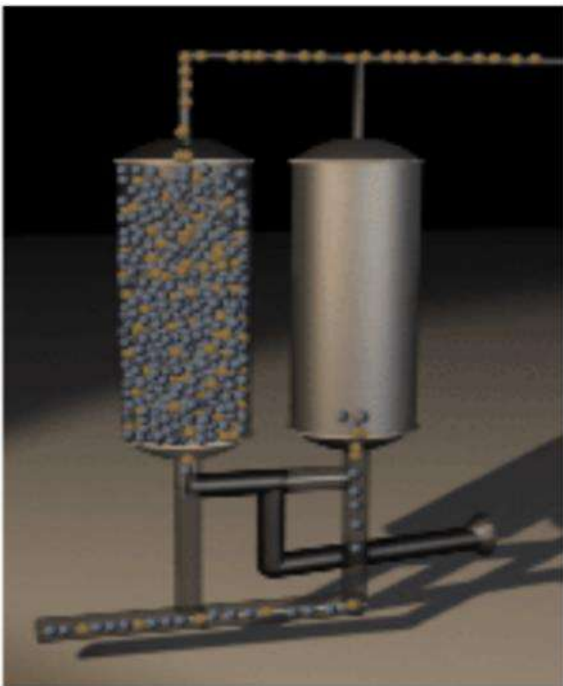


Figure-5<sup>[14]</sup> stage – 2

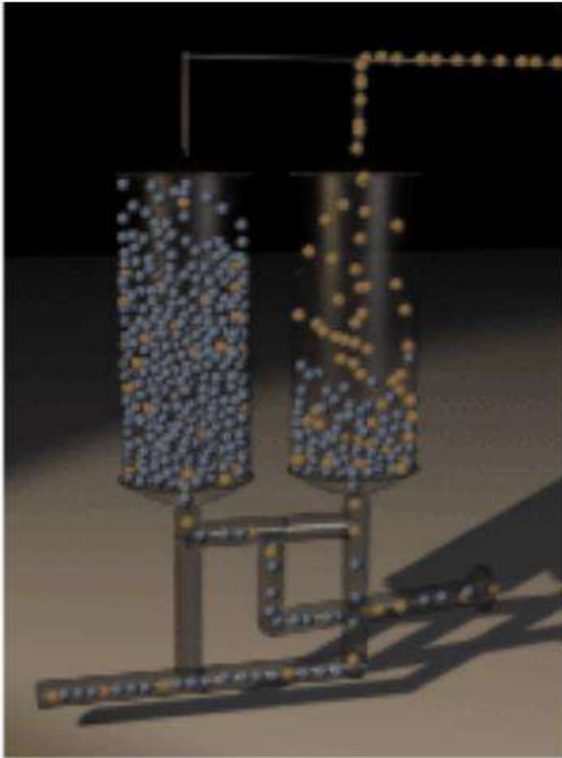


Figure-6<sup>[14]</sup> Stage – 3

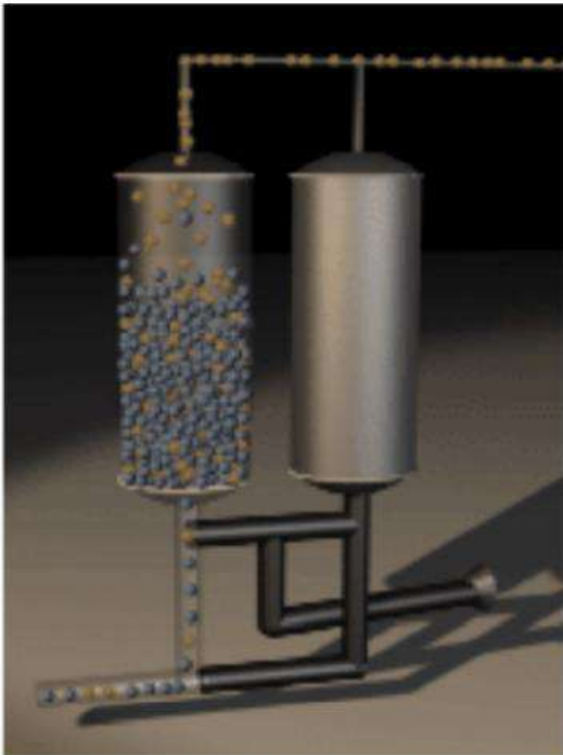


Figure-7<sup>[14]</sup> Stage – 4

Oxygen production using 13X zeolite by using PSA process has noticeably increased in the past decades. But the concentration of the products is limited to 95% oxygen due to presence of argon in air. Because the adsorbent present has the similar adsorption capacities for oxygen and argon. Actually in PSA cycle desorption take place at a pressure much lower than adsorption<sup>[15]</sup>.

There are many application observed for PSA unit such as producing oxygen for medical use. In 1975 this unit was started to use in a wide range for treating patient with respiratory illness. This provide 2-4 L/min of 85-95% oxygen. In this year Ruder and Isles also patented a PSA unit for producing enriched air(use onboard jet aircraft) (U.S. Patent 3,922,149). Just one year latter an electric powered compact PSA apparatus (DE Patent 2,559,120) was described by Armond. He use zeolite molecular sieve to generate breathing air for medical use. In 1984, Kratz and Sircar patented a medical oxygen generator for domiciliary use (U.S.Patent 4,477,265). This process generated 90% of oxygen<sup>[16]</sup>.

In this work, nitrogen adsorption process using 13X zeolite as a molecular sieve is simulated. So the process is dynamic<sup>[4]</sup>.

## Method of pressure swing adsorption

### Equilibrium adsorption

Air mainly contains three components, nitrogen, oxygen and argon. In between 1916 to 1918, Langmuir proposed the theoretical basis of adsorption which is based on kinetic theory of gases<sup>[17]</sup>. This phenomena explain the type 1 adsorption curve(HKC). Multicomponent adsorption equilibria theory (competition between the different molecules on the adsorbent) is required for designing purposes.

$$\theta_i = \frac{b_i P_i}{1 + \sum_{j=1}^N b_j P_j} \quad (\text{Equation 1})$$

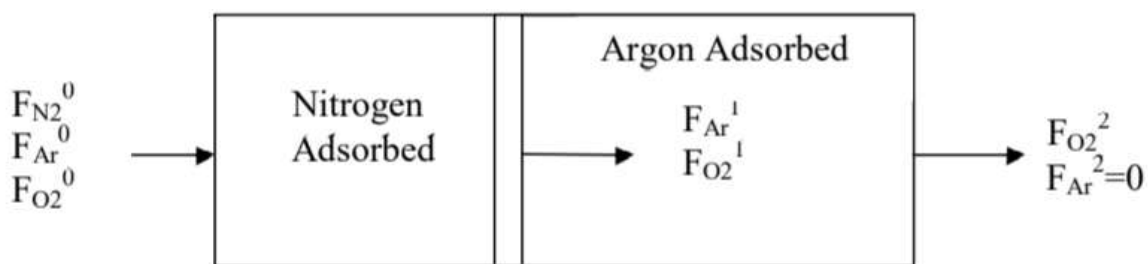
Fractional loading contributed by  $\theta_i$  and  $i$ .

$b_i$  and  $b_j$  are the rate constants of adsorption to that for desorption for component  $i$  and component  $j$  respectively.  $P_i$  – Partial pressure of component  $i$ ,  $P_j$  – Partial pressure of component  $j$ .  $N$  is the number of species.

Equation 1 gives the adsorbed amount of species  $i$  on the adsorbent in the multi component system. The selectivity describes how one species is selective to bind to the adsorbent over another species. The selectivity of a species  $i$  in relation to species  $j$  is given as

$$S_{i,j} = \frac{b_i}{b_j} \quad (\text{Equation 2})$$

A transport phenomena is observed to study how each species is adsorbed in the adsorbent bed. Material balance equations are used to determine these parameters.



Air component through adsorbent bed<sup>[1]</sup>.

Material balances are performed for the components in each section of the adsorbent bed.

$$\text{Nitrogen : } F_{N_2}^0 \Delta t = \Delta L_1 A N_{N_2}^1 = v_1 A N_{N_2}^1 \quad (\text{Equation 3})$$

$$\text{Oxygen: } F_{O_2}^1 = F_{O_2}^0 + (N_{O_2}^2 - N_{O_2}^1) A v_1 \quad (\text{Equation 4})$$

$$\text{Argon: } F_{Ar}^1 = F_{Ar}^0 + (N_{Ar}^2 - N_{Ar}^1) A v_1 \quad (\text{Equation 5})$$

$$F_{Ar}^2 = 0 = F_{Ar}^1 + N_{Ar}^2 A v_2 \quad (\text{Equation 6})$$

Here,  $F$  stands for volumetric flowrate,  $\Delta t$  is the cycle time,  $\Delta L$  is the length of the bed,  $A$  is the area,  $N$  is the loading and  $v$  is the front velocity.

The velocity of the argon front must be greater than nitrogen front.

$$\frac{v_2}{v_1} = \frac{\frac{F_{Ar}^0}{F_{N_2}^0} + (N_{Ar}^2 - N_{Ar}^1)}{N_{Ar}^2} > 1 \quad (\text{Equation 7})$$

Nitrogen molecule has strong electrostatic interaction with 13X zeolite than do oxygen and argon molecules. The front moves with nitrogen front's velocity as a function of the adsorption and desorption of the molecules on the adsorbent sites. So nitrogen has a slower rate of desorption than oxygen and argon. So the velocity front of argon to nitrogen is greater than one<sup>[1]</sup>.

To get greater flexibility Langmuir–Freundlich equation is used which is

$$q = q_m(T) \frac{b(T).p^{n(T)}}{1+b(T).p^{n(T)}} \quad (\text{Equation 8})^{[21]}$$

## Details of PSA Columns and Adsorbent

Table-2<sup>[13]</sup>

Adsorbers		
Column Length	L	0.7 m
Column diamete	D	50 mm
Adsorbent Type		13X zeolite
Shape		Sphere
Particle diameter	$d_p$	1.7-2.6 mm
Particle density	$\rho_p$	1070 kg/m <sup>3</sup>
Bulk density	$\rho_B$	670 kg/m <sup>3</sup>
Bed porosity	$\epsilon$	0.4
Adsorbent weight	w	0.75 kg
Adsorbent bed length	$L_B$	0.57 m
Langmuir isotherm parameters	$q_{sO_2}$	3.091 mol/kg
Oxygen	$b_{O_2}$	0.0367 bar <sup>-1</sup>
Adsorption heat of O2	$\Delta H_{O_2}$	12.8 kJ/mole
Nitrogen	$q_{sN_2}$	3.091 mol/kg
	$b_{N_2}$	0.1006 bar <sup>-1</sup>
Adsorption heat of N2	$\Delta H_{N_2}$	17 kJ/mole

## Discussion of the experimental work for two column 4 step and 6 step PSA operation.

Two column: 4 step and 6 step PSA operation .

- Pressurizing time  $t_{prs} = 10$  s
- Depressurizing time  $t_{deprs} = 10$  s
- Equalization time  $t_{eq} = 20$  s

The operating parameters considered in the present work with their ranges are as follows; Adsorption time  $t_{ads} = 10, 20, \text{ and } 30$  s ,Adsorption pressure  $P_H = 2, 3, \text{ and } 4$  bar , Purge flow rate  $Q_{purg} = 1, 1.5, 2, 3, 4, 5, \text{ and } 6$  L/min<sup>[13]</sup>.



## Two Column Adsorption:

The PSA system preparation shown in figure using vacuum and O<sub>2</sub> pressurizing and purging to ensure the zeolite activity<sup>[13]</sup>.

Figure- 8 shows that the effect of adsorption on oxygen purity. Figure -9 shows that no noticeably change occurred between the pressure ratios 2 and 4 bar. This result is in agreement with that performed by Jee et al. (2001) for high purge to feed ratio, Yuwen et al.(2005). Jain et al (2003) stated that for constant selectivity systems, performance increases with increasing pressure according to adsorption equilibrium isotherm.

In figure- 10 it can be seen that breakthrough occurs at high adsorption time. Adsorption Step duration is needed for needed for breakthrough to occur<sup>[13]</sup>.

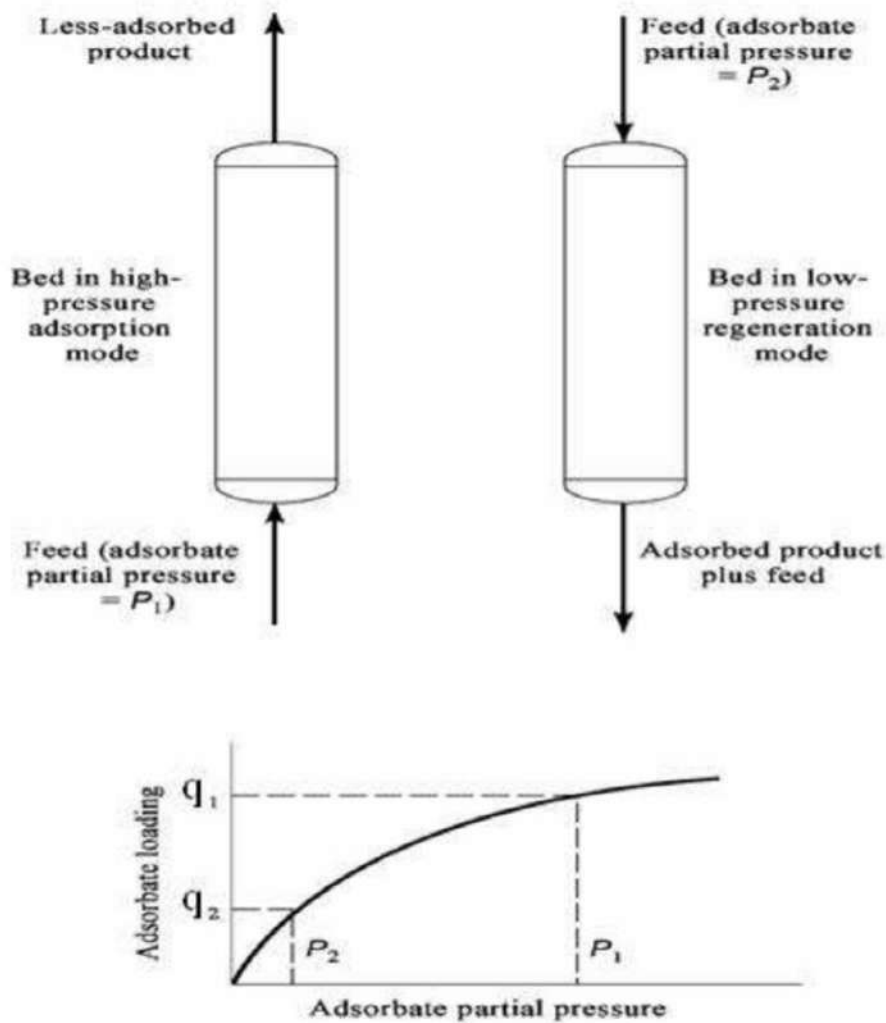


Figure – 8 Pressure swing cycle<sup>[13]</sup>.

## Product Oxygen Cycle for 4- step cycle

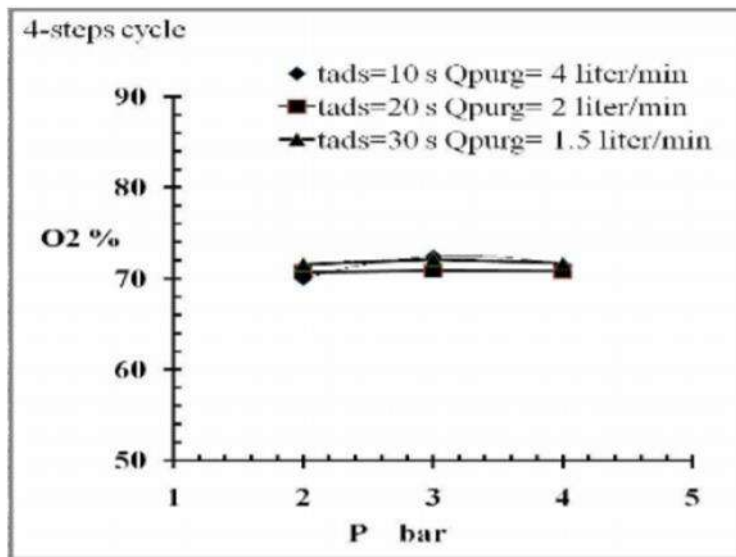


Figure - 9 The effect of the adsorption pressure ( $p_H$ ) on product oxygen purity for 2-column, 4-step operation<sup>[13]</sup>.

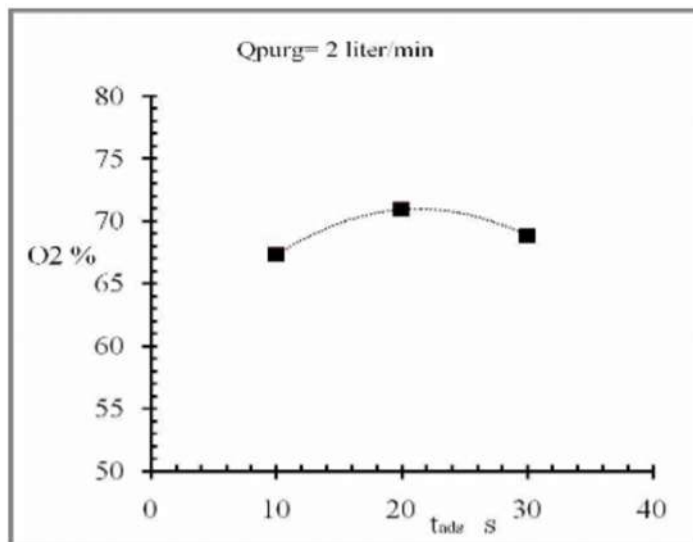


Figure - 10 Effect of the adsorption time ( $t_{ads}$ ) on product oxygen purity for 2-column, 4-step cycle, ( $Q_{purg}=2\text{ l/min}$ )<sup>[13]</sup>.

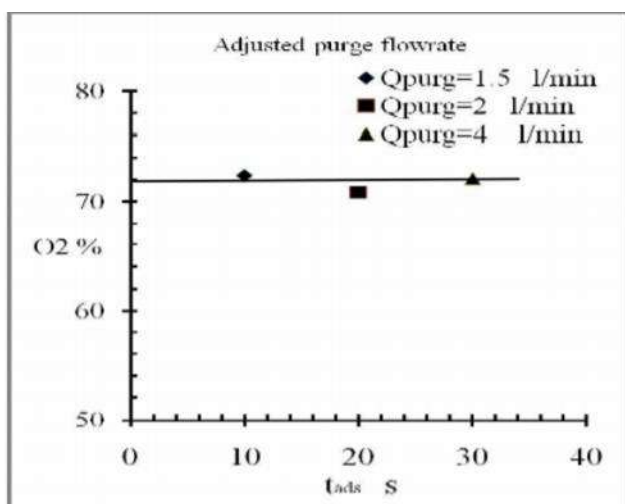


Figure -11 8 Effect of adsorption time ( $t_{\text{ads}}$ ) on product oxygen purity, for 4-step cycle, by adjusting the purge flowrate ( $Q_{\text{purg}}$ )<sup>[13]</sup>.

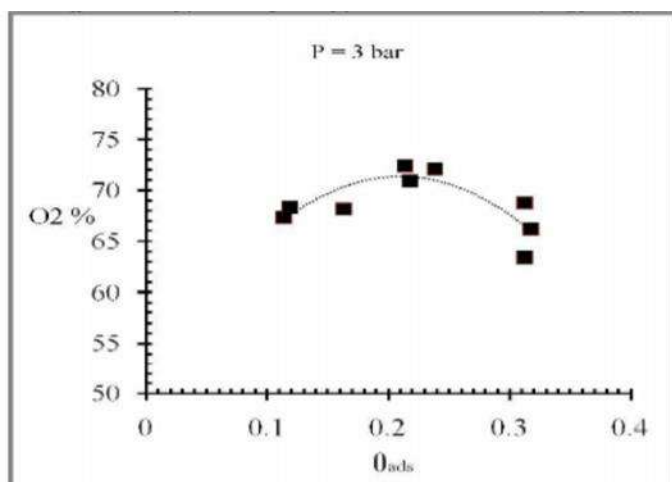


Figure- 12 9 Effect of the dimensionless adsorption time on product oxygen purity for 2-column, 4-step operation<sup>[13]</sup>.

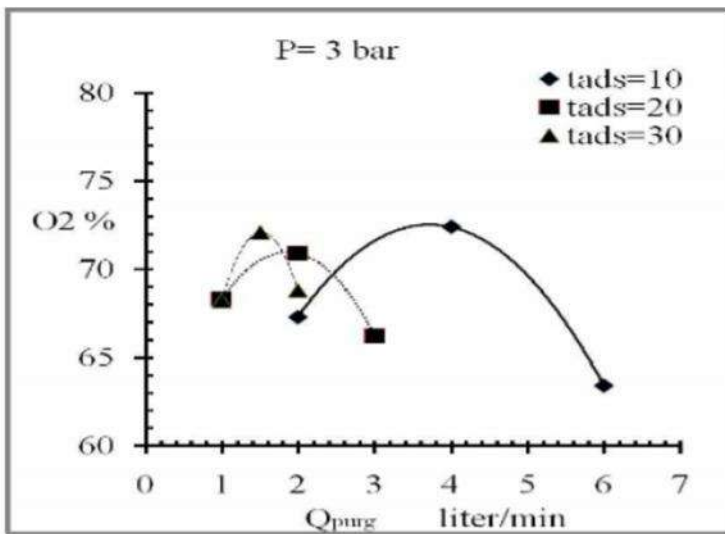


Figure- 13 The effect of the Purge Flow rate ( $Q_{\text{purg}}$ ) on product oxygen purity, for 2-column, 4-step cycle<sup>[13]</sup>.

From this Figure- 13 it is revealed that the nitrogen wave front is breakthrough. The maximum product oxygen is 70% pure because of both the effect of purge flowrate( $Q_{\text{purg}}$ ) and the adsorption time( $t_{\text{ads}}$ ).

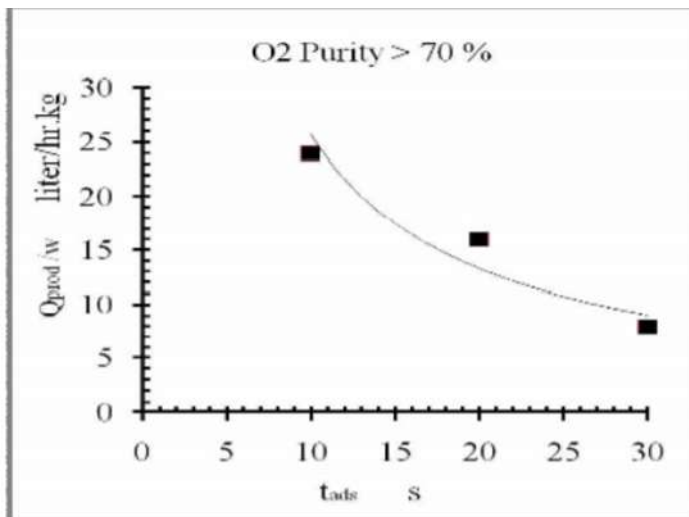


Figure-14 The effect of the adsorption times ( $t_{\text{ads}}$ ) on specific product Flowrate ( $Q_{\text{purg/w}}$ ) at maximum product oxygen purity<sup>[13]</sup>.

Product Oxygen Purity for 6- step cycle:

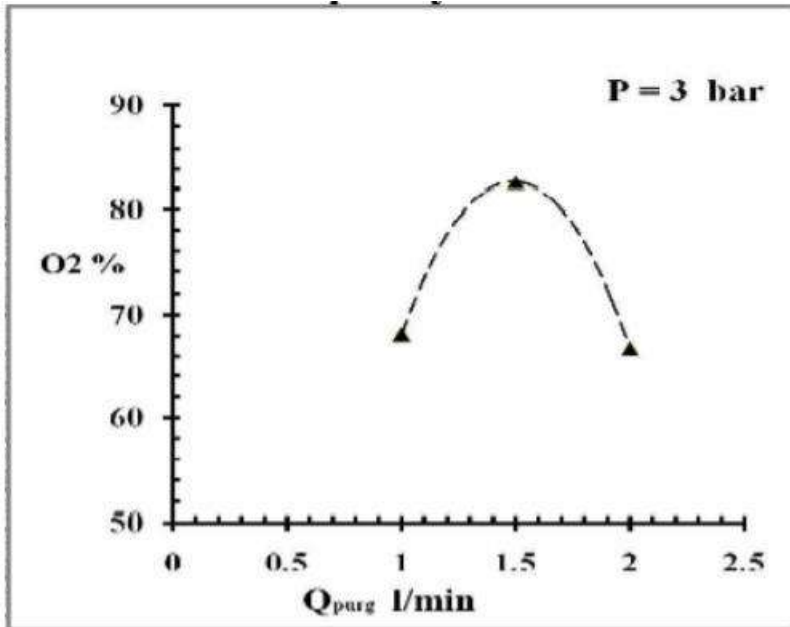


Figure -15 The effect of the purge flowrate ( $Q_{\text{purg}}$ ) on product oxygen purity for 6-Steps cycle, with air feed initial pressurizing<sup>[13]</sup>

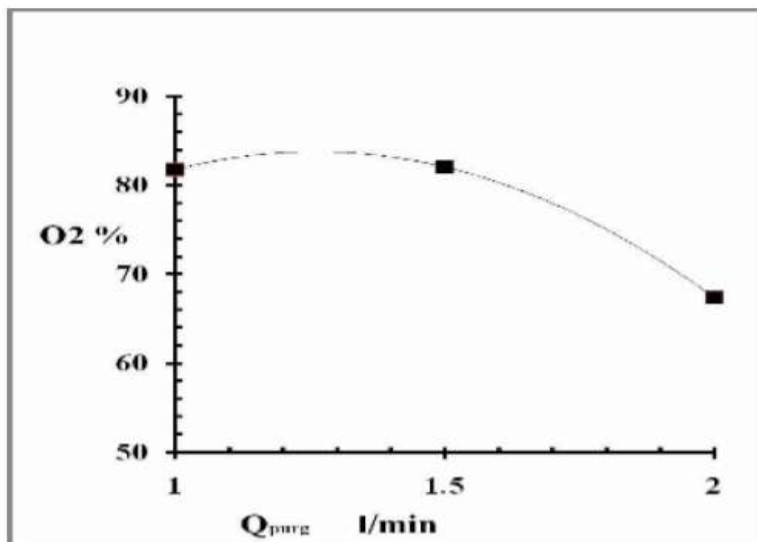


Figure -16 The effect of the purge flowrate ( $Q_{\text{purg}}$ ) on product oxygen purity for 6-Steps cycle, with O<sub>2</sub> initial pressurizing<sup>[13]</sup>.

Figure-16 shows that, with increasing purge flowrate above 1.5 lit/min , product purity decreases to that breakthrough point forming high effluent from the column<sup>[13]</sup>.

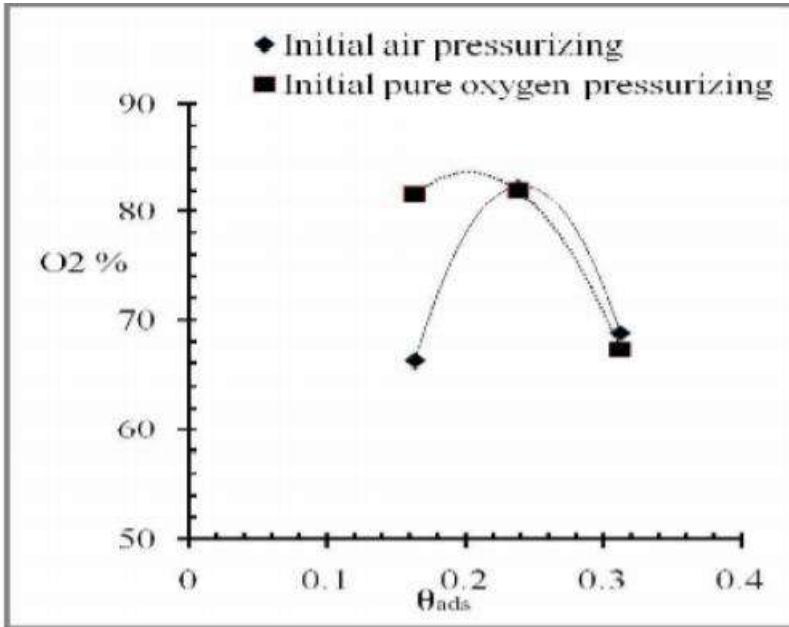


Figure -17 Effect of the dimensionless adsorption time ( $t_{ads}$ ) on product oxygen purity for 2-column, 6-step cycle<sup>[13]</sup>.

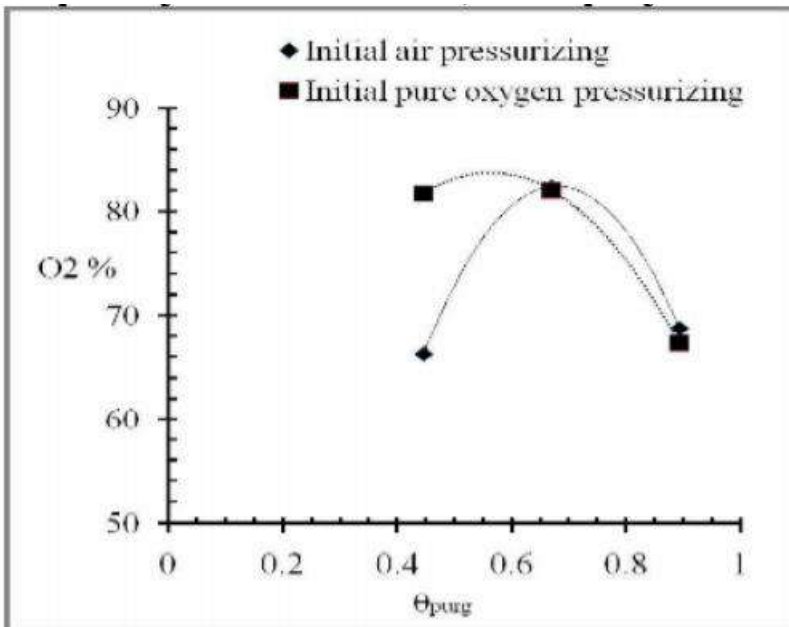
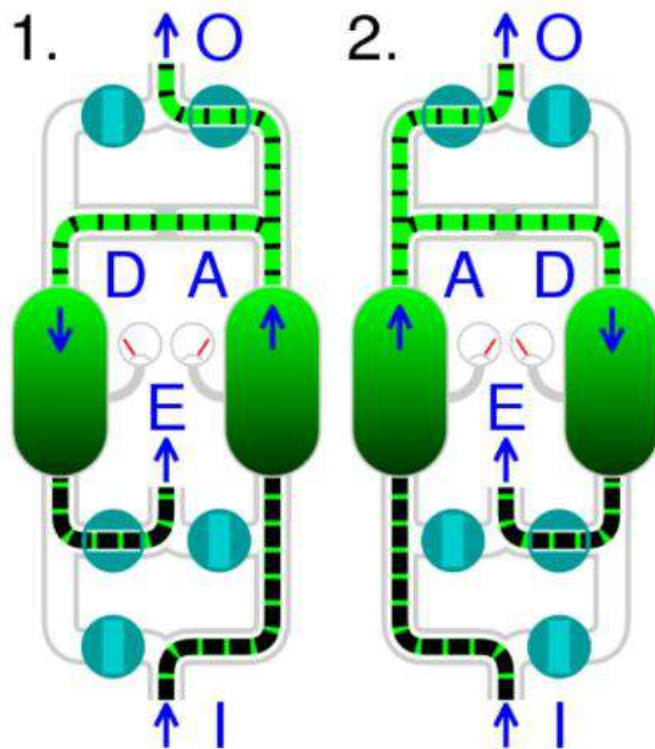


Figure -18 Effect of the dimensionless purge time ( $Q_{purg}$ ) on product oxygen purity for 2-column, 6-step cycle<sup>[13]</sup>



Animation of pressure swing adsorption, (1) and (2) showing alternating adsorption and desorption

I compressed air input    A adsorption  
 O oxygen output            D desorption  
 E exhaust

Figure– 19<sup>[20]</sup>

## Consideration for Mathematical Model for Dynamic modeling of N<sub>2</sub> adsorption on 13X bed.:-

To develop a mathematical model for adsorption bed, the following assumptions must be considered.

- Gas behaves as an ideal gas.
- The flow pattern is axially assumed as plug-flow model.
- Equilibrium equations for air are expressed as triple Langmuir-Freundlich isotherm (oxygen, nitrogen and argon);
- Mass transfer rate is presented by linear driving force (LDF) relations;
- At initial state bed is clean and there is no gas flow in it;
- Air is considered a mixture of oxygen and argon (21 %) and nitrogen (79 %) as feed<sup>[4]</sup>.

A four bed pressure swing adsorption for oxygen separation from air was proposed by Zahra et al(2008)<sup>[5]</sup>. Recently in 2017 Kakavandi et al proposed a dynamic modeling of nitrogen adsorption on 13X zeolite using two bed.

## Result and discussion :

The fourth order Runge-Kutta Gill method was used to solve the mathematical model. An experimental and simulation observation of the PSA unit running with a traditional Skarstrom cycle and a Skarstrom cycle with concurrent equalization in an attempt to separate oxygen from air using a 5A zeolite has been proposed by Mendes et al. Moreover, a small-scale two-bed six-step PSA process using zeolite 13X was performed by Jee et al.

Figures 20 and 21 indicate the effect of product flow rate and P/F on the purity and recovery of oxygen during PSA process, respectively<sup>[3]</sup>.



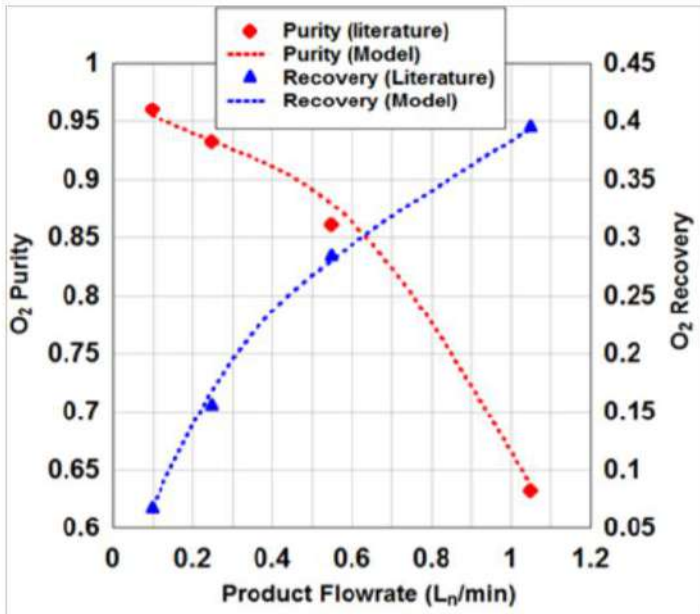


Figure -20<sup>[3]</sup>

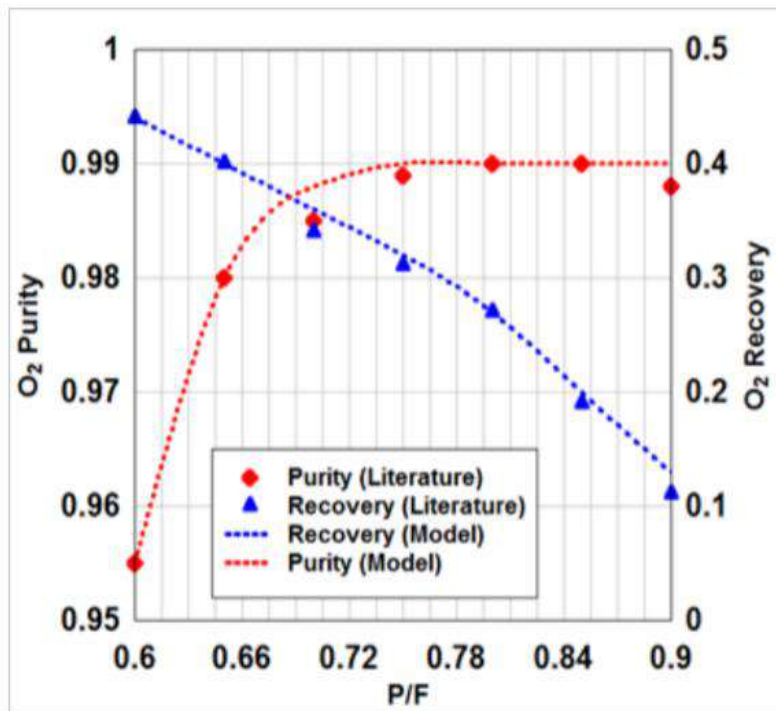


Figure-21<sup>[3]</sup>

Break through curves for nitrogen and oxygen on zeolite 13X is shown in the following Figure. The term “break through time” is developed by the response of initially clean bed per a flow with

constant composition. In Figure – 22 it is shown that oxygen exists from the top of the 13X zeolite earlier than nitrogen at about approximately 230 seconds.

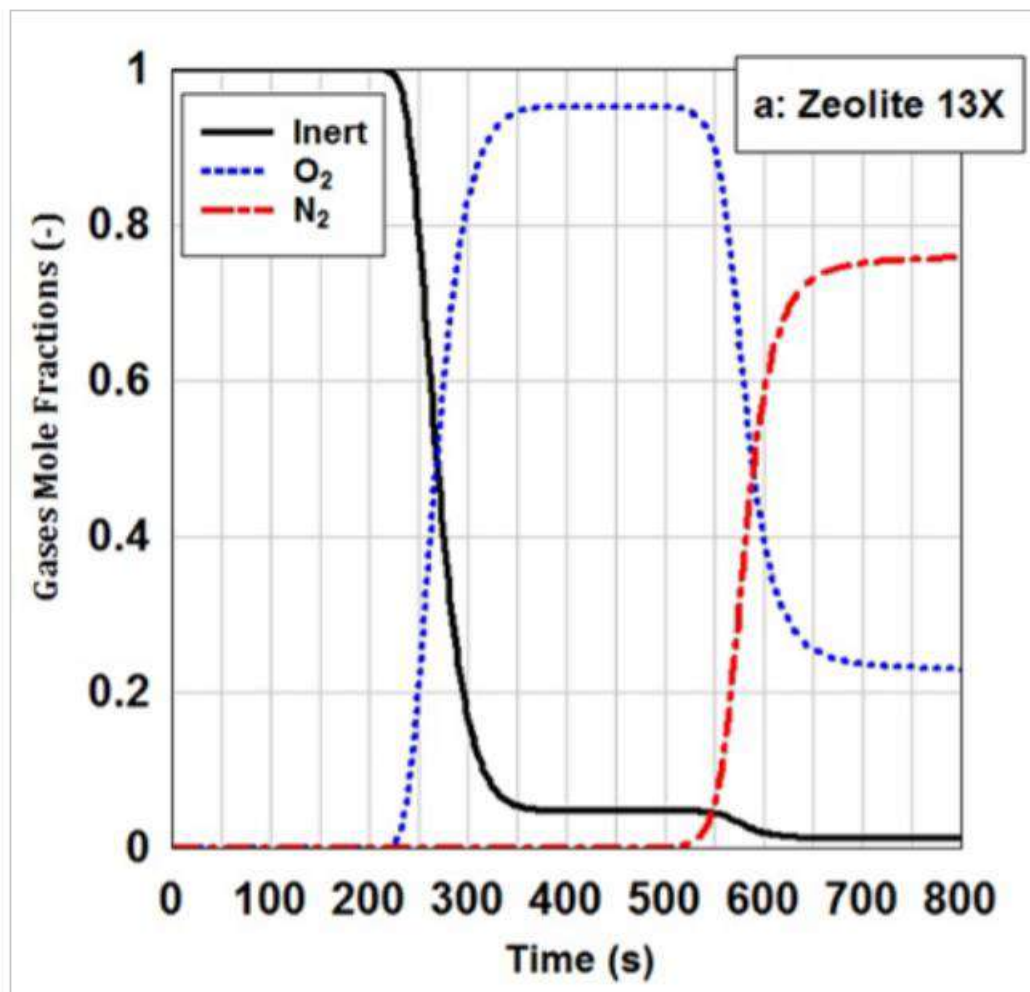


Figure -22<sup>[3]</sup>

(The simulated breakthrough curves of zeolite 13X for oxygen and nitrogen at adsorption pressure of 6 bar and feed flow rate of 5 LSTP/min. The adsorption bed was initially saturated with a non-adsorptive gas.)

With passing of time High roll-up phenomena is observed in case of oxygen. Because of this phenomena oxygen concentration is 4.5 times greater than feed concentration during the time of 400-500 seconds. Oxygen is affected by this phenomena because nitrogen adsorption on 13X zeolite is much more than that of oxygen. So oxygen concentration is relatively increased rather than feed concentration. Nitrogen breakthrough occurs at the time of 550 seconds and from this time oxygen concentration is starting to be reduced. In Figure- 22, it is clearly said that High roll-up phenomena in the case of nitrogen because of its strong adsorption on zeolite 13X. In PSA cycle adsorption and desorption process depends on pressure increasing and decreasing<sup>[18]</sup>.

Figure - 23 says that nitrogen concentration on zeolite 13X with respect to different adsorption pressures and time. With increasing pressure adsorption rate, of nitrogen increases. Figure- 24

says oxygen concentration along the bed length of the adsorbent (13X zeolite) in different times. The slope of oxygen concentration curve is fast. The desorption curve of zeolite 13X is depicted in Figure 25. The assumption is that a pure inter gas is utilized for cleaning the bed in order to simulate desorption over the beds<sup>[3]</sup>.

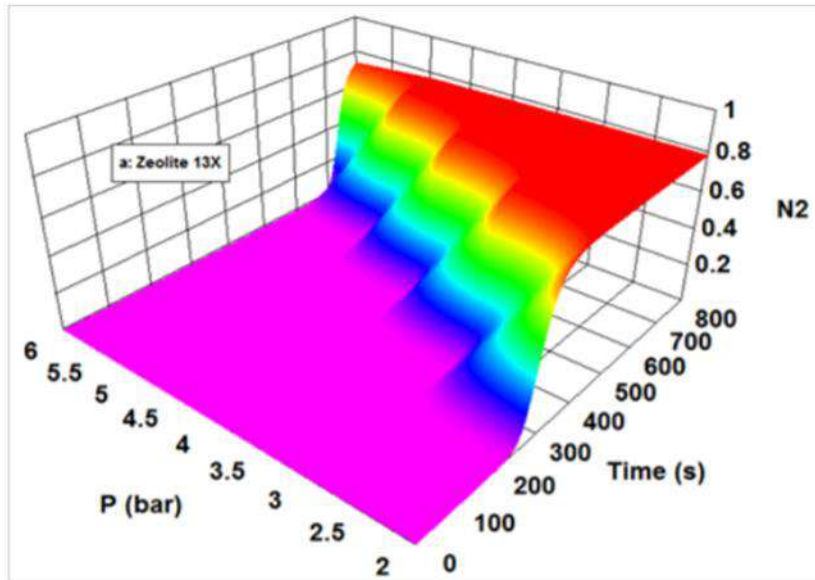


Figure -23 The outlet mole fraction of nitrogen from zeolite 13X at different adsorption pressures and feed flow rate of 4LSTP/min. The adsorption bed was initially saturated with a non-adsorptive gas<sup>[3]</sup>.

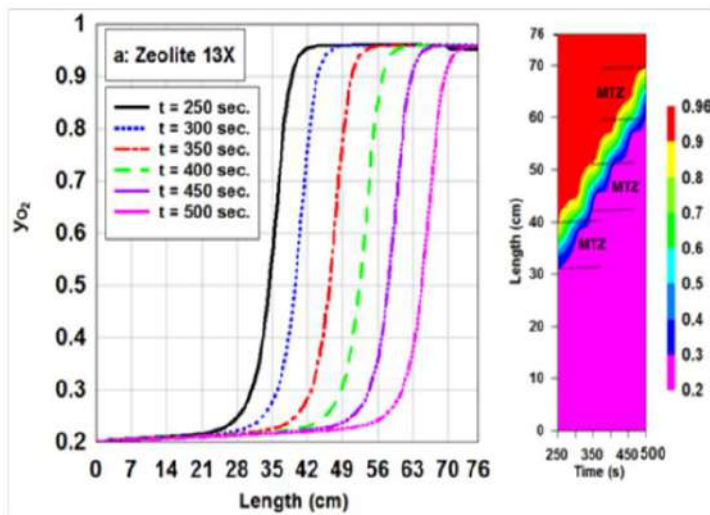


Figure – 24 Distribution of oxygen concentration along the length of zeolite 13X during adsorption process in different times. The feed flow rate is 5LSTP/min and the adsorption pressure is 6 bar<sup>[3]</sup>.

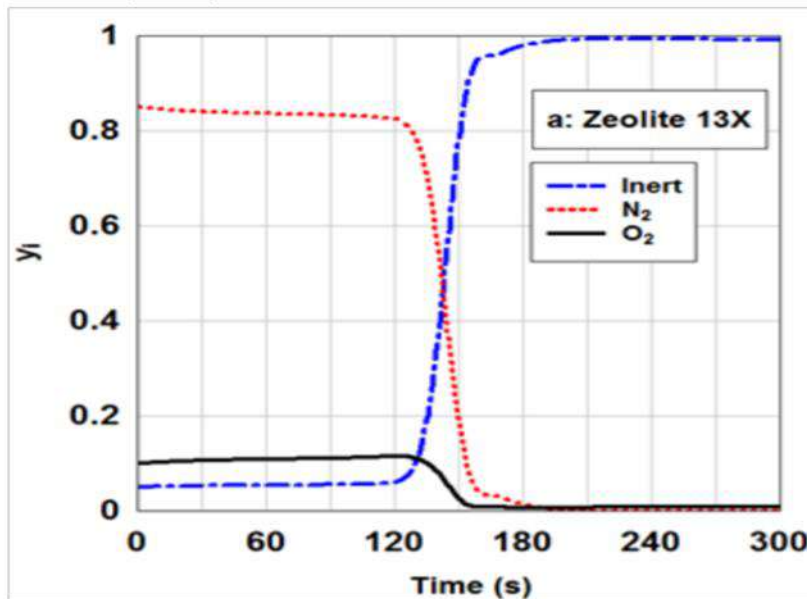


Figure – 25 The outlet

simulated concentration of gas phase from zeolite 13X during desorption at pressure of 0.1bar. The desorption bed was completely clean in the initial state<sup>[3]</sup>.

## Conclusion:-

It has been discussed that how the PSA process using 13X zeolite is effective to produce pure oxygen. Using this technology hospitals and nursing home can manage their oxygen deficiency. zeolite 13X is used in a wide range because it has outstanding nitrogen to oxygen adsorption selectivity and it is easily available in India. In this covid- 19 pandemic situation , this type of process for producing oxygen is really helpful. As evidenced by the discussion , there are numerous ways to operate the PSA process. The effect of adsorption pressure was also shown and it was clear that higher adsorption pressure will lower the recovery of the cycle. PSA method can produce almost 90% pure oxygen.

## Future Scope:-

Within the scope of the study , the effects of improvements on the pores, surface area increase the improvement of the process<sup>[23]</sup>. One major area of study that would be useful would be to optimizing cycles utilizing product pressurization instead of an equalization step and to get a fruitful result the effects of dead volume would need to be minimized by getting larger column . Additionally , more work is needed to find kinetic limit of the 13X zeolite in order to find what the maximum feed gas velocity is. Besides this future work could conclude a more in depth look at changing the adsorption pressure including operating the cycle as a pure PSA cycle<sup>[24]</sup>.

## REFERENCES:

1. Ashcraft,B.,and Swenton,J.(2007). Oxygen Production with Silver Zeolites and Pressure Swing Adsorption: Portable and Hospital Oxygen Concentrator Unit Designs with Economic Analysis. *chemical, biological and materials engineering*, pp. 1-100.
2. Davidescu,A.A., Apostu,S.A., and Mandruleanu,C.S.(2021). Shedding Light on the Main Characteristics and Perspectives of Romanian Medicinal Oxygen Market. *Healthcare*, 9,155,2-26. <https://doi.org/10.3390/healthcare9020155>
3. Kakavandi et al(2017). Dynamic modeling of nitrogen adsorption on zeolite 13x bed. *Fluid Mechanics Research International Journal*,1(1), 20-24.
4. Kakavandi,I.A., & Shokroo,E.J.(2016). Dynamic Survey of Nitrogen Adsorption on Zeolite 13X Bed. *3rd INTERNATIONAL CONFERENCE ON SCIENCE AND ENGINEERING*
5. Zahra,M., Jafar,T., andMasoud,M.(2008). Study of a Four-Bed Pressure Swing Adsorption for Oxygen Separation from Air. *International Journal of Chemical, Molecular, Nuclear, Materials and Metallurgical Engineering*, 2(11).
6. Pan,M., Omar,H.M.,& Rohani,S.(2017). Application of Nanosize Zeolite Molecular Sieves for Medical Oxygen Concentration. *Nanomaterials*,7,195,1-19. doi:10.3390/nano708019
7. 13X Molecular Sieve – Sorbead India. <https://www.sorbeadindia.com>
8. J, Mater.Chem,(2006). Novel porous materials for emerging applications. *Journal of Materials Chemistry*, 16, 623-625. DOI: 10.1039/B600327N
9. Kamarudin et al. (1998). ZEOLITE AS NATURAL GAS ADSORBENTS.
10. Mukherjee,N.(2021). PSA Oxygen: Conversion of N2 to O2 concentrator by Zeolite molecular sieve.
11. Prakash,M.(2021).India’s Oxygen emergency is more logistical.<http://theprint.in>
12. Ganley,J.C.(2018). PRESSURE SWING ADSORPTION IN THE UNIT OPERATIONS
13. Rahman,Z.A., Ali,A.J.,and Auob,H.S.(2010). A STUDY OF OXYGEN SEPARATION FROM AIR BY PRESSURE SWING ADSORPTION (PSA). *ACADEMIA*, 203-214.
14. Hamed,H.H.(2015). Oxygen and Nitrogen Separation from Air Using Zeolite Type 5A. *Al-Qadisiyah Journal For Engineering Sciences*, 8(2), 147-158.
15. Santos et al(2007). High-Purity Oxygen Production by Pressure Swing Adsorption. *Ind. Eng. Chem. Res*, 46, 591-599.
16. Santos,J.C., Portugal,A.F., Magalhaes,F.D., & Mendes ,A.(2006). Optimization of Medical PSA Units for Oxygen Production. *Ind. Eng. Chem. Res*, 45, 1085-1096.
17. Zabielska,K., Aleksandrak, T., & Gabrus, E. (2018). ADSORPTION EQUILIBRIUM OF CARBON DIOXIDE ON ZEOLITE 13X AT HIGH PRESSURES. *Chemical and Process Engineering*, 39 (3), 309–321. DOI: 10.24425/122952
18. Shokroo,E.J., Farniaei,M., and Beghbani,M.(2019). Simulation Study of Pressure Swing Adsorption to Purify Helium Using Zeolite 13X. *Applied Chemical Engineering*,2, 1-8.
19. Magee,H.M. Nitrogen Gas Adsorption in Zeolites 13X and 5A. pp. 1-13.

20. Pressure Swing adsorption- Wikipedia. <http://en.m.wikipedia.org>
21. Zabielska,K., Aleksandrak, T., & Gabrus, E. (2018). ADSORPTION EQUILIBRIUM OF CARBON DIOXIDE ON ZEOLITE 13X AT HIGH PRESSURES. *Chemical and Process Engineering*, 39 (3), 309–321. DOI: 10.24425/122952
22. Physical Chemistry (Volume-3) written by Hrishikesh Chatterjee.
23. Hazar,H., Tekdogan, R., and Sevinc, H. (2021). Investigating the effects of oxygen enrichment with modified zeolites on the performance and emissions of a diesel engine through experimental and ANN approach. *Fuel*,303,121318.
24. Moran, A.A. (2014). A PSA PROCESS FOR AN OXYGEN CONCENTRATOR. MSL, ACADEMIC ENDEAVORS, ETD Archive.

## Another sources which helped me to complete the review work.

- Bryan et al (2014). Development of mixed matrix membranes containing zeolites for post-combustion carbon capture. *Energy Procedia*, 63, 160-166.
- Karimi,A., Emrani,P., and Haghayegh,M.(2017). Experimental Verification of Dynamic Modelling of Nitrogen Adsorption on Zeolite 13X with VSA Process. *Science and Technology*, 7(1), 25-34. DOI: 10.5923/j.scit.20170701.03
- Shokroo et al (2015). Comparative study of zeolite 5A and zeolite 13X in air separation by pressure swing adsorption. *Korean J. Chem. Eng.*,33(4), 1391-1401. DOI: 10.1007/s11814-015-0232-6
- Khazraei,S., Soleimani,M., and Kargari,A.(2014). Investigation of Different Kinetic models of O<sub>2</sub> and N<sub>2</sub> adsorption on 13X Zeolite. *The 8th International Chemical Engineering Congress & Exhibition*, 1-5.
- Beaman,J.(1989). OXYGEN STORAGE ON ZEOLITES. USAFSAM-TR-88-26.
- Cavenati,S.(2004). Adsorption Equilibrium of Methane, Carbon Dioxide, and Nitrogen on Zeolite 13X at High Pressures. *Journal of Chemical & Engineering Data*, 49, 1095-1101.
- Bezerra et al (2011). Adsorption of CO<sub>2</sub> on nitrogen-enriched activated carbon and zeolite 13X. *Adsorption*,17, 235-246. DOI 10.1007/s10450-011-9320-z
- Chatti et al (2009). Amine loaded zeolites for carbon dioxide capture: Amine loading and adsorption studies. *The Official Journal of the International Zeolite Association*, 121, 84-89.
- Gizicki,W., and Banaszkiwicz,T.(2020). Performance Optimization of the Low-Capacity Adsorption Oxygen Generator. *Appl. Sci*, 7495, 1-11. doi:10.3390/app10217495
- Dantas et al(2011). Carbon dioxide–nitrogen separation through pressure swing adsorption. *Chemical Engineering Journal*,172, 698-704.
- Akulinin et al(2020). OPTIMIZATION AND ANALYSIS OF PRESSURE SWING ADSORPTION PROCESS FOR OXYGEN PRODUCTION FROM AIR UNDER UNCERTAINTY. *Chem. Ind. Chem. Eng. Q* , 26(1), 89-104.

- Montanari et al(2011). CO<sub>2</sub> separation and landfill biogas upgrading: A comparison of 4A and 13X zeolite adsorbents. *Energy*, 36, 314-319.
- Mofarahi,M.,and Shokroo, E.J.(2013). COMPARISON OF TWO PRESSURE SWING ADSORPTION PROCESSES FOR AIR SEPARATION USING ZEOLITE 5A AND ZEOLITE 13X. *Petroleum & Coal*, 55(3), 216-225.
- Shokroo,E.J., Farniaei,M., and Beghbani,M.(2019). Simulation Study of Pressure Swing Adsorption to Purify Helium Using Zeolite 13X. *Applied Chemical Engineering*,2, 1-8.
- Suraweera et al(2014). Hydrogen adsorption and diffusion in amorphous, metal-decorated nanoporous silica. *INTERNATIONAL JOURNAL OF HYDROJEN ENERGY*. 39,9241-9253
- Santos,J.C., Portugal,A.F., Magalhaes,F.D., & Mendes ,A.(2004). Simulation and Optimization of Small Oxygen Pressure Swing Adsorption Units. *Ind. Eng. Chem. Res.*, 43, 8328-8338.
- Zhu et al (2016). Study of a novel rapid vacuum pressure swing adsorption process with intermediate gas pressurization for producing oxygen. *Adsorption*, DOI 10.1007/s10450-016-9843-4
- Kroi,M.(2020). Natural vs. Synthetic Zeolites. *Crystals*, 10, 622, 1-8.

TITLE OF REVIEW - Producing Oxygen using 13X zeolite by PSA method.

NAME OF THE INSTITUTION - Scottish Church College

C.U. ROLL NO - 223/CEM/191026

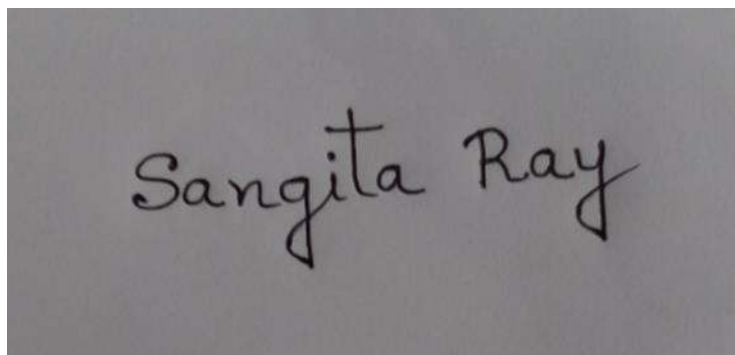
C.U. REGISTRATION NO - 613-1221-0683-16

SPECIAL PAPER : CHEM- SO 44

NAME OF CANDIDATE

Sangita Ray

SIGNATURE OF CANDIDATE

A rectangular box containing a handwritten signature in black ink on a light grey background. The signature reads "Sangita Ray" in a cursive script.

NAME OF EXAMINER

Dr. Sebanti Basu

SIGNATURE OF EXAMINER



## ACKNOWLEDGEMENT:

The review 'Producing Oxygen using 13X zeolite by PSA method' has provided me with an ample scope of learning through collaborative activities. I consider myself fortunate enough to work under Dr. Rama Ranjan Bhattacharjee whose guidance made my review work learning quite joyful. He has given important suggestions for the improvement of the review work. I am grateful to him.

I am also very thankful to Dr. Sebanti Basu, Associate professor, Scottish Church College for her continuous support.

I would like also to thank Dr. Sourav Chakrabarty, Assistant Professor, Scottish Church College for his precise suggestions which were very helpful to the accomplishment of the review work.

And I am also grateful to my parents and my friends who have helped me to carry out the review.

## CONTENT:

Introduction	1
Reason behind choosing zeolite	1
Why 13X zeolite	2
Table – 1 (Properties of zeolite)	3
Adsorption phenomena	4
A short view of PSA process	4-7
Methods of pressure swing adsorption	7-9
Table – 2 (Details of PSA Columns and Adsorbent)	9
Discussion of experimental work (two columns 4 step and 6 step)	9-15
Animation picture of PSA method	16
Consideration for Mathematical Model	17
Result and discussion (for Dynamic modeling of N <sub>2</sub> adsorption on 13X bed)	17-21
Conclusion	21
Future Scope	21
References	22-24

## Introduction:-

One of the most important clinical gas used in health care center is oxygen. There are no modern hospitals and nursing home which can manage without oxygen. Pure oxygen is too much essential for the respiration of the patients during anesthesia and in the intensive care or neonatal units<sup>[1]</sup>. Now in this covid pandemic situation oxygen is really too much necessary for survival of covid +ve patients. The challenge is appeared by increasing supply of medicinal oxygen with reducing cost<sup>[2]</sup>. In 1907, Linde built a first cryogenic distillation bed for air separation and this time oxygen was first produced<sup>[3]</sup>. Besides this in chemical industries oxygen is too much necessary for various processes like refinery industries, manufacturing metal etc. The most commonly adsorbent used in air separation for producing oxygen is zeolite 13X<sup>[4]</sup>. Here desorption and adsorption process mainly occurs. There are many process exists for separation of air to produce purified oxygen. Among them pressure swing adsorption (PSA) is very popular in the market because it is a safe process with reasonable energy and area requirements<sup>[1]</sup>. At first Skarstrom in 1958 proposed the simplest PSA process. Till now there are many process arises using different types of adsorbent for this purposes to purify oxygen. Farooq et al,(1989) used zeolite-5A for producing oxygen using PSA method by performing Sakrstrom cycle. In 1990 Keny and Liow used 5A zeolite for air separation<sup>[5]</sup>. But zeolite 13X is used in a wide range because it has outstanding nitrogen to oxygen adsorption selectivity. In recent time 13X zeolite is modified with Li<sup>+</sup> exchange method which shows a higher nitrogen adsorption capacity at the active cation sites of the zeolite framework<sup>[6]</sup>. Besides this zeolite 13X has large mass transfer zone, so the adsorption rate is high. Nitrogen concentrations mainly drop in the outlet of the zeolite 13X at the time of about 125 seconds and the concentrations reaches zero after about 180 seconds<sup>[3]</sup>.

## Reason behind choosing zeolite as a molecular sieve :

Porous materials are those materials which contain void space. There are many types of porous materials such as rocks and soil, zeolites, biological tissues and artificial materials such as cements and ceramics etc. The characteristics of a porous material vary depending on the size, arrangement and shape of the pores, as well as the porosity and composition of the material itself (porous materials latest research). According to the IUPAC, pores are classified into three categories, these are micropore – (pore sizes less than 2nm), mesopore (between 2 and 50 nm) and macropore ( with pore size larger than 50 nm)<sup>[8]</sup>. For PSA method zeolite is chosen as adsorbent. Zeolite has microporous crystalline structures. Zeolite framework is an assemblage of SiO<sub>4</sub> and AlO<sub>4</sub> tetrahedral joined together by sharing oxygen atoms<sup>[9]</sup>. This type of microporous solid such as zeolite (aluminosilicate member) is known as molecular sieves. Zeolite molecular sieve contains very small pores of uniform size<sup>[10]</sup>. Zeolite adsorbent has the selectivity to adsorb

nitrogen compared to oxygen because of the interaction between electrostatic field of the cationic zeolite and the quadrupole moment of the nitrogen and oxygen. The quadrupole of oxygen is three times lesser than that of nitrogen. And this fact leads to a selective adsorption on to the zeolite surface<sup>[6]</sup>.

## Why 13X zeolite:

So zeolite adsorbs nitrogen like it sponge adsorbs water . Converting medical air to medical oxygen using 13X zeolite is very practical. However LiX material is a good adsorbent for adsorption of nitrogen at ambient pressure and releases under vacuum. The operations are simpler and the system built will be simple and accomplished. But Lithium X can not be easily sourced in India. So the technology has to be based on more readily available 13X molecular sieve zeolite. Substitution of LiX by 13X change the operation from vacuum based to a pressure based (VPSA to PSA)<sup>[11]</sup>. There are three types of zeolite structure become dominant such as A,X and Y<sup>[1]</sup>. 13X zeolite is the sodium form of the type X crystal. It has pore diameter of 1nm . So it will adsorb molecules of A crystalline form that is 3 Angstrom,4 Angstrom and 5 Angstrom<sup>[7]</sup>. Zeolite 13X has the chemical formula  $\text{Na}_{86}[(\text{AlO}_2)_{86}(\text{SiO}_2)_{106}] \cdot \text{H}_2\text{O}$  having pore diameter less than 10 Angstrom( 1nm). X crystalline foam has a larger pore size than other types .

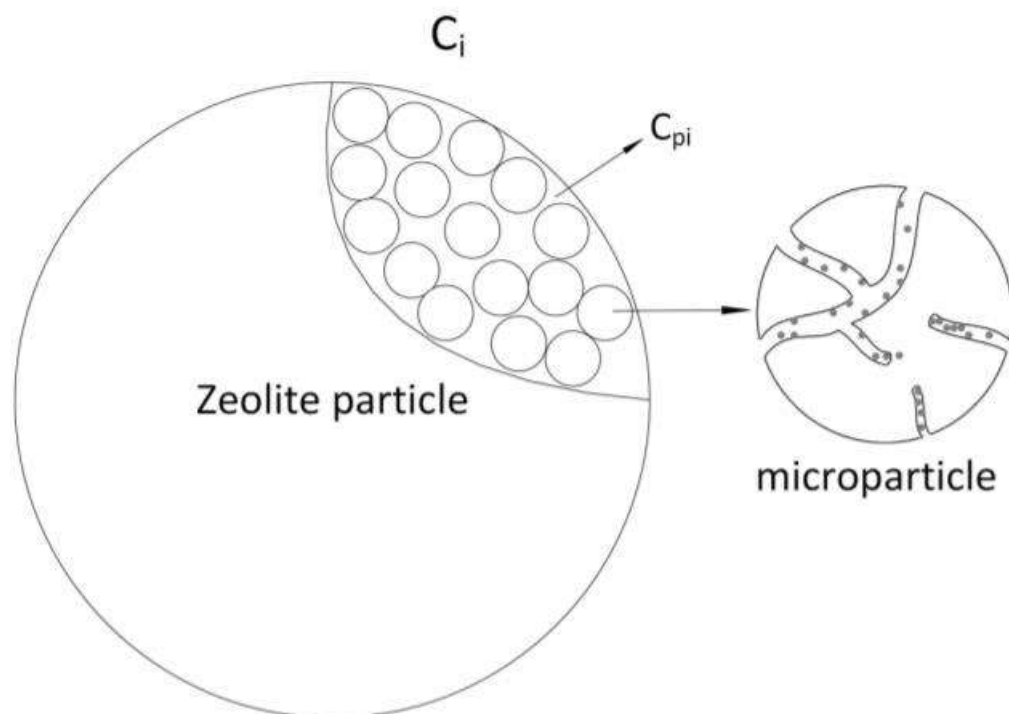
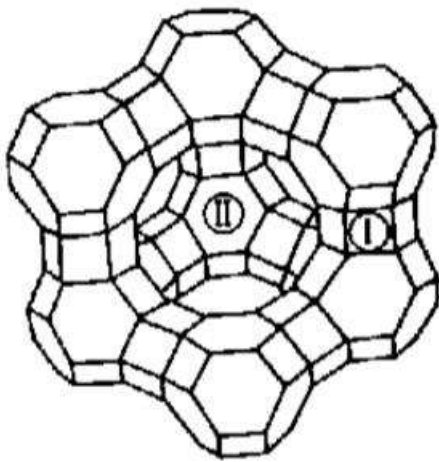


Figure-1 Schematics of zeolite particle structure<sup>[6]</sup>.

Table – 1 (Properties of zeolite)<sup>[19]</sup>

Chemical name	Na <sub>86</sub> [(AlO <sub>2</sub> ) <sub>86</sub> (SiO <sub>2</sub> ) <sub>106</sub> ]•H <sub>2</sub> O
Pore Diameter	~8Å
Mesopore volume	0.165 cm <sup>3</sup> /g
Micropore volume	0.17 cm <sup>3</sup> /g
Langmuir surface area	571 m <sup>2</sup> /g
Mass of pellet sample	2.37 g
Mass of crushed sample	2.49 g



Zeolite 13X molecular structure

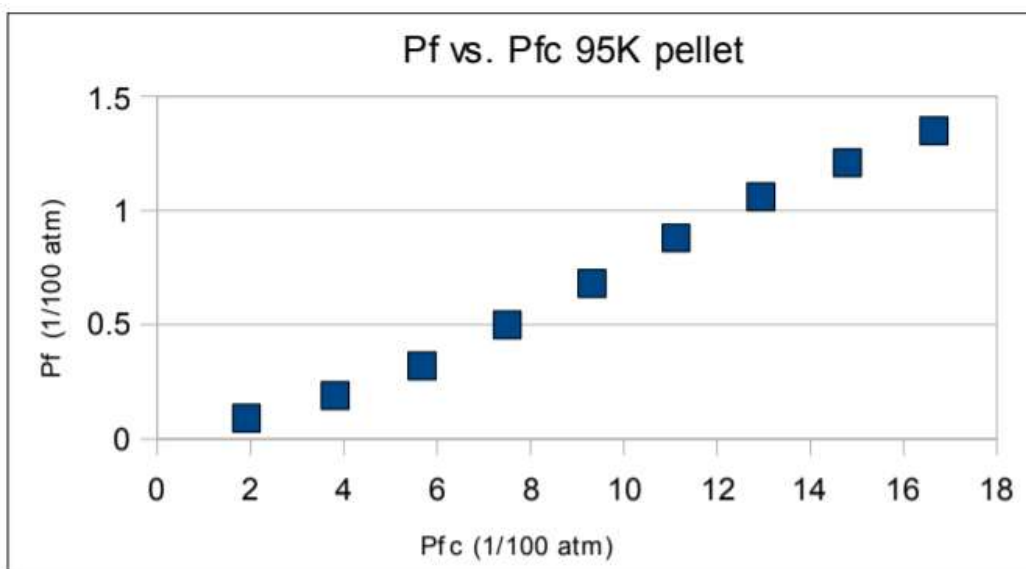
Figure-2<sup>[19]</sup>

Figure-3

Adsorption of nitrogen in zeolite 13X pellet at 95K<sup>[19]</sup>.

## Adsorption phenomena in PSA method:

Adsorption is the phenomenon where molecules of one phase remain preferentially concentrated at the surface of another phase<sup>[22]</sup>. Generally, gas adsorption in zeolite are of two types named physisorption and chemisorption. But physisorption is more preferable method for gas separation and purification because of the fact that the adsorbent can be regenerated by heating or flushed to remove the adsorbed gas molecules attaching to the solid. This make the process more economical and profitable<sup>[9]</sup>.

## A short view of PSA process:

Pressure swing adsorption is an industrial process which is generally used for the bulk separation of gas mixtures. It is a cyclic operation<sup>[12]</sup>. In 1960, Skarstrom patented the first PSA unit which was composed of two beds and using a zeolite<sup>[13]</sup>.

Stage 1- Compressed air is passed into the first bed. Nitrogen molecules are trapped and oxygen molecules is allowed to flow through.

Stage -2- At the time of saturation of the adsorbent in the first bed with nitrogen, the air flow feed is directed towards the second bed.

Stage -3- Nitrogen was adsorbed by the adsorbent (13X zeolite) in the second bed. The first bed is depressurized allowing nitrogen to be loosen out of the system and released to the atmosphere.

Stage- 4- The process starts over. Again compressed air is fed into the first bed. The second bed is relaxed by releasing nitrogen and oxygen to the atmosphere. The process is repeated continuously producing a constant flow of purify oxygen<sup>[14]</sup>.

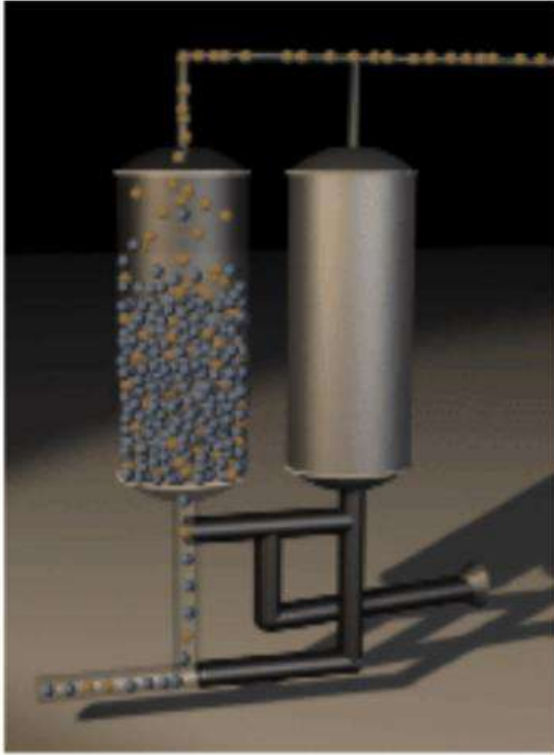


Figure-4<sup>[14]</sup> Stage – 1

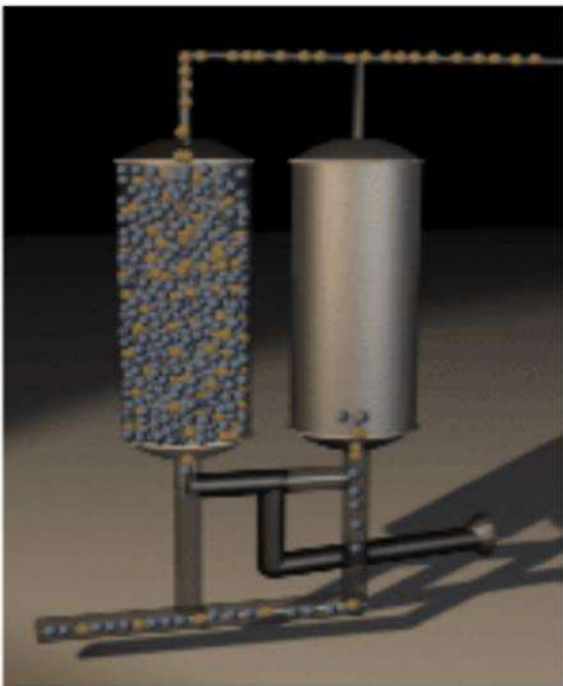


Figure-5<sup>[14]</sup> stage – 2

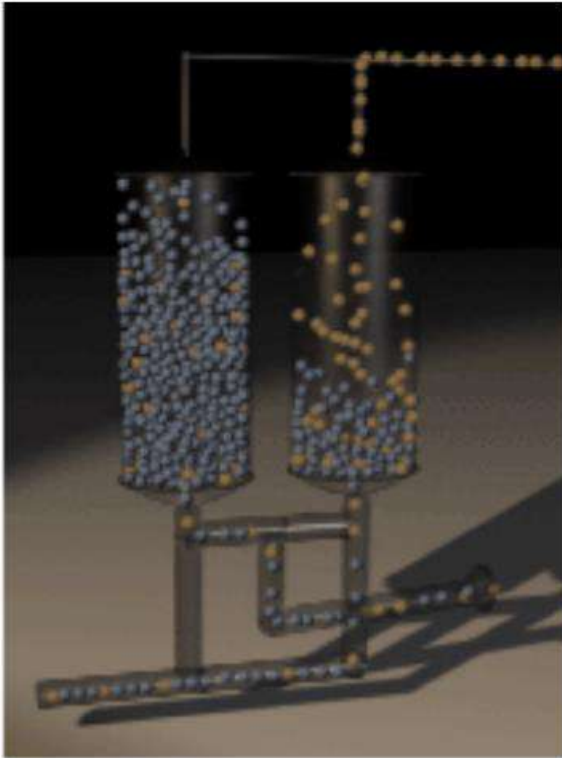


Figure-6<sup>[14]</sup> Stage – 3

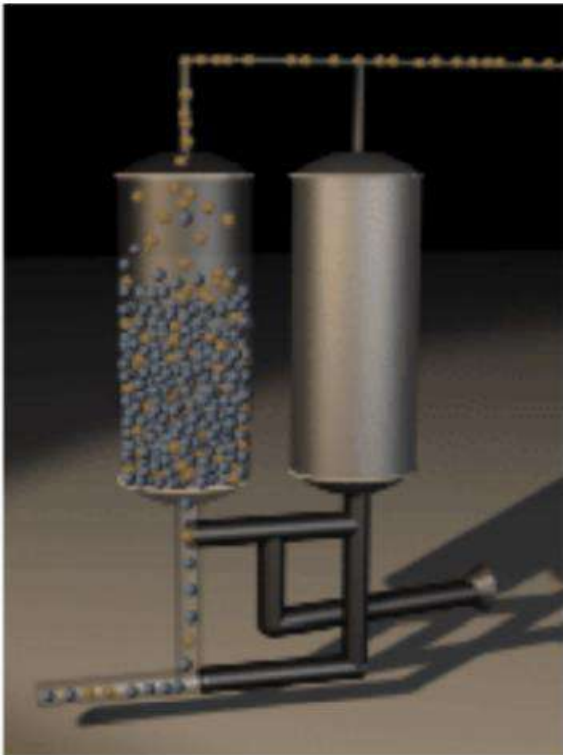


Figure-7<sup>[14]</sup> Stage – 4



Oxygen production using 13X zeolite by using PSA process has noticeably increased in the past decades. But the concentration of the products is limited to 95% oxygen due to presence of argon in air. Because the adsorbent present has the similar adsorption capacities for oxygen and argon. Actually in PSA cycle desorption take place at a pressure much lower than adsorption<sup>[15]</sup>.

There are many application observed for PSA unit such as producing oxygen for medical use. In 1975 this unit was started to use in a wide range for treating patient with respiratory illness. This provide 2-4 L/min of 85-95% oxygen. In this year Ruder and Isles also patented a PSA unit for producing enriched air(use onboard jet aircraft) (U.S. Patent 3,922,149). Just one year latter an electric powered compact PSA apparatus (DE Patent 2,559,120) was described by Armond. He use zeolite molecular sieve to generate breathing air for medical use. In 1984, Kratz and Sircar patented a medical oxygen generator for domiciliary use (U.S.Patent 4,477,265). This process generated 90% of oxygen<sup>[16]</sup>.

In this work, nitrogen adsorption process using 13X zeolite as a molecular sieve is simulated. So the process is dynamic<sup>[4]</sup>.

## Method of pressure swing adsorption

### Equilibrium adsorption

Air mainly contains three components, nitrogen, oxygen and argon. In between 1916 to 1918, Langmuir proposed the theoretical basis of adsorption which is based on kinetic theory of gases<sup>[17]</sup>. This phenomena explain the type 1 adsorption curve(HKC). Multicomponent adsorption equilibria theory (competition between the different molecules on the adsorbent) is required for designing purposes.

$$\theta_i = \frac{b_i P_i}{1 + \sum_{j=1}^N b_j P_j} \quad (\text{Equation 1})$$

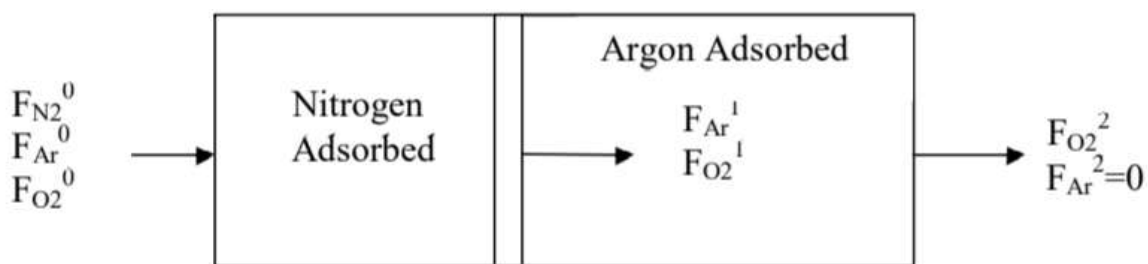
Fractional loading contributed by  $\theta_i$  and  $i$ .

$b_i$  and  $b_j$  are the rate constants of adsorption to that for desorption for component  $i$  and component  $j$  respectively.  $P_i$  – Partial pressure of component  $i$ ,  $P_j$  – Partial pressure of component  $j$ .  $N$  is the number of species.

Equation 1 gives the adsorbed amount of species  $i$  on the adsorbent in the multi component system. The selectivity describes how one species is selective to bind to the adsorbent over another species. The selectivity of a species  $i$  in relation to species  $j$  is given as

$$S_{i,j} = \frac{b_i}{b_j} \quad (\text{Equation 2})$$

A transport phenomena is observed to study how each species is adsorbed in the adsorbent bed. Material balance equations are used to determine these parameters.



Air component through adsorbent bed<sup>[1]</sup>.

Material balances are performed for the components in each section of the adsorbent bed.

$$\text{Nitrogen : } F_{N_2}^0 \Delta t = \Delta L_1 A N_{N_2}^1 = v_1 A N_{N_2}^1 \quad (\text{Equation 3})$$

$$\text{Oxygen: } F_{O_2}^1 = F_{O_2}^0 + (N_{O_2}^2 - N_{O_2}^1) A v_1 \quad (\text{Equation 4})$$

$$\text{Argon: } F_{Ar}^1 = F_{Ar}^0 + (N_{Ar}^2 - N_{Ar}^1) A v_1 \quad (\text{Equation 5})$$

$$F_{Ar}^2 = 0 = F_{Ar}^1 + N_{Ar}^2 A v_2 \quad (\text{Equation 6})$$

Here,  $F$  stands for volumetric flowrate,  $\Delta t$  is the cycle time,  $\Delta L$  is the length of the bed,  $A$  is the area,  $N$  is the loading and  $v$  is the front velocity.

The velocity of the argon front must be greater than nitrogen front.

$$\frac{v_2}{v_1} = \frac{\frac{F_{Ar}^0}{F_{N_2}^0} + (N_{Ar}^2 - N_{Ar}^1)}{N_{Ar}^2} > 1 \quad (\text{Equation 7})$$

Nitrogen molecule has strong electrostatic interaction with 13X zeolite than do oxygen and argon molecules. The front moves with nitrogen front's velocity as a function of the adsorption and desorption of the molecules on the adsorbent sites. So nitrogen has a slower rate of desorption than oxygen and argon. So the velocity front of argon to nitrogen is greater than one<sup>[1]</sup>.

To get greater flexibility Langmuir–Freundlich equation is used which is

$$q = q_m(T) \frac{b(T).p^{n(T)}}{1+b(T).p^{n(T)}} \quad (\text{Equation 8})^{[21]}$$

## Details of PSA Columns and Adsorbent

Table-2<sup>[13]</sup>

Adsorbers		
Column Length	L	0.7 m
Column diamete	D	50 mm
Adsorbent Type		13X zeolite
Shape		Sphere
Particle diameter	$d_p$	1.7-2.6 mm
Particle density	$\rho_p$	1070 kg/m <sup>3</sup>
Bulk density	$\rho_B$	670 kg/m <sup>3</sup>
Bed porosity	$\epsilon$	0.4
Adsorbent weight	w	0.75 kg
Adsorbent bed length	$L_B$	0.57 m
Langmuir isotherm parameters	$q_{sO_2}$	3.091 mol/kg
Oxygen	$b_{O_2}$	0.0367 bar <sup>-1</sup>
Adsorption heat of O2	$\Delta H_{O_2}$	12.8 kJ/mole
Nitrogen	$q_{sN_2}$	3.091 mol/kg
	$b_{N_2}$	0.1006 bar <sup>-1</sup>
Adsorption heat of N2	$\Delta H_{N_2}$	17 kJ/mole

## Discussion of the experimental work for two column 4 step and 6 step PSA operation.

Two column: 4 step and 6 step PSA operation .

- Pressurizing time  $t_{prs} = 10$  s
- Depressurizing time  $t_{deprs} = 10$  s
- Equalization time  $t_{eq} = 20$  s

The operating parameters considered in the present work with their ranges are as follows; Adsorption time  $t_{ads} = 10, 20, \text{ and } 30$  s ,Adsorption pressure  $P_H = 2, 3, \text{ and } 4$  bar , Purge flow rate  $Q_{purg} = 1, 1.5, 2, 3, 4, 5, \text{ and } 6$  L/min<sup>[13]</sup>.

## Two Column Adsorption:

The PSA system preparation shown in figure using vacuum and O<sub>2</sub> pressurizing and purging to ensure the zeolite activity<sup>[13]</sup>.

Figure- 8 shows that the effect of adsorption on oxygen purity. Figure -9 shows that no noticeably change occurred between the pressure ratios 2 and 4 bar. This result is in agreement with that performed by Jee et al. (2001) for high purge to feed ratio, Yuwen et al.(2005). Jain et al (2003) stated that for constant selectivity systems, performance increases with increasing pressure according to adsorption equilibrium isotherm.

In figure- 10 it can be seen that breakthrough occurs at high adsorption time. Adsorption Step duration is needed for needed for breakthrough to occur<sup>[13]</sup>.

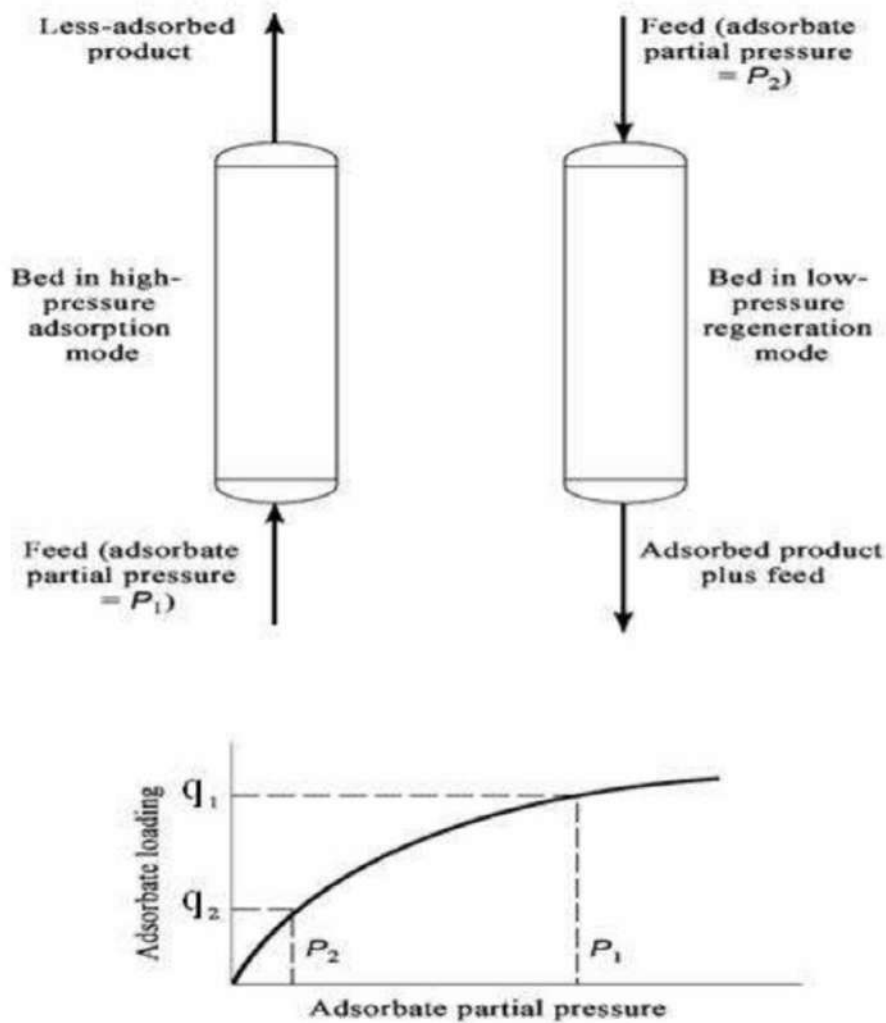


Figure – 8 Pressure swing cycle<sup>[13]</sup>.

## Product Oxygen Cycle for 4- step cycle

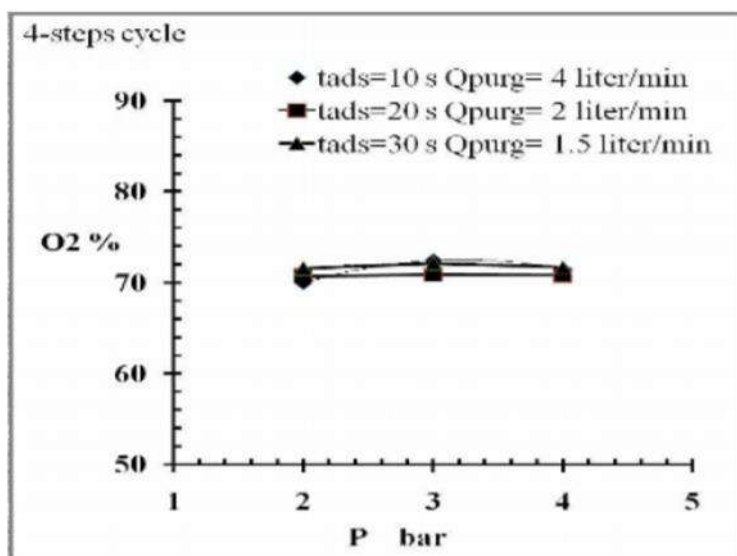


Figure - 9 The effect of the adsorption pressure ( $p_H$ ) on product oxygen purity for 2-column, 4-step operation<sup>[13]</sup>.

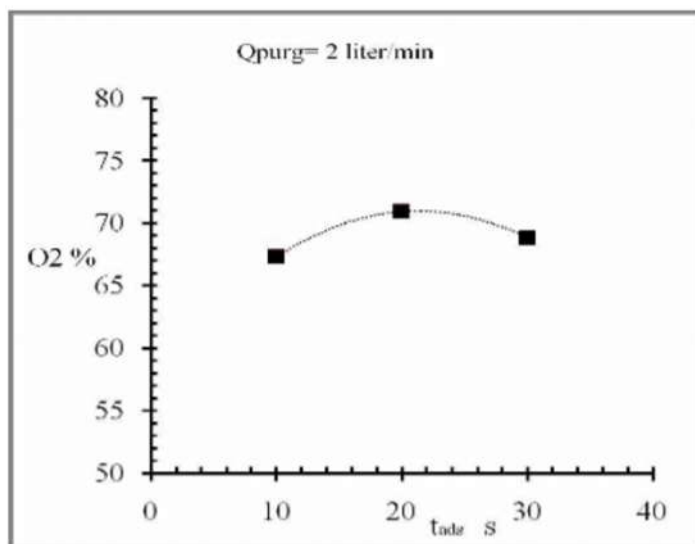


Figure - 10 Effect of the adsorption time ( $t_{ads}$ ) on product oxygen purity for 2-column, 4-step cycle, ( $Q_{purg}=2$  l/min)<sup>[13]</sup>.

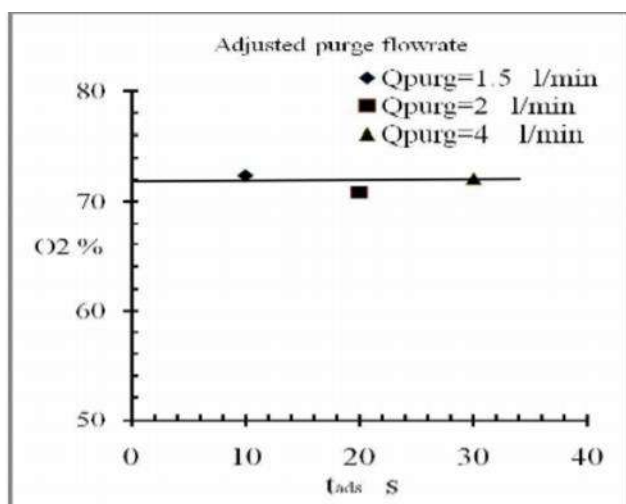


Figure -11 8 Effect of adsorption time ( $t_{\text{ads}}$ ) on product oxygen purity, for 4-step cycle, by adjusting the purge flowrate ( $Q_{\text{purg}}$ )<sup>[13]</sup>.

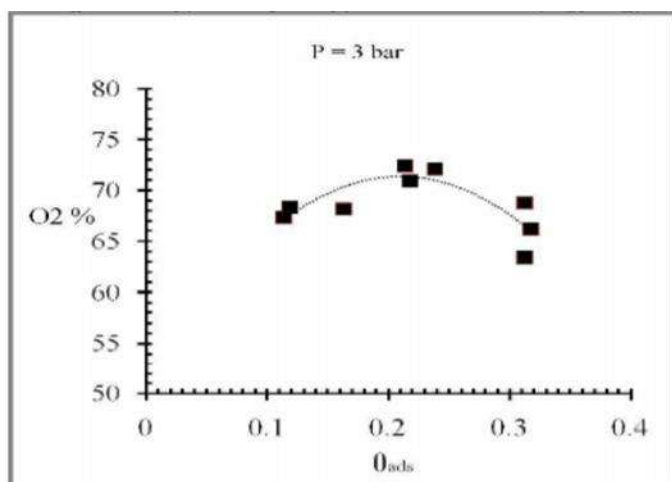


Figure- 12 9 Effect of the dimensionless adsorption time on product oxygen purity for 2-column, 4-step operation<sup>[13]</sup>.

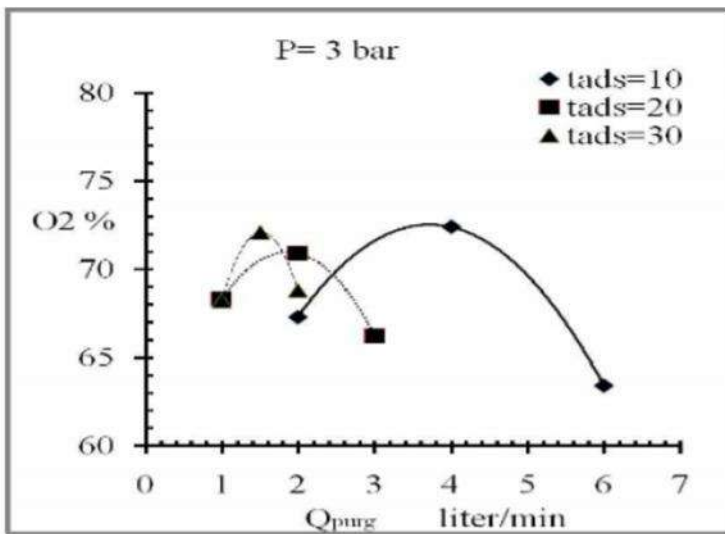


Figure- 13 The effect of the Purge Flow rate ( $Q_{\text{purg}}$ ) on product oxygen purity, for 2-column, 4-step cycle<sup>[13]</sup>.

From this Figure- 13 it is revealed that the nitrogen wave front is breakthrough. The maximum product oxygen is 70% pure because of both the effect of purge flowrate( $Q_{\text{purg}}$ ) and the adsorption time( $t_{\text{ads}}$ ).

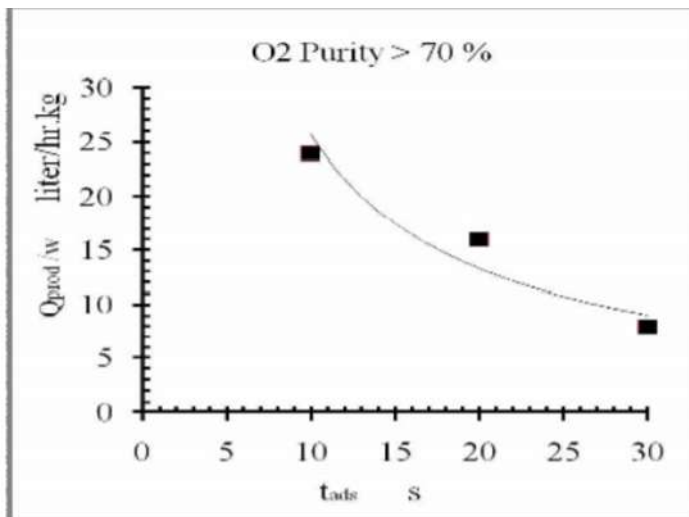


Figure-14 The effect of the adsorption times ( $t_{\text{ads}}$ ) on specific product Flowrate ( $Q_{\text{purg/w}}$ ) at maximum product oxygen purity<sup>[13]</sup>.

Product Oxygen Purity for 6- step cycle:

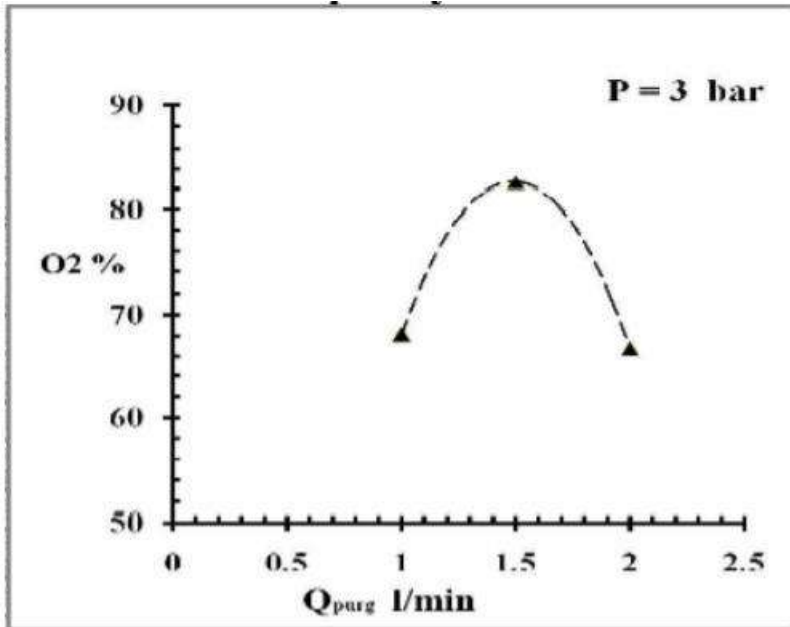


Figure -15 The effect of the purge flowrate ( $Q_{\text{purg}}$ ) on product oxygen purity for 6-Steps cycle, with air feed initial pressurizing<sup>[13]</sup>

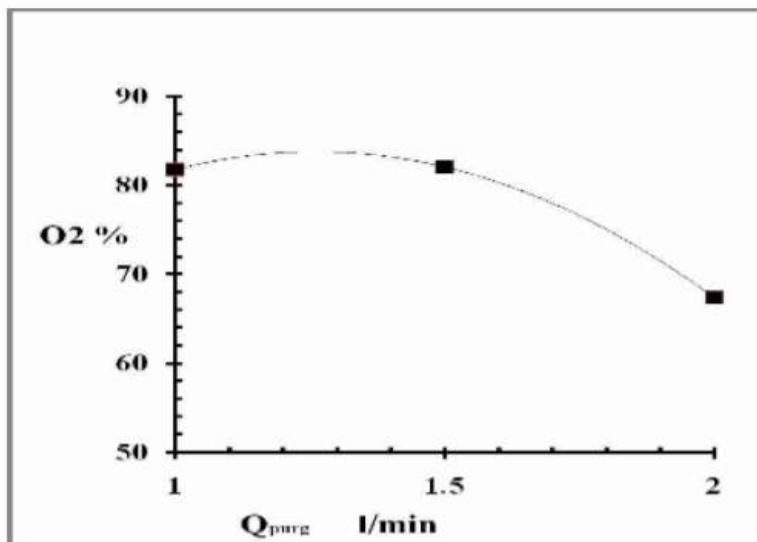


Figure -16 The effect of the purge flowrate ( $Q_{\text{purg}}$ ) on product oxygen purity for 6-Steps cycle, with O<sub>2</sub> initial pressurizing<sup>[13]</sup>.



Figure-16 shows that, with increasing purge flowrate above 1.5 lit/min , product purity decreases to that breakthrough point forming high effluent from the column<sup>[13]</sup>.

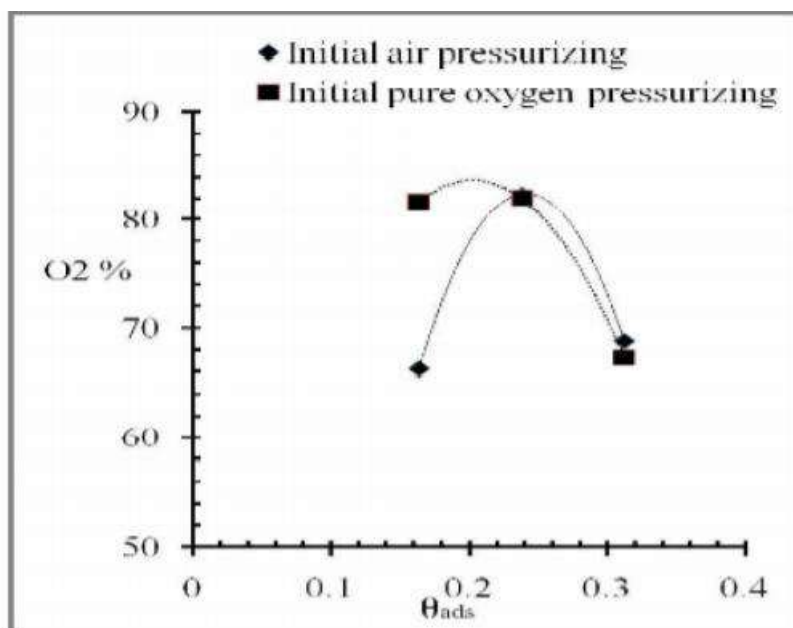


Figure -17 Effect of the dimensionless adsorption time ( $t_{ads}$ ) on product oxygen purity for 2-column, 6-step cycle<sup>[13]</sup>.

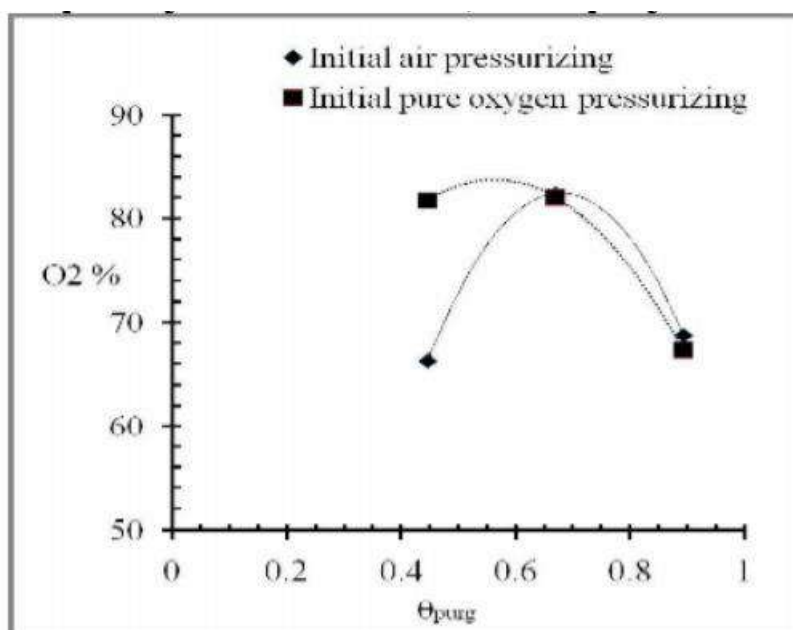
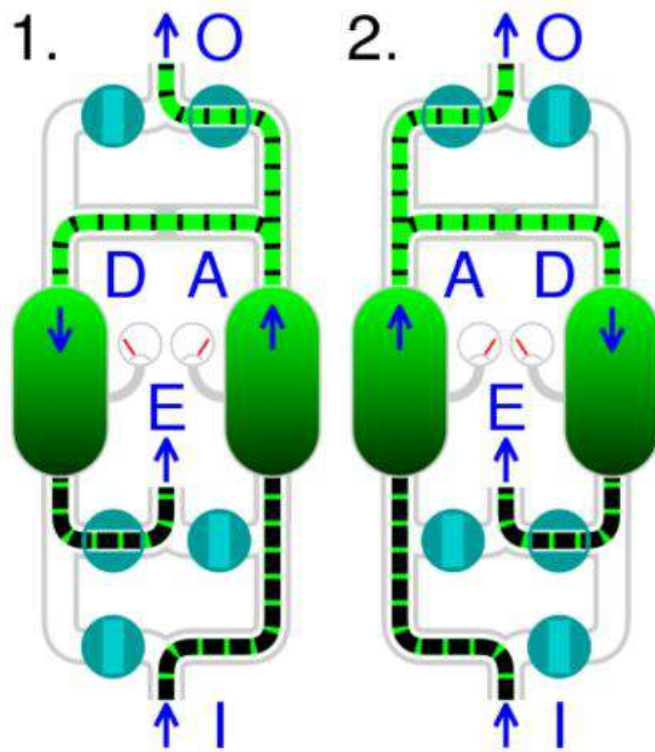


Figure -18 Effect of the dimensionless purge time ( $Q_{purg}$ ) on product oxygen purity for 2-column, 6-step cycle<sup>[13]</sup>



Animation of pressure swing adsorption, (1) and (2) showing alternating adsorption and desorption

I compressed air input    A adsorption  
 O oxygen output            D desorption  
 E exhaust

Figure– 19<sup>[20]</sup>

## Consideration for Mathematical Model for Dynamic modeling of N<sub>2</sub> adsorption on 13X bed.:-

To develop a mathematical model for adsorption bed, the following assumptions must be considered.

- Gas behaves as an ideal gas.
- The flow pattern is axially assumed as plug-flow model.
- Equilibrium equations for air are expressed as triple Langmuir-Freundlich isotherm (oxygen, nitrogen and argon);
- Mass transfer rate is presented by linear driving force (LDF) relations;
- At initial state bed is clean and there is no gas flow in it;
- Air is considered a mixture of oxygen and argon (21 %) and nitrogen (79 %) as feed<sup>[4]</sup>.

A four bed pressure swing adsorption for oxygen separation from air was proposed by Zahra et al(2008)<sup>[5]</sup>. Recently in 2017 Kakavandi et al proposed a dynamic modeling of nitrogen adsorption on 13X zeolite using two bed.

## Result and discussion :

The fourth order Runge-Kutta Gill method was used to solve the mathematical model. An experimental and simulation observation of the PSA unit running with a traditional Skarstrom cycle and a Skarstrom cycle with concurrent equalization in an attempt to separate oxygen from air using a 5A zeolite has been proposed by Mendes et al. Moreover, a small-scale two-bed six-step PSA process using zeolite 13X was performed by Jee et al.

Figures 20 and 21 indicate the effect of product flow rate and P/F on the purity and recovery of oxygen during PSA process, respectively<sup>[3]</sup>.

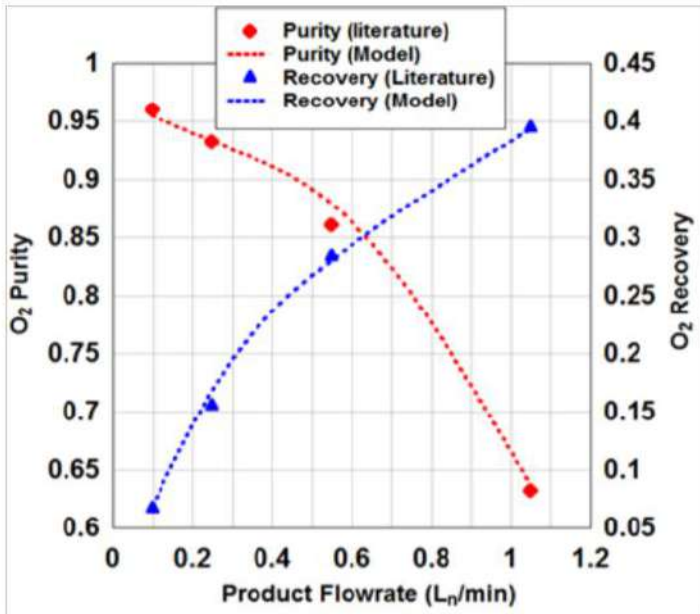


Figure -20<sup>[3]</sup>

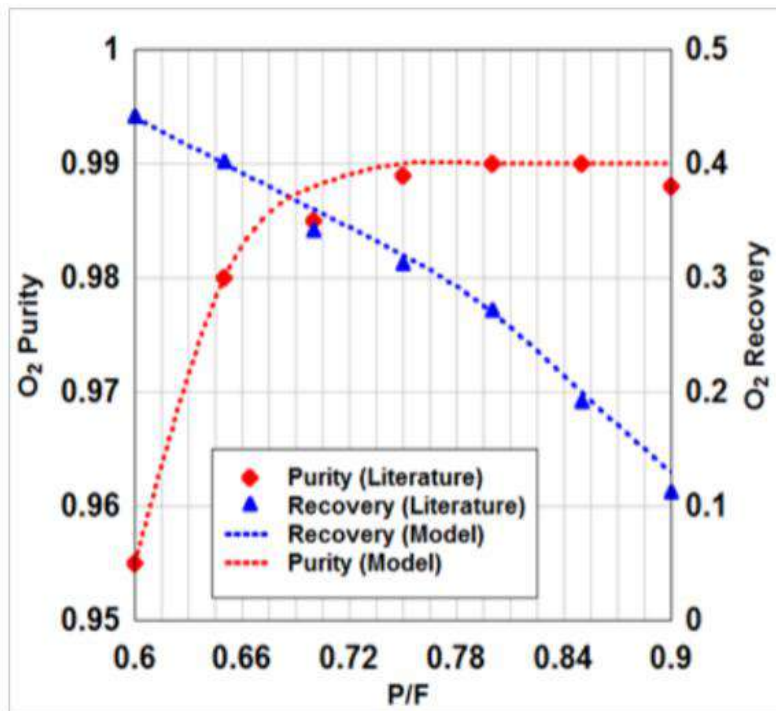


Figure-21<sup>[3]</sup>

Break through curves for nitrogen and oxygen on zeolite 13X is shown in the following Figure. The term “break through time” is developed by the response of initially clean bed per a flow with

constant composition. In Figure – 22 it is shown that oxygen exists from the top of the 13X zeolite earlier than nitrogen at about approximately 230 seconds.

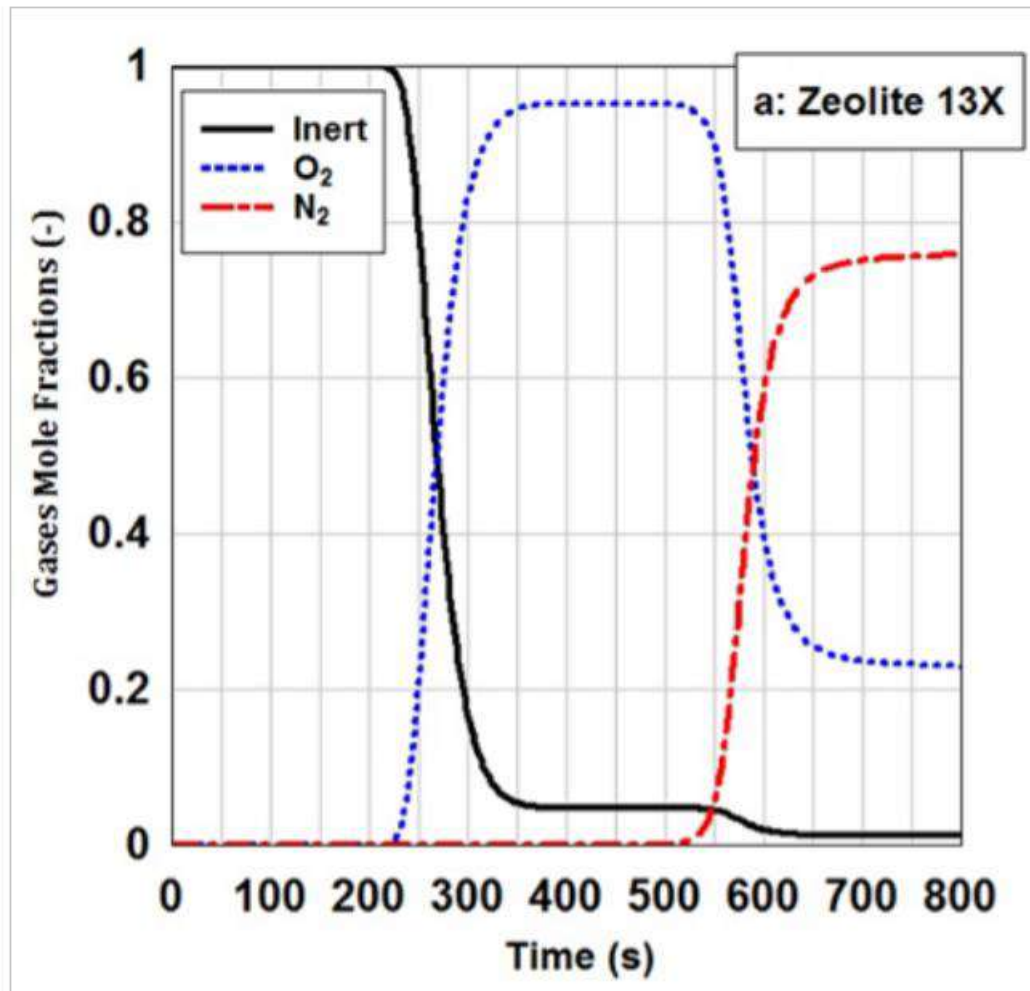


Figure -22<sup>[3]</sup>

(The simulated breakthrough curves of zeolite 13X for oxygen and nitrogen at adsorption pressure of 6 bar and feed flow rate of 5 LSTP/min. The adsorption bed was initially saturated with a non-adsorptive gas.)

With passing of time High roll-up phenomena is observed in case of oxygen. Because of this phenomena oxygen concentration is 4.5 times greater than feed concentration during the time of 400-500 seconds. Oxygen is affected by this phenomena because nitrogen adsorption on 13X zeolite is much more than that of oxygen. So oxygen concentration is relatively increased rather than feed concentration. Nitrogen breakthrough occurs at the time of 550 seconds and from this time oxygen concentration is starting to be reduced. In Figure- 22, it is clearly said that High roll-up phenomena in the case of nitrogen because of its strong adsorption on zeolite 13X. In PSA cycle adsorption and desorption process depends on pressure increasing and decreasing<sup>[18]</sup>.

Figure - 23 says that nitrogen concentration on zeolite 13X with respect to different adsorption pressures and time. With increasing pressure adsorption rate, of nitrogen increases. Figure- 24

says oxygen concentration along the bed length of the adsorbent (13X zeolite) in different times. The slope of oxygen concentration curve is fast. The desorption curve of zeolite 13X is depicted in Figure 25. The assumption is that a pure inter gas is utilized for cleaning the bed in order to simulate desorption over the beds<sup>[3]</sup>.

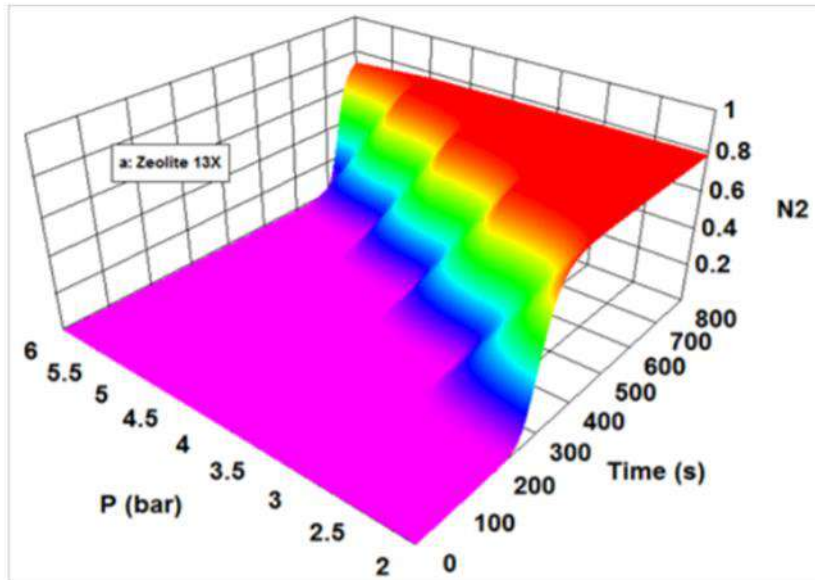


Figure -23 The outlet mole fraction of nitrogen from zeolite 13X at different adsorption pressures and feed flow rate of 4LSTP/min. The adsorption bed was initially saturated with a non-adsorptive gas<sup>[3]</sup>.

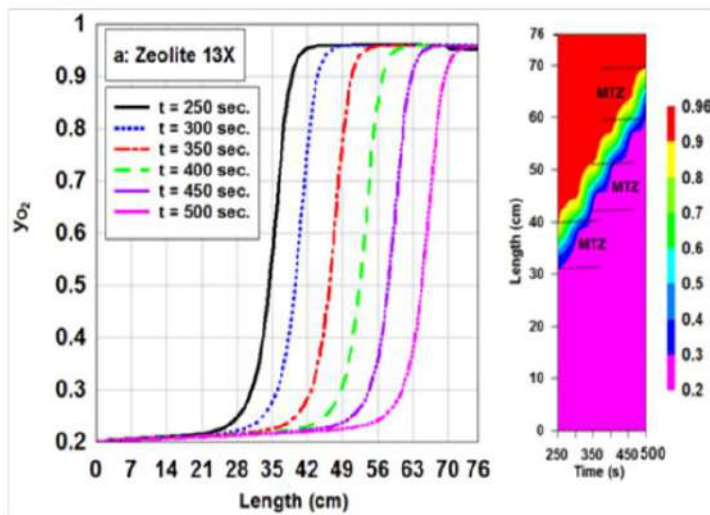


Figure – 24 Distribution of oxygen concentration along the length of zeolite 13X during adsorption process in different times. The feed flow rate is 5LSTP/min and the adsorption pressure is 6 bar<sup>[3]</sup>.

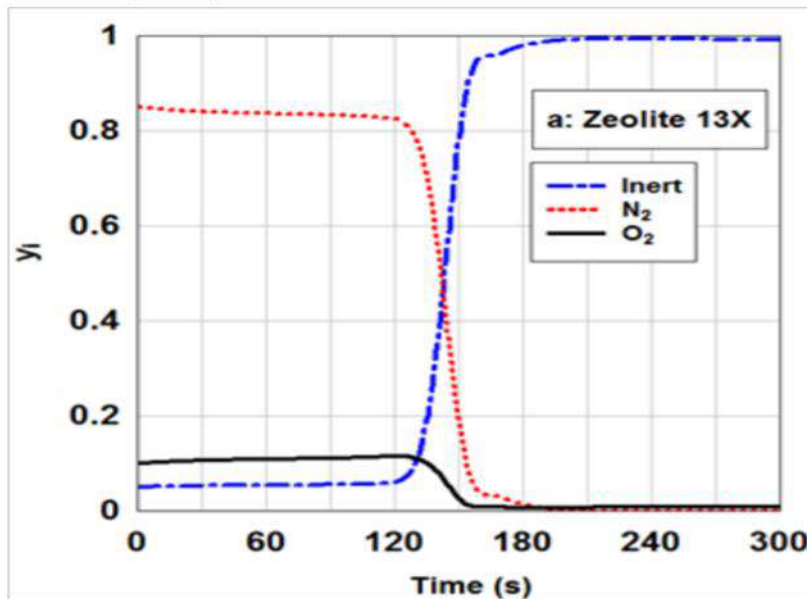


Figure – 25 The outlet

simulated concentration of gas phase from zeolite 13X during desorption at pressure of 0.1bar. The desorption bed was completely clean in the initial state<sup>[3]</sup>.

## Conclusion:-

It has been discussed that how the PSA process using 13X zeolite is effective to produce pure oxygen. Using this technology hospitals and nursing home can manage their oxygen deficiency. zeolite 13X is used in a wide range because it has outstanding nitrogen to oxygen adsorption selectivity and it is easily available in India. In this covid- 19 pandemic situation , this type of process for producing oxygen is really helpful. As evidenced by the discussion , there are numerous ways to operate the PSA process. The effect of adsorption pressure was also shown and it was clear that higher adsorption pressure will lower the recovery of the cycle. PSA method can produce almost 90% pure oxygen.

## Future Scope:-

Within the scope of the study , the effects of improvements on the pores, surface area increase the improvement of the process<sup>[23]</sup>. One major area of study that would be useful would be to optimizing cycles utilizing product pressurization instead of an equalization step and to get a fruitful result the effects of dead volume would need to be minimized by getting larger column . Additionally , more work is needed to find kinetic limit of the 13X zeolite in order to find what the maximum feed gas velocity is. Besides this future work could conclude a more in depth look at changing the adsorption pressure including operating the cycle as a pure PSA cycle<sup>[24]</sup>.

## REFERENCES:

1. Ashcraft,B.,and Swenton,J.(2007). Oxygen Production with Silver Zeolites and Pressure Swing Adsorption: Portable and Hospital Oxygen Concentrator Unit Designs with Economic Analysis. *chemical, biological and materials engineering*, pp. 1-100.
2. Davidescu,A.A., Apostu,S.A., and Mandruleanu,C.S.(2021). Shedding Light on the Main Characteristics and Perspectives of Romanian Medicinal Oxygen Market. *Healthcare*, 9,155,2-26. <https://doi.org/10.3390/healthcare9020155>
3. Kakavandi et al(2017). Dynamic modeling of nitrogen adsorption on zeolite 13x bed. *Fluid Mechanics Research International Journal*,1(1), 20-24.
4. Kakavandi,I.A., & Shokroo,E.J.(2016). Dynamic Survey of Nitrogen Adsorption on Zeolite 13X Bed. *3rd INTERNATIONAL CONFERENCE ON SCIENCE AND ENGINEERING*
5. Zahra,M., Jafar,T., andMasoud,M.(2008). Study of a Four-Bed Pressure Swing Adsorption for Oxygen Separation from Air. *International Journal of Chemical, Molecular, Nuclear, Materials and Metallurgical Engineering*, 2(11).
6. Pan,M., Omar,H.M.,& Rohani,S.(2017). Application of Nanosize Zeolite Molecular Sieves for Medical Oxygen Concentration. *Nanomaterials*,7,195,1-19. doi:10.3390/nano708019
7. 13X Molecular Sieve – Sorbead India. <https://www.sorbeadindia.com>
8. J, Mater.Chem,(2006). Novel porous materials for emerging applications. *Journal of Materials Chemistry*, 16, 623-625. DOI: 10.1039/B600327N
9. Kamarudin et al. (1998). ZEOLITE AS NATURAL GAS ADSORBENTS.
10. Mukherjee,N.(2021). PSA Oxygen: Conversion of N2 to O2 concentrator by Zeolite molecular sieve.
11. Prakash,M.(2021).India’s Oxygen emergency is more logistical.<http://theprint.in>
12. Ganley,J.C.(2018). PRESSURE SWING ADSORPTION IN THE UNIT OPERATIONS
13. Rahman,Z.A., Ali,A.J.,and Auob,H.S.(2010). A STUDY OF OXYGEN SEPARATION FROM AIR BY PRESSURE SWING ADSORPTION (PSA). *ACADEMIA*, 203-214.
14. Hamed,H.H.(2015). Oxygen and Nitrogen Separation from Air Using Zeolite Type 5A. *Al-Qadisiyah Journal For Engineering Sciences*, 8(2), 147-158.
15. Santos et al(2007). High-Purity Oxygen Production by Pressure Swing Adsorption. *Ind. Eng. Chem. Res*, 46, 591-599.
16. Santos,J.C., Portugal,A.F., Magalhaes,F.D., & Mendes ,A.(2006). Optimization of Medical PSA Units for Oxygen Production. *Ind. Eng. Chem. Res*, 45, 1085-1096.
17. Zabielska,K., Aleksandrak, T., & Gabrus, E. (2018). ADSORPTION EQUILIBRIUM OF CARBON DIOXIDE ON ZEOLITE 13X AT HIGH PRESSURES. *Chemical and Process Engineering*, 39 (3), 309–321. DOI: 10.24425/122952
18. Shokroo,E.J., Farniaei,M., and Beghbani,M.(2019). Simulation Study of Pressure Swing Adsorption to Purify Helium Using Zeolite 13X. *Applied Chemical Engineering*,2, 1-8.
19. Magee,H.M. Nitrogen Gas Adsorption in Zeolites 13X and 5A. pp. 1-13.



20. Pressure Swing adsorption- Wikipedia. <http://en.m.wikipedia.org>
21. Zabielska,K., Aleksandrak, T., & Gabrus, E. (2018). ADSORPTION EQUILIBRIUM OF CARBON DIOXIDE ON ZEOLITE 13X AT HIGH PRESSURES. *Chemical and Process Engineering*, 39 (3), 309–321. DOI: 10.24425/122952
22. Physical Chemistry (Volume-3) written by Hrishikesh Chatterjee.
23. Hazar,H., Tekdogan, R., and Sevinc, H. (2021). Investigating the effects of oxygen enrichment with modified zeolites on the performance and emissions of a diesel engine through experimental and ANN approach. *Fuel*,303,121318.
24. Moran, A.A. (2014). A PSA PROCESS FOR AN OXYGEN CONCENTRATOR. MSL, ACADEMIC ENDEAVORS, ETD Archive.

## Another sources which helped me to complete the review work.

- Bryan et al (2014). Development of mixed matrix membranes containing zeolites for post-combustion carbon capture. *Energy Procedia*, 63, 160-166.
- Karimi,A., Emrani,P., and Haghayegh,M.(2017). Experimental Verification of Dynamic Modelling of Nitrogen Adsorption on Zeolite 13X with VSA Process. *Science and Technology*, 7(1), 25-34. DOI: 10.5923/j.scit.20170701.03
- Shokroo et al (2015). Comparative study of zeolite 5A and zeolite 13X in air separation by pressure swing adsorption. *Korean J. Chem. Eng.*,33(4), 1391-1401. DOI: 10.1007/s11814-015-0232-6
- Khazraei,S., Soleimani,M., and Kargari,A.(2014). Investigation of Different Kinetic models of O<sub>2</sub> and N<sub>2</sub> adsorption on 13X Zeolite. *The 8th International Chemical Engineering Congress & Exhibition*, 1-5.
- Beaman,J.(1989). OXYGEN STORAGE ON ZEOLITES. USAFSAM-TR-88-26.
- Cavenati,S.(2004). Adsorption Equilibrium of Methane, Carbon Dioxide, and Nitrogen on Zeolite 13X at High Pressures. *Journal of Chemical & Engineering Data*, 49, 1095-1101.
- Bezerra et al (2011). Adsorption of CO<sub>2</sub> on nitrogen-enriched activated carbon and zeolite 13X. *Adsorption*,17, 235-246. DOI 10.1007/s10450-011-9320-z
- Chatti et al (2009). Amine loaded zeolites for carbon dioxide capture: Amine loading and adsorption studies. *The Official Journal of the International Zeolite Association*, 121, 84-89.
- Gizicki,W., and Banaszkiwicz,T.(2020). Performance Optimization of the Low-Capacity Adsorption Oxygen Generator. *Appl. Sci*, 7495, 1-11. doi:10.3390/app10217495
- Dantas et al(2011). Carbon dioxide–nitrogen separation through pressure swing adsorption. *Chemical Engineering Journal*,172, 698-704.
- Akulinin et al(2020). OPTIMIZATION AND ANALYSIS OF PRESSURE SWING ADSORPTION PROCESS FOR OXYGEN PRODUCTION FROM AIR UNDER UNCERTAINTY. *Chem. Ind. Chem. Eng. Q* , 26(1), 89-104.

- Montanari et al(2011). CO<sub>2</sub> separation and landfill biogas upgrading: A comparison of 4A and 13X zeolite adsorbents. *Energy*, 36, 314-319.
- Mofarahi,M.,and Shokroo, E.J.(2013). COMPARISON OF TWO PRESSURE SWING ADSORPTION PROCESSES FOR AIR SEPARATION USING ZEOLITE 5A AND ZEOLITE 13X. *Petroleum & Coal*, 55(3), 216-225.
- Shokroo,E.J., Farniaei,M., and Beghbani,M.(2019). Simulation Study of Pressure Swing Adsorption to Purify Helium Using Zeolite 13X. *Applied Chemical Engineering*,2, 1-8.
- Suraweera et al(2014). Hydrogen adsorption and diffusion in amorphous, metal-decorated nanoporous silica. *INTERNATIONAL JOURNAL OF HYDROJEN ENERGY*. 39,9241-9253
- Santos,J.C., Portugal,A.F., Magalhaes,F.D., & Mendes ,A.(2004). Simulation and Optimization of Small Oxygen Pressure Swing Adsorption Units. *Ind. Eng. Chem. Res.*, 43, 8328-8338.
- Zhu et al (2016). Study of a novel rapid vacuum pressure swing adsorption process with intermediate gas pressurization for producing oxygen. *Adsorption*, DOI 10.1007/s10450-016-9843-4
- Kroi,M.(2020). Natural vs. Synthetic Zeolites. *Crystals*, 10, 622, 1-8.

TITLE OF REVIEW - Producing Oxygen using 13X zeolite by PSA method.

NAME OF THE INSTITUTION - Scottish Church College

C.U. ROLL NO - 223/CEM/191026

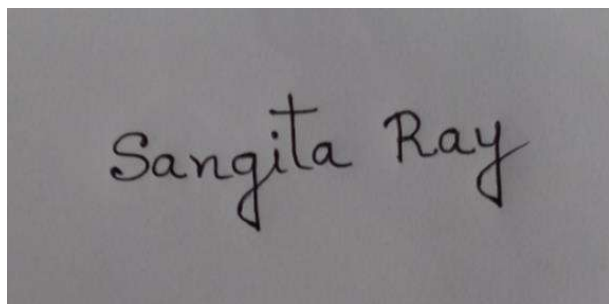
C.U. REGISTRATION NO - 613-1221-0683-16

SPECIAL PAPER : CHEM- SO 44

NAME OF CANDIDATE

Sangita Ray

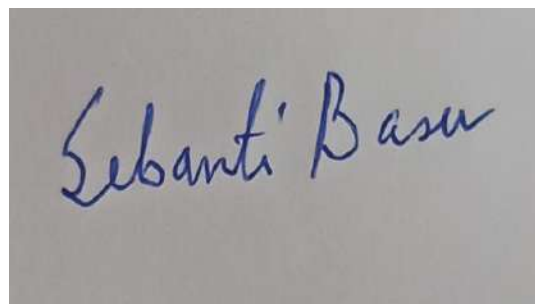
SIGNATURE OF CANDIDATE

A photograph of a handwritten signature in black ink on a light-colored background. The signature reads "Sangita Ray" in a cursive script.

NAME OF EXAMINER

Dr. Sebanti Basu

SIGNATURE OF EXAMINER

A photograph of a handwritten signature in blue ink on a light-colored background. The signature reads "Sebanti Basu" in a cursive script.

## ACKNOWLEDGEMENT:

The review 'Producing Oxygen using 13X zeolite by PSA method' has provided me with an ample scope of learning through collaborative activities. I consider myself fortunate enough to work under Dr. Rama Ranjan Bhattacharjee whose guidance made my review work learning quite joyful. He has given important suggestions for the improvement of the review work. I am grateful to him.

I am also very thankful to Dr. Sebanti Basu, Associate professor, Scottish Church College for her continuous support.

I would like also to thank Dr. Sourav Chakrabarty, Assistant Professor, Scottish Church College for his precise suggestions which were very helpful to the accomplishment of the review work.

And I am also grateful to my parents and my friends who have helped me to carry out the review.

## CONTENT:

Introduction	1
Reason behind choosing zeolite	1
Why 13X zeolite	2
Table – 1 (Properties of zeolite)	3
Adsorption phenomena	4
A short view of PSA process	4-7
Methods of pressure swing adsorption	7-9
Table – 2 (Details of PSA Columns and Adsorbent)	9
Discussion of experimental work (two columns 4 step and 6 step)	9-15
Animation picture of PSA method	16
Consideration for Mathematical Model	17
Result and discussion (for Dynamic modeling of N <sub>2</sub> adsorption on 13X bed)	17-21
Conclusion	21
Future Scope	21
References	22-24

## Introduction:-

One of the most important clinical gas used in health care center is oxygen. There are no modern hospitals and nursing home which can manage without oxygen. Pure oxygen is too much essential for the respiration of the patients during anesthesia and in the intensive care or neonatal units<sup>[1]</sup>. Now in this covid pandemic situation oxygen is really too much necessary for survival of covid +ve patients. The challenge is appeared by increasing supply of medicinal oxygen with reducing cost<sup>[2]</sup>. In 1907, Linde built a first cryogenic distillation bed for air separation and this time oxygen was first produced<sup>[3]</sup>. Besides this in chemical industries oxygen is too much necessary for various processes like refinery industries, manufacturing metal etc. The most commonly adsorbent used in air separation for producing oxygen is zeolite 13X<sup>[4]</sup>. Here desorption and adsorption process mainly occurs. There are many process exists for separation of air to produce purified oxygen. Among them pressure swing adsorption (PSA) is very popular in the market because it is a safe process with reasonable energy and area requirements<sup>[1]</sup>. At first Skarstrom in 1958 proposed the simplest PSA process. Till now there are many process arises using different types of adsorbent for this purposes to purify oxygen. Farooq et al,(1989) used zeolite-5A for producing oxygen using PSA method by performing Sakrstrom cycle. In 1990 Keny and Liow used 5A zeolite for air separation<sup>[5]</sup>. But zeolite 13X is used in a wide range because it has outstanding nitrogen to oxygen adsorption selectivity. In recent time 13X zeolite is modified with Li<sup>+</sup> exchange method which shows a higher nitrogen adsorption capacity at the active cation sites of the zeolite framework<sup>[6]</sup>. Besides this zeolite 13X has large mass transfer zone, so the adsorption rate is high. Nitrogen concentrations mainly drop in the outlet of the zeolite 13X at the time of about 125 seconds and the concentrations reaches zero after about 180 seconds<sup>[3]</sup>.

## Reason behind choosing zeolite as a molecular sieve :

Porous materials are those materials which contain void space. There are many types of porous materials such as rocks and soil, zeolites, biological tissues and artificial materials such as cements and ceramics etc. The characteristics of a porous material vary depending on the size, arrangement and shape of the pores, as well as the porosity and composition of the material itself (porous materials latest research). According to the IUPAC, pores are classified into three categories, these are micropore – (pore sizes less than 2nm), mesopore (between 2 and 50 nm) and macropore ( with pore size larger than 50 nm)<sup>[8]</sup>. For PSA method zeolite is chosen as adsorbent. Zeolite has microporous crystalline structures. Zeolite framework is an assemblage of SiO<sub>4</sub> and AlO<sub>4</sub> tetrahedral joined together by sharing oxygen atoms<sup>[9]</sup>. This type of microporous solid such as zeolite (aluminosilicate member) is known as molecular sieves. Zeolite molecular sieve contains very small pores of uniform size<sup>[10]</sup>. Zeolite adsorbent has the selectivity to adsorb

nitrogen compared to oxygen because of the interaction between electrostatic field of the cationic zeolite and the quadrupole moment of the nitrogen and oxygen. The quadrupole of oxygen is three times lesser than that of nitrogen. And this fact leads to a selective adsorption on to the zeolite surface<sup>[6]</sup>.

## Why 13X zeolite:

So zeolite adsorbs nitrogen like it sponge adsorbs water . Converting medical air to medical oxygen using 13X zeolite is very practical. However LiX material is a good adsorbent for adsorption of nitrogen at ambient pressure and releases under vacuum. The operations are simpler and the system built will be simple and accomplished. But Lithium X can not be easily sourced in India. So the technology has to be based on more readily available 13X molecular sieve zeolite. Substitution of LiX by 13X change the operation from vacuum based to a pressure based (VPSA to PSA)<sup>[11]</sup>. There are three types of zeolite structure become dominant such as A,X and Y<sup>[1]</sup>. 13X zeolite is the sodium form of the type X crystal. It has pore diameter of 1nm . So it will adsorb molecules of A crystalline form that is 3 Angstrom,4 Angstrom and 5 Angstrom<sup>[7]</sup>. Zeolite 13X has the chemical formula  $\text{Na}_{86}[(\text{AlO}_2)_{86}(\text{SiO}_2)_{106}] \cdot \text{H}_2\text{O}$  having pore diameter less than 10 Angstrom( 1nm). X crystalline foam has a larger pore size than other types .

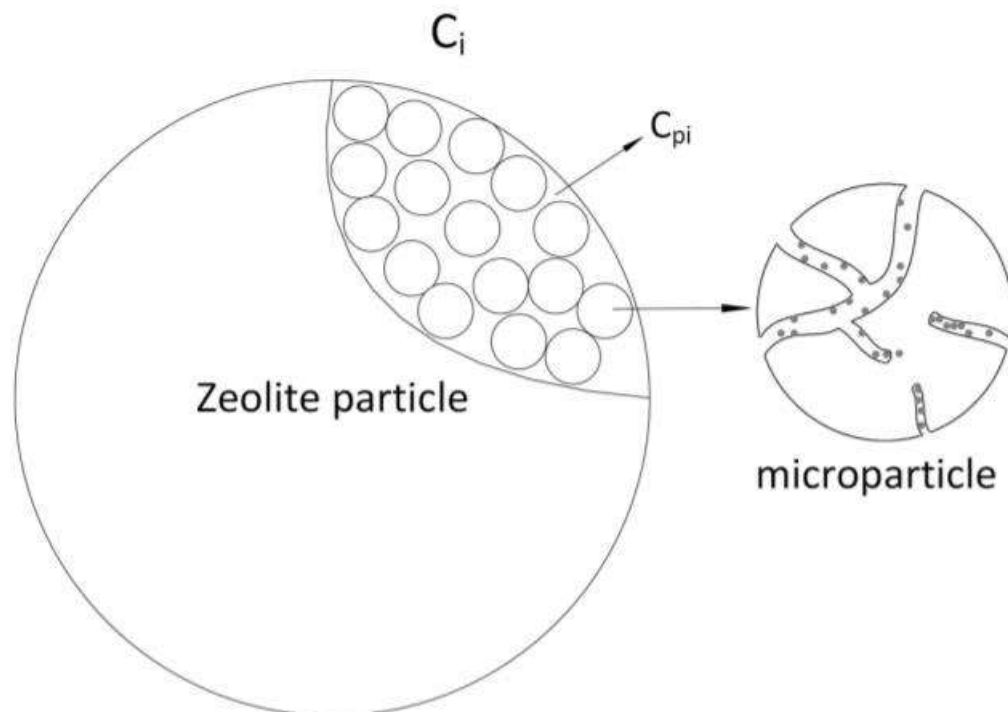
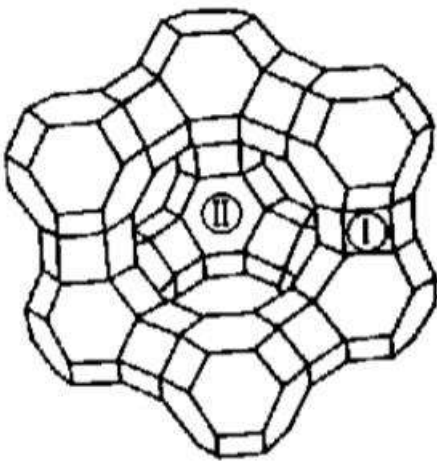


Figure-1 Schematics of zeolite particle structure<sup>[6]</sup>.

Table – 1 (Properties of zeolite)<sup>[19]</sup>

Chemical name	Na <sub>86</sub> [(AlO <sub>2</sub> ) <sub>86</sub> (SiO <sub>2</sub> ) <sub>106</sub> ]•H <sub>2</sub> O
Pore Diameter	~8Å
Mesopore volume	0.165 cm <sup>3</sup> /g
Micropore volume	0.17 cm <sup>3</sup> /g
Langmuir surface area	571 m <sup>2</sup> /g
Mass of pellet sample	2.37 g
Mass of crushed sample	2.49 g



Zeolite 13X molecular structure

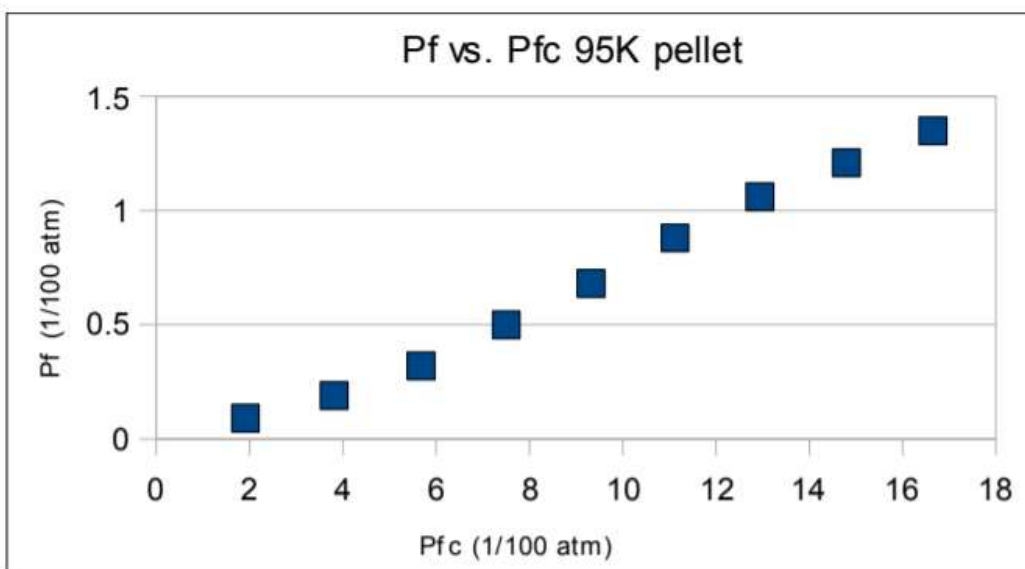
Figure-2<sup>[19]</sup>

Figure-3

Adsorption of nitrogen in zeolite 13X pellet at 95K<sup>[19]</sup>.



## Adsorption phenomena in PSA method:

Adsorption is the phenomenon where molecules of one phase remain preferentially concentrated at the surface of another phase<sup>[22]</sup>. Generally, gas adsorption in zeolite are of two types named physisorption and chemisorption. But physisorption is more preferable method for gas separation and purification because of the fact that the adsorbent can be regenerated by heating or flushed to remove the adsorbed gas molecules attaching to the solid. This make the process more economical and profitable<sup>[9]</sup>.

## A short view of PSA process:

Pressure swing adsorption is an industrial process which is generally used for the bulk separation of gas mixtures. It is a cyclic operation<sup>[12]</sup>. In 1960, Skarstrom patented the first PSA unit which was composed of two beds and using a zeolite<sup>[13]</sup>.

Stage 1- Compressed air is passed into the first bed. Nitrogen molecules are trapped and oxygen molecules is allowed to flow through.

Stage -2- At the time of saturation of the adsorbent in the first bed with nitrogen, the air flow feed is directed towards the second bed.

Stage -3- Nitrogen was adsorbed by the adsorbent (13X zeolite) in the second bed. The first bed is depressurized allowing nitrogen to be loosen out of the system and released to the atmosphere.

Stage- 4- The process starts over. Again compressed air is fed into the first bed. The second bed is relaxed by releasing nitrogen and oxygen to the atmosphere. The process is repeated continuously producing a constant flow of purify oxygen<sup>[14]</sup>.

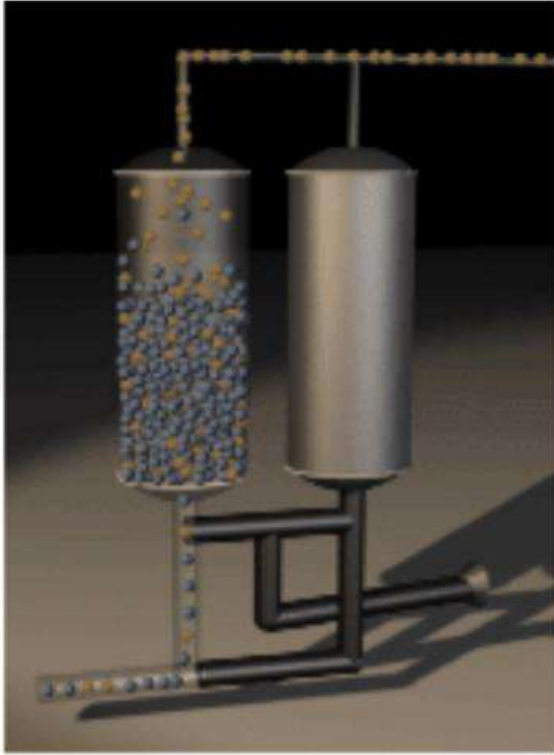


Figure-4<sup>[14]</sup> Stage – 1

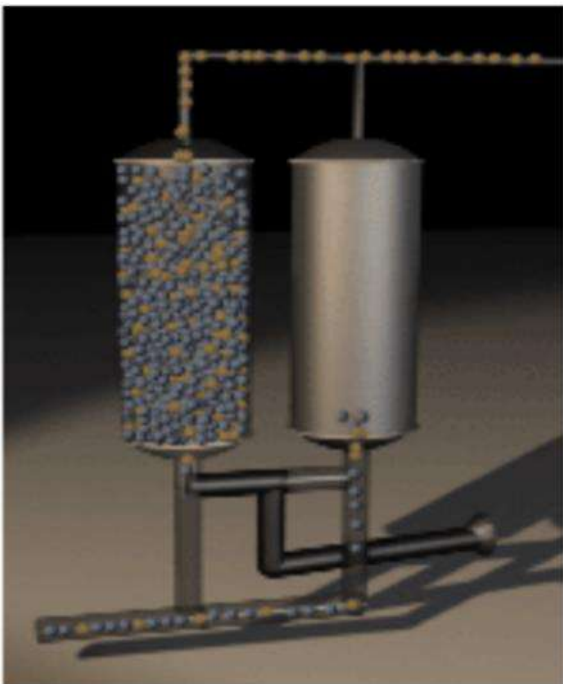


Figure-5<sup>[14]</sup> stage – 2

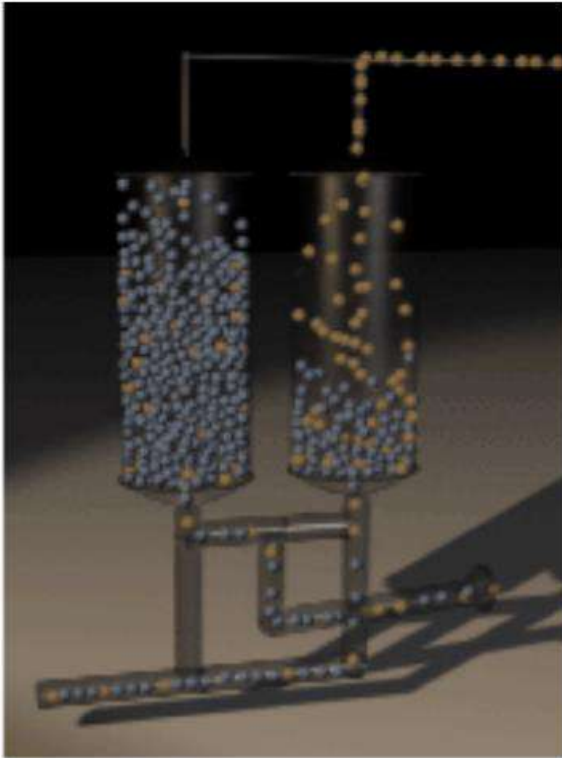


Figure-6<sup>[14]</sup> Stage – 3

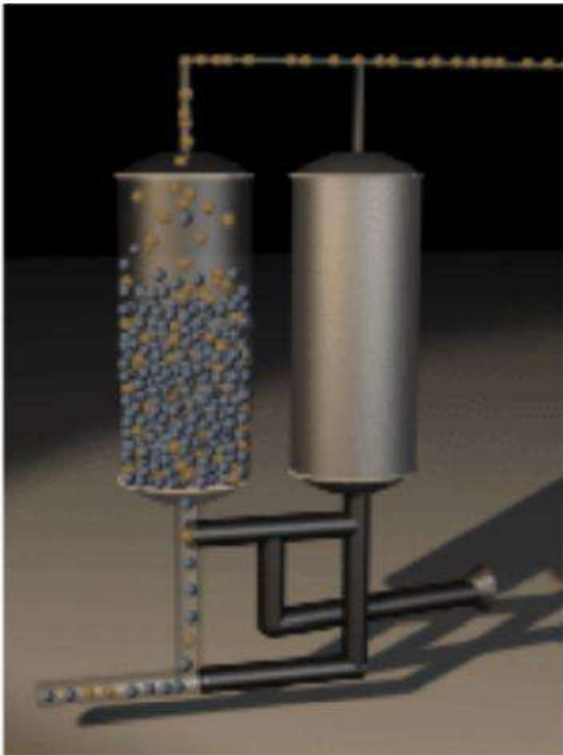


Figure-7<sup>[14]</sup> Stage – 4

Oxygen production using 13X zeolite by using PSA process has noticeably increased in the past decades. But the concentration of the products is limited to 95% oxygen due to presence of argon in air. Because the adsorbent present has the similar adsorption capacities for oxygen and argon. Actually in PSA cycle desorption take place at a pressure much lower than adsorption<sup>[15]</sup>.

There are many application observed for PSA unit such as producing oxygen for medical use. In 1975 this unit was started to use in a wide range for treating patient with respiratory illness. This provide 2-4 L/min of 85-95% oxygen. In this year Ruder and Isles also patented a PSA unit for producing enriched air(use onboard jet aircraft) (U.S. Patent 3,922,149). Just one year latter an electric powered compact PSA apparatus (DE Patent 2,559,120) was described by Armond. He use zeolite molecular sieve to generate breathing air for medical use. In 1984, Kratz and Sircar patented a medical oxygen generator for domiciliary use (U.S.Patent 4,477,265). This process generated 90% of oxygen<sup>[16]</sup>.

In this work, nitrogen adsorption process using 13X zeolite as a molecular sieve is simulated. So the process is dynamic<sup>[4]</sup>.

## Method of pressure swing adsorption

### Equilibrium adsorption

Air mainly contains three components, nitrogen, oxygen and argon. In between 1916 to 1918, Langmuir proposed the theoretical basis of adsorption which is based on kinetic theory of gases<sup>[17]</sup>. This phenomena explain the type 1 adsorption curve(HKC). Multicomponent adsorption equilibria theory (competition between the different molecules on the adsorbent) is required for designing purposes.

$$\theta_i = \frac{b_i P_i}{1 + \sum_{j=1}^N b_j P_j} \quad (\text{Equation 1})$$

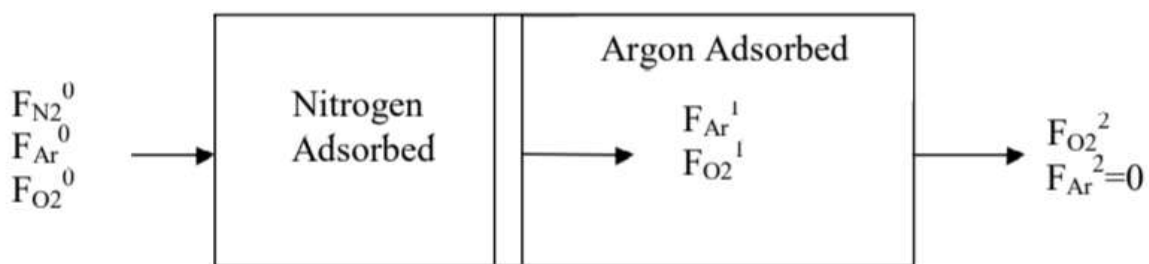
Fractional loading contributed by  $\theta_i$  and  $i$ .

$b_i$  and  $b_j$  are the rate constants of adsorption to that for desorption for component  $i$  and component  $j$  respectively.  $P_i$  – Partial pressure of component  $i$ ,  $P_j$  – Partial pressure of component  $j$ .  $N$  is the number of species.

Equation 1 gives the adsorbed amount of species  $i$  on the adsorbent in the multi component system. The selectivity describes how one species is selective to bind to the adsorbent over another species. The selectivity of a species  $i$  in relation to species  $j$  is given as

$$S_{i,j} = \frac{b_i}{b_j} \quad (\text{Equation 2})$$

A transport phenomena is observed to study how each species is adsorbed in the adsorbent bed. Material balance equations are used to determine these parameters.



Air component through adsorbent bed<sup>[1]</sup>.

Material balances are performed for the components in each section of the adsorbent bed.

$$\text{Nitrogen : } F_{N_2}^0 \Delta t = \Delta L_1 A N_{N_2}^1 = v_1 A N_{N_2}^1 \quad (\text{Equation 3})$$

$$\text{Oxygen: } F_{O_2}^1 = F_{O_2}^0 + (N_{O_2}^2 - N_{O_2}^1) A v_1 \quad (\text{Equation 4})$$

$$\text{Argon: } F_{Ar}^1 = F_{Ar}^0 + (N_{Ar}^2 - N_{Ar}^1) A v_1 \quad (\text{Equation 5})$$

$$F_{Ar}^2 = 0 = F_{Ar}^1 + N_{Ar}^2 A v_2 \quad (\text{Equation 6})$$

Here,  $F$  stands for volumetric flowrate,  $\Delta t$  is the cycle time,  $\Delta L$  is the length of the bed,  $A$  is the area,  $N$  is the loading and  $v$  is the front velocity.

The velocity of the argon front must be greater than nitrogen front.

$$\frac{v_2}{v_1} = \frac{\frac{F_{Ar}^0}{F_{N_2}^0} + (N_{Ar}^2 - N_{Ar}^1)}{N_{Ar}^2} > 1 \quad (\text{Equation 7})$$

Nitrogen molecule has strong electrostatic interaction with 13X zeolite than do oxygen and argon molecules. The front moves with nitrogen front's velocity as a function of the adsorption and desorption of the molecules on the adsorbent sites. So nitrogen has a slower rate of desorption than oxygen and argon. So the velocity front of argon to nitrogen is greater than one<sup>[1]</sup>.

To get greater flexibility Langmuir–Freundlich equation is used which is

$$q = q_m(T) \frac{b(T).p^{n(T)}}{1+b(T).p^{n(T)}} \quad (\text{Equation 8})^{[21]}$$

## Details of PSA Columns and Adsorbent

Table-2<sup>[13]</sup>

Adsorbers		
Column Length	L	0.7 m
Column diamete	D	50 mm
Adsorbent Type		13X zeolite
Shape		Sphere
Particle diameter	$d_p$	1.7-2.6 mm
Particle density	$\rho_p$	1070 kg/m <sup>3</sup>
Bulk density	$\rho_B$	670 kg/m <sup>3</sup>
Bed porosity	$\epsilon$	0.4
Adsorbent weight	w	0.75 kg
Adsorbent bed length	$L_B$	0.57 m
Langmuir isotherm parameters	$q_{sO_2}$	3.091 mol/kg
Oxygen	$b_{O_2}$	0.0367 bar <sup>-1</sup>
Adsorption heat of O2	$\Delta H_{O_2}$	12.8 kJ/mole
Nitrogen	$q_{sN_2}$	3.091 mol/kg
	$b_{N_2}$	0.1006 bar <sup>-1</sup>
Adsorption heat of N2	$\Delta H_{N_2}$	17 kJ/mole

## Discussion of the experimental work for two column 4 step and 6 step PSA operation.

Two column: 4 step and 6 step PSA operation .

- Pressurizing time  $t_{prs} = 10$  s
- Depressurizing time  $t_{deprs} = 10$  s
- Equalization time  $t_{eq} = 20$  s

The operating parameters considered in the present work with their ranges are as follows; Adsorption time  $t_{ads} = 10, 20, \text{ and } 30$  s ,Adsorption pressure  $P_H = 2, 3, \text{ and } 4$  bar , Purge flow rate  $Q_{purg} = 1, 1.5, 2, 3, 4, 5, \text{ and } 6$  L/min<sup>[13]</sup>.

## Two Column Adsorption:

The PSA system preparation shown in figure using vacuum and O<sub>2</sub> pressurizing and purging to ensure the zeolite activity<sup>[13]</sup>.

Figure- 8 shows that the effect of adsorption on oxygen purity. Figure -9 shows that no noticeably change occurred between the pressure ratios 2 and 4 bar. This result is in agreement with that performed by Jee et al. (2001) for high purge to feed ratio, Yuwen et al.(2005). Jain et al (2003) stated that for constant selectivity systems, performance increases with increasing pressure according to adsorption equilibrium isotherm.

In figure- 10 it can be seen that breakthrough occurs at high adsorption time. Adsorption Step duration is needed for needed for breakthrough to occur<sup>[13]</sup>.

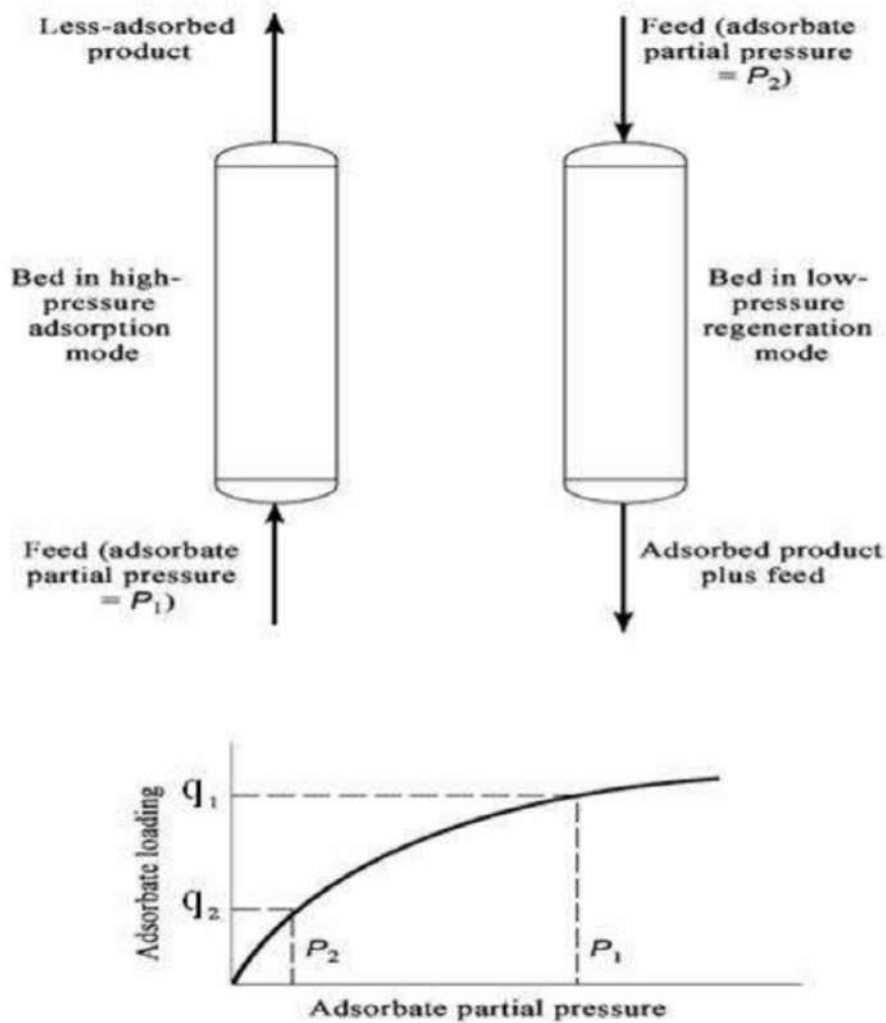


Figure – 8 Pressure swing cycle<sup>[13]</sup>.

## Product Oxygen Cycle for 4- step cycle

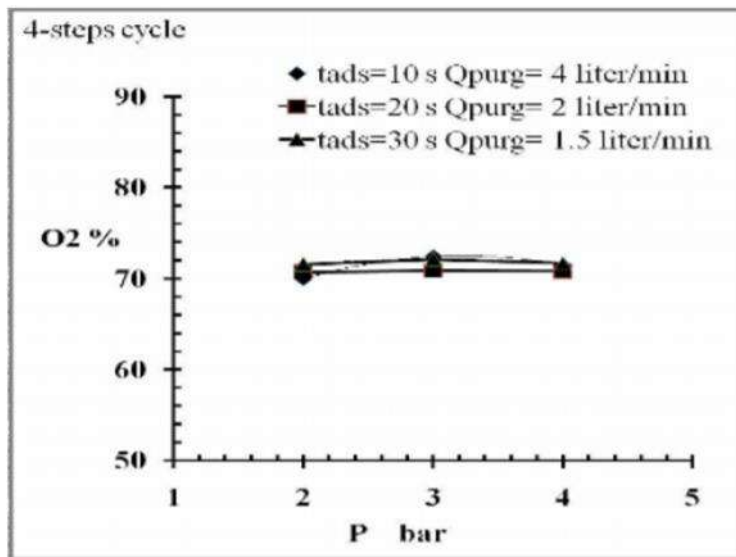


Figure - 9 The effect of the adsorption pressure ( $p_H$ ) on product oxygen purity for 2-column, 4-step operation<sup>[13]</sup>.

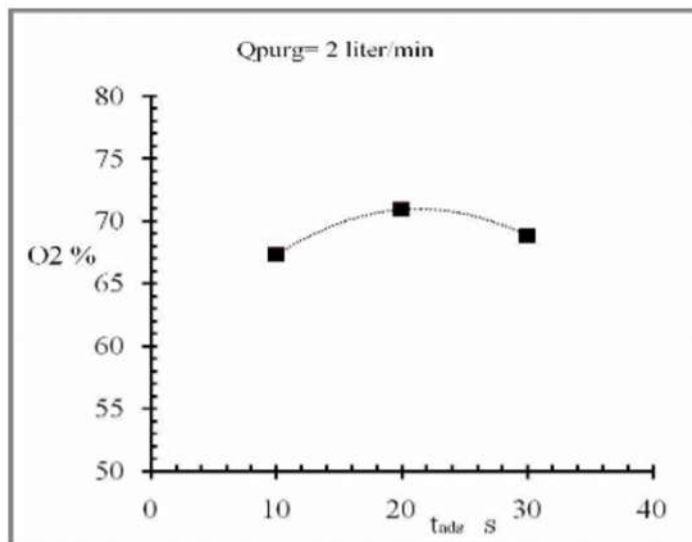


Figure - 10 Effect of the adsorption time ( $t_{ads}$ ) on product oxygen purity for 2-column, 4-step cycle, ( $Q_{purg}=2\text{ l/min}$ )<sup>[13]</sup>.



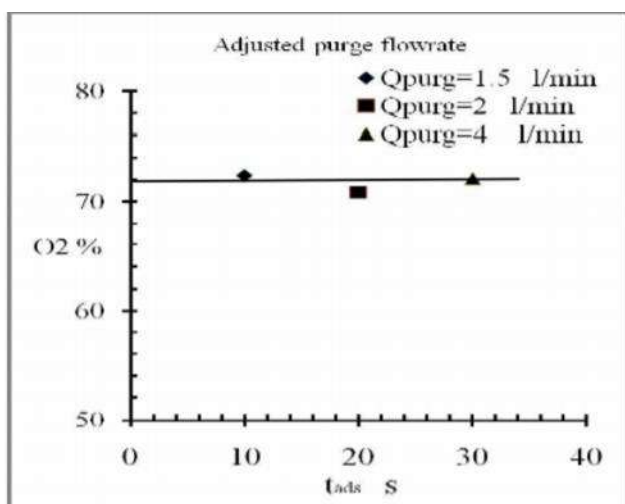


Figure -11 8 Effect of adsorption time ( $t_{\text{ads}}$ ) on product oxygen purity, for 4-step cycle, by adjusting the purge flowrate ( $Q_{\text{purg}}$ )<sup>[13]</sup>.

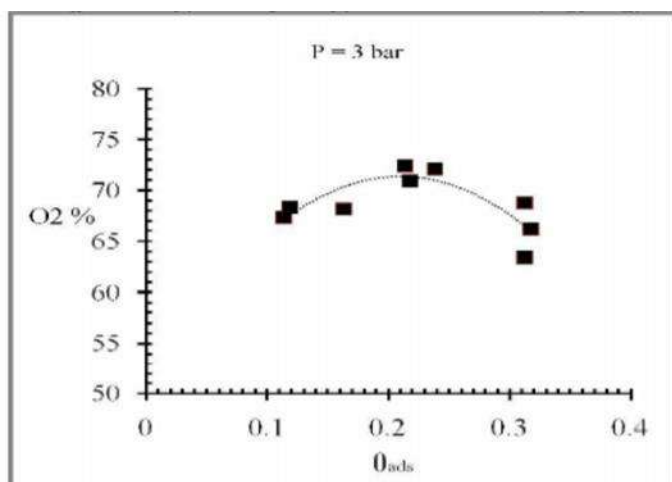


Figure- 12 9 Effect of the dimensionless adsorption time on product oxygen purity for 2-column, 4-step operation<sup>[13]</sup>.

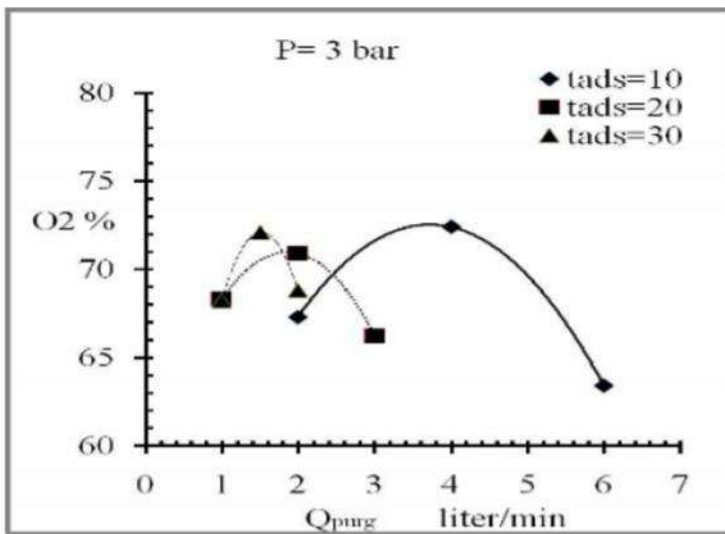


Figure- 13 The effect of the Purge Flow rate ( $Q_{\text{purg}}$ ) on product oxygen purity, for 2-column, 4-step cycle<sup>[13]</sup>.

From this Figure- 13 it is revealed that the nitrogen wave front is breakthrough. The maximum product oxygen is 70% pure because of both the effect of purge flowrate( $Q_{\text{purg}}$ ) and the adsorption time( $t_{\text{ads}}$ ).

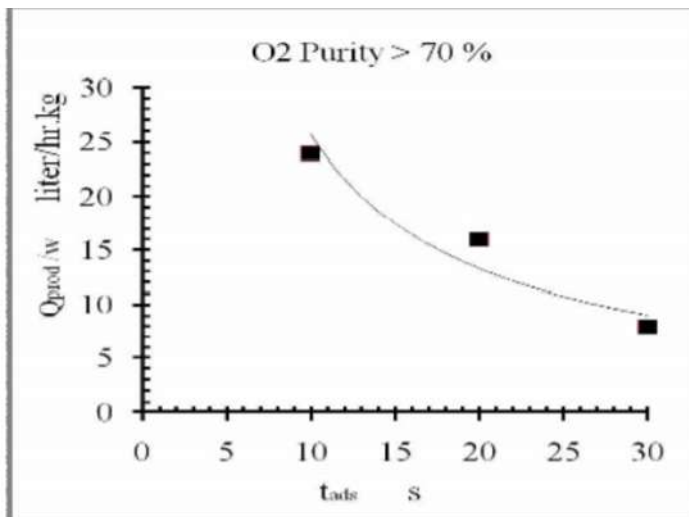


Figure-14 The effect of the adsorption times ( $t_{\text{ads}}$ ) on specific product Flowrate ( $Q_{\text{purg/w}}$ ) at maximum product oxygen purity<sup>[13]</sup>.

Product Oxygen Purity for 6- step cycle:

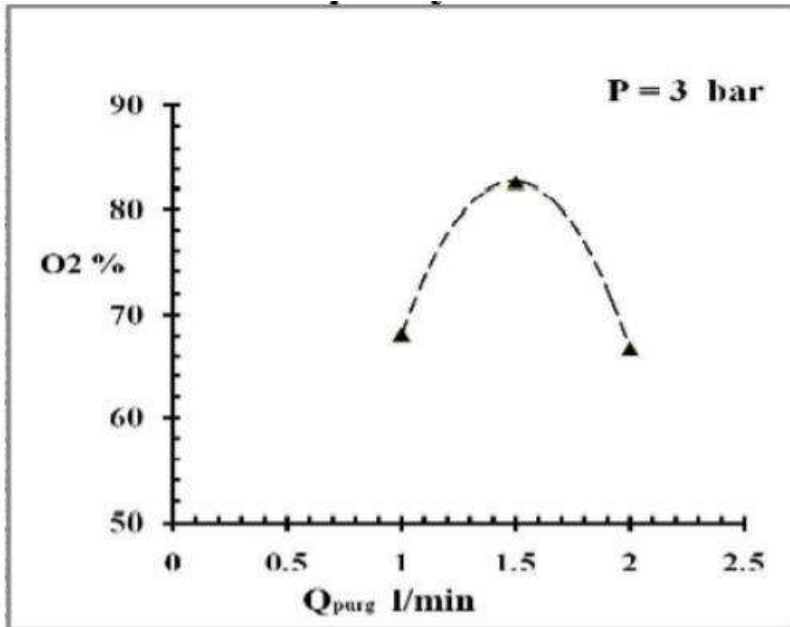


Figure -15 The effect of the purge flowrate ( $Q_{\text{purg}}$ ) on product oxygen purity for 6-Steps cycle, with air feed initial pressurizing<sup>[13]</sup>

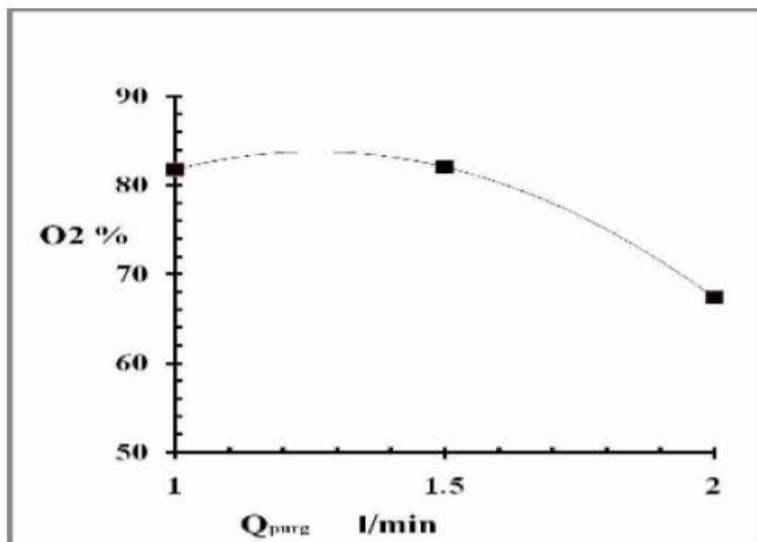


Figure -16 The effect of the purge flowrate ( $Q_{\text{purg}}$ ) on product oxygen purity for 6-Steps cycle, with O<sub>2</sub> initial pressurizing<sup>[13]</sup>.

Figure-16 shows that, with increasing purge flowrate above 1.5 lit/min , product purity decreases to that breakthrough point forming high effluent from the column<sup>[13]</sup>.

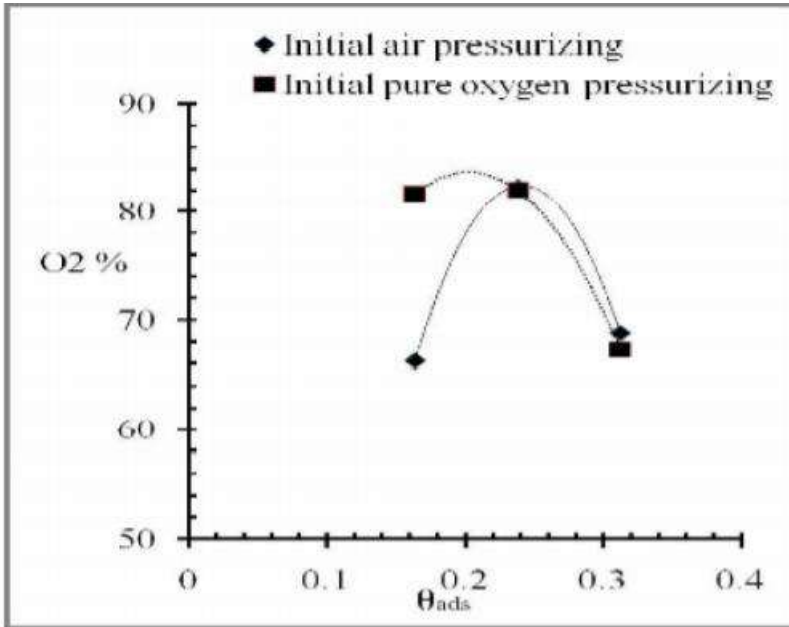


Figure -17 Effect of the dimensionless adsorption time ( $t_{ads}$ ) on product oxygen purity for 2-column, 6-step cycle<sup>[13]</sup>.

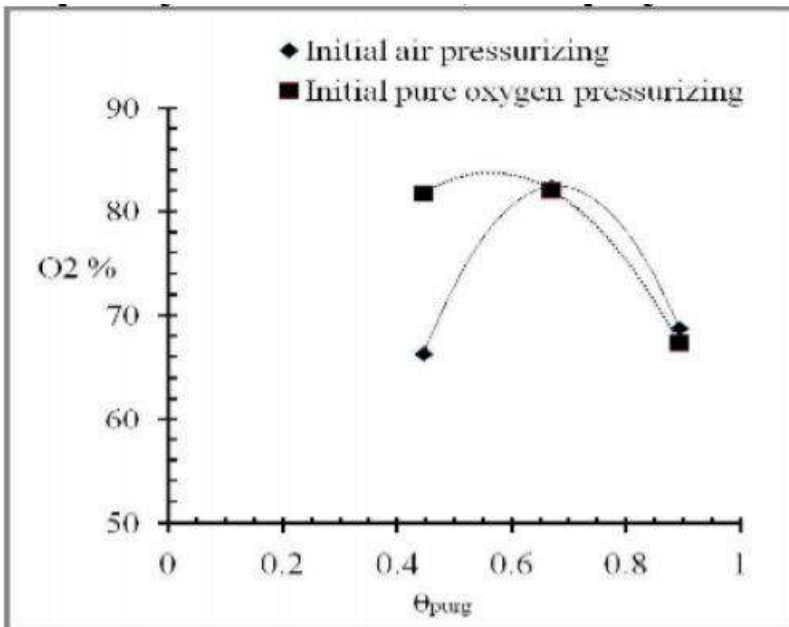
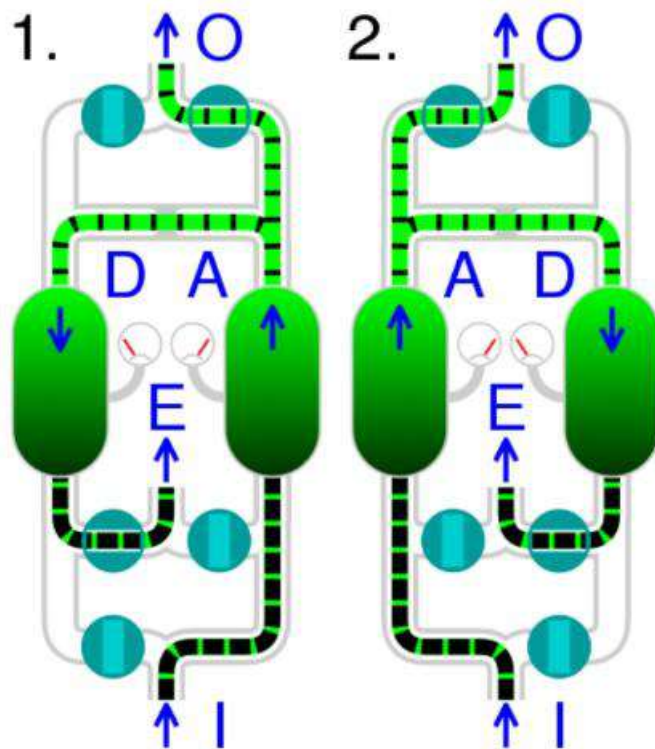


Figure -18 Effect of the dimensionless purge time ( $Q_{purg}$ ) on product oxygen purity for 2-column, 6-step cycle<sup>[13]</sup>



Animation of pressure swing adsorption, (1) and (2) showing alternating adsorption and desorption

I compressed air input    A adsorption  
 O oxygen output            D desorption  
 E exhaust

Figure– 19<sup>[20]</sup>

## Consideration for Mathematical Model for Dynamic modeling of N<sub>2</sub> adsorption on 13X bed.:-

To develop a mathematical model for adsorption bed, the following assumptions must be considered.

- Gas behaves as an ideal gas.
- The flow pattern is axially assumed as plug-flow model.
- Equilibrium equations for air are expressed as triple Langmuir-Freundlich isotherm (oxygen, nitrogen and argon);
- Mass transfer rate is presented by linear driving force (LDF) relations;
- At initial state bed is clean and there is no gas flow in it;
- Air is considered a mixture of oxygen and argon (21 %) and nitrogen (79 %) as feed<sup>[4]</sup>.

A four bed pressure swing adsorption for oxygen separation from air was proposed by Zahra et al(2008)<sup>[5]</sup>. Recently in 2017 Kakavandi et al proposed a dynamic modeling of nitrogen adsorption on 13X zeolite using two bed.

## Result and discussion :

The fourth order Runge-Kutta Gill method was used to solve the mathematical model. An experimental and simulation observation of the PSA unit running with a traditional Skarstrom cycle and a Skarstrom cycle with concurrent equalization in an attempt to separate oxygen from air using a 5A zeolite has been proposed by Mendes et al. Moreover, a small-scale two-bed six-step PSA process using zeolite 13X was performed by Jee et al.

Figures 20 and 21 indicate the effect of product flow rate and P/F on the purity and recovery of oxygen during PSA process, respectively<sup>[3]</sup>.

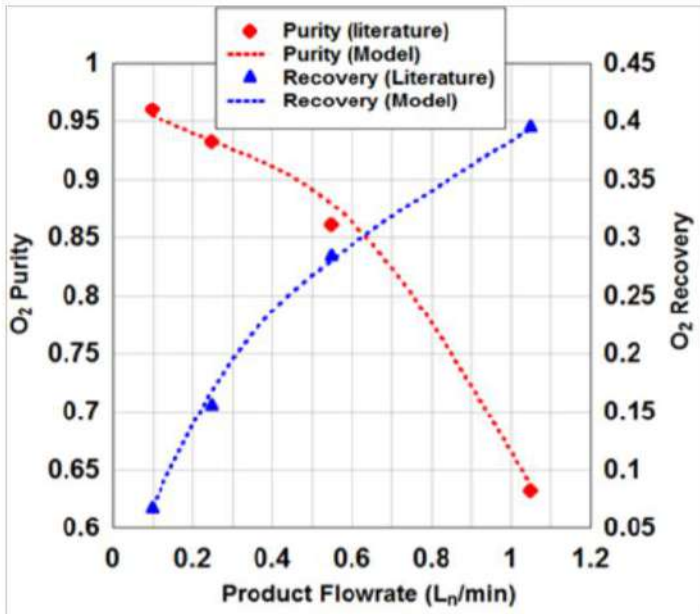


Figure -20<sup>[3]</sup>

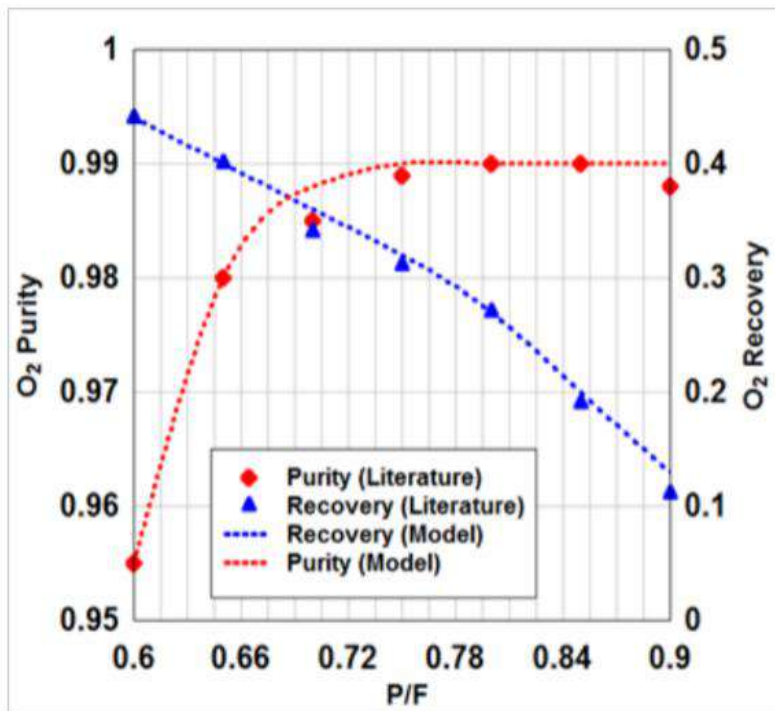


Figure-21<sup>[3]</sup>

Break through curves for nitrogen and oxygen on zeolite 13X is shown in the following Figure. The term “break through time” is developed by the response of initially clean bed per a flow with

constant composition. In Figure – 22 it is shown that oxygen exists from the top of the 13X zeolite earlier than nitrogen at about approximately 230 seconds.

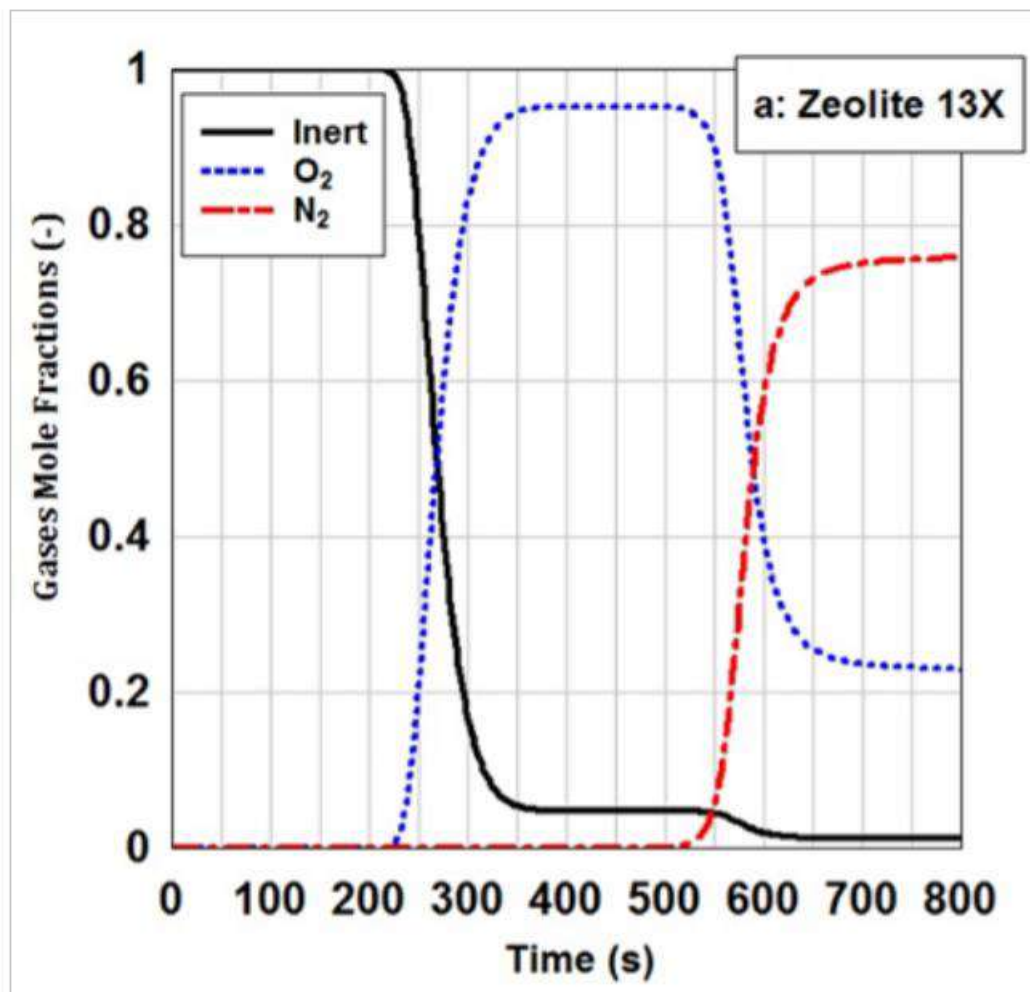


Figure -22<sup>[3]</sup>

(The simulated breakthrough curves of zeolite 13X for oxygen and nitrogen at adsorption pressure of 6 bar and feed flow rate of 5 LSTP/min. The adsorption bed was initially saturated with a non-adsorptive gas.)

With passing of time High roll-up phenomena is observed in case of oxygen. Because of this phenomena oxygen concentration is 4.5 times greater than feed concentration during the time of 400-500 seconds. Oxygen is affected by this phenomena because nitrogen adsorption on 13X zeolite is much more than that of oxygen. So oxygen concentration is relatively increased rather than feed concentration. Nitrogen breakthrough occurs at the time of 550 seconds and from this time oxygen concentration is starting to be reduced. In Figure- 22, it is clearly said that High roll-up phenomena in the case of nitrogen because of its strong adsorption on zeolite 13X. In PSA cycle adsorption and desorption process depends on pressure increasing and decreasing<sup>[18]</sup>.

Figure - 23 says that nitrogen concentration on zeolite 13X with respect to different adsorption pressures and time. With increasing pressure adsorption rate, of nitrogen increases. Figure- 24



says oxygen concentration along the bed length of the adsorbent (13X zeolite) in different times. The slope of oxygen concentration curve is fast. The desorption curve of zeolite 13X is depicted in Figure 25. The assumption is that a pure inter gas is utilized for cleaning the bed in order to simulate desorption over the beds<sup>[3]</sup>.

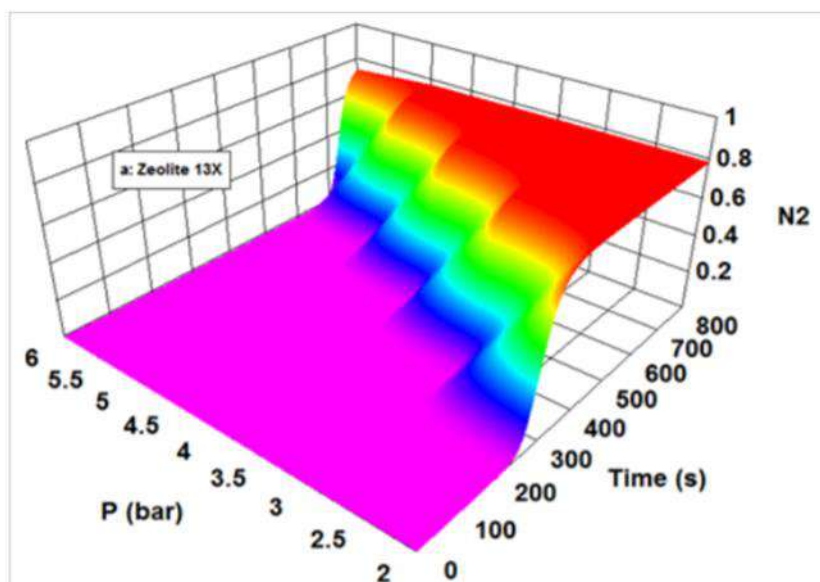


Figure -23 The outlet mole fraction of nitrogen from zeolite 13X at different adsorption pressures and feed flow rate of 4LSTP/min. The adsorption bed was initially saturated with a non-adsorptive gas<sup>[3]</sup>.

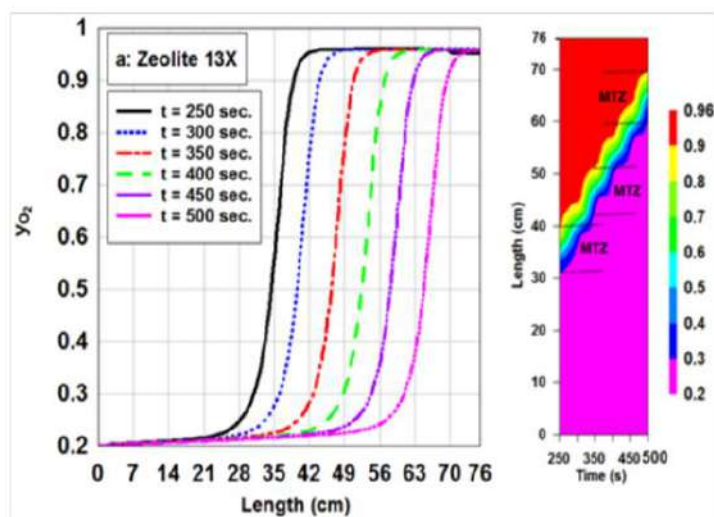


Figure – 24 Distribution of oxygen concentration along the length of zeolite 13X during adsorption process in different times. The feed flow rate is 5LSTP/min and the adsorption pressure is 6 bar<sup>[3]</sup>.

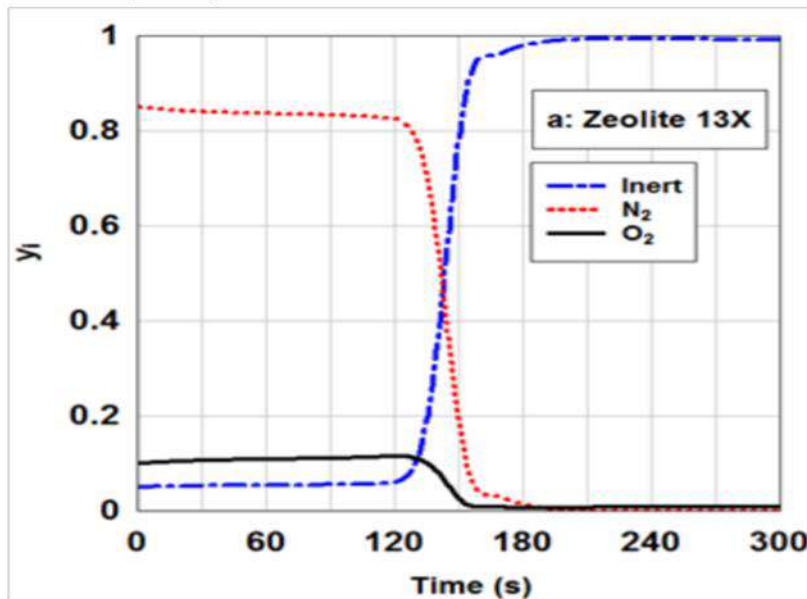


Figure – 25 The outlet

simulated concentration of gas phase from zeolite 13X during desorption at pressure of 0.1bar. The desorption bed was completely clean in the initial state<sup>[3]</sup>.

## Conclusion:-

It has been discussed that how the PSA process using 13X zeolite is effective to produce pure oxygen. Using this technology hospitals and nursing home can manage their oxygen deficiency. zeolite 13X is used in a wide range because it has outstanding nitrogen to oxygen adsorption selectivity and it is easily available in India. In this covid- 19 pandemic situation , this type of process for producing oxygen is really helpful. As evidenced by the discussion , there are numerous ways to operate the PSA process. The effect of adsorption pressure was also shown and it was clear that higher adsorption pressure will lower the recovery of the cycle. PSA method can produce almost 90% pure oxygen.

## Future Scope:-

Within the scope of the study , the effects of improvements on the pores, surface area increase the improvement of the process<sup>[23]</sup>. One major area of study that would be useful would be to optimizing cycles utilizing product pressurization instead of an equalization step and to get a fruitful result the effects of dead volume would need to be minimized by getting larger column . Additionally , more work is needed to find kinetic limit of the 13X zeolite in order to find what the maximum feed gas velocity is. Besides this future work could conclude a more in depth look at changing the adsorption pressure including operating the cycle as a pure PSA cycle<sup>[24]</sup>.

## REFERENCES:

1. Ashcraft,B.,and Swenton,J.(2007). Oxygen Production with Silver Zeolites and Pressure Swing Adsorption: Portable and Hospital Oxygen Concentrator Unit Designs with Economic Analysis. *chemical, biological and materials engineering*, pp. 1-100.
2. Davidescu,A.A., Apostu,S.A., and Mandruleanu,C.S.(2021). Shedding Light on the Main Characteristics and Perspectives of Romanian Medicinal Oxygen Market. *Healthcare*, 9,155,2-26. <https://doi.org/10.3390/healthcare9020155>
3. Kakavandi et al(2017). Dynamic modeling of nitrogen adsorption on zeolite 13x bed. *Fluid Mechanics Research International Journal*,1(1), 20-24.
4. Kakavandi,I.A., & Shokroo,E.J.(2016). Dynamic Survey of Nitrogen Adsorption on Zeolite 13X Bed. *3rd INTERNATIONAL CONFERENCE ON SCIENCE AND ENGINEERING*
5. Zahra,M., Jafar,T., andMasoud,M.(2008). Study of a Four-Bed Pressure Swing Adsorption for Oxygen Separation from Air. *International Journal of Chemical, Molecular, Nuclear, Materials and Metallurgical Engineering*, 2(11).
6. Pan,M., Omar,H.M.,& Rohani,S.(2017). Application of Nanosize Zeolite Molecular Sieves for Medical Oxygen Concentration. *Nanomaterials*,7,195,1-19. doi:10.3390/nano708019
7. 13X Molecular Sieve – Sorbead India. <https://www.sorbeadindia.com>
8. J, Mater.Chem,(2006). Novel porous materials for emerging applications. *Journal of Materials Chemistry*, 16, 623-625. DOI: 10.1039/B600327N
9. Kamarudin et al. (1998). ZEOLITE AS NATURAL GAS ADSORBENTS.
10. Mukherjee,N.(2021). PSA Oxygen: Conversion of N2 to O2 concentrator by Zeolite molecular sieve.
11. Prakash,M.(2021).India’s Oxygen emergency is more logistical.<http://theprint.in>
12. Ganley,J.C.(2018). PRESSURE SWING ADSORPTION IN THE UNIT OPERATIONS
13. Rahman,Z.A., Ali,A.J.,and Auob,H.S.(2010). A STUDY OF OXYGEN SEPARATION FROM AIR BY PRESSURE SWING ADSORPTION (PSA). *ACADEMIA*, 203-214.
14. Hamed,H.H.(2015). Oxygen and Nitrogen Separation from Air Using Zeolite Type 5A. *Al-Qadisiyah Journal For Engineering Sciences*, 8(2), 147-158.
15. Santos et al(2007). High-Purity Oxygen Production by Pressure Swing Adsorption. *Ind. Eng. Chem. Res*, 46, 591-599.
16. Santos,J.C., Portugal,A.F., Magalhaes,F.D., & Mendes ,A.(2006). Optimization of Medical PSA Units for Oxygen Production. *Ind. Eng. Chem. Res*, 45, 1085-1096.
17. Zabielska,K., Aleksandrak, T., & Gabrus, E. (2018). ADSORPTION EQUILIBRIUM OF CARBON DIOXIDE ON ZEOLITE 13X AT HIGH PRESSURES. *Chemical and Process Engineering*, 39 (3), 309–321. DOI: 10.24425/122952
18. Shokroo,E.J., Farniaei,M., and Beghbani,M.(2019). Simulation Study of Pressure Swing Adsorption to Purify Helium Using Zeolite 13X. *Applied Chemical Engineering*,2, 1-8.
19. Magee,H.M. Nitrogen Gas Adsorption in Zeolites 13X and 5A. pp. 1-13.

20. Pressure Swing adsorption- Wikipedia. <http://en.m.wikipedia.org>
21. Zabielska, K., Aleksandrak, T., & Gabrus, E. (2018). ADSORPTION EQUILIBRIUM OF CARBON DIOXIDE ON ZEOLITE 13X AT HIGH PRESSURES. *Chemical and Process Engineering*, 39 (3), 309–321. DOI: 10.24425/122952
22. Physical Chemistry (Volume-3) written by Hrishikesh Chatterjee.
23. Hazar, H., Tekdogan, R., and Sevinc, H. (2021). Investigating the effects of oxygen enrichment with modified zeolites on the performance and emissions of a diesel engine through experimental and ANN approach. *Fuel*, 303, 121318.
24. Moran, A.A. (2014). A PSA PROCESS FOR AN OXYGEN CONCENTRATOR. MSL, ACADEMIC ENDEAVORS, ETD Archive.

## Another sources which helped me to complete the review work.

- Bryan et al (2014). Development of mixed matrix membranes containing zeolites for post-combustion carbon capture. *Energy Procedia*, 63, 160-166.
- Karimi, A., Emrani, P., and Haghayegh, M. (2017). Experimental Verification of Dynamic Modelling of Nitrogen Adsorption on Zeolite 13X with VSA Process. *Science and Technology*, 7(1), 25-34. DOI: 10.5923/j.scit.20170701.03
- Shokroo et al (2015). Comparative study of zeolite 5A and zeolite 13X in air separation by pressure swing adsorption. *Korean J. Chem. Eng.*, 33(4), 1391-1401. DOI: 10.1007/s11814-015-0232-6
- Khazraei, S., Soleimani, M., and Kargari, A. (2014). Investigation of Different Kinetic models of O<sub>2</sub> and N<sub>2</sub> adsorption on 13X Zeolite. *The 8th International Chemical Engineering Congress & Exhibition*, 1-5.
- Beaman, J. (1989). OXYGEN STORAGE ON ZEOLITES. USAFSAM-TR-88-26.
- Cavenati, S. (2004). Adsorption Equilibrium of Methane, Carbon Dioxide, and Nitrogen on Zeolite 13X at High Pressures. *Journal of Chemical & Engineering Data*, 49, 1095-1101.
- Bezerra et al (2011). Adsorption of CO<sub>2</sub> on nitrogen-enriched activated carbon and zeolite 13X. *Adsorption*, 17, 235-246. DOI 10.1007/s10450-011-9320-z
- Chatti et al (2009). Amine loaded zeolites for carbon dioxide capture: Amine loading and adsorption studies. *The Official Journal of the International Zeolite Association*, 121, 84-89.
- Gizicki, W., and Banaszkiwicz, T. (2020). Performance Optimization of the Low-Capacity Adsorption Oxygen Generator. *Appl. Sci*, 7495, 1-11. doi:10.3390/app10217495
- Dantas et al (2011). Carbon dioxide–nitrogen separation through pressure swing adsorption. *Chemical Engineering Journal*, 172, 698-704.
- Akulinin et al (2020). OPTIMIZATION AND ANALYSIS OF PRESSURE SWING ADSORPTION PROCESS FOR OXYGEN PRODUCTION FROM AIR UNDER UNCERTAINTY. *Chem. Ind. Chem. Eng. Q*, 26(1), 89-104.

- Montanari et al(2011). CO<sub>2</sub> separation and landfill biogas upgrading: A comparison of 4A and 13X zeolite adsorbents. *Energy*, 36, 314-319.
- Mofarahi,M.,and Shokroo, E.J.(2013). COMPARISON OF TWO PRESSURE SWING ADSORPTION PROCESSES FOR AIR SEPARATION USING ZEOLITE 5A AND ZEOLITE 13X. *Petroleum & Coal*, 55(3), 216-225.
- Shokroo,E.J., Farniaei,M., and Beghbani,M.(2019). Simulation Study of Pressure Swing Adsorption to Purify Helium Using Zeolite 13X. *Applied Chemical Engineering*,2, 1-8.
- Suraweera et al(2014). Hydrogen adsorption and diffusion in amorphous, metal-decorated nanoporous silica. *INTERNATIONAL JOURNAL OF HYDROJEN ENERGY*. 39,9241-9253
- Santos,J.C., Portugal,A.F., Magalhaes,F.D., & Mendes ,A.(2004). Simulation and Optimization of Small Oxygen Pressure Swing Adsorption Units. *Ind. Eng. Chem. Res.*, 43, 8328-8338.
- Zhu et al (2016). Study of a novel rapid vacuum pressure swing adsorption process with intermediate gas pressurization for producing oxygen. *Adsorption*, DOI 10.1007/s10450-016-9843-4
- Kroi,M.(2020). Natural vs. Synthetic Zeolites. *Crystals*, 10, 622, 1-8.

---

A REVIEW ON

**DNA-SMALL MOLECULE BINDING:  
IMPORTANCE IN ANTI-CANCER DRUG  
DESIGN**

**Scottish Church College**



**University Registration no. : 223-1211-0015-19**

**University Roll no. : 223/CEM/191027**

**Special Paper: CHEM-SO 44**

Name of the candidate:

**SARMITA NEOGI**

Signature of the candidate:

A rectangular box containing the handwritten signature "Sarmita Neogi" in black ink.

Name of the examiner:

**DR. SEBANTI BASU**

Signature of the Examiner:

---

July, 2021

---

## **Acknowledgement**

I would like to extend my sincere thanks and gratitude to **Dr. PRABUDDHA BHATTACHARYA** for providing all the necessary support in preparing this systematic review article. Without his consistent guidance and help, it would have been very difficult to complete this work. I would like to thank **Dr. Sebanti Basu** and all the guiding faculties of the department for their kind words and continuous support. Without their guidance, my education would have been largely incomplete.

I am literally indebted to my friends and as well as my seniors for providing me with unfailing support and continuous encouragement throughout my years of study, and for motivating me in every possible way.

Finally, I would like to express my very profound gratitude to my father **Mr. Sisir Neogi** and my mother **Mrs. Mamata Neogi**. Without their moral support and prayer, it would not have been possible for me to achieve all this.

## Contents

<b>Serial No.</b>		<b>Page no.</b>
<b>1.</b>	<b>Abstract</b>	<b>4</b>
<b>2.</b>	<b>Introduction</b>	<b>5</b>
<b>3.</b>	<b>A brief discussion on the physico-chemical properties of DNA</b>	<b>7</b>
<b>4.</b>	<b>DNA as drug target</b>	<b>13</b>
<b>5.</b>	<b>DNA-Small Molecule Interactions</b> <ul style="list-style-type: none"><li>• <b>Covalent interactions of DNA with small molecules</b></li><li>• <b>Non-covalent binding</b></li></ul>	<b>15-21</b> <b>16</b> <b>17</b>
<b>6.</b>	<b>Therapeutic significance of DNA – Small Molecule Intercalation</b>	<b>21</b>
<b>7.</b>	<b>Conclusion</b>	<b>22</b>
<b>8.</b>	<b>References</b>	<b>23</b>



## **Abstract**

The review article focuses on the drug-DNA interactions and their types. DNA has been known to be the cellular target for many cytotoxic anticancer agents for several decades. Understanding how drug molecules interact with DNA has become a crucial and active area of research at the interface between chemistry, molecular biology and medicine. This field promises a better understanding of intracellular processes like replication, transcription and translation. While proteins help to control these processes by binding to DNA (sequence specific binding), certain small molecules (sequence non-specific binding) hinder these processes, thereby rendering them the potential to be anticancer drugs. This review article summarizes the importance of DNA-small molecule binding in anticancer drug design.

## **1. Introduction**

Cancer still remains one of the most feared diseases in the modern world. According to the World Health Organisation, it affected one person in three and caused a quarter of all deaths in the developed world during the year 2000. Cancer cells are formed when normal cells lose the normal regulatory mechanisms that control growth and multiplication. Any error during the sequence of DNA replication may interrupt the genetic code. If left unrepaired, an incorrect transmission of genetic information by DNA in replication may lead to a mutation. Such mutations are also caused upon exposure to light, radiation, viruses, transposons and mutagenic chemicals. Some mutations may lead to uncontrolled replication. In most DNA sequences, our body knows when replication should be controlled, but when mutations occur, the body is overridden, and replication does not stop. During the process of cell division if uncontrolled replication of the mutated DNA occurs, the daughter cell may acquire some genetic mutation that would alter the cell division control mechanisms of that cell. This altered cell no longer listens to the control signals for cell division and may continue to divide and multiply. The cells replicate so rapidly and continuously that they will have a very high error rate in DNA replication. The population of oncogenic cells is highly varied and some are able to avoid normal tumor necrosis factors and T cell mediated destruction. This differential survival from a varied population of replicating cells makes for a rapid evolution, resulting in a tumor with abnormal numbers of chromosomes, an over expression of telomerase to resist cell death, and a lack of response to normal growth regulating factors. The cells then continue to replicate without recognition of normal tissue cell-to-cell boundaries so they become invasive. This uncontrolled cell division and growth ultimately results in malignant tumors, and cancer.

A major problem in treating cancer is the fact that it is not a single disease. In an effort to fight this uncontrolled growth of cells, chemists have been trying to find molecules to arrest

formation of the malignant tumors. These molecules are known as antitumor antibiotics. There are various approaches towards anti-cancer chemotherapy based on the nature of the drug and the drug-targets (**Figure 1**).

The following classifications for the mode of action of an anti-cancer drug can be considered:

**(a) According to chemical structure and resource of the drug:**

Alkylating Agents; Antimetabolite; Antibiotics; Plant Extracts; Hormones

**(b) According to biochemistry mechanisms of anticancer action:**

i) Block nucleic acid biosynthesis (antimetabolites); ii) Direct influence the structure and function of DNA (Intercalating agents, alkylating agents, chain cutters - Antibiotics, topoisomerase inhibitors); iii) Interfere transcription and block RNA synthesis (Intercalator, groove-binders); iv) Interfere protein synthesis and function (Antitubulin, harringtonines, L-asparaginase); v) Influence hormone homeostasis (Estrogens and estrogen antagonistic drug, Androgens and androgen antagonistic drug, Progestogen drug, Glucocorticoid drug, gonadotropin-releasing hormone inhibitor: leuprolide, goserelin, aromatase inhibitor: aminoglutethimide, anastrozole)

**(c) According to the cycle or phase specificity of the drug**

i) Cell cycle nonspecific agents (CCNSA) (drugs that are active throughout the cell cycle):

Alkylating Agents, Platinum Compounds, Antibiotics

ii) Cell cycle specific agents (CCSA) (drugs that act during a specific phase of the cell cycle)

a) S Phase Specific Drug: Antimetabolites, Topoisomerase Inhibitors

b) M Phase Specific Drug: Vinca Alkaloids, Taxanes

c) G2 Phase Specific Drug: Bleomycin

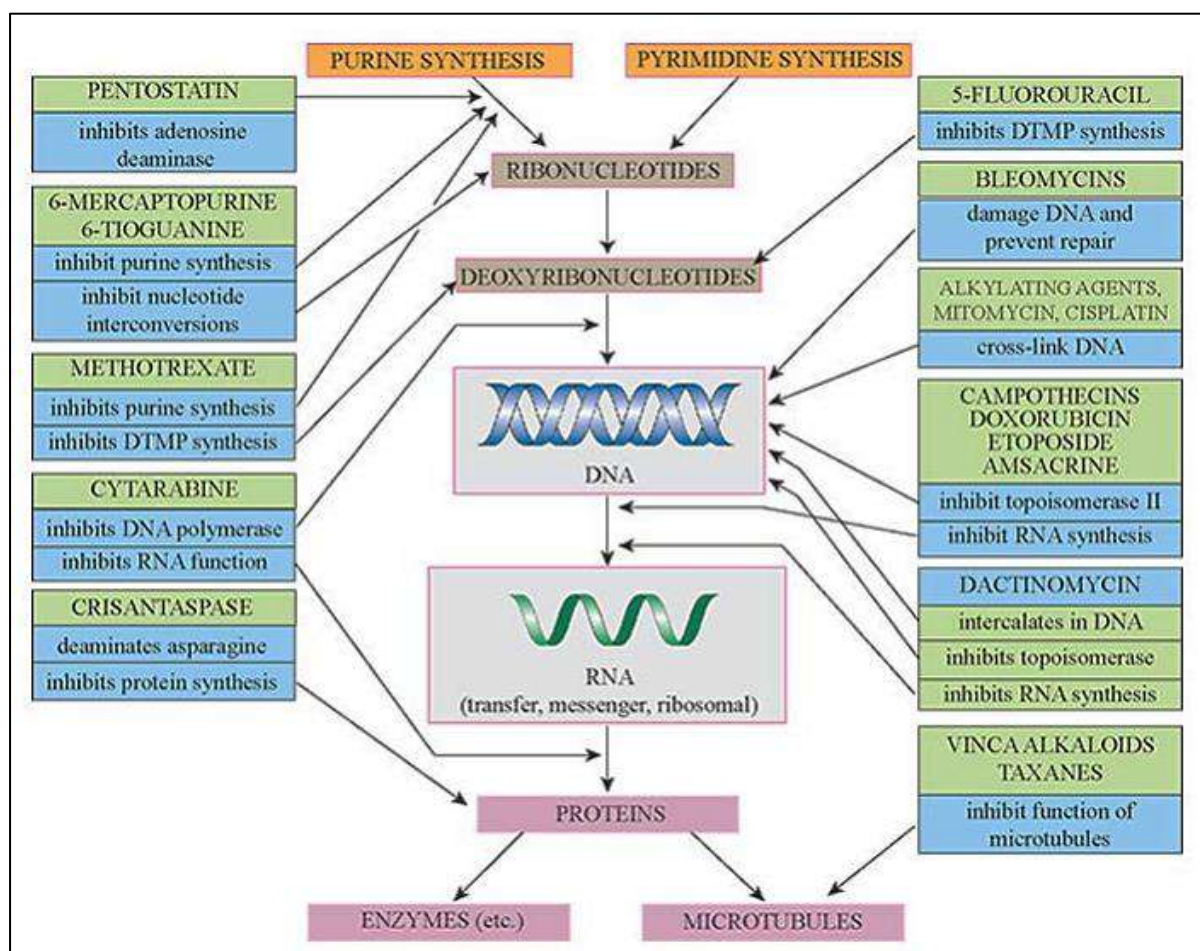
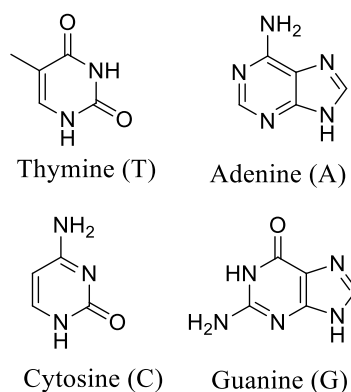


Figure 1. Variable drug-targets in anti-cancer chemotherapy

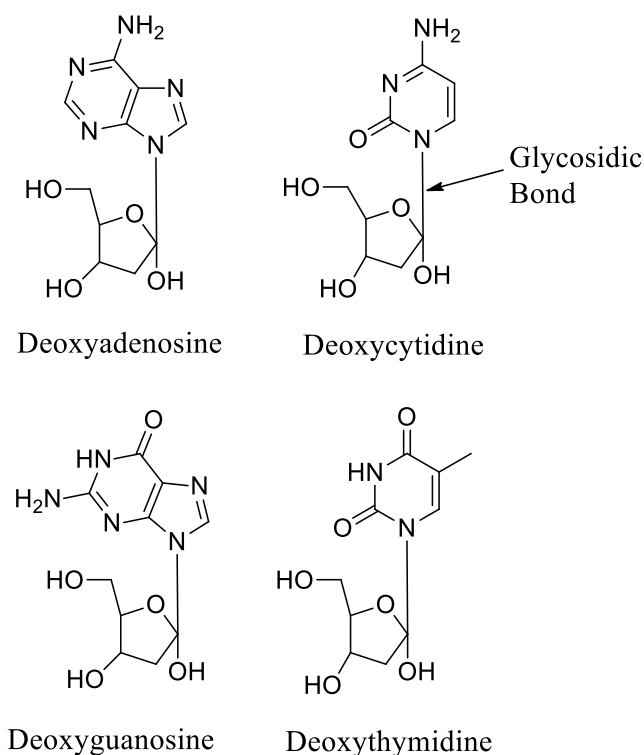
## 2. A brief discussion on the physico-chemical properties of DNA.

DNA (Deoxyribonucleic acid) is a polymer of phosphate containing pentose sugar (deoxyribose) attached to nucleobases, i.e. purines and pyrimidines, which are also known as nucleotides. Nucleotides are phosphates of base containing pentose sugar units known as nucleosides. The purines and pyrimidines are known as nucleobases.



**Figure 2.** The four nucleobases found in DNA.

The two purine bases – Adenine (A) and Guanine (G) – and the two pyrimidine bases – Cytosine (C) and Thymine (T) – are linked by bonds joining the 5' phosphate group of one nucleotide to a 3'-hydroxyl group on the sugar the adjacent nucleotide to form 3',5'-phosphodiester linkages. The phosphodiester bonds are stable because they are negatively charged, thereby repelling nucleophilic attack (Todd).



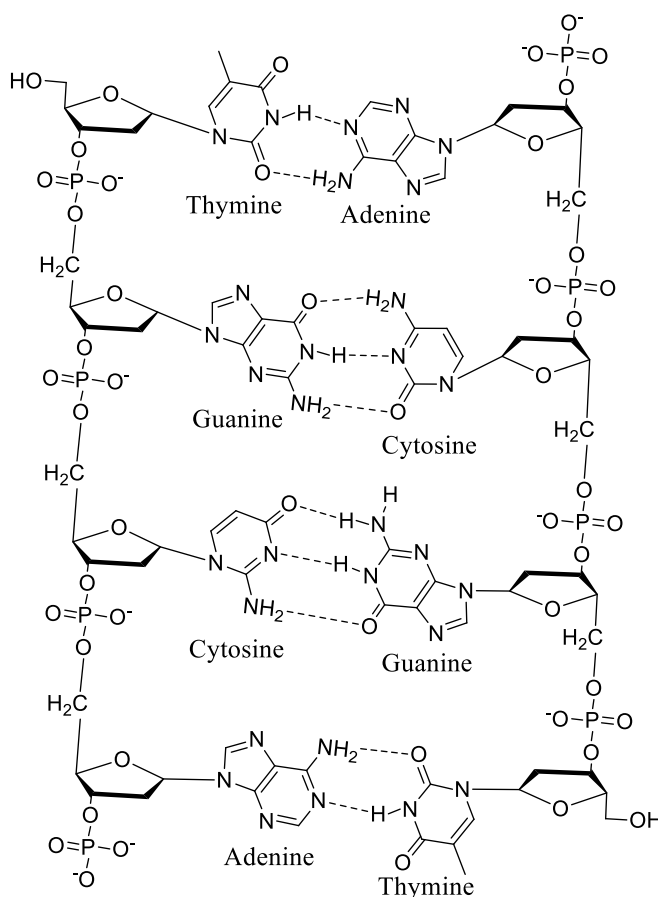
**Figure 3.** The Nucleosides of DNA

For any duplex DNA molecule, the ratios of A/T and G/C are always equal to one regardless of the base composition of the DNA. The number of adenines and thymines relative to the

number of guanines and cytosines is characteristic of a given species but varies from species to species (in humans, for example, 60.4% of DNA is composed of adenine and thymine bases) (Chargaff).

The bases are stacked upon each other at a distance of 3.4 Å (as described by Astbury in 1938). The nucleotide bases were linked by hydrogen bonding (**Figure 4**) (Gulland, 1947). DNA is a helical molecule that is able to adopt a variety of conformations (**Figure 5**) (Wilkins and Franklin).

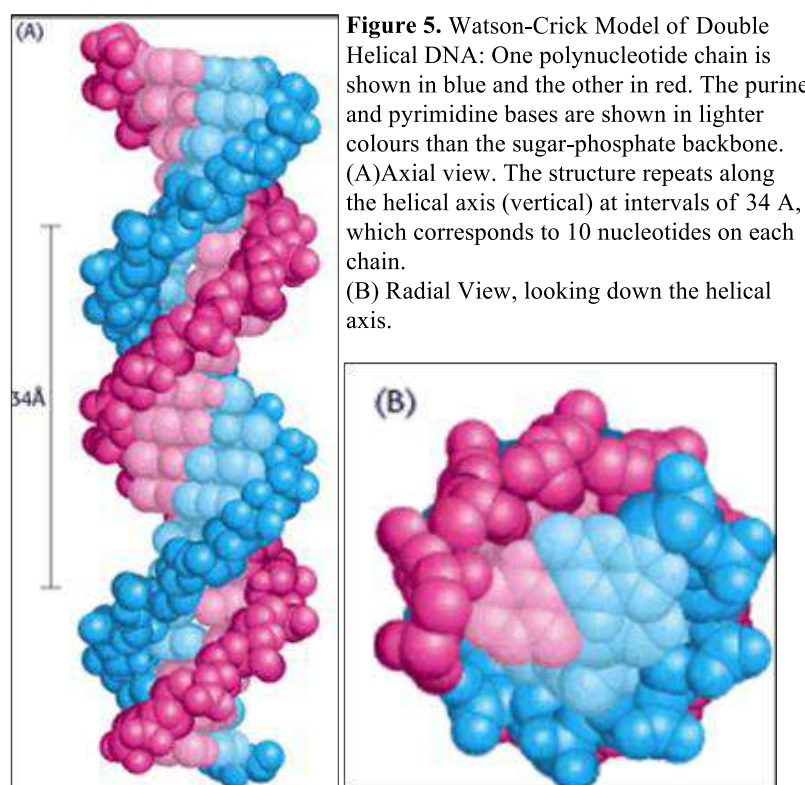
Two strands of DNA are intertwined into a helical duplex, which is held together by specific hydrogen bonding (**Figure 4**) between base pairs of adenine with thymine and guanine with cytosine and these base pairs are stacked at 3.4 Å distance (Watson and Crick). Furthermore, right handed rotation between adjacent base pairs by about 36° produces a double helix with 10 base pairs (bp) per turn.



**Figure 4.** Nucleotides and their hydrogen bonding

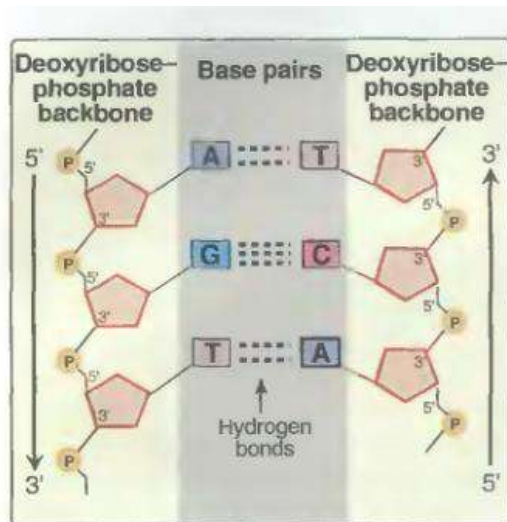
The bases are located along the axis of the helix with sugar phosphate backbones winding in an antiparallel orientation along the periphery. The order (or sequence) of the nucleotides along the chain differs from one DNA molecule to another. The purine and pyrimidine bases are flat and tend to stack above each other approximately perpendicular to the helical axis; this base stacking is stabilized mainly by London dispersion forces and by hydrophobic effects.

The two chains of the double helix are gripped together by hydrogen bonds between the bases. All the bases of the DNA are on the inside of the double helix, and the sugar phosphates are on the outside; therefore, the bases on one strand are close to those on the other. Because of this fit, specific base pairings between a large purine base (either A or G) on one chain and a smaller pyrimidine base (T or C) on the other chain are essential.



Base pairing between two purines would occupy too much space to allow a regular helix, and base pairing between two pyrimidines would occupy too little space. In fact, hydrogen bonds between G and C or A and T are more effective than any other combination. Therefore,

complementary base pairs form between guanines and cytosines or adenines and thymines only, resulting in a complementary relation between sequences of bases on the two polynucleotide strands of the double helix.

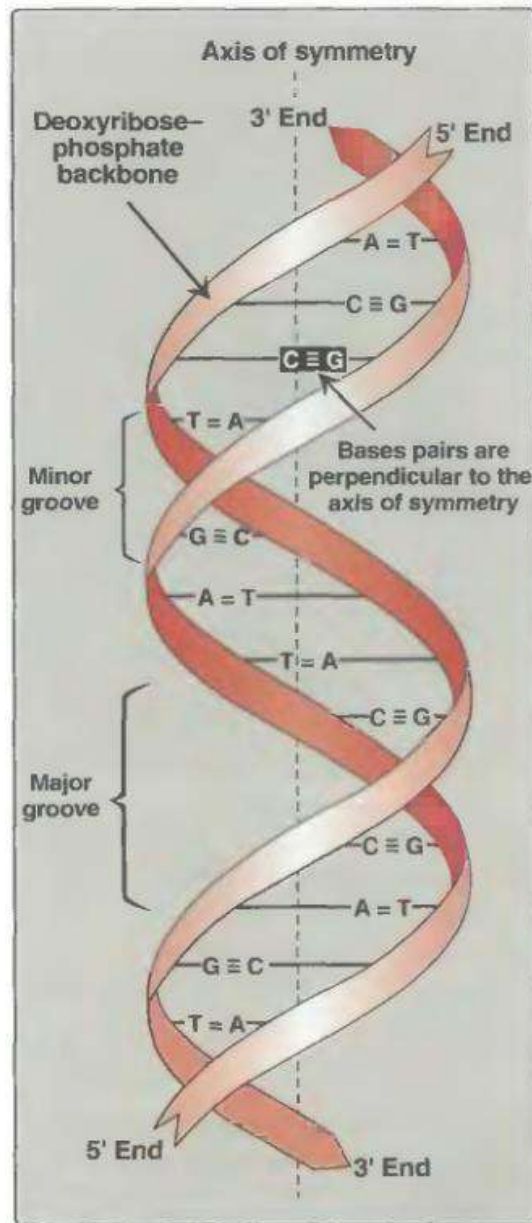


**Figure 6.** Two complementary DNA sequences

The two glycosidic bonds (**Figure 3**) that connect the base pair to its sugar rings are not directly opposite to each other, and, therefore, the two sugar-phosphate backbones of the double helix are not equally spaced along the helical axis. As a result, the grooves that are formed between the backbones are not of equal size; the larger groove is called the **major groove** and the smaller one is called the **minor groove**. One side of each base pair faces into the major groove, while the other side faces into the minor groove.

There are evidences of 3 types of DNA: A, B and Z. The B form is the most stable structure for a random-sequence DNA molecule under physiological conditions and is therefore the standard point of reference in any study of the properties of DNA.





**Figure 7.** DNA double helix, illustrating some of its major structural features

### Differences between A, B and Z-DNA

Helical Sense: A-DNA and B-DNA are right handed DNA helix whereas Z-DNA is left-handed.

Diameter of helix: Diameter of A-DNA is about 26 Å, that of B-DNA is 20 Å and that of Z-DNA is 18 Å.

Base Pairs per helical turn: A-DNA has 11 base pairs per helical turn, B-DNA has 10.5, Z-DNA has 12.

Helix rise per base pair: A-DNA has a helix rise per base pair of 2.6 Å, B-DNA has that of 3.4 Å and Z-DNA has that of 3.7 Å.

Base tilt normal to the helix axis: The base tilt normal to the helix axis of A-DNA is 20°, that of B-DNA is 6° degrees and that of Z-DNA is 7°.

Glycosyl bond conformation: It is ANTI for A-DNA and B-DNA and for Z-DNA, it is ANTI for Pyrimidines and SYN for Purines.

### **3. DNA as a drug target**

There are many important drugs which target nucleic acids, especially in the areas of antibacterial and anticancer therapy. DNA is the presumed intracellular target of some of the more clinically important antitumor agents, including bleomycin, doxorubicin (adriamycin), cisplatin, actinomycin D, mitomycin and cyclophosphamide. In spite of the well accepted premise that DNA is the receptor for these drugs, definitive data that pin-point the exact mechanism of action for any DNA-reactive drug are as yet unavailable. For DNA to be a receptor in the strict pharmacological sense it must possess both cognitive and response characteristics. In addition to proteins, oligomeric single-stranded RNA and DNA molecules and low molecular weight ligands such as drugs and carcinogens bind to DNA with varying degrees of sequence selectivity. Binding of low molecular weight ligands to DNA can cause a wide variety of potent biological responses including inhibition of transcription and replication, as well as mutagenic and oncogenic effects.

We shall first consider the drugs that interact with DNA. In general, we can group these under the following categories:

- intercalating agents;
- topoisomerase poisons (non-intercalating);
- alkylating agents;

- chain cutters;
- chain terminators.

It is likely that the interaction of the vast majority of sites on DNA that are recognized by low molecular weight ligands such as drugs do not lead to a measurable pharmacological response. According to receptor terminology, these are acceptor sites (i.e. cognition but no response). Conversely, those recognition sites on DNA that are linked to a response are receptor sites. The number of recognition sites on DNA decreases with increasing specified sequence length; for example, DNA target sites 10, 11 and 12 base pairs in length would be expected to occur approximately 2080, 1024 and 528 times in the human genome, respectively. However, a longer target sequence (15 or 16 base pairs) may only occur a few times or just once, and consequently a single ‘hit’ may seriously impair the ability of a cell to survive if this is a critical sequence. Potential receptor sites on DNA may be protected by histone molecules which are involved in higher orders of DNA structure, or proteins involved in control and expression of DNA functions such as transcription and replication. When DNA is modified by a low molecular weight ligand it potentially becomes a substrate for DNA repair processes. Furthermore, replication may be inhibited until the lesion on DNA is removed and repair is completed.

A list of FDA approved anti-cancer drugs which act via binding to DNA are listed in **Table 1**.

**Table 1.** Drugs acting via covalent and non-covalent interactions

Groove Binding Agents	DNA intercalators	Covalent DNA-adducts
Berenil Bisbenzimidazoles Bleomycin Chloroquine Chromomycin A3 Diamidine – 2 – phenylindole Distamycin A Guanyl Bisfuramidine Mithramycin Netamycin Netropsin	Aminoacridines Arylaminoalcohols Coumarins Cystodytin J Diplamine YO and YOYO-1 Daunomycin Quinolines and Quinoxalines Ethidium Bromide Proflavine Echinomycin	Busulfan Camptothecin Chlorambucil Cis-platin Clomesone Cyclodisone

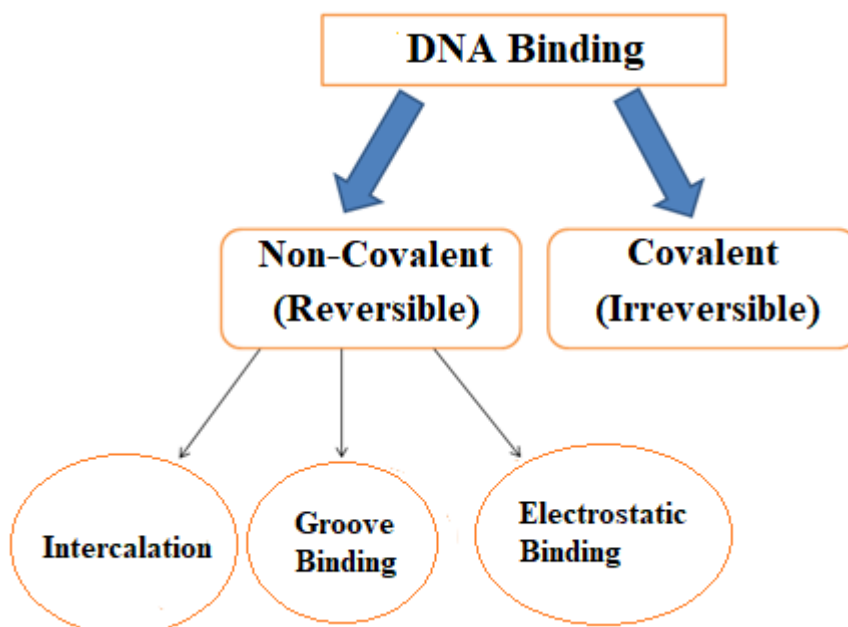
Pentamidine Pilocarpine SN 6999 SN 7167 Hoechst 33258	Chlorpheniramine Methapyrilene Tamoxifen Bis-naphthalene Doxorubicin M-AMSA Indoles	
---	---	--

## 4. DNA - Small Molecule Interactions

Binding of molecules to DNA is a crucial area of research, bridging chemistry and biology. This field promises a better understanding of intracellular processes like replication, transcription and translation. While proteins help control these processes by binding to DNA (sequence specific binding), certain small molecules (sequence non-specific binding) hinder these processes, thereby rendering them the potential to be anticancer drugs.

There are modes by which a foreign molecule can interact with the helix of DNA.

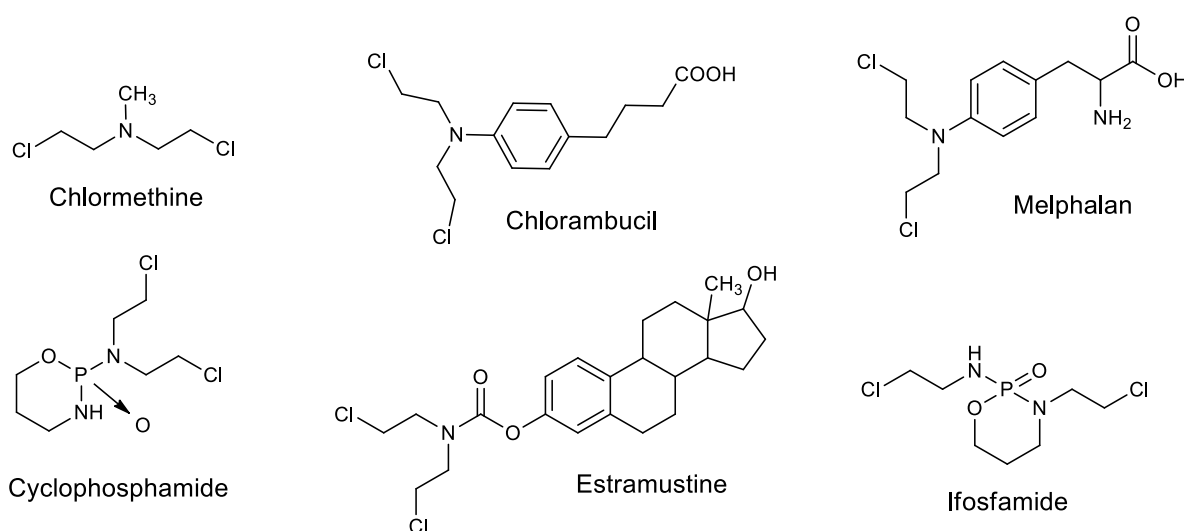
Interference with these interactions with these foreign molecules can disrupt the structure of DNA (shown in **Figure 8**).



**Figure 8.** Modes of binding of molecules in DNA

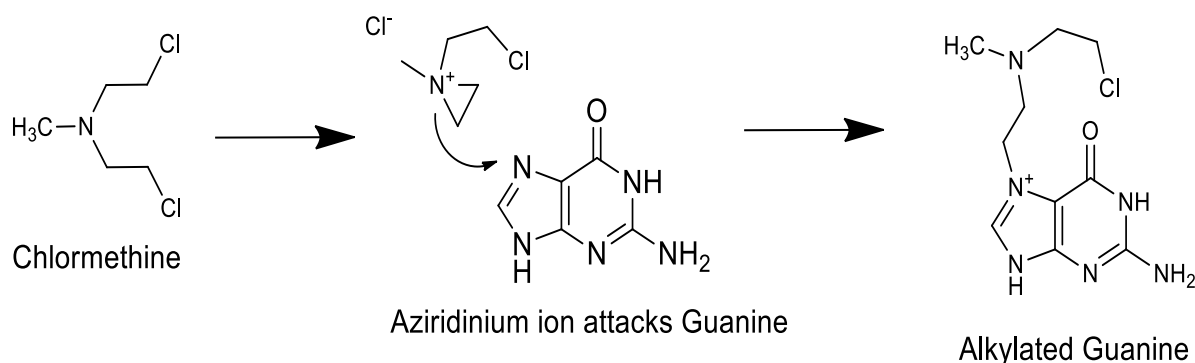
## Covalent Interaction of DNA with small molecules

This is done by highly electrophilic compounds named alkylating agents. There are many nucleophilic groups in the DNA and in particular the 7-nitrogen of guanine. Drugs with two such alkylating groups could therefore react with a guanine on each chain and cross-link the strands such that they cannot unravel during replication or transcription. Since alkylating agents are very reactive, they will react with any good nucleophile and so they are not very selective in their action. They will alkylate proteins and other macromolecules as well as DNA. Nevertheless, alkylating drugs have been useful in the treatment of cancer. Tumor cells often divide more rapidly than normal cells and so disruption of DNA function will affect these cells more drastically than normal cells.



**Figure 9.** DNA Alkylating agents

One bright example of such compounds is mechloroethamine, which gets converted to aziridine ion, which then interacts with the DNA duplex. Alkylation then takes place.<sup>2</sup>



**Figure 10.** Alkylation of guanine by chloromethine

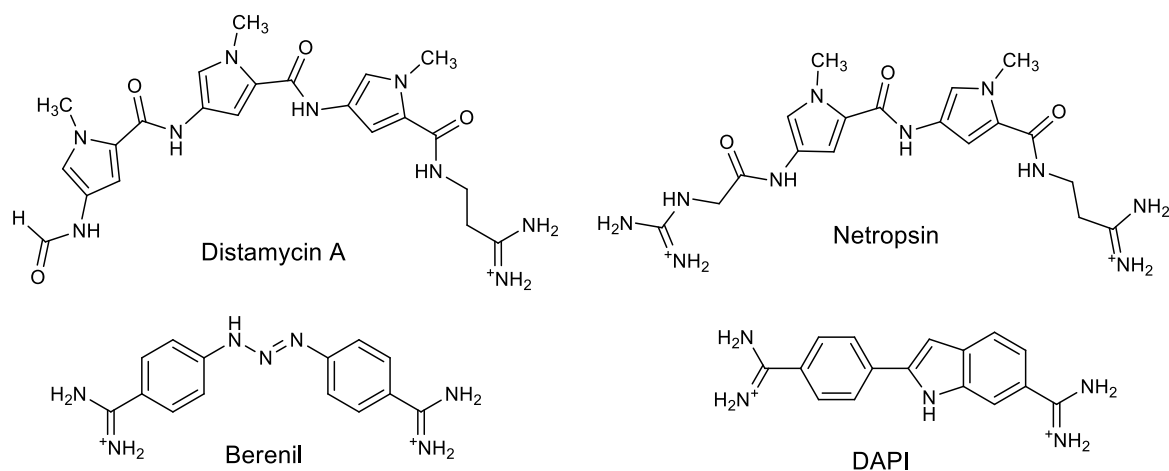
## Non-Covalent binding

### Groove Binding

Groove binders are a class of molecules that bind in major and minor grooves of the duplex DNA and play an important role in drug binding. As the dimensions of the grooves are different, targeting them requires vastly dissimilar and different shaped molecules.

Some small compounds bind to the minor groove of DNA by van der Waals interaction and hydrogen bonding. Minor groove binding drugs typically have several aromatic rings, such as pyrrole, furan or benzene connected by bonds possessing torsional freedom. Minor groove binding drugs are usually narrow curved shaped, which is isohelical to the curve of the minor groove, and facilitates binding by promoting van der Waals interactions. Additionally, these drugs can form hydrogen bonds to bases, typically to N3 of adenine and O2 of thymine.

The groove-binding molecules are commonly specific to adenine–thymine (AT) rich sequences. This preference in addition to the designed propensity for the electronegative pockets of AT sequences is probably due to better van der Waals contacts between the ligand and groove walls in this region, since AT regions are narrower than GC groove regions and also because of the steric hindrance in the latter, presented by the C2 amino group of the guanine base. Hydrophobic and/or hydrogen bonding are usually important components of this binding process, and provide stabilization. The antibiotic netropsin is a model groove-binder.



**Figure 11.** Well Known Groove Binders

### Intercalation of small molecules in the DNA duplex

There are several ways molecules (in this case also known as ligands) can interact with DNA. Ligands may interact with DNA by covalently binding, electrostatically, or intercalating. Intercalation, first described in 1961 by Lerman, is a non-covalent interaction where ligands of an appropriate size and chemical nature fit themselves in between base pairs of DNA. The ligand (molecule) is held rigidly perpendicular to the helix axis. This causes the base pairs to separate vertically, thereby distorting the sugar-phosphate backbone and decreasing the pitch of the helix. The phenomenon of intercalation involves the aromatic portion of a ligand positioning itself between base-pairs. The principal driving forces for intercalation are stacking and charge transfer interactions, but hydrogen bonding and electrostatic forces also play a role in stabilization.

Intercalation increases the separation of adjacent base pairs and the resultant helix distortion is compensated by adjustments in the sugar-phosphate backbone and an unwinding of the duplex. Aromatic stacking interactions between the bases and the intercalating molecule are a major stabilizing feature of the complexes formed.<sup>11</sup> Intercalation, apparently, is an energetically favorable process, because it occurs so readily. Presumably, the van der Waals forces that hold the intercalated molecules to the base pairs are stronger than those found between the stacked base pairs. Much of the binding energy is the result of the removal of the

drug molecule from the aqueous medium and a hydrophobic effect. Intercalators do not bind between every base pair. In general, intercalation does not disrupt the Watson–Crick hydrogen bonding, but it does destroy the regular helical structure, unwinds the DNA at the site of binding, and as a result of this, interferes with the action of DNA-binding enzymes such as DNA topoisomerases and DNA polymerases. Intercalation may not be the outright reason for DNA damage, but it does produce a conformational change (unwinding) in the double helix.

The large size of the intercalation system can be reflected in two aspects. First, intercalator molecules usually have side chains of various sizes. To capture the binding properties, at least one intercalator and one DNA base pair have to be included in the calculation. Intercalator and DNA base pairs, as well as water molecules and the DNA backbone, can be included without introducing too much computational cost. Thermodynamic processes can be simulated by computational experiments, e.g., via molecular dynamics. To gain more reliable information for the DNA intercalation process, an efficient higher level computational technique is desirable. Thus, the planar aromatic moiety of many carcinogens may well play a role in early stages of DNA recognition and binding, and intercalation of aromatic amino acid residues into DNA can impart enhanced stability to protein-DNA interactions. Hydrogen bonding involving substituent groups attached to complex intercalating molecules frequently imparts sequence selectivity to the binding process.

Anticancer activity and cytotoxicity of intercalative agents are associated with interference in at least some aspects of transcriptional, translational, and replicative processes, as well as with gross DNA damage and consequent inability to repair. Breakage of cellular DNA and interference with topoisomerase activity may well be a peculiar property of anticancer intercalating drugs.



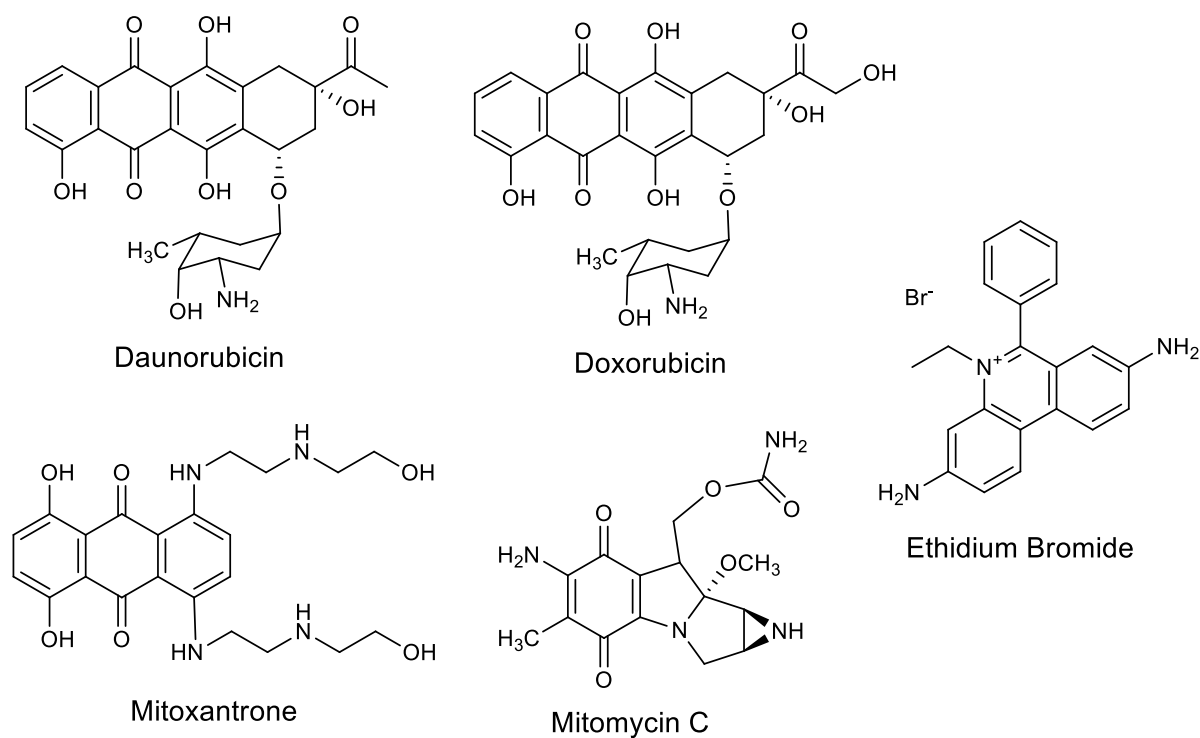


Figure 12. The Popular Intercalating Agents

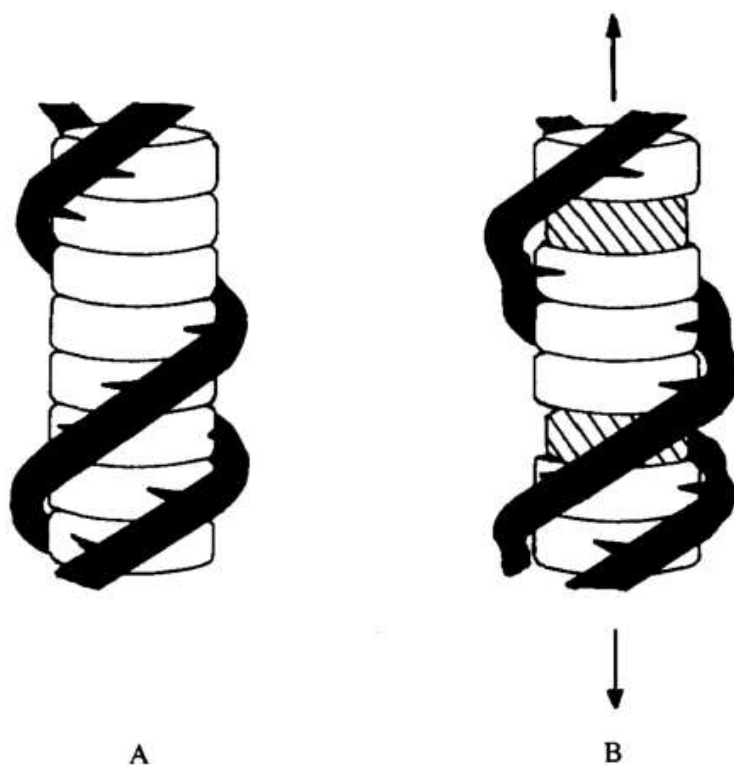
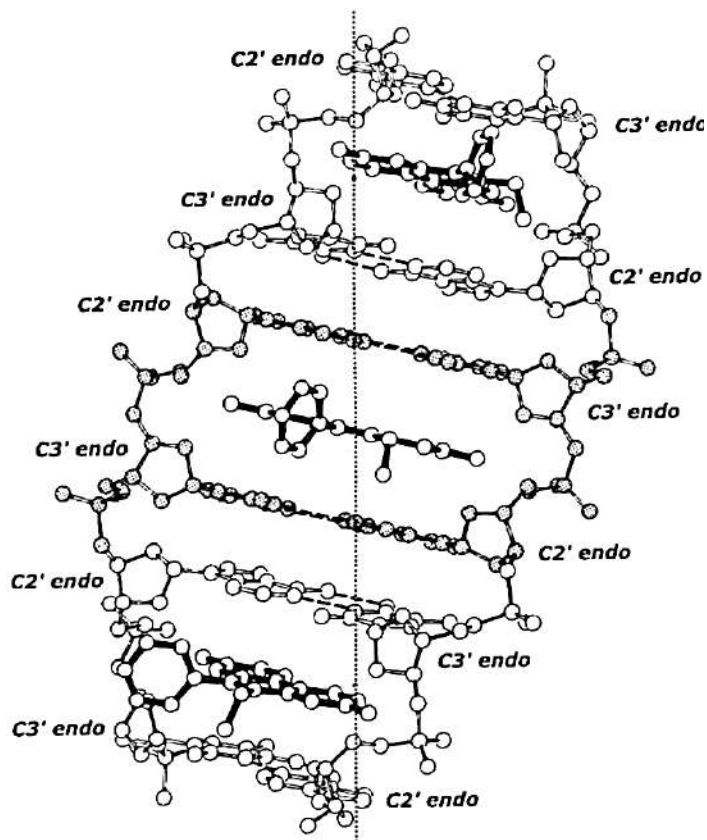


Figure 13. The Lerman Intercalation Model, in schematic form. (A) Illustrates the double-stranded DNA helix; (B) shows DNA with bound-ligand molecules as shaded discs intercalated between base pairs, shown as unshaded discs.

## The Rule of Neighbour Exclusion

The rule of neighbour-exclusion states that the two sites directly neighbouring an occupied intercalation site must remain unoccupied or, in less absolute terms, intercalation is an anti-cooperative at adjacent sites. **Figure 14** can make this rule quite clear.



**Figure 14.** The Rule of Neighbour-Exclusion

## 5. Therapeutic significance of DNA – Small Molecule Intercalation

Intercalation occurs when ligands of an appropriate size and chemical nature fit themselves in between base pairs of DNA. These ligands are mostly polycyclic, aromatic, and planar, and therefore often make good nucleic acid stains. Intensively studied DNA intercalators include berberine, ethidium bromide, proflavine, daunomycin, doxorubicin, and thalidomide. DNA

intercalators are used in chemotherapeutic treatment to inhibit DNA replication in rapidly growing cancer cells. Examples include doxorubicin (adriamycin) and daunorubicin (both of which are used in treatment of Hodgkin's lymphoma), and dactinomycin (used in Wilm's tumour, Ewing's Sarcoma, rhabdomyosarcoma).

## 6. Conclusion

In this article we have discussed the different types of small organic molecules which target DNA and DNA-associated processes. But many of these when used as chemotherapeutic agents manifest one or more side effects. Therefore, there is always a challenge remaining with these designer DNA-binding molecules, to achieve maximum specific DNA-binding affinity, and cellular and nuclear transport activity without affecting the functions of the normal cells. For many of the newer targeted therapeutics that are under development for the treatment of cancer, it is however, expected that these new putative drugs will be used in combination with the more traditional drugs molecule such as *cis*-platin or doxorubicin. In combination with a DNA-interactive drug, the chemotherapeutic agent might exert considerably enhanced clinical efficacy as anticancer agents. The future challenge will be to 'conjugate' these agents appropriately on the basis of firm scientific principles. Combination of the other tools of genomics and proteomics might provide a new opportunity towards this end.

## References

1. Hurley, L.; Boyd, F. L. *TIPS*, **1988**, *9*, 402-407
2. Sirajuddin, M.; Ali, S.; Badshah, A. *J. Photochem. Photobiol. B.* **2013**, *124*, 1-19
3. Ghosh, D.; Basu, S.; Singha M.; Das, J.; Bhattacharya, P.; Basak, A. *Tetrahedron Letters*, **2017**, *58*, 2014–2018
4. Paul, A.; Bhattacharya, S. *CURRENT SCIENCE*, **2012**, *102*, 212-231
5. Kennard, O. *Pure & Appl. Chem.*, **1993**, *65*, 1213-1222
6. Bhattacharya, P.; Mandal, S. M.; Basak, A. *Eur. J. Org. Chem.* **2016**, 1439–1448
7. Macindoe, G.; Mavridis, L.; Venkatraman, V.; Devignes, M.; Ritchie, D. W. *Nucleic Acids Res.*, **2010**, *38*, W445–W449, <http://hexserver.loria.fr/>
8. Bikadi, Z.; Hazai, E. *J. Cheminf.* **2009**, *1*, 15, 1-16
9. Hanwell, M. D.; Curtis, D. E.; Lonie, D. C.; Vandermeersch, T.; Zurek E.; Hutchison, G. R. *J. Cheminf.* **2012**, *4*:17.
10. Li, S.; Cooper, V. R.; Thonhauser, T.; Lundqvist, B. I.; Langreth, D. C. *J. Phys. Chem. B* **2009**, *113*, 11166–11172
11. Neidle, S.; Abraham, Z. *CRC Critical Reviews in Biochemistry*, **1984**, *17*, 73-121
12. Ahmed, M. S. ; Ramesh, V.; Nagaraja, V.; Parish, J.H.; Hadi, S. M. *Mutagenesis*, **1994**, *9*, 193-197
13. Hunter, C. A.; Sanders, J. K. M. *J. Am. Chem. Soc.* **1990**, *112*, 5525-5534
14. Seleem, D.; Pardi, V.; Murata, R. M. *Arch. Oral Biol.*, **2017**, *76*, 76-83
15. García-Zubiri IX, Burrows HD, de Melo JSS, Pina J, Monteserín M, Tapia M. *J. Photochem Photobiol.* **2007**, *83*,1455–1464
16. Ralph, R.K.; Marshall, B.; Darkin, S. *Trends Biochem Sci*, **1983**, *8*, 212 - 214

---

A REVIEW ON

**DNA-SMALL MOLECULE BINDING:  
IMPORTANCE IN ANTI-CANCER DRUG  
DESIGN**

**Scottish Church College**



**University Registration no. : 223-1211-0015-19**

**University Roll no. : 223/CEM/191027**

**Special Paper: CHEM-SO 44**

Name of the candidate:

**SARMITA NEOGI**

Signature of the candidate:

A rectangular box containing the handwritten signature "Sarmita Neogi" in black ink.

Name of the examiner:

**DR. SEBANTI BASU**

Signature of the Examiner:

A rectangular box containing the handwritten signature "Sebanti Basu" in blue ink.

---

July, 2021

---

## **Acknowledgement**

I would like to extend my sincere thanks and gratitude to **Dr. PRABUDDHA BHATTACHARYA** for providing all the necessary support in preparing this systematic review article. Without his consistent guidance and help, it would have been very difficult to complete this work. I would like to thank **Dr. Sebanti Basu** and all the guiding faculties of the department for their kind words and continuous support. Without their guidance, my education would have been largely incomplete.

I am literally indebted to my friends and as well as my seniors for providing me with unfailing support and continuous encouragement throughout my years of study, and for motivating me in every possible way.

Finally, I would like to express my very profound gratitude to my father **Mr. Sisir Neogi** and my mother **Mrs. Mamata Neogi**. Without their moral support and prayer, it would not have been possible for me to achieve all this.

## Contents

<b>Serial No.</b>		<b>Page no.</b>
<b>1.</b>	<b>Abstract</b>	<b>4</b>
<b>2.</b>	<b>Introduction</b>	<b>5</b>
<b>3.</b>	<b>A brief discussion on the physico-chemical properties of DNA</b>	<b>7</b>
<b>4.</b>	<b>DNA as drug target</b>	<b>13</b>
<b>5.</b>	<b>DNA-Small Molecule Interactions</b> <ul style="list-style-type: none"><li>• <b>Covalent interactions of DNA with small molecules</b></li><li>• <b>Non-covalent binding</b></li></ul>	<b>15-21</b> <b>16</b> <b>17</b>
<b>6.</b>	<b>Therapeutic significance of DNA – Small Molecule Intercalation</b>	<b>21</b>
<b>7.</b>	<b>Conclusion</b>	<b>22</b>
<b>8.</b>	<b>References</b>	<b>23</b>

## **Abstract**

The review article focuses on the drug-DNA interactions and their types. DNA has been known to be the cellular target for many cytotoxic anticancer agents for several decades. Understanding how drug molecules interact with DNA has become a crucial and active area of research at the interface between chemistry, molecular biology and medicine. This field promises a better understanding of intracellular processes like replication, transcription and translation. While proteins help to control these processes by binding to DNA (sequence specific binding), certain small molecules (sequence non-specific binding) hinder these processes, thereby rendering them the potential to be anticancer drugs. This review article summarizes the importance of DNA-small molecule binding in anticancer drug design.



## **1. Introduction**

Cancer still remains one of the most feared diseases in the modern world. According to the World Health Organisation, it affected one person in three and caused a quarter of all deaths in the developed world during the year 2000. Cancer cells are formed when normal cells lose the normal regulatory mechanisms that control growth and multiplication. Any error during the sequence of DNA replication may interrupt the genetic code. If left unrepaired, an incorrect transmission of genetic information by DNA in replication may lead to a mutation. Such mutations are also caused upon exposure to light, radiation, viruses, transposons and mutagenic chemicals. Some mutations may lead to uncontrolled replication. In most DNA sequences, our body knows when replication should be controlled, but when mutations occur, the body is overridden, and replication does not stop. During the process of cell division if uncontrolled replication of the mutated DNA occurs, the daughter cell may acquire some genetic mutation that would alter the cell division control mechanisms of that cell. This altered cell no longer listens to the control signals for cell division and may continue to divide and multiply. The cells replicate so rapidly and continuously that they will have a very high error rate in DNA replication. The population of oncogenic cells is highly varied and some are able to avoid normal tumor necrosis factors and T cell mediated destruction. This differential survival from a varied population of replicating cells makes for a rapid evolution, resulting in a tumor with abnormal numbers of chromosomes, an over expression of telomerase to resist cell death, and a lack of response to normal growth regulating factors. The cells then continue to replicate without recognition of normal tissue cell-to-cell boundaries so they become invasive. This uncontrolled cell division and growth ultimately results in malignant tumors, and cancer.

A major problem in treating cancer is the fact that it is not a single disease. In an effort to fight this uncontrolled growth of cells, chemists have been trying to find molecules to arrest

formation of the malignant tumors. These molecules are known as antitumor antibiotics. There are various approaches towards anti-cancer chemotherapy based on the nature of the drug and the drug-targets (**Figure 1**).

The following classifications for the mode of action of an anti-cancer drug can be considered:

**(a) According to chemical structure and resource of the drug:**

Alkylating Agents; Antimetabolite; Antibiotics; Plant Extracts; Hormones

**(b) According to biochemistry mechanisms of anticancer action:**

i) Block nucleic acid biosynthesis (antimetabolites); ii) Direct influence the structure and function of DNA (Intercalating agents, alkylating agents, chain cutters - Antibiotics, topoisomerase inhibitors); iii) Interfere transcription and block RNA synthesis (Intercalator, groove-binders); iv) Interfere protein synthesis and function (Antitubulin, harringtonines, L-asparaginase); v) Influence hormone homeostasis (Estrogens and estrogen antagonistic drug, Androgens and androgen antagonistic drug, Progestogen drug, Glucocorticoid drug, gonadotropin-releasing hormone inhibitor: leuprolide, goserelin, aromatase inhibitor: aminoglutethimide, anastrozole)

**(c) According to the cycle or phase specificity of the drug**

i) Cell cycle nonspecific agents (CCNSA) (drugs that are active throughout the cell cycle):

Alkylating Agents, Platinum Compounds, Antibiotics

ii) Cell cycle specific agents (CCSA) (drugs that act during a specific phase of the cell cycle)

a) S Phase Specific Drug: Antimetabolites, Topoisomerase Inhibitors

b) M Phase Specific Drug: Vinca Alkaloids, Taxanes

c) G2 Phase Specific Drug: Bleomycin

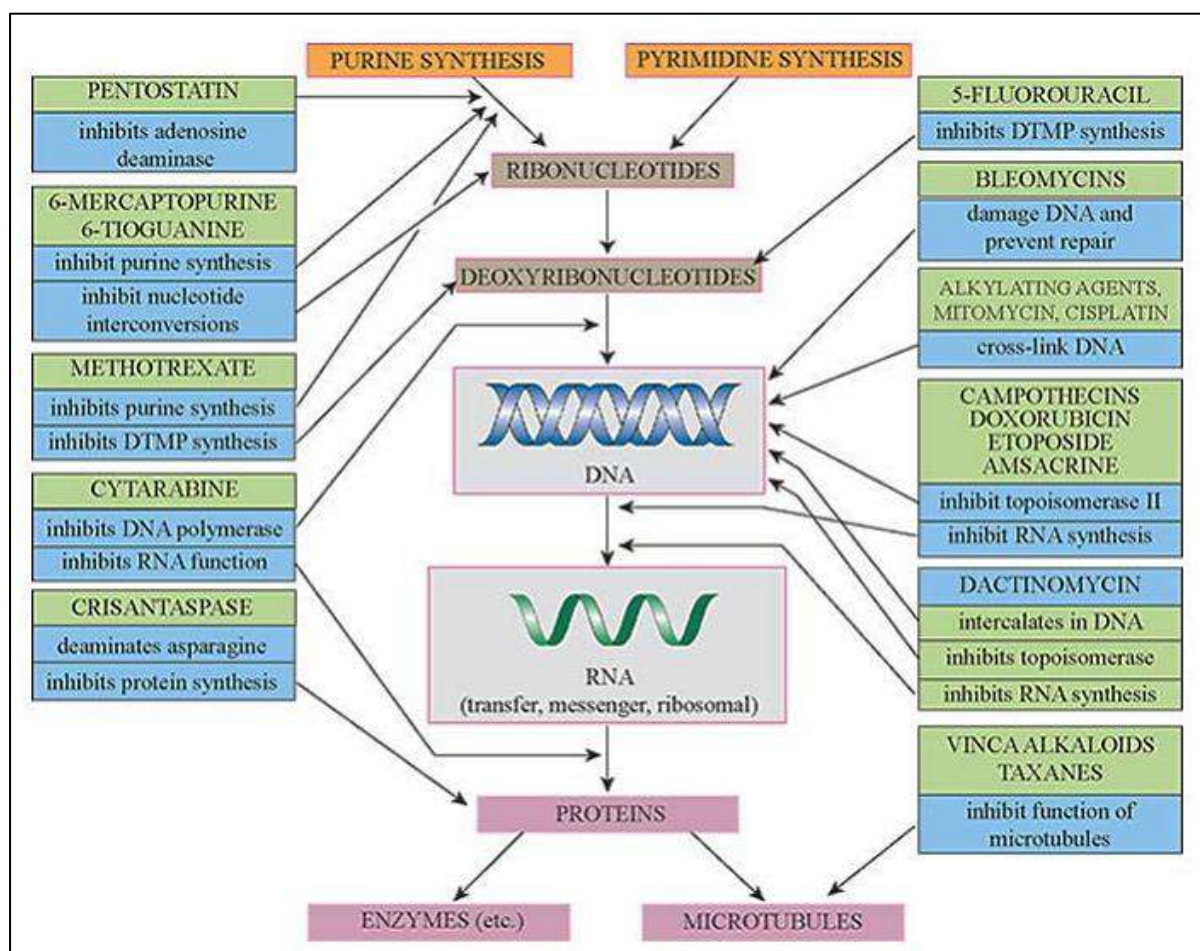
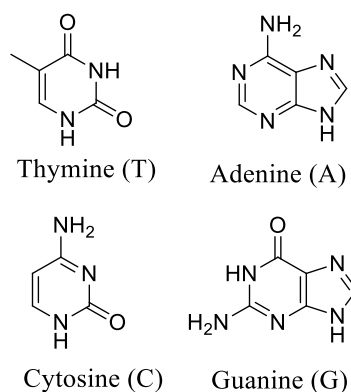


Figure 1. Variable drug-targets in anti-cancer chemotherapy

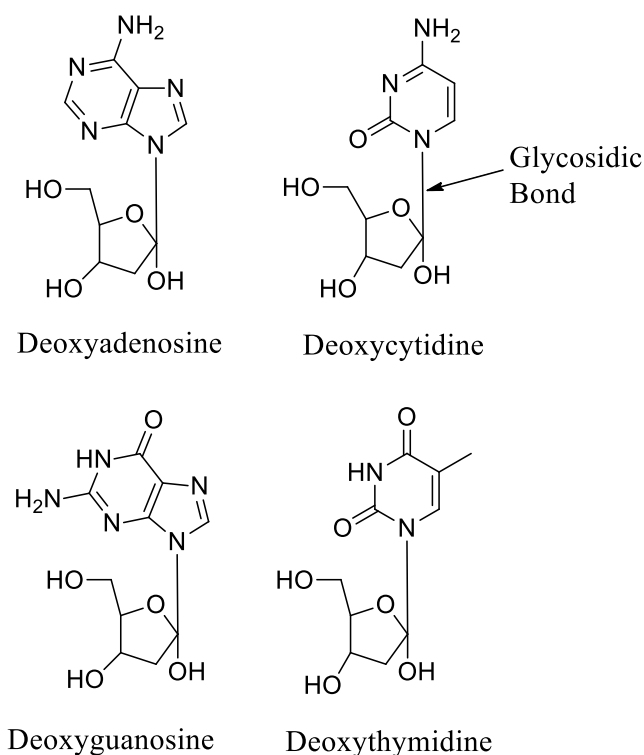
## 2. A brief discussion on the physico-chemical properties of DNA.

DNA (Deoxyribonucleic acid) is a polymer of phosphate containing pentose sugar (deoxyribose) attached to nucleobases, i.e. purines and pyrimidines, which are also known as nucleotides. Nucleotides are phosphates of base containing pentose sugar units known as nucleosides. The purines and pyrimidines are known as nucleobases.



**Figure 2.** The four nucleobases found in DNA.

The two purine bases – Adenine (A) and Guanine (G) – and the two pyrimidine bases – Cytosine (C) and Thymine (T) – are linked by bonds joining the 5' phosphate group of one nucleotide to a 3'-hydroxyl group on the sugar the adjacent nucleotide to form 3',5'-phosphodiester linkages. The phosphodiester bonds are stable because they are negatively charged, thereby repelling nucleophilic attack (Todd).



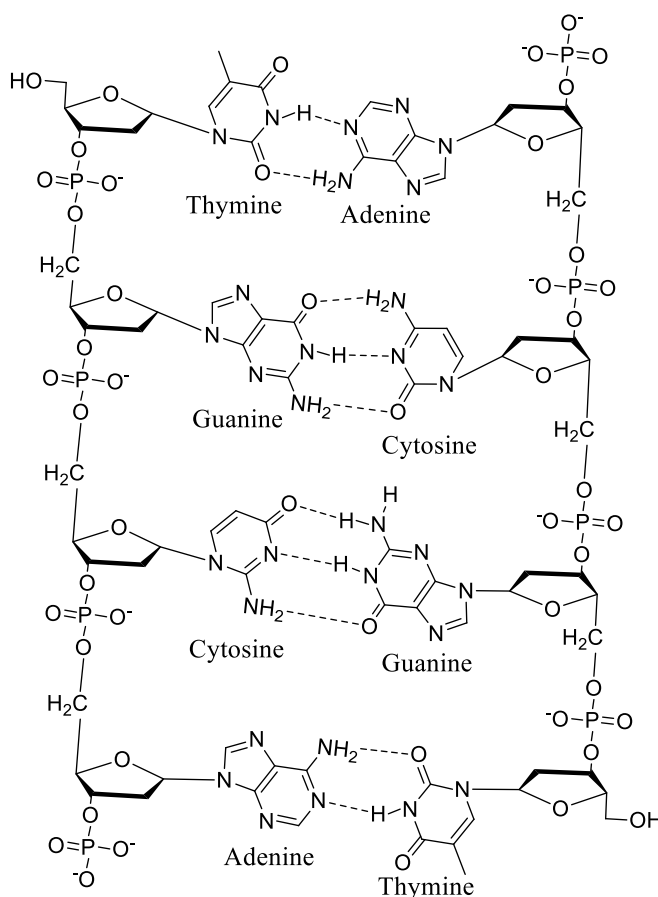
**Figure 3.** The Nucleosides of DNA

For any duplex DNA molecule, the ratios of A/T and G/C are always equal to one regardless of the base composition of the DNA. The number of adenines and thymines relative to the

number of guanines and cytosines is characteristic of a given species but varies from species to species (in humans, for example, 60.4% of DNA is composed of adenine and thymine bases) (Chargaff).

The bases are stacked upon each other at a distance of 3.4 Å (as described by Astbury in 1938). The nucleotide bases were linked by hydrogen bonding (**Figure 4**) (Gulland, 1947). DNA is a helical molecule that is able to adopt a variety of conformations (**Figure 5**) (Wilkins and Franklin).

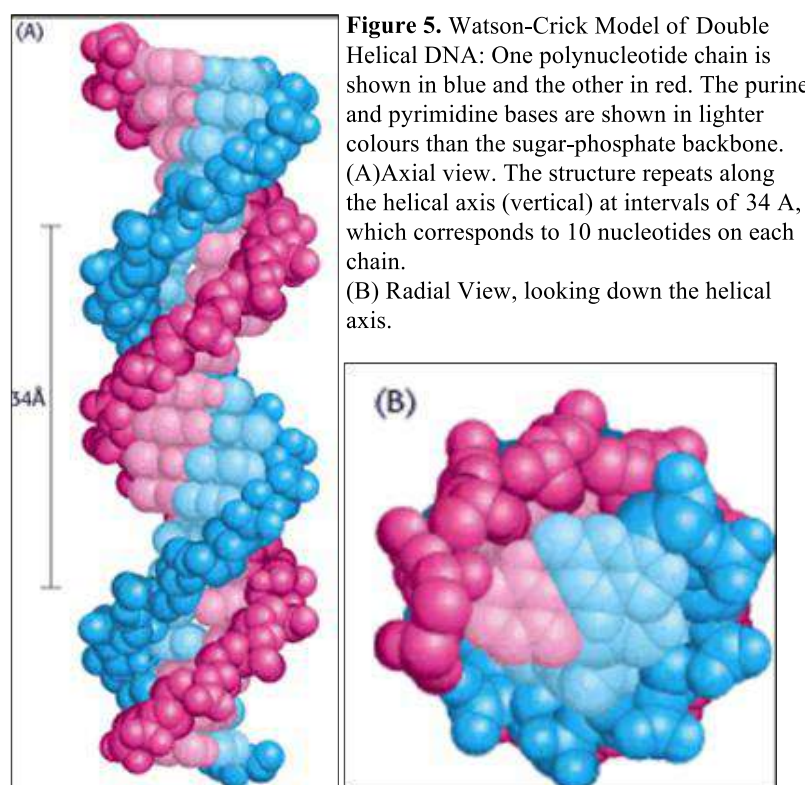
Two strands of DNA are intertwined into a helical duplex, which is held together by specific hydrogen bonding (**Figure 4**) between base pairs of adenine with thymine and guanine with cytosine and these base pairs are stacked at 3.4 Å distance (Watson and Crick). Furthermore, right handed rotation between adjacent base pairs by about 36° produces a double helix with 10 base pairs (bp) per turn.



**Figure 4.** Nucleotides and their hydrogen bonding

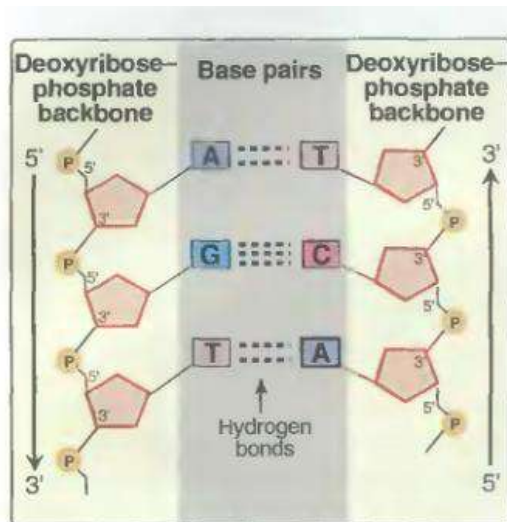
The bases are located along the axis of the helix with sugar phosphate backbones winding in an antiparallel orientation along the periphery. The order (or sequence) of the nucleotides along the chain differs from one DNA molecule to another. The purine and pyrimidine bases are flat and tend to stack above each other approximately perpendicular to the helical axis; this base stacking is stabilized mainly by London dispersion forces and by hydrophobic effects.

The two chains of the double helix are gripped together by hydrogen bonds between the bases. All the bases of the DNA are on the inside of the double helix, and the sugar phosphates are on the outside; therefore, the bases on one strand are close to those on the other. Because of this fit, specific base pairings between a large purine base (either A or G) on one chain and a smaller pyrimidine base (T or C) on the other chain are essential.



Base pairing between two purines would occupy too much space to allow a regular helix, and base pairing between two pyrimidines would occupy too little space. In fact, hydrogen bonds between G and C or A and T are more effective than any other combination. Therefore,

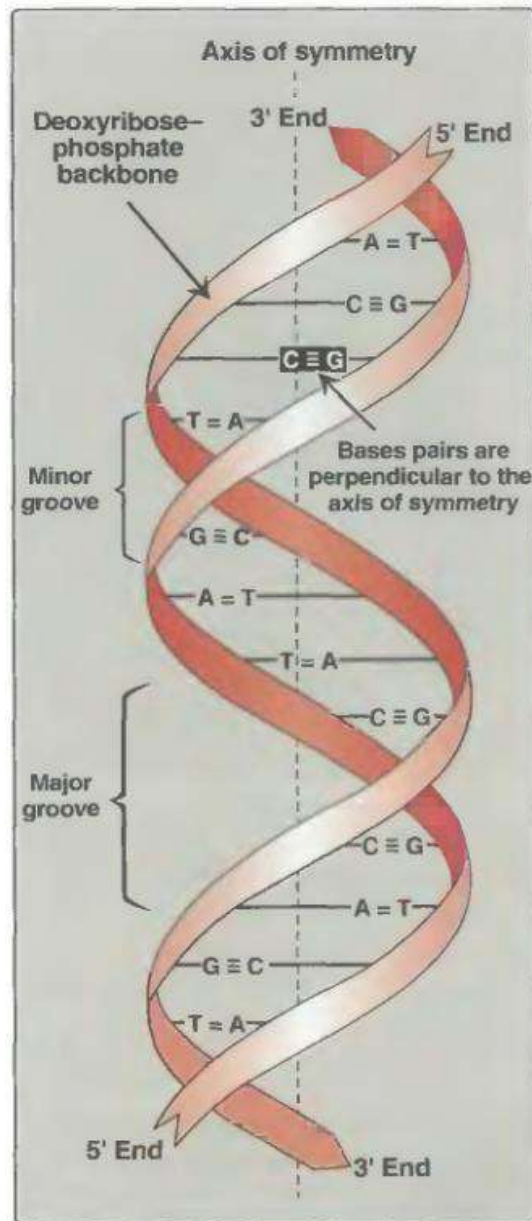
complementary base pairs form between guanines and cytosines or adenines and thymines only, resulting in a complementary relation between sequences of bases on the two polynucleotide strands of the double helix.



**Figure 6.** Two complementary DNA sequences

The two glycosidic bonds (**Figure 3**) that connect the base pair to its sugar rings are not directly opposite to each other, and, therefore, the two sugar-phosphate backbones of the double helix are not equally spaced along the helical axis. As a result, the grooves that are formed between the backbones are not of equal size; the larger groove is called the **major groove** and the smaller one is called the **minor groove**. One side of each base pair faces into the major groove, while the other side faces into the minor groove.

There are evidences of 3 types of DNA: A, B and Z. The B form is the most stable structure for a random-sequence DNA molecule under physiological conditions and is therefore the standard point of reference in any study of the properties of DNA.



**Figure 7.** DNA double helix, illustrating some of its major structural features

### Differences between A, B and Z-DNA

Helical Sense: A-DNA and B-DNA are right handed DNA helix whereas Z-DNA is left-handed.

Diameter of helix: Diameter of A-DNA is about 26 Å, that of B-DNA is 20 Å and that of Z-DNA is 18 Å.

Base Pairs per helical turn: A-DNA has 11 base pairs per helical turn, B-DNA has 10.5, Z-DNA has 12.



Helix rise per base pair: A-DNA has a helix rise per base pair of 2.6 Å, B-DNA has that of 3.4 Å and Z-DNA has that of 3.7 Å.

Base tilt normal to the helix axis: The base tilt normal to the helix axis of A-DNA is 20°, that of B-DNA is 6° degrees and that of Z-DNA is 7°.

Glycosyl bond conformation: It is ANTI for A-DNA and B-DNA and for Z-DNA, it is ANTI for Pyrimidines and SYN for Purines.

### **3. DNA as a drug target**

There are many important drugs which target nucleic acids, especially in the areas of antibacterial and anticancer therapy. DNA is the presumed intracellular target of some of the more clinically important antitumor agents, including bleomycin, doxorubicin (adriamycin), cisplatin, actinomycin D, mitomycin and cyclophosphamide. In spite of the well accepted premise that DNA is the receptor for these drugs, definitive data that pin-point the exact mechanism of action for any DNA-reactive drug are as yet unavailable. For DNA to be a receptor in the strict pharmacological sense it must possess both cognitive and response characteristics. In addition to proteins, oligomeric single-stranded RNA and DNA molecules and low molecular weight ligands such as drugs and carcinogens bind to DNA with varying degrees of sequence selectivity. Binding of low molecular weight ligands to DNA can cause a wide variety of potent biological responses including inhibition of transcription and replication, as well as mutagenic and oncogenic effects.

We shall first consider the drugs that interact with DNA. In general, we can group these under the following categories:

- intercalating agents;
- topoisomerase poisons (non-intercalating);
- alkylating agents;

- chain cutters;
- chain terminators.

It is likely that the interaction of the vast majority of sites on DNA that are recognized by low molecular weight ligands such as drugs do not lead to a measurable pharmacological response. According to receptor terminology, these are acceptor sites (i.e. cognition but no response). Conversely, those recognition sites on DNA that are linked to a response are receptor sites. The number of recognition sites on DNA decreases with increasing specified sequence length; for example, DNA target sites 10, 11 and 12 base pairs in length would be expected to occur approximately 2080, 1024 and 528 times in the human genome, respectively. However, a longer target sequence (15 or 16 base pairs) may only occur a few times or just once, and consequently a single ‘hit’ may seriously impair the ability of a cell to survive if this is a critical sequence. Potential receptor sites on DNA may be protected by histone molecules which are involved in higher orders of DNA structure, or proteins involved in control and expression of DNA functions such as transcription and replication. When DNA is modified by a low molecular weight ligand it potentially becomes a substrate for DNA repair processes. Furthermore, replication may be inhibited until the lesion on DNA is removed and repair is completed.

A list of FDA approved anti-cancer drugs which act via binding to DNA are listed in **Table 1**.

**Table 1.** Drugs acting via covalent and non-covalent interactions

Groove Binding Agents	DNA intercalators	Covalent DNA-adducts
Berenil Bisbenzimidazoles Bleomycin Chloroquine Chromomycin A3 Diamidine – 2 – phenylindole Distamycin A Guanyl Bisfuramidine Mithramycin Netamycin Netropsin	Aminoacridines Arylaminoalcohols Coumarins Cystodytin J Diplamine YO and YOYO-1 Daunomycin Quinolines and Quinoxalines Ethidium Bromide Proflavine Echinomycin	Busulfan Camptothecin Chlorambucil Cis-platin Clomesone Cyclodisone

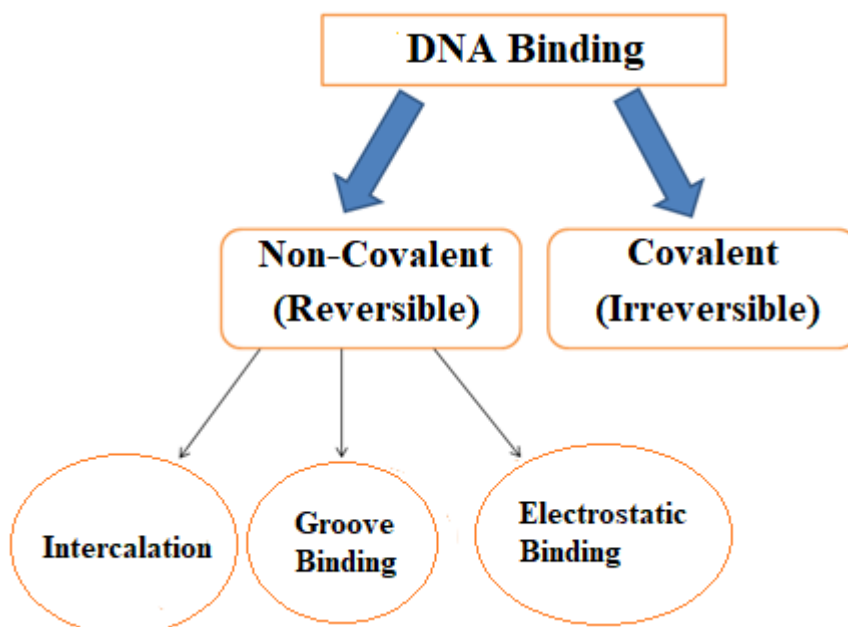
Pentamidine Pilocarpine SN 6999 SN 7167 Hoechst 33258	Chlorpheniramine Methapyrilene Tamoxifen Bis-naphthalene Doxorubicin M-AMSA Indoles	
---	---	--

## 4. DNA - Small Molecule Interactions

Binding of molecules to DNA is a crucial area of research, bridging chemistry and biology. This field promises a better understanding of intracellular processes like replication, transcription and translation. While proteins help control these processes by binding to DNA (sequence specific binding), certain small molecules (sequence non-specific binding) hinder these processes, thereby rendering them the potential to be anticancer drugs.

There are modes by which a foreign molecule can interact with the helix of DNA.

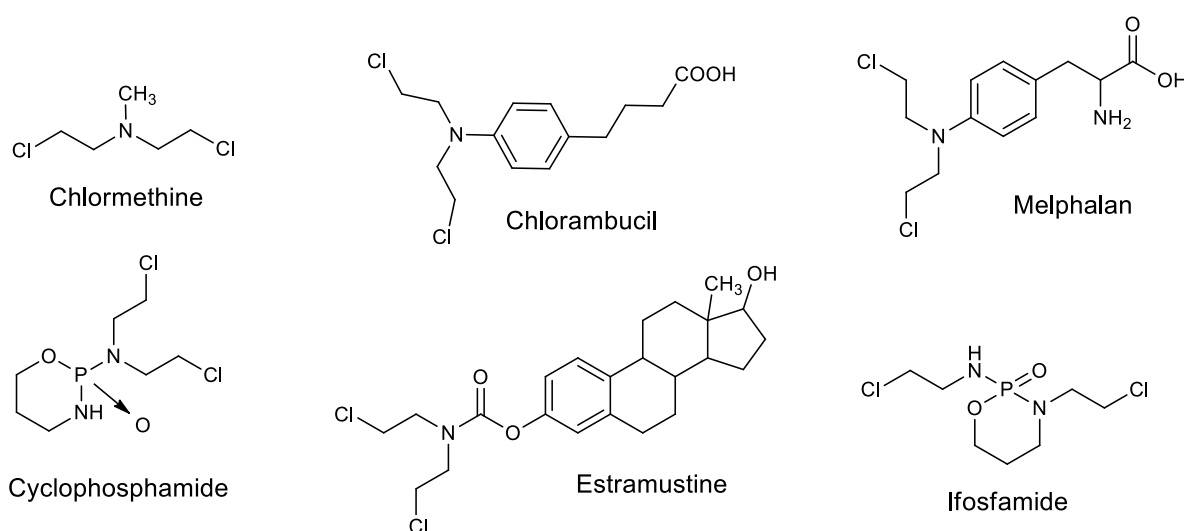
Interference with these interactions with these foreign molecules can disrupt the structure of DNA (shown in **Figure 8**).



**Figure 8.** Modes of binding of molecules in DNA

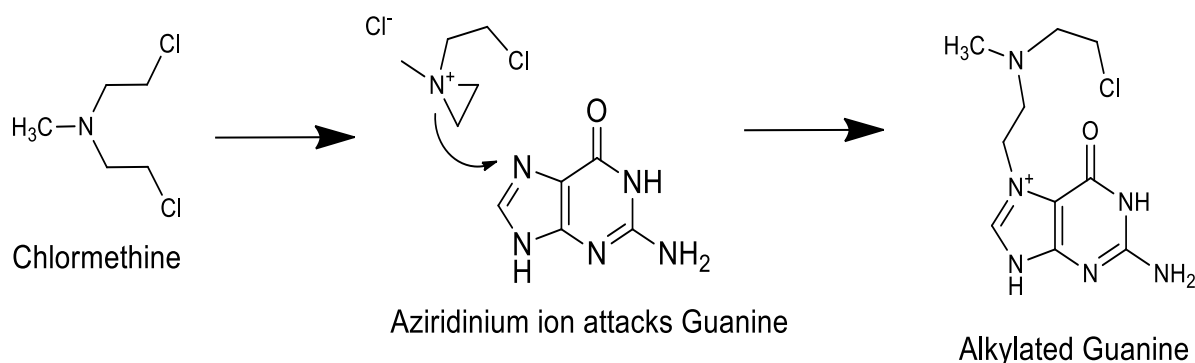
## Covalent Interaction of DNA with small molecules

This is done by highly electrophilic compounds named alkylating agents. There are many nucleophilic groups in the DNA and in particular the 7-nitrogen of guanine. Drugs with two such alkylating groups could therefore react with a guanine on each chain and cross-link the strands such that they cannot unravel during replication or transcription. Since alkylating agents are very reactive, they will react with any good nucleophile and so they are not very selective in their action. They will alkylate proteins and other macromolecules as well as DNA. Nevertheless, alkylating drugs have been useful in the treatment of cancer. Tumor cells often divide more rapidly than normal cells and so disruption of DNA function will affect these cells more drastically than normal cells.



**Figure 9.** DNA Alkylating agents

One bright example of such compounds is mechloroethamine, which gets converted to aziridine ion, which then interacts with the DNA duplex. Alkylation then takes place.<sup>2</sup>



**Figure 10.** Alkylation of guanine by chloromethine

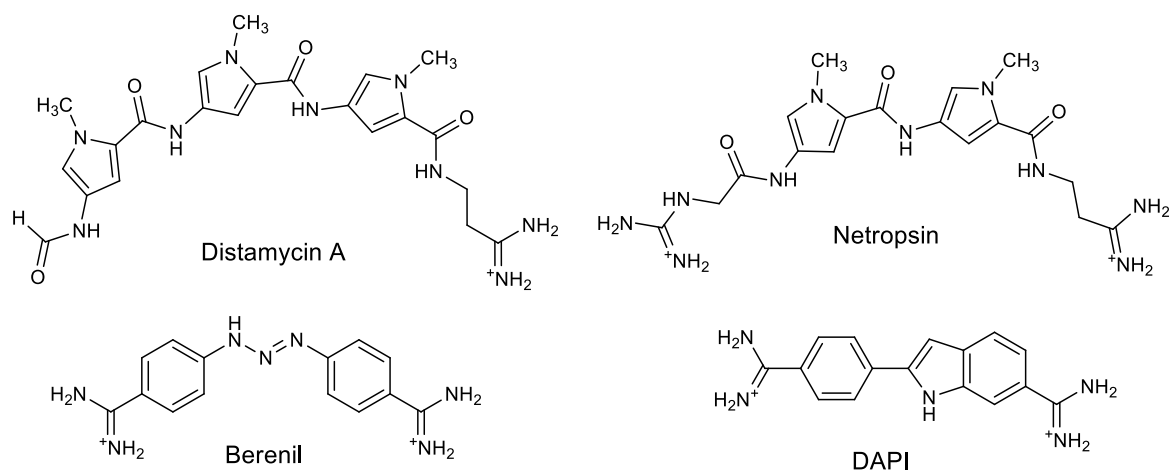
## Non-Covalent binding

### Groove Binding

Groove binders are a class of molecules that bind in major and minor grooves of the duplex DNA and play an important role in drug binding. As the dimensions of the grooves are different, targeting them requires vastly dissimilar and different shaped molecules.

Some small compounds bind to the minor groove of DNA by van der Waals interaction and hydrogen bonding. Minor groove binding drugs typically have several aromatic rings, such as pyrrole, furan or benzene connected by bonds possessing torsional freedom. Minor groove binding drugs are usually narrow curved shaped, which is isohelical to the curve of the minor groove, and facilitates binding by promoting van der Waals interactions. Additionally, these drugs can form hydrogen bonds to bases, typically to N3 of adenine and O2 of thymine.

The groove-binding molecules are commonly specific to adenine–thymine (AT) rich sequences. This preference in addition to the designed propensity for the electronegative pockets of AT sequences is probably due to better van der Waals contacts between the ligand and groove walls in this region, since AT regions are narrower than GC groove regions and also because of the steric hindrance in the latter, presented by the C2 amino group of the guanine base. Hydrophobic and/or hydrogen bonding are usually important components of this binding process, and provide stabilization. The antibiotic netropsin is a model groove-binder.



**Figure 11.** Well Known Groove Binders

### Intercalation of small molecules in the DNA duplex

There are several ways molecules (in this case also known as ligands) can interact with DNA. Ligands may interact with DNA by covalently binding, electrostatically, or intercalating. Intercalation, first described in 1961 by Lerman, is a non-covalent interaction where ligands of an appropriate size and chemical nature fit themselves in between base pairs of DNA. The ligand (molecule) is held rigidly perpendicular to the helix axis. This causes the base pairs to separate vertically, thereby distorting the sugar-phosphate backbone and decreasing the pitch of the helix. The phenomenon of intercalation involves the aromatic portion of a ligand positioning itself between base-pairs. The principal driving forces for intercalation are stacking and charge transfer interactions, but hydrogen bonding and electrostatic forces also play a role in stabilization.

Intercalation increases the separation of adjacent base pairs and the resultant helix distortion is compensated by adjustments in the sugar-phosphate backbone and an unwinding of the duplex. Aromatic stacking interactions between the bases and the intercalating molecule are a major stabilizing feature of the complexes formed.<sup>11</sup> Intercalation, apparently, is an energetically favorable process, because it occurs so readily. Presumably, the van der Waals forces that hold the intercalated molecules to the base pairs are stronger than those found between the stacked base pairs. Much of the binding energy is the result of the removal of the

drug molecule from the aqueous medium and a hydrophobic effect. Intercalators do not bind between every base pair. In general, intercalation does not disrupt the Watson–Crick hydrogen bonding, but it does destroy the regular helical structure, unwinds the DNA at the site of binding, and as a result of this, interferes with the action of DNA-binding enzymes such as DNA topoisomerases and DNA polymerases. Intercalation may not be the outright reason for DNA damage, but it does produce a conformational change (unwinding) in the double helix.

The large size of the intercalation system can be reflected in two aspects. First, intercalator molecules usually have side chains of various sizes. To capture the binding properties, at least one intercalator and one DNA base pair have to be included in the calculation. Intercalator and DNA base pairs, as well as water molecules and the DNA backbone, can be included without introducing too much computational cost. Thermodynamic processes can be simulated by computational experiments, e.g., via molecular dynamics. To gain more reliable information for the DNA intercalation process, an efficient higher level computational technique is desirable. Thus, the planar aromatic moiety of many carcinogens may well play a role in early stages of DNA recognition and binding, and intercalation of aromatic amino acid residues into DNA can impart enhanced stability to protein-DNA interactions. Hydrogen bonding involving substituent groups attached to complex intercalating molecules frequently imparts sequence selectivity to the binding process.

Anticancer activity and cytotoxicity of intercalative agents are associated with interference in at least some aspects of transcriptional, translational, and replicative processes, as well as with gross DNA damage and consequent inability to repair. Breakage of cellular DNA and interference with topoisomerase activity may well be a peculiar property of anticancer intercalating drugs.

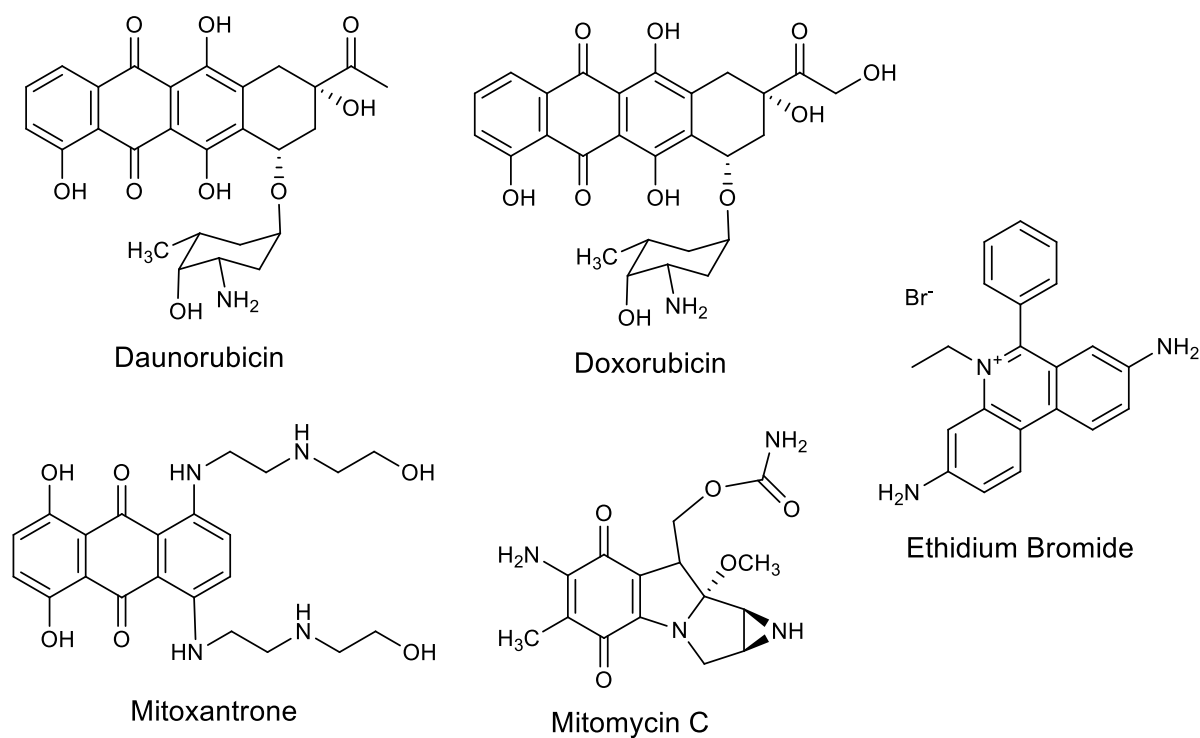


Figure 12. The Popular Intercalating Agents

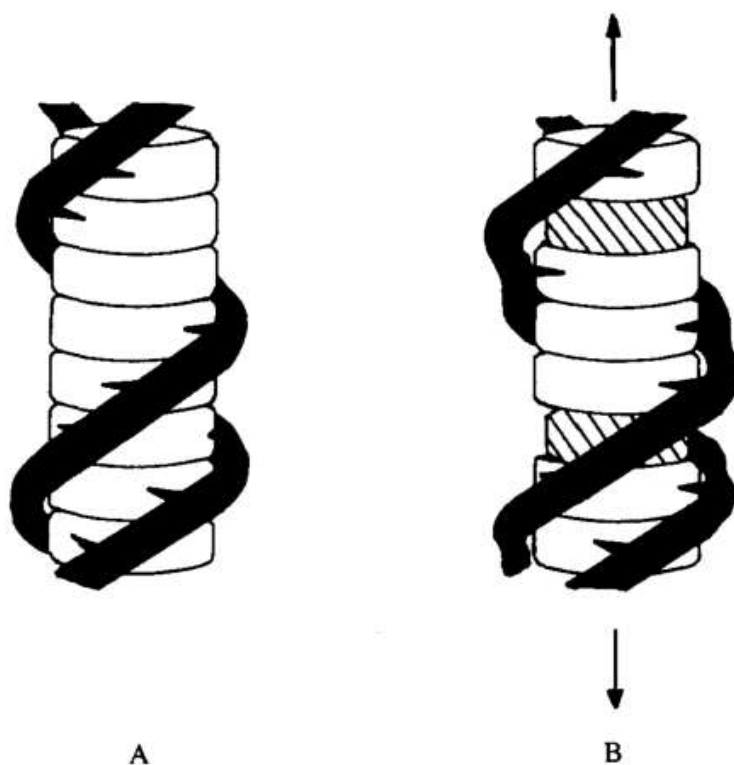
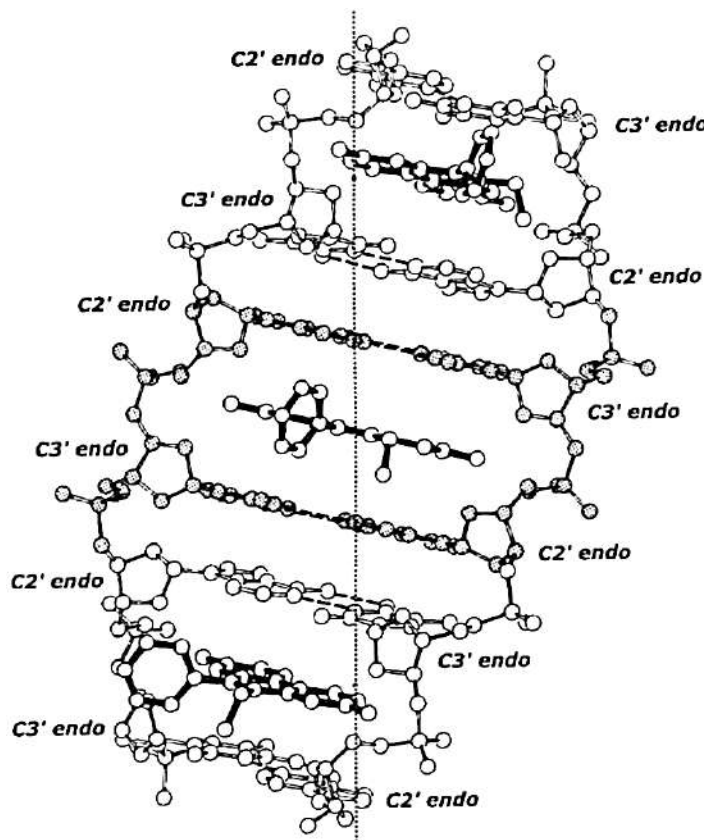


Figure 13. The Lerman Intercalation Model, in schematic form. (A) Illustrates the double-stranded DNA helix; (B) shows DNA with bound-ligand molecules as shaded discs intercalated between base pairs, shown as unshaded discs.



## The Rule of Neighbour Exclusion

The rule of neighbour-exclusion states that the two sites directly neighbouring an occupied intercalation site must remain unoccupied or, in less absolute terms, intercalation is an anti-cooperative at adjacent sites. **Figure 14** can make this rule quite clear.



**Figure 14.** The Rule of Neighbour-Exclusion

## 5. Therapeutic significance of DNA – Small Molecule Intercalation

Intercalation occurs when ligands of an appropriate size and chemical nature fit themselves in between base pairs of DNA. These ligands are mostly polycyclic, aromatic, and planar, and therefore often make good nucleic acid stains. Intensively studied DNA intercalators include berberine, ethidium bromide, proflavine, daunomycin, doxorubicin, and thalidomide. DNA

intercalators are used in chemotherapeutic treatment to inhibit DNA replication in rapidly growing cancer cells. Examples include doxorubicin (adriamycin) and daunorubicin (both of which are used in treatment of Hodgkin's lymphoma), and dactinomycin (used in Wilm's tumour, Ewing's Sarcoma, rhabdomyosarcoma).

## 6. Conclusion

In this article we have discussed the different types of small organic molecules which target DNA and DNA-associated processes. But many of these when used as chemotherapeutic agents manifest one or more side effects. Therefore, there is always a challenge remaining with these designer DNA-binding molecules, to achieve maximum specific DNA-binding affinity, and cellular and nuclear transport activity without affecting the functions of the normal cells. For many of the newer targeted therapeutics that are under development for the treatment of cancer, it is however, expected that these new putative drugs will be used in combination with the more traditional drugs molecule such as *cis*-platin or doxorubicin. In combination with a DNA-interactive drug, the chemotherapeutic agent might exert considerably enhanced clinical efficacy as anticancer agents. The future challenge will be to 'conjugate' these agents appropriately on the basis of firm scientific principles. Combination of the other tools of genomics and proteomics might provide a new opportunity towards this end.

## References

1. Hurley, L; Boyd, F. L. *TIPS*, **1988**, 9, 402-407
2. Sirajuddin, M.; Ali, S.; Badshah, A. *J. Photochem. Photobiol. B.* **2013**, 124, 1-19
3. Ghosh, D.; Basu, S.; Singha M.; Das, J.; Bhattacharya, P.; Basak, A. *Tetrahedron Letters*, **2017**, 58, 2014–2018
4. Paul, A.; Bhattacharya, S. *CURRENT SCIENCE*, **2012**, 102, 212-231
5. Kennard, O. *Pure & Appl. Chem.*, **1993**, 65, 1213-1222
6. Bhattacharya, P.; Mandal, S. M.; Basak, A. *Eur. J. Org. Chem.* **2016**, 1439–1448
7. Macindoe, G.; Mavridis, L.; Venkatraman, V.; Devignes, M.; Ritchie, D. W. *Nucleic Acids Res.*, **2010**, 38, W445–W449, <http://hexserver.loria.fr/>
8. Bikadi, Z.; Hazai, E. *J. Cheminf.* **2009**, 1, 15, 1-16
9. Hanwell, M. D.; Curtis, D. E.; Lonie, D. C.; Vandermeersch, T.; Zurek E.; Hutchison, G. R. *J. Cheminf.* **2012**, 4:17.
10. Li, S.; Cooper, V. R.; Thonhauser, T.; Lundqvist, B. I.; Langreth, D. C. *J. Phys. Chem. B* **2009**, 113, 11166–11172
11. Neidle, S.; Abraham, Z. *CRC Critical Reviews in Biochemistry*, **1984**, 17, 73-121
12. Ahmed, M. S. ; Ramesh, V.; Nagaraja, V.; Parish, J.H.; Hadi, S. M. *Mutagenesis*, **1994**, 9, 193-197
13. Hunter, C. A.; Sanders, J. K. M. *J. Am. Chem. Soc.* **1990**, 112, 5525-5534
14. Seleem, D.; Pardi, V.; Murata, R. M. *Arch. Oral Biol.*, **2017**, 76, 76-83
15. García-Zubiri IX, Burrows HD, de Melo JSS, Pina J, Monteserín M, Tapia M. *J. Photochem Photobiol.* **2007**, 83,1455–1464
16. Ralph, R.K.; Marshall, B.; Darkin, S. *Trends Biochem Sci*, **1983**, 8, 212 - 214

---

A REVIEW ON

**DNA-SMALL MOLECULE BINDING:  
IMPORTANCE IN ANTI-CANCER DRUG  
DESIGN**

**Scottish Church College**



**University Registration no. : 223-1211-0015-19**

**University Roll no. : 223/CEM/191027**

**Special Paper: CHEM-SO 44**

Name of the candidate:

**SARMITA NEOGI**

Signature of the candidate:

A rectangular box containing the handwritten signature "Sarmita Neogi" in black ink.

Name of the examiner:

**DR. SEBANTI BASU**

Signature of the Examiner:

A rectangular box containing the handwritten signature "Sebanti Basu" in blue ink.

---

July, 2021

---

## **Acknowledgement**

I would like to extend my sincere thanks and gratitude to **Dr. PRABUDDHA BHATTACHARYA** for providing all the necessary support in preparing this systematic review article. Without his consistent guidance and help, it would have been very difficult to complete this work. I would like to thank **Dr. Sebanti Basu** and all the guiding faculties of the department for their kind words and continuous support. Without their guidance, my education would have been largely incomplete.

I am literally indebted to my friends and as well as my seniors for providing me with unfailing support and continuous encouragement throughout my years of study, and for motivating me in every possible way.

Finally, I would like to express my very profound gratitude to my father **Mr. Sisir Neogi** and my mother **Mrs. Mamata Neogi**. Without their moral support and prayer, it would not have been possible for me to achieve all this.

## Contents

<b>Serial No.</b>		<b>Page no.</b>
<b>1.</b>	<b>Abstract</b>	<b>4</b>
<b>2.</b>	<b>Introduction</b>	<b>5</b>
<b>3.</b>	<b>A brief discussion on the physico-chemical properties of DNA</b>	<b>7</b>
<b>4.</b>	<b>DNA as drug target</b>	<b>13</b>
<b>5.</b>	<b>DNA-Small Molecule Interactions</b> <ul style="list-style-type: none"><li>• <b>Covalent interactions of DNA with small molecules</b></li><li>• <b>Non-covalent binding</b></li></ul>	<b>15-21</b> <b>16</b> <b>17</b>
<b>6.</b>	<b>Therapeutic significance of DNA – Small Molecule Intercalation</b>	<b>21</b>
<b>7.</b>	<b>Conclusion</b>	<b>22</b>
<b>8.</b>	<b>References</b>	<b>23</b>

## **Abstract**

The review article focuses on the drug-DNA interactions and their types. DNA has been known to be the cellular target for many cytotoxic anticancer agents for several decades. Understanding how drug molecules interact with DNA has become a crucial and active area of research at the interface between chemistry, molecular biology and medicine. This field promises a better understanding of intracellular processes like replication, transcription and translation. While proteins help to control these processes by binding to DNA (sequence specific binding), certain small molecules (sequence non-specific binding) hinder these processes, thereby rendering them the potential to be anticancer drugs. This review article summarizes the importance of DNA-small molecule binding in anticancer drug design.

## **1. Introduction**

Cancer still remains one of the most feared diseases in the modern world. According to the World Health Organisation, it affected one person in three and caused a quarter of all deaths in the developed world during the year 2000. Cancer cells are formed when normal cells lose the normal regulatory mechanisms that control growth and multiplication. Any error during the sequence of DNA replication may interrupt the genetic code. If left unrepaired, an incorrect transmission of genetic information by DNA in replication may lead to a mutation. Such mutations are also caused upon exposure to light, radiation, viruses, transposons and mutagenic chemicals. Some mutations may lead to uncontrolled replication. In most DNA sequences, our body knows when replication should be controlled, but when mutations occur, the body is overridden, and replication does not stop. During the process of cell division if uncontrolled replication of the mutated DNA occurs, the daughter cell may acquire some genetic mutation that would alter the cell division control mechanisms of that cell. This altered cell no longer listens to the control signals for cell division and may continue to divide and multiply. The cells replicate so rapidly and continuously that they will have a very high error rate in DNA replication. The population of oncogenic cells is highly varied and some are able to avoid normal tumor necrosis factors and T cell mediated destruction. This differential survival from a varied population of replicating cells makes for a rapid evolution, resulting in a tumor with abnormal numbers of chromosomes, an over expression of telomerase to resist cell death, and a lack of response to normal growth regulating factors. The cells then continue to replicate without recognition of normal tissue cell-to-cell boundaries so they become invasive. This uncontrolled cell division and growth ultimately results in malignant tumors, and cancer.

A major problem in treating cancer is the fact that it is not a single disease. In an effort to fight this uncontrolled growth of cells, chemists have been trying to find molecules to arrest



formation of the malignant tumors. These molecules are known as antitumor antibiotics. There are various approaches towards anti-cancer chemotherapy based on the nature of the drug and the drug-targets (**Figure 1**).

The following classifications for the mode of action of an anti-cancer drug can be considered:

**(a) According to chemical structure and resource of the drug:**

Alkylating Agents; Antimetabolite; Antibiotics; Plant Extracts; Hormones

**(b) According to biochemistry mechanisms of anticancer action:**

i) Block nucleic acid biosynthesis (antimetabolites); ii) Direct influence the structure and function of DNA (Intercalating agents, alkylating agents, chain cutters - Antibiotics, topoisomerase inhibitors); iii) Interfere transcription and block RNA synthesis (Intercalator, groove-binders); iv) Interfere protein synthesis and function (Antitubulin, harringtonines, L-asparaginase); v) Influence hormone homeostasis (Estrogens and estrogen antagonistic drug, Androgens and androgen antagonistic drug, Progestogen drug, Glucocorticoid drug, gonadotropin-releasing hormone inhibitor: leuprolide, goserelin, aromatase inhibitor: aminoglutethimide, anastrozole)

**(c) According to the cycle or phase specificity of the drug**

i) Cell cycle nonspecific agents (CCNSA) (drugs that are active throughout the cell cycle):

Alkylating Agents, Platinum Compounds, Antibiotics

ii) Cell cycle specific agents (CCSA) (drugs that act during a specific phase of the cell cycle)

a) S Phase Specific Drug: Antimetabolites, Topoisomerase Inhibitors

b) M Phase Specific Drug: Vinca Alkaloids, Taxanes

c) G2 Phase Specific Drug: Bleomycin

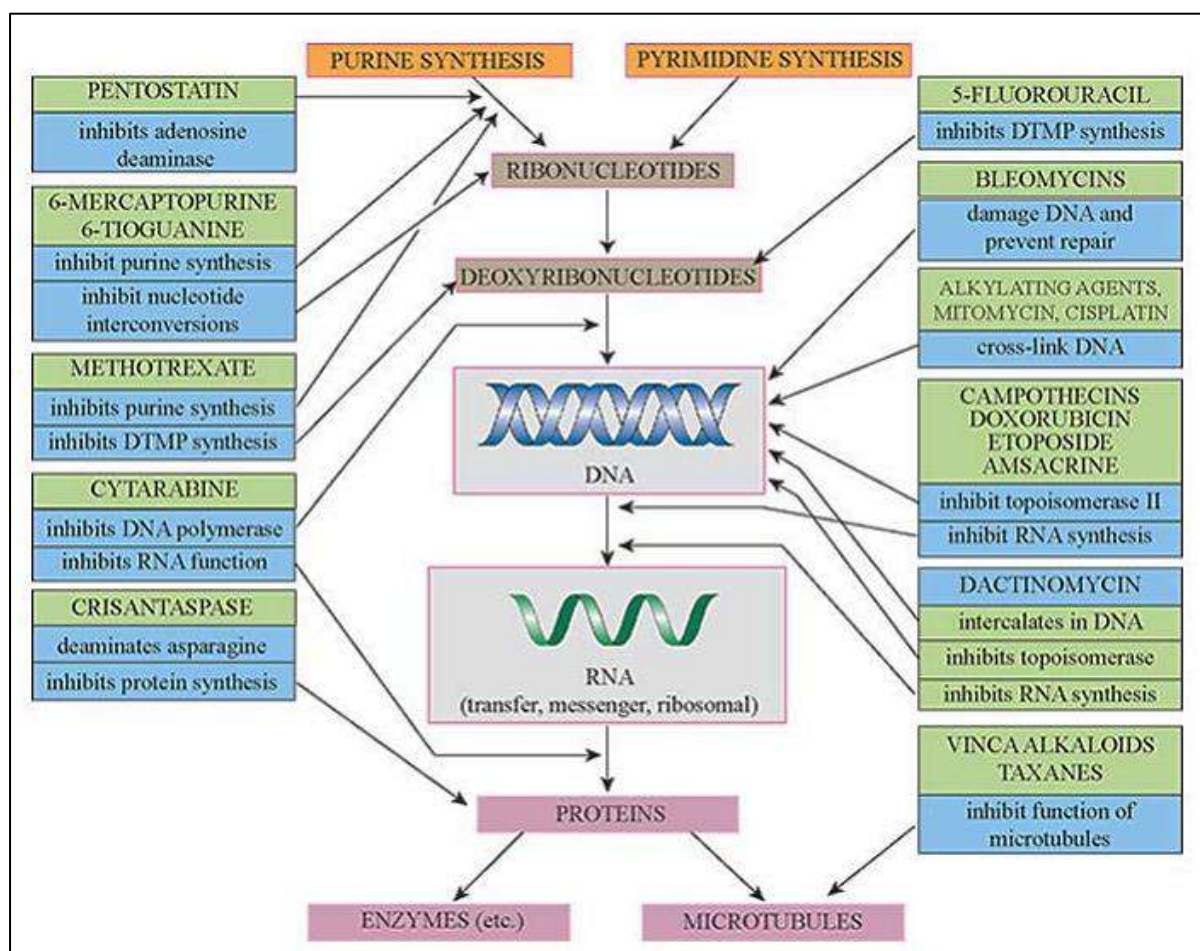
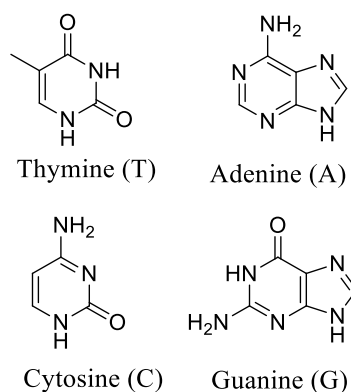


Figure 1. Variable drug-targets in anti-cancer chemotherapy

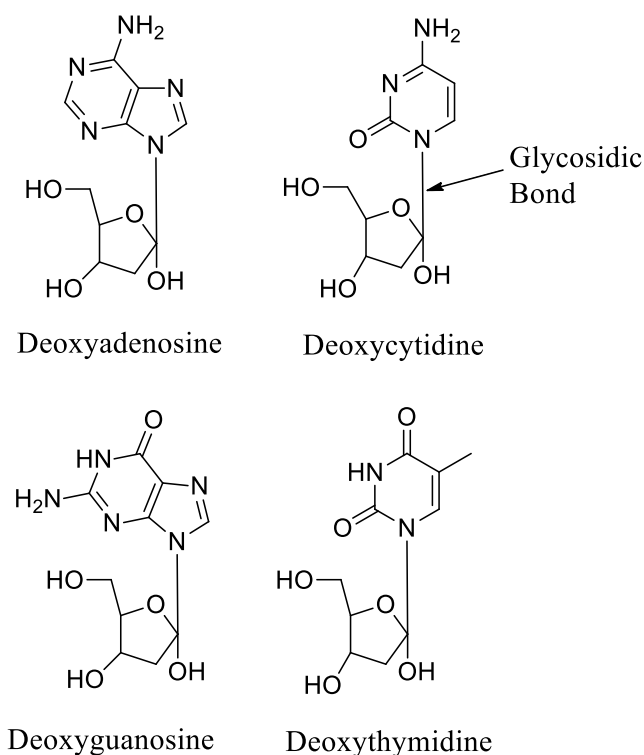
## 2. A brief discussion on the physico-chemical properties of DNA.

DNA (Deoxyribonucleic acid) is a polymer of phosphate containing pentose sugar (deoxyribose) attached to nucleobases, i.e. purines and pyrimidines, which are also known as nucleotides. Nucleotides are phosphates of base containing pentose sugar units known as nucleosides. The purines and pyrimidines are known as nucleobases.



**Figure 2.** The four nucleobases found in DNA.

The two purine bases – Adenine (A) and Guanine (G) – and the two pyrimidine bases – Cytosine (C) and Thymine (T) – are linked by bonds joining the 5' phosphate group of one nucleotide to a 3'-hydroxyl group on the sugar the adjacent nucleotide to form 3',5'-phosphodiester linkages. The phosphodiester bonds are stable because they are negatively charged, thereby repelling nucleophilic attack (Todd).



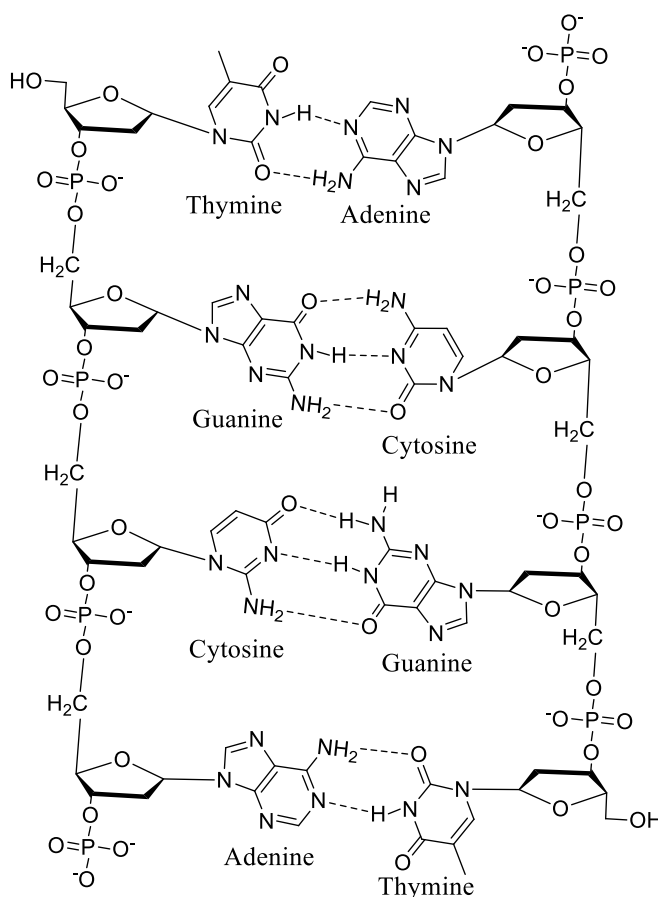
**Figure 3.** The Nucleosides of DNA

For any duplex DNA molecule, the ratios of A/T and G/C are always equal to one regardless of the base composition of the DNA. The number of adenines and thymines relative to the

number of guanines and cytosines is characteristic of a given species but varies from species to species (in humans, for example, 60.4% of DNA is composed of adenine and thymine bases) (Chargaff).

The bases are stacked upon each other at a distance of 3.4 Å (as described by Astbury in 1938). The nucleotide bases were linked by hydrogen bonding (**Figure 4**) (Gulland, 1947). DNA is a helical molecule that is able to adopt a variety of conformations (**Figure 5**) (Wilkins and Franklin).

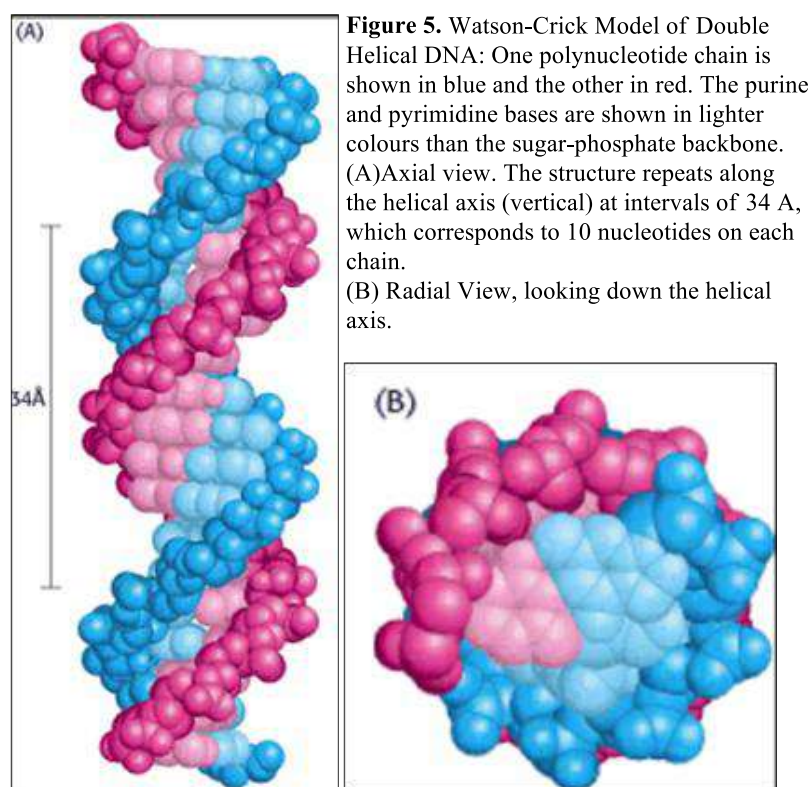
Two strands of DNA are intertwined into a helical duplex, which is held together by specific hydrogen bonding (**Figure 4**) between base pairs of adenine with thymine and guanine with cytosine and these base pairs are stacked at 3.4 Å distance (Watson and Crick). Furthermore, right handed rotation between adjacent base pairs by about 36° produces a double helix with 10 base pairs (bp) per turn.



**Figure 4.** Nucleotides and their hydrogen bonding

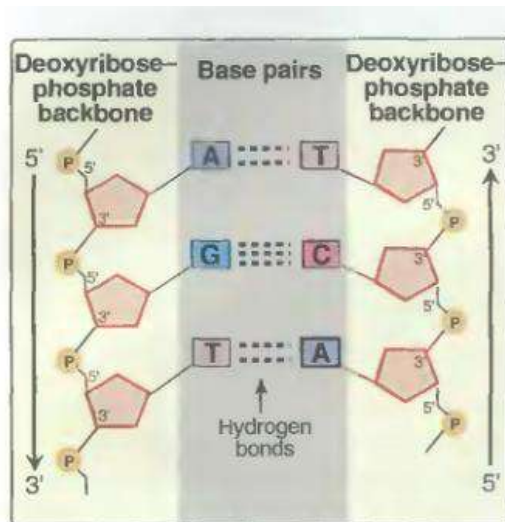
The bases are located along the axis of the helix with sugar phosphate backbones winding in an antiparallel orientation along the periphery. The order (or sequence) of the nucleotides along the chain differs from one DNA molecule to another. The purine and pyrimidine bases are flat and tend to stack above each other approximately perpendicular to the helical axis; this base stacking is stabilized mainly by London dispersion forces and by hydrophobic effects.

The two chains of the double helix are gripped together by hydrogen bonds between the bases. All the bases of the DNA are on the inside of the double helix, and the sugar phosphates are on the outside; therefore, the bases on one strand are close to those on the other. Because of this fit, specific base pairings between a large purine base (either A or G) on one chain and a smaller pyrimidine base (T or C) on the other chain are essential.



Base pairing between two purines would occupy too much space to allow a regular helix, and base pairing between two pyrimidines would occupy too little space. In fact, hydrogen bonds between G and C or A and T are more effective than any other combination. Therefore,

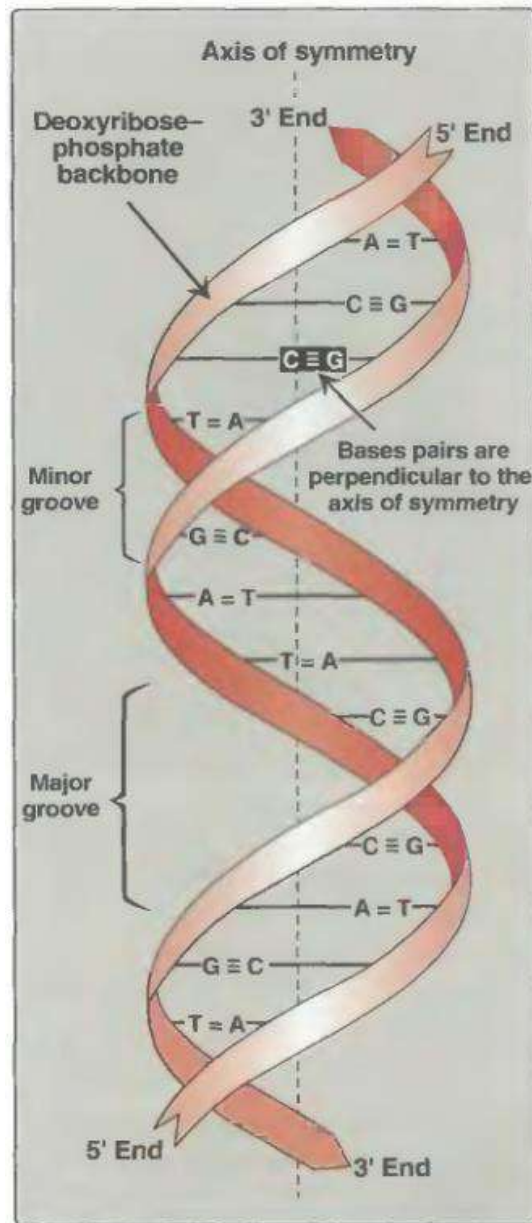
complementary base pairs form between guanines and cytosines or adenines and thymines only, resulting in a complementary relation between sequences of bases on the two polynucleotide strands of the double helix.



**Figure 6.** Two complementary DNA sequences

The two glycosidic bonds (**Figure 3**) that connect the base pair to its sugar rings are not directly opposite to each other, and, therefore, the two sugar-phosphate backbones of the double helix are not equally spaced along the helical axis. As a result, the grooves that are formed between the backbones are not of equal size; the larger groove is called the **major groove** and the smaller one is called the **minor groove**. One side of each base pair faces into the major groove, while the other side faces into the minor groove.

There are evidences of 3 types of DNA: A, B and Z. The B form is the most stable structure for a random-sequence DNA molecule under physiological conditions and is therefore the standard point of reference in any study of the properties of DNA.



**Figure 7.** DNA double helix, illustrating some of its major structural features

### Differences between A, B and Z-DNA

Helical Sense: A-DNA and B-DNA are right handed DNA helix whereas Z-DNA is left-handed.

Diameter of helix: Diameter of A-DNA is about 26 Å, that of B-DNA is 20 Å and that of Z-DNA is 18 Å.

Base Pairs per helical turn: A-DNA has 11 base pairs per helical turn, B-DNA has 10.5, Z-DNA has 12.

Helix rise per base pair: A-DNA has a helix rise per base pair of 2.6 Å, B-DNA has that of 3.4 Å and Z-DNA has that of 3.7 Å.

Base tilt normal to the helix axis: The base tilt normal to the helix axis of A-DNA is 20°, that of B-DNA is 6° degrees and that of Z-DNA is 7°.

Glycosyl bond conformation: It is ANTI for A-DNA and B-DNA and for Z-DNA, it is ANTI for Pyrimidines and SYN for Purines.

### **3. DNA as a drug target**

There are many important drugs which target nucleic acids, especially in the areas of antibacterial and anticancer therapy. DNA is the presumed intracellular target of some of the more clinically important antitumor agents, including bleomycin, doxorubicin (adriamycin), cisplatin, actinomycin D, mitomycin and cyclophosphamide. In spite of the well accepted premise that DNA is the receptor for these drugs, definitive data that pin-point the exact mechanism of action for any DNA-reactive drug are as yet unavailable. For DNA to be a receptor in the strict pharmacological sense it must possess both cognitive and response characteristics. In addition to proteins, oligomeric single-stranded RNA and DNA molecules and low molecular weight ligands such as drugs and carcinogens bind to DNA with varying degrees of sequence selectivity. Binding of low molecular weight ligands to DNA can cause a wide variety of potent biological responses including inhibition of transcription and replication, as well as mutagenic and oncogenic effects.

We shall first consider the drugs that interact with DNA. In general, we can group these under the following categories:

- intercalating agents;
- topoisomerase poisons (non-intercalating);
- alkylating agents;



- chain cutters;
- chain terminators.

It is likely that the interaction of the vast majority of sites on DNA that are recognized by low molecular weight ligands such as drugs do not lead to a measurable pharmacological response. According to receptor terminology, these are acceptor sites (i.e. cognition but no response). Conversely, those recognition sites on DNA that are linked to a response are receptor sites. The number of recognition sites on DNA decreases with increasing specified sequence length; for example, DNA target sites 10, 11 and 12 base pairs in length would be expected to occur approximately 2080, 1024 and 528 times in the human genome, respectively. However, a longer target sequence (15 or 16 base pairs) may only occur a few times or just once, and consequently a single ‘hit’ may seriously impair the ability of a cell to survive if this is a critical sequence. Potential receptor sites on DNA may be protected by histone molecules which are involved in higher orders of DNA structure, or proteins involved in control and expression of DNA functions such as transcription and replication. When DNA is modified by a low molecular weight ligand it potentially becomes a substrate for DNA repair processes. Furthermore, replication may be inhibited until the lesion on DNA is removed and repair is completed.

A list of FDA approved anti-cancer drugs which act via binding to DNA are listed in **Table 1**.

**Table 1.** Drugs acting via covalent and non-covalent interactions

Groove Binding Agents	DNA intercalators	Covalent DNA-adducts
Berenil Bisbenzimidazoles Bleomycin Chloroquine Chromomycin A3 Diamidine – 2 – phenylindole Distamycin A Guanyl Bisfuramidine Mithramycin Netamycin Netropsin	Aminoacridines Arylaminoalcohols Coumarins Cystodytin J Diplamine YO and YOYO-1 Daunomycin Quinolines and Quinoxalines Ethidium Bromide Proflavine Echinomycin	Busulfan Camptothecin Chlorambucil Cis-platin Clomesone Cyclodisone

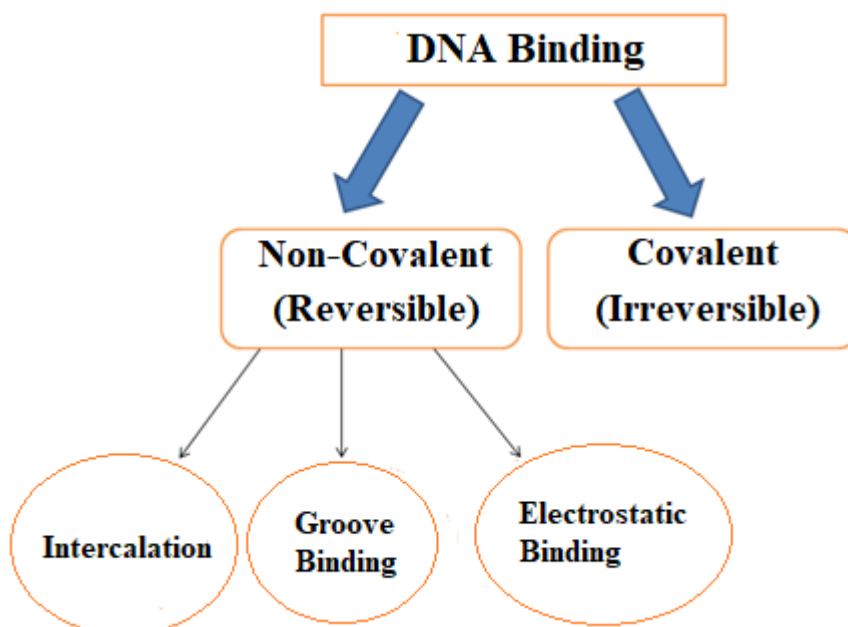
Pentamidine Pilocamycin SN 6999 SN 7167 Hoechst 33258	Chlorpheniramine Methapyrilene Tamoxifen Bis-naphthalene Doxorubicin M-AMSA Indoles	
---	---	--

## 4. DNA - Small Molecule Interactions

Binding of molecules to DNA is a crucial area of research, bridging chemistry and biology. This field promises a better understanding of intracellular processes like replication, transcription and translation. While proteins help control these processes by binding to DNA (sequence specific binding), certain small molecules (sequence non-specific binding) hinder these processes, thereby rendering them the potential to be anticancer drugs.

There are modes by which a foreign molecule can interact with the helix of DNA.

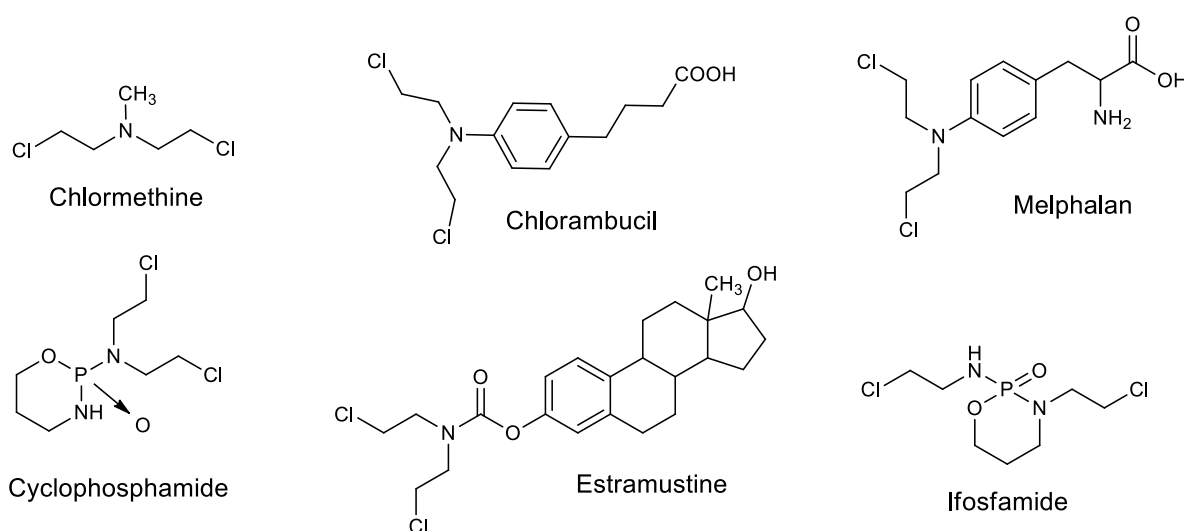
Interference with these interactions with these foreign molecules can disrupt the structure of DNA (shown in **Figure 8**).



**Figure 8.** Modes of binding of molecules in DNA

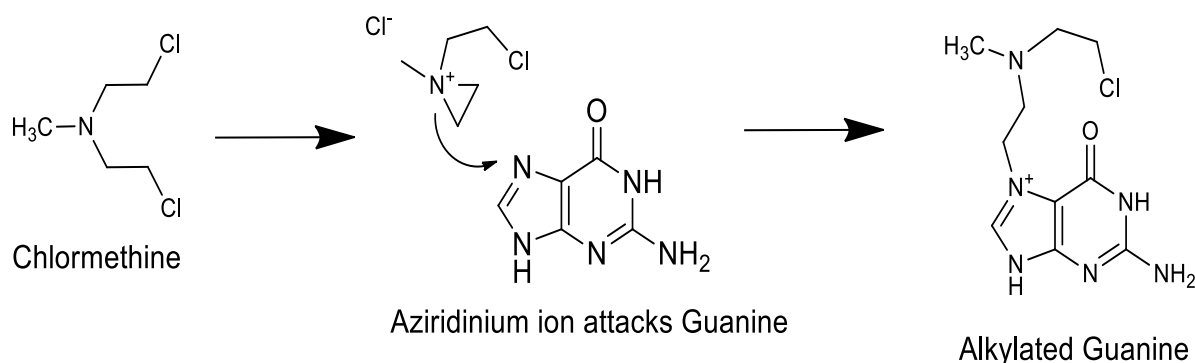
## Covalent Interaction of DNA with small molecules

This is done by highly electrophilic compounds named alkylating agents. There are many nucleophilic groups in the DNA and in particular the 7-nitrogen of guanine. Drugs with two such alkylating groups could therefore react with a guanine on each chain and cross-link the strands such that they cannot unravel during replication or transcription. Since alkylating agents are very reactive, they will react with any good nucleophile and so they are not very selective in their action. They will alkylate proteins and other macromolecules as well as DNA. Nevertheless, alkylating drugs have been useful in the treatment of cancer. Tumor cells often divide more rapidly than normal cells and so disruption of DNA function will affect these cells more drastically than normal cells.



**Figure 9.** DNA Alkylating agents

One bright example of such compounds is mechloroethamine, which gets converted to aziridine ion, which then interacts with the DNA duplex. Alkylation then takes place.<sup>2</sup>



**Figure 10.** Alkylation of guanine by chloromethine

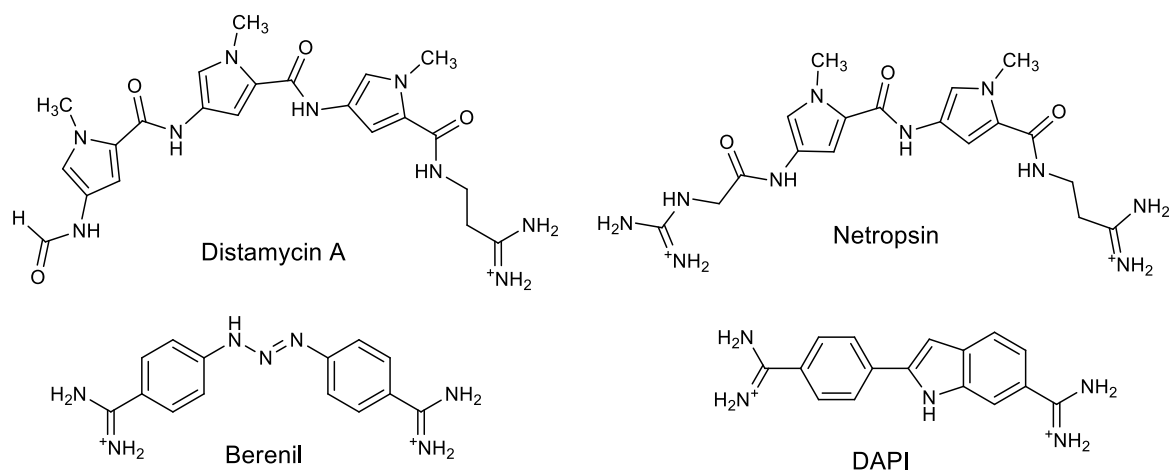
## Non-Covalent binding

### Groove Binding

Groove binders are a class of molecules that bind in major and minor grooves of the duplex DNA and play an important role in drug binding. As the dimensions of the grooves are different, targeting them requires vastly dissimilar and different shaped molecules.

Some small compounds bind to the minor groove of DNA by van der Waals interaction and hydrogen bonding. Minor groove binding drugs typically have several aromatic rings, such as pyrrole, furan or benzene connected by bonds possessing torsional freedom. Minor groove binding drugs are usually narrow curved shaped, which is isohelical to the curve of the minor groove, and facilitates binding by promoting van der Waals interactions. Additionally, these drugs can form hydrogen bonds to bases, typically to N3 of adenine and O2 of thymine.

The groove-binding molecules are commonly specific to adenine–thymine (AT) rich sequences. This preference in addition to the designed propensity for the electronegative pockets of AT sequences is probably due to better van der Waals contacts between the ligand and groove walls in this region, since AT regions are narrower than GC groove regions and also because of the steric hindrance in the latter, presented by the C2 amino group of the guanine base. Hydrophobic and/or hydrogen bonding are usually important components of this binding process, and provide stabilization. The antibiotic netropsin is a model groove-binder.



**Figure 11.** Well Known Groove Binders

### Intercalation of small molecules in the DNA duplex

There are several ways molecules (in this case also known as ligands) can interact with DNA. Ligands may interact with DNA by covalently binding, electrostatically, or intercalating. Intercalation, first described in 1961 by Lerman, is a non-covalent interaction where ligands of an appropriate size and chemical nature fit themselves in between base pairs of DNA. The ligand (molecule) is held rigidly perpendicular to the helix axis. This causes the base pairs to separate vertically, thereby distorting the sugar-phosphate backbone and decreasing the pitch of the helix. The phenomenon of intercalation involves the aromatic portion of a ligand positioning itself between base-pairs. The principal driving forces for intercalation are stacking and charge transfer interactions, but hydrogen bonding and electrostatic forces also play a role in stabilization.

Intercalation increases the separation of adjacent base pairs and the resultant helix distortion is compensated by adjustments in the sugar-phosphate backbone and an unwinding of the duplex. Aromatic stacking interactions between the bases and the intercalating molecule are a major stabilizing feature of the complexes formed.<sup>11</sup> Intercalation, apparently, is an energetically favorable process, because it occurs so readily. Presumably, the van der Waals forces that hold the intercalated molecules to the base pairs are stronger than those found between the stacked base pairs. Much of the binding energy is the result of the removal of the

drug molecule from the aqueous medium and a hydrophobic effect. Intercalators do not bind between every base pair. In general, intercalation does not disrupt the Watson–Crick hydrogen bonding, but it does destroy the regular helical structure, unwinds the DNA at the site of binding, and as a result of this, interferes with the action of DNA-binding enzymes such as DNA topoisomerases and DNA polymerases. Intercalation may not be the outright reason for DNA damage, but it does produce a conformational change (unwinding) in the double helix.

The large size of the intercalation system can be reflected in two aspects. First, intercalator molecules usually have side chains of various sizes. To capture the binding properties, at least one intercalator and one DNA base pair have to be included in the calculation. Intercalator and DNA base pairs, as well as water molecules and the DNA backbone, can be included without introducing too much computational cost. Thermodynamic processes can be simulated by computational experiments, e.g., via molecular dynamics. To gain more reliable information for the DNA intercalation process, an efficient higher level computational technique is desirable. Thus, the planar aromatic moiety of many carcinogens may well play a role in early stages of DNA recognition and binding, and intercalation of aromatic amino acid residues into DNA can impart enhanced stability to protein-DNA interactions. Hydrogen bonding involving substituent groups attached to complex intercalating molecules frequently imparts sequence selectivity to the binding process.

Anticancer activity and cytotoxicity of intercalative agents are associated with interference in at least some aspects of transcriptional, translational, and replicative processes, as well as with gross DNA damage and consequent inability to repair. Breakage of cellular DNA and interference with topoisomerase activity may well be a peculiar property of anticancer intercalating drugs.

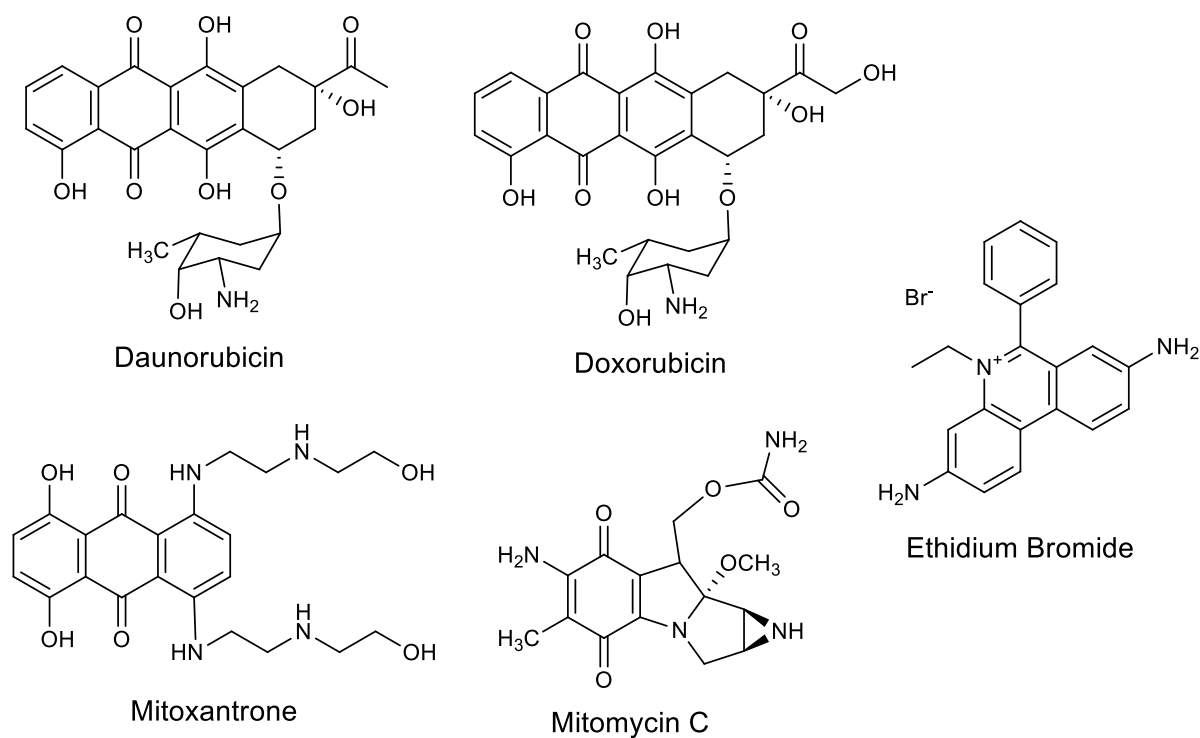


Figure 12. The Popular Intercalating Agents

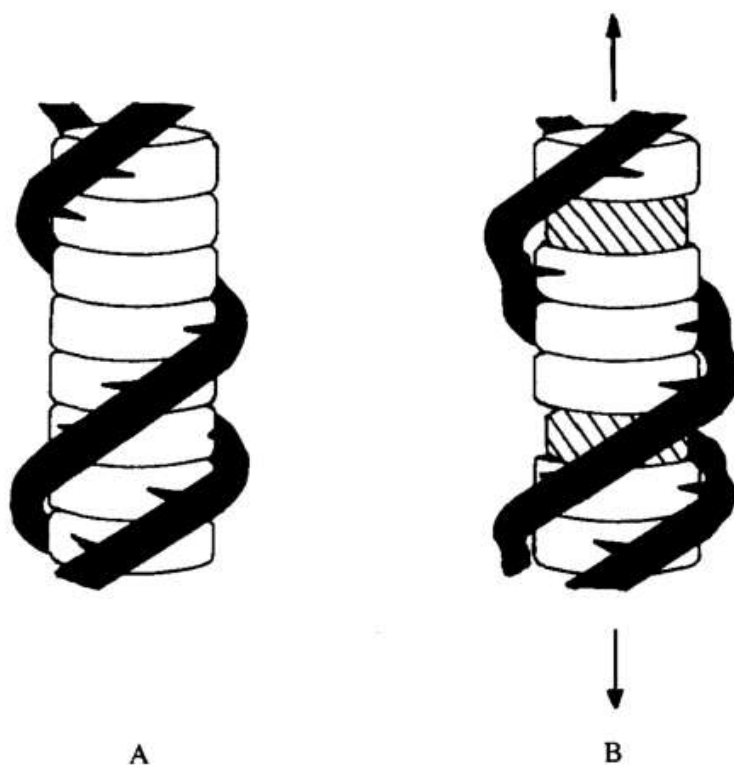
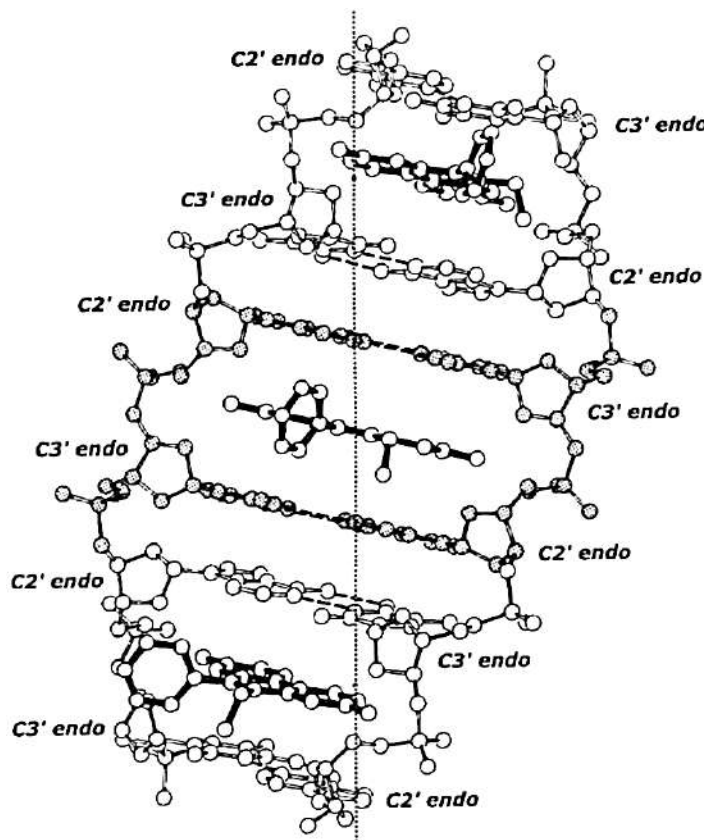


Figure 13. The Lerman Intercalation Model, in schematic form. (A) Illustrates the double-stranded DNA helix; (B) shows DNA with bound-ligand molecules as shaded discs intercalated between base pairs, shown as unshaded discs.

## The Rule of Neighbour Exclusion

The rule of neighbour-exclusion states that the two sites directly neighbouring an occupied intercalation site must remain unoccupied or, in less absolute terms, intercalation is an anti-cooperative at adjacent sites. **Figure 14** can make this rule quite clear.



**Figure 14.** The Rule of Neighbour-Exclusion

## 5. Therapeutic significance of DNA – Small Molecule Intercalation

Intercalation occurs when ligands of an appropriate size and chemical nature fit themselves in between base pairs of DNA. These ligands are mostly polycyclic, aromatic, and planar, and therefore often make good nucleic acid stains. Intensively studied DNA intercalators include berberine, ethidium bromide, proflavine, daunomycin, doxorubicin, and thalidomide. DNA



intercalators are used in chemotherapeutic treatment to inhibit DNA replication in rapidly growing cancer cells. Examples include doxorubicin (adriamycin) and daunorubicin (both of which are used in treatment of Hodgkin's lymphoma), and dactinomycin (used in Wilm's tumour, Ewing's Sarcoma, rhabdomyosarcoma).

## 6. Conclusion

In this article we have discussed the different types of small organic molecules which target DNA and DNA-associated processes. But many of these when used as chemotherapeutic agents manifest one or more side effects. Therefore, there is always a challenge remaining with these designer DNA-binding molecules, to achieve maximum specific DNA-binding affinity, and cellular and nuclear transport activity without affecting the functions of the normal cells. For many of the newer targeted therapeutics that are under development for the treatment of cancer, it is however, expected that these new putative drugs will be used in combination with the more traditional drugs molecule such as *cis*-platin or doxorubicin. In combination with a DNA-interactive drug, the chemotherapeutic agent might exert considerably enhanced clinical efficacy as anticancer agents. The future challenge will be to 'conjugate' these agents appropriately on the basis of firm scientific principles. Combination of the other tools of genomics and proteomics might provide a new opportunity towards this end.

## References

1. Hurley, L; Boyd, F. L. *TIPS*, **1988**, 9, 402-407
2. Sirajuddin, M.; Ali, S.; Badshah, A. *J. Photochem. Photobiol. B.* **2013**, 124, 1-19
3. Ghosh, D.; Basu, S.; Singha M.; Das, J.; Bhattacharya, P.; Basak, A. *Tetrahedron Letters*, **2017**, 58, 2014–2018
4. Paul, A.; Bhattacharya, S. *CURRENT SCIENCE*, **2012**, 102, 212-231
5. Kennard, O. *Pure & Appl. Chem.*, **1993**, 65, 1213-1222
6. Bhattacharya, P.; Mandal, S. M.; Basak, A. *Eur. J. Org. Chem.* **2016**, 1439–1448
7. Macindoe, G.; Mavridis, L.; Venkatraman, V.; Devignes, M.; Ritchie, D. W. *Nucleic Acids Res.*, **2010**, 38, W445–W449, <http://hexserver.loria.fr/>
8. Bikadi, Z.; Hazai, E. *J. Cheminf.* **2009**, 1, 15, 1-16
9. Hanwell, M. D.; Curtis, D. E.; Lonie, D. C.; Vandermeersch, T.; Zurek E.; Hutchison, G. R. *J. Cheminf.* **2012**, 4:17.
10. Li, S.; Cooper, V. R.; Thonhauser, T.; Lundqvist, B. I.; Langreth, D. C. *J. Phys. Chem. B* **2009**, 113, 11166–11172
11. Neidle, S.; Abraham, Z. *CRC Critical Reviews in Biochemistry*, **1984**, 17, 73-121
12. Ahmed, M. S. ; Ramesh, V.; Nagaraja, V.; Parish, J.H.; Hadi, S. M. *Mutagenesis*, **1994**, 9, 193-197
13. Hunter, C. A.; Sanders, J. K. M. *J. Am. Chem. Soc.* **1990**, 112, 5525-5534
14. Seleem, D.; Pardi, V.; Murata, R. M. *Arch. Oral Biol.*, **2017**, 76, 76-83
15. García-Zubiri IX, Burrows HD, de Melo JSS, Pina J, Monteserín M, Tapia M. *J. Photochem Photobiol.* **2007**, 83,1455–1464
16. Ralph, R.K.; Marshall, B.; Darkin, S. *Trends Biochem Sci*, **1983**, 8, 212 - 214

A LITERATURE SURVEY ON  
**STIMULI RESPONSIVE POLYMERS**

SCOTTISH CHURCH COLLEGE  
AFFILIATED TO  
UNIVERSITY OF CALCUTTA

ROLL NUMBER: 223/CEM/191028

REGISTRATION NUMBER: 223-1121-0186-16

P.G. SEMESTER IV

PHYSICAL CHEMISTRY SPECIAL PAPER: SP 44

Sayan Das

SAYAN DAS

Rana Sen.

DR. RANA SEN  
(SUPERVISOR)

# STIMULI RESPONSIVE POLYMERS

---

## ABSTRACT

Response to stimulus is a basic process of living systems. Based on the lessons from nature, scientists have been designing useful materials that respond to external stimuli such as temperature, pH, light, electric field, chemicals and ionic strength. These responses are manifested as dramatic changes in one of the following: shape, surface characteristics, solubility, formation of an intricate molecular self-assembly or a sol-to-gel transition. The functions of living cells are regulated by macromolecules that respond to changes in local environment and these biopolymers form the basis around which all major natural processes are controlled. Many synthetic polymers that exhibit environmentally responsive behaviour can thus be considered as biomimetic and their development is central to emerging 'smart' applications in biology and medicine. Stimuli-responsive polymers are capable of changing their chemical and/or physical properties in response to environmental stimuli. This unique feature has allowed stimuli-responsive polymers to be used in a variety of applications. This review will focus on the use of Stimuli Responsive Polymers in biological systems and cell targeting.

## INTRODUCTION

Polymers are large molecules, or macromolecules, composed of many repeating subunits (monomers), and can either be natural (e.g., cellulose, rubber, silk) or synthetic (e.g., polystyrene, polyethylene and polypropylene). Their large molecular mass yields physical properties that are significantly different than small molecules. Furthermore, the properties of polymers and polymer-based materials (e.g., toughness, elasticity, viscosity) can be tuned to fit a particular application.

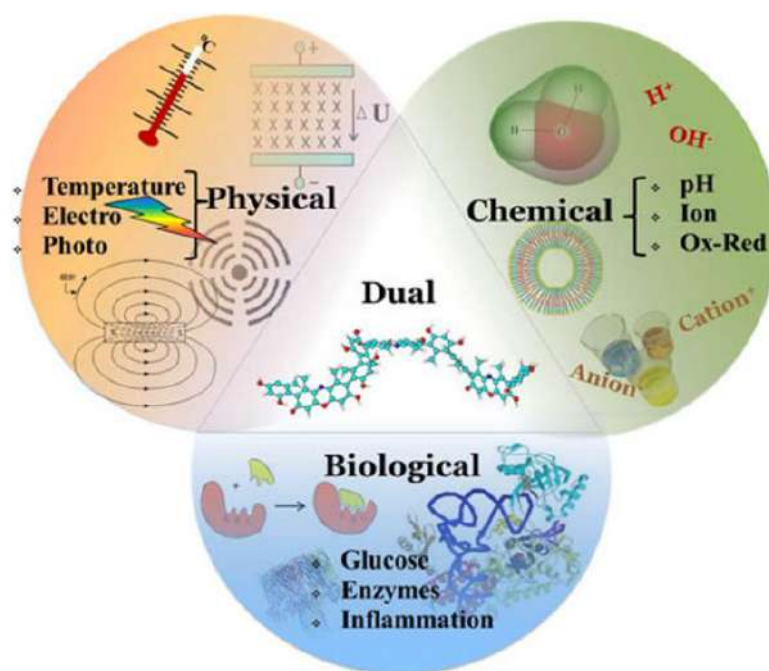
Stimuli-responsive polymers are polymers that respond sharply to small changes in physical or chemical conditions with relatively large phase or property changes. These polymers are also variously referred to as “environmentally-sensitive”, “smart” or “intelligent” polymers. Over the past 25 years they have been proposed for numerous biomedical uses, which are usually in an aqueous environment. When used as “smart biomaterials” they may be (a) dissolved in or phase separated out of aqueous solutions, (b) adsorbed on or (c) chemically grafted onto aqueous-solid interfaces, or the smart polymer molecules may be chemically cross-linked, H-bonded, and/or physically entangled in the form of (d) hydrogels. These properties led scientists to generate ‘smart’ materials that respond a variety of stimuli, e.g., pH, temperature, mechanical stress, the presence of various small molecules and biomolecules and electric/magnetic fields. Due to the breadth of the responsivities that can be built into stimuli-responsive polymers and materials, they have found applications as sensors and biosensors, for controlled and triggered drug delivery, for environmental remediation and as chemo mechanical actuators.

In biological systems and drug delivery, the design of new systems and approaches must meet challenges associated with administration in the body: (i) a simple route of administration, (ii) effective delivery to the desired biological compartment, (iii) response adapted to the pathological event, either rapid or slow, depending on the bio-specificity, and (iv) the use of non-toxic, biocompatible and biodegradable systems. In this review paper we will see how responsive polymers can be used to tackle such problems and provide an effective solution in drug delivery.

## STIMULI RESPONSIVE POLYMERS

The strategy underlying polymer-containing responsive systems is a dramatic physicochemical change caused by stimuli. At the macromolecular level, polymer chains can be altered in different ways, including changes in hydrophilic-to-hydrophobic balance, conformation, solubility, degradation, and bond cleavage, and these, in turn, will cause detectable behavioural changes to self-assembled structures. [1]

Stimuli are commonly classified in three categories: physical, chemical, or biological (Fig. 1) [2,3]. Physical stimuli (light, temperature, ultrasound, magnetic, mechanical, electrical) usually modify chain dynamics, i.e., the energy level of the polymer/solvent system, while chemical stimuli (solvent, ionic strength, electrochemical, pH) modulate molecular interactions, whether between polymer and solvent molecules, or between polymer chains [4]. Biological stimuli (enzymes, receptors) relate to the actual functioning of molecules: enzymatic reactions, receptor recognition of molecules [5]. In addition, there are dual stimuli-responsive polymers that simultaneously respond to more than one stimulus.



**Fig. 1** Classification of stimuli of stimuli-responsive polymers

Examples of stimuli responsive polymers are: -

**1. Physically Dependent Stimuli** - Physically dependent stimuli mainly include: temperature, electric field, light, ultrasound, magnetic fields and mechanical deformation. However, in this review we focus only on the stimuli-responsiveness of polymer/copolymer systems, hence, the physical stimuli reported as actively changing their properties/supramolecular structures are temperature, light, and electric field. We mention that magnetic fields and ultrasound have been used only for compounds that have been entrapped/encapsulated in polymer assemblies, and therefore we will not include them here.

**1.1 Temperature Responsive Polymers** - Temperature-responsive polymers have attracted great attention in bioengineering and biotechnology applications, because certain diseases manifest temperature changes [6]. Normally, these copolymers are characterized by a critical solution temperature around which the hydrophobic and hydrophilic interactions between the polymeric chains and the aqueous media abruptly change within a small temperature range. This induces the disruption of intra- and intermolecular electrostatic and hydrophobic interactions and results in chain collapse or expansion (a volume phase transition). Typically, these polymer solutions possess an upper critical solution temperature (UCST) above which one polymer phase exists, and below which a phase separation appears. Alternatively, polymer solutions that appear as monophasic below a specific temperature and biphasic above it generally possess a so-called lower critical solution temperature (LCST). Depending on the mechanism and chemistry of the groups, various temperature-responsive polymers have been reported: poly(N-alkyl substituted acrylamides), e.g., poly(N-isopropylacrylamide) (PNiPAAm) [7,8], poly (N-vinylalkylamides), e.g., poly(N-vinylcaprolactam) (PNVC) [9], and copolymers such as poly (L-lactic acid)-poly(ethylene glycol)-poly(L-lactic acid) (PLLA-PEG-PLLA) triblock copolymers [10], and poly (ethylene oxide)-poly(propylene oxide)-poly (ethylene oxide) (PEO-PPO-PEO) copolymers [11].

**1.2 Electro-Responsive Polymers** - Electrical and electrochemical stimuli are widely used in research and applications, due to their advantages of precise control via the magnitude of the current, the duration of an electrical pulse or the interval between pulses [12,13]. Typical electrically responsive polymers are conducting polymers, as for example polythiophene (PT) or sulphonated-polystyrene (PSS), which can show swelling, shrinking or bending in response to an external field [14,15]. There are different effects upon electrochemical stimulation: (a) an influx of counter ions and solvent molecules causes an increase in osmotic pressure in the polymer, resulting in a volumetric expansion, (b) control of the loading/adsorption of polyelectrolyte on to oppositely charged porous materials, (c) formation and swelling of redox-active polyelectrolyte multilayers. For example, when an electrochemical stimulus is applied to multilayer polyacrylamide films, the combined effects of H<sup>+</sup> ions migrating to the region of the cathode and the electrostatic attraction between the anode surface and the negatively charged acrylic acid groups lead to shrinking of the film on the anode side [16,17].

**1.3 Photo-Responsive Polymers** - Because light can be applied instantaneously and under specific conditions with high accuracy, it renders light-responsive polymers highly advantageous for applications. The light can be directly used at the polymer surface or can be delivered to distant locations using optical fibres. Ideally, the wavelength of the laser is tuned to the so-called biologically 'friendly' window [18], the near-infrared part of the spectrum, which is less harmful and has deeper penetration in tissues than visible light. In this case, the light is both minimally absorbed by cells/tissue and maximally so by the polymers. Most photo-responsive polymers contain light-sensitive chromophores such as azobenzene groups [19,20], spiropyran groups [21,22], or nitrobenzyl groups [23,24]. A variety of azobenzene or spiropyran-containing photo-responsive polymers, as for example PAA [25,26], PHPMAm [27,28], and PNIPAM [29,30], have been reported.

**2. Chemically-Dependent Stimuli** – Chemically dependent stimuli comprise pH, ionic strength, redox and solvent.

**2.1 pH-Responsive Polymers** - pH is an important environmental parameter for biomedical applications, because pH changes occur in many specific or pathological compartments. For example, there is an obvious change in pH along the gastrointestinal tract from the stomach (pH = 1–3) to the intestine (pH = 5–8),

chronic wounds have pH values between 7.4 and 5.4 [31], and tumour tissue is acidic extracellularly [32,33]. Therefore, unlike temperature changes, this property can be exploited for a direct response at a certain tissue or in a cellular compartment. The key element for pH responsive polymers is the presence of ionisable, weak acidic or basic moieties that attach to a hydrophobic backbone, such as polyelectrolytes [34]. Upon ionization, the electrostatic repulsions of the generated charges (anions or cations) cause a dramatic extension of coiled chains. The ionization of the pendant acidic or basic groups on polyelectrolytes can be partial, due to the electrostatic effect from other adjacent ionized groups [35]. Another typical pH responsive polymer exhibits protonation/deprotonation events by distributing the charge over the ionisable groups of the molecule, such as carboxyl or amino groups [36]. pH induces a phase transition in pH responsive polymers very abruptly. Usually, the phase switches within 0.2–0.3 U of pH [37]. pH responsive polymers typically include chitosan [38], albumin [39], gelatin [40], poly(acrylic acid) (PAAc)/chitosan IPN [41], poly(methacrylic acid-g-ethylene glycol) [P(MAA-g-EG)] [42,43], poly(ethylene imine) (PEI) [44], poly(N,N-diakylamino ethylmethacrylates) (PDAAEMA), and poly(lysine) (PL) [45,46].

**2.2 Ion-Responsive Polymers** - The responsiveness to ionic strength is a typical property of polymers containing ionisable groups. These polymer systems exhibit unusual rheological behaviour as a result of the attractive Coulombic interactions between oppositely charged species, which may render the polymer insoluble in deionized water but soluble in the presence of a critical concentration of added electrolytes where the attractive charge/charge interactions are shielded [47,48,49]. Therefore, changes in ionic strength cause changes in the length of the polymer chains, the polymer solubility and the fluorescence quenching kinetics of chromophores bound to electrolytes [48, 50, 51].

**2.3 Redox-Responsive Polymers** - containing labile groups present a beneficial opportunity to develop redox-responsive biodegradable or bio erodible systems. Acid labile moieties inside polyanhydrides [52,53], poly(lactic/glycolic acid) (PLGA) [54], and poly(b-amino esters) (PbAEs) [55] induce redox responsiveness. Disulphide groups have also been used to induce redox responsiveness, because they are unstable in a reducing environment, being cleaved in favour of corresponding thiol groups [56,57]. Polymers with disulphide cross-links degrade when exposed to cysteine or glutathione, which are reductive amino-acid based molecule [58]. Another typical redox responsive polymer is poly(NiPAAm-co-Ru(bpy)<sub>3</sub>), which can generate a chemical wave by the periodic redox change of Ru(bpy)<sub>3</sub> into an oxidized state of lighter colour [59]. This redox reaction alters the hydrophobic and the hydrophilic properties of the polymer chains and results in swelling and deswelling of the polymer.

**3 Biologically Dependent Stimuli** - Biologically dependent stimuli typically involve analytes and biomacromolecules such as glucose, glutathione, enzymes, receptors, and over-produced metabolites in inflammation.

**3.1 Glucose Responsive Polymers** - Precisely engineered glucose sensitive polymers have huge potential in the quest to generate, for example, self-regulated modes of insulin delivery [60]. For glucose responsive polymers, glucose oxidase (GOx) is conjugated to a smart, pH-sensitive polymer. GOx oxidizes glucose to gluconic acid, which causes a pH change in the environment. The pH sensitive polymer then exhibits a volume transition in response to the decreased pH [60]. In this way, drastic changes in the polymer conformation are regulated by the body's glucose level, which, in turn, significantly affects enzyme activity and substrate access.

**3.2 Enzyme-Responsive Polymers** - In nature, bacteria located mainly in the colon produce special enzymes, including reductive enzymes (e.g., azoreductase) or hydrolytic enzymes (e.g., glycosidases) which



are capable of degrading various types of polysaccharides, such as pectin, chitosan, amylase/amylopectin, cyclodextrin and dextrin [61, 62, 63]. In most enzyme-responsive polymer systems, enzymes are used to destroy the polymer or its assemblies. The biggest advantage of enzyme responsive polymers is that they do not require an external trigger for their decomposition, exhibit high selectivity, and work under mild conditions. For example, polymer systems based on alginate/chitosan or DEXS/chitosan microcapsules are responsive to chitosanase [64]. And azoaromatic bonds are sensitive to azoreductase [65]. In this respect, they have great potential for in vivo biological applications. However, the main disadvantage is the difficulty of establishing a precise initial response time.

**3.3 Inflammation-Responsive Polymers** - The inflammatory process is initiated by T- and B-lymphocytes, but amplified and perpetuated by polymorphonuclear (PMN) leukocytes and macrophages. Various chemical mediators in the process, including arachidonic acid metabolites, proteolytic enzymes and oxygen metabolites, can cause tissue damage. For inflammation-responsive systems, the reactive oxygen metabolites (oxygen free radicals) released by PMNs and macrophages during the initial phase of inflammation are the stimuli [66]. Such chemical mediators have been successfully used as stimuli for responsive drug delivery. For example, in vivo implantation experiments revealed that hyaluronic acid (HA) cross-linked with glycidyl ether can degrade in response to inflammation [67].

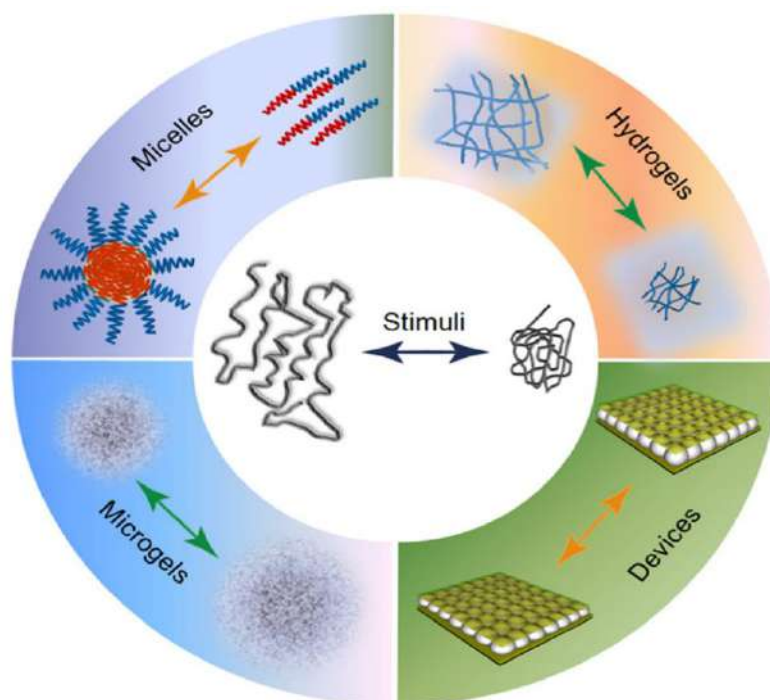
**4. Dual-Stimuli For biomedical applications**, a step forward is realized if the smart materials respond simultaneously to more than one stimulus. Therefore, increasing the efficacy of drug therapies may require polymeric materials, which are responsive to several kinds of stimuli. These will support the diagnosis of patients by monitoring several physiological changes at once. The dual-stimuli responsive approach is ideally suited for theragnostic (a combination of diagnostics and therapy) because some functionalities can provide on-site feedback and diagnostics, while others could initiate curing and therapy. Availability of various physical, chemical and biological stimuli is indispensable for multiple response functions. Therefore, multi-stimuli responsive polymers, especially dual temperature and pH-responsive systems, are attracting increasing attention recently for their advantages in biotechnological and biomedical applications. For example, a dual-stimuli responsive delivery system, using both pH and glutathione-responsive polymeric modules, was developed to therapeutically deliver medicinal molecules. It was possible to tune the release kinetics by systematically varying the composition of the pH-sensitive hydrophobic moiety (butyl acrylate), by modifying the glutathione-responsive moiety (pyridyl disulphide acrylate), or by modifying both of them. Table 1 summarizes stimuli responsive polymers grouped by stimulus–response, and contain information about the synthesis method and application.

**Table 1** Summary of stimuli responsive polymers grouped by stimulus–response, and contain information about the synthesis method and application

Type of stimulus–response	Stimulus-responsive polymers	Synthesis method	Application
<b>Physically dependent stimuli</b>			
Temperature-responsive polymers	PNiPAAm	Living radical polymerization	Water soluble polymer sensor, Tissue adhesion prevention material
	PNVC	Living radical polymerization	Thermosensitive hydrogel at any temperature
	PLLA/PEG/PLLA	Ring open polymerization	Potential anti-cancer drug carrier
	PEO–PPO–PEO	Crosslinking the ethoxysilane-cap	Drug carrier
Electro-responsive polymers	PT	Electrochemical Synthesis	Drug release and cancer chemotherapy
	PSS	Emulsion polymerization	Drug carrier
Photo-responsive polymers	Azobenzene or spiropyran-containing		
	PAA	} Copolymerization	Photocchromic polymer
	PHPMAm		Sensor
	PNIPAM		Photodegradation material
<b>Chemically dependent stimuli</b>			
pH-responsive polymers	chitosan	} Biosynthesis	Drug release
	Albumin		Enzyme immobilization
	Gelatin		Immunoassay
	PAAc/chitosan IPN	UV irradiation	Wound dressing material and drug release
	P(MAA- <i>g</i> -EG)	Free-radical, solution photopolymerization	Controlled insulin delivery
	PEI	Solution polymerization	pH-sensitive controlled release systems
	PDAAEMA		
Ion-responsive polymers	PL	Biosynthesis	Vectors for gene delivery
	<b>Redox-responsive polymers</b>		
Redox-responsive polymers	Polyanhydrides	Melt condensation polymerization	Potential oral drug delivery systems
	PLGA	Double emulsion solvent evaporation	Controlled delivery systems
	PbAEs	Addition solution polymerization	Efficient carrier for cytotoxic agents
	Poly(NiPAAm-co-Ru(bpy) <sub>3</sub> )	Living radical copolymerization	Artificial muscles, artificial reptile
<b>Biologically dependent stimuli</b>			
Glucose-responsive polymers	GOx conjugated chitosan	Carbodiimide chemistry	Self-regulated insulin delivery
Enzyme-responsive polymers	DEXS/chitosan	Layer-by-layer assembly	Local and sustained drug release
	Azoaromatic crosslinked hydrogel	Copolymerization	Specific delivery of peptides and proteins
Inflammation-responsive polymers	Glycidylether crosslinked HA	Suspension solution reaction	Implantable drug delivery
Dual-stimuli	PLL block PEG–PLL	Side chain reaction and crosslinking	Enhance gene expression

## CONTROLLED DRUG DELIVERY

Living systems respond to external stimuli by adapting themselves to changing conditions. Polymer scientists have been trying to mimic this behaviour by creating so called smart polymers. Smart polymers are very promising for biomedical applications, and have found use as controlled/triggered/targeted drug delivery vehicles, tissue engineering scaffolds, cell culture supports, bio separation devices, sensors, and actuators/ artificial muscles. The concept of stimuli-responsive polymer-based drug delivery systems was first reported in the late 1970s with the use of thermosensitive liposomes for the local release of drugs via hyperthermia. Subsequently, a great deal of research has been carried out on stimuli-responsive materials for drug delivery, especially concerning the design and application of responsive polymers. The design of new systems and approaches must meet the challenges associated with administration in the body. The systems must be: (i) simply administered, (ii) capable of delivery to the desired locations in response to a stimulus, (iii) composed of non-toxic, biocompatible and biodegradable components. A variety of stimuli-responsive polymer-based materials have been used for this application, including crosslinked gel networks, and non-crosslinked block copolymer assemblies. These, as well as other systems, are shown schematically in Figure 2.

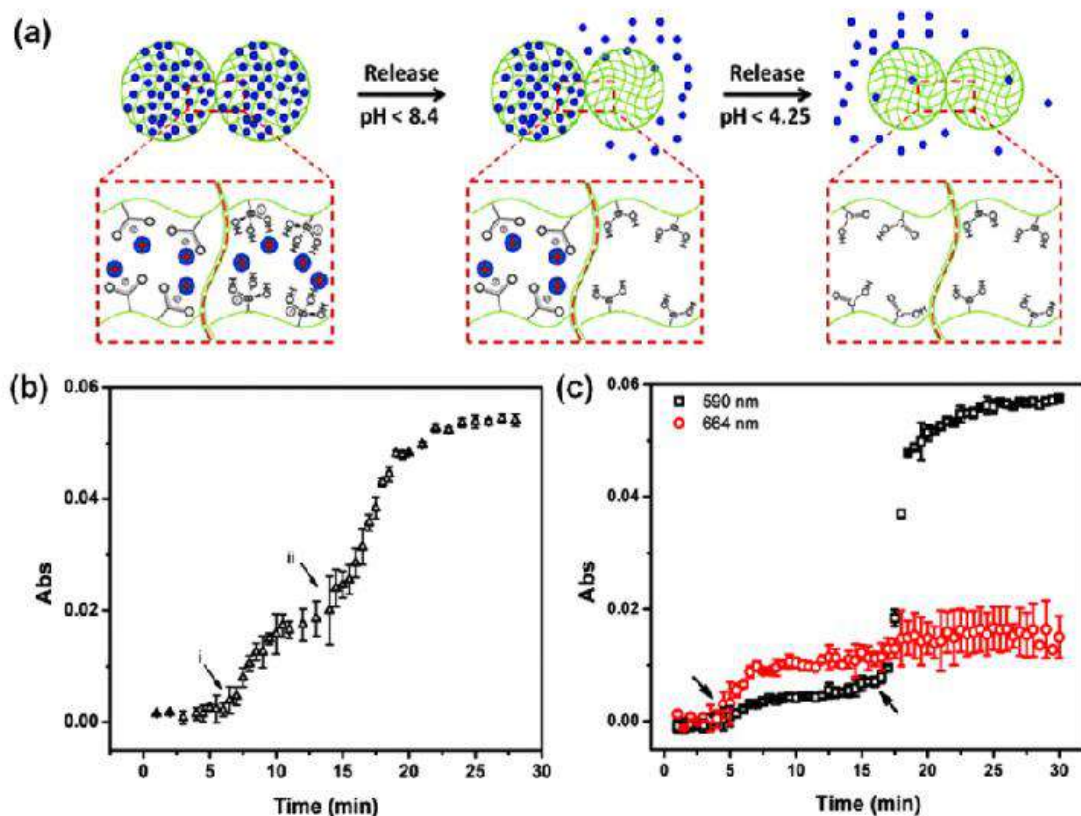


**Figure 2.** Various stimuli-responsive polymers that have been used for drug delivery applications.

In this section, we will discuss recent progress using these and related materials for controlled/triggered/targeted drug delivery. Some of the of drug delivery includes the use of crosslinked polymer networks, e.g., hydrogels and microgels; or the temperature responsive polymeric micelles. In this paper, there is a discussion of the pH responsive polymers.

As a drug carrier, pNIPAm-based microgels combine the advantages of both hydrogels and nanoparticles. PNIPAm microgel particles have a sponge-like structure with interstitial spaces filled with water. Drug molecules can be loaded by equilibrium partitioning between the solution and microgel phases. Electrostatic interaction, hydrophobic interaction, and/or hydrogen-bonding may play an important role for drug loading. The Serpe group developed a novel microgel-based assembly (reservoir device) as a new platform for drug delivery [68 – 72]. The structure of this device and the release mechanism is shown in Figure 4. The device is usually composed of a pNIPAm-co-AAc microgel layer sandwiched between two thin Au layers (all on a glass support) and was used as a novel platform for controlled and triggered small molecule delivery. Tris(4-(dimethylamino)phenyl)methyl chloride (crystal violet, CV), which is positively charged, was loaded into the microgel layer of the device and released in a pH dependent fashion, at a rate that could be controlled by the thickness of the Au layer coating the microgel [73]. The model drug could be released in an “on-off” fashion, by systematically varying the solution pH. Furthermore, by modifying the top layer Au surface, we can control the drug release with a lower thickness of Au [74]. By combining two oppositely charged microgel, we can control the microgels’ aggregation behaviour to control the drug release. In this case, the microgels copolymerized with acrylic acid exhibit a negative charge above pH 4.25, while the microgels copolymerized with N-[3-(dimethylamino)propyl]methacrylamide exhibit a positive charge below pH 8.4; these microgels are neutral outside of these pH ranges. We show that aggregates form when the two independent sets of microgels were exposed to one another in a solution that renders them both charged. In solutions of pH outside of this range, the microgels disaggregate because one of the microgels becomes neutralized. This behaviour was exploited to load (aggregation) and release (disaggregation) a small-molecule model drug [75]. This aggregate based system provides evidence how the charged pNIPAm-based microgels applied in controlled/triggered drug release.

Recently, we showed that the microgel-based reservoirs devices could be used for sequential and controlled release of more than one small molecule [76]. By incorporating the mixed microgels into reservoir devices, and varying their ratio, the small molecule release rate and release amount (dosage) can be easily tuned. Furthermore, two different small molecules can be loaded into the two distinct microgels, which allows for their sequential release at particular pHs (shown in Figure 3).



**Figure 3.** (a) Schematic of pH triggered MB release from APBA-MG and AAC-MG. As each microgel is neutralized, the electrostatic interactions between the microgel and the MB are diminished, and the MB is released from the microgel. (b) Sequential release of MB from a reservoir device with 1:1 APBA-MG and AAC-MG and 50 nm Au overlayer at 37 o C. The arrows indicate when the solution pH was changed to (i) 7.0 and (ii) 3.0. (c) The release profile for a device made of APBA-MG and AAC-MG loaded with MB and CV, respectively. The arrows are the time that pH adjusted

PNIPAm-co-AAC microgels (AAC-MG) and poly(N-isopropylacrylamide-3-(acrylamido)phenylboronic acid) (pNIPAm-co-APBA) microgels (APBAMG) were composed into the devices to load the drugs, MB and CV, respectively. At pH 10.0, methylene blue (MB, positively charged) exhibited strong electrostatic interactions with both the negatively charged AAC and APBA-modified microgels. This resulted in MB uptake into both of the microgels. At pH 7.0, the APBA groups were neutralized, allowing MB to be released from the APBA-MG only. When the solution pH was again lowered to 3.0, the AAC groups are neutralized allowing MB to be released from the AAC-MG. Furthermore, we demonstrated that two different small molecules could be delivered to a system when triggered at specific pHs. These systems represent a versatile approach to sequentially delivering small molecules to a system, in a triggered fashion, with tuneable release kinetics. Importantly, their release behaviour can be easily tuned by simply changing the microgel chemistry, e.g., by generating reservoir devices from microgels that ionize at different solution pH. This would allow one to deliver various small molecules to a system triggered by a variety of solution pHs. This, combined with the tuneable release kinetics and the ability to array these devices on a single substrate, makes this delivery platform extremely versatile, powerful, and unique.

## **CONCLUSION AND FUTURE PROSPECTS**

Although stimuli-responsive polymer-based systems have been known for many decades, it wasn't until relatively recently that their behaviour could be understood at a level deep enough to fully exploit their behaviour. This was initiated early on by theories used to describe the behaviour of polymers and polymer-based materials, later supported by experiment. Stimuli-responsive polymers have been synthesized using a variety of techniques, and employed for myriad applications; we describe only some of their applications here. In the future, combining stimuli responsive polymers with biological systems, and nanoscale materials, a variety of new functions (and properties) will be accessible. This development needs to be supported by new theories that can describe the newly found behaviours such that the development of new materials can be done in a smart fashion to meet the needs of a specific application. Another challenge is to develop systems that respond to multiple external stimuli in an “intelligent” and predictable manner. These materials are required to support the development of biomimetic systems with long-term stability and durability. The concepts presented in this review encompass both the introductory theory needed to understand polymers, and some of their applications. A more complete picture of this broad and complex topic can be obtained from the referenced articles.

## **ACKNOWLEDGEMENTS**

I would like to take this opportunity to thank the people without whom it would not have been possible without the kind support and help of my professors and University of Calcutta. I would like to extend my sincere thanks to all of them.

I am highly indebted to Professor Priyatosh Dutta and Professor Rana Sen for their guidance and constant supervision as well as for providing necessary information regarding the project & also for their support in completing the project.

I would like to express my special gratitude and thanks to the University of Calcutta for giving me the opportunity to present my views on this review.

My thanks and appreciations also go to my colleagues who have willingly helped me out with their abilities.

## REFERENCES

1. Schmaljohann D (2006) *Adv Drug Deliv Rev* 58:1655–1670
2. Gil ES, Hudson SM (2004) *Prog Polym Sci* 29:1173–1222
3. Delcea M, Mõhwald H, Skirtach AG (2011) *Adv Drug Deliv Rev* 63:730–747
4. Liechty WB, Kryscio DR, Slaughter BV, Peppas NA (2010) *Annu Rev Chem Biomol Eng* 1:149–173
5. Delcea M, Mõhwald H and Skirtach AG (2011) *Adv Drug Deliv Rev*. (In Press, Corrected Proof)
6. Zhang L, Xu T, Lin Z (2006) *J Membr Sci* 281:491–499
7. Liu Y, Meng L, Lu X, Zhang L, He Y (2008) *Polym Adv Technol* 19:137–143
8. Ohya S, Sonoda H, Nakayama Y, Matsuda T (2005) *Biomaterials* 26:655–659
9. Suwa K, Morishita K, Kishida A, Akashi M (1997) *J Polym Sci Part A Polym Chem* 35:3087–3094
10. Na K, Lee KH, Lee DH, Bae YH (2006) *Eur J Pharm Sci* 27:115–122
11. Sosnik A, Cohn D (2004) *Biomaterials* 25:2851–2858
12. Anal AK (2007) *Recent Pat Endocr Metab Immune Drug Discov* 1:83–90
13. Mendes PM (2008) *Chem Soc Rev* 37:2512–2529
14. Jones DP, Carlson JL, Samiec PS, Sternberg P Jr, Mody V C Jr, Reed RL, Brown LAS (1998) *Clinica Chimica Acta* 275:175–184
15. Koo AN, Lee HJ, Kim SE, Chang JH, Park C, Kim C, Park JH, Lee SC (2008) *Chem Commun* 44:6570–6572
16. Gong JP, Nitta T, Osada Y (1994) *J Phys Chem* 98:9583–9587
17. Tanaka T, Nishio I, Sun S-T, Ueno-Nishio S (1982) *Science* 218:467–469
18. Roggan A, Friebel M, Dõrschel K, Hahn A, Mũller G (1999) *J Biomed Opt* 4:36–46
19. Ichimura K, Oh S-K, Nakagawa M (2000) *Science* 288:1624–1626
20. Ichimura K, Suzuki Y, Seki T, Hosoki A, Aoki K (1988) *Langmuir* 4:1214–1216
21. Wang S, Song Y, Jiang L (2007) *J Photochem Photobiol C Photochem Rev* 8:18–29 3
22. Yoshida M, Lahann J (2008) *ACS Nano* 2:1101–1107
23. Jiang X, Lavender CA, Woodcock JW, Zhao B (2008) *Macromolecules* 41:2632–2643
24. Li Y, Jia X, Gao M, He H, Kuang G, Wei Y (2009) *J Polym Sci Part A Polym Chem* 48:551–557
25. Czaun M, Hevesi L, Takafuji M, Ihara H (2008) *Chem Commun* 44:2124–2126
26. Szabo´ D, Szeghy G, Zri´nyi M (1998) *Macromolecules* 31:6541–6548
27. Korth BD, Keng P, Shim I, Bowles SE, Tang C, Kowalewski T, Nebesny KW, Pyun J (2006) *J Am Chem Soc* 128:6562–6563
28. Marin A, Muniruzzaman M, Rapoport N (2001) *J Controlled Release* 71:239–249
29. Norris P, Noble M, Francolini I, Vinogradov AM, Stewart PS, Ratner BD, Costerton JW, Stoodley P (2005) *Antimicrob Agents Chemother* 49:4272–4279
30. Rapoport NY, Christensen DA, Fain HD, Barrows L, Gao Z (2004) *Ultrasonics* 42:943–950
31. Dissemond J, Witthoff M, Brauns TC, Haberer D, Goos M (2003) *Hautarzt* 54:959–965
32. Rofstad EK, Mathiesen B, Kindem K, Galappathi K (2006) *Cancer Res* 66:6699–6707
33. Vaupel P, Kallinowski F, Okunieff P (1989) *Cancer Res* 49:6449–6465
34. Gupta P, Virmani K, Garg S (2002) *Drug Discov Today* 7:569–579
35. Park SY, Bae YH (1999) *Macromol Rapid Commun* 20:269–273
36. Lee YM, Shim JK (1997) *Polymer* 38:1227–1232
37. Soppimath KS, Kulkarni AR, Aminabhavi TM (2001) *J Controlled Release* 75:331–345
38. Abdelaal MY, Abdel-Razik EA, Abdel-Bary EM, El-Sherbiny IM (2007) *J Appl Polym Sci* 103:2864–2874
39. Park H-Y, Song I-H, Kim J-H, Kim W-S (1998) *Int J Pharm* 175:231–236
40. Kurisawa M, Yui N (1998) *Macromol Chem Phys* 199:1547–1554
41. Lee JW, Kim SY, Kim SS, Lee YM, Lee KH, Kim SJ (1999) *J Appl Polym Sci* 73:113–120
42. Nakamura K, Murray RJ, Joseph JI, Peppas NA, Morishita M, Lowman AM (2004) *J Controlled Release* 95:589–599
43. Zhang J, Peppas NA (1999) *Macromolecules* 33:102–107



44. Sideratou Z, Tsiourvas D, Paleos CM (2000) *Langmuir* 16:1766–1769
45. Burke SE, Barrett CJ (2003) *Biomacromolecules* 4:1773–1783
46. Toncheva V, Wolfert MA, Dash PR, Oupicky D, Ulbrich K, Seymour LW (1998) *Biochim Biophys Acta* 1380:354–368
47. Corpart JM, Candau F (1993) *Macromolecules* 26:1333–1343
48. Kathmann EEL, White LA, McCormick CL (1997) *Macromolecules* 30:5297–5304
49. Salamone JC, Rodriguez EL, Lin KC, Quach L, Watterson AC, Ahmed I (1985) *Polymer* 26:1234–1238
50. Morrison ME, Dorfman RC, Clendening WD, Kiserow DJ, Rosky PJ, Webber SE (1994) *J Phys Chem* 98:5534–5540
51. Szczubiałka K, Jankowska M, Nowakowska M (2003) *J Mater Sci Mater Med* 14:699–703
52. Leong KW, Brott BC, Langer R (1985) *J Biomed Mater Res* 19:941–955
53. Mathiowitz E, Jacob JS, Jong YS, Carino GP, Chickering DE, Chaturvedi P, Santos CA, Vijayaraghavan K, Montgomery S, Bassett M, Morrell C (1997) *Nature* 386:410–414
54. Cohen S, Yoshioka T, Lucarelli M, Hwang LH, Langer R (1991) *Pharm Res* 8:713–720
55. Shenoy D, Little S, Langer R, Amiji M (2005) *Pharm Res* 22:2107–2114
56. Cerritelli S, Velluto D, Hubbell JA (2007) *Biomacromolecules* 8:1966–1972
57. Oh JK, Siegwart DJ, Lee H-I, Sherwood G, Peteanu L, Hollinger JO, Kataoka K, Matyjaszewski K (2007) *J Am Chem Soc* 129:5939–5945
58. Matsumoto S, Christie RJ, Nishiyama N, Miyata K, Ishii A, Oba M, Koyama H, Yamasaki Y, Kataoka K (2008) *Biomacromolecules* 10:119–127
59. Yoshida R, Yamaguchi T, Kokufuta E (1999) *J Artif Organs* 2:135–140
60. Chaterji S, Kwon IK, Park K (2007) *Prog Polym Sci* 32:1083–1122
61. Chambin O, Dupuis G, Champion D, Voilley A, Pourcelot Y (2006) *Int J Pharm* 321:86–93
62. Sinha VR, Kumria R (2001) *Int J Pharm* 224:19–38
63. Vandamme TF, Lenourry A, Charrueau C, Chaumeil JC (2002) *Carbohydr Polym* 48:219–231
64. Itoh Y, Matsusaki M, Kida T, Akashi M (2006) *Biomacromolecules* 7:2715–2718
65. Akala EO, Kopec'kova' P, Kopec'ek J (1998) *Biomaterials* 19:1037–1047
66. Rao NA (1990) *Trans Am Ophthalmol Soc* 88:787–850
67. Nobuhiko Y, Jun N, Teruo O, Yasuhisa S (1993) *J Controlled Release* 25:133–143
68. Y. Gao, G. P. Zago, Z. Jia, and M. J. Serpe, *ACS Appl. Mater. Interfaces*, 5, 9803 (2013).
69. S. Guo, Y. Gao, M. Wei, Q. M. Zhang, and M. J. Serpe, *J. Mater. Chem. B*, 3, 2516 (2015).
70. Y. Gao, K. Y. Wong, A. Ahiabu, and M. J. Serpe, *J. Mater. Chem. B*, 4, 5144 (2016).
71. Y. Gao, A. Ahiabu, and M. J. Serpe, *ACS Appl. Mater. Interfaces*, 6, 13749 (2014).
72. Y. Gao, W. Xu, and M. J. Serpe, *J. Mater. Chem. C*, 2, 5878 (2014)
73. M. Topp, P. Dijkstra, H. Talsma, and J. Feijen, *Macromolecules*, 30, 8518 (1997).
74. J. Virtanen, S. Holappa, H. Lemmetyinen, and H. Tenhu, *Macromolecules*, 35, 4763 (2002).
75. R. Motokawa, K. Morishita, S. Koizumi, T. Nakahira, and M. Annaka, *Macromolecules*, 38, 5748 (2005).
76. W. Zhang, L. Shi, K. Wu, and Y. An, *Macromolecules*, 38, 5743 (2005).

*A LITERATURE REVIEW ON*

# **SERS BASED OPTICAL NANOSENSORS**

SCOTTISH CHURCH COLLEGE

(UNIVERSITY OF CALCUTTA)

ROLL NO - 223/CEM/191025

REGISTRATION NO – 221-1221-0333-15

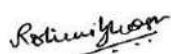
SPECIAL PAPER – SP44

NAME OF CANDIDATE

ROHINI GHOSH

NAME OF SUPERVISOR

Dr. ANIRUDDHA GANGULY



SIGNATURE OF CANDIDATE



SIGNATURE OF SUPERVISOR

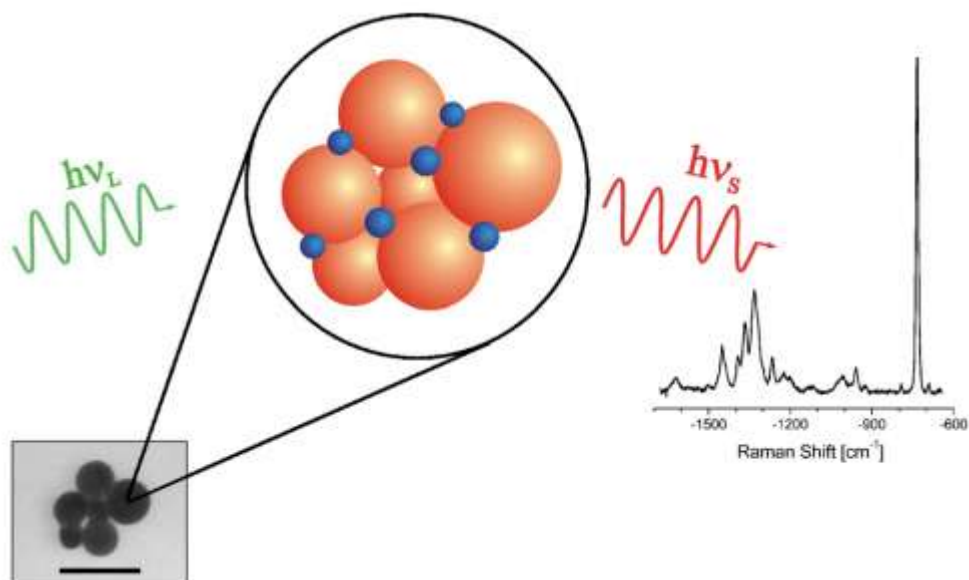
# **SERS BASED OPTICAL NANOSENSORS**

## **INTRODUCTION**

Metallic nanoparticles exhibit remarkable physical and chemical properties that are different from those of the bulk metals. In the context of nanophotonics, a key property of these nanostructures is the so-called localized surface plasmon resonance (LSPR), which is generated by the collective oscillation of conduction electrons upon excitation with the appropriate electromagnetic radiation (a laser beam). As a consequence of this excitation, a high electromagnetic field is generated at the surface of the nanoparticle which can be applied for the enhancement of spontaneous Raman scattering of the molecular species placed in close vicinity to these surfaces. This effect gives rise to a new powerful analytical tool, known as surface-enhanced Raman scattering (SERS) spectroscopy. The concept of SERS sensors can be extended to two-photon excitation using SEHRS. Particularly for applications in biological objects, sensors based on two-photon excitation benefit from excitation at longer wavelengths in the near-IR. Moreover, due to selection rules different from those of SERS, SEHRS spectra can provide additional molecular structural information on native cellular molecules.

## SURFACE ENHANCED RAMAN SCATTERING (SERS)

The surface enhanced Raman scattering (SERS) spectroscopy is based on the enhancement of nanostructured metallic surface. The SERS effect was discovered in 1974 by Fleischman, Hendra and McQuillan. The group reported an abnormally large Raman signal of pyridine measured on top of a roughened silver electrode. The enhancement was initially attributed to a punctual high concentration of adsorbed pyridine due to the extra surface area generated by the redox cycles in the electrode.



SCHEMATIC OF SERS PHENOMENON. MOLECULES (BLUE DOTS) ARE ATTACHED TO Ag OR Au NPs (ORANGE BALLS). FOR COMPARISON, THE TRANSMISSION ELECTRON

MICROGRAPH SHOWS SERS ACTIVE Au NANOAGGREGATE. THE SERS SPECTRUM SHOWN HERE WAS COLLECTED FROM  $10^{-9}$  M ADENINE IN A SOLUTION OF Ag NANOAGGREGATES.

In 1977, two independent reports, by Jean Maire and Van Duyne and Albrecht and Creighton, demonstrated that this intensity could not be accounted for by an increased surface. In fact, both papers reported on a new physical phenomenon, giving rise to the idea of the **SERS cross section**. They also noted that the scattering intensity from the adsorbed molecules was  $10^5 - 10^6$  times stronger than that of conventional Raman signal making SERS a powerful tool for sensing molecules in a trace amount, previously undetectable by spontaneous Raman scattering spectroscopy. Nowadays, **enhancement factors (EF)** have been reported up to  $10^{14} - 10^{15}$ -fold, which allows SERS to be sensitive enough to detect single molecules. The EFs depend on the structure of the metal and on the nature of the molecule. The most commonly used metallic surfaces for SERS are based on **silver and gold nanostructures**, which bring together chemical stability with the appropriate optical properties.

$$P_{SERS} \propto N \cdot I_L \cdot |A(\nu_L)|^2 \cdot |A(\nu_S)|^2 \cdot \sigma_{ads}^R$$

The equation shown above estimates the scattering signal for SERS. The total Stokes SERS signal  $P_{SERS}(\nu_S)$  is proportional to the Raman cross section  $\sigma_{ads}^{RS}$ , the excitation laser intensity  $I(\nu_L)$ , and the number of molecules  $N$  involved in the SERS process.  $\sigma_{ads}^{RS}$  describes the Raman cross section of the molecule in contact with the metal compared to the cross section  $\sigma_{free}^{RS}$  of a free molecule in a normal Raman experiment; thus, it includes the chemical or electronic enhancement.  $A(\nu_L)$  and  $A(\nu_S)$  express the local enhancement factors for the laser and for the Raman scattered field, respectively; accounting for the electromagnetic enhancement.

SERS has been extended to other metals like copper, platinum, lithium, sodium, potassium, indium, aluminium and rhodium. The signal enhancement provided by the metallic nanostructures resolves the problem of the intrinsic inefficiency of the Raman process, combining the ultrasensitive potential of this technique with the rich chemical and structural information characteristic of the vibrational spectroscopy. Further, the fact that SERS can be

carried out under environmental or biological conditions make it an ideal detection platform for (bio) chemical sensing, diagnostics, (bio)analytical chemistry, or environmental monitoring.

An additional benefit of SERS is that fluorescence is quenched for molecules close to the surface, due to the additional relaxation pathway available through transfer of energy to the metal surface, which facilitates signal detection.

The SERS effect has been deeply studied over the last 30 years. In general, two broad enhancement mechanisms have been proposed, the electromagnetic mechanism (EM) and the chemical (CT) mechanism. Nowadays, it is recognized that although EM is essential for SERS, CT plays a key role in the really ultrasensitive application of the technique.[1-7]

## ELECTROMAGNETIC ENHANCEMENT:

The SERS enhancement is due to an EM that is a direct consequence of the presence of the metallic nanostructures (also known as optical enhancers). In fact, the EM can be interpreted as, essentially, a redistribution of the electromagnetic field around the optical enhancer. Electromagnetic field enhancement exists as a result of resonances of the optical fields with surface plasmons. This leads to a redistribution of field intensities in the vicinity of nanoparticles resulting in areas of enhanced excitation intensities for the Raman process.

**Plasmons** are collective excitations of the surface conduction electrons that propagate along the metal surface. At certain frequencies of incident light, these electrons become highly polarizable, giving rise to large electromagnetic fields.

Additionally, based on the same resonance mechanism, nanostructures can be considered as nano-antennas for transmitting and enhancing Raman scattered light. In general, the shift in frequencies between excitation and scattered light is small as compared with the width of the plasmon resonance. Therefore, laser and Raman scattered field gain are approximately the same because of field enhancement. With  $A(\nu_L) \sim A(\nu_S) \sim A(\nu)$ , the electromagnetic SERS enhancement scales with the fourth power of the field enhancement factor  $A(\nu)$ . The electromagnetic enhancement is highly confined within a few nano-meters in the vicinity of the metal nanoparticles. Electromagnetic field enhancement depends on the resonance between plasmons and excitation and scattered fields, where plasmon frequencies are determined by the material and the morphology of the metal nanostructures. [8-11]

## CHEMICAL ENHANCEMENT:

The other mechanism postulated to occur in SERS is chemical enhancement. This effect requires the vibrational probe to be chemically bound to the SERS substrate.

Chemical effects have been proposed to explain changes in the relative intensities (and frequencies) in the vibrational modes of a molecule as compared with the normal Raman spectra, and to account for perceived discrepancies between the maximum EFs found experimentally and the maximum values from the electromagnetic calculations. The proposed chemical mechanism is associated with two processes:

1. Charge-transfer states involving transitions from the Fermi level of the metal to an unoccupied orbital of the molecule (or vice versa); and/or
2. Formation of a surface complex involving the metal and the analyte molecule, leading to a change in the properties of the molecule (such as the possibility of resonance RS).

The surface complexation of the analyte to the metallic nanostructure makes possible the transfer of charge. Basically, the enhancement proceeds via new electronic states, which arise from the formation of the molecule–metal complex. These new states are believed to be resonant intermediates in the RS. Thus, as opposed to the radiation being adsorbed or scattered through the plasmons on the surface (electromagnetic enhancement), the radiation is supposed to be absorbed into the metal. A hole is transferred into the adsorbate–metal atom cluster, then RS occurs and excitation is transferred back into the metal and re-radiation occurs from the metal surface.

Electromagnetic and chemical SERS enhancement can result in total enhancement factors on the order of  $10^{14}$ . Still, the relative contributions of electromagnetic and chemical effects to the total SERS enhancement and possible mechanism(s) behind a chemical enhancement remain under discussion. Nevertheless, many experimental observations available so far and theoretical results provide evidence that electromagnetic enhancement based on plasmon resonances gives mostly important contribution to high SERS enhancement.

Local optical fields also provide the key effect for the observation of surface-enhanced hyper Raman scattering (SEHRS). The enhancement of the 2-photon phenomenon of HRS is analogous to the enhancement of 1-photon excited Raman signals in SERS. Interestingly, HRS benefits even to a greater extent from the high local optical fields than normal Raman scattering does in the case of SERS because of its nonlinear dependence on the enhanced excitation field. The strong field enhancement for the two-photon process can compensate for the extremely small cross section of HRS and allows the measurement of SEHRS spectra at unexpectedly high signal level for a 2-photon process.[12-14]

## **SERS-ACTIVE SUBSTRATES:**

In order to maximize the SERS effect, the optical enhancers should accomplish several requirements including:

Large EFs, good reproducibility from one sample to another, stable SERS signal with time, simple preparation process, and easiness to be applied to many analytes in parallel. Moreover, these platforms should be inert, mechanically stable, and not lead to additional spurious peaks in the SERS spectrum.

However, SERS cannot only be achieved and maximized through a detailed design of the optical substrates, but also by improving the adsorption of the molecules of interest. For these reasons, the fabrication of active optical substrates with optimized properties has been a field of research with a great development during the last decades.

Nanotechnology shows potential applicability for the fabrication of new and specific SERS-active platforms by producing, assembling and ordering nanostructures. In fact, nanofabrication has solved two problems:

1. The engineering of well-defined structures which can be optimally tuned to maximize the EF; and
2. The fabrication of reproducible SERS platforms, which is a key request for SERS to be implemented as a quantitative analytical technique.

Normally, SERS has been obtained on electrodes, solid metal thin films and colloidal dispersions. Nowadays, **metallic nanoparticles** are considered one of the main SERS platforms. Since colloids are easy to produce in the laboratory and tend to generate large EFs, most researchers are still involved in the development of **colloid-based SERS**. Metallic nanoparticles are also of historical significance related to the development of SERS, as the first single-molecule SERS (SM-SERS) detections were reported using colloid particles.

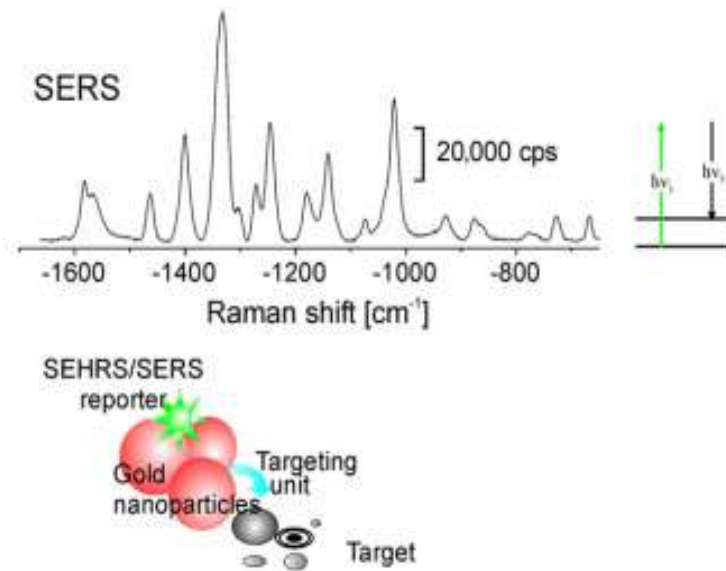
Besides, utilization of nanoparticles allows direct SERS analysis within the analyte natural solution medium. The presence of the solvent and the Brownian motion of the analyte–particle complexes minimize damage to the sample, even when using more energetic laser lines and higher power at the sample for excitation. Also, colloidal metals can also be used for the preparation of thin films, which add portability and versatility to on-field SERS analysis, over the regular physical fabrication techniques such as sputtering, physical vapour deposition or electron beam lithography, which are difficult to find in conventional laboratories.[15]

## FABRICATION OF SERS NANOSENSORS :

The key component for creating hybrid SERS nanosensors for biological applications is a nanostructure that provides a high level of electromagnetic field enhancement. This is the



prerequisite for an intense and stable spectroscopic signature of the reporter but also for an efficient and sensitive Raman probe of the cellular environment. Reporter molecules permit detection and imaging of the sensor based on their specific SERS spectrum. Potential reporters should be biocompatible molecules showing a strong and specific SERS spectrum. Moreover, the nanostructures should be small enough to cross cell membranes, and they should allow probing of cells without inducing any perturbation or toxicity. Measurements can be performed on the second and millisecond time scales.



Schematic of a multifunctional surface-enhanced Raman scattering (SERS) nano sensor built from silver nanoaggregates with Rose bengal as the reporter molecule attached along with its one-photon-excited spectral signature. One photon-excited SERS spectra were collected using 785-nm continuous-wave light.

Reporter molecules permit detection and imaging of the sensor based on their specific SERS spectrum. Potential reporters should be biocompatible molecules showing a strong and specific SERS spectrum. In this way, SERS sensors can label and highlight cellular structures. Also, gold or silver nanoparticles with reporter molecules attached that show a known and calibrated pH-dependent SERS signature can act also as an intracellular pH meter. In general, all three purposes can be combined, and the SERS signature of a reporter on a gold nanoparticle can be obtained along with the enhanced Raman signature of its cellular environment. As a further advantage, the SERS sensor can be functionalized using a specific linker (targeting unit) so as to target specific cellular compartments or structures. This functionalization of gold nanoparticles for targeted probing can be undertaken based on established methods used for electron microscopy and other labelling methods.

So far, Ag and Au have been the metals that provide the highest enhancement observed in SERS experiments with near-infrared excitation, yielding enhancement factors up to 14 orders of magnitude.[16-24]

## APPLICATIONS OF SERS NANOSENSORS

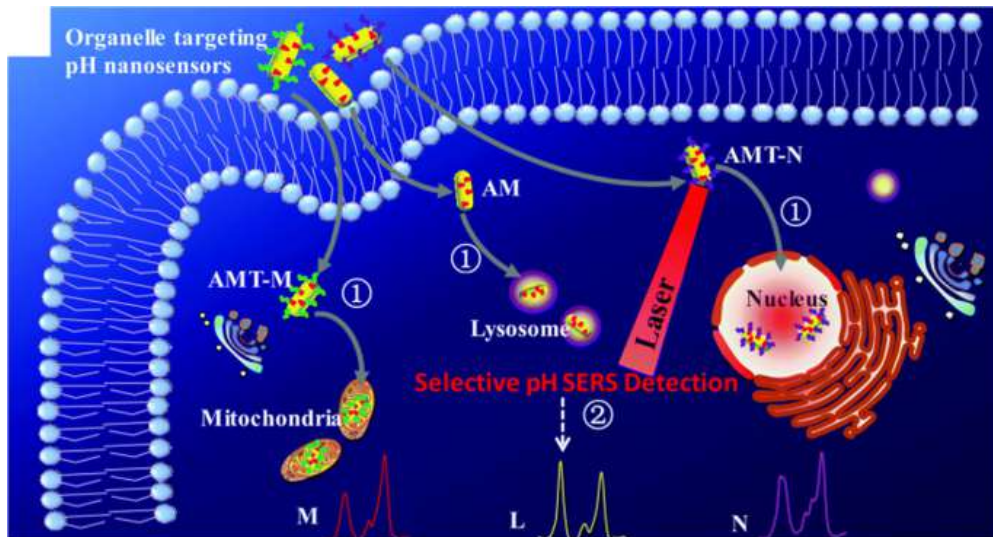
### Cellular microsensing

Smartly designed SERS tags can access information such as on the complex processes taking place in living cells that no other technique can, in situ monitoring of pH, gaseous content or ROS during cell proliferation.

The intra- and extracellular pH ( $pH_i$  and  $pH_e$ ) values of living cells play a major role in the physiology and pathology of diseases. The sensitive and reliable determination of these values could be important for the early diagnosis of many medical conditions.

4-Mercaptopyridine (4MPy) and 4-mercaptobenzoic acid (4MBA) are the two pH sensing molecules mostly used for SERS-based detection. They offer the possibility to monitor the pH variations over a large window (pH 4 to 9) and they also show good chemical affinity towards the surface of AuNPs. Generally, NP uptake by living cells is governed by endocytosis and it results in heterogeneous distribution. In order to achieve a targeted uptake, the NPs can be modified with cell-penetrating peptides. Shen et al. prepared gold nanorods functionalized with 4MPy and anchored a nucleus- or a mitochondrion-targeting peptide on their surface. The localization of the SERS tags in the cells was confirmed by super-high-resolution fluorescence imaging and biotransmission electron microscopy. As proof of concept, a tumour and a normal cell line have been investigated. The NPs showed good biocompatibility and the pH value, determined applying the ratiometric approach, of tumour cells showed an acidic character as compared with normal cells. [25]

---



Intracellular pH sensing with targeted AuNP distribution due to a cell-penetrating peptide-mediated method.

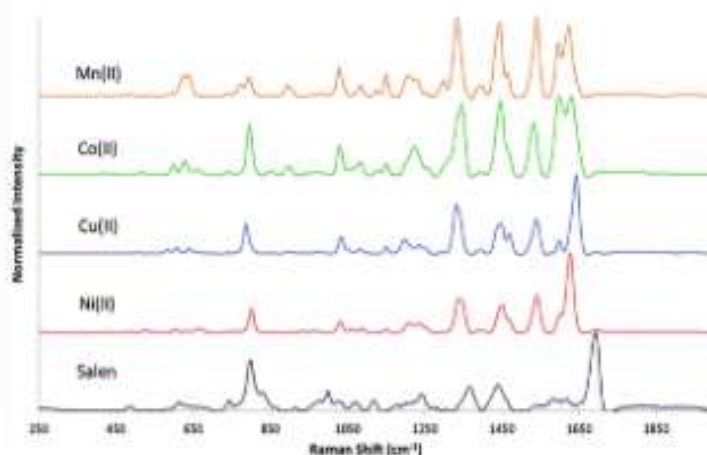
The presence of small molecules such as reactive oxygen species (ROS) in living cells can give important information regarding the cellular microenvironment. ROS are formed as a natural by-product of the normal metabolism of oxygen and have important roles in cell signalling and homeostasis. These by-products are not Raman active in order to be directly detected by SERS, molecules that show chemical reactivity with ROS have to be assembled on the surface of the plasmonic NPs. For example,  $H_2O_2$  was detected using 4-mercaptophenylboronic ester (4-MPBE), HClO with 2-mercapto-4-methoxy-phenol (MMP).

## Environmental sensing -

Environmental sensing with molecular SERS sensors, is more application oriented. The aim is to create accessible commercial analytical platforms that cover existing niches in environmental and food monitoring. Due to their toxicity, the detection of heavy metal ions is of special interest in environmental and food analyses.

For multi metal detection, Docherty et al. used a [O,N,N,O] tetradentate bis-Schiff base ligand that was synthesized by reacting salicylaldehyde with 1,2-diaminoethane. With this

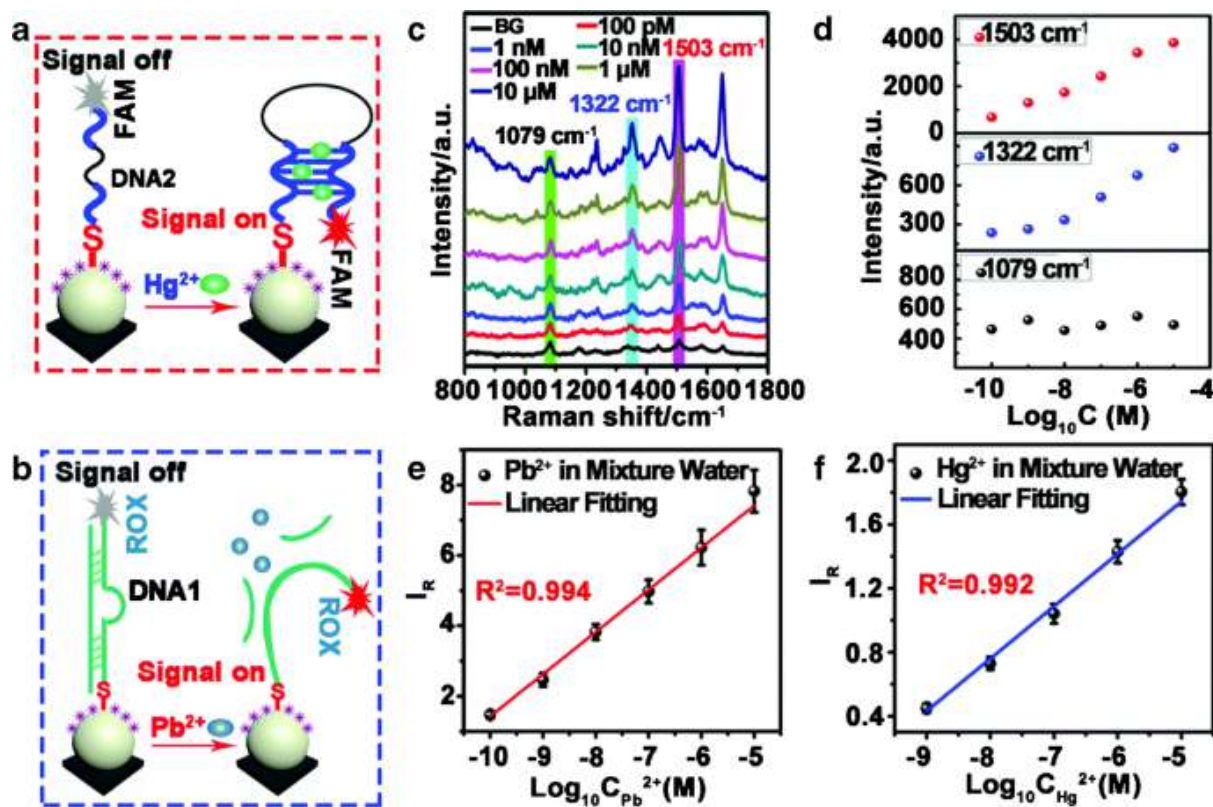
ligand, named salen, the researchers were able to detect  $\text{Ni}^{2+}$ ,  $\text{Co}^{2+}$ ,  $\text{Cu}^{2+}$  and  $\text{Mn}^{2+}$ . Each metal-salen complex results in significantly different SERS spectra. Thus, the unique spectral shape could be used to identify which metal ion was present. Remarkable changes between each of the complexes were recognized for the two peaks around  $1600\text{ cm}^{-1}$ . These two bands are assigned to the C=N stretching of Schiff bases. For  $\text{Cu}^{2+}$ , a strong band is observed at  $1641\text{ cm}^{-1}$  with a weaker band at  $1597\text{ cm}^{-1}$ . However, for  $\text{Co}^{2+}$  ions, this band shifts to  $1628\text{ cm}^{-1}$  and  $1597\text{ cm}^{-1}$ . For  $\text{Ni}^{2+}$  and  $\text{Mn}^{2+}$ , these bands again significantly shifted to  $1628\text{ cm}^{-1}$ , with a shoulder at  $1600\text{ cm}^{-1}$  for nickel ions, and to  $1621\text{ cm}^{-1}$  and  $1597\text{ cm}^{-1}$  for manganese ions, respectively. These bands were assigned to the C=N stretch of salen. Due to the changes induced by the binding of different metal ions to the nitrogen atoms of the Schiff base, the detected position of the bands around  $1600\text{ cm}^{-1}$  was altered. Thus, these peaks were used as marker bands for the identification and quantitation.[26]



Comparison of the baseline-corrected SERS spectra of the salen complexes studied, using  $2.5\text{-}\mu\text{M}$  solutions of each metal ion. Salen, black; Ni(II), red; Cu(II), blue; Co(II), green; Mn(II), orange ( $\lambda_{\text{exc}} = 532\text{ nm}$ ; acc. time = 10 s).

For the simultaneous detection of lead ( $\text{Pb}^{2+}$ ) and mercury ( $\text{Hg}^{2+}$ ), Shi et al. developed silicon SERS chips including an internal standard sensing strategy. For the detection in industrial wastewater, a silicon wafer was coated with Ag NPs as an internal standard and the NPs were modified with 4-aminothiophenol (4-ATP).  $\text{Pb}^{2+}/\text{Hg}^{2+}$ -responsive DNA strands were conjugated to the chip. The characteristic SERS band was found at  $1322\text{ cm}^{-1}$  for FAM and at  $1503\text{ cm}^{-1}$  for ROX, the marker band of 4-ATP ( $1079\text{ cm}^{-1}$ ) was used for normalization. Thus, the LOD was found to be  $99\text{ pM}$  ( $19.8\text{ ppt}$ ) for

Pb<sup>2+</sup> and 0.84 nM (168 ppt) for Hg<sup>2+</sup>. The specificity of this SERS application was investigated by mixing twelve metal ions (Zn<sup>2+</sup>, Ni<sup>2+</sup>, Na<sup>+</sup>, Mn<sup>2+</sup>, Mg<sup>2+</sup>, Fe<sup>2+</sup>, Cu<sup>2+</sup>, Co<sup>2+</sup>, Ca<sup>2+</sup>, Ba<sup>2+</sup>, Pb<sup>2+</sup>, Hg<sup>2+</sup>) and the mixed samples containing Pb<sup>2+</sup> and Hg<sup>2+</sup> at a concentration of 100 nM. Out of these twelve tested metals, only Pb<sup>2+</sup> and Hg<sup>2+</sup> exhibit strong SERS responses at 1503 cm<sup>-1</sup> or 1322 cm<sup>-1</sup>, respectively. To demonstrate the application, the developed chip was combined with a portable Raman microscope and employed for the simultaneous quantitative detection of Hg<sup>2+</sup> and Pb<sup>2+</sup> in industrial wastewater. Thereby, the achieved relative standard deviation values were less than 15%. [27]



a - Schematic of IS-Si@Ag NPs for Hg<sup>2+</sup> and

b - for Pb<sup>2+</sup> detection.

c - SERS spectra of the functionalized silicon SERS chip in the presence of Pb<sup>2+</sup> and Hg<sup>2+</sup> with the same concentrations ranging from 100 pM to 10 μM. Background (BG) stands for the distilled water.

d - Corresponding plots of the SERS intensities of the 4-ATP (1079 cm<sup>-1</sup>), FAM (1322 cm<sup>-1</sup>) and ROX (1503 cm<sup>-1</sup>).

**e** - The linear fitting of the SERS relative intensities ( $IR = I_{1503}/I_{1079}$ ) versus the logarithmic  $Pb^{2+}$  concentration ( $1.0 \times 10^{-10}$  to  $1.0 \times 10^{-5}$  M).

**f** - The linear fitting of the SERS relative intensities ( $IR = I_{1322}/I_{1079}$ ) versus the logarithmic  $Hg^{2+}$  concentration ( $1.0 \times 10^{-9}$  to  $1.0 \times 10^{-5}$  M).

Excitation wavelength, 633 nm; laser power, 0.2 mW.

## RECENT DEVELOPMENTS

Uranium is one of the main natural nuclides for producing nuclear energy in a variety of areas such as nuclear power and weapons. It may enter into the environment during the process of mining, producing, utilizing and after-dealing, thus proposing a threat to human health and environment because of its chemical and radiological toxicity. Uranium possesses a number of forms under different conditions and the most stable one in aqueous solution is uranyl  $UO_2^{2+}$ , which is soluble in water and is able to migrate in the environment. As a result, it is of great strategic importance to monitor the uranyl ion in the environment.

Uranyl can be detected by using SERS substrates coated with functionalized gold nanoparticles. GNPs are functionalized with a complexing agent such as **aminomethyl phosphonic acid (APA)**. On a Raman spectrum, formation of stable uranyl-APA complex is correlated to  $UO_2^{2+}$  symmetric stretching vibrational changes at frequencies ranging between 800 and 900  $cm^{-1}$ . APA modification of GNPs offer enhanced Raman signal of uranyl at a frequency of 828  $cm^{-1}$ . The quantitative performance of the APA modified GNP SERS sensor suggests that it can detect the presence of uranyl at concentrations as low as  $8E-05$  M. Furthermore, the APA modified GNPs are able to produce a distinct SERS signal of uranyl even in the presence of interfering compounds such as humic acids, total organic carbon (TOC) and nitrates.

SERS sensors utilising Ag as substrate material has also been employed for uranyl determination. The presence of uranyl on the surface of thermally vapor deposited silver nanoparticle caused appearance of stretching frequency at 700  $cm^{-1}$  and disappearance of 854  $cm^{-1}$  band because of interaction between them. Based on which, detection of uranyl

can be achieved with a detect limit of  $40 \text{ nmol L}^{-1}$ . Silver nanoparticle modified reduced graphene oxide (rGO) nanosheets was judiciously synthesized employing dimethylformamide as reducing agent in the presence of polyvinylpyrrolidone. The composite material was applied for selective detection of uranyl ion. As low as  $1 \text{ nmol L}^{-1}$  uranyl could be detected when  $\text{Al}_2\text{O}_3$  layers wrapped silver nanorods ( $\text{AgNR@Al}_2\text{O}_3$ ) was used as sensor, detection being stable and could be performed in acidic or basic solutions. A rapid detection of uranyl ions was also achieved by self-assembly of silver nanoparticles on modified silicon wafer.[28-35]

## LIMITATIONS OF SERS BASED NANOSENSORS

Key limitations of the SERS technique are -

To obtain a large effect, SERS can be used only for adsorbates on a limited number of metal surfaces in correctly prepared roughened form. The method requires intimate contact between the enhancing surface and the analyte.

Limited re-usability of the substrates and problems with homogeneity and reproducibility of the SERS signal within a substrate.

Contaminants that give strong surface enhancement can be detected in much lower concentration than the adsorbate studied, leading to problems in identification.

Finally, there is a tendency in SERS for photodecomposition to occur on the surface.

Despite its limitations, the sensitivity of SERS, as well as its exceptional spectral selectivity, has made SERS an attractive technique to detect a wide range of chemical species. SERS is unique in providing a fascinating insight into the adsorption mechanisms of molecules on suitable surfaces *in situ*.

## CONCLUSION

After its discovery, SERS was primarily used to probe electrochemical reactions and adsorption of molecular species on metal surfaces. Because of its inherent molecular fingerprint specificity and potential for single-molecule detection, SERS became an attractive tool for sensing molecules in trace amounts in the field of chemical analysis. Continuing advancements in nanostructure fabrication have dramatically advanced SERS capabilities as a powerful chemical sensing platform.

In parallel, advancements in the field of photonics has led to the availability of low-power, compact, robust, inexpensive, field-deployable Raman systems. SERS based nanosensors and labels offer several advantages over other optical sensors with respect to versatility, sensitivity, selectivity, and biocompatibility. Future challenges include the development of multifunctional SERS sensors with optimized plasmonic nanostructures as basic building blocks. Plasmonic structures, as key components of SERS sensors, can offer high local optical fields for sensitive diagnostic probing with SERS, with much lower acquisition times. This later parameter is of paramount importance due to the sample volumes commonly screened in actual medical practice. Utilizing the progress that has been made in the design of SERS-encoded particles, the application of SERS nanosensors is about to revolutionize bioanalysis.

SERS has been used to detect heavy metals, toxic anions, explosives, pesticides, toxic industrial chemicals (TICs), and drugs. Consequently, SERS has great applicability in the areas of homeland security, environmental monitoring, process control, and criminal forensics, and has the potential to become the next generation sensor technology.

## ACKNOWLEDGEMENT

I take this opportunity to express my sincere gratitude to the entire Physical Chemistry faculty of Scottish Church College, Kolkata, as without their valuable guidance and support, it would not have been possible to successfully complete this review paper.

## REFERENCES

1. Jeanmaire, D. L. and Van Duyne, R. P. (1977). Surface Raman spectroelectrochemistry Part I. Heterocyclic, aromatic, and aliphatic amines adsorbed on the anodized silver electrode. J. Electroanal. Chem.,
2. Alvarez-Puebla, R. A., Liz-Marzan, L. M. and Garcia De Abajo, F. J. (2010). Light concentration at the nanometer scale. J. Phys. Chem. Lett., 1, 2428–2434.
3. Aroca, R. (2006). Surface-Enhancement Vibrational Spectroscopy, New York, John Wiley and Sons, Ltd.



4. Banholzer, M. J., Millstone, J. E., Qin, L. and Mirkin, C. A. (2008). Rationally designed nanostructures for surface-enhanced Raman spectroscopy. Chem. Soc. Rev., 37 ,885–897.
5. Fleischmann, M., Hendra, P. J. and Mcquillan, A. J. (1974). Raman spectra of pyridine adsorbed at a silver electrode. Chem. Phys. Lett., 26 , 163–166.
6. Kneipp, K., Kneipp, H. and Moskovits, M. (2006). Surface-Enhanced Raman Scattering, Berlin Heidelberg, Springer-Verlag
7. Otto, A. (2002). What is observed in single molecule Sers, and why? J. Raman Spectra., 33 , 593–598.
8. Le Ru, E. C. and Etchegoin, P. G. (2006). Rigorous justification of the  $|E|^4$  enhancement factor in Surface Enhanced Raman scattering. Chem. Phys. Lett., 42363–66.
9. Mayer, K. M. and Hafner, J. H. (2011). Localized surface plasmon Resonance sensor, Chem. Rev., 111 , 3828–3857
10. Myroshnychenko, V., Rodriguez-Fernandez, J., Pastoriza-Santos, I., Funston, A. M., Novo, C., Liz-Marzan, L. M. and Garcia De Abajo, F. J. (2008). Modelling the optical response of gold nanoparticles
11. Xu, Y.-L. (1995). Electromagnetic scattering by an aggregate of spheres. Appl. Opt.,34 , 4573–4588.
12. Smith, E. and Dent, G. (2005). Modern Raman Spectroscopy – A Practical Approach ,Chichester: John Wiley and Sons Ltd.
13. Moskovits, M. (2005). Surface-enhanced Raman spectroscopy: a brief retrospective.J. Raman Spectrosc., 36 , 485–496.
14. Natan, M. J. (2006). Concluding remarks. surface enhanced Raman scattering.Faraday Discuss, 132 , 321–328.
15. Abalde-Cela, S., Ho, S., Rodriguez-Gonzalez, B., Correa-Duarte, M. A., Alvarez-Puebla, R. A., Liz-Marzan, L. M. and Kotov, N. A. (2009). Loading of exponentially grown LBL lms with silver nanoparticles and their application to generalized SERS detection. Angew. Chem.Int. Ed., 48 , 5326–5329
16. Lombardi JR, Birke RL, Tianhong L, Jia X. Charge-transfer theory of surface enhanced Raman spectroscopy: Herzberg-Teller contributions. J Chem Phys 1986;84:4174-80.

17. Kambhampati P, Child CM, Foster MC, Campion A. On the chemical mechanism of surface enhanced Raman scattering: experiment and theory. J Chem Phys 1998;108:5013-26.
18. Brus L. Noble metal nanocrystals: plasmon electron transfer photochemistry and single-molecule Raman spectroscopy. Accounts Chem Res 2008;41:1742-9.
19. Persson BNJ, Zhao K, Zhang ZY. Chemical contribution to surface-enhanced Raman scattering. Phys Rev Lett 2006;96:207401.
20. Kinnan MK, Chumanov G. Surface enhanced Raman scattering from silver nanoparticle arrays on silver mirror films: plasmon-induced electronic coupling as the enhancement mechanism. J Phys Chem C X-S,
21. Talley CE, Jusinski L, Hollars CW, Lane SM, Huser T. Intracellular pH sensors based on surface-enhanced Raman scattering. Anal Chem 2004; 76:7064-8
22. Jensen RA, Sherin J, Emory SR. Single nanoparticle based optical pH probe. Appl Spectrosc 2007;61:832-8.
23. Wu X, Liu H, Liu J, Haley KN, Treadway JA, Larson JP, et al. Biological pH sensing based on surface enhanced Raman scattering through a 2-aminothiophenol-silver probe. Biosen Bioelectron 2008;23: 886-91.
24. Tkachenko AG, Xie H, Liu YL, Coleman D, Ryan J, Glomm WR, et al. Cellular trajectories of peptide-modified gold particle complexes:
25. Shen YT, Liang LJ, Zhang SQ, Huang DS, Zhang J, Xu SP, et al. Organelle-targeting surface-enhanced Raman scattering (SERS) nanosensors for subcellular pH sensing. Nanoscale. 2018;10(4):1622–30. <https://doi.org/10.1039/c7nr08636a>.
26. Docherty J, Mabbott S, Smith E, Faulds K, Davidson C, Reglinski J, et al. Detection of potentially toxic metals by SERS using salen complexes. Analyst. 2016;141(20):5857–63.
27. Shi Y, Chen N, Su Y, Wang H, He Y. Silicon nanohybrid-based SERS chips armed with an internal standard for broad-range, sensitive and reproducible simultaneous quantification of lead (II) and mercury (II) in real systems. Nanoscale. 2018;10(8):4010–8.

28. C. Ruan, W. Luo, W. Wang, B. Gu, Surface-enhanced Raman spectroscopy for uranium detection and analysis in environmental samples, Anal. Chim. Acta 605 (2007) 80–86.
29. Z. Jiang, D. Yao, G. Wen, T. Li, B. Chen, A. Liang, A label-free nanogold DNAzyme-cleaved surface-enhanced resonance Raman scattering method for trace  $\text{UO}_2^{2+}$  using rhodamine 6G as probe, Plasmonics 8 (2013) 803–810.
30. R. Gwak, H. Kim, S.M. Yoo, S.Y. Lee, G.J. Lee, M.K. Lee, C.K. Rhee, T. Kang, B. Kim, Precisely determining ultralow level  $\text{UO}_2^{2+}$  in natural water with plasmonic nanowire interstice sensor, Sci. Rep. 6 (2016).
31. D. Bhandari, S.M. Wells, S.T. Retterer, M.J. Sepaniak, Characterization and detection of uranyl ion sorption on silver surfaces using surface enhanced Raman spectroscopy, Anal. Chem. 81 (2009) 8061–8067.
32. S. Dutta, C. Ray, S. Sarkar, M. Pradhan, Y. Negishi, T. Pal, Silver nanoparticle decorated reduced graphene oxide (rGO) nanosheet: a platform for SERS based low level detection of uranyl ion, ACS Appl. Mater. Interfaces 5 (2013) 8724–8732.
33. S. Wang, J. Jiang, H. Wu, J. Jia, L. Shao, H. Tang, Y. Ren, M. Chu, X. Wang, Self-assembly of silver nanoparticles as high active surface-enhanced Raman scattering substrate for rapid and trace analysis of uranyl(VI) ions, Spectrochim. Acta Part A, Mol. Biomol. Spectrosc. 180 (2017) 23–28.
34. J. Jiang, L. Ma, J. Chen, P. Zhang, H. Wu, Z. Zhang, S. Wang, W. Yun, Y. Li, J. Jia, J. Liao, SERS detection and characterization of uranyl ion sorption on silver nanorods wrapped with  $\text{Al}_2\text{O}_3$  layers, Microchim. Acta

**A REVIEW ON**  
**UTILIZATION OF WASTE CO<sub>2</sub> AS A BUILDING**  
**BLOCK FROM AN INDUSTRIAL PERSPECTIVE**



**Scottish Church College**

**Roll No.** - 223/CEM/191032  
**Registration No.** - 114-1221-0387-16  
**Special Paper** - CHEM-SO44  
**Name of the candidate** - Srabani Dutta  
**Name of the examiner** - Dr. Sebanti Basu

*Srabani Dutta.*

.....  
**Signature of the candidate**

.....  
**Signature of the examiner**

## ➤ **Contents**

- ❖ **Introduction**
- ❖ **General consideration**
- ❖ **Formic Acid and Carboxylation Reactions**
- ❖ **Carboxylation of olefins**
- ❖ **Carboxylation of aromatics**
- ❖ **Carboxylation of alkynes**
- ❖ **Lactones from dienes**
- ❖ **Organic carbonates**
- ❖ **Polycarbonates and Polyetheral carbonates**
- ❖ **Methylation reactions**
- ❖ **Conclusion**
- ❖ **Acknowledgement**
- ❖ **Reference**

## ❖ **Introduction**

The use of carbon dioxide (CO<sub>2</sub>) as a building block for the production of chemicals is a topic of high interest and importance nowadays. From an industrial perspective, CO<sub>2</sub> on the one hand is waste that is to be minimized, especially in the context of the global warming, but on the other hand is also a cheap and abundant C1 -building block. In this context, utilizing CO<sub>2</sub> is not a new topic from an industrial perspective, but has been gaining more and more attraction over the last years due to the discussions about a raw material change away from fossil carbon sources and global warming. This review reflects potential industrially relevant approaches for the use of CO<sub>2</sub> as an alternative building block in the synthesis of organic compounds which are produced on a significant industrial scale or for new CO<sub>2</sub>-based compounds, having the potential of scaling up. This review will not focus on the production of fuels like methanol based on CO<sub>2</sub>, energy as well as hydrogen storage utilizing CO<sub>2</sub>. For example for the synthesis of methanol, CO<sub>2</sub> is nowadays used in significant amounts as a co-feed in the syngas-based route. Also for methodologies based only on CO<sub>2</sub> and H<sub>2</sub>, the technology using heterogeneous catalysts is relatively mature and currently being operated on a pilot scale. The utilization of carbon dioxide (CO<sub>2</sub>) as a sustainable and renewable one-carbon (C1) building block in organic synthesis has attracted great attention since it may provide access to profitable chemicals from an abundant, non-toxic, non-flammable and inexpensive resource. Among these transformations, synthesis of biologically and synthetically important six-membered cyclic carbamates employing CO<sub>2</sub> as building block represents one of the hottest and attractive research topics in the field.

## ❖ General Consideration

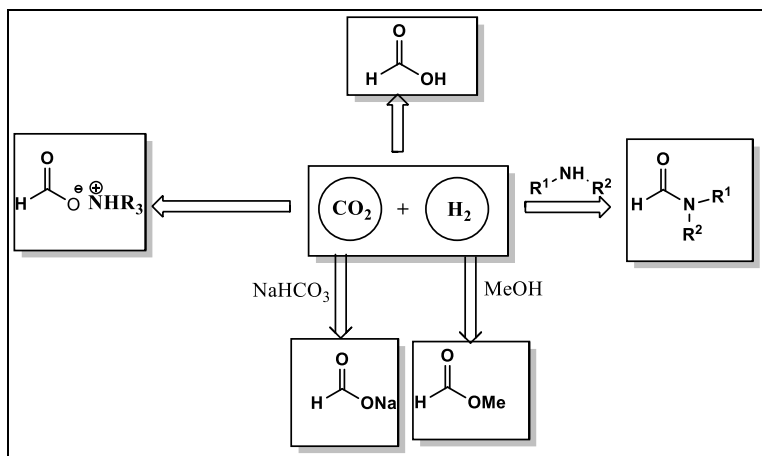
CO<sub>2</sub>, as the final product from the oxidation of organic molecules, is a very stable energetic molecule ( $\Delta H_{0\sim} -400 \text{ KJ mole}^{-1}$ ). It does not matter which organic product one wants to prepare using CO<sub>2</sub> as the building block, the reaction needs a driving force, either from a higher energetic reaction partner (e.g., H<sub>2</sub>, NH<sub>3</sub>, epoxides, bases, metals, organometallics) or by energy input to the process (heat, light, electricity). Nevertheless, for a series of compounds it is an ideal building block and has been applied since decades for the synthesis of urea and inorganic as well as organic carbonates on a large industrial scale. Therefore, there is potential to extend the use of CO<sub>2</sub> as a building block for industrial organic synthesis in near future within certain boundaries.

For synthetic use, the CO<sub>2</sub> must be relatively pure and available on chemical production sites. In certain processes, pure CO<sub>2</sub> is isolated as a by-product, for example, from ammonia plants, steam reforming units, or ethylene oxide plants. Despite the current use for the above-mentioned products, these processes are very large and much more pure CO<sub>2</sub> is released to the atmosphere than can be utilized. Therefore, on bigger chemical production sites, pure CO<sub>2</sub> for synthetic purposes is nowadays available in sufficient amounts to produce the chemicals discussed herein. For sure, one must think about other CO<sub>2</sub> sources (e.g., isolation from fuel gas or even the atmosphere), while going into a large-scale fuel production based on CO<sub>2</sub> or if industry moves completely away from fossil carbon-based resources in a future scenario.

For an economic and sustainable utilization of CO<sub>2</sub> in synthesis, it is essential that the reaction has a high atom economy, avoiding the formation of by-products and waste. Especially for the bulk chemicals mentioned in this review, the use of relatively expensive co-reagents which are delivering the driving force for the reaction but are ending up as wastes after the reaction is not desirable. For most of the reactions requiring at least stoichiometric amounts of co-reagents like organometallics, metals or bases. This review describes only synthetic protocols where the co-reagents used to drive the reaction are also relatively easy to regenerate. The overall energy consumption for a synthesis utilizing CO<sub>2</sub> is equally important and must be critically evaluated and compared with other alternatives not employing CO<sub>2</sub>.

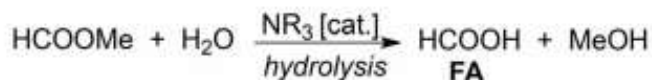
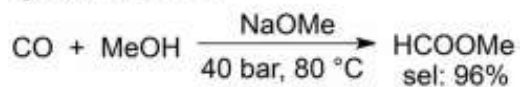
# ❖ Formic Acid and Carboxylation Reactions

Formic acid (HCOOH; FA) and its derivatives such as formamides or formic acid esters can be easily accessed by the hydrogenation of CO<sub>2</sub> using homogeneous or heterogeneous catalysts. Within the past 20 years, several catalytic systems have been reported for these transformations, including those involving the hydrogenations performed in the presence of inorganic bases (Scheme 1)

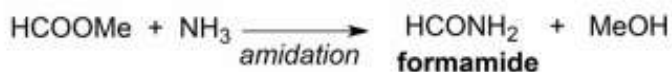
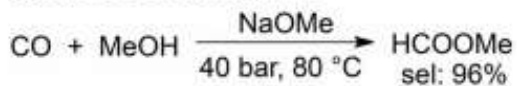


( Scheme 1)

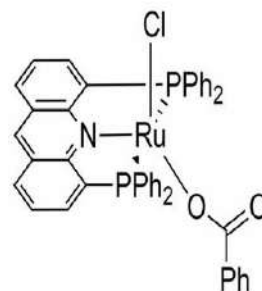
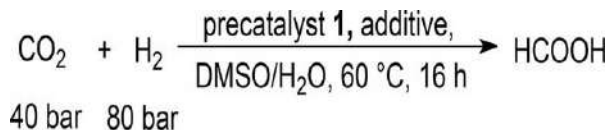
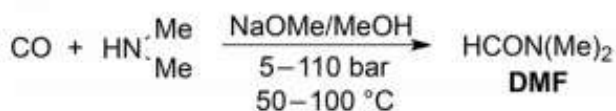
## **synthesis of FA**



## **synthesis of formamide**



## **synthesis of DMF**



1 = [Ru(Acriphos)(PPh<sub>3</sub>)(Cl)(PhCO<sub>2</sub>)]

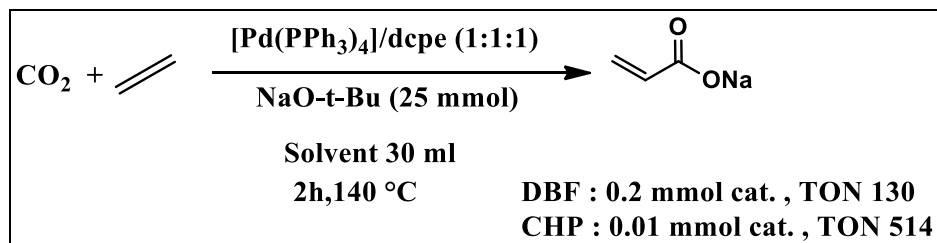
Current industrial routes for the Production of FA and its derivatives based on CO.



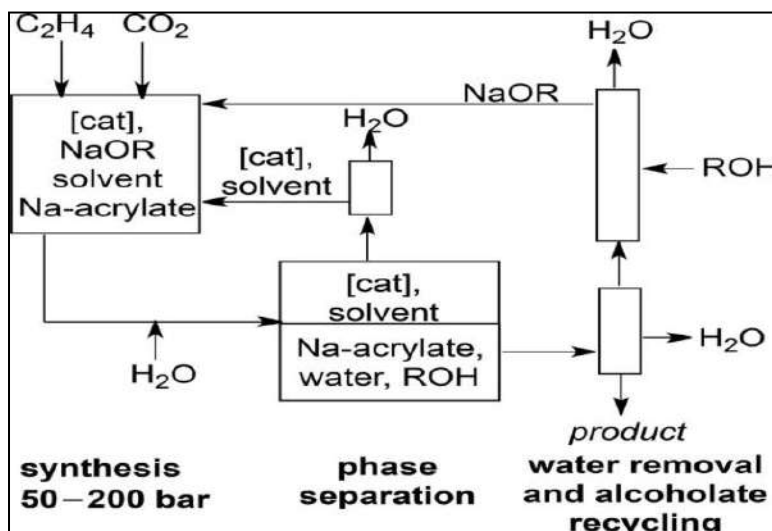
## ❖ Carboxylation of Olefins

The carboxylation of olefins to the corresponding unsaturated carboxylic acids is another attractive way to use CO<sub>2</sub> as a building block. The carboxylation of ethylene has the highest potential, since the formed sodium acrylate is the desired product and is currently used industrially on a multimillion ton scale for the production of super-adsorbents or dispersants. This carboxylation reaction has been achieved in the last years by using homogeneous nickel or palladium catalysts in the presence of an appropriate sodium base. Use of NaOH itself results in the formation of a stable carbonate (NaHCO<sub>3</sub>) under a given CO<sub>2</sub> pressure. Therefore, sodium bases that are basic enough to allow the sodium acrylate formation but do not form irreversible carbonates under the reaction conditions are needed.

After an extensive screening, it was found that certain sodium phenolates and alkoxides like Na<sup>t</sup>BuO or Na<sup>i</sup>PrO do fulfill these requirements and can be used. As an example, use of a homogeneous Pd-dcpe catalyst with NaO-t-Bu as the base and cyclohexylpyrrolidone as the solvent resulted in a TON of up to 514 in the first run (Scheme 2)

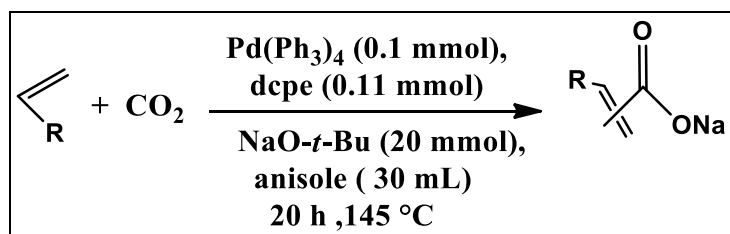


**Scheme 2.** arboxylation of ethylene in N-cyclohexylpyrrolidone (CHP) and N,N-dibutylformamide (DBF) using [Pd(PPh<sub>3</sub>)<sub>4</sub>]/dcpe as the catalyst



From an economic perspective, the CO<sub>2</sub> route is also of high interest.

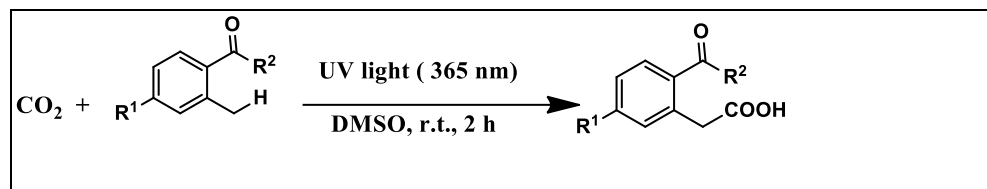
Additionally, under similar reaction conditions, it has been possible to carry out carboxylation reactions with other olefins like butadiene or propylene, whereby the corresponding sodium salts of the unsaturated carboxylic acids were obtained (Scheme 3).



**Scheme 3.** Synthesis of sodium acrylates from olefins and CO<sub>2</sub> using sodium tert-butoxide as base

### ❖ Carboxylation of Aromatics

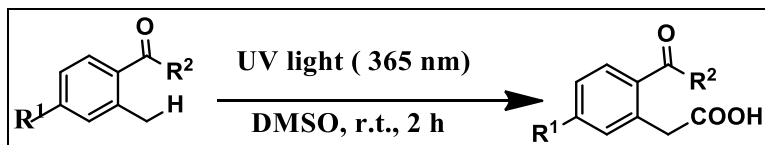
The carboxylation of phenolate salts with CO<sub>2</sub>, named as the Kolbe–Schmitt reaction (Scheme 4), is one of the oldest processes in organic synthesis uses CO<sub>2</sub> as a building block. This reaction is mainly employed to produce salicylic acid. The synthesis of salicylic acid from this route was first accomplished in 1860s.



**Scheme 4.** Kolbe–Schmitt carboxylation of phenol to salicylic acid

In spite of the technical usage of this reaction for the production of salicylic acid, its main drawback is the need for stoichiometric amounts of strong bases that results in the formation of stoichiometric amounts of salts as by-products, when the free acid is needed. Nevertheless, the whole reaction is driven by the salt formation step to achieve functionalisation of the aromatics with CO<sub>2</sub>.

In a parallel context, a unique carboxylation reaction of  $\alpha$ -alkylphenyl ketones has also been developed that utilizes UV irradiation for the production of *o*-acylphenylacetic acids (Scheme 5). Interestingly this methodology avoids the use of stoichiometric amounts of sacrificial reagents. Furthermore, the reaction has been proposed to proceed through the formation of highly reactive *o*-quinodimethane intermediates that are energetically susceptible to undergo cycloaddition reactions with CO<sub>2</sub>.



R1= H, R2= Me; 63%  
 R1= H, R2 = CH<sub>2</sub>Ph; 87%  
 R1= H, R2 = p-ClC<sub>6</sub>H<sub>4</sub>; 61%  
 R1= OMe, R2 = Ph; 65%  
 R1= CF<sub>3</sub>, R2= Ph; 83%

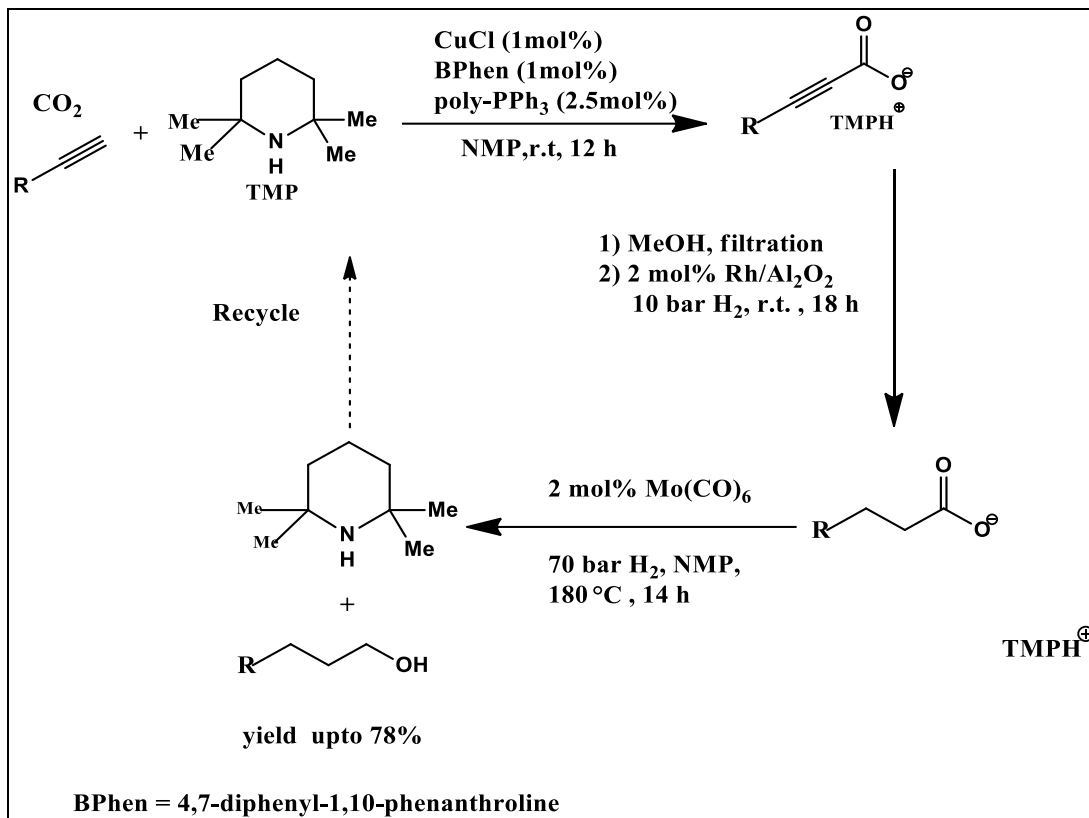
**Scheme 5.** Carboxylation of ortho-alkylphenyl ketones with CO<sub>2</sub> under UV light irradiation.

### ❖ Carboxylation of Alkynes

The carboxylation of terminal alkynes to propargylic acids in the presence of bases is also well known. But its industrial applicability on a larger scale is limited by the fact that an acid has to be added to form the free carboxylic acid, which again results in stoichiometric salt formation as waste (usually propargylic acids were produced via oxidation of the corresponding propargylic alcohols).

To overcome this issue, an elegant system was reported recently using propargylic acid salts as intermediates to produce alcohols. By using tetramethylpiperidine (TMP) as the base, the carboxylation of alkynes was achieved with a copper catalyst (Scheme 6). This salt could further be hydrogenated in two steps to the corresponding saturated alcohol and the free amine, which can be recycled back to the first step. No stoichiometric amounts of salts were formed as waste in this approach.

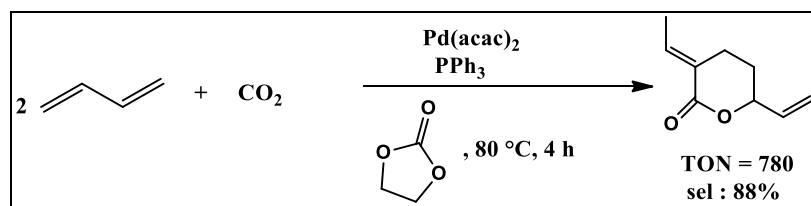
If successfully transferred to acetylene, the most frequently used alkyne in the industry, this concept could allow access to the bulk chemical 1,4-butanediol based on CO<sub>2</sub>, acetylene and H<sub>2</sub> without the use of formaldehyde (1,4-butanediol is currently mainly produced by the reaction of acetylene with formaldehyde to afford 1,4-butyndiol followed by hydrogenation).



Scheme 6. Sequential synthesis of alcohols by carboxylation of terminal alkynes

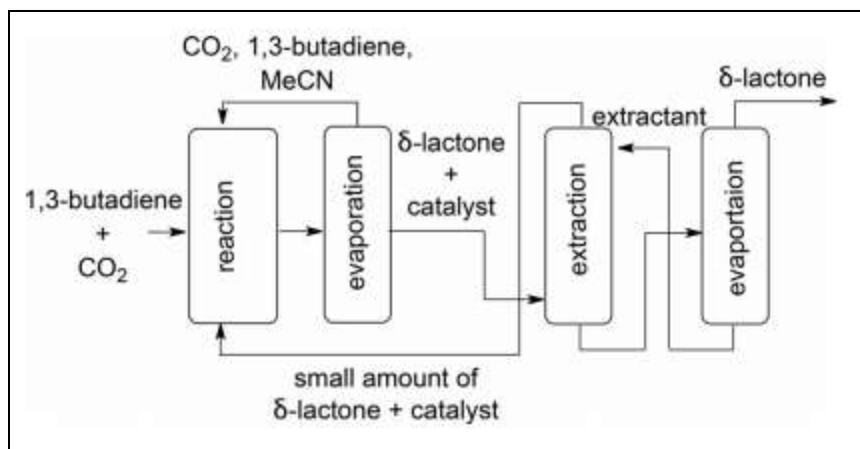
## ❖ Lactones from Dienes

The telomerization of butadiene with  $\text{CO}_2$  by using homogeneous Pd catalysts has been known since the 1970s. Subsequent research initiatives over the past years have led to catalytic systems constituting Pd associated with phosphine ligands that provide the best selectivities towards the unsaturated  $\delta$ -lactone (3-ethylidene-6-vinyltetrahydro-2H-pyran-2-one), without the use of stoichiometric reagents (Scheme 7)



Scheme 7. Palladium-catalyzed telomerization of 1,3-butadiene and  $\text{CO}_2$  to a  $\delta$ -lactone

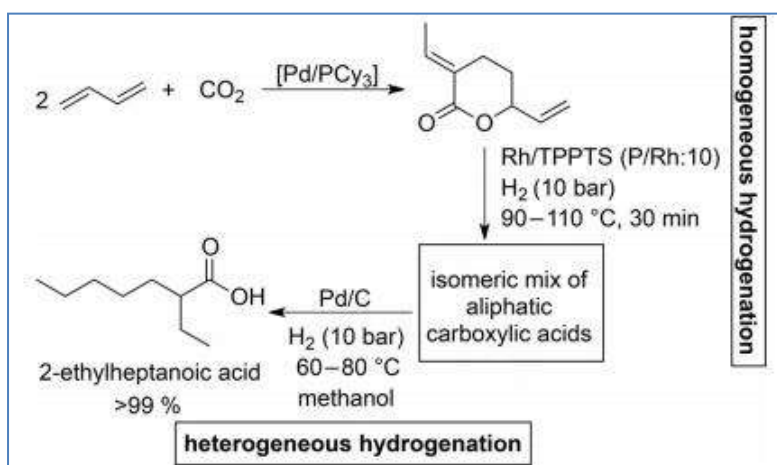
In industries, extraction technique is being used to carry out telomerization, where the  $\delta$ -lactone is extracted out of the product mixture [after evaporating the reaction solvent (MeCN)] by using a solvent such as 1,2,4-butanetriol and the catalyst left behind is recycled back to the reactor (Scheme 8).



**Scheme 8.** Continuous miniplant for the telomerization of 1,3-butadiene and CO<sub>2</sub> to a  $\delta$ -lactone using extractive catalyst recycle.

Due to the straightforward approaches available for its synthesis, the  $\delta$ -lactone was further evaluated as a potential platform chemical for its transformation into a variety of chemical intermediates. For example, starting from butadiene by following a two step hydrogenation route, 2-ethylheptanoic acid can be obtained in excellent yields through the  $\delta$ -lactone intermediate, on the other hand a methoxycarbonylation, followed by hydrogenation of the  $\delta$ -lactone resulted in a branched C10-diol (Scheme 9).

Although the products derived from the  $\delta$ -lactone are discussed as new intermediates but so far, they do not fit in existing industrial value chains like those for polymers. Therefore, the potential of these intermediates and the resulting products must be further evaluated to determine whether or not they are economic alternatives to the current related products.



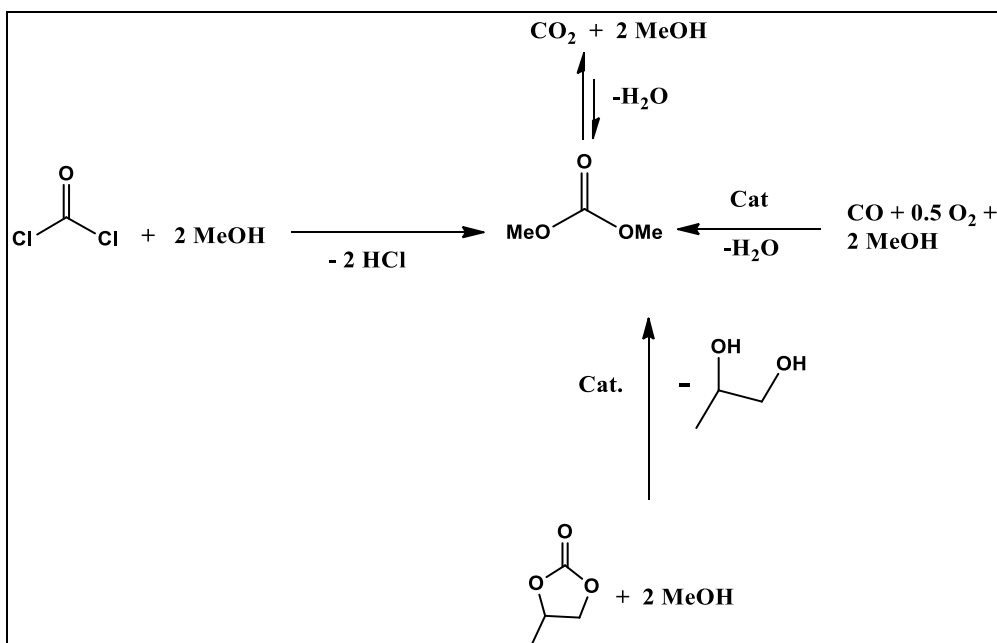
**Scheme 9.** Three-step process for the synthesis of 2-ethylheptanoic acid starting from 1,3-butadiene and CO<sub>2</sub>.

## ❖ Organic Carbonates

Linear and cyclic organic carbonates are widely used in the chemical industry as solvents, alkylating agents, monomers or in transesterification reactions. The most important carbonates are dimethyl carbonate (DMC), diethyl carbonate (DEC), diphenyl carbonate (DPC), ethylene carbonate (EC) as well as propylene carbonate (PC) and they are produced on an overall scale of a several 100 kilotons p.a.

### ❖ Linear Carbonates

Linear carbonates are nowadays mainly produced by two different routes: (i) the oxidative carbonylation of an alcohol, whereby good yields and selectivities are achieved (right arrow) and (ii) the transesterification of PC with methanol, which is nowadays the major industrial route for the synthesis of DMC in China. (lower arrow). Also carbonates like diphenyl carbonate (DPC) are best obtained by reacting dimethyl carbonate (DMC) with phenol. The conventional  $\text{COCl}_2$  route (left arrow) is nowadays hardly used for the synthesis of bulk carbonates.



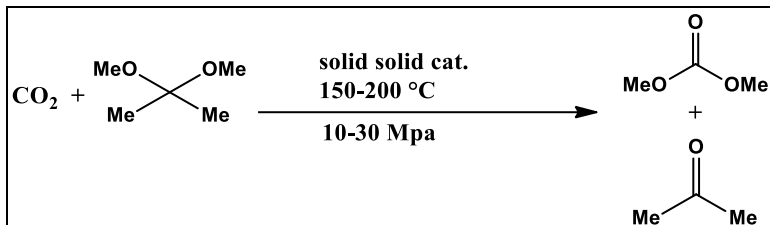
Comparison of routes for the synthesis of dimethyl carbonate (DMC)

The transesterification of PC, made from propylene oxide and  $\text{CO}_2$  is an indirect way to utilize  $\text{CO}_2$  in the synthesis of linear carbonates. As a significant amount of industrially produced propylene oxide is anyway transformed to propylene glycol by hydrolysis, one can get to DMC by a process based on the  $\text{CO}_2$  utilization route without forming any unwanted by-products or the need for additional drying agents. Drawbacks of this method

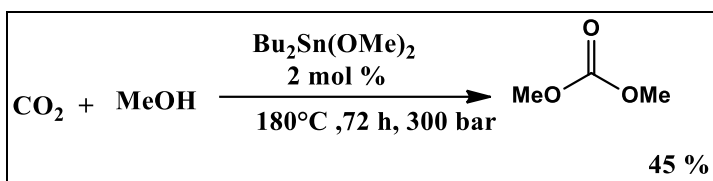
are 1) the energy consumption to separate the azeotropes is very high 2) not much economic.

There are many other methods to convert CO<sub>2</sub> into linear carbonates-

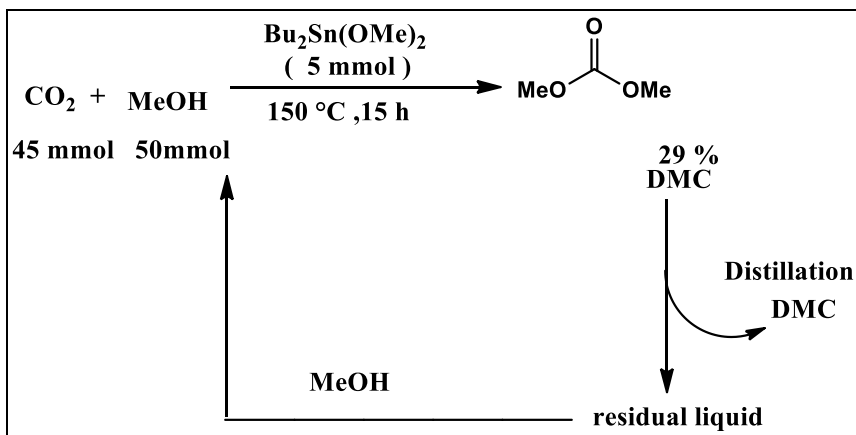
### Mitubishi heavy industries



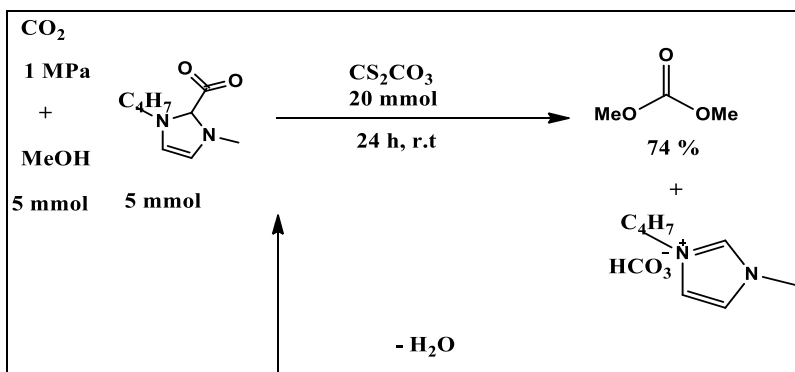
### Toshiyasu Sakakura et. al.



### Asahi Kasei Chemical Corporation



### X. Hu and Y. Wu et. al

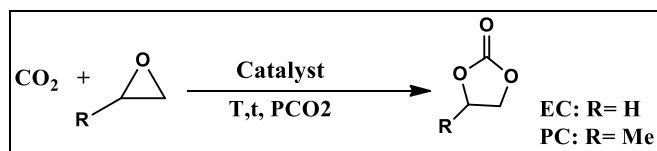


## ❖ Cyclic Carbonates

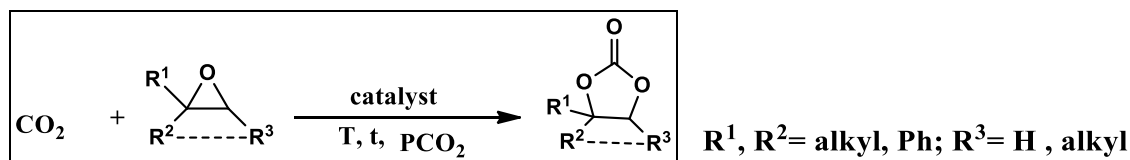
Five-membered cyclic carbonates are usually obtained by the reaction of the corresponding oxiranes with CO<sub>2</sub>. The driving force for this reaction is the high energy content of the oxirane. Industrially EC and PC are produced on a significant scale, starting from the corresponding ethylene and propylene oxides.

A broad series of substituted cyclic carbonates was also formed in moderate to good yields, from the corresponding oxiranes, whereby also different catalysts are applied. But in all these cases, first the reactive oxiranes must be produced, in order to utilize CO<sub>2</sub> as the building block. The cyclic carbonates can also be obtained from 1,2- or 1,3-diols, but like linear alkyl carbonates, the yields in the equilibrium are usually low when no water trapping agent is added. In the presence of water trapping agents like a zeolite or 2-cyanopyridine, from which the corresponding amide is formed via hydrolysis, significantly higher yields of the cyclic carbonate of up to 99% are possible. Another interesting cyclic carbonate is glycerol carbonate, which can be used as a bio-based monomer or solvent. It is usually produced by the reaction of DMC with glycerol, but can also be obtained directly from glycerol and CO<sub>2</sub>.

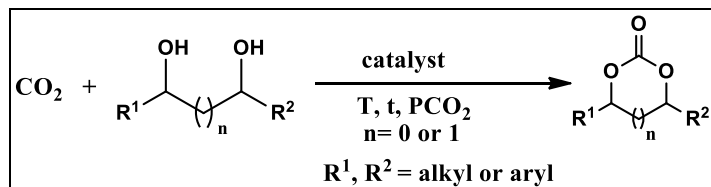
### Synthesis of five-membered cyclic carbonates from oxiranes.



### Recent synthesis routes for cyclic carbonates from CO<sub>2</sub> and epoxides.

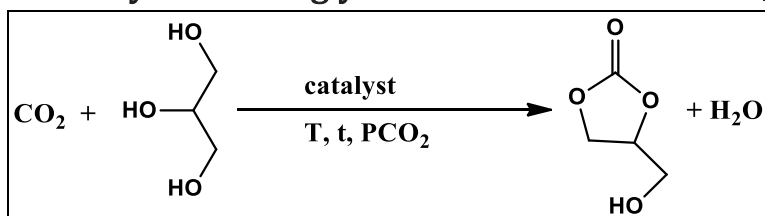


### Synthesis of cyclic carbonates from CO<sub>2</sub> and diol.





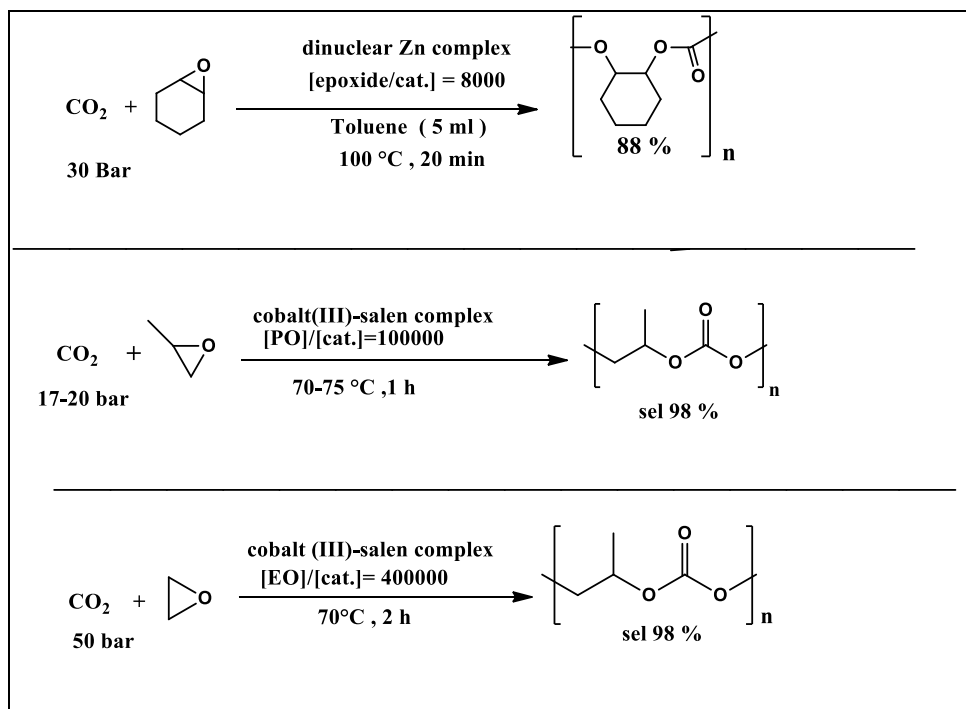
## Direct synthesis of glycerol carbonates from CO<sub>2</sub> and glycerol.



## ❖ Polycarbonates and Polyetherol Carbonates

The copolymerization of propylene oxide with CO<sub>2</sub> using ZnEt<sub>2</sub> in combination with water was first reported in 1969 and the synthesis of polycarbonates and polyetherols based on the copolymerization of oxiranes with CO<sub>2</sub> has attracted a lot of attention during the last years. From an industrial point of view, this reaction highly is attractive: (i) it is in principle by-product free, (ii) it does not require the addition of stoichiometric co-reagents, (iii) the products contain up to 50% CO<sub>2</sub> /O<sub>2</sub> and especially the oxiranes ethylene oxide and propylene oxide are industrially available on a large scale.

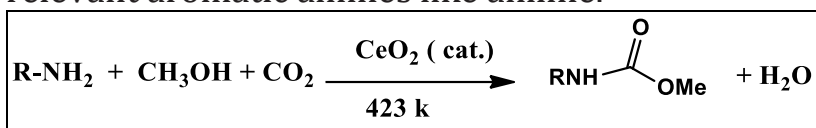
For the synthesis of polycarbonates, several active catalysts based on Zn or Co were reported. Unfortunately, the pure polymers based on ethylene oxide and propylene oxide do not show very good properties thus limiting their commercial attractiveness, but they can be utilized in blends with other polymers. The first commercial application of these polycarbonates was announced by SK innovation under the brand GreenPol.



## ❖ Linear Carbamates and Isocyanates

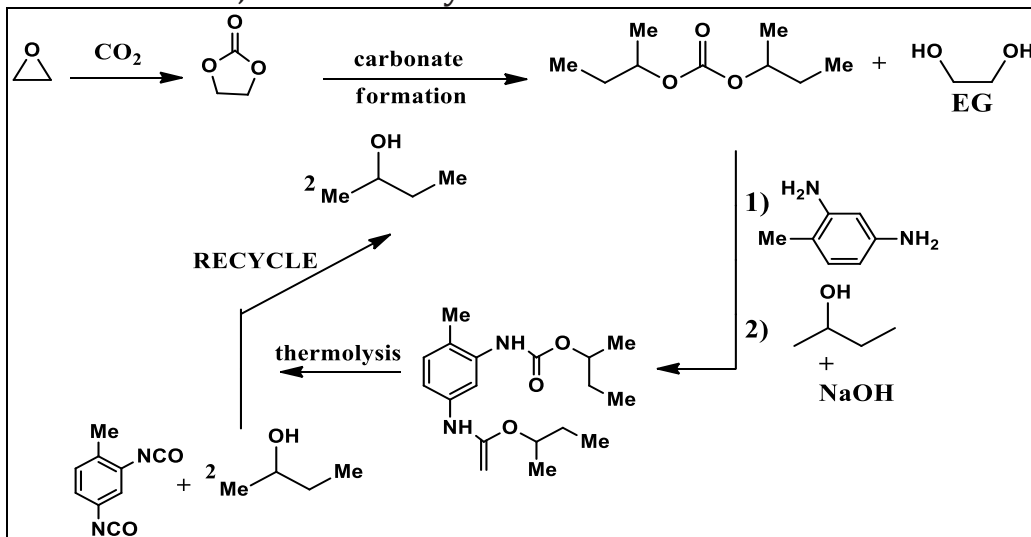
Isocyanates are important monomers produced on a large scale, and are mainly used for the production of polyurethanes. Currently, most of the isocyanates are produced by reacting the corresponding amines with phosgene. But this method is a bit costly (energy consumption, investments). Therefore, phosgene-free alternatives for isocyanate synthesis were investigated. One approach is the use of CO<sub>2</sub>-based carbamates as intermediates in isocyanate synthesis.

Carbamates can, in principle, be accessed by the reaction of the corresponding amine with CO<sub>2</sub> in the presence of an alcohol (Scheme 10). For the technically not relevant benzylamine or aminomethylcyclohexane, the carbamates are directly accessible in good yields without the use of drying agents, but this attempt fails for the commercially relevant aromatic amines like aniline.



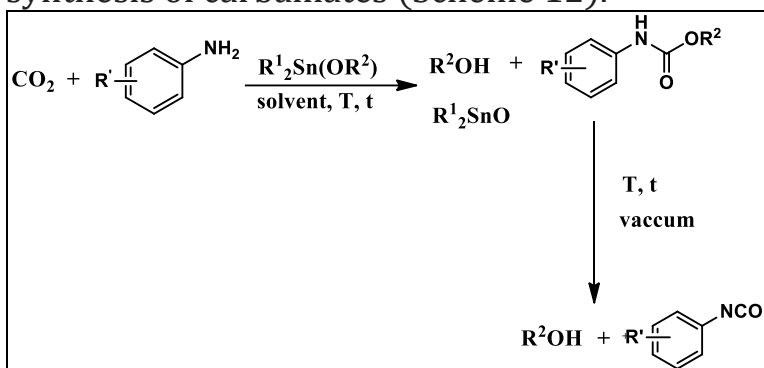
**Scheme 10.** Synthesis of carbamates directly from amine, CO<sub>2</sub> and alcohol.

Different concepts were presented to prepare aromatic carbamates based on CO<sub>2</sub> as the building block. In a concept reported by BASF, the initial step involves the production of ethylene carbonate from ethylene oxide and CO<sub>2</sub>. By using 2-butanol, a transesterification is performed to obtain diisobutyl carbonate and ethylene glycol as a valuable by-product. The linear carbonate is then reacted with toluenediamine to afford the corresponding bis-carbamate and 2-butanol. For high conversions, sodium 2-butylate is required as a co-reagent, which has to be synthesized in another energy-demanding step from the alcohol and NaOH. The obtained bis-carbamate can then be thermally cracked to the bisisocyanate and 2-butanol, which is recycled in to the carbonate formation step (Scheme 11).



**Scheme 11.** Process concept for the combined production of ethylene glycol (EG) and 2,4-toluene diisocyanate (TDI).

To simplify the synthesis of the carbamates based on CO<sub>2</sub>, the Ashai concept for the production of carbonates based on CO<sub>2</sub> and organotin reagents was modified for the synthesis of carbamates (Scheme 12).

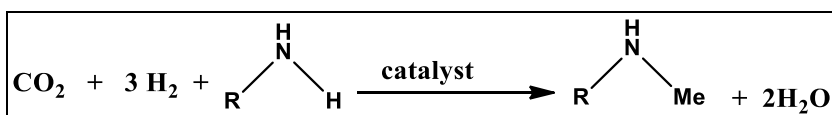


**Scheme 12.** Organotin(IV) alkoxide-catalyzed synthesis of industrially relevant carbamates and isocyanates.

## ❖ Methylation Reactions

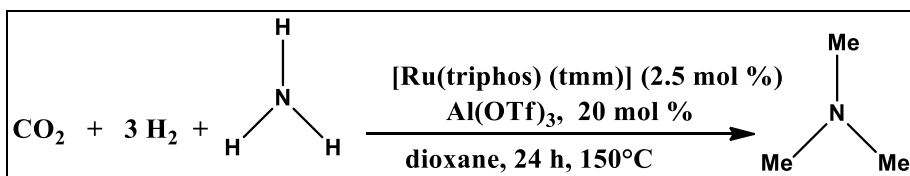
### ❖ N-Methylation

CO<sub>2</sub> in combination with H<sub>2</sub> can also be utilized in several N-methylations so far achieved on different substrates by the use of homogeneous ruthenium-triphos catalysts in combination with additives like acids or LiCl or with heterogeneous catalysts.



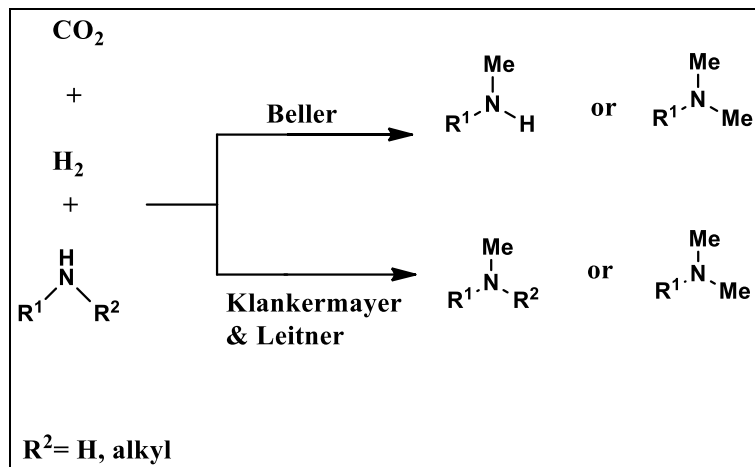
**Scheme 13.** General scheme for the N-methylation of amines using CO<sub>2</sub> and H<sub>2</sub>.

In the state of the art production of bulk methylamines, usually MeOH is employed as the methylating agent with the use of heterogeneous catalysts. MeOH-based methyl- and dimethylamine routes are frequently used to introduce methylamine functionalities. For an industrial application, the CO<sub>2</sub>/H<sub>2</sub>-based routes have to be competitive with the established and optimized systems based on MeOH, especially as MeOH can easily be obtained from CO<sub>2</sub>/H<sub>2</sub>. Using Ru-triphos with Al(OTf)<sub>3</sub> as co-catalyst, trimethylamine is accessible from ammonia and CO<sub>2</sub>/H<sub>2</sub> (Scheme 14).



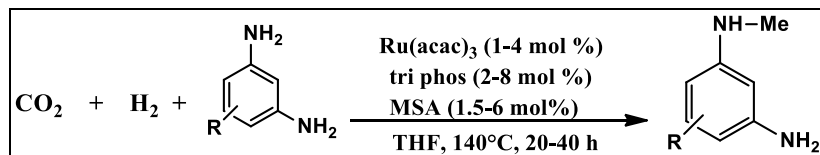
**Scheme 14.** Synthesis of trimethylamine TMA from NH<sub>3</sub> with CO<sub>2</sub> and H<sub>2</sub>

The reaction proceeds via formamides as intermediates, which are further deoxygenated to the N-methylamines. The Ru-triphos system can also be used for a series of other aliphatic and aromatic amines, as shown by the groups of Beller, Klankermayer and Leitner during the last years (Scheme 15).



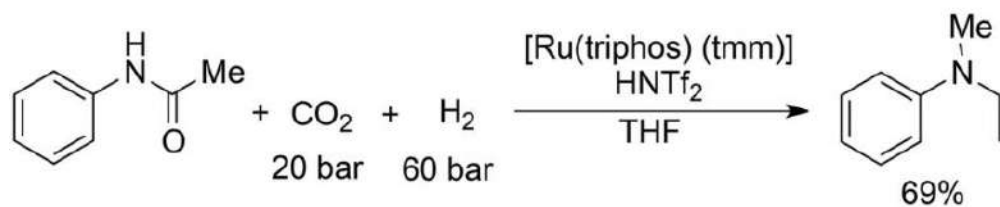
**Scheme 15.** N-Methylation of aliphatic and aromatic amines using  $\text{CO}_2$  and  $\text{H}_2$ .

For aromatic diamines, a selective N-monomethylation is possible, which is difficult to achieve when MeOH and the established catalysts are used.

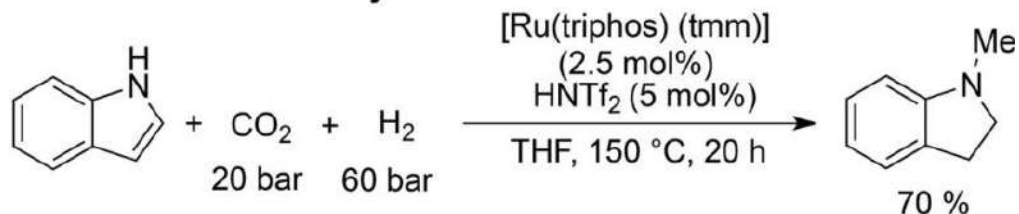


Selective N-monomethylation of diamines

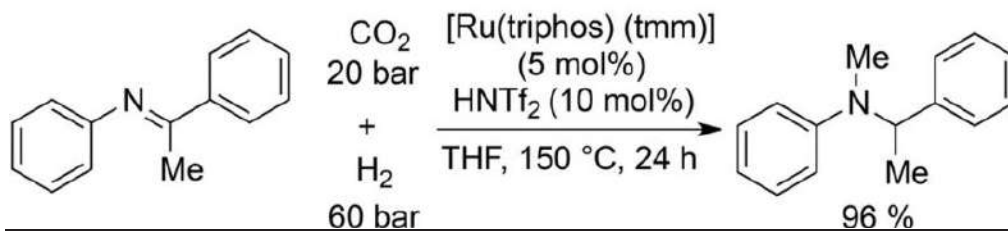
### amide reduction + methylation



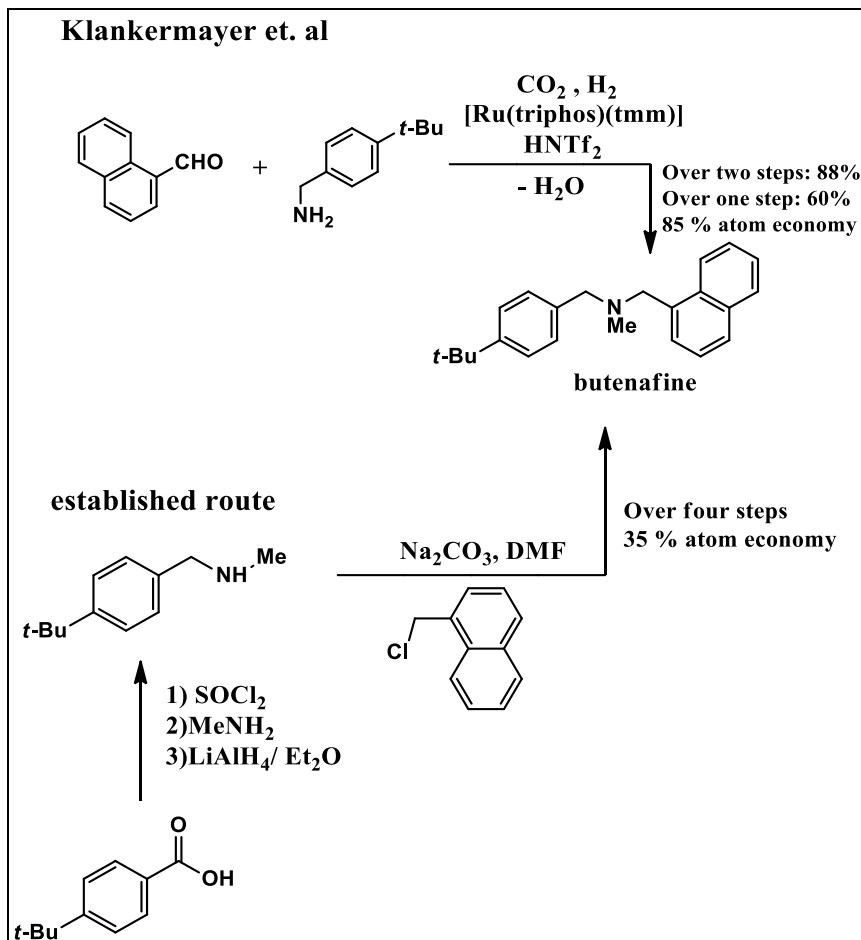
### olefin reduction + methylation



### imine reduction + methylation



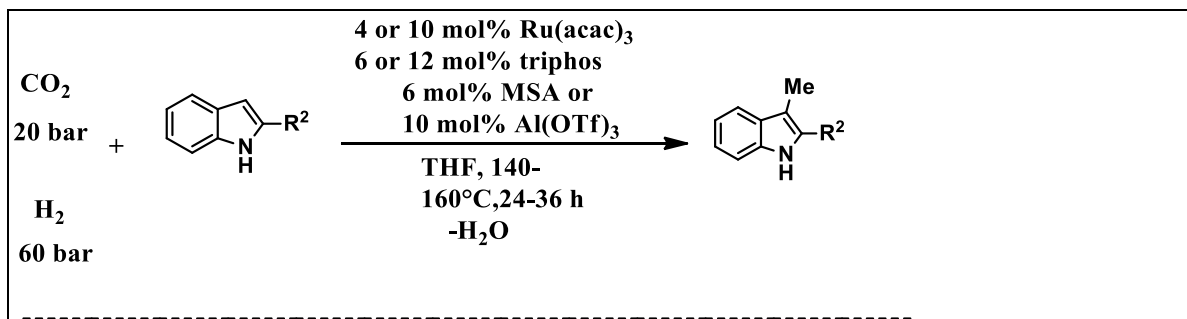
Sequential hydrogenation/N-methylation of acetanilide, indole and imines.

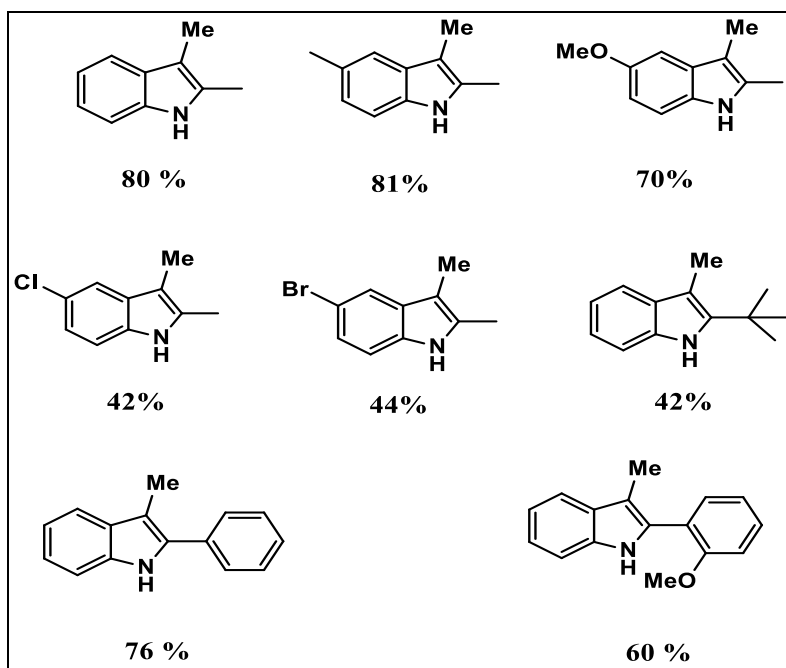


**Scheme 16.** Application of N-methylation for the synthesis of the antifungal agent butenafine with  $\text{CO}_2$  and  $\text{H}_2$  in comparison to the established methods.

## ➤ C-Methylation

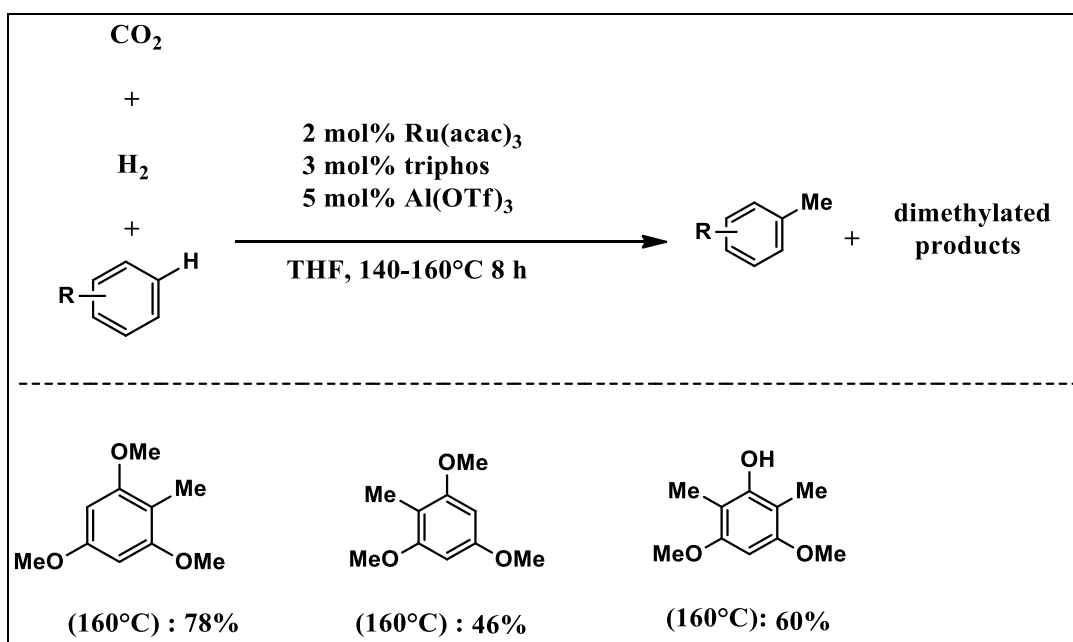
Like in the N-methylation,  $\text{CO}_2/\text{H}_2$  can also be used for the methylation of aromatic compounds to replace  $\text{MeOH}$  as the  $\text{CH}_3$  source. For example, heteroarenes can be methylated on the heteroarene ring by again using a Ru-triphos catalyst in combination with an acidic co-catalyst (Scheme 17).





### Scheme 17.C-H methylation of heteroarenes with CO<sub>2</sub> and H<sub>2</sub>

It is also possible to perform the methylation on electron-rich arenes at temperatures of up to 160°C (Scheme 18). This approach could be an alternative to the methylation of electron-rich arenes, like phenol to ortho-cresol with MeOH which is carried out at 350–400°C in the liquid phase, if the reaction could be extended to the less reactive phenol and related substrates.



### Scheme 18.C-H methylation of arenes with CO<sub>2</sub> and H<sub>2</sub>

## ❖ Conclusion

The utilization of CO<sub>2</sub> as a building block to produce a wide variety of chemicals and materials poses a challenge but also provides new opportunities to diverse industrial methods. Within the large number of reports in the last decades on the utilization of CO<sub>2</sub> as a building block, several methods have the potential for industrial usage. For example, Polyetherol carbonates and polycarbonates synthesis based on CO<sub>2</sub> are starting to be commercialized and will extend the industrial portfolio on CO<sub>2</sub> -based chemicals. On the other hand, many other approaches are not competitive yet in the current stage of development compared to the state of the art routes, due to a significantly higher energy consumption or the use of expensive co-reagents. But as a shift away from the fossil carbon sources is only a matter of time, there is still a high demand to develop new and elegant concepts for a sustainable and economic utilization of CO<sub>2</sub> as a building block in industrial organic synthesis.

## ❖ Acknowledgement

I would like to express my special thanks to my guide **Dr. Somjit Hajra** for his guidance and support in completing my presentation. I would also like to extend my gratitude to **Dr. Sebanti Basu** and to all the Professors of the chemistry department for guiding me in the completion of the presentation.

## ❖ Reference

- [1] T. Schaub, R. A. Paciello, M. Limbach, in: Applied Homogeneous Catalysis with Organometallic Compounds: A Comprehensive Handbook in Four Volumes, (Eds.: B. Cornils, W. A. Hermann, M. Beller, R. A. Paciello), Wiley-VCH, Weinheim, 2018, pp 1601–1614.
- [2] S. Topham, A. Bazzanella, S. Schiebahn, S. Luhr, L. Zha, A. Otto, D. Stolten, in Ullmann's Encyclopaedia of Industrial Chemistry, Wiley-VCH, Weinheim, 2014, DOI: 10.1002/14356007.a05165.pub2.
- [3] R. Schlögel, (Ed.), Chemical Energy Storage, de Gruyter, Berlin, Boston, 2013.
- [4] J. H. Meessen, in: Ullmann's Encyclopedia of Industrial Chemistry, Wiley-VCH, Weinheim, 2012, Vol. 37, pp 657–695.



[5] a) J. Ott, V. Gronemann, F. Pontzen, E. Fiedler, G. Grossmann, D. B. Kersebohm, G. Weiss, C. Witte, in: Ullmann's Encyclopedia of Industrial Chemistry, Wiley-VCH, Weinheim, 2012,

DOI: 10.1002/14356007.a16465.pub3; b) E. Kunkes, M. Behrens, in: Chemical Energy Storage,

(Ed.: R. Schlögl), de Gruyter, Berlin, Boston, 2013; pp 413–443; c) <http://carbonrecycling.is/george-olah/> (accessed 25.08.2018).

[6] F. Ausfelder, A. Bazzanella, Diskussionspapier: Verwertung und Speicherung von CO<sub>2</sub>, 2008, Dechema, Frankfurt. a) W. Leitner, *Angew. Chem* 1995, 107, 2391–2405; *Angew. Chem. Int. Ed. Engl.* 1995, 34, 2207–2221; b) P. G. Jessop, T. Ikariya, R. Noyori, *Chem. Rev.* 1995, 95, 259–272; c) P. G. Jessop, F. Jol, C.-C. Tai, *Coord. Chem. Rev.* 2004, 248, 2425–2442; d) P. G. Jessop, in: *The Handbook of Homogeneous Hydrogenation*, (Eds.: J. G. de Vries, C. J. Elsevier), WileyVCH, Weinheim, 2008, pp 489–511; e) W. Wang, S. Wang, X. Ma, J. Gong, *Chem. Soc. Rev.* 2011, 40, 3703–3727; f) M. Aresta, A. Dibenedetto, A. Angelini, *Chem. Rev.* 2014, 114, 1709–1742; g) W.-H. Wang, Y. Himeda, J. T. Muckerman, G. F. Manbeck, E. Fujita, *Chem. Rev.* 2015, 115, 12936–12973; h) J. Klankermayer, W. Leitner, *Science* 2015, 350, 629–630; i) G. H. Gunasekar, K. Park, K. D. Jung, S. Yoon, *Inorg.*

*Chem. Front.* 2016, 3, 882–895; j) A. Alvarez, A. Bansode, A. Urakawa, A. V. Bavykina, T. A. Wezendonk,

M. Makkee, J. Gascon, F. Kapteijn, *Chem. Rev.* 2017, 117, 9804–9838; k) W.-H. Wang, X. Feng, M. Bao, in: *Transformation of Carbon Dioxide to Formic Acid and Methanol*, Springer, Singapore, 2018, pp 7–42.

[10] S. C. E. Stieber, N. Huguet, T. Kageyama, I. Jevtovikj, P. Ariyananda, A. Gordillo, S. A. Schunk, F. Roming

er, P. Hofmann, M. Limbach, *Chem. Commun.* 2015, 51, 10907–10909.

[7] S. Manzini, N. Huguet, O. Trapp, T. Schaub, *Eur. J. Org. Chem.* 2015, 7122–7130.

[8] S. Manzini, A. Cadu, A. C. Schmidt, N. Huguet, O. Trapp, R. Paciello, T. Schaub, *ChemCatChem* 2017, 9, 2269–2274.

[9] a) H. Kolbe, *Justus Liebigs Ann. Chem.* 1860, 113, 125–127; b) A. S. Lindsey, H. Jeskey, *Chem. Rev.* 1957, 57, 583–620

[10] For selected examples of Kolbe–Schmitt carboxylation, see: a) D. Cameron, H. Jeskey, O. Baine, *J. Org. Chem.* 1950, 15, 233–236; b) J. Cason, G. O. Dyke, *J. Am. Chem. Soc.* 1950, 72, 621–622; c) O. Baine, G. F. Adamson, J. W. Barton, J. L. Fitch, D. R. Swayampati, H. J. Jeskey, *J. Org. Chem.* 1954, 19, 510–514; d) F. Wessely, K. Benedikt, H. Benger, H. Friedrich, F. Prillinger, *Monatsh. Chem.* 1950, 81, 1071–1091; e) J. M. Gnaim, B. S. Green, R. Arad-Yellin, P. M. Keehn, *J. Org. Chem.* 1991, 56, 4525–4529; f) Y. Kosugi, Y. Imaoka, F. Gotoh, M. A. Rahim, Y. Matsui, K. Sakanishi, *Org. Biomol. Chem.* 2003, 1, 817–821; g) Z. Markovic', S. Markovic', N. Begovic', *J. Chem. Inf. Model.* 2006, 46, 1957–1964; h) Z. Markovic', S. Markovic', N. Manojlovic', J. Predojevic'-Simovic', *J. Chem. Inf. Model.* 2007, 47, 1520–1525; i) X. Yan, Z. Cheng, Z. Yue, P. Yuan, *Res. Chem. Intermed.* 2014, 40, 3059–3071.

[11] a) L. J. Gooßen, N. Rodríguez, F. Manjolinho, P. P. Lange, *Adv. Synth. Catal.* 2010, 352, 2913–2917; b) X.

Zhang, W.-Z. Zhang, X. Ren, L.-L. Zhang, X.-B. Lu, *Org. Lett.* 2011, 13, 2402–2405; c) D. Y. Yu, Y. G. Zhang, *Green Chem.* 2011, 13, 1275–1279; d) D. Yu, M. X. Tan, Y. Zhang, *Adv. Synth. Catal.* 2012, 354, 969–974; e) M. Arndt, E. Risto, T. Krause, L. J. Gooßen, *ChemCatChem* 2012, 4, 484–487.

[12] K. Buchmüller, N. Dahmen, E. Dinjus, D. Neumann, B. Powietzka, S. Pitter, J. Schön, *Green Chem.* 2003, 5, 218–223.

[13] A. Behr, M. Becker, *Dalton Trans.* 2006, 4607–4613.

[14] A. Behr, P. Bahke, B. Klinger, M. Becker, *J. Mol. Catal. A: Chem.* 2007, 267, 149–156.

[15] H. J. Buysch, in: *Ullmann's Encyclopaedia of Industrial Chemistry*, Vol. 7, Wiley-VCH, Weinheim, 2012, pp 45–71.

[16] T. Sakakura, K. Kohno, *Chem. Commun.* 2009, 1312–1330.

[17] Reviews highlighting the direct synthesis of linear carbonates from CO<sub>2</sub> and alcohol and references therein: a) K. Shukla, V. C. Srivastava, *RSC Adv.* 2016, 6, 32624–32645; b)

- N. Kindermann, T. Jose, A. W. Kleij, *Top. Curr. Chem.* 2017, 375, 15; c) A. A. Chaugule, A. H. Tamboli, H. Kim, *Fuel* 2017, 200, 316–332;
- d) H.-Z. Tan, Z.-Q. Wang, Z.-N. Xu, J. Sun, Y.-P. Xu, Q.-S. Chen, Y. Chen, G.-C. Guo, *Catal. Today* 2018, doi.org/10.1016/j.cattod.2018.02.021.
- [18] J. Steinbauer, T. Werner, *ChemSusChem* 2017, 10, 3025–30
- [19] M. Aresta, A. Dibenedetto, F. Nocito, C. Pastore, *J. Mol. Catal. A* 2006, 257, 149–153.
- [20] L. P. Ozorio, C. J. A. Mota, *ChemPhysChem* 2017, 18, 3260–3265.29.
- [21] R. Ugajin, S. Kikuchi, T. Yamada, *Synlett* 2014, 25, 1178–1180.
- [22] H.-F. Jiang, A.-Z. Wang, H.-L. Liu, C.-R. Qi, *Eur. J. Org. Chem.* 2008, 2309–2312.
- [23] a) C. Gg r tler, in: *Technologie fg r Nachhaltigkeit und Klimaschutz - Chemische Prozesse und stoffliche Nutzung von CO<sub>2</sub>*, (Eds.: A. Bazzanella, D. Kr- mer), DECHEMA, Frankfurt, 2017, pp 44–49; b) A. Wolf, in: *Technologie fg r Nachhaltigkeit und Klimaschutz - Chemische Prozesse und stoffliche Nutzung von CO<sub>2</sub>*, (Eds.: A. Bazzanella, D. Kr- mer), DECHEMA, Frankfurt, 2017, pp 32–36.
- [24] G. Reuss, W. Disteldorf, A. O. Gamer, A. Hilt, in: *UllmannQ s Encyclopaedia of Industrial Chemistry*, Vol. 15, Wiley-VCH, Weinheim, 2012, pp 735–768.
- [25] K. I. Tominaga, Y. Sasaki, *Catal. Commun.* 2000, 1, 1– 3.
- [26] Q. Liu, L. Wu, I. Fleischer, D. Selent, R. Franke, R. Jackstell, M. Beller, *Chem. Eur. J.* 2014, 20, 6888–6894.
- [27] V. K. Srivastava, P. Eilbracht, *Catal. Commun.* 2009, 10, 1791–1795.
- [28] P. Kalck, M. Urrutigoity, *Chem. Rev.* 2018, 118, 3833– 3861.
- [29] Y. Li, I. Sorribes, T. Yan, K. Junge, M. Beller, *Angew. Chem.* 2013, 125, 12378–12382; *Angew. Chem. Int. Ed.* 2013, 52, 12156–12160.

- [30] K. Beydoun, T. V. Stein, J. Klankermayer, W. Leitner, *Angew. Chem.* 2013, 125, 9733–9736; *Angew. Chem. Int. Ed.* 2013, 52, 9554–9557.
- [31] K. Beydoun, G. Ghattas, K. Thenert, J. Klankermayer, W. Leitner, *Angew. Chem.* 2014, 126, 11190–11194; *Angew. Chem. Int. Ed.* 2014, 53, 11010–11014
- [32] K. Beydoun, K. Thenert, E. S. Streng, S. Brosinski, W. Leitner, J. Klankermayer, *ChemCatChem* 2016, 8, 135–138[137] Y. Li, X. Cui, K. Dong, K. Junge, M. Beller, *ACS Catal.* 2017, 7, 1077–1086.
- [33] a) S. V. Gredig, R. A. Koepfel, A. Baiker, *J. Chem. Soc. Chem. Commun.* 1995, 73–74; b) S. V. Gredig, R. A. Koepfel, A. Baiker, *Catal. Today* 1996, 29, 339–342; c) S. V. Gredig, R. A. Koepfel, A. Baiker, *Appl. Catal. A: General* 1997, 162, 249–260; d) K. Kon, S. M. A. H. Siddiki, W. Onodera, K. I. Shimizu, *Chem. Eur. J.* 2014, 20, 6264–6267; e) X. Cui, X. Dai, Y. Zhang, Y. Deng, F. Shi, *Chem. Sci.* 2014, 5, 649–655; f) X. Cui, Y. Zhang, Y. Deng, F. Shi, *Chem. Commun.* 2014, 50, 13521–13524; g) G. Tang, H.-L. Bao, C. Jin, X. H. Zhong, X. L. Du, *RSC Adv.* 2015, 5, 99678–99687; h) X. L. Du, G. Tang, H. L. Bao, Z. Jiang, X. H. Zhong, D. S. Su, J. Q. Wang, *ChemSusChem* 2015, 8, 3489–3496.
- [34] P. Roose, in: *Ullmann's Encyclopedia of Industrial Chemistry*, Wiley-VCH, Weinheim, 2015, DOI: 10.1002/14356007.a16 535.pub5.
- [35] P. Roose, K. Eller, E. Henkes, R. Roszbacher, H. Hçke, in: *Ullmann's Encyclopedia of Industrial Chemistry*, Wiley-VCH, Weinheim, 2015, DOI: 10.1002/14356007.a02 001.pub2.
- [36] Y. Li, T. Yan, K. Junge, M. Beller, *Angew. Chem.* 2014, 126, 10644–10648; *Angew. Chem. Int. Ed.* 2014, 53, 10476–10480.
- [37] H. G. Franck, J. W. Stadelhofer, in *Industrielle Aromatenchemie*, Springer Verlag, Berlin, 1987, p 173.

**A REVIEW ON**  
**UTILIZATION OF WASTE CO<sub>2</sub> AS A BUILDING**  
**BLOCK FROM AN INDUSTRIAL PERSPECTIVE**



**Scottish Church College**

**Roll No.** - 223/CEM/191032  
**Registration No.** - 114-1221-0387-16  
**Special Paper** - CHEM-SO44  
**Name of the candidate** - Srabani Dutta  
**Name of the examiner** - Dr. Sebanti Basu

*Srabani Dutta.*

**Signature of the candidate**

*Sebanti Basu*

**Signature of the examiner**

## ➤ **Contents**

- ❖ **Introduction**
- ❖ **General consideration**
- ❖ **Formic Acid and Carboxylation Reactions**
- ❖ **Carboxylation of olefins**
- ❖ **Carboxylation of aromatics**
- ❖ **Carboxylation of alkynes**
- ❖ **Lactones from dienes**
- ❖ **Organic carbonates**
- ❖ **Polycarbonates and Polyetheral carbonates**
- ❖ **Methylation reactions**
- ❖ **Conclusion**
- ❖ **Acknowledgement**
- ❖ **Reference**

## ❖ **Introduction**

The use of carbon dioxide (CO<sub>2</sub>) as a building block for the production of chemicals is a topic of high interest and importance nowadays. From an industrial perspective, CO<sub>2</sub> on the one hand is waste that is to be minimized, especially in the context of the global warming, but on the other hand is also a cheap and abundant C1 -building block. In this context, utilizing CO<sub>2</sub> is not a new topic from an industrial perspective, but has been gaining more and more attraction over the last years due to the discussions about a raw material change away from fossil carbon sources and global warming. This review reflects potential industrially relevant approaches for the use of CO<sub>2</sub> as an alternative building block in the synthesis of organic compounds which are produced on a significant industrial scale or for new CO<sub>2</sub>-based compounds, having the potential of scaling up. This review will not focus on the production of fuels like methanol based on CO<sub>2</sub>, energy as well as hydrogen storage utilizing CO<sub>2</sub>. For example for the synthesis of methanol, CO<sub>2</sub> is nowadays used in significant amounts as a co-feed in the syngas-based route. Also for methodologies based only on CO<sub>2</sub> and H<sub>2</sub>, the technology using heterogeneous catalysts is relatively mature and currently being operated on a pilot scale. The utilization of carbon dioxide (CO<sub>2</sub>) as a sustainable and renewable one-carbon (C1) building block in organic synthesis has attracted great attention since it may provide access to profitable chemicals from an abundant, non-toxic, non-flammable and inexpensive resource. Among these transformations, synthesis of biologically and synthetically important six-membered cyclic carbamates employing CO<sub>2</sub> as building block represents one of the hottest and attractive research topics in the field.

## ❖ General Consideration

CO<sub>2</sub>, as the final product from the oxidation of organic molecules, is a very stable energetic molecule ( $\Delta H_{0\sim} -400 \text{ KJ mole}^{-1}$ ). It does not matter which organic product one wants to prepare using CO<sub>2</sub> as the building block, the reaction needs a driving force, either from a higher energetic reaction partner (e.g., H<sub>2</sub>, NH<sub>3</sub>, epoxides, bases, metals, organometallics) or by energy input to the process (heat, light, electricity). Nevertheless, for a series of compounds it is an ideal building block and has been applied since decades for the synthesis of urea and inorganic as well as organic carbonates on a large industrial scale. Therefore, there is potential to extend the use of CO<sub>2</sub> as a building block for industrial organic synthesis in near future within certain boundaries.

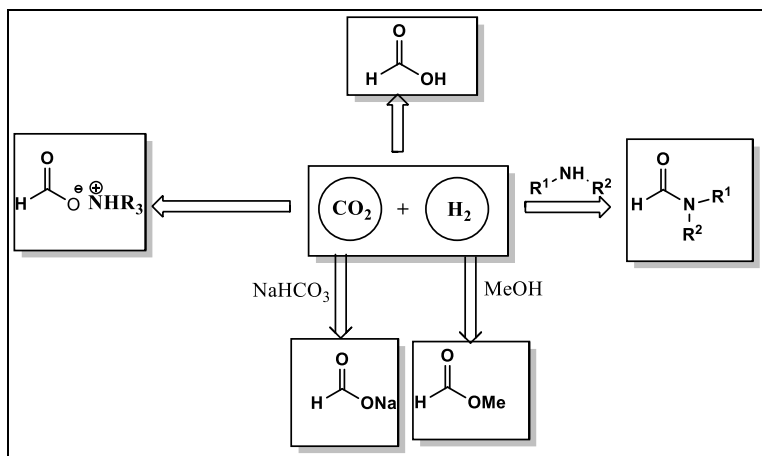
For synthetic use, the CO<sub>2</sub> must be relatively pure and available on chemical production sites. In certain processes, pure CO<sub>2</sub> is isolated as a by-product, for example, from ammonia plants, steam reforming units, or ethylene oxide plants. Despite the current use for the above-mentioned products, these processes are very large and much more pure CO<sub>2</sub> is released to the atmosphere than can be utilized. Therefore, on bigger chemical production sites, pure CO<sub>2</sub> for synthetic purposes is nowadays available in sufficient amounts to produce the chemicals discussed herein. For sure, one must think about other CO<sub>2</sub> sources (e.g., isolation from fuel gas or even the atmosphere), while going into a large-scale fuel production based on CO<sub>2</sub> or if industry moves completely away from fossil carbon-based resources in a future scenario.

For an economic and sustainable utilization of CO<sub>2</sub> in synthesis, it is essential that the reaction has a high atom economy, avoiding the formation of by-products and waste. Especially for the bulk chemicals mentioned in this review, the use of relatively expensive co-reagents which are delivering the driving force for the reaction but are ending up as wastes after the reaction is not desirable. For most of the reactions requiring at least stoichiometric amounts of co-reagents like organometallics, metals or bases. This review describes only synthetic protocols where the co-reagents used to drive the reaction are also relatively easy to regenerate. The overall energy consumption for a synthesis utilizing CO<sub>2</sub> is equally important and must be critically evaluated and compared with other alternatives not employing CO<sub>2</sub>.



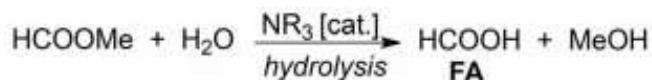
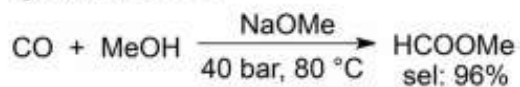
# ❖ Formic Acid and Carboxylation Reactions

Formic acid (HCOOH; FA) and its derivatives such as formamides or formic acid esters can be easily accessed by the hydrogenation of CO<sub>2</sub> using homogeneous or heterogeneous catalysts. Within the past 20 years, several catalytic systems have been reported for these transformations, including those involving the hydrogenations performed in the presence of inorganic bases (Scheme 1)

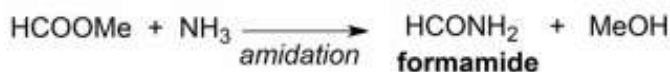
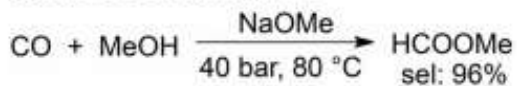


**Scheme 1**

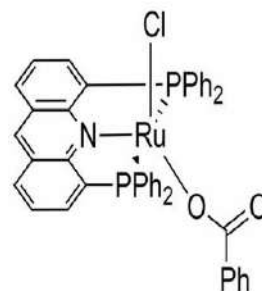
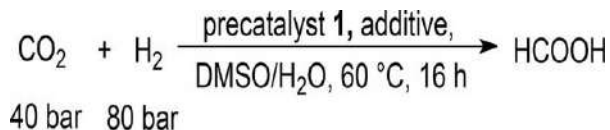
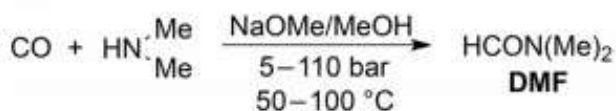
## **synthesis of FA**



## **synthesis of formamide**



## **synthesis of DMF**



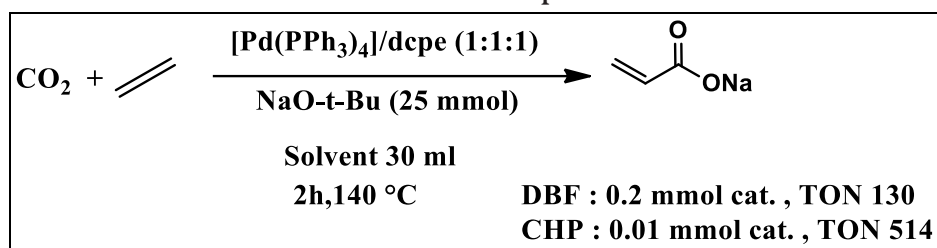
**1 = [Ru(Acriphos)(PPh<sub>3</sub>)(Cl)(PhCO<sub>2</sub>)]**

Current industrial routes for the Production of FA and its derivatives based on CO.

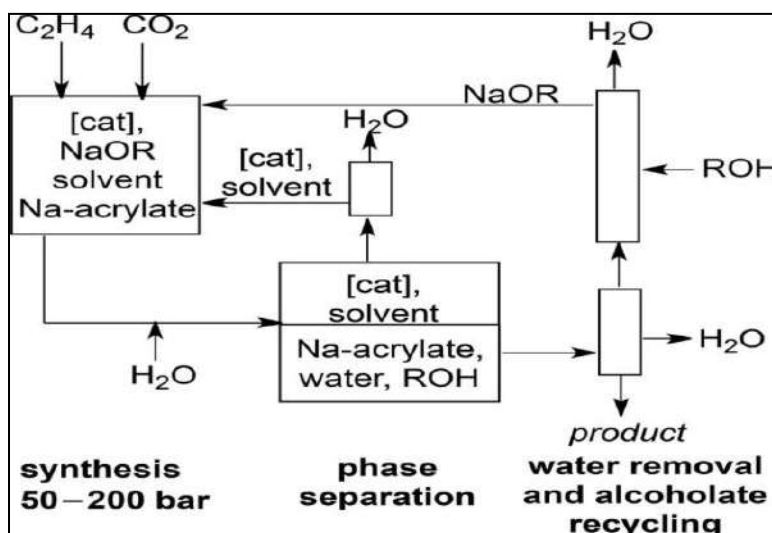
## ❖ Carboxylation of Olefins

The carboxylation of olefins to the corresponding unsaturated carboxylic acids is another attractive way to use CO<sub>2</sub> as a building block. The carboxylation of ethylene has the highest potential, since the formed sodium acrylate is the desired product and is currently used industrially on a multimillion ton scale for the production of super-adsorbents or dispersants. This carboxylation reaction has been achieved in the last years by using homogeneous nickel or palladium catalysts in the presence of an appropriate sodium base. Use of NaOH itself results in the formation of a stable carbonate (NaHCO<sub>3</sub>) under a given CO<sub>2</sub> pressure. Therefore, sodium bases that are basic enough to allow the sodium acrylate formation but do not form irreversible carbonates under the reaction conditions are needed.

After an extensive screening, it was found that certain sodium phenolates and alkoxides like Na<sup>t</sup>BuO or Na<sup>i</sup>PrO do fulfill these requirements and can be used. As an example, use of a homogeneous Pd-dcpe catalyst with NaO-t-Bu as the base and cyclohexylpyrrolidone as the solvent resulted in a TON of up to 514 in the first run.

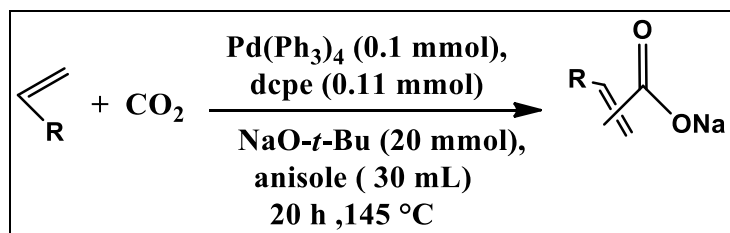


Carboxylation of ethylene in N-cyclohexylpyrrolidone (CHP) and N,N-dibutylformamide (DBF) using [Pd(PPh<sub>3</sub>)<sub>4</sub>]/dcpe as the catalyst



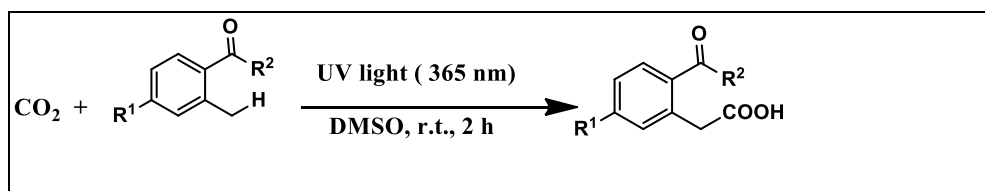
From an economic perspective, the CO<sub>2</sub> route is also of high interest.

Additionally, under similar reaction conditions, it has been possible to carry out carboxylation reactions with other olefins like butadiene or propylene, whereby the corresponding sodium salts of the unsaturated carboxylic acids were obtained



## ❖ Carboxylation of Aromatics

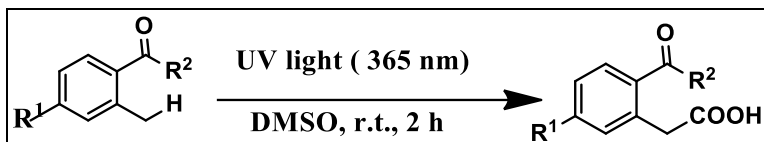
The carboxylation of phenolate salts with  $\text{CO}_2$ , named as the Kolbe–Schmitt reaction, is one of the oldest processes in organic synthesis uses  $\text{CO}_2$  as a building block. This reaction is mainly employed to produce salicylic acid. The synthesis of salicylic acid from this route was first accomplished in 1860s.



Kolbe–Schmitt carboxylation of phenol to salicylic acid

In spite of the technical usage of this reaction for the production of salicylic acid, its main drawback is the need for stoichiometric amounts of strong bases that results in the formation of stoichiometric amounts of salts as by-products, when the free acid is needed. Nevertheless, the whole reaction is driven by the salt formation step to achieve functionalisation of the aromatics with  $\text{CO}_2$ .

In a parallel context, a unique carboxylation reaction of  $\alpha$ -alkylphenyl ketones has also been developed that utilizes UV irradiation for the production of *o*-acylphenylacetic acids. Interestingly this methodology avoids the use of stoichiometric amounts of sacrificial reagents. Furthermore, the reaction has been proposed to proceed through the formation of highly reactive *o*-quinodimethane intermediates that are energetically susceptible to undergo cycloaddition reactions with  $\text{CO}_2$ .



R1= H, R2= Me; 63%  
 R1= H, R2 = CH<sub>2</sub>Ph; 87%  
 R1= H, R2 = p-ClC<sub>6</sub>H<sub>4</sub>; 61%  
 R1= OMe, R2 = Ph; 65%  
 R1= CF<sub>3</sub>, R2= Ph; 83%

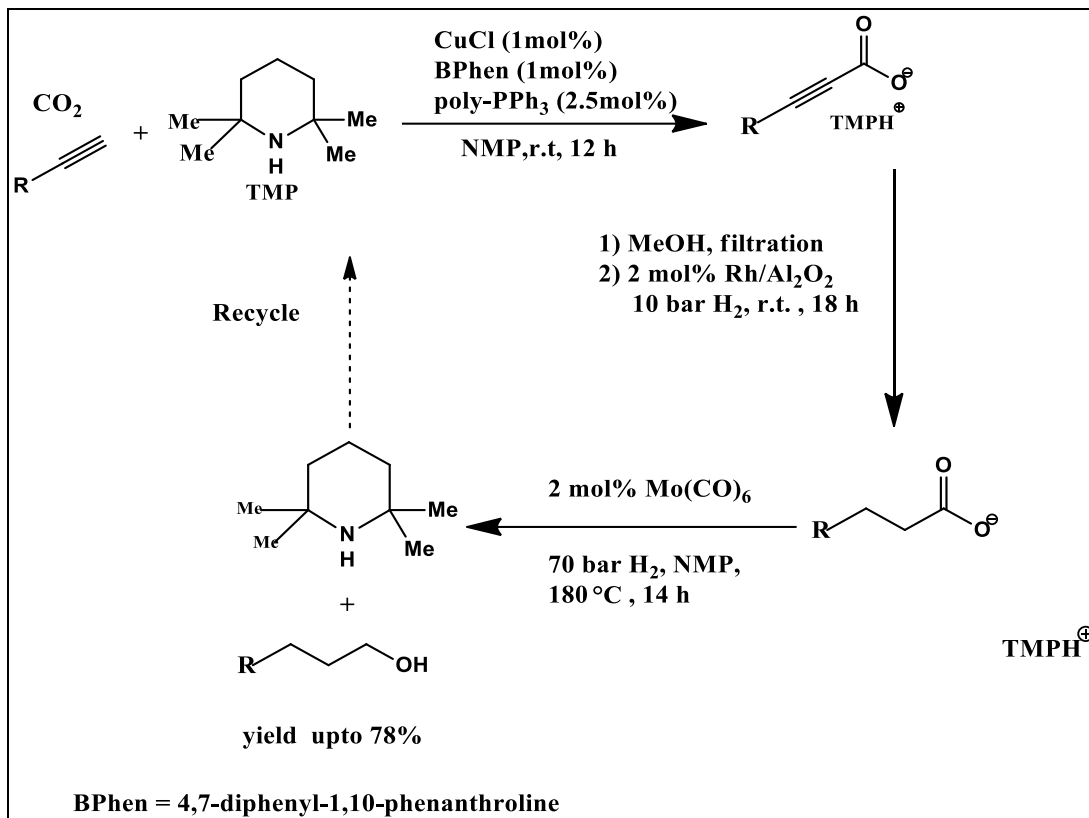
Carboxylation of ortho-alkylphenyl ketones with CO<sub>2</sub> under UV light irradiation.

### ❖ Carboxylation of Alkynes

The carboxylation of terminal alkynes to propargylic acids in the presence of bases is also well known. But its industrial applicability on a larger scale is limited by the fact that an acid has to be added to form the free carboxylic acid, which again results in stoichiometric salt formation as waste (usually propargylic acids were produced via oxidation of the corresponding propargylic alcohols).

To overcome this issue, an elegant system was reported recently using propargylic acid salts as intermediates to produce alcohols. By using tetramethylpiperidine (TMP) as the base, the carboxylation of alkynes was achieved with a copper catalyst. This salt could further be hydrogenated in two steps to the corresponding saturated alcohol and the free amine, which can be recycled back to the first step. No stoichiometric amounts of salts were formed as waste in this approach.

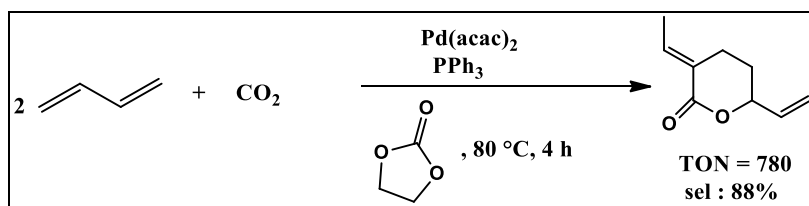
If successfully transferred to acetylene, the most frequently used alkyne in the industry, this concept could allow access to the bulk chemical 1,4-butanediol based on CO<sub>2</sub>, acetylene and H<sub>2</sub> without the use of formaldehyde (1,4-butanediol is currently mainly produced by the reaction of acetylene with formaldehyde to afford 1,4-butyne-3,5-diol followed by hydrogenation).



Sequential synthesis of alcohols by carboxylation of terminal alkynes

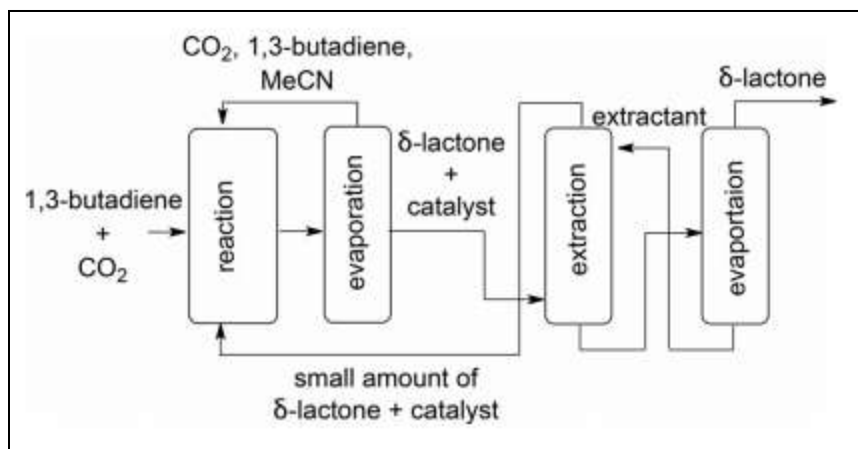
## ❖ Lactones from Dienes

The telomerization of butadiene with CO<sub>2</sub> by using homogeneous Pd catalysts has been known since the 1970s. Subsequent research initiatives over the past years have led to catalytic systems constituting Pd associated with phosphine ligands that provide the best selectivities towards the unsaturated  $\delta$ -lactone (3-ethylidene-6-vinyltetrahydro-2H-pyran-2-one), without the use of stoichiometric reagents.



### Palladium-catalyzed telomerization of 1,3-butadiene and CO<sub>2</sub> to a $\delta$ -lactone

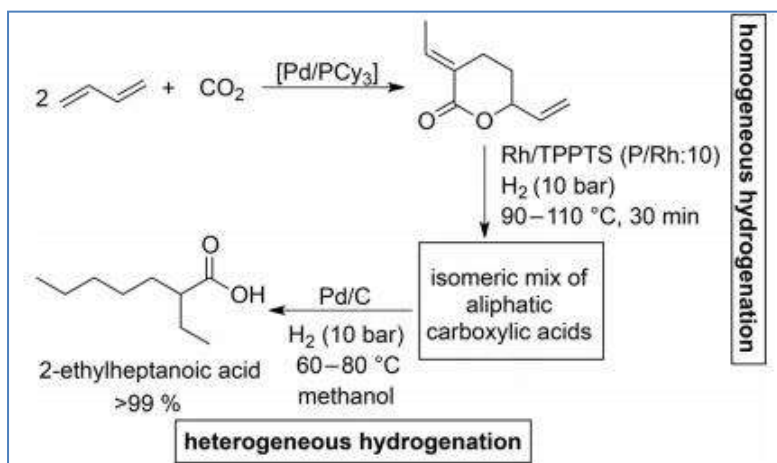
In industries, extraction technique is being used to carry out telomerization, where the  $\delta$ -lactone is extracted out of the product mixture [after evaporating the reaction solvent (MeCN)] by using a solvent such as 1,2,4-butanetriol and the catalyst left behind is recycled back to the reactor.



Continuous miniplant for the telomerization of 1,3-butadiene and  $\text{CO}_2$  to a  $\delta$ -lactone using extractive catalyst recycle.

Due to the straightforward approaches available for its synthesis, the  $\delta$ -lactone was further evaluated as a potential platform chemical for its transformation into a variety of chemical intermediates. For example, starting from butadiene by following a two step hydrogenation route, 2-ethylheptanoic acid can be obtained in excellent yields through the  $\delta$ -lactone intermediate, on the other hand a methoxycarbonylation, followed by hydrogenation of the  $\delta$ -lactone resulted in a branched C10-diol.

Although the products derived from the  $\delta$ -lactone are discussed as new intermediates but so far, they do not fit in existing industrial value chains like those for polymers. Therefore, the potential of these intermediates and the resulting products must be further evaluated to determine whether or not they are economic alternatives to the current related products.



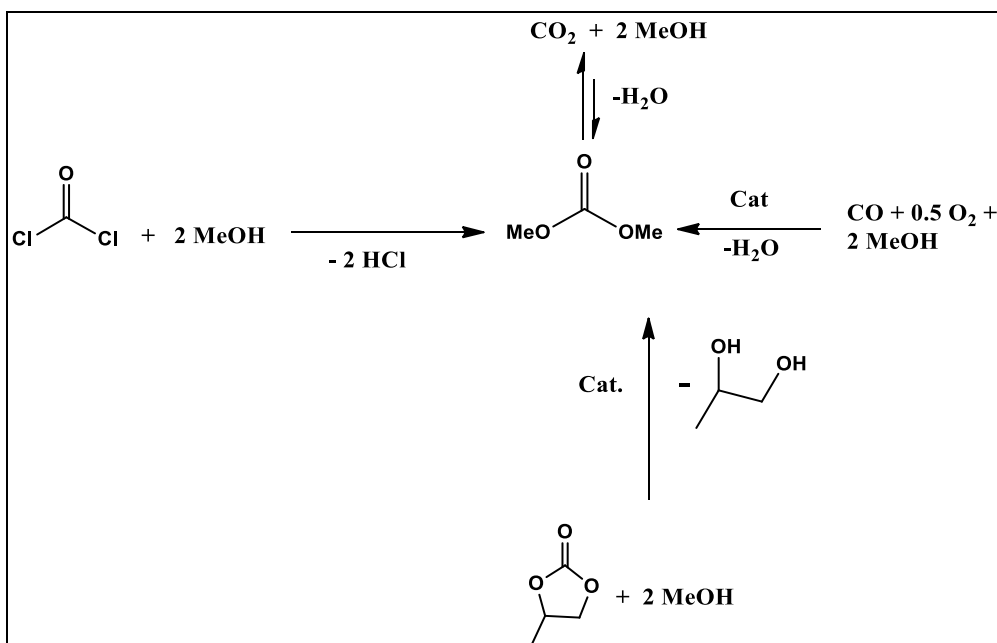
Three-step process for the synthesis of 2-ethylheptanoic acid starting from 1,3-butadiene and  $\text{CO}_2$ .

## ❖ Organic Carbonates

Linear and cyclic organic carbonates are widely used in the chemical industry as solvents, alkylating agents, monomers or in transesterification reactions. The most important carbonates are dimethyl carbonate (DMC), diethyl carbonate (DEC), diphenyl carbonate (DPC), ethylene carbonate (EC) as well as propylene carbonate (PC) and they are produced on an overall scale of a several 100 kilotons p.a.

## ❖ Linear Carbonates

Linear carbonates are nowadays mainly produced by two different route: (i) the oxidative carbonylation of an alcohol, whereby good yields and selectivities are achieved ( right arrow) and (ii) the transesterification of PC with methanol, which is nowadays the major industrial route for the synthesis of DMC in China. lower arrow). Also carbonates like diphenyl carbonate (DPC) are best obtained by reacting dimethyl carbonate (DMC) with phenol. The conventional  $\text{COCl}_2$  route ( left arrow) is nowadays hardly used for the synthesis of bulk carbonates.



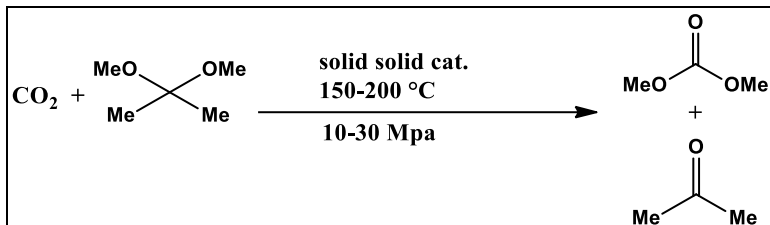
### Comparison of routes for the synthesis of dimethyl carbonate (DMC)

The transesterification of PC, made from propylene oxide and  $\text{CO}_2$  is an indirect way to utilize  $\text{CO}_2$  in the synthesis of linear carbonates. As a significant amount of industrially produced propylene oxide is anyway transformed to propylene glycol by hydrolysis, one can get to DMC by a process based on the  $\text{CO}_2$  utilization route without forming any unwanted by-products or the need for additional drying agents. Drawbacks of this method

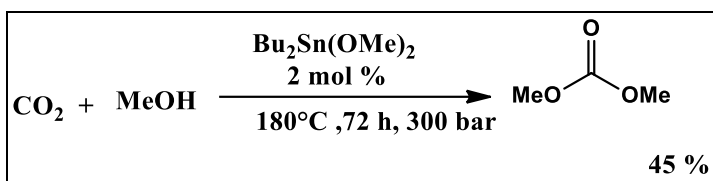
are 1) the energy consumption to separate the azeotropes is very high 2) not much economic.

There are many other methods to convert CO<sub>2</sub> into linear carbonates-

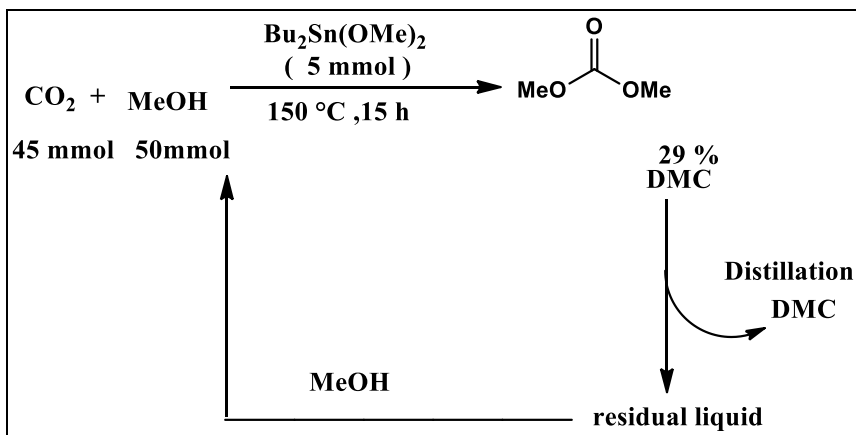
### Mitubishi heavy industries



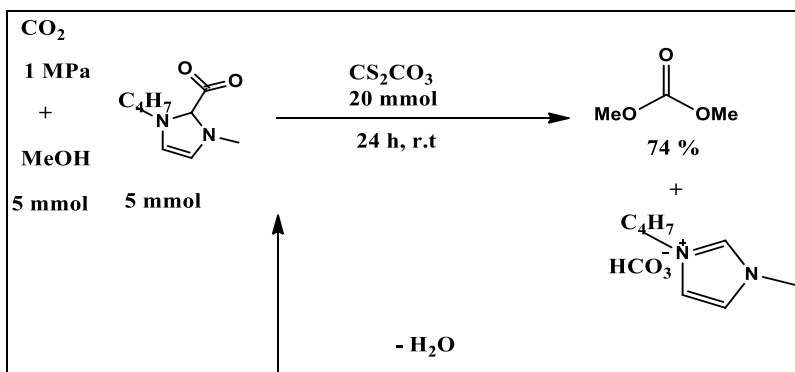
### Toshiyasu Sakakura et. al.



### Asahi Kasei Chemical Corporation



### X. Hu and Y. Wu et. al



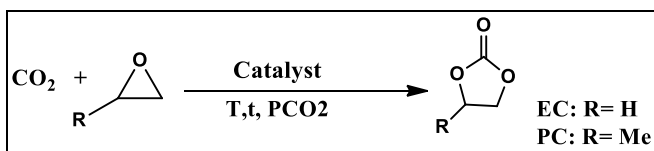


## ❖ Cyclic Carbonates

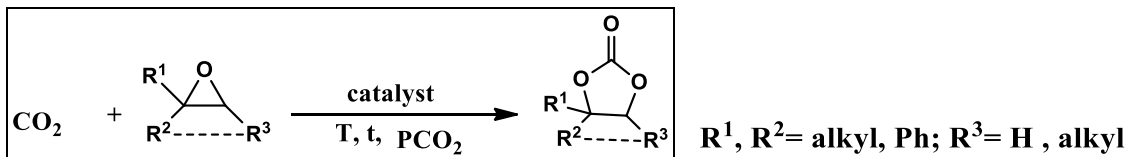
Five-membered cyclic carbonates are usually obtained by the reaction of the corresponding oxiranes with CO<sub>2</sub>. The driving force for this reaction is the high energy content of the oxirane. Industrially EC and PC are produced on a significant scale, starting from the corresponding ethylene and propylene oxides.

A broad series of substituted cyclic carbonates was also formed in moderate to good yields, from the corresponding oxiranes, whereby also different catalysts are applied. But in all these cases, first the reactive oxiranes must be produced, in order to utilize CO<sub>2</sub> as the building block. The cyclic carbonates can also be obtained from 1,2- or 1,3-diols, but like linear alkyl carbonates, the yields in the equilibrium are usually low when no water trapping agent is added. In the presence of water trapping agents like a zeolite or 2-cyanopyridine, from which the corresponding amide is formed via hydrolysis, significantly higher yields of the cyclic carbonate of up to 99% are possible. Another interesting cyclic carbonate is glycerol carbonate, which can be used as a bio-based monomer or solvent. It is usually produced by the reaction of DMC with glycerol, but can also be obtained directly from glycerol and CO<sub>2</sub>.

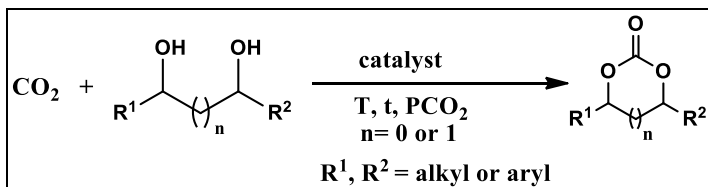
### Synthesis of five-membered cyclic carbonates from oxiranes.



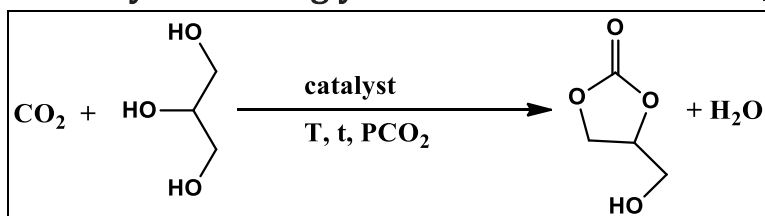
### Recent synthesis routes for cyclic carbonates from CO<sub>2</sub> and epoxides.



### Synthesis of cyclic carbonates from CO<sub>2</sub> and diol.



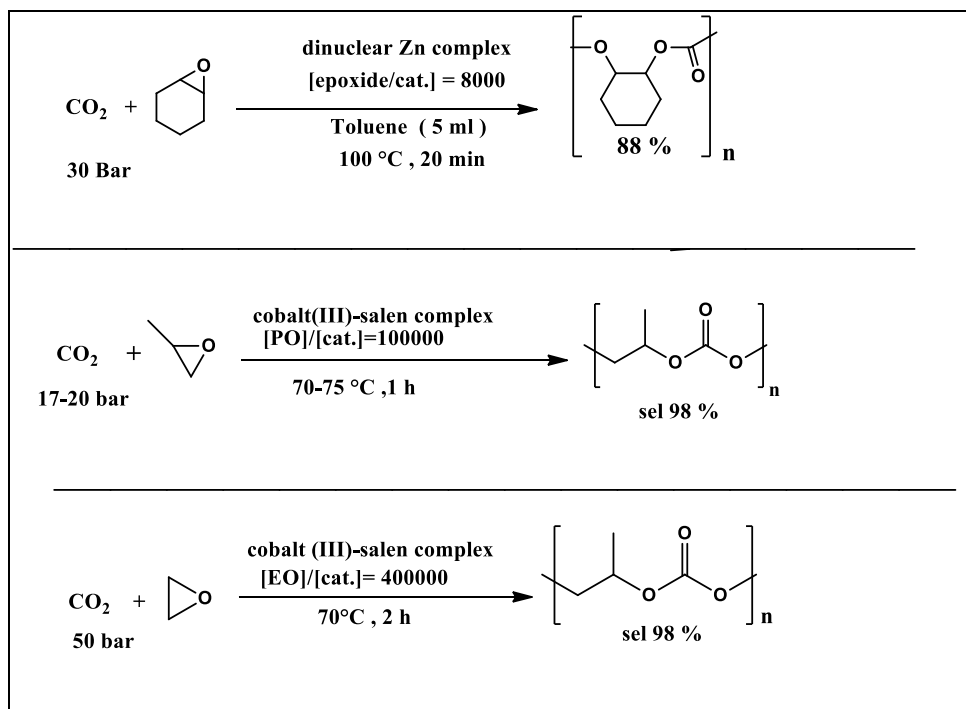
## Direct synthesis of glycerol carbonates from CO<sub>2</sub> and glycerol.



## ❖ Polycarbonates and Polyetherol Carbonates

The copolymerization of propylene oxide with CO<sub>2</sub> using ZnEt<sub>2</sub> in combination with water was first reported in 1969 and the synthesis of polycarbonates and polyetherols based on the copolymerization of oxiranes with CO<sub>2</sub> has attracted a lot of attention during the last years. From an industrial point of view, this reaction highly is attractive: (i) it is in principle by-product free, (ii) it does not require the addition of stoichiometric co-reagents, (iii) the products contain up to 50% CO<sub>2</sub> /O<sub>2</sub> and especially the oxiranes ethylene oxide and propylene oxide are industrially available on a large scale.

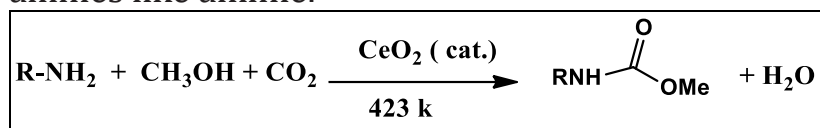
For the synthesis of polycarbonates, several active catalysts based on Zn or Co were reported. Unfortunately, the pure polymers based on ethylene oxide and propylene oxide do not show very good properties thus limiting their commercial attractiveness, but they can be utilized in blends with other polymers. The first commercial application of these polycarbonates was announced by SK innovation under the brand GreenPol.



## ❖ Linear Carbamates and Isocyanates

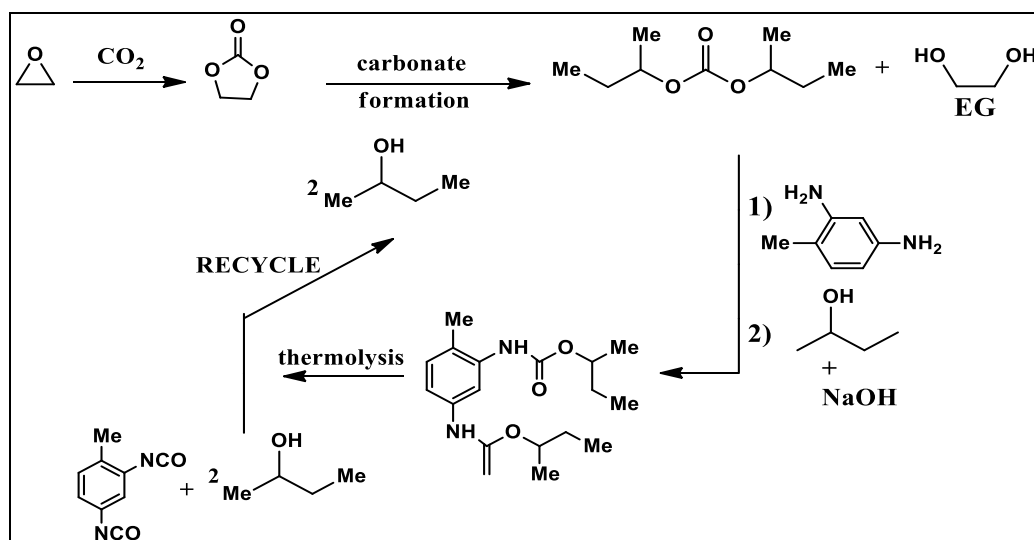
Isocyanates are important monomers produced on a large scale, and are mainly used for the production of polyurethanes. Currently, most of the isocyanates are produced by reacting the corresponding amines with phosgene. But this method is a bit costly (energy consumption, investments). Therefore, phosgene-free alternatives for isocyanate synthesis were investigated. One approach is the use of CO<sub>2</sub>-based carbamates as intermediates in isocyanate synthesis.

Carbamates can, in principle, be accessed by the reaction of the corresponding amine with CO<sub>2</sub> in the presence of an alcohol. For the technically not relevant benzylamine or aminomethylcyclohexane, the carbamates are directly accessible in good yields without the use of drying agents, but this attempt fails for the commercially relevant aromatic amines like aniline.



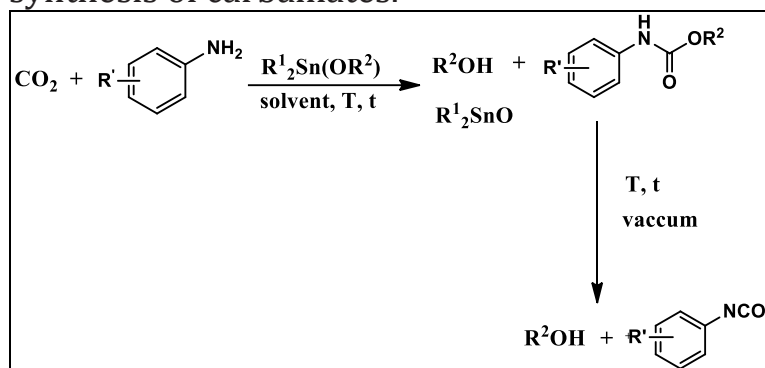
### Synthesis of carbamates directly from amine, CO<sub>2</sub> and alcohol.

Different concepts were presented to prepare aromatic carbamates based on CO<sub>2</sub> as the building block. In a concept reported by BASF, the initial step involves the production of ethylene carbonate from ethylene oxide and CO<sub>2</sub>. By using 2-butanol, a transesterification is performed to obtain diisobutyl carbonate and ethylene glycol as a valuable by-product. The linear carbonate is then reacted with toluenediamine to afford the corresponding bis-carbamate and 2-butanol. For high conversions, sodium 2-butylate is required as a co-reagent, which has to be synthesized in another energy-demanding step from the alcohol and NaOH. The obtained bis-carbamate can then be thermally cracked to the bisisocyanate and 2-butanol, which is recycled in to the carbonate formation step.



Process concept for the combined production of ethylene glycol (EG) and 2,4-toluene diisocyanate (TDI).

To simplify the synthesis of the carbamates based on CO<sub>2</sub>, the Ashai concept for the production of carbonates based on CO<sub>2</sub> and organotin reagents was modified for the synthesis of carbamates.

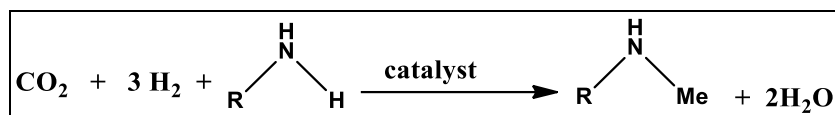


Organotin(IV) alkoxide-catalyzed synthesis of industrially relevant carbamates and isocyanates.

## ❖ Methylation Reactions

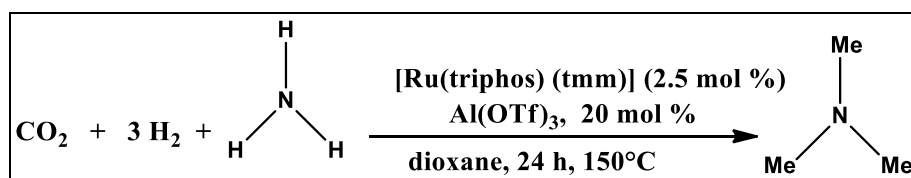
### ❖ N-Methylation

CO<sub>2</sub> in combination with H<sub>2</sub> can also be utilized in several N-methylations so far achieved on different substrates by the use of homogeneous ruthenium-triphos catalysts in combination with additives like acids or LiCl or with heterogeneous catalysts.



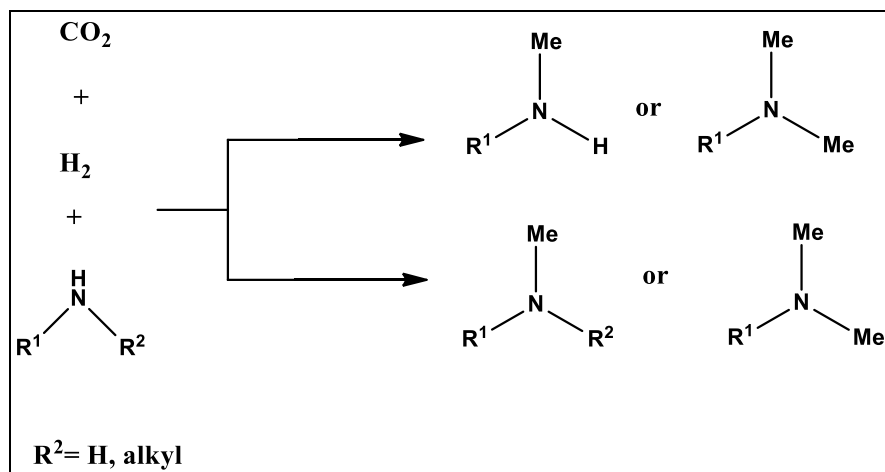
General scheme for the N-methylation of amines using CO<sub>2</sub> and H<sub>2</sub>.

In the state of the art production of bulk methylamines, usually MeOH is employed as the methylating agent with the use of heterogeneous catalysts. MeOH-based methyl- and dimethylamine routes are frequently used to introduce methylamine functionalities. For an industrial application, the CO<sub>2</sub>/H<sub>2</sub>-based routes have to be competitive with the established and optimized systems based on MeOH, especially as MeOH can easily be obtained from CO<sub>2</sub>/H<sub>2</sub>. Using Ru-triphos with Al(OTf)<sub>3</sub> as co-catalyst, trimethylamine is accessible from ammonia and CO<sub>2</sub>/H<sub>2</sub>.



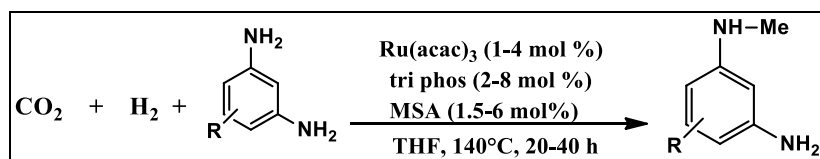
## Synthesis of trimethylamine TMA from NH<sub>3</sub> with CO<sub>2</sub> and H<sub>2</sub>

The reaction proceeds via formamides as intermediates, which are further deoxygenated to the N-methylamines. The Ru-triphos system can also be used for a series of other aliphatic and aromatic amines, as shown by the groups of Beller, Klankermayer and Leitner during the last years.



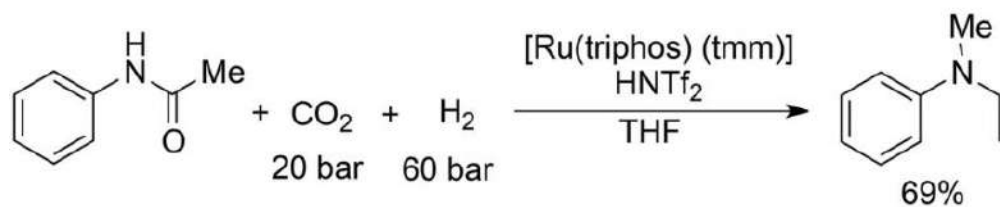
## N-Methylation of aliphatic and aromatic amines using CO<sub>2</sub> and H<sub>2</sub>.

For aromatic diamines, a selective N-monomethylation is possible, which is difficult to achieve when MeOH and the established catalysts are used.

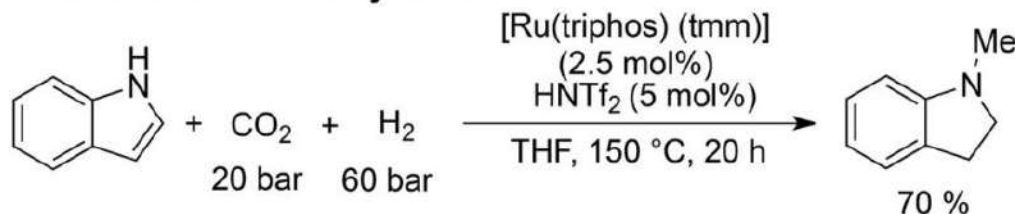


## Selective N-monomethylation of diamines

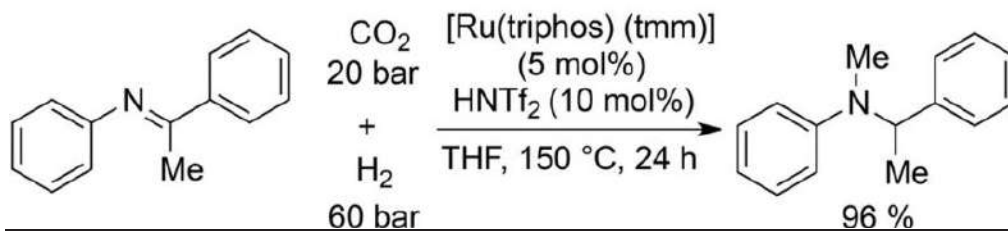
### amide reduction + methylation



### olefin reduction + methylation

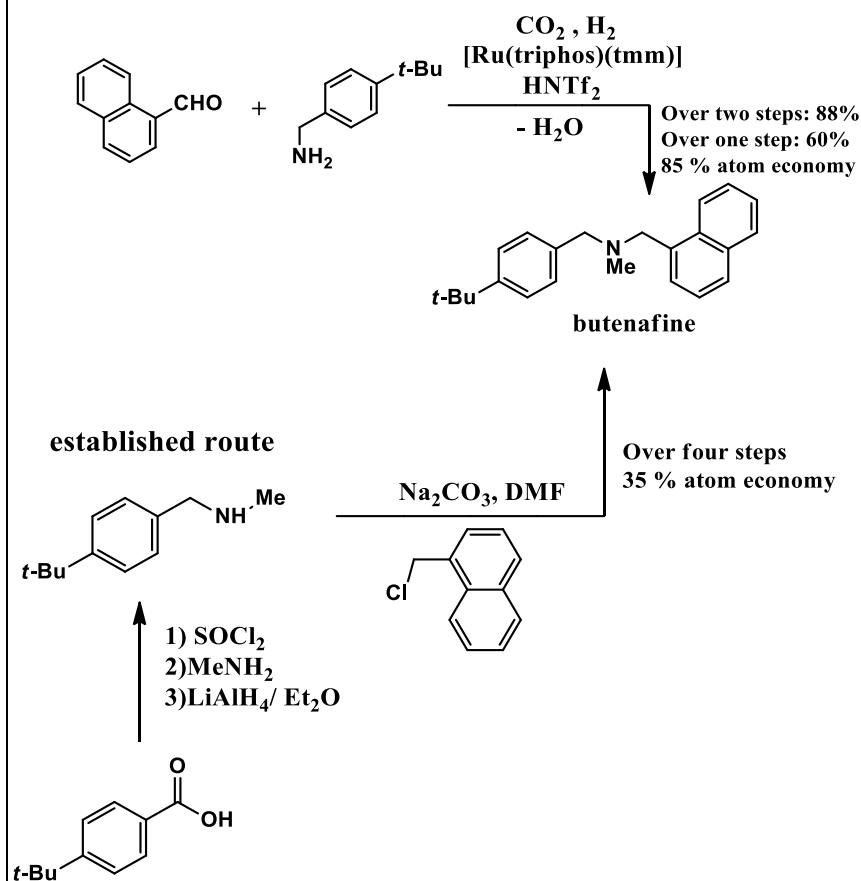


### imine reduction + methylation



Sequential hydrogenation/N-methylation of acetanilide, indole and imines.

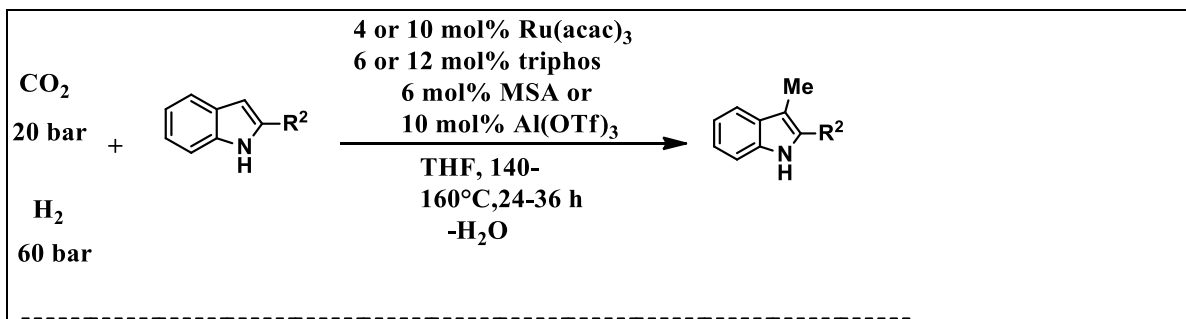
Klankermayer et. al

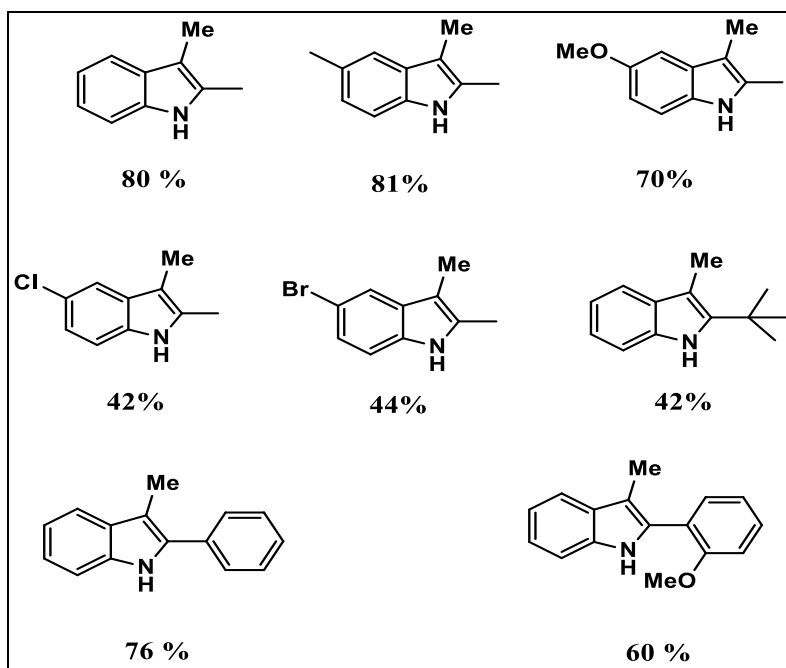


Application of N-methylation for the synthesis of the antifungal agent butenafine with CO<sub>2</sub> and H<sub>2</sub> in comparison to the established methods.

## ➤ C-Methylation

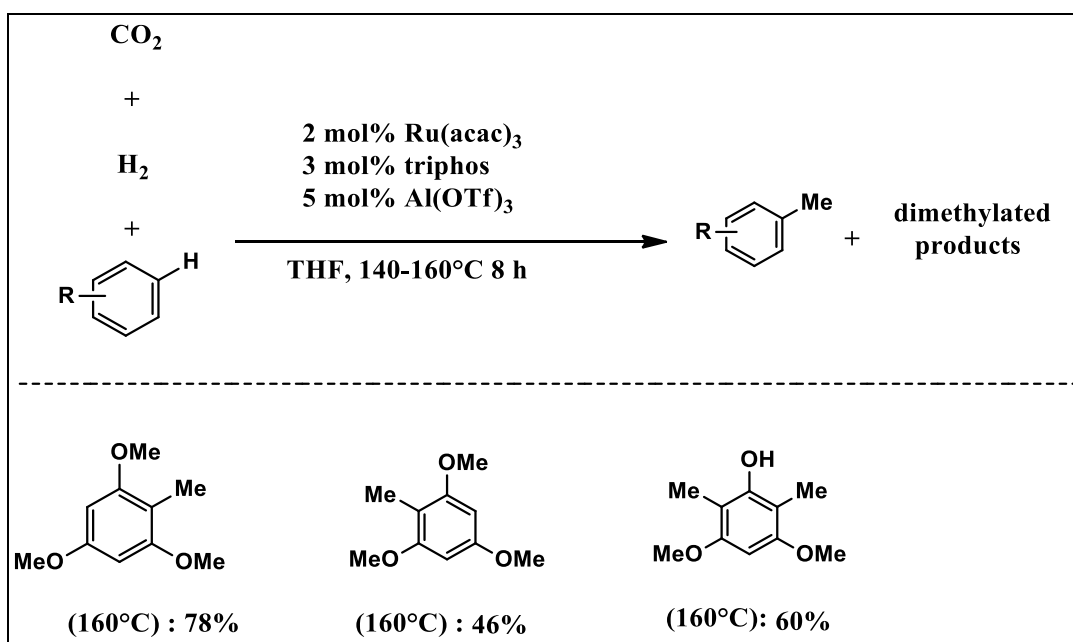
Like in the N-methylation, CO<sub>2</sub> /H<sub>2</sub> can also be used for the methylation of aromatic compounds to replace MeOH as the CH<sub>3</sub> source. For example, heteroarenes can be methylated on the heteroarene ring by again using a Ru-triphos catalyst in combination with an acidic co-catalyst.





### C-H methylation of heteroarenes with CO<sub>2</sub> and H<sub>2</sub>

It is also possible to perform the methylation on electron-rich arenes at temperatures of up to 160°C. This approach could be an alternative to the methylation of electron-rich arenes, like phenol to ortho-cresol with MeOH which is carried out at 350–400°C in the liquid phase, if the reaction could be extended to the less reactive phenol and related substrates.



### C-H methylation of arenes with CO<sub>2</sub> and H<sub>2</sub>



## ❖ Conclusion

The utilization of CO<sub>2</sub> as a building block to produce a wide variety of chemicals and materials poses a challenge but also provides new opportunities to diverse industrial methods. Within the large number of reports in the last decades on the utilization of CO<sub>2</sub> as a building block, several methods have the potential for industrial usage. For example, Polyetherol carbonates and polycarbonates synthesis based on CO<sub>2</sub> are starting to be commercialized and will extend the industrial portfolio on CO<sub>2</sub>-based chemicals. On the other hand, many other approaches are not competitive yet in the current stage of development compared to the state of the art routes, due to a significantly higher energy consumption or the use of expensive co-reagents. But as a shift away from the fossil carbon sources is only a matter of time, there is still a high demand to develop new and elegant concepts for a sustainable and economic utilization of CO<sub>2</sub> as a building block in industrial organic synthesis.

## ❖ Acknowledgement

I would like to express my special thanks to my guide **Dr. Somjit Hajra** for his guidance and support in completing my presentation. I would also like to extend my gratitude to **Dr. Sebanti Basu** and to all the Professors of the chemistry department for guiding me in the completion of the presentation.

## ❖ Reference

- [1] T. Schaub, R. A. Paciello, M. Limbach, in: Applied Homogeneous Catalysis with Organometallic Compounds: A Comprehensive Handbook in Four Volumes, (Eds.: B. Cornils, W. A. Hermann, M. Beller, R. A. Paciello), Wiley-VCH, Weinheim, 2018, pp 1601–1614.
- [2] S. Topham, A. Bazzanella, S. Schiebahn, S. Luhr, L. Zha, A. Otto, D. Stolten, in Ullmann's Encyclopedia of Industrial Chemistry, Wiley-VCH, Weinheim, 2014, DOI: 10.1002/14356007.a05165.pub2.
- [3] R. Schlögel, (Ed.), Chemical Energy Storage, de Gruyter, Berlin, Boston, 2013.
- [4] J. H. Meessen, in: Ullmann's Encyclopedia of Industrial Chemistry, Wiley-VCH, Weinheim, 2012, Vol. 37, pp 657–695.

[5] a) J. Ott, V. Gronemann, F. Pontzen, E. Fiedler, G. Grossmann, D. B. Kersebohm, G. Weiss, C. Witte, in: Ullmann's Encyclopedia of Industrial Chemistry, Wiley-VCH, Weinheim, 2012,

DOI: 10.1002/14356007.a16465.pub3; b) E. Kunkes, M. Behrens, in: Chemical Energy Storage,

(Ed.: R. Schlögl), de Gruyter, Berlin, Boston, 2013; pp 413–443; c) <http://carbonrecycling.is/george-olah/> (accessed 25.08.2018).

[6] F. Ausfelder, A. Bazzanella, Diskussionspapier: Verwertung und Speicherung von CO<sub>2</sub>, 2008, Dechema, Frankfurt. a) W. Leitner, *Angew. Chem* 1995, 107, 2391–2405; *Angew. Chem. Int. Ed. Engl.* 1995, 34, 2207–2221; b) P. G. Jessop, T. Ikariya, R. Noyori, *Chem. Rev.* 1995, 95, 259–272; c) P. G. Jessop, F. Jol, C.-C. Tai, *Coord. Chem. Rev.* 2004, 248, 2425–2442; d) P. G. Jessop, in: *The Handbook of Homogeneous Hydrogenation*, (Eds.: J. G. de Vries, C. J. Elsevier), WileyVCH, Weinheim, 2008, pp 489–511; e) W. Wang, S. Wang, X. Ma, J. Gong, *Chem. Soc. Rev.* 2011, 40, 3703–3727; f) M. Aresta, A. Dibenedetto, A. Angelini, *Chem. Rev.* 2014, 114, 1709–1742; g) W.-H. Wang, Y. Himeda, J. T. Muckerman, G. F. Manbeck, E. Fujita, *Chem. Rev.* 2015, 115, 12936–12973; h) J. Klankermayer, W. Leitner, *Science* 2015, 350, 629–630; i) G. H. Gunasekar, K. Park, K. D. Jung, S. Yoon, *Inorg.*

*Chem. Front.* 2016, 3, 882–895; j) A. Alvarez, A. Bansode, A. Urakawa, A. V. Bavykina, T. A. Wezendonk,

M. Makkee, J. Gascon, F. Kapteijn, *Chem. Rev.* 2017, 117, 9804–9838; k) W.-H. Wang, X. Feng, M. Bao, in: *Transformation of Carbon Dioxide to Formic Acid and Methanol*, Springer, Singapore, 2018, pp 7–42.

[10] S. C. E. Stieber, N. Huguet, T. Kageyama, I. Jevtovic, P. Ariyananda, A. Gordillo, S. A. Schunk, F. Roming

er, P. Hofmann, M. Limbach, *Chem. Commun.* 2015, 51, 10907–10909.

[7] S. Manzini, N. Huguet, O. Trapp, T. Schaub, *Eur. J. Org. Chem.* 2015, 7122–7130.

[8] S. Manzini, A. Cadu, A. C. Schmidt, N. Huguet, O. Trapp, R. Paciello, T. Schaub, *ChemCatChem* 2017, 9, 2269–2274.

[9] a) H. Kolbe, *Justus Liebigs Ann. Chem.* 1860, 113, 125–127; b) A. S. Lindsey, H. Jeskey, *Chem. Rev.* 1957, 57, 583–620

[10] For selected examples of Kolbe–Schmitt carboxylation, see: a) D. Cameron, H. Jeskey, O. Baine, *J. Org. Chem.* 1950, 15, 233–236; b) J. Cason, G. O. Dyke, *J. Am. Chem. Soc.* 1950, 72, 621–622; c) O. Baine, G. F. Adamson, J. W. Barton, J. L. Fitch, D. R. Swayampati, H. J. Jeskey, *J. Org. Chem.* 1954, 19, 510–514; d) F. Wessely, K. Benedikt, H. Benger, H. Friedrich, F. Prillinger, *Monatsh. Chem.* 1950, 81, 1071–1091; e) J. M. Gnam, B. S. Green, R. Arad-Yellin, P. M. Keehn, *J. Org. Chem.* 1991, 56, 4525–4529; f) Y. Kosugi, Y. Imaoka, F. Gotoh, M. A. Rahim, Y. Matsui, K. Sakanishi, *Org. Biomol. Chem.* 2003, 1, 817–821; g) Z. Markovic', S. Markovic', N. Begovic', *J. Chem. Inf. Model.* 2006, 46, 1957–1964; h) Z. Markovic', S. Markovic', N. Manojlovic', J. Predojevic'-Simovic', *J. Chem. Inf. Model.* 2007, 47, 1520–1525; i) X. Yan, Z. Cheng, Z. Yue, P. Yuan, *Res. Chem. Intermed.* 2014, 40, 3059–3071.

[11] a) L. J. Gooßen, N. Rodríguez, F. Manjolinho, P. P. Lange, *Adv. Synth. Catal.* 2010, 352, 2913–2917; b) X.

Zhang, W.-Z. Zhang, X. Ren, L.-L. Zhang, X.-B. Lu, *Org. Lett.* 2011, 13, 2402–2405; c) D. Y. Yu, Y. G. Zhang, *Green Chem.* 2011, 13, 1275–1279; d) D. Yu, M. X. Tan, Y. Zhang, *Adv. Synth. Catal.* 2012, 354, 969–974; e) M. Arndt, E. Risto, T. Krause, L. J. Gooßen, *ChemCatChem* 2012, 4, 484–487.

[12] K. Buchmüller, N. Dahmen, E. Dinjus, D. Neumann, B. Powietzka, S. Pitter, J. Schön, *Green Chem.* 2003, 5, 218–223.

[13] A. Behr, M. Becker, *Dalton Trans.* 2006, 4607–4613.

[14] A. Behr, P. Bahke, B. Klinger, M. Becker, *J. Mol. Catal. A: Chem.* 2007, 267, 149–156.

[15] H. J. Buysch, in: *Ullmann's Encyclopaedia of Industrial Chemistry*, Vol. 7, Wiley-VCH, Weinheim, 2012, pp 45–71.

[16] T. Sakakura, K. Kohno, *Chem. Commun.* 2009, 1312–1330.

[17] Reviews highlighting the direct synthesis of linear carbonates from CO<sub>2</sub> and alcohol and references therein: a) K. Shukla, V. C. Srivastava, *RSC Adv.* 2016, 6, 32624–32645; b)

- N. Kindermann, T. Jose, A. W. Kleij, *Top. Curr. Chem.* 2017, 375, 15; c) A. A. Chaugule, A. H. Tamboli, H. Kim, *Fuel* 2017, 200, 316–332;
- d) H.-Z. Tan, Z.-Q. Wang, Z.-N. Xu, J. Sun, Y.-P. Xu, Q.-S. Chen, Y. Chen, G.-C. Guo, *Catal. Today* 2018, doi.org/10.1016/j.cattod.2018.02.021.
- [18] J. Steinbauer, T. Werner, *ChemSusChem* 2017, 10, 3025–30
- [19] M. Aresta, A. Dibenedetto, F. Nocito, C. Pastore, *J. Mol. Catal. A* 2006, 257, 149–153.
- [20] L. P. Ozorio, C. J. A. Mota, *ChemPhysChem* 2017, 18, 3260–3265.29.
- [21] R. Ugajin, S. Kikuchi, T. Yamada, *Synlett* 2014, 25, 1178–1180.
- [22] H.-F. Jiang, A.-Z. Wang, H.-L. Liu, C.-R. Qi, *Eur. J. Org. Chem.* 2008, 2309–2312.
- [23] a) C. Gg r tler, in: *Technologie fg r Nachhaltigkeit und Klimaschutz - Chemische Prozesse und stoffliche Nutzung von CO<sub>2</sub>*, (Eds.: A. Bazzanella, D. Kr- mer), DECHEMA, Frankfurt, 2017, pp 44–49; b) A. Wolf, in: *Technologie fg r Nachhaltigkeit und Klimaschutz - Chemische Prozesse und stoffliche Nutzung von CO<sub>2</sub>*, (Eds.: A. Bazzanella, D. Kr- mer), DECHEMA, Frankfurt, 2017, pp 32–36.
- [24] G. Reuss, W. Disteldorf, A. O. Gamer, A. Hilt, in: *UllmannQ s Encyclopaedia of Industrial Chemistry*, Vol. 15, Wiley-VCH, Weinheim, 2012, pp 735–768.
- [25] K. I. Tominaga, Y. Sasaki, *Catal. Commun.* 2000, 1, 1– 3.
- [26] Q. Liu, L. Wu, I. Fleischer, D. Selent, R. Franke, R. Jackstell, M. Beller, *Chem. Eur. J.* 2014, 20, 6888–6894.
- [27] V. K. Srivastava, P. Eilbracht, *Catal. Commun.* 2009, 10, 1791–1795.
- [28] P. Kalck, M. Urrutigoity, *Chem. Rev.* 2018, 118, 3833– 3861.
- [29] Y. Li, I. Sorribes, T. Yan, K. Junge, M. Beller, *Angew. Chem.* 2013, 125, 12378–12382; *Angew. Chem. Int. Ed.* 2013, 52, 12156–12160.

- [30] K. Beydoun, T. V. Stein, J. Klankermayer, W. Leitner, *Angew. Chem.* 2013, 125, 9733–9736; *Angew. Chem. Int. Ed.* 2013, 52, 9554–9557.
- [31] K. Beydoun, G. Ghattas, K. Thenert, J. Klankermayer, W. Leitner, *Angew. Chem.* 2014, 126, 11190–11194; *Angew. Chem. Int. Ed.* 2014, 53, 11010–11014
- [32] K. Beydoun, K. Thenert, E. S. Streng, S. Brosinski, W. Leitner, J. Klankermayer, *ChemCatChem* 2016, 8, 135–138[137] Y. Li, X. Cui, K. Dong, K. Junge, M. Beller, *ACS Catal.* 2017, 7, 1077–1086.
- [33] a) S. V. Gredig, R. A. Koepfel, A. Baiker, *J. Chem. Soc. Chem. Commun.* 1995, 73–74; b) S. V. Gredig, R. A. Koepfel, A. Baiker, *Catal. Today* 1996, 29, 339–342; c) S. V. Gredig, R. A. Koepfel, A. Baiker, *Appl. Catal. A: General* 1997, 162, 249–260; d) K. Kon, S. M. A. H. Siddiki, W. Onodera, K. I. Shimizu, *Chem. Eur. J.* 2014, 20, 6264–6267; e) X. Cui, X. Dai, Y. Zhang, Y. Deng, F. Shi, *Chem. Sci.* 2014, 5, 649–655; f) X. Cui, Y. Zhang, Y. Deng, F. Shi, *Chem. Commun.* 2014, 50, 13521–13524; g) G. Tang, H.-L. Bao, C. Jin, X. H. Zhong, X. L. Du, *RSC Adv.* 2015, 5, 99678–99687; h) X. L. Du, G. Tang, H. L. Bao, Z. Jiang, X. H. Zhong, D. S. Su, J. Q. Wang, *ChemSusChem* 2015, 8, 3489–3496.
- [34] P. Roose, in: *Ullmann's Encyclopedia of Industrial Chemistry*, Wiley-VCH, Weinheim, 2015, DOI: 10.1002/14356007.a16535.pub5.
- [35] P. Roose, K. Eller, E. Henkes, R. Roszbacher, H. Hçke, in: *Ullmann's Encyclopedia of Industrial Chemistry*, Wiley-VCH, Weinheim, 2015, DOI: 10.1002/14356007.a02001.pub2.
- [36] Y. Li, T. Yan, K. Junge, M. Beller, *Angew. Chem.* 2014, 126, 10644–10648; *Angew. Chem. Int. Ed.* 2014, 53, 10476–10480.
- [37] H. G. Franck, J. W. Stadelhofer, in *Industrielle Aromatenchemie*, Springer Verlag, Berlin, 1987, p 173.

A LITERATURE REVIEW ON

# **A REFLECTION ON LITHIUM ION BATTERIES**

## **CATHODE CHEMISTRY**

(OXIDE CATHODES)



# **SCOTTISH CHURCH COLLEGE**

(UNIVERSITY OF CALCUTTA)

CU ROLL NO-223/CEM/1910/34  
CU REGISTRATION NUMBER:223-1211-0010-19  
SPECIAL PAPER: SP 44

NAME OF CANDIDATE  
SUMANNA SARANGI

NAME OF SUPERVISOR  
PROF. ANIRUDDHA GANGULY

*Sumanna Sarangi*  
SIGNATURE OF CANDIDATE

*Aniruddha Ganguly*  
SIGNATURE OF SUPERVISOR

**TABLE OF CONTENTS:**

Sl. No	Content	Page no.
1	ABSTRACT	3
2	INTRODUCTION	4
3	THE LITHIUM ION BATTERIES	5
4	DISCOVERY OF OXIDE CATHODES	6-8
5	CLASSIFICATION OF OXIDE CATHODES i. Layered oxides ii. Spinel oxides iii Polyanion oxides	8-12
6	ADVANTAGES AND DISADVANTAGES OF OXIDE CATHODES	12-13
7	OUTLOOK	13-15
8	THE NEED FOR RECYCLING	16
9	CONCLUSION	16
10	REFERENCES	16-18

## **ABSTRACT:**

The requirement of energy and power has pushed the civilization to the brink of exhaustion of non-renewable energy sources, which was somehow answered by the development of rechargeable batteries connected to renewable energy sources. However, the flow of time demands the cost of such contraption to be cheaper and long-lived in terms of life span. This has also brought us to the point of addressing the question regarding sustainable development. The study gives a brief insight on the history of rechargeable Li Batteries including the discovery of oxide cathodes, classification of these cathode materials and the merits and demerits of oxide cathodes in general. Furthermore, strategies that can help in achieving our objectives have been discussed as the outlook of the process. In addition to all this, we have also addressed the need for the recycling of cathode materials to help avoid exhaustion of finite resources in our usage. The resources at hand are helpful but finite as well. Therefore, the approach towards their usage should also regard the angle of sustainable development. Replacement should be a final solution instead of being an immediate solution. The 3 R's of energy: Reduce, Reuse and Recycle and the 5S's i.e Sort, Set in Order, Shine, Standardize, and Sustain should be promoted to achieve the goal of sustainability, the question at hand.



## INTRODUCTION:

Modern civilization has become dependent on fossil fuels of finite supply and uneven global distribution, which has two problematic consequences:

- (1) vulnerability of nation states to fossil-fuel imports and
- (2) Carbon dioxide emissions that are acidifying our oceans and creating global warming.

The lithium ion batteries – a type of a rechargeable batteries commonly termed LIBs , which infact have become an integral part of our daily life, powering the cellphones , laptops,digital cameras, ipads etc that have revolutionized the modern society, are now on the verge of transforming the transportation sector with electric cars, buses, and bikes are anticipated to be critical for enabling a widespread replacement of fossil-fuel-based power generation with renewable energy sources like solar and wind, providing a cleaner, more sustainable planet thereby giving us a solution to the above stated problem. The lithium ion batteries are far superior from their counter systems such as lead acid (Pb-acid), nickel-cadmium (Ni-Cd), and nickel-metal hydride (Ni-MH) batteries. The relatively high gravimetric and volumetric energy density of lithium ion batteries replaced other batteries in todays' consumer electronics and leading steps towards green energy. The award of the 2019 Nobel Prize in Chemistry to John Goodenough, StanleyWhittingham, and Akira Yoshino emboldens this assertion. (fig 1)

The development of lithium-ion battery technology to date is the result of a concerted effort on basic solid-state chemistry of materials for nearly half a century now. Discovery of new materials and a growth of our fundamental understanding of their structure-composition-property performance relationships have played a major role in advancing the field. Among the various components involved in a lithium-ion cell, the major factor that determines the energy density, rate capability (i.e., power density), and cost of Li-ion batteries is the cathode (positive electrode). And this paper discusses about the three leading type of cathodes which definitely will follow the path of five5s(sort,set in order,shine,standardize,sustain) methodology (REF 1-3).




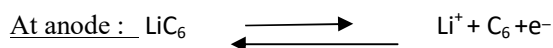
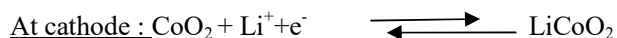
		
<b>John B. Goodenough</b> The University of Texas at Austin, USA	<b>M. Stanley Whittingham</b> Binghamton University, State University of New York, USA	<b>Akira Yoshino</b> AsahiKaseiCorporation, Tokyo, Japan & Meijo University, Nagoya, Japan
Metal oxides as lithium intercalating cathodes e.g. Lithium cobalt oxide	Metal sulphide as lithium intercalating cathode e.g. titanium disulphide	Carbon material as an alternative anode material

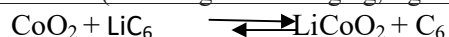
Fig.1- Nobel prize winners and their contribution in the field of rechargeable energy storage, especially in lithium ion batteries.)

## THE LITHIUM ION BATTERY:

The three primary functional components of a lithium-ion battery are the cathode, anode (electrodes) and electrolyte. Generally, the anode of a conventional lithium-ion cell is made from carbon (graphite with doped lithium ( $\text{LiC}_6$ )). The cathode is typically a metal oxide (cobalt oxide which we will discuss later in this paper). The electrolyte is a lithium salt (it is so chosen that as soon as the anode comes in contact with the electrolyte it disintegrates it into  $\text{Li}^+$ ,  $\text{C}_6\text{e}^-$ ) in an organic solvent (lithium hexafluorophosphate  $\text{LiPF}_6$ , in ethylene carbonate) a material allowing ions to travel through while electrically insulating avoiding electrical conduction through it, and a separator, a mesoporous material, allowing ions and also prevents electrical shorting between cathode and anode. All these components with representative materials are shown in fig 2. During discharge (fig 2a), an oxidation half-reaction at the anode produces positively charged lithium ions and negatively charged electrons. The oxidation half-reaction may also produce uncharged material that remains at the anode. Lithium ions move through the electrolyte, electrons move through the external circuit, and then they recombine at the cathode (together with the cathode material) in a reduction half-reaction. The electrolyte and external circuit provide conductive media for lithium ions and electrons, respectively, but do not partake in the electrochemical reaction. During discharge, electrons flow from the anode towards the cathode through the external circuit. The reactions during discharge lower the chemical potential of the cell, so discharging transfers energy from the cell to wherever the electric current dissipates its energy, mostly in the external circuit. During charging (fig 2b) these reactions and transports go in the opposite direction: electrons move from the positive electrode to the negative electrode through the external circuit. To charge the cell the external circuit has to provide electric energy. This energy is then stored as chemical energy in the cell. Both electrodes allow lithium ions to move in and out of their structures with a process called intercalation i.e a reversible insertion of a molecule or ion into layered materials with layered structures or deintercalation; the removal or the extraction of the ion/molecule that had been intercalated, respectively. As the lithium ions "rock" back and forth between the two electrodes, these batteries are also known as "rocking-chair batteries" or "swing batteries". This is illustrated below by taking lithium cobalt oxide as cathode and graphite as anode.



The full reaction (left to right: discharging, right to left: charging) being



In a lithium-ion battery, the lithium ions are transported to and from the cathode and anode by oxidizing the transition metal cobalt (Co), in  $\text{Li}_{1-x}\text{CoO}_2$  from  $\text{Co}^{3+}$  to  $\text{Co}^{4+}$  during charge, and reducing from  $\text{Co}^{4+}$  to  $\text{Co}^{3+}$  during discharge.

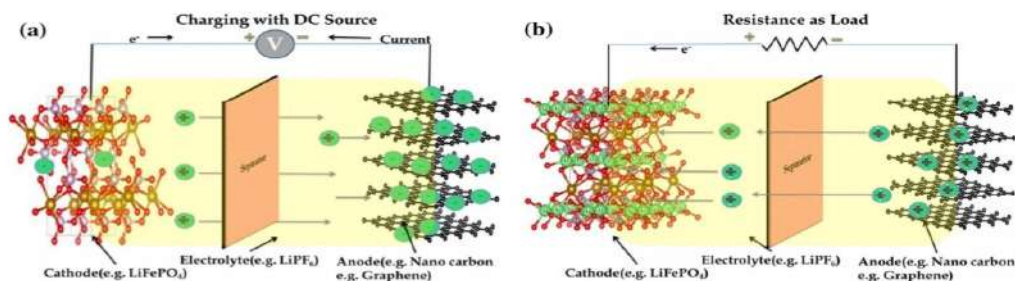


Figure 2: Schematic representation of (a) charging using an external DC source and (b) discharging using an external load for a rechargeable Li-ion battery.

### THE DISCOVERY of OXIDE CATHODES:

Even though intercalation chemistry was introduced in 1841 it took the interest of scientists in 1960s, particularly on altering the electronic and optical properties of materials through intercalation. A few transition-metal disulfides  $MS_2$  as well as oxides such as  $WO_3$  were investigated by intercalating  $A = H^+, Li^+, \text{ and } Na^+$  ions. For instance, the intercalation of these monovalent ions into  $WO_3$  to produce  $A_xWO_3$  altered the electronic conductivity from insulator to semiconductor to metallic depending on the value of  $x$ .

With the chemical intercalation reactions on metal disulfides in place Professor Whittingham, around 1970s, discovered titanium disulfide ( $TiS_2$ ) as a cathode material, a lithium metal anode and a liquid electrolyte in which a lithium salt like  $LiClO_4$  was dissolved in an organic solvent like dimethoxyethane (glyme) and tetrahydrofuran (THF). The  $Li-TiS_2$  cell displayed a discharge voltage of  $<2.5$  V with good reversibility for one lithium per  $TiS_2$  molecule. Following the demonstration with  $TiS_2$ , a number of metal dichalcogenides were investigated by various groups as electrode materials for lithium batteries. However, there were two major issues. First, the cell voltage was limited to  $<2.5$  V, limiting the energy density. Second, dendrite growth on lithium-metal anodes during cell cycling caused internal shorting and caused a fire hazard. In fact, there were attempts to put cells consisting of sulfide cathodes and lithium-metal anodes into market, but they were then abandoned due to safety issues. (REF 4-7)

Further, around 1980s, the work on metal oxide particularly lithium cobalt oxide by Professor Goodenough became an alternative cathode material to metal sulphide for lithium ion batteries which could operate at higher voltage  $\sim 3.5 - 4$  V and thereby providing higher energy/power density. The cell voltage is determined by the energy difference between the redox energies of the anode and the cathode which implies the cathode energy should lie as low as possible and the anode energy should lie as high as possible, meaning the cathode would require the stabilization of higher oxidation state with a lower-lying energy band while the anode would require the stabilization of lower oxidation states with a higher lying energy band. Therefore, the question is how to access the lower-lying energy band of a metal ion with high enough oxidation states in a material so that the cell voltage can be increased. After three decades (1950-1980) of research on the properties of transition-metal oxides, Goodenough utilized the basic understanding that the top of the  $S^{2-}:3p$  band lies at a higher energy than the top of the  $O^{2-}:2p$  band to design oxide cathodes (Fig. 3). This means that the access to lower-lying energy bands with higher oxidation states such as  $Co^{3+/4+}$  and hence the higher cell voltage will be limited by the top of the  $S^{2-}:3p$  band, and attempts to lower the cathode redox energy by accessing higher oxidation states in a sulfide will result in an oxidation of  $S^{2-}$  ions to molecular disulfide ions  $(S_2)^{2-}$ . In contrast, in an oxide, the cathode redox energy can be significantly lowered by accessing lower-lying energy bands such as  $Co^{3+/4+}$  and hence the cell voltage can be increased to as high as 4V, as the top of the  $O^{2-}:2p$  band lies at a lower energy compared to the top of the  $S^{2-}:3p$  band. (REF-8)

This basic idea led to the discovery of three classes of oxide cathodes by Goodenough's group in the 1980s, involving three visiting scientists from three different parts of the world, including Koichi Mizushima from Japan who worked on the layered oxide cathodes, Michael Thackeray from South Africa who worked on the spinel oxide cathodes, and Arumugam Manthiram from India who worked on the polyanion cathodes (fig 4). Later around 1985, Professor Akira Yoshino used a carbon material (petroleum coke) as an anode in place of lithium together with lithium cobalt oxide as cathode material to fabricate a lithium ion battery. This is considered as the birth point for the current commercially used lithium ion batteries. The advantage of such lithium ion batteries is that these are not based on any chemical reaction but intercalation of lithium ions via lithium ion movement between cathode and anode during charging and discharging. With the emergence of LIBs continuous researches been going on for new battery materials which can provide enhanced energy and power density and give a world an alternative grid energy storage. Further, large energy to power density aspect ratio together with higher operating voltage, large charge-discharge cyclability without the degradation in capacity and safety issues are other important points needs to be prioritized while developing such high energy and power density materials. Thus, we are in the need of substantial efforts to innovate such materials which can meet these requirements. This paper discusses the chronological development of cathode materials together with issues and challenges in realizing efficient rechargeable LIBs. (REF 9)

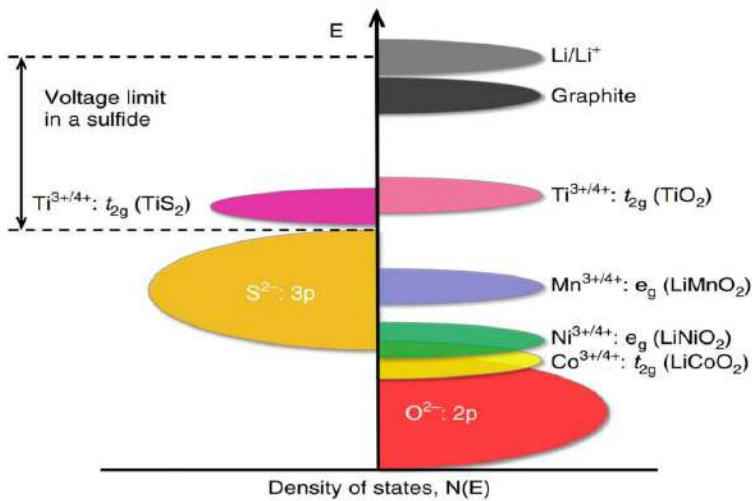


Fig. 2 Positions of the redox energies relative to the top of the anion:p bands. The top of the S<sup>2-</sup>:3p band lying at a higher energy limits the cell voltage to <2.5 V with a sulfide cathode. In contrast, the top of the O<sup>2-</sup>:2p band lying at a lower energy enables access to lower-lying energy bands with higher oxidation states and increases the cell voltage substantially to ~4

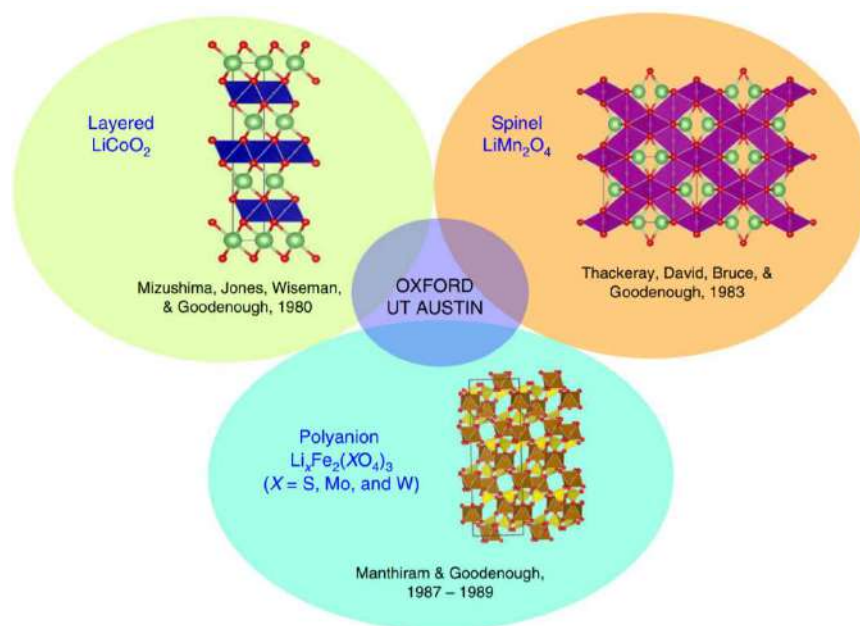


Fig. 4 Discovery of three classes of oxide cathodes in the 1980s. Layered  $\text{LiCoO}_2$  with octahedral-site lithium ions offered an increase in the cell voltage from  $<2.5$  V in  $\text{TiS}_2$  to  $\sim 4$  V. Spinel  $\text{LiMn}_2\text{O}_4$  with tetrahedral-site lithium ions offered an increase in cell voltage from 3V for octahedral-site lithium ions with  $\text{Mn}^{3+/4+}$  couple to  $\sim 4$  V, with an accompanying cost reduction. Polyanion oxide  $\text{Li}_x\text{Fe}_2(\text{SO}_4)_3$  offered yet another way to increase the cell voltage through inductive effect from  $<2.5$  V in a simple oxide like  $\text{Fe}_2\text{O}_3$  to 3.6 V, with a further reduction in cost and improved thermal stability and safety.

### CLASSIFICATION OF CATHODE MATERIALS:

#### Cathode class I: layered oxides

The first oxide cathode investigated is the layered  $\text{LiCoO}_2$  (Fig. 2), in which the monovalent  $\text{Li}^+$  and trivalent  $\text{Co}^{3+}$  ions are ordered on the alternate (111) planes of the rock salt structure with a cubic close-packed array of oxide ions: this structure is referred to as the O3 structure (ABCABC type). The large charge and size differences between  $\text{Li}^+$  and  $\text{Co}^{3+}$  ions lead to good cation ordering, which is critical to support fast two-dimensional lithium-ion diffusion and conductivity in the lithium plane. The lithium-ion conduction in the lithium plane occurs from one octahedral site to another via a neighboring tetrahedral void that shares faces with three octahedral within the lithium layer as it offers the lowest energy barrier (Fig. 5a). With a good cation ordering, the direct interaction between Co-Co across the shared octahedral edges in the cobalt plane gives a good electronic conductivity as well; in fact, due to the introduction of holes into the low-spin  $\text{Co}^{3+/4+} : t_{2g}^{6-x}$  band  $\text{Li}_{1-x}\text{CoO}_2$  becomes metallic on charging. The good structural stability along with high electrical and lithium-ion conductivity proffers fast charge-discharge good reversible cyclability. With these features,  $\text{LiCoO}_2$  remains as one of the best cathodes to date with a high operating voltage of  $\sim 4$  V. The  $\text{LiCoO}_2$  cathode solved two major challenges associated with the sulfide cathodes proposed in the 1970s. It enabled not only a increase in the operating voltage from  $<2.5$  V to  $\sim 4$  V but also fabricated the LIB without the need to employ a metallic lithium anode. As the as-synthesized cathode contained lithium, a lithium-free anode like graphite can be paired with  $\text{LiCoO}_2$  to give the modern-day lithium-ion cell. However, the

$\text{Co}^{3+/4+}$  band overlaps with the top of the  $\text{O}^{2-}:2p$  band as seen in Fig. 3, which leads to a release of oxygen from the crystal lattice on charging more than 50% with  $(1-x) < 0.5$  in the  $\text{Li}_{1-x}\text{CoO}_2$  cathode. Therefore, despite good electrochemical performance, the practical capacity of  $\text{LiCoO}_2$  is limited to  $\sim 140 \text{ mA h g}^{-1}$ . Following  $\text{LiCoO}_2$ , a number of layered  $\text{LiMO}_2$  oxides have been investigated over the years where  $M = 3d$  transition metals (Table 2). Some of them can be directly synthesized by direct high-temperature reactions as indicated by “yes” in Table 2.

With further researches it was found when  $M = \text{V, Mn, and Fe}$ , the members suffer from layered to spinel transitions or other structural changes during charge–discharge due to a low octahedral-site stabilization energy (OSSE) (a slight difference in CFSE of octahedral and tetrahedral sites) (Table 3), so they are not good cathodes.  $\text{LiTiO}_2$  operates at a lower voltage of  $\sim 1.5 \text{ V}$ , so it is not suitable as a cathode (Fig. 1). In addition, it is rather tedious to synthesize it with lower-valent  $\text{Ti}^{3+}$ .  $\text{LiCrO}_2$  is difficult to charge as it displays a large polarization with an increase in charge voltage.  $\text{LiNiO}_2$  is also difficult to synthesize as a well ordered material, unlike  $\text{LiCoO}_2$ , as  $\text{Ni}^{3+}$  tends to be reduced to  $\text{Ni}^{2+}$  and result in  $\text{Li}_{1-y}\text{Ni}_{1+y}\text{O}_2$  at the high-temperature synthesis conditions of  $700\text{--}800 \text{ }^\circ\text{C}$ , accompanied by a volatilization of some lithium from the reaction mixture.

However the high cost and limited capacity of  $\text{LiCoO}_2$  led the work on the substitution of cobalt with Mn and Ni during the past couple of decades to give  $\text{LiNi}_{1-y-z}\text{Mn}_y\text{Co}_z\text{O}_2$  (NMC). The question is why use NMC with three transition-metal ions? In NMC,  $\text{Mn}^{3+}$  tends to get oxidized during synthesis to  $\text{Mn}^{4+}$  by reducing  $\text{Ni}^{3+}$  to  $\text{Ni}^{2+}$  as the  $\text{Mn}^{3+/4+}$  band lies above the  $\text{Ni}^{2+/3+}$  band. Thus,  $\text{Mn}^{4+}$  helps the inclusion of Ni as a stable  $\text{Ni}^{2+}$  into NMC giving a structural stability without participating in the charge–discharge process. In NMC, each transition-metal ion has its own advantages and disadvantages (Table 4). The two major factors are chemical stability and structural stability, in which Co and Mn are diametrically opposite to each other. Since the  $\text{Mn}^{3+/4+}$  band lies well above the top of the  $\text{O}^{2-}:2p$  band (Fig. 4), Mn does not suffer from any chemical instability involving oxygen release from the lattice in contrast to Co as the  $\text{Co}^{3+/4+}$  band overlaps with the top of the  $\text{O}^{2-}:2p$  band. On the other hand, Mn suffers from structural instability as it can readily migrate from the octahedral sites in the transition-metal plane to the octahedral sites in the lithium plane through a neighboring tetrahedral site due to the smaller OSSE as seen in Table 3, resulting in a layered to spinel transition and accompanying voltage decay during cycling. In contrast, Co enjoys good structural stability without such cation migration due to the large OSSE. In addition to the above two critical differences,  $\text{Co}^{3+/4+}$  becomes metallic on charging due to the partially filled  $t_{2g}$  orbitals interacting along the shared edges while  $\text{Mn}^{4+}$  remains semiconducting. Also, Mn is abundant and environmentally benign compared to Co. Interestingly, Ni lies in between Mn and Co in all the five criteria (table 4) as:

(i) the  $\text{Ni}^{3+/4+}$  band barely touches the top of the  $\text{O}^{2-}:2p$  band so that  $\text{Ni}^{3+}$  can be charged all the way to  $\text{Ni}^{4+}$  without the removal of electron density from the  $\text{O}^{2-}:2p$  band and loss of oxygen from the lattice and

(ii)  $\text{Ni}^{3+}$  exhibits an OSSE value intermediate between those of  $\text{Mn}^{3+}$  and  $\text{Co}^{3+}$ , offering reasonably good structural stability. That is why the trend is to progressively increase the Ni content and decrease the Co content in NMC so that the capacity can be increased while lowering the cost. (REF 11-14)

Table 2:  $\text{LiMO}_2$  oxides crystallising in the O3 layered structure of the  $\text{LiCoO}_2$

$M^{3+}$ ion	Sc	Ti	V	Cr	Mn	Fe	Co	Ni	Cu
$\text{LiMO}_2$	no	yes	Yes	yes	No	No	Yes	yes	No

Table 3: comparison of the CFSE of the transition metal ions  $M^{3+}$  in NMC cathodes

ion	Octahedral cfse ( $\Delta_o$ )	Tetrahedral cfse ( $\Delta_o$ )	Octahedral site stabilization energy(osse)( $\Delta_o$ )
$\text{Mn}^{3+}$	$t_2^3 e^1, -0.6$	$e^2 t_2^2, -.18$	-.42
$\text{Ni}^{3+}$	$t_2^6 e^1, =1.88$	$e^4 t_2^3, -.53$	-1.35
$\text{Co}^{3+}$	$t_2^6 e^0, -2.4$	$e^3 t_2^3, -.27$	-2.13

TABLE 4: Comparison of the characteristics of manganese, cobalt, nickel in NMC cathodes :

PARAMETER	TREND
Chemical stability	Mn > Ni > Co
structural stability	Co > Ni > Mn
Electrical conductivity	Co > Ni > Mn
Abundance	Mn > Ni > Co
Environmental benignity	Mn > Ni > Co

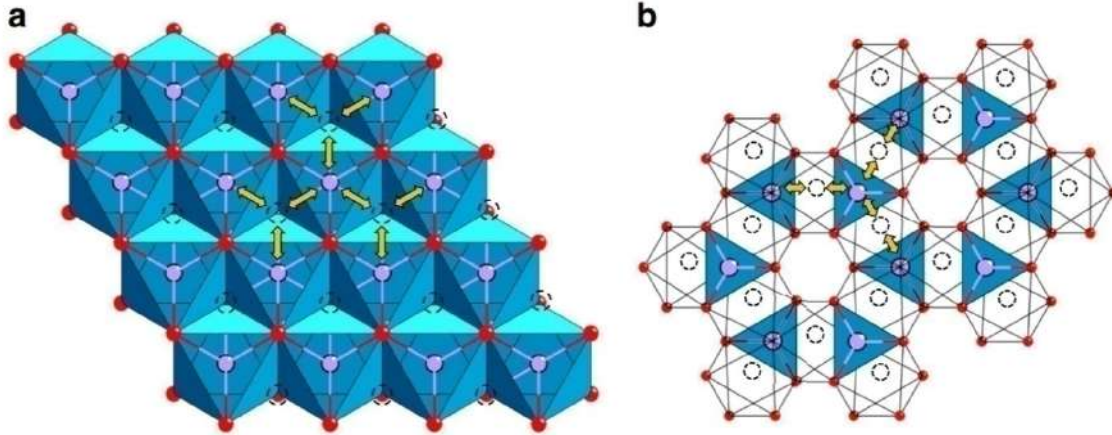


Fig. 5 Lithium-diffusion pathways with lower energy barriers in close-packed oxides. a Two-dimensional lithium diffusion from one octahedral site to another octahedral site in the lithium plane through a neighboring empty tetrahedral site in the O3 layered  $\text{LiMO}_2$  cathodes. b Three-dimensional lithium diffusion from one 8a tetrahedral site to another 8a tetrahedral site through a neighboring empty 16c octahedral site in the spinel cathodes.

## Cathode class II: spinel oxides

With a prior demonstration of lithium insertion into magnetite ( $\text{Fe}_3\text{O}_4$ ) crystallizing in the spinel structure by Thackeray in South Africa, the second class of cathode discovered is the spinel  $\text{LiMn}_2\text{O}_4$  at the University of Oxford (Fig. 4), in which the  $\text{Mn}^{3+/4+}$  ions occupy the 16d octahedral sites and the  $\text{Li}^+$  ions occupy the 8a tetrahedral sites of the spinel framework with a cubic close-packed array of oxide-ions. The stable  $[\text{Mn}_2]_{16d}\text{O}_4$  framework with edge-shared octahedra offers a three-dimensional lithium-ion diffusion pathway with fast lithium-ion conductivity. The lithium-ion conduction occurs from one 8a tetrahedral site to another 8a tetrahedral site via a neighboring empty 16c octahedral site as it offers the lowest energy barrier (Fig. 5b). The direct Mn–Mn interaction across the shared  $\text{MnO}_6$  octahedral edges as in  $\text{LiCoO}_2$  with mixed-valent high-spin  $\text{Mn}^{3+/4+}:t_{2g}^3e_g^{1-x}$  in  $(\text{Li}_{1-x})_{8a}[\text{Mn}_2]_{16d}\text{O}_4$  facilitates good hopping electronic conduction, but it remains as a small-polaron semiconductor during the charge–discharge process, unlike  $\text{Li}_{1-x}\text{CoO}_2$ . The good three dimensional structural stability along with high electrical and lithium-ion conductivity offers even faster charge–discharge characteristics for  $\text{Li}_{1-x}\text{Mn}_2\text{O}_4$  with good reversibility compared to  $\text{LiCoO}_2$ . The insertion/extraction of lithium into/from the tetrahedral sites with a deep site energy in  $\text{Li}_{1-x}\text{Mn}_2\text{O}_4$  offers a high operating voltage of 4 V with a practical capacity of  $<130 \text{ mA h g}^{-1}$  as close to one lithium per two Mn ions can be reversibly extracted from the tetrahedral sites. Interestingly, an additional lithium can be inserted into the empty 16c octahedral sites at 3 V to form the lithiated spinel  $[\text{Li}_2]_{16c}[\text{Mn}_2]_{16d}\text{O}_4$  that is accompanied by a spontaneous displacement into the empty 16c octahedral sites. It is interesting to

note that the operating voltage drops by 1 V on going from a tetrahedral site to octahedral-site lithium, despite the same  $\text{Mn}^{3+/4+}$  redox couple. This illustrates the significant role of site energy in addition to electron transfer in controlling the voltage in solids, unlike in solutions where no site energy contribution is involved. However, the accompanying Jahn-Teller distortion caused by a single eg electron in  $\text{Mn}^{3+}$ :  $t_{2g}^3 e_g^1$  in  $[\text{Li}_2]_{16c}[\text{Mn}_2]_{16d}\text{O}_4$  causes a cubic to tetragonal phase transition with a two-phase reaction involving a large instantaneous c/a ratio and volume changes. Therefore, the capacity in the 3 V region could not be utilized in practical cells. One important advantage on going from  $\text{LiCoO}_2$  to  $\text{LiMn}_2\text{O}_4$  is the significant reduction in cost as Mn is two orders of magnitude lower in cost than Co. However, one critical issue with  $\text{LiMn}_2\text{O}_4$  is the dissolution of Mn from the lattice into the electrolyte in presence of trace amounts (ppm levels) of  $\text{H}^+$  ions (acidity) in the electrolyte due to the well-known disproportionation of  $\text{Mn}^{3+}$  to  $\text{Mn}^{4+}$  and  $\text{Mn}^{2+}$  in acid. During such a disproportionation,  $\text{Mn}^{4+}$  is retained in the solid and  $\text{Mn}^{2+}$  is leached out into the solution. In addition to degrading the cathode, the Mn dissolution and its migration to the anode severely poison the graphite anode and limit the cycle life of lithium-ion cells. Interestingly, substituting a small amount of lithium (e.g., 5 atom %) for Mn in  $\text{LiMn}_2\text{O}_4$  perturbs the long range Mn–Mn interaction/contact, frustrates the  $\text{Mn}^{3+}$  disproportionation reaction, reduces Mn dissolution, and thereby improves the cyclability. Unfortunately,  $\text{LiM}_2\text{O}_4$  spinel oxides are known only with  $M=\text{Ti}, \text{V},$  and  $\text{Mn}$ , unlike the layered  $\text{LiMO}_2$  oxides (Table 4). This is because of the difficulty of stabilizing the highly oxidized  $M^{3+/4+}$  oxidation states by conventional high-temperature synthesis. Among the known three spinel oxides,  $\text{LiTi}_2\text{O}_4$  operates around 1.5 V, so it is not a suitable cathode. Nor is  $\text{LiV}_2\text{O}_4$  a practical choice since it suffers from structural changes and a lower voltage of around 3 V. There have been efforts to prepare both  $\text{LiCo}_2\text{O}_4$  and  $\text{LiNi}_2\text{O}_4$  spinel oxides by chemically extracting 50% lithium, respectively, from  $\text{LiCoO}_2$  and  $\text{LiNiO}_2$  to obtain  $\text{Li}_{0.5}\text{CoO}_2$  and  $\text{Li}_{0.5}\text{NiO}_2$ , followed by calcining them at moderate temperatures of 200–400 °C to transform the layered phase to spinel phase. However, such attempts result in either incomplete transformation at low enough temperatures or loss of oxygen and formation of a mixture of spinel-like phases and reduced  $\text{Co}_3\text{O}_4$  or  $\text{NiO}$  phases due to the instability of  $\text{Co}^{3+/4+}$  and  $\text{Ni}^{3+/4+}$  at high enough temperatures. Such spinel-like phases also exhibit poor electrochemical performance due to a lack of well-formed crystalline spinel phases. Another approach has been to partially substitute Mn with other ions like Cr, Co, and Ni. One example is  $\text{LiMn}_{1.5}\text{Ni}_{0.5}\text{O}_4$  spinel in which Mn exists as  $\text{Mn}^{4+}$  and Ni exists as  $\text{Ni}^{2+}$  as in NMC cathodes. With  $\text{Ni}^{2+/3+}$  and  $\text{Ni}^{3+/4+}$  couples and tetrahedral-site lithium ions,  $\text{LiMn}_{1.5}\text{Ni}_{0.5}\text{O}_4$  operates at ~4.7 V with a reversible capacity of ~135 mA h g<sup>-1</sup>. However,  $\text{LiMn}_{1.5}\text{Ni}_{0.5}\text{O}_4$  spinel suffers from capacity fade due to the lack of suitable electrolyte that can be stable at such high voltages. (REF15-18)

### Cathode class III: Polyanion Oxides

Departing from the previous two simple oxide classes of cathodes, the third class of cathode investigated is the polyanion oxides. (Based on Manthiram's Ph.D. dissertation work in India on the hydrogen reduction of the polyanion oxides  $\text{Ln}_2(\text{MoO}_4)_3$  (Ln =lanthanide and Y) to obtain lower-valent  $\text{Mo}^{4+}$  oxides  $\text{Ln}_2(\text{MoO}_3)_3$ , analogous polyanion oxides  $\text{Fe}_2(\text{MoO}_4)_3$  and  $\text{Fe}_2(\text{WO}_4)_3$  were prepared by Manthiram, crystallizing in a NASICON-related framework structure (Fig. 3).) These polyanion oxides were found to undergo reversible insertion/extraction of two lithium ions per formula unit to give  $\text{Li}_2\text{Fe}_2(\text{MoO}_4)_3$  or  $\text{Li}_2\text{Fe}_2(\text{WO}_4)_3$  both by chemical and electrochemical methods. Interestingly, both  $\text{Fe}_2(\text{MoO}_4)_3$  and  $\text{Li}_2\text{Fe}_2(\text{WO}_4)_3$  exhibited a flat discharge voltage of 3 V, which was significantly higher than that seen with simple oxides like  $\text{Fe}_2\text{O}_3$  or  $\text{Fe}_3\text{O}_4$  (<2.5 V) operating with the same  $\text{Fe}^{2+/3+}$  redox couple. Motivated by the increase in voltage on going from a simple oxide to a polyanion oxide,  $\text{Fe}_2(\text{SO}_4)_3$  having the same structure as  $\text{Fe}_2(\text{MoO}_4)_3$  was then investigated. Surprisingly,  $\text{Fe}_2(\text{SO}_4)_3$  displayed a much higher flat discharge voltage of 3.6 V. A comparison of the operating voltages of the isostructural  $\text{Fe}_2(\text{MoO}_4)_3$  (3.0 V),  $\text{Fe}_2(\text{WO}_4)_3$  (3.0 V), and  $\text{Fe}_2(\text{SO}_4)_3$  (3.6 V) with that of  $\text{Fe}_2\text{O}_3$  (<2.5 V), all operating with the same  $\text{Fe}^{2+/3+}$  couple (Fig. 5), led to a recognition of the role of the counter cations  $\text{Mo}^{6+}$ ,  $\text{W}^{6+}$ , and  $\text{S}^{6+}$  in drastically shifting the redox energy of the  $\text{Fe}^{2+/3+}$  couple by altering the characteristics of the Fe–O bond. In the  $\text{Fe}_2(\text{XO}_4)_3$  (X=Mo, W, and S) structure (Fig. 4), the  $\text{FeO}_6$  octahedra share their corners with  $\text{XO}_4$  tetrahedra, providing an extended, three-dimensional –O–Fe–O–X–O–Fe–O– linkage. As a result, the more covalent Mo–O or W–O bond weakens the Fe–O bond covalency through inductive effect compared to that in the simple iron



oxide  $\text{Fe}_2\text{O}_3$ , resulting in a lowering of the  $\text{Fe}^{2+/3+}$  redox energy and a consequent increase in the operating voltage from  $<2.5$  to  $3.0$  V in  $\text{Fe}_2(\text{MoO}_4)_3$  and  $\text{Fe}_2(\text{WO}_4)_3$ . An even more covalent S-O bond in  $\text{Fe}_2(\text{SO}_4)_3$  weakens the Fe-O covalency even further, resulting in a further lowering of the  $\text{Fe}^{2+/3+}$  redox energy and a much more significant increase in the operating voltage from  $3.0$  V in  $\text{Fe}_2(\text{MoO}_4)_3$  and  $\text{Fe}_2(\text{WO}_4)_3$  to  $3.6$  V in  $\text{Fe}_2(\text{SO}_4)_3$  (Fig. 6).

Intrigued by the ability to increase the operating voltage by going from simple oxides to polyanion oxides in addition to the increase in voltage from a sulfide to an oxide in the previous two classes of cathodes, polyanion oxides with phosphate groups were investigated by Manthiram and Goodenough in the late 1980s. In the meantime, Sony Corporation announced in 1991 the commercialization of lithium ion batteries with  $\text{LiCoO}_2$  cathode and graphite anode. Motivated by this announcement and based on the previous work on molybdate, sulfate, and phosphates, exploration of other lithium-containing phosphates as cathodes led to the identification of olivine  $\text{LiFePO}_4$  as a cathode in 1997, ten years after the initial identification in 1987 of the polyanion class of cathodes and the inductive effect. The ability to increase the voltage drastically to as high as  $\sim 5$  V in polyanion oxide cathodes, for example, in  $\text{LiMPO}_4$  even with lower-valent couples like  $\text{Co}^{2+/3+}$  or  $\text{Ni}^{2+/3+}$  illustrates the power of the inductive effect imparted by the changes in metal oxygen bonding in tuning the operating voltages. Accordingly, the polyanion oxide class with sulfates, phosphates, and silicates has become diverse compared to the first two classes of oxide cathodes (layered and spinel oxides) in terms of versatility and number of materials, not only for lithium-ion batteries, but also for sodium-ion batteries. For example, polyanion oxides like  $\text{Li}_3\text{V}_2(\text{PO}_4)_3$ ,  $\text{Na}_3\text{V}_2(\text{PO}_4)_3$ , and  $\text{Na}_3\text{V}_2(\text{PO}_4)_2\text{F}_3$ , and  $\text{LiFePO}_4$  have become appealing cathodes for lithium-ion or sodium-ion batteries.

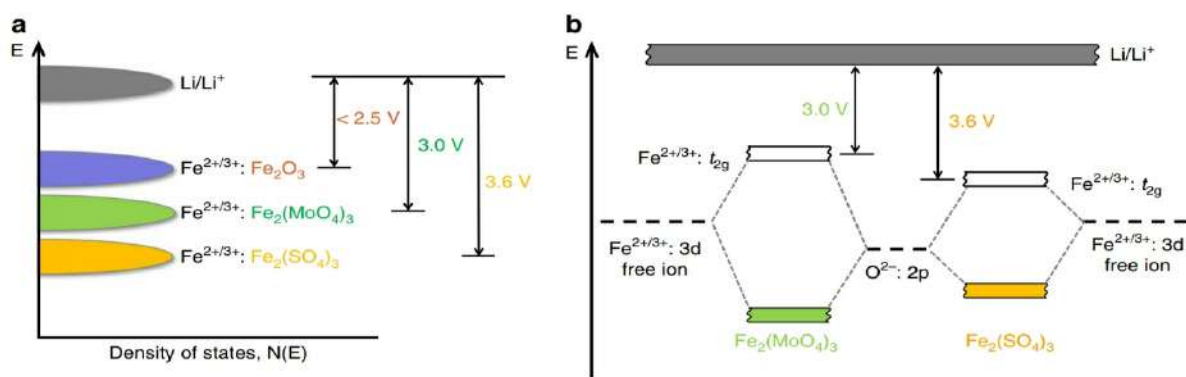


Fig. 6 Role of counter-cations in shifting the redox energies in polyanion oxides. a Lowering of the redox energies of the  $\text{Fe}^{2+/3+}$  couple and the consequent increase in cell voltage on going from a simple oxide  $\text{Fe}_2\text{O}_3$  to a polyanion oxide  $\text{Fe}_2(\text{MoO}_4)_3$  and then to another polyanion oxide  $\text{Fe}_2(\text{SO}_4)_3$  with a more electronegative counter-cation  $\text{S}^{6+}$  vs.  $\text{Mo}^{6+}$ , i.e., with a more covalent S-O bond than the Mo-O bond. b Molecular orbital energy diagram illustrating the lowering of the  $\text{Fe}^{2+/3+}$  redox energy in  $\text{Fe}_2(\text{SO}_4)_3$  compared to that in the isostructural  $\text{Fe}_2(\text{MoO}_4)_3$ , due to a weakening of the Fe-O covalency by a more covalent S-O bond than the Mo-O bond through inductive effect. (REF 19-24)

## ADVANTAGES AND DISADVANTAGES OF OXIDE CATHODES

Both the layered and spinel class of oxides offer good electronic conductivity but the polyanion oxide class have poor electronic conductivity. Therefore, the particles for the polyanion oxide cathodes are required to be synthesized small and coated with conductive carbon, which often increases the processing cost and introduces inconsistencies in performances. Both layered and spinel oxides have close-packed structure with high densities, while the polyanion class of oxides generally have lower densities, which is further reduced by the necessity to make them as small particles coated with

carbon, leading to a lower volumetric energy density. Thus, the polyanion cathodes are generally less attractive for applications that require high volumetric energy density, such as portable electronic devices and electric vehicles, than the layered oxide cathodes. However, the polyanion class of cathodes offer an important advantage of high thermal stability and better safety than the layered and spinel oxide cathodes as the oxygen is tightly bound to P, S, or Si with strong covalent bonds. Also, the polyanion cathodes with optimally small particles coated with carbon can sustain high charge–discharge rates due to good structural integrity, despite a lower volumetric energy density. Moreover, polyanion cathodes are known with abundant transition metals like Fe, unlike the layered and spinel oxides, offering sustainability advantages; therefore, they are appealing for grid storage of electricity produced from renewable energy sources like solar and wind. Between the layered and spinel oxides, layered oxides are more appealing with a wide range of compositions than spinel oxides due to the inability to stabilize highly oxidized  $M^{3+/4+}$  states by conventional synthetic processes for the spinel oxides. In fact, the spinel cathodes are largely limited to  $\text{LiMn}_2\text{O}_4$ , but even that is plagued by Mn dissolution and the consequent poisoning of graphite anodes and capacity fade particularly at elevated temperatures. However, substituting a small amount of lithium (e.g., 5 atom %) for Mn helps to reduce the problems to some extent. On the other hand, although  $\text{LiMn}_{1.5}\text{Ni}_{0.5}\text{O}_4$  is appealing due to the high operating voltage of  $\sim 4.7$  V and the consequent power capability, its practical viability is hampered by the lack of adequate electrolytes that can survive at such high operating voltages. (REF26)

## OUTLOOK

In the near future layered oxides due to their high gravimetric and volumetric energy densities will be more favoured than the other three oxides. However, cost and sustainability becomes critical as we move forward with large-scale development of lithium-ion batteries for electric vehicles and for grid storage. Also, there is a demand to increase the energy density beyond the current level to keep up with the advances in portable electronic devices and enhance the driving range of electric vehicles. Hence efforts are being made to increase the cathode capacity and lower the cost. In this regard, lithium-rich layered oxides, such as  $\text{Li}_{1.2}\text{Mn}_{0.6}\text{Ni}_{0.2}\text{O}_2$ , rich in Mn and Co free became appealing due to lower cost and capacities as high as  $300 \text{ mA h g}^{-1}$  in the last two decades. However, as discussed above the layered to spinel transitions due to the low OSSE of  $\text{Mn}^{3+}$  and the consequent voltage decay during cycling as well as Mn dissolution and the consequent poisoning of the graphite anode have been a challenge to employ them as a practical cathode. Intrigued by the involvement of oxide ions in the redox process of lithium-rich layered oxides, cathodes based on anion redox have become recently appealing, at least from a basic science point of view. However, the longterm cycle stability of such cathodes in full cells needs to be fully evaluated as we move forward to assess their practical viability. More recently, increasing the Ni content and lowering or eliminating the cobalt content in NMC cathodes is becoming much more prominent. Intensive efforts are underway around the world with this strategy as  $\text{Ni}^{2+}$  or  $\text{Ni}^{3+}$  can be oxidized all the way to  $\text{Ni}^{4+}$  without encountering much oxygen loss from the lattice, unlike with Co, as discussed earlier in the layered oxide section. However, layered oxides with high Ni contents have three critical challenges: cycle instability, thermal instability, and air instability, all of which are related to the instability of  $\text{Ni}^{3+}$  or  $\text{Ni}^{4+}$  in contact with the liquid organic electrolyte. This is understandable considering that only NiO with  $\text{Ni}^{2+}$  is known as a binary oxide and oxides like  $\text{Ni}_3\text{O}_4$  or  $\text{Ni}_2\text{O}_3$  with  $\text{Ni}^{3+}$  do not exist. Therefore, the chemically unstable  $\text{Ni}^{4+}$  ions that are generated on charging layered oxides with high Ni contents react aggressively with the electrolyte to form thick solid-electrolyte interphase (SEI) layers along with the dissolution of Ni and Mn, which then migrate towards graphite anode and deposits on them to limit the cyclability. The transition-metal deposition on graphite anodes catalyzes electrolyte decomposition and leads to the formation of a thick SEI layer with a multilayer structure as seen in Fig. 7, which increases with increasing number of cycles as more transition-metal ions dissolve and migrate to the anode. After a specific number of cycles, the SEI layer thickness also increases with

increasing Ni content due to the increasing transition-metal dissolution and deposition on the graphite anode. Furthermore, the phase transitions occurring in high nickel cathodes at a high state-of-charge with volume changes introduce cracks with new surfaces on cycling, which further exaggerate the surface reactivity with the electrolyte and increase metal dissolution and SEI formation, resulting in rapid capacity fade as cycling progresses. This issue becomes much more prominent and serious particularly after large number of cycles, extending beyond, for example, 500 cycles. Intuitive bulk cation doping as well as surface stabilization strategies to minimize the volume changes, crack formation, and surface reactivity can help to overcome the challenges as we move forward. For example, doping with a small amount of inert  $\text{Al}^{3+}$  for the transition-metal ions as seen in Fig. 7b increases electron localization by perturbing the long-range metal-metal interaction, decreases the long-range metal-oxygen covalence, makes the lattice robust with strong metal-oxygen bonds, and thereby suppresses transition-metal ion dissolution and improves the long-term cycle life. Such strategies also help to improve the thermal stability and air stability. Overall, both controlled materials synthesis and advanced bulk and surface characterization methodologies can help to develop an in-depth basic science understanding and mitigate the issues as we move forward. The capacity of the three classes of insertion-reaction oxide cathodes discussed above are generally limited due to the limited number of crystallographic sites available as well as the large voltage steps encountered on going from one redox couple to another. For example, the voltage drops by more than 1 V on going from the  $\text{V}^{4+/5+}$  couple to the  $\text{V}^{3+/4+}$  couple, introducing challenges to employ them in practical applications. Ni is one unique candidate, which does not experience a voltage step on going through multiple redox couples, i.e., from the  $\text{Ni}^{3+/4+}$  couple to the  $\text{Ni}^{2+/3+}$  couple, as illustrated by the high-voltage  $\text{LiMn}_{1.5}\text{Ni}_{0.5}\text{O}_4$  spinel and layered NMC oxides. Considering the limitations in the capacity of insertion-reaction oxide cathodes, the alternative is to focus on conversion-reaction cathodes, such as sulfur and oxygen. However, both lithium-sulfur and lithium-oxygen batteries face challenges, much more so with lithium-oxygen batteries than with lithium-sulfur batteries. Catalytic decomposition of electrolytes resulting in poor cycle life as well as sluggish reaction kinetics resulting in a large hysteresis between the charge and discharge voltages remain as daunting issues for lithium-oxygen batteries. On the other hand, enormous progress is being made with lithium-sulfur batteries in recent years, hopefully making them viable. However, the necessary practical parameters and metrics need to be seriously considered and followed through to make the lithium-sulfur technology successful. In this regard, a target consisting of “five 5s” and employing such targets in pouch cells could help as we move forward with lithium-sulfur batteries. The five targets are a sulfur loading of  $>5 \text{ mg cm}^{-2}$ , a carbon content of  $<5\%$ , an electrolyte to sulfur (E/S) ratio of  $<5 \mu\text{L mg}^{-1}$ , an electrolyte to capacity (E/C) ratio of  $<5 \mu\text{L (mA h)}^{-1}$ , and a negative to positive (N/P) ratio of  $<5$ .(REF 25-31)

## THE NEED FOR RECYCLING CATHODE MATERIALS

Lithium-ion batteries consist of five primary metals: aluminium and copper as collectors, cobalt, iron, and lithium. Of these cobalt and nickel being rare are available in only selected regions of the world. With the ever-growing need for lithium-ion batteries, particularly from the electric transportation industry, a large amount of lithium-ion batteries is bound to retire in the near future, thereby leading to serious disposal problems and detrimental impacts on environment and energy conservation. Also, the precious metals comprising these batteries would be lost forever. As per Bloomberg New Energy Finance, the global consumption of lithium-ion battery raw materials such as cobalt, lithium, and copper is expected to increase 20 times by 2030. (fig 8) So the best way to treat such batteries is to recycle the metals and other natural resources from a spent battery using different mechanical and metallurgical processes. These precious extracts can be re-used to manufacture more batteries.

The high percentage of heavy metals like copper, nickel, and organic chemicals may contaminate soil and water if disposed of along with municipal waste ending up in landfills. Additionally, incinerating lithium-ion batteries releases toxic gases resulting in air pollution. Lithium requires proper handling as it poses health risks to humans and animals. It can get absorbed and accumulated in edible plants and can enter the food chain, causing various genetic, reproductive, and gastrointestinal problems.

The raw materials used in the batteries are mined from select places on earth. Transportation of these materials to different parts of the world for the production of lithium-ion batteries results in increasing its carbon footprint, the cause of greenhouse gas emissions. Usage of recycled materials can reduce the CO<sub>2</sub> emissions from the production cycle by up to 90%. Therefore, to reduce dependence on imports of key metals of lithium-ion batteries, recycling of spent batteries to extract the precious metals makes complete sense. Also, a proper disposal of batteries should be made mandatory by the government to safeguard against potential environmental and health hazards associated with lithium-ion batteries waste. There are short term and long term processes to manage the LIB waste and researches being going on for the reuse of the recycled cathode materials. As replacement cannot be a permanent solution as it will lead to the scarcity of other metals hence the 3Rs should be the priority which will also lead a path of sustainable development. (REF 32)

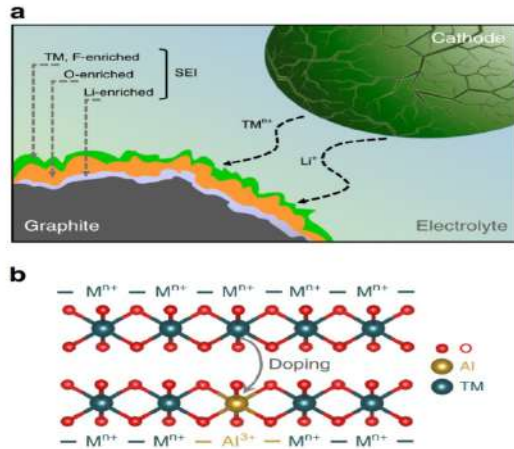


Fig7:Challenges associated with high-nickel layered oxide cathodes and the role of cation doping. (a)Schematic illustration of the dissolution and migration of transition-metal ions from the cathode to the graphite anodeand the consequent catalytic formation of thick SEI layers on the graphiteanode. (b) Substitution of transition-metal ions with a small amount of inert ion like Al<sup>3+</sup> that makes the lattice robust by perturbing the long-range metal-metal interaction and increasing the metal-oxygen bond strength and thereby suppressing metal-ion dissolution.

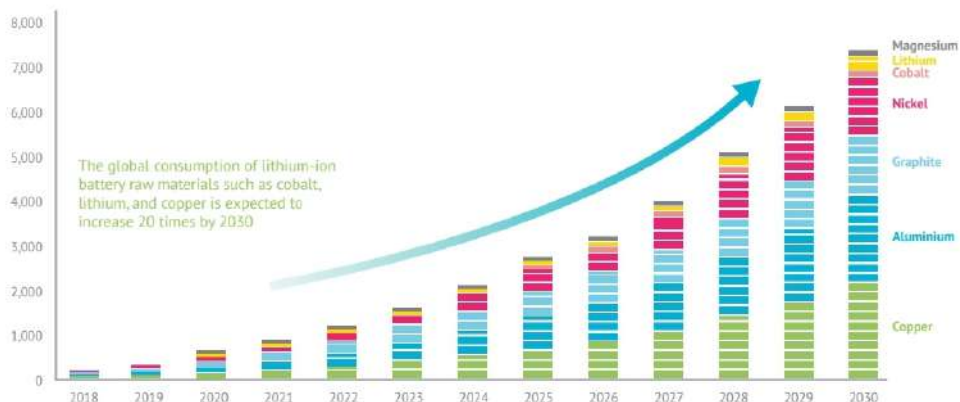


Fig-8-metals and materials demand from LIB in EVs.

## CONCLUSION:

Basic science researches led to the identification of three classes of transition-metal oxide cathodes in the 1980s with much higher operating voltages than the preused sulfide cathodes in 1960s for lithium-based batteries. They are layered oxides, spinel oxides, and polyanion oxides, and these three classes remain the leading cathodes and serve as a basis for future developments. The jump from sulfide cathodes to oxide cathodes was based on a simple idea that the top of the  $O^{2-} 2p$  band lies at a lower energy than the top of the  $S^{2-} 3p$  band, enabling access to lower-lying energy bands with higher oxidation states of transition-metal ions and a consequent increase in the operating voltage. The transition from simple oxide cathodes to polyanion oxide cathodes was based on the basic idea that a decrease in the covalency of the metal-oxygen bond by counter-cations (inductive effect) lowers the cathode redox energy and increases the operating voltage further compared to a simple oxide with the same redox couple. The higher operating voltages of oxide cathodes leading to higher energy densities and the presence of lithium in the as-synthesized cathodes prompted the commercialization of the modern-day lithium-ion batteries in the 1990s. With the increase in population there is demand of developments in LIBs with higher energy density and low cost. So there is a dire need of layered cathodes with high nickel content and cobalt content as much low as possible, but it needs to overcome certain hindrances like surface stabilizations, thermal and air instabilities etc.. Intense researches been going on conversion reaction cathodes like oxygen and sulphur for improving the capacity as in the present cathodes the intercalation and deintercalation is limited due to the availability of less number of crystallographic sites. Progresses are on for the development of Lithium-sulfur batteries and with more intensive researches keeping 3Rs and 5Ss in mind we can make earth cleaner and livable.

## REFERENCE

1. Armand, M. & Tarascon, J. M. Building better batteries. *Nature* 451, 652–657 (2008).
2. Manthiram, A. An outlook on lithium ion battery technology. *ACS Cent. Sci.* 3, 1063–1069 (2017).
3. Goodenough, J. B. & Park, K.-S. The Li-ion rechargeable battery: a perspective. *J. Am. Chem. Soc.* 135, 1167–1176 (2013).
4. Aronson, S., Salzano, F. J. & Bellafiore, D. Thermodynamic properties of the potassium–graphite lamellar compounds from solid-state emf measurements. *J. Chem. Phys.* 49, 434–439 (1968).
5. Whittingham, M. S. Electrical energy storage and intercalation chemistry.
6. Koch, V. R. Status of the secondary lithium electrode. *J. Power Sources* 6, 357–370 (1981).
7. Brandt, K. Historical development of secondary lithium batteries. *Solid State Ion.* 69, 173–183 (1994).
8. Goodenough, J. B. *Metallic Oxides*. *Prog. Solid State Chem.* 5, 145–399.
9. Mizushima, K., Jones, P. C., Wiseman, P. J. & Goodenough, J. B.  $Li_xCoO_2$  ( $0 < x < 1$ ): A new cathode material for batteries of high energy density. *Mater. Res. Bull.* 15, 783–798 (1980)
10. Nishizawa, M., Yamamura, S., Itoh, T. & Uchida, I. Irreversible conductivity change of  $Li_{1-x}CoO_2$  on electrochemical lithium insertion/extraction, desirable for battery applications. *Chem. Comm.* 1631 (1998).
11. Lithium-ion rechargeable cells with  $LiCoO_2$  and carbon Electrodes K. Sekai, H. Azuma, A. Omaru, S. Fujita, H. Imoto, T. Endo, K. Yamaura.
12. Bruce, P. G. & Armstrong, A. R. Synthesis of layered  $LiMnO_2$  as an electrode for rechargeable lithium batteries. *Nature* 381, 499–500 (1996).
13. DePicciotto, L. A., Thackeray, M. M., David, W. I. F., Bruce, P. G. & Goodenough, J. B. Structural characterization of delithiated  $LiVO_2$ . *Mater. Res. Bull.* 19, 1497–1506 (1984).
14. Dutta, G., Manthiram, A. & Goodenough, J. B. Chemical synthesis and

- properties of  $\text{Li}_{1-\delta-x}\text{Ni}_{1+\delta}\text{O}_2$  and  $\text{Li}[\text{Ni}_2]\text{O}_4$ . *J. Solid State Chem.* 96, 123–131
15. Choi, W. & Manthiram, A. Comparison of metal ion dissolutions from lithium ion battery cathodes. *J. Electrochem. Soc.* 153, A1760–A1764 (2006)
16. de Picciotto, L. A. & Thackeray, M. M. Insertion/extraction reactions of lithium with  $\text{LiV}_2\text{O}_4$ . *Mater. Res. Bull.* 20, 1409–1420 (1985).
17. First-principles Study of Lithium Cobalt Spinel Oxides: Correlating Structure and Electrochemistry Soo Kim,<sup>a,1</sup> Vinay I. Hegde,<sup>a</sup> Zhenpeng Yao,<sup>a</sup> Zhi Lu,<sup>a</sup> Maximilian Amsler,<sup>a,2</sup> Jiangang He,<sup>a</sup> Shiqiang Hao,<sup>a</sup> Jason R. Croy,<sup>b</sup> Eungje Lee,<sup>\*,b</sup> Michael M. Thackeray,<sup>b</sup> and Chris Wolverton.
18. Manthiram, A., Chemelewski, K. & Lee, E.-S. A perspective on the high voltage  $\text{LiMn}_{1.5}\text{Ni}_{0.5}\text{O}_4$  spinel cathode for lithium-ion batteries. *Energy Environ. Sci.* 7, 1339–1350 (2014).
19. Manthiram, A. & Goodenough, J. B. Lithium insertion into  $\text{Fe}_2(\text{MO}_4)_3$  frameworks: comparison of  $\text{M} = \text{W}$  with  $\text{M} = \text{Mo}$ . *J. Solid State Chem.* 71, 349–360 (1987).
20. Manthiram, A. & Goodenough, J. B. Lithium insertion into  $\text{Fe}_2(\text{SO}_4)_3$  framework. *J. Power Sources* 26, 403–406 (1989).
21. Manthiram, A., Swinnea, J. S., Sui, Z. T., Steinfink, H. & Goodenough, J. B. The influence of oxygen variation on the crystal structure and phase composition of the superconductor  $\text{YBa}_2\text{Cu}_3\text{O}_{7-x}$ . *J. Am. Chem. Soc.* 109
22. Padhi, A. K., Nanjundaswamy, K. S. & Goodenough, J. B. Phospho-Olivines as positive electrode materials for rechargeable lithium batteries. *J. Electrochem. Soc.* 144, 1188–1194 (1997).
23. Masquelier, C. & Croguennec, L. Polyanionic (phosphates, silicates, sulfates) frameworks as electrode materials for rechargeable Li (or Na) batteries. *Chem. Rev.* 113, 6552–6591 (2013).
24. Huang, H., Yin, S. C., Kerr, T., Taylor, N. & Nazar, L. F. Nanostructured composites: a high capacity, fast rate  $\text{Li}_3\text{V}_2(\text{PO}_4)_3/\text{carbon}$  cathode for rechargeable lithium batteries. *Adv. Mater.* 14, 1525–1528 (2002).
25. Cathode Materials for Lithium Ion Batteries (LIBs): A Review on Materials related aspects towards High Energy Density LIBs Ambesh Dixit
26. Nitta, N., Wu, F., Lee, J. T. & Yushin, G. Li-ion battery materials: present and future. *Mater. Today* 18, 252–264 (2015).
27. Doughty, D. H. & Roth, E. P. A general discussion of Li ion battery safety. *Electrochem. Soc. Interface* 21, 37–44 (2012).
28. Dunn, B., Kamath, H. & Tarascon, J.-M. Electrical energy storage for the grid: a battery of Choice. *Science* 334, 928–935 (2011).
29. Armstrong, A. R. et al. Demonstrating oxygen loss and associated structural reorganization in the lithium battery cathode  $\text{Li}[\text{Ni}_{0.2}\text{Li}_{0.2}\text{Mn}_{0.6}]\text{O}_2$ . *J. Am. Chem. Soc.* 128, 8694–8698 (2006).
30. Chung, S.-H. & Manthiram, A. Current status and future prospects of metal-sulfur batteries. *Adv. Mater.* 31, 1901125 (2019).
31. Bhargava, A., He, J., Gupta, A. & Manthiram, A. Lithium-sulfur batteries: attaining the critical metrics. *Joule* 4, 285–291 (2020)..
32. recycling of cathode materials of LIBs. JMK RESEARCH analytes 2020.

### ACKNOWLEDGEMENT:

I owe a debt of gratitude to the entire Physical Chemistry faculty, Scottish Church College kolakata, for the vision and foresight that inspired me to write this paper.

I am indebted to my parents and friends who kept encouraging me and inspiring me .

Special thanks to Professor Priyatosh Dutta, my mentor Professor Rana Sen , my guide Professor Aniruddha Ganguly and Professor Susmita Kar, for helping me in the entire journey.

Finally , I take this opportunity to acknowledge everyone who helped me writing this paper.

**A REVIEW ON SPIKE GLYCOPROTEIN OF**  
**COVID-19**

**SCOTTISH CHURCH COLLEGE,**  
**UNIVERSITY OF CALCUTTA**



University Roll Number:- **223/CEM/191036**

University Registration Number:- **223-1211-0011-19**

**SPECIAL PAPER:- CHEM-SO44**

Name of the Candidate: **TRISANDHYA BANDOPADHYAY**

Name of the Examiner: **Dr. SEBANTI BASU**

A handwritten signature in black ink that reads 'Trisandhya Bandopadhyay'.

Signature of the Candidate

A handwritten signature in blue ink that reads 'Sebanti Basu'.

Signature of the Examiner



## **ACKNOWLEDGEMENT**

I would like to express my special thanks of gratitude to Dr. Asish Kumar Sen, Ex. Chief Scientist and Emeritus Scientist-CSIR, Department of Chemistry, Indian Institute of Chemical Biology, for his constant guidance, support and encouragement throughout this review work, which was accomplished during my 4<sup>th</sup> and final semester (Jan-July, 2021) in partial fulfilment of Master degree in Chemistry under Scottish Church College, University of Calcutta.

I would also like to extend my special thanks to my College Professors and the University of Calcutta for giving me this golden opportunity to write this review paper.

<b><u>CONTENTS</u></b>	<b><u>PAGE NO.</u></b>
1. INTRODUCTION	4
1.1 Glycoproteins	4
1.1.1. Oligosaccharide linkages in Glycoproteins	4
1.1.2. Function and Importance of Glycoproteins	5
1.2. CORONAVIRUSES: ORIGIN AND EMERGENCE	6
2. GENOME AND STRUCTURE OF SARS-CoV-2	7
3. STRUCTURE OF SARS-CoV-2 S-GLYCOPROTEIN	9
3.1. Structure of the S1 subunit	11
3.2. Structure of the S2 subunit	12
4. FUNCTION OF THE SARS-CoV-2 S-GLYCOPROTEIN	13
4.1. Receptor binding	14
4.2. Viral fusion	14
5. POST TRANSLATIONAL MODIFICATIONS OF S-GLYCOPROTEIN	16
5.1. N-linked glycosylation	16
5.2. Palmitoylation	16
6. CONCLUSION	17
7. REFERENCES	18

## 1. INTRODUCTION

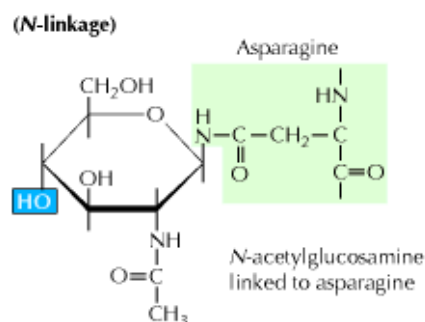
### 1.1. Glycoproteins

Glycoproteins are proteins that contain covalently attached sugar or oligosaccharides residues [1]. The hydrophilic and polar characteristics of sugars may dramatically change the chemical characteristics of the protein to which they are attached [1]. Glycoproteins are frequently present at the surface of the cells where they function as membrane proteins or as part of the extracellular matrix [2]. Inside cells they are found in specific organelles such as Golgi complexes, secretory granules, and lysosomes [3]. The oligosaccharide portions of glycoproteins are very heterogeneous and, like glycosaminoglycans, they are rich in information, forming highly specific sites for recognition and high affinity binding by carbohydrate-binding proteins called lectins. Some cytosolic and nuclear proteins can be glycosylated as well [2].

#### 1.1.1. Oligosaccharide linkages in glycoproteins

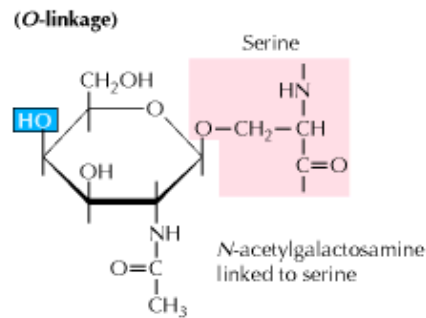
Protein glycosylation is abundant than all other types of post-translational modifications of proteins. Oligosaccharides are attached to the proteins molecules through two type of linkages such as: *N*-linked and *O*-linked.

1. *N*-Linked Glycoproteins [4]: In the vast majority of *N*-glycosidic (*N*-linked) attachments, an NAG (N-Acetyl Glucosamine) is  $\beta$ -linked to the amide nitrogen of an Asn in the sequence Asn-X-Ser or Asn-X-Thr, where X is any amino acid residue except Pro and only rarely Asp, Glu, Leu, or Trp. The oligosaccharides in these linkages usually have a distinctive **core** (innermost sequence) whose peripheral mannose residues are linked to either mannose or NAG residues. These terminal mannose residues may, in turn, be linked to other sugar/oligosaccharides residues, so that an enormous diversity of *N*-linked oligosaccharides is possible.



*N*-linked oligosaccharides have an *N*-glycosyl bond to the amide nitrogen of an Asn residue.

2. *O*-Linked Glycoproteins [4]: The most common *O*-glycosidic (*O*-linked) attachment involves the disaccharide core  $\beta$ -galactosyl-(1 $\rightarrow$ 3)- $\alpha$ -N-acetylgalactosamine  $\alpha$ -linked to the OH group of either Ser or Thr. Less commonly, glucose, galactose, mannose, and xylose form  $\alpha$ -*O*-glycosides with Ser or Thr.



*O*-linked oligosaccharides have an *O*-glycosidic bond to the hydroxyl group of Ser or Thr residues

### 1.1.2. Function and importance of glycoproteins

Glycoproteins are heavily involved in the immune system, where they allow white blood cells to move around the body, initiate immune responses, and identify other cells. They are also involved in creating mucus to protect various organs in our body. Glycoproteins are essential for keeping our bodies healthy and functional. Some of the common glycoproteins are described below:

❖ Mucins [2]: Mucins are a category of glycoproteins which are the major components of the mucus membrane in our body. Mucins are basically heavily glycosylated proteins that are produced and released by epithelial tissues. When the sequence of amino acids of the protein is examined, a high density of serine and threonine residues is found which are required to form the glycosidic bonds between the protein and sugar molecules. This means that they can form many *O*-glycosidic linkages. The oligosaccharide contains negative charges and these negative charges attract water molecules. These water molecules get attached to mucins and hence to the mucus membrane giving them the ability to lubricate the epithelial tissues. The carbohydrates are very sticky in nature and thus the pathogenic and infectious agents are trapped and in this way mucins protect the epithelial tissues.

❖ Erythropoietin [5]: Erythropoietin is a glycoprotein containing 165 amino acids sequence. Three of these amino acids are asparagine residues and are N-glycosylated whereas one of them is a serine residue and is *O*-glycosylated. Erythropoietin is produced by special cells in our kidney and is released into the blood plasma and acts as a hormone

that stimulates the production of erythrocytes. The glycosylation of erythropoietin helps to stabilise its structure and keep it in the blood plasma.

❖ Tissue factor [2]: Tissue factor is a transmembrane glycoprotein that is exposed during trauma. It's exposure initiates the formation of blood clotting process.

The bulkiness and negative charge of oligosaccharide chains also protect some proteins from attack by proteolytic enzymes. The importance of normal protein glycosylation is clear from the finding of at least 18 different genetic disorders of glycosylation in humans, all causing severely defective physical or mental development; some of these disorders are fatal [3].

Glycoproteins are also important mediators of cell–cell recognition and, in many cases, are the receptors for bacterial attachment, via adhesins, in the initial stages of infection [2].

## 1.2. Coronaviruses: origin and emergence

❖ Coronaviruses infect humans and animals that cause variety of diseases/disorders which include respiratory, enteric, renal and neurological diseases. Since the beginning of the 21<sup>st</sup> century, three coronaviruses have crossed the species barrier to cause deadly pneumonia in humans: Severe Acute Respiratory Syndrome Coronavirus (SARS-CoV), Middle East Respiratory Syndrome Coronavirus (MERS-CoV) and SARS-CoV-2. SARS-Cov emerged in Guangdong, China in 2002 and spread to five continents through air travel routes, infecting 8098 individuals and causing 774 deaths. In 2012, MERS-CoV emerged in the Arabia Peninsula and spread to 27 other countries infecting 2494 individuals and causing 858 deaths [6].

❖ MERS-CoV is believed to have originated from bats and was transmitted to dromedary camels in the distant past. Both SARS-CoV and SARS-CoV-2 are closely related and originated in bats who most likely serve as reservoir host for these two viruses [6]. In addition to highly pathogenic zoonotic pathogens SARS-CoV, MERS\_CoV and SARS-Cov-2, all belonging to the  $\beta$ -Coronavirus genus, four low pathogenic coronavirus are endemic in humans: HCoV-OC43, HCoV-HKU1, HCoV-NL63 and HCoV-229E.

❖ The ongoing pandemic of a novel strain of Coronavirus, SARS-CoV-2 was discovered in Wuhan, China and has resulted in >19.7Cr infections and >42L deaths [7]. On 31<sup>st</sup> January, 2020 the World Health Organisation (WHO) confirmed this novel Corona virus as a public health emergency of international concern.

## 2. GENOME AND STRUCTURE OF SARS-CoV-2

Coronaviruses are non-segmented, enveloped virus with single stranded positive sense RNA (+ssRNA) with 5'cap structure and 3'-poly-A tail ranging between 26 to 32kb in length. Coronaviruses belong to the family of Coronaviridae, of the sub family Coronavirinae, order Nidovirales, which include four genera: Alpha Coronavirus, Beta Coronavirus, Gamma Coronavirus and Delta Coronavirus (Fig. 1). Coronaviruses are the largest member of RNA viruses with a diameter of 80-160 nm. Phylogenetic analysis of 2019 novel Coronavirus indicates that SARS-CoV-2 shares 79% and 55% genome identity to SARS-CoV and MERS-CoV respectively and belongs to same family of virus as SARS and MERS [8].

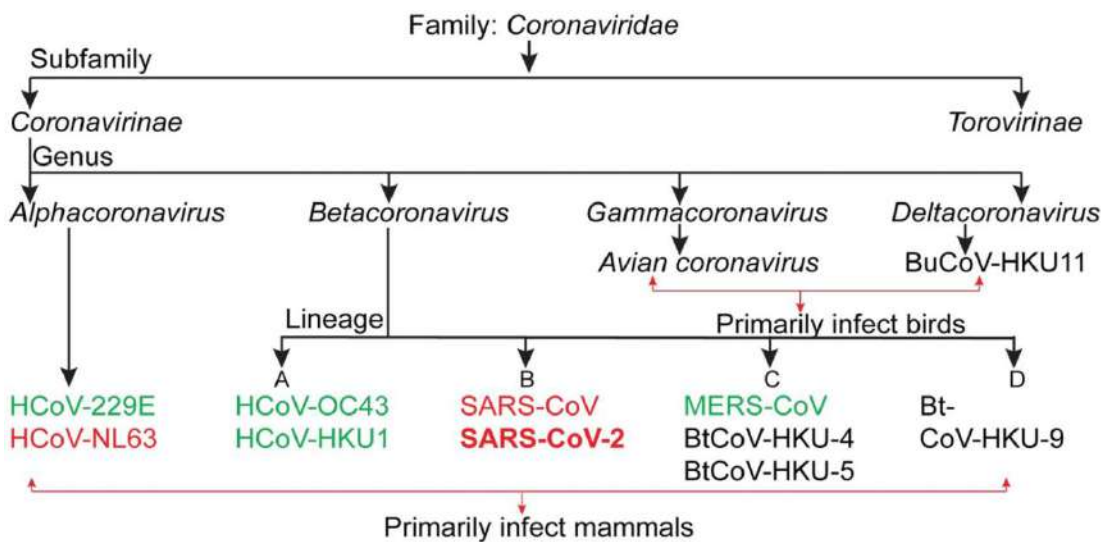


Fig. 1. Classification of coronaviruses; the 7 known HCoVs are shown in green and red.

- ❖ The observed morphology of SARS-CoV-2 is consistent with the other members of Coronaviridae family. It has a core of tightly packed RNA and is surrounded by an envelope of proteins, glycoproteins and lipids. SARS-CoV-2 comprises of approximately 30,000 bp-long RNA.
- ❖ Structurally, SARS-CoV-2 has four main structural proteins: Spike (S)-Glycoprotein, Envelope (E)-Protein, Membrane (M)-Glycoprotein and Nucleocapsid (N)-Protein and other accessory proteins (Fig. 2). The genome is arranged in the order of a non-coding 5'-UTR-replicase gene (ORF1ab)- structural proteins and accessory proteins- non-coding 3'-UTR. Hemagglutinin-esterase gene, a common feature of lineage Betacoronavirus, is absent in SARS-CoV-2.

- ❖ The E-protein is the smallest of all structural proteins found in the viral membrane and localises to the endoplasmic reticulum and Golgi complex in the host cell and is known to facilitate virus like particle formation. It helps in production and maturation of this virus [9].
- ❖ The M-glycoprotein is a transmembrane protein that helps in determining the shape of the virus envelope. It is the most abundant structural protein in a virion (ineffective virus) and can bind to all other structural proteins [10].
- ❖ N-proteins gets stabilised by binding with M-glycoproteins and viral assembly is completed. The N-protein is responsible for packaging of the viral genome RNA into a helical ribonucleocapsid (RNP). It is the structural component of CoV in the endoplasmic reticulum-Golgi region [11].
- ❖ The S-glycoprotein is a transmembrane protein (Fig. 3) that mediates the entry of Coronavirus into the host cells. Its molecular weight is about 150kDa and is found in the outer portion of the virus. S-proteins form homotrimers protruding from the viral surface. It has two functional subunits: S1 subunit and S2 subunit. S1 subunit is responsible for binding to the host cell receptor and S2 subunit functions to mediate virus fusion in transmitting host cells (Fig. 4). S-protein facilitates binding of envelope viruses to host cells by attraction with Angiotensin-Converting Enzyme 2 (ACE2), expressed in lower respiratory tract cells [12].

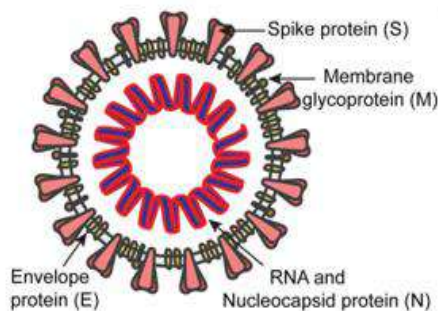


Fig. 2. Schematic of SARS-CoV-2 structure.

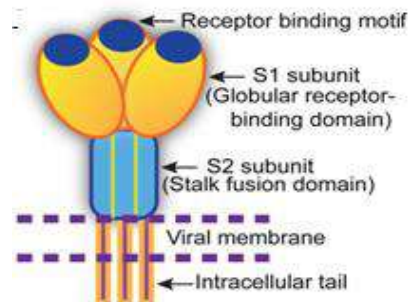


Fig. 3. Cartoon depicts key features and the trimeric structure of the SARS-CoV-2 S-protein.

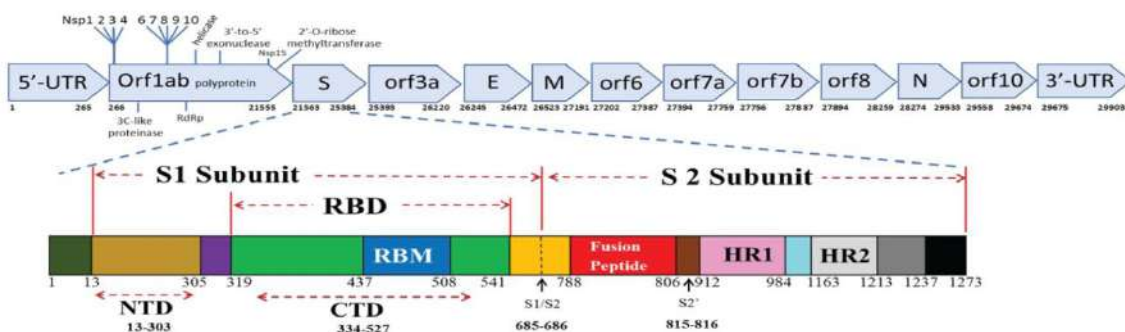
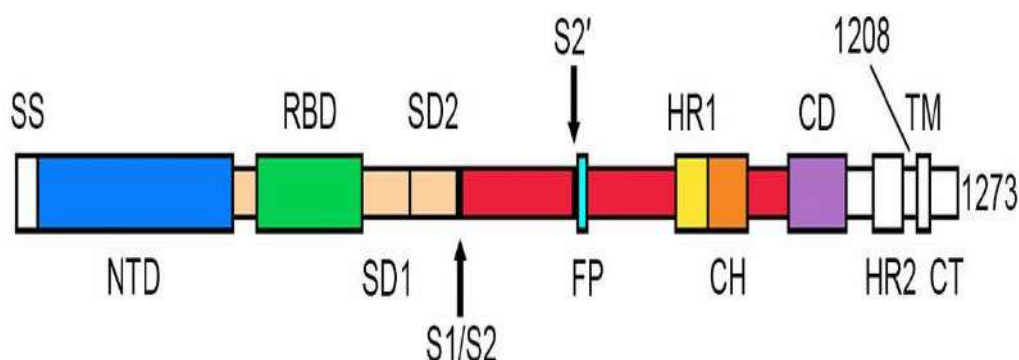


Fig. 4. Schematic of SARS-CoV-2 genome (top) and S-protein (bottom).

### 3. STRUCTURE OF SARS-CoV-2 S-GLYCOPROTEIN

The SARS-CoV-2 S-glycoprotein plays important roles in viral infection and pathogenesis. The mature S-glycoprotein on the surface of the virus is a heavily glycosylated trimer. Each protomer of this consists of 1260 amino acids residues. The surface subunit S1 is composed of 672 amino acids residues and arranged into four domains which are: an N-terminal domain (NTD), a C-terminal domain (CTD) which is also known as the receptor-binding domain, and two subdomains, SD1 and SD2 [13]. The transmembrane S2 subunit is composed of 588 amino acids residues and contains an N-terminal hydrophobic fusion peptide (FP), two heptad repeats (HR1 and HR2), a transmembrane domain (TM), and a cytoplasmic tail (CT), arranged as FP-HR1-HR2-TM-CT (Fig. 5) [13]. The distal S1 subunit contains the receptor-binding domain(s) and support the prefusion state of the membrane-anchored S2 subunit that contains the fusion machinery [6].

The SARS-CoV-2 S glycoprotein is a part of the typical class I viral fusion protein, it therefore shares some common structural and mechanistic features with other class I viral fusion proteins. Like other class I viral fusion proteins, the SARS-CoV-2 S glycoprotein is also a conformational machine which mediates viral entry by switching from a metastable unliganded state, through a prehairpin intermediate state, to a stable postfusion state. Determination of the SARS-CoV-2 S glycoprotein trimer fragments have been done in both the prefusion and postfusion states (Fig. 6) [14,15,16].



(Fig. 5. Overall structure of the SARS-CoV-2 S glycoprotein trimer in different conformations: Schematic representation of the domain arrangement of the SARS-CoV-2 S-protein precursor.

NTD: N-terminal domain; RBD: receptor-binding domain; RBM: receptor-binding motif; SD1/2: Sub domain 1/2; FP: Fusion peptide; HR1/2: Heptad repeat 1/2; CH: Central Helix; CD: Connector



domain; TM: Transmembrane domain; CT: Cytoplasmic Tail; Arrows denote proteases cleavage sites.)

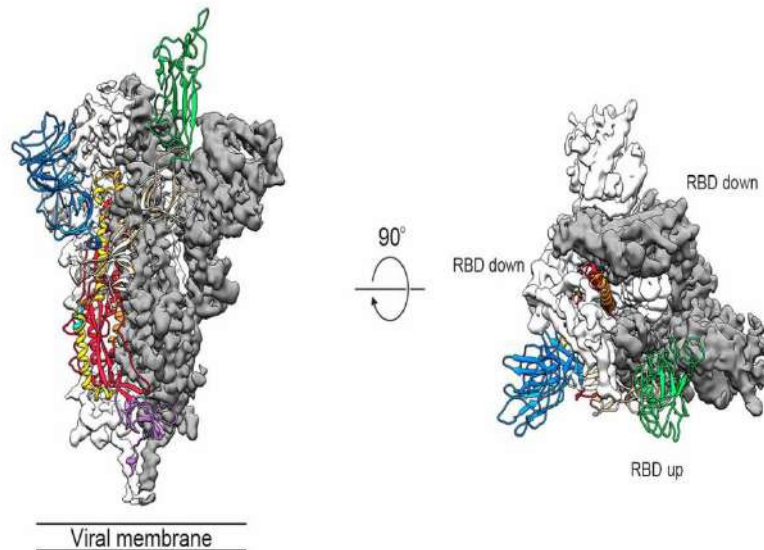


Fig. 6. Side and top views of the prefusion structure of the SARS-CoV-2 S ectodomain trimer with two RBDs in the down conformation and one RBD assumes the up conformation.

The life cycle (Fig. 7) of SARS-CoV-2 begins with membrane fusion occurring at the plasma membrane or within acidified endosomes after endocytosis, which is mediated by conformational changes in the S-glycoprotein triggered by angiotensin-converting enzyme 2 (ACE2) binding. Following viral entry, SARS-CoV-2 releases its genomic RNA into the host cell cytoplasm. Genome RNA is first translated into viral replicase polyproteins (pp1a and 1ab), which are further cleaved by viral proteases into a total of 16 nonstructural proteins. A replication-transcription complex (RTC) is formed based on many of these nonstructural proteins. In the process of genome replication and transcription mediated by RTC, the negative-sense (- sense) genomic RNA is synthesized and used as a template to produce positive-sense (+ sense) genomic RNA and subgenomic RNAs. The nucleocapsid (N) structural protein and viral RNA are replicated, transcribed, and synthesized in the cytoplasm, whereas other viral structural proteins, including the S protein, membrane (M) protein and envelope (E) protein, are transcribed and then translated in the rough endoplasmic reticulum (RER) and transported to the Golgi complex. In the RER and Golgi complex, the SARS-CoV-2 glycoprotein is subjected to co-translational and post-translational processing, including signal peptide removal, trimerization, extensive glycosylation and subunit cleavage. The N protein is subsequently associated with the positive sense genomic RNA to become a nucleoprotein complex (nucleocapsid), which together with S, M, and E proteins as well as other viral proteins, is further assembled and

followed by budding into the lumen of the ER-Golgi intermediate compartment (ERGIC) to form mature virions. Finally, the mature virions are released from the host cell, waiting for a new life cycle to start.

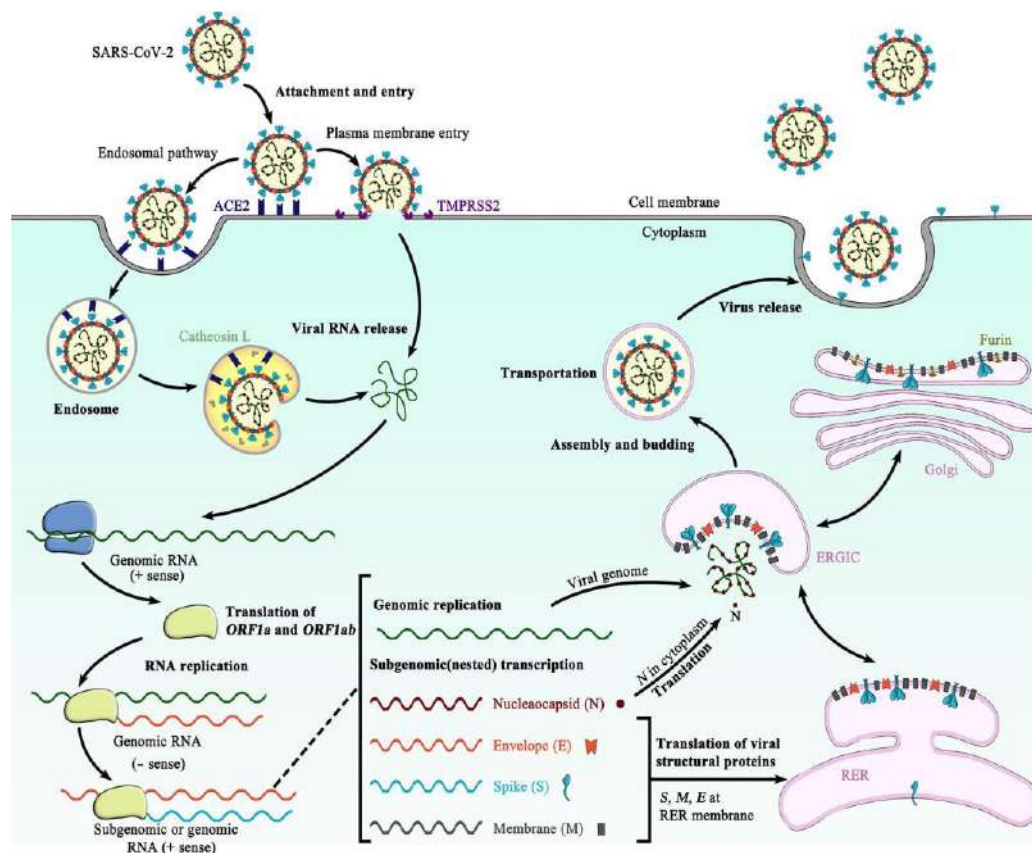


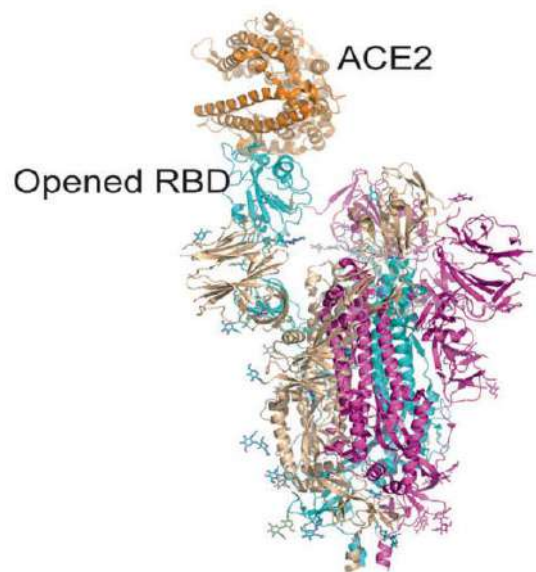
Fig. 7. Schematic representation of the life cycle of SARS-CoV-2.

### 3.1. Structure of the S1 subunit

The virus particles get attached to cell receptors to the surface of the host cell. This is the starting of the infection of virus. Therefore, receptor recognition is important to the entry of virus.

The RBD which is situated in the S1 subunit gets attached to the cell receptor, ACE2, in the region of aminopeptidase N. The S1 region consists of the NTD and CTD, and atomic details at the binding interface. The SARS-CoV-2 S CTD binding interface has more residues that gets to interact directly with the receptor ACE2 than does SARS-RBD, and a larger surface area is buried with SARS CoV-2 S CTD in complex with ACE2 than with SARS S RBD. There are mutations in the key residues which plays an important role in enhancing the interaction with ACE2. F486 in SARS-CoV-2, instead of I472 in SARS RBD, forms strong aromatic–aromatic interactions with ACE2 Y83, and E484 in SARS-CoV-2-CTD, instead of P470 in SARS RBD, forms ionic interactions with K31, which leads to higher affinity for receptor binding than RBD of SARS-CoV (Fig. 8) [17, 18, 19, 20]. The RBD region is a target

for neutralizing antibodies (nAbs), and SARS-CoV-2 and SARS-CoV RBD are ~73%–76% similar in sequence. Nine ACE2-contacting residues in CoV RBD are fully conserved, and four are partially conserved. The analysis of the RBM (receptor-binding motif) of SARS-CoV and SARS-CoV-2 revealed that most residues essential for ACE2 binding in the SARS-CoV S protein are conserved in the SARS-CoV-2 S protein. Studies have shown that there are some differences in antigenicity between SARS-CoV and SARS-CoV-2. It is revealed by the studies on the murine monoclonal antibodies and polyclonal antibodies against SARS-RBD [19].



*Fig. 8. The S protein binds to ACE2 with opened RBD in the S1 subunit.*

### **3.2. Structure of the S2 subunit**

The S2 subunit consists of a FP, HR1, HR2, TM domain, and cytoplasmic domain fusion (CT). It is responsible for viral fusion and entry of the virus. FP is a short section consisting of 15–20 conserved amino acids of the family of virus, such as glycine (G) or alanine (A). It anchors to the target membrane once the S protein adopts the prehairpin conformation. Previously it was shown that FP plays a necessary role in media membrane fusion by disrupting and connecting lipid bilayers of the host plasma membrane [21]. HR1 and HR2 are composed of a repetitive heptapeptide: HPPHCPC, where H is a hydrophobic or large residue, P is a polar or hydrophilic residue, and C is another charged residue [22]. HR1 and HR2 form the six-helical bundle (6-HB). This is essential for the function of the S2 subunit in viral fusion and entry [23]. HR1 is found at the C-terminus of a hydrophobic FP, and HR2 is found at the N-terminus of the TM domain [24]. The downstream TM domain anchors the S protein to the viral membrane, and therefore the S2 subunit ends in a CT tail [25]. RBD binds to ACE2, and S2 changes conformation by inserting FP into the target cell

membrane, exposing the prehairpin coiledcoil of the HR1 domain and triggering interaction between the HR2 domain and HR1 trimer to create 6-HB, thus bringing the viral envelope and cell membrane into proximity for viral fusion and entry. HR1 forms a homotrimeric assembly during which three extremely preserved hydrophobic grooves on the surface that bind to HR2 are exposed. The HR2 domain forms each a rigid helix and a versatile loop to interact with the HR1 domain. In the postfusion hairpin conformation of CoVs, there are many strong interactions between the HR1 and HR2 domains inside the helical region, which is designated the “fusion core region” (HR1core and HR2core regions, respectively). Targeting the heptad repeat (HR) has attracted the greatest interest in therapeutic drug discovery. The S protein is an important target protein for the development of specific drugs, while the S1 RBD domain is part of a highly mutable region and is not an ideal target site for broad-spectrum antiviral inhibitor development [26]. In contrast, the HR region of the S2 subunit plays a necessary role in HCoV infections and is preserved among HCoVs, as is the mode of interaction between HR1 and HR2 [27]. An artificial peptide derived from the stem region of the ZIKV envelope protein was demonstrated in 2017 to powerfully inhibit infection by ZIKV and other flaviviruses in vitro [28], implying antiviral potency of peptides derived from preserved regions of viral proteins. Peptides derived from the HR2 region of class I viral fusion proteins of enveloped viruses competitively bind to viral HR1 and effectively inhibit viral infection. Therefore, HR1 has become a promising target for the development of fusion inhibitors against SARS-CoV-2 infection [29].

#### **4. FUNCTION OF THE SARS-CoV-2 S-GLYCOPROTEIN**

The S protein on the surface of the virus may be a key issue which is involved in infection. It is a trimeric class I TM glycoprotein which causes the entry of the virus, and it is present in all kinds of HCoVs, as well as in other viruses [30]. Similar to other coronaviruses, the S protein of SARS-CoV-2 mediates receptor recognition, cell attachment, and fusion throughout the viral infection [18, 19, 20, 31, 32,33]. The basic unit by which the S protein binds to the receptor is the trimer of the S protein which is located on the surface of the viral envelope [18, 33]. The S1 domain containing the RBD is primarily responsible for the attachment of the virus to the receptor, while the S2 domain mainly contains the HR domain, that is HR1 and HR2, which is associated to virus fusion [29, 34].

#### 4.1. Receptor binding

The SARS-CoV-2 S protein gets attached to the host cell by recognizing the receptor ACE2 (Angiotensin Converting Enzyme 2) [33]. ACE2 converts angiotensin I to angiotensin [35]. ACE2 is distributed primarily in the lungs, intestine, heart, and kidney, and alveolar epithelial type II cells [36]. ACE2 is additionally an identified receptor for SARS-CoV. The S1 subunit of the SARS-CoV S protein binds with ACE2 to promote the formation of endosomes, which triggers viral fusion activity underneath Hydrogen ion concentration (Fig. 9a,b) [37]. Since ACE2 from different species, such as amphibians, birds, and mammals, has a preserved primary structure, the interaction between the S protein and ACE2 may be used to identify intermediate hosts of SARS-CoV-2 [38]. The S protein gets attached to ACE2 through the RBD region of the S1 subunit, mediating viral attachment to host cells in the form of a trimer [17]. The dissociation constant ( $K_D$ ) of attachment of SARS-CoV-2 S protein to human ACE2 is 14.7 nM which is less than that of SARS-CoV for which the  $K_D$  is 325.8 nM. This indicates that SARS-CoV-2 S is much more sensitive to ACE2 than that of SARS-CoV S. An approximate 24% difference is found in S-protein between SARS-CoV-2 and SARS-CoV whereas that of RBD is 23% [39].

#### 4.2. Viral fusion

The fusion of the viral membrane and host cell membrane is referred to as Viral Fusion (Fig. 9 a,b). This results in the discharge of the viral genome into the host cell. Cleavage of the SARS-CoV-2 S1 and S2 subunits is the basis of fusion. The S protein is cleaved in 2 components which are the S1 subunit and S2 subunit, by the host proteases. The subunits, S1 and S2 exist in a non-covalent form till viral fusion occurs [40]. It is discovered that the precise furin cleavage site is at the cleavage site of SARS-CoV-2 but not in other SARS like CoVs [41, 42]. The S protein of SARS-CoV-2 exists in an uncleaved state. This is discovered from the mutation of the cleavage site in SARS-CoV-2. The others are primarily in a cleaved state. Multiple furin cleavage sites are present in SARS-CoV-2 and therefore the probability of being cleaved by furin like proteases increases and thereby enhances its infectivity [43, 44]. Host cell proteases, such as TMPRSS2, are essential for S protein priming, and they have been shown to be activated in the entry of SARS-CoV and influenza A virus [47, 48]. Another host cell protease that has been proven to cleave viral S protein is trypsin [49].

Therefore we can conclude that the S protein of SARS-CoV-2 is similar to that of SARS-CoV, and host cell proteases are required for promoting S protein cleavage of both SARS-

CoV-2 and SARS-CoV. The presence of a selected furin cleavage site on SARS-CoV-2 S might be one reason that SARS-CoV-2 is more contagious than SARS-CoV. The formation of 6-HB is essential for viral fusion. The FP within the N-terminus of SARS-CoV-2 and the two HR domains on S2 is essential for viral fusion [50]. After cleavage of the S protein, the FP of SARS-CoV-2 is exposed and triggers viral fusion. Under the action of some special ligands, the fusion protein undergoes a conformational change and then inserts into the host cell membrane (Fig. 9c) [51]. The distance between the viral membrane and host cell membrane is shortened, and the HR1 domain of the S protein is in close proximity to the host cell membrane, whereas the HR2 domain is closer to the viral membrane side. Then, HR2 folds back to HR1, the two HR domains form a six-helix structure in an antiparallel format of the fusion core, the viral membrane is pulled toward the host cell membrane and tightly binds to it, and the two membranes fuse [52].

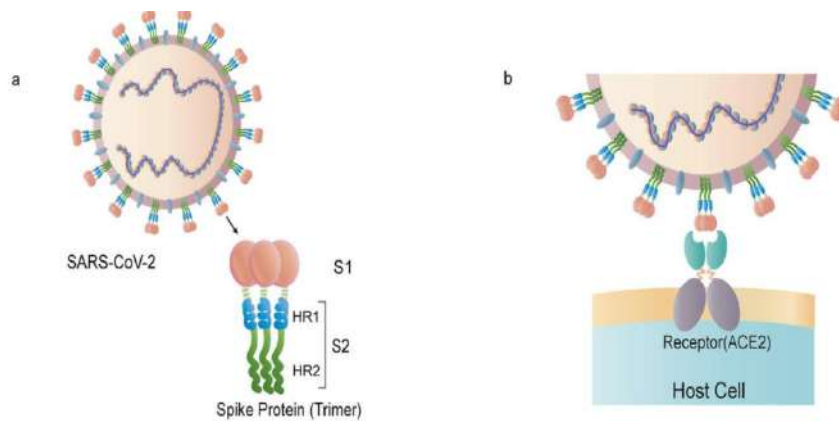


Fig. 9a. The schematic structure of the S protein. Fig. 9b. The S protein binds to the receptor ACE2.

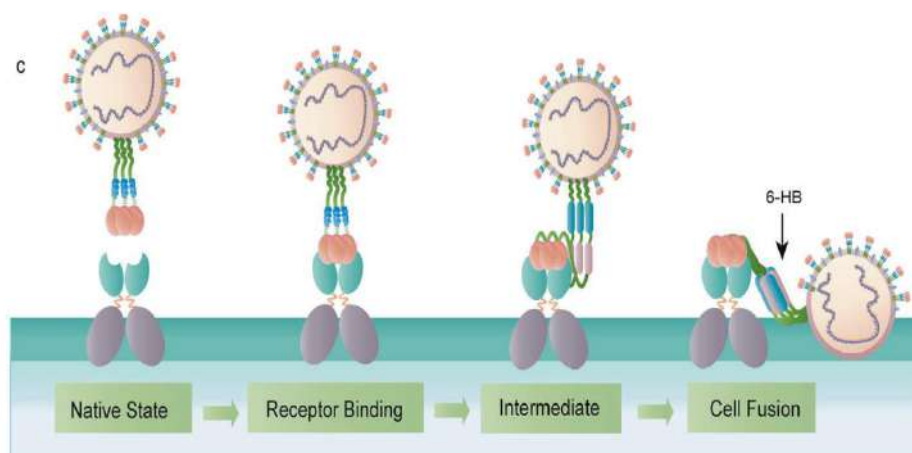


Fig. 9c. The binding and virus-cell fusion process mediated by the S protein.

## **5. POST TRANSLATIONAL MODIFICATIONS OF S-GLYCOPROTEIN**

Numerous CoV proteins undergo post translational modifications (PTMs) which include glycosylation and palmitoylation of the E and S-glycoprotein. More specifically, glycosylation at Asn residues (N linked) or hydroxyl group of Ser and Thr (O-linked) of the M-protein, ADP-ribosylation of N-protein and other PTMs on NSPs and accessory protein have been observed in CoVs. In addition, incorporation of disulfide bonds in S-glycoprotein and conserved cysteine residues into its cytosolic domain have been reported with palmitoylation.

### **5.1. N-linked glycosylation**

The N-linked glycosylation in S-glycoprotein of CoVs was first reported for mouse hepatitis virus. S-glycoprotein of SARS-CoV-2 has exhibits oligosaccharides containing high mannose and trimers within 30 min after the entry into endoplasmic reticulum, former to the acquirement of multifaceted glycans present in Golgi apparatus. Monitoring of SARS-CoV S-glycoprotein susceptibility to endoglycosidase H (endo H), shows its maturation status. Using molecular cloning techniques, the S glycoprotein coding sequences of various CoVs were cloned, following determination of N-linked glycosylation sites. However, all the putative glycosylation sites were not functional. In SARS-CoV S-glycoprotein, 12 sites were found glycosylated out of the 23 putative sites [53]. N-linked glycosylation is associated with protein conformation, and hence intensely affects the antigenicity of S-glycoprotein and receptor binding. Similarly, S-glycoprotein of SARS-CoV-2 has been found to exhibit 22 N-linked glycan structure detected using mass spectrometry which showed complex and hybrid glycans likely to play an important role in protein folding and immune evasion.

### **5.2. Palmitoylation**

Palmitoylation is a process of the covalent attachment of fatty acids like palmitic acid, to cysteine etc. Four cysteine rich clusters are present in the cytoplasmic ends of SARSCoV S-glycoprotein. Mutational study revealed palmitoylation of cysteine clusters I and II. Even though the cellular expression of SARS-CoV S-glycoprotein was unaffected considerably by cysteine clusters I and II mutations, S mediated fusion of cells was clearly reduced as compared with the wild type protein. This suggests the requirement of palmitoylation in the endodomain for the SARS-CoV S-glycoprotein fusogenic activity [53] [54].

## 6. CONCLUSION

Seventeen years after the short outbreak of the severe acute respiratory syndrome (SARS) in 2003, another coronavirus-related epidemic disease, coronavirus disease 2019 (COVID-19) has now spread globally and has jeopardized the lives of almost everyone on this planet. SARS coronavirus (SARS-CoV) and SARS-CoV-2 are the etiological agents of SARS and COVID-19, respectively.

SARS-CoV-2 shows many similarities with SARS-CoV on sequence alignment, structural, and antigen basis. The SARS-CoV and SARS-CoV-2 particles are roughly spherical with a diameter of 80–120 nm. Protruding spikes decorate the surface of the viral particles. These spikes are glycoprotein in nature and are termed as S-glycoprotein. S-glycoprotein plays essential roles in host-pathogen interaction, such as, in mediating the entry of the virus into host cells through binding with human Angiotensin-converting enzyme 2 (hACE2) as a functional receptor, a main target for neutralization antibody, immunological functions etc.

All coronaviruses display lectin like spike glycoproteins on their surface. *O*-acetylated sialic acid binding by the S1 spike protein subunits is crucial for coronavirus to engage host cells, while the S2 domain initiates viral fusion. Enhanced binding affinity between SARS-CoV-2 S-glycoprotein and hACE2 was proposed to correlate with increased virus transmissibility and disease severity in humans.

The complete chemical structure of the S-glycoprotein is still unknown especially for the glycan part. However, it is clear that the S-glycoprotein play the most crucial role in viral infection and propagation. More research findings will help to understand the function and role of the S-glycoprotein.

Till today, there is no effective drug to cure coronavirus infection. Several vaccines have been developed on emergency basic with varied efficacy against different mutant stains of covid-19. More efficient SARS-CoV-2 vaccines are therefore crucial to reduce the severity and transmission of the disease. In the quest for better vaccine, vaccine development targeting the cell surface S-glycoprotein is being investigated.

Spike glycoprotein is now known to bind with *O*-acetylated sialic acids. Based on this observation, research is being conducted to develop simple COVID-19 diagnostic kit instead of complicated RNA based detection process. Currently S-glycoprotein is one of the most vital targets for the development of vaccine and therapeutics for COVID-19.



## 7. REFERENCES

1. "Glycoprotein - Wikipedia". 2021. *En.Wikipedia.Org*. <https://en.wikipedia.org/wiki/Glycoprotein>.
2. Nelson, David L, Michael M Cox, Aaron A Hoskins, and Albert L Lehninger. n.d. *Lehninger Principles Of Biochemistry*.
3. Voet, Donald, Judith G Voet, and Charlotte W Pratt. 2016. *Fundamentals Of Biochemistry*. New York: Wiley.
4. "What Glycoproteins Are And What They Do". 2021. *Thoughtco*. <https://www.thoughtco.com/glycoprotein-definition-and-function-4134331>.
5. <https://www.ncbi.nlm.nih.gov/pmc/articles/PMC3822280/>.
6. Walls, Alexandra C., Young-Jun Park, M. Alejandra Tortorici, Abigail Wall, Andrew T. McGuire, and David Veasley. 2020. "Structure, Function, And Antigenicity Of The SARS-Cov-2 Spike Glycoprotein". *Cell* 181 (2): 281-292.e6. doi:10.1016/j.cell.2020.02.058.
7. "COVID Live Update: From The Coronavirus - Worldometer". 2021. *Worldometers*. *Info*. [https://www.worldometers.info/coronavirus/?utm\\_campaign=homeAdvegas1?%22](https://www.worldometers.info/coronavirus/?utm_campaign=homeAdvegas1?%22).
8. Kim, Cheorl-Ho. 2020. "SARS-Cov-2 Evolutionary Adaptation Toward Host Entry And Recognition Of Receptor O-Acetyl Sialylation In Virus-Host Interaction". *International Journal Of Molecular Sciences* 21 (12): 4549. doi:10.3390/ijms21124549.
9. Venkatagopalan, Pavithra, Sasha M. Daskalova, Lisa A. Lopez, Kelly A. Dolezal, and Brenda G. Hogue. 2015. "Coronavirus Envelope (E) Protein Remains At The Site Of Assembly". *Virology* 478: 75-85. doi:10.1016/j.virol.2015.02.005.
10. Nakauchi, Mina, Hiroaki Kariwa, Yasuhiro Kon, Kentaro Yoshii, Akihiko Maeda, and Ikuo Takashima. 2008. "Analysis Of Severe Acute Respiratory Syndrome Coronavirus Structural Proteins In Virus-Like Particle Assembly". *Microbiology And Immunology* 52 (12): 625-630. doi:10.1111/j.1348-0421.2008.00079.x.
11. Wu, Chia-Hsin, Shiou-Hwei Yeh, Yeou-Guang Tsay, Ya-Hsiung Shieh, Chuan-Liang Kao, Yen-Shun Chen, Sheng-Han Wang, Ti-Jung Kuo, Ding-Shinn Chen, and Pei-Jer Chen. 2009. "Glycogen Synthase Kinase-3 Regulates The Phosphorylation Of Severe Acute Respiratory Syndrome Coronavirus Nucleocapsid Protein And Viral Replication". *Journal Of Biological Chemistry* 284 (8): 5229-5239. doi:10.1074/jbc.m805747200.

12. Simmons, Graham, Pawel Zmora, Stefanie Gierer, Adeline Heurich, and Stefan Pöhlmann. 2013. "Proteolytic Activation Of The SARS-Coronavirus Spike Protein: Cutting Enzymes At The Cutting Edge Of Antiviral Research". *Antiviral Research* 100 (3): 605-614. doi:10.1016/j.antiviral.2013.09.028.
13. Wrapp, Daniel, Nianshuang Wang, Kizzmekia S. Corbett, Jory A. Goldsmith, Ching-Lin Hsieh, Olubukola Abiona, Barney S. Graham, and Jason S. McLellan. 2020. "Cryo-EM Structure Of The 2019-Ncov Spike In The Prefusion Conformation". *Science* 367 (6483): 1260-1263. doi:10.1126/science.abb2507.
14. Wrapp, Daniel, Nianshuang Wang, Kizzmekia S. Corbett, Jory A. Goldsmith, Ching-Lin Hsieh, Olubukola Abiona, Barney S. Graham, and Jason S. McLellan. 2020. "Cryo-EM Structure Of The 2019-Ncov Spike In The Prefusion Conformation". *Science* 367 (6483): 1260-1263. doi:10.1126/science.abb2507.
15. Harrison, Stephen C. 2008. "Viral Membrane Fusion". *Nature Structural & Molecular Biology* 15 (7): 690-698. doi:10.1038/nsmb.1456.
16. Duan, Liangwei, Qianqian Zheng, Hongxia Zhang, Yuna Niu, Yunwei Lou, and Hui Wang. 2020. "The SARS-Cov-2 Spike Glycoprotein Biosynthesis, Structure, Function, And Antigenicity: Implications For The Design Of Spike-Based Vaccine Immunogens". *Frontiers In Immunology* 11. doi:10.3389/fimmu.2020.576622.
17. Wrapp, Daniel, Nianshuang Wang, Kizzmekia S. Corbett, Jory A. Goldsmith, Ching-Lin Hsieh, Olubukola Abiona, Barney S. Graham, and Jason S. McLellan. 2020. "Cryo-EM Structure Of The 2019-Ncov Spike In The Prefusion Conformation". *Science* 367 (6483): 1260-1263. doi:10.1126/science.abb2507.
18. Walls, Alexandra C., Young-Jun Park, M. Alejandra Tortorici, Abigail Wall, Andrew T. McGuire, and David Veasley. 2020. "Structure, Function, And Antigenicity Of The SARS-Cov-2 Spike Glycoprotein". *Cell* 183 (6): 1735. doi:10.1016/j.cell.2020.11.032.
19. Wang, Qihui, Yanfang Zhang, Lili Wu, Sheng Niu, Chunli Song, Zengyuan Zhang, and Guangwen Lu et al. 2020. "Structural And Functional Basis Of SARS-Cov-2 Entry By Using Human ACE2". *Cell* 181 (4): 894-904.e9. doi:10.1016/j.cell.2020.03.045.
20. Lan, Jun, Jiwan Ge, Jinfang Yu, Sisi Shan, Huan Zhou, Shilong Fan, and Qi Zhang et al. 2020. "Structure Of The SARS-Cov-2 Spike Receptor-Binding Domain Bound To The ACE2 Receptor". *Nature* 581 (7807): 215-220. doi:10.1038/s41586-020-2180-5.
21. Millet, Jean Kaoru, and Gary R. Whittaker. 2018. "Physiological And Molecular Triggers For SARS-Cov Membrane Fusion And Entry Into Host Cells". *Virology* 517: 3-8. doi:10.1016/j.virol.2017.12.015.
22. Chambers, P., C. R. Pringle, and A. J. Easton. 1990. "Heptad Repeat Sequences Are Located Adjacent To Hydrophobic Regions In Several Types Of Virus Fusion

- Glycoproteins". *Journal Of General Virology* 71 (12): 3075-3080. doi:10.1099/0022-1317-71-12-3075.
23. Xia, Shuai, Yun Zhu, Meiqin Liu, Qiaoshuai Lan, Wei Xu, Yanling Wu, and Tianlei Ying et al. 2020. "Fusion Mechanism Of 2019-Ncov And Fusion Inhibitors Targeting HR1 Domain In Spike Protein". *Cellular & Molecular Immunology* 17 (7): 765-767. doi:10.1038/s41423-020-0374-2.
  24. Robson, B. 2020. "Computers And Viral Diseases. Preliminary Bioinformatics Studies On The Design Of A Synthetic Vaccine And A Preventative Peptidomimetic Antagonist Against The SARS-Cov-2 (2019-Ncov, COVID-19) Coronavirus". *Computers In Biology And Medicine* 119: 103670. doi:10.1016/j.compbiomed.2020.103670.
  25. Tang, Tiffany, Miya Bidon, Javier A. Jaimes, Gary R. Whittaker, and Susan Daniel. 2020. "Coronavirus Membrane Fusion Mechanism Offers A Potential Target For Antiviral Development". *Antiviral Research* 178: 104792. doi:10.1016/j.antiviral.2020.104792.
  26. Lu, Guangwen, Qihui Wang, and George F. Gao. 2015. "Bat-To-Human: Spike Features Determining 'Host Jump' Of Coronaviruses SARS-Cov, MERS-Cov, And Beyond". *Trends In Microbiology* 23 (8): 468-478. doi:10.1016/j.tim.2015.06.003.
  27. Liu, Shuwen, Gengfu Xiao, Yibang Chen, Yuxian He, Jinkui Niu, Carlos R Escalante, and Huabao Xiong et al. 2004. "Interaction Between Heptad Repeat 1 And 2 Regions In Spike Protein Of SARS-Associated Coronavirus: Implications For Virus Fusogenic Mechanism And Identification Of Fusion Inhibitors". *The Lancet* 363 (9413): 938-947. doi:10.1016/s0140-6736(04)15788-7.
  28. Yu, Yufeng, Yong-Qiang Deng, Peng Zou, Qian Wang, Yanyan Dai, Fei Yu, and Lanying Du et al. 2017. "A Peptide-Based Viral Inactivator Inhibits Zika Virus Infection In Pregnant Mice And Fetuses". *Nature Communications* 8 (1). doi:10.1038/ncomms15672.
  29. Huang, Yuan, Chan Yang, Xin-feng Xu, Wei Xu, and Shu-wen Liu. 2020. "Structural And Functional Properties Of SARS-Cov-2 Spike Protein: Potential Antivirus Drug Development For COVID-19". *Acta Pharmacologica Sinica* 41 (9): 1141-1149. doi:10.1038/s41401-020-0485-4.
  30. Weissenhorn,, W., A. Dessen, L. J. Calder, S. C. Harrison, J. J. Skehel, and D. C. Wiley. 1999. "Structural Basis For Membrane Fusion By Enveloped Viruses". *Molecular Membrane Biology* 16 (1): 3-9. doi:10.1080/096876899294706.
  31. Gui, Miao, Wenfei Song, Haixia Zhou, Jingwei Xu, Silian Chen, Ye Xiang, and Xinquan Wang. 2016. "Cryo-Electron Microscopy Structures Of The SARS-Cov Spike Glycoprotein Reveal A Prerequisite Conformational State For Receptor Binding". *Cell Research* 27 (1): 119-129. doi:10.1038/cr.2016.152.

32. Bosch, Berend Jan, Ruurd van der Zee, Cornelis A. M. de Haan, and Peter J. M. Rottier. 2003. "The Coronavirus Spike Protein Is A Class I Virus Fusion Protein: Structural And Functional Characterization Of The Fusion Core Complex". *Journal Of Virology* 77 (16): 8801-8811. doi:10.1128/jvi.77.16.8801-8811.2003.
33. Yan, Renhong, Yuanyuan Zhang, Yanning Li, Lu Xia, Yingying Guo, and Qiang Zhou. 2020. "Structural Basis For The Recognition Of SARS-Cov-2 By Full-Length Human ACE2". *Science* 367 (6485): 1444-1448. doi:10.1126/science.abb2762.
34. Cui, Jie, Fang Li, and Zheng-Li Shi. 2018. "Origin And Evolution Of Pathogenic Coronaviruses". *Nature Reviews Microbiology* 17 (3): 181-192. doi:10.1038/s41579-018-0118-9.
35. Donoghue, Mary, Frank Hsieh, Elizabeth Baronas, Kevin Godbout, Michael Gosselin, Nancy Stagliano, and Michael Donovan et al. 2000. "A Novel Angiotensin-Converting Enzyme-Related Carboxypeptidase (ACE2) Converts Angiotensin I To Angiotensin 1-9". *Circulation Research* 87 (5). doi:10.1161/01.res.87.5.e1.
36. Zhang, Haibo, Josef M. Penninger, Yimin Li, Nanshan Zhong, and Arthur S. Slutsky. 2020. "Angiotensin-Converting Enzyme 2 (ACE2) As A SARS-Cov-2 Receptor: Molecular Mechanisms And Potential Therapeutic Target". *Intensive Care Medicine* 46 (4): 586-590. doi:10.1007/s00134-020-05985-9.
37. Shang, Jian, Yushun Wan, Chuming Luo, Gang Ye, Qibin Geng, Ashley Auerbach, and Fang Li. 2020. "Cell Entry Mechanisms Of SARS-Cov-2". *Proceedings Of The National Academy Of Sciences* 117 (21): 11727-11734. doi:10.1073/pnas.2003138117.
38. Chen, Yun, Yao Guo, Yihang Pan, and Zhizhuang Joe Zhao. 2020. "Structure Analysis Of The Receptor Binding Of 2019-Ncov". *Biochemical And Biophysical Research Communications* 525 (1): 135-140. doi:10.1016/j.bbrc.2020.02.071.
39. Wan, Yushun, Jian Shang, Rachel Graham, Ralph S. Baric, and Fang Li. 2020. "Receptor Recognition By The Novel Coronavirus From Wuhan: An Analysis Based On Decade-Long Structural Studies Of SARS Coronavirus". *Journal Of Virology* 94 (7). doi:10.1128/jvi.00127-20.
40. Tortorici, M. Alejandra, Alexandra C. Walls, Yifei Lang, Chunyan Wang, Zeshi Li, Danielle Koerhuis, and Geert-Jan Boons et al. 2019. "Structural Basis For Human Coronavirus Attachment To Sialic Acid Receptors". *Nature Structural & Molecular Biology* 26 (6): 481-489. doi:10.1038/s41594-019-0233-y.
41. Coutard, B., C. Valle, X. de Lamballerie, B. Canard, N.G. Seidah, and E. Decroly. 2020. "The Spike Glycoprotein Of The New Coronavirus 2019-Ncov Contains A Furin-Like Cleavage Site Absent In Cov Of The Same Clade". *Antiviral Research* 176: 104742. doi:10.1016/j.antiviral.2020.104742.

42. Al-Tawfiq, Jaffar A. 2020. "Viral Loads Of SARS-Cov, MERS-Cov And SARS-Cov-2 In Respiratory Specimens: What Have We Learned?". *Travel Medicine And Infectious Disease* 34: 101629. doi:10.1016/j.tmaid.2020.101629.
43. Hasan, Anwarul, Bilal Ahamad Paray, Arif Hussain, Fikry Ali Qadir, Farnoosh Attar, Falah Mohammad Aziz, and Majid Sharifi et al. 2020. "A Review On The Cleavage Priming Of The Spike Protein On Coronavirus By Angiotensin-Converting Enzyme-2 And Furin". *Journal Of Biomolecular Structure And Dynamics* 39 (8): 3025-3033. doi:10.1080/07391102.2020.1754293.
44. Millet, Jean Kaoru, and Gary R. Whittaker. 2015. "Host Cell Proteases: Critical Determinants of Coronavirus Tropism And Pathogenesis". *Virus Research* 202: 120-134. doi:10.1016/j.virusres.2014.11.021.
45. Claas, Eric CJ, Albert DME Osterhaus, Ruud van Beek, Jan C De Jong, Guus F Rimmelzwaan, Dennis A Senne, Scott Krauss, Kennedy F Shortridge, and Robert G Webster. 1998. "Human Influenza A H5N1 Virus Related To A Highly Pathogenic Avian Influenza Virus". *The Lancet* 351 (9101): 472-477. doi:10.1016/s0140-6736(97)11212-0.
46. Kido, Hiroshi, Yuushi Okumura, Etsuhisa Takahashi, Hai-Yan Pan, Siye Wang, Dengbing Yao, Min Yao, Junji Chida, and Mihiro Yano. 2012. "Role Of Host Cellular Proteases In The Pathogenesis Of Influenza And Influenza-Induced Multiple Organ Failure". *Biochimica Et Biophysica Acta (BBA) - Proteins And Proteomics* 1824 (1): 186-194. doi:10.1016/j.bbapap.2011.07.001.
47. Heurich, A., H. Hofmann-Winkler, S. Gierer, T. Liepold, O. Jahn, and S. Pohlmann. 2013. "TMPRSS2 And ADAM17 Cleave ACE2 Differentially And Only Proteolysis By TMPRSS2 Augments Entry Driven By The Severe Acute Respiratory Syndrome Coronavirus Spike Protein". *Journal Of Virology* 88 (2): 1293-1307. doi:10.1128/jvi.02202-13.
48. Limburg, Hannah, Anne Harbig, Dorothea Bestle, David A. Stein, Hong M. Moulton, Julia Jaeger, and Harshavardhan Janga et al. 2019. "TMPRSS2 Is The Major Activating Protease Of Influenza A Virus In Primary Human Airway Cells And Influenza B Virus In Human Type II Pneumocytes". *Journal Of Virology* 93 (21). doi:10.1128/jvi.00649-19.
49. Ou, Xiuyuan, Yan Liu, Xiaobo Lei, Pei Li, Dan Mi, Lili Ren, and Li Guo et al. 2020. "Characterization Of Spike Glycoprotein Of SARS-Cov-2 On Virus Entry And Its Immune Cross-Reactivity With SARS-Cov". *Nature Communications* 11 (1). doi:10.1038/s41467-020-15562-9.
50. Kawase, Miyuki, Michiyo Kataoka, Kazuya Shirato, and Shutoku Matsuyama. 2019. "Biochemical Analysis Of Coronavirus Spike Glycoprotein Conformational

- Intermediates During Membrane Fusion". *Journal Of Virology* 93 (19). doi:10.1128/jvi.00785-19.
51. Harrison, Stephen C. 2015. "Viral Membrane Fusion". *Virology* 479-480: 498-507. doi:10.1016/j.virol.2015.03.043.
  52. Eckert, Debra M., and Peter S. Kim. 2001. "Mechanisms Of Viral Membrane Fusion And Its Inhibition". *Annual Review Of Biochemistry* 70 (1): 777-810. doi:10.1146/annurev.biochem.70.1.777.
  53. Saxena, Shailendra K., Swatantra Kumar, Preeti Baxi, Nishant Srivastava, Bipin Puri, and R. K. Ratho. 2020. "Chasing COVID-19 Through SARS-Cov-2 Spike Glycoprotein". *Virusdisease* 31 (4): 399-407. doi:10.1007/s13337-020-00642-7.
  54. Krokhin, Oleg, Yan Li, Anton Andonov, Heinz Feldmann, Ramon Flick, Steven Jones, and Ute Stroehrer et al. 2003. "Mass Spectrometric Characterization of Proteins From The SARS Virus". *Molecular & Cellular Proteomics* 2 (5): 346-356. doi:10.1074/mcp.m300048-mcp200.

**A REVIEW ON SPIKE GLYCOPROTEIN OF**  
**COVID-19**

**SCOTTISH CHURCH COLLEGE,**  
**UNIVERSITY OF CALCUTTA**



University Roll Number:- **223/CEM/191036**

University Registration Number:- **223-1211-0011-19**

**SPECIAL PAPER:- CHEM-SO44**

Name of the Candidate: **TRISANDHYA BANDOPADHYAY**

Name of the Examiner: **Dr. SEBANTI BASU**

A handwritten signature in black ink that reads 'Trisandhya Bandopadhyay'.

Signature of the Candidate

Signature of the Examiner

## **ACKNOWLEDGEMENT**

I would like to express my special thanks of gratitude to Dr. Asish Kumar Sen, Ex. Chief Scientist and Emeritus Scientist-CSIR, Department of Chemistry, Indian Institute of Chemical Biology, for his constant guidance, support and encouragement throughout this review work, which was accomplished during my 4<sup>th</sup> and final semester (Jan-July, 2021) in partial fulfilment of Master degree in Chemistry under Scottish Church College, University of Calcutta.

I would also like to extend my special thanks to my College Professors and the University of Calcutta for giving me this golden opportunity to write this review paper.



<b><u>CONTENTS</u></b>	<b><u>PAGE NO.</u></b>
1. INTRODUCTION	4
1.1 Glycoproteins	4
1.1.1. Oligosaccharide linkages in Glycoproteins	4
1.1.2. Function and Importance of Glycoproteins	5
1.2. CORONAVIRUSES: ORIGIN AND EMERGENCE	6
2. GENOME AND STRUCTURE OF SARS-CoV-2	7
3. STRUCTURE OF SARS-CoV-2 S-GLYCOPROTEIN	9
3.1. Structure of the S1 subunit	11
3.2. Structure of the S2 subunit	12
4. FUNCTION OF THE SARS-CoV-2 S-GLYCOPROTEIN	13
4.1. Receptor binding	14
4.2. Viral fusion	14
5. POST TRANSLATIONAL MODIFICATIONS OF S-GLYCOPROTEIN	16
5.1. N-linked glycosylation	16
5.2. Palmitoylation	16
6. CONCLUSION	17
7. REFERENCES	18

## 1. INTRODUCTION

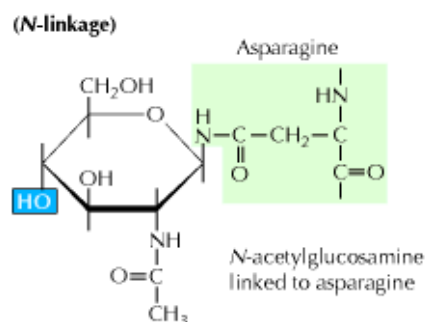
### 1.1. Glycoproteins

Glycoproteins are proteins that contain covalently attached sugar or oligosaccharides residues [1]. The hydrophilic and polar characteristics of sugars may dramatically change the chemical characteristics of the protein to which they are attached [1]. Glycoproteins are frequently present at the surface of the cells where they function as membrane proteins or as part of the extracellular matrix [2]. Inside cells they are found in specific organelles such as Golgi complexes, secretory granules, and lysosomes [3]. The oligosaccharide portions of glycoproteins are very heterogeneous and, like glycosaminoglycans, they are rich in information, forming highly specific sites for recognition and high affinity binding by carbohydrate-binding proteins called lectins. Some cytosolic and nuclear proteins can be glycosylated as well [2].

#### 1.1.1. Oligosaccharide linkages in glycoproteins

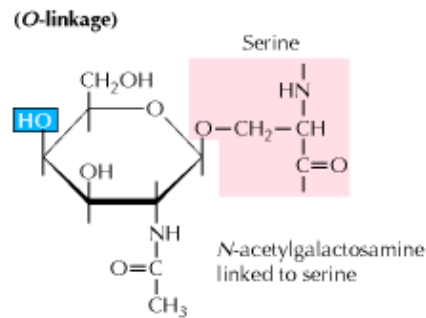
Protein glycosylation is abundant than all other types of post-translational modifications of proteins. Oligosaccharides are attached to the proteins molecules through two type of linkages such as: *N*-linked and *O*-linked.

1. *N*-Linked Glycoproteins [4]: In the vast majority of *N*-glycosidic (*N*-linked) attachments, an NAG (N-Acetyl Glucosamine) is  $\beta$ -linked to the amide nitrogen of an Asn in the sequence Asn-X-Ser or Asn-X-Thr, where X is any amino acid residue except Pro and only rarely Asp, Glu, Leu, or Trp. The oligosaccharides in these linkages usually have a distinctive **core** (innermost sequence) whose peripheral mannose residues are linked to either mannose or NAG residues. These terminal mannose residues may, in turn, be linked to other sugar/oligosaccharides residues, so that an enormous diversity of *N*-linked oligosaccharides is possible.



*N*-linked oligosaccharides have an *N*-glycosyl bond to the amide nitrogen of an Asn residue.

2. *O*-Linked Glycoproteins [4]: The most common *O*-glycosidic (*O*-linked) attachment involves the disaccharide core  $\beta$ -galactosyl-(1 $\rightarrow$ 3)- $\alpha$ -N-acetylgalactosamine  $\alpha$ -linked to the OH group of either Ser or Thr. Less commonly, glucose, galactose, mannose, and xylose form  $\alpha$ -*O*-glycosides with Ser or Thr.



*O*-linked oligosaccharides have an *O*-glycosidic bond to the hydroxyl group of Ser or Thr residues

### 1.1.2. Function and importance of glycoproteins

Glycoproteins are heavily involved in the immune system, where they allow white blood cells to move around the body, initiate immune responses, and identify other cells. They are also involved in creating mucus to protect various organs in our body. Glycoproteins are essential for keeping our bodies healthy and functional. Some of the common glycoproteins are described below:

❖ Mucins [2]: Mucins are a category of glycoproteins which are the major components of the mucus membrane in our body. Mucins are basically heavily glycosylated proteins that are produced and released by epithelial tissues. When the sequence of amino acids of the protein is examined, a high density of serine and threonine residues is found which are required to form the glycosidic bonds between the protein and sugar molecules. This means that they can form many *O*-glycosidic linkages. The oligosaccharide contains negative charges and these negative charges attract water molecules. These water molecules get attached to mucins and hence to the mucus membrane giving them the ability to lubricate the epithelial tissues. The carbohydrates are very sticky in nature and thus the pathogenic and infectious agents are trapped and in this way mucins protect the epithelial tissues.

❖ Erythropoietin [5]: Erythropoietin is a glycoprotein containing 165 amino acids sequence. Three of these amino acids are asparagine residues and are N-glycosylated whereas one of them is a serine residue and is *O*-glycosylated. Erythropoietin is produced by special cells in our kidney and is released into the blood plasma and acts as a hormone

that stimulates the production of erythrocytes. The glycosylation of erythropoietin helps to stabilise its structure and keep it in the blood plasma.

❖ Tissue factor [2]: Tissue factor is a transmembrane glycoprotein that is exposed during trauma. It's exposure initiates the formation of blood clotting process.

The bulkiness and negative charge of oligosaccharide chains also protect some proteins from attack by proteolytic enzymes. The importance of normal protein glycosylation is clear from the finding of at least 18 different genetic disorders of glycosylation in humans, all causing severely defective physical or mental development; some of these disorders are fatal [3].

Glycoproteins are also important mediators of cell–cell recognition and, in many cases, are the receptors for bacterial attachment, via adhesins, in the initial stages of infection [2].

## **1.2. Coronaviruses: origin and emergence**

❖ Coronaviruses infect humans and animals that cause variety of diseases/disorders which include respiratory, enteric, renal and neurological diseases. Since the beginning of the 21<sup>st</sup> century, three coronaviruses have crossed the species barrier to cause deadly pneumonia in humans: Severe Acute Respiratory Syndrome Coronavirus (SARS-CoV), Middle East Respiratory Syndrome Coronavirus (MERS-CoV) and SARS-CoV-2. SARS-Cov emerged in Guangdong, China in 2002 and spread to five continents through air travel routes, infecting 8098 individuals and causing 774 deaths. In 2012, MERS-CoV emerged in the Arabia Peninsula and spread to 27 other countries infecting 2494 individuals and causing 858 deaths [6].

❖ MERS-CoV is believed to have originated from bats and was transmitted to dromedary camels in the distant past. Both SARS-CoV and SARS-CoV-2 are closely related and originated in bats who most likely serve as reservoir host for these two viruses [6]. In addition to highly pathogenic zoonotic pathogens SARS-CoV, MERS\_CoV and SARS-Cov-2, all belonging to the  $\beta$ -Coronavirus genus, four low pathogenic coronavirus are endemic in humans: HCoV-OC43, HCoV-HKU1, HCoV-NL63 and HCoV-229E.

❖ The ongoing pandemic of a novel strain of Coronavirus, SARS-CoV-2 was discovered in Wuhan, China and has resulted in >19.7Cr infections and >42L deaths [7]. On 31<sup>st</sup> January, 2020 the World Health Organisation (WHO) confirmed this novel Corona virus as a public health emergency of international concern.

## 2. GENOME AND STRUCTURE OF SARS-CoV-2

Coronaviruses are non-segmented, enveloped virus with single stranded positive sense RNA (+ssRNA) with 5'cap structure and 3'-poly-A tail ranging between 26 to 32kb in length. Coronaviruses belong to the family of Coronaviridae, of the sub family Coronavirinae, order Nidovirales, which include four genera: Alpha Coronavirus, Beta Coronavirus, Gamma Coronavirus and Delta Coronavirus (Fig. 1). Coronaviruses are the largest member of RNA viruses with a diameter of 80-160 nm. Phylogenetic analysis of 2019 novel Coronavirus indicates that SARS-CoV-2 shares 79% and 55% genome identity to SARS-CoV and MERS-CoV respectively and belongs to same family of virus as SARS and MERS [8].

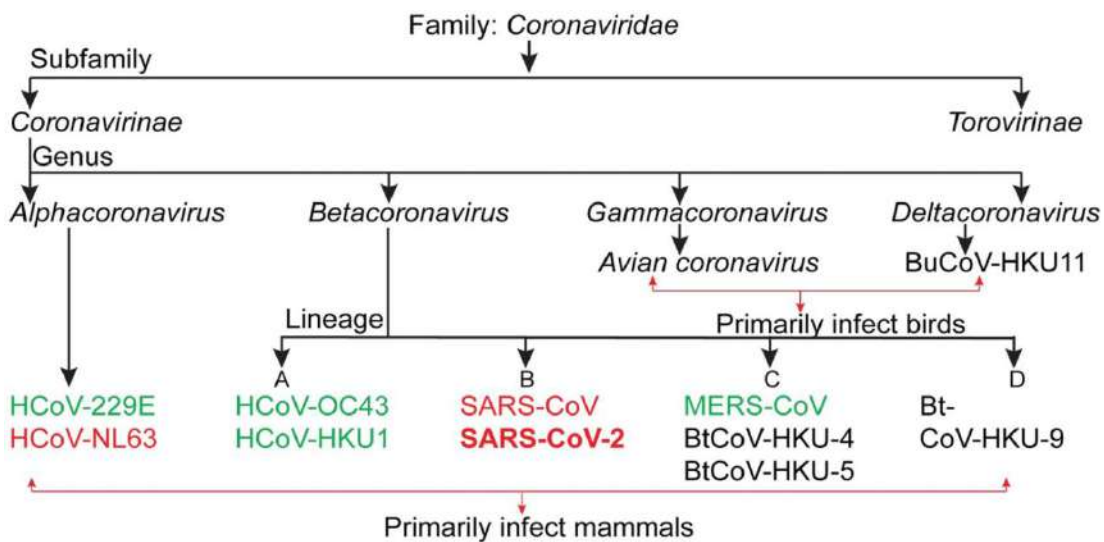


Fig. 1. Classification of coronaviruses; the 7 known HCoVs are shown in green and red.

- ❖ The observed morphology of SARS-CoV-2 is consistent with the other members of Coronaviridae family. It has a core of tightly packed RNA and is surrounded by an envelope of proteins, glycoproteins and lipids. SARS-CoV-2 comprises of approximately 30,000 bp-long RNA.
- ❖ Structurally, SARS-CoV-2 has four main structural proteins: Spike (S)-Glycoprotein, Envelope (E)-Protein, Membrane (M)-Glycoprotein and Nucleocapsid (N)-Protein and other accessory proteins (Fig. 2). The genome is arranged in the order of a non-coding 5'-UTR-replicase gene (ORF1ab)- structural proteins and accessory proteins- non-coding 3'-UTR. Hemagglutinin-esterase gene, a common feature of lineage Betacoronavirus, is absent in SARS-CoV-2.

- ❖ The E-protein is the smallest of all structural proteins found in the viral membrane and localises to the endoplasmic reticulum and Golgi complex in the host cell and is known to facilitate virus like particle formation. It helps in production and maturation of this virus [9].
- ❖ The M-glycoprotein is a transmembrane protein that helps in determining the shape of the virus envelope. It is the most abundant structural protein in a virion (ineffective virus) and can bind to all other structural proteins [10].
- ❖ N-proteins gets stabilised by binding with M-glycoproteins and viral assembly is completed. The N-protein is responsible for packaging of the viral genome RNA into a helical ribonucleocapsid (RNP). It is the structural component of CoV in the endoplasmic reticulum-Golgi region [11].
- ❖ The S-glycoprotein is a transmembrane protein (Fig. 3) that mediates the entry of Coronavirus into the host cells. Its molecular weight is about 150kDa and is found in the outer portion of the virus. S-proteins form homotrimers protruding from the viral surface. It has two functional subunits: S1 subunit and S2 subunit. S1 subunit is responsible for binding to the host cell receptor and S2 subunit functions to mediate virus fusion in transmitting host cells (Fig. 4). S-protein facilitates binding of envelope viruses to host cells by attraction with Angiotensin-Converting Enzyme 2 (ACE2), expressed in lower respiratory tract cells [12].

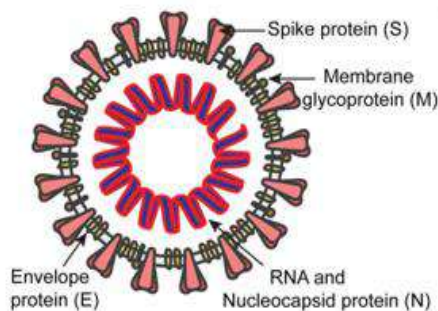


Fig. 2. Schematic of SARS-CoV-2 structure.

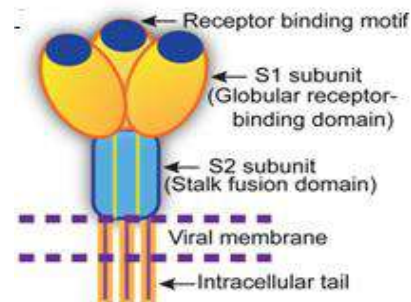


Fig. 3. Cartoon depicts key features and the trimeric structure of the SARS-CoV-2 S-protein.

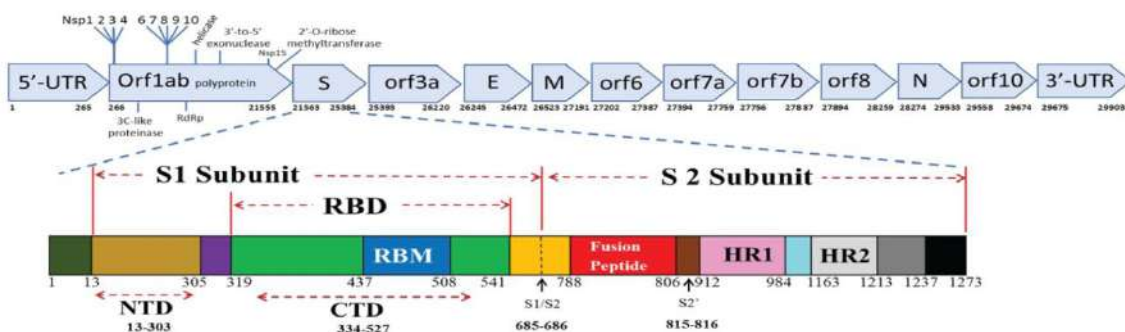
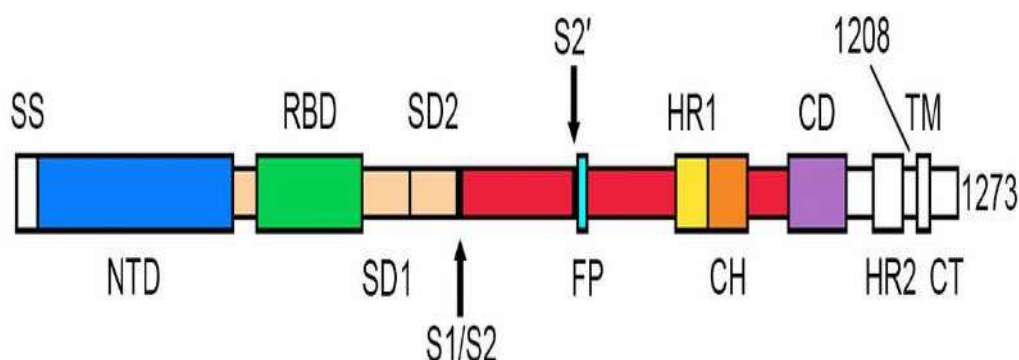


Fig. 4. Schematic of SARS-CoV-2 genome (top) and S-protein (bottom).

### 3. STRUCTURE OF SARS-CoV-2 S-GLYCOPROTEIN

The SARS-CoV-2 S-glycoprotein plays important roles in viral infection and pathogenesis. The mature S-glycoprotein on the surface of the virus is a heavily glycosylated trimer. Each protomer of this consists of 1260 amino acids residues. The surface subunit S1 is composed of 672 amino acids residues and arranged into four domains which are: an N-terminal domain (NTD), a C-terminal domain (CTD) which is also known as the receptor-binding domain, and two subdomains, SD1 and SD2 [13]. The transmembrane S2 subunit is composed of 588 amino acids residues and contains an N-terminal hydrophobic fusion peptide (FP), two heptad repeats (HR1 and HR2), a transmembrane domain (TM), and a cytoplasmic tail (CT), arranged as FP-HR1-HR2-TM-CT (Fig. 5) [13]. The distal S1 subunit contains the receptor-binding domain(s) and support the prefusion state of the membrane-anchored S2 subunit that contains the fusion machinery [6].

The SARS-CoV-2 S glycoprotein is a part of the typical class I viral fusion protein, it therefore shares some common structural and mechanistic features with other class I viral fusion proteins. Like other class I viral fusion proteins, the SARS-CoV-2 S glycoprotein is also a conformational machine which mediates viral entry by switching from a metastable unliganded state, through a prehairpin intermediate state, to a stable postfusion state. Determination of the SARS-CoV-2 S glycoprotein trimer fragments have been done in both the prefusion and postfusion states (Fig. 6) [14,15,16].



(Fig. 5. Overall structure of the SARS-CoV-2 S glycoprotein trimer in different conformations: Schematic representation of the domain arrangement of the SARS-CoV-2 S-protein precursor.

NTD: N-terminal domain; RBD: receptor-binding domain; RBM: receptor-binding motif; SD1/2: Sub domain 1/2; FP: Fusion peptide; HR1/2: Heptad repeat 1/2; CH: Central Helix; CD: Connector

domain; TM: Transmembrane domain; CT: Cytoplasmic Tail; Arrows denote proteases cleavage sites.)

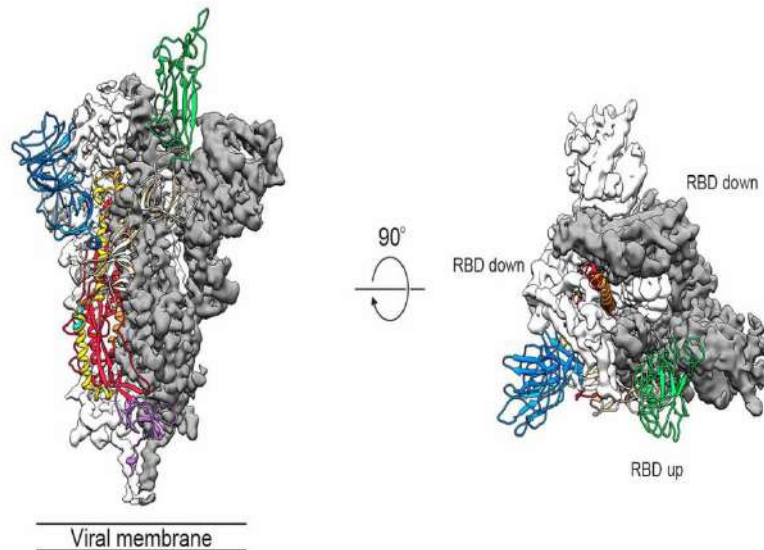


Fig. 6. Side and top views of the prefusion structure of the SARS-CoV-2 S ectodomain trimer with two RBDs in the down conformation and one RBD assumes the up conformation.

The life cycle (Fig. 7) of SARS-CoV-2 begins with membrane fusion occurring at the plasma membrane or within acidified endosomes after endocytosis, which is mediated by conformational changes in the S-glycoprotein triggered by angiotensin-converting enzyme 2 (ACE2) binding. Following viral entry, SARS-CoV-2 releases its genomic RNA into the host cell cytoplasm. Genome RNA is first translated into viral replicase polyproteins (pp1a and 1ab), which are further cleaved by viral proteases into a total of 16 nonstructural proteins. A replication-transcription complex (RTC) is formed based on many of these nonstructural proteins. In the process of genome replication and transcription mediated by RTC, the negative-sense (- sense) genomic RNA is synthesized and used as a template to produce positive-sense (+ sense) genomic RNA and subgenomic RNAs. The nucleocapsid (N) structural protein and viral RNA are replicated, transcribed, and synthesized in the cytoplasm, whereas other viral structural proteins, including the S protein, membrane (M) protein and envelope (E) protein, are transcribed and then translated in the rough endoplasmic reticulum (RER) and transported to the Golgi complex. In the RER and Golgi complex, the SARS-CoV-2 glycoprotein is subjected to co-translational and post-translational processing, including signal peptide removal, trimerization, extensive glycosylation and subunit cleavage. The N protein is subsequently associated with the positive sense genomic RNA to become a nucleoprotein complex (nucleocapsid), which together with S, M, and E proteins as well as other viral proteins, is further assembled and



followed by budding into the lumen of the ER-Golgi intermediate compartment (ERGIC) to form mature virions. Finally, the mature virions are released from the host cell, waiting for a new life cycle to start.

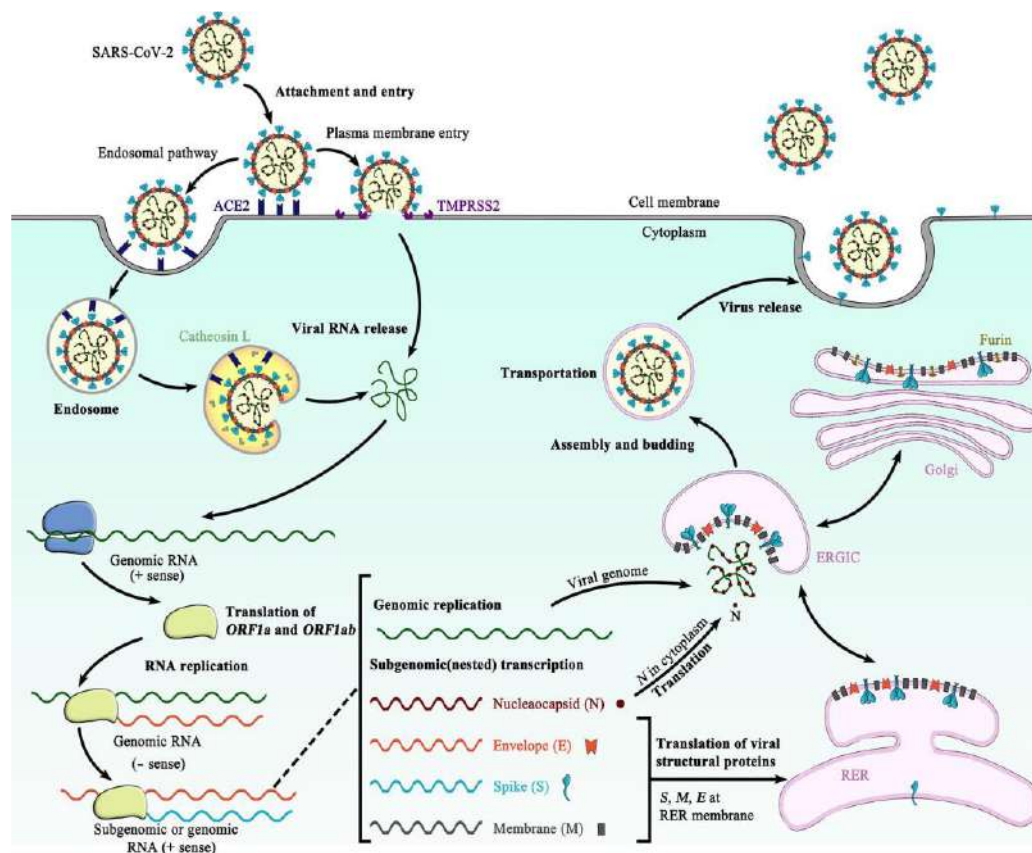


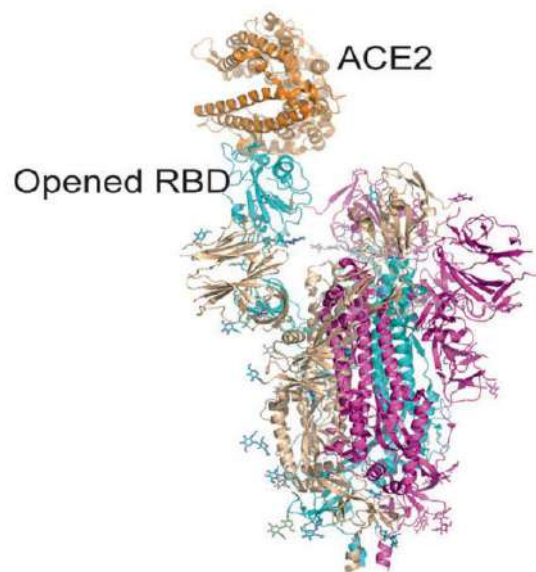
Fig. 7. Schematic representation of the life cycle of SARS-CoV-2.

### 3.1. Structure of the S1 subunit

The virus particles get attached to cell receptors to the surface of the host cell. This is the starting of the infection of virus. Therefore, receptor recognition is important to the entry of virus.

The RBD which is situated in the S1 subunit gets attached to the cell receptor, ACE2, in the region of aminopeptidase N. The S1 region consists of the NTD and CTD, and atomic details at the binding interface. The SARS-CoV-2 S CTD binding interface has more residues that gets to interact directly with the receptor ACE2 than does SARS-RBD, and a larger surface area is buried with SARS CoV-2 S CTD in complex with ACE2 than with SARS S RBD. There are mutations in the key residues which plays an important role in enhancing the interaction with ACE2. F486 in SARS-CoV-2, instead of I472 in SARS RBD, forms strong aromatic–aromatic interactions with ACE2 Y83, and E484 in SARS-CoV-2-CTD, instead of P470 in SARS RBD, forms ionic interactions with K31, which leads to higher affinity for receptor binding than RBD of SARS-CoV (Fig. 8) [17, 18, 19, 20]. The RBD region is a target

for neutralizing antibodies (nAbs), and SARS-CoV-2 and SARS-CoV RBD are ~73%–76% similar in sequence. Nine ACE2-contacting residues in CoV RBD are fully conserved, and four are partially conserved. The analysis of the RBM (receptor-binding motif) of SARS-CoV and SARS-CoV-2 revealed that most residues essential for ACE2 binding in the SARS-CoV S protein are conserved in the SARS-CoV-2 S protein. Studies have shown that there are some differences in antigenicity between SARS-CoV and SARS-CoV-2. It is revealed by the studies on the murine monoclonal antibodies and polyclonal antibodies against SARS-RBD [19].



*Fig. 8. The S protein binds to ACE2 with opened RBD in the S1 subunit.*

### **3.2. Structure of the S2 subunit**

The S2 subunit consists of a FP, HR1, HR2, TM domain, and cytoplasmic domain fusion (CT). It is responsible for viral fusion and entry of the virus. FP is a short section consisting of 15–20 conserved amino acids of the family of virus, such as glycine (G) or alanine (A). It anchors to the target membrane once the S protein adopts the prehairpin conformation. Previously it was shown that FP plays a necessary role in media membrane fusion by disrupting and connecting lipid bilayers of the host plasma membrane [21]. HR1 and HR2 are composed of a repetitive heptapeptide: HPPHCPC, where H is a hydrophobic or large residue, P is a polar or hydrophilic residue, and C is another charged residue [22]. HR1 and HR2 form the six-helical bundle (6-HB). This is essential for the function of the S2 subunit in viral fusion and entry [23]. HR1 is found at the C-terminus of a hydrophobic FP, and HR2 is found at the N-terminus of the TM domain [24]. The downstream TM domain anchors the S protein to the viral membrane, and therefore the S2 subunit ends in a CT tail [25]. RBD binds to ACE2, and S2 changes conformation by inserting FP into the target cell

membrane, exposing the prehairpin coiledcoil of the HR1 domain and triggering interaction between the HR2 domain and HR1 trimer to create 6-HB, thus bringing the viral envelope and cell membrane into proximity for viral fusion and entry. HR1 forms a homotrimeric assembly during which three extremely preserved hydrophobic grooves on the surface that bind to HR2 are exposed. The HR2 domain forms each a rigid helix and a versatile loop to interact with the HR1 domain. In the postfusion hairpin conformation of CoVs, there are many strong interactions between the HR1 and HR2 domains inside the helical region, which is designated the “fusion core region” (HR1core and HR2core regions, respectively). Targeting the heptad repeat (HR) has attracted the greatest interest in therapeutic drug discovery. The S protein is an important target protein for the development of specific drugs, while the S1 RBD domain is part of a highly mutable region and is not an ideal target site for broad-spectrum antiviral inhibitor development [26]. In contrast, the HR region of the S2 subunit plays a necessary role in HCoV infections and is preserved among HCoVs, as is the mode of interaction between HR1 and HR2 [27]. An artificial peptide derived from the stem region of the ZIKV envelope protein was demonstrated in 2017 to powerfully inhibit infection by ZIKV and other flaviviruses in vitro [28], implying antiviral potency of peptides derived from preserved regions of viral proteins. Peptides derived from the HR2 region of class I viral fusion proteins of enveloped viruses competitively bind to viral HR1 and effectively inhibit viral infection. Therefore, HR1 has become a promising target for the development of fusion inhibitors against SARS-CoV-2 infection [29].

#### **4. FUNCTION OF THE SARS-CoV-2 S-GLYCOPROTEIN**

The S protein on the surface of the virus may be a key issue which is involved in infection. It is a trimeric class I TM glycoprotein which causes the entry of the virus, and it is present in all kinds of HCoVs, as well as in other viruses [30]. Similar to other coronaviruses, the S protein of SARS-CoV-2 mediates receptor recognition, cell attachment, and fusion throughout the viral infection [18, 19, 20, 31, 32,33]. The basic unit by which the S protein binds to the receptor is the trimer of the S protein which is located on the surface of the viral envelope [18, 33]. The S1 domain containing the RBD is primarily responsible for the attachment of the virus to the receptor, while the S2 domain mainly contains the HR domain, that is HR1 and HR2, which is associated to virus fusion [29, 34].

#### 4.1. Receptor binding

The SARS-CoV-2 S protein gets attached to the host cell by recognizing the receptor ACE2 (Angiotensin Converting Enzyme 2) [33]. ACE2 converts angiotensin I to angiotensin [35]. ACE2 is distributed primarily in the lungs, intestine, heart, and kidney, and alveolar epithelial type II cells [36]. ACE2 is additionally an identified receptor for SARS-CoV. The S1 subunit of the SARS-CoV S protein binds with ACE2 to promote the formation of endosomes, which triggers viral fusion activity underneath Hydrogen ion concentration (Fig. 9a,b) [37]. Since ACE2 from different species, such as amphibians, birds, and mammals, has a preserved primary structure, the interaction between the S protein and ACE2 may be used to identify intermediate hosts of SARS-CoV-2 [38]. The S protein gets attached to ACE2 through the RBD region of the S1 subunit, mediating viral attachment to host cells in the form of a trimer [17]. The dissociation constant ( $K_D$ ) of attachment of SARS-CoV-2 S protein to human ACE2 is 14.7 nM which is less than that of SARS-CoV for which the  $K_D$  is 325.8 nM. This indicates that SARS-CoV-2 S is much more sensitive to ACE2 than that of SARS-CoV S. An approximate 24% difference is found in S-protein between SARS-CoV-2 and SARS-CoV whereas that of RBD is 23% [39].

#### 4.2. Viral fusion

The fusion of the viral membrane and host cell membrane is referred to as Viral Fusion (Fig. 9 a,b). This results in the discharge of the viral genome into the host cell. Cleavage of the SARS-CoV-2 S1 and S2 subunits is the basis of fusion. The S protein is cleaved in 2 components which are the S1 subunit and S2 subunit, by the host proteases. The subunits, S1 and S2 exist in a non-covalent form till viral fusion occurs [40]. It is discovered that the precise furin cleavage site is at the cleavage site of SARS-CoV-2 but not in other SARS like CoVs [41, 42]. The S protein of SARS-CoV-2 exists in an uncleaved state. This is discovered from the mutation of the cleavage site in SARS-CoV-2. The others are primarily in a cleaved state. Multiple furin cleavage sites are present in SARS-CoV-2 and therefore the probability of being cleaved by furin like proteases increases and thereby enhances its infectivity [43, 44]. Host cell proteases, such as TMPRSS2, are essential for S protein priming, and they have been shown to be activated in the entry of SARS-CoV and influenza A virus [47, 48]. Another host cell protease that has been proven to cleave viral S protein is trypsin [49].

Therefore we can conclude that the S protein of SARS-CoV-2 is similar to that of SARS-CoV, and host cell proteases are required for promoting S protein cleavage of both SARS-

CoV-2 and SARS-CoV. The presence of a selected furin cleavage site on SARS-CoV-2 S might be one reason that SARS-CoV-2 is more contagious than SARS-CoV. The formation of 6-HB is essential for viral fusion. The FP within the N-terminus of SARS-CoV-2 and the two HR domains on S2 is essential for viral fusion [50]. After cleavage of the S protein, the FP of SARS-CoV-2 is exposed and triggers viral fusion. Under the action of some special ligands, the fusion protein undergoes a conformational change and then inserts into the host cell membrane (Fig. 9c) [51]. The distance between the viral membrane and host cell membrane is shortened, and the HR1 domain of the S protein is in close proximity to the host cell membrane, whereas the HR2 domain is closer to the viral membrane side. Then, HR2 folds back to HR1, the two HR domains form a six-helix structure in an antiparallel format of the fusion core, the viral membrane is pulled toward the host cell membrane and tightly binds to it, and the two membranes fuse [52].

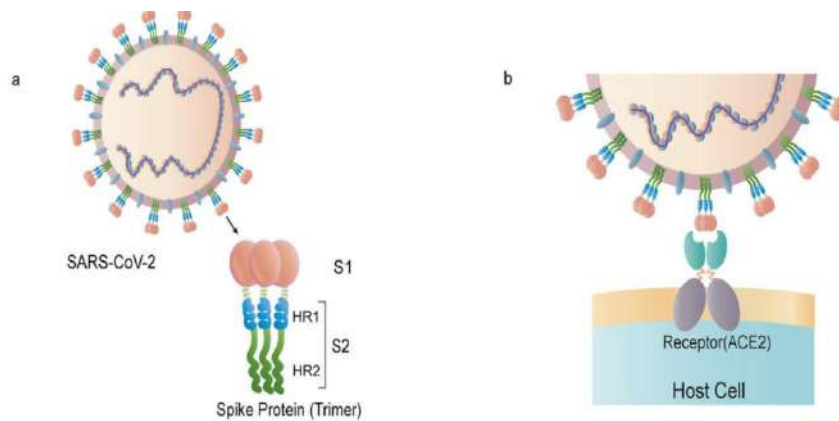


Fig. 9a. The schematic structure of the S protein. Fig. 9b. The S protein binds to the receptor ACE2.

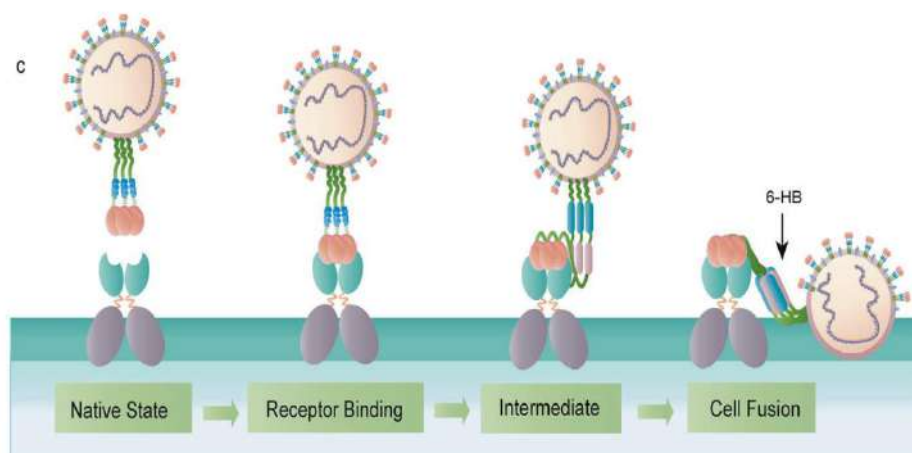


Fig. 9c. The binding and virus-cell fusion process mediated by the S protein.

## **5. POST TRANSLATIONAL MODIFICATIONS OF S-GLYCOPROTEIN**

Numerous CoV proteins undergo post translational modifications (PTMs) which include glycosylation and palmitoylation of the E and S-glycoprotein. More specifically, glycosylation at Asn residues (N linked) or hydroxyl group of Ser and Thr (O-linked) of the M-protein, ADP-ribosylation of N-protein and other PTMs on NSPs and accessory protein have been observed in CoVs. In addition, incorporation of disulfide bonds in S-glycoprotein and conserved cysteine residues into its cytosolic domain have been reported with palmitoylation.

### **5.1. N-linked glycosylation**

The N-linked glycosylation in S-glycoprotein of CoVs was first reported for mouse hepatitis virus. S-glycoprotein of SARS-CoV-2 has exhibits oligosaccharides containing high mannose and trimers within 30 min after the entry into endoplasmic reticulum, former to the acquirement of multifaceted glycans present in Golgi apparatus. Monitoring of SARS-CoV S-glycoprotein susceptibility to endoglycosidase H (endo H), shows its maturation status. Using molecular cloning techniques, the S glycoprotein coding sequences of various CoVs were cloned, following determination of N-linked glycosylation sites. However, all the putative glycosylation sites were not functional. In SARS-CoV S-glycoprotein, 12 sites were found glycosylated out of the 23 putative sites [53]. N-linked glycosylation is associated with protein conformation, and hence intensely affects the antigenicity of S-glycoprotein and receptor binding. Similarly, S-glycoprotein of SARS-CoV-2 has been found to exhibit 22 N-linked glycan structure detected using mass spectrometry which showed complex and hybrid glycans likely to play an important role in protein folding and immune evasion.

### **5.2. Palmitoylation**

Palmitoylation is a process of the covalent attachment of fatty acids like palmitic acid, to cysteine etc. Four cysteine rich clusters are present in the cytoplasmic ends of SARSCoV S-glycoprotein. Mutational study revealed palmitoylation of cysteine clusters I and II. Even though the cellular expression of SARS-CoV S-glycoprotein was unaffected considerably by cysteine clusters I and II mutations, S mediated fusion of cells was clearly reduced as compared with the wild type protein. This suggests the requirement of palmitoylation in the endodomain for the SARS-CoV S-glycoprotein fusogenic activity [53] [54].

## 6. CONCLUSION

Seventeen years after the short outbreak of the severe acute respiratory syndrome (SARS) in 2003, another coronavirus-related epidemic disease, coronavirus disease 2019 (COVID-19) has now spread globally and has jeopardized the lives of almost everyone on this planet. SARS coronavirus (SARS-CoV) and SARS-CoV-2 are the etiological agents of SARS and COVID-19, respectively.

SARS-CoV-2 shows many similarities with SARS-CoV on sequence alignment, structural, and antigen basis. The SARS-CoV and SARS-CoV-2 particles are roughly spherical with a diameter of 80–120 nm. Protruding spikes decorate the surface of the viral particles. These spikes are glycoprotein in nature and are termed as S-glycoprotein. S-glycoprotein plays essential roles in host-pathogen interaction, such as, in mediating the entry of the virus into host cells through binding with human Angiotensin-converting enzyme 2 (hACE2) as a functional receptor, a main target for neutralization antibody, immunological functions etc.

All coronaviruses display lectin like spike glycoproteins on their surface. *O*-acetylated sialic acid binding by the S1 spike protein subunits is crucial for coronavirus to engage host cells, while the S2 domain initiates viral fusion. Enhanced binding affinity between SARS-CoV-2 S-glycoprotein and hACE2 was proposed to correlate with increased virus transmissibility and disease severity in humans.

The complete chemical structure of the S-glycoprotein is still unknown especially for the glycan part. However, it is clear that the S-glycoprotein play the most crucial role in viral infection and propagation. More research findings will help to understand the function and role of the S-glycoprotein.

Till today, there is no effective drug to cure coronavirus infection. Several vaccines have been developed on emergency basic with varied efficacy against different mutant stains of covid-19. More efficient SARS-CoV-2 vaccines are therefore crucial to reduce the severity and transmission of the disease. In the quest for better vaccine, vaccine development targeting the cell surface S-glycoprotein is being investigated.

Spike glycoprotein is now known to bind with *O*-acetylated sialic acids. Based on this observation, research is being conducted to develop simple COVID-19 diagnostic kit instead of complicated RNA based detection process. Currently S-glycoprotein is one of the most vital targets for the development of vaccine and therapeutics for COVID-19.

## 7. REFERENCES

1. "Glycoprotein - Wikipedia". 2021. *En.Wikipedia.Org*. <https://en.wikipedia.org/wiki/Glycoprotein>.
2. Nelson, David L, Michael M Cox, Aaron A Hoskins, and Albert L Lehninger. n.d. *Lehninger Principles Of Biochemistry*.
3. Voet, Donald, Judith G Voet, and Charlotte W Pratt. 2016. *Fundamentals Of Biochemistry*. New York: Wiley.
4. "What Glycoproteins Are And What They Do". 2021. *Thoughtco*. <https://www.thoughtco.com/glycoprotein-definition-and-function-4134331>.
5. <https://www.ncbi.nlm.nih.gov/pmc/articles/PMC3822280/>.
6. Walls, Alexandra C., Young-Jun Park, M. Alejandra Tortorici, Abigail Wall, Andrew T. McGuire, and David Veessler. 2020. "Structure, Function, And Antigenicity Of The SARS-Cov-2 Spike Glycoprotein". *Cell* 181 (2): 281-292.e6. doi:10.1016/j.cell.2020.02.058.
7. "COVID Live Update: From The Coronavirus - Worldometer". 2021. *Worldometers*. [https://www.worldometers.info/coronavirus/?utm\\_campaign=homeAdvegas1?%22](https://www.worldometers.info/coronavirus/?utm_campaign=homeAdvegas1?%22).
8. Kim, Cheorl-Ho. 2020. "SARS-Cov-2 Evolutionary Adaptation Toward Host Entry And Recognition Of Receptor O-Acetyl Sialylation In Virus-Host Interaction". *International Journal Of Molecular Sciences* 21 (12): 4549. doi:10.3390/ijms21124549.
9. Venkatagopalan, Pavithra, Sasha M. Daskalova, Lisa A. Lopez, Kelly A. Dolezal, and Brenda G. Hogue. 2015. "Coronavirus Envelope (E) Protein Remains At The Site Of Assembly". *Virology* 478: 75-85. doi:10.1016/j.virol.2015.02.005.
10. Nakauchi, Mina, Hiroaki Kariwa, Yasuhiro Kon, Kentaro Yoshii, Akihiko Maeda, and Ikuo Takashima. 2008. "Analysis Of Severe Acute Respiratory Syndrome Coronavirus Structural Proteins In Virus-Like Particle Assembly". *Microbiology And Immunology* 52 (12): 625-630. doi:10.1111/j.1348-0421.2008.00079.x.
11. Wu, Chia-Hsin, Shiou-Hwei Yeh, Yeou-Guang Tsay, Ya-Hsiung Shieh, Chuan-Liang Kao, Yen-Shun Chen, Sheng-Han Wang, Ti-Jung Kuo, Ding-Shinn Chen, and Pei-Jer Chen. 2009. "Glycogen Synthase Kinase-3 Regulates The Phosphorylation Of Severe Acute Respiratory Syndrome Coronavirus Nucleocapsid Protein And Viral Replication". *Journal Of Biological Chemistry* 284 (8): 5229-5239. doi:10.1074/jbc.m805747200.



12. Simmons, Graham, Pawel Zmora, Stefanie Gierer, Adeline Heurich, and Stefan Pöhlmann. 2013. "Proteolytic Activation Of The SARS-Coronavirus Spike Protein: Cutting Enzymes At The Cutting Edge Of Antiviral Research". *Antiviral Research* 100 (3): 605-614. doi:10.1016/j.antiviral.2013.09.028.
13. Wrapp, Daniel, Nianshuang Wang, Kizzmekia S. Corbett, Jory A. Goldsmith, Ching-Lin Hsieh, Olubukola Abiona, Barney S. Graham, and Jason S. McLellan. 2020. "Cryo-EM Structure Of The 2019-Ncov Spike In The Prefusion Conformation". *Science* 367 (6483): 1260-1263. doi:10.1126/science.abb2507.
14. Wrapp, Daniel, Nianshuang Wang, Kizzmekia S. Corbett, Jory A. Goldsmith, Ching-Lin Hsieh, Olubukola Abiona, Barney S. Graham, and Jason S. McLellan. 2020. "Cryo-EM Structure Of The 2019-Ncov Spike In The Prefusion Conformation". *Science* 367 (6483): 1260-1263. doi:10.1126/science.abb2507.
15. Harrison, Stephen C. 2008. "Viral Membrane Fusion". *Nature Structural & Molecular Biology* 15 (7): 690-698. doi:10.1038/nsmb.1456.
16. Duan, Liangwei, Qianqian Zheng, Hongxia Zhang, Yuna Niu, Yunwei Lou, and Hui Wang. 2020. "The SARS-Cov-2 Spike Glycoprotein Biosynthesis, Structure, Function, And Antigenicity: Implications For The Design Of Spike-Based Vaccine Immunogens". *Frontiers In Immunology* 11. doi:10.3389/fimmu.2020.576622.
17. Wrapp, Daniel, Nianshuang Wang, Kizzmekia S. Corbett, Jory A. Goldsmith, Ching-Lin Hsieh, Olubukola Abiona, Barney S. Graham, and Jason S. McLellan. 2020. "Cryo-EM Structure Of The 2019-Ncov Spike In The Prefusion Conformation". *Science* 367 (6483): 1260-1263. doi:10.1126/science.abb2507.
18. Walls, Alexandra C., Young-Jun Park, M. Alejandra Tortorici, Abigail Wall, Andrew T. McGuire, and David Veasley. 2020. "Structure, Function, And Antigenicity Of The SARS-Cov-2 Spike Glycoprotein". *Cell* 183 (6): 1735. doi:10.1016/j.cell.2020.11.032.
19. Wang, Qihui, Yanfang Zhang, Lili Wu, Sheng Niu, Chunli Song, Zengyuan Zhang, and Guangwen Lu et al. 2020. "Structural And Functional Basis Of SARS-Cov-2 Entry By Using Human ACE2". *Cell* 181 (4): 894-904.e9. doi:10.1016/j.cell.2020.03.045.
20. Lan, Jun, Jiwan Ge, Jinfang Yu, Sisi Shan, Huan Zhou, Shilong Fan, and Qi Zhang et al. 2020. "Structure Of The SARS-Cov-2 Spike Receptor-Binding Domain Bound To The ACE2 Receptor". *Nature* 581 (7807): 215-220. doi:10.1038/s41586-020-2180-5.
21. Millet, Jean Kaoru, and Gary R. Whittaker. 2018. "Physiological And Molecular Triggers For SARS-Cov Membrane Fusion And Entry Into Host Cells". *Virology* 517: 3-8. doi:10.1016/j.virol.2017.12.015.
22. Chambers, P., C. R. Pringle, and A. J. Easton. 1990. "Heptad Repeat Sequences Are Located Adjacent To Hydrophobic Regions In Several Types Of Virus Fusion

- Glycoproteins". *Journal Of General Virology* 71 (12): 3075-3080. doi:10.1099/0022-1317-71-12-3075.
23. Xia, Shuai, Yun Zhu, Meiqin Liu, Qiaoshuai Lan, Wei Xu, Yanling Wu, and Tianlei Ying et al. 2020. "Fusion Mechanism Of 2019-Ncov And Fusion Inhibitors Targeting HR1 Domain In Spike Protein". *Cellular & Molecular Immunology* 17 (7): 765-767. doi:10.1038/s41423-020-0374-2.
  24. Robson, B. 2020. "Computers And Viral Diseases. Preliminary Bioinformatics Studies On The Design Of A Synthetic Vaccine And A Preventative Peptidomimetic Antagonist Against The SARS-Cov-2 (2019-Ncov, COVID-19) Coronavirus". *Computers In Biology And Medicine* 119: 103670. doi:10.1016/j.compbiomed.2020.103670.
  25. Tang, Tiffany, Miya Bidon, Javier A. Jaimes, Gary R. Whittaker, and Susan Daniel. 2020. "Coronavirus Membrane Fusion Mechanism Offers A Potential Target For Antiviral Development". *Antiviral Research* 178: 104792. doi:10.1016/j.antiviral.2020.104792.
  26. Lu, Guangwen, Qihui Wang, and George F. Gao. 2015. "Bat-To-Human: Spike Features Determining 'Host Jump' Of Coronaviruses SARS-Cov, MERS-Cov, And Beyond". *Trends In Microbiology* 23 (8): 468-478. doi:10.1016/j.tim.2015.06.003.
  27. Liu, Shuwen, Gengfu Xiao, Yibang Chen, Yuxian He, Jinkui Niu, Carlos R Escalante, and Huabao Xiong et al. 2004. "Interaction Between Heptad Repeat 1 And 2 Regions In Spike Protein Of SARS-Associated Coronavirus: Implications For Virus Fusogenic Mechanism And Identification Of Fusion Inhibitors". *The Lancet* 363 (9413): 938-947. doi:10.1016/s0140-6736(04)15788-7.
  28. Yu, Yufeng, Yong-Qiang Deng, Peng Zou, Qian Wang, Yanyan Dai, Fei Yu, and Lanying Du et al. 2017. "A Peptide-Based Viral Inactivator Inhibits Zika Virus Infection In Pregnant Mice And Fetuses". *Nature Communications* 8 (1). doi:10.1038/ncomms15672.
  29. Huang, Yuan, Chan Yang, Xin-feng Xu, Wei Xu, and Shu-wen Liu. 2020. "Structural And Functional Properties Of SARS-Cov-2 Spike Protein: Potential Antivirus Drug Development For COVID-19". *Acta Pharmacologica Sinica* 41 (9): 1141-1149. doi:10.1038/s41401-020-0485-4.
  30. Weissenhorn,, W., A. Dessen, L. J. Calder, S. C. Harrison, J. J. Skehel, and D. C. Wiley. 1999. "Structural Basis For Membrane Fusion By Enveloped Viruses". *Molecular Membrane Biology* 16 (1): 3-9. doi:10.1080/096876899294706.
  31. Gui, Miao, Wenfei Song, Haixia Zhou, Jingwei Xu, Silian Chen, Ye Xiang, and Xinquan Wang. 2016. "Cryo-Electron Microscopy Structures Of The SARS-Cov Spike Glycoprotein Reveal A Prerequisite Conformational State For Receptor Binding". *Cell Research* 27 (1): 119-129. doi:10.1038/cr.2016.152.

32. Bosch, Berend Jan, Ruurd van der Zee, Cornelis A. M. de Haan, and Peter J. M. Rottier. 2003. "The Coronavirus Spike Protein Is A Class I Virus Fusion Protein: Structural And Functional Characterization Of The Fusion Core Complex". *Journal Of Virology* 77 (16): 8801-8811. doi:10.1128/jvi.77.16.8801-8811.2003.
33. Yan, Renhong, Yuanyuan Zhang, Yanning Li, Lu Xia, Yingying Guo, and Qiang Zhou. 2020. "Structural Basis For The Recognition Of SARS-Cov-2 By Full-Length Human ACE2". *Science* 367 (6485): 1444-1448. doi:10.1126/science.abb2762.
34. Cui, Jie, Fang Li, and Zheng-Li Shi. 2018. "Origin And Evolution Of Pathogenic Coronaviruses". *Nature Reviews Microbiology* 17 (3): 181-192. doi:10.1038/s41579-018-0118-9.
35. Donoghue, Mary, Frank Hsieh, Elizabeth Baronas, Kevin Godbout, Michael Gosselin, Nancy Stagliano, and Michael Donovan et al. 2000. "A Novel Angiotensin-Converting Enzyme-Related Carboxypeptidase (ACE2) Converts Angiotensin I To Angiotensin 1-9". *Circulation Research* 87 (5). doi:10.1161/01.res.87.5.e1.
36. Zhang, Haibo, Josef M. Penninger, Yimin Li, Nanshan Zhong, and Arthur S. Slutsky. 2020. "Angiotensin-Converting Enzyme 2 (ACE2) As A SARS-Cov-2 Receptor: Molecular Mechanisms And Potential Therapeutic Target". *Intensive Care Medicine* 46 (4): 586-590. doi:10.1007/s00134-020-05985-9.
37. Shang, Jian, Yushun Wan, Chuming Luo, Gang Ye, Qibin Geng, Ashley Auerbach, and Fang Li. 2020. "Cell Entry Mechanisms Of SARS-Cov-2". *Proceedings Of The National Academy Of Sciences* 117 (21): 11727-11734. doi:10.1073/pnas.2003138117.
38. Chen, Yun, Yao Guo, Yihang Pan, and Zhizhuang Joe Zhao. 2020. "Structure Analysis Of The Receptor Binding Of 2019-Ncov". *Biochemical And Biophysical Research Communications* 525 (1): 135-140. doi:10.1016/j.bbrc.2020.02.071.
39. Wan, Yushun, Jian Shang, Rachel Graham, Ralph S. Baric, and Fang Li. 2020. "Receptor Recognition By The Novel Coronavirus From Wuhan: An Analysis Based On Decade-Long Structural Studies Of SARS Coronavirus". *Journal Of Virology* 94 (7). doi:10.1128/jvi.00127-20.
40. Tortorici, M. Alejandra, Alexandra C. Walls, Yifei Lang, Chunyan Wang, Zeshi Li, Danielle Koerhuis, and Geert-Jan Boons et al. 2019. "Structural Basis For Human Coronavirus Attachment To Sialic Acid Receptors". *Nature Structural & Molecular Biology* 26 (6): 481-489. doi:10.1038/s41594-019-0233-y.
41. Coutard, B., C. Valle, X. de Lamballerie, B. Canard, N.G. Seidah, and E. Decroly. 2020. "The Spike Glycoprotein Of The New Coronavirus 2019-Ncov Contains A Furin-Like Cleavage Site Absent In Cov Of The Same Clade". *Antiviral Research* 176: 104742. doi:10.1016/j.antiviral.2020.104742.

42. Al-Tawfiq, Jaffar A. 2020. "Viral Loads Of SARS-Cov, MERS-Cov And SARS-Cov-2 In Respiratory Specimens: What Have We Learned?". *Travel Medicine And Infectious Disease* 34: 101629. doi:10.1016/j.tmaid.2020.101629.
43. Hasan, Anwarul, Bilal Ahamad Paray, Arif Hussain, Fikry Ali Qadir, Farnoosh Attar, Falah Mohammad Aziz, and Majid Sharifi et al. 2020. "A Review On The Cleavage Priming Of The Spike Protein On Coronavirus By Angiotensin-Converting Enzyme-2 And Furin". *Journal Of Biomolecular Structure And Dynamics* 39 (8): 3025-3033. doi:10.1080/07391102.2020.1754293.
44. Millet, Jean Kaoru, and Gary R. Whittaker. 2015. "Host Cell Proteases: Critical Determinants of Coronavirus Tropism And Pathogenesis". *Virus Research* 202: 120-134. doi:10.1016/j.virusres.2014.11.021.
45. Claas, Eric CJ, Albert DME Osterhaus, Ruud van Beek, Jan C De Jong, Guus F Rimmelzwaan, Dennis A Senne, Scott Krauss, Kennedy F Shortridge, and Robert G Webster. 1998. "Human Influenza A H5N1 Virus Related To A Highly Pathogenic Avian Influenza Virus". *The Lancet* 351 (9101): 472-477. doi:10.1016/s0140-6736(97)11212-0.
46. Kido, Hiroshi, Yuushi Okumura, Etsuhisa Takahashi, Hai-Yan Pan, Siye Wang, Dengbing Yao, Min Yao, Junji Chida, and Mihiro Yano. 2012. "Role Of Host Cellular Proteases In The Pathogenesis Of Influenza And Influenza-Induced Multiple Organ Failure". *Biochimica Et Biophysica Acta (BBA) - Proteins And Proteomics* 1824 (1): 186-194. doi:10.1016/j.bbapap.2011.07.001.
47. Heurich, A., H. Hofmann-Winkler, S. Gierer, T. Liepold, O. Jahn, and S. Pohlmann. 2013. "TMPRSS2 And ADAM17 Cleave ACE2 Differentially And Only Proteolysis By TMPRSS2 Augments Entry Driven By The Severe Acute Respiratory Syndrome Coronavirus Spike Protein". *Journal Of Virology* 88 (2): 1293-1307. doi:10.1128/jvi.02202-13.
48. Limburg, Hannah, Anne Harbig, Dorothea Bestle, David A. Stein, Hong M. Moulton, Julia Jaeger, and Harshavardhan Janga et al. 2019. "TMPRSS2 Is The Major Activating Protease Of Influenza A Virus In Primary Human Airway Cells And Influenza B Virus In Human Type II Pneumocytes". *Journal Of Virology* 93 (21). doi:10.1128/jvi.00649-19.
49. Ou, Xiuyuan, Yan Liu, Xiaobo Lei, Pei Li, Dan Mi, Lili Ren, and Li Guo et al. 2020. "Characterization Of Spike Glycoprotein Of SARS-Cov-2 On Virus Entry And Its Immune Cross-Reactivity With SARS-Cov". *Nature Communications* 11 (1). doi:10.1038/s41467-020-15562-9.
50. Kawase, Miyuki, Michiyo Kataoka, Kazuya Shirato, and Shutoku Matsuyama. 2019. "Biochemical Analysis Of Coronavirus Spike Glycoprotein Conformational

- Intermediates During Membrane Fusion". *Journal Of Virology* 93 (19). doi:10.1128/jvi.00785-19.
51. Harrison, Stephen C. 2015. "Viral Membrane Fusion". *Virology* 479-480: 498-507. doi:10.1016/j.virol.2015.03.043.
  52. Eckert, Debra M., and Peter S. Kim. 2001. "Mechanisms Of Viral Membrane Fusion And Its Inhibition". *Annual Review Of Biochemistry* 70 (1): 777-810. doi:10.1146/annurev.biochem.70.1.777.
  53. Saxena, Shailendra K., Swatantra Kumar, Preeti Baxi, Nishant Srivastava, Bipin Puri, and R. K. Ratho. 2020. "Chasing COVID-19 Through SARS-Cov-2 Spike Glycoprotein". *Virusdisease* 31 (4): 399-407. doi:10.1007/s13337-020-00642-7.
  54. Krokhin, Oleg, Yan Li, Anton Andonov, Heinz Feldmann, Ramon Flick, Steven Jones, and Ute Stroehrer et al. 2003. "Mass Spectrometric Characterization of Proteins From The SARS Virus". *Molecular & Cellular Proteomics* 2 (5): 346-356. doi:10.1074/mcp.m300048-mcp200.